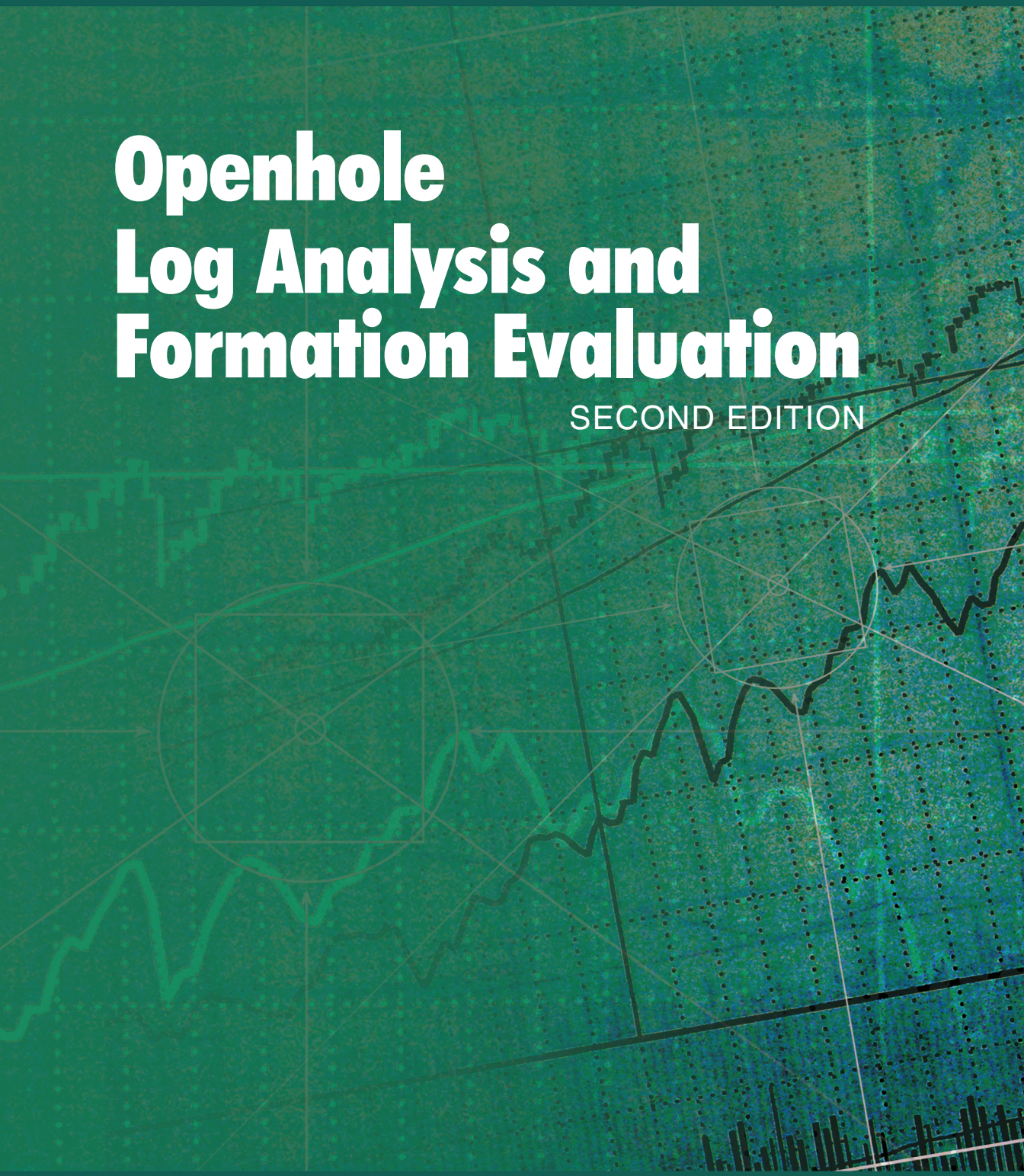
SOCIETY OF PETROLEUM ENGINEERS



Openhole Log Analysis and Formation Evaluation

SECOND EDITION

Richard M. Bateman

Openhole Log Analysis and Formation Evaluation

Openhole Log Analysis and Formation Evaluation

Richard M. Bateman
Faculty Member, Texas Tech University

Second Edition

Society of Petroleum Engineers

© Copyright 2012 Society of Petroleum Engineers

All rights reserved. No portion of this book may be reproduced in any form or by any means, including electronic storage and retrieval systems, except by explicit, prior written permission of the publisher except for brief passages excerpted for review and critical purposes.

Printed in the United States of America.

Disclaimer

This book was prepared by members of the Society of Petroleum Engineers and their well-qualified colleagues from material published in the recognized technical literature and from their own individual experience and expertise. While the material presented is believed to be based on sound technical knowledge, neither the Society of Petroleum Engineers nor any of the authors or editors herein provide a warranty either expressed or implied in its application. Correspondingly, the discussion of materials, methods, or techniques that may be covered by letters patents implies no freedom to use such materials, methods, or techniques without permission through appropriate licensing. Nothing described within this book should be construed to lessen the need to apply sound engineering judgment nor to carefully apply accepted engineering practices in the design, implementation, or application of the techniques described herein.

ISBN 978-1-61399-156-5
ISBN 978-1-61399-269-2 (Digital)

Society of Petroleum Engineers
222 Palisades Creek Drive
Richardson, TX 75080-2040 USA

http://www.spe.org/store
service@spe.org
1.972.952.9393

Preface

Formation evaluation is an extremely broad term and can encompass many different disciplines. Thus, any work that includes the phrase in its title runs a double risk. An attempt to cover all possible methods of data gathering and analysis would appear presumptuous and overly ambitious, and yet the omission of any of the methods would rightly leave the work incomplete. In its broadest sense, formation evaluation can include everything from macroscopic studies of an entire geologic basin down to microscopic studies of individual mineral grains. Central to both extremes are borehole geophysical well logs. In the practical sense, each formation evaluation method leans on its neighbor for support. Seismic interpretation can be refined in the light of logging data, log response can be calibrated by reference to core analysis, flow testing can refine log-based productivity estimates, etc.

It is this interaction between a spectrum of different formation evaluation methods that makes the whole process of evaluating subsurface formations a dynamic and viable science. Thus, although logs and log analysis are central to this work, it should never be thought that logs alone are sufficient to define entirely the properties of a formation.

The student of formation evaluation should therefore be familiar with geology, geophysics, geochemistry, petrophysics, reservoir engineering, drilling technology, computer science, economics, mathematics, and probability theory. Few occupations require such a wide overall familiarity with so many disciplines. Unfortunately, this has led the formation evaluator to be labeled as the jack of all trades and master of none. However, because of an awareness of the interaction between so many disciplines, he or she is in fact a better master of many trades than many of the jacks of individual ones. It is hoped that this work reflects these sentiments by stressing the fruitfulness of combining neighboring sciences to produce a whole that is greater than the sum of its parts.

This book is divided into sections that address a number of formation evaluation themes. *Part I, Methods of Gathering Formation Evaluation Data,* includes Chapters 1 through 5. These chapters address methods of gathering data needed to evaluate a formation. Chapters 6 through 8 comprise *Part II, Methods of Analysis and Application of Results,* and discuss analysis methods in general and the end use of the results of analysis. *Part III, Openhole Logging Measurements* (Chapters 9 through 20), addresses openhole logging measurements; each tool's principle of operation and contribution to the overall evaluation problem is covered. *Part IV, Analysis of Logs and Cores,* includes Chapters 21 through 30. These chapters address more subtle details of log analysis and its integration with core analysis. In *Part V, Formation Testing,* Chapters 31 and 32 cover formation testing. *Part VI, Integrated Formation-Evaluation Plan,* consists of Chapter 33. This final chapter gives an overall "game plan" for the formation evaluator. An appendix to the volume summarizes important log analysis equations.

Since the first publication of this book in 1985, the science and art of formation evaluation has seen many innovations. In particular, measurements of formation resistivity have advanced with the introduction of array tools that allow improved measurement of formation resistivity at a range of distances from the borehole itself. Likewise, advances in the design of sonic tools and in the processing of their recorded signals afford the analyst a better insight into the nature of the rocks surrounding the borehole. Also, new methods of looking at the distribution of pore sizes, their fluid content, and formation flow potential have come into wide use with advances in microcore scanning, nuclear magnetic resonance technology, and wireline formation testing improvements.

Finally, what was previously considered unworthy of consideration is now the item on which many analysts spend the majority of their time, namely shales!

Apart from the tools themselves, and their additions to the petrophysicists arsenal, the mode of data capture, too, has changed. Whereas previously all data was recorded from a wireline logging tool suspended on a cable, today many, if not all, of the conventional wireline measurements can be made from logging while drilling tools run on the end of the drillpipe itself. Thus, this revised and updated edition will prepare the reader for a fuller understanding of modern formation evaluation data gathering methods as well as illuminate advanced analysis techniques afforded by these new and improved sensors.

Acknowledgments

This work is based on many years of practical experience with the vicissitudes of evaluating subsurface formation properties. In the course of compiling materials, I have leaned heavily on friends, coworkers, other authors, oil companies, service companies, and professional societies. Where humanly possible, I have given credit where credit is due. In some cases, it has proved difficult to trace the origin of some figures, and I must thank those who have unknowingly assisted me with such material. I also owe a debt of gratitude to the many students who have attended my courses and provided me with valuable feedback on both the style and content of this work.

I also owe a debt of gratitude to Tarek Ghazi, who volunteered his time for the thankless task of being my go-between with the SPE Books Development Committee. Lastly, this revised edition would have been much the poorer if it had not been for the dedicated industry professionals who reviewed the manuscript and provided invaluable suggestions for its improvement. They included Matt Bratovich, Quinn Passey, Dare Keelan, Jeff Williams, Professor Richard Dawe, and Professor Donald Hill.

My thanks to Jennifer Wegman of the SPE, without whose tireless efforts the publication of this work would have been impossible.

Richard M. Bateman
Canton, North Carolina
April 2012

SPE would like to thank Tarek Ghazi for his generous contributions to the oversight of this book project on behalf of the Books Development Committee. We appreciate his contributions in working with the author and ensuring that timelines and quality standards were upheld throughout the process.

Contents

Preface ..... **v**
Acknowledgments ..... **vii**
Part I—Methods of Gathering Formation Evaluation Data **1**
1. Formation Evaluation Overview **3**
1.1 The Scope of Formation Evaluation 3
1.2 Formation Evaluation 3
1.3 Formation-Evaluation Methods 5
1.4 Mud Logging 6
1.5 Coring 6
1.6 Measurements While Drilling (MWD) 7
1.7 Logging While Drilling (LWD) 7
1.8 Testing 7
1.9 Openhole Logging 7
1.10 Modern Logging Tools 8
1.11 Evolution of Logging Devices 9
1.12 Categorization of Logging Devices 11
1.13 Summary 15
2. Mud Logging **39**
2.1 Measurements Related to the Drilling Process 39
2.2 Measurements Relevant to Formation Evaluation 40
2.3 Measurement Techniques 41
2.4 Summary 45
3. Measurements on Drillpipe **59**
3.1 Terminology: MOD, MWD, and LWD 59
3.2 MOD Telemetry 60
3.3 Morphing From Wireline to MOD 62
3.4 Petrophysical Considerations for MOD Measurements 63
3.5 Logs Provided by MOD 64
3.6 Other MOD Sensors 66
3.7 MOD Quality Control and Sensor Calibration 66
3.8 The Future of MOD 68
4. Wireline Logging Operations **71**
4.2 Logging Trucks 71
4.3 Logging Cables 73
4.4 Logging Tools 77
4.5 The Borehole Environment 79
4.6 Choosing a Logging Suite 81
4.7 Computerized Logging Units 84
4.8 Log-Quality Control 87
5. Coring **93**
5.1 Objectives 93
5.2 Wireline Coring 93

5.3 Conventional Coring 96
5.4 Coring Fluids 97
5.5 Special Core Handling 99
5.6 Summary 100
Part II—Methods of Analysis and Application of Results 101
6. The Physics of Rock/Fluid Systems 103
6.1 The Genesis of Reservoir Rocks 103
6.2 Fluid Distribution in the Reservoir 106
6.3 Relative Permeability 109
6.4 Measurement of Porosity 113
6.5 Measurements of Permeability 113
6.6 Measurements of Saturation 116
6.7 Practical Petrophysics 120
6.8 Averaging 120
6.9 Summary 123
7. Basic Concepts of Log Analysis 125
7.1 Log Analysis Overview 125
7.2 Lithology 126
7.3 Porosity 127
7.4 Water Saturation: S_w 131
7.5 Hydrocarbon Type 132
7.6 Pay Counting 133
7.7 Permeability 134
7.8 Generalized Log Analysis 134
7.9 Summary 136
8. Volumetrics and Reserve Estimation 139
8.1 Oil and Gas in Place Estimates 139
8.2 Reserve Estimates 141
8.3 Recovery Factors 141
8.4 Formation Volume Factors 142
8.5 Depth and Net Pay Measurements 142
8.6 Special Cases of Deviated Wells and Dipping Beds 143
8.7 Reservoir Volumes 147
8.8 Reserves 148
8.9 Uncertainty 149
Part III—Openhole Logging Measurements 153
9. The Spontaneous Potential Log 155
9.1 History of the Spontaneous Potential (SP) 155
9.2 Recording the SP 155
9.3 Source of the SP 156
9.4 R_W From the SP 159
9.5 Alternative One-Step Method for Obtaining R_W From the SP 166
9.6 Factors Affecting the SP 168
9.7 The SP as a Shale Indicator 172
9.8 SP Depositional Patterns 173
9.9 SP Quality Control 173
10. The Gamma Ray Log 179
10.1 Origin of Natural Gamma Rays 179
10.2 Abundance of Naturally Occurring Radioactive Minerals 180
10.3 Operating Principle of Gamma Ray Tools 180
10.4 Calibration of Gamma Ray Detectors and Logs 180

10.5 Time Constants....182
10.6 Perturbing Effects on Gamma Ray Logs....185
10.7 Estimating Clay Content From Gamma Ray Logs....186
10.8 Gamma Ray Spectroscopy....189
10.9 Interpretation of Gamma Ray Spectral Logs....191
10.10 Summary....194
11. Resistivity Measurements....203
11.1 Definitions....203
11.2 Typical Resistivities....204
11.3 Ideal Resistivity Measurements....204
11.4 Evolution of Modern Resistivity Devices....208
11.5 Philosophy of Measuring Formation Resistivity....209
11.6 Summary....209
12. Induction Logging....213
12.1 Induction Basics....213
12.2 When To Use an Induction Logging Device....214
12.3 Induction-Tool Development History....214
12.4 Theory of Induction Devices....215
12.5 Practice of Induction Logging....216
12.6 Phasor Induction....223
12.7 High-Resolution Induction....223
12.8 Array Induction Tool (AIT)....225
12.9 3D Induction....226
12.10 Calibration....226
12.11 Summary....228
13. The Laterolog....231
13.1 Early Laterolog Devices....231
13.2 When To Use a Laterolog....231
13.3 The DLL Tool....232
13.4 Borehole and Invasion Corrections....237
13.5 The Butterfly Chart....239
13.6 DLL Fingerprints....240
13.7 Anomalous Behavior....241
13.8 Summary....245
14. Microresistivity Measurements....249
14.1 Microresistivity Tools....249
14.2 Depth of Investigation....253
14.3 Bed Resolution....254
14.4 Environmental Corrections....254
14.5 S_{xo} and Hydrocarbon Movability....256
14.6 Hydrocarbon Density....257
14.7 Calibration and Quality Control....258
15. Dielectric Measurements....259
15.1 Electromagnetic Propagation Tools (EPT)....259
15.2 Physical Principle....259
15.3 Measurement Principles for Dielectric Logging Tools....261
15.4 Summary....270
16. Sonic (Acoustic) Logging and Elastic Formation Properties....273
16.1 Propagation of Elastic Waves....273
16.2 Elastic Constants....274
16.3 Sonic Logging Tools....275

16.4 Operating Principles 275
16.5 LSS Tools 278
16.6 Array Sonic Tools 281
16.7 Dipole Sonic Tools 282
16.8 Cycle Skipping and Noise 284
16.9 Waveform Recording 285
16.10 Sonic Porosity (ϕ_s) 286
16.11 Sonic Combination for R_{wa} 291
16.12 Δt Ratio 291
16.13 Mechanical Properties of a Formation 292
16.14 Seismic Applications 293
16.15 Cement Bond Log (CBL) 296
16.16 Log Quality Control 299
17. Formation Density Log 305
17.1 Operating Principle 305
17.2 Mudcake Compensation 307
17.3 Electron Density 310
17.4 Density Porosity (ϕ_D) 312
17.5 Shale Effects 314
17.6 Gas Effects 315
17.7 Depth of Investigation 317
17.8 Lithologic Density Tool 318
17.9 Density Log Quality Control 321
17.10 Safety 322
18. Neutron Logs 327
18.1 The Physics of Neutrons 327
18.2 The Compensated Neutron Tool 329
18.3 CNL Operating Principle 330
18.4 CNL Environmental Corrections 334
18.5 Depth of Investigation 334
18.6 Matrix Settings and Lithology Effects 334
18.7 Gas Effects 335
18.8 Shale Effects 337
18.9 Other Neutron-Logging Tools 337
18.10 CNL Calibration and Quality Control 338
19. Nuclear Magnetic Resonance 341
19.1 Applications of NMR 341
19.2 NMR vs. Conventional Logging and Log Analysis 341
19.3 NMR Measurements 343
19.4 NMR Free Fluid and Permeability 344
19.5 The Physics of NMR 345
19.6 NMR Logging 346
19.7 NMR Log Interpretation 352
19.8 NMR Vertical and Horizontal Resolution 357
19.9 NMR Calibration 357
19.10 NMR Limitations 358
20. Dipmeter and Borehole Imaging 361
20.1 Definitions 361
20.2 Applications of Dipmeters and Borehole Imaging Devices 362
20.3 Tools Available 363

20.4 Field Presentation....364
20.5 Dipmeter Computation....364
20.6 Computed Log Presentations....367
20.7 Interpretation....370
20.8 Fracture Finding....375
20.9 Dipmeter Log-Quality Control....375
20.10 Borehole Imaging....376
Part IV—Analysis of Logs and Cores....389
21. Interpretation Techniques....391
21.1 Models....393
21.2 Structured Approach....394
22. Quick-Look Interpretation, Crossplots, and Overlays....397
22.1 Compatibly Scaled Overlays....397
22.2 Crossplots....408
22.3 Histograms....412
22.4 Quick-Look Algorithms....413
23. Porosity....415
23.1 Reading Porosity From the Density Log....415
23.2 Combinations of Porosity Tools....416
23.3 Density Porosity (ϕ_D)....417
23.4 Neutron Porosity (ϕ_N)....418
23.5 Sonic Porosity....419
23.6 Neutron-Density Crossplot....420
23.7 Neutron-Sonic Crossplot....420
23.8 Shaly Formations....420
23.9 Secondary Porosity in Complex Lithology....424
23.10 Hydrocarbon Effects....424
23.11 Hydrocarbon Density....427
23.12 Summary....427
24. Lithology/Mineralogy....429
24.1 The Neutron-Density Crossplot....429
24.2 The Neutron-Sonic Crossplot....432
24.3 The Sonic-Density Crossplot....433
24.4 The M-N Plot....434
24.5 The Matrix Identification Plot (MID)....435
24.6 The Litho-Density Log and the Photoelectric Factor P_e....437
25. R_w Determination....447
25.1 Direct Measurement....447
25.2 R_w Computed From Chemical Analysis....449
25.3 R_w From the SP....452
25.4 The R_{wa} Method....452
25.5 The Ratio Technique....456
25.6 R_w From Crossplots....456
25.7 *F*-Overlay Technique....457
25.8 R_w Catalogs....459
26. Water Saturation....461
26.1 Methods Available To Determine S_w....461
26.2 The Basic Method: Archie's Equation....462
26.3 The Saturation Exponent *n*....463

26.4 Formation Factor and Porosity: Finding *a* and *m* 465
26.5 Determination of S_w in Clean Formations 466
26.6 Shaly Sand Methods 472
26.7 Summary 474
27. Core Analysis 477
27.1 Sample Selection and Preparation 478
27.2 Measurement of Basic Rock Properties 479
27.3 Effects of Overburden Pressure 485
27.4 Measurements of Capillary Pressure 485
27.5 Petrographic and Other Measurements 487
27.6 Electrical and Related Measurements 492
27.7 Summary 493
28. Formation Evaluation in Shaly Sands 497
28.1 Objectives 497
28.2 Clay Types and Distributions 497
28.3 Models 502
28.4 Other Shaly Sand Models 510
28.5 Quick-Look Computer Analysis 512
28.6 Practical Log Analysis in Shaly Sands 512
28.7 Low-Resistivity Pay 516
28.8 Unconventional Reservoirs 517
28.9 Summary 519
29. Formation Evaluation in Complex Lithology 523
29.1 Objectives 523
29.2 Exactly Determined Systems 523
29.3 Overdetermined Systems 525
29.4 Crossplot-Based Systems 528
29.5 Practical Quick-Look Methods 531
29.6 Neural Networks 532
29.7 Elemental Logging Tools 533
29.8 Logging-Tool Responses to Reservoir Rocks and Minerals 536
29.9 Summary 536
30. Formation Evaluation in Unconventional Reservoirs 545
30.1 Overview of Unconventional Reservoirs 545
30.2 Geochemistry of Unconventional Rocks 548
30.3 Unconventional Formation Evaluation 551
30.4 Assessment of TOC 563
30.5 Matrix and Pore Volumetrics 571
30.6 Geomechanics 579
30.7 Unconventional Well Construction 582
Part V—Formation Testing 595
31. Wireline Formation Testing 597
31.1 Tool Characteristics and Applications 597
31.2 Operating Principles 598
31.3 Interpretation 600
31.4 Fluid Sampling 609
31.5 Sequential Pressure Readings vs. Depth for Pore-Pressure Gradient 610
31.6 Formation Production Estimates 611
32. Drillstem-Testing Objectives 617
32.1 Mechanics of DST 617
32.2 Pressure Recording 617

32.3 Planning the DST 618
32.4 Perspective 619
Part VI—Integrated Formation-Evaluation Plan 621
33. Integrated Formation-Evaluation Plan 623
33.2 Planning 623
33.3 Monitoring 624
33.4 Data Analysis 625
33.5 Summary 626
Appendix—Log Analysis Equation Summary 629
Author Index 641
Subject Index 643

Part I—Methods of Gathering Formation Evaluation Data

Chapter 1

Formation Evaluation Overview

1.1 The Scope of Formation Evaluation

Formation evaluation covers a very wide range of measurement and analytic techniques. The purpose of this work is to expose the reader to all the available methods and to provide a perspective with reference to borehole geophysics or well logs. Although the emphasis will be on well logging techniques and log analysis methods, these are not the only tools available to the formation evaluator. Well logs are central only in the sense that they are universally recorded in practically all wellbores and can be directly related to all the other parameters available from the associated sciences. For example, a geophysicist needs borehole measurements to determine a time-depth relationship, and a petrophysicist needs a core analysis to determine log response properly, but a thin section or a scanning electron microscope (SEM) photograph of a rock sample is of no direct help in the interpretation of a seismic section, nor is a vertical seismic profile (VSP) of any help in determining relative permeability. However, all these measurements are pertinent to the overall task of defining a reservoir's limits, storage capacity, hydrocarbon content, produceability, and economic value.

To place the various disciplines in perspective, it is valuable to consider the overall problem of formation evaluation in terms of orders of magnitude. If one meter is taken as a unit of measurement, then the various formation evaluation techniques can be placed in order as shown in **Table 1.1.**

It can be seen that these formation evaluation techniques cover at least 12 orders of magnitude. The physical principles used to make the basic measurements are equally far-ranging. An enlightening way of viewing this vast spread is to consider the frequencies used by the measuring processes available, as illustrated in **Table 1.2.** Again, a span of many orders of magnitude can be observed. Few other sciences require or use such a wide range of measurement techniques over such a wide range of physical dimensions.

1.2 Formation Evaluation

The initial discovery of a reservoir lies squarely in the hands of the explorer who uses seismic records, gravity, and magnetics. Formation evaluation presupposes that a reservoir has been located and is to be defined by drilling as few wells as possible. In these wells, enough data should be gathered to extrapolate reservoir parameters throughout the field to arrive at realistic figures for both economic evaluation of the reservoir and planning of the optimum recovery method. Formation evaluation offers a way of gathering the data needed for both economic analysis and production planning.

What, then, are the parameters that the manager, the geologist, the geophysicist, and the reservoir and production engineers need? Which of them can be provided by seismic records, by coring, by mud logging, by formation testing, or by conventional logging?

- The geophysicist needs to know the time-depth relationship to calibrate conventional seismic and VSP surveys.

TABLE 1.1—FORMATION EVALUATION PERSPECTIVE

Meters	Formation Evaluation Technique	Purpose
10^{6}	Satellite imagery	
10^{5}	Basin geologic studies	Gross structure
10^{4}	Seismic, gravity, magnetics	
10^{3}	Gravimeter, ultralong spaced electrical logs	Local structure
10^{2}	Drillstem tests	Productivity and reserves
10^{1}	Wireline formation tests	
10^{0}	Full diameter cores	Local porosity, permeability and lithology
10^{-1}	Sidewall cores, well logs, MWD, LWD	
10^{-2}	Micro-focused logs, coreplug analysis	
10^{-3}	Cuttings analysis (mud logging)	Local hydrocarbon content
10^{-4}	Core analysis	Rock properties
10^{-5}	X-ray mineralogy	Rock and clay typing
10^{-6}	Scanning electron microscope (SEM)	Micropore structure

TABLE 1.2—RANGE OF PHYSICAL PRINCIPLES USED IN FORMATION EVALUATION

Measurement Frequency	Measurement Type
Hertz	
10^{9} to 10^{7}	Dielectric
10^{3}	Induction, sonic
10^{2}	Laterolog, seismic
10^{1}	Old electric logs
10^{-4}	Step-rate well testing
10^{-8} to 10^{-9}	Material balance

- The geologist needs to know the stratigraphy of the formations, the structural and sedimentary features, and the mineralogy of the formations through which the well was drilled.
- The reservoir engineer needs to know the vertical and lateral extent of the reservoir, its porosity (and type of porosity), and its permeability, fluid content, and recoverability.
- The production engineer needs to know the rock properties, to be aware of overpressure if it exists, and to be able to assess sanding and associated completion problems and the need for secondary recovery efforts or pressure maintenance at a future date. Once the well is on

production, the production engineer will also need to diagnose problems as the well ages and may also need to know formation injectivity and residual water saturations to plan waterflooding and to be able to monitor the progress of the waterflood when it becomes operational.
- The manager needs to know the vital inputs to an economic study, namely the original amount of hydrocarbons in place, their recoverability, the cost of development, and on the basis of these factors, the profitability of producing the reservoir.

Log measurements, when properly calibrated, can provide most of the parameters required. Specifically, logs can provide either a direct measurement or a good indication of

- Porosity, both primary and secondary (fractures and vugs)
- Permeability
- Water saturation and hydrocarbon movability
- Hydrocarbon type (oil, gas, or condensate)
- Lithology
- Formation dip and structure
- Sedimentary environment
- Travel times of elastic waves in a formation

From these data, good estimates can be made of reservoir size and hydrocarbons in place. Logging techniques in cased holes can provide much of the data needed to monitor primary production and also to gauge the applicability of waterflooding and to monitor its progress once initiated. In producing wells, logging can provide measurements of

- Flow rates
- Fluid type
- Pressure
- Residual oil saturation

From these measurements, dynamic well behavior can be understood better, remedial work planned, and secondary or tertiary recovery proposals evaluated and monitored.

In summary, when properly used, logging can answer many questions from a wide spectrum of special-interest groups on topics ranging from basic geology to economics. Of equal importance, however, is the fact that logging by itself cannot answer all formation-evaluation questions. Coring, core analysis, and formation testing are integral parts of any formation-evaluation effort.

1.3 Formation-Evaluation Methods

In practice, the order in which formation-evaluation methods are used tends to follow the orders-of-magnitude table (Table 1.1), that is, to move from the macroscopic to the microscopic. Thus, a prospective structure will first be defined by seismic records, gravity, magnetics, or a combination of these. A wellbore drilled through such a structure may involve mud logging, logging while drilling (LWD), measurements while drilling (MWD), or a combination of these, and in that wellbore, cores may be cut or sidewall samples taken. Once the well has reached the prescribed depth, conventional wireline logs will be run. An initial analysis of mud-log shows, together with initial log analysis, may indicate zones that merit testing by either wireline formation testing or drillstem testing. Should such tests prove the formation to be productive, a more exhaustive analysis will be performed of all available data, including a core analysis. The whole process can be summarized as shown in **Table 1.3.**

The exploration phase, involving seismic records, gravity, and magnetics, will not be covered in this book. However, the use of logs to refine seismic interpretation will be covered, as will the VSP. The drilling phase will be covered by discussion of mud logging, coring, LWD, and MWD. The testing phase will be covered by sections dealing with both DSTs and wireline formation tests. Core analysis will be covered to the extent that the results of core analysis have a direct effect on log analysis.

TABLE 1.3—FORMATION EVALUATION OVERVIEW

Phase	Activity	Formation Evaluation Method
Exploration	Define structure	Seismic, gravity, magnetics
Drilling	Drill well	Mud logging, coring, MWD, LWD
Logging	Log well	Openhole logs
Primary evaluation	Log analysis and testing	Sidewall cores, VSP, wireline FT, DST
Completion	Cementing, shooting, fracturing	CBL, mech props, frac monitoring
Analysis	Core and fluid analysis	Laboratory studies
Feedback	Refinement of seismic model	Time/depth calibration
	Integrated field study	Log/core calibration
Exploitation	Producing hydrocarbons	Material balance analysis
Secondary recovery	Production logging	Production log analysis
	Assisted lifting	Flood efficiency analysis
	Water or gas injection	Rock microproperty analysis
Abandonment	Economic decisions	

Production logging merits a book of its own, and the reader is referred to a companion volume to this work by the same author, *Cased-Hole Log Analysis and Reservoir Performance Monitoring* (Bateman 1985).

Economic analysis is outside the scope of this book, but the vital inputs to any economic analysis still must come from the formation-evaluation methods discussed here. For those unfamiliar with some or all of the formation-evaluation methods mentioned, the following brief summaries will serve as an introduction. Those familiar with the topics under discussion may forge ahead in the text to the relevant sections where each is discussed in detail.

1.4 Mud Logging

Mud logging, more elegantly referred to as hydrocarbon mud logging, is a process whereby the circulating mud and cuttings in a well being drilled are continuously monitored by a variety of sensors. A combined analysis of all the measurements provides indications of the rock type and its fluid content. The various measurements are displayed on a log as curves or notations as a function of depth. Not all wells are logged in this manner. Development wells, for example, are usually drilled and logged with wireline logging tools only. Wildcat wells, however, are nearly always monitored by the mud-logging process. The great merits of mud logging include the availability on a semicontinuous basis of an actual formation cuttings analysis (which in turn gives immediate indications of rock type and hydrocarbon presence) and the ability to predict drilling problems (such as overpressure) before they become unmanageable. Chapter 2 addresses this topic in more detail.

1.5 Coring

A number of methods are in use to cut cores in a wellbore. Conventional cores are cut using a special core bit by means of which a long core barrel is retrieved and brought back to the surface. The formation sample recovered may undergo physical changes on its journey from the bottom of the well, where it is cut, to the surface, where it can be analyzed. More sophisticated coring mechanisms are now in use that conserve the orientation, pressure, and original fluid saturations of the rock sample gathered. An awareness of these methods is essential to an understanding of core analysis results.

Other coring methods are available for cases in which additional rock samples are required after the well has been drilled, but before it has been cased. These methods require wireline tools that cut core plugs from the side of the well.

Many of the parameters needed to interpret openhole wireline logs correctly can be determined only from an accurate core analysis. This presupposes that cores have been cut. Therefore, in the initial stages of a field development, coring plays an essential part. Chapter 5 covers methods of recovering core samples, and Chapter 27 covers their analysis.

1.6 Measurements While Drilling (MWD)

The term MWD originally referred to the data that were of interest to the driller and that could be recorded in real time as the well was drilled. These measurements, made by sensors in a drill collar close to the bit itself, were transmitted to surface by mud pressure pulses and included the parameters needed for well steering such as weight on bit, hole deviation, and hole direction. With time, additional sensors to assist in the drilling operation were added, including gamma ray and resistivity measurements. This ushered in the age of *geosteering,* which enabled the geologist-driller team to "steer" the wellbore path to intersect the formation of interest at the desired position in the reservoir. Today full logging suites may be run on drill collars and are referred to as "logging while drilling"; therefore, the MWD name is now reserved for the measurements related to well construction rather than to formation evaluation.

1.7 Logging While Drilling (LWD)

More and more, formation properties are being measured at the time the formation is drilled by use of special drill collars that house formation logging devices. These LWD tools are particularly valuable in deviated extended-reach wells where wellbore path control is of critical importance and where an immediate knowledge of the formation properties is vital for decision-making on such matters as the choice of coring and casing points. The measurements obtained by LWD are rapidly becoming just as accurate and useful in log analysis procedures as the measurements obtained with wireline logging tools. Indeed, there are LWD sensors now available that are competitive with, and in some cases exceed, the capabilities of wireline logging sensors. Chapter 3 discusses in more detail the full range of measurements available on the drillpipe.

1.8 Testing

Formation testing is the proof of the pudding. If hydrocarbons flow from the well on a DST, no amount of logging data or core analysis can deny that a productive zone has been found. However, a DST not only provides proof that hydrocarbons exist in the formation and will flow, but also supplies vital data on both the capacity of the reservoir and its ability to produce in the long term. Correct interpretation of pressure records from DSTs add immensely to the overall formation-evaluation task.

Wireline formation testers complement DSTs by their ability to sample many different horizons in the well and produce not only fluid samples, but also detailed formation pressure data that are almost impossible to obtain from a DST alone. Chapter 30 covers wireline formation testing and Chapter 31 drillstem testing.

1.9 Openhole Logging

Openhole logging provides the great meeting place of all the other formation-evaluation methods. Only through openhole logging can a continuous record of measurement vs. depth be made for so many formation properties. In particular, wireline logs can record formation electrical resistivity, bulk density, natural and induced radioactivity, hydrogen content, and elastic moduli. These raw measurements can then be interpreted to give a continuous measurement-vs.-depth record of formation properties such as porosity, water saturation, and rock type. Almost without exception, every well drilled for hydrocarbons is logged with wireline instruments.

Unfortunately, the logs so acquired are not always analyzed in detail or are incorrectly analyzed because of a lack of training on the part of the analyst or a lack of understanding of where wireline logs fit in relation to other methods of formation evaluation. All too often, logs are seen as an end in themselves and are considered in isolation. It is hoped that this book will assist the reader in taking a broader view of log analysis in the context of overall formation evaluation. Chapter 4 covers the "how" of wireline logging operations in general, and Chapters 9 through 20, in Part III of this work, give further details of each of the openhole logging measurements available.

Fig. 1.1 illustrates the overall formation evaluation picture and the central role of openhole logging and log analysis.

1.10 Modern Logging Tools

The actual running of a log involves as much the tool on the end of the logging cable as the cable itself and the surface controlling and recording apparatus. Therefore, before discussing downhole tools, the common elements of all logs will be presented. **Fig. 1.2** illustrates the basic components of any logging system.

A sensor, incorporated in a sonde together with its associated electronics, is suspended in the hole by a multiconductor cable. The sensor is separated from the virgin (undisturbed) formation by a portion of the mud column, by mudcake, and more often than not, by an invaded zone in the surrounding formation. The signals from the sensor are conditioned by the electronics for transmission up the cable to the surface control computer, which in turn conditions the signals for recording and transmission. As the cable is raised or lowered, it activates a depth-measuring device, for example a sheave wheel, which in turn activates a recording device, either an analog device or a digital system that makes digital recordings on magnetic media. Finally, some form of reproduction takes place to provide a hard copy of the recorded data.

In general, well-logging jargon distinguishes between a *logging survey,* a *logging tool*, and a *log* as well as a *curve.* To avoid confusion about these terms when logging matters are discussed, it should be noted that a *logging survey* is provided by a logging-service company for a client.

During the course of the survey, the logger may use several different logging tools and may record several different logs, on each of which are presented several different curves. The logging

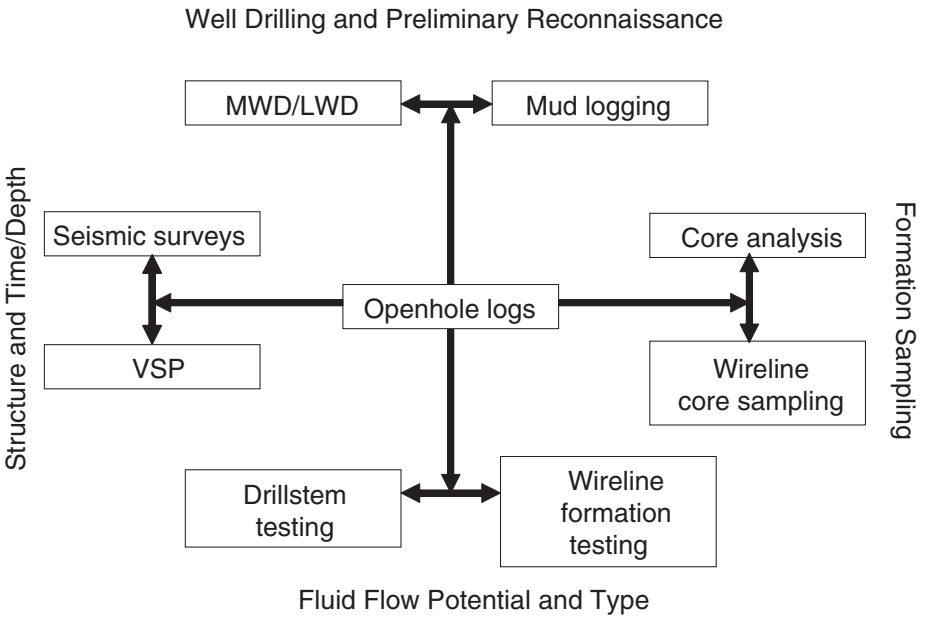


Fig. 1.1—Interrelationships between formation evaluation methods.

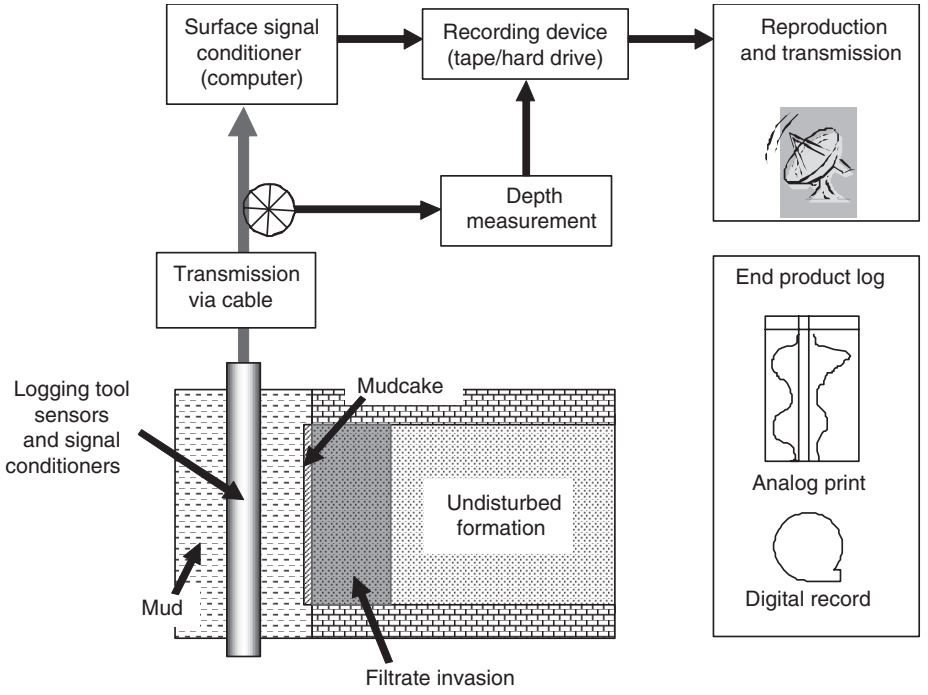


Fig. 1.2—Components of a logging system.

tools used, in turn, may be composed of multiple sensors. **Fig. 1.3** illustrates these terms and their interrelationship.

The openhole logging tools in use today are normally provided by a single run in the borehole using what is referred to as a *triple- or quad-combo tool string*. An example of such a log presentation is given in **Fig. 1.4.**

The components of a combination tool string vary depending on the mud system used to drill the well and the needs of the client, but a commonly used combination might include the following:

- Array resistivity tool (either induction or laterolog)
- Compensated neutron tool
- Compensated density/litho-density tool (including photoelectric factor, P_e)
- Gamma ray/spectral gamma ray
- Sonic (simple, array and/or dipole)

It is also common practice to run such combination tool strings with a standard utility tool sub that records such useful items as

- Spontaneous potential (SP)
- Caliper
- Mud resistivity
- Mud temperature
- Hydrostatic pressure

1.11 Evolution of Logging Devices

Although the analyst must be equipped to interpret the logging measurements of the day, it is also important to realize that in the past, logging tools were less sophisticated, and therefore handling their measurements requires additional skills. While the inexorable march of technology propels

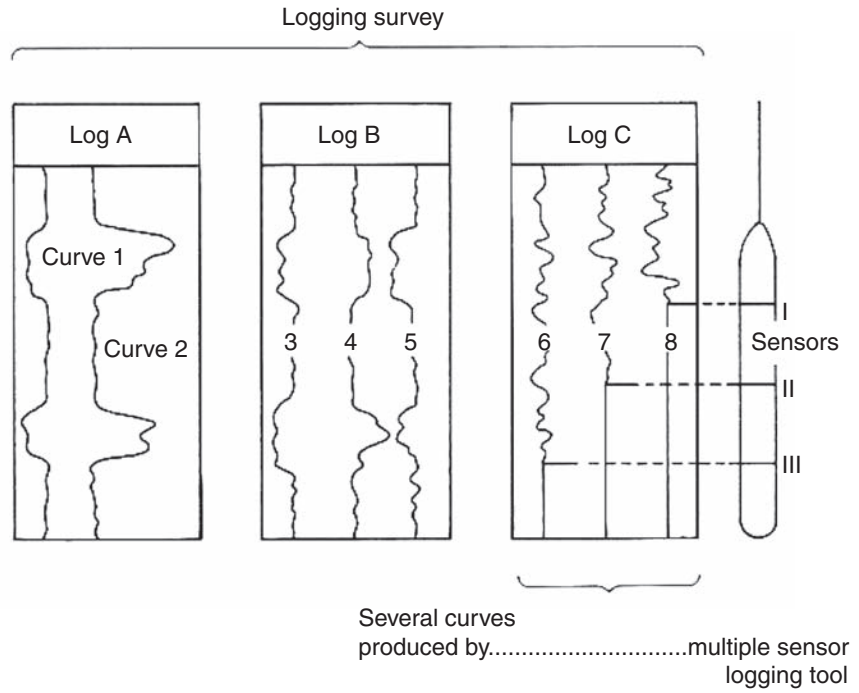


Fig. 1.3—Logging terms.

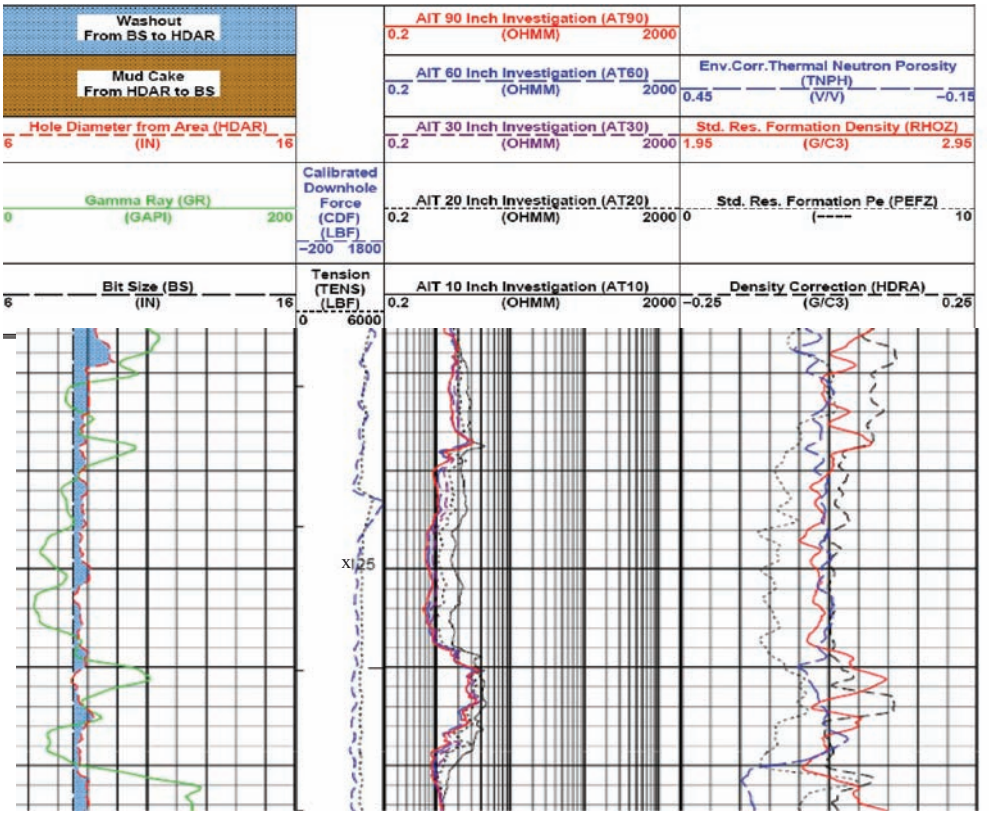


Fig. 1.4—Triple combo example.

the industry ever forward, it is worth reflecting that much of the "legacy" material that the analyst may be required to evaluate still exist in well files on analog film stock or on paper prints. Even today, a visit to a data room to consider the worth of an old file that is for sale is bound to expose the analyst to older logs and logging curves generated by devices and methods that no longer exist.

In general the historical progress of the logging industry can be categorized into three generations. The first generation included the "proof of principle" type of tool that demonstrated that a particular physical measurement could be made on wireline. The second-generation tools elaborated on these basic devices and introduced additional transmitters, receivers, and spacings to attempt to defeat ever-present threats such as filtrate invasion and thin beds. The third generation made great strides forward by taking advantage of

- Downhole and surface computerization
- High-speed logging cable data transmission schemes
- Innovative technologies such as
  - Optical fluid analysis
  - Dipole sonic sources
  - Advanced NMR technology
  - Drillpipe-conveyed logging sensors
  - Borehole imaging devices

Table 1.4 summarizes the evolution of these logging devices. Useful guides to the less modern devices are enumerated in the bibliography section of this chapter.

1.12 Categorization of Logging Devices

From the point of view of the analyst, it is convenient to categorize the various logging tools according to their intended use. Where pertinent to openhole log analysis and formation evaluation, the corresponding chapter in this work is noted.

1.12.1 Formation Fluid Content Indicators. ***Induction Tools*** (see Chapter 12) belong to the resistivity-tool family and measure formation resistivity. They work like mine detectors by inducing currents in the formation. Induction logs are called by a variety of names such as

- Induction
- Dual induction
- High-resolution induction
- Phasor induction
- Array induction
- 3D induction

They may be run simultaneously with neutron, density, SP, or gamma ray logs, or a combination of these.

Laterolog Tools (see Chapter 13) belong to the resistivity-tool family and measure formation resistivity. They work by focusing a beam of current into the formation. Laterologs are known by a variety of names such as

- Laterolog 3
- Laterolog 7
- Dual laterolog
- Array laterolog

As with the induction tools, they may be run simultaneously with neutron, density, SP, or GR logs, or a combination of these.

TABLE 1.4—GENERATIONAL EVOLUTION OF LOGGING DEVICES

	Generations			
Logging Tool	First	Second	Third	Drillpipe
Electric (deep reading)	Single E-log	Normals and Laterals	Ultralong spacing	Resistivity at Bit
Electric (shallow reading)		16" SN; SFL	Resistivity through casing	—
Induction	5FF40	6FF40; dual induction	Array and 3D induction	—
		High resolution (HRI)		—
Laterolog	LL-3 and LL-7	Dual laterolog	Array laterolog	Azimuthal resistivity imaging
Microresistivity	Microlog			—
	Microlaterolog	μ-spherically focused	μ-cylindrically focused	—
	Proximity log			—
Dielectric	—	1T-2R single f (EPT)	Multi T and R + Multi f	"E wave" measurements
Sonic	1T-2R	2T-4R (BHC)	Array (Multi-R) and Dipole	—
Density	Uncompensated	Compensated	Litho-density (P_e)	Azimuthal density imaging
Neutron	N-γ	N-epithermal N (SNP)		
		N-thermal N (CNL)		
Pulsed neutron	TDT and NLL	Multigating	Elemental GR spectral	—
Gamma ray	GM detectors	Scintillation detectors	Spectral GR	—
Hole geometry	2- and 3-arm calipers	4- and 6-arm calipers	Borehole cameras	—
Dipmeter	SP and 3-arm	4- and 6-arm	Dips from borehole imaging	—
Imaging	—	Multi-electrode (FMI)	Ultrasonic	—
Nuclear magnetic resonance	—	NMR (with mud doping)	MRIL and CMR	—
Coring	Percussion sidewall	Core slicer	Rotary sidewall	—
Formation testing	Limited samples (FT)	Repeat sampling (RFT)	Multiprobe; pump out	
			Optical flow stream analysis	

Microfocused and Microresistivity Tools (see Chapter 14) belong to a family of devices that measure the formation resistivity close to the borehole where invasion may have taken place. They are known by a variety of names such as

- Proximity log
- Microlaterolog

- Microspherically focused log
- Microcylindrically focused log
- Microlog

Dielectric Logging Tools (see Chapter 15) measure the speed of electromagnetic waves sent along the wall of the formation. From the measured speed, the dielectric constant of the formation can be deduced. Oil and water, which have very different dielectric constants, can be distinguished. Other measurements, such as attenuation of microwaves, can indicate porosity and other resistivity-related parameters. These tools are used in open holes where formation waters are fresh. They are limited by a very shallow depth of investigation.

Pulsed Neutron Tools measure the neutron-capture cross section of the formation, which helps to distinguish oil from saltwater. The primary application of these tools is in cased holes. However, they may also be used in an open hole. The tools are limited in use to those formations that have fairly salty formation water. The curves that appear on the log are

- Σ the formation neutron capture cross section
- τ the thermal neutron decay time
- ϕ a porosity-type ratio curve

Carbon/Oxygen Logging uses inelastic fast neutron scattering to measure directly the relative abundance of carbon and oxygen in a formation. Carbon/oxygen logging is used in cased holes and is a natural candidate for those parts of the world where fresh formation waters preclude the use of a pulsed-neutron logging survey.

1.12.2 Porosity-Lithology Indicators. ***Sonic/Acoustic Logging*** (see Chapter 16) was originally developed as a primary porosity device, but it has since been superseded in that role by the neutron-density combination. However, its use has grown in other directions to cover a wide range of borehole seismic measurements that assist the analyst in such tasks as integration of time/depth analysis with conventional seismic traces, fracture detection, permeability indication, and determination of formation mechanical properties. The modern sonic log is known as an array sonic and may operate with multiple transmitters and receivers at multiple frequencies with both compression and shear excitation modes.

Density Tools (see Chapter 17) send gamma rays into the formation and detect gamma rays coming back. A more sophisticated version of the density tool is the litho-density tool. In addition to measuring bulk density, it also measures the photoelectric factor P_e, which is a direct indicator of formation lithology and as such is a valuable adjunct to the basic density measurement.

Neutron Tools (see Chapter 18) emit fast neutrons (from either a chemical source or a downhole accelerator), which are then slowed as they pass through the surrounding formations. Eventually they are detected at the thermal or epithermal stages of their brief lives, depending on the type of tool in question. Earlier versions of the tool detected gamma rays captured rather than making a measurement of the residual neutron flux. There are several types of neutron tools including:

Natural and Spectral Gamma Ray Logging (see Chapters 10 and 24) distinguishes reservoir rocks from nonreservoir rocks. Conventional gamma ray logging records the total gamma ray activity of the formation being logged, whereas gamma ray spectrometry measures the number and energy of naturally occurring gamma rays in the formation and distinguishes between elements and daughter products of three main radioactive families: uranium, thorium, and potassium. Because these elements and their decay products are associated with certain distinct types of mineralogy, sedimentology, and formation waters, gamma ray spectral logging has obvious appeal.

Nuclear Magnetic Resonance Tools (see Chapter 19) measure the precession rate of atomic nuclei after the removal of an intense magnetic field. The measured quantity is related to pore-size distribution, electrostatically (clay) bound water, capillary-bound water, and the free fluid content of the formation. It is perhaps the only logging measurement that can be directly related

to formation porosity and permeability. Basic signal processing can also reveal useful information about the hydrocarbon types occupying the pore space.

Sidewall Coring (see Chapter 5) provides the analyst with a physical sample of the formation, which can then be subjected to laboratory analysis under controlled conditions to determine porosity, permeability, and grain density. Additional petrophysical properties add to the understanding of the reservoir and help to predict what the performance may be when wells are placed on production. These special parameters include the Archie constants (*a, m,* and *n*; see Chapters 6 and 27), wettability, relative permeability, and capillary pressure, among others.

1.12.3 Reservoir Geometry Indicators. ***Dipmeters and Borehole Imaging Devices*** (see Chapter 20) afford the analyst the means either to compute or to view directly both the bed dip and azimuth and the formation texture. Gross structural features such as faults, folds, and unconformities can be deduced from the trends in dip patterns with depth, and at the same time, sedimentary features can be revealed. Depositional features such as forests and cross bedding can be followed and vugs and fractures mapped quasidirectly from the borehole images. Devices in use include

- Four- and six-arm dipmeters
- Oil-based mud dipmeters
- Multielectrode resistivity imagers
- Ultrasonic rotating scanners

Borehole Gravimeters measure perturbations in the gravitational acceleration constant caused by the proximity to the borehole of formation material that is lighter or heavier than normal. Thus, this tool can spot higher porosities (such as gas-bearing zones) some distance from the borehole. Its use requires that an exacting set of prerequisites regarding depth, temperature, and time be satisfied, which may not be possible in all wells everywhere.

Ultralong-Spacing Electric logs are used in rare circumstances to gauge the proximity of one borehole to another, for example when drilling a relief well to one that is in an uncontrolled blowout condition.

1.12.4 Formation Productivity Indicators. ***Nuclear Magnetic Resonance*** (see Chapter 19), already mentioned as a "porosity-lithology" indicator, deserves a double mention because it also indicates the ability of the formation to flow. One of the outputs from the basic tool measurement is referred to as the *free fluid index*, which is a measure of flow potential.

Wireline Formation Testers (see Chapter 30) enable limited samples of formation fluid to be sucked out of the formation and brought to the surface for further analysis. These wireline formation testers also enable multiple formation pressure tests to be performed in one run into the hole; these can be used to compute fluid pressure gradients and thus determine precisely gas/oil and oil/water contact regions. The more sophisticated versions of this tool include a number of advanced features such as the ability to pump out unwanted mud filtrate before capturing an uncontaminated sample of reservoir fluid. Furthermore, optical fluid analyzers now inform the operator before sampling whether the fluid flowing from the formation is oil or water.

1.12.5 Auxiliary Tools. ***SP*** (see Chapter 9) is a standard auxiliary parameter recorded with a resistivity tool provided that the mud system is water-based.

Caliper Logs are recorded on almost every wireline logging run and are very useful for determining where the hole is rugose or greatly out of round, places where pad-contact-type tools cannot be expected to operate correctly.

Mud Properties such as temperature, pressure, and resistivity are routinely monitored by a utility sub that accompanies the conventional formation-measuring devices. These environmental properties are later used for making appropriate environmental corrections semiautomatically.

1.13 Summary

The basic devices described above will answer the majority of questions about the formation. To put all these tools, surveys, and curves in perspective, the reader is invited to peruse a summary of all the common logging tools, their measurements, and the uses to which they may be put, which is offered in the appendices to this work.

References

Bateman, R.M. 1985. *Cased-Hole Log Analysis and Reservoir Performance Monitoring*. Boston, Massachusetts: International Human Resources Development Corporation (IHRDC).

Halliburton Wireline and Perforating Services, http://www.halliburton.com/public/lp/contents/Books_and_Catalogs/web/WPS_PS_Catalog/Web/WPS_PS_CAT.pdf (downloaded 26 March 2012).

Introduction to Open Hole Logging. Schlumberger Educational Services (05/96).

Schlumberger. A.G. 1982. *The Schlumberger Adventure*. New York: Arco Publishing.

Schlumberger. 2007. *80 Years of Innovation*. Sugar Land, Texas: Oilfield Services Marketing Communications.

General References

Allaud, L.A. and Martin, M.H. 1977. *Schlumberger: The History of a Technique*. New York: John Wiley.

Bateman, R.M. 2009. Petrophysical Data Acquisition, Transmission, Recording and Processing: A Brief History of Change From Dots to Digits. *Trans.,* SPWLA 50th Annual Logging Symposium, The Woodlands, Texas, USA, 21–24 June.

Oristaglio, M. and Dorozynski, A. 2009. *A Sixth Sense: The Life and Science of Henri-Georges Doll*. New York: Overlook Duckworth.

Société de Prospection Electrique. 1949. *Les Méthodes Schlumberger dans Les Sondages*, Paris.

Appendix 1A: Symbols

TABLE APPENDIX 1A: SYMBOLS

Symbol	Units	Description
a		Archie constant
A		Atomic weight
BVI	% or decimal	Bulk volume irreducible
D		Diffusivity coefficient
d_h	in. or cm	Hole diameter
d_i	in. or cm	Invasion diameter
Δ_ρ	g/cm^3	Density correction
Δt	s/ft or /m	Slowness (sonic travel time)
Δt_c	µs/ft or /m	Slowness for compressional waves (sonic travel time)
Δt_f	µs/ft or /m	Δt fluid
Δt_{ma}	µs/ft or /m	Δt matrix
Δt_{maa}	µs/ft or /m	Apparent Δt matrix
Δt_s	µs/ft or /m	Slowness for shear waves (sonic travel time)
F	unitless ratio	Formation factor
ϕ_D	unitless ratio	Porosity from density
ϕ_{Dsh}	unitless ratio	Apparent density porosity in shale
FFI	% or decimal	Free fluid index
ϕ_G	unitless ratio	Gaymard porosity
ϕ_N	unitless ratio	Porosity from neutron
ϕ_{Nsh}	unitless ratio	Apparent neutron porosity in shale
ϕ_S	unitless ratio	Porosity from sonic
ϕ_X	unitless ratio	Crossplot porosity
G	% or decimal	Radial geometric factor (induction devices)
h	ft or meters	Bed thickness
J	% or decimal	Radial pseudogeometric factor (laterolog devices)
k	md or Darcy	Permeability
k_{rg}	% or decimal	Relative permeability to gas
k_{ro}	% or decimal	Relative permeability to oil
k_{rw}	% or decimal	Relative permeability to water

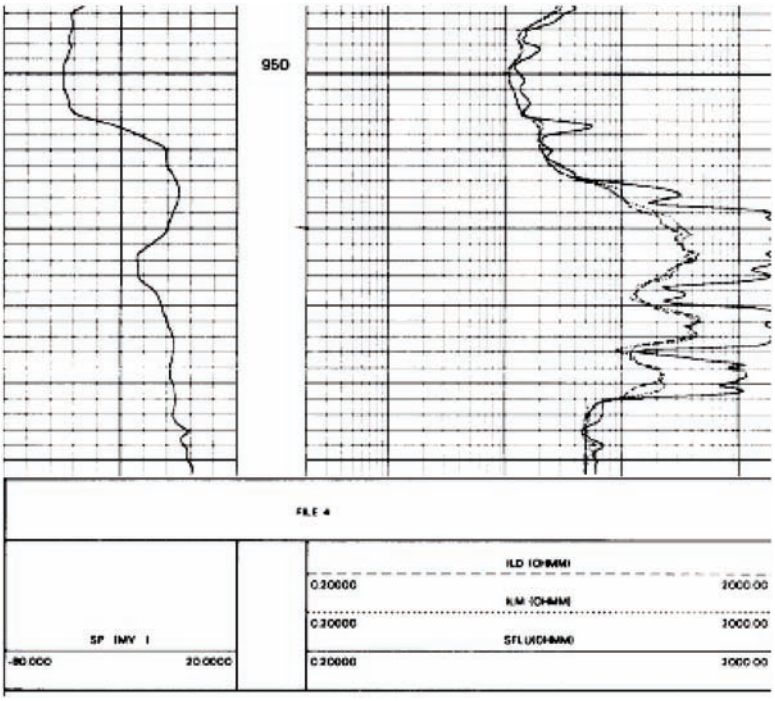
TABLE APPENDIX 1A: SYMBOLS (CONT'D)

Symbol	Units	Description
m		Cementation exponent
n		Saturation exponent
P_e	Barns per electron	Photoelectric factor
ρ_B	g/cm^3	Bulk density
ρ_b	g/cm^3	Bulk density
ρ_e		Electron density
ρ_g	g/cm^3	Gas density
ρ_{gr}	g/cm^3	Grain density
RI	unitless ratio	Resistivity Index (R_o/R_t)
R_m	$\Omega \cdot$m	Mud resistivity
ρ_{ma}	g/cm^3	Matrix density
ρ_{maa}	g/cm^3	Apparent matrix density
R_{mc}	$\Omega \cdot$m	Mudcake resistivity
R_{mf}	$\Omega \cdot$m	Mud filtrate resistivity
R_s	$\Omega \cdot$m	Shoulder bed resistivity
R_{sh}	$\Omega \cdot$m	Shale resistivity
R_t	$\Omega \cdot$m	Undisturbed formation resistivity
R_w	$\Omega \cdot$m	Connate water resistivity
R_{xo}	$\Omega \cdot$m	Invaded zone formation resistivity
SP	mV	Spontaneous potential
S_w	% or decimal	Water saturation—undisturbed formation
S_{wb}	% or decimal	Bound-water saturation
S_{wf}	% or decimal	Free-water saturation
S_{wi}	% or decimal	Irreducible water saturation
S_{xo}	% or decimal	Water saturation—invaded formation
T_1	msec	Longitudinal relaxation time
T_2	msec	Transverse relaxation time
U		Volumetric photoelectric absorption index
U_{ma}		U matrix apparent
V_{cl}	% or decimal	Clay volume
V_{sh}	% or decimal	Shale volume
Z		Atomic number

Appendix 1B: Log Analysis Abbreviations

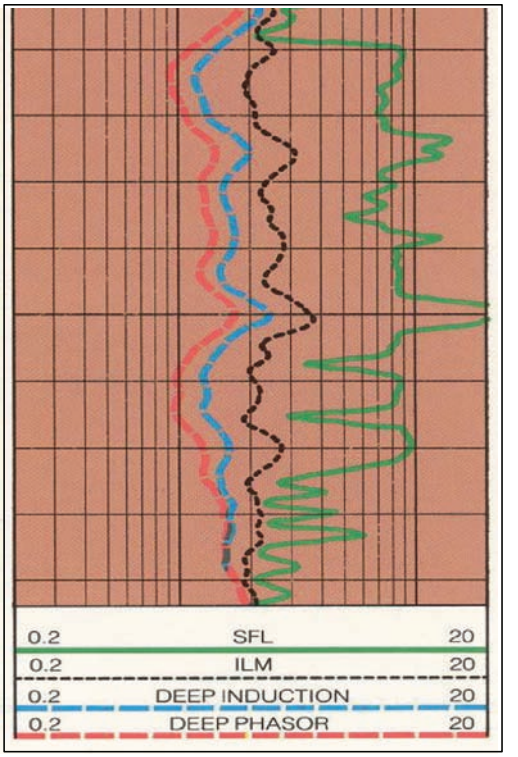
TABLE APPENDIX 1B—LOG ANALYSIS ABBREVIATIONS	
AHBDF	Along hole below drill floor
API	American Petroleum Institute
BHT	Bottomhole temperature
C1	Methane
C2	Ethane
C3	Propane
C4	Butane
C5	Pentane
CCD	Catalytic combustion detector
DST	Drillstem test
EMA	Equivalent methane in air
EPT	Electromagnetic propagation tool
EWR	Electric wave resistivity
FID	Flame ionization detector
GOC	Gas oil contact
GWC	Gas water contact
GWR	Gas wetness ratio
K	Potassium
LHR	Light heavy ratio
LWD	Logging while drilling
MCFL	Microcylindrically focused
MOD	Measurements on drillpipe
MSFL	Microspherically focused
MWD	Measurements while drilling
OCQ	Oil character qualifier
OWC	Oil water contact
PSI	Pounds per square inch
RAB	Resistivity at bit
RFT	Repeat formation tester
SEM	Scanning electron microscope
TCD	Thermal conductivity detector
Th	Thorium
TST	True stratigraphic thickness
TVD	True vertical depth
TVT	True vertical thickness
U	Uranium
VSP	Vertical seismic profile
WC	Water cut

Appendix 1C: Openhole Logging Tools: Measurements and Uses



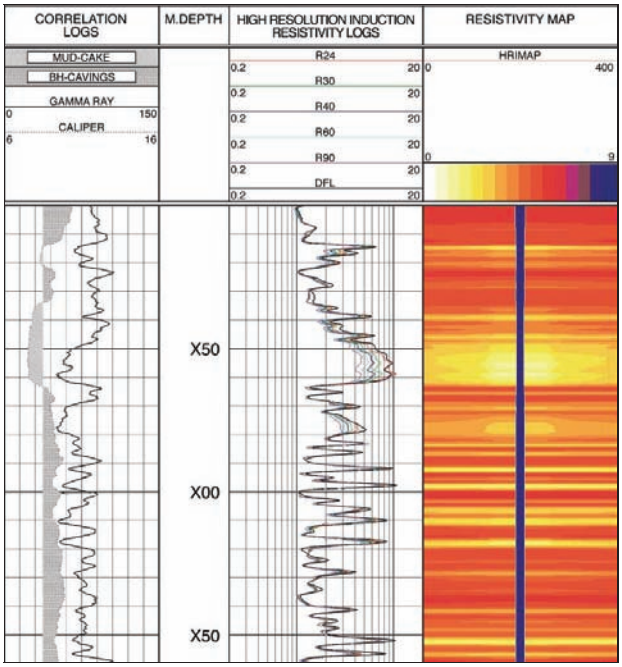
Generic name of log:	Dual induction
Type of tool:	Resistivity
Name and abbreviations:	DIL
When run:	Primary log in fresh or oil-based mud
Purpose:	Measures formation resistivity, R_t
Limitations:	Behaves badly in salt muds and/or large boreholes
Often combined with:	Neutron, Density, Sonic
Operating principle:	20-kHz coil induces current in formation
Curves recorded:	R_{ID} — deep induction R_{IM} — medium induction R_{SFL} — spherically focused *SP*, *GR*

Fig. 1-C1—Dual induction log (*Introduction to Open Hole Logging*). Courtesy of Schlumberger.



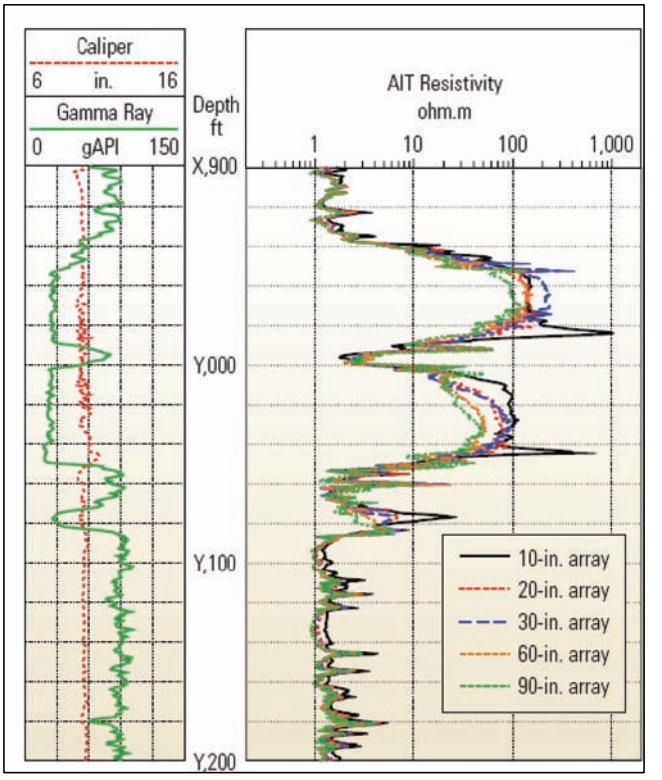
Generic name of log:	Phasor induction
Type of tool:	Resistivity
Names and abbreviations:	Phasor
When run:	Primary log in fresh or oil-based mud
Purpose:	Measures formation resistivity, R_t
Limitations:	Behaves badly in salt muds and/or large boreholes
Often combied with:	Neutron, Density, Sonic
Operating principle:	Multi-frequency coils and enhanced focusing
Curves recorded:	$R_{Deep\ Phasor}$ $R_{ID,\ \mathrm{RIM}}$ — deep and medium induction R_{SFL} — spherically focused *SP*, *GR*

Fig. 1-C2—Phasor induction.



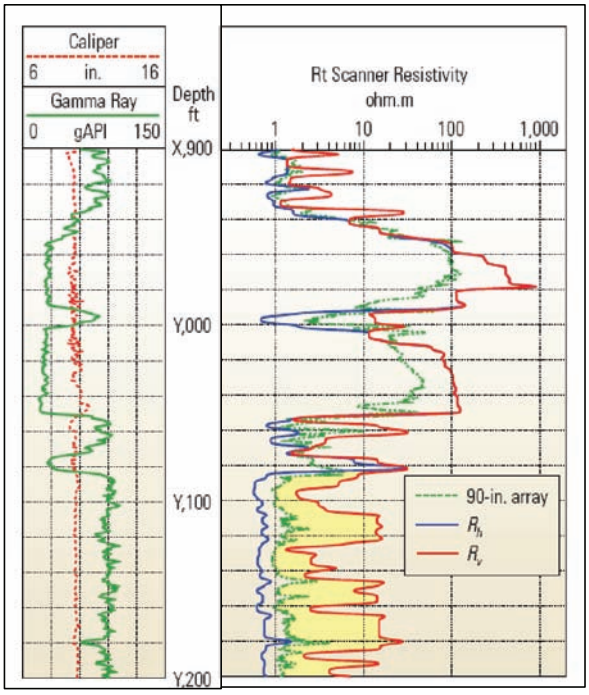
Generic name of log:	High-resolution induction
Type of tool:	Resistivity
Names and abbreviations:	HRI
When run:	Specialty log in fresh or oil-based mud
Purpose:	Measures formation resistivity, R_t
Limitations:	Behaves badly in salt muds and/or large boreholes
Often combined with:	Neutron, Density, Sonic
Operating principle:	Enhanced vertical resolution
Curves recorded:	5 induction resistivities HRI 24, 30, 40, 60 and 90-in. depths of investigation *SP, GR*

Fig. 1-C3—High-resolution induction (*Introduction to Open Hole Logging*). Courtesy of Schlumberger.



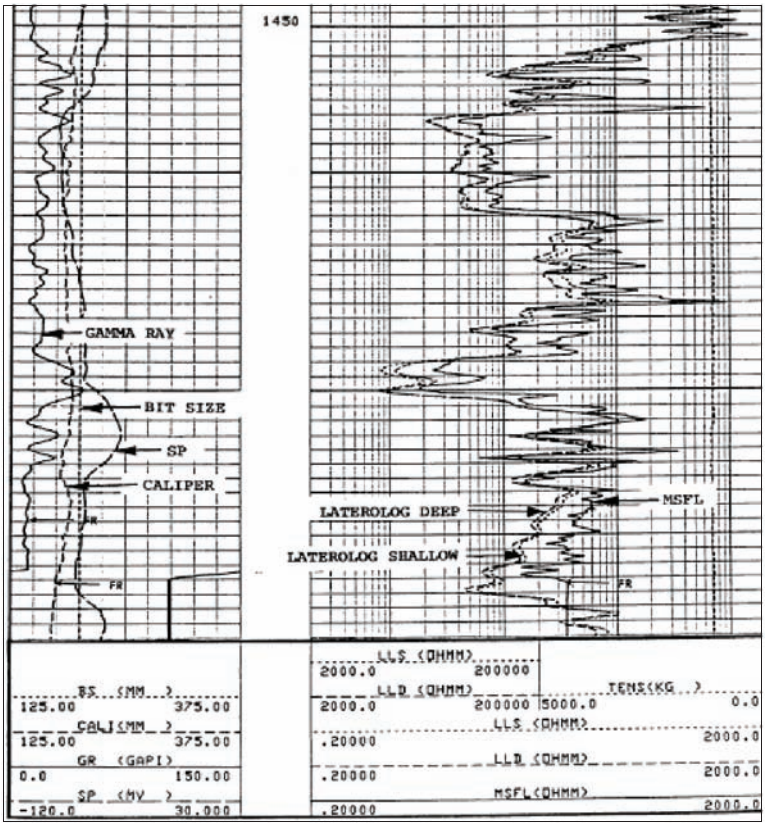
Generic name of log:	Array induction
Type of tool:	Resistivity
Name and abbreviations:	AIT
When run:	Primary log in fresh or oil-based mud
Purpose:	Measures formation resistivity, R_t
Limitations:	Behaves badly in salt muds and/or large boreholes
Often combined with:	Neutron, Density, Sonic
Operating principle:	Multicoil, multifrequency induction device
Curves recorded:	5 induction resistivities AIT 10, 20, 30, 60 and 90-in. depths of investigation

Fig. 1-C4—Array induction (*Introduction to Open Hole Logging*). Courtesy of Schlumberger.



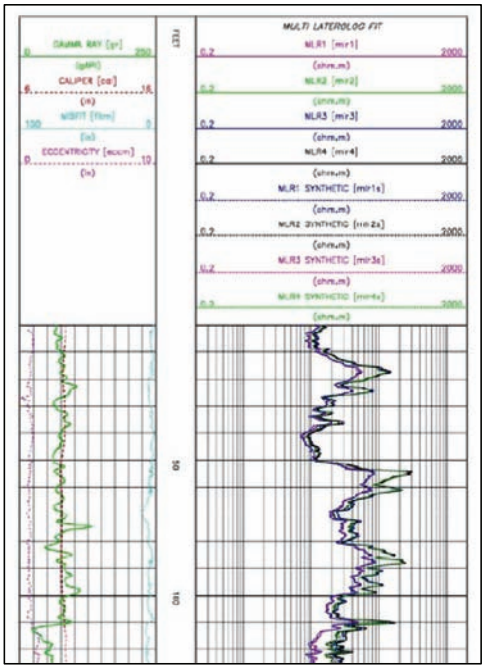
Generic name of log:	3D induction
Type of tool:	Resistivity
Name and abbreviations:	Rt scanner
When run:	Specialty log in fresh or oil-based mud for anisotropy
Purpose:	Measures formation resistivity, R_t on both vertical and horizontal axis
Limitations:	Behaves badly in salt muds and/or large boreholes
Often combined with:	Neutron, Density, Sonic
Operating principle:	20-kHz coil induces current in formation
Curves recorded:	Orthogonal coins used for resistivity in x-, y- and z-axis R_h and R_v

Fig. 1-C5—3D induction.



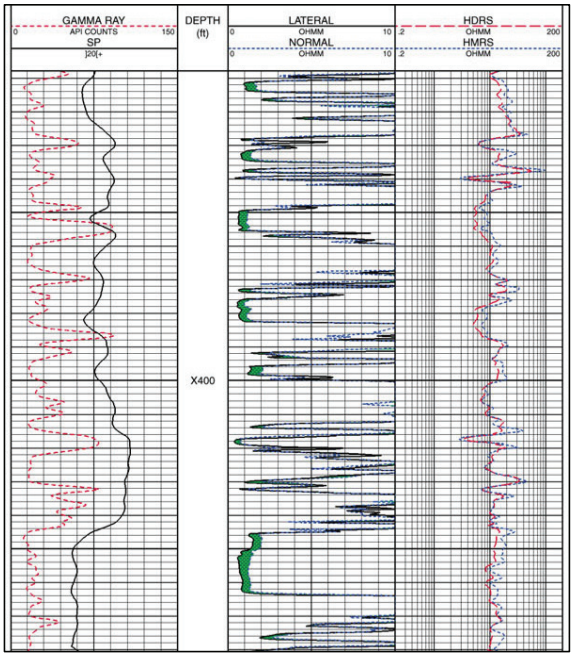
Generic name of log:	Dual laterolog
Type of tool:	Resistivity
Names and abbreviations:	DLL
When run:	Primary log in salt mud
Purpose:	Measures formation resistivity, R_t
Limitations:	Cannot be used in oil-based muds
Often combined with:	Neutron, Density, Sonic
Operating principle:	Focused horizontal beam of current sent into formation
Curves recorded:	R_{LLD} — deep laterolog R_{LLS} — shallow laterolog $R_{\mu SFL}$ — microspherically focused *SP*, *GR*, *Caliper*

Fig. 1-C6—Dual laterolog (*Introduction to Open Hole Logging*). Courtesy of Schlumberger.



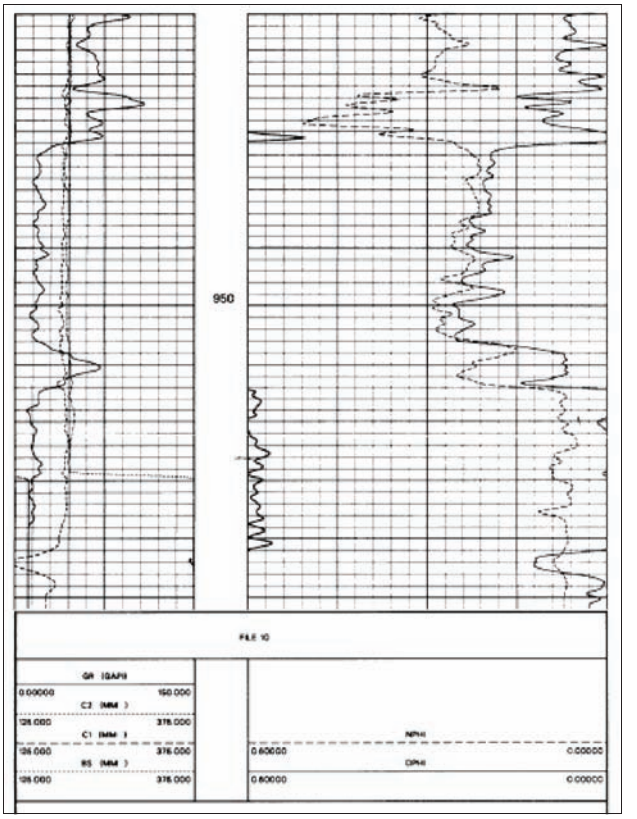
Generic name of log:	Array laterolog
Type of tool:	Resistivity
Names and abbreviations:	Rt Explorer, RTeX
When run:	Primary resisitivity log in salt mud
Purpose:	Measures formation resistivity, R_t
Limitations:	Cannot be used in oil-based muds
Often combined with:	Neutron, Density, Sonic
Operating principle:	Mulitple laterlog electrode arrays provide multiple depths of investigation
Curves recorded:	Verry shallow laterolog — 9-in. Shallow laterolog — 13-in. Medium laterolog — 19-in. Deep laterolog — 37-in.

Fig. 1-C7—Array laterolog. Courtesy of Baker Hughes.



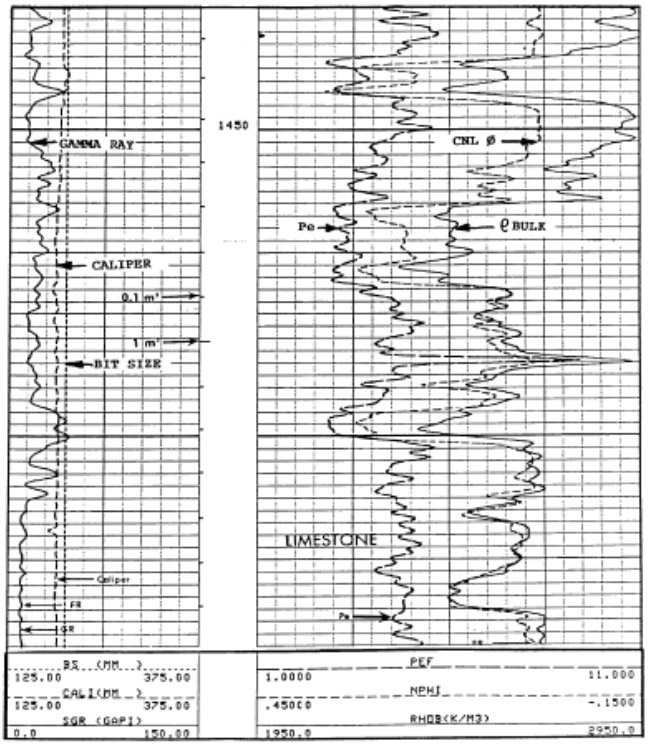
Generic name of log:	Microlog
Type of tool:	Microresistivity
Names and abbreviations:	ML
When run:	Water based muds
Purpose:	Highlights porous and perm zones: measures R_{xo}
Limitations:	Cannot be used in oil-based muds
Often combined with:	Triple combo
Operating principle:	Pad contact, reveals Δ res between mudcake and form resisitivity
Curves recorded:	$R_{1''\times1''}$ — micronormal $R_{2''}$ — micro-inverse *SP*, *GR*, *Micro-caliper*

Fig. 1-C8—Microlog. Courtesy of Halliburton.



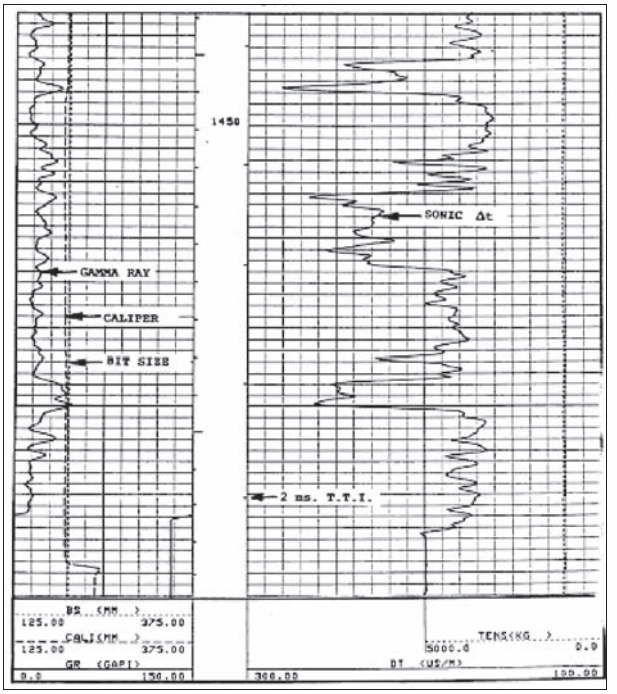
Generic name of log:	Neutron density
Type of tool:	Porosity
Names and abbreviations:	CNL-FDC
When run:	Standard porosity log
Purpose:	Measures formation porosity, ϕ; indicates lithogy and gas
Limitations:	Requires fluid-filled borehole
Often combined with:	Induction or laterolog
Operating principle:	Tools emit neutrons and γ rays — and detect returning radiation
Curves recorded:	ϕ_N — thermal neutron porosity ρ_B — formation bulk density and $\Delta\rho$-density correction *SP*, *GR*, *Caliper*

Fig. 1-C9—Neutron-density.



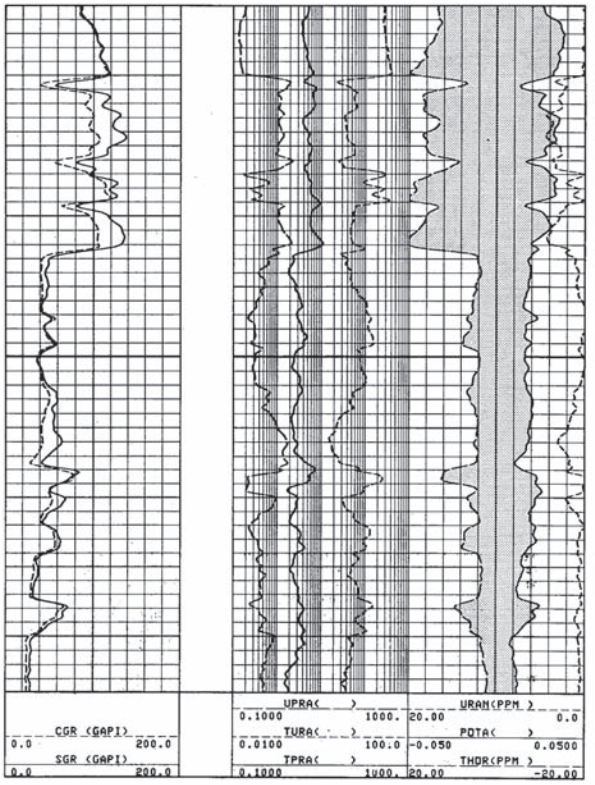
Generic name of log:	Litho-density
Type of tool:	Lithology indicator
Names and abbreviations:	LDT
When run:	Standard + porosity log
Purpose:	Measures ρ_B and P_e (photoelectric factor)
Limitations:	Behaves poorly in rugose hole
Often combined with:	Induction or laterolog as part of triple-combo
Operating principle:	Tools emits γ rays and detects returning γ's and energy spectrum
Curves recorded:	P_e — photoelectric factor ρ_B — formation and $\Delta\rho$-density correction *Caliper, GR*

Fig. 1-C10—Litho-density log (*Introduction to Open Hole Logging*). Courtesy of Schlumberger.



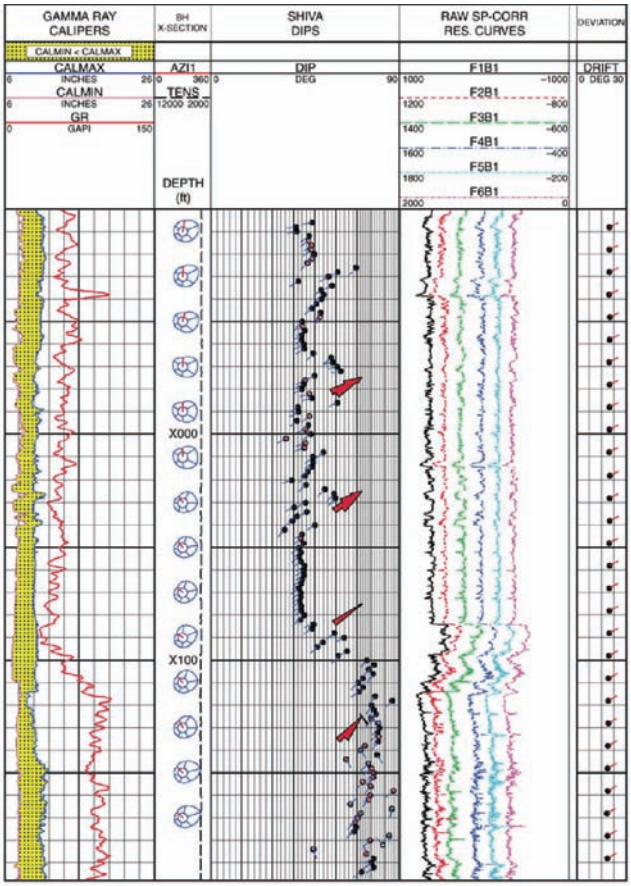
Generic name of log:	Sonic
Type of tool:	Porosity and elastic formation properties
Names and abbreviations:	BHC, Acoustilog, Long Spacing Sonic, Dipole Sonic, Waveform Sonic
When run:	Stand-alone or as part of quad-combo
Purpose:	Measures Δt comp. and shear, indicates lithology, fractures, and elastic constant
Limitations:	Requires fluid-filled borehole
Often combined with:	Induction or laterolog
Operating principle:	Ultrasonic transmitters and receivers measure signal speed and amplitude
Curves recorded:	Δt_c — compressional slowness Δt_s — shear slowness *SP*, *GR*, *Caliper*

Fig. 1-C11—Sonic log (*Introduction to Open Hole Logging*). Courtesy of Schlumberger.



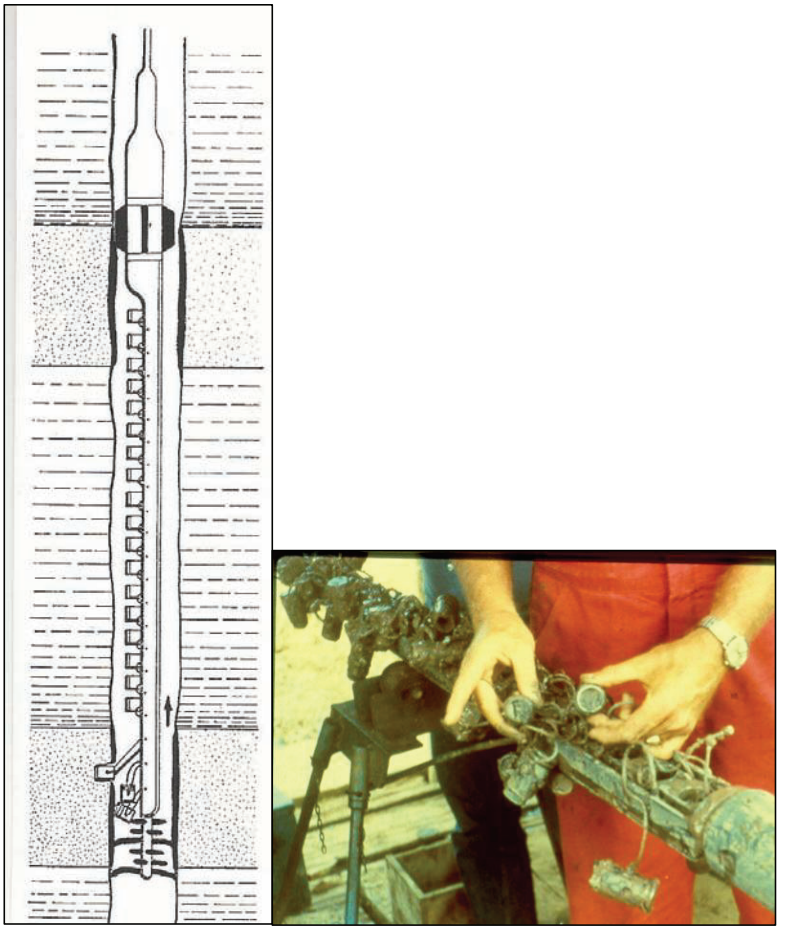
Generic name of log:	Spectral gamma ray
Type of tool:	Radioactive
Names and abbreviations:	NGS, Spectralog
When run:	Stand-alone or as part of triple-combo in open- or cased-hole
Purpose:	Natural γ ray activity and components; clay typing; source rock detection
Limitations:	Slow logging speed
Often combined with:	Neutron-density
Operating principle:	γ ray energy spectrum characterizes source elements emitting γ's
Curves recorded:	K — potassium, Th — thorium and U — uranium

Fig. 1-C12—Natural gamma ray spectral log.



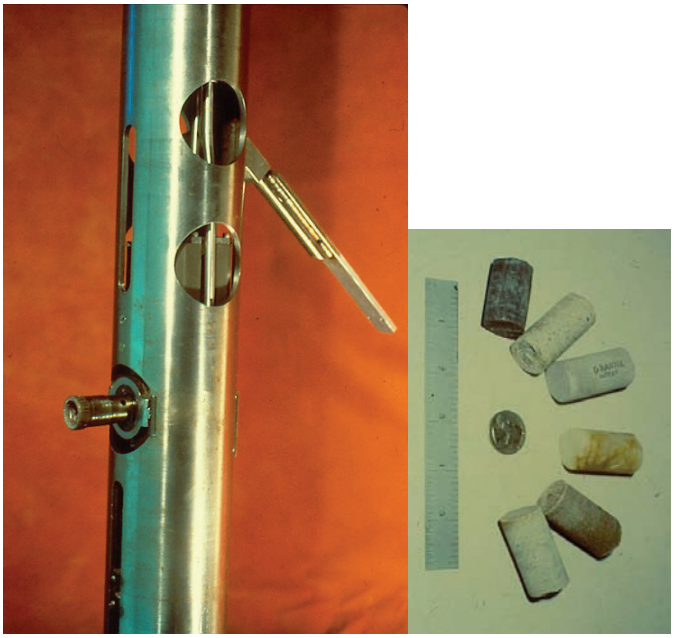
Generic name of log:	Dipmeter
Type of tool:	4-arm or 6-arm dipmeter
Names and abbreviations:	HDT, SHDT, HEDT, SED
When run:	In openhole; water- and oil-based mud versions available
Purpose:	Computer formation dip and azimuth
Limitations:	Slow logging speed
Often combined with:	Neutron-density
Operating principle:	Independent pad electrodes record multiple correlation curves
Curves recorded:	Correlation curves, hole dev, hole azimuth, tool orientation

Fig. 1-C13—Dipmeter (Halliburton Wireline and Perforating Services). Courtesy of Halliburton.



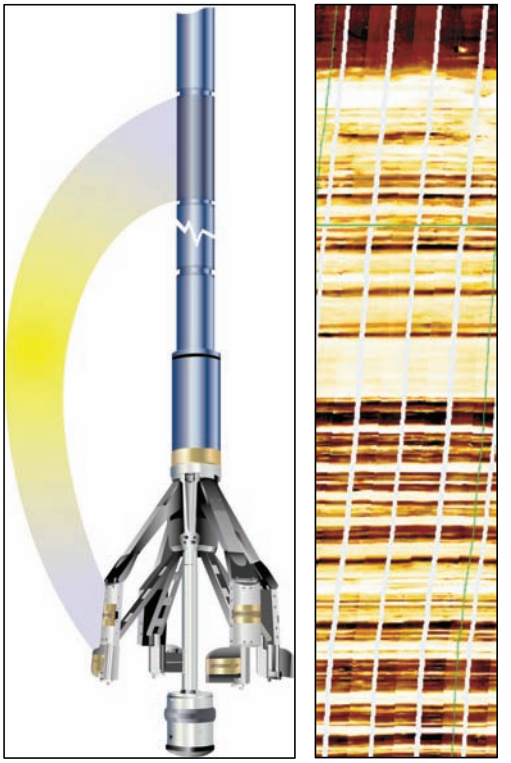
Generic name of log:	Percussion sidewall coring
Type of tool:	Multiple percussion sidewall cores
Names and abbreviations:	SWC
When run:	In openhole
Purpose:	Obtain rock samples
Limitations:	May induce fractures in samples of hard rock
Often combined with:	GR for depth correlation
Operating principle:	Gunpower charge propels coring cylinder into formation

Fig. 1-C14—Percussion sidewall coring.



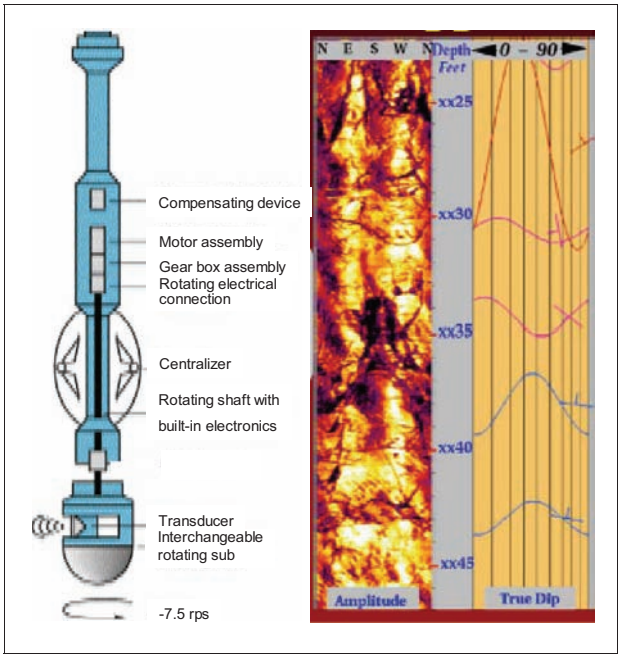
Generic name of log:	Rotary sidewall coring
Type of tool:	Multiple drilled sidewall cores
Names and abbreviations:	RSCT
When run:	In openhole
Purpose:	Obtain undamaged rock samples
Limitations:	Requires fluid-filled borehole
Often combined with:	Difficult to use in very large holes and/or unconsolidated formations
Operating principle:	GR for depth correlation
Curves recorded:	Hydraulic motor rotates cylindrical core barrel and bit

Fig. 1-C15—Rotary sidewall coring.



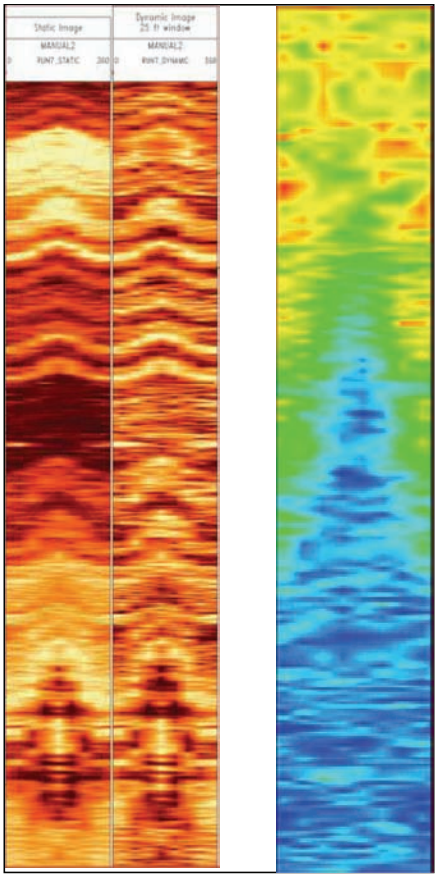
Generic name of log:	Formation micro imager
Type of tool:	Electrical borehole imaging device
Names and abbreviations:	FMI, FMS, FRI, EMI, STAR
When run:	In openhole
Purpose:	Obtain image of borehole wall by means of electrical contrast
Limitations:	Difficult to use in very large holes; requires special version for oil-based muds
Often combined with:	GR for depth correlation
Operating principle:	Multiple pads with multiple electrodes record formation resistivity details

Fig. 1-C16—Electrical borehole imager.



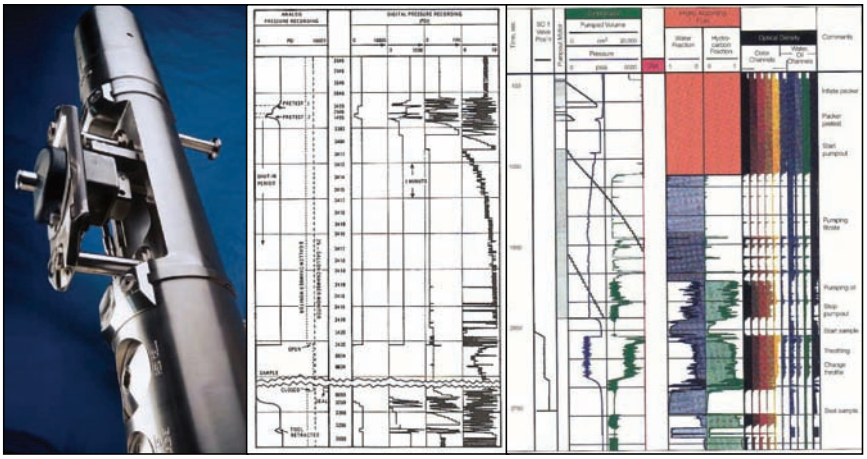
Generic name of log:	Ultrasonic formation imager
Type of tool:	Acoustic (sonar) imaging device
Names and abbreviations:	CAST, CBIL, UBI, AST
When run:	In openhole for formation images; in cased-hole for tubular inspection
Purpose:	Obtain image of borehole wall/casing through acoustic travel time and reflectivity
Limitations:	Difficult to use in very large holes
Often combined with:	GR for depth correlation
Operating principle:	Revolving transducer scans 360°; records echo time and amplitude

Fig. 1-C17—Ultrasonic borehole imager.



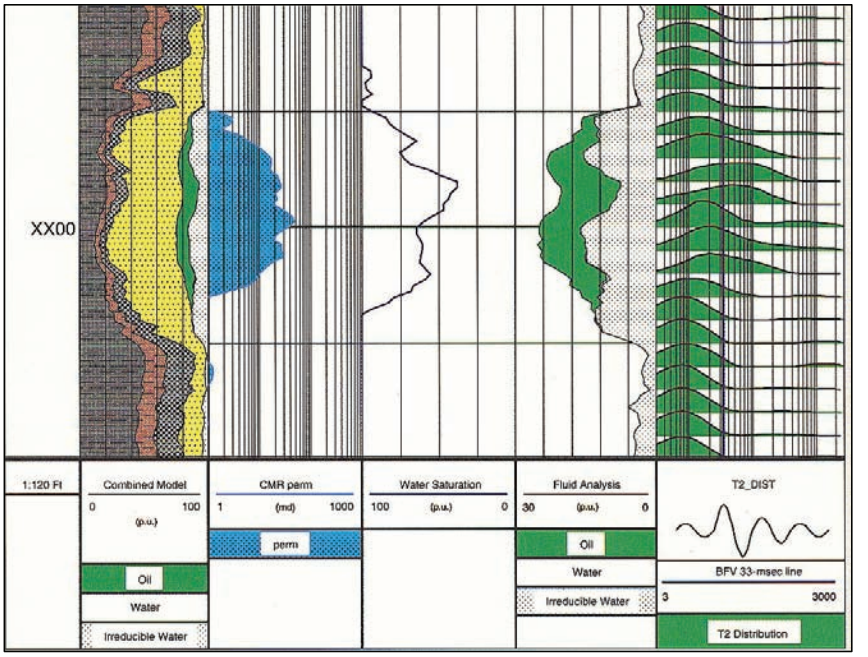
Generic name of log:	LWD imaging
Type of tool:	Density or gamma ray sensors on rotated drillpipe
Names and abbreviations:	In openhole while drilling
When run:	Obtain image of borehole wall while drilling
Purpose:	Requires rotation of the drillstring
Limitations:	Requires fluid-filled borehole
Often combined with:	Other LWD sensors
Operating principle:	Oriented sensor records segmented readings as pipe is rotated

Fig. 1-C18—LWD formation density image (left), LWD gamma ray image (right).



Generic name of log:	Wireline formation tester
Type of tool:	Fluid sampler and pressure tester
Names and abbreviations:	RFT, MDT
When run:	In openhole
Purpose:	Obtain sample of formation fluid and record formation pressures and transients
Limitations:	Propensity to get stuck
Often combined with:	Multiple mix-and-match components for fluid ID and capture
Operating principle:	Fluid from probe pumped through sensors and rejected or captured
Parameters recorded:	Pressures, fluid resistivity and pH, $T_{2bulk(NMR)}$

Fig. 1-C19—Wireline formation tester.



Generic name of log:	Nuclear magnetic resonance
Type of tool:	Rock pore space analyzer
Names and abbreviations:	CMR, MRIL
When run:	In openhole
Purpose:	Determine porosity, pore-size distribution, and permeability
Limitations:	Reads close to the borehole in the invaded (S_{xo}) zone
Often combined with:	Run as a stand-alone tool
Operating principle:	Polarizes H nuclei with magnet then uses RF to sense proton precession
Parameters recorded:	Free fluid index, clay-bound water, irreducible water, pore-size distribution

Fig. 1-C20—NMR.

Chapter 2

Mud Logging

As the old saying goes, "If you throw enough mud, some of it is bound to stick." In the case of mud logging, the name stuck. Today, however, mud logging embraces far more than just monitoring mud returns during the drilling process. It would be more elegant and more informative to refer to it as "hydrocarbon well logging." Mud logging includes measurements of both the progress of the drilling operation itself and the contents and properties of the formations drilled. Some of the information gathered is vital to the drilling engineer, but of little use to the formation evaluator. Other items are vitally important to the seeker of porous and permeable formations with recoverable hydrocarbons.

Not all wells are drilled with a mud logging unit in operation, and where mud logging equipment is present, all possible measurements are not necessarily recorded. The objective here is to summarize the most commonly recorded parameters and to review their use, interpretation, and integration into the overall formation evaluation effort.

During well drilling, the drill bit crushes the rock it encounters, and cuttings are circulated to the surface by the mud. If the rock being drilled is hydrocarbon-bearing, traces of oil, gas, or both will reach the surface in both the mud and the bit cuttings. These traces can be quantified, recorded, and interpreted using a number of measurement techniques, the purpose of which is to provide indications of formation porosity, lithology, and hydrocarbon content **(Fig. 2.1)**. It is important to bear in mind when discussing mud logging that actual samples of the formation and its contents are physically available for inspection, usually within a relatively short time after drilling through them. No other form of formation evaluation (except coring) can offer such incontrovertible evidence—unless an uncontrolled blowout, offering proof positive, is included as a formation evaluation method, something most would prefer to avoid.

2.1 Measurements Related to the Drilling Process

Many of the measurements appearing on a mud log are of direct interest only to the drilling engineer. Such measurements may include continuous monitoring of

- Mud properties (e.g., weight, viscosity, salinity, temperature)
- Weight on bit, hook load, pump speed, etc.
- Pit levels
- Presence of H_2S

Many of these parameters may be combined in an interpretative fashion to give indirect indications of porosity and pore pressure. Through the use of the "d" exponent, for example, the driller may be forewarned of the approach of an overpressured zone and may take appropriate action to increase the mud weight. Although these measurements are of importance to those charged with

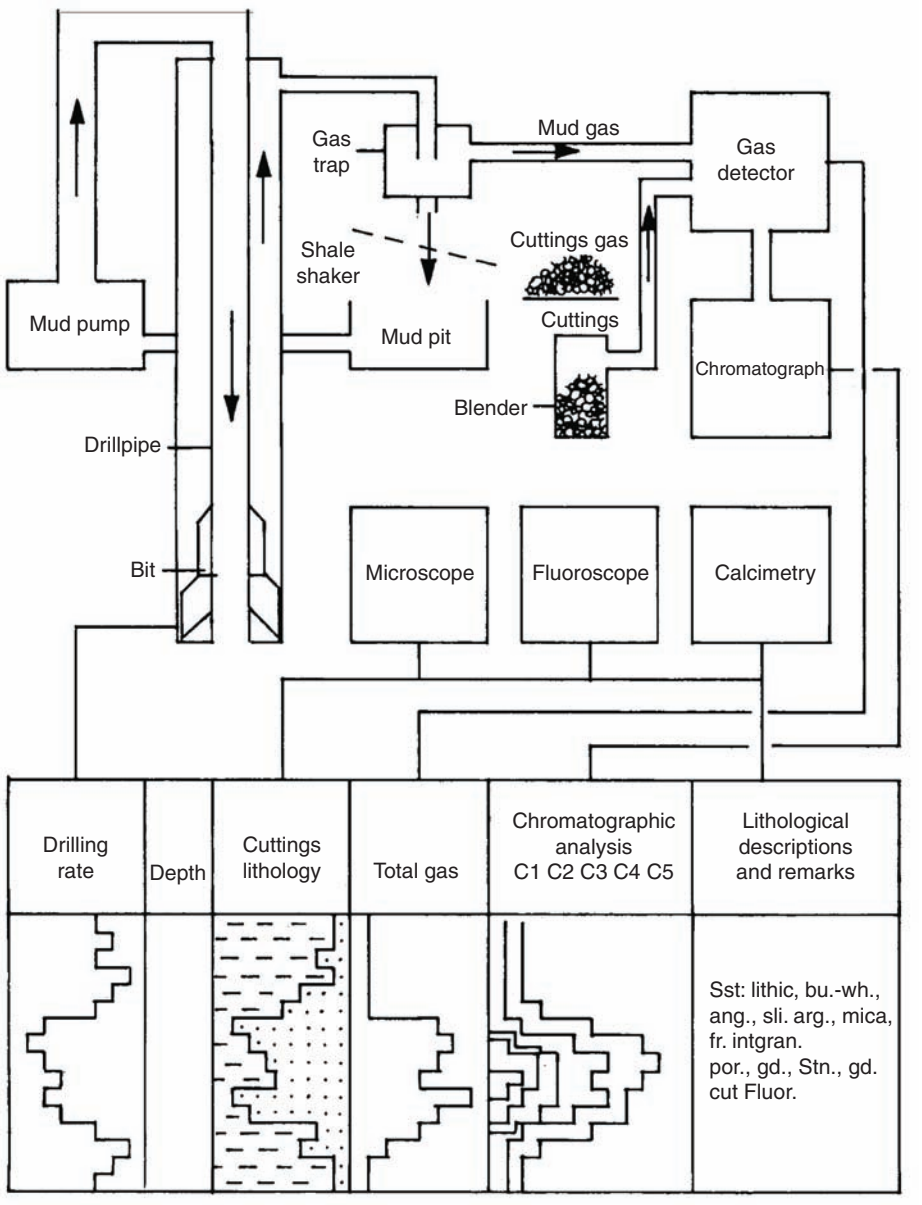


Fig. 2.1—Schematic of mud logging data gathering and presentation.

the expedient and economic drilling of the well, the formation evaluator is more interested in records that give direct or indirect indications of hydrocarbons.

2.2 Measurements Relevant to Formation Evaluation

The measurements of interest to the analyst are

- Penetration rate
- Mud gas detection and chromatographic gas analysis
- Cuttings gas detection and analysis
- Cuttings description and analysis for shows

Except for the penetration rate, all these measurements are lagged (i.e., a time lag exists between the moment the bit liberates cuttings and fluids into the wellbore and the time these same fluids and bit cuttings reach the surface). Considerable care is therefore required to place mud and cuttings samples correctly at the proper depth on the well's mud log. Lag times in deep wells may reach several hours. The lag time may be calculated provided that the pump capacity and pump stroke rate are known and that the annular volume between the drillpipe and the formation or casing can be estimated. In washed-out holes, this value can be difficult to estimate. An alternative method is to drop a carbide pill into the drillstring at the surface. When the pill reaches the bit, it is broken open and, reacting chemically with the water in the mud, produces acetylene gas, which is circulated from the bottom up to the surface and detected. Because the dimensions of the drillstring are accurately known, the time for the downward journey of the pill can be calculated exactly.

If properly lagged, all measurements should appear on the mud log on depth with each other. When correlating a mud log with a wireline log, the best curve to use is the rate of penetration (ROP). This usually shows a good correlation with a gamma ray or SP curve.

The mud logger's sources of data include

- Gas extracted from the mud at the gas trap
- Cuttings collected at the shale shaker
- Gas liberated from cuttings in the blender

The types of measurement possible include

- Total gas concentration, from either the mud or the cuttings
- Chromatographic gas analysis
- Visual inspection of cuttings by normal and ultraviolet light
- Calcimetry for carbonate analysis

2.3 Measurement Techniques

2.3.1 Gas Concentration. The measurement of gas concentration in the mud is made by use of either a hot-wire detector, a flame-ionization detector (FID), or a Katharometer. All three types of detectors produce a total gas reading. The modern norm (SPWLA 1983) is to report total gas in universal volumetric units (i.e., in terms of volume/volume) and standardized to equivalent methane in air (EMA). Therefore, the units on the mud log may be quoted as percent, ppk, or ppm.

Hot-Wire Gas Detector [Catalytic Combustion Detector (CCD)]. The principle of the hot-wire detector is simple. A wire resistor is heated to a temperature that ensures combustion of any hydrocarbons flowed past it in a mixture with air. The combustion of hydrocarbon gas, when present, heats the wire and thus raises its electrical resistance, which in turn is monitored by a bridge circuit. Such a device can be accurately calibrated. Regulators assure a constant flow of air and mud or cuttings gas, and the output can be continuously recorded as total gas on the mud log.

FID. A high-temperature hydrogen flame is maintained in a chamber through which mud or cuttings gas is circulated. When hydrocarbons are encountered, the heat of the hydrogen flame is sufficient to ionize the hydrocarbons. A pair of electrodes in the chamber senses the presence of the ions by the small current that can flow through the ionized gas.

Katharometer [Thermal Conductivity Detector (TCD)]. This device responds to the thermal conductivity of the mixture of mud or cuttings and the carrier gas (air) as measured by a heated platinum wire. It is less sensitive than either the FID or the CCD.

2.3.2 Detector Calibration. Calibration of any of these total-gas detectors should be carried out in terms of EMA. The response of the device will then be a function of both the gas concentration

and the gas composition. For example, if a mixture of 25% methane and 75% air passes through the detector, then the response will be

$$25 \times 1 = 25\% \text{ EMA} \quad (2.1)$$

If, on the other hand, a mixture containing gases with more carbon atoms per molecule (higher C number) passes through the detector, the percentage of each gas is weighted by its C number, as shown in **Table 2.1**. Thus, the same total gas reading could be obtained with only half as much ethane, a third as much propane, etc.

It is also common to correct the raw readings for a number of variables related to the drilling process. These include

- Mud-pump output
- Penetration rate
- Volume of mud per unit length of hole
- Bit size

These are combined to obtain a dilution ratio that is multiplied by the raw total gas reading to give a normalized reading that is independent of the mechanical details of the drilling process.

2.3.3 Gas Chromatography. To determine the composition of the gas, a chromatograph is used. Gas is passed through a column packed with an inert powdered solid **(Fig. 2.2)**. Different components of the gas mixture take different times to travel the length of the column and on exiting may be detected by one or another of the gas detectors already discussed. Output from the chromatograph is recorded on the log in ppm or ppk of each component.

2.3.4 Visual Inspection. Cuttings are visually inspected on a regular basis to determine

- Approximate porosity, lithology, and texture
- Presence of hydrocarbons
- Chemical makeup

Because it takes about 15 minutes to process each sample, the frequency (by depth) of the reported results will be a function of the drilling rate. In other words, if the drilling rate is 100 ft/hr, the best that a mud logger can do to keep up is to report samples every 25 ft (4 per hour). Therefore, in hard rock with a drilling rate of 8 ft/hr, samples can be processed every 2 ft.

TABLE 2.1—MUD GAS CARBON NUMBERS AND EMA

C Number	Gas	Formula	% Present	% EMA
C 1	Methane	CH_4	8	8 × 1 = 8
C 2	Ethane	C_2H_6	6	6 × 2 = 12
C 3	Propane	C_3H_8	4	4 × 3 = 12
I C 4	Iso-Butane	C_4H_{10}	4	6 × 4 = 24
n C 4	Butane	C_4H_{10}	2	
C 5	Pentane	C_5H_{12}	1	5 × 1 = 5
Totals			25%	61%

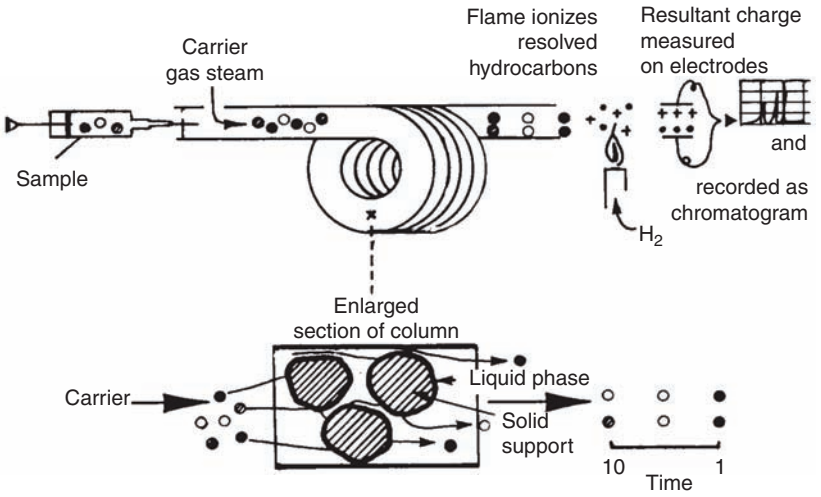


Fig. 2.2—Gas chromatography. Courtesy of Continental Laboratories.

2.3.5 Written Description. A written description follows a set of rules so that a fixed order is used:

- Rock type, underlined and followed by classification
- Color
- Texture, including grain size, roundness, and sorting
- Cement or matrix materials
- Fossils and accessories
- Sedimentary structures
- Porosity and oil shows

For example

> *Ls: ool, Grst, brn, med-crs, arg, Brach-Bry, glauc, gd intpar, por, gd Stn, gd cut Fluor*

can be translated to mean

> *limestone, oolitic, grainstone, brown, medium coarse, argillaceous, brachiopod bryozoa, glauconitic, good interparticle porosity, good stain, good cut fluorescence*.

Appendix 2B to this chapter lists all the abbreviations commonly used to describe rocks in this geological telegraphese.

2.3.6 Hydrocarbon Determination. If hydrocarbons are still present in the cuttings after their journey up through the mud column, they can be detected with a number of techniques. These include

- Smelling the sample
- Visual inspection under ultraviolet light
- Subjecting the sample to chemical reagents

A trained nose can distinguish an oil odor from a condensate odor. In ordinary light, the cuttings may have a visible oil stain, or oil may be seen bleeding from the rock fragments. Under ultraviolet light, these hydrocarbons will fluoresce, and the API gravity of the oil will influence the color seen, as detailed in **Table 2.2**.

TABLE 2.2—API GRAVITY AND COLOR OF FLUORESCENCE

API Gravity	Color of Fluorescence
less than 15	Brown
15 to 25	Orange
25 to 35	Cream or yellow
35 to 45	White
45 or over	Blue-white to violet

If no fluorescence is seen on the untreated sample, then a chemical reagent is added. This is usually a solvent (chlorothene or acetone, for example) that brings out any hydrocarbon still in the sample. Such solvent-extracted hydrocarbon is referred to as a *cut.* Other chemicals used include hydrochloric acid, which will cause bubbling on contact with carbonates, a reaction that forms the basis for calcimetry.

2.3.7 Calcimetry. A weighed sample of cuttings (usually one gram) is placed in contact with a standard volume of HCl (a few cubic centimeters) in a closed chamber. If either limestone ($CaCO_3$) or dolomite ($CaMgCO_3$) is present, the acid reacts with the rock to form carbon dioxide gas (CO_2). The calcimeter measures both the volume of CO_2 liberated and the rate at which it is liberated. Because the reaction with dolomite proceeds more slowly than the reaction with limestone, it is possible to distinguish the relative concentrations of these two carbonates in a sample.

2.3.8 Evaluation of Shows. When reading a mud log, it is useful to be able to estimate formation productivity in a semiquantitative manner. A number of authors have suggested ways to combine the readings from chromatographic analysis to fingerprint the true formation content. One method (Haworth et al. 1984) suggests using three ratios to type the formation. These are

Gas wetness ratio (GWR) = C2 + / C1 +
Light-to-heavy ratio (LHR) = (C1 + C2) / (C3 + C4 + C5)
Oil character qualifier (OCQ) = (C4 + C5) / C3.

The diagnostics reported are as shown in **Table 2.3**. The LHR correlates well with the API gravity, that is, a high LHR corresponds to low-density (high-API) hydrocarbons. The OCQ ratio is useful as a qualifier when excessive methane is present.

Another technique is to plot straight C-number ratios on a special logarithmic grid, as shown in **Fig. 2.3**. The type of production is predicted according to the area of the graph on which the points fall.

TABLE 2.3—HYDROCARBON POTENTIAL [After Haworth et al. (1984)]

Hydrocarbon	GWR (%)	LHR (%)	OCQ Ratio
Light dry gas	< 0.5	100 +	Very low
Medium density gas	0.5–17.5	< 100	< 0.5
Light oil	5–10	17.5	> 0.5
Medium gravity oil	17.5–40	< 10	> 1
Residual oil	> 40	5–10	> 2
Coal bed	15–20	< 100	Very low

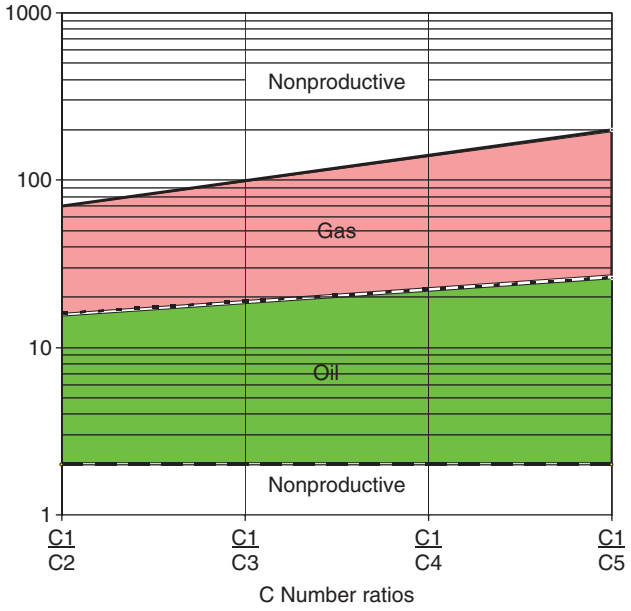


Fig. 2.3—Formation production potential from carbon number ratios.

2.4 Summary

Hydrocarbon well logging can supply real-time data to both the formation evaluator and the drilling engineer and enables a hands-on investigation of both the rocks penetrated and their pore fluids, subject to the vagaries of the process by which the samples arrive in the analyst's hands. When the measurements are made using calibrated equipment, the analyst can hope to know, before running wireline logs, the location of reservoir rocks in the column drilled and to have a semiquantitative idea of their porosity and hydrocarbon content. Apart from these considerations, use of a mud logging unit will help in making decisions on coring and testing depths.

References

Haworth, J.H., Gurvis, R.L., and Sellens, M.P. 1984. Reservoir Characterization by Mathematical Treatment of Hydrocarbon Gas Show. *Proc.,* SPWLA 25th Annual Logging Symposium, New Orleans, June 10–13.

SPWLA. 1983. *Hydrocarbon Well Logging Recommended Practice,* second edition. Houston: Society of Professional Well Log Analysts.

General References

API RP 34, Recommended Practice: Standard Hydrocarbon Mud Log Form. 1958. Dallas, API.

API 2564, Conversion of Operational and Process Measurement Units to the Metric (SI) System, first edition. 1974. Washington, DC: API.

API RP 31, Recommended Practice and Standard Form for Electrical Logs, third edition. 1976. Dallas: API.

Association of Desk and Derrick Clubs. 1973. *D&D Standard Oil Abbreviator*, second edition. Tulsa: Penn Well.

Helender, D.P. 1969. Drilling-Mud Logging Becoming More Important in Formation Evaluation. In *Oil and Gas Equipment,* four-part series (February, March, April, May).

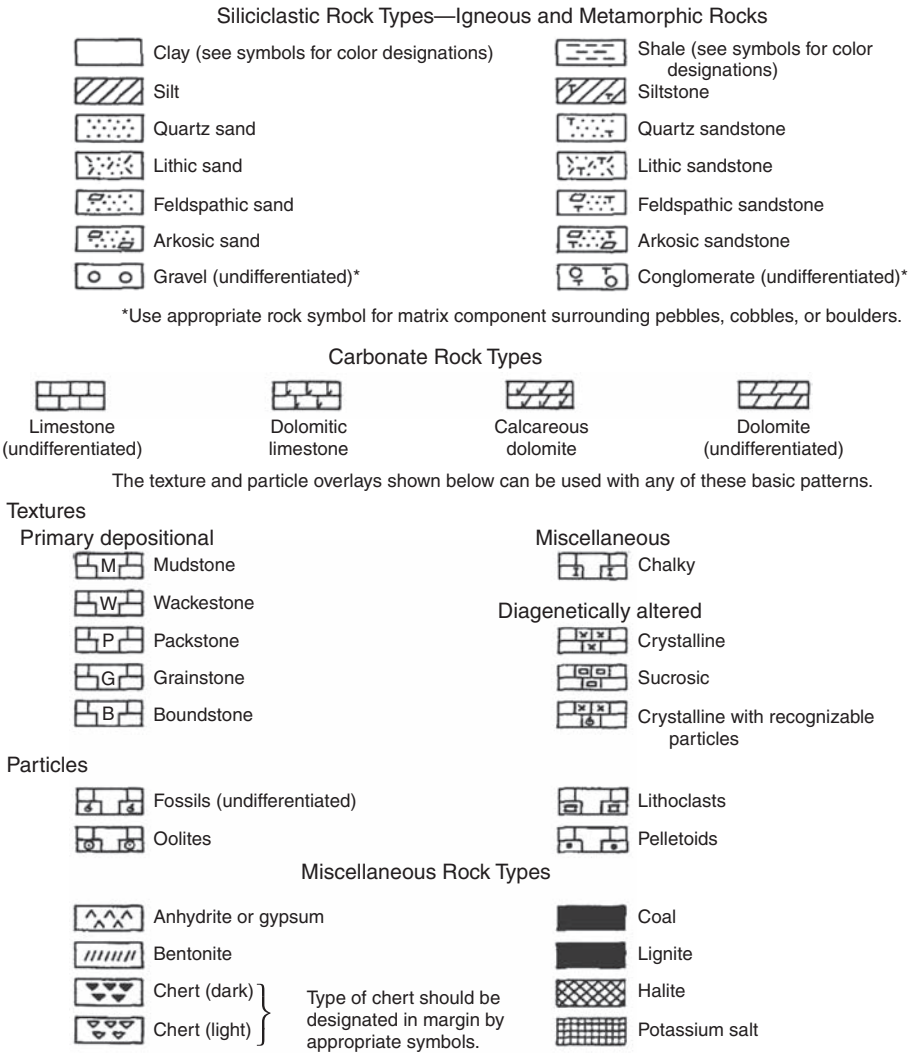
Mercer, R.F. 1974. Liberated, Produced, Recycled, or Contamination? *Proc.,* SPWLA 15th Annual Logging Symposium, New Orleans, June 4–7.

Pixler, B.O. 1969. Formation Evaluation by Analysis of Hydrocarbon Ratios. *J. Pet Tech* **21** (6): 665–670. http://dx.doi.org/ 10.2118/2254-PA.

Swanson, R.G. 1981. *Sample Examination Manual*. Tulsa: Methods in Exploration Series, American Association of Petroleum Geologists.

Appendix 2A: Symbols Used to Describe Lithology

Reprinted by permission of the SPWLA from *Hydrocarbon Well Logging Recommended Practice*, second edition, December 1983.




Extrusive


Metamorphic


Intrusive


Pyroclastic

Specific rock types can be designated by using symbols and/or inserting the first two letters of rock name in center of lithic column.

Secondary Components

Modifying Components


Anhydritic


Cherty


Very sandy


Argillaceous


Dolomitic


Sandy


Calcareous


Micaceous


Slightly sandy


Carbonaceous


Salt hoppers


Silty

Cements


Anhydrite


Calcite


Chert


Dolomite


Quartz

Streaks and Lenses


Argillaceous


Calcareous


Dolomitic


Sandy


Silty

Interbeds and Intercalations





Use same symbols as for streaks and lenses enclosed within above symbols.

Concretions and Nodules


anhy.
Anhydritic


calc.
Calcareous


ch
Cherty or siliceous


fe.
Ironstone or other ferruginous material


phos.
Phosphatic

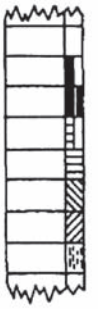

sid.
Sideritic

Miscellaneous Symbols

N.S. No sample

No Information

Lst
Dol
Ss
Can be used for long continuous sections of uniform lithology in place of drafted symbols.



Colors

Color description for shales can be illustrated in column (½ in.) along right margin of log with these symbols.

Fossils

rd. Red algae

gn. Green algae

Accessories

Ash or tuff

Chlorite

Quartz crystals

Siderite grains

Mineralization

Cal.

Cal.

Type of vein, fracture or vug filling indicated by abbreviation of mineral

Cherts

Transparent

bl

gy

Use appropriate chert symbol followed by abbreviation of color.

Oil Shows

Poor oil stain

Good to excellent oil stain

Dead oil stain

Appendix 2B: Abbreviations Used to Describe Lithology

TABLE B-1—ABBREVIATIONS USED TO DESCRIBE LITHOLOGY (SPWLA 1983)

above	ab	biosparite	Biosp
absent	abs	biostrom (-al)	Biost, biost
abundant	abd	biotite	Biot
acicular	acic	bioturbated	bioturb
after	aft	birdseye	Bdeye
agglomerate	Aglm	bitumen (-inous)	Bit, bit
aggregate	Agg	black (-ish)	blk; blksh
algae, algal	Alg, alg	blade (-ed)	Bid, bid
allochem	Allo	blocky	blky
altered	alt	blue (-ish)	bl, bish
alternating	altg	bored (-ing)	Bor, bor
amber	amb	botryoid (-al)	Bot, bot
ammonite	Amm	bottom	Btm
amorphous	amor	boudinage	boudg
amount	amt	boulder	Bld
amphipora	Amph	boundstone	Bdst
and	&	brachiopod	Brach
angular	ang	brackish	brak
anhedral	ahd	branching	brhg
anhydrite (-ic)	Anhy, anhy	break (-en)	Brk, brk
anthracite	Anthr	breccia (-ted)	Brec, brec
aphanitic	aph	brighter	brt
apparent	apt	brittle	brit
appears	ap	brown	bm
approximate	apprx	bryozoan	Bry
aragonite	Arag	bubble	Bubl
arenaceous	aren	buff	bu
argillaceous	arg	bulbous	bulb
argillite	argl	burrow (-ed)	Bur, bur
arkose (-ic)	Ark, ark		
as above	a. a.	calcarenite	Clcar
asphalt (-ic)	Asph, asph	calcareous	calc
assemblage	Assem	calcilutite	Clcit
associated	assoc	calcirudite	Clcrd
at	@	calcisiltite	Clsit
authigenic	authg	calcisphaera	Casph
average	Av, av	calcisphere	Clcsp
		calcite (-ic)	Calc, calctc
band (-ed)	Bnd, bnd	caliche	cche
barite (-ic)	bar	carbonaceous	carb
basalt (-ic)	Bas, bas	carbonate	crbnt
basement	Bsmt	carbonized	cb
become(-ing)	bcm	cavern (-ous)	Cav, cav
bed (-ed)	Bd, bd	caving	Cvg
bedding	Bdg	cement (-ed, -ing)	Cmt, cmt
belemnites	Belm	center (-ed)	cntr
bentonite (-ic)	Bent, bent	cephalopod	Ceph
bioclastic	biocl	chaetetes	Chaet
bioherm (al)	Bioh, bioh	chalcedony (-ic)	Chal, chal
biomicrite	Biomi	chalk (-y)	Chk, chky

TABLE B-1—ABBREVIATIONS USED TO DES CRIBE LITHOLOGY (SPWLA 1983) (CONT'D)			
charophyte	Char	crystal (-line)	XI, xin
chert (-y)	Cht, cht	cube, cubic	Cub, cub
chitin (-ous)	Chit, chit	cuttings	Ctgs
chitinozoa	Chtz	cypridopsis	Cyp
chlorite (-ic)	Chlor, chlor		
chocolate	choc	dark (-er)	dk, dkr
circulate (-ion)	circ, Circ	dead	dd
clastic	clas	debris	Deb
clay (-ey)	Cl, cl	decrease (-ing)	Decr, decr
claystone	Clst	dendrite (-ic)	dend
clean	cln	dense	dns
clear	clr	depauperate	depau
cleavage	Clvg	description	Descr
cluster	Clus	desiccation	dess
coal	C	detrital	detr
coarse	crs	devitrified	devit
coated (-ing)	cotd, cotg, Cotg	diabase	Db
coated grains	cold gn	diagenesis (-etic)	Diagn, diagn
cobble	Cbl	diameter	Dia
colonial	coin	disseminated	dissem
color	Col, cot	distillate	Dist
common	com	ditto	" or do
compact	cpct	dolomite (-ic)	Dol, dot
compare	cf	dolostone	dolst
concentric	cncn	dominant (-ly)	dom
conchoidal	conch	drillstem test	DST
concretion (-ary)	Conc, conc	drilling	drig
conglomerate (-ic)	Cgl, cgl	drusy	dru
conodont	Cono		
conquina (-oid)	coqid	earthy	ea
considerable	cons	east	E
consolidated	consol	echinoid	Ech
conspicuous	conspic	elevation	Elev
contact	Ctc	elongate	elong
contamination (-ed)	Contam, contam	embedded	embd
content	Cont	endothrya	Endo
contorted	cntrt	equant	eqnt
coral, coralline	Cor, corin	equivalent	Equiv
core	c	euhedral	euhd
covered	cov	euryamphipora	Euryamph
cream	crm	euxinic	eux
crenulated	cren	evaporite (-itic)	Evap, evap
crinkled	crnk	excellent	ex
crinoid (-al)	Crin, crinal	exposed	exp
cross	x	extraclast (-ic)	Exclas, exclas
cross-bedded	x-bd	extremely	extr
cross-laminated	x-lam	extrusive	exv
cross-stratified	x-strat		
crumpled	crpld	facet (-ed)	Fac, fac
crypridopsis	Cyp	faint	fnt
cryptocrystalline	crpxin	fair	fr

TABLE B-1—ABBREVIATIONS USED TO DESCRIBE LITHOLOGY (SPWLA 1983) (CONT'D)			
fault (-ed)	Flt, ft	grading	grad
fauna	Fau	grain (-s, -ed)	Gr, gr
favosites	Fvst	grainstone	Grst
feet	Ft	granite	Grt
feldspar (-athic)	Fspr, fspr	granite wash	G.W.
fenestra (-al)	Fen, fen	granule (-ar)	Gran, gran
ferro-magnesian	Fe-mag	grapestone	Grapst
ferruginous	ferr	graptolite	Grap
fibrous	fibr	gravel	Grv
fill (-ed)	fd	gray, grey (-ish)	gry, grysh
fine (ly)	f, fnly	graywacke	Gwke
fissile	fis	greasy	gsy
flaggy	fig	green (-ish)	gn, gnsh
flake, flaky	Flk, fk	grit (-ty)	Gt, gt
flat	f	gypsum (-iferous)	Gyp, gyp
flesh	fls		
floating	fltg	hackly	hkl
flora	Flo	halite (-iferous)	Hal, hal
fluorescence (-ent)	Fluor, fluor	hard	hd
foliated	fol	heavy	hvy
foot	Ft	hematite (-ic)	Hem, hem
foraminifer	Foram	heterogeneous	hetr
foraminiferal	foram	heterostegina	Het
formation	Fm	hexagonal	hex
fossil (-iferous)	Foss, foss	high (-ly)	hi
fracture (-d)	Frac, frac	homogeneous	horn
fragment (-al)	Frag, frag	horizontal	hor
framework	frmwk	hornblende	hornbd
frequent	freq	hydrocarbon	Hydc
fresh	frs		
friable	fri	igneous rock	Ig, ig
fringe (-ing)	Frg, frg	imbedded	imbd
frosted	fros	impression	imp
frosted quartz	F.Q.G.	in part	I.P.
fucoid (-al)	Fuc, fuc	inch	in
fusulinid	Fus	inclusion (-ded)	Incl, incl
		increasing	incr
gabbro	Gab	indistinct	indst
galeolaria	Gal	indurated	ind
gas	G	inoceramus	inoc
gastropod	Gast	insoluble	insl
generally	gen	interbedded	intbd
geopetal	gept	intercalated	intercal
gilsonite	Gil	intercrystalline	intxin
girvanella	Girv	interfragmental	intfrag
glass (-y)	Glas, glas	intergranular	intgran
glauconite (-itic)	Glauc, glauc	intergrown	intgn
globigerina (-inal)	Glob, glob	interlaminated	intrlam
gloss (-y)	Glos, glos	interparticle	intpar
gneiss (-ic)	Gns, gns	interpretation	intpt
good	gd	intersticies	inst, intstl

TABLE B-1—ABBREVIATIONS USED TO DESCRIBE LITHOLOGY (SPWLA 1983) (CONT'D)

interval	intvl	maroon	mar
intraclast (-ic)	Intclas, intclas	massive	mass
intraparticle	intrapar	material	Mat
intrusive	Intr, intr	matrix	Mtrx
invertebrate	invtb	maximum	max
iridescent	irid	medium	m or med
ironstone	Fe-st	member	Mbr
irregular (-ly)	irr	meniscus	men
isopachous	iso	metamorphic (-osed)	meta, metaph
ivanovia	ivan	metamorphic rock	Meta
		metasomatic	msm
jasper	jasp	mica (-aceous)	Mic, mic
joint (ed, -ing)	Jt, jt	micrite (-ic)	Micr, micr
		micro	mic
kaolin (-itic)	Kao, kao	micro-oolite	Microol
		microcrystalline	microxin
lacustrine	lac	microfossil	microfos
lamina (-itions, -ated)	Lam, lam	micrograined	micgr
large	lge	micropore (-osity)	micropor
laterite (-itic)	tat, lat	microspar	Microspr
lavender	lav	microstylolite	Microstyl
layer	Lyr	middle	Mid
leached	lchd	millolid	Millid
lens, lenticular	Len, lent	milky	mky
lentil (-cular)	len	mineral (-ized)	Min, min
light	lt	minor	mnr
lignite (-itic)	Lig, lig	minute	mnut
limestone	Ls	moderate	mod
limonite (-itic)	Lim, lim	mold (-ic)	Mol, mol
limy	lmy	mollusc	Moll
lithic	lit	mosaic	mos
lithographic	lithgr	mottled	mott
lithology (-ic)	Lith, lith	mud (-dy)	md, mdy
little	Ltl	mudstone	Mdst
littoral	litt	muscovite	Musc
local	loc		
long	lg	nacreous	nac
loose	lse	no sample	n.s.
lower	l	no show	n/s
lumpy	lmpy	no visible porosity	n.v.p.
luster	Lstr	nodules (-ar)	Nod, nod
lustre	Lstr	north	N
lutite	Lut	novaculite	Novac
		numerous	num
macrofossil	Macrofos		
magnetite, magnetic	Mag, mag	occasional	occ
manganese	Mn, mn	ochre	och
marble	Mbl	odor	od
marine	marn	oil	O
marl (-y)	Mrl, mrl	oil source rock	OSR
marlstone	Mrlst	olive	olv

TABLE B-1—ABBREVIATIONS USED TO DESCRIBE LITHOLOGY (SPWLA 1983) (CONT'D)			
olivine	olvn	poor (-ly)	p
oncolite (-oidal)	Onc, onc	porcelaneous	porcel
ooid (-al)	Oo, oo	porosity, porous	Por, por
oolicast (-ic)	Ooc, ooc	porous (-sity)	por
oolite (-itic)	Ool, oo1	porphyry (-itic)	prphy
oomold (-ic)	Oomol, oomol	possible (-ly)	poss
opaque	op	predominant (-ly)	pred
orange (-ish)	or, orsh	preserved	pres
orbitolina	Orbit	primary	prim
organic	org	prism (-atic)	pris
orthoclase	Orth	probable (-ly)	prob
orthoquartzite	O-Qtz	production	Prod
ostracod	Ostr	prominent	prom
overgrowth	ovgth	pseudo-oolite (-ic)	Psool, psool
oxidized	ox	pseudo-	ps
oyster	Oyst	pumice stone	Pst
		purple	purp
packstone	Pkst	pyrite (-ized, -itic)	Pyr, pyr
paper (-y)	Pap, pap	pyrobitumen	Pybit
paraparchites	Para	pyroclastic	pyrcl
part (-ly)	Pt, pt	pyroxene	pyrxn
particle	Par, par		
parting	Ptg	quartz (-ose)	Qtz, qtz
parts per million	PPM	quartzite (-ic)	Qtzt, qtzt
patch (-y)	Pch, pch		
pearly	prly	radial (-ating)	Rad, rad
pebble (-ly)	Pbl, pbl	radiaxial	Radax
pelecypod	Pelec	range	rng
pellet (-al)	Pel, pel	rare	r
pelletoid (-al)	Peld, peld	recemented	recem
pendular (-ous)	Pend, pend	recovery (-erect)	Rec, rec
pentamerus	Pent	recrystallized	rexizd
permeability (-able)	Perm, k, perm	red (-ish)	rd, rdsh
petroleum	Pet, pet	reef (-oid)	Rf, rf
phlogopite	Phlog	remains	Rem
phosphate (-atic)	Phos, phos	renalcis	Ren
phreatic	phr	replaced (-ment)	rep, Repl
phyllite, (-itic)	Phyl, phyl	residue (-ual)	Res, res
pin-point (porosity)	p.p.	resinous	rsns
pink	pk	rhomb (-ic)	Rhb, rhb
pinkish	pkish	ripple	Rpl
pisold (-al)	Piso, piso	rounded, frosted, pitted	r.f.p.
pisolite (-itic)	Pisol, pisol	rock	Rk
pitted	pit	round (-ed)	rnd, rndd
plagioclase	Plag	rubble (-bly)	Rbl, rbl
plant	Plt	rudistid	Rud
plastic	plas	rugose	rug
platy	plty		
polish, polished	Pol, pol	saccharoidal	sacc
pollen	Poln	salt (-y)	Sa, sa
polygonal	poly	salt and pepper	s&p

TABLE B-1—ABBREVIATIONS USED TO DESCRIBE LITHOLOGY (SPWLA 1983) (CONT'D)

salt cast (-ic)	sa-c	splintery	Splin
salt water	S.W.	sponge	Spg
same as above	a.a.	spore	Spo
sample	Spl	spotted (-y)	sptd, spry
sand (-y)	Sd, sdy	stachyode	Stach
sandstone	Sst	stain (-ed, -ing)	Stn, stn
saturation (-ated)	Sat, sat	stalactitic	stal
scales	sc	strata (-ified)	Strat, strat
scaphopod	Scaph	streak (-ed)	Strk, strk
scarce	scs	streaming	stmg
scattered	scat	striae (-ted)	Strl, strl
schist (-ose)	Sch, sch	stringer	strgr
scolecodont	Scol	stromatolite	Stromit, stromlt
secondary	sec	stromatoporoid	Strom
sediment (-ary)	Sed, sed	structure	Str
selenite	Sel	styliolina	Stylio
septate	Sept	stylolite (-itic)	Styl, styl
shadow	shad	sub	sb
shale (-y)	Sh, sh	subangular	sbang
shell	Shl	sublithic	sblit
shelter porosity	Shlt por	subrounded	sbrndd
show	shw	sucrosic	suc
siderite (-itic)	Sid, Sid	sugary	sug
sidewall core	S.W.C.	sulfur (-ous)	Su, su
silica (-iceous)	Sil, sil	superficial oolite	Spfool, spfool
silky	slky	surface	Surf
silt (-y)	Slt, slty	syntaxial	syn
siltstone	Sltst	syringopora	Syring
similar	sim		
size	sz	tabular (-ate)	tab
skeletal	skel	tan	tn
slabby	slb	tasmanites	Tas
slate (-y)	Sl, sl	tension	tns
slickenside (-d)	Slick, slick	tentaculites	Tent
slight (-ly)	sil, silly	terriginous	ter
small	sml	texture (-d)	Tex, tex
smooth	sm	thamnopora	Tham
soft	sft	thick	thk
solenpora	Solen	thin	thn
solitary	sol	thin section	T.S.
solution, soluble	Sol, sol	thin-bedded	t.b.
somewhat	smwt	throughout	thru
sorted (-ing)	srt, srtg	tight	ti
south	S	top	Tp
spar (-ry)	Spr, spr	tough	tgh
sparse (-ly)	sps, spsly	trace	Tr
speck (-led)	Spk, spkld	translucent	trnsl
sphaerocodium	Sphaer	transparent	trnsp
sphalerite	Sphal	trilobite	Tril
spherule (-itic)	Spher, spher	tripoli (-itic)	Trip, trip
spicule	Spic, spic	tube (-ular)	Tub, tub

TABLE B-1—ABBREVIATIONS USED TO DESCRIBE LITHOLOGY (SPWLA 1983) (CONT'D)

tuff (-aceous)	Tf, tf
type (-ical)	Typ, typ
unconformity	Unconf
unconsolidated	uncons
underclay	Uc
underlying	undly
unidentfiable	unident
uniform	uni
upper	u
vadose	Vad, vad
variation (-able)	Var, var
varicolored	vatic
variegated	vgt
varved	vrvd
vein (-ing, -ed)	Vn, vn
veinlet	Vnlet
vermilion	verm
vertebrate	vrtb
vertical	vert
very	v
very poor sample	V.P.S.
vesicular	ves
violet	vl
visible	vis
vitreous (-ified)	vit
volatile	volat
volcanic rock,	Volc, volc
vug (-gy)	Vug vug
wackestone	Wkst
washed residue	W.R.
water	Wtr
wavy	wvy
waxy	wxy
weak	wk
weathered	wthd
well	Wl, wl
west	W
white	wh
with	w/
without	w/o
wood	Wd
yellow (-ish)	yel, yelsh
zeolite	zeo
zircon	Zr
zone	Zn

Appendix 2C: Abbreviations Used by Engineers

Reprinted by permission of the SPWLA from *Hydrocarbon Well Logging Recommended Practice*, second edition, December 1983.

absolute open flow	AOP	gas/oil ratio	GOR
		gauged	ga
barrel of oil	BO	good air blow	GAB
barrels of oil per day	BOPD	good initial puff	GIP
barrels of oil per hour	BOPH	gravity	gty
barrels of water	BW	ground	GR
barrels of water per day	BWPD	ground level	GL
barrels of water per hour	BWPH		
bottomhole flow pressure	BHFP	heavy oil	HO
bottomhole pressure	BHP		
bottomhole shut-in pressure	BHSIP	initial air blow	IAB
bottomhole temperature	BHT	initial production	IP
brackish	brk		
		kelly bushing	KB
casing	csg		
choke	ck	legal subdivision	LSD
circulated out	CO	location	loc
circulate (-ed) (-tion)	circ		
completed (tion)	comp	million cubic feet of gas	MCFG
connection gas	CG	mud-cut oil	MCO
cored	crd	mud-cut water	MCW
		mud resistivity	RM
decreasing	decr		
depth correction	DC	new bit	NB
derrick floor	DF	new core bit	NCB
development	(D)	no returns	NR
directional survey	DS	no returns	NR
distillate	dist		
drillstem test	DST	oil and gas	O&G
driller	drir	oil and salt water	O&SW
dry and abandoned	D&A	oil cut	OC
		oil-cut mud	OCM
estimated	est	oil-flecked mud	OCM
		oil to surface	OTS
faint air blow	FTAB	old total depth	OTD
fair air blow	FAB	old well drilled deeper	OWDD
filter cake	CK	old well plugged back	OWPB
filtrate, API, cc's	F	old well worked over	OWWO
flowed (ing)	fl/	open	op
flowing pressure	FP		
flowline temperature	F/T	packer	pk
		per day	PD
gas- and oil-cut mud	G&OCM	per hour	PH
gas-cut mud	GCM	perforated	perf
gas-cut water	GCW	plugged back	PB
gas to surface	GTS	pounds per square inch	psi

pump pressure	PP
pump strokes	SPM
recovered	rec
rotary speed	RPM
rotary table	RT
salinity - PPMCL	CL
saltwater	SW
show of oil	SO
show of oil and gas	SO&G
show of oil and water	SO&W
shut in	SI
shut-in pressure	SIP
slight gas-cut mud	SGCM
slight gas-cut water	SGCW
slight oil-cut mud	SOCM
slight oil-cut water	SOCW
slight show of oil	SSO
squeezed	sqz
strong air blow	SAB
suction temperature	S/T
swabbed	swbd
testing	tstg
too small to measure	TSTM
total depth	T.D.
trip gas	TG
valve open	V.op
viscosity, API, sec.	V
water	wtr
water cushion	wtr cush
water-cut mud	WCM
weak air blow	WAB
weak initial puff	WIP
weight of mud	W
weight on bit	WOB
wildcat	(W)

Chapter 3

Measurements on Drillpipe

Measurements on drillpipe (MOD) play an increasingly important role in modern drilling and formation evaluation practices. They provide an operator with almost immediate feedback on both the trajectory of the hole being drilled and the characteristics of the formations penetrated. This kind of information is unavailable in real time from conventional sources such as deviation surveys or wireline logs that, a priori, must be run after the drilling has taken place. MOD is of particular benefit in that it can be applied while geosteering a wellbore to a target zone, maintaining an extended reach section in the zone and at the same time performing formation evaluation comparable with that available from conventional wireline sensors.

3.1 Terminology: MOD, MWD, and LWD

Traditionally, the industry has used two terms to describe MOD activities. The first term, introduced in the 1980s, referred to measurements made during well construction to inform the driller about the subsurface location of the drill bit. By today's standards, these measurements while drilling (MWD) were fairly basic, but they enabled wells deviated from the vertical to be nudged in the desired direction and the wellbore path to be accurately described. This was a reactive process and was not truly equivalent to today's proactive "steering." The engineering emphasis was on well drilling and concentrated on such parameters as the well deviation from vertical and the compass direction in which the well was heading. With the kind of information that MWD supplies, more or less in real time, the driller can take appropriate actions, such as changing the weight on bit, increasing the mud weight, pulling out of the hole for a conventional logging run (once the objective formation has been reached), or running back in with a whipstock.

The second term, logging while drilling (LWD), refers to measurement of the formation's petrophysical properties. Because the mechanics of MWD enabled the transmission of downhole data to surface using mud pulse technology, it was natural that formation evaluators would want to incorporate the same sensors that were used on the wireline into the drill collars that also housed the MWD sensors. As the industry has advanced, the dividing lines between what is an MWD measurement and what is an LWD measurement have become blurred, and the current author favors the more general term MOD to describe both. Today, scanning-type petrophysical measurements are used to correct wellbore steering, and drilling metrics are used as indicators of mechanical formation properties, so there is little reason left to treat these sister technologies as being different and many good reasons to consider them all as part and parcel of MOD.

3.1.1 MOD Common Elements. Many different MOD systems are in commercial use today; they all have the following common characteristics:

- Downhole sensor subs mounted on special drill collars
- A power source

- A telemetry system
- Surface equipment

For the task of controlling the drilling process, the downhole sensor subs typically contain instrumentation capable of measuring the following parameters:

- Torque
- Weight on bit
- Borehole pressure
- Borehole temperature
- Tool-face angle
- Hole deviation from vertical
- Hole azimuth with respect to geographic coordinates

For the task of real-time formation evaluation and intelligent geosteering with respect to geologic and reservoir features and characteristics, downhole sensors typically provide measurements of:

- Natural formation gamma ray activity
- Formation acoustical travel time (slowness, both compression and shear)
- Mud resistivity
- Formation resistivity
- Formation density
- Formation thermal neutron-derived porosity
- Formation pressure
- Nuclear magnetic resonance

3.2 MOD Telemetry

The power source for activation of the sensors and the telemetry system can be one of three types:

- Surface power source
- Downhole turbine
- Downhole batteries

In the case of a surface power source, it is necessary to make electrical connections between the surface and the downhole sensors; this in turn requires either special wired drillpipe or an electric cable.

In the case of a downhole turbine, the circulating mud itself drives an electric generator located in the MOD drill collar. This in turn leads to an increase in the hydraulic horsepower required of the mud pumps to maintain circulation.

In the case of batteries, no special cabling or additional mud pumping is required, but the MOD system is limited by the life of the batteries used. Once the batteries are discharged, no further measurements can be made, and the MOD sub must be retrieved and redressed with fresh batteries.

The telemetry system most commonly used is coded mud-pressure pulses. The output from a specific sensor is converted from analog to digital form and encoded as a series of pressure pulses that are detected and decoded at the surface. The pressure pulses may be in the form of overpressure or underpressure anomalies introduced respectively by either a relief valve that shorts the mud circulation or a check valve that chokes it. Data transmission rates for mud-pulse systems are typically 5 to 20 bits per second (bps).

Coded mud-pressure pulses are, however, not the only means available for telemetry. Other methods, either in use or under experimental development, include electromagnetic e-mode

TABLE 3.1—MOD DATA TRANSMISSION METHODS AND SPEEDS

Method	Data Rate	
Mud pulse	5–20	bps
Electromagnetic telemetry	2–25	bps
Short hop radio waves	0.2–2	Kbps
Wired drillpipe	50	Kbps

(electric current) or h-mode (magnetic field) systems; acoustic telemetry through drillpipe, tubing in a straight hole, or both, or through the earth by use of seismic waves; hardwired systems; systems with self-energizing repeaters; and hybrid systems that combine various transmission methods. These methods, while suffering some depth limitations, can offer much higher data transmission rates, as shown in **Table 3.1**.

The surface equipment consists of a mud-pulse decoder (or a decoder of some other parameter, depending on the telemetry system in use) together with signal-processing hardware and software that together produce the output that the drilling engineer wishes to use. Output may be in the form of a visual display (either on the rig floor or at a remote site) or as a hard-copy listing or log of the parameters recorded. Data may also be recorded on magnetic media for future use.

In most systems, the transmission of data to the surface is selective. For example, a measurement of hole deviation and azimuth may require that the drilling process be temporarily suspended and the drillstring held motionless for a short period. Readings are then accumulated in a buffer and transmitted to the surface only when mud circulation recommences.

Fig. 3.1 illustrates an MOD downhole assembly with its mud-pulse transmitter, turbine generator, and sensor sub, as well as details of the mud siren and the mechanics of creating either positive or negative mud-pressure pulses. Typically, each measurement or "word" is transmitted as part of a data frame. Some measurements are transmitted more than once in each frame.

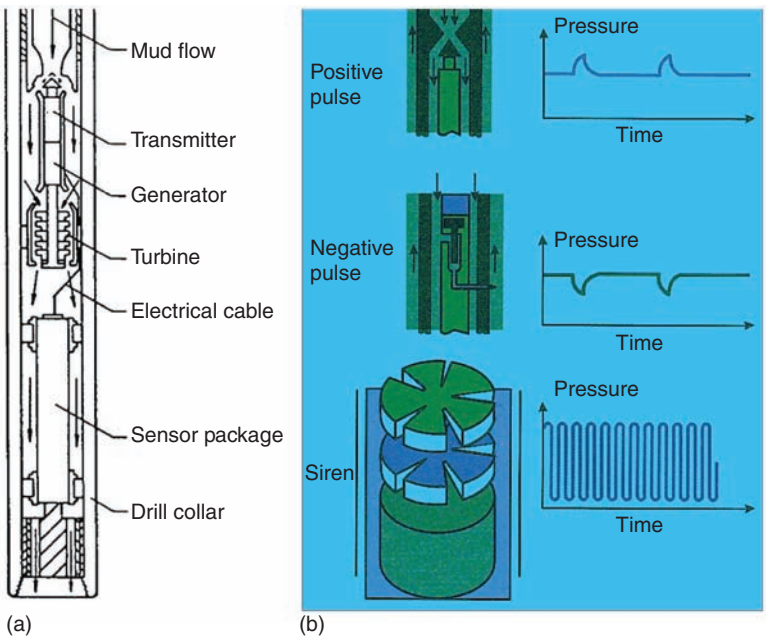


Fig. 3.1—(a) Typical MOD downhole assembly (Grosso et al. 1983); (b) close-up of mud pulse siren, negative and positive pulses (Grosso et al. 1983).

Current telemetry systems are capable of transmitting a complete frame in a matter of one or 2 minutes. The actual sampling rate in terms of measurements per unit of depth is inversely proportional to the rate of penetration (unit of depth per unit of time).

3.3 Morphing From Wireline to MOD

Since the 1990s, the process of morphing wireline logging technology into the MOD sphere has gained momentum to the point where, almost without exception, any petrophysical measurement available on wireline is now also available on drillpipe. Moreover, in some cases, the basic wireline sensor has been enhanced during its journey from wireline to drillpipe. MOD and wireline logging differ in three major areas: sensor rotation, invasion-free reading of R_t, and ease of use in highly deviated or horizontal wells.

3.3.1 Sensor Rotation. In particular, it should be noted that by placing a wireline logging sensor on a drill collar that can rotate, the unidirectional wireline tool is converted into a 360° scanning tool. **Fig. 3.2** shows an example of a borehole image obtained from an azimuthal MOD resistivity device.

3.3.2 Mud Filtrate Invasion Effects. The different modes of operation of the two measurement systems (wireline- and drillpipe-conveyed) introduce additional advantages for the MOD version. For example, the wireline log can be recorded only while the logging tool string is being raised up the borehole, some significant time *after* drilling has been completed and mud filtrate invasion has taken place. By contrast, MOD logging sensors record as the drill bit progresses downhole and make their measurements within minutes of the exposure of the virgin formation to the drilling mud. This is particularly valuable to the log analyst who is thus afforded a measurement of R_t that is virtually free of the effects of mud-filtrate invasion.

Fig. 3.3 illustrates the progress of the mud-filtrate invasion front as a function of time and depth as the bit penetrates the formation and the MOD resistivity sensor makes its measurement.

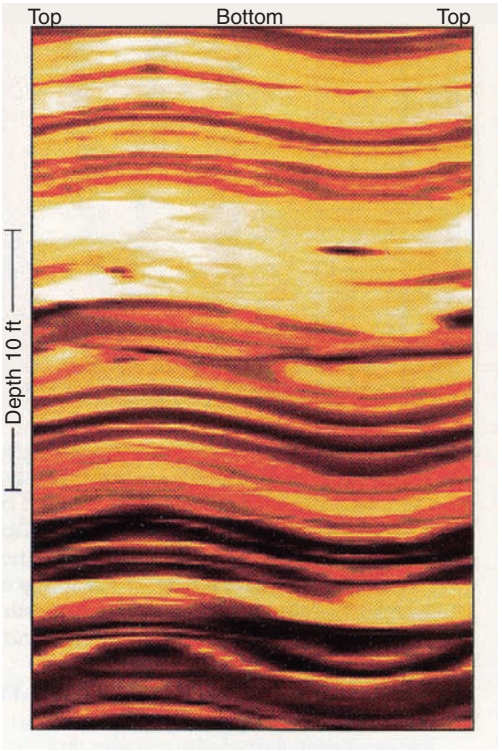


Fig. 3.2—Electrical borehole image made with MOD rotating sensor (Bonner et al. 1996). Courtesy of Schlumberger.

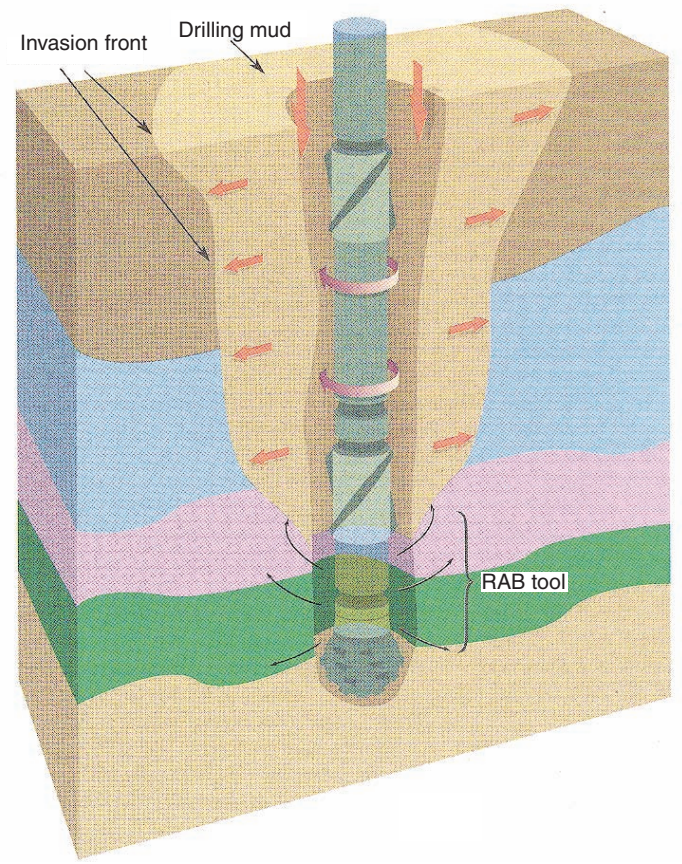


Fig. 3.3—Invasion-free resistivity measurement near bit with measurement on drillpipe sensor.

3.3.3 Measurements in Extended-Reach Wells. Wireline logging in highly deviated or extended-reach horizontal wells is problematic (see Chapter 4). However, this task is greatly simplified by the use of MOD and has come to be the preferred mode of real-time geosteering and formation evaluation in such cases.

3.4 Petrophysical Considerations for MOD Measurements

In vertical holes crossing horizontal beds, there is little difference between the way in which an analyst handles resistivity and porosity data measured by wireline or by MOD sensors. However, in horizontal wells, a number of new factors enter the picture and complicate the analyst's task.

3.4.1 Asymmetrical Invasion Effects. Fig. 3.4a shows a view in a plane normal to the logging-tool axis, with an MOD logging device lying on the low side of a horizontal well drilled through a target bed that has shoulder beds both above and below the well trajectory. The tool's response volume is shown as a dotted circle around the axis of the tool. Because of directional permeability effects and gravity, the invasion profile is not circular, but oval.

Effectively, there are four regions surrounding the tool, as indicated in **Table 3.2**. Each of the four regions has a different resistivity and a different response to porosity and lithology sensing devices such as neutron and density tools. The task of the analyst is therefore somewhat complicated because the parameter required for log analysis is simply the resistivity of the non-invaded target bed (Zone 2, shown in yellow in Fig. 3.4b), but the tool's response includes the disturbing effects from Zones 1, 3, and 4. Given these circumstances, modeling is required to resolve the issue completely.

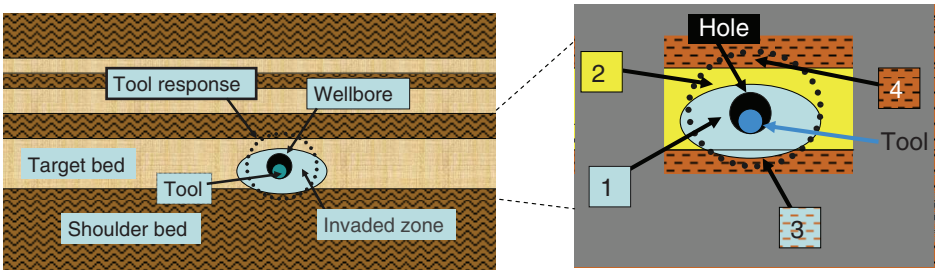


Fig. 3.4—(a) Asymmetrical invasion effects in horizontal wells; (b) detail of the four zones surrounding the MOD device in a horizontal hole.

TABLE 3.2—ZONES SURROUNDING MOD TOOL IN HORIZONTAL HOLE

Zone	Bed	Condition
1	Target bed	Invaded
2	Target bed	Noninvaded
3	Shoulder bed	Invaded
4	Shoulder bed	Noninvaded

3.5 Logs Provided by MOD

3.5.1 MOD for Resistivity. The presence of steel drillpipe in the borehole precludes the use of standard wireline induction logging technology (discussed in more detail in Chapter 12). Instead, the industry has moved to a related technology known as electric wave resistivity (EWR). A high-frequency electric wave is propagated through the surrounding formation, and the phase and amplitude of the received signals are used to deduce formation resistivity and formation dielectric constant. In this respect, the underlying physics of the measurement is akin to that used by the wireline electromagnetic propagation tool (EPT) covered in Chapter 15. Although the number of transmitter and receiver coils and their relative spacing vary somewhat between the different service companies, they all use common frequencies of 400 KHz and 2 MHz to make the basic EWR measurements.

Fig. 3.5 illustrates one EWR implementation with six transmitter coils and three receiver coils that are angled at 45° to the transmitter coils, thus providing directionality to the measured formation resistivity. This in turn aids in geosteering by providing a warning during drilling that, for example, the bit is approaching a boundary with another bed of markedly different resistivity, as may occur, for example, when leaving the pay zone and entering a shale or dropping below the oil/water contact zone.

Resistivity at Bit (RAB). **Fig. 3.6** shows a MOD sub for recording the formation resistivity at the bit. Note that the tool incorporates both azimuthal resistivity button electrodes and an azimuthal natural gamma ray detector. These can be used in normal (rotational) drilling to create both resistivity borehole images and gamma ray images.

Fig. 3.7a gives a pictorial representation of the measurement of formation resistivity at the bit, and the panel shown in Fig. 3.7b shows an application for this kind of measurement.



Fig. 3.5—EWR device (azimuthal deep resistivity). Courtesy of Halliburton.

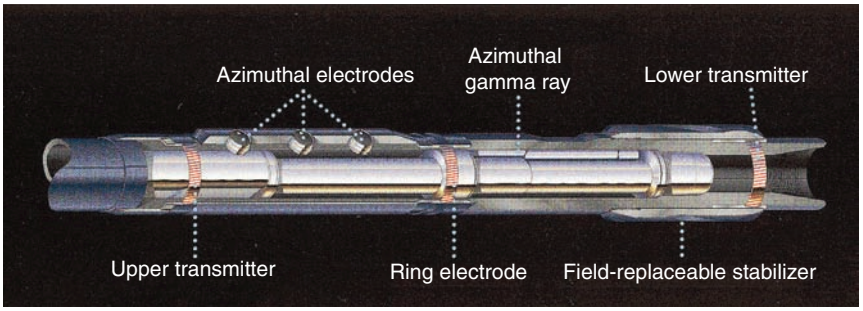


Fig. 3.6—MOD sub for RAB and gamma ray detection. Courtesy of Schlumberger.

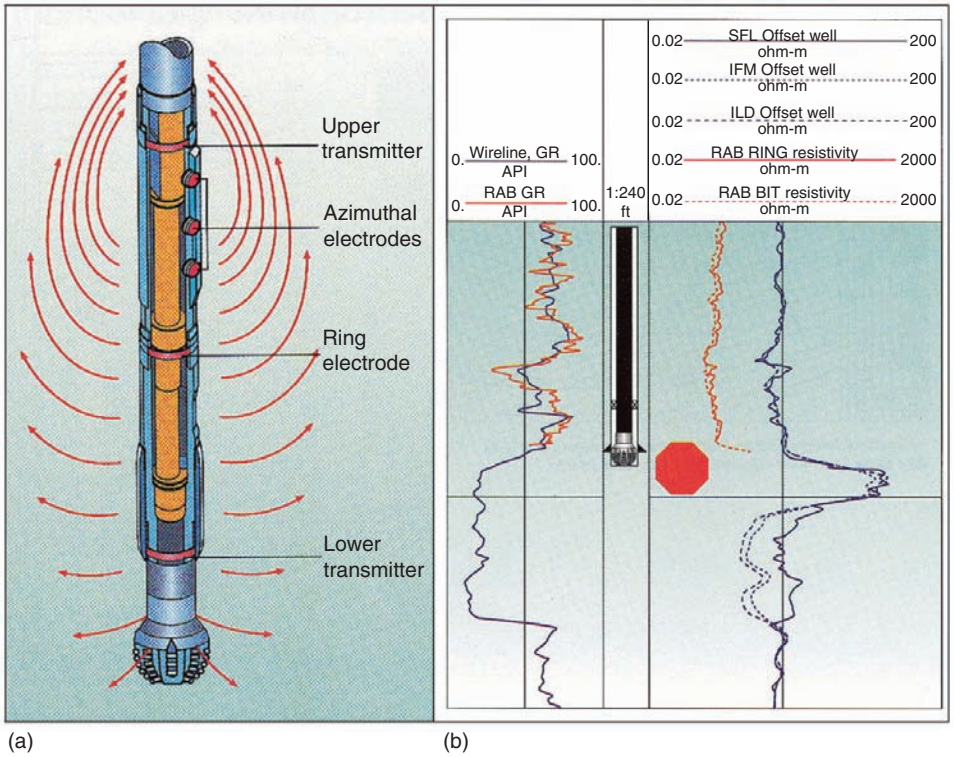


Fig. 3.7—(a) Measurement of RAB (Bonner et al. 1993); (b) application of RAB measurement (Bonner et al. 1996). Courtesy of Schlumberger.

In the example shown, an initial field well penetrated a hydrocarbon-bearing interval. For reservoir characterization purposes, a full-diameter core was required in this interval in the adjoining offset well. During drilling of the offset well, the RAB resistivity curves gave the needed indication that the top of the zone of interest had been penetrated and drilling could therefore be suspended and the drillstring tripped out of the hole before running back in with a core barrel.

3.5.2 MOD for Porosity and Lithology. ***Sonic Logging on Drillpipe***. The principles of sonic logging and the application of slowness measurements to petrophysical evaluations are covered in Chapter 16 and will not be discussed here. However, substantially the same *modus operandi* for wireline sonic logging is used by its sister application for MOD work.

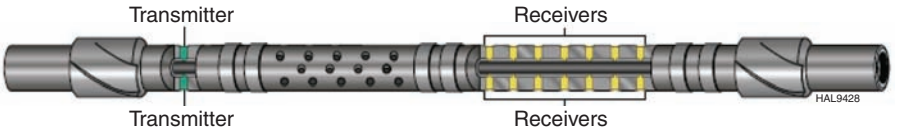


Fig. 3.8—MOD sonic logging sub. Courtesy of Halliburton.

Fig. 3.8 illustrates a sonic logging MOD sub with radially opposed, dual-frequency transmitters and multi-receiver arrays that can produce a conventional log of slowness (Δt_c and Δt_s) against depth as well as waveforms. Chapter 20 (Dipmeter and Borehole Imaging) discusses ultrasonic borehole imaging applications on wireline; equivalent MOD sonic imaging devices are in the experimental stages.

Neutron-Density Logging on Drillpipe. The principles of formation-density logging are covered in Chapter 17 and those of neutron logging in Chapter 18. The use of both measurements for porosity, lithology, and hydrocarbon typing are covered at various points in Chapters 22 through 24. Suffice it to say that substantially the same hardware is used in the MOD implementations as for the wireline versions. **Fig. 3.9** illustrates a MOD sub for recording compensated thermal neutron porosity (ϕ_N) and formation bulk density (ρ_B).

3.6 Other MOD Sensors

Other MOD sensors continue to be added to the analyst's arsenal. The most recent additions have been

- Nuclear magnetic resonance (NMR) measurements (see Chapter 19 for discussion of the basic NMR principles and their application to wireline logging).
- Formation pressure testing (see Chapter 31) for a discussion of wireline formation testing and the use of formation pressure data to determine formation fluid gradients and contacts).

Fig. 3.10 illustrates a combination log obtained from MOD sensors alone that includes gamma ray, hole size, deep, medium, and shallow resistivities, neutron porosity, formation density, and sonic travel time for both compression and shear waves. This is effectively the MOD equivalent of a wireline quad combo.

3.7 MOD Quality Control and Sensor Calibration

As with wireline logging tools, the sensors used on MOD subs are subject to quality standards through a system of shop, prelogging, and post-logging calibrations. These enable the user to monitor any departures from established norms that may arise in the course of tool mobilization and handling during a given run in the hole. **Fig. 3.11** shows a typical MOD calibration "tail."

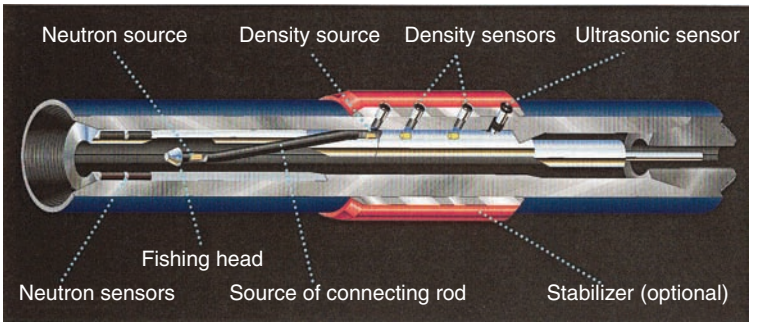


Fig. 3.9—MOD neutron-density sub. Courtesy of Schlumberger.

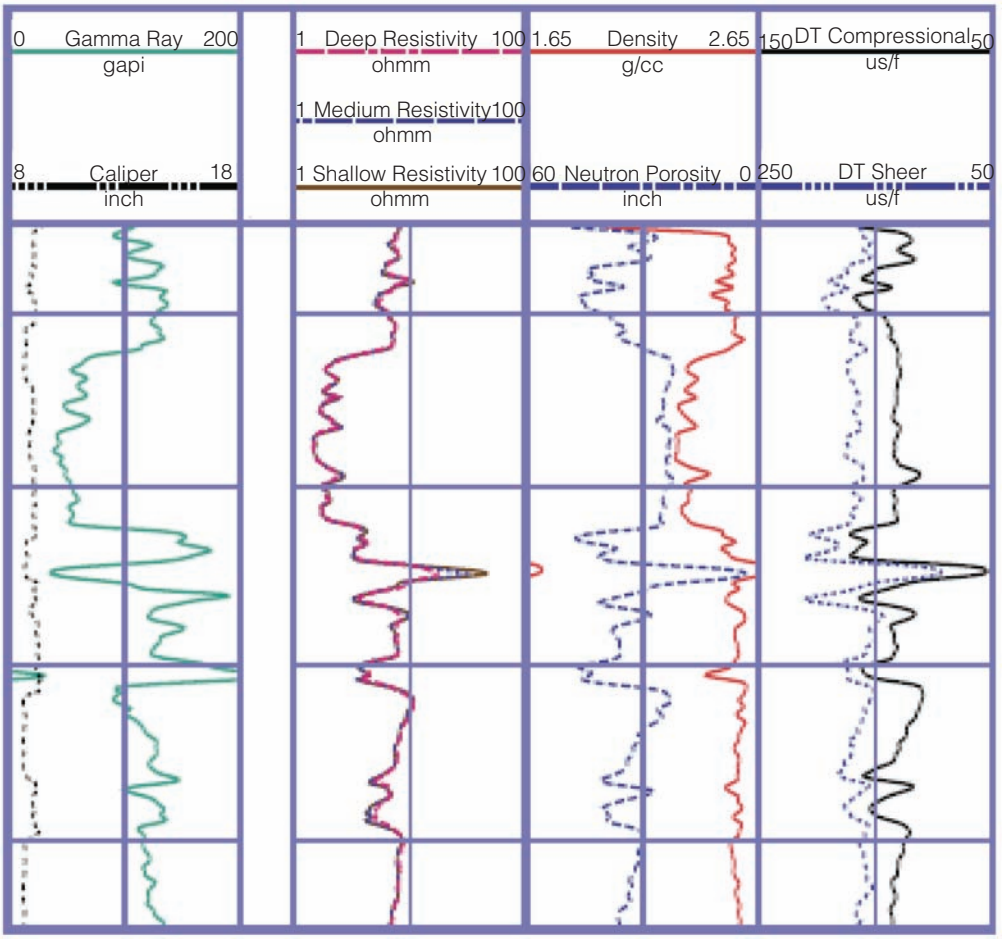


Fig. 3.10—Combination log from MOD including GR, hole size, R_{Deep}, R_{Medium}, and $R_{Shallow}$, ϕ_N, ρ_B, Δt_c, and Δt_s. Courtesy of Halliburton.

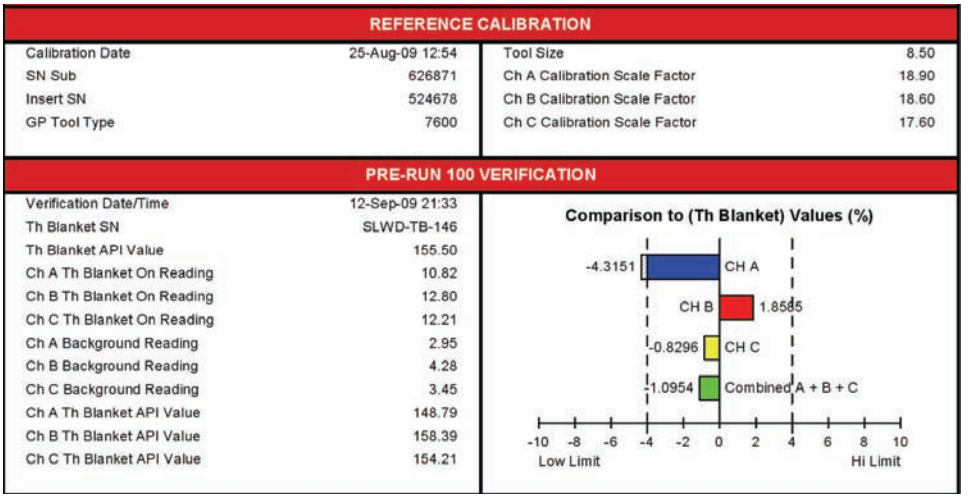


Fig 3.11—Example MOD calibration. Courtesy of Halliburton.

3.8 The Future of MOD

It seems safe to assume that in the future, the use of MOD for formation evaluation will become the norm. Technological advances will enable more wireline-type logging measurements to be made by MOD subs. Telemetry will improve to the point where a full suite of logs will be available effectively in real time. This in turn will enable almost instant evaluation of a formation within minutes of drilling. Such advances are to be encouraged because any improvement in one formation evaluation technique helps all the others.

References

Bonner, S., Burgess, T., Clark, B., et al. 1993. Measurements at the Bit: A New Generation of MWD Tools. *Oilfield Review* **5** (2): 44–54.

Bonner, S., Fredette, M., Lovell, J., et al. 1996. Resistivity While Drilling—Images From the String. *Oilfield Review* **8** (1): 4–19.

Grosso, D.S., Raynal, J.C., and Radar, D. 1983. Report on MWD Experimental Downhole Sensors. *J. Pet Tech* **35** (5): 899–904. http://dx.doi.org/10.2118/10058-PA.

Schlumberger. *Measurements While Drilling (M.W.D): Technical Specifications*.

General References

Anderson, B. 1986. The Analysis of Some Unresolved Induction Interpretation Problems Using Computer Modeling. *The Log Analyst* **27** (5): 60–73.

Anderson, B.I. Druskin, V., Lee, P., Lüling, M.G., Schoen, E., Tabanou, J., Wu, P., Davydycheva, S., and Knisherman, L. 1997. Modeling 3D Effects on 2-MHz LWD Resistivity Logs. *Proc.,* SPWLA 38th Annual Logging Symposium, Houston, June 15–18.

Anderson, B., Barber T., Druskin, V., Lee, P., and Dussan, E.V. 1999. The Response of Multiarray Induction Tools in Highly Dipping Formations With Invasion and in Arbitrary 3D Geometries. *The Log Analyst* **40** (5): 327–344.

Bell, C., Hampson, J., Eadsforth, P., Chemali, R., Helgesen, T., Meyer, H., Peveto, C., Poppitt, A., Randall, R., Signorelli, J., and Wang, T. 2006. Navigating and Imaging in Complex Geology With Azimuthal Propagation Resistivity While Drilling. Paper SPE 102637 presented at the 2006 SPE Annual Technical Conference and Exhibition, San Antonio, Texas, USA, 24–27 September. http://dx.doi.org/10.2118/102637-MS.

Bittar, M., Klein, J., Beste, R., Hu, G., Pitcher, J., Golla, C., Althoff, C. et al. 2007. A New Azimuthal Deep Reading Resistivity Tool for Geosteering and Advanced Formation Evaluation. Paper SPE 109971 presented at the SPE Annual Technical Conference and Exhibition, Anaheim, California, USA, 11–14 November. http://dx.doi.org/10.2118/109971-MS.

Bittar, M., Hveding, F., Clegg, N., Johnston, J., Solberg, P., and Mangeroy, G. 2008. Maximizing Reservoir Contact in the Oseberg Field Using a New Azimuthal Deep-Reading Technology. Paper SPE 116071 presented at the SPE Annual Technical Conference and Exhibition, Denver, 21–24 September. http://dx.doi.org/10.2118/116071-MS.

Brami, J.B. 1991. Current Calibration and Quality Control Practices for Selected Measurement-While-Drilling Tools. Paper SPE 22540 presented at the SPE Annual Technical Conference and Exhibition of the Society of Petroleum Engineers, Dallas, 6–9 October. http://dx.doi.org/10.2118/22540-MS.

Kamp, A.W. 1983. Downhole Telemetry From the User's Point of View. *J. Pet Tech* **35** (10): 1792–1796. http://dx.doi.org/10.2118/11227-PA.

Kriegshäuser, B.F., Fanini, O.N., Forgang, S., Mollison, R.A., Yu, L., Gupta, P.K., Koelman, J.M.V., and van Popta, J. 2000. Increased Oil-In-Place in Low-Resistivity Reservoirs from Multicomponent Induction Log Data. *Proc.,* SPWLA 41st Annual Logging Symposium, Dallas, 4–7 June.

Meyer, W.H., Hart, E., and Jensen, K. 2008. Geosteering with a Combination of Extra Deep and Azimuthal Resistivity Tools. Paper SPE 115675 presented at the SPE Annual Technical Conference and Exhibition, Denver, 21–24 September. http://dx.doi.org/10.2118/115675-MS.

Meador, R.A. 2009. Logging-While-Drilling: a Story of Dreams, Accomplishments and Bright Futures. *Proc.,* SPWLA 50th Annual Logging Symposium, The Woodlands, Texas, USA, 21–24 June.

Roberts, A., Newton, R., and Stone, F. 1982, MWD Field Use and Results in the Gulf of Mexico. Paper SPE 11226 presented at the SPE Annual Technical Conference and Exhibition, New Orleans, 16–19 September. http://dx.doi.org/10.2118/11226-MS.

Tanguy, D.R. and Zoeller, W.A. 1981. Applications of Measurements While Drilling. Paper SPE 10324 presented at the SPE Annual Technical Conference and Exhibition, San Antonio, 5–7 October. http://dx.doi.org/10.2118/10324-MS.

Zoeller, W.A. 1983. Pore Pressure Detection From the MWD Gamma Ray. Paper SPE 12166 presented at the SPE Annual Technical Conference and Exhibition, San Francisco, 5–8 October. http://dx.doi.org/10.2118/12166-MS.

Chapter 4

Wireline Logging Operations

4.1 Rigging Up To Run a Log

Fig. 4.1 shows a typical setup for a logging job. A logging truck is anchored about 100 to 200 ft from the well. Two sheaves are mounted in the derrick with one suspended from the crown block and the other chained down near the rotary table. The logging cable from the truck winch is then passed over the sheaves, attached to the logging toolstring and lowered into the hole. A more detailed diagram of this hookup is shown in **Fig. 4.2**.

Two mechanical details of this method of rigging up are worth noting. Between the top sheave and the elevators, there is a tension device **(Fig. 4.3)** that measures the strain on the logging cable and displays it in the logging truck. The tension on the elevators is twice the tension on the cable. The elevators should be securely locked and the traveling block braked and chained.

The tie-down chain for the lower sheave is also of great importance. If it breaks or comes untied, then the cable, too, may break and the sheave be catapulted several hundred feet away **(Fig. 4.4)**.

QUESTION 4.1. If the tension in the logging cable is 5,000 lbm, estimate the tension in the tiedown chain if it forms an angle of 45° with each of the two cable directions on either side of the sheave.

4.2 Logging Trucks

Logging service companies offer a variety of logging units. Each type of unit has the following components:

- Logging cable
- Winch to raise and lower the cable in the well
- Downhole logging tools
- Self-contained 120-VAC generator
- Surface computer and control equipment
- Data recording media (disk and/or magnetic tape)
- Data display equipment (e.g., computer monitor, printer)
- Data transmission equipment (e.g., satellite link, internet connection)

Fig. 4.5 shows a cutaway of a typical logging truck. Land units are mounted on a specially adapted truck chassis reinforced to bear the load of a full winch of cable (up to 30,000 ft long). The instrument and recorder cabs are usually cramped and either too hot or too cold. Although not designed to do so, this keeps the merely curious onlooker away. Do not be deterred. If you have good reason to be in the logging unit, stay there and do what you must.



Fig. 4.1—Setup for a logging job.

Offshore units **(Fig. 4.6)** are mounted on skids and bolted (or welded) to the deck of the drilling barge, vessel, or platform. Some logging units can be disassembled into many small components and flown into remote jungles suspended under helicopters. Nevertheless, all logging units are basically the same.

Good mechanical maintenance is required to avoid problems during logging operations. An engine that stops during logging operations will leave the logging tool dangling in the well. If it stays there too long without moving, it may become stuck. In that case, the traveling block, from which the top sheave is suspended, can be raised and lowered by the driller so

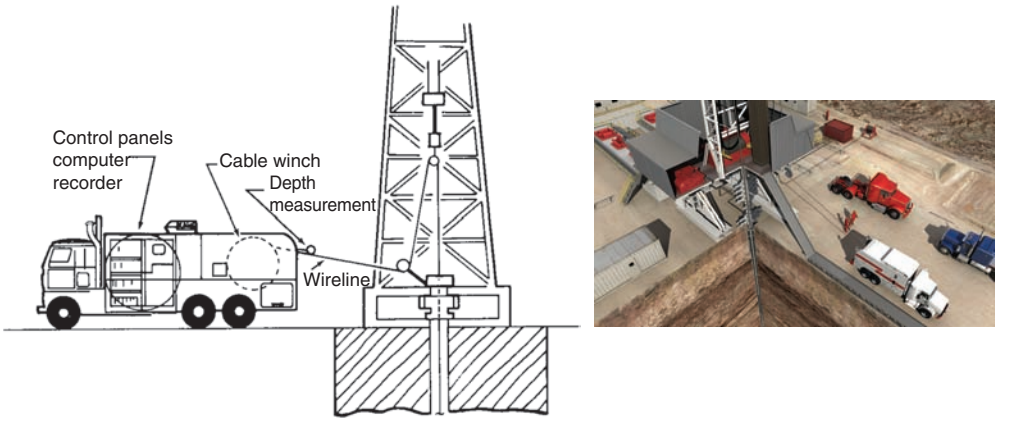


Fig. 4.2—Details of a wireline logging setup. Courtesy of Halliburton.

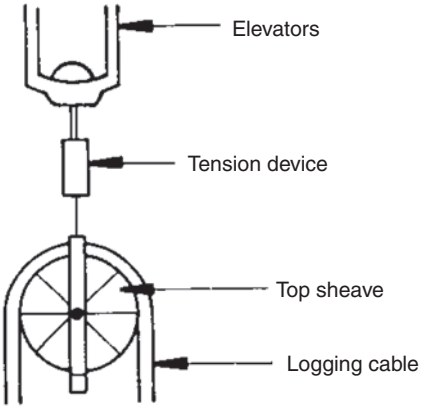


Fig. 4.3—Top sheave and elevator arrangement for a logging job.

that the tool is kept in motion. Another item that can cause a problem is the 120-V generator. If it fails, all surface logging equipment and downhole tools go dead. Rig power may then be substituted.

4.3 Logging Cables

Modern logging cables are of two types: monoconductor and multiconductor. Monoconductor cables are used for completion services—such as shooting perforating guns, setting wireline packers and plugs—and for production logging surveys—such as flowmeter and temperature logs in producing wells. Multiconductor cables are used by most logging-service companies for recording openhole surveys.

The monoconductor cables are approximately ½ or ¼ in. in diameter—the smaller cable is used for jobs where high wellhead pressure is encountered. The multiconductor cables contain six or seven individual insulated conductors in the core. The outer sheath is composed of two counterwound layers of steel wire. Such a cable has a breaking strength of 14,000 to 18,000 lbm and weighs 300 to 400 lbm per 1,000 ft. It is quite elastic and has a stretch coefficient close to10^{-6} ft/ft/lbm. Although desirable, it is worth noting that fiber optics has yet to be universally adopted as an alternative to conventional electric conductor cables.

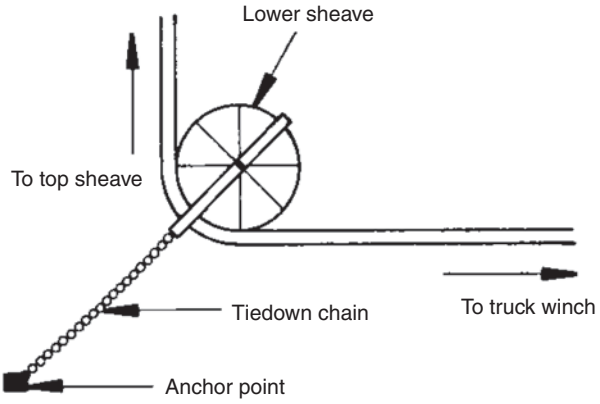


Fig. 4.4—Lower sheave tie-down arrangement.



Fig. 4.5—Computerized logging truck. Photo taken by the author with permission of Baker Hughes.

4.3.1 The Head and the Weakpoint. The cable ends at the logging head. The head anchors the cable and attaches to the logging tool by means of a threaded ring. Thus, the head provides the electrical connection between the individual cable conductors and the various pins in the top of the tool as well as the mechanical connection. Built into the head is a weakpoint, which is a short

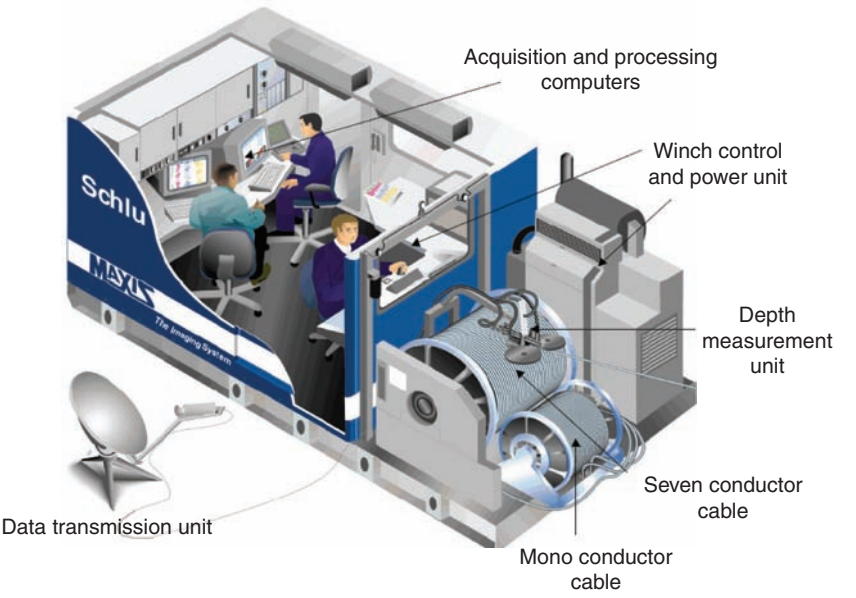


Fig. 4.6—Offshore wireline logging unit. Courtesy of Schlumberger.

length of aircraft cable, designed to break at some given tension. The standard breaking point is 6,000 lbm, but deep-hole weakpoints break at 3,500 lbm. The weakpoint is necessary to provide a means to free the cable from the tool in case the tool has become irrevocably stuck in the wellbore. To explain fully the function of the weakpoint, a discussion of the various ways the tool can become stuck is in order.

4.3.2 Getting Stuck. There are two ways of getting stuck. Either the tool will stick and the cable in the hole above the tool will remain free, or the tool will remain free and the cable will become keyseated further up the hole above the tool. **Fig. 4.7** illustrates the difference.

Once the tool or cable is stuck, the first thing to do is to determine whether it is the tool or the cable that is stuck. The standard procedure is to put normal logging tension on the cable and let it sit for a few minutes while the following data are gathered:

a. The present depth of the tool
b. The surface tension that was on the cable just before it got stuck
c. The cable type, size, etc.
d. The cable-head weakpoint rating

Once these data have been gathered, make certain that the tie-down chain on the lower sheave is secure. Then mark the cable (using chalk or friction tape) at the rotary table. Securely position a T-bar clamp around the cable just above the rotary table. (If, in the subsequent tug-of-war, the cable breaks at the top sheave, this clamp will hold the cable at the surface and prevent it from snaking down the hole on top of the tool.) Next apply 1,000 lbm over the tension already on the cable and measure the distance the cable mark has moved. This will be the stretch produced in the elastic cable as a result of 1,000 lbm extra tension. Knowing this distance, the length of free cable can be estimated from a stretch chart or from knowledge of the stretch coefficient. If the length of free cable so determined proves to be the present logging depth, then the tool is evidently stuck and the cable is free. On the other hand, if the length of free cable is less than the present logging depth, the cable itself must be stuck higher up the hole. If the cable proves to be stuck, it is counterproductive to apply any further tension because this will merely compound the problem by aggravating the differential pressure sticking of the cable.

If it is the tool that is stuck, pulling on the cable will have one of three results. The tool will pop free, the weakpoint will break (leaving the tool in the hole but saving the cable), or the cable will

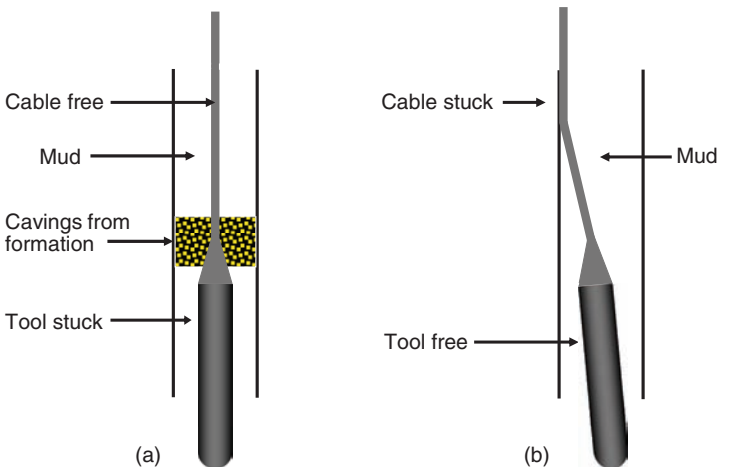


Fig. 4.7—Two ways of getting stuck: (a) tool stuck, (b) tool free, cable keyseated.

break at the point of maximum tension at the top sheave. Of the three, the first is to be preferred. Of the other two, the breaking of the weakpoint is preferred. But which will occur first? Will the cable part at the surface before the weakpoint breaks? **Fig. 4.8** will help to explain the tensions involved.

If the cable weakpoint is 6,000 lbm, and 10,000 ft of cable weighing 3,500 lbm is in the hole, it will be necessary to apply 9,500 lbm (6,000 + 3,500) at the surface in order to apply 6,000 lbm at the weakpoint. At greater depths, the surface tension required to break the weakpoint will be even higher and may exceed the breaking strength (14,000 to 18,000 lbm) of the cable itself. Thus, for deep holes, a weakpoint of only 3,500 lbm is preferred.

Differential pressure sticking of the cable is caused when the cable cuts through the mudcake. One side of the cable is exposed to formation pressure while the other side is exposed to the hydrostatic mud column. When the hydrostatic pressure is significantly higher than the formation pressure, the cable is forced against the formation, and the resulting friction stops any further cable movement **(Fig. 4.9)**.

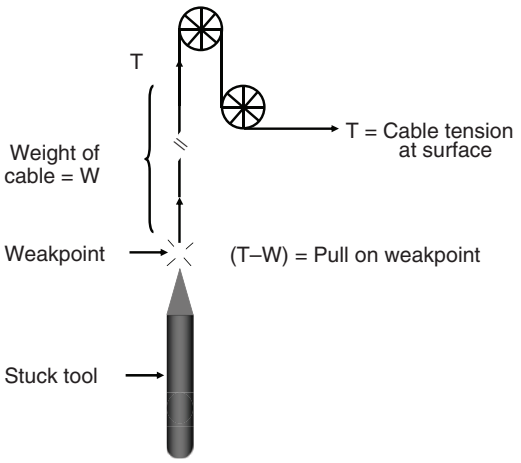


Fig. 4.8—Breaking the cable at the weakpoint.

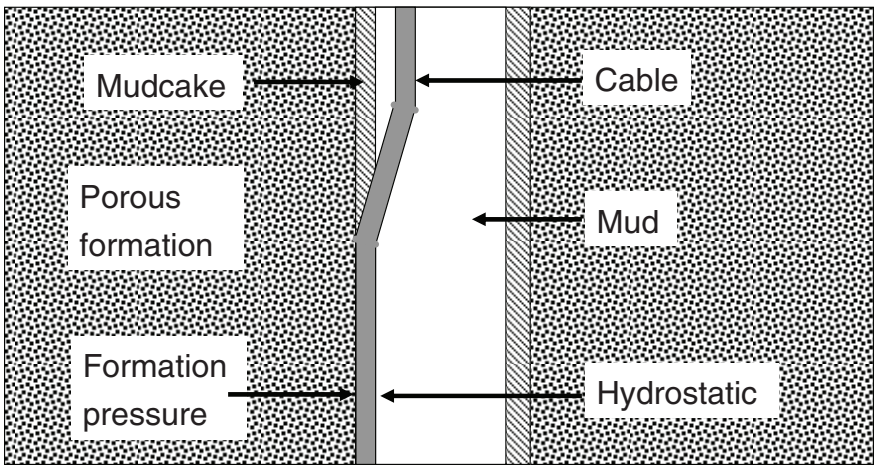


Fig. 4.9—Differential pressure sticking of the cable.

An example will illustrate this phenomenon: mud weight is 10 lbm/gal. At 5,000 ft, the hydrostatic pressure is 2,600 psi, but formation pressure is 2,250 psi; there is thus a differential pressure of 350 psi. If the diameter of the cable is ½ in., and only 10 ft of the cable is stuck, the force on the cable will be 21,000 lbm (350 psi × 120 in. × ½ in.). If the coefficient of friction is 0.1, the pull required to overcome the friction will be 2,100 lbm.

4.3.4 Fishing Alternatives. There are several alternatives available for recovering a stuck tool and/or cable:

1. Leave the cable attached to the tool and run a side-door overshot.
2. Use the cut-and-thread technique.
3. Break the weakpoint, recover the cable, and fish for the logging tool with the drillpipe, or push it to the bottom of the hole and mill it up.

Fig. 4.10 illustrates these three methods. The side-door overshot is not recommended at depths greater than 3,000 ft. Historically, the cut-and-thread technique is the surest way to recover a stuck logging tool.

4.4 Logging Tools

Logging tools are cylindrical tubes containing sensors and associated electronics. These tubes can be attached to the logging cable at the logging head. Although there are large variations in size and shape, a typical logging tool is 3⅝ in. in diameter and 10 to 30 ft long. They are built to withstand pressures up to 20,000 psi and temperatures of 300 to 400°F. The internal sensors and electronics are ruggedly built to withstand physical abuse. Modern tools are modularized to allow combination tool strings. By appropriate mixing and matching, various logging sensors can be connected together. This technique has obvious limitations; for example, very long tools are difficult to handle and the conductors in the cable have limited information transmitting power.

Because the multiple sensors of logging tools are located at different points along the axis of the tool, their respective measurements have to be memorized and placed on a common depth reference. Thus, the signal from the sensor highest on the tool string must be remembered until

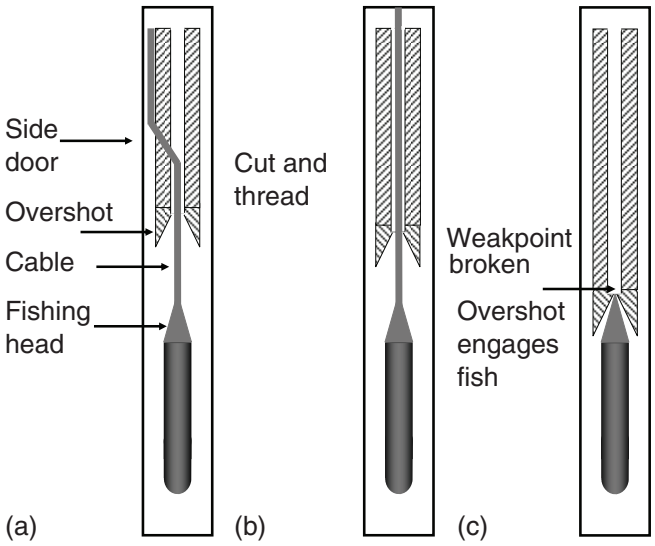


Fig. 4.10—Fishing alternatives: (a) Side-door overshot, (b) cut-and-thread, (c) fishing with drillpipe.

the signal from the lowest sensor arrives (see **Figs. 4.11 and 4.12**). In Fig. 4.12, the reference point for the survey is the sensor producing the curve marked **A**. Higher up on the tool are two more sensors, **B** and **C**. If recorded unmemorized, the formations would appear off-depth (e.g., Sand 2 appears at different depths for each of the sensors). Note that Sand 1 can only be logged by Sensor **A**. It is important, therefore, to make certain that all curves recorded simultaneously are on-depth on the log.

Another depth problem arises when several surveys are recorded on different trips into the hole. Unless care is taken, these surveys may not be on-depth with each other. The only method of assuring good depth control is to insist on a repeat section that passes a good marker bed. Each subsequent log should be placed on-depth using this repeat section as a depth reference before the main logging run is made.

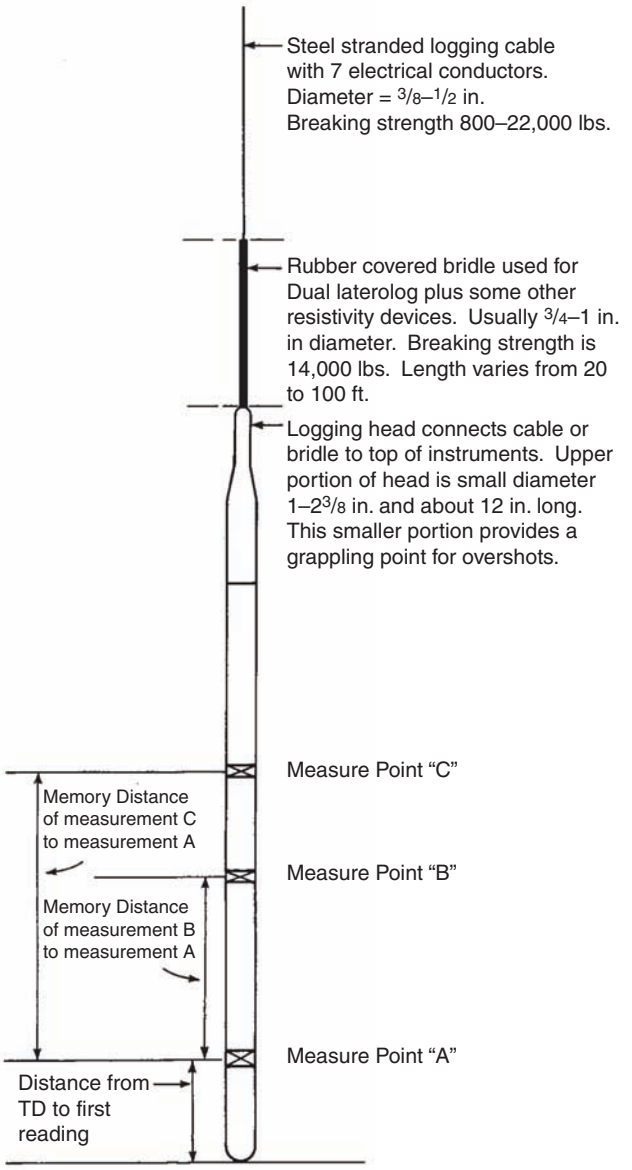


Fig. 4.11—Measure points and memorization distances.

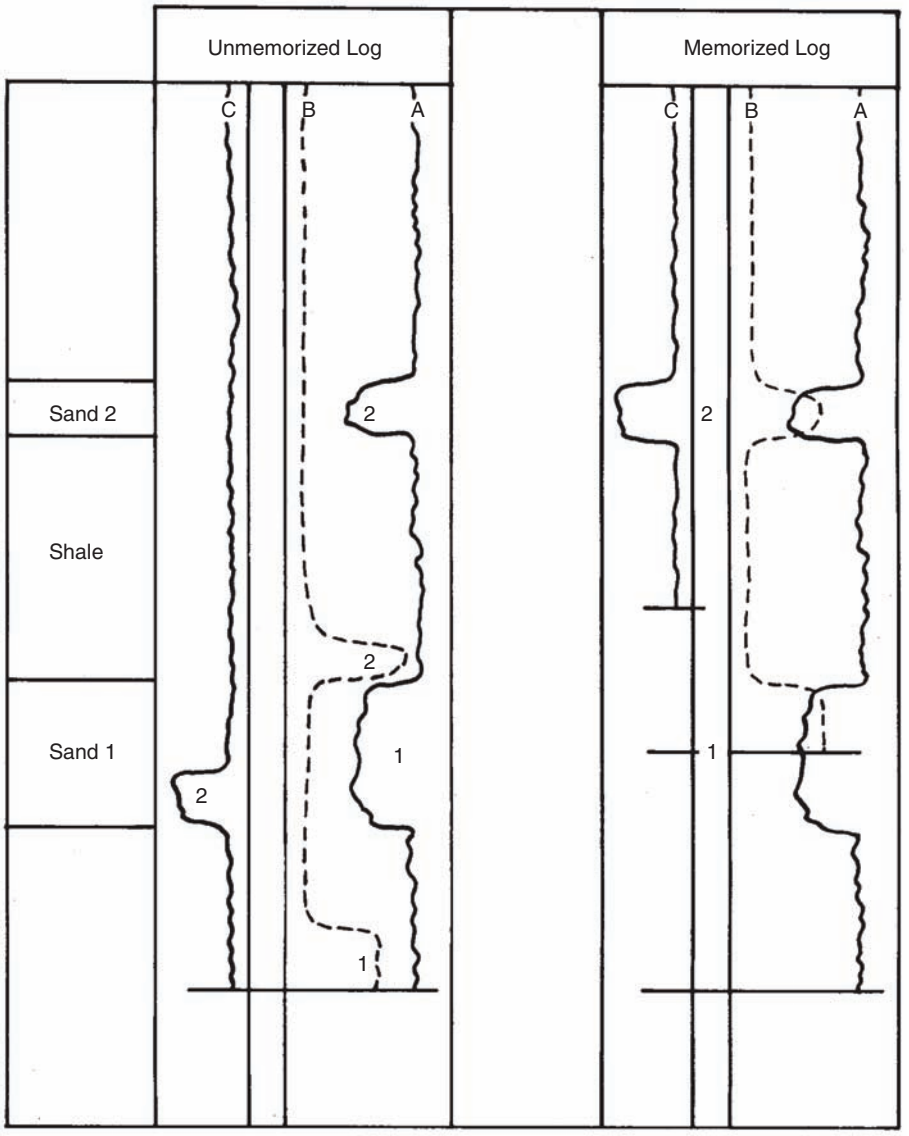


Fig. 4.12—Unmemorized and memorized logs.

4.5 The Borehole Environment

As the drill bit penetrates a permeable formation, an invasion process begins. Because the pressure in the mud column exceeds formation pressure, fluid from the mud will move into the formation (provided it is porous and permeable) and deposit a mudcake on the borehole wall. **Fig. 4.13** illustrates the process and the names used in logging literature for the various zones that surround the borehole.

It is important to distinguish between the resistivity of the fluid within the pore space and the resistivity of the rock/fluid system itself. The terms used in **Table 4.1** should be well known to everyone involved in the evaluation of well logs. The flushed (invaded) zone is important because it affects the readings of some logging tools and because it forms a reservoir of mud filtrate that will be recovered on a drillstem or wireline formation test before formation fluids are recovered.

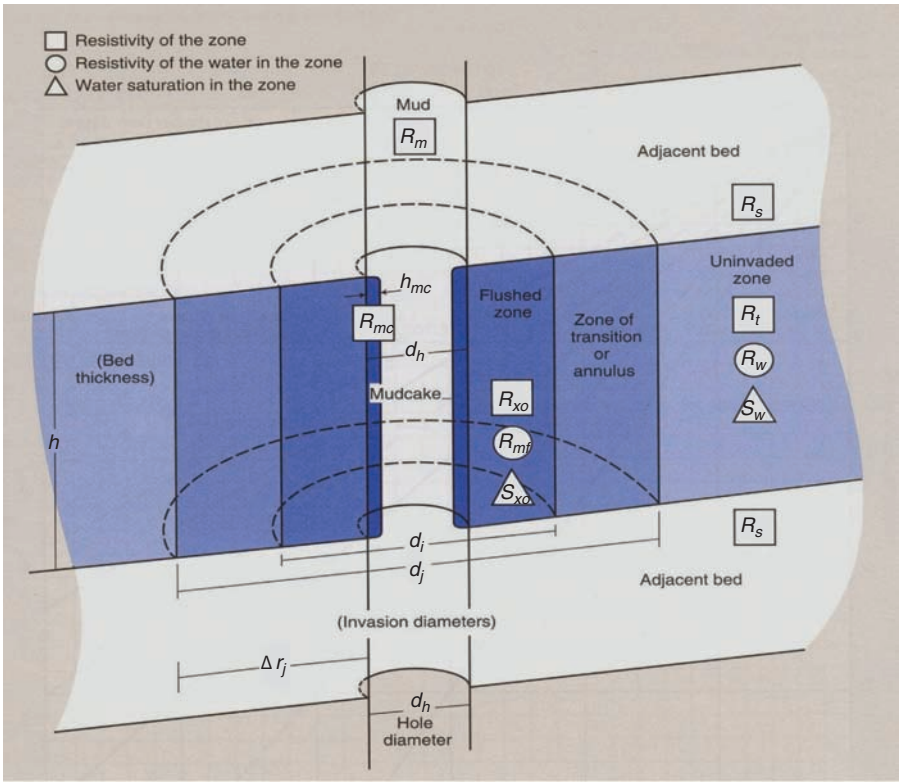


Fig. 4.13—Symbols used in log interpretation (Schlumberger 2009). Courtesy of Schlumberger.

TABLE 4.1—NOMENCLATURE FOR ZONES IN AND AROUND THE BOREHOLE

Name of Zone	Dimension	Fluid Content	Fluid/Water Resistivity	Rock Resistivity
Bed	h	—	—	—
Adjacent bed	—	—	—	R_s
Mud	d_h	Mud	R_m	—
Mudcake	h_{mc}	—	—	R_{mc}
Flushed or invaded	d_i	Mud filtrate + residual oil	R_{mf}	R_{xo}
Transition	d_j	Mixed + hydrocarbons	—	—
Uninvaded (undisturbed)		Connate water + hydrocarbons	R_w	R_t

QUESTION 4.2. A 30% porous sandstone bed is 100 ft thick. It is 100% saturated with mud filtrate (S_{xo} = 100%) to an invasion diameter of 40 in. The hole diameter is 8½ in. Estimate the volume of filtrate that will be recovered from this sandstone before connate water or oil begins to be recovered.

QUESTION 4.3. How many linear feet of 3½-in. drillpipe will the volume calculated in Question 4.2 occupy? (Note: for this size drillpipe there are 27.1 linear ft/ft^3.)

The invasion process may change the resistivity profile around the borehole. Whether resistivity increases or decreases with distance from the borehole wall depends on the type of mud used (oil-based or water-based) and the relative values of R_{mf} and R_w. A schematic illustration of what may be expected for a number of cases is shown in **Fig. 4.14**.

4.6 Choosing a Logging Suite

Choice of a logging suite will be influenced by:

- Type of well—wildcat or development well
- Hole conditions—depth, deviation from vertical, hole size, mud type
- Formation—fluid content, fresh or salt connate water
- Economics—rig time, logging dollars, etc.

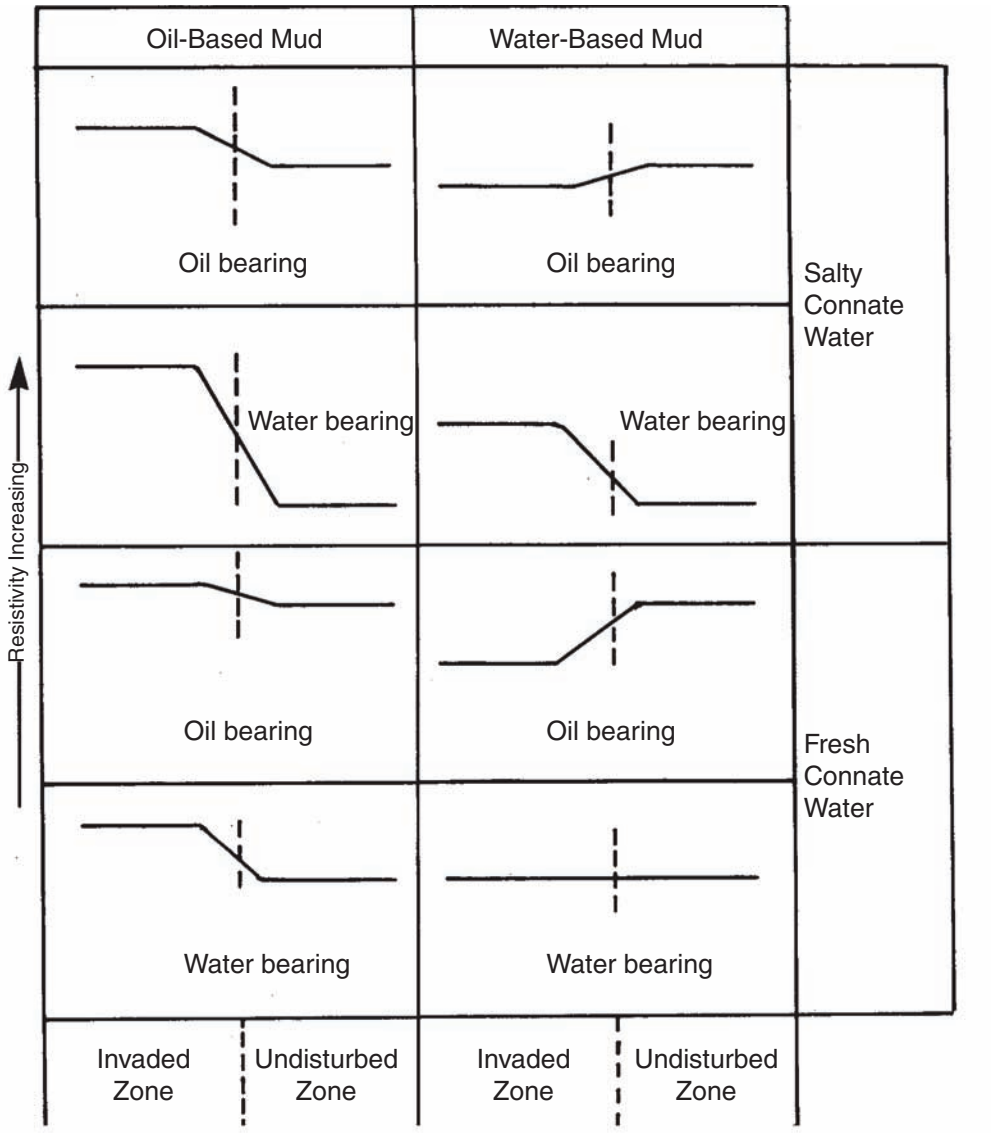


Fig. 4.14—Radial resistivity profile as a function of mud type and formation content.

Each tool is designed for a specific set of conditions. Outside these limitations, the tool fails to provide the required measurements and its use is thus discouraged.

4.6.1 Depth, Pressure, and Temperature. The majority of logging tools are rated at 20,000 psi and 350°F. This is adequate for most holes to be logged. For higher temperatures, special tools (hostile environment) are available from the logging-service companies.

4.6.2 Hole Size. The standard minimum hole size is 6 in. for correct and safe operation of normal logging tools. A limited number of slim-line, small-diameter tools are available for smaller holes. Maximum hole size is hard to define. Most pad-contact tools (compensated neutron logs, compensated formation density logs, microfocused logs, dipmeters, etc.) have spring-loaded, hydraulically operated arms that push the relevant sensor against the borehole wall. The arms will open to a diameter of about 20 in., although this limit varies a little from tool to tool. If holes are deviated, good pad contact may still be obtained since the tool will lean on the low side of the hole, although this cannot be guaranteed. Running a pad-contact tool in a hole with a diameter of more than 20 in. is risky because the pad may not be able to make contact with the wall of the wellbore.

Resistivity devices such as induction logs and laterologs suffer in a progressive fashion as the borehole gets bigger. Theoretically, there is no fixed limit to the hole size, but practically there is a limit because borehole corrections to the raw data become so large that nothing useful can be determined from the logs. Logging of large-diameter surface holes may, thus, cause a problem and require logging in a specially drilled medium-sized hole, which is subsequently under-reamed to the desired gauge.

4.6.3 Hole Deviation. In today's offshore environment, the deviated hole is the norm rather than the exception. The greater the angle of deviation of the hole from vertical, the greater the difficulties of physically getting a logging tool to the bottom of the hole. In general, hole deviation above 40° from vertical causes problems. A number of techniques have been tried to get logging tools safely to bottom; these include:

- Keeping the openhole section as short as possible
- Removal of centralizers and standoff pads
- Use of a hole finder—a rubber snout on the bottom of the logging tool string
- Use of logging tools specially adapted to be run to the bottom of the hole on drillpipe
- Use of a motorized "tractor" to drag the logging tools to target depth

In difficult situations, the hole may have to be logged through open-ended drillpipe with a slim logging tool physically pumped down by mud circulation. Holes with deviations as high as 65° have been logged with this technique.

4.6.4 Types of Logs To Be Run. Logging combinations (chosen according to the type of mud, lithology, and information needed) generally consist of resistivity devices and porosity/lithology devices. Where hydrocarbon reservoirs are difficult to evaluate, two or more porosity devices are needed to differentiate oil from gas and to differentiate between rock types in order to provide more accurate porosity data. Additional tools are also needed when the reservoir engineer, the completion engineer, and the geophysicist want specialized information for formation evaluation and well completion planning.

To a large degree, the choice of a logging program will depend on two main factors—the drilling objective (exploration or development) and the mud system chosen (fresh, salt, or oil-based). With this in mind **Table 4.2** gives general recommended logging suites. Within the broad categories listed, there are further choices such as an array or scanning tool over a simpler, more economic, basic version of the same measurement. This would be particularly true in the case of

TABLE 4.2—RECOMMENDED GENERAL LOGGING PROGRAMS

	Exploration			Development		
Mud System	Fresh	Salt	Oil Based	Fresh	Salt	Oil Based
Neutron	X	X	X	X	X	X
Density				X	X	X
Density + Pe	X	X	X			
Sonic	X	X	X			
Induction	X		X	X		X
Laterolog		X			X	
Micro-XX	X	X		X	X	
Sidewall Coring	X	X	X			
Dipmeter	X	X				
Borehole Imaging	X	X	X			
GR				X	X	X
Spectral GR	X	X	X			
SP	X	X		X	X	
NMR	X	X	X			
Formation Tester	X	X	X			

induction and sonic logging. The extent of the logging program is also a function of the information obtained on previous wells.

4.6.5 Influence of the Mud Program. Mud type influences the choice of a logging tool, especially the choice of a resistivity tool. Air-drilled holes, which have nonconductive fluid in them, must be logged with an induction device. Air-drilled holes also need an Epithermal Neutron device rather than a conventional Compensated (Thermal) Neutron (see Chapter 18 for further details). Likewise, holes drilled with oil-based mud can only be logged with an induction log. Where conductive fluids are in the borehole for logging operations, the choice between induction and laterolog devices is controlled by the salinities of the mud and the connate water in the formation. In general, fresh muds and salty formation waters favor the induction log and salty muds favor the laterolog.

All formations should be protected from excessive fluid losses so that porosity and saturation can be adequately determined. Bit-cutting sample recovery should be efficient enough to help in interpretation of lithology so that proper constants for log evaluation formula can be established. Thus, the mud program should be designed for both the drilling and the logging operations.

It is possible for a logging program to succeed or fail solely because of the way the mud program is designed. For example, filtrate from a high-water-loss mud can invade a formation so deeply as to mask the measurement of true resistivity, reduce the amplitude of the spontaneous potential curve, obscure the detection of the residual hydrocarbons, and result in water recovery on a drillstem test from zones that would otherwise produce oil. Invasion of oil from oil-based or oil-emulsion muds can affect resistivity readings and erroneously indicate oil in water-bearing formations or reduce the formation porosity values calculated from microresistivity devices.

The practice of mudding up just before reaching the objective zone can adversely affect interpretation when mud filtrate invades the formation beyond the radius of investigation of the resistivity device. Also, friable formations drilled with natural high-water-loss muds are usually badly washed out and can prevent the logging tools from going down the hole because they hang up on ledges and/or bridges. Borehole contact devices cannot obtain effective contact with the side of the borehole in highly rugose holes and will give erroneous measurements.

The decision to drill through shallow formations with natural high-water-loss muds is normally based on the erroneous assumption that the shallow formations are of no interest. Nevertheless,

logs through the shallow formations are invariably consulted later to find zones for recompletion, to determine prospects for new hydrocarbon-bearing zones in the area, to locate and evaluate high pressure zones, and for general correlation work.

4.6.6 Choosing When To Log. Logs should be run just before the running and setting of a casing string. Once casing is set, the choices for logging are severely limited. Logs should also be run if hole conditions suggest that a section of hole could be lost (caving, washouts, etc., which would negate running a logging tool), if cuttings indicate that an unexpected formation has been encountered, or if one is otherwise lost structurally.

However, one's enthusiasm for running logs should be tempered somewhat by the economic and practical realities of service-company price lists and fee structures. Each time a logging truck is called, some kind of setup charge is assessed to cover costs of mobilization; a depth charge is assessed per foot of hole from surface to total depth; and a survey charge is assessed over the actual interval logged. The full cost of a logging operation is, more than anything else, a function of the depth of the well. To log a 100-ft section at 10,000 ft is an expensive proposition, while a 4,000-ft survey at 5,000 ft total depth is probably less expensive.

4.7 Computerized Logging Units

Major service companies now offer logging services from computer-based logging units. The advantages of using these computer-based units are many, and their use is to be encouraged because they offer the following features:

- All logs are directly recorded on digitally.
- Logs can be recorded while logging up or logging down, with all curves mutually on depth.
- Calibrations are performed under programmed control.
- Logs can be played back from the digital recordings on many different scales (both depth and response scales).
- Wellsite computation of raw data is commonly available. These computations range from completion aids (hole-volume integration for cement volumes) to dipmeter computations and complete log analysis.

Fig. 4.15 shows the logging engineers console inside a logging unit with a computer-based logging system. The logging engineer interacts with the system using the keyboard. At a command, the computer will load programs to perform such functions as calibration, logging, computation, and playback.



Fig. 4.15—Computerized logging system. Photo taken by the author of a Baker Atlas logging truck with permission of Baker Hughes.

4.7.1 Log Presentations and Calibrations. The analog presentation of a wireline log is comprised by a header that identifies the well and the intervals logged (see **Fig 4.16**), curve headers that identify the parameters recorded and their scaling (see **Fig. 4.17**).

Conventional logging systems require human operation of both sensitivity and zero offset control. The variable offset resistor **(Fig. 4.18)** is adjusted when the logging sensor is at the low end of its range of measurement (e.g., the caliper tool in a 6-in. ring), and the variable gain resistor is adjusted when the sensor is at the high end (e.g., the caliper tool in a 12-in. ring).

Computer systems eliminate the need for human intervention—other than to place the tool to be calibrated in the correct environment (putting the 6-in. ring over the caliper arms, for example).

Logging Date			23-Jan-2009		
Run Number			1		
Depth Driller			3320 m		
Schlumberger Depth			3324 m		
Bottom Log Interval			3321.5 m		
Top Log Interval			2886.7 m		
Casing Driller Size @ Depth			9.625 m	@	2886 m
Casing Schlumberger			2886.7 m		
Bit Size			8.500 in		
Type Fluid In Hole			Versadrill OBM		
MUD	Density	Viscosity	1.27016 g/cm^3	56 s	
	Fluid Loss	PH	4.1 cm^3		
	Source of Sample				
RM @ Measured Temperature				@	
RMF @ Measured Temperature				@	
RMC @ Measured Temperature				@	
Source RMF	RMC				
RM @ MRT	RMF @ MRT		@ 102		@ 102
Maximum Recorded Temperatures			102°C	102	102
Circulation Stopped		Time	22-Jan-2009		18:30
Logger on Bottom		Time	23-Jan-2009		9:00
Unit Number		Location	5525		
Recorded By					
Witnessed By					

Fig. 4.16—Example of a computerized log heading.

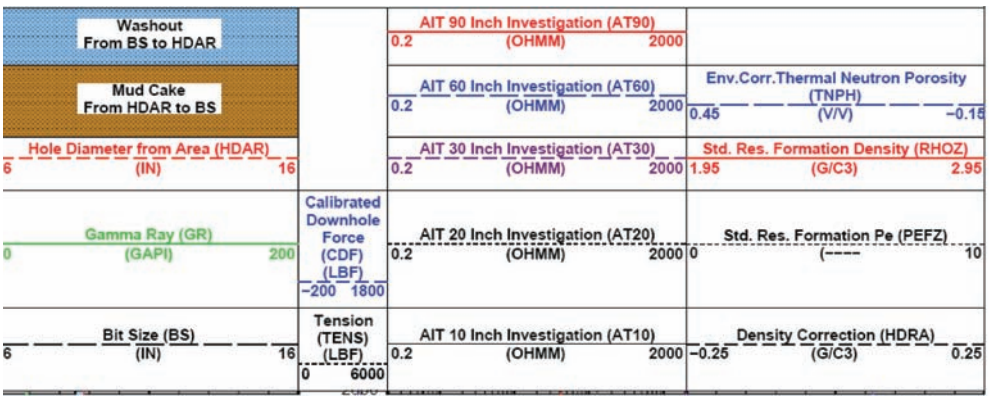


Fig. 4.17—Example of a computerized logging curve header.

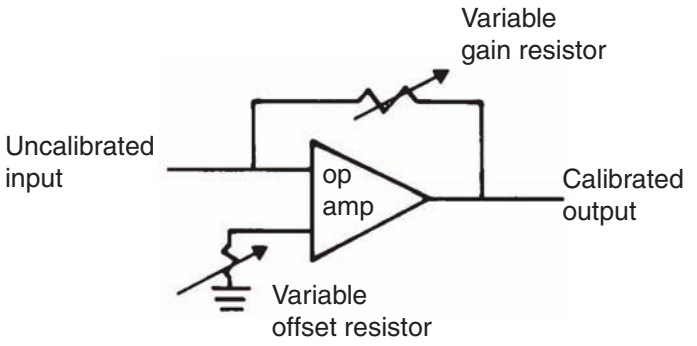


Fig. 4.18—Conventional calibration method.

The computer system accepts the raw, uncalibrated readings of the tool and computes a calibration equation to transform the raw data into calibrated data (see **Fig. 4.19**). For example, a caliper may read 7.2 in. in an 8-in. ring and 13.6 in. in a 16-in. ring. The computer solves the equation relating calibrated readings to raw readings:

$$\text{calibrated caliper} = A + B \times \text{raw caliper}, \quad \ldots\ldots\ldots\

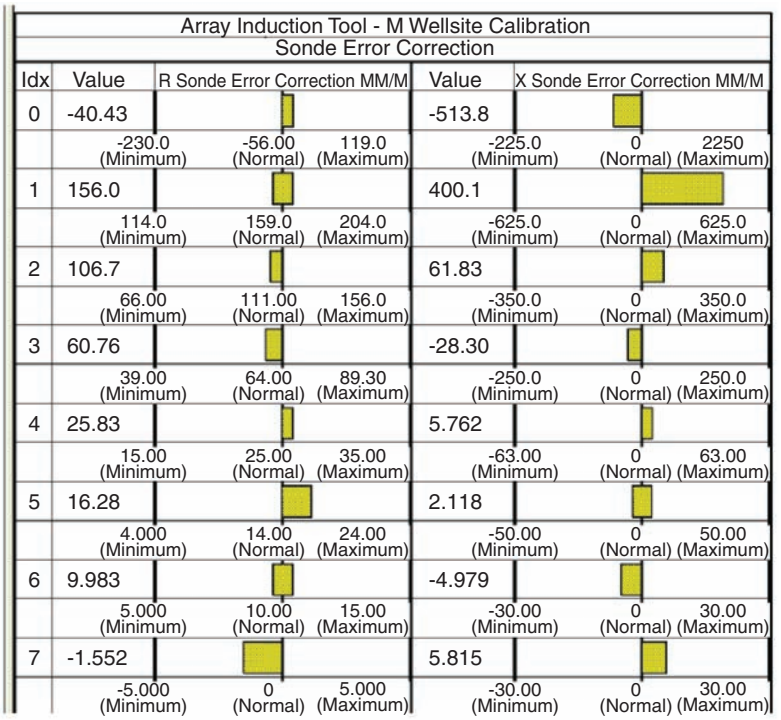


Fig. 4.20—Computer unit calibrations for an array induction log (Schlumberger 2008). Courtesy of Schlumberger.

Note that these calibration tails record the actual value of some parameter as a number expressed in engineering units. Computerized calibrations fall into three categories:

1. Shop calibrations
2. Before survey calibration
3. After survey calibration

The important things to check include good agreement of all three calibration values within the specified tolerances as specified by the corresponding service company log quality guidelines, which can be obtained from logging company sales personnel. For further details on log calibrations please refer to Bateman (1985) and Theys (1999 and 2010).

4.8 Log-Quality Control

4.8.1 The Need for Log-Quality Control. The need for log-quality control has been documented in various studies, such as the one by Neinast and Knox of Sun Oil Company (1973). As these studies have shown, poor log-quality control can result in a large percentage of logs being in error. Frequently, the errors made in recording the logs render them useless as formation evaluation tools.

It is the function of the well operator's representative to ensure that the logs obtained are of the best quality. Service-company personnel expect a representative to be available and in the logging unit during the logging operation. Logging operations should be discussed with the logging engineer before and after the job. The most critical time during a logging operation is when the tool is within 1,000 ft of the bottom of the well. Do not distract the logging engineer during this time. Even the best engineers may make mistakes when they are distracted. Give the engineer a chance to perform the operation with minimum interruption.

After each log is complete, discuss it with the engineer as thoroughly as possible. Ask for an explanation of any abnormal curve responses, equipment failure, or hole problems, and enter the information in the "remarks" column of the log heading. If there is any question about validity, request a rerun of the log before the crew rigs down. Generally, 200 ft of repeat in relatively smooth hole should be enough to verify the log. Everyone is reluctant to go back in the hole after rigging down, but once pipe is set, it will be impossible to get another resistivity survey of any type.

No matter how competent and conscientious an observer may be, there are ways in which bad logs can defy detection at the wellsite. To this degree, log quality also depends on the competence and integrity of the logging company's engineer. Perhaps the most important objective is to develop relationships of mutual trust with the logging company personnel with whom you work.

4.8.2 Practical Log Quality Checks. Calibrations are the only completely objective verifications of log quality available. Learn what they mean and how to use them. The depth-related log measurements will include one or more repeat sections, usually of about 200 ft. These records are valuable, though not conclusive, indications of correct tool operation and should be examined carefully on every log run.

4.8.3 Acceptance Standards for Logs. Although a large percentage of all logs might contain erroneous data of some nature, it would be unfair to intimate that all such logs are worthless. Often a log can be corrected visually or mathematically, but sometimes the log must be rerun before valid conclusions can be made. If so, the cost of rerunning the log might outweigh the importance of the error. When the log is not rerun, the error should be noted on the heading in the remarks column and also noted on the log opposite any zone of interest.

For the most serious errors, it is a mistake to think a bad log is better than none; a bad log may influence important decisions. Consequently, it is imperative that the log be rerun. The problem, of course, is to determine whether to accept or reject the questionable log. One reliable method for determination of a bad log is to ask the question, Is the interpretation accurate? If in doubt, rerun the log. Also ask, Can everyone who will use this log see the error and/or be able to perform an accurate interpretation? If in doubt, rerun the log.

A definite criterion for acceptance or rejection of a log is difficult to establish; each situation will be somewhat different. Good judgment should outweigh written instructions when deciding whether to accept or rerun a log. The following guidelines should assist in making such decisions.

Overall Technical Quality. Many things may adversely affect the technical quality of logging data. The most obvious is equipment malfunction. Other possible causes of poor data are rugose boreholes, sticking tools, logging engineer's errors, tool rotation, excess logging speed, deviated wells, poor centralization or eccentralization, and formation alteration. Many times an anomaly over a logged interval will suggest the possibility of a malfunction. This should be resolved by repeating the log in that section. After all, it may be significant. It is interesting to recall that the SP was originally an anomaly that interfered with measurement of formation resistivity.

Repeatability. Properly functioning resistivity tools, run under conditions that are within their capability, will nearly always repeat very well. As a functional check of the equipment, a repeat section of 200 ft or more is routinely run and should be required except in unusual circumstances. Aside from equipment failures, factors that could cause poor repeats include:

- Washed-out holes, particularly those of extremely noncircular cross sections
- Variable tool centering, particularly in large holes with fairly high mud conductivities
- The presence of metallic fish in the borehole
- Comparing an up-run with a down-run (which may appear quite different with some types of equipment)

The repeatability of a log run may be affected by time-related phenomena too, such as varying invasion profiles. Invading filtrate can penetrate deeper, migrate vertically, accumulate as

annuli, or dissipate altogether with the passage of time. The log response, particularly of the shallow reading devices, may continue to change for many days after the well is logged. Though unusual, such changes can be very troublesome; but from the viewpoint of log quality, they are usually recognizable. The changes occur only in the invaded sections, not the shales or other impervious rocks.

Offset Logs. If the well is in a developing field, or in a consistent geological block, available offset logs are likely to be useful. This is especially true in an unfamiliar area.

Absolute Log Values. Comparison of log readings with known absolute values is seldom possible, but when it can be done, this positive crosscheck should be used. Formations that consist of pure, zero-porosity minerals such as halite, anhydrite, or limestone, can be used to check log readings. These natural benchmarks are listed, for several of the more common tools, in **Table 4.3**.

A casing can sometimes be used as a check. All caliper tools should read the same in casing. The diameter indicated is usually slightly greater than that of new casing owing to drillpipe wear. The two diameters measured by a four-arm caliper should be equal. The sonic should read about 56 μsec/ft in unbonded casing.

Depth Measurements. Measurement of depth is perhaps the logging company's most basic function but one that tends to get lost among the more glamorous parameters. Absolute depth control is provided either by a calibrated sheave or by magnetic marks placed on the logging cable every 100 ft (or 50 m). In either case, the operational procedure for obtaining accurate depth control is rather rigorous and if followed properly, will almost always result in accurate depth measurements. This is one of the places where it is advisable to be on terms of mutual trust with the logging engineer. It may be possible to detect evidence of inaccurate depth measurements, but absolute verification is very difficult. Compare the logger's total depth and casing depth with the depths reported by the driller, watch for excessive tie-in corrections with previous log runs, and check the apparent depths of known markers.

Relative depth control means ensuring that all measurements are on-depth with each other. All curves that are recorded on the same trip in the hole should be on-depth with each other within ± 6 in. In addition, each subsequent log should match the base log within 2 ft in straight holes and 4 ft in highly deviated wells (greater than 30°).

TABLE 4.3—TOOL RESPONSE IN COMMON BENCHMARKS

Benchmark	Sonic (μ-sec/ft)	Density (g/cm^3)	Compensated Neutron Limestone %	Photoelectric Factor (Pe)
Salt	67	2.04	–2	4.65
Anhydrite	50	2.98	–1	5.05
Sulfur	122	2.02	–3	5.43
Casing	56	—	—	—

TABLE 4.4—RECOMMENDED LOGGING SPEEDS

Tool	Ft/min	Ft/hr	Remarks
Resistivity log	100	6000	
Resistivity + GR log	60	3600	GR for correlation
Sonic log	60	3600	Slower if the sonic is noisy
Dipmeter	60	3600	
Microresistivity	40	2400	
Radiation log	30	1800	
NMR	15	900	

Logging Speeds. The logging speed in feet or meters per minute is indicated by gaps or ticks along the edge of log print. Acceptable logging speeds depend on the type of log, the intended use of the data, and the type of formation being logged. Normal routine logging speeds are given in **Table 4.4**.

Logging Service Company Nomenclature. In general the same logging measurement is called by a slightly different name by each of the major wireline service companies. To offer some clarification, an appendix to this chapter lists some of the more common logging tools and their names by service company. However this table is continuously changing and the reader is recommended to obtain wireline service catalogs from the service providers to have the most up-to-date information at hand. When the generic equivalents that are offered for measurements on drillpipe are added, keeping these types of tables up to date is difficult.

References

Bateman, R.M. 1985. *Log Quality Control*. Boston, Massachusetts: International Human Resources Development Corporation (IHRDC).

Neinast, G.S. and Knox, C.C. 1973. Normalization of Well Log Data. Paper 1973-I presented at the SPWLA 14th Annual Logging Symposium, Lafayette, Louisiana, USA, 6–9 May.

This is Schlumberger. 1988. New York: Schlumberger Limited.

Schlumberger. 2008. *Log Calibration Guide*, client version. Sugar Land, Texas: Schlumberger Limited.

Schlumberger. 2009. *Log Interpretation Charts*. Sugar Land, Texas: Schlumberger.

Theys, P. 1999. *Log Data Acquisition and Quality Control*, second edition. Paris: Editions TECHNIP.

Theys, P. 2010. *Quest for Quality Data*. Paris, France: Editions TECHNIP.

Answers to Questions

QUESTION 4.1. 2T COS 45° = 10,000 × 0.7071 = 7,707 lbm.

QUESTION 4.2. 250 ft^3 or 44.5 bbl.

QUESTION 4.3. 6,774.44 ft.

Appendix—Service Company Nomenclature

APPENDIX—SERVICE COMPANY NOMENCLATURE

Schlumberger	Halliburton	Baker Atlas	Weatherford
Electrical log (ES)	Electric log	Electrolog	Electric log
Induction electric log	Induction electrical log	Induction electrolog	Induction electric log
Induction spherically focused			
Dual induction SFL	Dual induction-laterolog	Dual induction focused log	Dual induction log
Laterolog-3	Laterolog-3	Focused log	Guard log
Dual laterolog	Dual laterolog	Dual laterolog	Dual guard log
Microlog	Micro-electrical log	Minilog	Contact log
Microlaterolog	Microlaterolog	Microlaterolog	F_o R_{xo} log
Proximity log		Proximity log	
Microspherically focused log			
Borehole compensated sonic	Borehole compensated sonic	Borehole compensated acoustilog	Acoustic velocity log
Long spaced sonic log		Long spacing BHC acoustilog	
Cement bond/variable density	Sonic cement bond system	Acoustic cement bond log	Microseismogram
Gamma ray neutron	Gamma ray neutron	Gamma ray neutron	Gamma ray neutron
Sidewall neutron porosity log	Sidewall neutron porosity log	Sidewall epithermal neutron log	Sidewall neutron log
Compensated neutron log	Compensated neutron log	Compensated neutron log	Dual spaced neutron
Acoustilog			
Thermal neutron decay time		Neutron lifetime log	Thermal multigate decay
Formation density log	Compensated density log	Compensated densilog	Density log
Litho-density log		Z-densilog	
High resolution dipmeter	Four-electrode dipmeter	Diplog	Diplog
Formation interval tester		Formation tester	Formation test
Repeat formation tester	Selective formation tester	Formation multitester	Multiset tester
Sidewall sampler	Sidewall core gun	Corgun	Sidewall coring
Electromagnetic propagation log	Dielectric constant log	Dielectric log	Dielectric constant log
Borehole geometry tool	X-Y caliper log	Caliper log	Caliper
Ultra long spacing electric log			Compensated
Natural gamma ray		Spectralog	Spectral natural
Spectrometry			Gamma
General spectroscopy tool		Carbon/oxygen log	
Well seismic tool		Borehole seismic record	
Fracture identification log	Fracture detection log		

Chapter 5

Coring

5.1 Objectives

The objectives of coring are to bring a sample of the formation and its pore fluids to the surface in an unaltered state, to preserve the sample, and then to transport it to a laboratory for analysis. These objectives are hard to meet because the very act of cutting a core will, to some extent, alter both the properties of the rock itself and the saturation of the fluids in its pores.

A number of techniques exist for minimizing damage to formation samples. These will be discussed in this chapter. Other techniques, aimed at restoring the original state of the formation sample when it was at reservoir conditions, may be brought into play at the time the core is analyzed. These will be discussed in Chapter 27, which deals with core analysis.

5.2 Wireline Coring

Two primary methods of retrieving formation samples with wireline tools are currently in use: the conventional percussion sidewall core gun and the rotary sidewall coring tool.

5.2.1 Percussion Sidewall Cores. Fig. 5.1 illustrates a percussion sidewall core gun. The body of the gun carries a number of hollow steel bullets that can be fired selectively into the formation by means of explosive charges. Once lodged in the formation, the bullet can be retrieved by means of flexible steel wires attached to the bullet. Raising the gun in the borehole usually provides sufficient tension on the wires to dislodge the bullet. Note that the gun is equipped with an SP electrode. This allows the tool to be placed at the correct depth in the well before sampling by correlation of a short section of SP log with other openhole logs already run.

These guns come in a variety of shapes and sizes. On average, they are capable of retrieving 60 to 90 samples in one trip in the hole. The diameter of the core barrel may be anywhere between ¾ and 1⅛ in. Typical core size is 1 in. in diameter and 1¾ in. long.

The length of the core retrieved is a function of many variables. The strength of the explosive charge used, the type of core barrel selected, and the hardness of the formation determine the length of the recovered sample; it may be as long as 2 in. or as short as nothing at all. Occasionally, the retainer wires used to retrieve the core barrel will break and the bullet will be lost in the hole. **Fig. 5.2** is a close-up view of a core gun.

When all the samples have been collected, the gun is raised to the surface and each core plug is extracted from the coring bullet and stored in a glass jar marked with the well name and the depth from which it was cut. Subsequently, these cores may be analyzed for porosity, permeability, grain density, grain size and distribution, and hydrocarbon content. There are obvious limitations to the amount of data that can be obtained from sidewall cores. In the first place, the sample is taken from a part of the formation that has been flushed with mud filtrate. Second, the act of explosively firing the core barrel into the formation may induce local fracturing or sample compaction. Last, the trip up the hole to the surface involves reservoir pressure depletion and a considerable amount

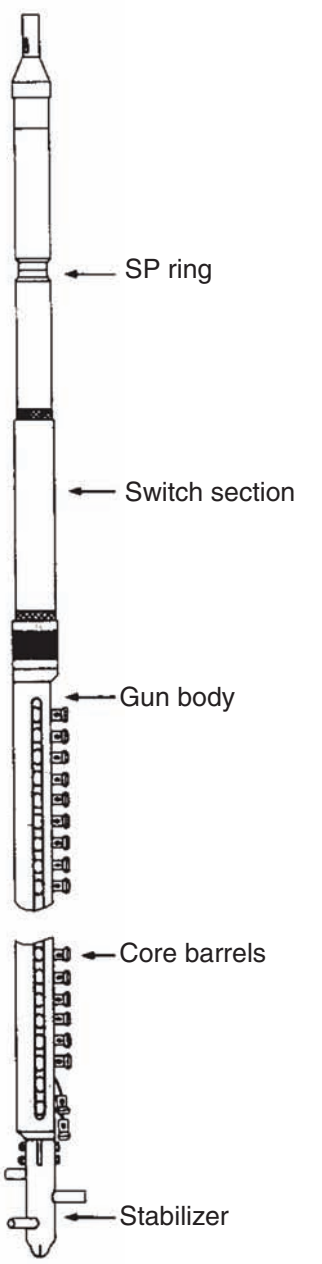


Fig. 5.1—Conventional sidewall core gun. Courtesy of Halliburton.

of flushing through the mud column. Despite these drawbacks, sidewall cores are still good quick-look indicators of formation properties. It is normal practice to inspect these cores at the wellsite for lithology and grain size, hydrocarbon odor, fluorescence, stain, and cut when a mud logging unit or geologist's dog house is available.

5.2.2 Rotary Sidewall Coring. The rotary sidewall coring tool uses a motorized circular bit to bore physically into the wall of the formation to retrieve its samples. It is capable of cutting up to 30 core samples in one run in the hole. With this tool, core size is 15/16 in. in diameter and 1¾ in. long. Each core takes about 5 minutes to cut. This device works better than the conventional percussion sidewall core gun in consolidated formations and causes no physical damage to the sample. **Fig. 5.3** shows the tool and **Fig. 5.4** shows samples of rotary sidewall cores recovered by the device.

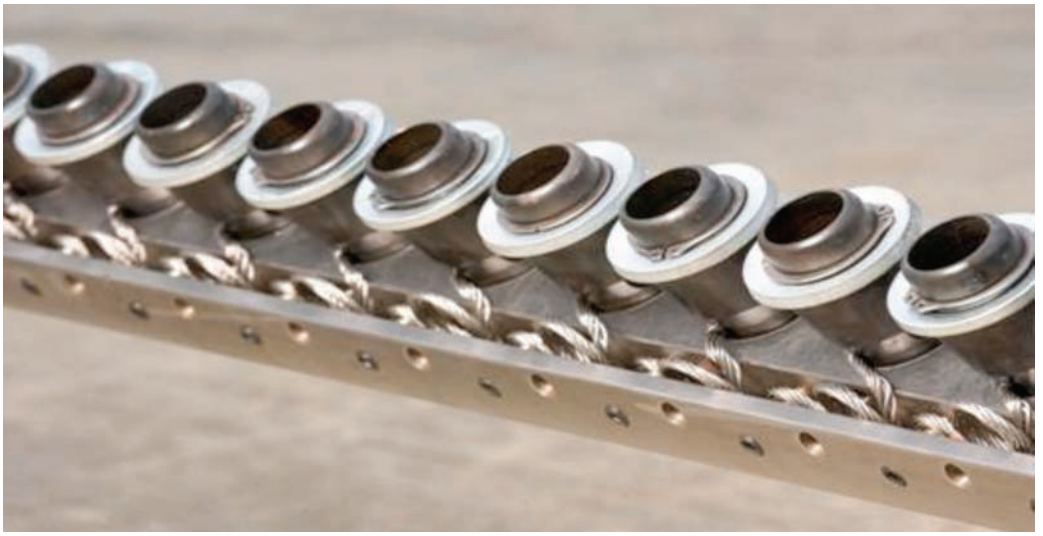


Fig. 5.2—Close-up view of sidewall core gun. Courtesy of Halliburton.

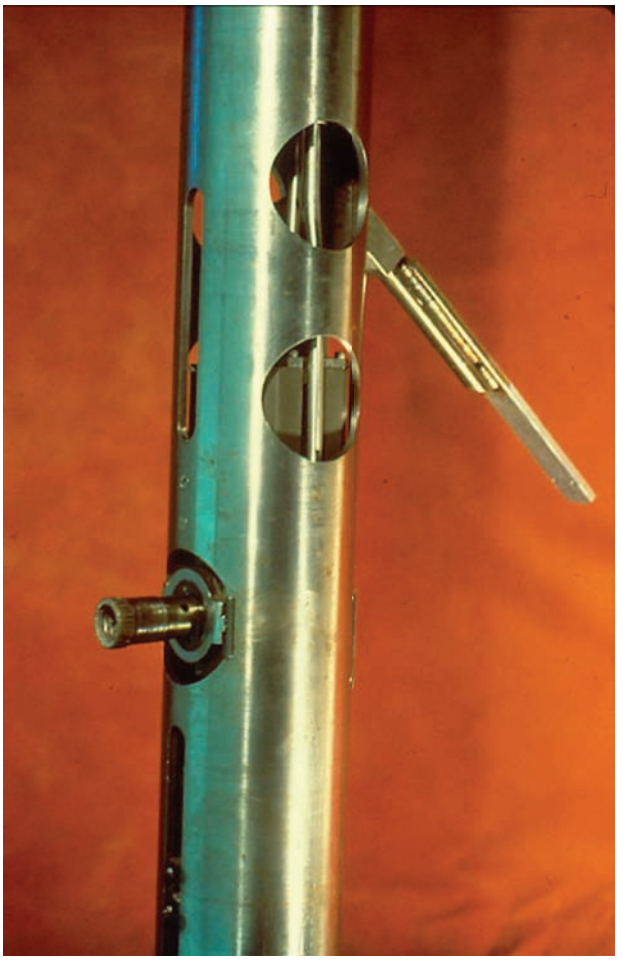


Fig. 5.3—Rotary sidewall coring tool.



Fig. 5.4—Rotary sidewall cores.

5.3 Conventional Coring

When the decision is reached to cut a conventional core (e.g., at a drilling break, a planned depth reached), the drillpipe is removed from the hole and dressed with a hollow core bit and a hollow barrel equipped with a nonrotating inner barrel as shown in **Fig. 5.5**. Cores can be from 400 ft

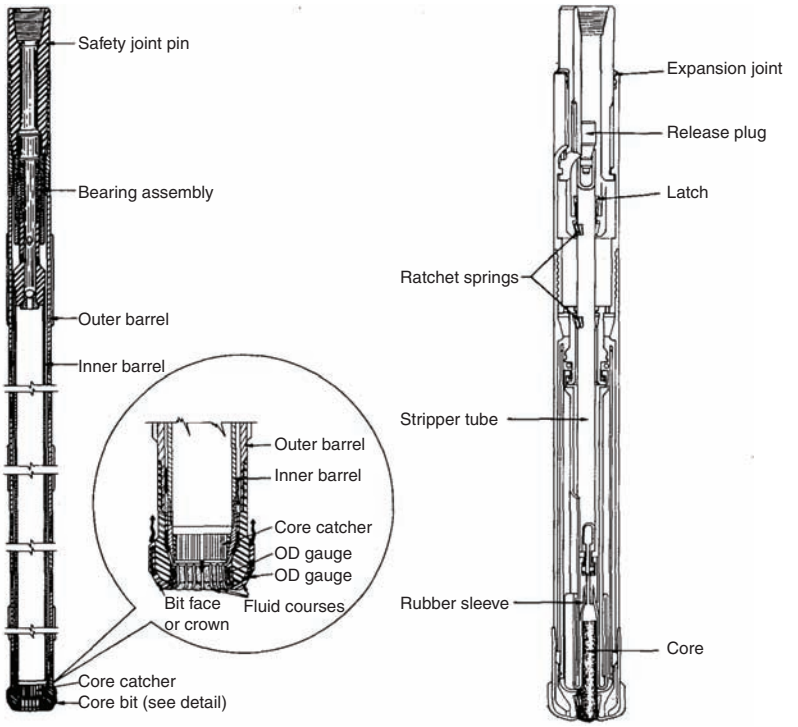


Fig. 5.5—Conventional coring devices (Park 1985). Reprinted by permission of *World Oil*.

down to 1.5 ft long (for short radius horizontal well applications) and have a diameter of 1⅞ to 5¼ in. If unconsolidated formations are to be cored, an inner removable core barrel or inner core barrel removable liner is used to hold friable material more securely. In addition, a full closure core catcher prevents soft formations from falling out of the barrel during core retrieval.

For some applications, a special pressure core can be cut (see **Fig. 5.6**). The core barrel is designed so that after the core is cut, it is maintained at original reservoir pressure until it arrives at the laboratory for analysis. Normally, pressure cores are frozen at the wellsite for transportation. For other applications, oriented cores may be cut. The original orientation of the core relative to north is maintained by use of a special key that cuts grooves in the core. This kind of core is valuable in fractured reservoirs, where fracture orientation or directional permeability is of interest. Both bed dip and azimuth may be deduced from such a core.

5.4 Coring Fluids

The coring fluid used will either increase or decrease the initial saturations of gas, oil, and water in the formation. Water-based muds, for example, produce a water filtrate that invades the core, displacing hydrocarbons. Low invasion coring bits can minimize or eliminate this effect. Tracer data indicate that nonflushed plugs can be obtained for analysis. Oil-based muds having an oil filtrate may replace reservoir oil by the flushing mechanism but do not substantially alter the original oil saturation. **Table 5.1** summarizes the effects of various coring fluids.

Oil or gas will displace water unless the sample or formation is already at irreducible water saturation. The fact that fluid saturations are changed by the coring fluid is not always of

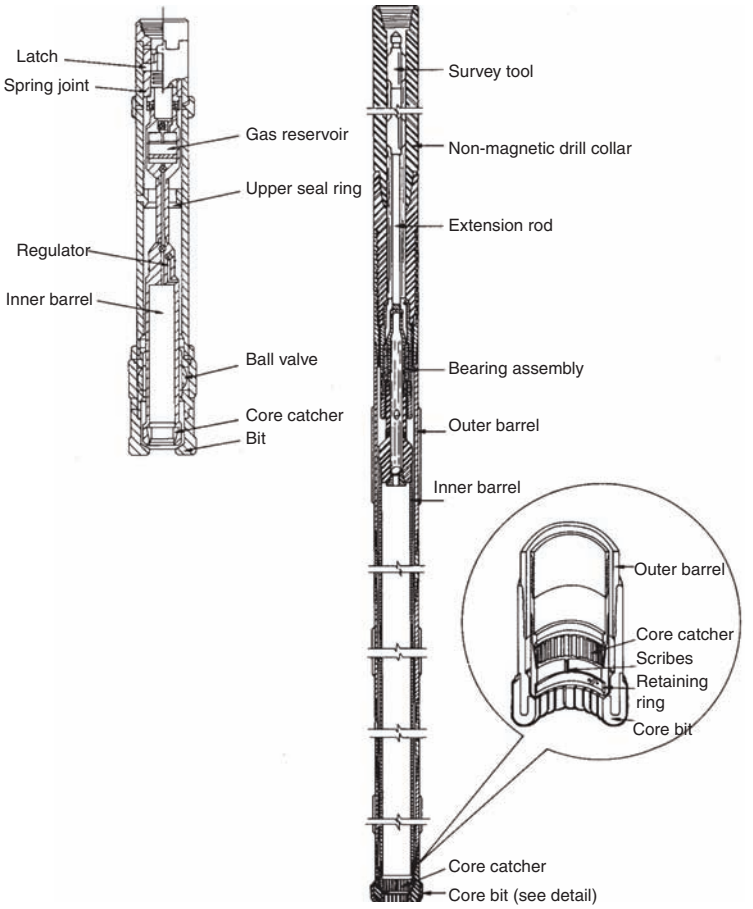


Fig. 5.6—Pressure core barrel (Park 1985). Reprinted by permission of *World Oil*.

TABLE 5.1—EFFECTS OF CORING FLUIDS ON RESERVOIR FLUID SATURATION

		Effect on Core Saturations	
Coring Fluid	Filtrate	Water	Hydrocarbon
Water based	Water	Increased	Decreased
Oil based	Oil	No change*	Replaced
Inverted oil emulsion	Oil	No change*	Replaced
Oil emulsion	Water	Increased	Decreased
Gas	Gas	No change*	Replaced
Air	Uncertain	Uncertain	Decreased

*Oil or gas will displace water unless the sample or formation is already at irreducible water saturation.

consequence—for example, if the core is being cut only for porosity and permeability estimates, the change of water or hydrocarbon saturation is not important. **Table 5.2** lists the most suitable coring fluid for a given objective.

Saturation changes in cores can take place at three different times: at the time the core is cut, as it travels in the core barrel from the reservoir to the surface, and at the surface during transportation and storage. It is worthwhile to review the causes and approximate magnitudes of these saturation changes. **Table 5.3** documents 10 different cases covering a range of coring fluids and initial reservoir saturations. Saturations at surface vary with rock pore geometry and with oil viscosity and formation volume factor. Once the core is retrieved at surface, precautions must be taken to ensure that no further saturation changes occur.

TABLE 5.2—RECOMMENDED CORING FLUIDS TO MEET CORE ANALYSIS OBJECTIVES

	Measurements Suited ✓											
	Water Wet Rock						Oil Wet Rock					
Coring Fluid[1]	Sw[2]	Rel k[3]	Pc[5]	Pc[6] Air-Hg	Wet[4]	EP	Sw[2]	Rel k[3]	Pc[5]	Pc[6] Air-Hg	Wet[4]	EP[3]
Water based	—	✓	✓	✓	✓	✓	—	—	—	✓	✓	—
Oil based	✓	—	—	✓	—	—	✓	✓	—	✓	✓	✓
Invert oil emulsion	✓	—	—	✓	—	—	✓	✓	—	✓	✓	✓
Gas	✓	✓	✓	✓	✓	✓	✓	✓	—	✓	✓	✓
Water	—	✓	✓	✓	✓	✓	—	✓	—	✓	✓	—
Non-oxidized crude	✓	✓	✓	✓	✓	✓	✓	✓	—	✓	✓	✓

1. Porosity, permeability, grain density, lithology, and residual fluids are available for all coring fluids.

2. Reservoir values of water saturation (S_w) require that the coring fluid not add water to the core and that S_w be at irreducible saturation. Water-based fluid is only satisfactory if low invasion coring is used.

3. Oil wet formation cores require crude oil, or low/nonsurface active oil-based mud additives with low water content. Relative permeability (Rel k) tests should be made on fresh, nonextracted core. Resistivity (EP) measurements can be made on fresh core plugs to be combined with S_w.

4. Wettability (Wet) of the reservoir can best be run on fresh, nonextracted core. The coring fluid should contain nonsurface active agents. Techniques are available to use reservoir crude oil to restore cleaned and dried samples to reservoir wettability conditions. However, this may not always be successful and the location of water in the restored core may not be the same as it was in the reservoir.

5. Capillary pressure tests with various fluids (P_c) can be used such as air-water, oil-water, etc. These are typically made on extracted restored core. Oil wet rock measurements require special considerations as to suitability.

6. Air-mercury capillary pressure tests are suitable for all nonshaly rocks. This is the best test for pore throat distribution determination. Hill et al. (1979) described adjustments to air-mercury data for hydratable clay content.

TABLE 5.3—CHANGES IN SATURATION AS A FUNCTION OF RESERVOIR CONTENT AND CORING FLUID

Case	Formation Content	Coring Fluid	Initial Saturations		Change Due to	Saturations in Core Barrel	Change Due to	Saturations at Surface	
1	Oil/water	Water based,	O	70	Flushing	30	Shrinkage	12	O
	oil	badly	G	0		0	Expansion	40	G
	Productive	flushed	W	30	Invasion	70	Expulsion	48	W
2	Oil/water	Water based,	O	70	—	70	Shrinkage	20	O
	oil	Unflushed	G	0	—	0	Expansion	50	G
	Productive		W	30	—	30	—	30	W
3	Oil/water	Oil based,	O	70	Flushing	70	Shrinkage	40	O
	Oil	badly	G	0	—	0	Expansion	30	G
	productive	flushed	W	30	—	30	—	30	W
4	Gas/water	Water based,	O	0	—	0	Condensation	1	O
	Gas	Badly	G	70	Flushing	30	Expansion	49	G
	Productive	Flushed	W	30	Invasion	70	Expulsion	50	W
5	Gas/water	Water based,	O	0	—	0	Condensation	2	O
	Gas	Unflushed	G	70	—	70	—	68	G
	Productive		W	30	—	30	—	30	W
6	Gas/water	Oil based,	O	0	Invasion	50	Expulsion	40	O
	gas	badly	G	70	Flushing	20	Expansion	30	G
	productive	flushed	W	30	—	30	—	30	W
7	Water	Water based	O	0	—	0	—	0	O
	Water		G	0	—	0	Expansion	10	G
	Productive		W	100	Flushing	100	Expulsion	90	W
8	Water	Oil based,	O	0	Invasion	40	Shrinkage	35	O
	water	badly	G	0	—	0	Expansion	10	G
	productive	flushed	W	100	Flushing	60	Expulsion	48	W
9	Oil/water	Water based,	O	30	—	30	Shrinkage	12	O
	at original	badly	G	0	—	0	Expansion	40	G
	reservoir pressure	flushed	W	70	Flushing	70	Expulsion	48	W
10	Oil/water	Water based,	0	155	Flushing	25	Shrinkage	22	O
	after solution	badly	G	15	Flushing	5	Expansion	10	G
	gas drive	flushed	W	30	Invasion	70	Expulsion	68	W

5.5 Special Core Handling

On surface, the core is exposed to the atmosphere, and evaporation of water and light hydrocarbons can occur. Thus, it is normal practice to store the core immediately in a protective environment. Storage methods include:

- Freezing the core with dry ice
- Containing cores in plastic bags
- Wrapping cores in plastic and/or aluminum foil and sealing them with special dips

- Submergence under deaerated water (this may alter pore saturations)
- Submergence under nonoxidizing crude (this also may alter pore saturations)
- Containment within inner core barrels, liners, and tubes

Rubber sleeve cores are normally left in their sleeves, although they may be cut into shorter lengths for ease of handling. Cores with inner core barrel liners may be cut into shorter lengths, capped, and shipped in a frozen state. In some cases the total core barrel liner is frozen at the wellsite before transportation.

5.6 Summary

Cores can be cut in a variety of ways. Great care should be taken in planning the coring fluid and in the transportation and storage of cores once cut to preserve the fluid saturation of interest. The coring fluid used and/or the initial reservoir conditions may make the saturation of oil, water, or gas in the core arriving at the lab considerably higher, or lower, than it was in the formation.

References

Park, A. 1985. Coring: Part 2—Core Barrel Types and Uses. *World Oil* (April): 83–90.

General References

API RP 40, Recommended Practices for Core Analysis, second edition. 1998. Washington, DC: API.

Hill, H.J., Shirley, O.J., and Klein, G.E. 1979. Bound Water in Shaly Sands—Its Relation to Q and Other Formation Properties. *The Log Analyst* **20** (3): 3–19.

Hyland, C.R. 1983. Pressure Coring—An Oilfield Tool. Paper SPE 12093 presented at the SPE Annual Technical Conference and Exhibition, San Francisco, California, 5–8 October. http://dx.doi.org/10.2118/12093-MS.

Pallatt, N., Stockden, I.L.M., Mitchell, P.S.H., and Woodhouse, R. 1991. Low Invasion Coring Gives "Native" Reservoir Water Saturations. In *Theory and Application of Multidisciplinary Evaluations: 14th European Formation Evaluation Symposium*. SPWLA, London Chapter.

Rathmell, J.J., Tibbitts, G.A., Gremley, R.B. et al. 1995. Development of a Method for Partially Uninvaded Coring in High Permeability Sandstones. *SPE Form Eval* **10** (2): 65–71. SPE 20413-PA. http://dx.doi.org/10.2118/20413-PA.

Rathmell, J.J., Gremley, R.R., and Tibbitts, G.A. 1994. Field Applications of Low Invasion Coring. Paper SPE 27045 presented at the SPE Latin America/Caribbean Petroleum Engineering Conference, Buenos Aires, Argentina, 27–29 April. http://dx.doi.org/10.2118/27045-MS.

Rathmell, J.J., Wilston, B.S., Gale, B.A., et al. 1998. Development and Application of PDC Core Bits for Downhole Low Invasion Coring in the Arab Carbonates. *SPE Drill & Compl* **13** (1): 56–65. http://dx.doi.org/10.2118/36263-PA.

Rathmell, J.J., Atkins, L.K., and Kralik, J.G. 1999. Application of Low Invasion Coring and Outcrop Studies to Reservoir Development Planning for the Villano Field. Paper SPE 53718 presented at the Latin American and Caribbean Petroleum Engineering Conference, Caracas, Venezuela, 21–23 April. http://dx.doi.org/10.2118/53718-MS.

Woodhouse, R. 1998. Accurate Reservoir Water Saturations From Oil-Mud Cores: Questions and Answers from Prudhoe Bay and Beyond. *The Log Analyst* **39** (3): 23–47.

Part II—Methods of Analysis and Application of Results

Chapter 6

The Physics of Rock/Fluid Systems

Petrophysics is the name given to the study of rock/fluid systems. It is particularly important that the log analyst be aware of the way in which rocks and fluids interact in both static and dynamic situations. Although logging measurements are made under static reservoir conditions, the prediction of reservoir behavior under dynamic flow conditions can be made only if the physics of fluid flow is understood. The objective of this discussion is to equip the formation evaluator with the information needed to relate log response to reservoir performance (which is what really counts), rather than just to static reservoir content. It is hoped that from the following discussion, the reader will develop a feel for why some reservoirs with low water saturations produce with high water cut, while other reservoirs with much higher computed water saturations produce water-free hydrocarbons.

6.1 The Genesis of Reservoir Rocks

A reservoir rock is one that has both storage capacity and the ability to allow fluids to flow through it; that is, it must possess both porosity and permeability. Porosity can develop as the void space between grains of sediments as they are laid down. Typical reservoirs with intergranular porosity are sandstone reservoirs. Porosity can also develop when chemicals react with rocks after the rocks have been deposited. Typical reservoirs with this solution type of porosity are carbonate reservoirs. Porosity can also develop in the form of fractures induced by the stresses of tectonic movement. Porosity per se does not guarantee permeability. Swiss cheese, for example, is highly porous, but impermeable.

6.1.1 Porosity. The porosity developed in sedimentary rocks is a function of many variables, such as grain shape, size, orientation, and sorting, which can be broadly grouped under the term *rock texture*. If all the grains are of the same size, sorting is said to be good. If grains of many diverse sizes are mixed together, sorting is said to be poor. The packing of the grains (see **Fig. 6.1**) determines the porosity. For a given quality of sorting, porosity is independent of grain size. For example, if spheres of diameter d are packed in a cubic lattice arrangement, the porosity can be calculated in the following manner.

In a unit volume, n^3 spheres are packed n to a side. The total volume is $(nd)^3$. The volume of any one sphere is $(4/3)\ \pi\ (d/2)^3$, and therefore the volume occupied by n^3 spheres is $(4/3)\ \pi\ (nd/2)^3$. The porosity is therefore

$$\phi = \frac{(nd)^3 - \left(\frac{4}{3}\right)\pi\left(\frac{nd}{2}\right)^3}{(nd)^3}, \quad \text{(6.1)}$$

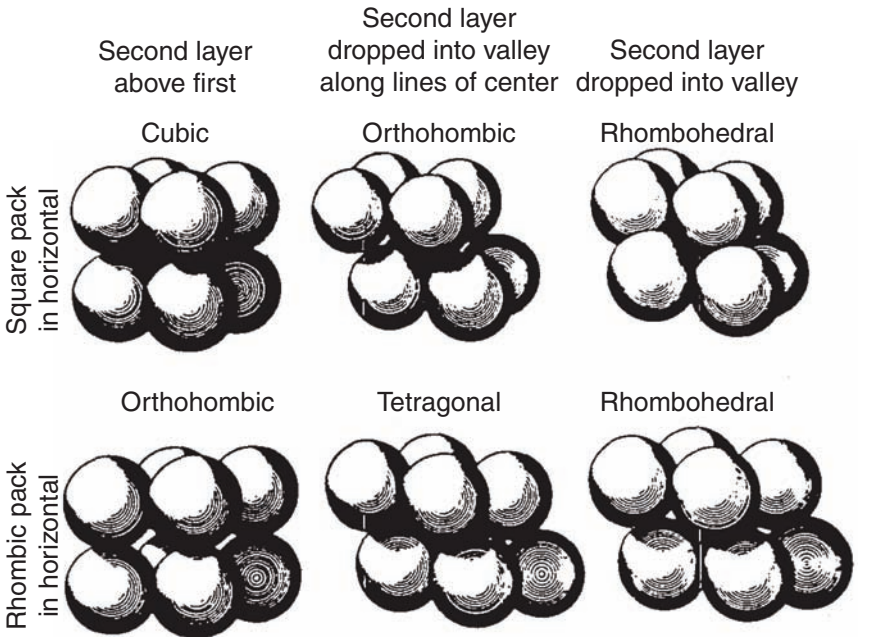


Fig. 6.1— Packing of spheres (Graton and Fraser 1935). Reprinted by permission of the University of Chicago Press.

which simplifies to $(1 - \pi/6)$, or 0.4764. Note that the term d cancels out and is not a determining factor.

Cubic packing is not an efficient way to store spheres in a box, and nature seeks more compact packing mechanisms, such as rhombohedral packing, which produces a porosity of 25.95% (as opposed to 47.64% for cubic packing). For a given grain size, porosity will decrease as sorting becomes poorer, because intergranular pores can be occupied by ever-smaller grains.

Quite apart from the mechanics of how sand grains are packed, their degree of compaction with depth of burial is another matter. Porosity decreases with increasing depth in a predictable manner. A relationship of the form

$$\phi = \phi_0 e^{-\text{depth}/\alpha}, \quad (6.2)$$

where α is a compaction constant for a particular geologic area, generally fits most normally pressured reservoirs; that is, the log of porosity is linear with depth. For example, if ϕ_0, the porosity at surface, is 45%, and depth is in feet, a typical value of α might be 12,000, resulting in a porosity of 12.9% at 15,000 ft and 8.5% at 20,000 ft.

6.1.2 Permeability. Although porosity is a static property of a rock, permeability is a dynamic one. Permeability is a measure of the ability of a rock to allow fluids to flow through it. Darcy's law for flow through a porous medium is:

$$q = \frac{kA\Delta p}{\mu L}, \quad (6.3)$$

where q is the flow rate through a body of length L with cross-sectional area A open to flow under a pressure differential of Δp for a fluid with viscosity μ. If flow is laminar, Darcy's relation can be used to define the permeability k as follows:

$$k = \frac{q\mu L}{\Delta p A} \quad \ldots\ldots (6.4)$$

If only one fluid is present in the pore system, this relation defines absolute permeability—that is, it is a rock property independent of the fluid flowing through the rock. If q is in cm^3/s, A is in cm^2, $\Delta p/L$ is in atm/cm, and μ is in cp, then k is in darcies. (The practical unit is the millidarcy, abbreviated md and equal to 0.001 of a darcy.)

The relationship between permeability and porosity depends on rock type. In general, the log of permeability is linear with porosity for a given rock type; however, the precise relationship can be found only through direct measurements of representative rock samples. **Fig. 6.2** shows some of these trends. Various investigators have, over the years, developed theoretical permeability-to-porosity relationships that account for textural features such as the size, shape, and distribution of pore channels in the rock. One such relationship is the Kozeny relationship:

$$k = (\text{const})\, d^2 \frac{\phi^3}{(1-\phi)^2} \quad \ldots\ldots (6.5)$$

For fracture systems, generalized formulas have been developed that relate permeability to the square of fracture width.

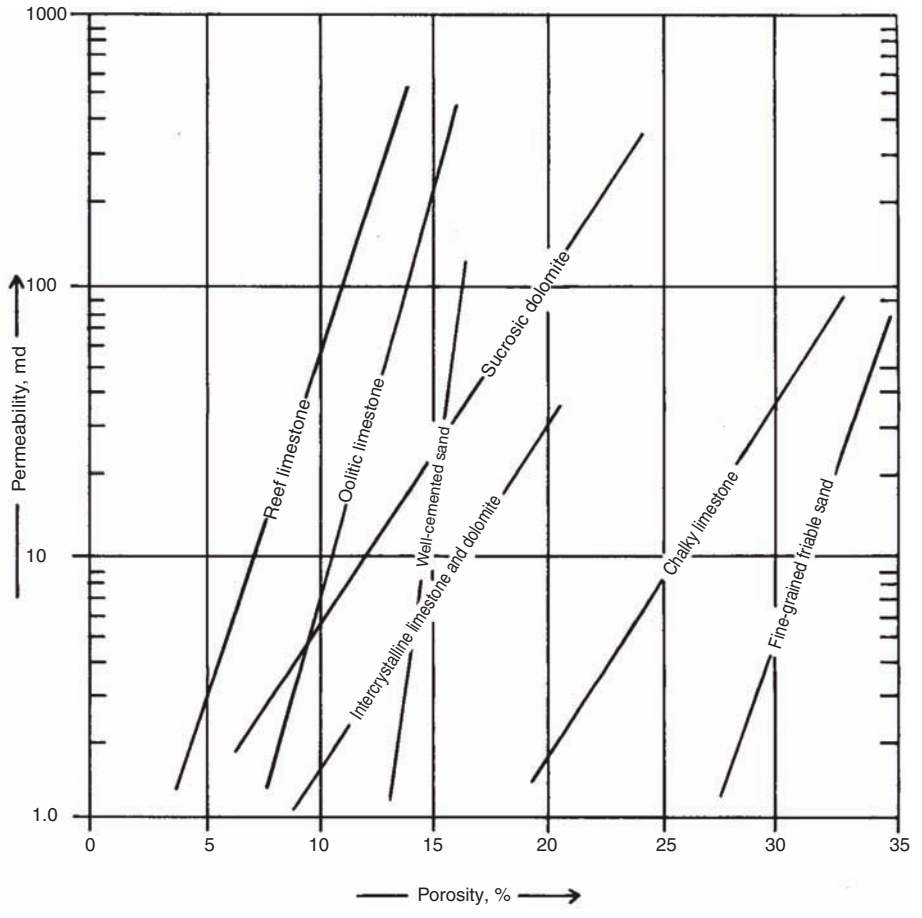


Fig. 6.2—Permeability/porosity relationships. After Core Lab.

In some reservoirs, permeability is a vector, that is, it has directional properties. Depositional effects may tend to align grains along their long axis, thus increasing the permeability in that direction. Moreover, vertical permeability may be different from horizontal permeability. In fractured reservoirs, permeability is likely to be highly directional depending on the azimuth of the fracture planes.

6.2 Fluid Distribution in the Reservoir

Initially, sediments are laid down in water, either in river and lake beds (continental), in deltas and along shorelines (transitional), or on continental shelves (marine), as illustrated in **Fig. 6.3**. (Exceptions to this rule are eolian dune sediments, which are initially deposited in a water-free environment). Later in geologic time, after the reservoir rock has been buried, hydrocarbons from neighboring source rocks migrate into the reservoir. By simple gravity segregation, gas accumulates above oil, which overlies water. In the absence of any rock matrix, gas, oil, and water form distinct layers with sharp contacts between each phase, but in the reservoir, the lines of demarcation between gas, oil, and water become blurred. Some common observations from a physics laboratory will serve to explain why this occurs.

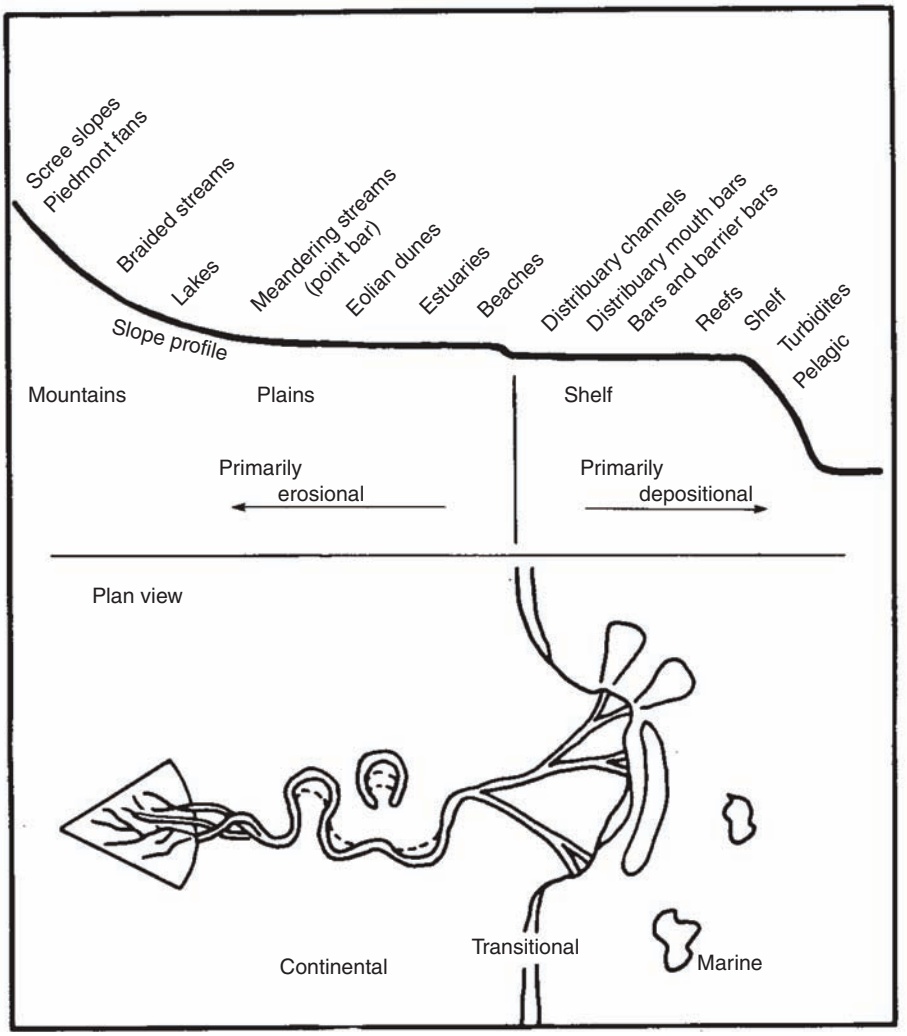


Fig. 6.3—Interrelationships of depositional environments (Goetz et al. 1977). Reprinted by permission of the Indonesian Petroleum Association.

Fig. 6.4 shows a simple reservoir containing oil and water. It is divided into three sections. The section at the top is mainly oil, the section at the bottom is all water, and the section in the middle has increasing amounts of water with increasing depth. Plotted on the right side of the figure is a water-saturation curve, together with a plot of fluid pressure in the pore space.

To understand the shape of the water-saturation curve in the transition zone, consider the case of a small glass tube held in a beaker of water, as shown in **Fig. 6.5**. A capillary tube of radius r will support a column of water of height h. If the density of air is ρ_a and the density of water is ρ_w, the pressure differential at the air/water contact is simply $(\rho_w - \rho_a)\, h$. This pressure differential acting across the cross-sectional area of the capillary is exactly counterbalanced by the surface tension, T, of the water film acting around the inner circumference of the capillary tube.

If, at the water/glass interface, the contact angle is θ, then at equilibrium

$$2\pi rT\cos\theta = (\rho_w - \rho_a)\pi r^2$$

force = pressure × area. . . . . (6.6)

Simplifying this expression and rearranging,

$$h = \frac{2T\cos\theta}{r(\rho_w - \rho_a)} \quad \ldots\ldots\ldots\

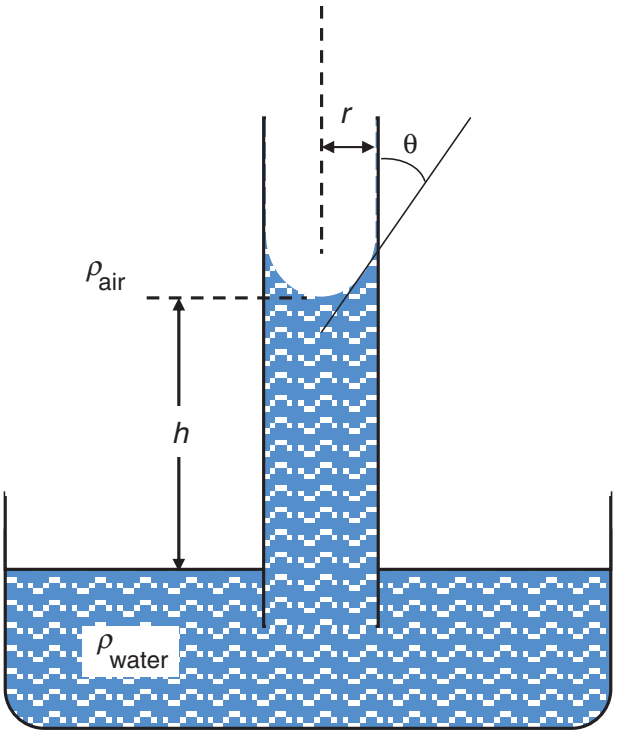


Fig. 6.5—Capillary tube in water.

Inspection of this equation shows that the smaller the value of r, the larger h becomes. When this laboratory observation is translated into reservoir-fluid terms, it is clear that water can be drawn up into what would otherwise be a 100%-oil column by the capillary effect of the small pores in the rock system that act like tiny tubes. The air in Fig. 6.5 can be equated with oil, the water with water, and the tube with the pore throats. Thus the maximum height, h, to which water can be raised by capillary action, is controlled by the following factors:

- The interfacial tension, T, between the two phases (oil and water in this case)
- The contact angle, θ, between the wetting fluid (water in this case) and the rock
- The radius, r, of the pore throats
- The density difference between the phases, $(\rho_w - \rho_a)$ in this case

Given these factors, it is simple to predict the length of a transition zone in a reservoir. Reservoirs with large pore throats and high permeability will have short transition zones, and the transition zone at a gas/oil contact will be shorter than that at an oil/water contact simply because of the interphase density differences involved **(Fig. 6.6)**.

Obviously, a pore system is made up of a variety of pore sizes and shapes. As a result, no single value of r can be assigned to a particular reservoir. Therefore, depending on the distribution of the pore throat radii, as well as their actual size, either many or few of the available pore channels will raise water above the free-water level. The water saturation above the top of the transition zone will therefore be a function of porosity and of pore-size distribution. In a water-wet system, water wets the surface of each grain or lines the walls of the capillary tubes. When oil migrates into the reservoir, the effects of the capillary pressure are such that the downward progress of oil in the reservoir is most strongly resisted in the smallest capillaries. There is a distinct limit to the amount of oil that can be expected to fill the pores. Large-diameter pores offer little resistance (capillary pressure, P_c, is low because r is large). Small-diameter pores

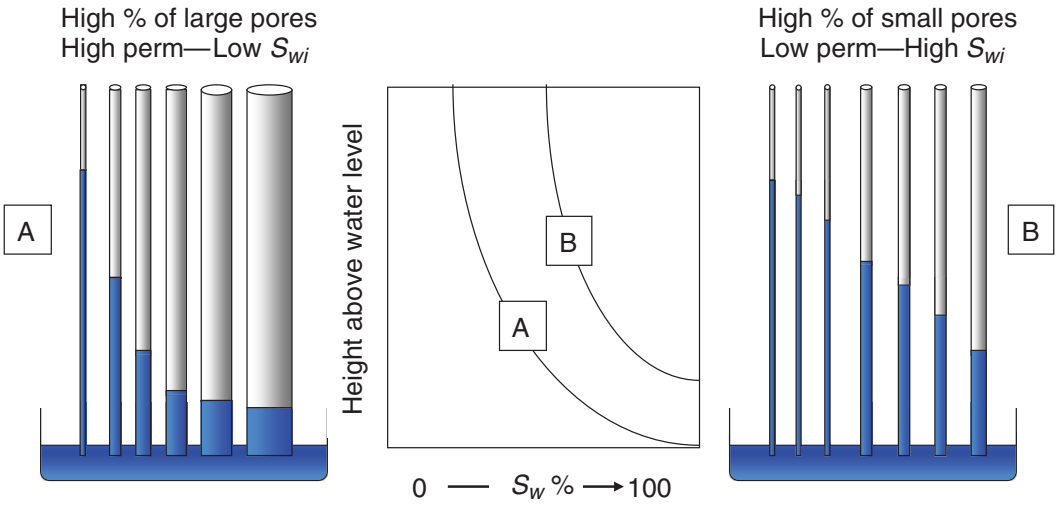


Fig. 6.6—Capillary pressure effects in reservoirs. After Core Labs.

offer greater resistance (P_c is high because r is small). For a given reservoir, ρ_o and ρ_w determine the pressure differential that an oil/water meniscus can support. Therefore, the maximum possible oil saturation is controlled by the relative number of small and large capillaries or pore throats. This maximum possible oil saturation, if looked at in terms of water saturation, translates into a minimum possible water saturation, which is referred to as the irreducible water saturation, S_{wi}. Shaly, silty, low-permeability rocks, with their attendant small pore throats, tend to have very high irreducible water saturation. Clean sands of high permeability have very low irreducible water saturation. **Fig. 6.7** illustrates this important concept by comparing capillary pressure curves for four rock systems of different porosity and permeability.

Some rock/fluid systems are preferentially oil-wet rather than water-wet, the distinguishing trait being the contact angle θ at the oil-water interface at the rock surface (**Fig. 6.8**). Traditionally, rock/fluid systems exhibiting contact angles less than 75° are considered water-wet, those with more than 105° are considered oil-wet, and systems in between are considered neutral. Note that the contact angle is a combined rock/fluid property, and studies show that it is dependent on the wetting history of the rock and the concentrations of polar compounds in the oil. Oil-wet reservoirs have very low S_{wi} values because, in effect, the capillary forces assist oil in the displacement of water.

6.3 Relative Permeability

If only one fluid is present in a pore system, fluid flow is well governed by Darcy's law. If two or more fluids are present together in a pore system, the dynamic behavior of the individual phases is not quite so straightforward. Consider the case of oil and water together in a pore system. Effective permeability is defined as the permeability of the rock to a particular fluid phase at a particular saturation. Therefore, if, under a given pressure gradient, oil and water flow through a pore system together, the effective permeabilities k_o (for oil) and k_w (for water) are:

$$k_o = \frac{q_o \mu_o L}{\Delta p A} \quad \text{and} \quad k_w = \frac{q_w \mu_w L}{\Delta p A} \qquad \text{(6.8)}$$

The total flow rate q_t (= q_o+ q_w) is less than the flow rate that either phase would have if it were present at 100% saturation. Therefore, it appears that the two phases interfere with each other's progress through the pore system.

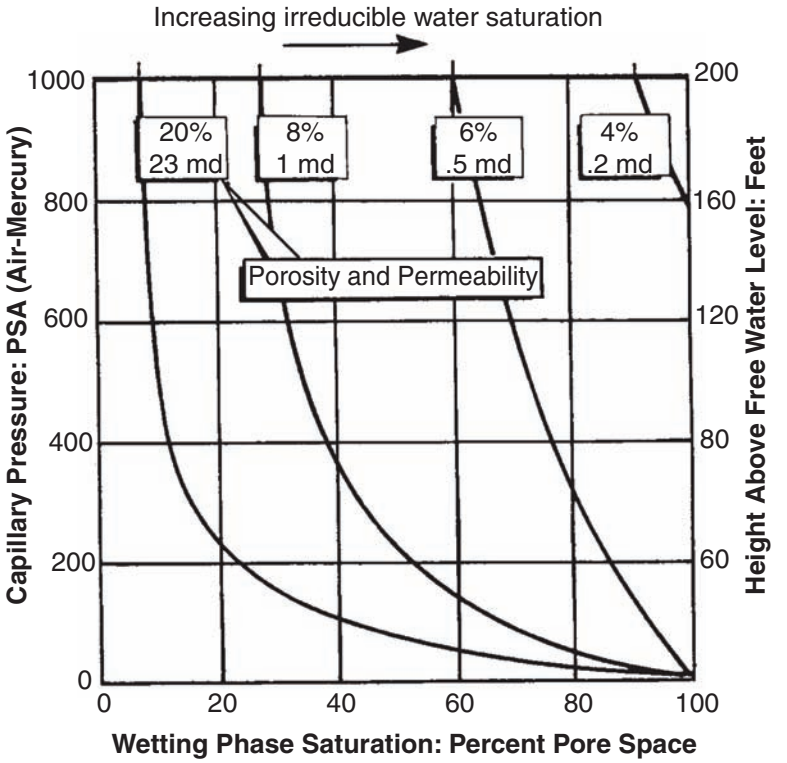


Fig. 6.7—Capillary pressure curves as a function of permeability and porosity. After Core Labs.

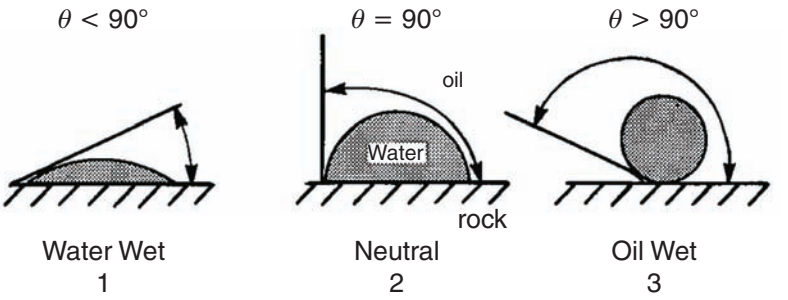


Fig. 6.8—Rock/fluid wettability and contact angle. After Core Labs.

Relative permeability, k_r, is the ratio of effective permeability to one phase to absolute permeability, and it is quoted at a particular saturation value. Thus,

$$k_{ro} = k_o / k \quad \text{and} \quad k_{rw} = k_w / k. \qquad (6.9)$$

Fig. 6.9 shows typical relative permeability curves. Several aspects of these are worth noting. Relative permeability to oil at irreducible water saturation is 100% or 1, as water saturation increases, k_{ro} decreases until it effectively reaches zero at some high water saturation corresponding to S_{or}, the residual oil saturation. Relative permeability to water, on the other hand, commences effectively at zero when the rock is at S_{wi} and thereafter increases as S_w increases. Note also that for a given S_w, k_{ro} is always less for an oil-wet system than for a water-wet system. Conversely, k_{rw} is always greater in an oil-wet system than in a water-wet one.

A common way of representing this difference between oil-wet and water-wet systems is to plot the relative permeability ratio k_{rw}/k_{ro} versus the water saturation S_w. **Fig. 6.10** shows that in

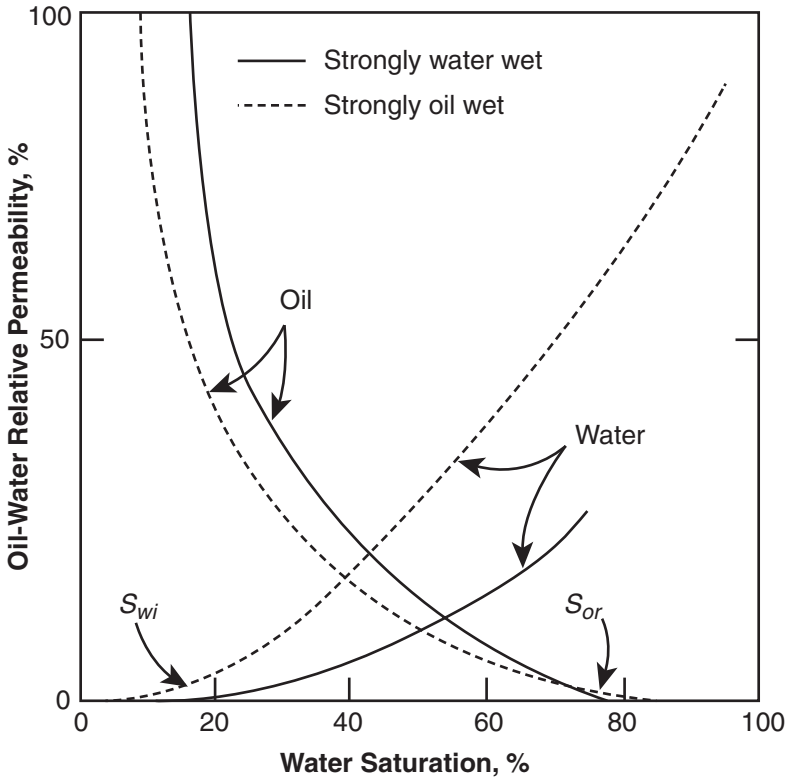


Fig. 6.9—Relative-permeability curves. Reprinted from Raza et al. (1968).

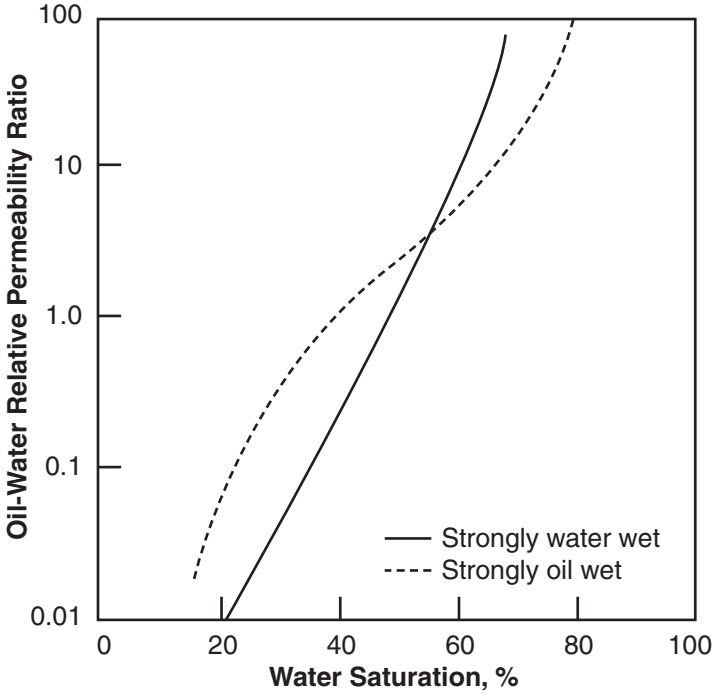


Fig. 6.10—Relative-permeability ratio plot. Reprinted from Raza et al. (1968).

water-wet systems, the relation is such that if the k_{rw}/k_{ro} ratio is plotted on a log scale and S_w on a linear scale, a straight line is obtained, but in an oil-wet system, an S-shaped line results.

When plotting relative-permeability curves, a distinction is usually made between two possible scenarios, imbibition and drainage. Imbibition refers to the case in which the saturation of the wetting fluid increases. For example, in a water-wet reservoir, a rise in the water table subjects the transition zone to imbibition of water.

Drainage refers to the case in which the saturation of the wetting fluid decreases, for example when oil first migrates into a water-wet rock. The difference between the two sets of relative-permeability curves reflects the saturation history and the trapping of the nonwetting phase that occurs after it has been imbibed. **Fig. 6.11** illustrates these various cases.

Many workers in this field have proposed generalized empirical equations to relate k_{ro} and k_{rw} to S_w, S_{wi}, and S_{or}. Particularly worthy of note are those cited in Honarpour et al. (1982), Molina (1983), and Pirson et al. (1964). A commonly used approximation gives:

$$k_{ro} = \left(\frac{0.9 - S_w}{0.9 - S_{wi}}\right)^2 \quad \text{and} \quad k_{rw} = \left(\frac{S_w - S_{wi}}{1 - S_{wi}}\right)^3 \ldots\ldots\ldots\

Therefore, the water/oil ratio (WOR) is given by:

$$WOR = k_w \mu_o / k_o \mu_w. \quad \ldots\ldots (6.13)$$

The k_w/k_o ratio is numerically equivalent to k_{rw}/k_{ro}, which can be deduced from measured relative-permeability ratios or estimated from one of the generalized correlations. The actual water cut (WC) of the production into the wellbore will be given by:

$$WC = q_w / (q_w + q_o), \quad \ldots\ldots (6.14)$$

which is equivalent to:

$$WC = WOR / (1 + WOR). \quad \ldots\ldots (6.15)$$

Surface water cut will be a function of the formation volume factors (β) of oil and water, and therefore the complete expression will be:

$$WC = WOR\beta_o / (\beta_w + WOR\beta_o). \quad \ldots\ldots (6.16)$$

6.4 Measurement of Porosity

Porosity may be measured by a variety of methods, including:

- Borehole gravimetrics
- Wireline logging
- Core analysis

Each method investigates a different volume of the formation. The borehole gravimeter samples very large volumes on the order of 10^3 to 10^6 ft^3. Wireline logging tools investigate a much smaller volume, on the order of 1 to 10 ft^3, depending on the specific porosity device used. Core analysis investigates much smaller volumes, ranging from 10^{-3} to 10^{-1} ft^3. From one extreme to the other, there are nine orders of magnitude, and therefore one should not be needlessly surprised to learn that porosity estimates using different tools and techniques do not always agree. This general problem is discussed further in Chapter 21. Porosity determination from wireline logs is covered in Chapter 23 and core analysis in Chapter 27.

6.5 Measurements of Permeability

As with porosity, there are many ways to estimate permeability. These include:

- Pressure buildup from drillstem tests (Chapter 31)
- Pressure drawdown and buildup from wireline formation testers (Chapter 30)
- Log analysis
- Core analysis (Chapter 27)

Again, many orders of magnitude separate the effective radii of investigation of the various methods, as shown in **Table 6.1.**

Obviously, these different methods of measurement may well produce different results. Disparate results are also to be expected in a heterogeneous reservoir. Where the drilling process has caused clay swelling in the invaded zone, it is to be expected that measurements made near the wellbore (logs, cores, wireline formation tests) will reflect permeabilities that are lower than the true permeabilities. Disparities can also be expected in the permeability measurements made on cores because they are influenced by the type of fluid (air or brine) used for the measurement and

TABLE 6.1—RADIUS OF INVESTIGATION OF ROCK PERMEABILITY MEASUREMENTS

Method	Approximate Radius of Investigation, ft
DST	10^2 to 10^4
Wireline formation tester buildup	10 to 10^2
Wireline formation tester drawdown	10^{-2} to 10^0
Log analysis	5 to 10^{-1}
Core analysis	8×10^{-2} to 3×10^{-1}

the pressure and temperature of the sample at the time of the measurement (standard or reservoir conditions).

Many investigators have attempted to correlate rock permeability with measurements made by wireline logging tools. These relationships fall into two categories: those that apply above the transition zone, and those that apply only in the transition zone. A few examples are:

$$k = \frac{8581\phi^{4.4}}{S_{wi}^{\ 2}} \quad \text{(Timur 1968)} \quad (6.17)$$

$$k = \left(\frac{250\phi^3}{S_{wi}}\right)^2 \quad \text{(Oils-Wyllie and Rose 1950)} \quad (6.18)$$

$$k = \left(\frac{79\phi^3}{S_{wi}}\right)^2 \quad \text{(Dry Gas-Wyllie and Rose 1950)} \quad (6.19)$$

$$k = \frac{10000\phi^{4.5}}{S_{wi}^{\ 2}} \quad \text{(Schlumberger Perm-1)} \quad (6.20)$$

$$k = \phi\left\{\frac{122}{h\left(\rho_w - \rho_o\right)}\right\}^2 \quad \text{(Oil/Water-Raymer and Freeman 1984)} \quad (6.21)$$

$$k = \phi\left\{\frac{140}{h\left(\rho_w - \rho_g\right)}\right\}^2, \quad \text{(Gas/Water-Raymer and Freeman 1984)} \quad (6.22)$$

where

S_{wi} is fractional irreducible water saturation
ϕ is fractional porosity
h is height in feet from free-water level to the top of the transition zone
ρ_w is the water density in g/cm^3
ρ_o is the oil density in g/cm^3
ρ_g is the gas density in g/cm^3.

Fig. 6.12 shows a graphic representation of the Wyllie and Rose relationship above the transition zone; ϕ and S_{wi} are crossplotted to yield values of k.

In the transition zone, the resistivity gradient is commonly linear, that is, a resistivity log on a linear scale will frequently show a straight line in a transition zone. The resistivity gradient ($\Delta R/\Delta D$) measured in Ω·m/ft is first normalized by division by R_o (the wet-rock resistivity; see Chapter 7) and then related to k provided that the density difference ($\rho_w - \rho_h$) between the wetting and nonwetting phases is known (here the subscript h refers to hydrocarbon). **Fig. 6.13** gives a graphic solution to the equation

$$k = c\left(\frac{2.3a}{(\rho_w - \rho_h)}\right)^2, \quad \ldots\ldots(6.23)$$

where

$$a = \frac{\Delta R}{\Delta D} \times \frac{1}{R_o} \quad \ldots\ldots(6.24)$$

c = 20 (a constant to take care of units)
ρ_w and ρ_h are in g/cm^3
$\Delta R/\Delta D$ is expressed in Ω/ft
k is in md.

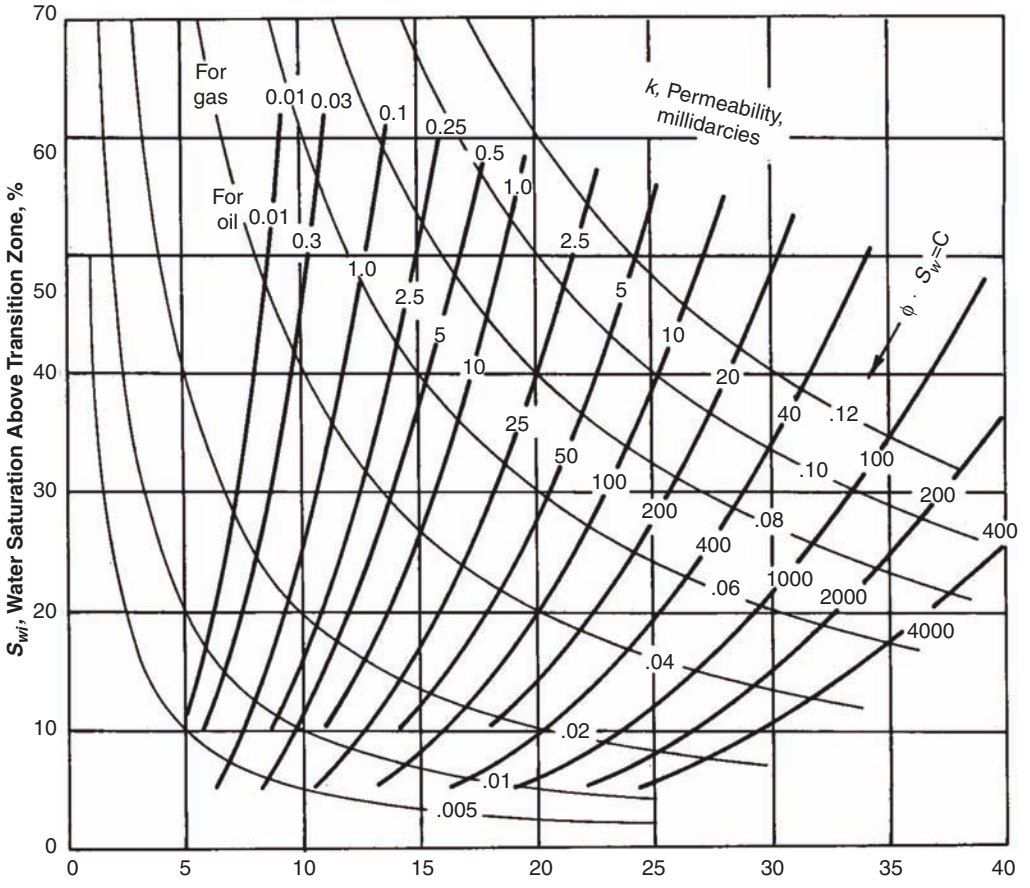


Fig. 6.12—Permeability estimation above the transition zone (Schlumberger 2009). Courtesy of Schlumberger.

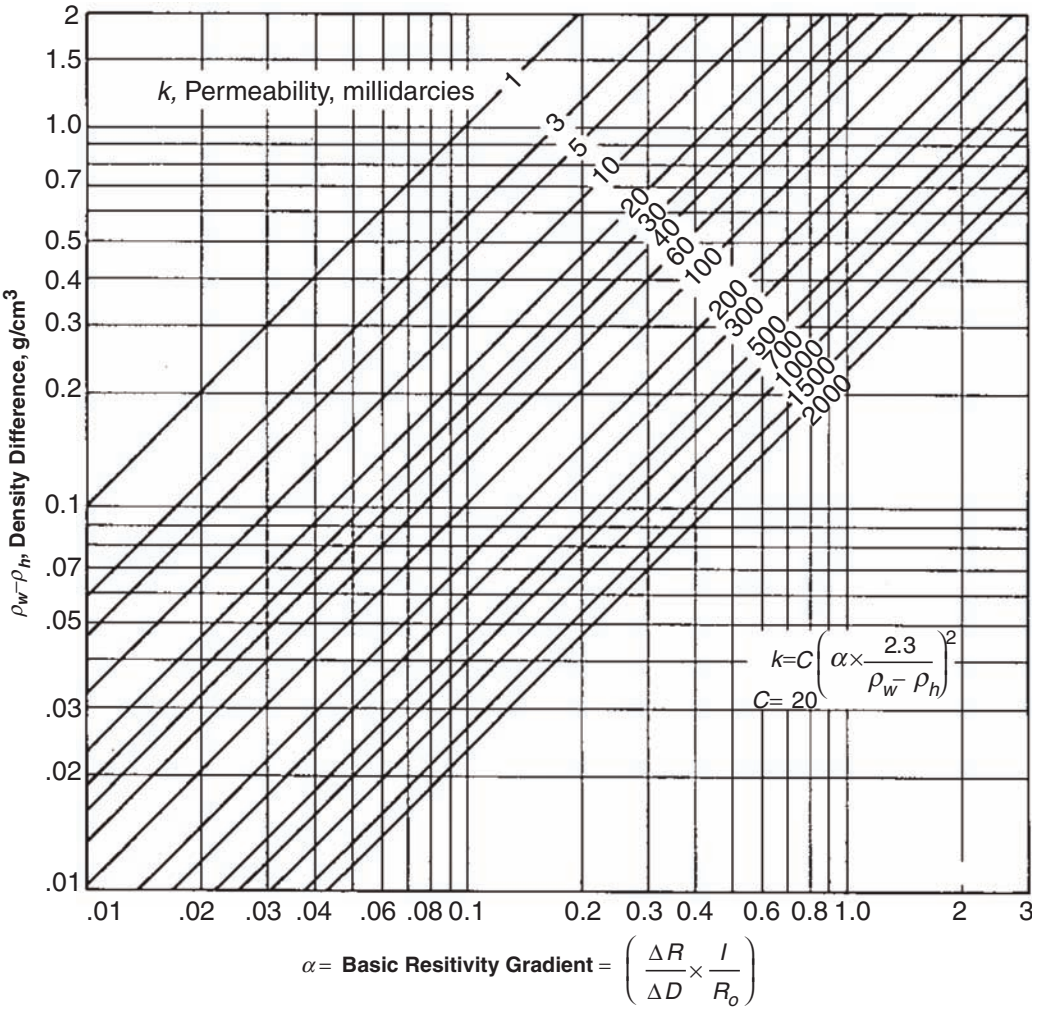


Fig. 6.13—Permeability estimates from transition zone resistivity gradient. Courtesy of Schlumberger.

6.6 Measurements of Saturation

Fluid saturations, for the most part, are well measured by log analysis techniques provided that formations are clean and connate waters are saline. Problems arise with shaly formations and fresh formation waters (see Chapters 26 and 28). Other methods of saturation determination are available from proper coring and core analysis techniques (see Chapters 5 and 27). Mud logging can provide a qualitative measure of oil and gas saturations, as described in Chapter 2.

Many similarities exist between the flow of fluids through a rock and the flow of electric current through a rock. The permeability to water, for example, can be equated with the electrical conductivity of a porous system because both depend on interconnected pores. In the case in which both oil and water are present in a pore system, there is a parallel between relative permeability to water and the electrical conductivity of an oil-bearing sand. Investigation of the electrical properties of wet and oil-bearing rocks was pioneered by Archie (1942). A good starting point for following the development of his experimental observations is the electrical behavior of electrolytes and water-filled rocks.

6.6.1 Water Resistivity, R_w. Connate waters range in resistivity from approximately 0.01 Ω·m up to several Ω·m, depending on the salinity and temperature of the solution. To determine water saturation by quantitative analysis of porosity and resistivity logs, a value of R_w is required.

Chapter 25 is dedicated exclusively to the methods available for finding R_w. Here, it is necessary to understand only that the ability of a rock to conduct electricity is due entirely to the ions in the water found in the pore spaces. **Fig. 6.14** shows a cube of rock with a system of cylindrical tubes drilled through it. If these cylindrical pores are filled with water of resistivity R_w, their total area is A, and their length is L, the resistivity of the total rock system can be estimated as proportional to R_w (L/A). If the area A is small, there is a small conductive path of length L, and the resistivity of the rock system is high. Conversely, if A is large, the resistivity is low. The resistivity of a rock 100% saturated with water is referred to as R_o. Because A is proportional to the porosity itself,

$$R_o = f\left(R_w, \phi\right). \quad (6.25)$$

It can also be said that R_o is related to R_w by some formation factor F such that

$$R_o = FR_w. \quad (6.26)$$

6.6.2 Electrical Formation Factor. Archie used a simple method to arrive at this conclusion. He took a number of cores of different porosity and saturated each one with a variety of brines. He then measured, at each brine salinity, the resistivity of the water, R_w, and the resistivity of the 100%-water-saturated rock system, R_o. When the results were plotted, he found a series of straight lines of slope F **(Fig. 6.15)**.

F, determined in this manner, is referred to as the electrical formation factor. Archie conducted many experiments in an attempt to link the electrical formation factor to porosity in a predictable manner. (The simple tubular model bears little relationship to the tortuous paths that pores actually take. See **Fig. 6.16**.)

The factor L, the length of the tubular pore, grows larger as the tortuosity of the pore system increases. It was therefore a logical step to propose that F and ϕ had to be related by some inverse

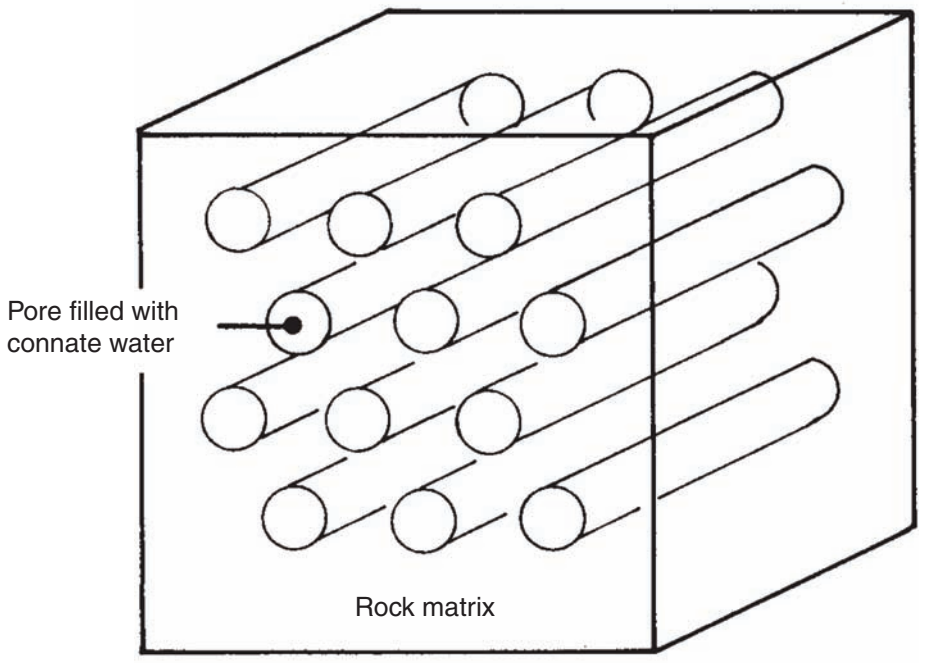


Fig. 6.14—Simplified model of water-filled rock system.

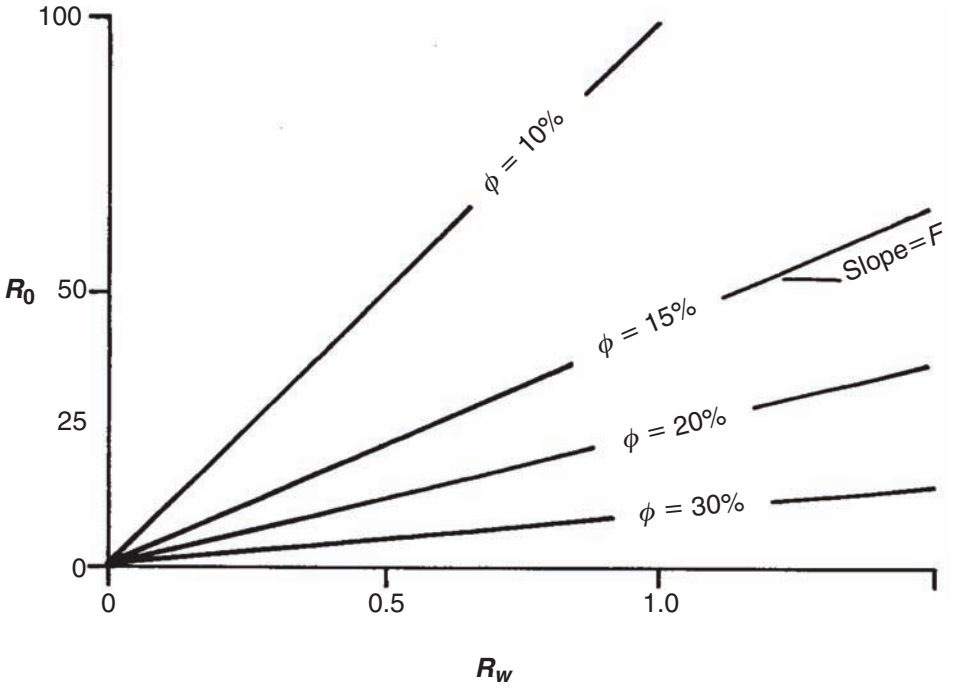


Fig. 6.15—R_o as a function of R_w for rocks of different porosity.

power function. Note that by definition the formation factor is the ratio of R_o/R_w, that is, the ratio of the resistivity of a rock sample 100% saturated with water to the resistivity of the water itself. Eventually, Archie found that laboratory-measured values of F could be related to the rock porosity by an equation of the form

$$F = a / \phi^m, \quad \ldots\ldots\ldots\

where a and m are experimentally determined constants; a is usually close to one, and m is usually close to two **(Fig. 6.17)**. Three commonly used relations linking formation factor to porosity are:

$$F = 1/\phi^2 \quad \text{Carbonates} \quad (6.28)$$

$$F = 0.62/\phi^{2.15} \quad \text{Humble formula for soft formations} \quad (6.29)$$

$$F = 0.81/\phi^2 \quad \text{Sands} \quad (6.30)$$

In a wet formation, the F-to-ϕ relationship can therefore be combined with the definition of F to arrive at

$$R_w = R_o/F = R_o\phi^m/a \quad (6.31)$$

6.6.3 Saturation. Archie's experiments showed that the saturation of a core could be related to its resistivity. He found that the fractional water saturation, S_w, was approximately equal to the square root of the ratio of the wet formation resistivity, R_o, to the formation resistivity R_t, that is:

$$S_w^2 = R_o/R_t \quad (6.32)$$

In a more generalized form, this equation can be written as

$$S_w^n = R_o/R_t \quad (6.33)$$

where n is the saturation exponent and is usually set to 2 **(Fig. 6.18).**

Because Archie's model considers the electrolyte in the pores as the only conductive path, his relationships work well in clean formations. However, in shaly formations or where the connate water is fresh, they do not work as well.

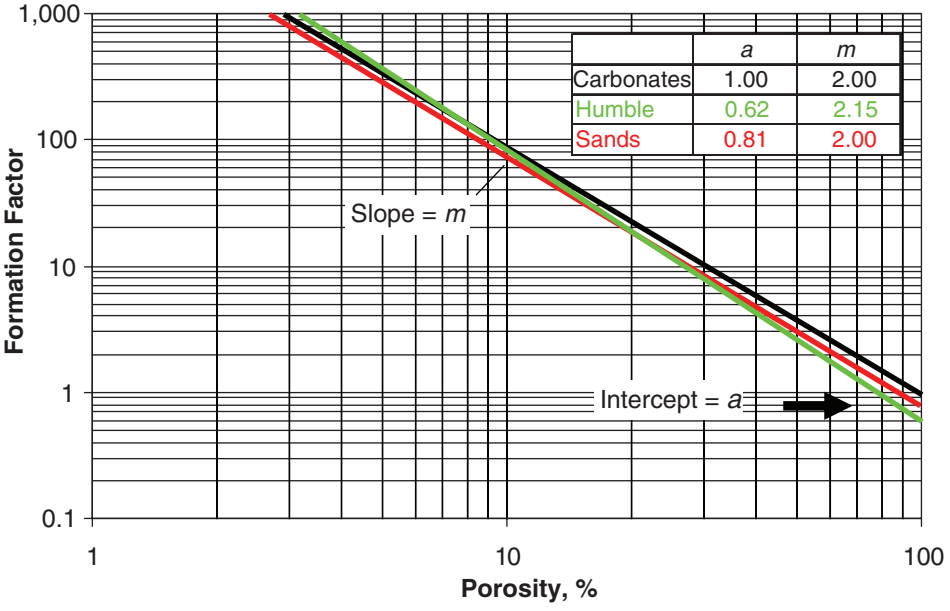


Fig. 6.17—Generalized *F*-to-ϕ relationship.

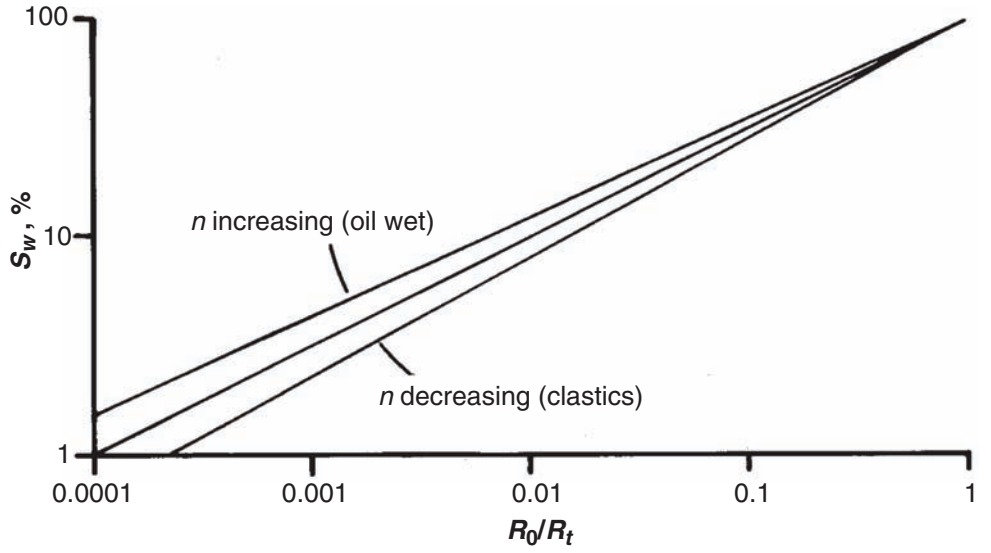


Fig. 6.18—S_w as a function of R_o/R_t and n.

6.7 Practical Petrophysics

A proper marriage between petrophysics and log analysis can produce some spectacular results. One of the most interesting is that when a formation is above the transition zone and therefore at irreducible water saturation, the product of porosity (ϕ) and water saturation (S_w) is a constant. Variations of porosity are normal on a local scale because of changes in the depositional environment at the time the sediments were laid down and because of subsequent diagenesis. If porosity is locally reduced, more of the pore throats are small, or there are simply fewer pore throats. Either way, the mean radius r is smaller, and therefore p_c is larger, and more water can be held in the pores, maintaining a constant value of ϕS_{wi}.

This observation has a practical application. After a zone has been analyzed on a foot-by-foot basis for porosity and water saturation, a plot of ϕ vs. S_w will reveal the presence or absence of a transition zone. **Fig. 6.19** illustrates this phenomenon. Note that on Fig. 6.19, ϕ and S_w are on linear scales, and the points at irreducible saturation fall on a hyperbola. **Fig. 6.20** shows a similar plot on log-log paper, where the points at irreducible saturation plot on a straight line. Points in the transition zone plot to the right of the irreducible line.

A reservoir can be characterized by its ϕS_{wi} product, and this knowledge can be used as a basis for predicting production characteristics. For points that are not at irreducible saturation, some water production is to be expected, depending on the mobility ratio ($k_w\mu_o/k_o\mu_w$) for the particular fluids present. **Fig. 6.21** shows the ϕS_{wi} product at irreducible saturation for a number of formations. Note that in a low-porosity, low-permeability formation, surprisingly high water saturations can be tolerated without fear of water production. Conversely, in formations with good porosity and permeability, even when they have moderate values of S_w, water production can be expected. This salient fact is all too often overlooked by those who were once taught that (1) if S_w is less than 50% (or 60%, or whatever), there should be no trouble, and (2) do not attempt completions if S_w is greater than a certain percentage. From those who are now enlightened and emboldened by petrophysics, let us see some completions in zones of 65%, 70%, and even 75% S_w, provided that permeability is low.

6.8 Averaging

Averaging is a dangerous pastime. The average depth of the Mississippi is 3 ft, but that does not mean you can try to wade from one side to the other at New Orleans without being prepared either

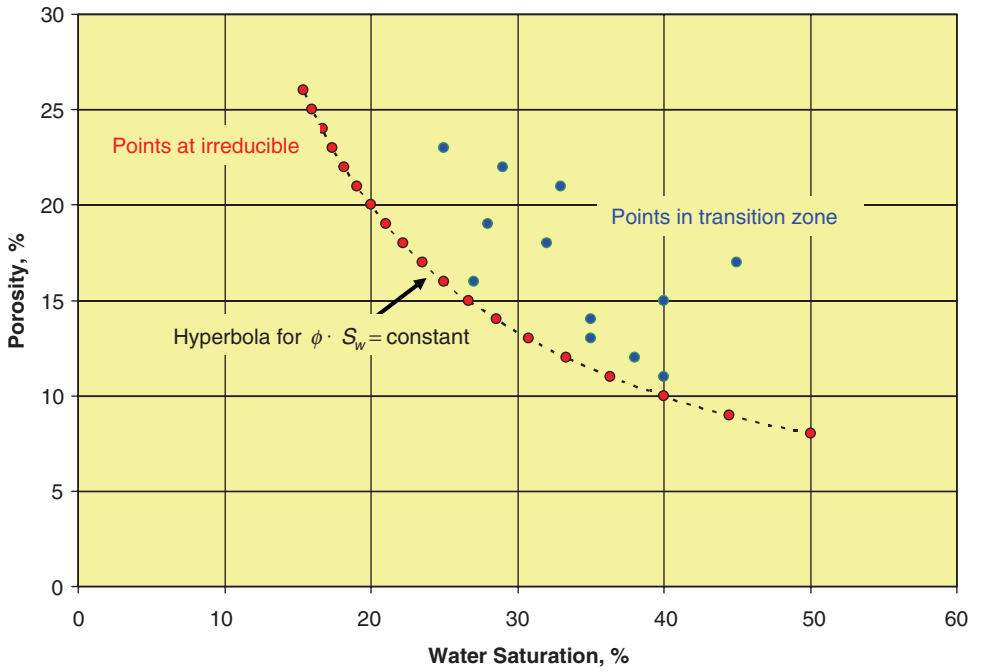


Fig. 6.19—ϕ-S_w crossplot on linear grids (Bateman 1984). Reprinted by permission from the SPWLA.

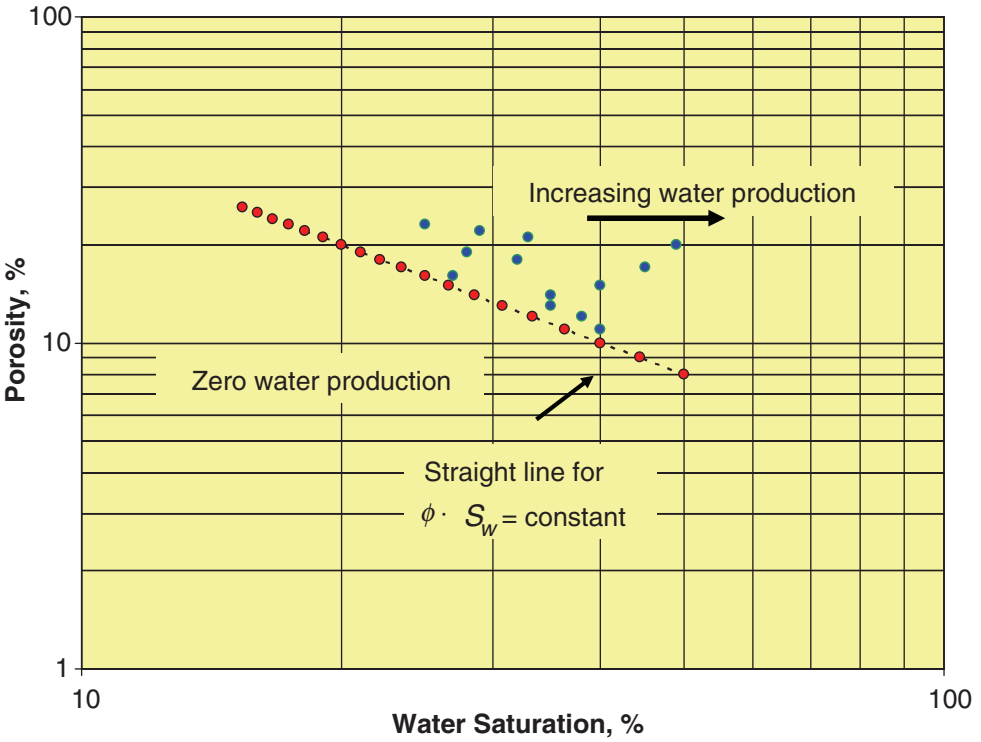


Fig. 6.20—ϕ-S_w crossplot on logarithmic grids (Bateman 1984). Reprinted by permission from the SPWLA.

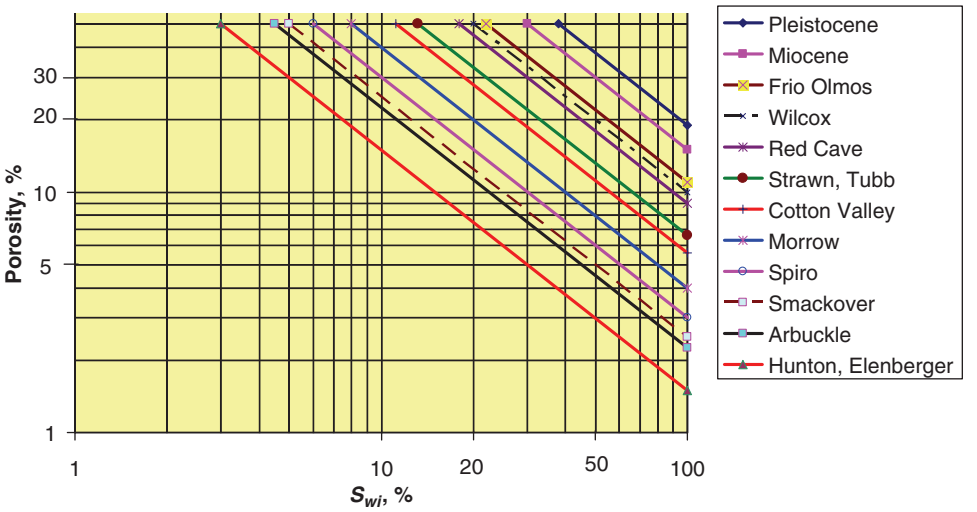


Fig. 6.21—ϕS_{wi} for various formations.

to swim or to drown. Therefore, when talking about average porosity, average saturation, and average permeability, be careful how these are calculated and used.

For example, suppose that a well has two zones. One is at 10% porosity, and the other is at 20% porosity. Is the average porosity 15%? Not necessarily. If the 10% zone is 30 ft long and the 20% zone is 50 ft long, obviously the average is skewed in favor of the longer zone. The correct way to average porosities is therefore to use

$$\phi_{av} = \frac{\sum \phi h}{\sum h} \quad \ldots\ldots\ldots\

Therefore, the two zones combined have 13.00 porosity feet and 10.05 hydrocarbon porosity feet, the average oil saturation is 77.31% (10.05/13.00), and the average water saturation is 22.69% (2.95/13.00). S_{wav}, therefore, can be defined as:

$$S_{wav} = \frac{\sum \phi S_w h}{\sum \phi h} \quad \ldots\ldots (6.36)$$

These sums and averages are most conveniently calculated by means of computers working with a digital log base. Permeability averaging may be achieved in a number of ways depending on the intended use of the average itself.

For parallel flow, use the *arithmetic average*:

$$\overline{k_a} = \left(k_1 + k_2 + k_3 \cdots + k_n\right)/n \quad \ldots\ldots (6.37)$$

For series flow, use the *harmonic average*:

$$\overline{k_h} = \left(1/k_1 + 1/k_2 + 1/k_3 \cdots + 1/k_n\right)/n \quad \ldots\ldots (6.38)$$

For random flow, use the *geometric average*:

$$\overline{k_g} = \left(k_1 k_2 k_3 \cdots k_n\right)^{1/n} \quad \ldots\ldots (6.39)$$

6.9 Summary

The conduction of electric current through a porous rock is conceptually similar to the flow of fluid through the rock. Therefore, wireline-tool measurements of formation conductivity are related to formation porosity, permeability, and fluid saturation. By combining the basic relationships established by Archie with the physics of fluid distribution and flow in a reservoir, the analyst can determine the free-water level, the length of the transition zone, and the irreducible water saturation. From these parameters, productivity can be estimated.

References

Archie, G.E. 1942. The Electrical Resistivity Log as an Aid in Determining Some Reservoir Characteristics. *J. Pet Tech* **5:** 1–8.

Bateman, R.M. 1984. Watercut Prediction From Logs Run in Feldspathic Sandstone With Fresh Formation Waters. SPWLA 25th Annual Logging Symposium, New Orleans, 10–13 June, Paper EE.

Bradley, J.S. 1980. Fluid and Electrical Formation Conductivity Factors Calculated for a Spherical-Grain Onion-Skin Model. *The Log Analyst* **21:** 24–32.

Coates, G.R. and Dumanoir, J.L. 1974. A New Approach to Improved Log-Derived Permeability. *The Log Analyst* **15** (1): 17–29.

de Witte, L. 1950. Relations Between Resistivities and Fluid Contents of Porous Rocks. *Oil & Gas J.* **49** (16): 120.

Goetz, J.F., Prins, W.J., and Logar, J.F. 1977. Reservoir Delineation by Wireline Techniques. *Proc.,* 6th Annual Convention of the Indonesia Petroleum Association, Jakarta, May.

Graton, L.C., and Fraser, H.J. 1935. Systematic Packing of Spheres With Particular Relation to Porosity and Permeability. *J. Geol.* **43:** 785–909.

Honarpour, M., Koederitz, L.F., and Harvey, A.H. 1982. Empirical Equations for Estimating Two-Phase Relative Permeability in Consolidated Rock. *J. Pet Tech* **34** (12): 2905–2908. http://dx.doi.org/10.2118/9966-PA.

Le Blanc, R.J. Sr. 1977. Distribution and Continuity of Sandstone Reservoirs (Parts 1 and 2). *J. Pet Tech* **29** (7): 776–804. http://dx.doi.org/10.2118/6137-PA.

Leverett, M.C. 1941. Capillary Behavior in Porous Solids. SPE- 941152-G. *Trans.,* AIME **142:** 152–169.

Molina, N.N. 1983. Systematic Approach Aids Reservoir Simulation. *Oil & Gas J.* (April).

Morris, R.L. and Biggs, W.P. 1967. Using Log-Derived Values of Water Saturation and Porosity. *Proc.,* SPWLA 8th Annual Logging Symposium, 11–14 June.

Pirson, S.J., Boatman, E.M., and Nettle, R.L. 1964. Prediction of Relative Permeability Characteristics of Intergranular Reservoir Rocks from Electrical Resistivity Measurements. *J. Pet Tech* **16** (5): 564–570. http://dx.doi.org/10.2118/749-PA.

Raymer, L.L. 1981. Elevation and Hydrocarbon Density Correction for Log Derived Permeability Relationships. *The Log Analyst* **22** (3)**:** 3–7.

Raymer, L.L. and Freeman, P.M. 1984. In-Situ Determination of Capillary Pressure, Pore Throat Size and Distribution, and Permeability From Wireline Data. SPWLA 25th Annual Logging Symposium, 10–13 June, Paper CCC.

Raza, S.H., Treiber, L.E., and Archer, D.L. 1968. Wettability of Reservoir Rocks and Its Evaluation. *Producers Monthly* (April).

Rockwood, S.H., Lair, G.H., and Langford, B.J. 1957. Reservoir Volumetric Parameters Defined by Capillary Pressure Studies. SPE-710-G. *Trans.*, AIME **210:** 252–259.

Schlumberger. 1969. *Log Interpretation Principles*.

Schlumberger. 1972. *Log Interpretation: Volume 1—Principles*.

Schlumberger. 1977. *Log Interpretation Charts*.

Schlumberger. 2009. *Log Interpretation Charts*, 09-FE-0058. Sugar Land, Texas: Schlumberger.

Timur, A. 1968. An Investigation of Permeability, Porosity, and Residual Water Saturation Relationship for Sandstone Reservoirs. *The Log Analyst* **9** (4): 8–17.

Tixier, M.P. 1949. Evaluation of Permeability from Electric-Log Resistivity Gradients. *Oil & Gas J.* **48:** 113.

Wyllie, M.R.J. and Rose, W.D. 1950. Some Theoretical Considerations Related to the Quantitative Evaluation of the Physical Characteristics of Reservoir Rock From Electrical Log Data. *J. Pet Tech* **189:** 105–108.

General References

Bobek, J.E., Mattax, C.C., and Denekas, M.O. 1958. Reservoir Rock Wettability: Its Significance and Evaluation. *Trans.,* AIME **213:** 155–160.

Chapter 7

Basic Concepts of Log Analysis

7.1 Log Analysis Overview

Successful completion of this section will enable the reader to pick up a suite of logs and perform basic formation evaluation, including:

- Identification of porous and permeable reservoir rocks
- Porosity estimation
- Water saturation calculation
- Differentiation between oil- and gas-bearing sections

Before confronting these tasks, it may be profitable to reflect for a moment on the general scope of log analysis and the tasks that a log analyst must address. An easy-to-grasp example of the sort of problem facing the log analyst would be to consider 1 cubic foot of rock of reasonable porosity and containing one gallon of oil **(Fig. 7.1).**[*] The surface area of the grains of sand in that cubic foot of rock might be 1 acre. Spreading the gallon of oil over an area of one acre results in a layer only 37 millionths of an inch thick.

The task of the log analyst is to detect this thin layer of oil and then to assist in producing it. The fundamental questions to be answered by the analyst are:

- What kind of rock is present?
- Are any hydrocarbons present, and if so, should a test be run and the well completed?
- What kind(s) of hydrocarbons are there: oil, gas, or condensate?
- How much is there? (Net pay, porosity, water saturation, etc.)
- What will flow and how quickly?

The parameters needed to answer these questions are:

- Porosity and lithology
- Permeability
- Water saturation
- Bed thickness

and the skill required to find on a log the data necessary for the relevant quantitative calculations.

[*]In metric terms, the equivalent is a cubic meter of sand containing 133 L of oil. The surface area of the 70 billion grains is 4,047 m^2, and the thickness of the layer is 94 millionths of a centimeter.

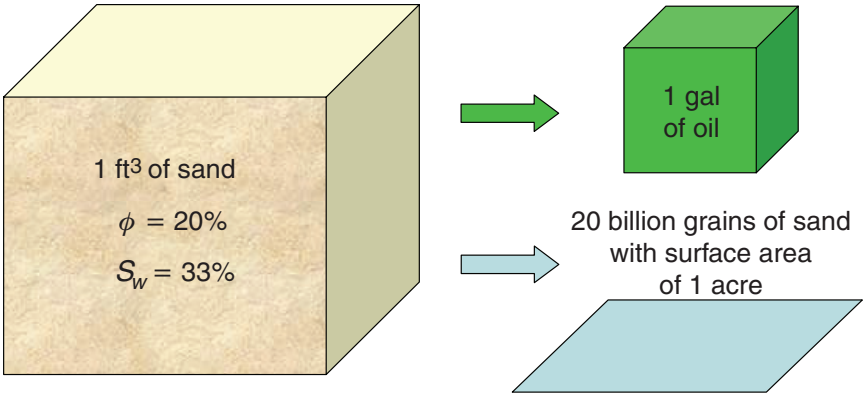


Fig. 7.1—Reservoir perspective.

The generalized answer log (plotted at subsea depths) shown in **Fig. 7.2** was derived from an analysis of the logs shown in **Figs 7.3 and 7.4.** The computed log gives a visual account of the main formation characteristics of interest: porosity, permeability, water saturation, rock type, and hydrocarbon type. More sophisticated presentations might include other parameters, and these will be covered later, once a better understanding has been gained of the principles of measurement of the various logging tools available and a more detailed treatment of interpretation has been provided.

On the answer log shown in Fig. 7.2, the logged column, from top to bottom, shows a shale section over a porous and permeable section containing both a gas cap and an oil column. Below the oil leg, a transition zone leads into a water column. The log is divided into four tracks. From left to right: the depth column shows a gas flag; Track 1 shows shale content and permeability; Track 2 shows the porosity and the distribution of fluids within the pore space; Track 3 shows water saturation and highlights intervals with a water saturation less than 50%; Track 4 provides a picture of the bulk rock volume by splitting it into three components, sand, shale, and pore space. From these four tracks, the analyst can deduce almost all that needs to be known about the logged column. All the necessary information is available for making decisions about completion and testing and also for calculation of the hydrocarbons in place.

Let us review the steps that went into evolving an answer log of this sort and trace how a log analyst proceeds when studying a suite of logs. This review will cover all the basic steps involved; the chapters that follow will add many refinements.

7.2 Lithology

The starting point will be to inspect the section that has been logged and discard from further attention any unwanted parts. Zones of no further interest will be shales and evaporites with zero porosity and permeability (i.e., nonreservoir rocks). As a rule, this step can be accomplished by taking a marker pen and color-coding only those sections that are of interest, that is, those showing porosity and permeability. The criteria used for this visual sifting of the data are documented in **Table 7.1.**

The logs in Figs 7.3 and 7.4 are from a sand-shale sequence. Fig. 7.3 shows a dual laterolog-GR, and Fig. 7.4 shows a neutron-density-GR log.

As an exercise in log analysis, it is suggested that the first step should be to delineate the porous and permeable sections on the example log. With a yellow highlighter, mark up the gamma ray log in Fig. 7.3 or 7.4 to show the clean (shale-free) zones. A practical way to do this is to color from the middle of Track 1 leftward to the gamma ray curve. This should give a good visual image of the sand and shale sections. Attention can then be concentrated in the sections containing reservoir rock.

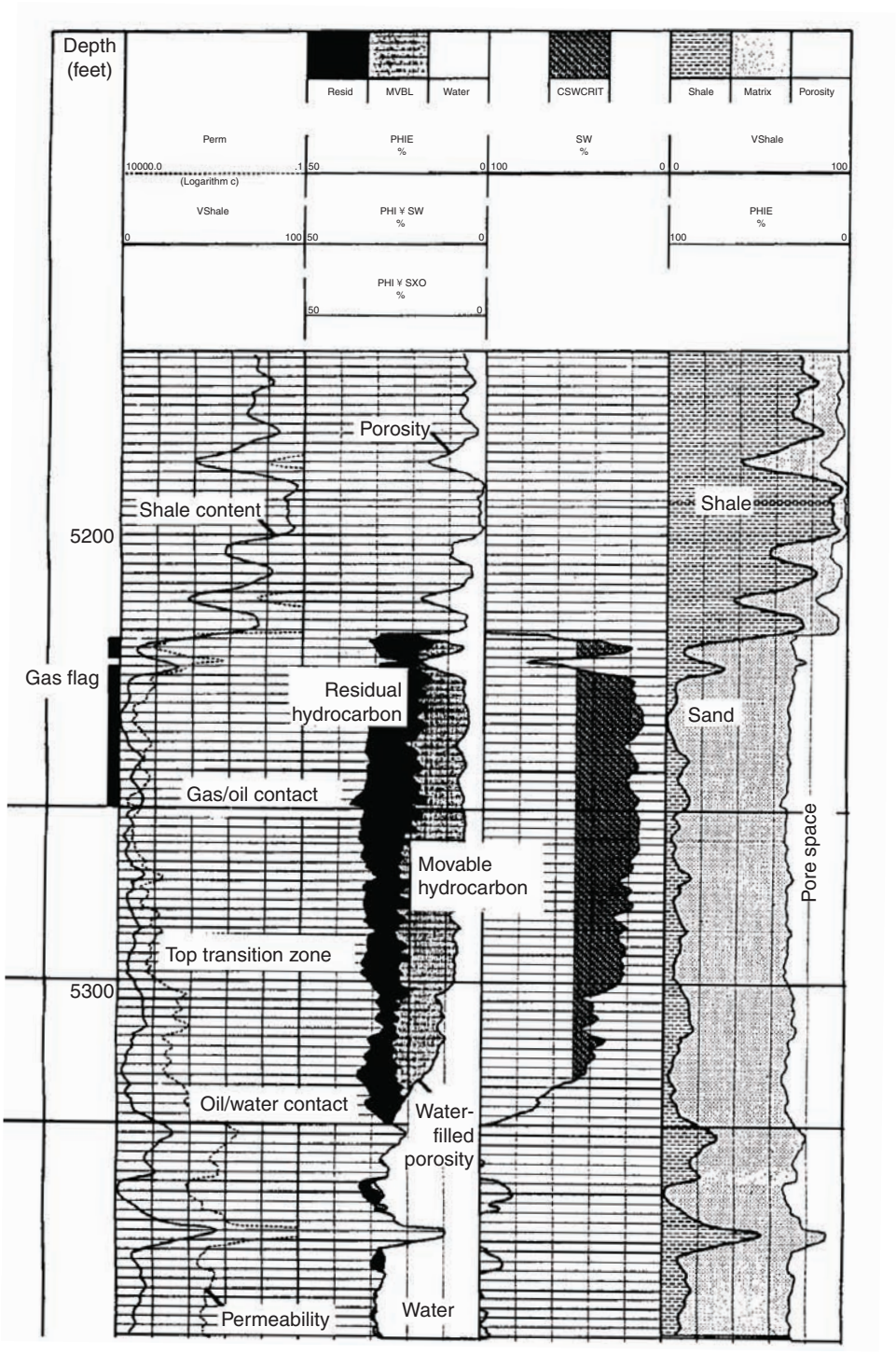


Fig. 7.2—Generalized answerlog.

7.3 Porosity

The porosity of a formation is defined as the volume of the pore space divided by the volume of the rock containing the pore space. This definition of porosity ignores the question of whether the pores are interconnected. Swiss cheese, for example, is quite porous but is of very low permeability

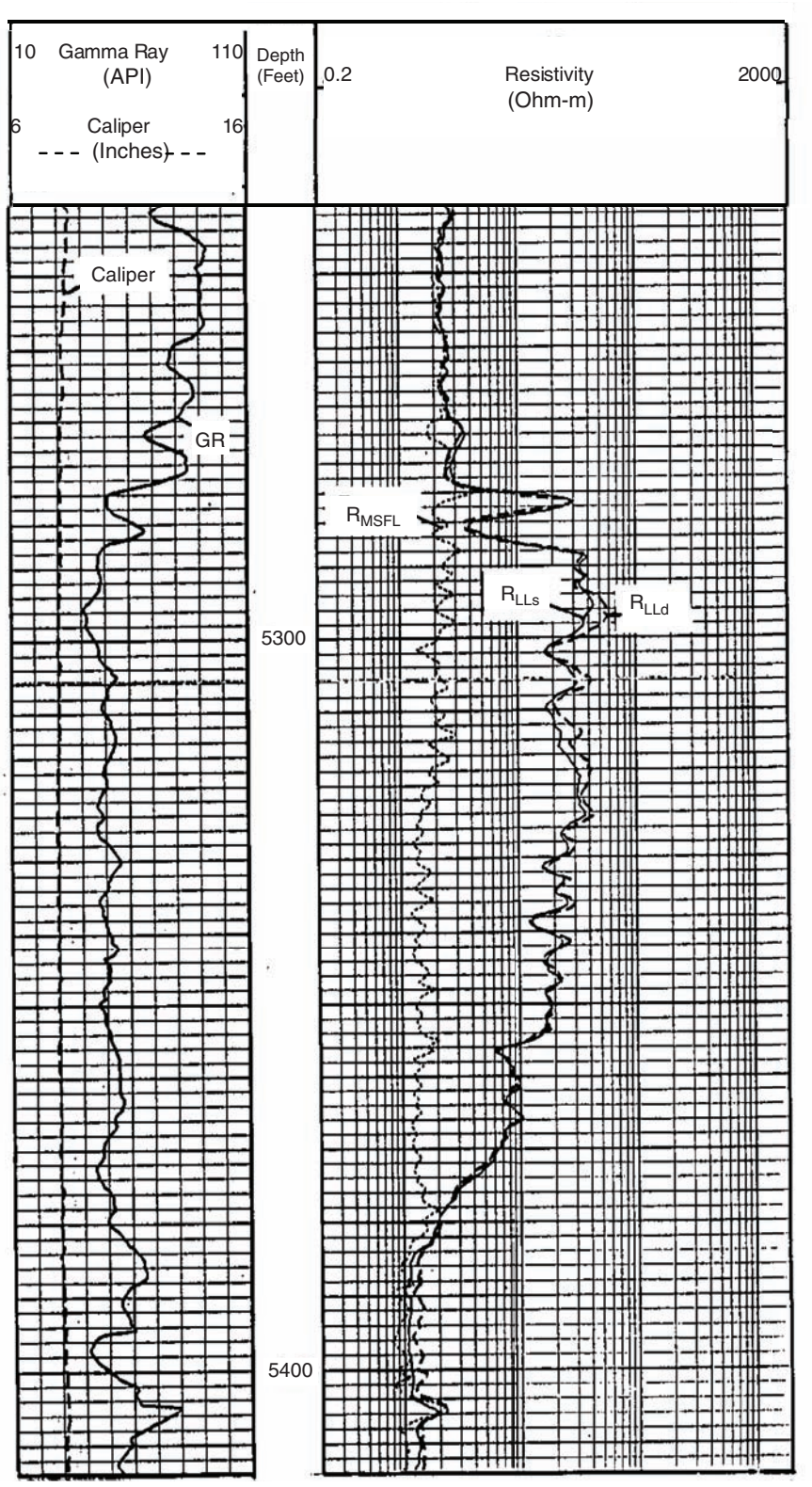


Fig. 7.3—A dual laterolog resistivity log.

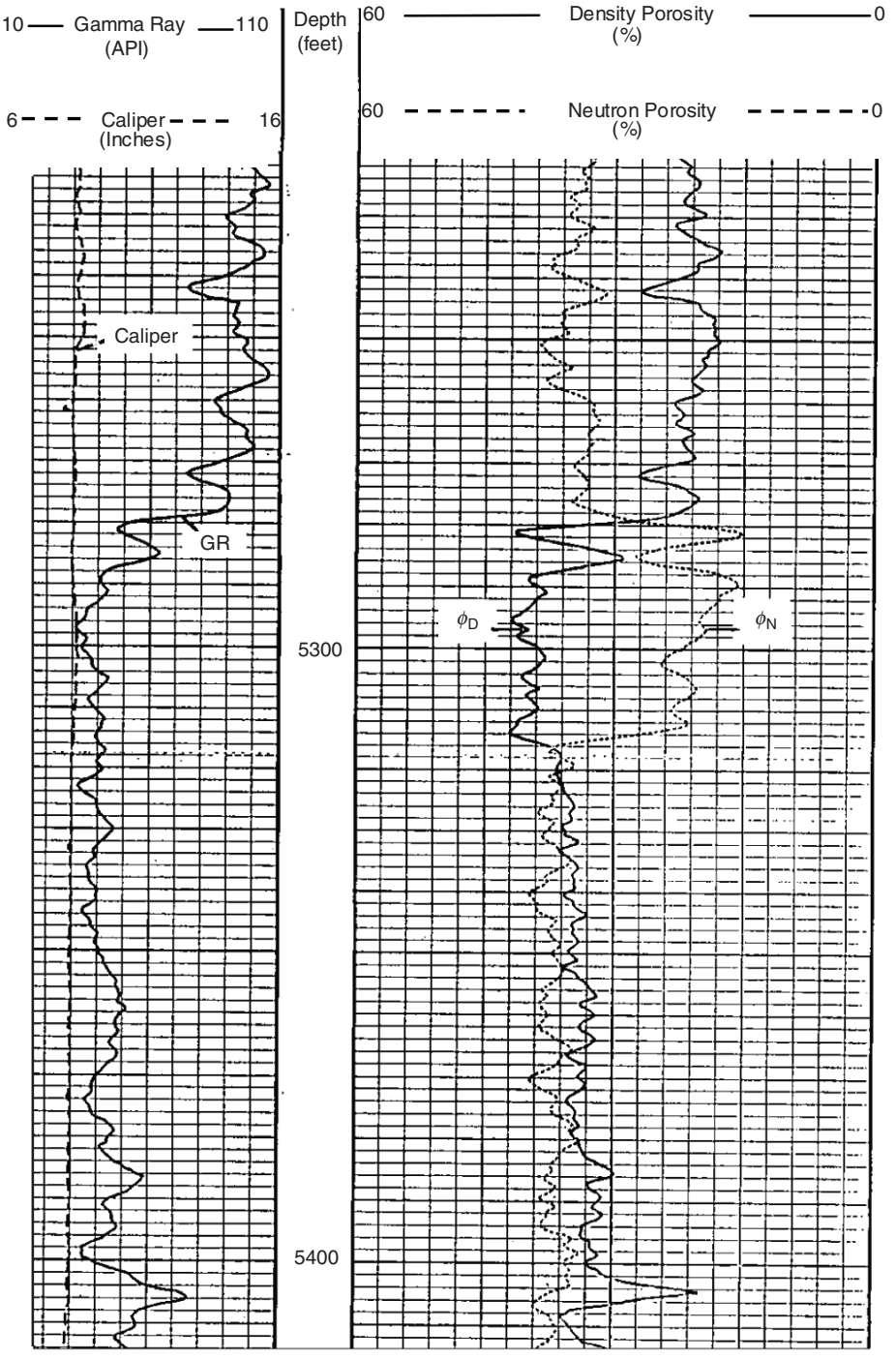


Fig. 7.4—A neutron-density porosity log.

because the void spaces are not interconnected. Intergranular porosity that is interconnected is effective porosity. Pores that are blocked in some way (by clay particles, silt, etc.) are ineffective. Therefore, a preferred definition gives total porosity (ϕ_t) as the volume of the pores divided by the volume of rock and effective porosity (ϕ_e) as the volume of the interconnected pores divided by the volume of rock **(Fig. 7.5).**

TABLE 7.1—DISCRIMINATION BETWEEN RESERVOIR AND NONRESERVOIR ROCKS

Reservoir Rocks	Nonreservoir Rocks
Low gamma ray	High gamma ray
Good SP development	Flat SP
Relative separation of resistivity curves	Stacked resistivity curves

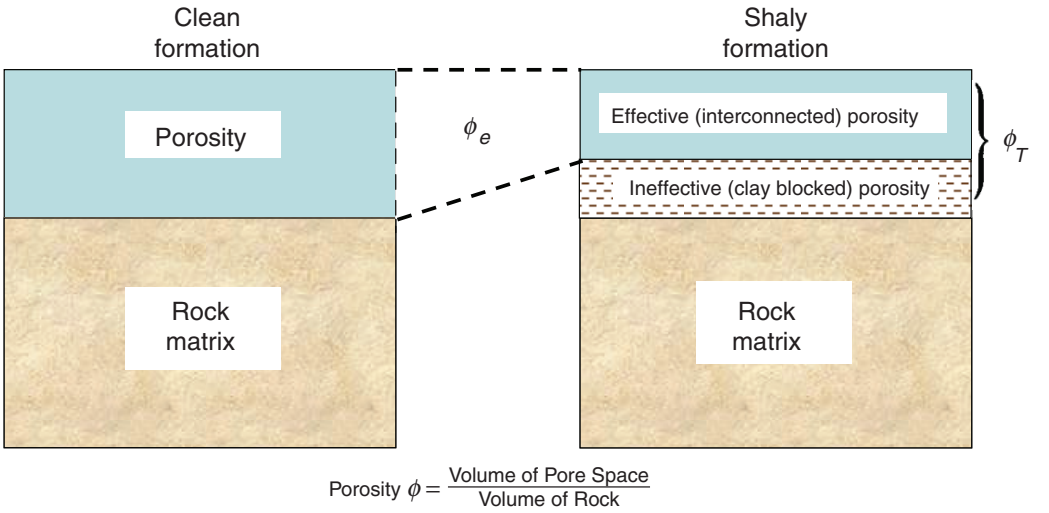


Fig. 7.5—Definitions of total and effective porosity.

In a laboratory, porosity can be measured in a number of ways. One of the simplest is to weigh a sample of rock when it is 100% saturated with water, and then to remove all the water and reweigh the sample. Provided that the density of the rock matrix (or the volume of the rock sample) is known, the porosity can be calculated.

QUESTION 7.1. A sample of porous sandstone saturated with water is found to weigh 215.5 g. After all the water is removed from the sample, it weighs 185.5 g. If the density of the sandstone matrix is 2.65 g/cm^3 and the density of the water is 1.0 g/cm^3, what is the porosity of the sample?

The density logging tool provides an in-situ bulk-rock density measurement that, if properly rescaled, can be displayed as a porosity trace. The solid curve in Tracks 2 and 3 in Fig. 7.4 is such a recording. For the time being, the dashed curve (neutron log) may be ignored.

QUESTION 7.2. On the example log shown in Fig. 7.4, the porosity scale is marked from 0 to 60% (right to left) over Tracks 2 and 3. Using the density-porosity curve (the solid trace), read the average porosity in the zone from 5,320 to 5,350 ft.

On the example log (Fig. 7.4), good porosity development (33–36%) is seen for the sand section. The shale section at the top of the log appears to show approximately 21% porosity and the gas cap approximately 40%. Both these apparent porosities reflect the effects of shale and light hydrocarbons and, for present purposes, can be ignored.

7.4 Water Saturation: S_w

Water saturation is defined as the volume fraction of the pore space occupied by water **(Fig. 7.6).** Note that the bulk volume of water is given by the product $\phi\ S_w$, the hydrocarbon saturation is given by $(1 - S_w)$, and the bulk volume of hydrocarbons is $\phi\ (1 - S_w)$. In the event that gas, oil, and water are all present in the pore space, then the individual saturations of the water and hydrocarbon phases are as shown in **Fig. 7.7.**

From Chapter 6, in which the relationship between rock resistivity and water saturation was defined, it is known that

$$S_W = \left(R_0 / R_t\right)^{1/2} \quad \text{.....(7.1)}$$

This equation can be put to good use on the example logs. If, on Fig. 7.3, it is possible to read a value for R_o in the wet zone and a value for R_t in a hydrocarbon zone; then, if the porosities in each zone are the same, a water saturation value can be computed using Archie's equation.

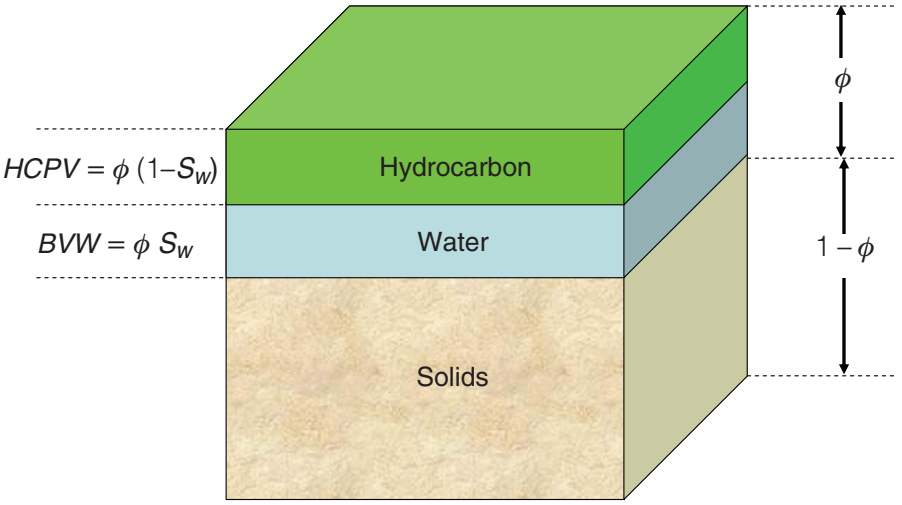


Fig. 7.6—Porosity, water saturation, bulk water volume, and hydrocarbon pore volume.

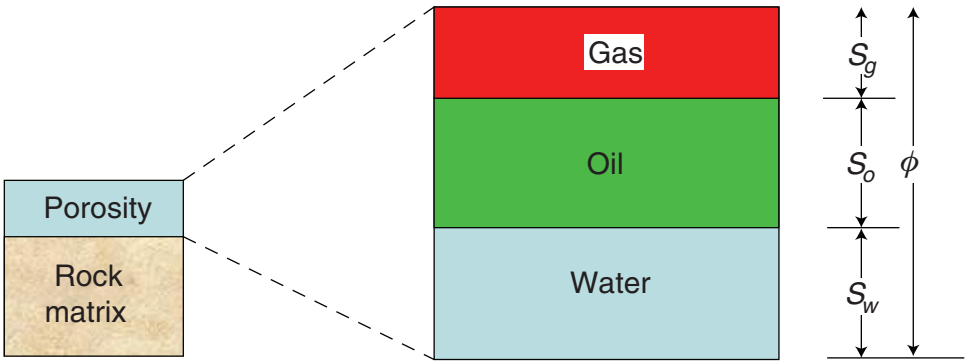


Fig. 7.7—Definitions of porosity and water, oil, and gas saturations.

QUESTION 7.3.
Read R_o at 5,420 ft.
Read R_t at 5,297 ft.
Compute S_w.

In cases where R_o cannot be read in a wet zone of equal porosity, recourse can be had to Archie's equation written in the form:

$$S_w^n = FR_w / R_t \quad \ldots\ldots (7.2)$$

Solution of this equation requires knowledge of both F, the formation factor, and R_w, the connate-water resistivity. Again from Chapter 6,

$$R_w = R_o / F = R_o \phi^m / a, \quad \ldots\ldots (7.3)$$

which can be used to find R_w from the logs shown in Figs. 7.3 and 7.4. The oil/water contact in this well is at 5,384 feet. Below this level, a value for R_o can be read from the dual laterolog and a value (ϕ_D) for porosity in the wet zone can be read from the density log. These can be combined to find a value for R_w.

QUESTION 7.4.
Read R_o in the interval 5,390–5,400 ft.
Read ϕ_D in the same interval.
Assume $F = 0.62 / \phi^{2.15}$.
Calculate R_w.

With R_w defined, Archie's equation can be solved.

QUESTION 7.5.
Read the porosity at 5,350 ft.
Convert this to an F value using $a = 0.62$, $m = 2.15$.
Read R_t at 5,350 ft.
Use $R_w = 0.18\ \Omega \cdot m^2/m$.
Compute S_w at 5,350 ft.

A useful chart for solving Archie's equation is shown in **Fig. 7.8.** To use this chart (known as a nomogram), draw a first line from R_w through ϕ to find R_o. Then draw a second line from R_o through R_t to find S_w.

Thus, water saturation can be calculated on a point-by-point basis algebraically or by use of a nomogram. With laptop computers, the calculation of water saturation from Archie's equation is trivial. However, the practicing log analyst may not always have access to a portable computing device or one that has a fully charged battery, and in these cases, the nomogram is king because it requires only a straight edge and a pencil.

7.5 Hydrocarbon Type

The neutron-density log (Fig. 7.4) can be used to distinguish between oil and gas. For reasons that will be covered later when discussing the neutron and density tools and their interpretation in Chapter 23, gas can be expected to leave its "fingerprint" on the neutron-density combination. The neutron log (dashed curve) will read less than true porosity, and the density log (solid curve) will read more than true porosity in gas-bearing formations.

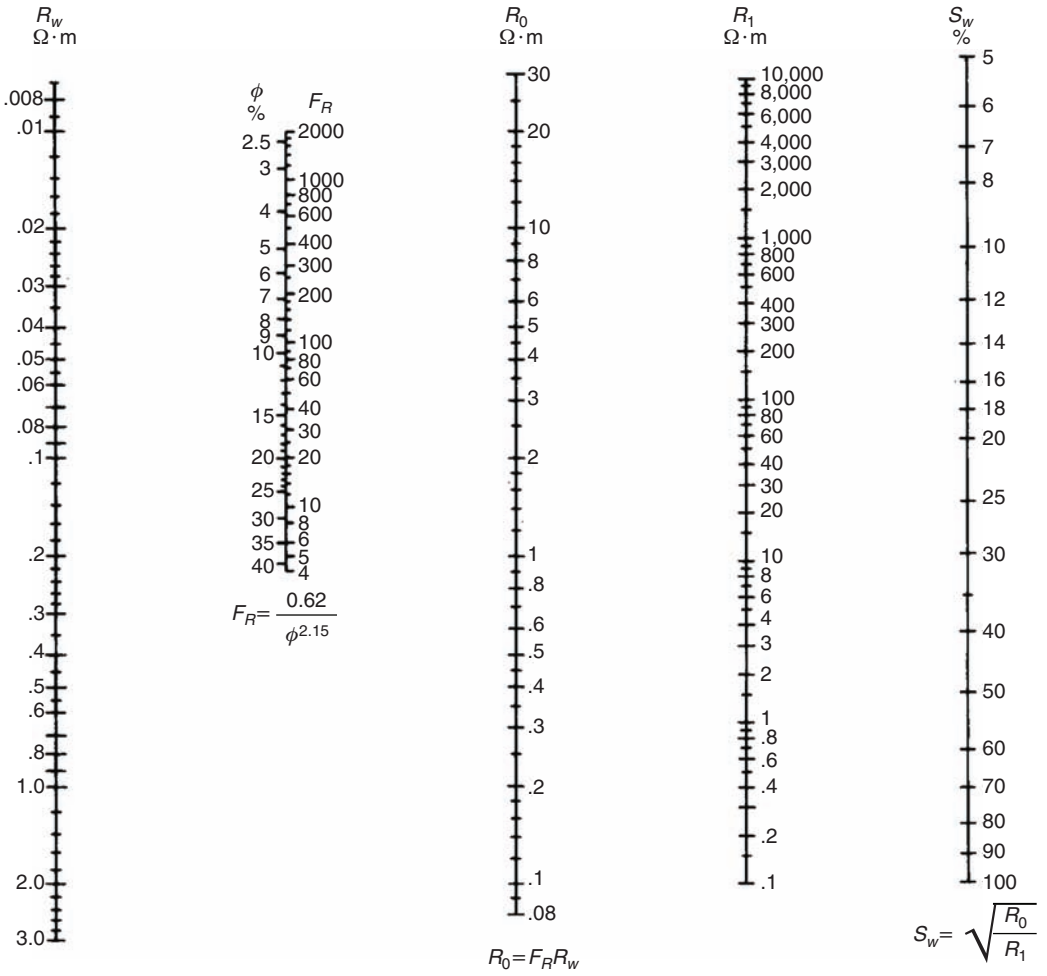


Fig. 7.8—Nomogram for saturation determination (Schlumberger 2009). Courtesy of Schlumberger.

QUESTION 7.6. Inspect Fig. 7.4. Color-code (red) between the neutron and density logs only where the neutron value is less than the density value. From the result, determine the gas/oil contact (GOC).

7.6 Pay Counting

Chapter 8 covers the hydrocarbons-in-place calculations in detail. Here a preview will be provided of the various ways to quantify pay, that is, the amount of hydrocarbon calculated from logs.

Net pay is measured in feet. For example, the well logged in Fig. 7.3 has a gross pay section from 5,280 ft down to 5,384 ft (dual-laterolog depths). However, not all this section will produce hydrocarbons. There are low-porosity shale streaks that will not produce, and there are sections at the base of the interval that will produce water because S_w is too high.

QUESTION 7.7. Find the net pay in feet for the example well.

This net pay can be further classified by a breakdown into so many feet of oil and so many feet of gas.

QUESTION 7.8. Subdivide the net pay into oil and gas pay.

However, "X feet of pay" is not very informative unless you know how good or bad each foot is. It is necessary to quantify "net pay" with reference to hydrocarbon pore volumes.

Oil in place is defined as the fraction of the rock volume occupied by hydrocarbons. For each foot of formation, the water saturation and porosity can be used to define the hydrocarbon pore volume (HCPV):

$$HCPV = \phi(1 - S_w) \quad \ldots\ldots\ldots\

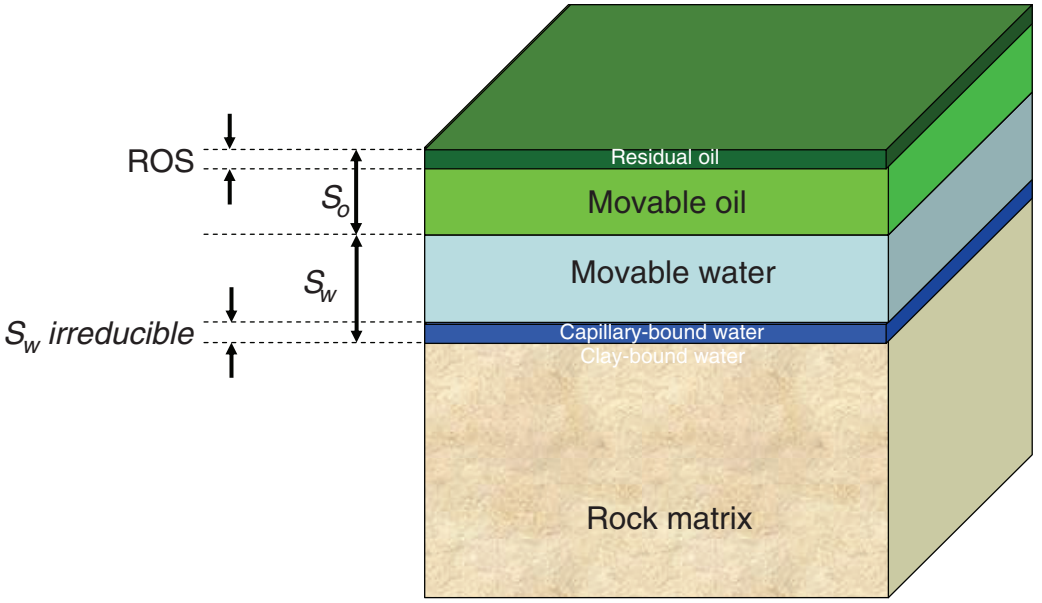


Fig. 7.9—Concepts of movable and bound fluids in the pore space.

- Irreducible water saturation, S_{wi}
- Residual oil saturation (ROS)

In clean formations with high permeability, the volume of bound water is very small. In tighter, more shaly formations of low permeability, the volume of bound water can be substantially greater, as illustrated in **Fig. 7.10.**

This difference is due, not only to additional small pores in the matrix material itself, but also to the adsorption of water onto the surfaces of clay crystals present in the formation. A full treatment

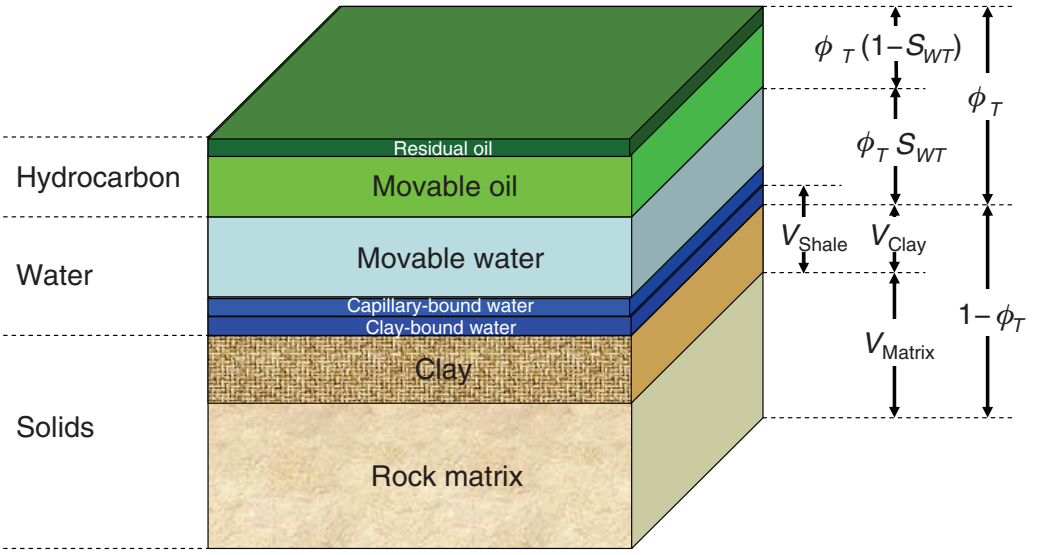


Fig. 7.10—Concepts of clay, shale, total and effective porosities, and clay-bound water.

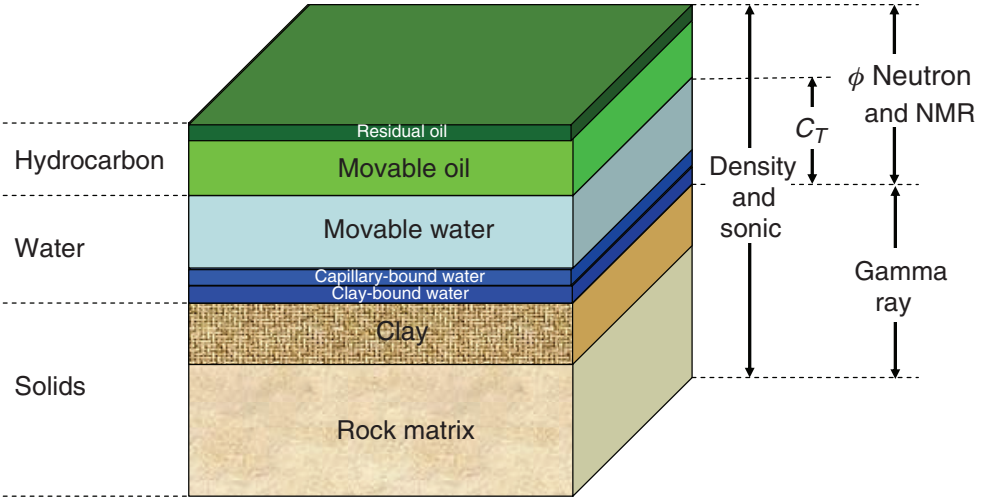


Fig. 7.11—Logging sensors and the seven-component formation model.

of these concepts is given in Chapter 28. The expanded formation model presented there is made up of seven components **(Fig. 7.11).** The challenge for the log analyst is to combine the measurements from the various logging sensors in such a way that the precise value of each of the seven components is accounted for.

7.9 Summary

Application of a few basic principles enables the analyst to work from raw logs through to quantitative pay counts. The steps involved included

- Defining porous and permeable zones
- Reading porosity values from a porosity log
- Recognizing hydrocarbon- and water-bearing zones by inspection of a resistivity log
- Applying Archie's relationships to find R_w and S_w
- Distinguishing gas from oil
- Summarizing pay thickness and quality
- Estimating permeability

Refinements of these clean-formation procedures, to be studied later, will not in any way alter this basic method of formation evaluation from logs.

Reference

Schlumberger. 2009. *Log Interpretation Charts*, 09-FE-0058. Sugar Land, Texas: Schlumberger.

Answers to Questions

QUESTION 7.1. Two quantities must be known: the volume of the rock sample, including its pores, and the volume of the pore space itself. Because the water removed from the sample entirely filled the pore space, it follows that the volume of the water equals the pore volume. Therefore, the

pore volume is (215.5 – 185.5) g at 1 g/cm^3 = 30 cm^3. The volume of the rock itself is given by its weight divided by its density, or 185.5/2.65, which gives 70 cm^3 of dry rock. This total volume of the rock + the pores is therefore 100 cm^3. The porosity of this system is therefore 30/100 = 0.3, or 30%.

QUESTION 7.2. ϕ_{av} = 35%.

QUESTION 7.3. S_w = 14.4%.

QUESTION 7.4. R_w = 0.18 Ω·m.

QUESTION 7.5. S_w = 24.7%.

QUESTION 7.6. GOC is at 5,314 ft.

QUESTION 7.7. 72 ft of net pay.

QUESTION 7.8. 38 ft net oil pay.
34 ft net gas pay.

QUESTION 7.9. k = 2500 md.

QUESTION 7.10. k = 500 md.

QUESTION 7.11. 0.5 Ω /ft, hence k = 700 md.

Chapter 8

Volumetrics and Reserve Estimation

For many end users of log data, the single most important calculation is that of the hydrocarbon reserves in the reservoir. This chapter will cover the mathematics and philosophy of reserve estimation. It should be noted that accurate reserve figures rely not only on log data and computations based on logs, but on other data as well. The size and shape of a reservoir are determined by seismic records and other means independently of the log data gathered in one or many wells. Correlation of logs from many wells in a field will undoubtedly help in defining the size, shape, and limits of the subsurface trap. Dipmeter data will also be of assistance. However, in the final analysis, logs define only the concentration of oil- or gas-in-place in terms of bulk-volume fractions. The extrapolation of these figures to reserves requires more information than logs alone can provide. In summary, a log analyst can say with a reasonable degree of certainty that, for example, 10% of the volume of a bottle is full of oil. It is up to others to determine the size of the bottle and hence to deduce the actual volume of oil available.

8.1 Oil and Gas in Place Estimates

Consider the circumstances depicted in **Fig. 8.1.** A cylindrical block of porous rock has a height h and an area A, giving rise to a rock volume $V = h\,A$. If the porosity is ϕ and the water saturation is S_w, then the oil-in-place is $\phi\,V\,(1 - S_w)$ in the same units as V. Therefore, if V is expressed in cubic feet or cubic meters, then the oil-in-place is expressed in the same units because ϕ and S_w are simply fractions of one.

In the more general case, the units of h and A must be considered to calculate a volume V. If h is measured in feet and A in acres, then the reservoir volume V is expressed in acre-feet. If h is in meters and A in hectares, then V is expressed in hectare-meters.

So far, only reservoir units at constant porosity and saturation have been considered. In actual reservoirs, both porosity and saturation vary both laterally and vertically. A useful quantity for oil-in-place measurements is therefore the hydrocarbon pore volume, or *HCPV*, which is defined as

$$HCPV = \phi\left(1 - S_w\right) \quad \text{(8.1)}$$

Therefore, at any depth in a well, if both porosity and saturation can be deduced from logs, the concentration of hydrocarbons in the reservoir at that depth can be estimated. For example, if porosity is 30% and water saturation is 40%, then the $HCPV = 0.3\ (1 - 0.4) = 0.18$, and 18% of the reservoir bulk volume contains oil. At a neighboring point in the same well, the value of

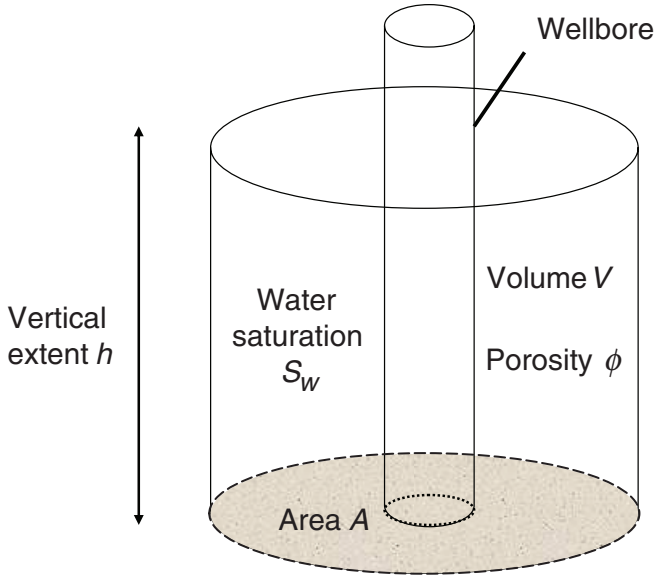


Fig. 8.1—OIP (generalized reservoir units).

HCPV may be different. Therefore, to sum the total oil in place (OIP), an integration of *HCPV* with respect to depth and area is called for:

$$OIP = \Sigma\phi(1-S_w)hA \quad \ldots\ldots\ldots\

TABLE 8.1—UNITS MULTIPLIER *C* FOR RESERVES

Use C =	Where A Is in	h is in	Hydrocarbon is	To Find N in
7.7579×10^{-3}	acres	feet	oil	MMSTB
43.56×10^{-6}	acres	feet	gas	BCF
10×10^{-3}	hectares	meters	oil	MM m^3
10×10^{-3}	hectares	meters	gas	MM m^3

MM STB = 10^6 stock tank barrels

BCF = 10^9 standard cubic feet

MM m^3 = 10^6 cubic meters

8.2 Reserve Estimates

So far, only the volume of hydrocarbons found in a trap has been discussed. Although this is of course fundamental, the bottom line is the number of stock-tank barrels that can be recovered from the trap. The conversion of OIP to reserves requires two additional pieces of data: the recovery factor, r, and the formation volume factor, B. Neither of these can be estimated from logs. The recovery factor is a function of the type of reservoir and the drive mechanism, and the formation volume factor is a function of the hydrocarbon properties. The reserves, N, can therefore be expressed in terms of stock-tank volumes as:

$$N = C\Sigma\phi(1-S_w)hAr/B, \quad \ldots\ldots\ldots\

$c = -0.1903$,
$d = -0.2159$,
p_i = initial reservoir pressure, psia,
p_a = abandonment reservoir pressure, psia,
μ_w = water viscosity, cp,
μ_o = oil viscosity, cp,

and

$$r_{SG} = 41.82\left[\phi(1-S_w)/B_{ob}\right]^a \left(k/\mu_{ob}\right)^b \left(S_w\right)^c \left(p_b/p_a\right)^d, \quad \ldots\ldots\ldots\ldots\ldots\ldots\ldots\ldots\ldots\ldots\ldots\ldots (8.6)$$

where
r_{SG} = recovery factor for solution-gas-drive reservoirs,
B_{ob} = oil formation volume factor at bubblepoint pressure,
μ_{ob} = oil viscosity at bubblepoint pressure,
p_b = bubblepoint pressure,
$a = 0.1611$,
$b = 0.0979$,
$c = 0.3722$, and
$d = 0.1741$.
For both equations, k is in darcys, and ϕ and S_w are fractions.

QUESTION 8.2. Calculate the primary recovery in a waterdrive reservoir given the following data:

$\phi = 20\%$.
$S_w = 35\%$.
$k = 250$ md.
$B_o = 1.25$.
$\mu_w = 0.5$ cp.
$\mu_o = 1.5$ cp.
$p_i = 2000$ psia.
$p_a = 750$ psia.

8.4 Formation Volume Factors

Because of the dissolved gas present in oil at reservoir conditions, the volume of oil recovered at surface is less than the volume of oil in the formation. The shrinkage can be quantified by use of the oil formation volume factor, B_o. This is a function of the gas gravity, γ_g, the solution gas/oil ratio, R_{sb}, and the formation temperature, T. The factors required are not always available in a wildcat situation, and oil and gas samples may need to be collected and submitted for PVT analysis.

Gas-formation volume factors depend on formation pressure and temperature and on the supercompressibility factor Z for a particular gas. In general, B_g will be a small fraction of one; that is, many tens or hundreds of times as much gas will be recovered at surface as exist at formation conditions. For further details, the reader is referred to Bateman (1984).

8.5 Depth and Net Pay Measurements

When summing pay, it is normal practice to compute a number of useful items such as:

- Gross section
- Net porous and permeable section
- Gross pay section
- Net pay section

Referring to **Fig. 8.2,**

- The gross section represents the distance A–D.
- The net porous and permeable section is the gross section less shale or other low-porosity, low-permeability sections such as a, b, and c.
- The gross pay is represented by A–C less a and b (i.e., gross pay includes all hydrocarbon-bearing sections from the top of the formation down to the oil/water contact, less any shale sections, etc.).
- Net pay is represented by A–B less a and b (i.e., it only includes sections above the transition zone likely to produce water-free hydrocarbons).
- Net pay figures are the ones to use for *h* in the HCPV, OIP, and reserve calculations.

8.6 Special Cases of Deviated Wells and Dipping Beds

So far, only vertical wells with horizontal beds have been considered. However, when the wellbore is deviated, the beds are dipping, or both, it is important to make allowances for these effects.

Offshore exploration and development require the drilling of multiple deviated wells from fixed platforms. As a result, the thickness of a formation as measured from a log made in a deviated hole reflects neither its true stratigraphic thickness (TST) nor its true vertical thickness (TVT). The geologist who tries to trace a given bed across the field finds it difficult to deduce whether variations in bed thickness measured from a log are due to legitimate bed-thickness variations or whether they are geometrical distortions resulting from hole deviation and bed-dip effects. The engineer trying to compute reserves is faced with the same type of problem. Measured bed thickness can be less than true vertical bed thickness in some cases and greater in other cases. A need for a quick and simple solution to the problem is evident, and a method will be presented here to satisfy the demands of both the explorer and the engineer.

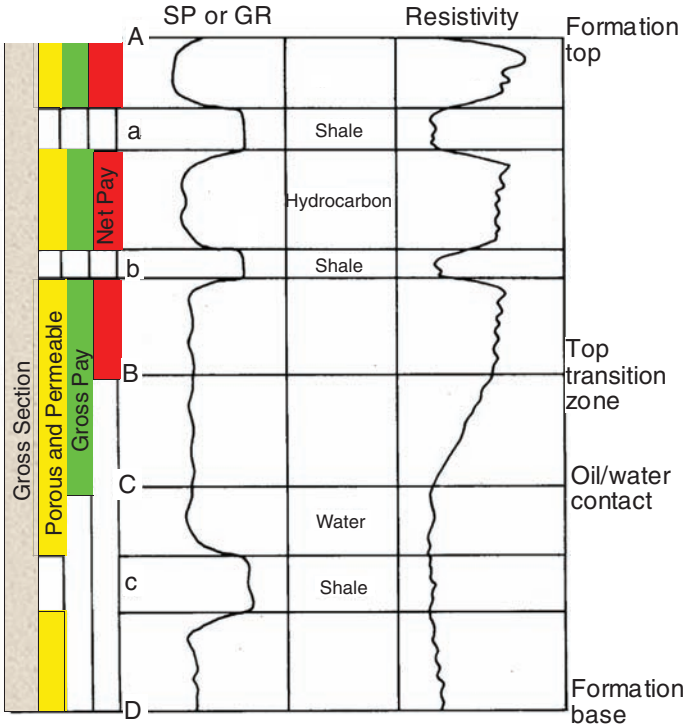


Fig. 8.2—Gross and net pay.

Fig. 8.3 illustrates the case of a well that is deviated by $\alpha°$ from the vertical and that crosses a horizontal bed of measured thickness (MT). If the well enters the bed at A and leaves the bed at B, the measured thickness is AB, and the *TST* is related to the measured thickness by:

$$\mathrm{TST} = \mathrm{MT}\cos\alpha \quad \ldots\ldots (8.7)$$

Fig. 8.4 illustrates the case of a straight hole crossing a bed of *MT* that dips at $\beta°$ from the horizontal. If the hole enters the bed at A and leaves the bed at B, the measured thickness is AB, and the *TST* is given by

$$\mathrm{TST} = \mathrm{MT}\cos\beta \quad \ldots\ldots (8.8)$$

Note that when the well is vertical, the azimuth of the dipping bed is immaterial and that when the bed is horizontal, the well azimuth is likewise not required for calculating *TST*.

Fig. 8.5 illustrates the case of a well that deviates at $\alpha°$ from the vertical and that crosses a bed that dips at $\beta°$ from the horizontal. Note that both the bed azimuth and the well azimuth are the same for this particular illustration. Again, the measured thickness is AB. It is of interest to note that the true vertical depth difference between A and B is AC, where AC = AB cos α. However, the engineer is interested in the *TVT*, given by AE, and the geologist is seeking the *TST*, given by BD.

For the case in which both well and bed dip are oriented in the same azimuth, it is a trivial exercise to deduce *TVT* (distance AE on Fig. 8.5) and *TST* (distance BD):

$$\mathrm{TST} = \mathrm{MT}\cos(\alpha+\beta) \quad \ldots\ldots (8.9)$$

$$\mathrm{TVT} = \frac{\mathrm{TST}}{\cos\beta} = \frac{\mathrm{MT}\cos(\alpha+\beta)}{\cos\beta}. \quad \ldots\ldots (8.10)$$

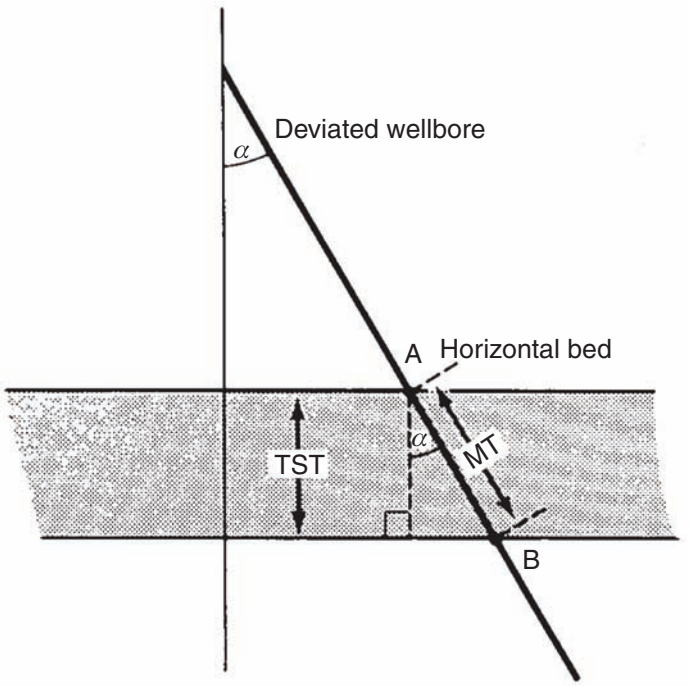


Fig. 8.3—Deviated well and horizontal bed (Bateman and Konen 1979). Reprinted by permission of the SPWLA.

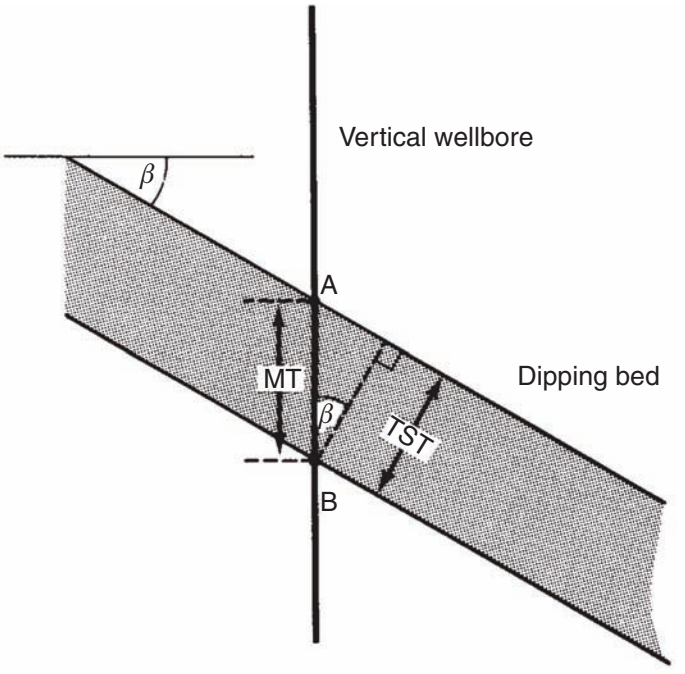


Fig. 8.4—Vertical well and dipping bed (Bateman and Konen 1979). Reprinted by permission of the SPWLA.

Note that Eqs. 8.9 and 8.10 hold only for the case in which bed-dip azimuth and well-deviation azimuth are exactly the same. In the general case, the well azimuth is different from the bed azimuth, and the simple relationships deduced for the special case illustrated in Fig. 8.5 do not hold.

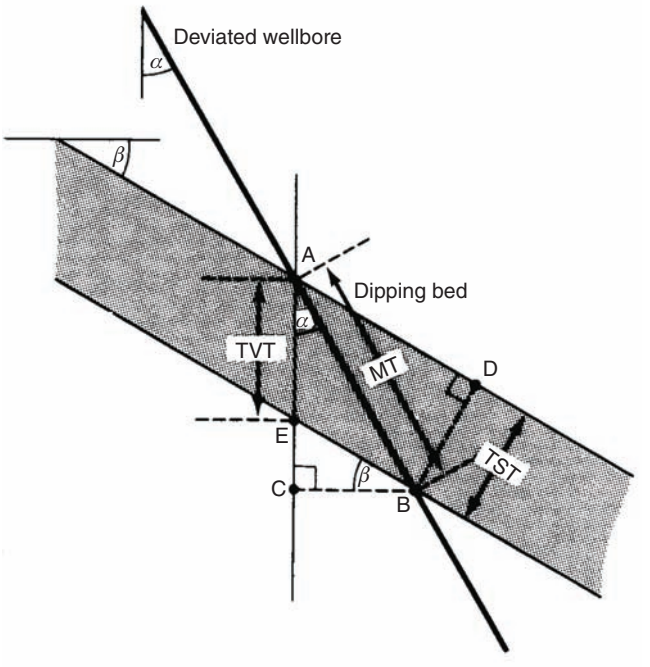


Fig. 8.5—Deviated well and dipping bed (Bateman and Konen 1979). Reprinted by permission of the SPWLA.

The practicing log analyst who has had to deal with dipmeter-related problems will appreciate the similarity between structural dip subtraction and the solution described here. The basic idea is to consider the well as one dip vector and the bed as another and to perform a dip rotation. In this method, the bed is brought back to the horizontal, and the well deviation and azimuth assume new values in the geographical frame of reference, while maintaining the same orientation relative to the bed itself. The reader may better understand the principle by imagining a pencil (representing the well) stuck through a slab of cheese (representing the dipping bed). If the cheese is initially dipping to north and the pencil transverses the cheese deviated to the west, then the result of placing the cheese on a horizontal surface will be to move the azimuth of the pencil from west to somewhere north of west and at the same time to increase the deviation of the pencil from the vertical.

Another approach would be to allow the pencil to rotate until it were vertical, in which case the cheese slab would dip at an increased angle to some point west of north.

Either of these rotations can be performed by treating the problem as a structural dip subtraction. The manipulation can be made graphically by using a stereo net with a rotating overlay, or it can be made mathematically using the cosine law of spherical triangles. Once the bed has been rotated back to horizontal (or the hole back to vertical), the simple relationships illustrated in Figs. 8.3 and 8.4 can be used. Because the new azimuth of the bed or the hole is not required, the only parameter needed is the new bed dip or the new hole deviation, depending on which approach has been used. In this illustration, the bed will be rotated back to horizontal. Therefore, if

α° = well deviation from vertical,
β° = bed dip from horizontal,
HAZ° = hole azimuth,
DAZ° = dip azimuth, and
MT = measured bed thickness,

then the well deviation from the vertical after the bed has been rotated to horizontal is given by α', where:

$$\cos\alpha' = \cos\alpha\cos\beta - \sin\alpha\sin\beta\cos(\mathrm{HAZ} - \mathrm{DAZ}) \quad (8.11)$$

If the bed is now horizontal, the true stratigraphic bed thickness is given by:

$$\mathrm{TST} = \mathrm{MT}\cos\alpha' \quad (8.12)$$

or

$$\mathrm{TST} = \mathrm{MT}\left[\cos\alpha\cos\beta - \sin\alpha\sin\beta\cos(\mathrm{HAZ} - \mathrm{DAZ})\right], \quad (8.13)$$

and the *TVT* of the bed is given by:

$$\mathrm{TVT} = \frac{\mathrm{TST}}{\cos\beta} \quad (8.14)$$

or

$$\mathrm{TVT} = \mathrm{MT}\left[\cos\alpha - \sin\alpha\tan\beta\cos(\mathrm{HAZ} - \mathrm{DAZ})\right] \quad (8.15)$$

It is assumed that the *TST* is the same at the point where the well enters the bed as it is at the point where the well leaves the bed. It is also assumed that the well deviation and azimuth do not change as the well crosses the bed. If the bed is highly dipping, it is possible that the well will in fact enter the bed from the bottom side and exit from the top side. If this occurs, the calculated results for *TST* and *TVT* will appear as negative numbers.

QUESTION 8.3. From the log, the following data are collected:

Top of bed = 5,642 ft.
Bottom of bed = 5,878 ft.
Well deviation = 30° to azimuth 128°.
Bed dip = 25° to azimuth 45°.

Find

a. Measured thickness.
b. TVD difference between top and bottom of bed.
c. TST of bed.
d. TVT of bed.

8.7 Reservoir Volumes

The gross rock volume enclosed within a hydrocarbon-bearing structure cannot be deduced from a single log. Even with the aid of seismic mapping, many uncertainties remain. However, after enough wells have been drilled, it is usually possible to prepare maps showing how many net feet of pay exist above the oil/water (or gas/oil or gas/water) contact. Such maps are known as isopachs. **Fig. 8.6** shows a cross section through an oil-bearing structure together with an isopach map contouring the net feet of pay above the oil/water contact.

Once such a map has been drawn, the area enclosed within each contour can be found with a planimeter. A plot can then be made showing the area contained within each contour as a function of depth, as shown in **Fig. 8.7.** The volume is then calculated as an integration of Adh, either by planimeter or by numerical integration.

With the advent of geocellular modeling and its associated software, it has become common practice to build a reservoir model first using geophysical and geological data and then to populate

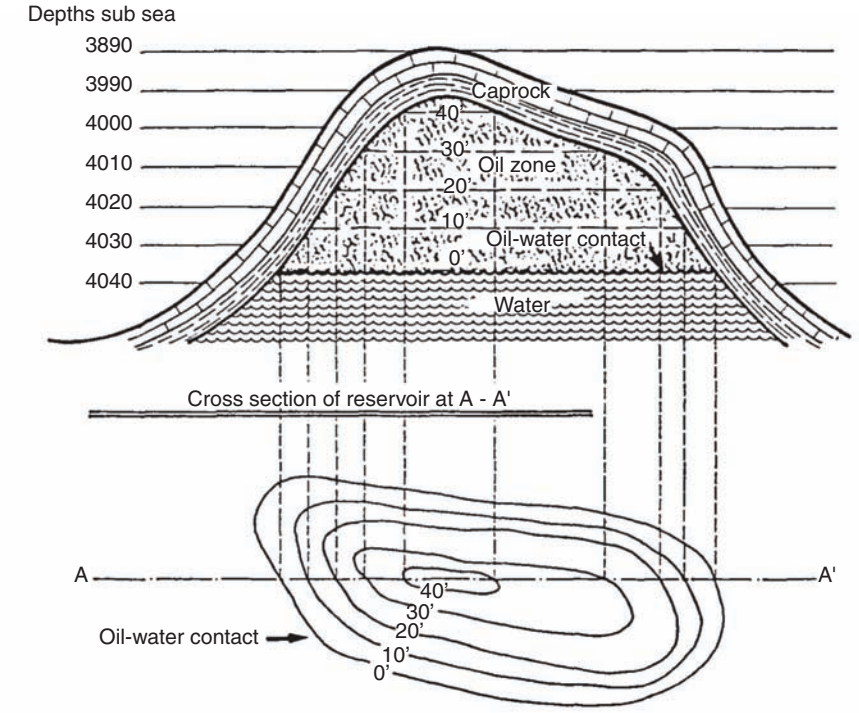


Fig. 8.6—Net pay thickness isopach and structure cross section (Schlumberger 1980). Courtesy of Schlumberger.

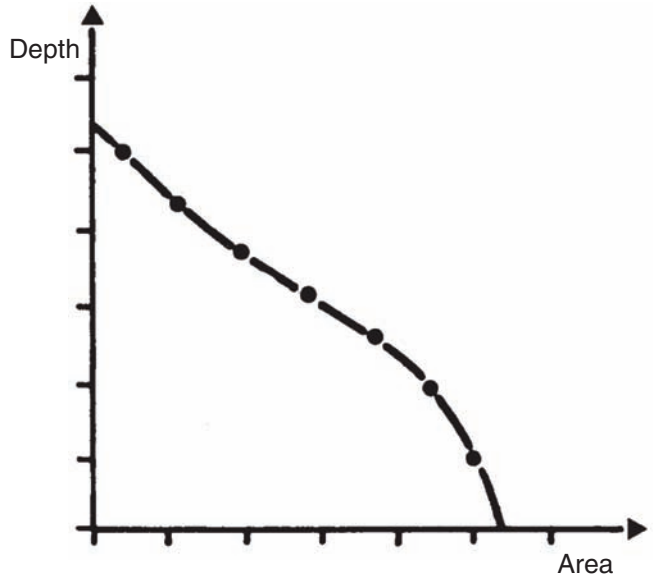


Fig. 8.7—Area within net pay contour vs. depth (Schlumberger 1980). Courtesy of Schlumberger.

the model with petrophysical properties that are based on log readings made in the wellbores that have penetrated the reservoir. Then cell-by-cell, layer-by-layer values for porosity, saturation, and permeability can be distributed using techniques such as Krieging. Once all the cells have been populated, sums and averages can be calculated that lead directly to the required numbers for reservoir pore volume and hydrocarbons-in-place.

8.8 Reserves

Although reserves are measured in barrels (or cubic meters), these are in fact economic measures of a resource. When estimating reserves, part of the exercise involves geology, geophysics, petrophysics, and reservoir engineering, but an equally important part involves economics. Although geoscientists can provide exact answers for ϕ, S_w, A, h, B_o (or $1/B_g$), and recovery factor, there are other factors that are beyond their scope and responsibility. A reserve is a volume of hydrocarbon that can be profitably recovered in the future from a known reservoir (the key word here being "profitably").

How then are reserves calculated? The key parameters in making these determinations are

- Future production profile
- Future capital costs for drilling, plant, and pipelines to connect to market
- Prices at which oil and gas can be sold
- Operating costs, royalties, and taxes that must be paid

The future production profile will depend on the development program (how many wells, their placement and productivity) and a calculated future production decline rate. The geocellular models already referred to are useful in this exercise. Material balance calculations can also play a part in predicting future production. For a reservoir in secondary or tertiary recovery, the oil-water ratio may be plotted against cumulative oil production to gain insight into the all-important future production profile. But where along the time axis is the analyst obliged to cut off accumulating future production and call it a reserve? This will depend on the expected income from the sale of the hydrocarbons produced, on the costs to drill and operate the wells, and on the royalties and taxes (or production shares) that must be paid out of the income stream. The economic decision point determining when the field should be abandoned is therefore dictated by many factors that are beyond the scope of the analyst. Hydrocarbons may well remain underground because of the

cost of water disposal, for example, or because of a ban on associated gas flaring, neither of which can be controlled by the log analyst or the petrophysicist.

Over the life of a field, the inputs to an original oil in place figure (OOIP) are not likely to change dramatically. It is possible that with development drilling, a better understanding of the reservoir geometry will result or a more exact value of porosity may be obtained, but these changes are small compared with the enormous swings in world oil and gas prices and the fickle changes in royalties and taxes that confound the economic side of the equation far too often.

Logging and log analysis can provide a stable basis for the chain of reserve calculations, but the final numbers depend on factors beyond the realm of formation properties or of those who attempt to measure them scientifically. **Table 8.2** provides a handy guide for conversions between English and metric volumetric units.

8.9 Uncertainty

The calculation of the volume of recoverable hydrocarbons (N) follows a long sequence and involves many parameters. Uncertainties in the true value of each parameter, therefore, compound to contribute to the uncertainty in the final answer. Basically, there are three components involved: the reservoir volume, the hydrocarbon concentration, and the recovery factor. Reservoir pore volume is the product of mapped area A, net pay h, and porosity ϕ. Hydrocarbon concentration (saturation) is given by $(1 - S_w)$. Recovery factor is a combination of the formation volume factor (B_o or $1/B_g$) and the percentage of the original hydrocarbons in place that will be produced economically, r. No single geoscientific discipline is the owner of these key parameters; rather, each contributes something to the whole. **Table 8.3** summarizes the parties involved and

TABLE 8.2—CONVERSION FACTORS IN RESERVE ESTIMATION

1 acre-foot	=	43,560	cu ft	=	7,758	barrels
1 hectare-meter	=	353,147	cu ft	=	62,893	barrels
1 acre-foot	=	0.1233	m-ha		1,233.5	m^3
1 hectare-meter	=	8.107	acre-ft		10,000	m^3
1 barrel	=	5.615	cu ft	=	0.159	m^3
1 cubic meter	=	35.31	cu ft	=	6.289	barrels
1 BCF	=	178.1	MMB	=	28.32	MMm^3
1 MMB	=	5.615	MMCF	=	159	Mm^3
1 hectare	=	2.471	acres		10,000	m^3

TABLE 8.3—CONTRIBUTORS TO THE RESERVE CALCULATION

	Geologist	Log Analyst	Reservoir	
	Geophysicist	Petrophysicist	Engineer	Economist
A	X			
h	X	X		
ϕ		X		
S_w		X		
r			X	X
B_o or B_g			X	

their responsibilities, and **Table 8.4** summarizes the effect of an increase in the value of each parameter on computed porosity, water saturation, HCPV, and reserves.

Although this table indicates the effect on the final answer, up or down, of an increase in any given parameter that goes into the calculation, it does not give any indication of the magnitude of change involved. As it turns out, some of the parameters that the petrophysicists or log analysts provide are relatively forgiving. **Table 8.5** gives the order of sensitivity of the final answer to a change of plus or minus 10% in each of the input parameters.

TABLE 8.4—SENSITIVITY OF HCPV AND *N* TO CHANGES IN INPUT PARAMETERS

Parameter	Δ	Porosity	Water Saturation	HC Pore Volume	Stock Tank bbl
R_w	⇧	—	⇧	⇩	⇩
ρ_{ma}	⇧	⇧	⇩	⇧	⇧
ρ_{mf}	⇧	⇧	⇩	⇧	⇧
Archie "*a*"	⇧	—	⇧	⇩	⇩
Archie "*m*"	⇧	—	⇧	⇩	⇩
Archie "*n*"	⇧	—	⇧	⇩	⇩
h	⇧	—	—	⇧	⇧
Area	⇧	—	—	⇧	⇧
FVF	⇧	—	—	—	⇩
Rec Factor	⇧	—	—	—	⇧

TABLE 8.5—ORDER OF IMPORTANCE OF INPUTS TO RESERVE ESTIMATES

Parameter Δ +/−10%	Influence %	Importance
ρ_B	131	Least forgiving
ρ_{ma}	118	
Field radius	40	
B_o or $1/B_g$	20	
Thickness *h*	20	
Net to gross	20	
Recovery factor	20	
ρ_{Fluid}	16	
Archie "*m*"	7	
Archie "*n*"	7	
R_t	3	
R_w	3	Most forgiving

References

Bateman, R.M. 1984. *Cased-Hole Log Analysis and Reservoir Performance Monitoring,* Chap. 3. Boston: International Human Resources Development Corporation (IHRDC).

Bateman, R.M., and Konen, C.E. 1979. Finding True Stratigraphic Thickness and True Vertical Thickness of Dipping Beds Cut by Directional Wells. *The Log Analyst* **20** (2): 3–6.

Muskat, M. 1949 (reprinted 1981). *Physical Principles of Oil Production,* Chap. 14. Boston: International Human Resources Development Corporation (IHRDC).

Poston, S.W. 1984. Numerical Simulation of Reservoir Sandstone Models. Paper SPE 13135 presented at the SPE Annual Technical Conference and Exhibition, Houston, 16–19 September. http://dx.doi.org/10.2118/13135-PA.

Schlumberger. 1980. *Reservoir and Production Fundamentals*.

General References

Bull. D 14, *A Statistical Study of Recovery Efficiency*. 1967. Washington, DC: API.

Banks, R.B. 1982. New Thoughts on an Old Topic: Reservoir Integration (Volumetrics). Paper SPE 11339 presented at the 1982 Production Technology Symposium, Hobbs New Mexico, USA, 8–9 November. http://dx.doi.org/10.2118/11339-MS.

Answers to Questions

QUESTION 8.1.

a. HCPV = 3.5 ft.
b. Oil-in-place = 27,153 bbl/acre.
c. Reserves = 1.253 MMSTB.

QUESTION 8.2.

Oil-in-place term = $54.9\ [0.2\ (1 - 0.35)/1.25]^{0.0422} = 49.99$.
Mobility term = $[(0.25 \times 0.5)/1.5]^{0.077} = 0.826$.
Water saturation term = $0.35^{-0.1903} = 1.221$.
Pressure ratio term = $(2000/750)^{-0.2159} = 0.809$.
Hence $r_{WD} = 49.99 \times 0.826 \times 1.221 \times 0.809 = 0.408$
or 40.8% of the oil in place will be recovered.

QUESTION 8.3.

a. MT = 236 ft.
b. TVD difference = 204.38 ft.
c. TST = 179.16 ft.
d. TVT = 197.68 ft.

Part III—Openhole Logging Measurements

Chapter 9

The Spontaneous Potential Log

9.1 History of the Spontaneous Potential (SP)

The SP, one of the first logging measurements ever made, was discovered by accident. It appeared in the borehole as a DC potential that caused perturbations to the old electric logging systems. Its usefulness was soon realized, and it has remained one of the few well log measurements to have been in continuous use for over 80 years.

The SP log has a number of useful functions, including:

- Correlation
- Lithology indication
- Porosity and permeability indications
- Measurement of R_w and hence of formation water salinity

Fig. 9.1 shows a typical SP log, which is represented in Track 1 as a solid curve and shows departures to the left from a base line (or shale line) reading on the right to a sand line on the left in the cleanest nonshale zones. The scale of the log is in millivolts, abbreviated mV. Notice that there is no absolute scale in mV, but only a relative scale of so many mV per log chart division (20 in this example).

How this measurement can be used quantitatively will be explained later in this section.

QUESTION 9.1. On the log shown in Fig. 9.1, read the maximum SP deflection from the shale line to the sand line:

SP = mV.

9.2 Recording the SP

The SP can be recorded very simply by suspending a single electrode in the borehole and measuring the voltage difference between the electrode and a ground electrode, which usually takes the form of a "fish" making electrical contact with the earth at the surface. A generalized illustration of the SP recording system is shown in **Fig. 9.2.** Such SP electrodes are built into nearly all logging tools. For example, the SP can be recorded using an induction log, a laterolog, a sonic log, a sidewall core gun, or other device.

However, the SP cannot be recorded in oil-based muds because there is no electrically conductive path through the mud and a conductive path is essential to generate a spontaneous potential. The SP is a sort of self-calibrating indicator of formation-water salinity. To understand how the SP can be used to find R_w, a little should first be known about the origin of the SP.

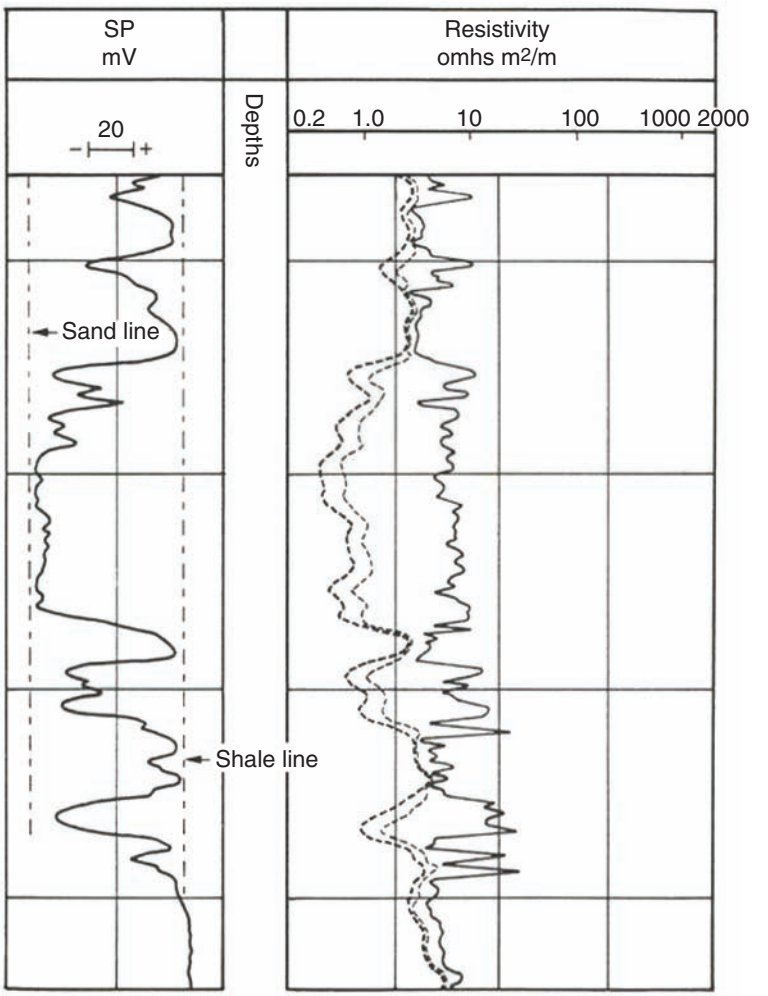


Fig. 9.1—Typical SP log with resistivity recording.

9.3 Source of the SP

If two sodium chloride solutions of different concentrations are separated by a permeable membrane, then ions from the most concentrated solution will tend to migrate into the less concentrated solution **(Fig. 9.3).**

However, Na^+ and Cl^- ions do not move with the same alacrity. Cl^- ions move faster than Na^+ ions. The result is a conventional current flowing from the weaker solution to the more concentrated solution. This is known as a *liquid junction effect*. In terms of the solutions present in a formation, mud filtrate can be substituted for the weak solution and formation water for the more concentrated solution **(Fig. 9.4).** The potential is referred to as the *liquid-junction potential* (E_{lj}). The greater the contrast in salinity between the mud filtrate and the formation water, the larger this potential will be.

A similar battery effect arises in the formation because of the molecular construction of shale beds. Shales are permeable to Na^+ ions, but not so permeable to Cl^- ions. A shale, therefore, acts as an ionic sieve. This phenomenon occurs because of the crystalline structure of clay minerals, which have exterior surfaces with exchange sites to which cations can temporarily cling. (This same surface conductance effect manifests itself in the electrical behavior of shaly sands; see Chapter 28). Because Na^+ ions effectively manage to penetrate the shale bed from the saline

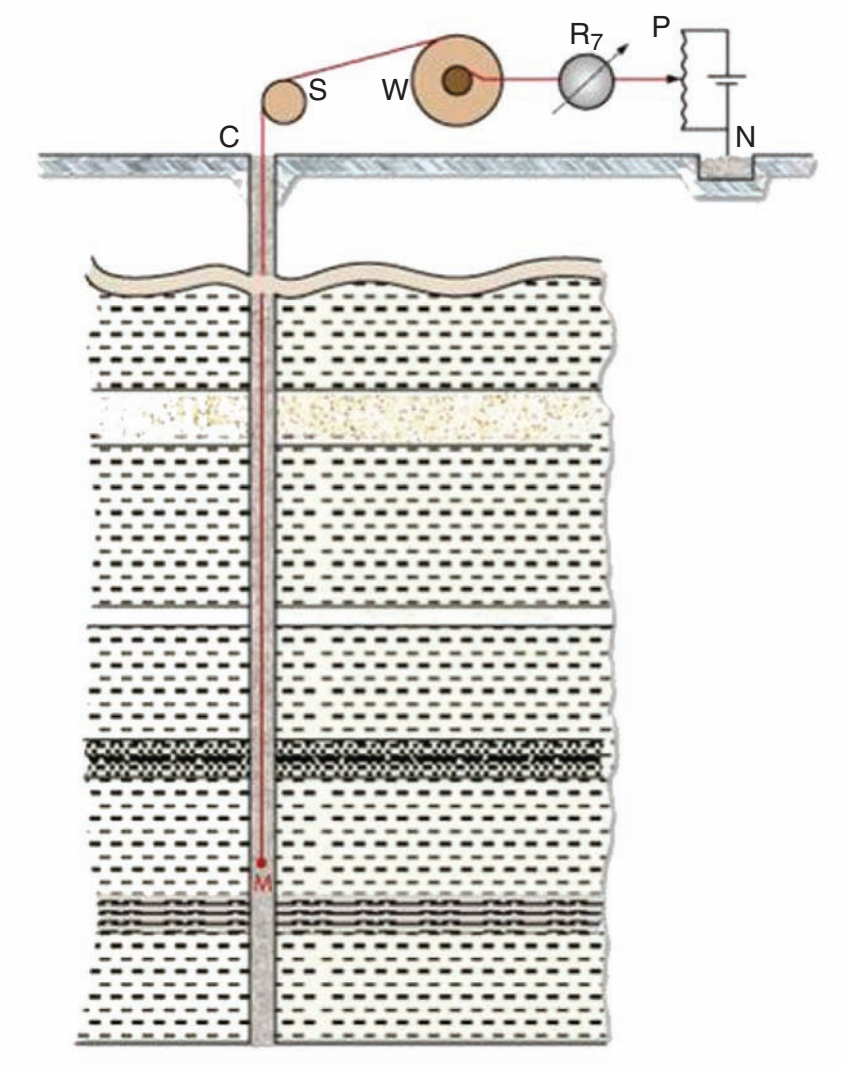


Fig. 9.2—Recording the SP.

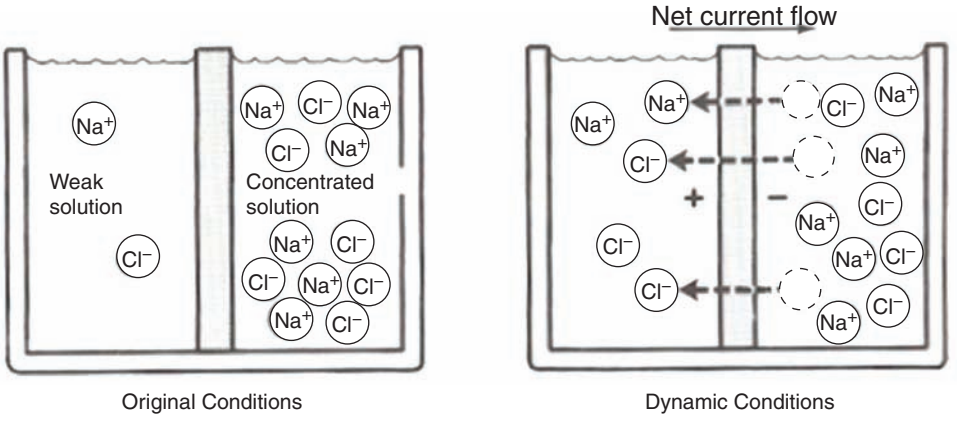


Fig. 9.3—Liquid junction effect.

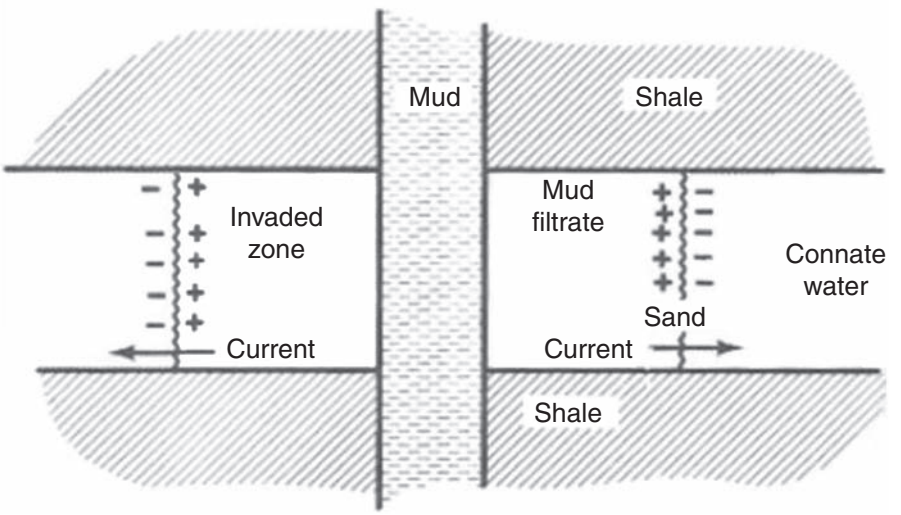


Fig. 9.4—Liquid junction SP.

formation water to the less saline mud column, a so-called *membrane potential* (E_m) is created **(Fig. 9.5).**

The total electrical potential can now be appreciated to be the sum of these two components:

$$E_{\text{Total}} = E_{lj} + E_m = SP. \quad \ldots\ldots\ldots\

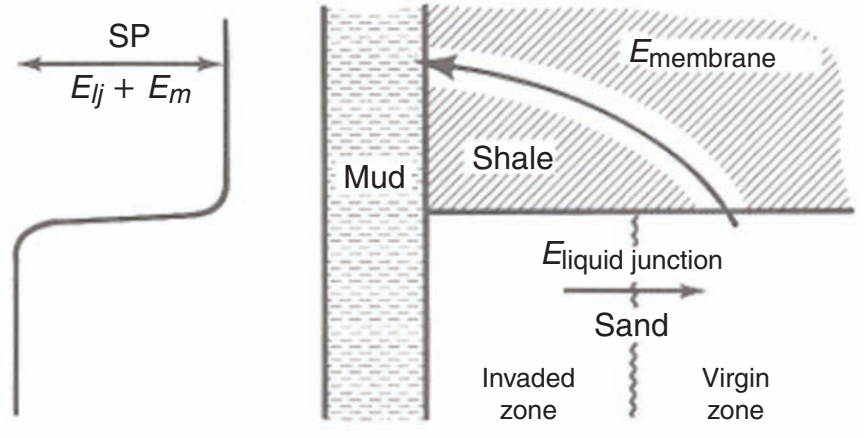


Fig. 9.6—Overall SP picture.

It is quite common to find fresh water in shallow sands and increasingly saline water as depth increases. Such a progression is shown in **Fig. 9.7,** where the SP appears deflected to the left deep in the well but is reversed nearer the surface.

In Sand A, R_w is less than R_{mf} (i.e., the formation water is saltier than the mud filtrate). In Sand B, the SP deflection is less than in Sand A, indicating fresher formation water. In Sand C, the SP is reversed, indicating formation water that is fresher than the mud filtrate, so that R_w is greater than R_{mf}. It is a safe guess that somewhere in the vicinity of 7,000 ft, R_{mf} and R_w are equal.

9.4 R_w From the SP

In order to quantitative analysis of the SP, the relationship between the SP and the resistivities of the mud filtrate and the formation water must be determined. Analysis of a series of complicated paths of logic based on various laws of physical chemistry leads to the equation:

$$\mathrm{SP} = -K \log(R_{mf}/R_w), \quad \ldots\ldots\ldots\

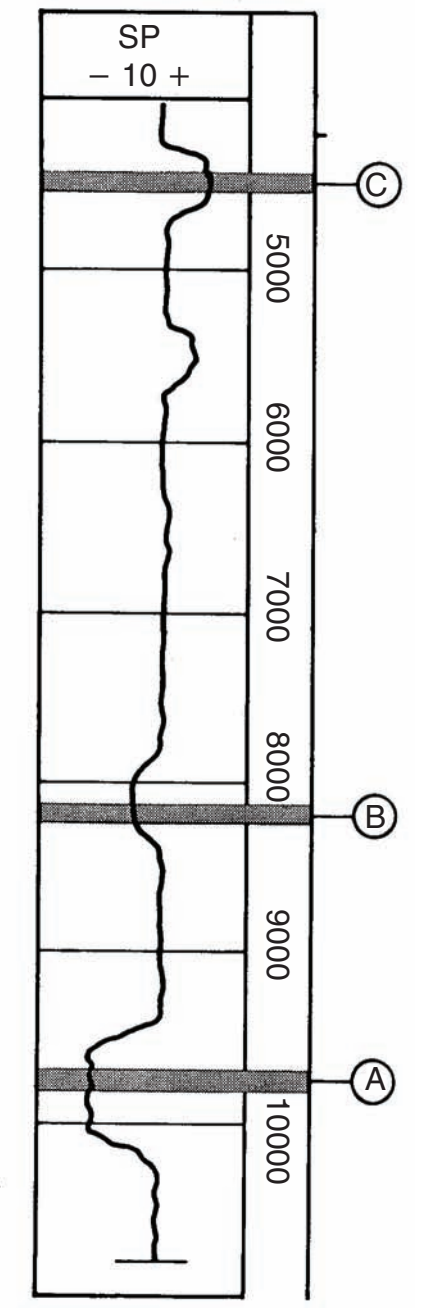


Fig. 9.7—Normal and reverse SP deflections.

(Mud engineers love to sprinkle sundry additives into the system daily to maintain the appearance of being busy.)

Experiments of the sort reported by Williams and Dunlap (1984), in which R_m and R_{mf} were measured daily as a well was being drilled, tend to support the contention that R_{mf} is the least well-defined parameter in SP log analysis. A comparison between the values of R_m and R_{mf} as reported on log headings with the actual daily measured values can show alarmingly large differences. **Fig. 9.8** shows such a plot. As can be seen, the values for both R_m and R_{mf} reported on the log heading for this well are low by a substantial factor.

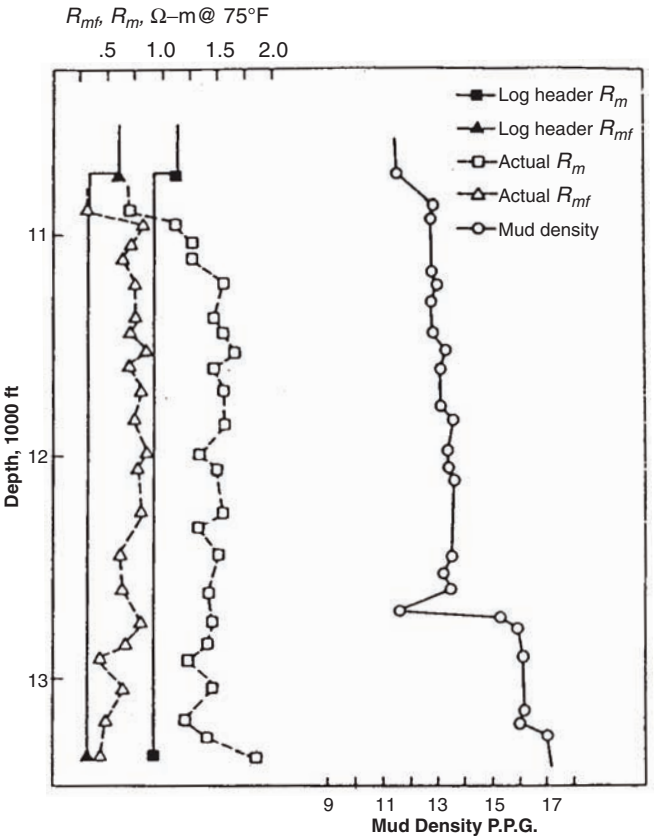


Fig. 9.8—Log header R_m and R_{mf} vs. short-term variations in R_m, R_{mf}, and mud density (Williams and Dunlap 1984). Reprinted by permission from the SPWLA.

In the absence of any reported value for R_{mf} and given a value for R_m, a value for R_{mf} can be estimated from **Fig. 9.9,** which also serves for estimation of R_{mc}. A fit of this empirical chart gives

$$R_{mf} = \left\{R_m^{\,1.065}\right\} \times 10^{\left[(9-W)/13\right]} \quad \ldots\ldots\ldots\

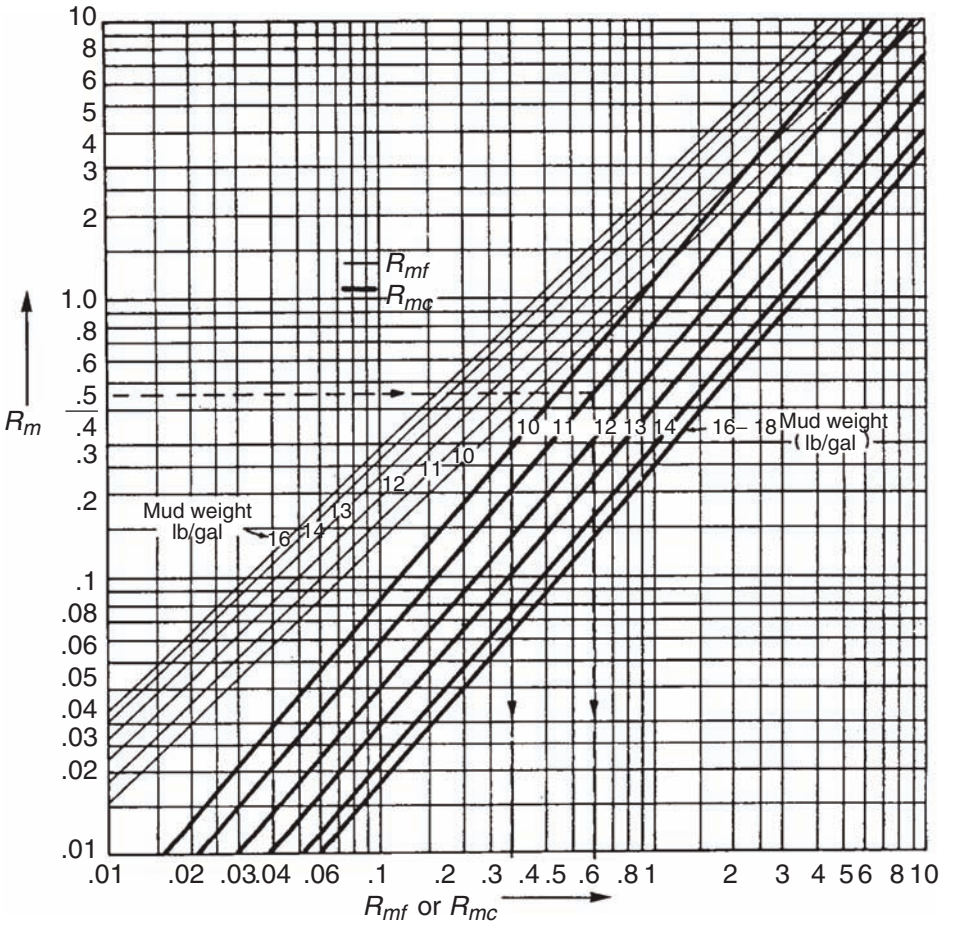


Fig. 9.9—Estimation of R_{mf} and R_{mc}. Courtesy of Schlumberger.

solutions. The actual development of the SP is controlled by the relative *activity* of the formation water and the mud filtrate solutions. Therefore, the SP equation should read:

$$\mathrm{SP} = -K \log(A_w / A_{mf}) \quad \ldots\ldots\ldots\

4. Compute the R_{mfe}/R_{we} ratio from the SP.
5. Compute R_{we}.
6. Convert R_{we} at formation temperature to an R_w value.

9.4.1 Step 1: Formation Temperature. Formation temperature may be estimated from surface and bottomhole temperatures by simple extrapolation. Usually, log header data are sufficient. Alternatively, formation temperature may be calculated using

$$T_{\text{form}} = T_{\text{surf}} + \text{Depth} * \text{Temperature Gradient}. \quad \ldots\ldots\ldots\

9.4.2 Step 2: Conversion of R_{mf} to R_{mf} at Formation Temperature. The resistivity of any ionic solution decreases in a predictable fashion as temperature increases. Therefore, R_{mf} as measured at surface temperature needs to be converted to downhole conditions at formation temperature before it can be used as a parameter in the SP equation. Sodium chloride solutions behave as shown in **Fig. 9.11,** where solution resistivity in Ω·m is plotted against temperature for a number of solutions of different concentrations (ppm NaCl).

QUESTION 9.3. R_{mf} is reported on the log heading to be 0.08 Ω·m at 75°F. Use Fig. 9.11 to find:
a. R_{mf} at 180 °F
b. The salinity of the solution in ppm NaCl.

An approximation to the chart in Fig. 9.11 is given by the Arps formula*, which states:

$$R_2 = R_1 \frac{(T_1 + 7)}{(T_2 + 7)}, \quad \ldots\ldots\ldots\

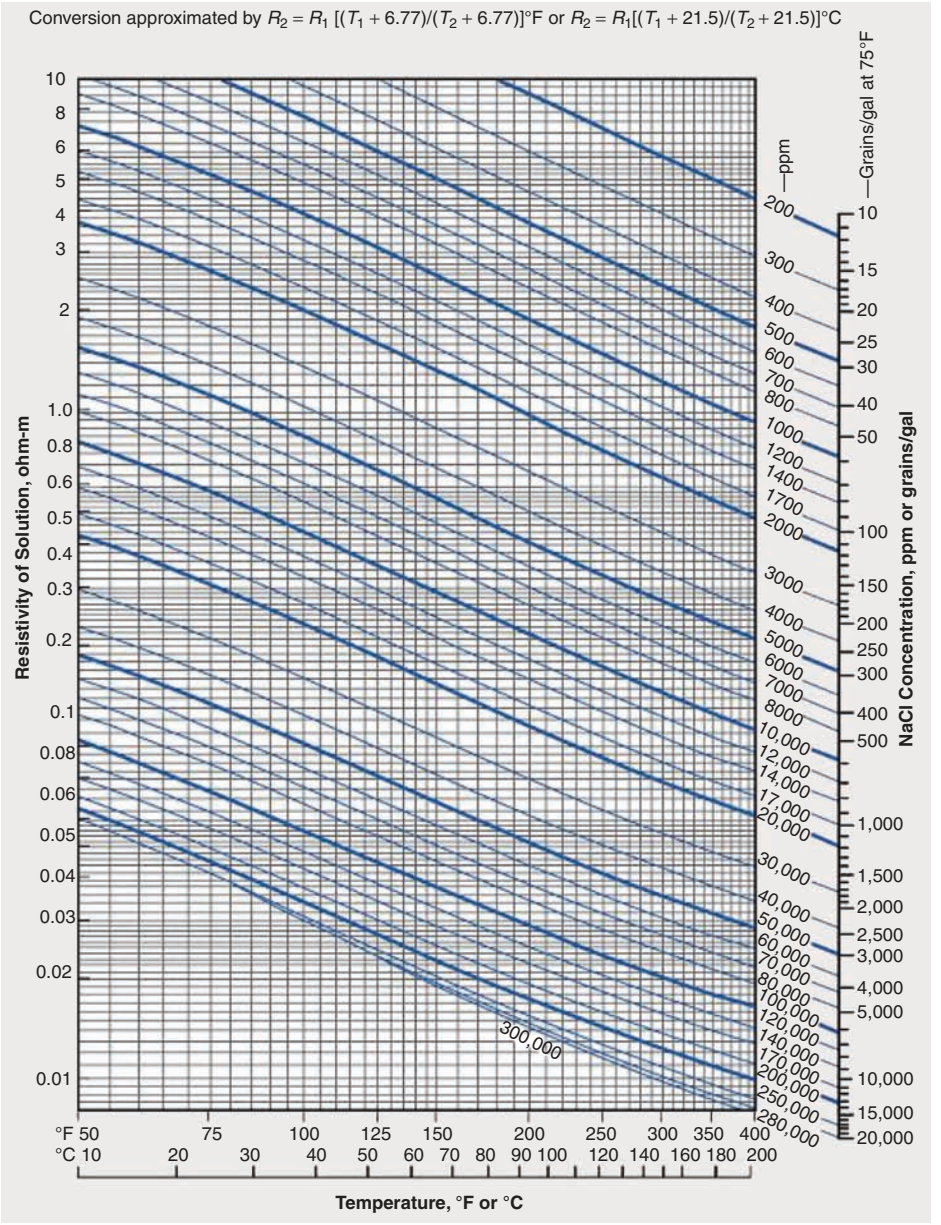


Fig. 9.11—Solution resistivity vs. temperature and concentration (Schlumberger 2009). Courtesy of Schlumberger.

9.4.5 Step 5: Computing R_{we}. R_{we} is found by dividing the known value of R_{mfe} by the R_{mfe}/R_{we} ratio found from the SP in Step 4.

QUESTION 9.6. If R_{mfe} = 0.031 and R_{mfe}/R_{we} = 3.84, find R_{we} using either a calculator or Fig. 9.13.

9.4.6 Step 6: Converting R_{we} to R_w. The conversion of R_{we} to R_w is a simple matter of reversing the process used to convert R_{mf} to R_{mfe} in Step 3. Fig. 9.12 is used.

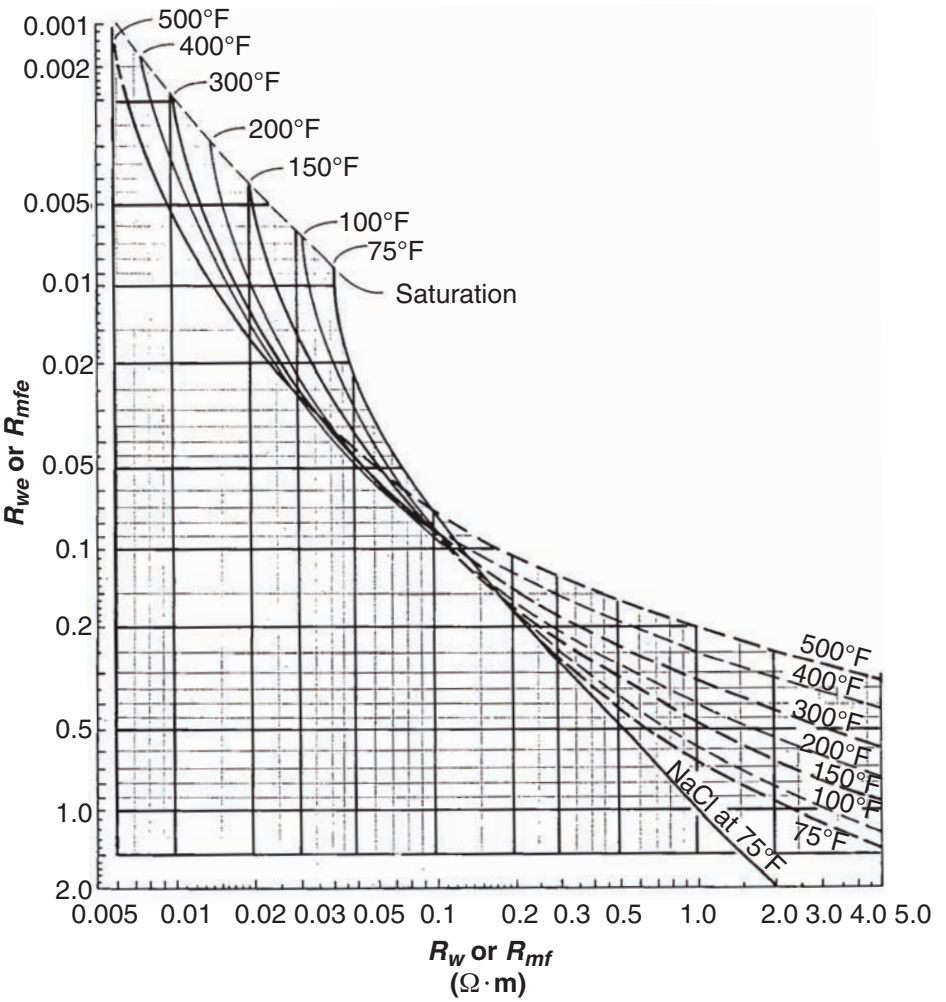


Fig. 9.12—Conversion of solution resistivities to equivalent resistivity (Schlumberger 2009). Courtesy of Schlumberger.

QUESTION 9.7. R_{we} has been found to be 0.0083 at a formation temperature of 180°F.

a. Use Fig. 9.12 to convert this to an R_w value.

b. Estimate the connate-water salinity from Fig. 9.11.

Fig. 9.14 is offered as a road map to place in perspective the six steps used for calculation of formation-water resistivity from the SP. For those inclined toward mechanization of the log interpretation process, the flow chart from Bateman and Konen (1977) is reproduced here as **Fig. 9.15.**

9.5 Alternative One-Step Method for Obtaining R_w From the SP

An alternative method for computing R_w from the SP is provided by Silva and Bassiouni (1981), using the chart shown in **Fig. 9.16.**

Essentially, the user enters the chart on the x-axis, which is scaled in resistivity units, with a value of R_{mf} at formation temperature. From this starting point, a first intersection is found by

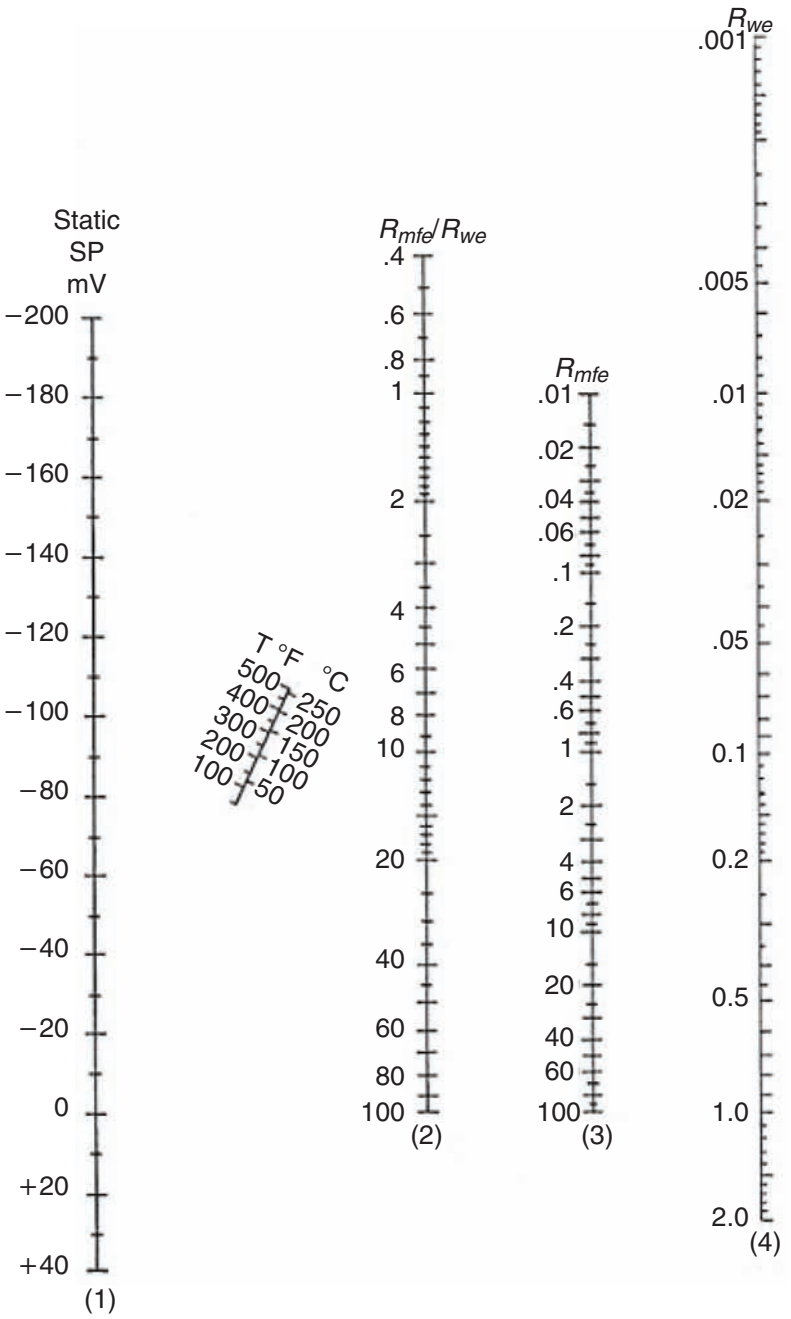


Fig. 9.13—Conversion of SP in mV to R_{we}. Courtesy of Schlumberger.

moving up the chart page to the appropriate formation-temperature line. From this point, a line is traced leftwards across the chart page to find a second intersection point with the *Y*-axis, which is an SP scale in mV. Next, the user moves along the SP scale for as many mV as the SP deflection in the water-bearing interval indicates and returns, parallel to the x-axis, to the previously used formation-temperature line. From this intersection point, a line is dropped to the resistivity axis, which will then indicate the value of R_w at formation temperature. **Fig. 9.17** provides a convenient guide for this procedure.

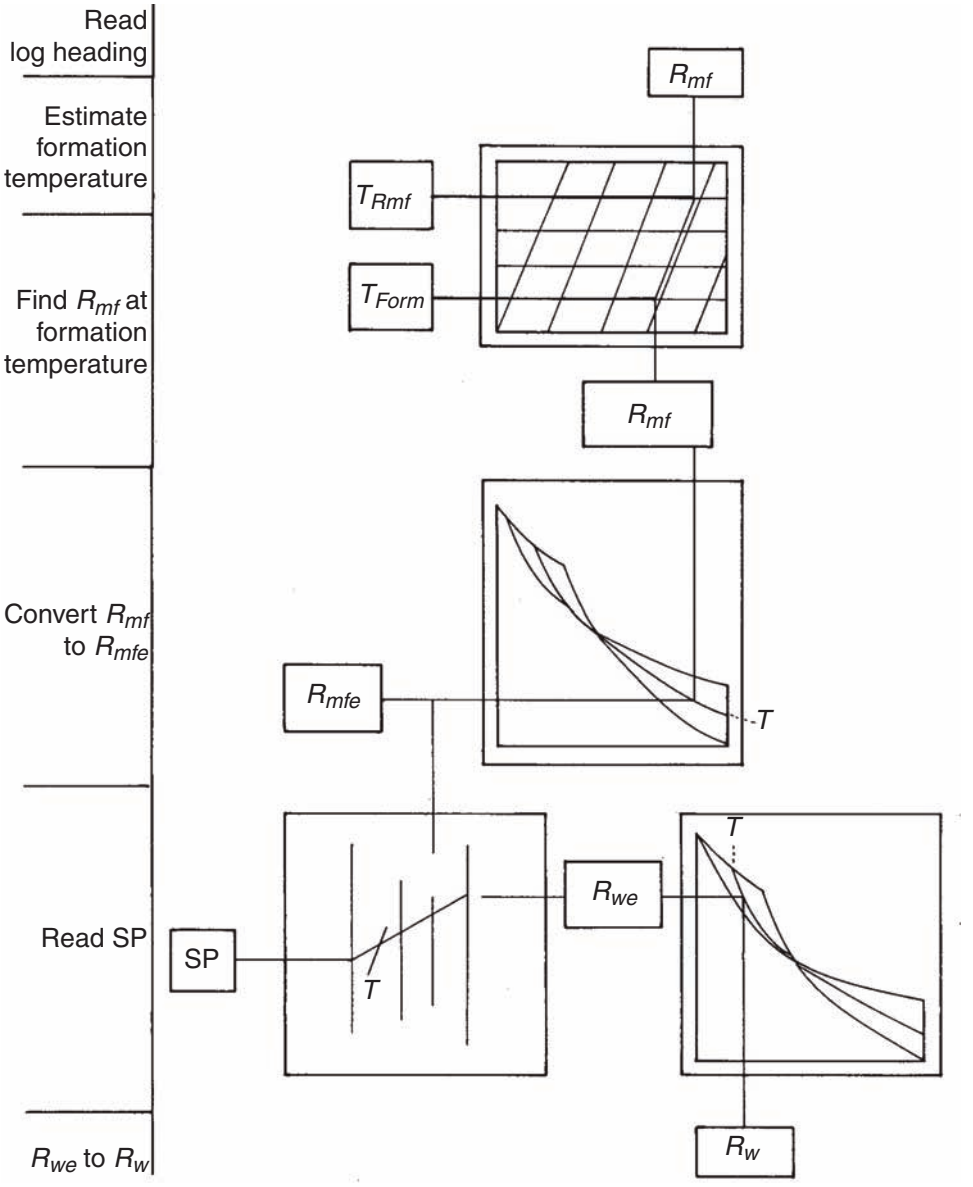


Fig. 9.14—Quick guide for obtaining R_w from the SP.

QUESTION 9.8. Use the Silva and Bassiouni "one-step" chart to compute R_w from the SP given that R_{mf} at the formation temperature of 180°F is 0.08 Ω·m and the SP deflection in the water-bearing section is –100 mV.

9.6 Factors Affecting the SP

Readings of spontaneous potential are usually accurately and easily measured. There are, however, some circumstances where SP readings need careful handling.

1. *No SP in oil-based muds*. Because of the absence of an electrical path in the mud column, no SP will be generated in oil-based muds.

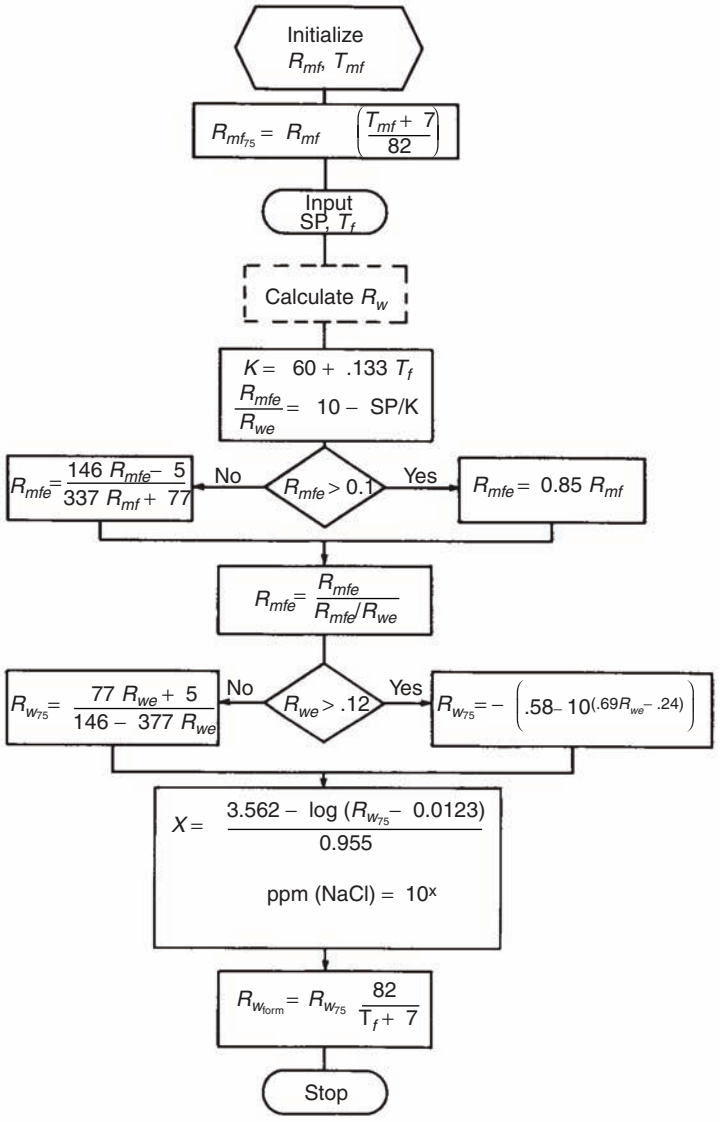


Fig. 9.15—Logic flow diagram for obtaining R_w from the SP (Bateman and Konen 1977). Reprinted by permission from the SPWLA.

2. *Shaly formation will reduce the measured SP*. This phenomenon permits the formation shaliness to be determined if a clean sand with the same water salinity is available for a legitimate comparison.
3. *Hydrocarbon saturation will reduce SP measurements*. Inasmuch as the amount of connate water in the undisturbed zone is reduced in hydrocarbon-bearing formations, the downhole battery will be somewhat weaker, and therefore the SP deflection will be diminished. For this reason, only water-bearing sands should be selected for R_w determination from the SP.
4. *Unbalanced mud columns, with differential pressure into the formation, can cause "streaming" potentials that augment the SP.* This effect is noticeable in depleted reservoirs. There is no way to handle it quantitatively. This phenomenon is called the *electrokinetic SP*.
5. *In hard formations.* Resistivities may be very high in hard (low-porosity) formations, except in permeable zones and shales. These high resistivities affect the distribution of

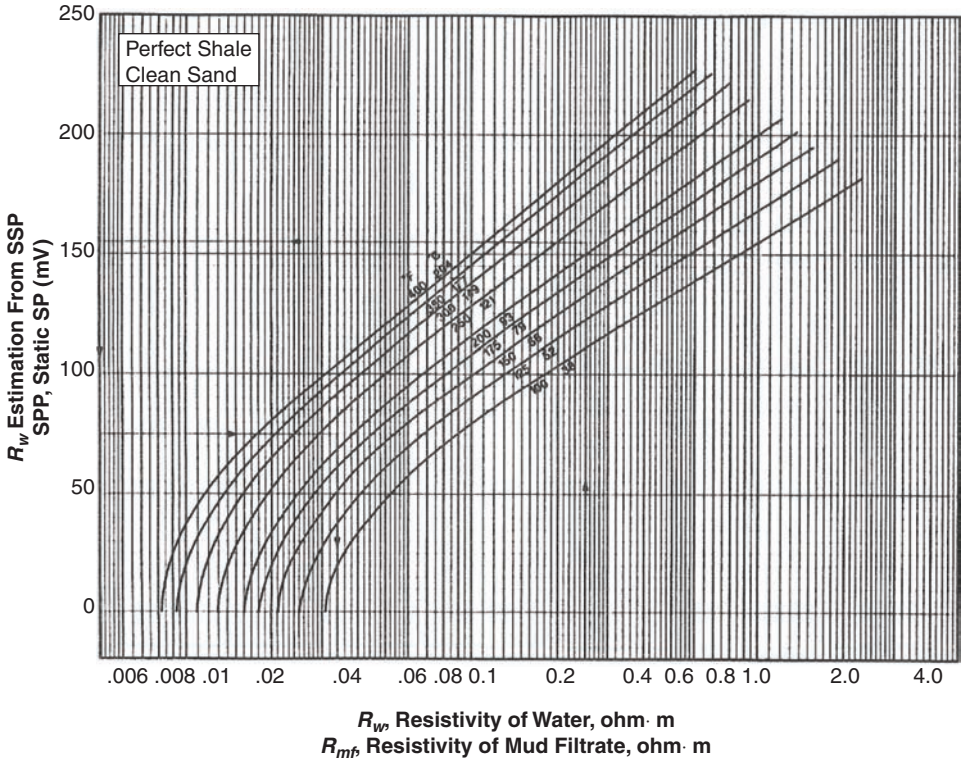


Fig. 9.16—Alternative method for determining R_w from the SP. After Silva and Bassiouni (1981). Reprinted by permission from the SPWLA.

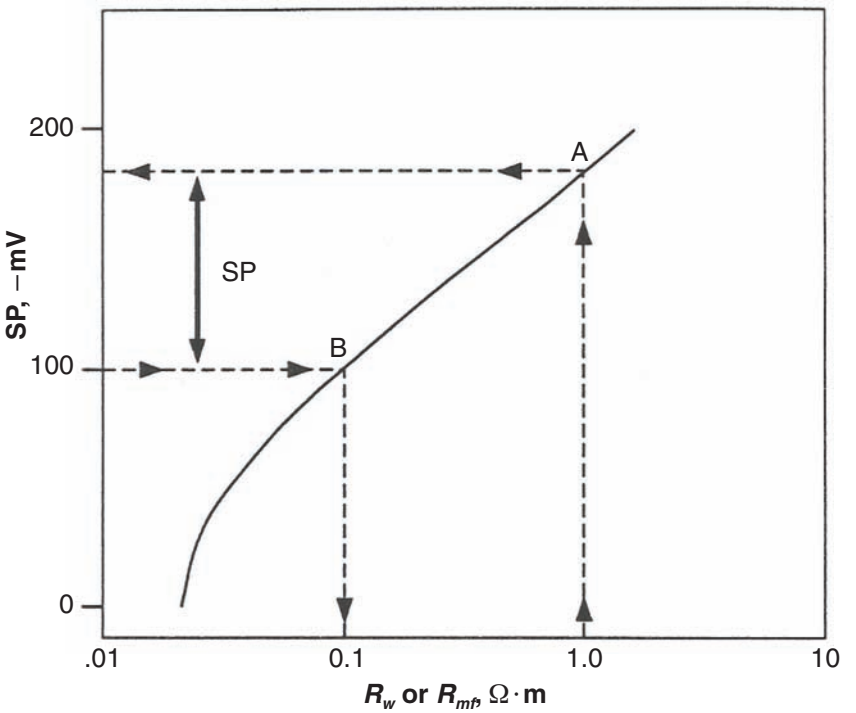


Fig. 9.17—Guide to the Silva and Bassiouni (1981) SP chart. Reprinted by permission from the SPWLA.

the SP currents and therefore the shape of the SP curve. This is illustrated in **Fig. 9.18**, where the SP currents flowing from shale bed Sh1 toward permeable bed P2 are largely confined to the borehole between Sh1 and P2 because of the very high resistivity in this interval.

Assuming that the borehole diameter is constant, the potential drop per foot will be constant, and the SP curve will be a straight line. In such formations, the SP current can leave or enter the borehole only opposite permeable beds or shales, and the SP curve will appear as a succession of straight-line portions with a change in slope opposite highly permeable intervals (with the concave side of the SP curve toward the shale line). The boundaries of the permeable beds cannot be located with accuracy by use of the SP in highly resistive beds.

6. *Bed thickness, diameter of invasion, the R_{xo}/R_t ratio, neighboring shale resistivity (R_{sh}), hole diameter (d_h), and mud resistivity (R_m) are all possible disturbing factors*. Bed thickness can affect the SP measurements very dramatically. In thin beds, where R_{xo}/R_m is high and invasion is deep, the SP does not fully develop. **Fig. 9.19** illustrates the factors that can cause SP reduction.

   In the terminology used here, SP refers to observed SP deflection on the log and SSP (static SP) to the value it would have had if all disturbing influences were removed. Many SP correction charts are available in the literature, some more complex than others. It is virtually impossible to include on one chart all the possible variables involved in making the necessary corrections. **Fig. 9.20** shows one of the more practically useful charts. Most of the variables required (d_i, R_{xo}/R_t, and h) are usually known or guessable.

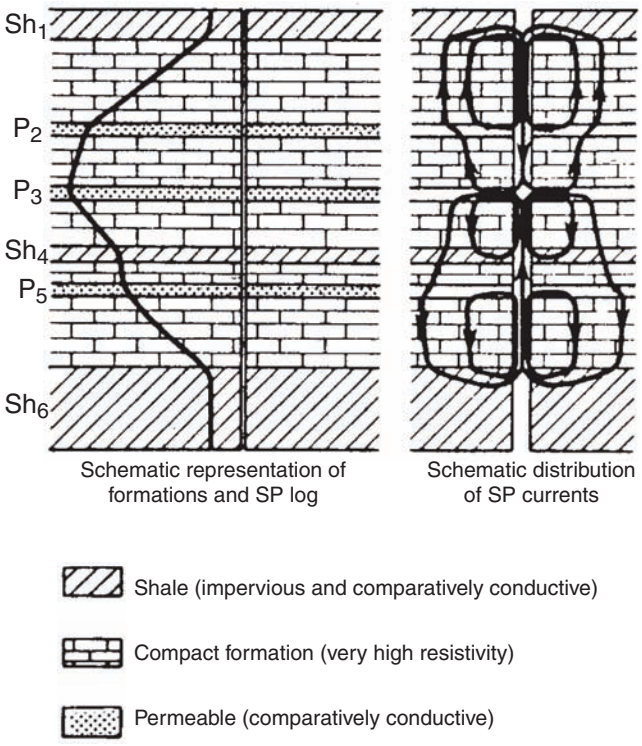


Fig. 9.18—Schematic representation of the SP in highly resistive formations. Courtesy of Schlumberger.

QUESTION 9.9. The SP deflects 25 mV from the baseline in a sand 4 ft thick. Given that $R_{xo}/R_m = 50$ and $d_i = 30$ in.:
a. Find out by what percentage the SP has been reduced.
b. Compute the corrected value for the SP.

7. *The use of potassium chloride muds affects the derivation of R_w from the SP*. Cox and Raymer (1976) cover this subject in detail. A quick solution to KCl mud perturbation is simply to take the observed SP deflection, subtract 25 mV, and then treat the computation as a NaCl mud case. The R_{mf} to R_{mfe} relationship is slightly different for KCl filtrates than for NaCl filtrates. Again, a quick working rule is to add 30% to the measured R_{mf} and proceed as for NaCl filtrate.

9.7 The SP as a Shale Indicator

The presence of shale in an otherwise clean sand will tend to reduce the SP. This fact can be used to estimate the shale content of a formation. If SP_{sand} is the value observed in a clean, water-bearing sand and SP_{shale} is the value observed in shale, then any intermediate value of the SP may be converted into a value for the shale volume (V_{sh}) by use of the following relationship:

$$(V_{sh})_{SP} = (SP - SP_{sand}) / (SP_{shale} - SP_{sand}) \quad \ldots\ldots\ldots\

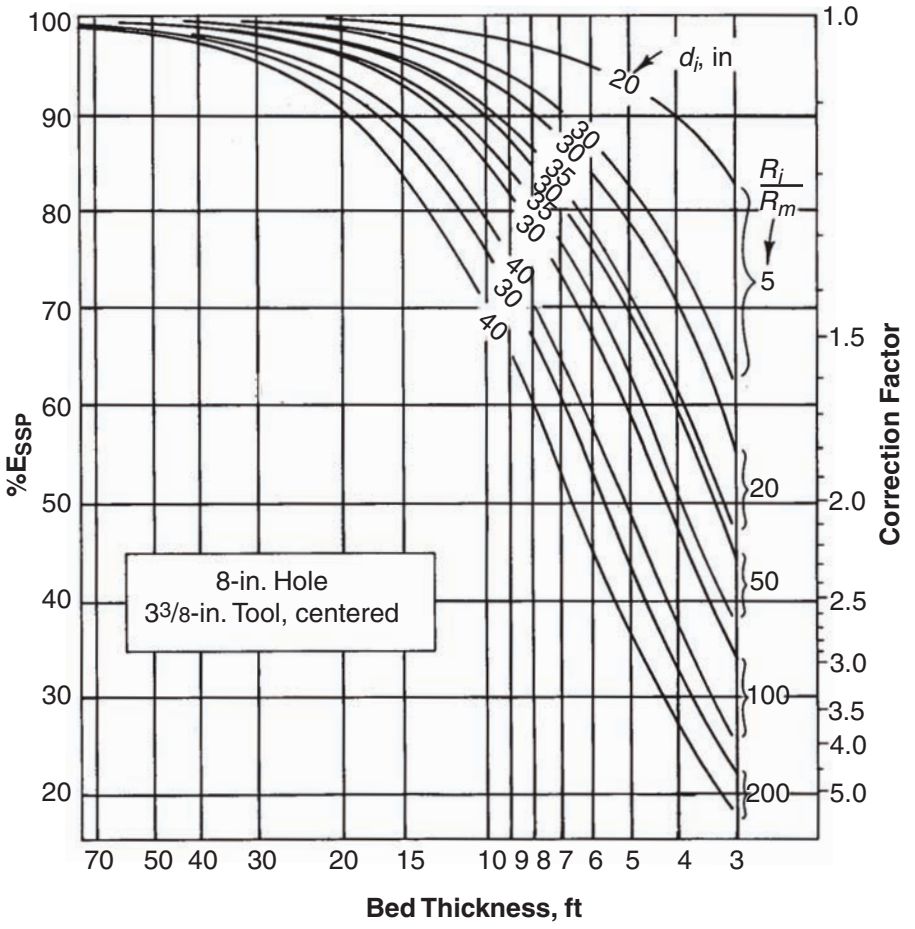


Fig. 9.20—SP correction for bed thickness. Courtesy of Schlumberger.

QUESTION 9.10. In **Fig. 9.21**, assume that Sand A is clean and wet. Use the SP deflection in Sand B to determine its shale content:

$(V_{sh})_{SP}$ =?

9.8 *SP* Depositional Patterns

Apart from water salinity variations, SP deflections also respond to depositional changes. In particular, channels, bars, and other depositional sequences where sorting, grain size, or cementation change with depth produce characteristic SP shapes. These are variously described as bells or funnels. **Fig. 9.22** illustrates some of these patterns.

9.9 SP Quality Control

Although SP logs are prone to errors, these errors can easily be detected in the field.

1. A poor ground can cause the SP baseline to move. For example, placing the SP ground in a mud pit with a changing level or on the ocean floor where currents can drag it back and forth can cause problems.

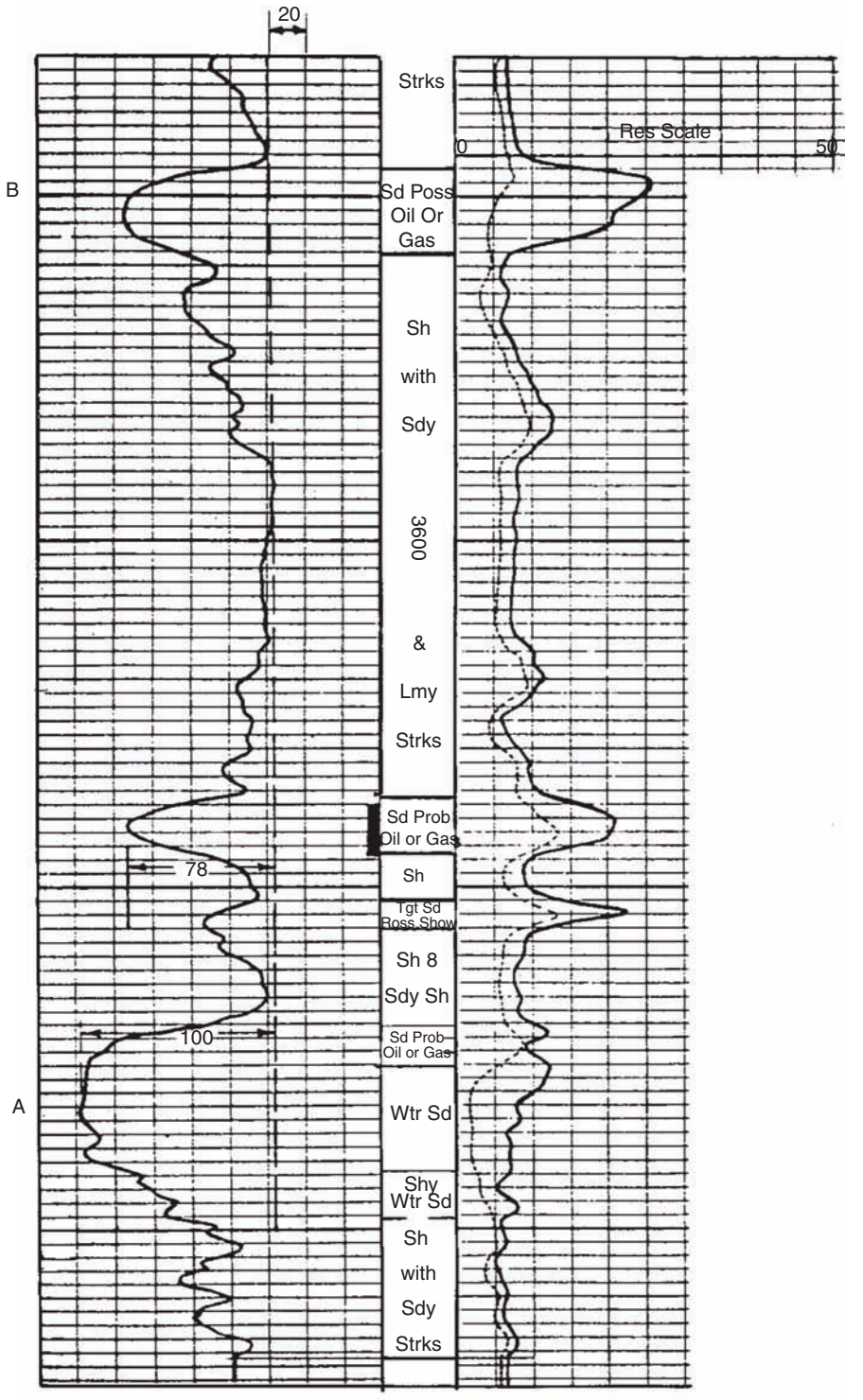


Fig. 9.21—Estimation of V_{sh} from SP.

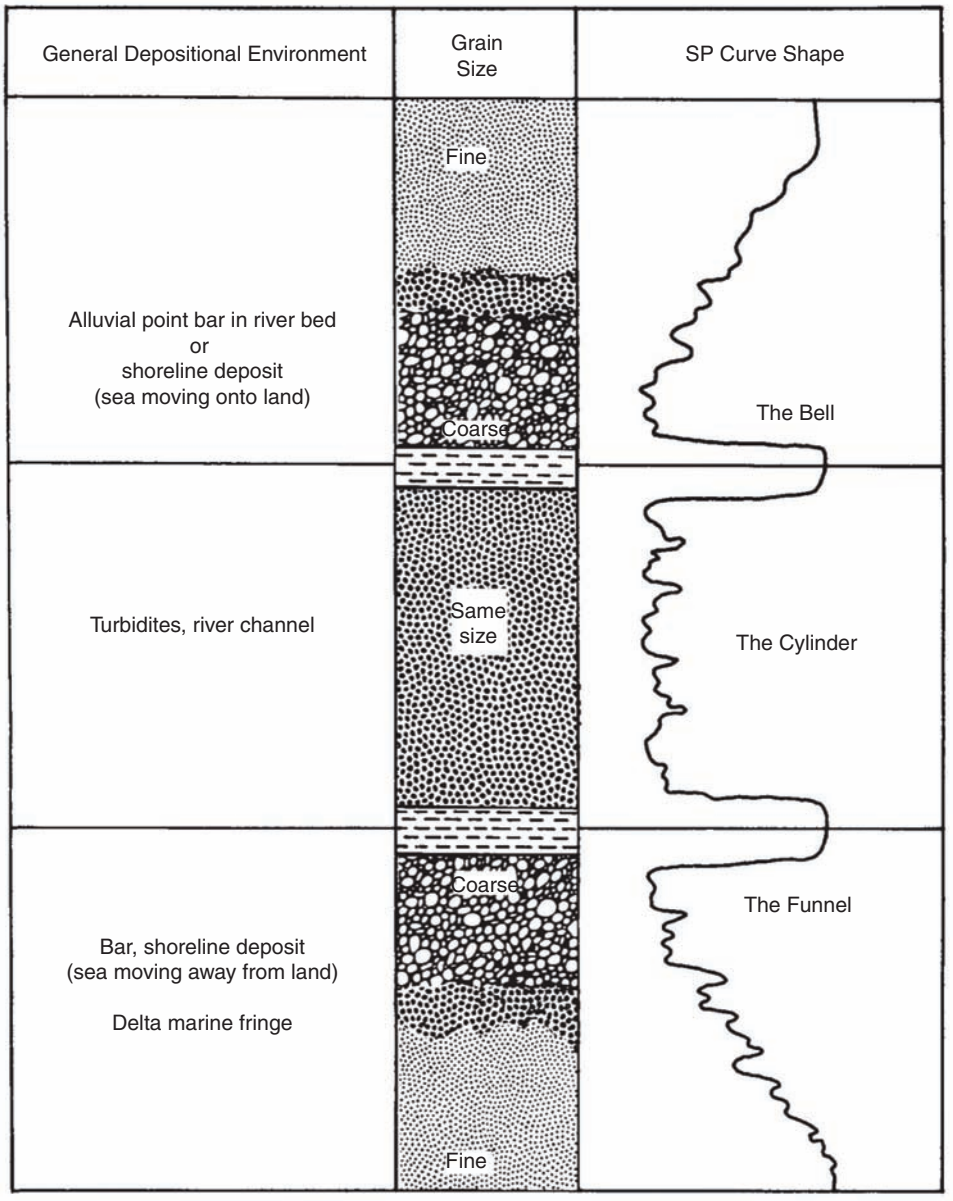


Fig. 9.22—SP shapes in different depositional sequences.

2. Cyclical or sawtooth SP profiles can indicate a magnetized cable winch drum or intermittent SP circuit contacts. In this case, the log is useless.
3. Baseline shifts can become very pronounced in some geographical areas. As the tool is raised up the hole, the SP baseline will gently shift to the left by a certain amount, typically a few mV per thousand feet. Eventually the SP will disappear off the left-hand edge of the track and reappear from the right-hand edge. This is normal. If a downhole ground is used (cable armor, for example), the baseline will move very rapidly near the casing shoe. Some service company engineers will ride the SP millivolts box and purposely keep the baseline straight. If this technique is used, a notation should be made on the log heading.

References

Bateman, R.M. and Konen, C.E. 1977. The Log Analyst and the Programmable Pocket Calculator. *The Log Analyst* **18** (5): 3–11.

Cox, J.W. and Raymer, L.L. 1976. The Effects of Potassium Salt Muds on Gamma Ray and Spontaneous Potential Measurements. *Proc.,* SPWLA 17th Annual Logging Symposium, New Orleans.

Doll, H.G. 1949. The SP Log: Theoretical Analysis and Principles of Interpretation. *Trans.,* AIME, **179:** 146–185.

Schlumberger. 1972. *Log Interpretation Charts*.

Schlumberger. 1984. *Log Interpretation Charts*.

Schlumberger. 1972. *Log Interpretation: Volume 1— Principles*, Chaps. 2 and 13.

Schlumberger. 2009. *Log Interpretation Charts*. Sugar Land, Texas: Schlumberger.

Segesman, F. 1962. New SP Correction Charts. *Geophysics* **27** (6): 815–828.

Silva, P. and Bassiouni, Z. 1981. A New Approach to the Determination of Formation Water Resistivity From the SP Log. *Proc.,* SPWLA 22nd Annual Logging Symposium, Mexico City, 23–26 June.

Williams, H. and Dunlap, H.F. 1984. Short-Term Variations in Drilling Parameters: Their Measurement and Implications. *The Log Analyst* **25** (5): 3–9.

General References

Doll, H.G. 1955. The Invasion Process in High-Permeability Sands. *Pet. Eng* (January).

Dresser Atlas. 1974. *Log Review 1*, REP 03/81, Section 4. Houston, Texas: Dresser Industries Inc.

Evers, J.F. and Iyer, B.G. 1975. A Statistical Study of the SP in Fresh Water Formations in Northern Wyoming. *Proc.,* SPWLA, 16th Annual Logging Symposium.

Gondouin, M., Tixier, M.P., and Simard, G.L. 1957. An Experimental Study on the Influence of the Chemical Composition of Electrolytes on the SP Curve. *Trans*., AIME **210**: 58–72.

Hilchie, D.W. 1984. A New Water Resistivity Versus Temperature Equation. *The Log Analyst* **25** (4): 20.

Kharaka, Y.K., Brown, P.M., and Carathers, W.W. 1978. Chemistry of Waters in the Geopressured Zone from Coastal Louisiana: Implications for Geothermal Development. In *Geothermal Resources Council Transactions,* **Vol. 2.** 371–374.

Overton, H.L. and Lipson, L.B. 1958. A Correlation of the Electrical Properties of Drilling Fluids With Solids Content. *Trans.,* AIME **213:** 333–336.

Presser, T.S. and Barnes, I. 1974. Special Techniques for Determining Chemical Properties of Geothermal Waters. *U.S. Geological Survey Water Resources Inv.*: 22–74.

Segesman, F. and Tixier, M.P. 1958. Some Effects of Invasion on the SP Curve. *Proc.,* SPE Annual Meeting, Houston, 5–8 October.

Ucok, H., Ershghi, I., and Olhoeft, G.R. 1980. Electrical Resistivity of Geothermal Brines. *J. Pet Tech* **32** (4): 717–727. http://dx.doi.org/10.2118/7878-PA.

Wyllie, M.R.J. 1949. A Quantitative Analysis of the Electrochemical Component of the SP Curve. *Trans.,* AIME **186:** 17–26.

Answers to Questions

QUESTION 9.1.
140 mV.

QUESTION 9.2.
a. 1.15 °F/100 ft.
b. 180°F.

QUESTION 9.3.
a. 0.036 Ω·m.
b. 90,000 ppm NaCl.

QUESTION 9.4.
$R_{mfe} = 0.032\ \Omega\cdot m$.

QUESTION 9.5.
$R_{mfe}/R_{we} = 3.84$.

QUESTION 9.6.
$R_{we} = 0.0083\ \Omega\cdot m$.

QUESTION 9.7.
a. $R_w = 0.02\ \Omega\cdot m$.
b. Salinity = 200,000 ppm NaCl.

QUESTION 9.8.
$R_w = 0.018\ \Omega\cdot m$.

QUESTION 9.9.
a. Reduced by 60%.
b. SSP = 25/0.6 = 41.7 mV.

QUESTION 9.10.
V_{sh} from the SP = 24%.

Chapter 10

The Gamma Ray Log

Gamma ray logs are used for three main purposes:

- Correlation
- Evaluation of the shale content of a formation
- Analysis of lithology and mineralogy

The gamma ray log measures the natural gamma ray emissions from subsurface formations. Because gamma rays can pass through steel casing, measurements can be made in both open and cased holes. In other applications, induced gamma rays are measured (e.g., in pulsed neutron logging), but that procedure will not be discussed in this section.

10.1 Origin of Natural Gamma Rays

Radioactive nuclei decay giving off alpha, beta, and gamma rays is illustrated in **Fig. 10.1.** The alpha and beta particles each carry an electric charge and do not travel far before being absorbed by another atom. However the gamma rays, which have no charge, travel effortlessly through what we perceive as solid matter.

Naturally occurring gamma radiation originates from three sources: the radioactive elements in the uranium, thorium, and potassium groups. Uranium 235, uranium 238, and thorium 232 all decay, through a long chain of daughter products, to stable lead isotopes (see **Fig. 10.2**).

An isotope of potassium, ${}^{40}_{19}K$, decays to argon, giving off a gamma ray as shown in **Fig. 10.3.** Each type of decay is characterized by a gamma ray of a specific energy (wavelength), and the frequency of occurrence of each decay energy is different.

The relationship between gamma ray energy and frequency of occurrence is shown in **Fig. 10.4.** This is an important concept because it is used as the basis for measurement in natural gamma ray spectroscopy tools.

Gamma ray tools consist of a gamma ray detector and the associated electronics for passing the gamma ray count rate to the surface. A variety of gamma ray logging tools is available in sizes that range from through-tubing versions (typically $1^{11}/_{16}$ in. in diameter) up to full-size openhole versions. These devices are also available in high-pressure, high-temperature (hostile logging) versions and in drillpipe-conveyed versions adapted for LWD.

A typical gamma ray log (see **Fig. 10.5**) is normally presented in Track 1 on a linear grid and is scaled in API units, which will be defined later. Gamma ray activity increases from left to right. Modern gamma ray tools are in the form of double-ended subs that can be sandwiched into practically any logging tool string; therefore, the gamma ray log can be run in combination with practically any tool available.

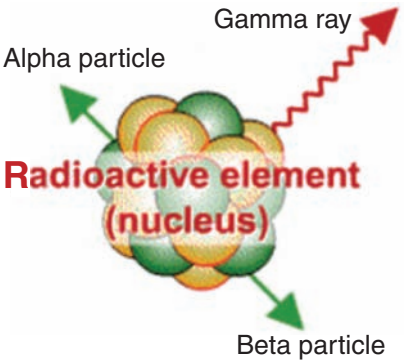


Fig. 10.1—Decay modes and products of radioactive atoms.

10.2 Abundance of Naturally Occurring Radioactive Minerals

An average shale contains 6 ppm uranium, 12 ppm thorium, and 2 ppm potassium. Because the various gamma ray radioactive sources are not all equally effective, it is more informative to consider this mix of radioactive materials on a common basis, for example, by reference to potassium equivalents (i.e., the amount of potassium that would produce the same number of gamma rays per unit of time). Reduced to a common denominator, the average shale contains uranium equivalent to 4.3% potassium, thorium equivalent to 3.5% potassium, and 2% potassium. However, an average shale is hard to find. Because shale is a mixture of clay minerals, sand, silts, and other extraneous materials, there can be no standard gamma ray activity figure for shale. Indeed, the main clay minerals vary enormously in their natural radioactivity. Kaolinite has practically no potassium, whereas illite contains between 4% and 8% potassium, and montmorillonite contains less than 1%. Occasionally, natural radioactivity may be due to the presence of dissolved potassium or other salts in water contained in the pores of the shale.

10.3 Operating Principle of Gamma Ray Tools

Traditionally, two types of gamma ray detectors have been used in the logging industry: Geiger-Mueller and scintillation detectors. Today, practically all gamma ray tools use scintillation detectors containing a sodium iodide crystal **(Fig. 10.6).** When a gamma ray strikes the crystal, a single photon of light is emitted. This tiny flash of light then strikes a photocathode made of cesium-antimony or silver-magnesium. Each photon, when it hits the photocathode, releases a bundle of electrons. These in turn are accelerated in an electrical field to strike another electrode, producing an even bigger shower of electrons. This process is repeated through a number of stages until a final electrode conducts a small current through a measurement resistor to give a voltage pulse that signals that a gamma ray has struck the sodium iodide crystal. The system has a very short "deadtime" and can register many counts per second without becoming swamped by a large number of signals.

10.4 Calibration of Gamma Ray Detectors and Logs

One of the problems of gamma ray logging is the choice of a standard calibration system, because various logging companies use counters of different sizes and shapes encased in steel housings of varying characteristics. On very old logs, the scale might be calibrated in micrograms of radium per ton of formation. For many reasons, this was found to be an unsatisfactory calibration method for gamma ray logs, and therefore an API standard was devised. A test pit installed at the University of Houston contains an artificial shale, as illustrated in **Fig. 10.7.** A cylinder 4 ft in diameter and 24 ft long contains a central 8-ft section consisting of cement mixed with 13 ppm uranium, 24 ppm thorium, and 4% potassium sandwiched by 8-ft sections of pure Portland cement on either side. This 24-ft sandwich is cased with 5½-in. J55 casing. The API standard defines the difference in radioactivity between the pure cement and the radioactive cement mixture as 200 API units.

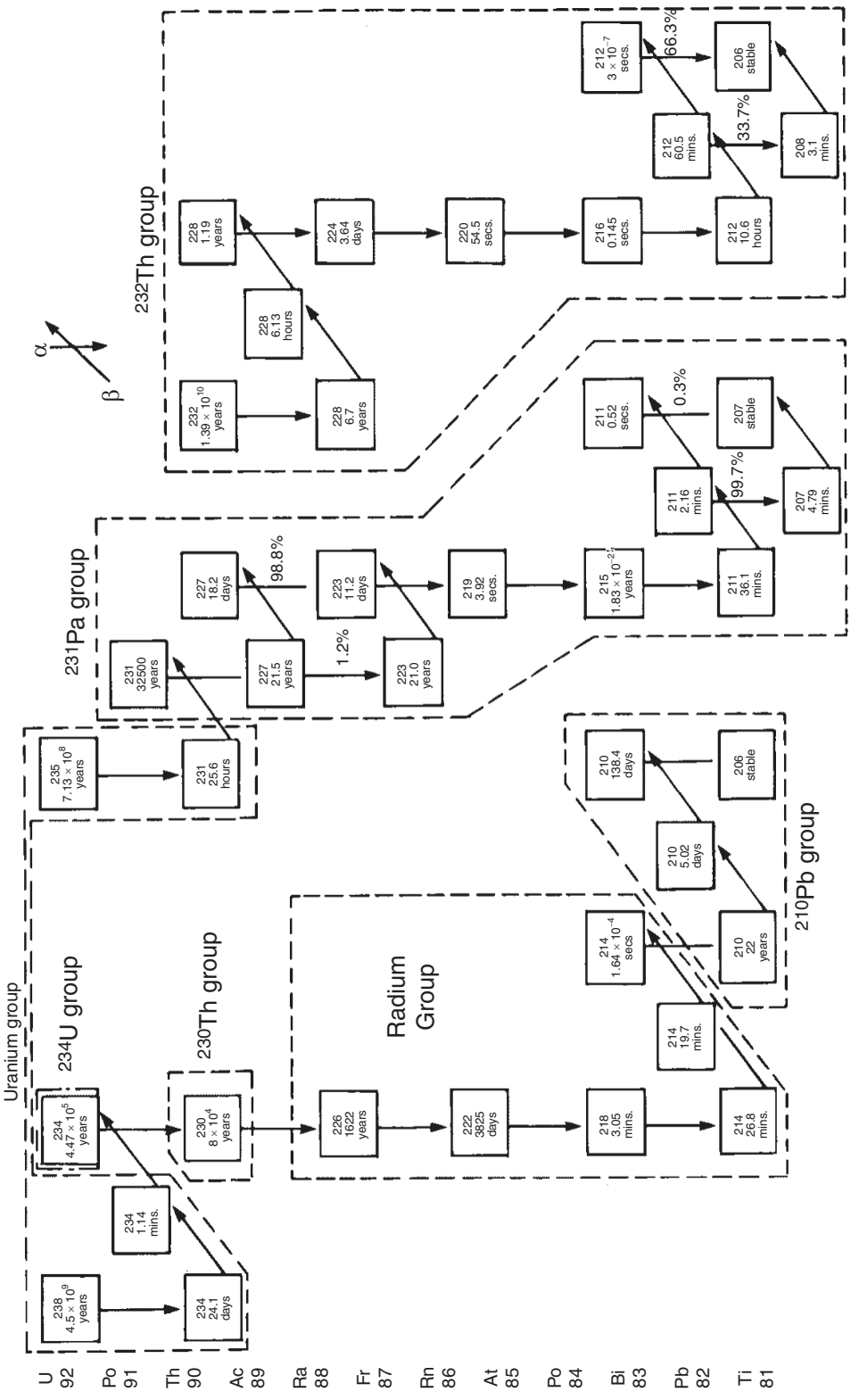


Fig. 10.2—Classification of the radioactive disintegration series.

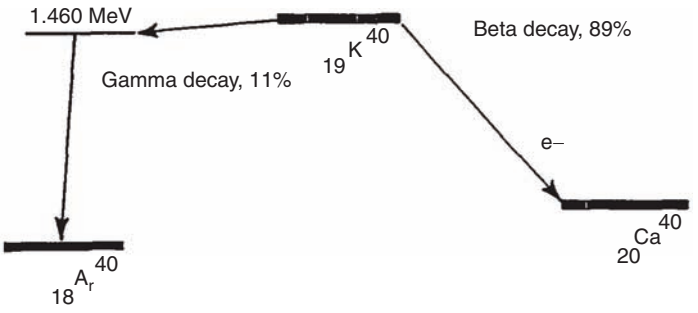


Fig. 10.3—Decay scheme of $^{40}_{19}K$. From Tittman (1956); used by permission from the University of Kansas.

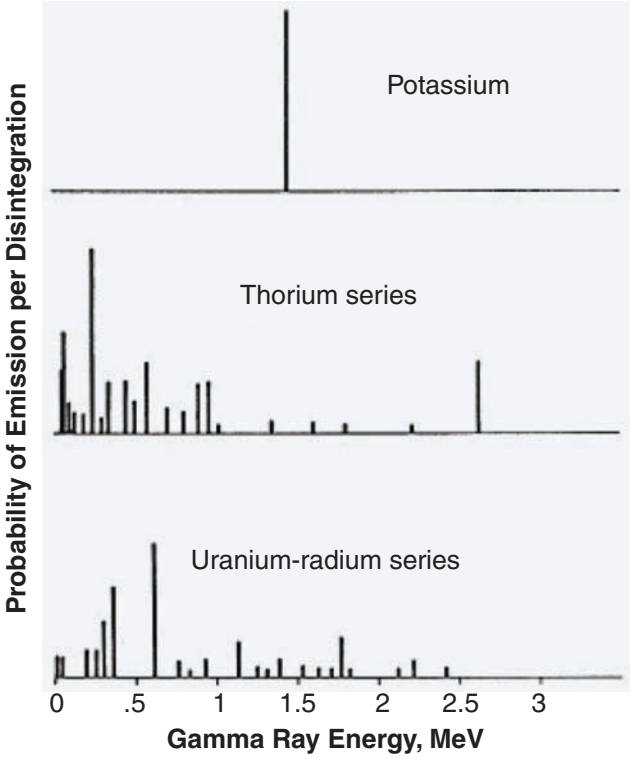


Fig. 10.4—Gamma ray emission spectra of radioactive minerals. From Tittman (1956); used by permission from the University of Kansas.

Any logging service company may place its tool in this pit to perform a calibration. Field calibration is performed with a portable jig that contains a radioactive *pill.* The pill is a 0.1-millicurie source of radium 226. When placed 53 in. from the center of the gamma ray detector, it produces a known increase over the background count rate. This increase is equivalent to a known number of API units, depending on the tool type and size and the counter that it encloses.

10.5 Time Constants

All radioactive processes are subject to statistical variations. For example, if a source of gamma rays emits an average of 100 gamma rays per second over a period of hours, the source will emit 360,000 gamma rays per hour (100 × 60 seconds × 60 minutes). However, if the count is measured for 1 second only, the actual count might be less than 100 or more than 100. Therefore, a choice must be made. Gamma rays can be counted for a very short interval of time, resulting in a poor

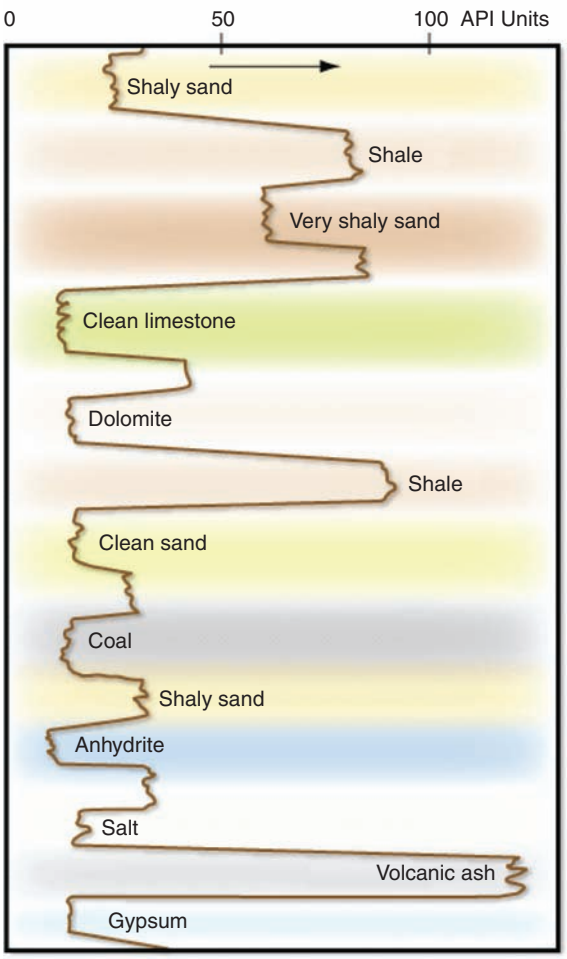


Fig. 10.5—Gamma ray log presentation.

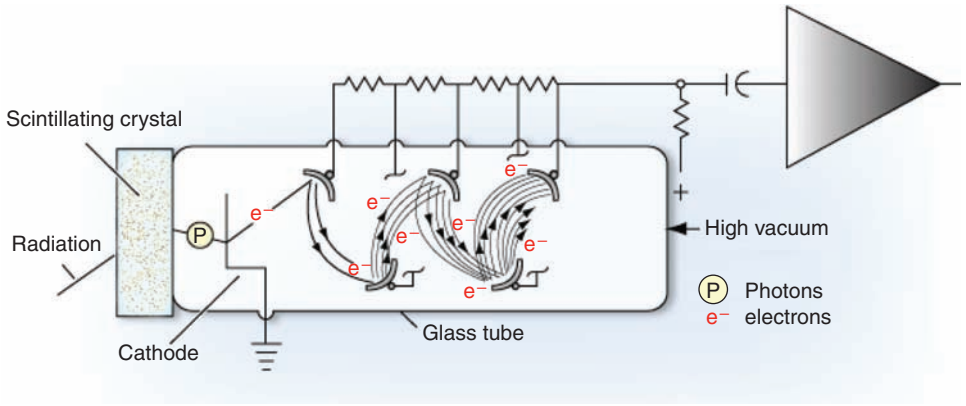


Fig. 10.6—Scintillation counter. Courtesy of Halliburton.

estimate of the real count rate, or they can be counted for a long time, resulting in a more accurate estimate of the count rate at the expense of an inordinately long measurement time period. To average out statistical variations, various time constants may be selected according to the radioactivity level measured. The lower the count rate, the longer is the time constant required for adequate averaging of the variations.

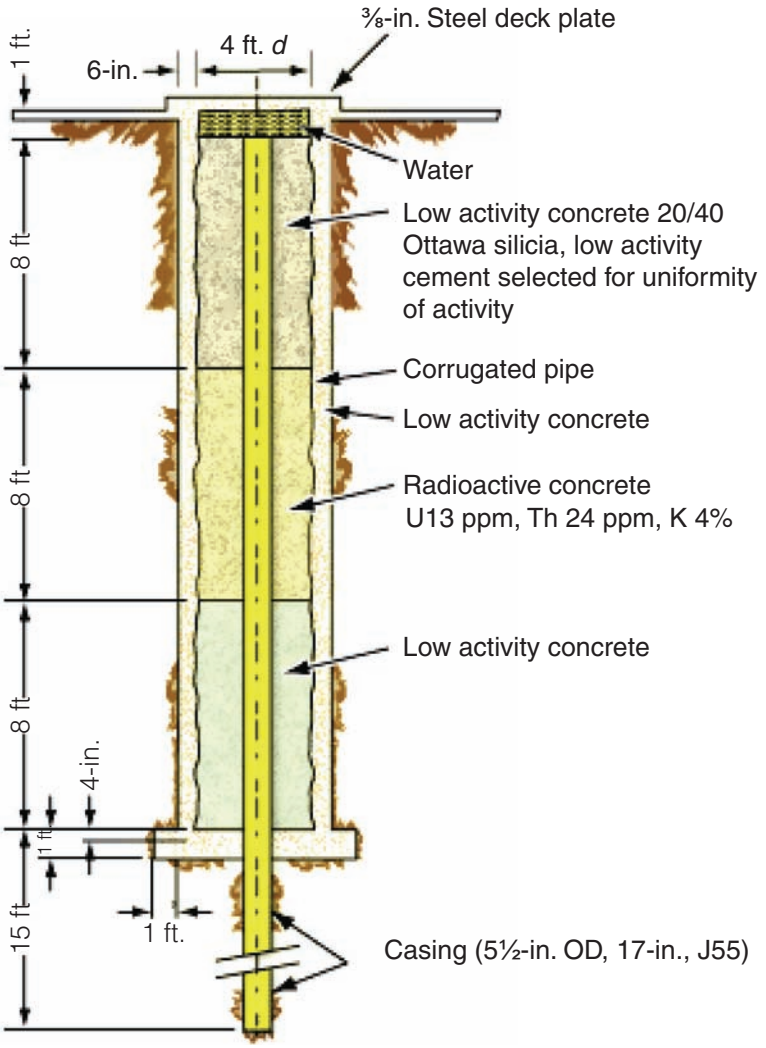


Fig. 10.7—API gamma ray standard.

In the logging environment, gamma rays can be counted for a short period of time (e.g., 1 second) with the knowledge that, during that time period, the detector will have moved past the formation whose activity is being measured. Therefore, the logging speed and the time interval used to average count rates are interrelated. **Table 10.1** documents the commonly followed working rules.

With very slow logging speeds (900 ft/hr = 0.25 ft/sec) and long time constants, a more accurate measurement of absolute activity is obtained at the expense of good bed resolution. With high logging speeds and short time constants, somewhat better bed resolution is obtained at the expense of absolute accuracy. At some future time, when the efficiency of gamma ray detectors and their associated electronics will have improved by one or two orders of magnitude, the use of a time constant will be obsolete except in the cases of extremely inactive formations with intrinsically low gamma ray count rates.

To illustrate the interdependence of logging speed and time constant, the same formation is shown logged at two different speeds in **Fig. 10.8.** On the first run, the logging speed was 80 ft/min and the time constant 1 second. On the second run, the speed was 30 ft/min and the time constant 2 seconds. Note the differences in both statistics and bed resolution between the two runs.

TABLE 10.1—LOGGING SPEEDS AND TIME CONSTANTS	
Logging Speed (in ft/hr)	Time Constant (in seconds)
3,600	1
1,800	2
1,200	3
900	4

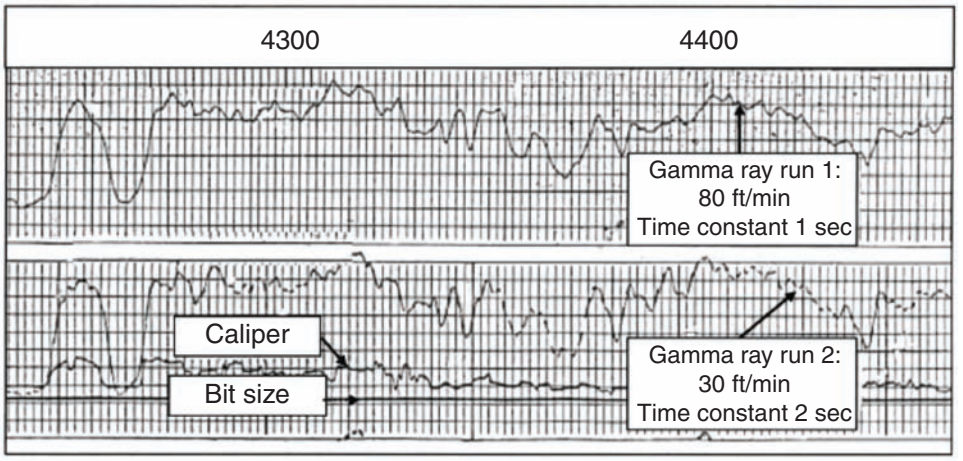


Fig. 10.8—Effects of logging speed and time constant on gamma ray log.

10.6 Perturbing Effects on Gamma Ray Logs

Gamma ray logs are subject to a number of perturbing effects, including:

- Sonde position in the hole (centering/eccentricity)
- Hole size
- Mud weight
- Casing size and weight
- Cement thickness

Because there are innumerable possible combinations of hole size, mud weight, and tool position, an arbitrary set of standard conditions has been defined as a 3 ⅛-in.-OD tool mounted off-center in an 8-in. hole filled with 10-lbm mud. A series of charts is available for making the appropriate corrections. **Fig. 10.9** applies to logs run in an open hole; it corrects for hole size and mud weight. **Fig. 10.10** applies to logs run in a cased hole; it corrects for casing and cement as well.

Note that if a gamma ray log is run in combination (for example as a component of the "triple combo"), it is run eccentered. If it is run singly with, for example, a laterolog or an induction log, it will be centered most of the time. GR_{cor} is defined as the response of a 3 ⅝-in. tool run off-center in an 8-in. hole with 10-lbm mud.

QUESTION 10.1. Use Fig. 10.9 to estimate GR_{cor} under the following conditions:
GR_{log} reads 67 API units.
Hole size = 8 in., mud weight = 16 lbm/gal.
Tool is centered.
$GR_{cor} = ?$

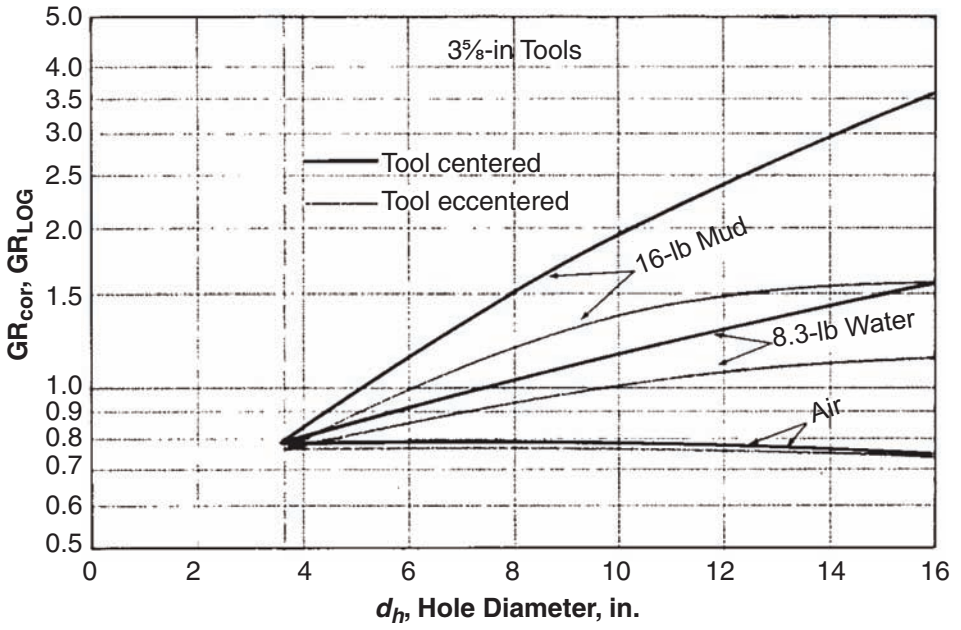


Fig. 10.9—Gamma ray corrections for hole size and mud weight (Schlumberger 1982). Courtesy of Schlumberger.

It should be noted that although these charts are reproduced here, modern logs usually have these environmental corrections applied automatically at the wellsite, and the user is not required to work laboriously through the appropriate charts. The purpose of including these charts here is to give the analyst a feel for the order of magnitude of the corrections that are being applied. Even a brief inspection of the charts shows that in heavy muds and large holes, it is not uncommon for the raw gamma ray values to be doubled after the corrections are applied. When working with "legacy" materials for which these corrections were not available at the wellsite, it is up to the analyst to apply them.

10.7 Estimating Clay Content From Gamma Ray Logs

Because it is common to find radioactive materials associated with the clay minerals that constitute shales, it is a commonly accepted practice to use the relative gamma ray deflection as a clay volume indicator. The simplest procedure is to rescale the gamma ray between its minimum (in a clean sand) and its maximum value (in a shale) from 0 to 100%. Because the amount of clay-bound water associated with the clay constituents of a shale is a function of the depth of burial and compaction of the shale, this linear scaling does not truly reflect the fractional clay volume in a given shaly sand. A number of different relationships have been proposed to relate the relative gamma ray deflection to the clay content of the formation. To explain these methods further, the *gamma ray index* is defined as a linear rescaling of the GR log between $GR_{\min}$ and $GR_{\max}$ such that

$$\text{Gamma Ray Index } (X) = \frac{GR - GR_{\min}}{GR_{\max} - GR_{\min}} \quad \ldots\ldots\ldots\

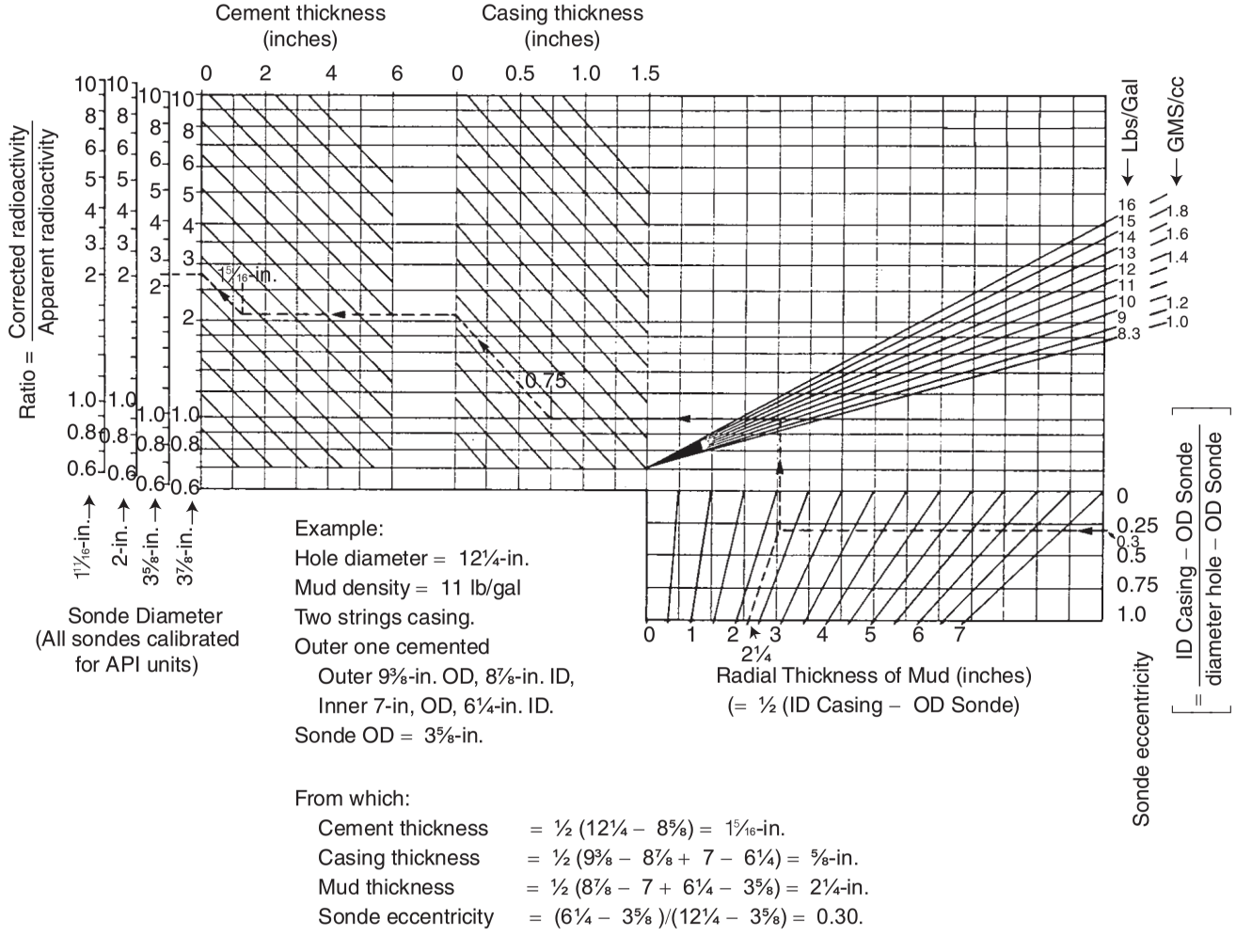


Fig. 10.10—Gamma ray corrections for cased holes (Schlumberger 1982). Courtesy of Schlumberger.

$$\text{Bateman } V_{clay} = X^{(X+GR\ \text{Factor})} \quad \ldots\ldots\ldots\

In the lower part of the same figure, the same logic is applied to a 100% shale formation that has a gamma ray reading of 120 API. The void ratio of the shale is 35%, implying that 65% of the volume is composed of radioactive clay solids and 35% of nonradioactive clay-bound water. This in turn indicates that the intrinsic API of the clay solids is 185.

Therefore, a 50:50 mixture of clean sand and shale produces a gamma ray response of 70 API, as shown in **Fig. 10.13.** This translates into an X-value of 50%. However, the actual clay volume fraction, V_{clay}, is only 32.5%. In Fig. 10.11, this plots on the Clavier line and corresponds to a Bateman factor of 1.25.

QUESTION 10.2. On the gamma ray log shown on **Fig. 10.14,** choose values for GR_{min} and GR_{max} and then compute X and V_{clay} in sand C using the linear, Clavier, and Stieber methods.

10.8 Gamma Ray Spectroscopy

Each radioactive decay event produces a unique gamma ray. These various gamma rays have characteristic energy levels and occur in characteristic abundances, as expressed in counts per time period. The simple method of counting how many gamma rays a formation produces can be carried a step further to count how many it produces from each gamma ray energy group. If the number of occurrences is plotted against the energy groups, a spectrum will be produced that is characteristic of the formation logged.

Such a spectrum is shown in **Fig. 10.15,** where energies from 0 to approximately 3 MeV have been divided into 256 specific energy bins. The number of gamma rays in each bin is plotted on the y-axis. This spectrum can be thought of as a mixture of the three individual spectra associated with uranium, thorium, and potassium. Some unique mixture of these three radioactive families would have the same spectrum as the observed one. The trick is to find a quick and easy method of discovering that unique mixture. Fortunately, onboard computers in logging trucks are capable of quickly finding a best fit and producing continuous curves showing the concentrations of U, Th, and K.

A gamma ray spectral log is shown in **Fig. 10.16.** Note that in Track 1, both total gamma ray activity (SGR) and a uranium-free version of total activity are displayed. Units are API. In Tracks 2 and 3, the concentrations of U, Th, and K are displayed. Logging service companies use various units for spectral logs, which may show counts, ppm, or percentages.

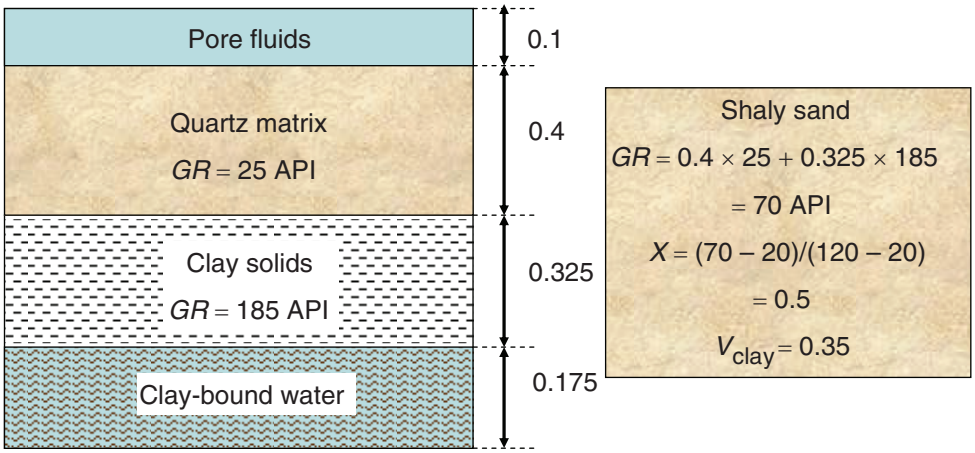


Fig 10.13—A 50:50 mix of clean sand and shale (X = 50%, but V_{clay} = 32.5%).

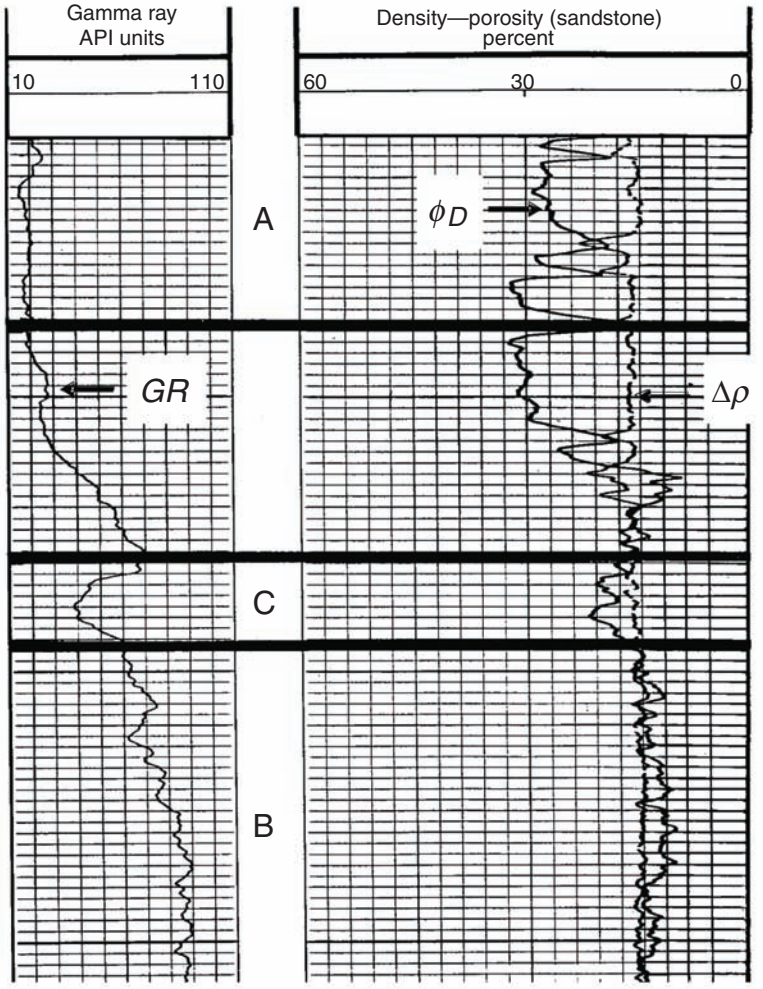


Fig. 10.14—Estimation of shale and clay content from a gamma ray log.

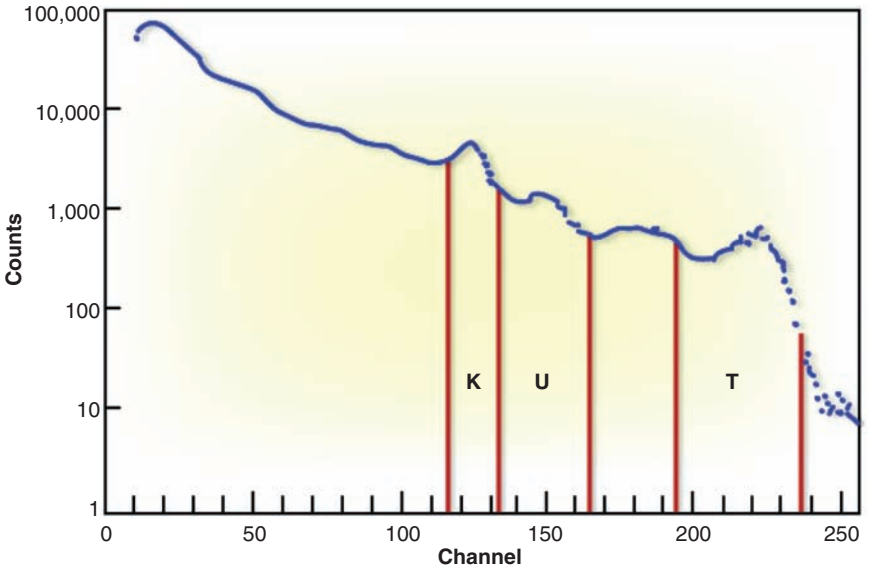


Fig. 10.15—Gamma ray spectrometry.

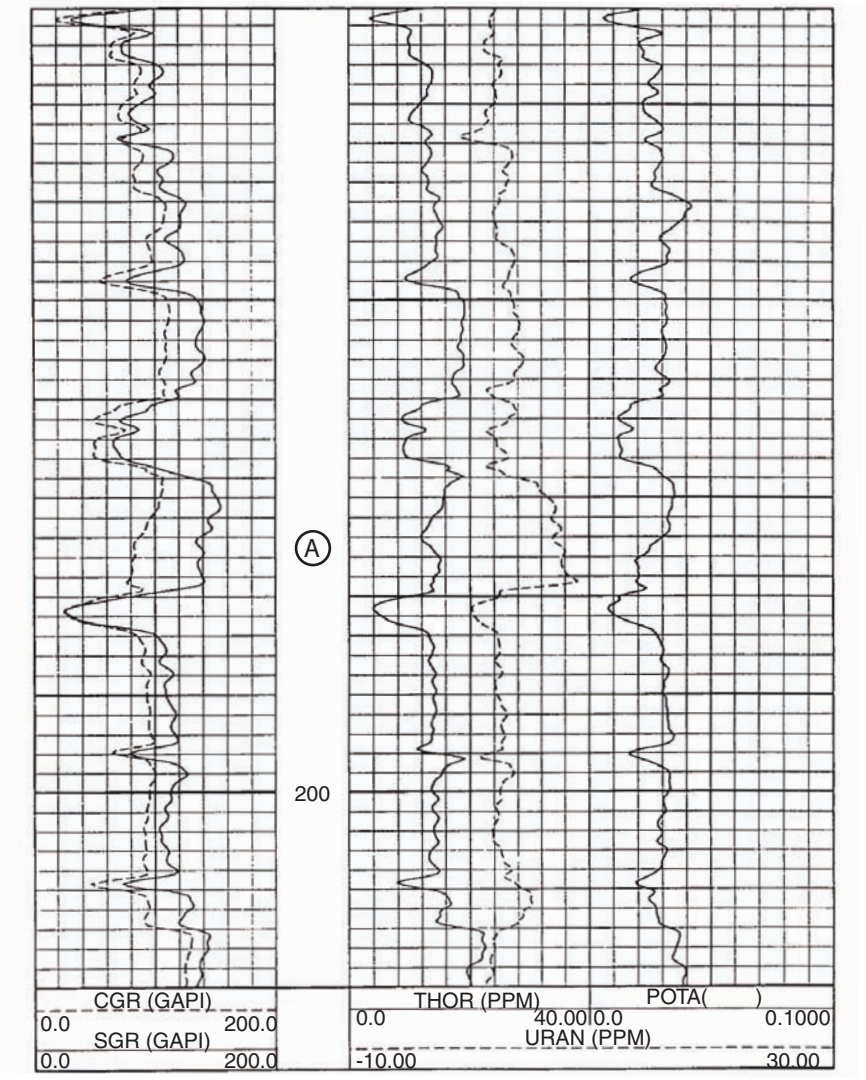


Fig. 10.16—Gamma ray spectral log (*Introduction to Open Hole Logging*). Courtesy of Schlumberger.

QUESTION 10.3. In the example shown in Fig. 10.16, determine which element is responsible for the high activity seen on the total gamma ray intensity curve at the point marked "A."

10.9 Interpretation of Gamma Ray Spectral Logs

The interpretation of natural gamma ray spectral logs uses two general techniques. One uses the uranium curve as an indicator of fractures and was described by Fertl et al. (1980). Another technique is to use the U, Th, and K concentrations in combination with other log data to determine lithology and clay type, as described by Marett et al. (1976). Still another approach, described by Hassan et al. (1976), could be called the geochemical method.

Fig. 10.17 illustrates the variation of the thorium-to-potassium ratio in a number of minerals ranging from potassium-feldspar to bauxite. A number of radioactive minerals are mapped as a function of their thorium and potassium contents in **Fig. 10.18.**

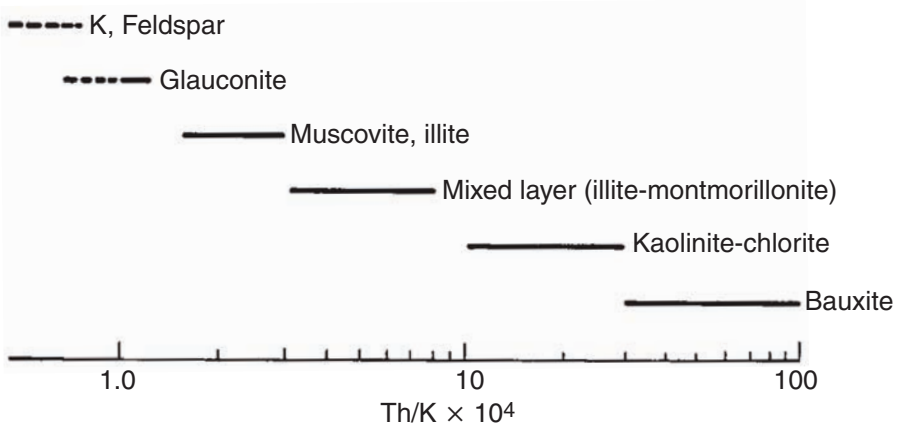


Fig. 10.17—Thorium/potassium ratios for various minerals (Hassan et al. 1976). Reprinted by permission from the SPWLA.

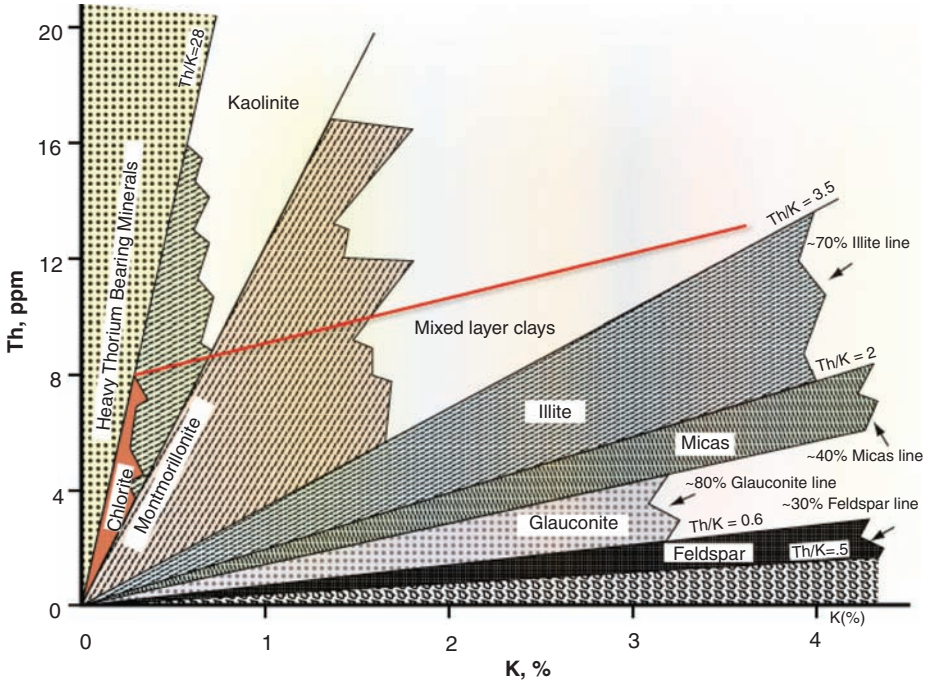


Fig. 10.18—Thorium/potassium crossplot for mineral identification. Courtesy of Schlumberger.

If additional data are available, for example, the photoelectric absorption coefficient (P_e) obtained from the litho-density tool, plots such as those shown in **Figs. 10.19 and 10.20** can be constructed to assist in mineral identification.

Other elemental ratios are also useful indicators. A low U to Th ratio, for example, indicates reduced black shales. Uranium by itself may indicate a high organic carbon content that is indicative of high total organic carbon (TOC) associated with source rocks.

Field presentations of gamma ray spectra can assist the analyst in the task of mineral identification by offering curve plots with ratios of the three components (U, Th, and K) already computed. **Fig. 10.21** gives an example of one such presentation.

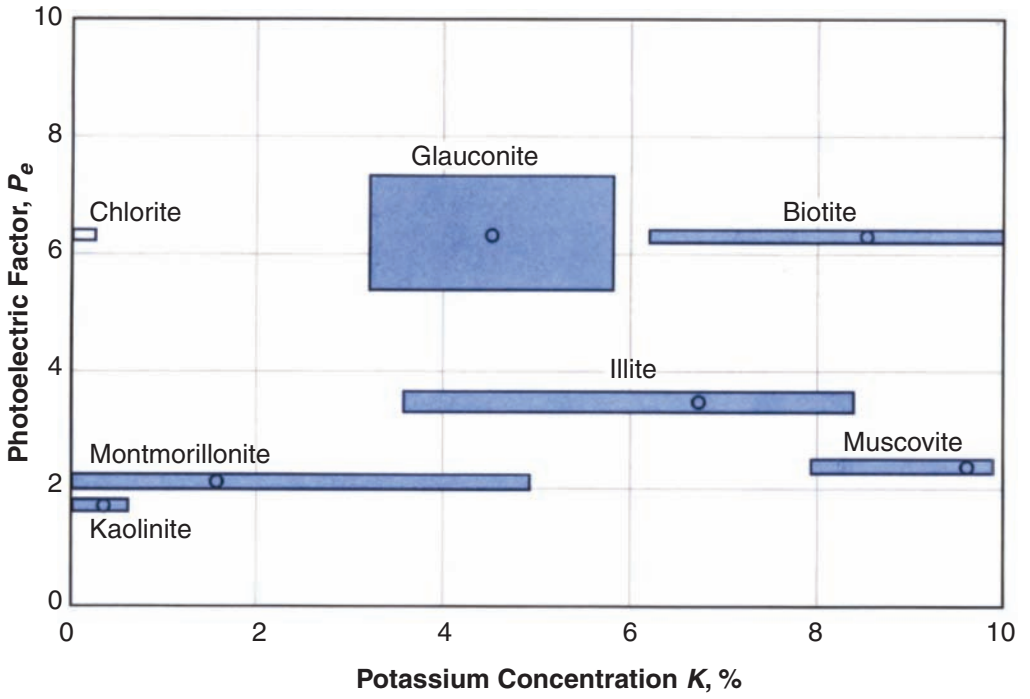


Fig. 10.19—Crossplot of P_e vs. K (Schlumberger 2009). Courtesy of Schlumberger.

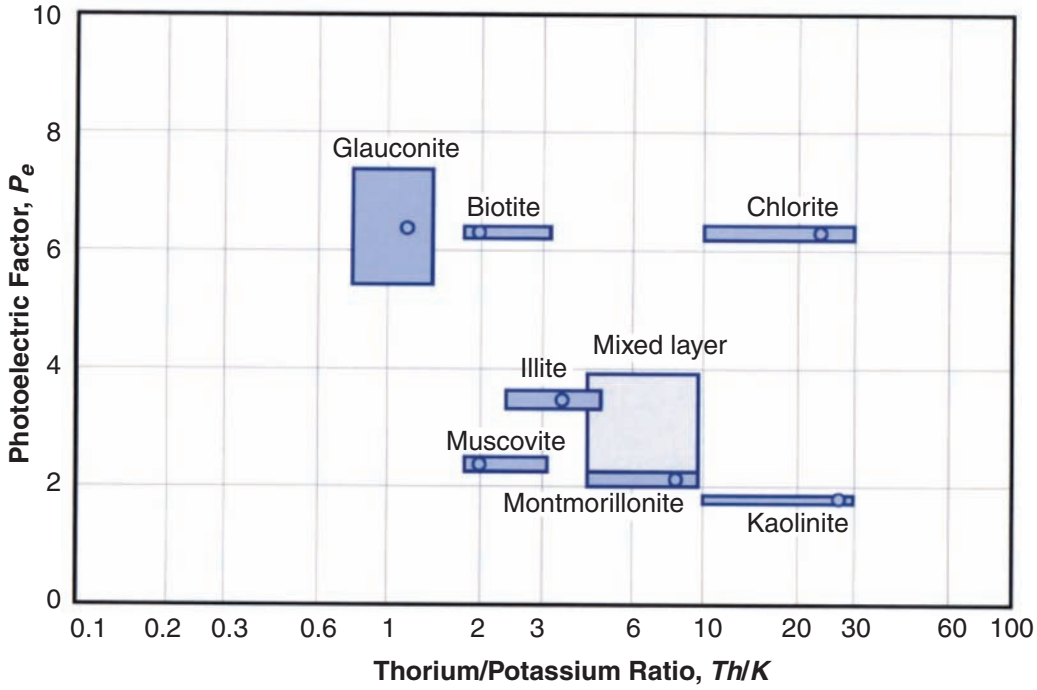


Fig. 10.20—Crossplot of P_e vs. Th/K (Schlumberger 2009). Courtesy of Schlumberger.

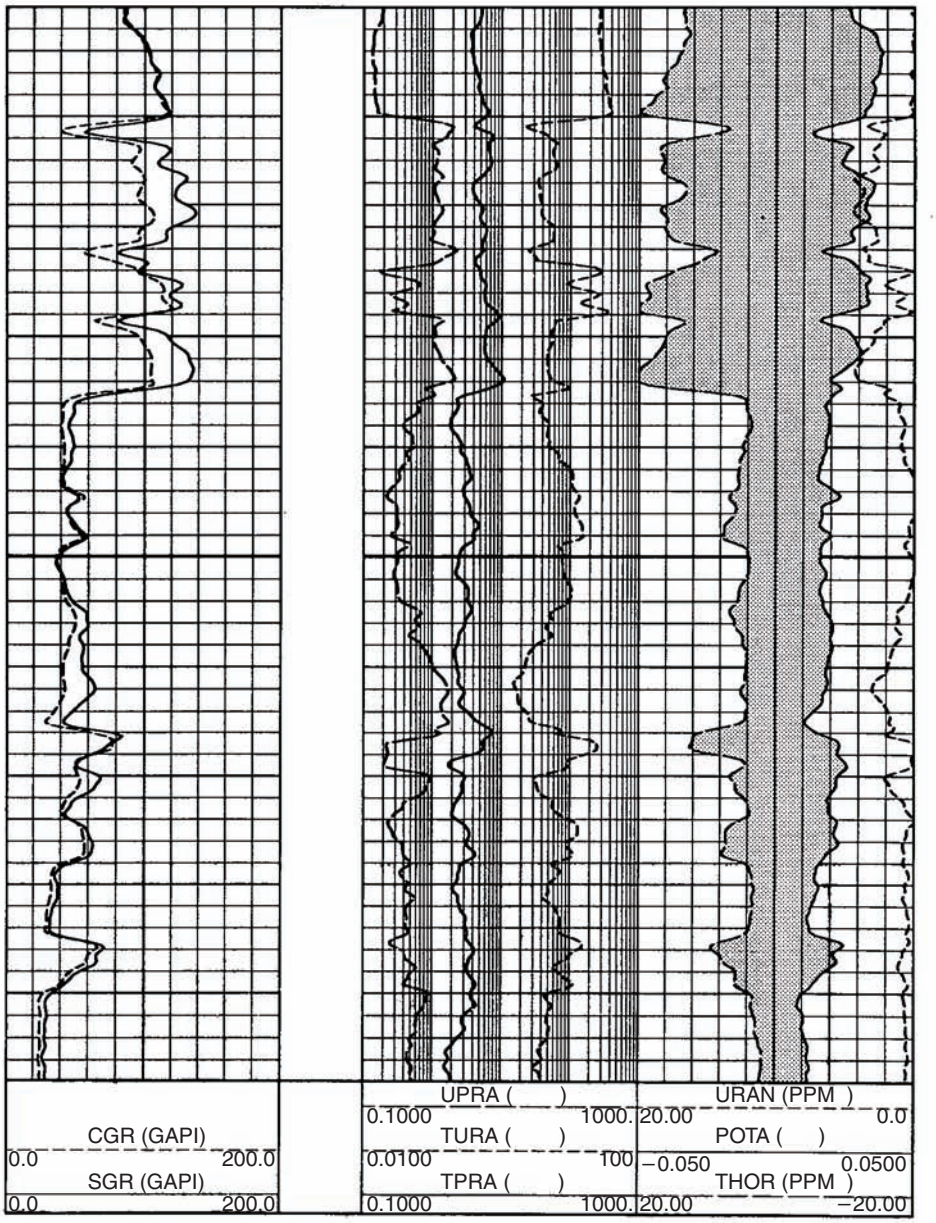


Fig. 10.21—Display of *Th*, *K*, and *U* ratios.

Track 1 shows a total gamma ray curve together with a uranium-free curve. Track 2 gives three ratios, uranium/potassium, thorium/uranium, and thorium/potassium. Track 3 gives a coded display on which the coded area represents the formations with both the highest potassium and the highest thorium content.

10.10 Summary

Gamma ray logs are particularly useful to the log analyst because they can be run in both open and cased holes. They are the primary diagnostic method for distinguishing between reservoir rocks and shales that contain radioactive clay minerals. In quantitative analysis, these measurements

are frequently used to compute the clay content of the formation. Gamma ray spectral logs add further to the usefulness of natural gamma ray logs by enabling the analyst to deduce the kinds of radioactive rock present as well as their abundance.

References

Fertl, W.H. 1979. Gamma Ray Spectral Data Assists in Complex Formation Evaluation. *The Log Analyst* **20** (5): 3–37.

Fertl, W.H., Stapp, W.L., Vaello, D.B. et al. 1980. Spectral Gamma-Ray Logging in the Texas Austin Chalk Trend. *J. Pet Tech* **32** (3): 481–488; presented at the 53rd Annual Technical Conference and Exhibition, Houston, 1–4 October 1978. http://dx.doi.org/10.2118/7431-PA.

Frondel, C. 1956. Mineralogy of Thorium. In *Contributions to the geology of uranium and thorium by the United States Geological Survey and Atomic Energy Commission for the United Nations International Conference on Peaceful Uses of Atomic Energy, Geneva, Switzerland, 1955*, compiled by L.R. Page, H.E. Stocking, and H.B. Smith, U.S. Geological Survey Professional Paper No. 300. Washington, DC: Professional Paper Series, U.S. Government Printing Office.

Hassan, M., Hossin, A., and Combaz, A. 1976. Fundamentals of the Differential Gamma Ray Log—Interpretation Technique. Paper presented at the SPWLA 17th Annual Logging Symposium, Denver, 9–12 June.

Introduction to Open Hole Logging. Schlumberger Educational Services (05/96).

Marett, G., Chevalier, P., Souhaite, P. et al. 1976. Shaly Sand Evaluation Using Gamma Ray Spectrometry Applied to the North Sea Jurassic. *Proc.,* SPWLA 17th Annual Logging Symposium, Denver.

Schlumberger. 1982. *Well Evaluation Developments: Continental Europe*.

Schlumberger. 2009. *Log Interpretation Charts*, 09-FE-0058. Sugar Land, Texas: Schlumberger.

Stieber, S.J. and Thomas, E.C. 1975. The Distribution of Shale in Sandstones and Its Effect Upon Porosity. Paper presented at the SPWLA 16th Annual Logging Symposium, New Orleans, 4–7 June.

Tittman, J. 1956. Radiation Logging: Lecture 1—Physical Principles and Lecture 2—Applications. *Proc*., Petroleum Engineering Conference on the Fundamental Theory and Quantitative Analysis of Electric and Radioactivity Logs, University of Kansas, Lawrence, Kansas, 2–3 April.

General References

Bhuyan, K. and Passey, Q.R. 1994. Clay Estimation from GR and Neutron-Density Porosity Logs. *Trans.,* SPWLA 35th Annual Logging Symposium, Tulsa, June 19–22.

Dresser Atlas. 1981. Spectralog. Publication No. 3334, Dresser Industries, Inc, Houston, Texas.

Fertl, W.H., and Frost, E. Jr. 1982. Experiences with Natural Gamma Ray Spectral Logging in North America. Paper SPE 11145 presented at the SPE Annual Technical Conference and Exhibition, New Orleans, 25–29 September. http://dx.doi.org/10.2118/11145-MS.

Kokesh, F.P. 1951. Gamma Ray Logging. *Oil & Gas J.* **50:** 284–290.

Poupon, A., Clavier, C., Dumanoir, J., et al. 1970. Log Analysis of Sand-Shale Sequences—A Systematic Approach. *J. Pet Tech* **22** (7): 867–881. http://dx.doi.org/10.2118/2897-PA.

Quirein, J.A., Gardner, J.S., and Watson, J.T. 1982. Combined Natural Gamma Ray Spectral/ Litho-Density Measurements Applied to Complex Lithologies. Paper SPE 11143 presented at the SPE Annual Technical Conference and Exhibition, New Orleans, 25–29 September. http://dx.doi.org/10.2118/11143-MS.

Smith, H.D. Jr., Robbins, C.A., Arnold, D.M., and Deaton, J.G. 1983. A Multi-Function Compensated Spectral Natural Gamma Ray Logging System. Paper SPE 12050 presented at the SPE Annual Technical Conference and Exhibition, San Francisco, 5–8 October. http://dx.doi.org/10.2118/12050-MS.

Answers to Questions

QUESTION 10.1. $GR_{cor} = 100$.

QUESTION 10.2.
$GR_{min} = 20$.
$GR_{max} = 85$.
In sand C, $GR = 40$.
GR Index = 0.308.
V_{clay} linear = 30.8%.
V_{clay} Clavier = 16.2%.
V_{clay} Stieber = 12.9%.

QUESTION 10.3. Uranium.

Appendix 10A

TABLE A-1—NATURAL GAMMA RAY EMITTERS: URANIUM SERIES (Fertl 1979)

Nuclide		Mode of Disintegration	Half-Life
UI	$_{92}U^{238}$	α	4.51×10^4 yr
UX_1	$_{90}Th^{234}$	β	24.1 d
UX_2	$_{91}Pa^{234m}$	β, IT	1.18 min.
UZ	$_{91}Pa^{234}$	β	6.66 hours
UII	$_{92}U^{234}$	α	2.48×10^4 yr
Io	$_{90}Th^{230}$	α	8.0×10^4 yr
Ra	$_{88}Ra^{226}$	α	1620 yr
Rn	$_{86}Em^{222}$	α	3.82 d
RaA	$_{84}PO^{218}$	α, β	3.05 min.
RaA′	$_{85}At^{218}$	α, β	2 s
RaA″	$_{86}Em^{218}$	α	1.3 s
RaB	$_{82}Pb^{214}$	β	26.8 min.
RaC	$_{83}Bi^{214}$	α, β	19.7 min.
RaC′	$_{84}PO^{214}$	α	1.6×10^{-4} sec
RaC″	$_{81}T1^{210}$	β	1.32 min.
RaD	$_{82}Pb^{210}$	β	19.4 yr
RaE	$_{83}Bi^{210}$	α, β	5.01 d
RaF	$_{84}PO^{210}$	α	138.4 d
RaE′	$_{81}T1^{206}$	β	4.2 min.
RaG	$_{82}Pb^{206}$	Stable	

TABLE A-2—NATURAL GAMMA RAY EMITTERS CONTINUED: GAMMA RAY LINES* IN THE SPECTRA OF THE IMPORTANT NATURALLY OCCURRING RADIONUCLIDES (Fertl 1979)

Nuclide	Gamma Ray Energy, MeV	Number of Photons per Disintegration in Equilibrium Mixture
Bi^{214} (Rac)	0.609	0.47
	0.769	0.05
	1.12	0.17
	1.238	0.06
	1.379	0.05
	1.764	0.16
	2.204	0.05
$T4^{208}$ (ThC′)	0.511	0.11
	0.533	0.28
	2.614	0.35
K^{40}	1.46	0.11

*With intensities greater than 0.05 photons per disintegration and energies greater than 100 KeV.

TABLE A-3—URANIUM MINERALS (Fertl 1979)

Autunite	$Ca\ (UO_2)_2\ (PO_4)_2\ 10–12H_2O$
Tyuyamunite	$Ca\ (UO_2)_2\ (VO_4)_2\ 5–8H_2O$
Carnotite	$K_2(UO_2)_2\ (UO_4)_2\ 1–3H_2O$
Baltoodite	U-silicate high in K
Weeksite	U-silicate high in Ca

Appendix 10B

TABLE B-1—NATURAL GAMMA RAY EMITTERS: THORIUM SERIES

Name	Composition	ThO_2 Content (%)
Thorium Minerals		
Cheralite	$(Th, Ca, Ce)(PO_4SiO_4)$	30, variable
Huttonite	$ThSiO_4$	81.5 (ideal)
Pilbarite	$ThO_2 \cdot UO_3 \cdot PbO \cdot 2SiO_2 \cdot 4H_2O$	31, variable
Thorianite	ThO_2	Isomorphous series to UO_2
Thoritea	$ThSiO_4$	25 to 63–81.5 (ideal)
Thorogummite*	$Th(SiO_4)_{1-x}(OH)_{4-x}$; $x < 0.25$	24 to 58 or more
Thorium-Bearing Minerals		
Allanite	$(Ca, Ce, Th)_2(Al, Fe, Mg)_3Si_3O_{12}(OH)$	0 to about 3
Bastnaesite	$(Ce, La)Co_3F$	Less than 1
Betafite	About $(U, Ca)(Nb, Ta, Ti)_3O_9nH_2O$	0 to about 1
Brannerite	About $(U, Ca, Fe, Th, Y)_3Ti_5O_{16}$	0 to 12
Euxenite	$(Y, Ca, Ce, U, Th)(Nb, Ta,Ti)_2O_5$	0 to about 5
Eschynite	$(Ce, Ca, Fe, Th)(Ti, Nb)_2O_6$	0 to 17
FergusOnite	$(Y, Er, Ce, U, Th)(Nb, Ta, Ti)O_4$	0 to about 5
Monazite**	$(Ce, Y, La, Th)PO_4$	0 to about 30; usually 4 to 12
Samarskite	$(Y, Er, Ce, U, Fe, Th)(Nb, Ta)_2O_6$	0 to about 4
Thucholite	Hydrocarbon mixture containing U, Th, rare earth elements	
Uraninite	UO_2 (ideally) with Ce, Y, Ph, Th, etc.	0 to 14
Yttrocrasite	About $(Y, Th, U, Ca)_2(Ti, Fe, W)_4O_{11}$	7 to 9
Zircon	$ZrSiO_4$	Usually less than 1

Source: From Frondel (1956). Courtesy of the U.S. Geological Survey and U.S. Atomic Energy Commission.

*Potential thorium ore minerals.

**Most important commercial ore of thorium. Deposits are found in Brazil, India, Russia, Scandinavia, South Africa, and USA.

Appendix 10C

TABLE C-1—POTASSIUM, URANIUM, AND THORIUM DISTRIBUTION IN ROCKS AND MINERALS (Fertl 1979)

Rocks and Minerals	K (%)	U (ppm)	Th (ppm)
Accessory minerals			
Allanite		30–700	500–5000
Apatite		5–150	20–150
Epidote		20–50	50–500
Monazite		500–3000	$2.5 \times 10^4 - 20 \times 10^4$
Sphene		100–700	100–600
Xenotime		$500–3.4 \times 10^4$	Low
Zircon		300–3000	100–2500
Andesite (av.)	1.7	0.8	1.9
A., Oregon	2.9	2	2
Basalt			
Alkali basalt	0.61	0.99	4.6
Plateau basalt	0.61	0.53	1.96
Alkali olvine basalt	< 1.4	< 1.4	3.9
Tholeiites (orogene)	< 0.6	< 0.25	< 0.05
(non orogene)	< 1.3	< 0.50	< 2.0
Basalt in Oregon	1.7	1.7	6.8
Carbonates			
Range (average)	0.0–2.0 (0.3)	0.1–9.0 (2.2)	0.1–7.0 (1.7)
Calcite, chalk, limestone, dolomite (all pure)	< 0.1	< 0.1	< 0.5
Dolomite, West Texas (clean)	0.1–0.3	1.5–10	< 2.0
Limestone (clean)			
Florida	< 0.4	2	1.5
Cretaceous trend, Texas	< 0.3	1.5–15	< 2.0
Hunton lime, Oklahoma	< 0.2	< 1.0	<1.5
West Texas	< 0.3	< 1.5	<1.5
Clay Minerals			
Bauxite		3–30	10–130
Glauconite	5.08–5.30		
Bentonite	< 0.5	1–20	6–50
Montmorillonite	0.16	2–5	14–24
Kaolinite	0.42	1.5–3	6–19
Illite	4.5	1.5	
Mica			
Biotite	6.7–8.3		< 0.01
Muscovite	7.9–9.8		< 0.01

TABLE C-2—POTASSIUM, URANIUM, AND THORIUM DISTRIBUTION IN ROCKS AND MINERALS (Fertl 1979)

Rocks and Minerals	K (%)	U (ppm)	Th (ppm)
Diabase, Va.	< 1.0	< 1.0	2.4
Diorite, quartzodiorite	1.1	2	8.5
Dunite, Wa.	< 0.02	< 0.01	< 0.01
Feldspars			
Plagioclase	0.54		< 0.01
Orthoclase	11.8	–14	< 0.01
Microcline	10.9		< 0.01
Gabbro (mafic igneous)	0.46–0.58	0.84–0.9	2.7–3.85
Granite (silicic igneous)	2.75–4.26	3.6–4.7	19–20
Rhode Island	4.5–5	4.2	25–52
New Hampshire	3.5–5	12–16	50–62
Precambrian (Oklahoma)	2–6	3.2–4.6	14–27
Minnesota (Col. Texas)			
Granodiorite	2–2.5	2.6	9.3–11
Colorado, Idaho	5.5	2.5	11.0–12.1
Oil shales, Colorado	< 4.0	Up to 500	1–30
Peridotite	0.2	0.01	0.05
Phosphates		100–350	1–5
Rhyolite	4.2	5	
Sandstones, range (av.)	0.7–3.8 (1.1)	0.2–0.6 (0.5)	0.7–2.0 (0.7)
Silica, quartz, quartzite, (pure)	< 0.15	< 0.4	< 0.2
Beach Sands, Gulf Coast	< 1.2	0.84	2.8
Atlantic Coast (Fla., NC)	0.37	3.97	11.27
Atlantic Coast (NJ, Mass.)	0.3	0.8	2.07
Shales			
“Common” shales [range (av.)]	1.6–4.2 (2.7)	1.5–5.5 (3.7)	8–18 (12.0)
Shales (200 samples)	2	6	12
Schist (biotite)		2.4–4.7	13–25
Syenite	2.7	2500	1300
Tuff (feldspathic)	2.04	5.96	1.56

Appendix 10D

TABLE D-1—GEOLOGICAL SIGNIFICANCE OF NATURAL GAMMA RATIOS (Fertl 1979)

Ratios	Remarks
Thorium/uranium (Th/U)	In *sedimentary* rocks, Th/U varies with depositional environment
	Th/U > 7: continental, oxidizing environment, weathered soils, etc.
	< 7: marine deposits, gray and green shales, graywackes
	< 2: marine black shales, phosphates
	In *igneous* rocks, high Th/U indicative of oxidizing conditions by magma before crystallization and/or extensive leaching during postcrystallization history
	Source rock potential estimates of argillaceous sediments (shales)
	Major geologic unconformities
	Distance to ancient shore lines or location of rapid uplift during time of deposition
	Stratigraphic correlations, transgression vs. regression, oxidation vs. reduction regimes, etc.
Uranium/Potassium (U/K)	Source rock potential of argillaceous sediments
	Stratigraphic correlations
	Unconformities, diagenetic changes in argillaceous sediments, carbonates, etc.
	Frequent correlation with vugs and natural fracture systems in subsurface formations, including localized correlation with hydrocarbon shows on drilling mud logs and core samples both in clastic and carbonate reservoirs
Thorium/potassium (Th/K)	Recognition of rock types of different facies
	Paleographic and paleoclimatic interpretation of facies and characteristics
	Depositional environments, distance from ancient shore lines, etc.
	Diagenetic changes of argillaceous sediments
	Clay typing: Th/K increases from glauconite $\rightarrow$ muscovite $\rightarrow$ illite mixed-layer clays $\rightarrow$ kaolinite $\rightarrow$ chlorite $\rightarrow$ bauxite
	Correlation with crystallinity of illite, average reflectance power, paramagnetic electronic resonance

Chapter 11

Resistivity Measurements

The very first logging device ever designed was made to measure formation resistivity. It was a modification of a device previously used to detect underground resistivity anomalies associated with either geologic features or concentrations of metallic ores. This old surface surveying device is illustrated in **Fig. 11.1.** A voltage source sent a current through the ground between two widely spaced electrodes. The voltage drop between two other, more closely spaced, electrodes was used as a measure of the ground resistivity.

By moving the whole electrode array across the countryside, it was possible to map underground features, as shown in **Fig. 11.2.** When the entire setup was rotated through a 90° angle and lowered into a borehole, the electric log was born. The first electric log to be run (**Fig. 11.3**) was in the Pechelbronn field in France in 1927.

Since those early days, a series of improvements has resulted in five main families of resistivity tools:

- Electric logs
- Induction logs
- Laterologs
- Microresistivity devices
- Dielectric logs

11.1 Definitions

Ohm's law states that the potential difference, V, between two points on a conductor is equal to the product of the current flowing in the conductor, I, and the resistance of the conductor, R. Practical units of measurement are respectively the volt, the amp, and the ohm. Expressed as an equation, this relationship is:

$$V = I \times R$$

$$\text{Volts} = \text{Amps} \times \text{Ohms} \quad (11.1)$$

In logging, the resistivity of a rock is of more interest than its resistance. *Resistivity* is the specific electrical resistance of a given amount of material. The unit of resistivity is the ohm-meter^2/meter, abbreviated as $\Omega \cdot m^2/m$, that is, the voltage required to cause 1 amp to pass through a cube 1 m long and 1 m square **(Fig. 11.4).**

When discussing formation resistivities, it is common to say, "this is a 25-ohm sand," rather than, "this sand has a resistivity of 25 ohm-meters squared per meter." So the field jargon, when talking about resistivity logs, is to say "ohm" when $\Omega \cdot m^2/m$ is really meant.

Why the need to know the resistivity rather than the resistance? Because resistance is a function not only of the resistivity measured, but also of the geometry of the body of material on which the measurement is being made. The geometry of the body is not of prime interest to the well logger.

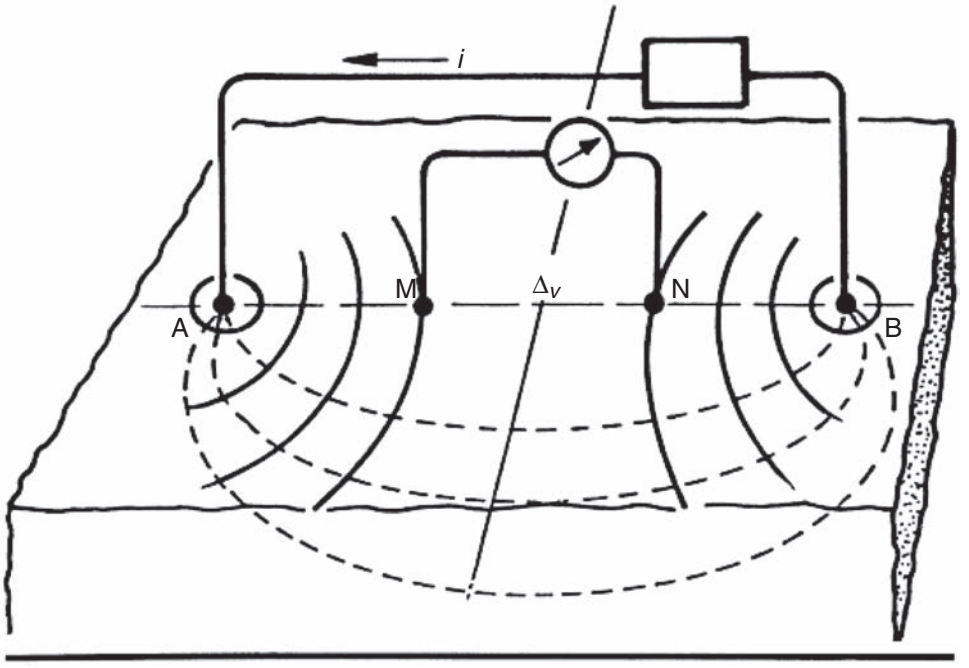


Fig. 11.1—Surface resistivity measurement device (Allaud and Martin 1977). Reprinted by permission from John Wiley & Sons.

The measurement that characterizes the rock, as far as fluid content is concerned, is the resistivity, not the resistance. The resistance of a wire stretching across the Pacific Ocean could be high, but the resistivity of the wire itself could be very low.

Conductivity is the reciprocal of resistivity. A substance with infinite resistivity (empty space) has a conductivity of zero, and a substance with low resistivity has high conductivity:

$$\text{conductivity} = \frac{1}{\text{resistivity}} \quad \ldots\ldots\ldots\

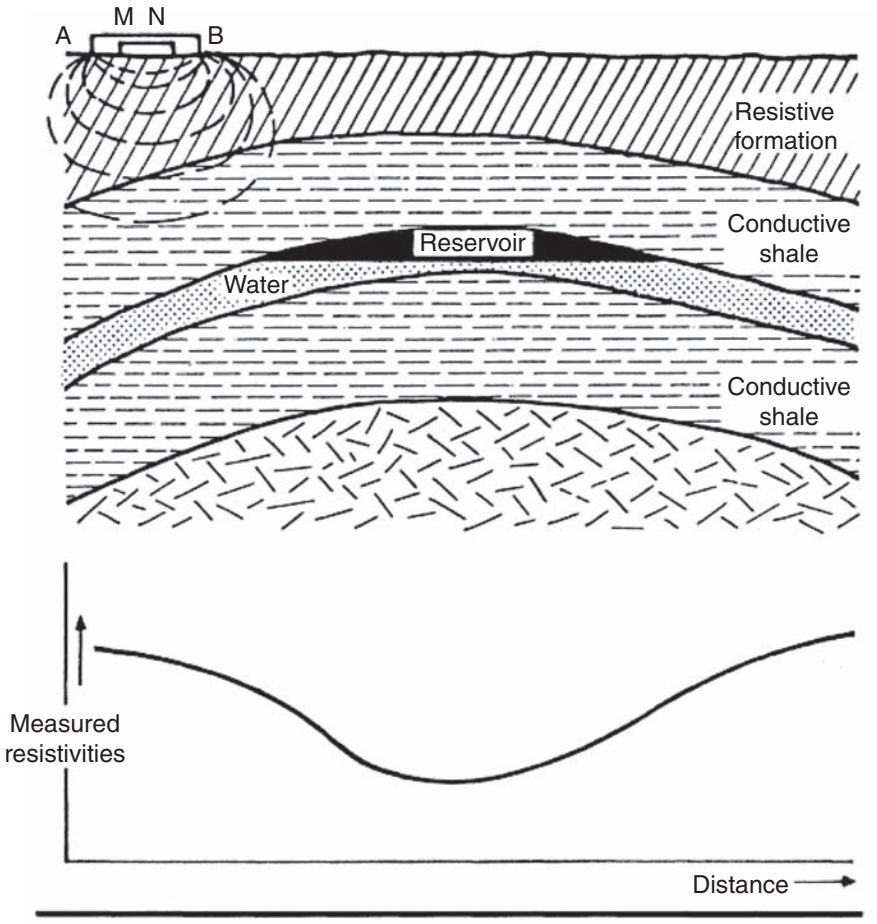


Fig. 11.2—Hypothetical cross section of an anticline and corresponding resistivity profile (Allaud and Martin 1977). Reprinted by permission from John Wiley & Sons.

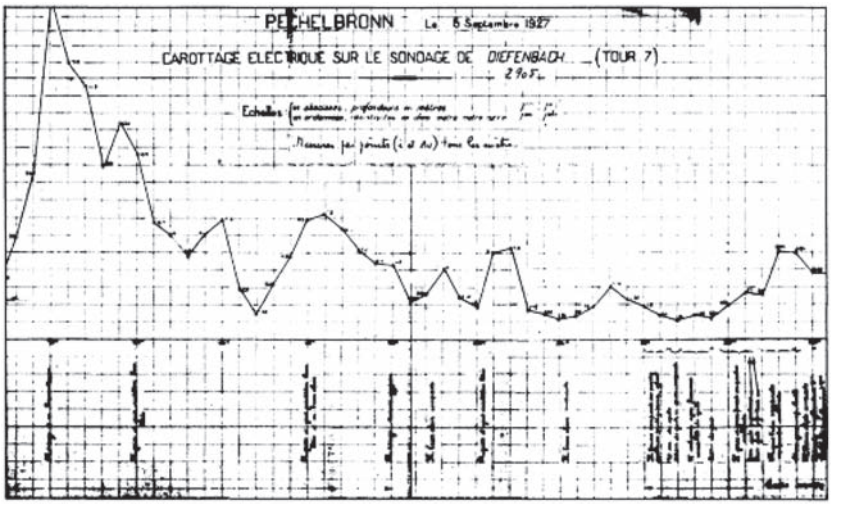


Fig. 11.3—The first electric log, a simple hand-plotted graph (Schlumberger 2007). Courtesy of Schlumberger.

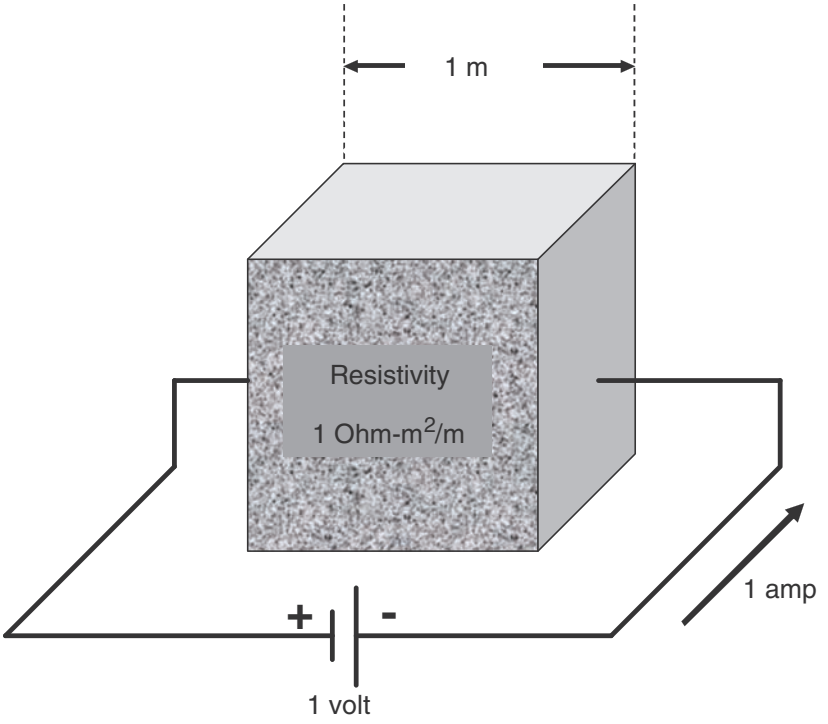


Fig. 11.4—Definition of the ohmmeter.

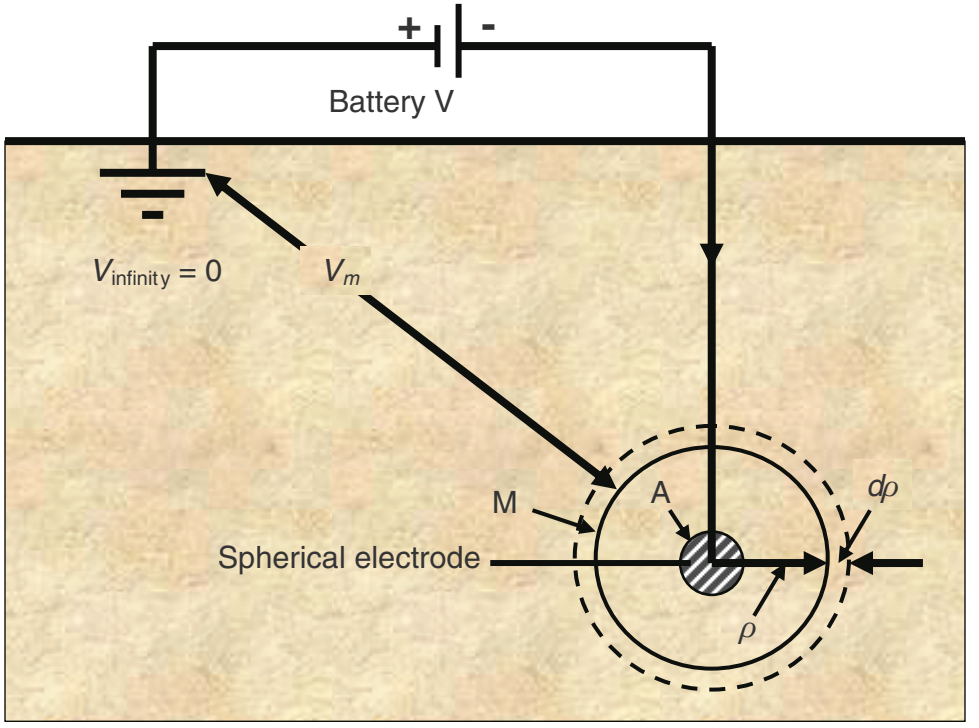


Fig. 11.5—Electrical logging schematic.

where dV is the voltage drop, I is the current, and dr is the resistance between the two shells. If the resistivity of the medium is R,

$$dr = R \times \frac{d\rho}{4\pi\rho^2} \text{ and } dV = I \times R \times \frac{d\rho}{4\pi\rho^2} \quad \ldots\ldots\ldots\

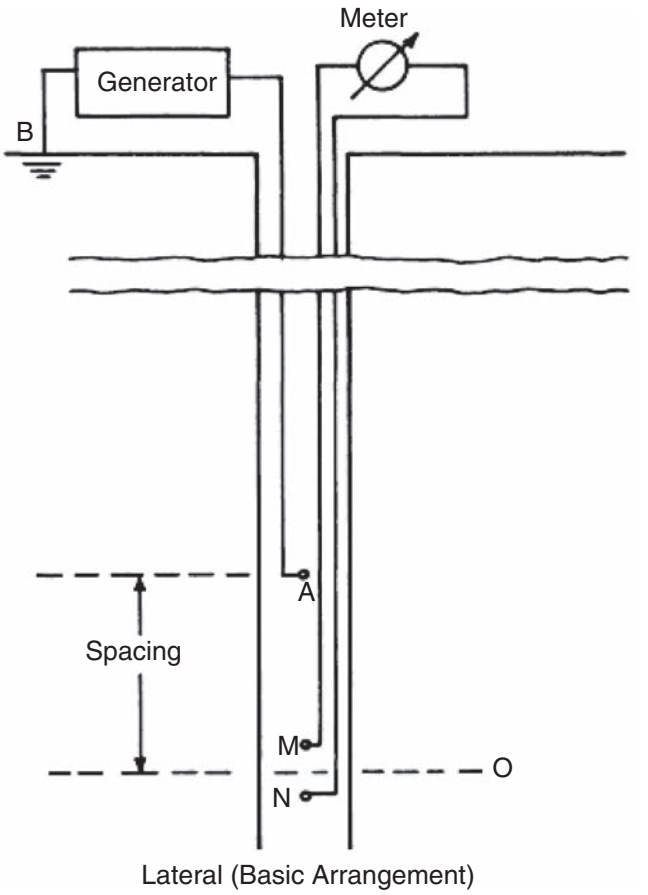


Fig. 11.7—Lateral resistivity device (after Kunz and Moran 1958). Reprinted by permission from the Society of Exploration Geophysicists (SEG).

Constant current is passed between electrodes A and B. The measured voltage appears between electrodes M and N. The distance *AM* is called the *spacing.* In the 16-in. *short normal* device, electrode A is 16 in. away from electrode M. A *lateral* device is illustrated in **Fig. 11.7.** Here, a constant current is sent between the A and B electrodes, and the measured voltage appears between the M and N electrodes. *Inverse* devices use another combination of electrode functions and will not be discussed here.

All these old electric devices, which were extensively used for many years, were plagued with inherent defects as a result of borehole and adjacent-bed effects. Their idiosyncrasies are legion. The student requiring further details to complete a study of old electric logs is directed to a volume published by the Society of Professional Well Log Analysts titled *The Art of Ancient Log Analysis.* The only survivors from among the early electric logs are the microlog and a device known as the ULSEL, the ultralong-spaced electric log, which is a normal device with an *AM* spacing of 100 to 1,000 ft. It is used for remote sensing of one borehole from another (blowout control) or remote sensing of resistive anomalies such as salt domes.

11.4 Evolution of Modern Resistivity Devices

Although the original principles of electric logging were sound, their practical implementations left much to be desired. Efforts to improve the measurement of formation resistivity have been actively pursued for the last 80 years at least. As a result, three main branches of resistivity logging have evolved: focused electric logs, induction logs, and microwave devices.

11.4.1 Focused Electric Logs. Focused electric logs were a logical successor to the early unfocused electric logs. Addition of focusing electrodes to the basic four-electrode array made it possible to steer the current in the right direction. The modern descendant of the early focused electric log is the laterolog (see Chapter 13), which uses a multiplicity of focusing electrodes to direct current into the formation and to eliminate most of the detrimental borehole effects that were present in early electric logs. Spherically focused logs also rely on focusing electrodes. Microfocused logging measurements are reviewed in Chapter 14.

11.4.2 Induction Logs. Induction logs broke the tradition of using current and voltage measurement electrodes by introducing a system of focused coils to induce currents to flow in the formation, away from the disturbing influence of the borehole and the invaded zone. Induction logs are discussed in Chapter 13.

11.4.3 Microwave Devices. More recently still, microwave devices have been used to measure the dielectric constant of the formation. Although, strictly speaking, these do not measure formation resistivity, they are usually classified as resistivity devices because the end use of their measurements is the same: determination of formation fluid saturation. These microwave devices are covered in Chapter 15.

11.5 Philosophy of Measuring Formation Resistivity

Whatever the device used to measure formation resistivity, there are common elements that conspire to confound its activity. These are the effects of:

- The borehole itself
- Neighboring beds
- Mud filtrate invasion

Although modern resistivity measurement devices represent a considerable improvement over the original unfocused electric log, there is still plenty of room for further development. Therefore, when using a resistivity log, the analyst should always bear in mind that the device used to produce the log is not perfect and that the measurement displayed on the log is a composite of four factors (R_s, R_t, R_m, and R_{xo}) as illustrated in **Fig. 11.8**.

Note that the tool is influenced not only by R_t, the resistivity of the undisturbed zone (which is what the tool trying to measure), but also, due to its design, by the resistivity of the borehole, the adjacent beds, and the invaded zone, if present. Therefore, there is evident danger in assuming that the reading from a resistivity log truly represents R_t. The device used, the particular circumstances of the well, and the nature of the formations logged all influence the actual reading, which may be greater or less than R_t. The chapters that follow will give instructions on how to recognize those cases where resistivity measurements may depart radically from R_t. For now, suffice it to say that, as a working rule, a large contrast between the resistivity of the bed of interest and the resistivity of either the mud column or the adjacent bed is a danger signal that calls for the use of correction charts. In this context, a large contrast could be considered to be a factor of 10 or more. Of particular note are conditions in which the bed of interest is thin (say, 15 ft or less), invasion is deep (d_i greater than 40 in.), or both.

11.6 Summary

By way of summary, it is safe to assume that a deep resistivity device measures R_t unless

1. R_t/R_m is greater than, say, 10,
2. R_t/R_s is greater than, say, 10,
3. Hole size is greater than, say, 12 in.,
4. Bed thickness is less than, say, 15 ft, or
5. Invasion diameter is greater than 40 in.

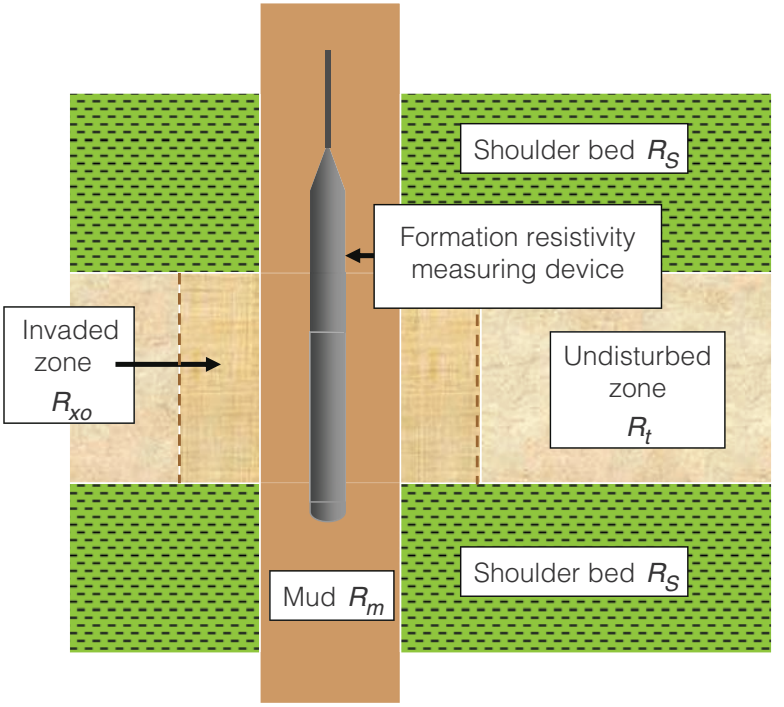


Fig. 11.8—Factors affecting resistivity measurement devices.

If any of these adverse conditions exist, the appropriate correction chart is called for. It will become apparent later that induction logs and focused electric logs (laterologs) behave differently when confronted with these problems, and in many cases, what is poison to an induction tool is an advantage to a laterolog, and vice versa.

References

Allaud, L. and Martin, M. 1977. *Schlumberger: The History of a Technique*. New York: John Wiley.

Kunz, K.S. and Moran, J.H. 1958. Some Effects of Formation Anisotropy on Resistivity Measurements in Boreholes. *Geophysics* **23** (4):770–794.

Schlumberger. 2007. *80 Years of Innovation*. Sugar Land, Texas: Oilfield Services Marketing Communications.

Schlumberger. 1972. *Log Interpretation: Volume 1—Principles.*

Schlumberger, C., Schlumberger, M., and Leonardon, E.G. 1934. Some Observation Concerning Electrical Measurements in Anisotropic Media, and their Interpretation. *Trans.,* AIME **110:** 159.

Schlumberger, C., Schlumberger, M., and Leonardon, E.G. 1934. Electrical Coring: a Method of Determining Bottom-Hole Data by Electrical Measurements. *Trans.,* AIME **110:** 237.

Schlumberger, C., Schlumberger, M., and Leonardon, E.G. 1934. A New Contribution to Subsurface Studies by Means of Electrical Measurements in Drill Holes. *Trans.,* AIME **110:** 273.

General References

Lynch, E.J. 1962. *Formation Evaluation*. New York: Geoscience Series, Harper & Row.

Oristaglio, M. and Dorozynski, A. 2009. *A Sixth Sense: The Life and Science of Henri-Georges Doll*. New York: The Overlook Press.

Runge, R.J., Worthington, A.E., and Lucas, D.R. 1969. Ultra-Long Spaced Electric Log (ULSEL). *The Log Analyst* **10** (5): 20–30.

SPWLA. 1979. *The Art of Ancient Log Analysis*. Houston: Society of Professional Well Log Analysts.

Answers to Questions

QUESTION 11.1. 200 millimhos; 0.5 ohms.

Chapter 12

Induction Logging

12.1 Induction Basics

Formation resistivity logging systems used before the introduction of induction logging depended on the presence of an electrically conductive fluid in the borehole to transmit electric current to the formation. In most rotary-drilled wells, the drilling fluid is a water-based mud that conducts electricity. However, some wells are drilled with nonconductive fluids such as oil-emulsion muds, oil-based muds, air, or gas. With such drilling fluids, it is impossible to obtain a satisfactory electrical log by use of conventional electric logging tools.

Induction logging does not depend on physical contact between the walls of the wellbore and the logging tool. The induction log is similar to a transformer in that a transmitter coil is energized with alternating current, which induces a secondary current in the formation. This current is proportional to the electrical conductivity of the formation and to the cross-sectional area affected by the energizing coil. The higher the conductivity of the formation (the lower its resistivity), the larger the formation current will be. This formation current in turn induces a signal in a receiver coil, and the intensity of this signal is proportional to the formation current, and hence to the formation conductivity. The signal detected by the receiver coil is amplified and recorded at the surface on the log.

The direct measurement made by induction logging devices represents conductivity. The reciprocal of the directly measured parameter is what the analyst normally works with, namely a logging curve on a resistivity scale. On some log presentations, both the conductivity and the reciprocal conductivity (resistivity) curves are shown on the log. Conductivity is measured in mhos or millimhos per meter. A mho is the reciprocal of an ohm, that is, 1 mho = 1/ Ω·m. A millimho equals 1/1000 of a mho. Therefore, formations with resistivities of 10, 100, or 1000 Ω·m have conductivities of 100, 10, and 1 mmho/m, respectively.

Induction logging equipment provides a record over a wide range of conductivity values. Accuracy is excellent for conductivity values higher than 20 mmho/m (resistivity values less than 50 Ω·m) and is acceptable in lower conductivity ranges (down to 5 mmho/m). Beyond this limit, the induction log continues to respond to variations in formation conductivity, but with diminished accuracy. There is a small uncertainty of about ±1 mmho/m on the zero of induction equipment.

The end purpose of measuring the formation resistivity is of course to distinguish hydrocarbon-bearing zones from water-bearing ones. The quest of the log analyst is therefore to obtain the value of R_t, which can then be used to compute the water saturation of a reservoir section. Conspiring against the analyst and the logging-tool designer are the effects of mud in the borehole, bed thickness, depth of invasion by the mud filtrate, and bed anisotropy. This chapter will describe how best to overcome these difficulties.

12.2 When To Use an Induction Logging Device

Induction logs are recommended for use where:

- Fresh or oil-based mud is used
- R_{mf}/R_w is greater than three
- R_t is less than 150 Ω·m
- Thin-bed resolution is not an issue for accurate log interpretation

Induction logs are the only resistivity devices that will work in oil-based mud (in which oil is the continuous phase) or in air-filled holes. **Fig. 12.1** illustrates the preferred working conditions for induction tools: R_{mf}/R_w is plotted against porosity, and the top right portion of the chart shows the conditions in which the induction log should be run.

12.3 Induction-Tool Development History

Induction logging has a long history, with the first tools introduced in the 1940s. Since then, successive generations of induction tools have come to market. Although the basic mode of operation has remained substantially unchanged, the refinements added by each improvement have been long in coming, but worth the wait. These can be chronicled as follows:

- Five-coil system (5FF40)
- Six-coil system (6FF40)
- Dual induction
- Phasor induction
- High-resolution induction
- Array induction
- 3D induction

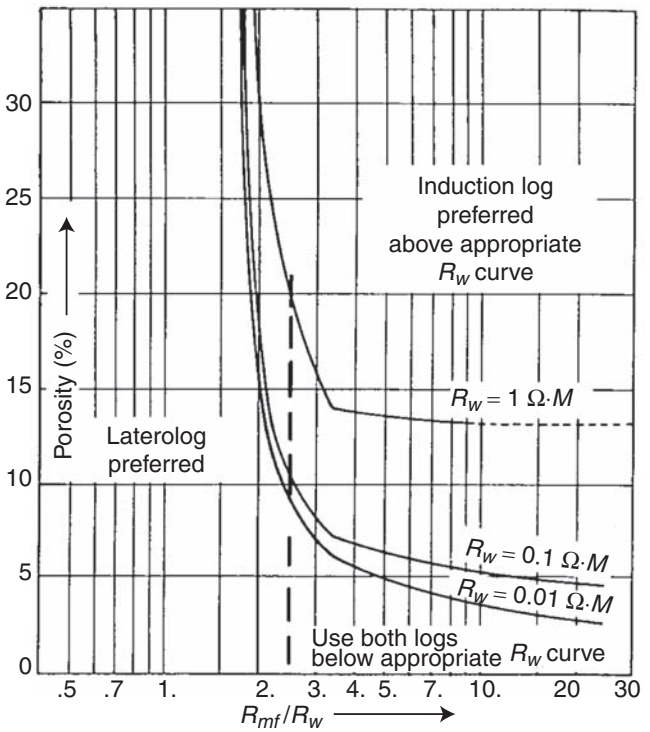


Fig. 12.1—Preferred conditions for induction tools (Schlumberger 1989a). Courtesy of Schlumberger.

Table 12.1 documents the chronology of improvements to induction devices in terms of their ability to resolve thin beds (vertically) and to read formation resistivity (R_t) farther and farther away from the disturbing effects of the invaded zone.

Each of these devices will be discussed briefly to give the reader a grasp of the practical advantages afforded to the user and the analyst by the historical progression of this key wireline logging technology. However, to appreciate these advances, the theory of induction devices must be further described.

12.4 Theory of Induction Devices

Induction tools work like mine detectors or airport security devices through which passengers walk. A transmitter coil, with an alternating current passing through it, sets up an alternating magnetic field. The alternating magnetic field induces an alternating potential in the formation. The conductivity of the formation material determines whether a large or a small alternating current is caused to flow in the formation. The alternating magnetic field associated with this current induces an AC potential in a receiving coil. This potential can be measured and used as an indicator of formation conductivity. **Fig. 12.2** illustrates this concept by reference to a simple two-coil device.

The oscillator attached to the transmitter is held at a constant 20-KHz frequency and a constant current, so that the strength of the magnetic field is also constant. The induced current in the formation is large when the resistivity is low (conductivity is high), and therefore the measured signal (the voltage appearing on the receiver coil) is greatest in low-resistivity formations. In very high-resistivity formations, the measured signal becomes very small, and resolution is lost. This loss of resolution at high resistivities becomes a problem at approximately 150 Ω·m. Above 250 Ω·m, induction tools are not very useful for quantitative measurements.

TABLE 12.1—HISTORICAL PERSPECTIVE OF INDUCTION TOOL DEVELOPMENT

Tool	Vertical Resolution, ft	Radial Investigation, in.	Year Introduced
5FF40	7	30	1947
6FF40	7	50	1956
Dual Induction			
Deep	7	50	
Medium	5	28	
Shallow	2.5	16	
Phasor Induction			1986
Deep	3	65	
Medium	3	40	
Shallow	2.5	16	
High Resolution Induction			1989
Deep	2	95	
Medium	2	60	
Shallow	2	16	
Array Induction Tool			1990
AT90	4	90	
AT60	3	60	
AT30	2	30	
AT20	2	20	
AT10	1	10	
3D Induction			2000

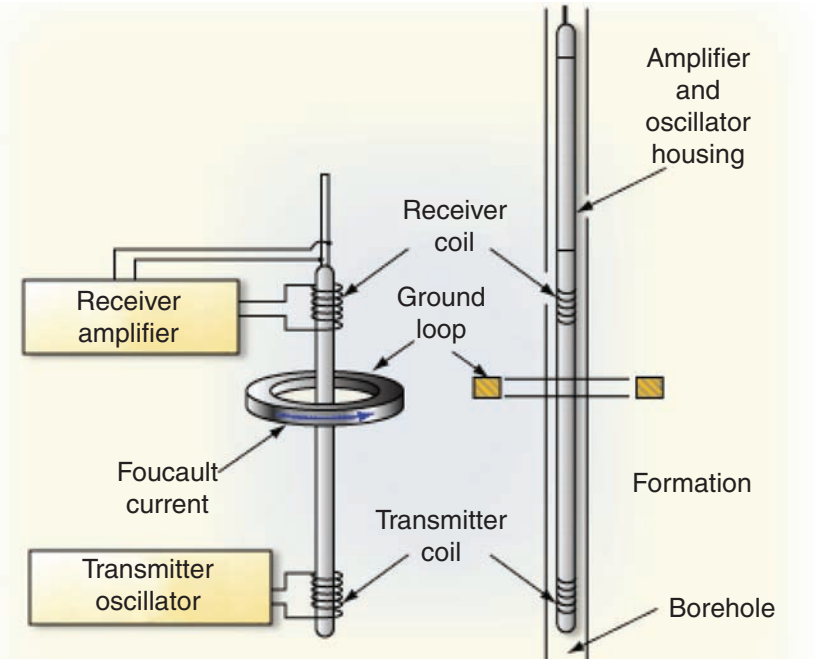


Fig. 12.2—Basic two-coil induction log system (Schlumberger 1989a). Courtesy of Schlumberger.

An induction tool requires no special borehole fluids and works equally well in air or in oil- or water-based muds. In fact, in air-filled holes or oil-based muds (where oil is the continuous phase), it is the only resistivity tool that will work.

12.5 Practice of Induction Logging

12.5.1 Calibration. An induction log system is calibrated by use of a two-point method. The sonde is suspended high off the ground and well away from conductive materials and is adjusted by zero shift to read zero conductivity (infinite resistivity). A circular ring of metal is then placed around the sonde as a test loop, and a scale-sensitivity adjustment is made to the known test-loop value. Depending on the tool, this value will be equivalent to a low-resistivity (1- or 2-Ω·m) formation. When the tool is at the bottom of a 10,000-ft well, there is no way that a test loop can be placed around the sonde. An internal calibrator is therefore included in the tool. This calibrator has a nominal value of 1 or 2 Ω·m, and its precise value is determined monthly by reference to the test loop. These internal calibrators shift with age, but behave reasonably well under normal use. A check of the zero-conductivity point when the tool is in the hole is accomplished simply by opening the receiving coil. Any extraneous signal is canceled out by a zero adjustment.

12.5.2 Skin Effect. To understand the induction response fully, several factors must be considered. In addition to the emf induced by the magnetic field of the transmitter coil, other emfs are induced in the ground loops, and these affect the amplitude and phase of the eddy currents. These additional emfs are produced by linkage of each ground loop with its own magnetic field (a ground loop has self-inductance), and with the magnetic fields of other nearby ground loops (there is mutual inductance between different ground loops). In this multiply cross-coupled system, the resultant eddy currents will not be quite as predicted on the basis of the simple tool theory already discussed. In other words, it cannot be assumed that the individual ground loops are independent of one another.

It can be predicted that, with increasing distance from the source (i.e., from the transmitter coil), the amount of transmitted power will be attenuated because:

1. The dissipation of energy by eddy-current flows in the region near the source decreases the energy available for transmission to regions farther out.
2. Regions at some distance from the source are shielded from the magnetic field of the transmitter coil by the canceling effect of magnetic fields of opposite sign from the eddy currents in the conductive medium closer to the transmitter. In a sense, this shielding of outer regions is equivalent to a reflection of energy back toward its source.

As a consequence of these interactions, a reduction of the receiver-coil signal, that is, a reduction in the measured conductivity value, occurs. This reduction in the apparent conductivity reading is commonly called the "skin effect." If σ_g is the conductivity reading that would be observed in a given media configuration without the skin effect and σ_a is the conductivity actually observed, the difference in conductivity, σ_s, is the skin effect:

$$\sigma_s = \sigma_g - \sigma_a \quad \ldots\ldots\ldots\

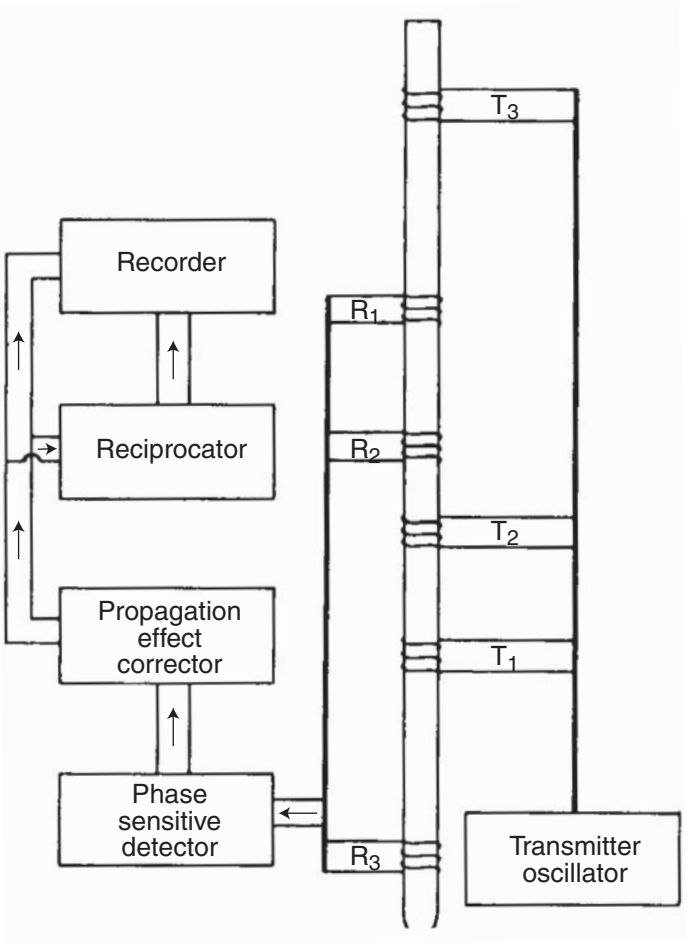


Fig. 12.4—Schematic diagram of a typical six-coil induction logging system. Courtesy of Baker Hughes.

poor vertical bed resolution. In effect, the signal received is a mixture of signals received from points both above and below the horizon being measured **(Fig. 12.5).**

Older induction equipment, before the digital age, attempted to correct for this lack of bed resolution by means of analog control equipment on the surface that emphasized the reading at the reference depth and played down the measurements made on either side. This was achieved by means of a shoulder-bed resistivity (SBR) correction routine that manipulated three measurements made at different depths (a central reading at the depth reference point, one deeper in the well, and one shallower) in such a way that the reading recorded on the log was equal to some weight value A times the value of the interval being measured plus B times the values at two points 78 in. above and below the point being measured. The values for A and B were chosen so that $A - 2B = 1$. This was logical because in a homogeneous formation (where all three measurements are the same), there is no net effect. This scheme assisted in correction for the effects of adjacent beds. Even so, it was insufficient to cure completely the problem of poor resolution, and correction charts were made available to the user for cases in which more precise measurements of formation resistivity were needed.

12.5.5 Induction Current Paths. Current loops flow around the borehole in a horizontal plane (assuming a vertical hole). The measured signal includes signals from the mud, the filtrate-invaded zone, and the undisturbed zone. The tool effectively sees three resistances in parallel **(Fig. 12.6).** The voltage drop around the loop can be considered constant at V, but

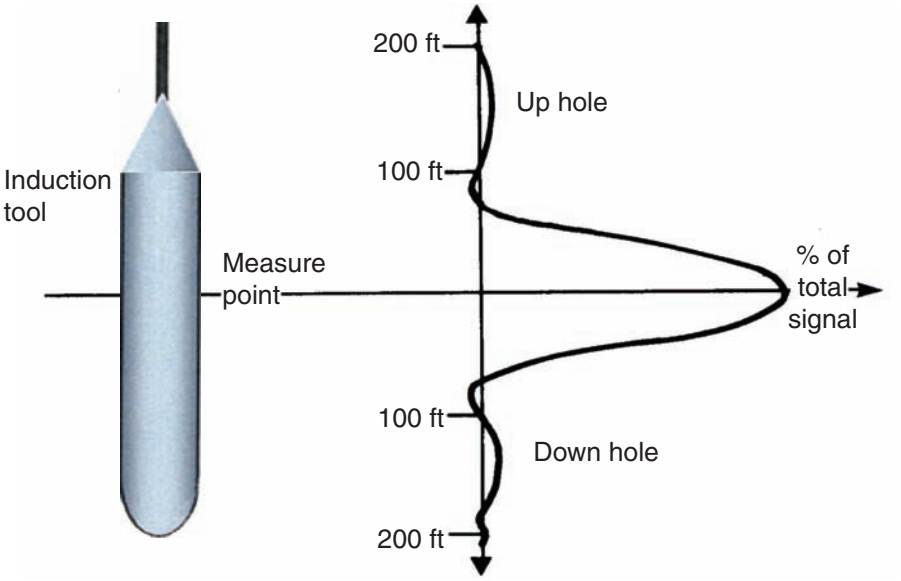


Fig. 12.5—Vertical response of induction tools.

in each zone from which signals are being recorded, the current flow will be different. The equations are:

$$V_{\text{mud}} = R_m \times i_m \times \alpha$$
$$V_{\text{invaded}} = R_{xo} \times i_{xo} \times \beta$$
$$V_{\text{undisturbed}} = R_t \times i_t \times \gamma, \quad \ldots\ldots\ldots\

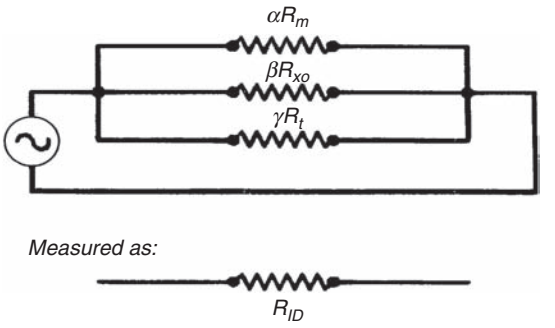


Fig. 12.7—An equivalent induction circuit.

where α, β, and γ are geometric constants dependent on the hole size and the diameter of the invaded zone. The total current flow is:

$$I = i_t + i_{xo} + i_m \quad \text{and} \quad V = I \times R_{ID} \ldots\ldots\ldots\

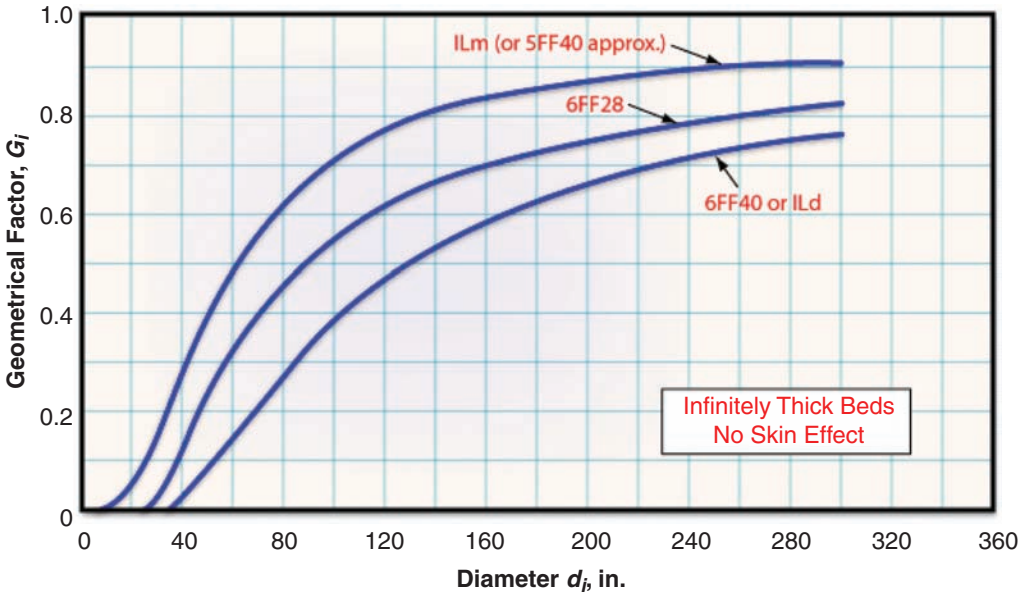


Fig. 12.8—Induction geometric factor (*G*). Courtesy of Schlumberger.

and therefore,

$$R_{ID} = 1/0.08 = 12.5\Omega \quad \ldots\ldots\ldots\

The solution is to use the dual induction-SFL combination logging tool. Because the geometric factor (G') for the medium induction log (R_{IM}) is different from the geometric factor (G) for the deep induction log (R_{ID}) and from the pseudogeometric factor (J) for the SFL (R_{SFL}) at the same d_i, the three equations can be solved simultaneously. Eqs. 12.8 and 12.9 can therefore be written as follows:

$$\frac{1}{R_{IM}} = \frac{G'}{R_{xo}} + \frac{1-G'}{R_t} \quad \ldots\ldots\ldots\

QUESTION 12.1. Use Fig. 12.10 to solve the following case:

R_{ID} = 10.0 Ω·m.
R_{IM} = 13.8 Ω·m.
R_{SFL} = 65.0 Ω·m.

Find the values of R_t, R_{xo}, and d_i.

12.6 Phasor Induction

The phasor induction tool improved on the basic six-coil induction design by incorporating additional focusing capability and additional operating frequencies which made many borehole and invasion corrections far less significant and enabled them to be applied semiautomatically. This meant that at the time of logging, a deep resistivity curve was part and parcel of the product delivered. **Fig. 12.11** shows an example of such a log.

It should be noted that although with this improved design, R_t was made easier to read directly from the log, the problem of poor vertical bed resolution was still unsolved.

12.7 High-Resolution Induction

High-resolution induction provided a much-needed mitigation of the poor bed-resolution problem by providing a bed resolution of approximately 2 ft instead of the conventional 6 or 7 ft. **Fig. 12.12** shows an example of such a log.

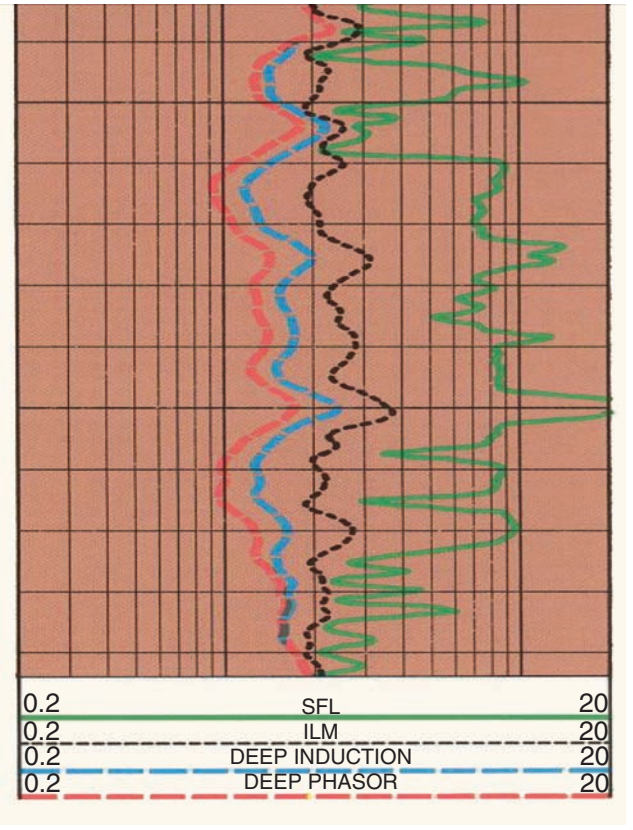


Fig. 12.11—Example of a phasor induction log.

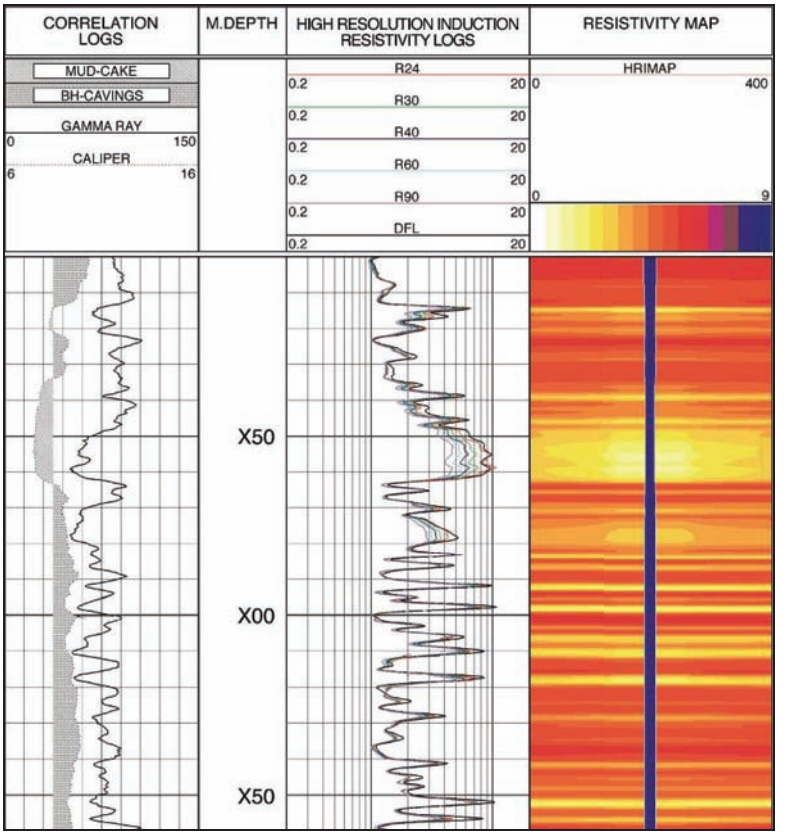


Fig. 12.12—Example of a high-resolution induction log. Courtesy of Halliburton.

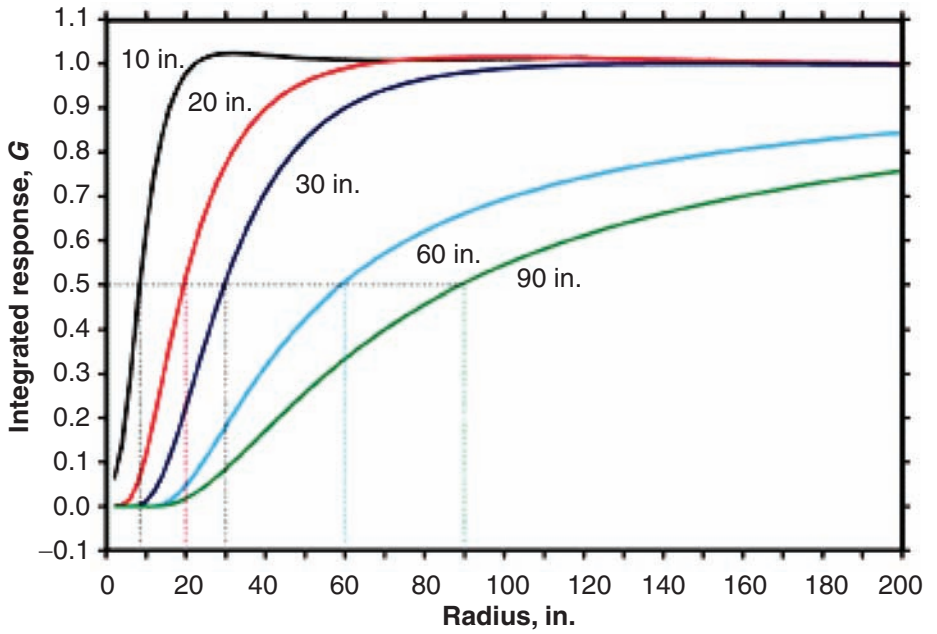


Fig. 12.13—Radial geometric factors for array induction measurements.

12.8 Array Induction Tool (AIT)

The AIT uses multiple transmitter and receiver coils set out along the axis of the tool so as to generate effectively eight different arrays. These produce 28 distinct formation resistivity measurements that are then combined to produce five formation resistivity measurements at five different radial depths of investigation, nominally at radial distances from the borehole wall of 10, 20, 30, 60, and 90 in. **Fig. 12.13** plots the geometric factors for the five measurements. It can be seen that the point at which 50% of the response is derived for each of the devices falls at the corresponding nominal depth of investigation.

Fig. 12.14 shows an example log with the five resistivity curves, with a section of impermeable formation (at the top of the logged section) and an invaded porous and permeable section lower down where all five curves diverge, as would be expected in a normal invasion profile with $R_t > R_{xo}$.

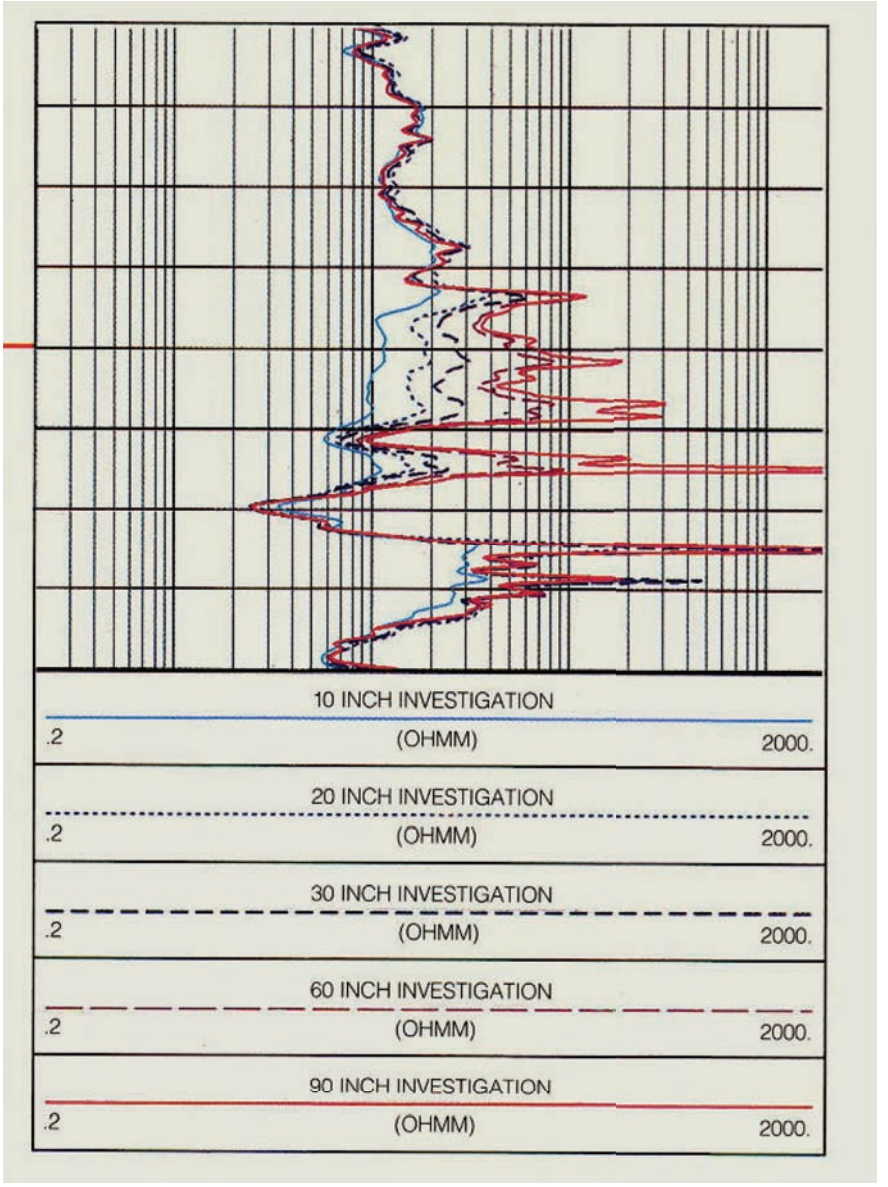


Fig. 12.14—Example of array induction with five resistivity curves.

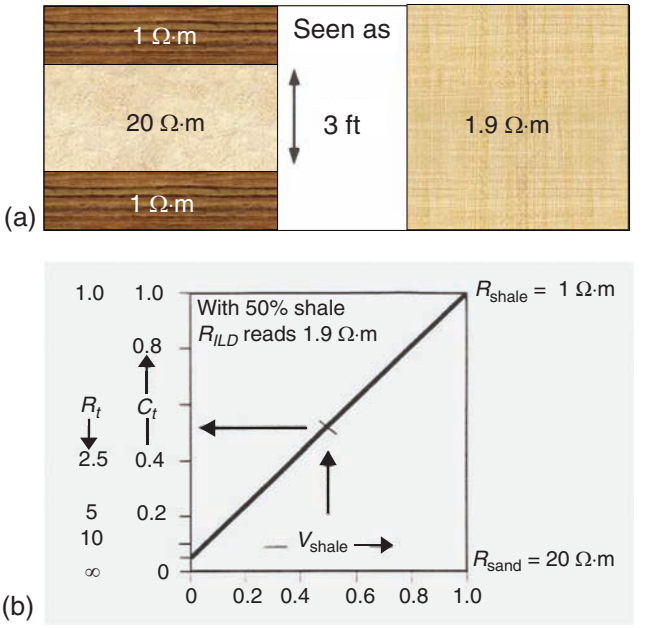


Fig. 12.15—Conventional induction log response in thin beds.

12.9 3D Induction

The basic design of induction logging tools used coils that were co-axial with the tool axis. Therefore, in a vertical well crossing horizontal beds, the induced current loops flowed parallel to the bedding planes. This system gave good results in thick homogeneous beds, but led to underestimation of reservoir-rock resistivity when (a) the beds were thin compared to the vertical resolution of the tool and (b) the formation was anisotropic, as for example in a thinly laminated sand-shale sequence. **Fig. 12.15** illustrates the parallel resistivity circuits by which the conventional induction log averages the conductivities of the sand laminae with those of the shale laminae, with the result that the apparent formation resistivity is very much lower than the true resistivity of the sand bed. This may lead to overlooked pay and missed production.

In the example shown, the upper part (a) shows a sand bed with an R_t of 20 Ω surrounded on either side by a shale bed with a resistivity of 1 Ω. Because the tool sees the sand and shale resistivities in parallel, the resistivity recorded on the log (R_{ILD}) is a mere 1.9 Ω. The lower part (b) shows the reason for this. As the percentage of shale in the sand/shale sandwich goes from 0 to 100%, the conductivity measurement goes from 0.05 mho to 1 mho. Therefore, at a V_{shale} value of 50%, the conductivity is given by (0.05+1)/2, or 0.525 mho, which is equivalent to 1.9 Ω.

The cure to this problem was the appearance on the scene of the so-called 3D induction log. This tool added coils that have their axes at right angles to the tool axis and that therefore produce current loops in a vertical plane parallel to the tool axis. The output of the tool is therefore a dual resistivity measurement: one for the horizontal direction, R_h, and one for the vertical, R_v. **Fig. 12.16** shows the tool configuration and **Fig. 12.17** some sample logs.

12.10 Calibration

Induction tools can be calibrated on land at any time. The sonde is placed in a zero-conductivity environment. This is normally done by raising the sonde up in the air well away from metallic objects. This defines a zero point. A calibration loop is then placed around the sonde to give a known conductivity signal, usually 500 mmhos. Calibration is performed monthly. It is almost

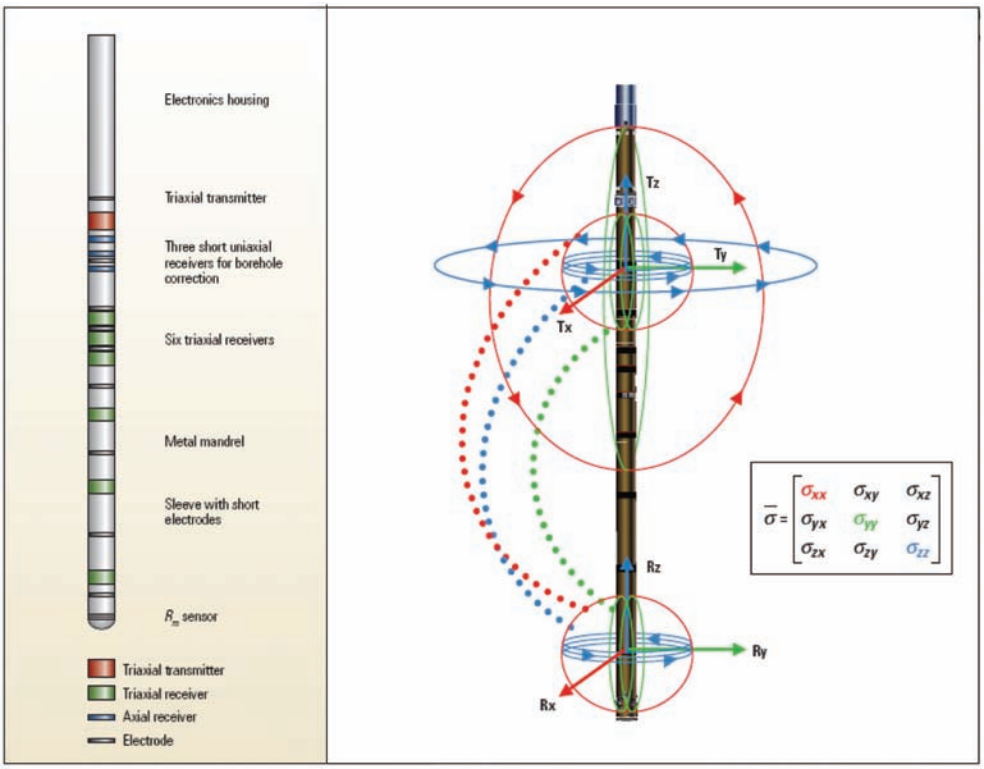


Fig. 12.16—(a) 3D induction tool and (b) horizontal and vertical current loops (Anderson et al. 2008). Courtesy of Schlumberger.

impossible to perform on an offshore rig because of the surrounding metal structure. In cases where it is not possible to set the zero point under controlled conditions at the surface, it is permissible to set it with the tool in the hole opposite a thick, very high-resistivity zone (e.g., salt, anhydrite, dense low-porosity carbonate) if such a zone exists. The sonde and its associated electronic cartridge form a matched set and should always be used together.

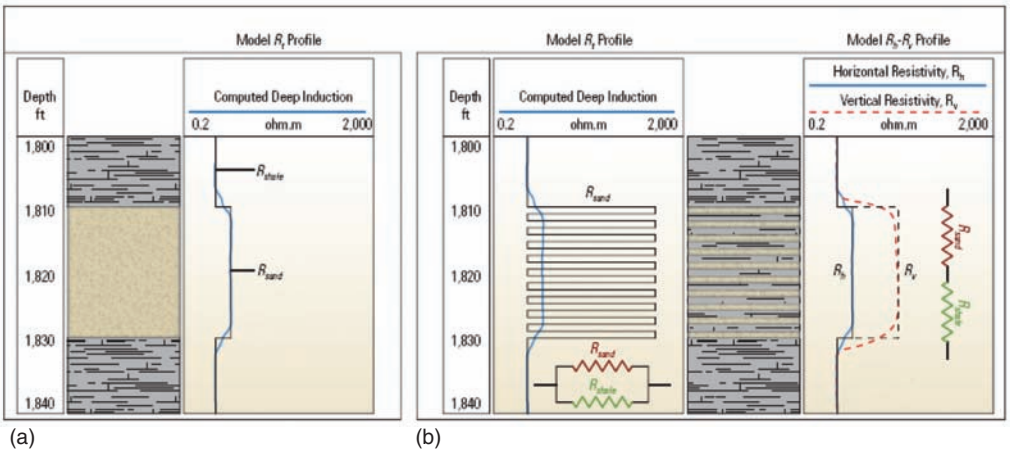


Fig. 12.17—3D induction response to (a) massive sand and (b) laminated sand-shale sequence (Anderson et al. 2008). Courtesy of Schlumberger.

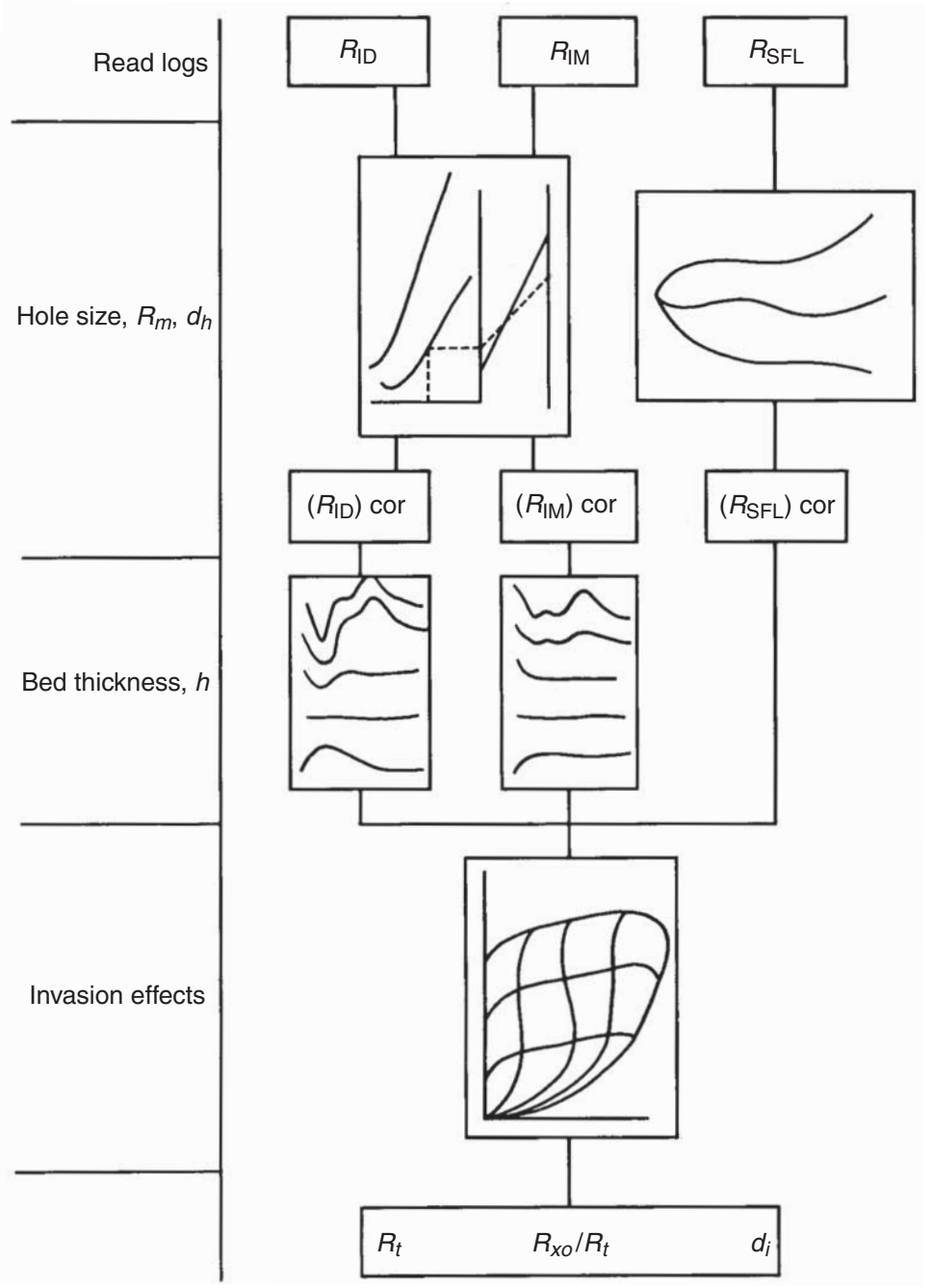


Fig. 12.18—Quick guide to R_t from dual induction logs.

12.11 Summary

In 90% of cases, it is permissible to assume that the deep induction reading is equal to the true formation resistivity, R_t. Conditions where this assumption is not valid include:

- Induction logs run in very large holes
- Induction logs run in salt muds
- Places where the bed of interest is thin

- Places where the shoulder-bed resistivity is markedly different from the resistivity of the bed under consideration
- Places where invasion is abnormally deep

Because all these perturbing effects are a matter of degree, it is suggested that for each log examined, a few quick calculations will show whether any of the various correction charts available introduce any substantial changes in the apparent resistivity. If they do not, it is safe to use R_{ID} as R_t in making an evaluation. If they do, the required corrections should be performed in the following order **(Fig. 12.18).**

- Hole-size and mud-resistivity corrections
- Bed-thickness corrections
- Invasion corrections

Modern logging systems incorporate environmental corrections on the fly, but to do so, the wellsite operator needs to select key inputs such as the source of hole-size information and the mud resistivity value. If there is any doubt about the correctness of these choices, an alternative environmental correction can be performed post-logging by effectively stripping out the corrections made at the wellsite and substituting more complete or accurate ones in the light of additional or more up-to-date information.

References

Anderson, B., Barber, T., Leveridge, R. et al. 2008. Triaxial Induction—A New Angle for an Old Measurement. *Oildfield Review* **20** (2): 64–84.

Schlumberger. 1989a. *Log Interpretation Principles/Applications*, seventh edition. Sugar Land, Texas: Schlumberger.

Schlumberger. 1989b. *Phasor Induction Tool*. Document SMP-9060.

Schlumberger. 2005. *Historical Log Interpretation Charts*.

General References

Anderson, B., Barber, T., and Lüling, M. 1995. The Response of Induction Tools to Dipping Anisotropic Formations. *Trans.,* SPWLA 36th Annual Logging Symposium, Paris, 26–29 June, Paper D.

Anderson, B., Sigal, R., Zouioueche, F., George, B.K., Torres-Verdin, C., and Delshad, M. 2003. A Case Study Integrating the Physics of Mud-Filtrate Invasion With the Physics of Induction Logging: Assessment of In-Situ Hydrocarbon Saturation in the Presence of Deep Invasion and Highly Saline Connate Water. *Proc.,* SPWLA 44th Annual Logging Symposium Galveston, Texas, USA, 22–25 June.

Archie, G.E. 1942. The Electrical Resistivity Log as an Aid in Determining Some Reservoir Characteristics. SPE-942054-G. *Trans.,* AIME **146:** 54–62.

Barber, T. 1985. Introduction to the Phasor Dual Induction Tool. *J. Pet Tech* **37** (9): 1699–1706.

Barber, T. 1985. Real-Time Environmental Corrections for the DIT-E Phasor Dual Induction Tool. *Trans.,* SPWLA 26th Annual Logging Symposium, Dallas, 17–20 June, Paper EE.

Barber, T. 1986. Invasion Profiling With the Phasor Induction Tool. *Trans.,* SPWLA 27th Annual Logging Symposium, Houston, 9–13 June, Paper EE.

Barber, T. 1988. Induction Vertical Resolution Enhancement—Physics and Limitations. *Trans.,* SPWLA 29th Annual Logging Symposium, San Antonio, 5–8 June, Paper O.

Barber, T., Orban, A., Hazen, G., et al. 1995. A Multiarray Induction Tool Optimized for Efficient Wellsite Operation. Paper SPE 30583 presented at the SPE Annual Technical Conference and Exhibition, Dallas, 22–25 October. http://dx.doi.org/10.2118/30583-MS.

Barber, T., Wang, H., Leveridge, R., Hazen, G., and Schlein, B. 2008. Principles of Log Quality Control for Complex Induction Logging Instruments. Paper MMMM presented at the SPWLA 49th Annual Logging Symposium, Austin, Texas, USA, 25–28 May.

Blakeman, E.R. 1962. A Method of Analyzing Electrical Logs Recorded on a Logarithmic Scale. *J. Pet Tech* **14** (8): 844–850. http://dx.doi.org/10.2118/375-PA.

Clavaud, J.-B. and Wang, H. 2008. Bed Boundaries From Multi-Component Induction Technology: Fact or Fiction and What To Do With Them. *Proc.,* SPWLA 49th Annual Logging Symposium, Austin, Texas, USA, 25–28 May, Paper K.

Doll, H.G. 1949. Introduction to Induction Logging and Application to Logging of Wells Drilled With Oil Base Mud. SPE- 949148-G. *Trans.,* AIME **186:** 148–162.

Dumanoir, J.L., Tixier, M.P., and Martin, M. 1957. Interpretation of the Induction-Electrical Log in Fresh Mud. SPE- 790-G. *Trans.,* AIME **210:** 202–217.

George, C.F., Smith, H.W, Bostick Jr., F.X. 1964. Application of Inverse Filters to Induction Log Analysis. *Geophysics* **29** (1): 93–104.

Meyer, W.H. 1987. Deconvolution of Invaded-Bed Induction Problems. *Trans.*, SPWLA 28th Annual Logging Symposium, London, 29 June–2 July, Paper P.

Minerbo, G.N. and Miles, J. 1991. Borehole Correction System for an Array Induction Well Logging Apparatus. US Patent No. 5,041,975.

Moran, J.H. 1964. Induction Method and Apparatus for Investigating Earth Formations Utilizing Two Quadrature Phase Components of a Detected Signal. US Patent No. 3,147,429.

Moran, J.H. 1982. Induction Logging—Geometrical Factors With Skin Effect. *The Log Analyst* **23** (6): 410.

Moran, J.H. and Gianzero, S. 1979. Effects of Formation Anisotropy on Resistivity Logging Measurements. *Geophysics* **44** (7): 1266–1286.

Moran, J.H. and Kunz, K.S. 1962. Basic Theory of Induction Logging and Application to Study of Two-Coil Sondes. *Geophysics* **27** (6): 829–858.

Souhaite, P., Misk, A., and Poupon, A. 1975. R_t Determination in the Eastern Hemisphere. *Trans.*, SPWLA 16th Annual Logging Symposium, New Orleans, 4–7 June, Paper LL.

Schuster, N.A., Badon, J.D., and Robbins, E.R. 1971. Application of the ISF/Sonic Combination Tool to Gulf Coast Formations. *Trans.,* Gulf Coast Association of Geological Societies, Vol. 21.

Singer, J. and Barber, T. 1988. The Effect of Transition Zones on the Response of Induction Logs. *Trans.*, SPWLA 29th Annual Logging Symposium, San Antonio, 5–8 June, Paper L.

SPWLA. 1992. *Resistivity Logging*. Houston: SPWLA Reprint Volume.

Strickland, R., Sinclair, P., Harber, J. et al. 1987. Introduction to the High-Resolution Induction Tool. *Trans.*, SPWLA 28th Annual Logging Symposium, London, 27 June –2 July, Paper E.

Strickland, R., Chemali, R., Su, S.M., et al. 1992. New Developments in the High-Resolution Induction Log. *Trans.,* SPWLA 33rd Annual Logging Symposium, Oklahoma City, Oklahoma, USA, 14–17 June.

Tixier, H.P., Alger, R.P., Biggs, W.P., et al. 1965. Combined Logs Pinpoint Reservoir Resistivity. *Pet. Eng.* (February-March).

Woodhouse, R., Threadgold, P. and Taylor, P.A. 1975. The Radial Response of the Induction Tool. *The Log Analyst* **16** (1): 39.

Answers to Questions

QUESTION 12.1.

$R_{IM}/R_{ID} = 1.38$.
$R_{SFL}/R_{ID} = 6.5$.
$R_t/R_{ID} = 0.9$.
$R_{xo}/R_t = 10$.
$R_t = 9\ \Omega\cdot m$.
$R_{xo} = 90\ \Omega\cdot m$.
$d_i = 50$ in.

Chapter 13

The Laterolog

13.1 Early Laterolog Devices

In the 1920s, Conrad Schlumberger put forward the idea of a guarded electrode in an attempt to improve on existing electrical logs, which had undesirable borehole effects. The idea was not put into practice until H.G. Doll designed a working guard-electrode system. From this starting point, laterologs evolved in a number of ways. The Laterolog-7, which used small guard electrodes, was later joined by the Laterolog-3, which used long guard electrodes **(Fig. 13.1).** Both operated on the same principle: a constant survey current (i_0) was forced into the formation by bucking currents from the guard electrodes. By monitoring the voltage required to maintain the fixed current i_0, the formation resistivity was measured. The conductivity laterolog evolved from these tools. It maintained a constant voltage on the measurement electrode, while current variations monitored the formation conductivity.

Improvements to the initial single laterolog tools came with the introduction of the dual laterolog (DLL), which was neither a conductivity nor a resistivity laterolog, but rather a hybrid which used a constant product of current and voltage (perhaps it should be called a joule laterolog). It solved many of the problems associated with the earlier laterologs and is the standard basic resistivity log for salt-mud environments. This workhorse makes measurements of formation resistivity at two different radial depths of investigation. The deep laterolog together with a shallower investigation laterolog, known as the shallow laterolog, provide the triangulation needed to solve the problem of making proper allowance for the effects of mud-filtrate invasion.

A more recent addition to the laterolog tool family is the array laterolog device. This tool adds measurements at graduated radial depths of investigation (up to four) and improves vertical resolution to approximately one foot.

13.2 When To Use a Laterolog

Laterologs should be used when the following conditions exist:

- Seawater or brine mud is in the hole
- The R_{mf}/R_w ratio is less than 3
- Hole size is less than 16 in.

The laterolog will produce better results than the induction log when R_t exceeds 150 Ω. It will also give a better estimate of R_t than the induction log when bed thickness is less than 10 ft. **Fig. 13.2** should be referred to when there is doubt as to whether a laterolog should be run. This figure shows a plot of the R_{mf}/R_w ratio vs. porosity. The laterolog is the tool of choice when the crossplot of R_{mf}/R_w vs. ϕ falls on the left side of the chart.

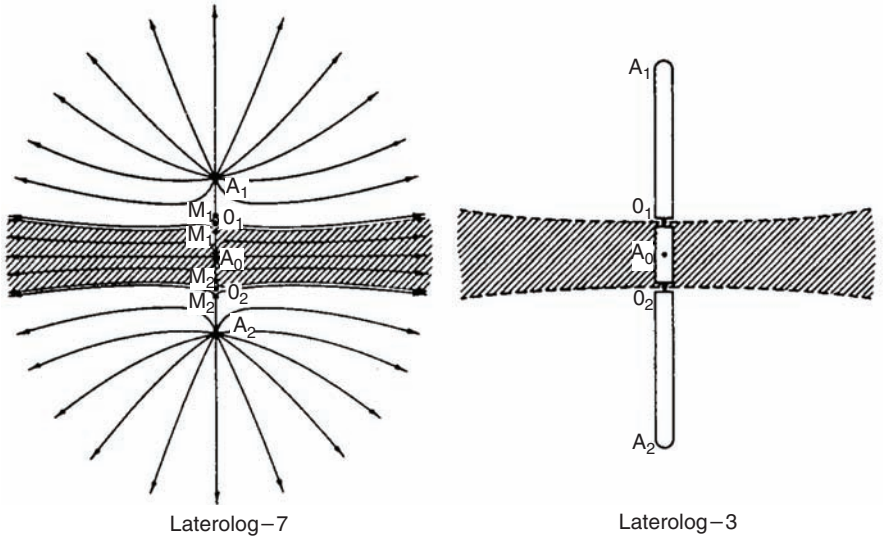


Fig. 13.1—Schematic diagrams of early laterologs (Schlumberger 1989). Courtesy of Schlumberger.

13.3 The DLL Tool

The DLL records three resistivity curves: the laterolog deep (*LLD* or LL_d), the laterolog shallow (*LLS* or LL_s), and a microspherically focused log (*MSFL*). Auxiliary curves such as caliper, gamma ray, and spontaneous potential may also be recorded. The resistivity curves are presented on a standard four-decade logarithmic scale **(Fig. 13.3).**

The principal of operation of laterolog tools may be illustrated by reference to the simultaneous DLL. **Fig. 13.4** is an illustration of the tool with its associated measurement electrodes.

As shown in Fig. 13.4, the R_{xo} measuring portion of this tool is a pad-type device. Once the tool is at the bottom of the well, arms with contact pads are extended to fit against the sides of the borehole. The mechanics of making both deep and shallow laterolog measurements with a single

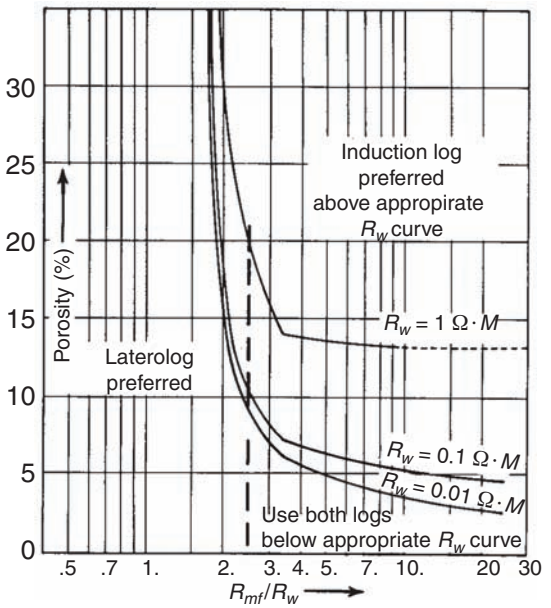


Fig. 13.2—Preferred ranges for application of induction logs and laterologs (Schlumberger 1989). Courtesy of Schlumberger.

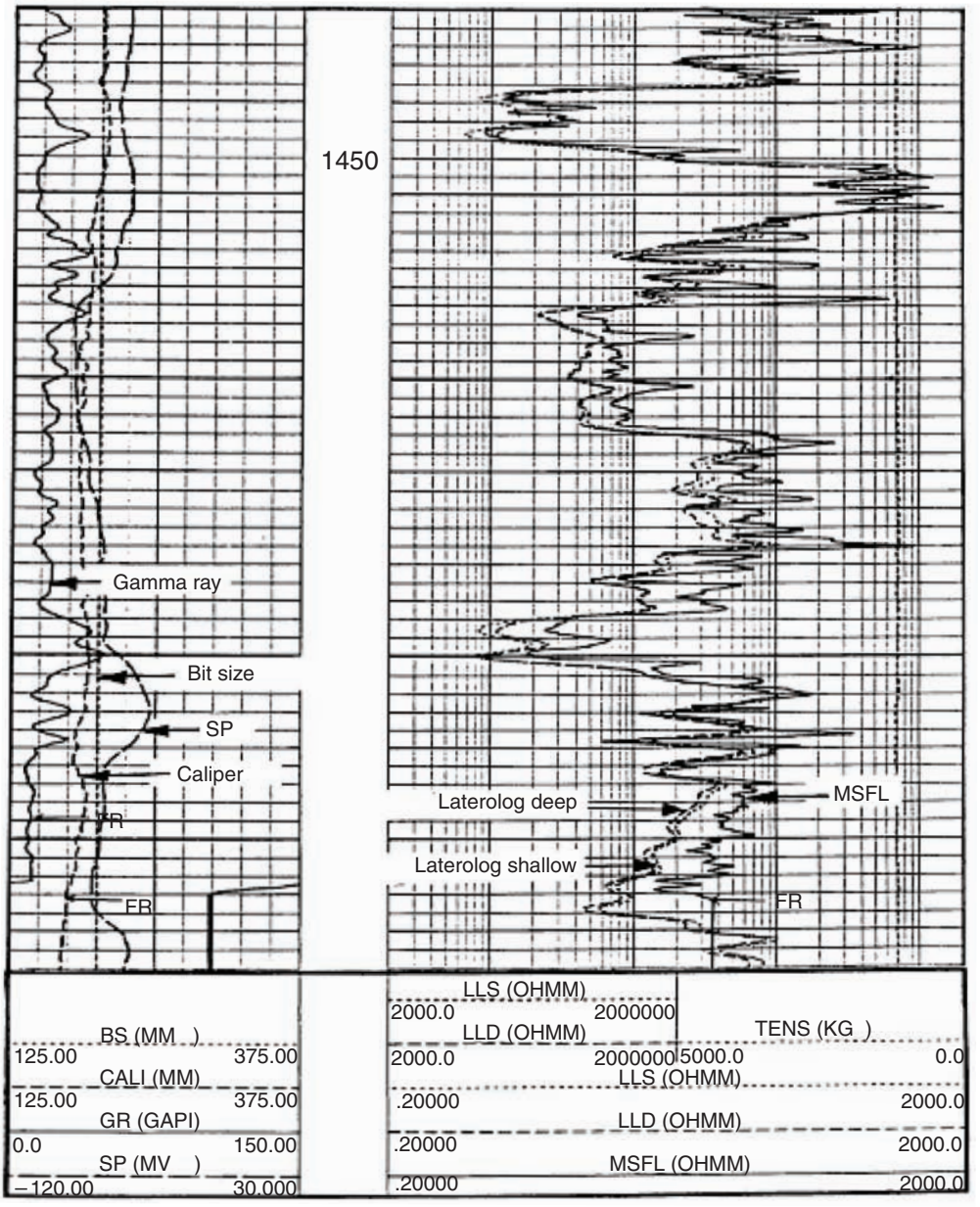


Fig. 13.3—Typical dual laterolog presentation.

set of electrodes are handled by circuitry inside the tool. The respective current paths for the LL_d and LL_s devices are shown in **Fig. 13.5**.

The LL_d uses long-focusing electrodes and a distant return electrode, while the shallow laterolog (LL_s) uses short-focusing electrodes and a close return electrode. The current paths for the *MSFL*, which has five rectangular electrodes mounted on a pad carried on one of the caliper arms, are shown in **Fig. 13.6** and are discussed more fully in Chapter 14 that covers microresistivity devices in detail.

Under normal conditions for use of a DLL, the radial profile of the resistivities is as shown in **Fig. 13.7** (i.e., $R_t > R_{xo} > R_m$). Between the invaded zone and the undisturbed formation, there is a transition zone that has a resistivity value between the values of R_t and R_{xo}.

Fig. 13.8 depicts a plan view of a horizontal slice made through the tool and the formation that surrounds it. This figure shows current flowing radially outward from the tool and

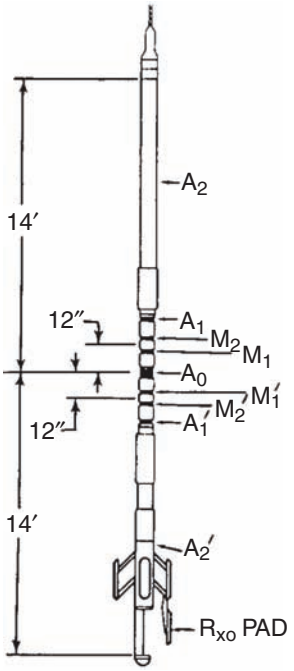


Fig. 13.4—Schematic diagram of the dual laterolog-R_{xo} tool (Suau et al. 1972).

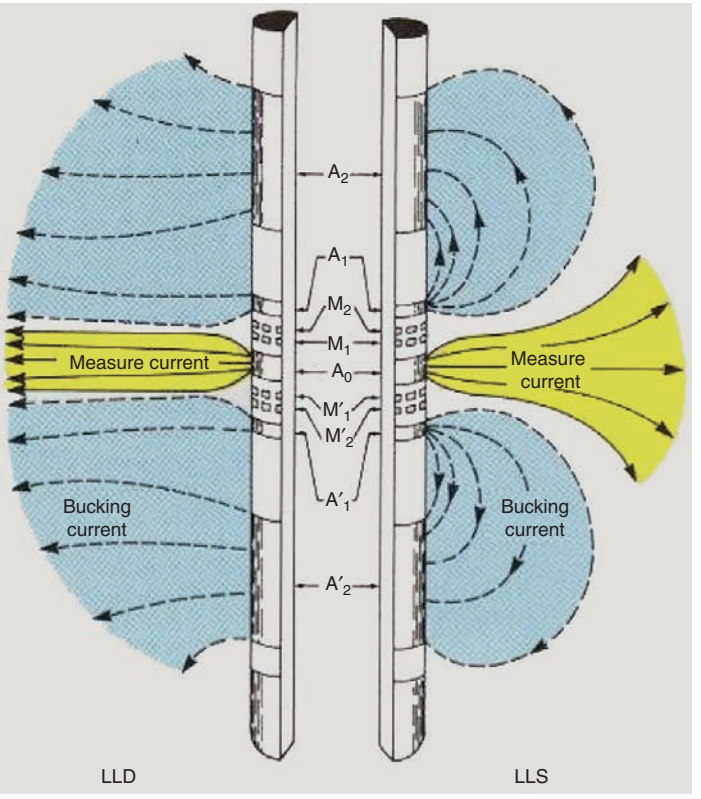


Fig. 13.5—Representative current patterns for deep and shallow laterologs. After Suau et al. (1972).

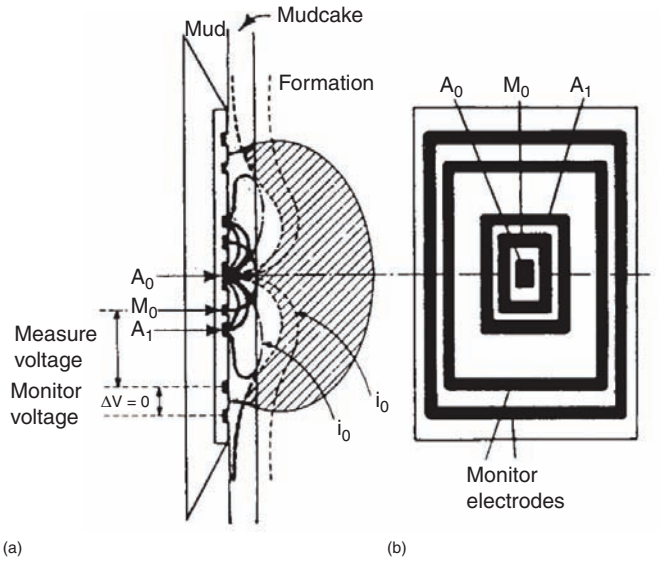


Fig. 13.6—(a) MSFL current distribution and (b) electrode arrangement (Suau et al. 1972).

passing through the mud, the invaded zone, and the undisturbed formation before arriving at the return electrode. If held constant, the current will therefore develop a series of voltage drops across each zone encountered. The relationship between these voltages can be simplistically written as:

$$V_{\text{total}} = V_{\text{mud}} + V_{\text{invaded}} + V_{\text{undisturbed}} \quad \ldots\ldots\ldots\

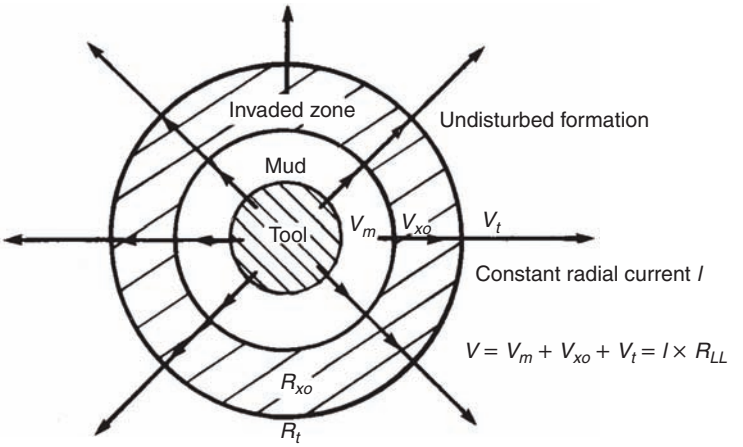


Fig. 13.8—Laterolog current paths.

V_{total} is related to the measured current I and the resistivity (R_{LL}) as measured by the tool:

$$V_{\text{total}} = I \times R_{LL} \quad \ldots\ldots\ldots\

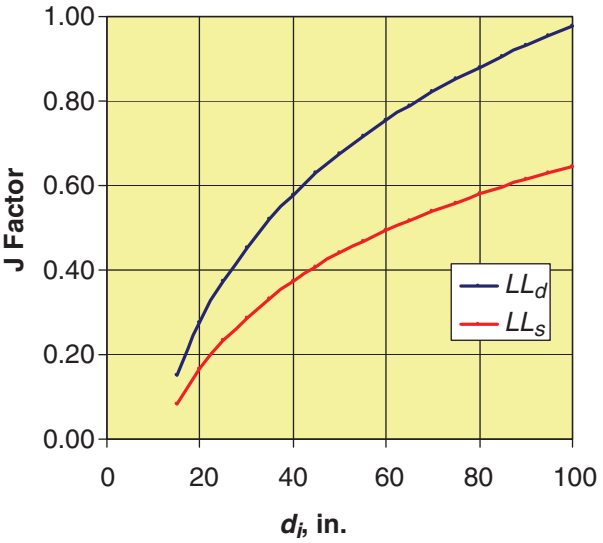


Fig. 13.10—Laterolog pseudogeometric factors.

there are three unknowns (R_t, R_{xo}, and d_i), three independent measurements are needed. This can be accomplished by means of the three measurements R_{LLd}, R_{LLs}, and R_{MSFL}. In most cases, R_{xo} can be equated to R_{MSFL}, thus eliminating one of the three unknowns. R_t and d_i are then determined by the shallow and deep laterologs that give different values for J at the same d_i (Fig. 13.10). For the same d_i, J for the deep measuring tool is less than J' for the shallow measuring tool. The deep measuring tool is more sensitive to R_t, and the shallow measuring tool is more sensitive to R_{xo}.

13.4 Borehole and Invasion Corrections

Before the three unknowns can be determined, the raw data must be corrected for borehole effects. Charts are available to achieve this. The MSFL, being a pad-contact device, is sensitive to mudcake thickness (h_{mc}) and mudcake resistivity (R_{mc}). **Fig. 13.11** shows a plot of R_{MSFL}/R_{mc} plotted against $(R_{MSFL})_{corr}/R_{MSFL}$. The lines on the chart represent various values of h_{mc}. The use of this chart corrects for the value of α discussed earlier. The value of h_{mc} is equal to half the difference between the borehole size and the caliper reading, and R_{mc} is the measured value of R_{mc} corrected back to formation temperature.

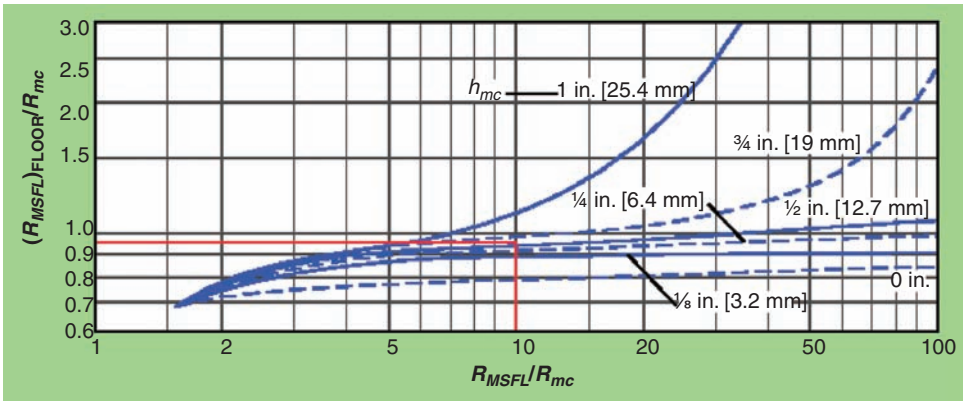


Fig. 13.11—Chart for correcting the measured value of R_{MSFL} for mudcake thickness (Schlumberger 2005). Courtesy of Schlumberger.

QUESTION 13.1.
Using Fig. 13.11, solve the following exercise:
$R_{MSFL} = 3.5\ \Omega\cdot m$.
$R_{mc} = 0.35\ \Omega\cdot m$.
$h_{mc} = 16$ mm.
$(R_{MSFL})_{corr} = ?$

The shallow laterolog hole-size correction can be accomplished by means of **Fig. 13.12,** in which R_{LLs}/R_m is plotted vs. $(R_{LLs})_{corr}/R_{LLs}$. The lines on the chart are for various values of hole diameter.

QUESTION 13.2.
$R_{LLs} = 25.0\ \Omega\cdot m$.
$R_m = 0.25\ \Omega\cdot m$.
Caliper = 14.0 in.
$(R_{LLs})_{corr} = ?$

The deep laterolog hole-size correction is accomplished by means of **Fig. 13.13,** in which R_{LLd}/R_m is plotted against $(R_{LLd})_{corr}/R_{LLd}$. The lines on the chart are for various values of hole diameter.

QUESTION 13.3.
$R_{LLd} = 50.0\ \Omega\cdot m$.
$R_m = 0.25\ \Omega\cdot m$.
Caliper = 16.0 in.
$(R_{LLd})_{corr} = ?$

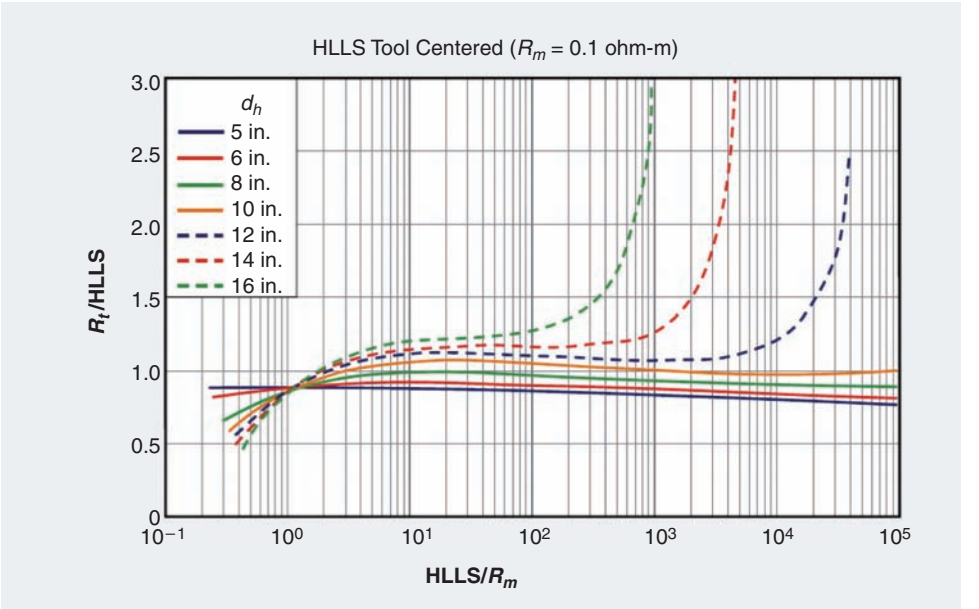


Fig. 13.12—Borehole correction chart for the shallow laterolog (after Schlumberger 2005). Courtesy of Schlumberger.

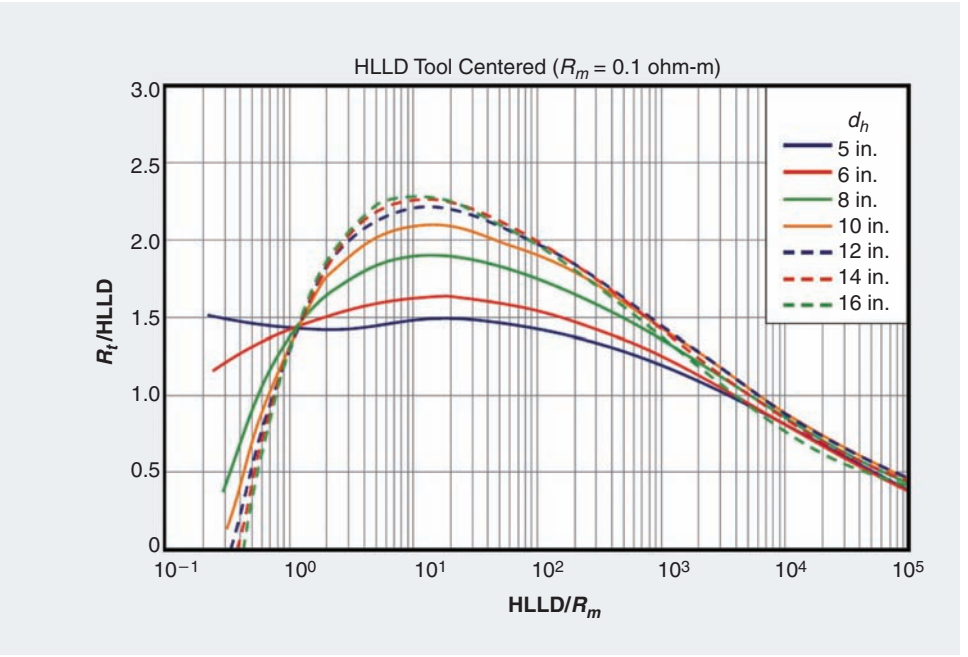


Fig. 13.13—Borehole correction chart for the deep laterolog (after Schlumberger 2005). Courtesy of Schlumberger.

In the range of normal interest, in which laterolog readings lie in the range $10 < (R_{LL}/R_m) < 100$, all corrections are within ±10%, but if hole diameters are large, the corrections needed to laterologs can become intolerably large.

Modern laterolog tools incorporate environmental corrections on the fly, and the analyst can take formation resistivity values directly from the log without resorting to the laborious use of the charts detailed here. However, it is sound practice to recognize conditions under which the tools are likely to be close to their reasonable limits for acceptable correction by even the best onboard wellsite software. In case of doubt, the "on the fly" corrections should be removed and the raw data reading corrected again in the light of better choices for environmental factors such as R_m and R_{mc}.

13.5 The Butterfly Chart

After the raw log readings have been corrected for borehole effects, they must also be corrected for invasion effects. **Fig. 13.14** can be used to compensate for the values of β and γ discussed earlier. This interpretation chart plots the ratio R_{LLd}/R_{LLS} against the ratio R_{LLd}/R_{xo}. There are three families of lines on the chart: constant values of R_t/R_{LLd}, constant values of R_t/R_{xo}, and constant values of d_i. To use the chart, it is first assumed that $(R_{MSFL})_{corr}$ is equal to R_{xo}. A point is then located on the chart at coordinates R_{LLd}/R_{LLS} and R_{LLd}/R_{xo}. This point uniquely defines the three unknowns: R_t, R_{xo}, and d_i.

QUESTION 13.4.
$R_{LLd} = 33$ Ω·m.
$R_{LLs} = 11$ Ω·m.
$R_{MSFL} = 3$ Ω·m.
$R_t = ?$
$d_i = ?$

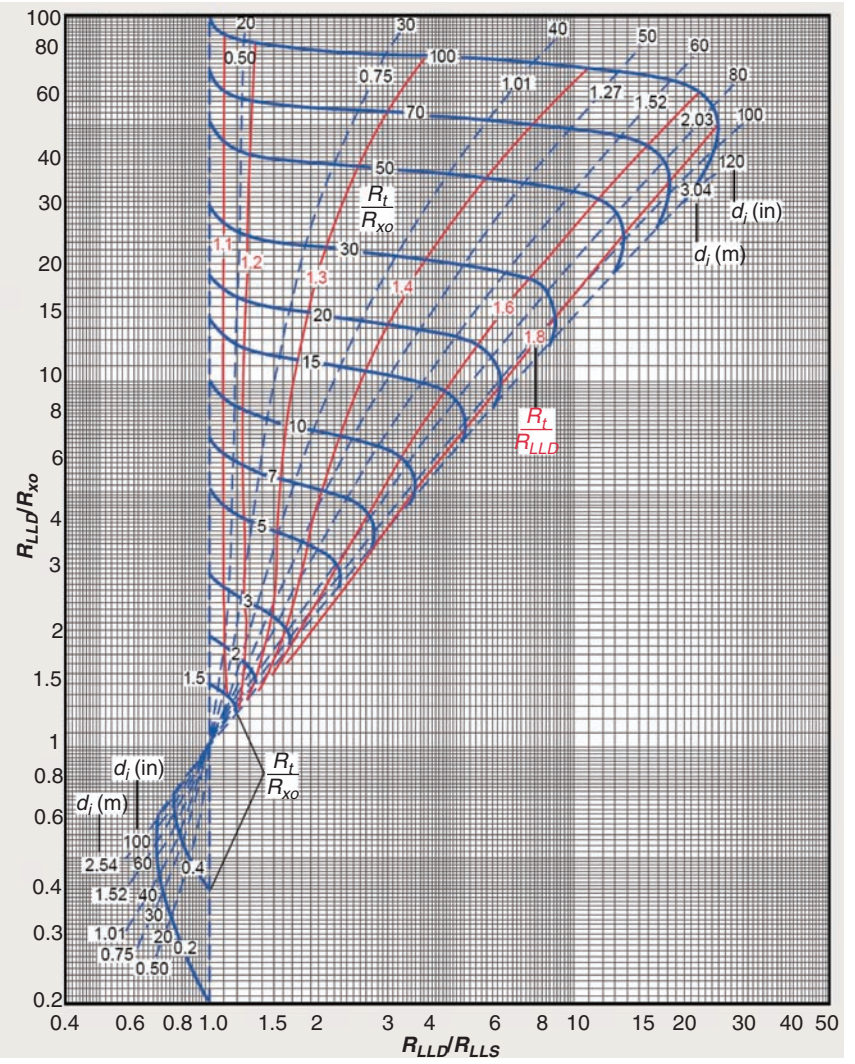


Fig. 13.14—Invasion correction chart for the DLL. Courtesy of Schlumberger.

The lower left portion of the chart corresponds to the invasion pattern $R_{MSFL} > R_{LLs} > R_{LLd}$, which usually occurs in water-saturated zones where $R_{mf} > R_w$. Because this area of the chart is rather ill-defined on Fig. 13.14, a better solution can be found using **Fig. 13.15**.

QUESTION 13.5.
$R_{LLd} = 5.0\ \Omega\cdot$m.
$R_{LLs} = 6.6\ \Omega\cdot$m.
$R_{MSFL} = 9.0\ \Omega\cdot$m.
$R_t = ?$
$d_i = ?$

13.6 DLL Fingerprints

The characteristic behavior of the DLL tool in zones with movable hydrocarbons makes quick-look interpretation very simple. The golden rule is that the pattern $R_{LLd} > R_{LLs} > R_{MSFL}$ **(Fig. 13.16a)**

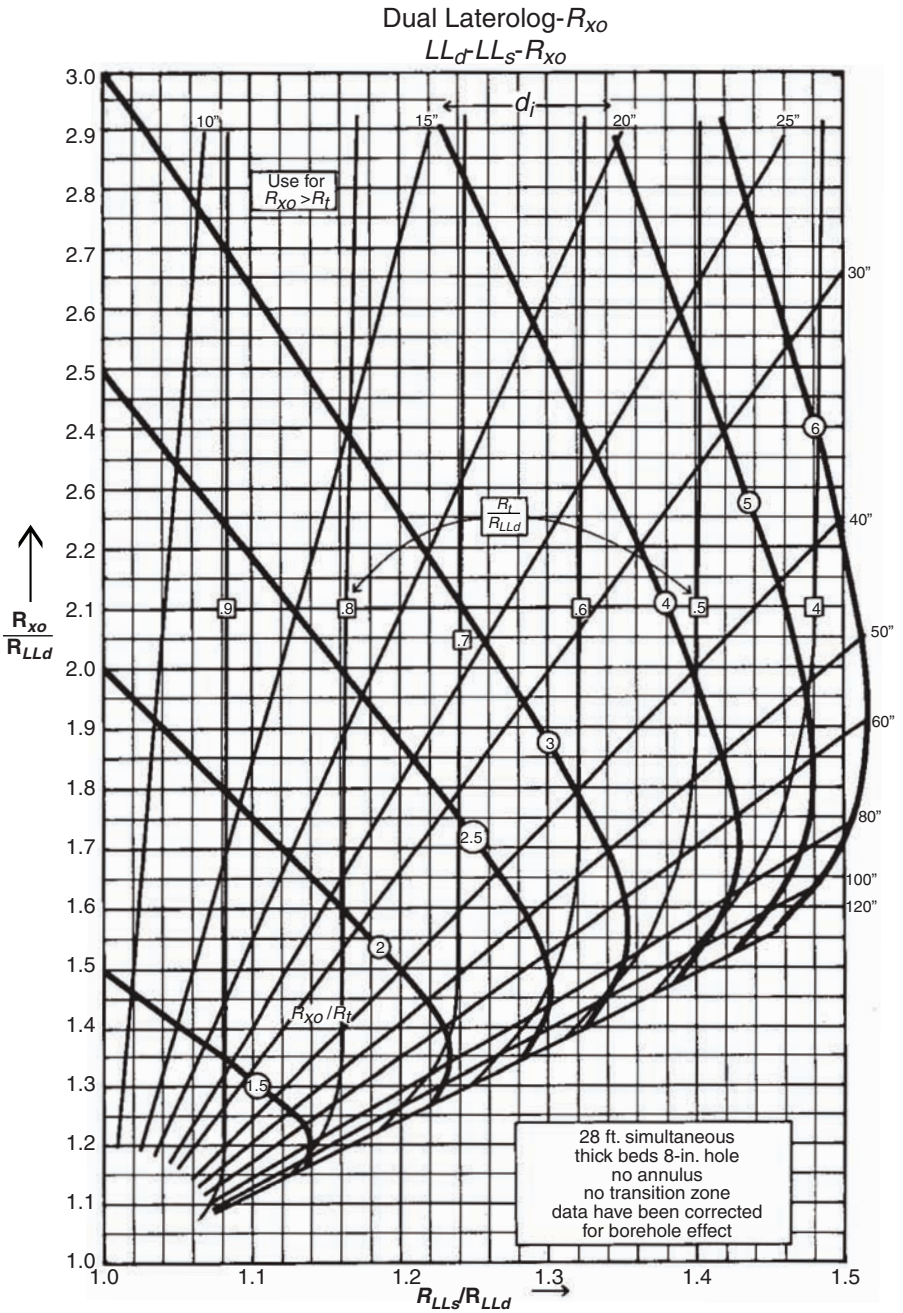


Fig. 13.15—Invasion correction chart ($R_{xo} > R_t$) for the DLL.

is a good indication that hydrocarbons are present. Conversely, the pattern $R_{MSFL} > R_{LLs} > R_{LLd}$ (Fig. 13.16b) is a good indication that the zone is wet (i.e., at 100% water saturation). Any relative ordering of the curves other than these two cases suggests little or no invasion and indicates that the zone is impermeable **(Fig. 13.17).**

13.7 Anomalous Behavior

The early laterologs were prone to various types of anomalous behavior, which are chronicled here to give some insight into the few anomalies that can still occur even with the DLL.

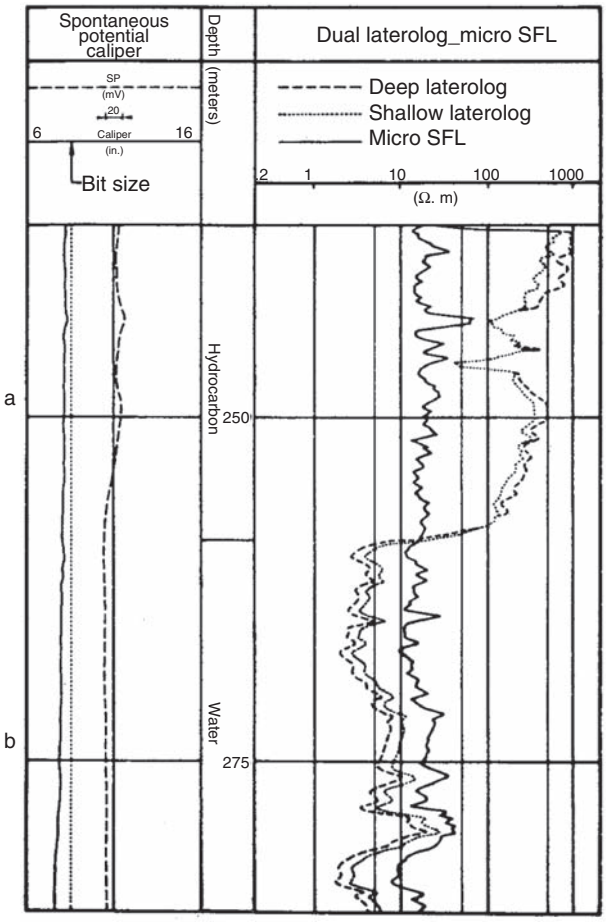


Fig. 13.16—DLL: (a) oil pattern; (b) wet pattern. Courtesy of Schlumberger.

13.7.1 The Delaware Effect. In the early 1950s in the Permian Basin, logging engineers found that laterologs behaved anomalously when approaching a thick resistive bed, such as the massive anhydrite that overlies the Delaware sand. The effect manifested itself by a gradual increase in apparent resistivity starting when the bridle entered the highly resistive bed.

Apparent resistivities would climb to as much as 10 times the value of R_t before the sonde itself entered the highly resistive bed. The solution for the Laterolog-7 was to place the B return electrode at the surface. For the conductivity laterolog, the solution was not as elegant because these devices were using a 280-Hz survey current generated in the cartridge. Locating the return at the surface did not solve the problem because the skin effect restricted the return current to a sheath around the borehole, and the lower part of the cable then became the effective return electrode **(Fig. 13.18).** Compensation for this effect with the laterolog-3 involved a messy setup with two sondes, one on each side of a cartridge, and a B return on the bottom for Delaware situations. Nevertheless, for all practical purposes, the laterolog-3 remained prone to the Delaware effect.

13.7.2 Anti-Delaware Effect. In an attempt to counteract this situation and to provide a dual-spacing laterolog, a tool was introduced with both deep and shallow devices. However, this device also exhibited anomalous behavior beneath highly resistive beds. The deep laterolog showed a decreasing resistivity gradient, the exact opposite of the Delaware effect. With the B electrode at surface (effectively at zero potential), the N electrode acted as the takeoff point for a potential

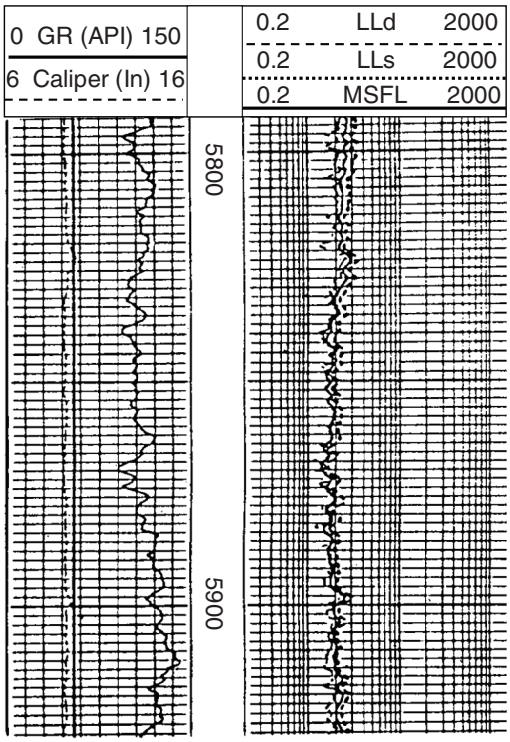


Fig. 13.17—DLL shale pattern.

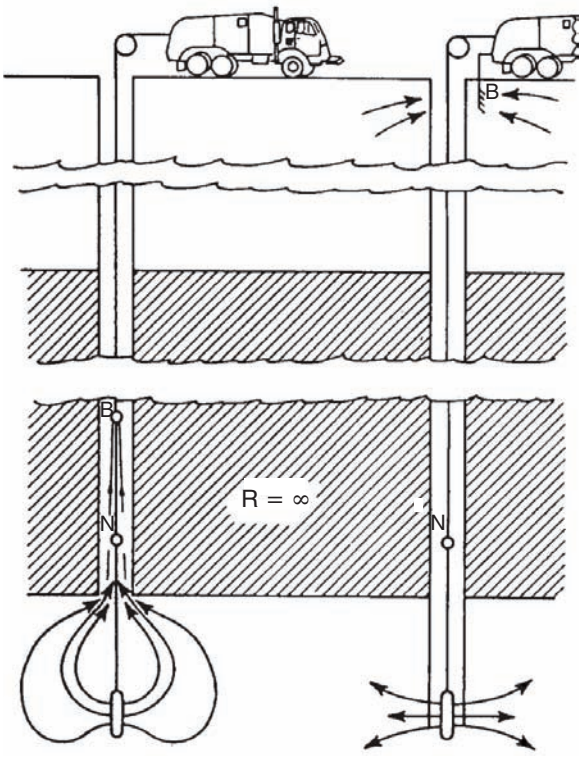


Fig. 13.18—Schematic of the Delaware effect (Suau et al. 1972).

divider formed by the borehole below and above N. The approaching sonde, at some positive potential, would then cause the potential of N to increase.

The anti-Delaware effect would at worst cause a 50% reduction in the deep-laterolog measurements and would be noticeable only within 35 ft of the resistive bed. In fact, the effect had been present on the earlier "B at surface" Delaware-free laterologs, but it had not been noticed because there was no shallow laterolog with which to compare the deep laterolog. The DLLs in use today incorporate features that ensure virtual freedom from both Delaware and anti-Delaware effects.

13.7.3 The Groningen Effect. First noticed during gas-well logging in Holland, the Groningen effect manifests itself as a too-high LL_d reading when the N electrode enters a highly resistive bed. From a distance of A_0N below the bed boundary (102 ft for the simultaneous DLT), the LL_d reading increases over a short distance to an anomalously high value, which it will then maintain until the bed is entered.

In some instances, the high-resistivity anomaly was misinterpreted as an indication of a hydrocarbon-bearing interval, with the result that the well was completed, at great expense, only to produce saltwater. Experiments have indicated that the effect is dependent on operating frequency and is troublesome only in low-resistivity formations immediately below a massive salt or anhydrite bed. Therefore, the Groningen effect will appear (if at all) within 102 ft (31 m) of a resistive bed and will be of interpretive importance only where R_t in the underlying bed is less than 10 Ω. It can still appear even if casing is set to the bottom of the resistive bed.

Even if resistive-bed effects do not distort the dual-laterolog measurements, other environmental influences will affect them, simply because a tool cannot be built that is entirely immune to the disturbing effects of the borehole and adjacent beds. For interpretative work, these distorting influences must be taken into account. Hole-size and invasion effects have been covered in the foregoing discussions; the need for shoulder-bed corrections is also worth noting.

13.7.4 Shoulder-Bed Corrections: Squeeze and Antisqueeze. When the sonde is in front of a bed, on either side of which there is a resistive shoulder, current tends to concentrate in the least resistive path; in other words, the current is "squeezed" between the resistive shoulders into the formation of interest. To correct for this effect, the charts in **Figs. 13.19 and 13.20** have been compiled.

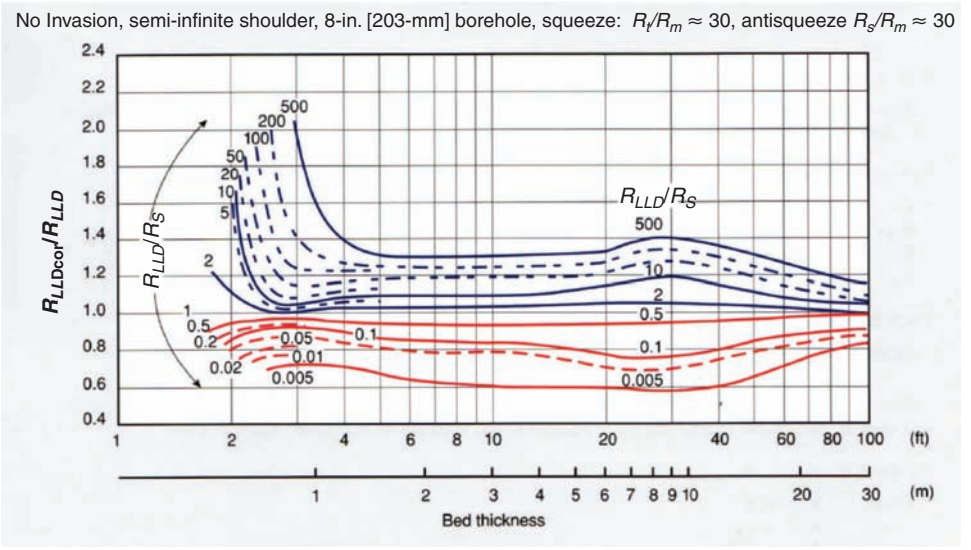


Fig. 13.19—Shoulder-bed correction chart for the deep laterolog. Courtesy of Schlumberger.

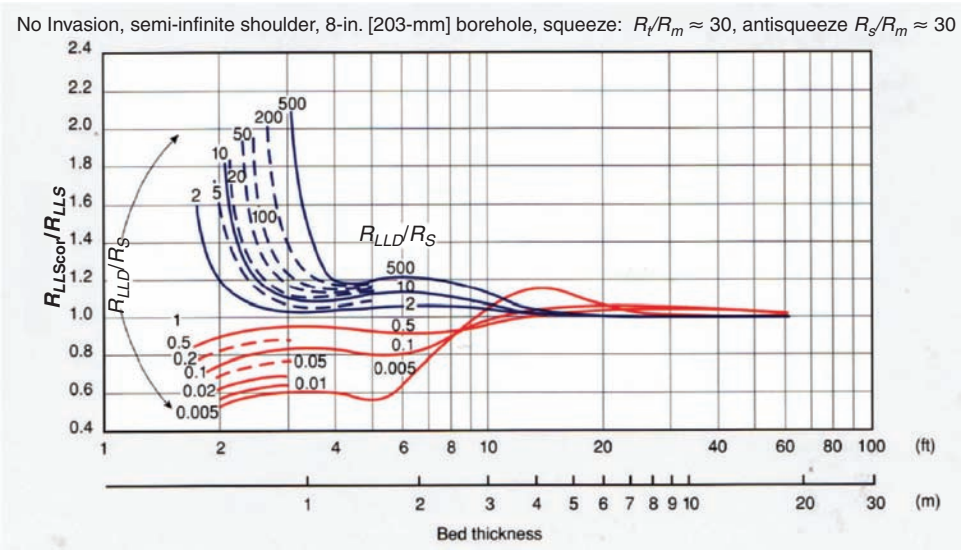


Fig. 13.20—Shoulder-bed correction chart for the shallow laterolog. Courtesy of Schlumberger.

The correction factor (R_c/R_a) to be applied to the borehole corrected log reading is shown as a function of bed thickness and R_a/R_s, which is the ratio of the apparent reading to the shoulder resistivity. If R_a/R_s is less than one, a squeeze situation exists, and the apparent log reading is too high (lower half of chart). If R_a/R_s is greater than one, the bed is surrounded by a conductive shoulder, and the current tends to fan out into the path of least resistance: the conductive shoulders. (Because this is the reverse of squeeze, it is referred to as antisqueeze). In this situation, the apparent log readings are too low.

Two observations should be made here. First, an inversion occurs as bed thickness increases through 9.5 ft for LL_s (this is not evident from the chart), and for formation thicknesses greater than 20 ft, LL_s is free from shoulder effects. Second, LL_d is much more affected by squeeze and antisqueeze than is LL_s, even in what might be considered thick beds (50 ft or more).

When making detailed interpretations, use the shoulder-bed correction charts for LL_d after borehole correction and before any other step. Invasion corrections may then be made using Fig. 13.14. A word of caution is in order. In general, an ideal laterolog has a J that varies logarithmically with d_i, but is also a function of the contrast between R_{xo} and R_t. In addition, one effect of a hole size larger than 8 in. is that part of the R_{xo} zone is replaced by mud; this changes the effective position of the origin on the J-versus-d_i plot. Fig. 13.14 therefore gives correct answers in 8-in. holes with thick beds. In larger holes or in thin beds, it will be in error. If the effect of antisqueeze is taken into account (resistive beds, conductive shoulders, pay sand with adjacent shaly shoulders), the effective depth of investigation of LL_d will be reduced. The difference between the LL_s and LL_d measurements will therefore also be reduced. A recent study has shown that even at a bed thickness of 8 ft, the effective depth of investigation of LL_d is close to that of LL_s. Under these conditions, there can be no solution for R_t unless d_i is known. Therefore, separation between LL_d and LL_s values will not be observed in beds thinner than 8 ft, even when R_t is greater than R_{xo}.

13.8 Summary

In low-resistivity (< 10 Ω·m) formations below a massive resistive bed, watch for the Groningen effect (R_{LLd} reads too high within a distance of A_0N of the bed boundary).

When interpreting laterologs, make borehole corrections first, shoulder-bed corrections second (if required), and invasion corrections last **(Fig. 13.21).**

Use Fig 13.14 with care in large holes and when the R_{xo}/R_t ratio is large in thin formations.

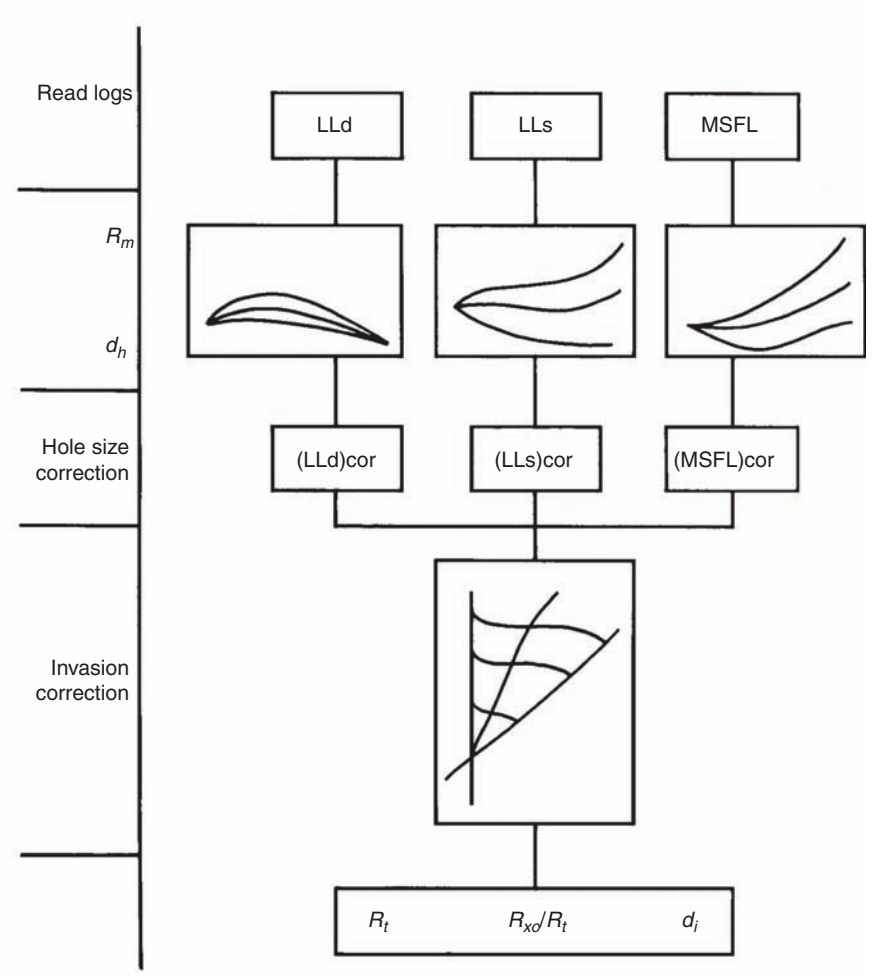


Fig. 13.21—Quick guide to R_t from the DLL.

References

Schlumberger. 1989. *Log Interpretation Principles/Applications*, seventh edition. Sugar Land, Texas: Schlumberger.

Schlumberger. 2005. *Historical Log Interpretation Charts*.

Suau, J., Grimaldi, P., Poupon, A., et al. 1972. The Dual Laterolog-R_{xo} Tool. Paper SPE 4018 presented at the SPE Annual Meeting, San Antonio, Texas, USA, 8–11 October. http://dx.doi.org/10.2118/4018-MS.

General References

Chemali, R., Gianzero, S., Strickland, R. et al. 1983. The Shoulder-Bed Effect on the Dual Laterolog and Its Variation With the Resistivity of the Borehole Fluid. *Trans*., 24th SPWLA Annual Logging Symposium, Calgary, 27–30 June, Paper UU.

Doll, H.G. 1951. The Laterolog: A New Resistivity Logging Method With Electrodes Using an Automatic Focusing System. *J. Pet Tech* **3** (11): 305–316; *Trans.,* AIME, **192**. SPE-951305-G.

Horst, G. and Creager, L. 1974. Progress Report on the Interpretation of the Dual Laterolog-R_{xo} Tool in the Permian Basin. *Trans.,* 15th Annual SPWLA Logging Symposium, Corpus Christi, Texas, USA, 2–5 June.

Maurer, H., Antonov, Y., Corley, B. et al. 2009. Advanced Processing for a New Array Laterolog Tool. *Trans.,* 50th Annual SPWLA Logging Symposium, The Woodlands, Texas, USA, 21–24 June, Paper AA.

Zhou, Z., Corley, B., Khokhar, R. et al. 2008. A New Multi-Laterolog Tool With Adaptive Borehole Correction. Paper SPE 114704 presented at the SPE Annual Technical Conference and Exhibition, Denver, 21–24 September. http://dx.doi.org/10.2118/114704-MS.

Answers to Questions

QUESTION 13.1.
$(R_{MSFL})_{corr} = 3.3\ \Omega\cdot m$.

QUESTION 13.2.
$(R_{LLs})_{corr} = 32.5\ \Omega\cdot m$.

QUESTION 13.3.
$(R_{LLd})_{corr} = 48.0\ \Omega\cdot m$.

QUESTION 13.4.
$R_t = 46.2\ \Omega\cdot m$.
$d_i = 40$ in.

QUESTION 13.5.
$R_t = 3.0\ \Omega\cdot m$.
$d_i = 40$ in.

Chapter 14

Microresistivity Measurements

Measurements made by use of microresistivity tools have a variety of uses, such as:

- Well-to-well correlation
- Thin-bed delineation
- Flushed- or invaded-zone saturation, S_{xo}
- Residual-oil saturation (ROS)
- Hydrocarbon movability
- Hydrocarbon density (ρ_{hy})
- Invasion diameter (d_i)
- Refinements to R_t by invasion corrections to readings from deep-resistivity devices

A variety of tools, both old and new, are available; each has its own special characteristics. This section will present the names, uses, and idiosyncrasies of microresistivity tools.

14.1 Microresistivity Tools

The following list covers most of the microresistivity tools available:

- 16-in. SN short normal log
- LL-8 laterolog-8
- SFL spherically focused log
- MLL microlaterolog
- PL proximity log
- MSFL microspherically focused log
- ML microlog

These tools can be divided into two main groups: *mandrel tools* and *pad-contact* tools. The electrodes of a mandrel tool are placed on a cylindrical mandrel that is run in the hole. They do not require physical contact with the formation, but they do require a conductive (water-based) mud system to function correctly. Strictly speaking, mandrel tools should not be considered *micro*-resistivity tools because they take their readings in the part of the formation that lies between the flushed zone (R_{xo}) and the undisturbed zone (R_t), but they are included in this discussion because they do not qualify as *bona fide* deep-resistivity devices.

The electrodes of a pad-contact tool are embedded in insulating pads that are carried on caliper arms, which are forced against the borehole wall. There are now microresistivity pad-contact tools that generate adequate readings in oil-based mud systems as well. The sizes and ratings of micro-resistivity tools are summarized in **Table 14.1.** These devices are usually run in combination with some specific deep-resistivity device, as shown in **Table 14.2.**

TABLE 14.1—MICRORESISTIVITY TOOLS: TYPES AND RATINGS

Name	OD (in.)		
16-in. SN	$2^3/_4$ to $3^7/_8$	Mandrels	All devices are rated for 20,000 psi and 350°F.
LL8	$3^3/_8$ and $3^7/_8$		
SFL	$3^1/_2$		
MLL	$5^1/_{16}$	Pads	
PL	$5^1/_2$		
MSFL	$5^1/_4$		
ML	$5^1/_{16}$		

TABLE 14.2—MICRORESISTIVITY TOOLS: APPLICATIONS

Microtool	Usually Run With	Main Tool
MSFL		Dual laterolog
LL-8 or SFL		Dual induction log
SFL or SN		Induction log
MLL or PL		Microlog
ML		Microlaterolog or Proximity log

14.1.1 The Microlog: ML. The microlog is worthy of special mention because it is an underrated device that should be run more frequently than it is. It was one of the first microresistivity devices on the market and has had a spectacular career. Originally, it was used as a pseudoporosity device. When modern improved porosity devices were developed, the microlog was relegated to the pile of "has-beens" by many people in the logging industry. Nevertheless, it is still a valuable tool because it offers a superb visual identification of porous and permeable zones**. Fig. 14.1a** illustrates the microlog tool, which carries an array of three electrodes on a pad that makes intimate contact with the formation. Fig. 14.1b shows the electrode arrangement on the microlog pad and the current paths through the mudcake and the invaded formation close to the borehole wall.

Effectively, the tool measures two resistivities, one very close to the pad where the measurement current passes through the mudcake (if present) and generates one reading on the log (the microinverse, $R_{1''x\,1''}$) that is close to the mudcake resistivity, R_{mc}, and a second that passes through the mudcake, "sees" the flushed or invaded zone, and generates a reading on the log (the micronormal, $R_{2''}$) that is closer to R_{xo}. In porous and permeable zones, the two curves are separated. In non-permeable zones, because of the lack of invasion and hence the absence of mudcake, the two read the same.

An example log showing porous and permeable sections (highlighted in red) is shown in **Fig. 14.2.** Note that where the two microresistivity curves diverge, the microcaliper (in Track 1) also shows a hole size less than the bit size because of mudcake buildup.

14.1.2 The Microlaterolog: MLL. The analyst may find examples in older well files of presentations showing a combination of both the microlog and microlaterolog plots, as shown in **Fig. 14.3.** On this log presentation, the presence of permeability is indicated wherever the micronormal curve reads higher than the microinverse curve (presented in Track 1). The main (logarithmic) resistivity track shows a near-wellbore measurement of formation resistivity that should be close to R_{xo}. In this example from 11,332 to 11,355 ft, the value of R_{MLL} lies between 10 and 20 Ω·m.

In the absence of modern porosity devices, it is possible to make certain formation evaluations based solely on the readings from a microlog. For example, **Fig. 14.4** crossplots $R_{2''}/R_{mc}$ against $R_{1''x1''}/R_{mc}$ (where the micronormal curve is referred to as $R_{2''}$ and the microinverse curve as $R_{1''x\,1''}$).

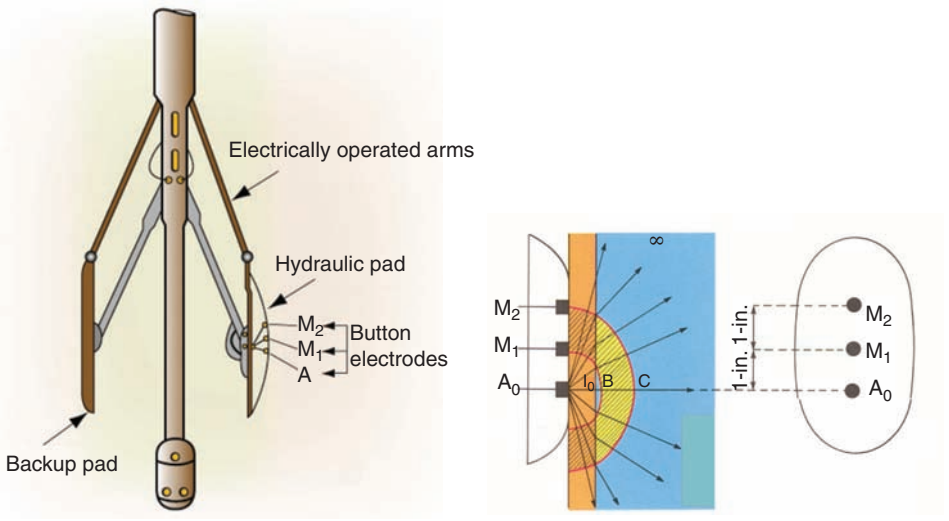


Fig. 14.1—(a) Microlog tool and (b) microlog electrode arrangement and current paths.

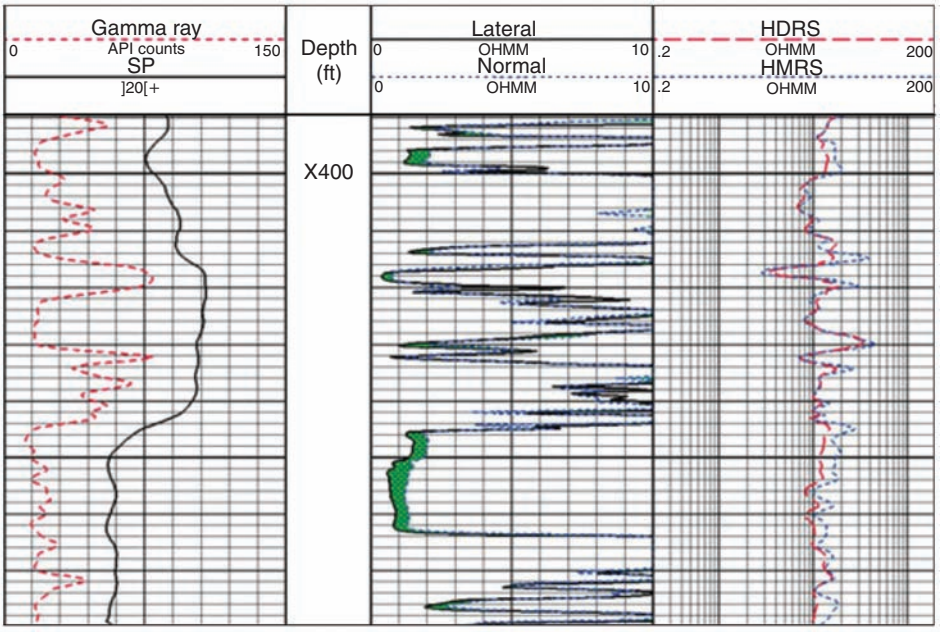


Fig. 14.2—Example microlog presentation.

The plotted points define values of R_{xo}/R_{mc} and mudcake thickness (h_{mc}). If the mudcake thickness is known from observation of the microcaliper, then the value of R_{xo} can be deduced. Going one step further, porosity may be deduced if R_{mf} is known and S_{xo} can be guessed using Archie's equation:

$$\phi^m = \frac{a \times R_{mf}}{R_{xo}\left(S_{xo}\right)^n} \quad \ldots\ldots\ldots\

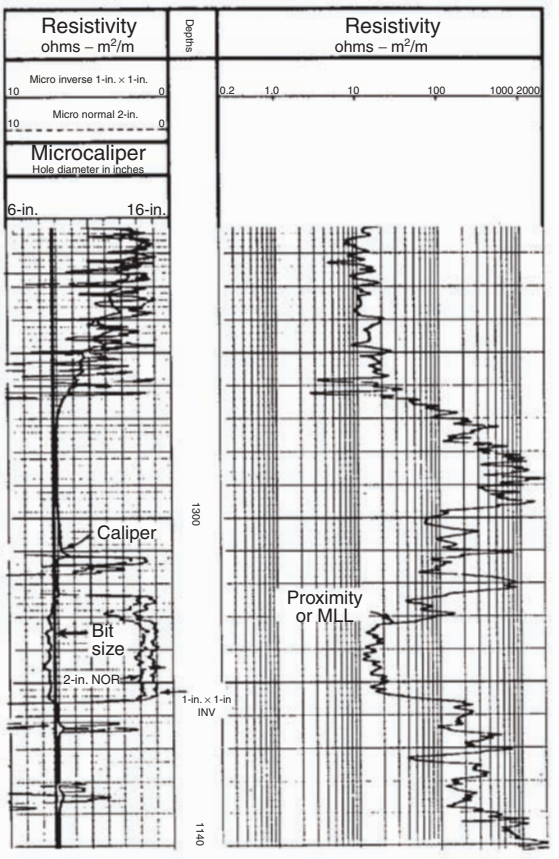


Fig. 14.3—Presentation of proximity log-microlog combination. Courtesy of Schlumberger.

In the case that $a = 1$ and $m = n = 2$, this expression reduces to

$$\phi = \frac{1}{S_{xo}} \sqrt{\frac{R_{mf}}{R_{xo}}} \quad \ldots\ldots\ldots\

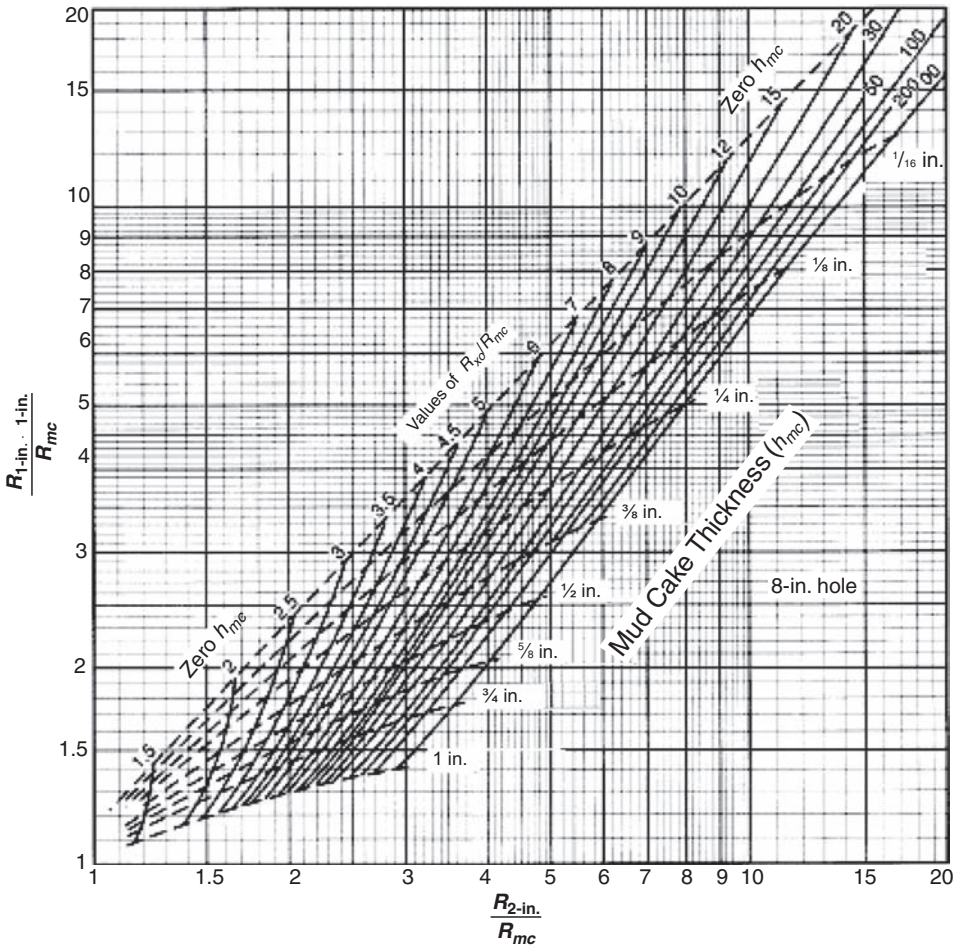


Fig. 14.4—Microlog interpretation chart (Schlumberger 2005). Courtesy of Schlumberger.

"intermediate"-resistivity devices, the SFL reads deeper than a proximity log and shallower than a laterolog-8. It also suffers less severely from the deleterious effects of large hole size and has the bonus of better bed resolution, as illustrated in the comparative figures given in **Table 14.3.**

The current-path focusing pattern associated with this tool **(Fig. 14.6)** leaves little doubt as to where the tool's name came from.

14.2 Depth of Investigation

Each microresistivity tool has its characteristic depth of investigation. It is important to know this depth for each tool to select the one with the right characteristics for the job. When invasion is shallow, a tool with a shallow depth of investigation is needed if the tool is to read R_{xo} without undue influence from R_t. Conversely, in situations in which deep invasion exists, a deep investigation tool will ensure a reading of R_{xo} free from any effects of R_{mc}.

As with other tools, no single value for depth of investigation can be used. Rather, a pseudogeometric factor must be used. This factor indicates how much of the total tool signal is received from an annular formation volume represented by a radial distance (expressed in inches) from the borehole wall **(Fig. 14.7).** Table 14.3 lists the radial depths of investigation for several microresistivity tools.

Many of the tools listed here are considered obsolete today. However, the analyst may encounter situations where an assessment needs to be made of the worth of an old field that may be

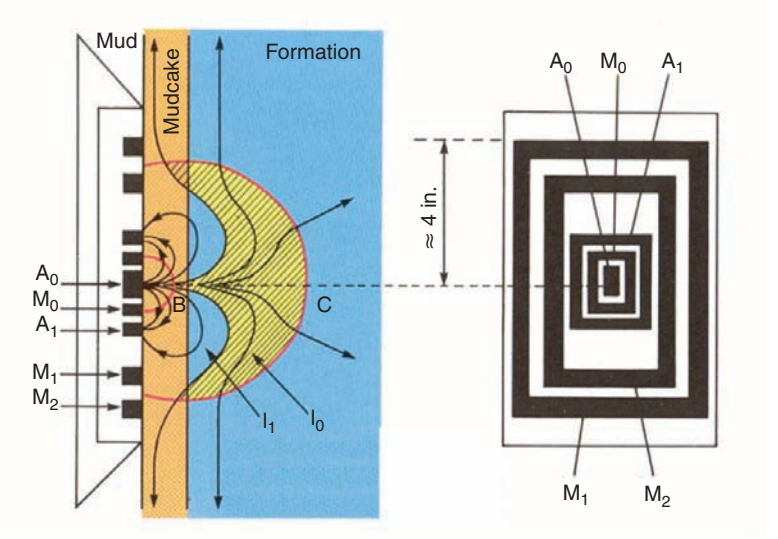


Fig. 14.5—Microspherically focused log electrode arrangement (Schlumberger 1989).

TABLE 14.3—MICRORESISTIVITY TOOLS: BED RESOLUTION AND RADIAL INVESTIGATION

Rank		Tool Name	Vertical Bed Resolution (in.)	Radial Distance for 90% Response (in.)
1.	ML	Microlog	3	1
2.	MII	Microlaterolog	6	4
3.	MSFL	Microspherically focused log	12	4.5
4.	PL	Proximity log	12	10
5.	SFL	Spherically focused log	12	24
6.	LL8	Laterolog-8	12	49
7.	SN	16-in. Short Normal log	24	70+

subject to trading. In such cases, it is useful to be able to work with such "legacy" materials that may lurk in the well files of fields drilled and produced decades in the past. An example of such an analysis can be seen in Question 14.1 in conjunction with the chart shown in Fig. 14.4.

14.3 Bed Resolution

As each microresistivity tool has its characteristic depth of investigation, each tool also has its own characteristic bed resolution; in other words, some tools are better than others at distinguishing thin beds. Tools with large bed-resolution values are "blind" to thin shale or sandstone layers. For example, 3-in. shale streaks will not be "seen" by a short normal log. Table 14.3 summarizes the bed resolution of each microresistivity device.

Fig. 14.8 shows a direct comparison of the results from SFL and MSFL devices run in the same well through a water-bearing section with an R_{mf}/R_w ratio of approximately 6:1. It is evident that the MSFL has superior vertical bed resolution and that the SFL is reading deeper into the formation than its microresistivity cousin.

14.4 Environmental Corrections

Microresistivity devices of the mandrel type are subject to aberrations resulting from the size of the wellbore. These effects can be quite severe. The pad-contact tools, however, are

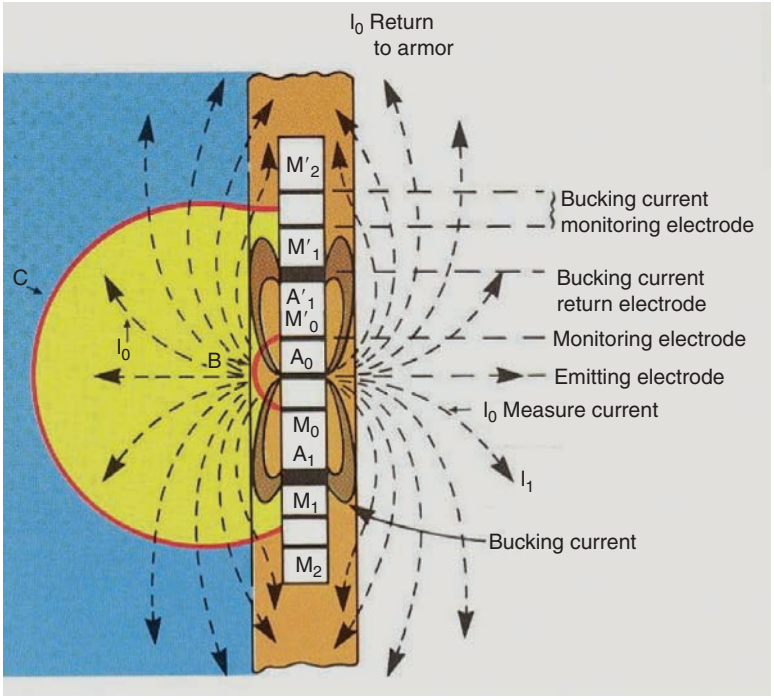


Fig. 14.6—SFL electrode arrangement and current paths.

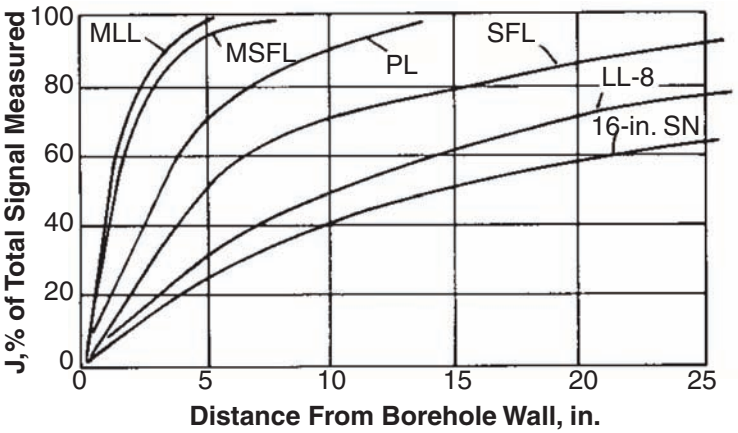


Fig. 14.7—Radial depth of investigation for microresistivity tools.

affected only by excessive mudcake thickness and loss of contact with the formation in rugose holes. If pad contact with the formation is maintained, the pad-contact tools are unaffected by the size of the wellbore. Mudcake corrections can be made for the microlaterolog and the proximity log by reference to (historic) service company correction charts (not shown here). Corrections for mandrel-type tools can be made by use of similar charts generated for the 16-in. SN, LL-8, and SFL tools. Modern microresistivity tools generally apply the environmental correction "on the fly" at the time of logging, sparing the analyst from using manual correction charts.

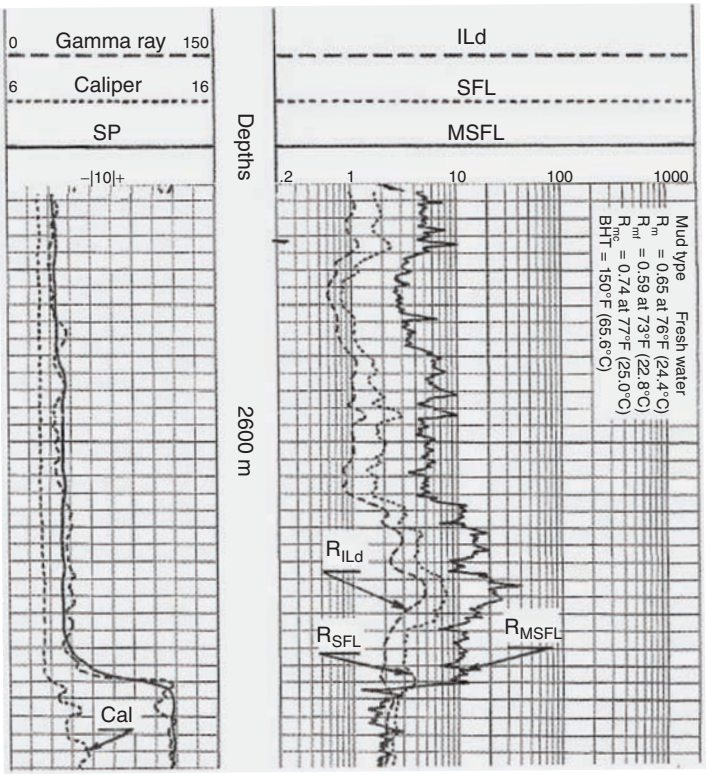


Fig. 14.8—Comparison of MSFL and SFL bed resolution and radial depth of investigation.

14.5 S_{xo} and Hydrocarbon Movability

The water (filtrate) saturation in the flushed zone (S_{xo}) can be estimated using Archie's equation:

$$\left(S_{xo}\right)^n = F\,R_{mf}/R_{xo} \quad \ldots\ldots\ldots\

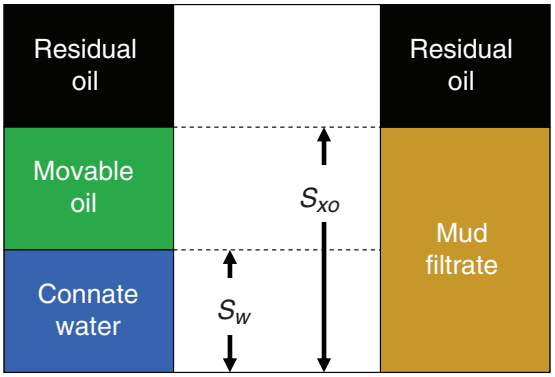


Fig. 14.9—Hydrocarbon movability.

determined by the relationship $\phi\ (S_{xo} - S_w)$. The percentage of the original oil in place that has moved is determined by

$$\%\,\text{OOIP moved} = \frac{S_{xo} - S_w}{1 - S_w} \times 100 \quad \ldots\ldots\ldots\

14.7 Calibration and Quality Control

Quality control for microresistivity devices can be summarized by the following maxims:

- Beware of washed-out holes because (a) pad-contact tools lose contact with the formation and float in the mud column and (b) mandrel tools give severely inaccurate readings.
- Beware of thick mudcakes because pad-contact tools require large corrections. If hole conditions are bad, do not try to measure R_{xo} because either the tool will stick or the pad will tear up. Either way, no usable log reading will be obtained.

References

Schlumberger. 1972. *Log Interpretation: Volume 1—Principles*.

Schlumberger. 1989. *Log Interpretation Principles/Applications*, seventh edition. Sugar Land, Texas: Schlumberger.

Schlumberger. 2005. *Historical Log Interpretation Charts*.

General References

Doll, H.G., 1950. The Microlog. SPE- 950155-G. *Trans.*, AIME **189:** 155–164.

Doll, H.G., 1955. Filtrate Invasion in Highly Permeable Sands. *Pet. Eng. J.* **27** (1): B53–B66. Dallas: Petroleum Engineer Publishing.

Doll, H.G., 1953. The Microlaterolog. *J. Pet Tech* **5** (1): 17–32; *Trans.,* AIME, **198.** SPE-217-G.

Doll, H.G., Dumanoir, J.L., and Martin, M. 1960. Suggestions for Better Electric Log Combinations and Improved Interpretations. *Geophysics* **25** (4): 854–882.

Answers to Questions

QUESTION 14.1.
$h_{mc} = 3/8$ in.
$R_{xo} = 7\ \Omega\cdot$m.

QUESTION 14.2.
$S_{xo} = 75\%$.

QUESTION 14.3.
% OOIP moved = 50%.

Chapter 15

Dielectric Measurements

The dielectric constant of a material affects how an electromagnetic wave passes through it. Because the dielectric constants of oil and water are different, the behavior of electromagnetic waves in reservoir rocks is of interest. The measurement of ultrahigh-frequency (microwave) electromagnetic propagation has therefore formed the basis for both wireline logging measurements and measurements on drillpipe (see Chapter 3).

15.1 Electromagnetic Propagation Tools (EPT)

Traditionally, measurement of the electrical conductivity or resistivity of a formation has been one of the main surveys performed in a borehole, primarily to determine water saturation. Development of the first dielectric device, the EPT, made it possible to use another electrical characteristic of the formation, the dielectric permittivity (or dielectric constant), to estimate formation water saturation. This dielectric permittivity is not read directly. The basic measurement made by a dielectric tool is the propagation time and attenuation of an electromagnetic wave as it passes through a specific formation interval. Because this propagation time is substantially higher in water than in hydrocarbons or minerals, the dielectric measurement is affected primarily by the water-filled porosity. (The nuclear porosity tools, on the other hand, are influenced by the total porosity.) Over a wide range of salinities, the propagation time in water is practically constant, and therefore saturation estimates can be made without resistivity data for water. When other openhole log data are available, it is possible to distinguish between oil, gas, and water in reservoirs with unknown or changing R_w. This is particularly useful in places where conventional resistivity logging has difficulty in distinguishing between hydrocarbons and fresh formation water.

15.2 Physical Principle

The dielectric constant is one of the main factors affecting how an electromagnetic wave propagates through a medium. In general, the electric field E resulting from an electromagnetic wave can be described by the equation:

$$\Delta E = \varepsilon\mu \frac{\partial^2 E}{\partial t^2}, \quad \text{.....(15.1)}$$

where μ is the magnetic permeability of the medium. In the case of a plane wave passing through a nonferromagnetic material, the general equation has the solution:

$$E = E_0 e^{j\omega t - \gamma x}, \quad \text{.....(15.2)}$$

where:

x is the distance traveled by the wave,
ω is the frequency of the wave,
E_0 is the value of E at time 0,

j is the square root of −1,
t is time, and
γ is the complex propagation constant ($\gamma^2 = -\omega^2 \mu_0 \varepsilon$).

ε is usually a complex number and can be written as $\varepsilon = \varepsilon' - j\varepsilon''$, where ε' is the permittivity of the medium and ε'' the loss factor. The term γ can be simplified to the form $\alpha + \beta j$, where α is the attenuation factor and β is the phase shift.

If the preceding relationships are known, the dielectric permittivity of the medium can be found by measuring the phase shift and attenuation of a single-frequency electromagnetic wave. By relating this permittivity to the dielectric permittivity of free space, ε_0, the dielectric constants ε_r' and ε_r'' can be calculated:

$$\varepsilon_r' = \frac{\varepsilon'}{\varepsilon_0} = \frac{1}{\varepsilon_0 \mu_0 \omega^2} (\beta^2 - \alpha^2) \quad \ldots\ldots\ldots\

This enables both shallow and deep readings into the formation radially away from the borehole and the invaded zone. These newer tools have the antenna array pad mounted on an articulated arm so that it is free to follow the wellbore contours and can provide more reliable readings in rugose holes.

Interpretation of these surveys is based on the same principles, although some adjustments are required to suit the idiosyncrasies of the various measurements. Detailed discussion of interpretation will be limited here to the 1.1-GHz measurement.

15.3 Measurement Principles for Dielectric Logging Tools

15.3.1 EPT. The EPT (shown in **Fig. 15.1**) is a pad-type tool with an antenna pad attached rigidly to the body of the tool. A backup arm has the dual purpose of pressing the pad against the borehole wall and providing a caliper measurement. A standard microlog pad is also attached to the main arm, enabling a resistivity measurement to be made with a vertical resolution similar to that of the electromagnetic measurement. A smaller arm, exerting less force, is mounted on the same side of the tool as the pad and is used to detect the degree of rugosity of the borehole. The borehole diameter is the sum of the measurements from these two independent arms.

Two microwave transmitters and two receivers are mounted in the antenna-pad assembly in a borehole-compensation (BHC) array that minimizes the effects of borehole rugosity and tool tilt **(Fig. 15.2)**. The two transmitter/receiver spacings, 8 and 12 cm, are chosen to achieve an acceptable depth of investigation while ensuring that the detected signals will have sufficient amplitude without the possibility of phase wraparound (see **Fig. 15.3**). A 1.1-GHz electromagnetic wave is sent sequentially from each of the two transmitters; the amplitude and phase shift of the wave are measured at each of the two receivers **(Fig. 15.4)**. The absolute values of the amplitude and phase shift are found by comparison with an accurate known reference signal generated in the tool. The phase shift β, the wave propagation time t_{pl}, and the attenuation A over the receiver/receiver spacing are calculated from the individual measurements. In each case, an average is taken of the measurements derived from the two transmitters. A complete BHC measurement is made 60 times per second; these individual measurements are accumulated and averaged over a formation interval of either 2 in. or 6 in. before being recorded on optical or magnetic media.

Because of the close proximity of the receivers to the transmitters, spherical waves are being measured. Therefore, a correction factor is applied to the measured attenuation so that the

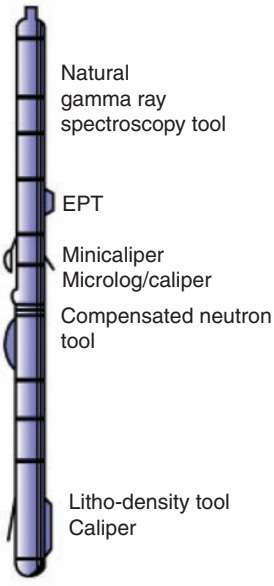


Fig. 15.1—EPT tool (Johnson and Evans 1983). Reprinted by permission from the SPWLA.

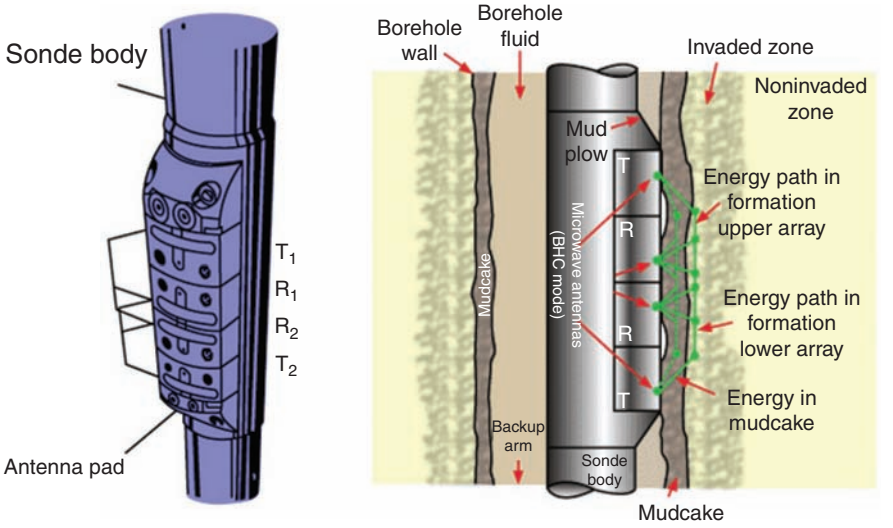


Fig. 15.2—EPT antenna configuration and signal paths (Johnson and Evans 1983). Reprinted by permission from the SPWLA.

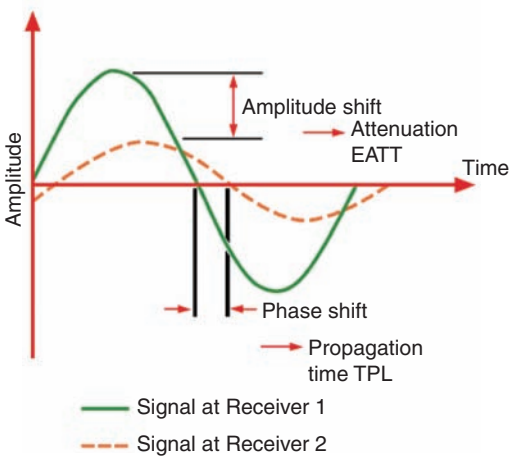


Fig. 15.3—Electromagnetic propagation signals (Johnson and Evans 1983). Reprinted by permission from the SPWLA.

plane-wave theory can be applied. The increased attenuation resulting from the spherical spreading of the wave is compensated for by applying a spherical loss correction factor, *SL*. Therefore, the corrected attenuation, A_c, is given by $A_c = A - SL$. In air, *SL* has a value of approximately 50 dB, but because the term is porosity-dependent, a more exact approach can be taken when correcting downhole measurements:

$$SL = 45 + 1.3t_{pl} + 0.18t_{pl}^2 \quad \ldots\ldots\ldots\

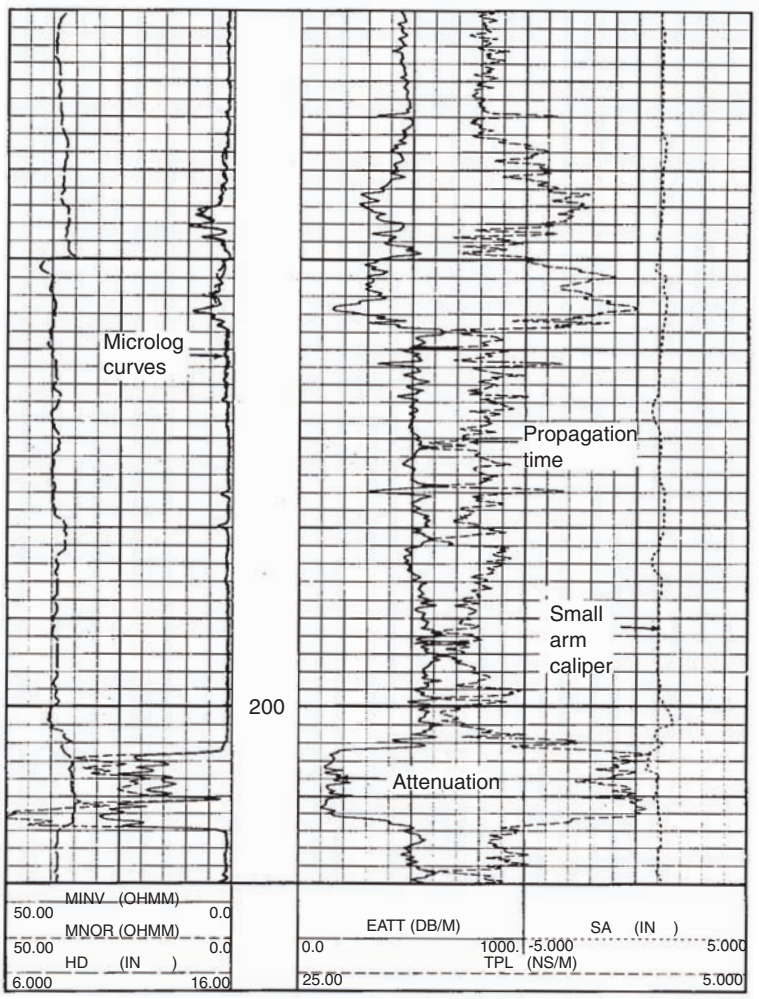


Fig. 15.4—Presentation of data available from an EPT survey. Courtesy of Schlumberger.

diameter (HD) and the micronormal (MNOR) and microinverse (MINV) resistivity curves. The electromagnetic wave attenuation (EATT) and propagation time (TPL) are recorded in Tracks 2 and 3. The measurement of the smaller caliper arm (SA) can be displayed to monitor the borehole rugosity and thereby the quality of the EPT data.

15.3.2 Multispacing, Multifrequency Dielectric Tools. The more-recently introduced multispacing, multifrequency dielectric tools offer many advantages over the older single-frequency two-transmitter, two-receiver skid-mounted devices. Specifically, they offer:

- Higher bed resolution
- Improved measurement accuracy in rugose boreholes
- Radial profiling
- Functionality in both water-based and oil-based muds

Fig. 15.5 illustrates one implementation of such a tool, which incorporates two transmitters and three receivers and mounts the antenna arrays on an articulated arm for improved formation contact in rugose holes.

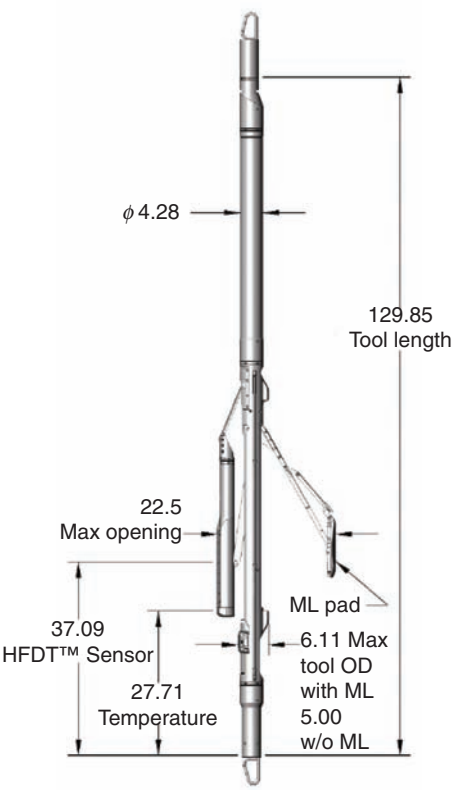


Fig. 15.5—High-frequency dielectric tool (HFDT) with two transmitters and three receivers. Courtesy of Halliburton.

Fig. 15.6 illustrates the transmitter and receiver arrangement of a two-transmitter, eight-receiver multifrequency tool that generates nine multifrequency BHC measurements of phase shift and attenuation. The frequencies used in these newer devices range from 20 MHz to 1 GHz and permit radial "profiling" of the formation properties, thus helping the analyst to determine the invasion profile and to understand better the properties of the undisturbed formation.

Fig. 15.7 illustrates log interpretation based on a multifrequency dielectric tool run in fresh-connate-water-bearing oil sands. The green-shaded area in the third track highlights the difference between the total pore space, indicated by the conventional neutron and density logs, and the water-filled pore, space delimited by the dielectric tool.

15.3.3 Interpretation Methods. The EPT measurement responds mainly to the water content of a formation, rather than to the matrix or any other fluid. The water present in a formation can be the original connate water, mud filtrate, or bound water associated with shales. Because of the shallow depth of investigation of the tool (1 to 6 in.), it can usually be assumed that only the flushed zone is influencing the measurement and that the free water is filtrate.

Under normal circumstances, if fresh muds are used, the propagation time of the electromagnetic waves is essentially unaffected by water salinity **(Fig. 15.8).** An increase in salinity increases the loss factor ε'' and decreases the permittivity ε', but these effects tend to cancel out. If salt-saturated fluids are encountered, the loss factor increases to the extent that the electromagnetic waves are highly attenuated, and therefore measurements are more difficult. EPT measurements are unaffected by mudcake up to a thickness of approximately 0.4 in., but rugosity can result in spurious readings because mud comes in between the antenna pad and the formation.

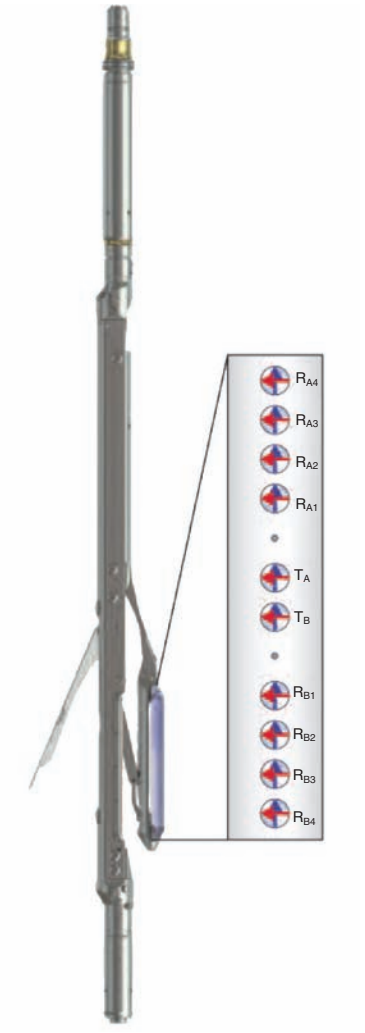


Fig. 15.6—Two-transmitter, eight-receiver antenna arrangement operating at four different frequencies. Courtesy of Schlumberger.

The situation can deteriorate further in boreholes filled with air or oil, when even a thin film of fluid results in the tool responding only to the fluid and not to the formation.

Measurements performed on various samples have produced an empirical relationship for the response of the EPT readings:

$$\gamma = \phi\gamma_f (1-\phi)\gamma_{ma}, \quad \ldots\ldots\ldots\

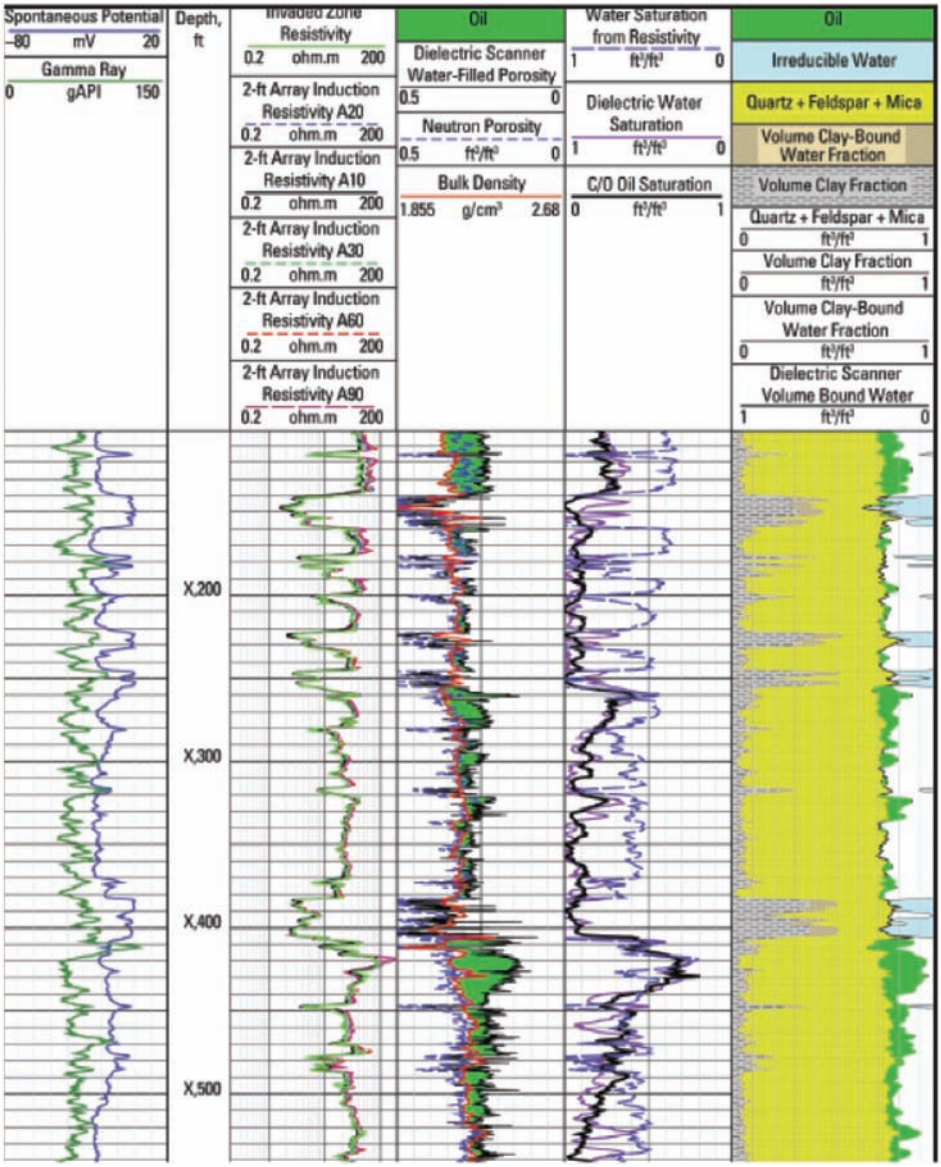


Fig. 15.7—Hydrocarbon zones revealed by multifrequency dielectric tool. Courtesy of Schlumberger.

where t_{pl}, t_{pf}, and t_{pma} are the propagation times for the total formation, the fluid, and the matrix, respectively, and A_c and A_{cf} are the corrected attenuations for the formation and the fluid, respectively. Normally, the matrices are lossless, so there is no corresponding term A_{cma}.

15.3.4 Wellsite Interpretation: t_{po} Method. The t_{po} interpretation method is used during the recording of an EPT log to determine porosity from measured values of attenuation and propagation time. The principle behind the method is that all values used in the computations are treated as if they were measured in a lossless formation. The measured data must therefore be related back to lossless conditions by applying a correction factor that is a function of the attenuation of electromagnetic waves in the lossy medium. If the measured propagation time is t_{pl}, then the propagation time in the lossless formation, t_{po}, is given by:

$$t_{po}^2 = t_{pl}^2 - \frac{A_c^2}{3{,}604}. \quad \ldots\ldots\ldots\

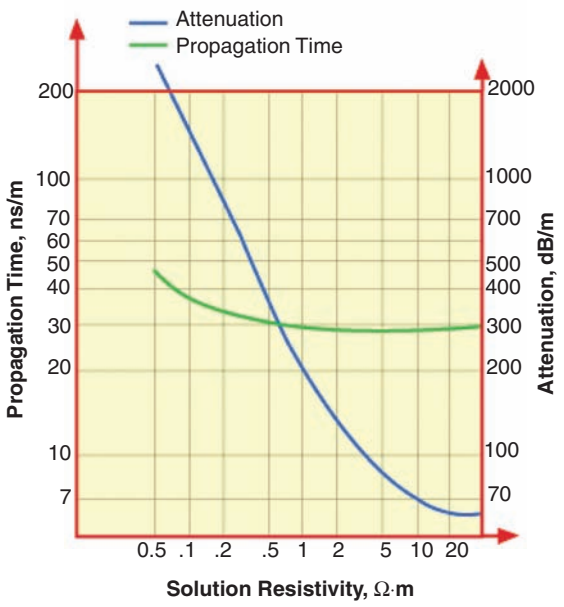


Fig. 15.8—Propagation time and attenuation as functions of water salinity. Courtesy of Schlumberger.

A similar correction can be applied to transform the water propagation time to lossless conditions, that is, t_{pw} to t_{w0}. The attenuation A_c is computed from the logged attenuation by applying a constant correction of −50 dB. Hydrocarbons and matrices are lossless media, and therefore $t_{pma0} = t_{pma}$ and $t_{ph0} = t_{ph}$. The lossless propagation time of water can be obtained from the temperature-related equation:

$$t_{pw0} = 20 \times \frac{710 - T/3}{444 + T/3}, \quad \ldots\ldots\ldots\

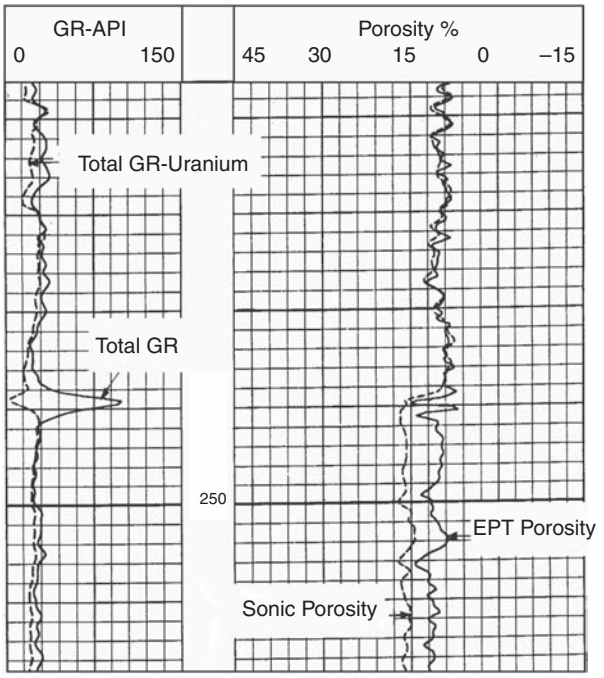


Fig. 15.9—Quick identification of hydrocarbon-bearing intervals through comparison of sonic and EPT porosity. Courtesy of Schlumberger.

upper section of the sand is clearly indicated by the separation of the two porosity curves. The original oil/water contact occurs at 267 m, while the present contact is at 261 m. Generally, the EPT porosity will read the same as a nuclear-derived porosity in water-bearing zones and shales. In hydrocarbon-bearing intervals, however, the EPT porosity will be less than either the total porosity or the density porosity. In gas zones, the separation between the neutron porosity and the EPT porosity will not be as apparent. **Fig. 15.10** illustrates these differences.

The value of the matrix propagation time to be used in the porosity computation is chosen by one of several available methods. If a simple known lithology is being dealt with, the values in Table 15.1 can be used directly. In a dual-mineral formation containing two of the most common matrices, the chart shown in **Fig. 15.11** can be used. If any other mineral is known to predominate in the formation, its matrix parameters can similarly be entered into the chart.

15.3.5 Derivation of the Cementation Exponent *m*. Because the dielectric tool responds to the water-filled pore space (more or less independently of water salinity), a value for bulk volume of water (BVW) can be derived from the tool measurement by means of the interpretation techniques already covered. If water-based mud is used to drill through the formation, then provided that the zone immediately adjacent to the wellbore has been completely flushed, the bulk volume of water detected will reflect the product ϕS_{xo}. If oil-based mud with an oil filtrate is used to drill, then the bulk volume of water detected will reflect the product ϕS_{wi}. An extension of this knowledge enables the analyst to derive the cementation exponent m by following a logical series of steps.

Assuming a water-based mud with a water–mud filtrate,

$$BVW = \phi \times S_{xo} \quad \ldots\ldots\ldots\

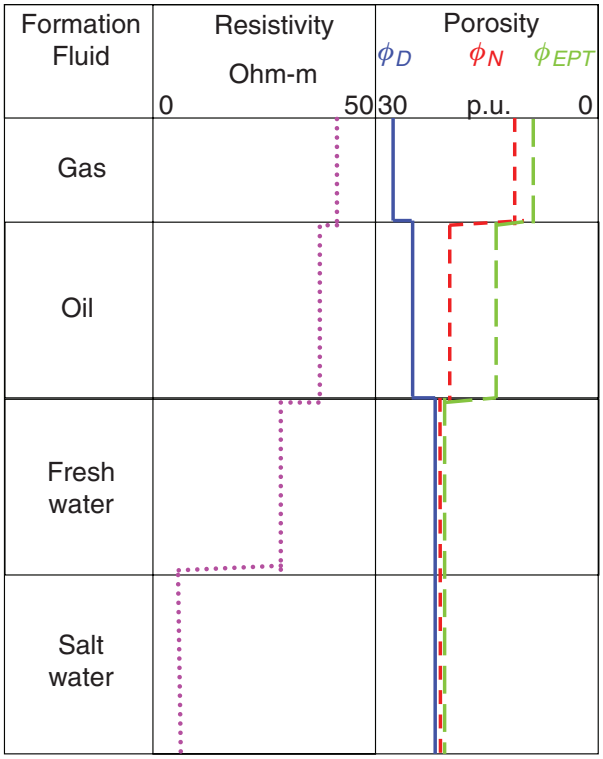


Fig. 15.10—Variation of log readings for water and hydrocarbons. Courtesy of Schlumberger.

Hence, if ϕ is known independently from conventional logs, S_{xo} can simply be derived as:

$$S_{xo} = \frac{BVW}{\phi} \quad \ldots\ldots\ldots\

However, Archie's equation (see Chapter 7) also relates S_{xo} to porosity and to both the flushed-zone resistivity, R_{xo}, and the mud-filtrate resistivity, R_{mf}:

$$S_{xo}^{n} = \frac{a}{\phi^{m}} \times \frac{R_{mf}}{R_{xo}} \quad \ldots\ldots\ldots\

Recently introduced multifunction wireline tools have improved the usefulness of dielectric logging in open holes by offering radial profiling of fluid saturations.

References

Johnson, R. and Evans, C.J. 1983. Results of Recent Electromagnetic Propagation Time Logging in the North Sea. Paper presented at the SPWLA 8th European Formation Evaluation Symposium, London, March 14–15.

Schlumberger. 1982. *Well Evaluation Developments, Continental Europe 1982*, 65–71.

General References

Amin, A.T., Watfa, M., and Awad, M.A. 1987. Accurate Estimation of Water Saturations in Complex Carbonate Reservoirs. Paper SPE 15714 presented at the Middle East Oil Show, Bahrain, 7–10 March. http://dx.doi.org/10.2118/15714-MS.

Anderson, B.I., Luling, M.G., Taherian, R. et al. 1994. The Response of Dielectric Logging Tools to Dipping Thin Beds. Paper SPE 28438 presented at the SPE Annual Technical Conference and Exhibition, New Orleans, 25–28 September. http://dx.doi.org/10.2118/28438-MS.

Chew, W.C. 1982. Response of the Deep Propagation Tool in Invaded Boreholes. Paper SPE 10989 presented at the SPE Annual Technical Conference and Exhibition, New Orleans, 25–29 September. http://dx.doi.org/10.2118/10989-MS.

Baker, P.L., Kenyon, W.E., and Kester, J.M. 1985. EPT Interpretation Using a Textural Model. *Trans.,* SPWLA 26th Annual Logging Symposium, Dallas, June 17–20, Paper DD.

Berry, W.R. II, Head, M.P., and Mougne, M.L. 1979. Dielectric Constant Logging: a Progress Report. *Trans.,* SPWLA 20th Annual Logging Symposium, Tulsa, 3–6 June, Paper W.

Blenkinsop, M., Baker, P., Clavier, C. et al. 1986. Deep Electromagnetic Propagation Tool Interpretation. *Trans.,* SPWLA 27th Logging Symposium, Dallas, 9–13 June.

Eck, M.E. and Powell, D.E. 1983. Application of Electromagnetic Propagation Logging in the Permian Basin of West Texas. Paper SPE 12183 presented at the SPE Annual Technical Conference and Exhibition, San Francisco, 5–8 October. http://dx.doi.org/10.2118/12183-MS.

Focke, J.W. and Munn, D. 1987. Cementation Exponents in Middle Eastern Carbonate Reservoirs. *SPE Form Eval* **2** (2): 155–167. http://dx.doi.org/10.2118/13735-PA.

Geng, X., Yong, Y., Lu, D. et al. 1983. Dielectric Logging: A Logging Method for Determining Oil Saturation. *J. Pet Tech* **35** (10): 1797–1805. http://dx.doi.org/10.2118/10565-PA.

Huchital, G.S., Hutin, R., Thoraval, Y. et al. 1981. The Deep Propagation Tool (a New Electromagnetic Logging Tool). Paper SPE 10988 presented at the SPE Annual Technical Conference and Exhibition, San Antonio, Texas, 5–7 October. http://dx.doi.org/10.2118/10988-MS.

Kenyon, W.E. and Baker, P.L. 1984. EPT Interpretation in Carbonates Drilled with Salt Muds. Paper SPE 13192 presented at the SPE Annual Technical Conference and Exhibition, Houston, 16–19 September. http://dx.doi.org/10.2118/13192-PA.

Lüling, M.G., Pettinicchio, L., Rosthal, R.A. et al. 2005. Dielectric Effects on Resistivity Anisotropy in Laminates, or, When Is $R_v < R_h$? *Trans.,* SPWLA 46th Annual Logging Symposium, New Orleans, 26–29 June, Paper QQQ.

Mazzagatti, R.P., Dowling, D.J., Sims, J.C. et al. 1983. Laboratory Measurement of Dielectric Constant Near 20 MHz. Paper SPE 12097 presented at the SPE Annual Technical Conference and Exhibition, San Francisco, 5–8 October. http://dx.doi.org/10.2118/12097-MS.

Meador, R.A. and Cox, P.T. 1975. Dielectric Constant Logging: a Salinity-Independent Estimation of Formation Water Volume. Paper SPE 5504 presented at the SPE Annual Technical Conference and Exhibition, Dallas, 28 September–1 October. http://dx.doi.org/10.2118/5504-MS.

Penney, R.K., Calcraft, A.P., and Pietsch, A.P. 1996. Quantitative EPT Interpretation in Australian Reservoirs. Paper SPE 36979 presented at the SPE Asia Pacific Oil and Gas Conference, Adelaide, Australia, 28–31 October. http://dx.doi.org/10.2118/36979-MS.

Pilman, D., Skinner, T., Denton, R. et al. 2009. Cost-Effective Reservoir Characterization Utilizing Dielectric Logging Measurements, San Joaquin Basin, California. Paper SPE 124206 presented at the SPE Annual Technical Conference and Exhibition, New Orleans, 4–7 October. http://dx.doi.org/10.2118/124206-MS.

Rau, R.N. and Wharton, R.P. 1980. Measurement of Core Electrical Parameters at Ultrahigh and Microwave Frequencies. Paper SPE 9380 presented at the SPE Annual Technical Conference and Exhibition, Dallas, 21–24 September. http://dx.doi.org/10.2118/9380-PA.

Seleznev, N., Boyd, A., Habashy, T. et al. 2004. Dielectric Mixing Laws for Fully and Partially Saturated Carbonate Rocks. *Trans.,* SPWLA 45th Annual Logging Symposium, Noordwijk, The Netherlands, June 6–9, Paper CCC.

Sen, P.N. 1980. The Dielectric and Conductivity Response of Sedimentary Rocks. Paper SPE 9379 presented at the SPE Annual Technical Conference and Exhibition, Dallas, 21–24 September. http://dx.doi.org/10.2118/9379-MS.

Watfa, M. 1991. Using Electric Logs to Obtain the Saturation Exponent (n) in the Article Equation. Paper SPE 21415 presented at the Middle East Oil Show, Bahrain, 16–19 November. http://dx.doi.org/10.2118/21415-MS.

Watfa, M. and Nurmi, R. 1987. Calculation of Saturation, Secondary Porosity, and Producibility in Complex Middle East Carbonate Reservoirs. *Trans.,* SPWLA 28th Annual Logging Symposium, London, 29 June–2 July, Paper CC.

Wharton, R.P., Hazen, G.A., Rau, R.N. et al. 1980. Electromagnetic Propagation Logging: Advances in Technique and Interpretation. Paper SPE 9267 presented at the SPE Annual Technical Conference and Exhibition, Dallas, 21–24 September. http://dx.doi.org/10.2118/9267-MS.

Zhang, T., Ligneul, P., Nicot, B. et al. 2010. Dielectric Response of Carbonate Core-Plugs: Influence of Heterogeneous Rock Properties on Permittivity. Paper presented at the SPE/DGS Saudi Arabia Section Technical Symposium and Exhibition, Al-Khobar, Saudi Arabia, 4–7 April. http://dx.doi.org/10.2118/136941-MS.

Answer to Question

QUESTION 15.1.

$$
\begin{aligned}
(m - 1.9) \times \log(0.25) &= \log(0.81) + \log(0.3) - \log(12) + 1.9 \times \log(5).\\
(m - 1.9) \times (-0.602) &= -0.092 - 0.523 - 1.079 + 1.328 = -0.366.\\
(m - 1.9) &= 0.608.\\
m &= 2.502.
\end{aligned}
$$

Chapter 16

Sonic (Acoustic) Logging and Elastic Formation Properties

Elastic formation properties control the transmission of elastic waves through subsurface formations, and the science of seismic evaluation is based on the physics of rock elasticity. Sonic logging is a localized downhole branch of geophysics. A wealth of information concerning formation properties can be gathered by properly combining surface and downhole measurements. For example:

- Sonic logs and checkshot surveys can be used to calibrate seismic surveys (time/depth relationships).
- Sonic and density logs can be combined to provide synthetic seismic traces.
- Sonic and density logs can be combined to deduce mechanical properties of the formation, and these in turn can be used to deduce pore pressure, rock compressibility, fracture gradients, along with sanding problems and other difficulties.
- Sonic and other logs can be combined to deduce porosity, lithology, and fluid saturations.
- Measurement of directional shear velocity can quantify formation anisotropy if present.
- Borehole measurements can produce a vertical seismic profile (VSP), which can "see" below the bottom of the well.
- Sonic tools may be used for cement-bond logging in cased holes.

Because the elasticity of subsurface formations is basic to all these measurements and their interpretation, an understanding of how elastic waves propagate through a medium is required.

16.1 Propagation of Elastic Waves

In an infinite medium, two types of sound waves are propagated: compressional waves and shear waves. In a finite medium (e.g., a borehole), guided waves may also be propagated.

Compressional waves (or pressure waves) are longitudinal; that is, the direction of propagation is parallel to the direction of particle displacement **(Fig. 16.1a).** Gases and liquids, as well as solids, tend to oppose compression, and compressional waves can therefore be propagated through all three.

Shear waves are transverse; that is, the direction of their propagation is perpendicular to the direction of particle displacement (Fig. 16.1b). Shear waves can be propagated through solids because solids are rigid. On the other hand, gases (and liquids with negligible viscosity) cannot oppose shearing, and shear waves therefore cannot be propagated through them. In practice, viscous fluids do permit some propagation of shear waves, although the waves become highly attenuated.

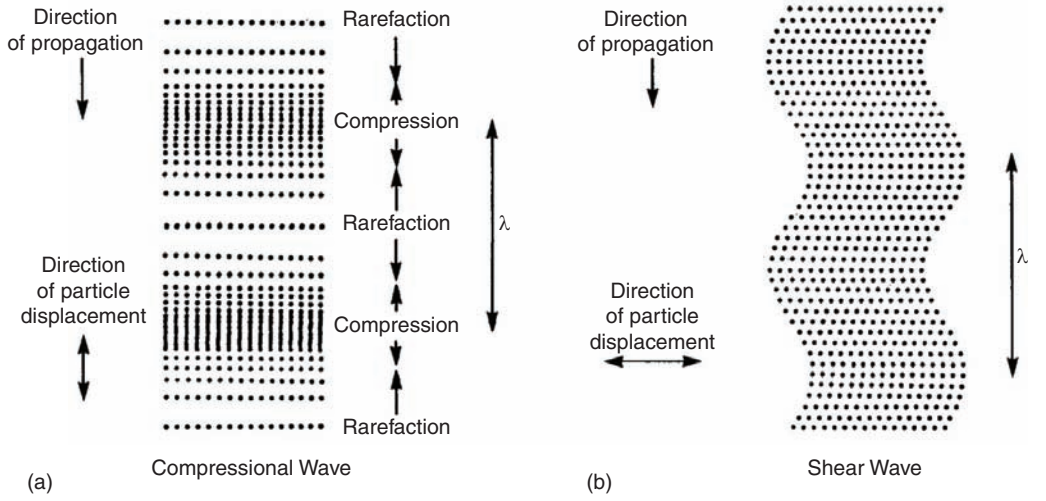


Fig. 16.1—(a) Compressional wave; (b) shear wave. Courtesy of Schlumberger.

Guided waves, or interface waves, include:

Rayleigh waves occur at the mud/formation interface and are a combination of two displacements, one parallel with and the other perpendicular to the interface. Their speed is slightly less than that of shear waves (V_{Rayleigh} is 86 to 96% of V_{shear}). Energy leaks away from the interface as compressional waves are set up in the mud. The waves are then referred to as pseudo-Rayleigh waves.

Stoneley waves travel in mud by interaction between the mud and the formation. Their amplitude decays exponentially, in both the mud and the formation, away from the borehole boundary. These low-frequency waves are called *tube waves.* Stoneley-wave velocity is lower than mud compressional-wave velocity.

16.2 Elastic Constants

Proper interpretation of any measurement made using elastic-wave data requires an understanding of the elastic properties of a medium.

The properties derived from testing rock samples in the laboratory (e.g., by measuring the strain for a given applied stress) are static elastic constants. Dynamic elastic constants are determined by measuring elastic-wave velocities in the material. Sonic logging and waveform analysis provide the means to obtain continuous velocity measurements and therefore knowledge of the dynamic mechanical properties of the rock in situ. Many geoscientific investigators have proposed models relating the basic formation properties (such as the speed of sound, matrix density, porosity, and fluid content) to elastic moduli. Chief among these is the Gassmann equation, which is documented in the Appendix 16B to this chapter.

The speed at which a wave travels through a medium may be expressed in two ways. Geophysicists think in terms of velocity—that is, distance traveled per unit of time. Subsurface formation velocities range from 6,000 to 25,000 ft/sec. Log analysts think in terms of time—that is, the time taken to travel one unit of distance. A convenient unit of measurement is the microsecond per foot (μs/ft), which is given the symbol Δt.* It is common to refer to this "reciprocal velocity" as *slowness*. With these definitions in mind, the dynamic elastic constants of a medium can be expressed as a function of bulk density (ρ_b) and travel time (Δt_c and Δt_s respectively, for compressional and

*Although Δt has been the conventional symbol, it is also common practice to use a script "t" or a plain "*dt*" in its place in many publications.

TABLE 16.1—DYNAMIC ELASTIC CONSTANTS

μ	Poisson's ratio	$\frac{\text{Lateral strain}}{\text{Longitudinal strain}}$	$\frac{\frac{1}{2}(\Delta t_s/\Delta t_c)^2 - 1}{(\Delta t_s/\Delta t_c)^2 - 1}$
G	Shear modulus	$\frac{\text{Applied stress}}{\text{Shear strain}}$	$\frac{\rho_b}{\Delta t_s^2} \times a$
E	Young's modulus	$\frac{\text{Applied stress}}{\text{Normal strain}}$	$2G(1+\mu) \times a$
K_B	Bulk modulus	$\frac{\text{Applied stress}}{\text{Volumetric strain}}$	$\rho_b\left(\frac{1}{\Delta t_c^2} - \frac{4}{3\Delta t_s^2}\right) \times a$
C_B	Bulk compressibility	$\frac{\text{Volumetric deformation}}{\text{Applied stress}}$	$\frac{1}{K_B}$

shear waves), as shown in **Table 16.1.** The coefficient ***a*** is equal to 1.34×10^{10} if ρ_b is in gm/cm^3 and Δt is in μs/ft. (Note: Poisson's ratio is dimensionless; *G, E,* and K_b are in Mpsi*, and C_b is in microsips.)

Discussions later in the text will show how both compressional and shear velocities can be measured by sonic tools or deduced by other means. Practical applications of these data will also be explained.

16.3 Sonic Logging Tools

Sonic logging tools attempt to measure the formation properties Δt_c and Δt_s by means of an apparatus suspended in the mud column. To ensure success in this task, a number of "tricks" are used. These include borehole compensation, long-spacing tools, mono- and dipole energy sources, multiple (array) receivers, waveform recording, and semblance processing.

The curves recorded on sonic logs may include the interval transit times Δt_s and Δt_c in μs/ft, waveforms, waveform amplitudes, caliper, gamma ray and/or SP values, and integrated travel time (discussed later in this chapter). Sonic logs may be recorded in conjunction with other porosity and resistivity devices with a so-called "quad-combo" tool string. A typical standalone sonic log is illustrated in **Fig. 16.2.**

Tools available for sonic measurement include borehole-compensated (BHC) tools, slimhole versions (that can be run through tubing), long-spacing sonic (LSS) tools, multiple-receiver array tools, and tools equipped with multipole energy sources (both compressional and shear).

In seismic-data gathering, a disturbance is created at the surface by means of explosives or by use of an air gun in water. In sonic logging, an acoustic pulse, produced by alternate expansions and contractions of a transducer, is emitted by a transmitter **(Fig. 16.3).**

This monopole-transmitter pulse generates a compressional wave through the mud. Part of the acoustic energy traverses the mud, impinges on the borehole wall at the critical angle of incidence, passes along the formation close to the borehole wall, re-enters the mud, and arrives at a receiver, where it is converted into an electrical signal **(Fig. 16.4).**

16.4 Operating Principles

Sonic tools consist of transmitter transducers that convert electrical energy into mechanical energy and receiver transducers that do the reverse. In its simplest form, the measurement is made in an uncompensated mode **(Fig. 16.5).**

At time T_0, the transmitter emits a small shock wave that travels through the mud to the borehole wall, where it is refracted through the formation. Part of the energy traveling through the formation is in turn refracted back into the mud column and finds its way to the first receiver at time T_1 and to the second receiver at time T_2. The difference in the two times is referred to as Δt and

*To convert Mpsi to GPa, multiply Mpsi by 6.895.

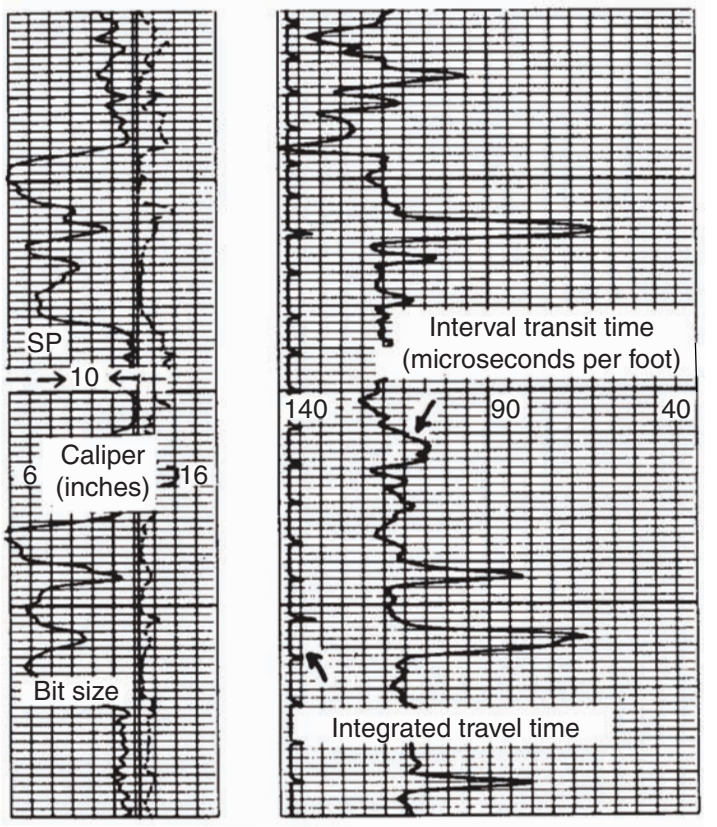


Fig. 16.2—Sonic log. Courtesy of Schlumberger.

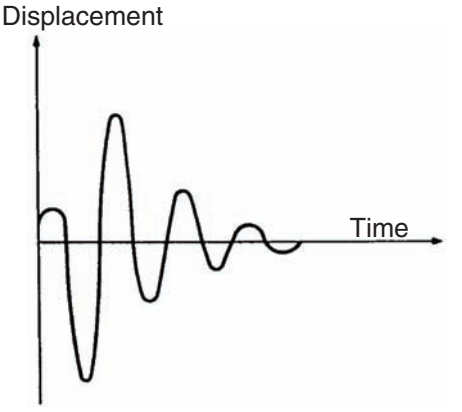


Fig. 16.3—Typical transmitter pulse. Courtesy of Schlumberger.

represents the time required for a compressional wave to travel through the formation over a distance equal to the spacing between the two receivers. The formation travel time, Δt, is expressed in μs/ft or in μs/m.

This early form of sonic tool worked on the assumption that in mud, the travel paths to the two receivers were equal. This was true in the case of a smooth borehole of unchanging size, but it was not true if the borehole was of varying size or if the sonde was tilted with respect to the

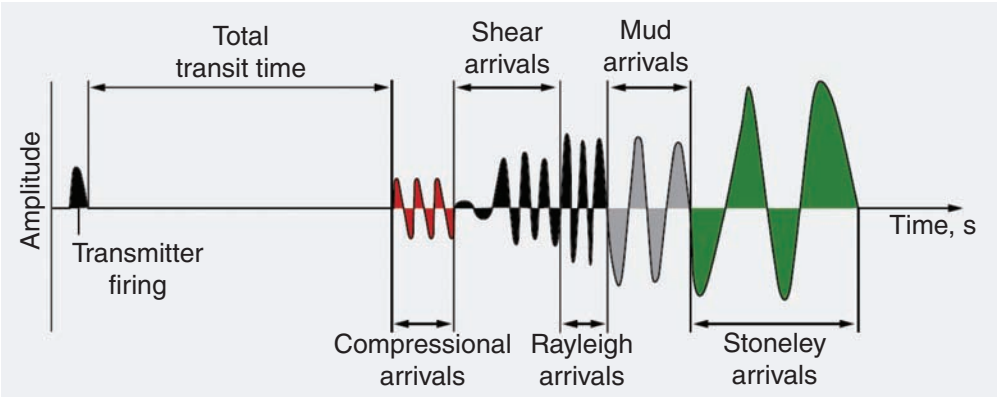


Fig. 16.4—Signal generated at the receiver by various wave arrivals. Courtesy of Schlumberger.

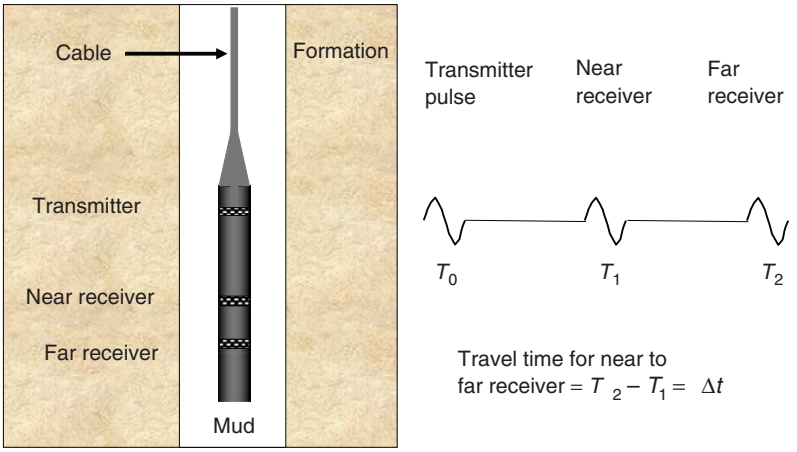


Fig. 16.5—Basic sonic device.

borehole axis. These difficulties were overcome by the introduction of the BHC sonic tool. **Fig. 16.6** illustrates the principle of the BHC sonic tool. Two transmitters and four receivers are used, and two values of Δt are measured and averaged. This system eliminated errors in Δt resulting from sonde tilt and hole-size variations. Even so, there are practical limits to the working range of the tool.

In large boreholes, for example, the time required for a compressional wave to travel from the transmitter to the formation, through the formation, and back through the mud to a receiver may exceed the time required for a direct transmission from the transmitter to the receiver through the mud. The critical factors in determining when this condition will exist are the transmitter/receiver spacing, the hole size, and the travel time in the formation.

The largest formation Δt that can be measured with conventional BHC sonic tools with 3-foot spacing is 175 μs/ft in a 12¼ -in. hole and 165 μs/ft in a 14-in. hole. These limitations are not serious ones if the formation is a reservoir rock with a Δt in the normal range of 40 to 140 μs/ft. It does become a serious defect if the rock is a shale with a long transit time and if the purpose of the log is to compute integrated travel time for geophysical purposes. Mathematically, the variables can be related as follows:

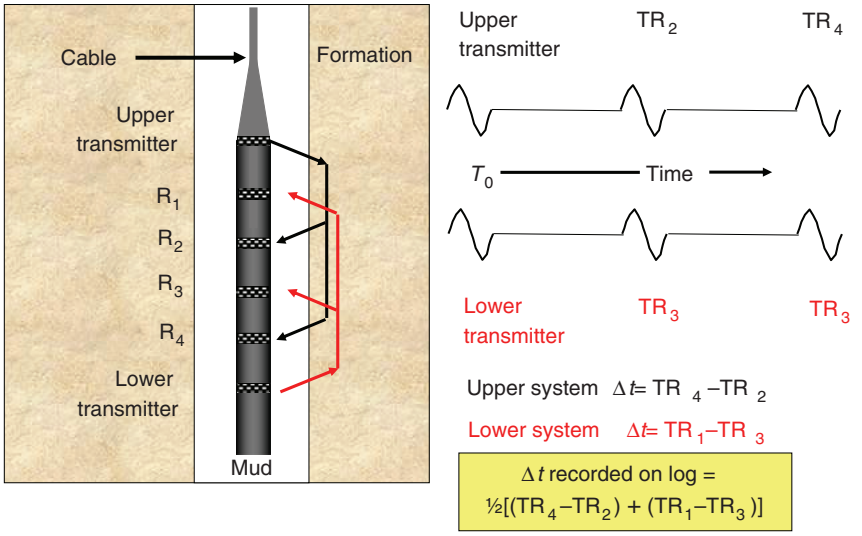


Fig. 16.6—BHC sonic tool.

$$S_{\min} = (D-d)\left\{\frac{V_{\text{form}}+V_m}{V_{\text{form}}-V_m}\right\}^{1/2} \quad \ldots\ldots\ldots\

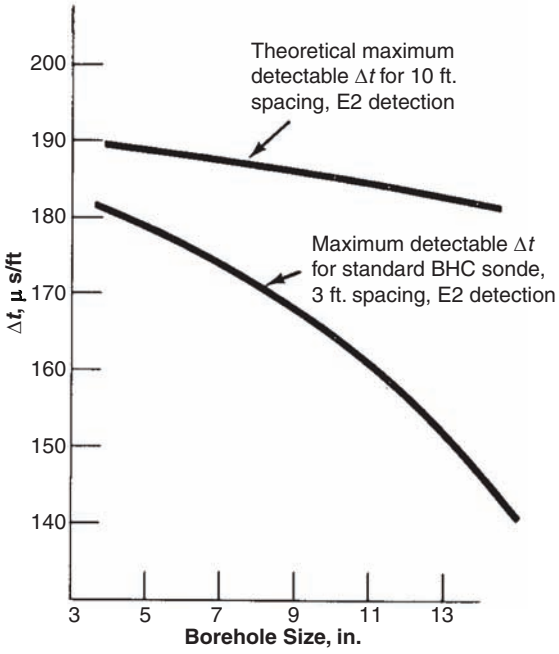


Fig. 16.7—Maximum detectable Δt for 3- and 10-ft spacings (Δt_f = 192 μs/ft, tool OD = 3 5/8 in.).

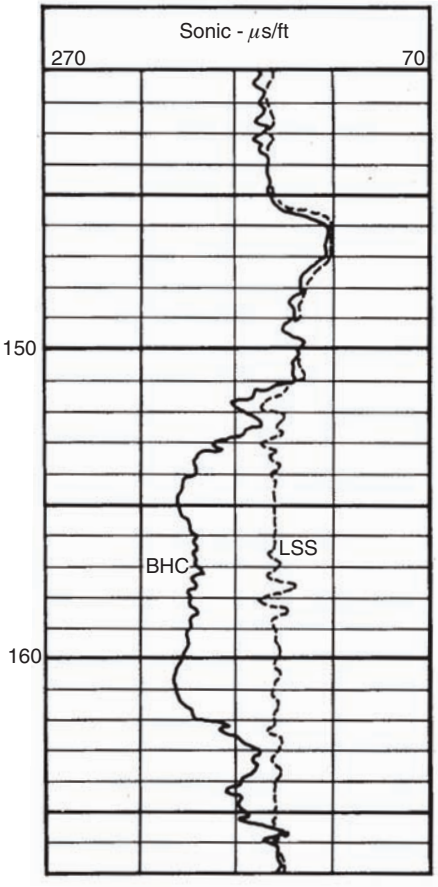


Fig. 16.8—Comparison of BHC and LSS logs. Courtesy of Schlumberger.

Lengthening the spacing on a sonic device achieves two ends:

1. A valid sonic log can be recorded in a bigger hole with a long-spacing device than with a conventionally spaced tool.
2. The zone investigated by the tool extends deeper into the formation with a long-spacing device than with a conventionally spaced tool.

Deeper investigation into the formation is of great value when logging through intervals of shale that have had their properties altered by the drilling process. If the Δt of the formation in the undisturbed state is less than the Δt of the formation in the altered state, the fastest route for a compressional wave will be through the undisturbed formation, or deep in the formation **(Fig. 16.9).**

LSS tools make their measurements in a depth-derived mode. In other words, the tool compensates for changes in borehole size by combining the travel times measured and memorized when the tool is at one depth with travel times recorded at a shallower depth when a different combination of transmitters and receivers is activated. Two transmitters spaced 2 ft apart are located 8 ft below a pair of receivers that are also 2 ft apart **(Fig. 16.10).** The first Δt reading is memorized and combined with a second Δt reading measured after the sonde has been pulled the appropriate distance further along the borehole; compensation for changes in the hole size is thus achieved.

Note (Fig. 16.10) that the first (memorized) Δt reading = T1R1 − T1R2 and the second Δt reading = T2R2 − T1R2. Then the 8- to 10-ft interval time DT = ½ (memorized first Δt reading +

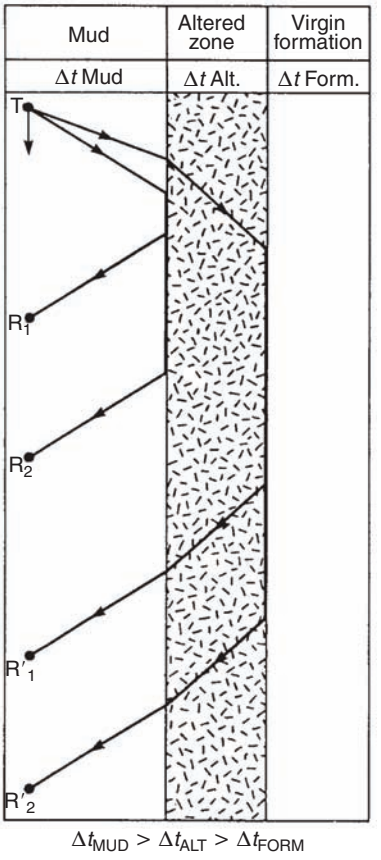


Fig. 16.9—Depth of investigation of long- and short-spacing sonic tools. Courtesy of Schlumberger.

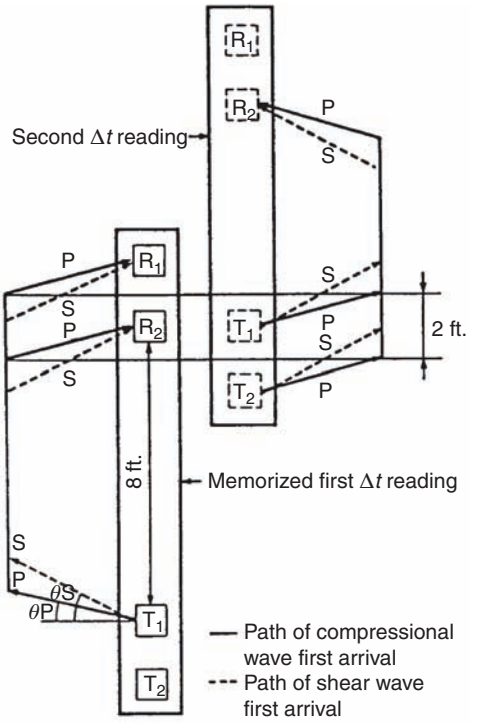


Fig. 16.10—Long-spaced sonic "depth-derived" principle. Courtesy of Schlumberger.

second Δt reading). The 10- to 12-ft measurement, known as *DTL,* uses T2 for the first (memorized) Δt and R1 for the second Δt reading.

Both *DT* and *DTL* are recorded on Tracks 2 and 3 of the long-spaced sonic log **(Fig. 16.11).** The four transit-time curves can be displayed in Track 1 if desired, either in real time or in the playback phase. The log illustrated in Fig. 16.11 was recorded through a shaly interval, thus accounting for the slight difference between *DT* and *DTL* due to alteration of the formation. Nevertheless, the two 10-ft curves (TT1 and TT4) virtually overlap each other, even though they were measured with different transmitter/receiver pairs, thereby confirming the validity of the measurement.

16.6 Array Sonic Tools

The incorporation of multiple receiver arrays and waveform recording methods has led to improvements over conventional sonic logging tools. **Fig. 16.12** illustrates such a tool. The combination and spacing of transmitters enables the tool to perform as a conventional short-spaced (BHC) sonic tool, a long-spaced sonic tool, or a cased-hole cement-bond logging device with variable density recording as well. It also makes possible (for the example illustrated) the recording of multiple waveforms at eight separate receivers. **Fig. 16.13** shows a typical recording in which compressional-, shear-, and Stoneley-wave arrivals are clearly visible.

Data processing is accomplished by software that seeks coherence between the time window of one waveform as it moves out along the other waveforms at the other receivers. The semblance algorithm used is entirely similar to that used in seismic processing. This makes it possible to plot the values of the coherence function as "contours" on a crossplot of slowness (Δt). **Fig. 16.14** shows such a crossplot.

The compressional, shear, and Stoneley arrivals appear as "peaks" from which it can be deduced that, in this example, $\Delta t_c \approx 60$ μs/ft, $\Delta t_s \approx 90$ μs/ft, and $\Delta t_{\text{Stoneley}} \approx 200$ μs/ft. This process can be

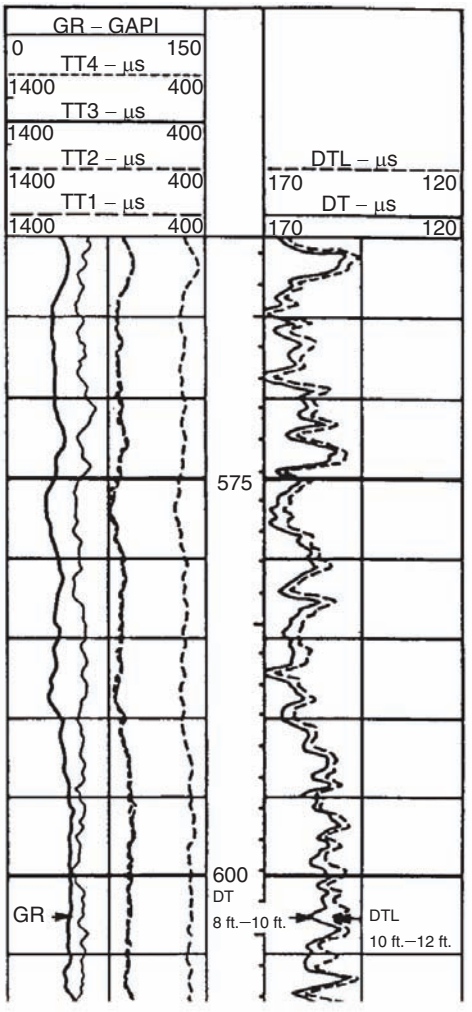


Fig. 16.11—LSS log with four transit-time curves displayed on Track 1. Courtesy of Schlumberger.

repeated at each depth interval in the well and the output of each array-processing repetition can be depicted as a log of slowness vs. depth, as illustrated in **Fig. 16.15.**

16.7 Dipole Sonic Tools

Dipole sonic logging tools incorporate directional energy sources for both compressional and shear waves. Proper use and interpretation of the signals received at directional receivers enable the analyst to detect azimuthal formation anisotropy and to determine the directions of maximum and minimum horizontal stress in a vertical or near-vertical borehole. This in turn offers the well builder or the geosteering expert the information needed to drill more efficiently (in the direction of maximum horizontal stress) and avoid borehole collapse. Likewise, the same information is vital for completion planning when fracturing in the direction of maximum stress.*

*Well production, however, is typically better if one drills in the more difficult direction of minimum horizontal stress.

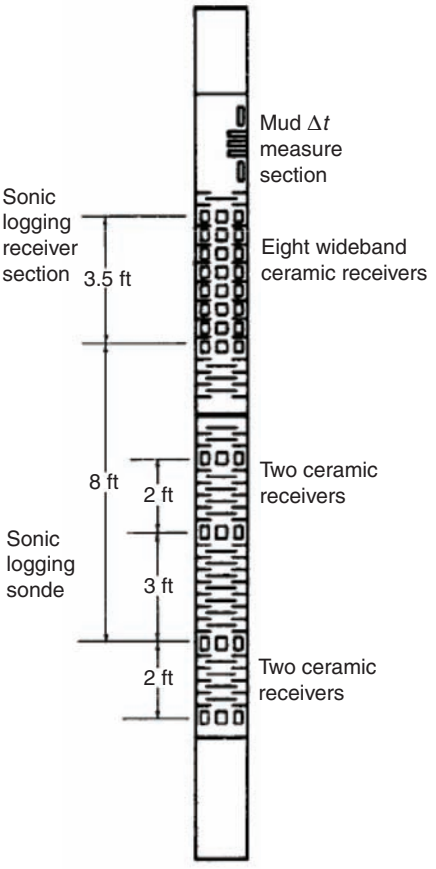


Fig. 16.12—Array sonic logging tool (after Morris et al. 1984).

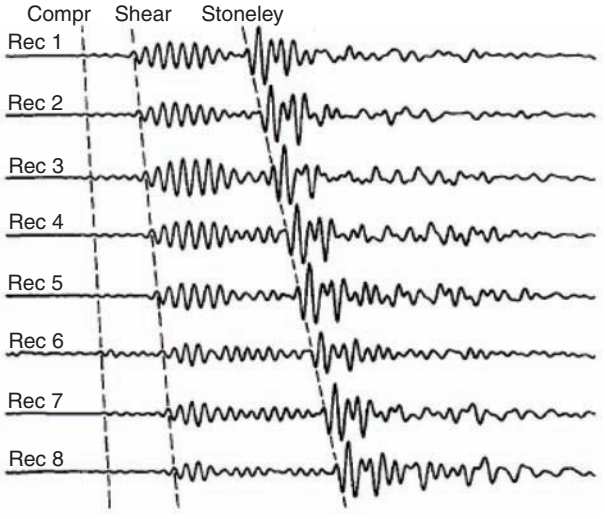


Fig. 16.13—Array sonic waveform recordings (after Morris et al. 1984).

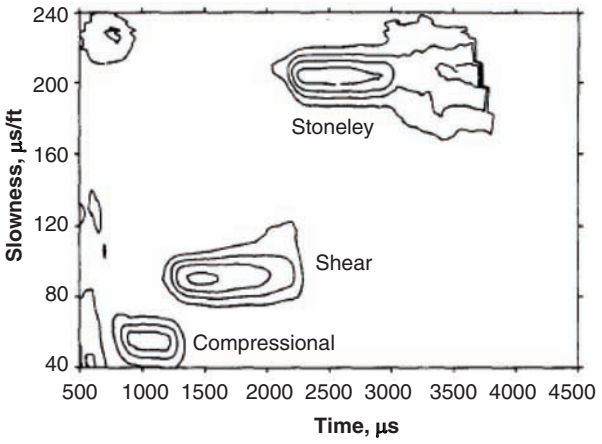


Fig. 16.14—Contour plot of coherence function (after Morris et al. 1984).

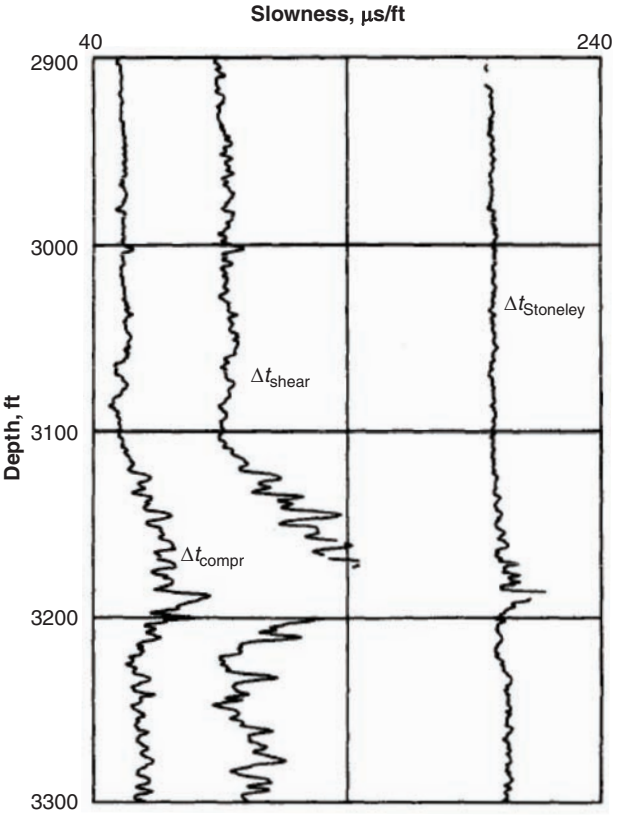


Fig. 16.15—Example log of slowness (after Morris et al. 1984).

16.8 Cycle Skipping and Noise

The actual travel-time measurement is determined at the first arrival peak. However, the tool's internal trigger mechanism for detecting this peak is subject to certain errors. **Fig. 16.16** illustrates two common problems. In the first, the bias level is set too high, and the travel time is triggered on a later peak, causing an erroneously long time to be measured (this is known as cycle skipping). In the second, the bias is set too low, and the travel time is triggered on noise, causing an erroneously short travel time (this problem is known as noise).

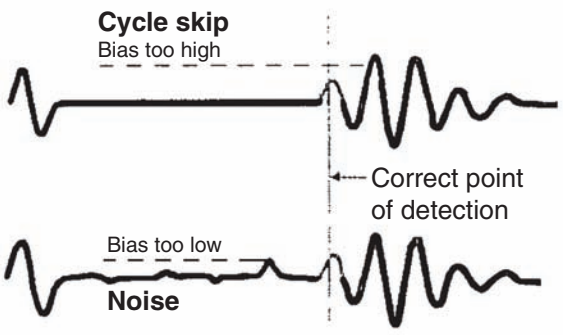


Fig. 16.16—Cycle skipping and noise.

It is not always possible to distinguish the difference between cycle skipping and noise in the BHC mode because two measurements are being averaged by the tool. **Fig. 16.17** illustrates a bad sonic log that had to be rerun as a result of cycle skipping and noise.

16.9 Waveform Recording

Waveforms may be recorded with an LSS tool. The longer spacing enables a longer time separation of the compressional- and shear-wave arrivals than that provided by short-spacing tools. Various LSS transmitter/receiver combinations permit four waveforms to be recorded at 6-in.

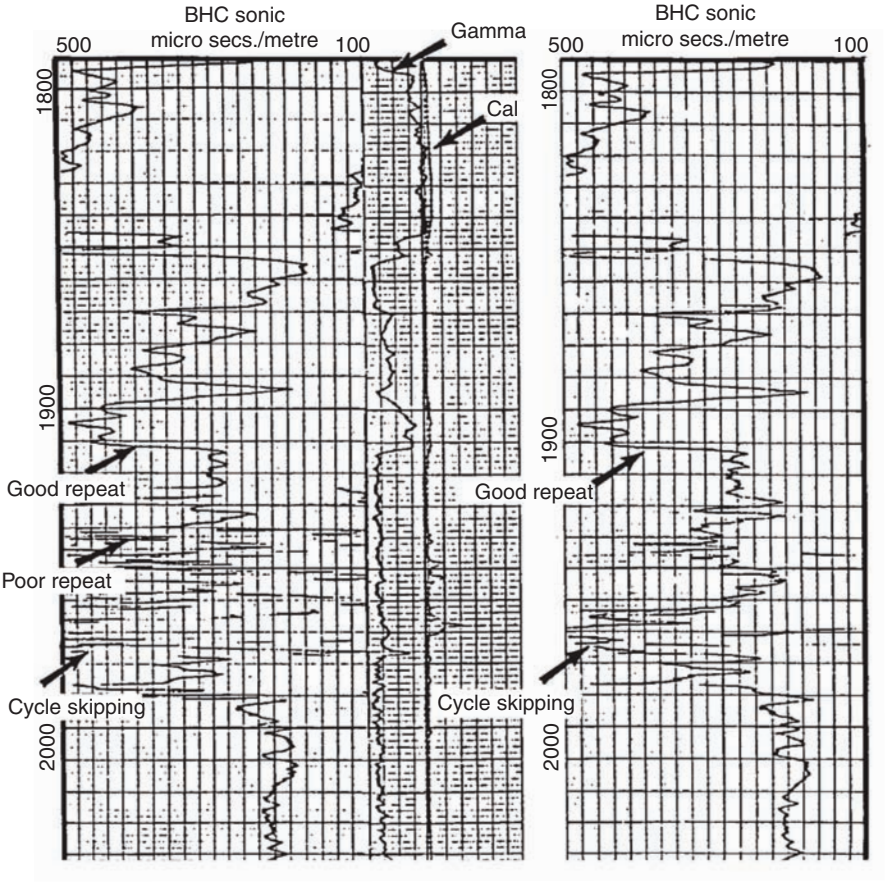


Fig. 16.17—Cycle skipping.

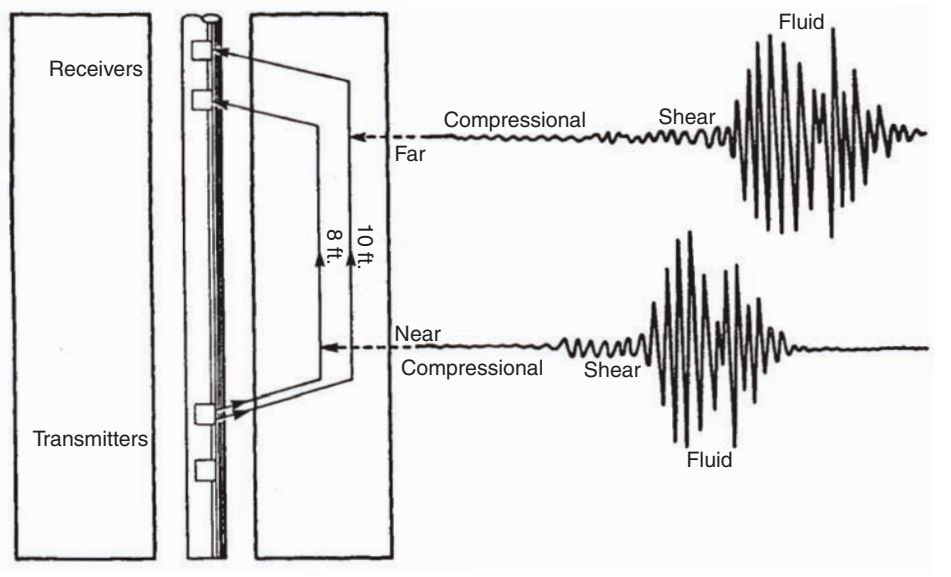


Fig. 16.18—Long-spaced sonic waveforms. Courtesy of Schlumberger.

intervals. **Fig. 16.18** illustrates composite waveforms received at the near and far receivers when the upper transmitter is fired.

Waveform recording considerably extends the range of sonic logging applications in both open and cased holes. The principal advantage of waveform recording is that the shear-wave velocity of the formation is specifically detected. The objective is to distinguish between the compressional- and shear-wave arrivals and to measure the compressional and shear interval transit times. In cased holes, the formation arrivals are usually distinct from the casing arrivals. This permits a viable sonic measurement where, without waveform recording, previous sonic devices would have been ineffective.

The data-processing methods used to extract shear-wave arrival times are somewhat complex and are similar to seismic processing methods; that is, multiple waveforms are stacked. It is quite common, however, to "see" shear arrivals on variable-density displays of the sort shown in **Fig. 16.19.**

16.10 Sonic Porosity (ϕ_S)

The fact that compressional waves travel faster through solid matrix material than through fluid is the basis for the method used to determine formation porosity from sonic logs. **Fig. 16.20** is a schematic in which the pore space and the solid matrix have been separated for purposes of illustration. If Δt_f is the time taken to travel through the pore space and Δt_{ma} is the time taken to travel through the matrix, the total measured travel time will be Δt, and the porosity will be given by:

$$\Delta t = \phi \Delta t_f + (1-\phi)\Delta t_{ma} \quad or \quad \phi_s = \frac{\Delta t - \Delta t_{ma}}{\Delta t_f - \Delta t_{ma}} \ldots\ldots\ldots\

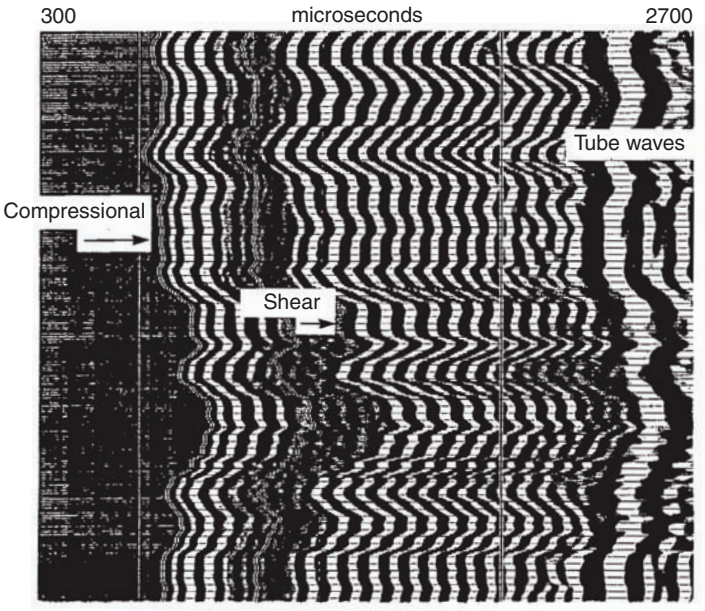


Fig. 16.19—Variable-density display with compressional- and shear-wave first-arrival detections highlighted. Courtesy of Schlumberger.

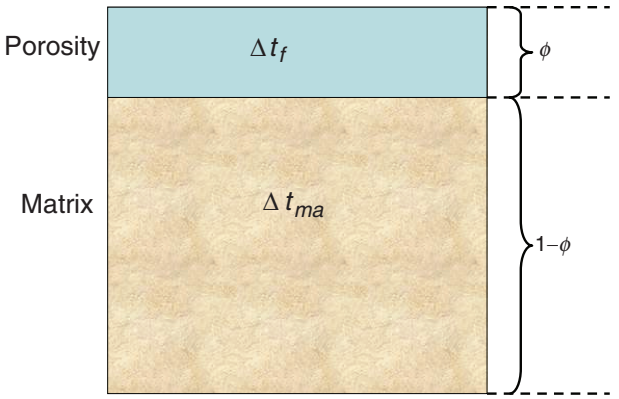


Fig. 16.20—Sonic porosity measurement.

16.10.1 Matrix Travel Times. The matrix travel time will depend on the matrix itself. **Table 16.2** gives a partial listing of common matrix materials. A more exhaustive list is provided in Appendix 16A.

16.10.2 Fluid Travel Time. Fluid travel time is a function of the temperature, pressure, and salinity of a solution **(Fig. 16.22).** To use the figure, enter the chart on the x-axis with the formation temperature and move up to the appropriate salinity line. For this purpose, the fluid in the pore space is normally considered to be mud filtrate. Proceed across to the right to find the fluid velocity at zero pressure. Now draw a projection parallel to the diagonal lines to a point directly above the estimated formation pressure. Proceed to the right and read the fluid velocity corrected for pressure, temperature, and salinity. Use of this chart will improve porosity determination by

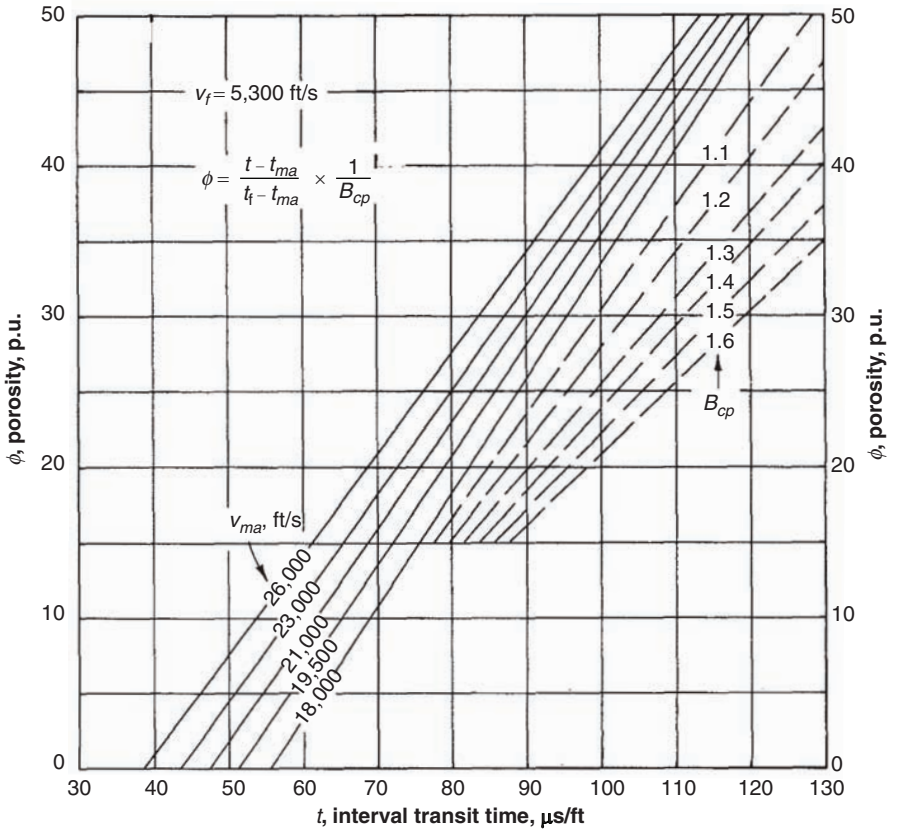


Fig. 16.21—Sonic porosity determination. Courtesy of Schlumberger.

TABLE 16.2—Δt_{ma} FOR COMMON MATRIX MATERIALS AND FLUIDS

Material	Travel Time Δt (μs/ft)	Velocity (ft/sec)	Density g/cm^3
Dolomite	43.5	23,000	2.87
Limestone	47.5	21,000	2.71
Sandstone	55.6	18,000	2.65
Anhydrite	50.0	20,000	2.97
Gypsum	52.5	19,000	2.35
Salt	67.0	15,000	2.03
Water (fresh)	200	5,000	1.00
Water (100,000 ppm NaCl)	189	5,300	1.06
Water (200,000 ppm NaCl)	176	5,700	1.14
Oil	232	4,300	
Air	919	1,088	
Casing	57	17,000	

eliminating empirical changes in the matrix velocity to some incorrect value to force a porosity value consistent with other measurements. To convert from ft/sec to ms/ft, the following relation can be used:

$$\Delta t\ (\mu s/ft) = 10^6/V \text{ in ft/s} \quad \ldots\ldots\ldots\

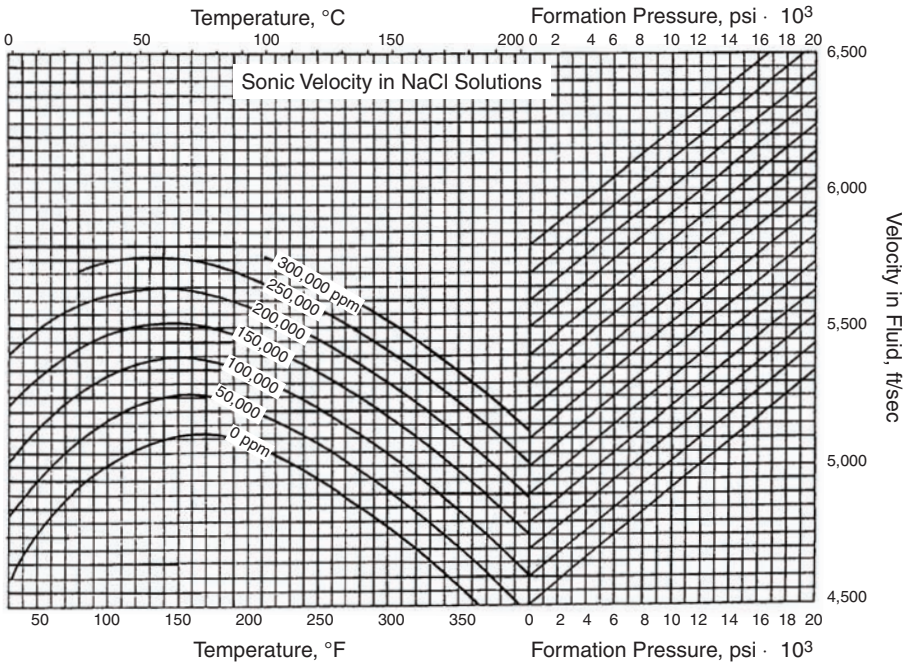


Fig. 16.22—Determination of V_f (and hence Δt_f). After Wyllie (1958) by permission from Society of Exploration Geophysicists (SEG).

QUESTION 16.2.
Temperature = 270°C
Salinity = 200,000 ppm
Formation Pressure = 6,000 psi.
Find V_f in ft/sec, and convert this value to Δt_f in μs/ft.

16.10.3 Compaction Effects and the Hunt-Raymer Transform. Unconsolidated formations exhibit travel times that are longer than can be accounted for by the Wyllie time-average equation. This situation can be handled in two ways: conventionally and by the Hunt-Raymer transform. The conventional method adapts the Wyllie time-average equation by introducing a fudge factor, B_{cp}, such that:

$$\phi_s = \frac{\Delta t - \Delta t_{ma}}{\Delta tf - \Delta t_{ma}} \times \frac{1}{B_{cp}}, \quad \ldots\ldots\ldots\

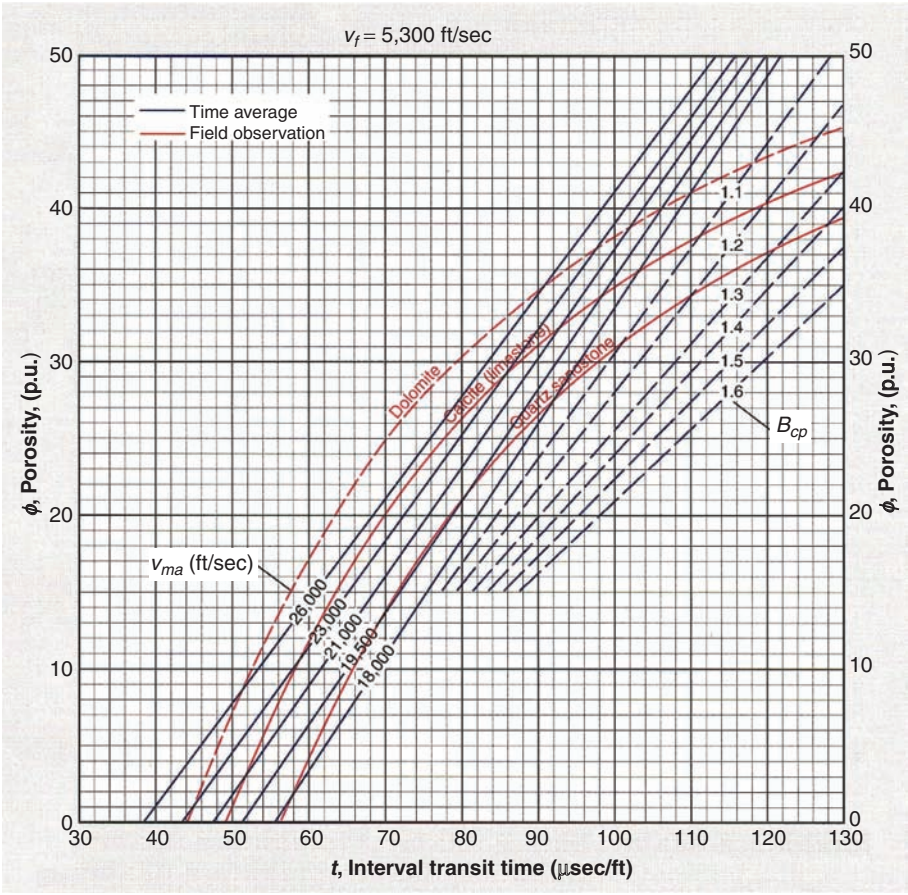


Fig. 16.23—Sonic porosity chart with Hunt-Raymer transform. Courtesy of Schlumberger.

The Hunt-Raymer transform is based on empirical observations from sonic logs and porosity determinations made by other means. **Fig. 16.23** shows the generalized form of the Hunt-Raymer transform and plots Δt against porosity for sandstone, limestone, and dolomite.

An acceptable equation relating porosity to Δt for this transform is given by:

$$\phi_S = \frac{1}{\rho_{ma} - \rho_f}\left(1 - \frac{\Delta t_{ma}}{\Delta t}\right) \quad \ldots\ldots\ldots\

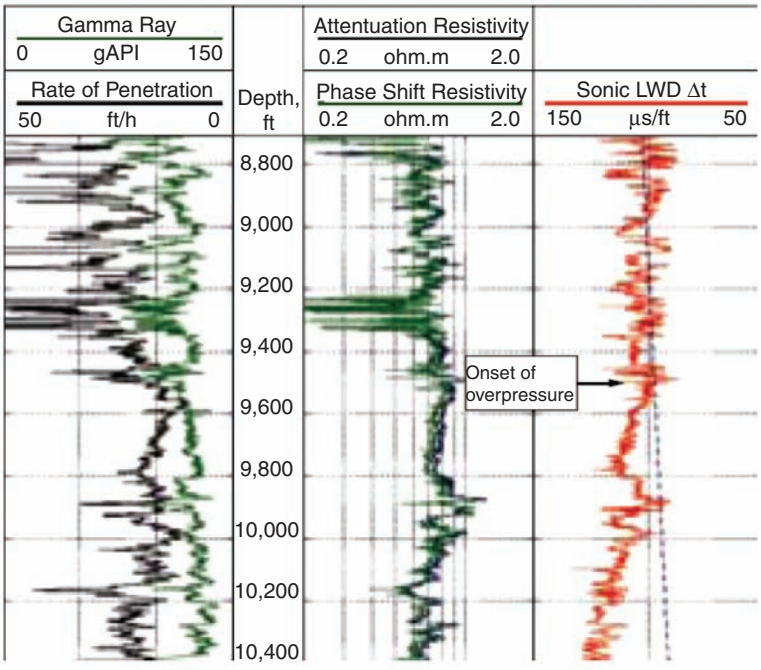


Fig. 16.24—Sonic indication of overburden pressure gradient and onset of overpressure. Courtesy of Schlumberger.

16.11 Sonic Combination for R_{wa}

Historically, the combination of the induction tool with the sonic tool was one of the first "combo" tools used by the logging industry. The analyst may find many examples of this in "legacy materials," and it is worthwhile to show here an example of such a combination log and its presentation **(Fig. 16.25).**

This combination was found particularly useful in shaly sand sequences. Note that a curve called R_{wa} is displayed in Track 1 along with the *SP*. This curve represents apparent water resistivity derived from both the induction and sonic measurements. Δt is then converted to a value of ϕ_S, the sonic porosity. This is then combined with the value of R_t from the induction log to give:

$$R_{wa}\,(\text{sonic}) = \frac{(\phi_S)^m \times R_t}{a} \qquad (16.9)$$

This curve affords a quick and easy visual method of spotting potential productive zones. A minimum value of R_{wa} can be chosen in a water-bearing zone, and then any point on the log exhibiting an R_{wa} value greater than three or four times that minimum is immediately of interest. This technique is discussed more fully in Chapter 25.

16.12 Δt Ratio

Determination of the ratio $\Delta t_s / \Delta t_c$ provides a useful contribution for formation evaluation. The principal areas of application are lithology identification, formation-fluid determination, and rock mechanical properties. The first example **(Fig. 16.26)** demonstrates an interesting property of the Δt ratio in micaceous sands. In the clean upper zone, the Δt ratio (called DTR on the log) correlates very well with the gamma ray curve. The lower zone is not shaly, as the gamma ray might suggest, but contains radioactive mica and heavy components. The Δt ratio remains substantially

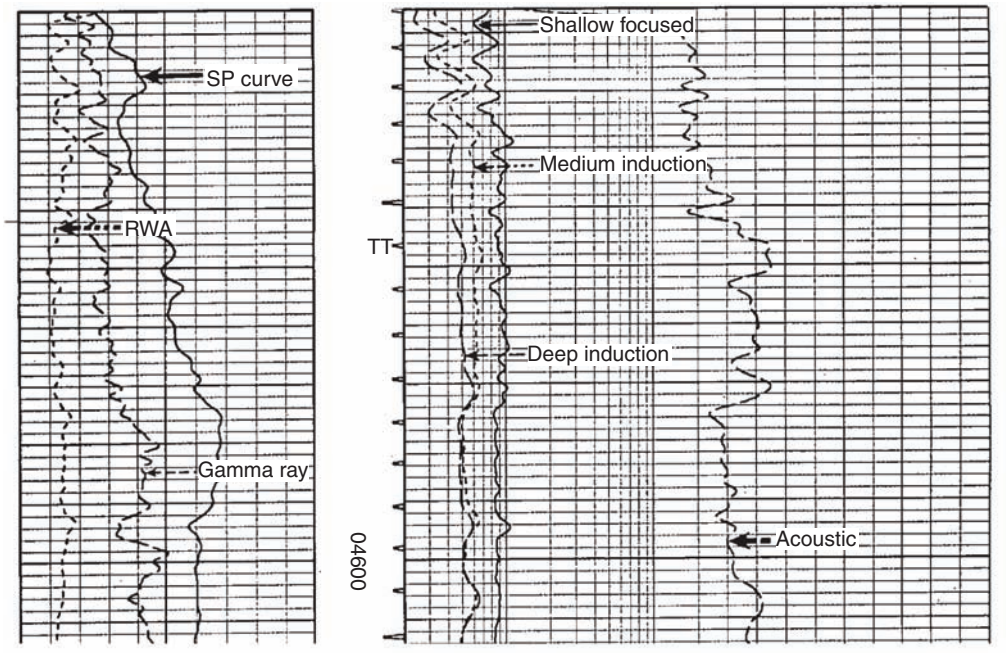


Fig. 16.25—Induction-sonic log presentations with R_{wa} curve.

the same in both zones, indicating a shale-free sandstone because it is unaffected by the other minerals. Therefore, the Δt ratio provides, in this type of lithology, a clay indicator unaffected by mica or other nonshale radioactive components such as feldspar.

Obviously, it is preferable to measure Δt_s and then to compute the $\Delta t_s/\Delta t_c$ ratio and use it as a lithology indicator. However, if the lithology is known, the $\Delta t_s/\Delta t_c$ ratio for that lithology can be used to compute Δt_s, which can then be used to calculate the formation elastic constants, which are in turn useful for inferring formation mechanical properties. Of help in this respect is **Table 16.3**, which lists the $\Delta t_s/\Delta t_c$ values for common rock types.

These data can be used as follows: Read the conventional Δt_c from the sonic log and multiply by the ratio of $\Delta t_s/\Delta t_c$ read from Table 16.3.

$$\Delta t_S = \Delta t_C \cdot \left(\Delta t_S/\Delta t_C\right) \quad \ldots\ldots\ldots\

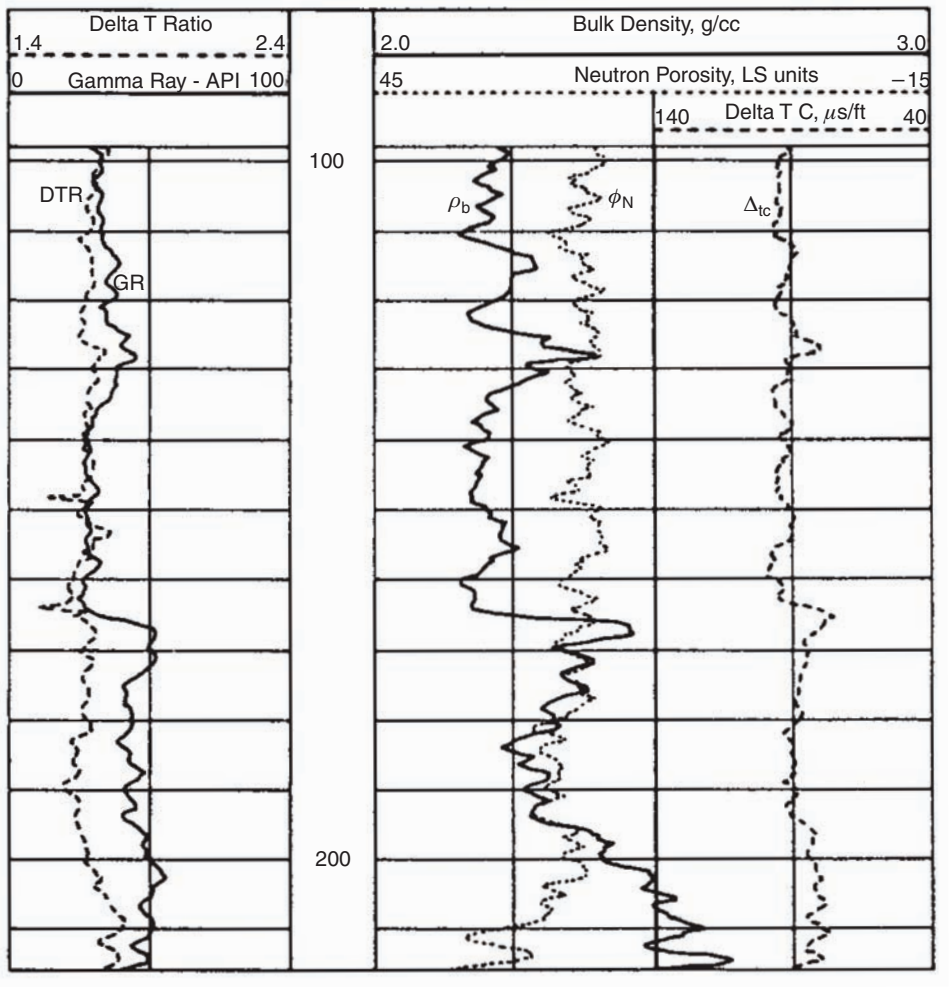


Fig. 16.26—Δ*t* ratio in micaceous sands. Courtesy of Schlumberger.

- Young's modulus
- Shear modulus

These parameters (discussed in more detail in Section 16.2 and documented in Table 16.1) may in turn be used for calculations in areas of interest to drilling and completion engineers, including:

- Prediction of the wellbore pressure at which shear failure will occur, resulting in sand production and need for gravel packing
- Avoidance of accidental fracturing while drilling or cementing
- Differential-pressure requirements for hydraulic-fracture initiation

Fig. 16.27 shows an example of a computed log illustrating an analysis of formation strength and propensity to sanding problems. The same logic can be applied to such diverse fields as bit selection and design of fracture treatments.

16.14 Seismic Applications

It is important to appreciate the difference in the scales of measurement and sensitivity that sonic logging measurements and seismic surveys offer. **Fig. 16.28** conveniently summarizes these scales. At the lowest end of the scales for range and resolution are the ultrasonic devices used in

TABLE 16.3—Δt RATIO FOR ROCK TYPES [AFTER MASON (1984)]

Formation Lithology	Ratio $\Delta t/\Delta t$
Anhydrite	2.45
Basalt	1.55
Chalk	2.45
Chert	1.6
Clay	3.2
Claystone	1.9
Diabase	1.7
Diorite	1.75
Dolomite	1.8
Epidosite	1.7
Gabbro	1.6
Gneiss	1.8
Granite	1.7
Gypsum	2.45
Hornstone	1.85
Limestone	1.9
Limestone (silty)	2.1
Limestone (argillaceous)	2.3
Marble	1.8
Mudstone	1.85
Pyrite	1.7
Quartz	1.55
Quartzite	1.5
Salt	2.15
Sandstone	1.6
Shale	1.7–1.75
Siltstone	1.8

TABLE 16.4—TRAVEL-TIME CORRECTION FACTOR α FOR GRAIN SIZE [AFTER MASON (1984)]

Wentworth's Classification	Grain Size (mm)	$\Delta t_s/\Delta t_c$ Correction Factor α
Silt	1/16	0.90
Very fine grained	1/16–1/8	0.95
Fine grained	1/8–1/4	1.00
Medium grained	1/4–1/2	1.05
Coarse grained	1/2–1.0	1.10
Very coarse grained	1.0–2.0	1.15
Granules	2.0–4.0	1.20
Granules	>4.0	>1.30

borehole imaging, casing inspection, and cement evaluation. These can resolve features at millimeter or centimeter scales. Moving up the plot, the borehole logging devices previously described are encountered. These easily resolve beds in the 10- to 20-cm thickness range. Cross-well tomography then bridges the gap between strictly localized wellbore measurements and imaging of interwell space. VSPs make use of the presence of a borehole and the wireline logging apparatus

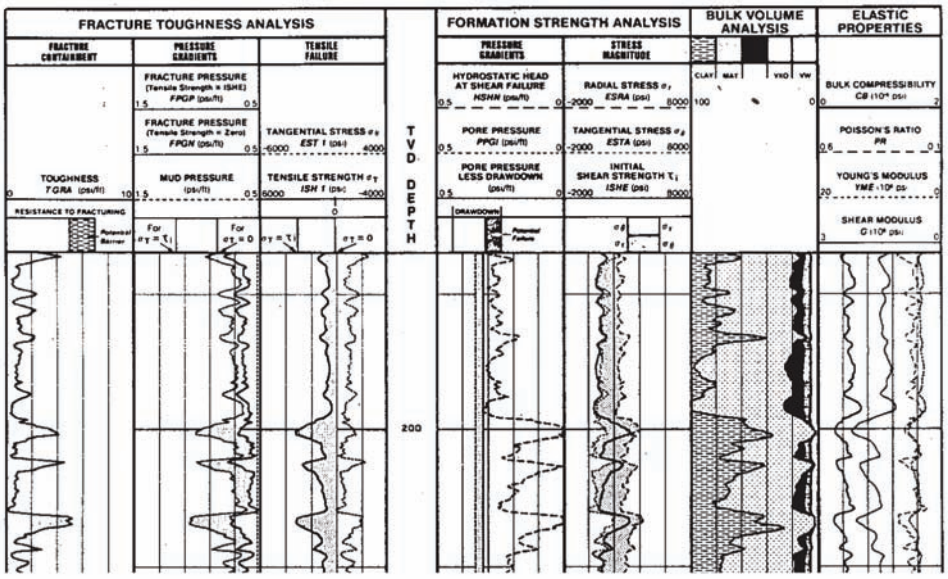


Fig. 16.27—Analysis of formation properties on a computed log. Courtesy of Schlumberger.

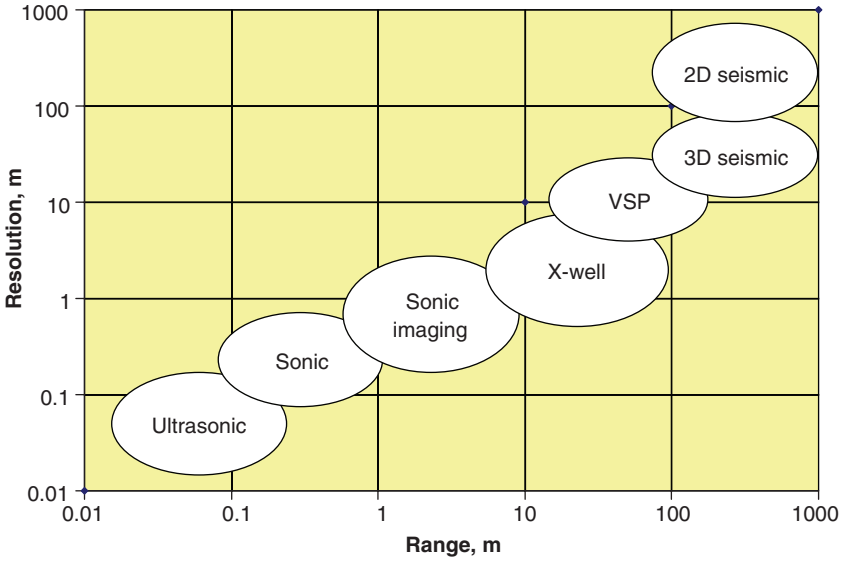


Fig. 16.28—Range and resolution of sonic and seismic measurements.

to image earth strata immediately surrounding the borehole and even beyond its total depth. Note that with each increase in range, there is a corresponding decrease in measurement resolution. At the high end of the scale shown, 2D and 3D seismic surveys suffer from the inability to resolve features (in the vertical direction) smaller than 10 to 100 m, even though they can illuminate a lateral extent of hundreds or thousands of meters.

The link between borehole sonic logging and seismic logging is best illustrated by **Fig. 16.29,** which superimposes a seismic wiggle trace on a typical earth formation and its corresponding sonic log trace.

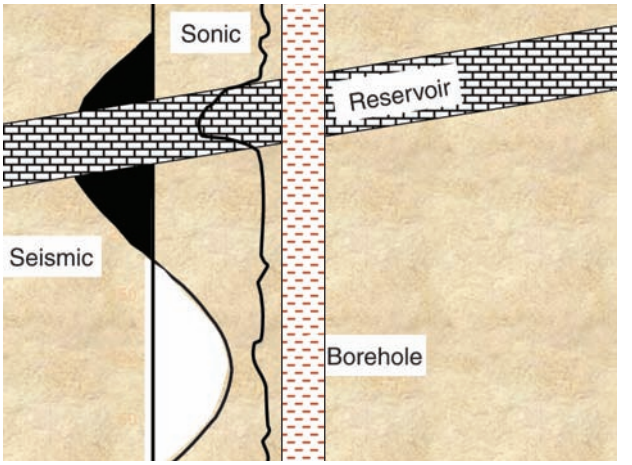


Fig. 16.29—Comparison of seismic trace with sonic log.

16.14.1 Transit-Time Integration. Sonic logs have important geophysical applications. Determining a time-vs.-depth relation for a particular geologic column is an essential step for proper analysis of seismic data. Sonic logs can be run in such a way that the integrated travel time is displayed as a series of time ticks **(Fig. 16.30).**

QUESTION 16.3. On the sonic log of Fig. 16.30, find the integrated travel time from 9,000 to 9,100 ft.

16.14.2 Synthetic Seismogram. Other seismic applications include the use of sonic logs, singly or in combination with density logs, to produce synthetic seismograms. The ability of an interface between two distinct geologic strata to reflect or transmit acoustic energy is related to the relative density and travel time in each stratum. A reflectivity coefficient can be calculated from the relationship:

$$\frac{\rho_1 V_1 - \rho_2 V_2}{\rho_1 V_1 + \rho_2 V_2}, \quad \ldots\ldots\ldots\

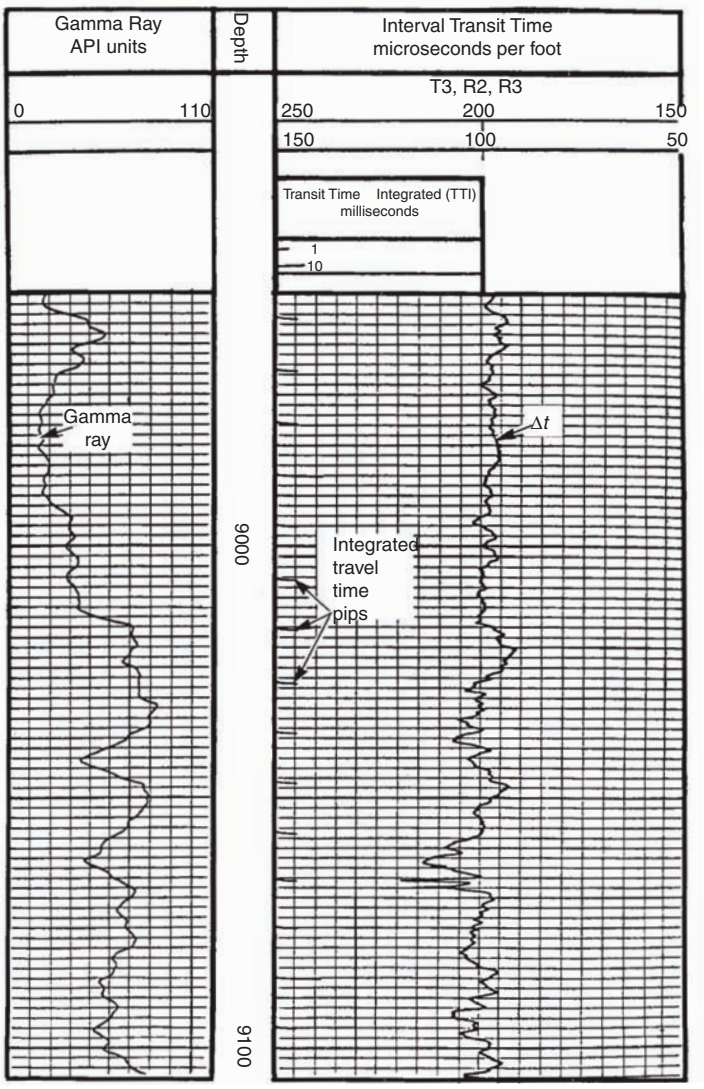


Fig. 16.30—Transit-time integration.

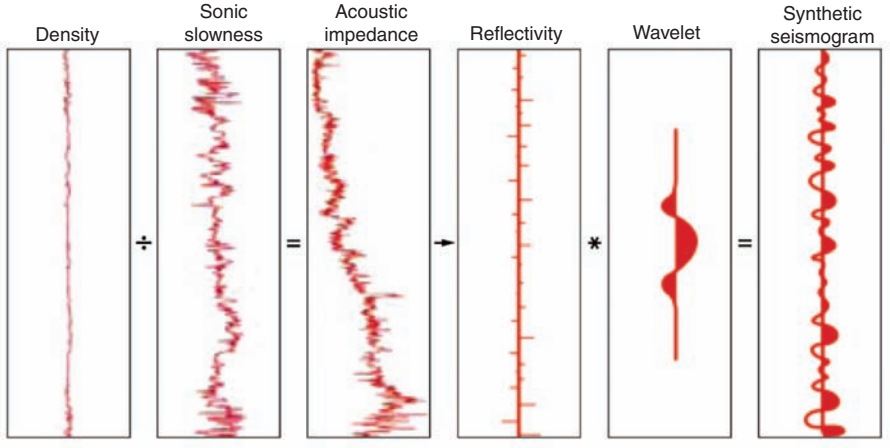


Fig. 16.31—Synthetic seismogram from density and sonic logs. Courtesy of Schlumberger.

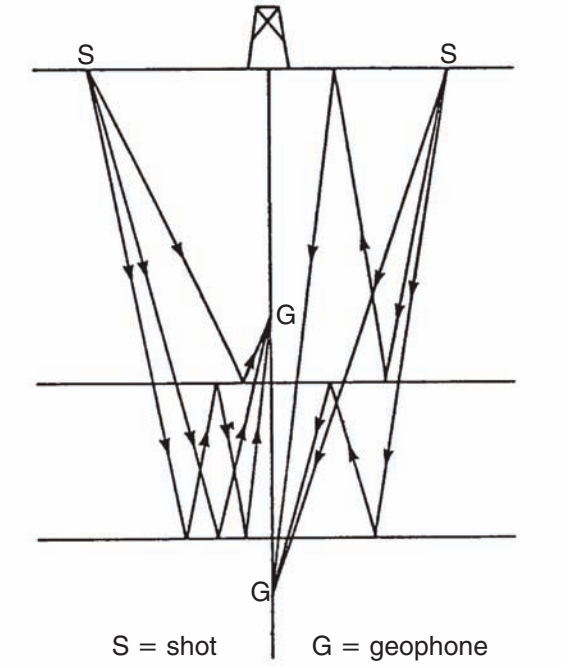


Fig. 16.32—Setup for VSP survey. Courtesy of Schlumberger.

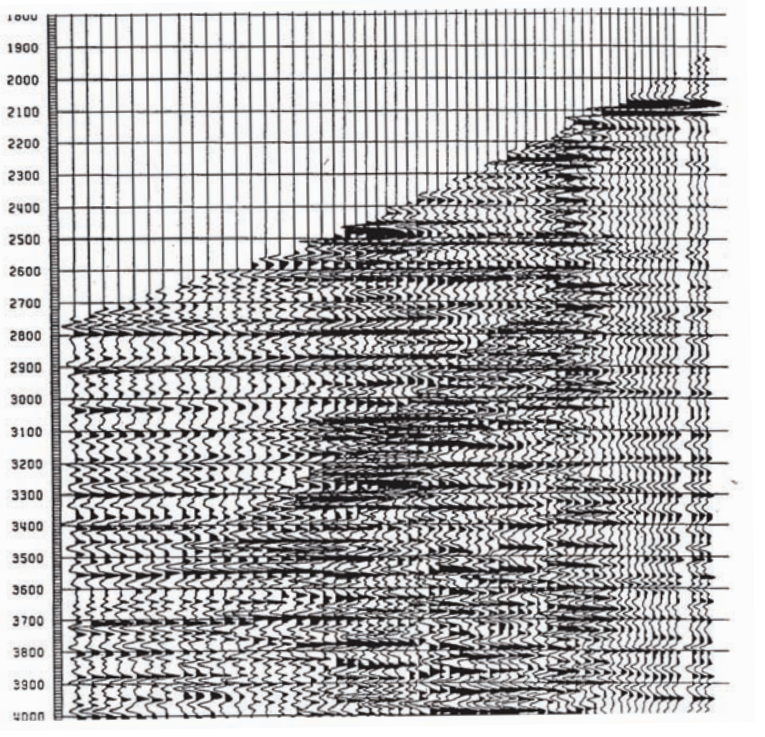


Fig. 16.33—Results of VSP survey. Courtesy of Schlumberger.

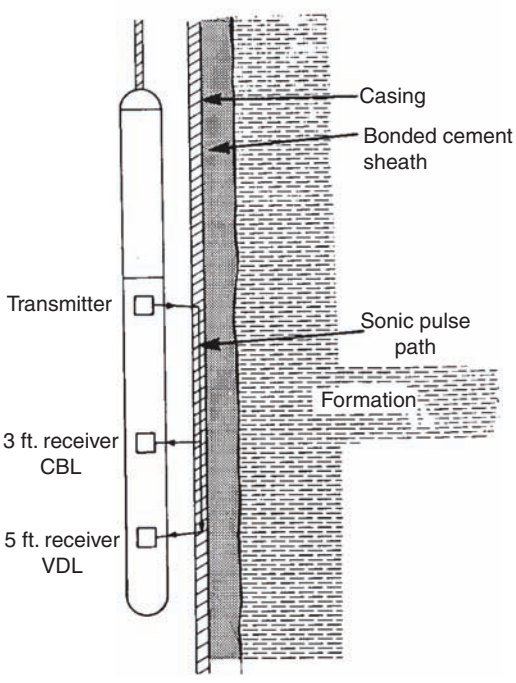


Fig. 16.34—CBL-VDL tool. Courtesy of Baker Hughes.

Fig. 16.35 illustrates the change in amplitude of the first-arrival peak when good bonding exists between the casing and the cement. The question of whether the cement sheath is bonded to the formation is solved by recourse to a wavetrain display known as the "variable density log" (VDL). A good bond between the cement and the formation is indicated when the later arrivals are strong and can be visually identified by the sharpness of the VDL traces which are on the extreme right of the display in **Fig. 16.36.** More details on CBL tools and logs are given by Bateman (1984).

16.16 Log Quality Control

Sonic logs are subject to very easily detected errors such as the cycle skips and noise already discussed. More-subtle errors can be pinned down if the log is run through marker beds such as a salt (Δt = 67 μs/ft) or anhydrite (Δt = 50 μs/ft), or into the casing where it should read 56 μs/ft (the travel time in steel).

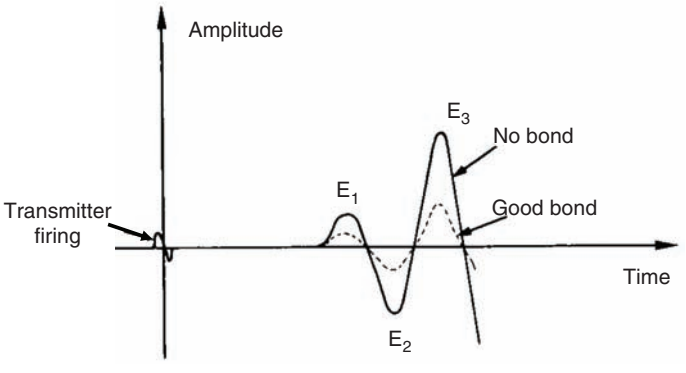


Fig. 16.35—Schematic of receiver output signal with bonded and unbonded casing. Courtesy of Schlumberger.

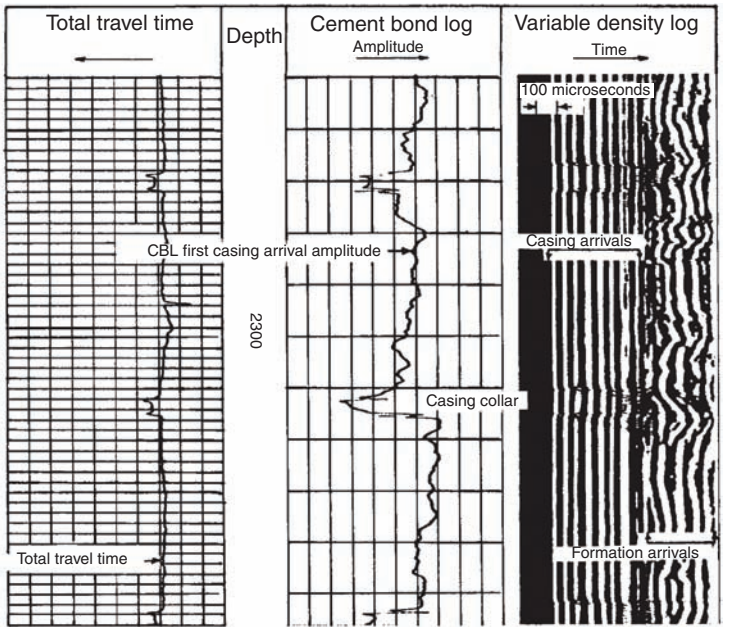


Fig. 16.36—CBL-VDL display (Brown et al. 1970). Courtesy of the SPWLA.

References

Bateman, R.M. 1984. *Cased-Hole Log Analysis and Reservoir Performance Monitoring.* Boston, IHRDC.

Brown, H.D., Grigalva, V.E., and Raymer, L.L. 1970. New Developments in Sonic Wave Train Display and Analysis in Cased Holes. *Trans.,* SPWLA 11th Annual Logging Symposium, Los Angeles, 3–6 May.

Mason, K.L. 1984. Tricone Bit Selection Using Sonic Logs. Paper SPE 13256 presented at the SPE Annual Technical Conference and Exhibition, Houston, 16–19 September.

Morris, C.F., Little, T.M., and Letton, W. 1984. A New Sonic Array Tool for Full Waveform Logging. Paper SPE 13285 presented at the SPE Annual Technical Conference and Exhibition, Houston, 16–19 September.

Wyllie, M.R.J., Gregory, A.R., and Gardner, G.H.F. 1958. An Experimental Investigation of Factors Affecting Elastic Wave Velocities in Porous Media. *Geophysics* **23** (3): 459–493.

Schlumberger. 1982. *Well Evaluation Developments, Continental Europe,* London.

General References

Asburn, B.E. 1977. Well Log Editing in Support of Detailed Seismic Studies. *Trans.,* SPWLA 18th Annual Logging Symposium, Houston, 5–8 June.

Castagna, J.P., Batzle, M.L., and Eastwood, R.L. 1985. Relationships between compressional-wave and shear-wave velocities in clastic silicate rocks. *Geophysics* **50** (4): 571–581.

Dominguez, H. and Perez, P. 1991. Permeability Estimation in Naturally Fractured Fields by Analysis of Stoneley Waves. *The Log Analyst* 32 (3): 120–128.

Garboczi, E.J. and Day, A.R. 1995. An algorithm for calculating the effective linear elastic properties of heterogeneous materials: three-dimensional results for composites with equal phase Poisson's ratios. *Journal of the Mechanics and Physics of Solids* **43:** 1349–1362.

Hicks, W.G. and Berry, J.E. 1956. Application of Continuous Velocity Logs to Determination of Fluid Saturation of Reservoir Rocks. *Geophysics* **21** (3): 739–754.

Kimball, C.V. and Marzetta, T.L. 1984. Semblance Processing of Borehole Acoustic Array Data. *Geophysics* **49** (3): 274–381.

Kokesh, F.P. and Blizard, R.B. 1959. Geometrical Factors in Sonic Logging. *Geophysics* **24** (1): 64–76.

Kokesh, F.P., Schwartz, R.J., Wall, W.B., and Morris, R.L. 1965. A New Approach to Sonic Logging and Other Acoustic Measurements. *J. Pet Tech* **17** (3): 282–286.

Knackstedt, M.A., Arns, C.H., and Pinczewski, W.V. 2003. Velocity-porosity relationships: I. Accurate velocity model for clean sandstones. *Geophysics* **68** (6): 1822–1834.

Krief, M., Garat, J., Stellingweff, J., and Ventre, J. 1990. A petrophysical interpretation using the velocities of P and S waves. *The Log Analyst* **31:** 355–369.

Leslie, H.D. and Mons, F. 1982. Sonic Waveform Analysis: Applications. Paper presented at the SPWLA Annual Logging Symposium, Corpus Christi, Texas, USA, 6–9 July.

Liu, O.Y. 1984. Stoneley Wave-Derived Dt Shear Log. Paper presented at the SPWLA Annual Logging Symposium, New Orleans, 10–13 June.

Marion, D., Nur, A., Yin, H., and Han, D. 1992. Compressional velocity and porosity in sand-clay mixtures. *Geophysics* **57** (4): 554–563.

Morris, R.L., Grine, D.R., and Arkfeld, T.E. 1964. Using Compressional and Shear Acoustic Amplitudes for the Location of Fractures. *J. Pet Tech* **16** (6): 623–632.

Pickett, G.R. 1963. Acoustic Character Logs and Their Applications in Formation Evaluations. *J. Pet Tech* **15** (6): 659–667.

Raymer, L.L., Hunt, E.R., and Gardner J.S. 1980. An Improved Sonic Transit Time-to-Porosity Transform. *Trans.,* SPWLA 21st Annual Logging Symposium, Lafayette, Louisiana, USA, 8–11 July, Paper P.

Stevens, J.L. and Day, S.M. 1983. Shear Velocity Logging in Slow Formations Using Stoneley Waves. Paper presented at the SEG Annual Meeting, Las Vegas, Nevada, 11–15 September.

Thomas, D.H. 1977. Seismic Applications of Sonic Logs. *Trans.,* 5th European SPWLA Logging Symposium, Paris, 20–21 October.

Tixier, M.P., Alger, R.P., and Doll, C.A. 1959. Sonic Logging. *J. Pet Tech* **11** (5): 106–114.

Tixier, M.P., Alger, R.P., and Tanguy, D.R. 1960. New Developments in Induction and Sonic Logging. *J. Pet Tech* **12** (5): 79–87.

Wyllie, M.R.J., Gregory, A.R., and Gardner, G.H.F. 1956. Elastic Wave Velocities in Heterogeneous and Porous Media. *Geophysics* **21** (1): 41–70.

Answers to Questions

QUESTION 16.1.
$\phi_s = 19\%$.

QUESTION 16.2.
$V_f = 5{,}650$ ft/sec.
$\Delta t_f = 177$ μs/ft.

QUESTION 16.3.
10 ms

Appendix 16A

TABLE A-1—COMPRESSIONAL WAVE VELOCITY AND INTERVAL TRANSIT TIME IN GEOLOGIC MATERIALS

	Matrix Travel Time (μsec/ft)		Matrix Velocity (ft/sec)	
Material	Average	Range	Average	Range
Dunite	38.2	(34.7–41.1)	26,174	(24,305–28,807)
Gabbro	42.4	(42.4–47.6)	23,586	(20,998–23,596)
Hematite	42.9		23,295	
Domotie	43.5	(40.0–45.0)	22,727	(22,222–25,000)
Norite	44.1	(43.5–49.0)	21,683	(20,400–22,967)
Diabase	44.6	(44.0–46.0)	22,435	(21,746–22,730)
Anorthosite	45.4		22,016	
Calcite	46.5	(45.5–47.5)	21,505	(21,053–22,000)
Aluminum	48.7		20,539	
Anhydrite	50.0		20,000	
Albitite	50.2	(49.5–50.6)	19,916	(19,752–20,212)
Granite	50.8	(46.8–53.5)	19,685	(18,691–21,367)
Steel	50.8		19,686	
Limestone	52.0	(47.7–53.0)	19,231	(18,750–21,000)
Angbeinite	52.0		19,231	
Iron	52.1		19,199	
Gypsum	53.0	(52.5–53.0)	19,047	(18,868–19,047)
Serpentine	53.9		18,702	
Quartzite	55.0	(52.5–57.7)	18,182	(17,390–19,047)
Quartz	55.1	(54.7–55.5)	18,149	
Sandstone	57.0	(53.8–100.0)	17,544	(17,390–19,030)
Casing* (steel)	57.1		17,500	(18,000–18,275)
Basalt	57.5		17,391	(10,000–19,500)
Polyhalite	57.5		17,391	
Aluminum tub	60.9		16,400	
Tiona	65.0		15,400	
Heulandite	66.1		15,355	
Halite	65.7		15,000	
Stilbite	68.0		14,699	
Sylvite	74.0		13,500	
Copper	78.7		12,700	
Crnallite	83.3		12,000	
Glacial ice	87.1		11,480	
Cement (wide variation)	95.0	(83.3–95.1)	10,526	(10,526–12,000)
Concrete (wide variation)	95.2	(83.3–125.0)	10,500	(8,000–12,000)
Shale	100.0	(60.0–170.0)	10,000	(5,882–16,667)

* Value of extensional (“first arrival”) wave in thin rods.

TABLE A-2—COMPRESSIONAL WAVE VELOCITY AND INTERVAL TRANSIT TIME IN GEOLOGIC MATERIALS

	Matrix Travel Time (μsec/ft)		Matrix Velocity (ft/sec)	
Material	Average	Range	Average	Range
Anthracite coal	105.0	(90.0–120.0)	9,524	(8,333–11,111)
Bituminous coal	120.0	(100.0–140.0)	8,333	(5,906–10,000)
Sulfur	122.0		8,200	
Lead	141.1		7,087	
Lignite	160.0	(140.0–180.0)	6,250	(3,281–7,143)
Water				
200 K ppm NaCl,15 psi	180.5		5,540	
150 K ppm NaCl, 15 psi	186.0		5,375	
100 K ppm NaCl, 15 psi	192.3		5,200	
Pure	207.0		4,380	
Rubber (Neoprene)	190.5		5,248	
Kerosene, 15 psi	214.5		4,659	
Oil	238.0		4,200	
Methane, 15 psi	626.0		1,600	
Air, 15 psi	919.0		1,088	
Ethane (10°C) 0.00125 g/cm^3	989.6		1,010	
CO_2 0.0019776 g/cm^3	1176.5		850	

Appendix 16B

The Gassmann equation relates the speed of a compressional wave, V_P, to porosity, ϕ, rock density, ρ, Poisson's ratio, σ, and pore fluid content:

$$V_P^2 = \frac{K_{ma}}{\rho}\left[\beta\gamma + \frac{(1-\beta)^2}{B+(1-\beta)}\right], \quad \text{(16A-1)}$$

where

K = compressibility modulus
ρ = density
σ = Poisson's ratio
ϕ = porosity

and

$$\gamma = \frac{3(1-\sigma_{ma})}{1+\sigma_{ma}} \quad \text{(16A-2)}$$

$$B = \phi\left(\frac{K_{ma}}{K_{fl}}\right) - 1 \quad \text{(16A-3)}$$

$$\beta = \frac{K_b}{K_{ma}} \quad \text{(16A-4)}$$

The subscripts are *ma* for matrix, *b* for bulk, and *fl* for fluid. Units are bulk modulus in dynes/cm^2, density in g/cm^3, velocity in cm/s, and porosity as a fraction.

It should be noted that the Gassmann equation calculates Δt_c from a knowledge of the elastic constants of a medium. In practice, the exact reverse process is followed in that Δt_c is measured using a sonic logging device and its value, along with other log-derived parameters (such as density and porosity), is used to determine the formation elastic constants in situ.

Chapter 17

Formation Density Log

The density of a formation is one of the most important pieces of data in formation evaluation. In the majority of the wells drilled, it is used as the primary indicator of porosity. In combination with other measurements, data from a formation density log may also be used to indicate lithology and formation-fluid type.

A conventional compensated density log is shown in **Fig. 17.1,** with the value of formation bulk density (ρ_b) in Tracks 2 and 3. The most frequently used scales are either 2.0 to 3.0 g/cm^3 or 1.95 to 2.95 g/cm^3 across two tracks. A correction curve, $\Delta\rho$, is sometimes displayed in Track 3 or, less frequently, in Track 2. Gamma ray and caliper curves usually appear in Track 1.

Compensated formation density tools are used alone or in combination with other tools, such as the compensated neutron tool. The density tool is a pad-type tool with a backup caliper arm that forces the skid against the side of the borehole. **Fig. 17.2** illustrates the articulated device (skid) that carries a gamma ray source and two detectors, which are referred to as the short-spacing and long-spacing detectors.

17.1 Operating Principle

Gamma rays are emitted continuously from the source. They pass through the mudcake and enter the formation, where they progressively lose energy until either they are completely absorbed by the rock matrix or they return to one or the other of the two gamma ray detectors in the tool. Dense formations absorb many gamma rays; low-density formations absorb fewer gamma rays. Therefore, high count rates at the detectors indicate low-density formations, and low count rates at the detectors indicate high-density formations.

Gamma rays can react with matter in three distinct ways:

1. Compton scattering: When a gamma ray collides with an electron orbiting a nucleus, the electron is ejected from its orbit, and the incident gamma ray loses energy.
2. Photoelectric effect: When a gamma ray collides with an electron, it loses all its energy, and the electron is ejected from the atom.
3. Pair production: A gamma ray interacts with an atom to produce an electron and a positron. These will later recombine to form another gamma ray.

If an incident beam of gamma rays strikes a target of thickness x, its intensity is reduced on passing through the target in such a way that:

$$I_{\text{out}} = I_{\text{in}} e^{-\mu x}, \quad \ldots\ldots\ldots\

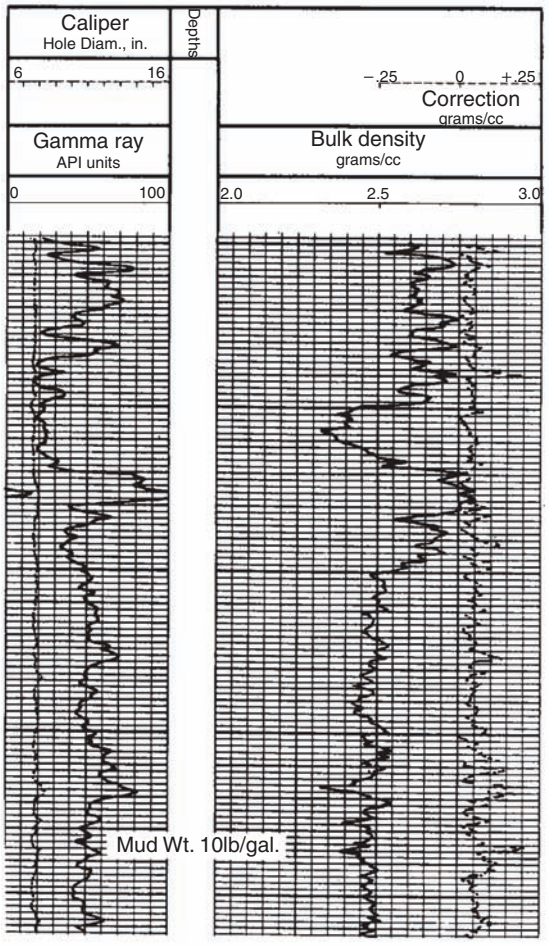


Fig. 17.1—Compensated formation density log presentation. Courtesy of Schlumberger.

Fig. 17.4 shows μ as a function of incident gamma ray energy for all three types of interaction. The conventional gamma ray source used in logging tools is made of cesium or cobalt, and the emitted gamma rays have an energy of 0.63 MeV. Because pair production requires energies higher than two or three MeV, it is obvious from Fig. 17.4 that this type of interaction will not occur.

The detectors used in conventional density tools have a practical lower limit to the gamma ray energy level that they can detect. This lower limit is approximately 0.2 MeV. Therefore, the operating range is between the two vertical lines (Fig. 17.4) that mark the energy range between the gamma rays emitted from the source and the detection limit of the detectors. Compton scattering, therefore, becomes the only possible form of gamma ray interaction that can be monitored by conventional density tools. The net effect of gamma ray Compton scattering and absorption is that the count rate seen at the detector is logarithmically proportional to the formation density **(Fig. 17.5):**

$$\log(\text{count rate}) = A + B\,(\text{formation density}). \quad \ldots\ldots\ldots\

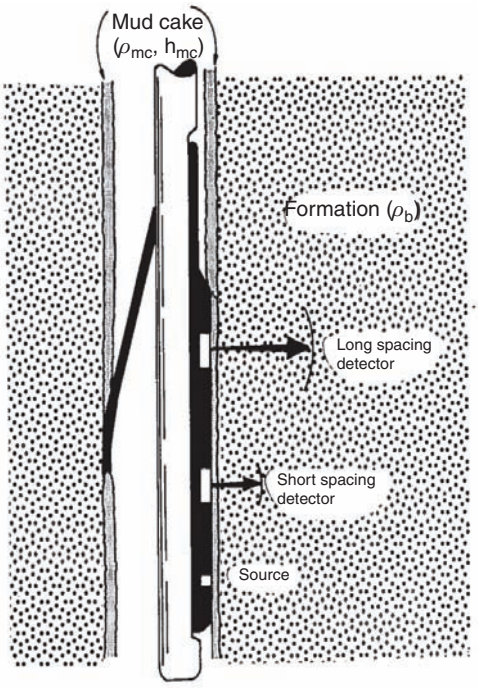


Fig. 17.2—Schematic of the dual-spacing formation density logging device. Courtesy of Schlumberger.

17.2 Mudcake Compensation

If the mudcake has a density different from that of the formation, both the near and far count rates will change. **Fig. 17.7** shows where a plotted point would fall if a formation with a bulk density of 2.7 g/cm^3 were to have an ever-increasing amount of mudcake with density of 1.5 g/cm^3 placed between it and the tool. In the extreme case of "infinite" mudcake thickness, both detectors will "see" only mudcake and read a value of 1.5 g/cm^3.

The arc describing the locus of the points is referred to as a rib. The zero-mudcake line is referred to as a spine. A complete set of spine and ribs can be drawn for various thicknesses

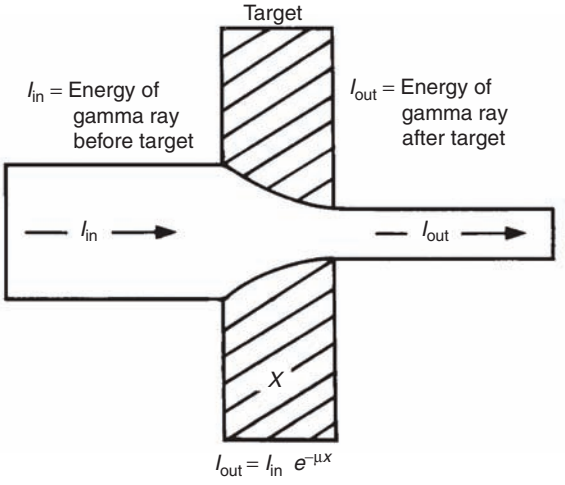


Fig. 17.3—Gamma ray mass absorption coefficient.

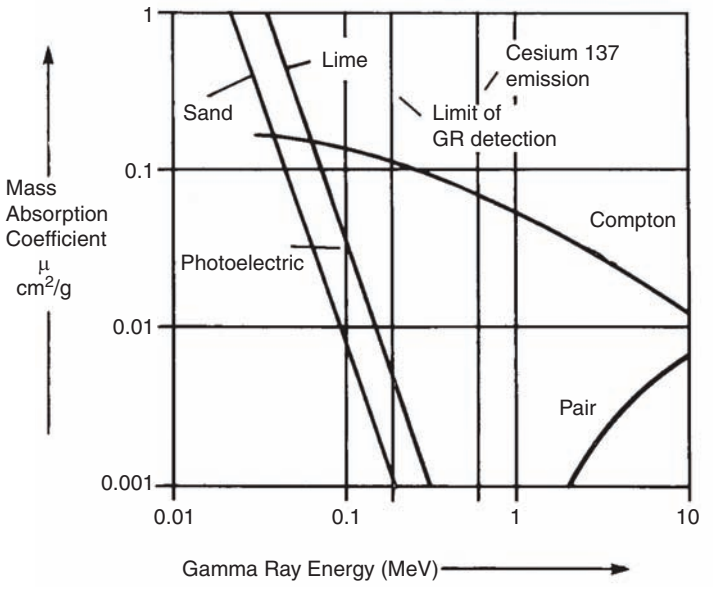


Fig. 17.4—Mass absorption coefficient vs. gamma ray energy.

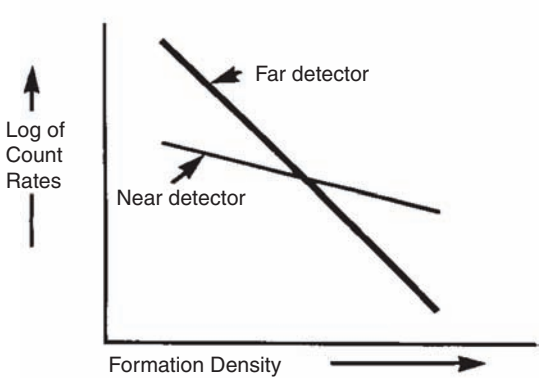


Fig. 17.5—Detector count rates vs. formation density measurements.

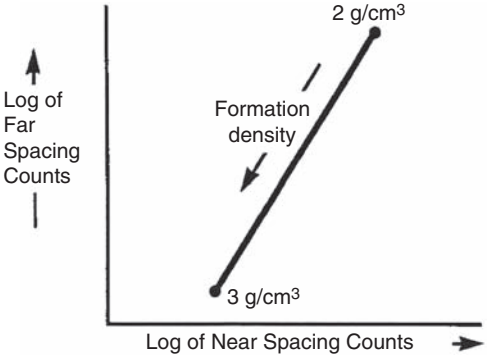


Fig. 17.6—Near and far count rates of the formation density tool.

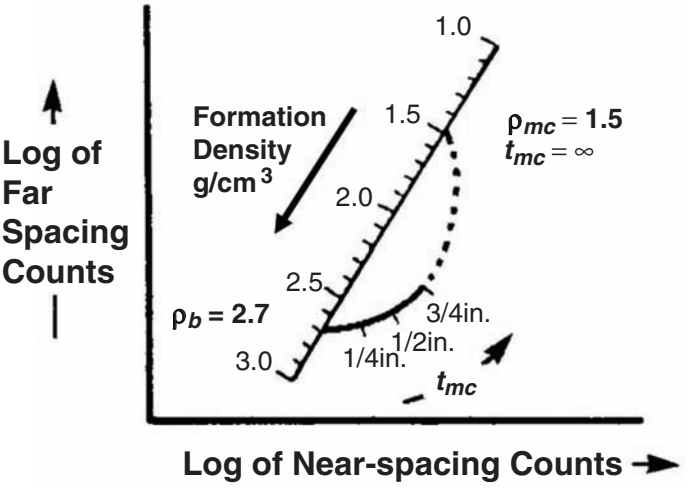


Fig. 17.7—Mudcake compensation.

and densities of mudcakes, as shown in **Fig. 17.8.** Note that the ribs also extend to the left of the spine for mudcakes with a density greater than the formation density (for example, in barite muds).

The surface equipment associated with the density tool computes the position of the point on the spine-and-ribs chart and then moves the point down the rib to intercept the spine. At this point, a corrected value of ρ is recorded in the log. The value of $\Delta\rho$ is calculated as the difference between ρ from the long spacing and ρ_{corr}. Therefore, $\Delta\rho$ is positive in light muds and negative in heavy muds.

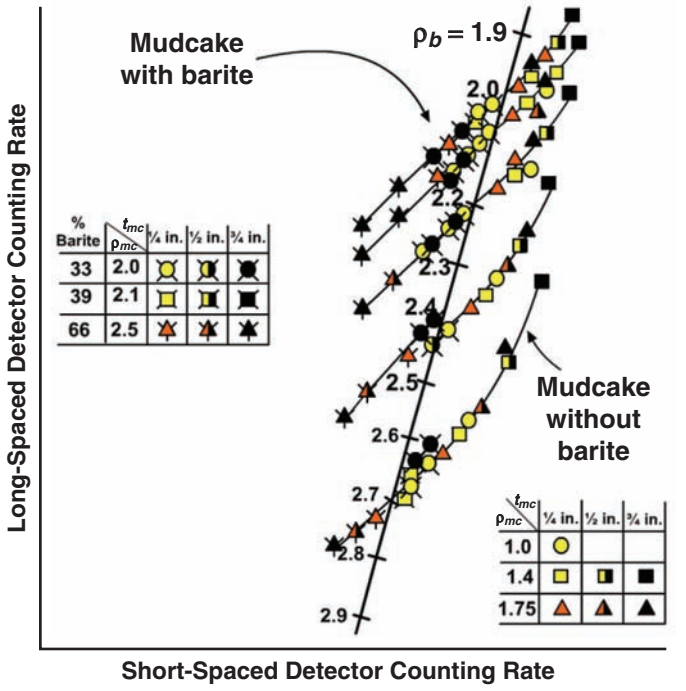


Fig. 17.8—Spine-and-ribs plot showing response of count rates to mudcake. Courtesy of Schlumberger.

17.3 Electron Density

Because Compton scattering is an interaction between gamma rays and electrons, the density actually measured is the electron density ρ_e, not the bulk density ρ_b. Therefore, the ratio between electron density and bulk density must be investigated.

An element is distinguished by its atomic weight, *A,* and its atomic number, *Z.* For example, oxygen has an atomic weight of 16 and an atomic number of 8. Electron density is related to bulk density by the equation

$$\rho_e = \rho_b \cdot 2(Z/A). \quad \ldots\ldots (17.3)$$

Therefore, for oxygen, $\rho_e = \rho_b$, because $2(Z/A) = 1$. Most elements also have $2(Z/A)$ equal or close to unity, but there are important exceptions. The most important exception is hydrogen, which has a $2(Z/A)$ value of 1.9841. **Table 17.1** lists some of the common elements found in hydrocarbon bearing formations along with their respective *A* and *Z* values. More values are listed later in Table 17.3.

The fact that hydrogen's $2(Z/A)$ value is closer to 2 than to unity causes calibration of the density tool to be a special case. By definition, the tool should give correct porosities in freshwater-filled limestone. Because the tool measures ρ_e, the ρ_e value of both water and limestone must be known. For an element, $\rho_e = \rho_b \cdot 2(Z/A)$, but for a compound molecule,

$$\rho_e = \rho_b \frac{2Z}{\text{molecular weight}} \quad \ldots\ldots (17.4)$$

For limestone, with chemical formula $CaCO_3$ and density 2.71 g/cm^3,

$$\begin{aligned} \rho_e &= \rho_b \frac{2(20+6+3\times 8)}{40.08+12.011+3\times 16} \\ &= \rho_b \times 0.9991 \\ &= 2.71\times 0.991 = 2.7076. \end{aligned} \quad \ldots\ldots (17.5)$$

For water, with chemical formula H_2O and density 1.0 g/cm^3,

$$\rho_e = \rho_b \frac{2(2+8)}{2.016+16} = 1\times 1.1101 = 1.1101 \quad \ldots\ldots (17.6)$$

TABLE 17.1—*A* AND *Z* VALUES FOR COMMON ELEMENTS

Element	*A*	*Z*	(*Z*/*A*)
H	1.008	1	1.9841
C	12.011	6	0.9991
O	16.000	8	1.0000
Na	22.990	11	0.9569
Mg	24.320	12	0.9868
Al	26.980	13	0.9637
Si	28.090	14	0.9968
Cl	35.460	17	0.9588
Ca	40.080	20	0.9980

Therefore, the tool must be calibrated to give a ρ_e reading in water of 1.1101 and a ρ_e in limestone of 2.7076. A linear conversion is all that is required:

$$\rho_a = A + B\rho_e, \quad \ldots\ldots\ldots\

TABLE 17.2—APPARENT DENSITY VALUES FOR VARIOUS MINERALS AND FLUIDS

Compound	Formula	Actual Density ρ_b	$\frac{2Z}{\text{Mol. Wt.}}$	ρ_e	ρ_a (as seen by tool)
Quartz	SiO_2	2.654	0.9985	2.650	2.648
Calcite	$CaCO_3$	2.710	0.9991	2.708	2.710
Dolomite	$CaCO_3MgCO_3$	2.870	0.9977	2.863	2.876
Anhydrite	$CaSO_4$	2.960	0.9990	2.957	2.977
Sylvite	KCl	1.984	0.9657	1.916	1.863
Halite	NaCl	2.165	0.9581	2.074	2.032
Gypsum	$CaSO_42H_2O$	2.320	1.0222	2.372	2.351
Anthracite Coal		1.400 1.800	1.030	1.442 1.852	1.355 1.796
Bituminous Coal		1.200 1.500	1.060	1.272 1.590	1.173 1.514
Fresh Water	H_2O	1.000	1.1101	1.110	1.00
Salt Water	200,000 ppm	1.146	1.0797	1.237	1.135
"Oil"	$n(CH_2)$	0.850	1.1407	0.970	0.850
Methane	CH_4	ρ_{meth}	1.247	1.247 ρ_{meth}	1.335 ρ_{meth}–0.188
"Gas"	$C_{1,1}H_{4,2}$	ρ_g	1.238	1.238 ρ_g	1.325 ρ_g–0.188

Source: Schlumberger

17.4 Density Porosity (ϕ_D)

Because the density of a mixture of components is a linear function of the densities of its individual constituents, it is a simple matter to calculate the porosity of a porous rock. For this purpose, it is useful to consider the bulk-volume model of a clean formation with water-filled pore spaces, as illustrated in **Fig. 17.10.**

A unit volume of porous rock consists of a fraction ϕ made up of water and a fraction $(1 - \phi)$ made up of solid rock matrix. Therefore, the bulk density of the sample can be written as:

$$\rho_b = \rho_{ma}(1-\phi) + \rho_f \phi, \quad \ldots\ldots\ldots\

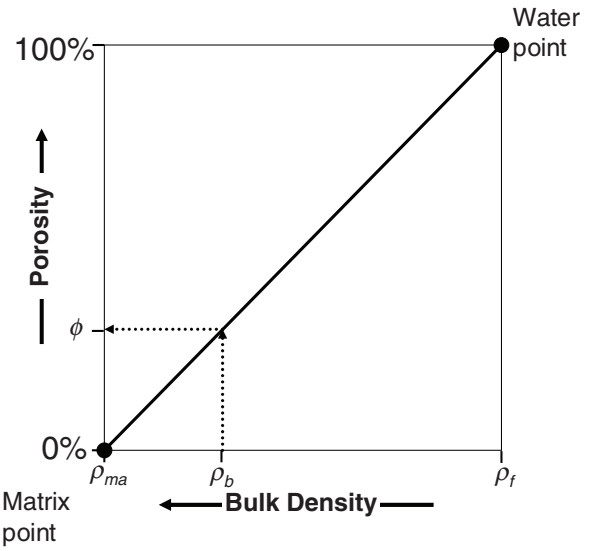


Fig. 17.11—Density-porosity graph.

where ϕ_D is used to denote a porosity value derived from a measurement of formation density. The same concept can be illustrated graphically, as shown in **Fig. 17.11,** where ρ_b is plotted against porosity. Note that points falling on the line connecting the matrix point (ρ_{ma}, $\phi = 0\%$) and the water point (ρ_f, $\phi = 100\%$) represent all possible cases extending from a zero-porosity rock matrix up to 100% porosity. Any intermediate value of ρ_b corresponds to some porosity ϕ.

Note that porosity, strictly speaking, is a decimal fraction and that the assumption is made that ρ_b is equal to ρ_a, the tool reading. Density porosity, given the assumptions made, can be found either using a calculator or graphically using **Fig. 17.12,** which generalizes the concept from Fig. 17.11 and builds in response lines for a number of different matrix materials and pore-filling fluids. To become familiar with this chart and its application, the reader is invited to work the following two examples.

QUESTION 17.3. In a dolomite formation, $\rho_{ma} = 2.87$, $\rho_b = 2.44$, and $\rho_f = 1.0$ (fresh water). Find $\phi_D = ?$

QUESTION 17.4. In a sandstone formation, $\rho_{ma} = 2.65$, $\rho_b = 2.40$, and $\rho_f = 1.1$ (salt-mud filtrate). Find $\phi_D = ?$

This derivation of porosity assumes a clean matrix of known density and a water-filled pore space. These computed values of ϕ_D can be incorrect when the lithology is mixed or unknown, when shale is present, when gas or light hydrocarbons are present in the flushed zone, or when pad contact with the formation is lost in washed-out holes.

Because the tool performs its reading in the zone adjacent to the borehole wall, where mud filtrate has flushed away most of the original formation fluids, the choice of a value for ρ_f is dictated by the density of the mud filtrate, which in turn is a function of its salinity, pressure, and temperature. **Fig. 17.13** is useful for estimating ρ_f in saltwater-filled formations.

QUESTION 17.5. Use Fig. 17.13 to find the density of a sodium chloride solution at 240°F and 4,000 psi if the concentration is 200,000 ppm.

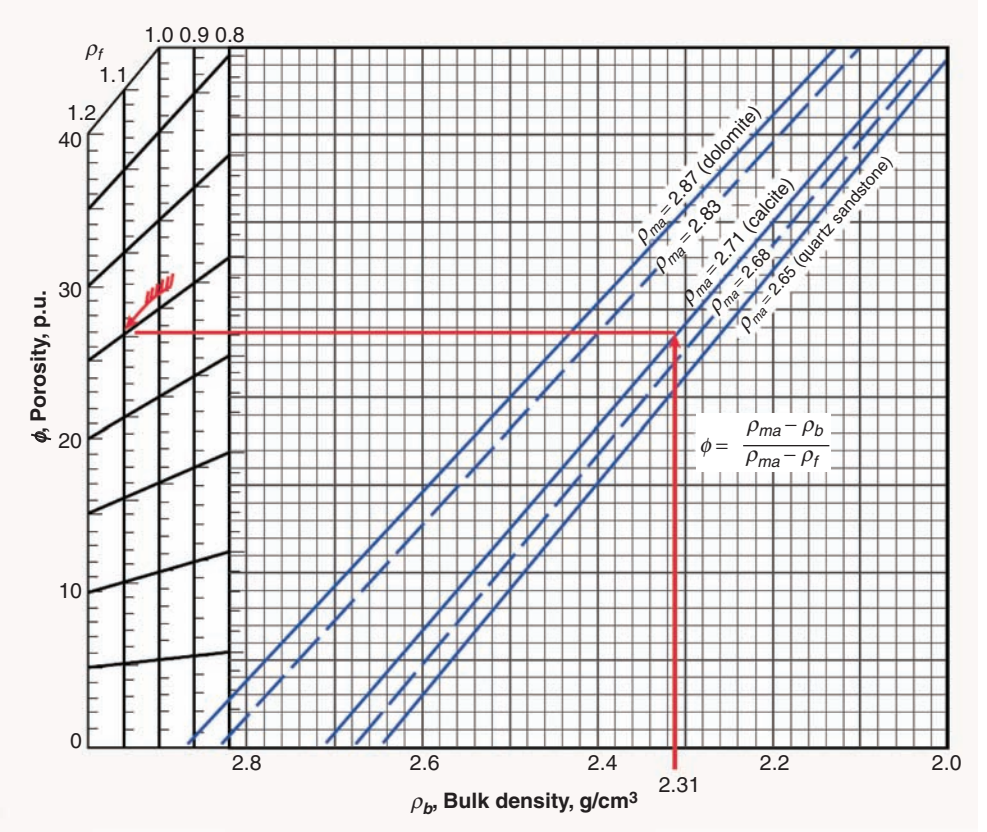


Fig. 17.12—Determination of porosity from formation density log. Courtesy of Schlumberger.

17.5 Shale Effects

When, in addition to matrix and fluid, a third component, shale, is introduced, the same principle can be applied as before. **Fig. 17.14** illustrates a bulk-volume model of a shaly formation. The volume fraction of shale is referred to as V_{sh}; the volume fraction of matrix is $(1 - \phi - V_{sh})$. As before, an equation may be written for the bulk density of such a mixture:

$$\rho = (1 - V_{sh} - \phi)\rho_{ma} + V_{sh}\rho_{sh} + \phi\rho_f \quad \ldots\ldots\ldots\

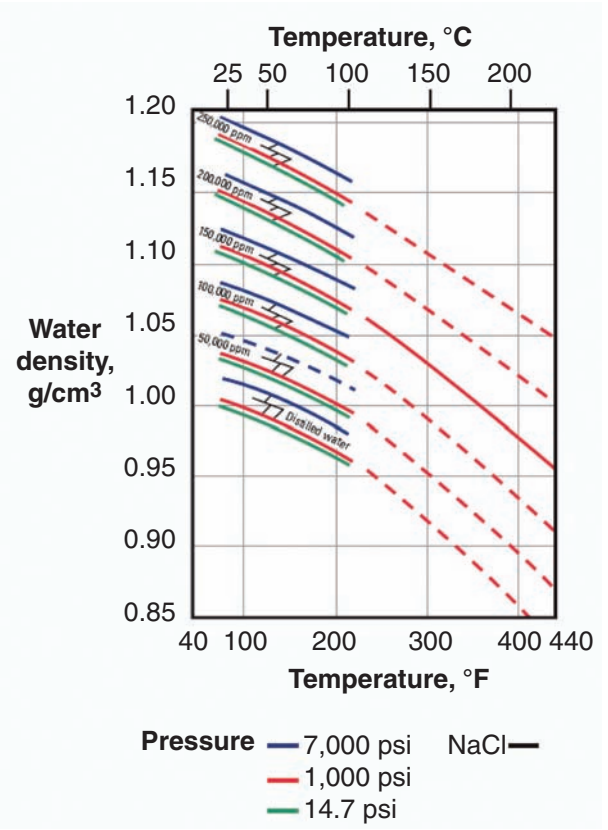


Fig. 17.13—Density of NaCl solutions vs. pressure and temperature. Courtesy of Schlumberger.

disseminated in a sand may not be the same as those deposited in a pure shale, it is still widely used for quick assessments and gives satisfactory results in most cases.

In this context, it is worth remembering that shales are in fact porous formations, albeit with effectively zero permeability and hence zero effective porosity. If the clay mineral in a shale has a matrix density of 3 g/cm^3 (which is a good average), a shale with a bulk density of 2.5 g/cm^3 has a total porosity of 25%. The same shale logged on an apparent sandstone-porosity scale would appear to have a porosity of approximately 9%.

17.6 Gas Effects

To quantify the effects of gas on the response of the density tool, both the gas saturation and the effective density of the gas (ρ_g) must be known. Once again, a bulk-volume model is useful in

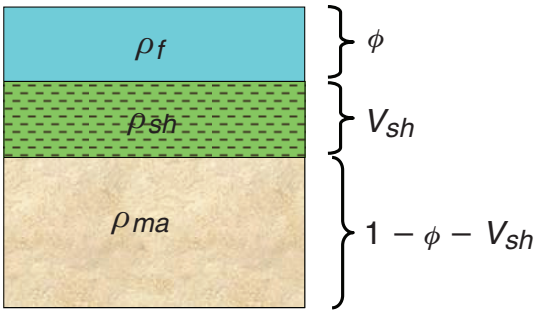


Fig. 17.14—Bulk-volume model of shaly formation.

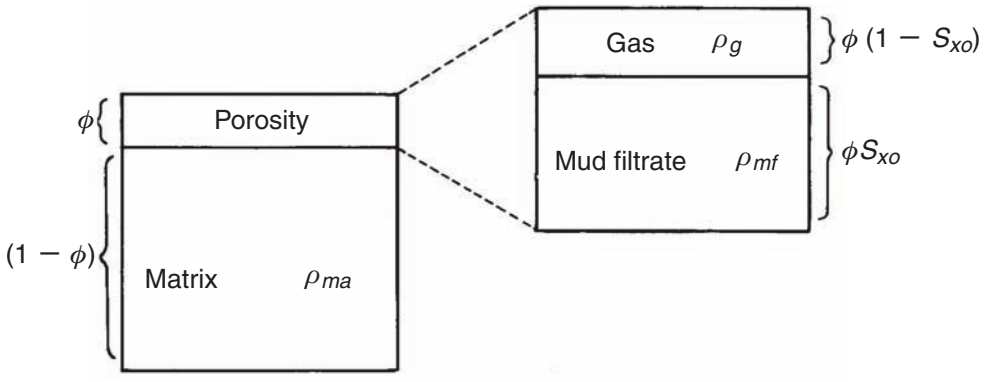


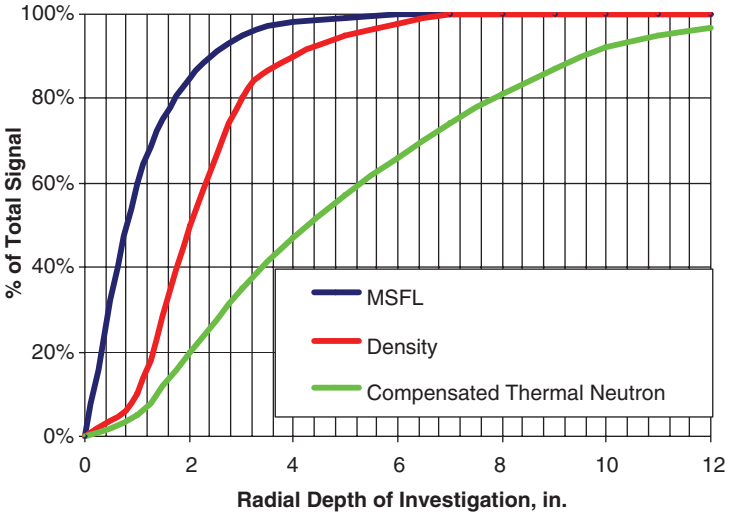
Fig. 17.15—Bulk-volume model of a clean gas-bearing formation.

quantifying the relationship between formation bulk density and the unknown quantities. Given a clean, gas-bearing formation **(Fig. 17.15),** the expression for formation bulk density is:

$$\rho_b = \rho_{ma}(1-\phi) + \rho_{mf}\phi\, S_{xo} + \rho_g \phi(1-S_{xo}) \quad \ldots\ldots\ldots\

All the terms in this expression are either known or can be read from the appropriate log, with the exception of ρ_g, which may be calculated from a knowledge of gas gravity to air and reservoir temperature and pressure. An approximation for ρ_g is given by the algorithm

$$\rho_g = \frac{0.18}{(7644/\text{depth in ft}) + 0.22}, \quad \ldots\ldots\ldots\



17.17—Comparison of depth of investigation of the density tool with that of other devices.

17.8 Lithologic Density Tool

Litho-density tools (LDTs) are improved and expanded versions of standard formation density logging tools. In addition to the bulk density (ρ_b), these tools also measure the photoelectric absorption index (P_e) of the formation. This parameter enables a lithological interpretation to be made without prior knowledge of porosity.

17.8.1 Physical Principle. Gamma rays interact with matter in various ways, depending on their energy. However, only two reactions are of interest when dealing with relatively low-energy gamma rays originating from the chemical sources currently used in logging tools. These reactions are the Compton scattering of gamma rays by electrons and the photoelectric absorption of gamma rays by electrons. Compton scattering has already been discussed in the context of conventional density-tool measurements.

The photoelectric effect occurs when a gamma ray collides with an electron and is absorbed in the process, so that all its energy is transferred to the electron. The probability of this reaction taking place depends upon the energy of the incident gamma rays and the type of atom. The photoelectric absorption index of an atom increases with increasing atomic number Z.

$$P_e = \left(0.1 \times Z_{\text{eff}}\right)^{3.6} \quad \text{.....(17.22)}$$

The Compton effect occurs over a wide energy range, whereas the photoelectric effect occurs only when lower-energy gamma rays are involved, as indicated in **Fig. 17.18,** which shows a plot of the mass absorption coefficient μ against the gamma ray energy. This figure also shows that the photoelectric effect, unlike Compton scattering, is dependent on the type of formation.

17.8.2 Measurement Theory. The LDT is similar to a conventional compensated density device and uses a skid containing a gamma ray source and two gamma ray detectors held against the borehole wall by a spring-actuated arm **(Fig. 17.19).** Gamma rays are emitted from the tool with an energy of 662 keV and are scattered by the formation, losing energy until they are absorbed through the photoelectric effect.

At a finite distance from the source, there is a gamma ray energy spectrum, as shown in **Fig. 17.20.** This figure also shows that an increase in the formation density results in a decrease in the number of gamma rays detected over the whole spectrum. For formations of constant density but

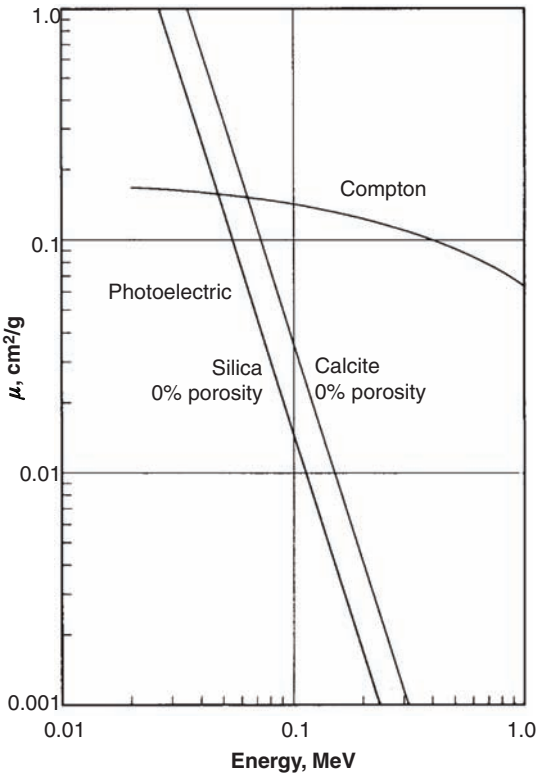


Fig. 17.18—Gamma ray mass absorption coefficients. Courtesy of Schlumberger.

different photoelectric absorption coefficients **(Fig. 17.21),** the gamma ray spectrum is altered only at lower energies.

Note in Fig. 17.21 that region H supplies only information related to the density of the formation, whereas region L provides data related to both the electron density and the photoelectric absorption index. By comparing the counts in the energy windows H and L, the photoelectric

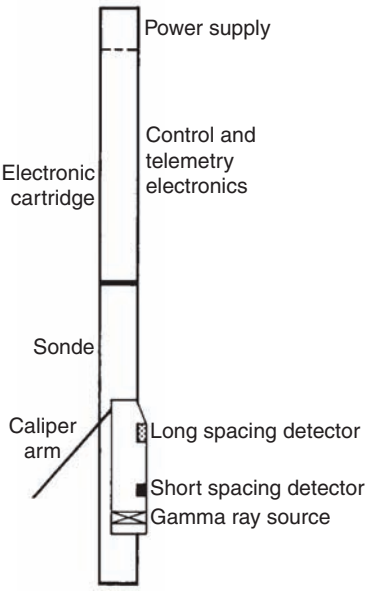


Fig. 17.19—The lithologic density tool. Courtesy of Schlumberger.

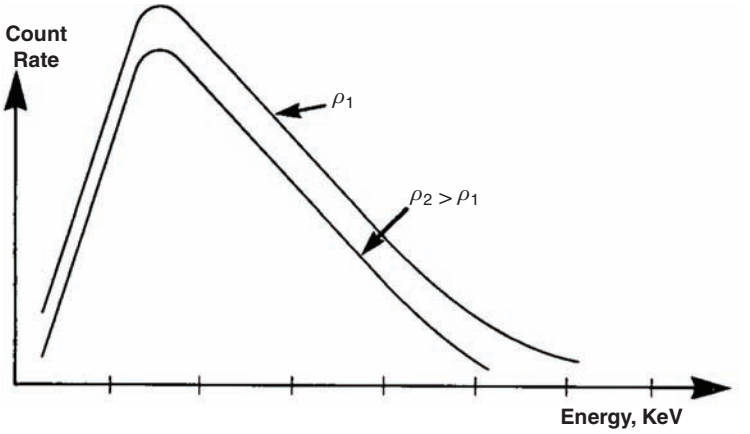


Fig. 17.20—Variations in gamma ray spectrum for formations of different densities. Courtesy of Schlumberger.

absorption index can be measured. The gamma ray spectrum at the short-spacing detector is analyzed only for a density measurement, which is used to correct the formation density determined from the long-spacing spectrum for the effects of mudcake and rugosity.

The LDT skid-and-detector system produces greater count rates than those obtained with conventional density tools. This leads to lower statistical variability and better repeatability of the measurements. The skid geometry is such that the density reading has a sharper vertical resolution than that of the conventional density measurement. The P_e measurement also has a high resolution, which is useful in identifying fractures and laminar formations.

17.8.3 Interpretation of the P_e Curve. The photoelectric absorption coefficient is virtually independent of porosity, with only a slight decrease in the coefficient as the porosity increases. Similarly, the fluid content of the formation has little effect on the coefficient. Simple lithologies, such as pure sandstone or anhydrite, can be read directly from logs using the P_e curve (PEF) alone **(Fig. 17.22). Table 17.3** lists the P_e values for the most commonly occurring reservoir rocks and evaporites.

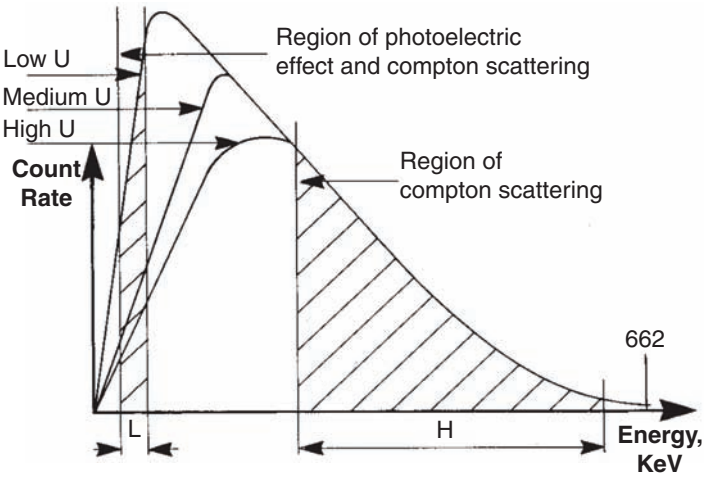


Fig. 17.21—Variations in gamma ray spectrum for formations of constant density but different photoelectric capture cross sections. Courtesy of Schlumberger.

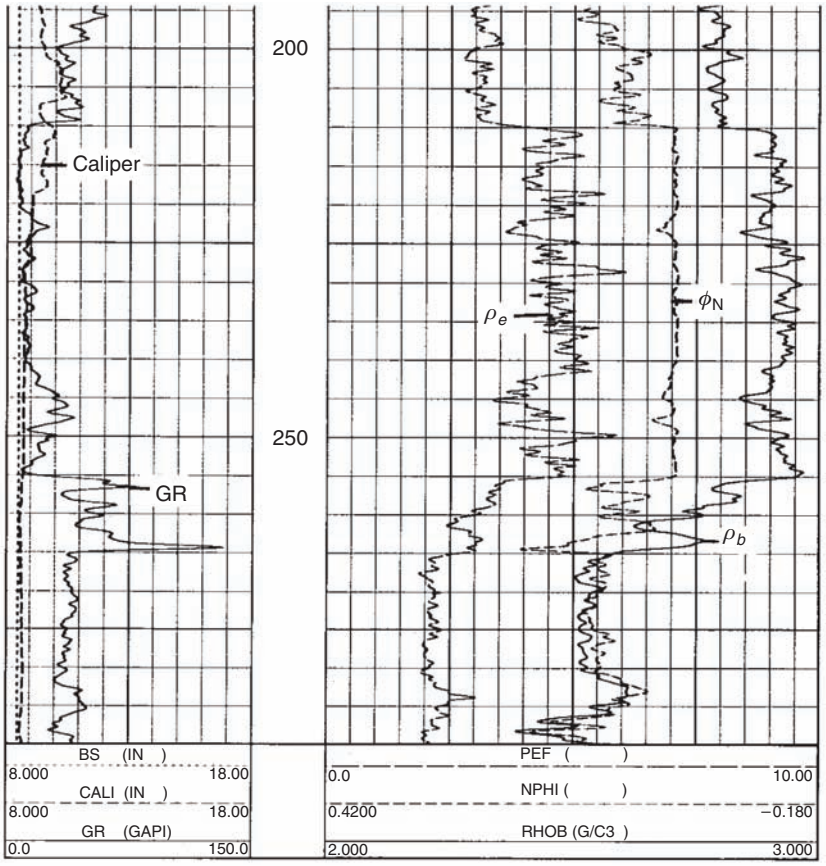


Fig. 17.22—Identification of simple lithologies with the photoelectric absorption coefficient. Courtesy of Schlumberger.

Although there is some degree of variation in the log readings because of impurities, four main lithologies can be identified in the example shown in Fig. 17.22: sandstone up to 265 m, anhydrite from 255 to 210 m, dolomite from 210 to 185 m, and halite above 185 m. In some ambiguous cases, the density and neutron porosity readings must also be considered. A more exhaustive treatment of interpretive techniques for the P_e measurement is given in Chapter 24.

17.9 Density Log Quality Control

Practical calibration of density tools is accomplished using a series of standards. The primary standard **(Fig. 17.23)** is established with reference to laboratory formations. Because these cannot be easily transported, a set of secondary standards is available at logging service

TABLE 17.3—P_e VALUES FOR COMMON FORMATIONS

Material	P_e
Sandstone	1.81
Limestone	5.08
Dolomite	3.14
Salt	4.65
Anhydrite	5.05

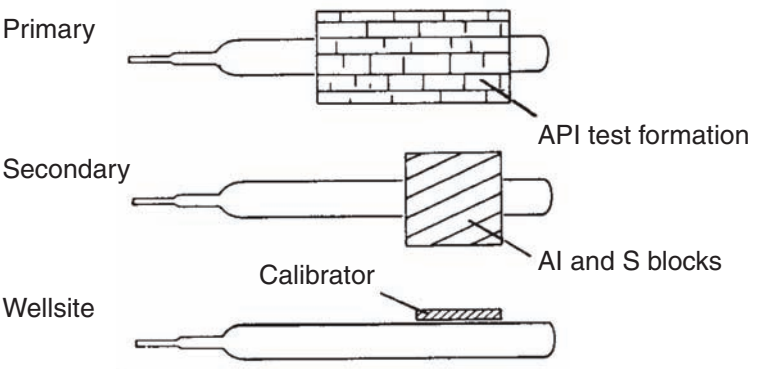


Fig. 17.23—Density-tool calibration.

company bases in the form of aluminum and sulfur blocks of accurately known density and geometry. These blocks, weighing 400 lbm, are not easily transportable, either, so a field calibrator containing two small gamma ray sources is used to reproduce the same count rates as those found in the aluminum block. The sulfur block is used as a check for the mudcake compensation.

Wellsite calibration should be performed before and after each log is run. Shop calibration should be run at least every 60 days, and a reproduction of it should form an integral part of the log record as delivered. Note that the field calibrator, the detector skid, and the source form a matched set. If any of the three does not match the serial numbers on the master calibration, the log should be rejected.

Natural benchmarks for checking the validity of a density log are salt, which has a ρ_a of 2.032 g/cm^3, and anhydrite, which has a ρ_a of 2.977 g/cm^3. These minerals may not appear in the wellbore being logged, and even if they do, they may not be 100% pure. Therefore, even these benchmarks should be used with caution. In general, density logs are either well-calibrated (and therefore correct) or very noticeably bad.

Apart from the natural benchmarks, the next-best quality check is a review of the $\Delta\rho$ curve. If the short-spacing detector fails, then the whole compensation mechanism is thrown out of kilter. If $\Delta\rho$ is generally within the limits of ±0.05 g/cm^3, the log may be assumed to be correct. However, if $\Delta\rho$ is negative in light muds, something is wrong. Likewise, a positive value for $\Delta\rho$ in heavy (barite) muds is a signal that something is wrong.

17.10 Safety

The standard compensated density tools use a cesium 137 radioactive source. Such sources are prone to becoming lost or stuck in the wells where they are used or even lost and unaccounted for during surface transportation in remote locations. Currently, there are regulatory efforts under way (Badruzzaman et al. 2009) to control these potentially hazardous sources more strictly. In the case of neutron sources, they can be replaced by particle accelerators that can be switched off when not in use and activated only when the logging tools are at depth in a borehole.

References

Badruzzaman, A., Barnes, S., Bair, F.K. et al. 2009. Radioactive Sources in Petroleum Industry: Applications: Concerns and Alternatives. Paper SPE 123593 presented at the SPE Asia Pacific Health, Safety, Security and Environment Conference, Jakarta, 4–6 August. http://dx.doi.org/10.2118/123593-MS.

Schlumberger. 1982a. *Litho-Density Tool Interpretation*. M 086108.

Schlumberger. 1982b. *Well Evaluation Developments, Continental Europe*.

Schlumberger. 2005. *Historical Log Interpretation Charts*. 05-FE-006.

General References

Alger, R.P., Raymer, L. Jr., Hoyle, W.R. et al. 1963. Formation Density Log Applications in Liquid-Filled Holes. *J. Pet Tech* **15** (3): 321–332. http://dx.doi.org/10.2118/435-PA.

Ellis, D., Flaum, C., Roulet, C. et al. 1983. Litho-Density Tool Calibration. Paper SPE 12048 presented at the SPE Annual Technical Conference and Exhibition, San Francisco, 5–8 October. http://dx.doi.org/10.2118/12048-PA.

Garner, J.S. and Dumanoir, J.L. 1980. Litho-Density Log Interpretation. *Trans.,* SPWLA 21st Annual Logging Symposium, Lafayette, Louisiana, USA, 8–11 July, Paper N.

Sherman, H. and Locke, S. 1975. Effect of Porosity on Depth of Investigation of Neutron and Density Sondes. Paper SPE 5510 presented at the SPE Annual Technical Conference and Exhibition, Dallas, 28 September–1 October. http://dx.doi.org/10.2118/5510-MS.

Tittman, J. and Wahl, J.S. 1965. The Physical Foundations of Formation Density Logging (Gamma-Gamma). *Geophysics* **30** (2): 284–294.

Wahl, J.S., Tittman, J., and Johnstone, C.W. 1964. The Dual Spacing Formation Density Log. *J. Pet Tech* **16** (12): 1411–1416. http://dx.doi.org/10.2118/989-PA.

Watson, C.C. 1983. Numerical Simulation of the Litho-Density Tool Lithology Response. Paper SPE 12051 presented at the SPE Annual Technical Conference and Exhibition, San Francisco, 5–8 October. http://dx.doi.org/10.2118/12051-MS.

Answers to Questions

QUESTION 17.1.
$\rho_a = 1.335\ \rho_{\text{meth}} - 0.188$.

QUESTION 17.2.
$\rho_{\text{meth}} = 0.079$ g/cm^3.

QUESTION 17.3.
$\phi_D = 23\%$.

QUESTION 17.4.
$\phi_D = 16\%$.

QUESTION 17.5.
$\rho_{mf} = 1.11$ g/cm^3.

QUESTION 17.6.
ρ_g at 10,000 ft (from Fig. 17.16) = 0.21 g/cm^3.
ρ_g as seen by density tool = $1.325 \times 0.21 - 0.188 = 0.090$.
$\phi = 0.293$ or 29.3%.

Appendix—Photoelectric Factors of Elements and Minerals

TABLE A-1—PHOTOELECTRIC FACTORS OF ELEMENTS AND MINERALS

Name	Formula	Molecular Weight	*Pe*	*Zeq*	*ρ*	*ρe*	*ρb*	*C*
Elements								
Hydrogen	H	1.000	0.00025	1				1.9840
Carbon	C	12.011	0.15898	6				0.991
Oxygen	O	16.000	0.44784	8				1.0000
Sodium	Na	22.991	1.4093	11				0.9566
Magnesium	Mg	24.320	1.9277	12				0.9868
Aluminum	Al	26.980	2.5715	13	2.700	2.602	2.596	0.9637
Silicon	Si	28.090	3.3579	14				0.9968
Sulfur	S	32.006	5.4304	16	2.070	2.066	2.022	0.9979
Chlorine	Cl	35.457	6.7549	17				0.9589
Potassium	K	39.100	10.081	19				0.9719
Calcium	Ca	40.080	12.126	20				0.9980
Titanium	Ti	47.900	17.089	22				0.9186
Iron	Fe	55.850	31.181	26				0.9311
Copper	Cu	63.500	43.500	29				
Strontium	Sr	87.630	122.240	38				0.8673
Zirconium	Zr	91.220	147.030	40				0.8770
Barium	Ba	137.360	493.720	56				0.8154
Minerals								
Anhydrite	$CaSO_4$	136.146	5.055	15.69	2.960	2.957	2.977	0.9989
Barite	$BaSO_4$	233.366	266.800	47.20	4.500	4.011		0.8913
Calcite	$CaCO_3$	100.090	5.084	15.71	2.710	2.708	2.710	0.9991
Carnalite	KCl· MGC12· $6H_2O$	277.880	4.089	14.79	1.610	1.645	1.573	1.0220
Celestite	$SrSO_4$	183.696	55.130	30.40	3.960	3.708		0.9363
Corundum	Al_2O_3	101.960	1.552	11.30	3.970	3.894		0.9808
Dolomite	$CaCO_3$· $MgCO_3$	184.420	3.142	13.74	2.870	2.864	2.877	0.9977
Gypsum	$CaSO_4$· $2H_2O$	172.180	3.990	14.07	2.320	2.372	2.350	1.0222
Halite	NaCl	58.450	4.650	15.30	2.165	2.074	2.040	0.9580
Hematite	Fe_2O_3	159.700	21.480	23.45	5.240	4.987		0.9518
Ilmenite	$FeOTiO_2$	151.750	16.630	21.87	4.700	4.460		0.9489
Magnesite	$MgCO_3$	84.330	0.829	9.49	3.037	3.025	3.049	0.9961
Magnetite	Fe_3O_4	231.550	22.080	23.65	5.180	4.922		0.9501
Marcasite	FeS_2	119.980	16.970	21.96	4.875	4.708		0.9668
Pyrite	FeS_2	119.980	16.970	21.96	5.000	4.834		0.9668
Quartz	SiO_2	60.090	1.081	11.78	2.654	2.650	2.648	0.9985
Rutile	TiO_2	79.900	10.080	19.02	4.260	4.052		0.9512
Siderite	$FeCO_3$	115.860	14.690	21.09	3.940		3.890	
Sylvite	KCl	74.557	8.510	18.13	1.984	1.916	1.862	0.9657
Zircon	$ZrSiO_4$	183.310	69.100	32.45	4.560	4.279		0.9383

TABLE A-1—PHOTOELECTRIC FACTORS OF ELEMENTS AND MINERALS (CONT'D)

Name	Formula	Molecular Weight	*Pe*	*Zeq*	*ρ*	*ρe*	*ρb*	*C*
Liquids								
Water	H_2O	18.016	0.358	7.52	1.000	1.110	1.0000	1.1101
Salt water	(120,000 ppm)		0.807	9.42	1.086	1.185	1.0800	1.0918
Oil	CH_{16}		0.119	5.53	0.850	0.948	0.8260	1.1157
	CH_2		0.125	5.61	0.850	0.970	0.8800	1.1407
Misc.								
Berea sandstone			1.745	11.67	2.308	2.330	2.3050	0.9993
Pecos sandstone			2.700	13.18	2.394	2.414	2.3950	1.0000
Average shale			3.420	14.07	2.650	2.645	2.6420	0.9980
Anthracite coal	C:H:O = 95:3:4		0.161	6.02	1.700	1.749	1.6830	1.0287
Bituminous coal	C:H:O = 82:5:13		0.180	6.21	1.400	1.468	1.3830	1.0485

Chapter 18

Neutron Logs

18.1 The Physics of Neutrons

The neutron is a fundamental particle found in the nucleus of all atoms except hydrogen, which contains only a proton. The neutron has approximately the same mass as the proton, but carries no electrical charge. These two properties, small size and electrical neutrality, make it an ideal projectile for penetrating matter. Neutrons pass through brick walls and steel plates with the greatest of ease. They can pass through steel casing and also penetrate rocks. It was logical, therefore, that they should find a place in the arsenal of logging tools. Over the years, a number of logging tools have appeared that rely on one or another of the many possible ways that the neutron can interact with matter. To understand these different tools fully, a review of some aspects of nuclear physics is required.

Two categories of neutron sources are found in the logging industry: chemical sources and pulsed sources. Chemical sources are composed of two elements that are in intimate contact with each other and react together to emit neutrons continuously. These sources are normally either plutonium-beryllium or americium-beryllium. Chemical sources need to be heavily shielded when not in use. Pulsed sources, on the other hand, are relatively harmless when not in use. They incorporate an ion accelerator and a target and can be activated by simply switching on the accelerator. Currently, the pulsed neutron sources are used for pulsed neutron logging (also known as thermal neutron decay time logging) and for inelastic neutron spectroscopy or so-called carbon/oxygen logs and other elemental assaying techniques.*

Near the chemical sources, neutrons are found with substantially all their initial energy of several MeV; these are called fast neutrons. These neutrons interact with other atoms in several ways (which will be discussed later), losing energy with each collision. Eventually, the neutrons reach an intermediate energy level where they have an energy of only a few eV; these neutrons are called epithermal neutrons. After still more interactions, a neutron may be slowed down to a point where it has the same energy as the surrounding matter; this energy level is a direct function of the absolute temperature. Such neutrons are called thermal neutrons. They have energies in the range of 0.025 eV. At this stage, the neutron is ripe for capture. Neutron capture is accomplished when a nucleus swallows a neutron, gets indigestion, and spits out a gamma ray. The whole sequence is summarized in **Table 18.1.**

When a neutron slows to this thermal stage, it is captured by a nucleus, which then emits a gamma ray. This gamma ray is called a capture gamma ray. The measurements of conventional neutron-logging tools, with the exception of pulsed neutron tools, are all predicated on the spatial distribution of the epithermal neutrons, thermal neutrons, or capture gamma rays that they produce. Pulsed neutron logs monitor the neutron distribution as a function of time. The elemental

*For further detailed discussion of elemental logging and analysis, see Chapter 29.

TABLE 18.1—STAGES IN THE LIFE OF A NEUTRON

Type	Energy	Encountered
1. Fast	Several MeV	Near source
2. Epithermal	A few eV	After collisions
3. Thermal	0.025 eV	At capture

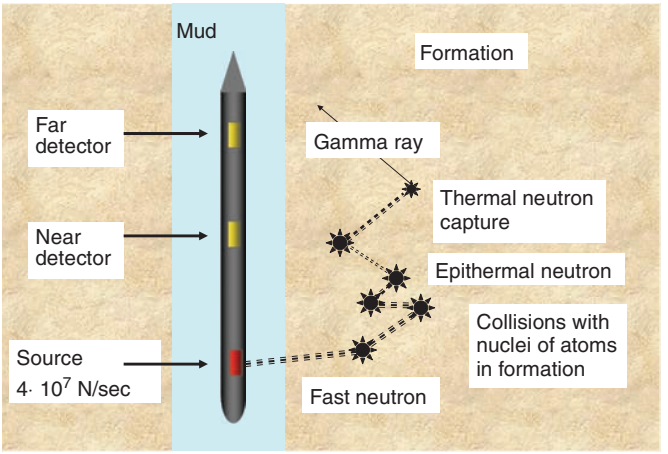


Fig. 18.1—Generalized neutron logging tool.

logging tools rely on the energy spectrum of gamma rays produced by inelastic collisions with the nuclei of the elements present in the formation.

The first neutron tools, known as gamma ray neutron tools (GNT), consisted of a chemical source and a single detector of the gamma rays produced by neutron capture. This tool gave a qualitative indication of porosity, but was severely affected by hole size and the salinity of the borehole fluid and of the formation water.

In an attempt to overcome these inherent problems, the sidewall neutron porosity (SNP) tool was introduced. It relied on a single detector of epithermal neutrons. This tool overcame salinity problems, but had its own unique problem in that mudcake could affect its readings, and estimation of the magnitude of the error was not always easy.

The compensated neutron log (CNL) was then introduced, with two detectors of thermal neutrons. It overcame most of the defects of previous tools, yet it also encountered problems with formations containing thermal-neutron absorbers. Tools with dual detectors of epithermal neutrons are also available and have applications in air-drilled (empty) boreholes. **Fig. 18.1** illustrates a generalized neutron-logging tool.

The ability of a nucleus to slow down or capture a neutron is governed by a property known as its cross section. In general, the slowing down cross section for any given nucleus may be quite different from its capture cross section; in other words, although some elements may be good at stopping neutrons, they may not be particularly hungry to swallow them once they are stopped. To add to the complexities of the process of neutron slowing and capture, it has been found that these cross sections are also a function of the energy of the neutron involved in the process. Therefore, an analysis of how fast neutrons are scattered and eventually captured in a subsurface formation is a complex task. **Table 18.2** lists the main elements found in the logging environment, together with their neutron-slowing and capture cross sections. Also listed are their natural abundance and the number of collisions required to slow a fast neutron down to the thermal energy level of 0.025 eV.

Two elements, hydrogen and chlorine, dominate the behavior of all neutron tools. Hydrogen, the element with only a proton for a nucleus, is the best material for slowing down a neutron. Simple mechanics reveals that when two balls collide, the maximum energy loss occurs when the

TABLE 18.2—SLOWING AND CAPTURE CROSS SECTIONS FOR 2-MeV NEUTRONS

		Cross Section		
Element Symbol	Abundance ppm	Capture	Slowing	Collisions to 0.025 eV
H	1,400	0.3	20	18
Be	—	0.01	6.1	87
B	—	700	3	105
C	320	0	4.8	115
N	—	1.88	10	130
O	466,000	0	4.1	150
Na	28,300	0.51	3.5	215
Mg	20,900	0.4	3.6	227
Al	81,000	0.23	1.5	251
Si	277,000	0.13	1.7	261
S	520	0.53	1.5	297
Cl	314	31.6	10	329
K	25,900	2.2	1.5	362
Ca	36,300	0.43	9.5	371
Fe	50,000	2.5	11	514
Cd	—	2500	5.3	1028

two balls are of equal mass. The neutron and the proton, being of equal mass, account for the prodigious powers of the hydrogen nucleus to slow neutrons. (A good place to hide in case of nuclear attack is therefore under water, provided that the problem of drowning has been solved first). The other dominant element affecting neutron tools is chlorine, which is a voracious devourer of thermal neutrons, absorbing them a hundred times faster than most other elements.

After accounting for the relative abundance of all the elements and their slowing down and capture cross sections, it can be determined that a neutron has to collide with a hydrogen nucleus an average of 18 times to reach thermal energy. However, once it reaches thermal energy, it is most likely to be absorbed by a chlorine nucleus. This explains why the original gamma ray neutron tools were so dependent on fluid salinity. A few parts per million of sodium chloride in the mud or the formation water could alter their response dramatically. It also explains why the SNP (epithermal neutron tool) was such an improvement. The SNP was completely blind to capture gamma rays; it detected only epithermal neutrons. The CNL (thermal-neutron) tools are theoretically just as blind to salinity effects because they also ignore the capture gamma rays from chlorine. However, inspection of Table 18.2 shows that small amounts of boron or cadmium in the formation can seriously affect the distribution of thermal neutrons.

18.2 The Compensated Neutron Tool

The compensated neutron tool **(Fig. 18.2)** measures a *neutron porosity index,* which can be related to formation porosity only if the lithology and formation fluid content are known. The tool consists of a chemical neutron source and two thermal-neutron detectors. It is run eccentered, with the source and detectors forced against the borehole wall by means of a bowspring. Conventional CNL tools are available in a variety of diameters and for a range of temperature and pressure ratings. They can be run equally well in open holes or in cased, liquid-filled holes. In an empty hole (gas-filled), they do not work. It is normal practice to run these tools in combination with at least the density and gamma ray tools or (more normally) as part of a "triple-combo" logging-tool string. If this tool is run alone, no caliper is recorded.

Fig. 18.3 shows a typical neutron-density field log. The neutron porosity index is the dashed curve recorded in Tracks 2 and 3. Broadly speaking, the compensated neutron log is an indicator of three quantities: porosity, lithology, and formation fluid type.

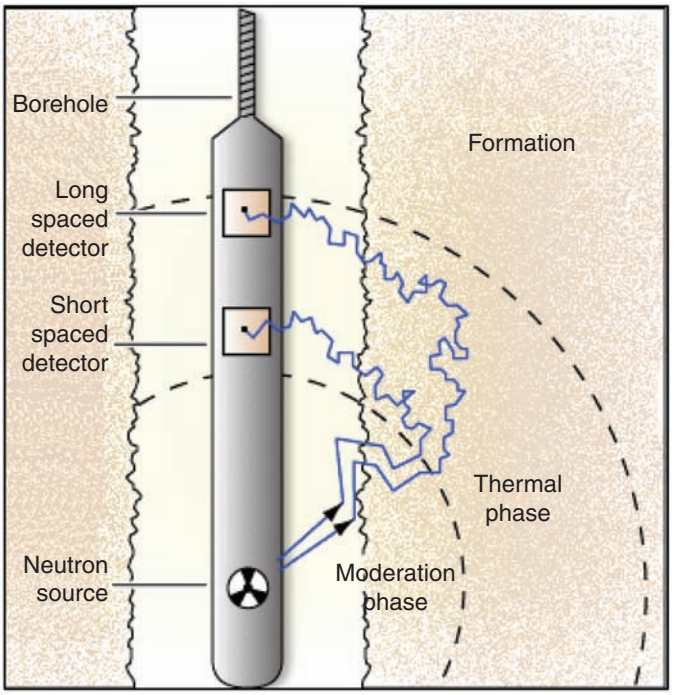


Fig. 18.2—Compensated dual-detector thermal neutron logging-tool schematic.

18.3 CNL Operating Principle

To understand properly the operation of the CNL logging tool, the distribution of the thermal neutrons as they move away from the source must be investigated. The *thermal neutron flux* is defined as the number of thermal neutrons crossing a unit area in unit time. This flux is controlled mainly by the hydrogen content of the formation. Hydrogen is found in the water molecules filling the pore space (assuming that the formation is water-bearing). Therefore, the hydrogen content of the formation is a direct indication of formation porosity.

Fig. 18.4 shows a plot of the thermal neutron flux as a function of the distance from the source for three different porosity values. Note that the lines cross each other at some distance from the source. At points closer to the source than the crossover region, high thermal neutron flux means high porosity, but at points further from the source than the crossover region, the reverse is true, that is, high thermal neutron flux indicates low porosity.

The absolute neutron count rate is a poor indication of porosity because a number of factors affect it. The actual count rate seen at any detector spacing from the source is a function not only of porosity, but also of such environmental factors as the hole size, the mud weight, and the casing size and weight. Therefore, the CNL reading must be normalized to correct for unknown environmental effects. This is done by taking two readings of thermal neutron flux at different spacings (from the source) and using them to define the slope of the response line. This slope is relatively unaltered by environmental effects, although the position of the response line on the graph may vary substantially in the y-direction **(Fig. 18.5).**

The primary measurement of the CNL tool is therefore a ratio of two-count rates. A high ratio is indicative of high porosity. The conversion of the ratio to a porosity value is based either on laboratory experiments conducted with rock samples of known porosity or on computer simulations. **Fig. 18.6** shows the results of such an experiment.

To record porosity directly, it is necessary to convert the near-count/far-count ratio into a porosity (ϕ) value. It can be seen in Fig. 18.6, for example, that a ratio of 2.0 means less than 10% porosity in dolomite or more than 20% in sandstone. The surface controls of the CNL tool enable

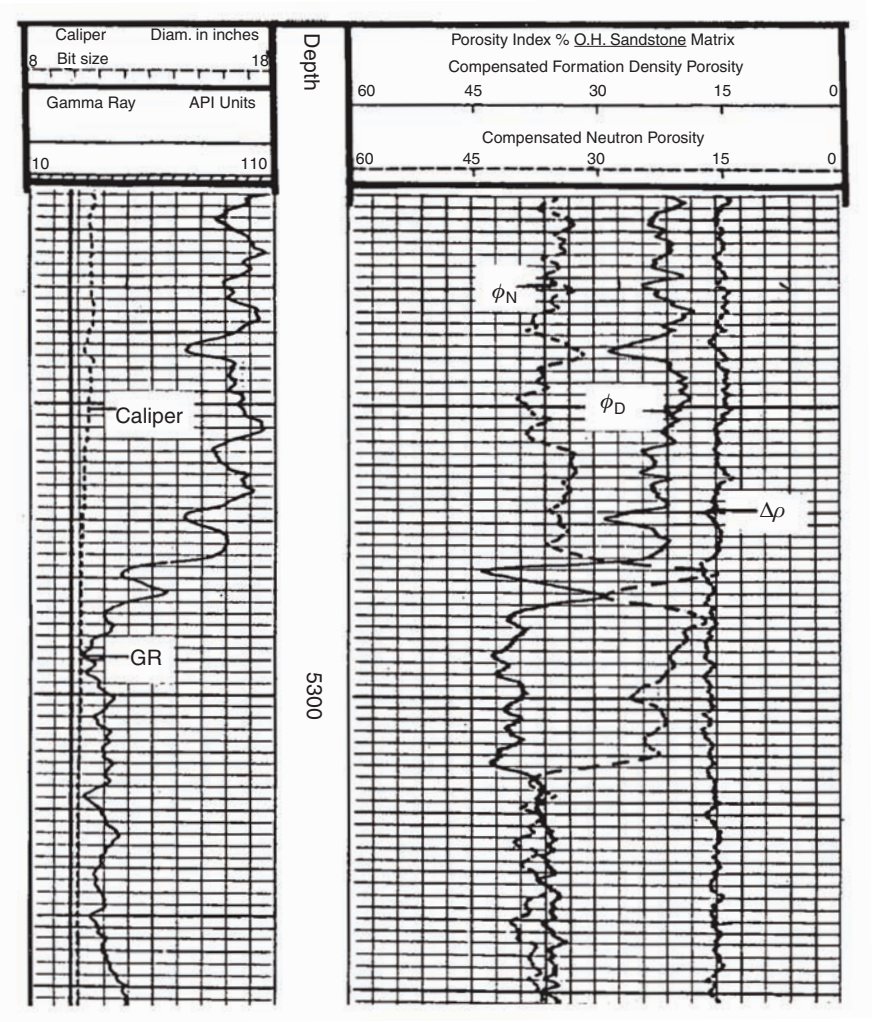


Fig. 18.3—Example of a compensated neutron log.

the operator to select the matrix for which a porosity value is required. If the operator chooses to run the CNL on a limestone setting, the conversion of ratio to porosity will follow the middle of the three response lines in Fig. 18.6.

If, subsequently, it is found that the actual matrix is not limestone, then the apparent limestone porosity must be converted to some other matrix porosity. This is accomplished by use of **Fig. 18.7,** which shows the relationship between apparent limestone porosity and the porosity values for dolomite and sandstone for two generations of compensated thermal neutron tools. The older family of tools corresponds to the blue lines marked "NPHI," and the more recent generation of tools corresponds to the red curves marked "TNPH." The adjustments between the different matrix materials are fairly uniform (except for very high or very low porosity values).

Approximate conversion rules can be used in the middle of the range of apparent limestone porosity values. For example, if ϕ_{NLM} is the CNL porosity recorded with a limestone/matrix setting and ϕ_T is the true porosity, **Table 18.3** can be used to convert the apparent porosity to dolomite and sandstone porosity values. The opposite problem can also be addressed; if the log is recorded on a matrix setting other than limestone, **Table 18.4** provides the means

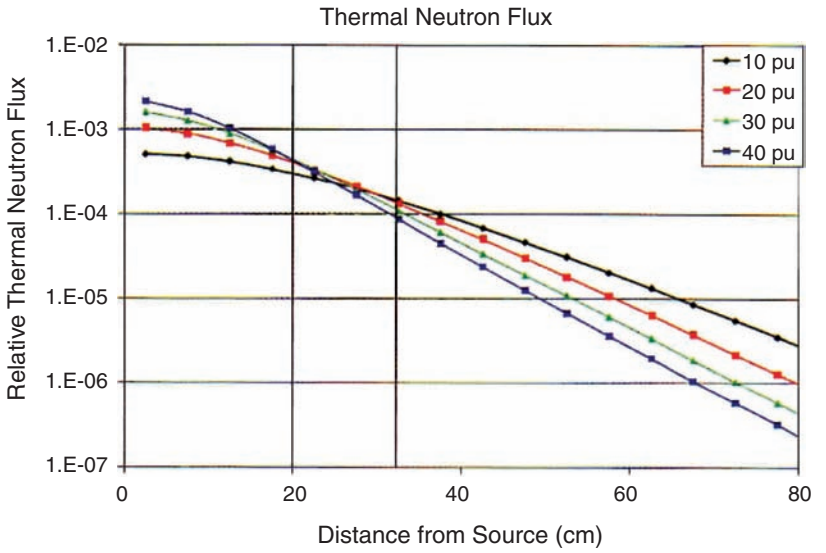


Fig. 18.4—Thermal neutron distribution as a function of distance from the source and porosity. After Gilchrist (2009).

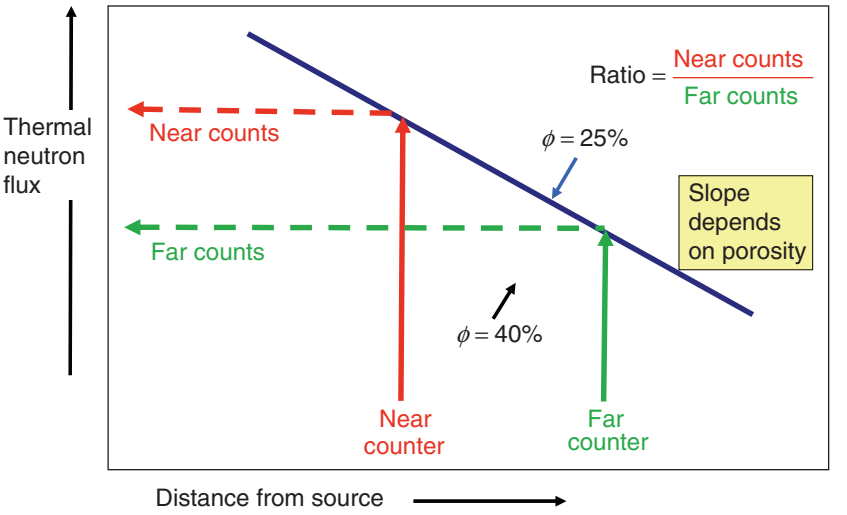


Fig. 18.5—Compensated neutron borehole compensation.

to convert it back to limestone. The following questions will acquaint the reader with these conversions.

QUESTION 18.1. The CNL is recorded on a limestone-matrix setting and gives a value of $\phi_{NLM} = 15\%$. However, the lithology is actually sandstone. What is ϕ_T, the true porosity?

QUESTION 18.2. The CNL is recorded on a sandstone-matrix setting and gives a value of $\phi_{NSD} = 22.5\%$. What would be the equivalent neutron porosity index (ϕ_{NLM})?

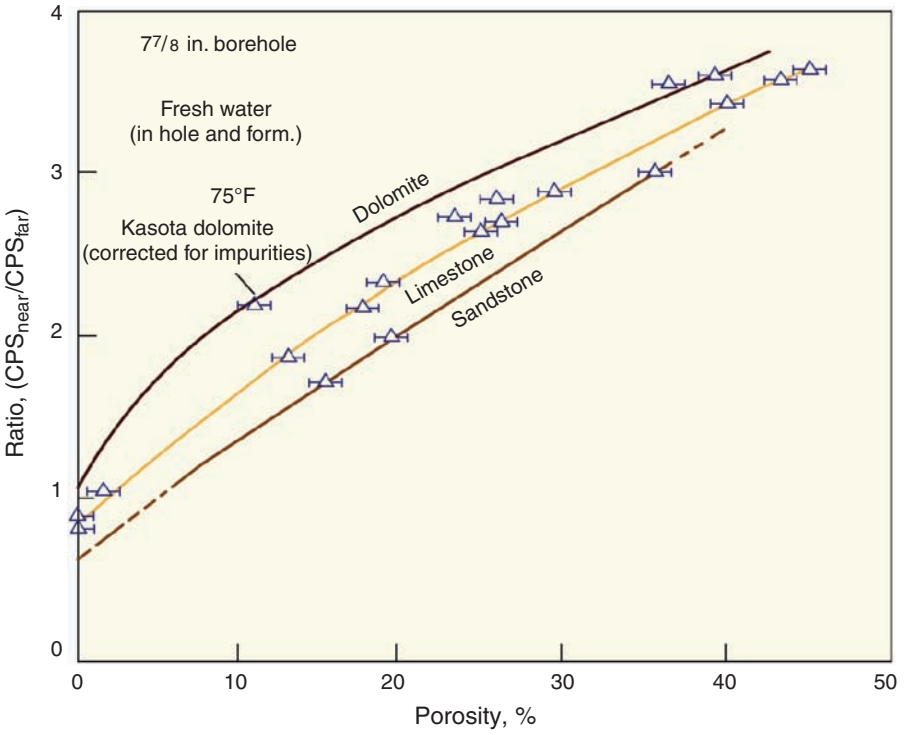


Fig. 18.6—Tool response for sandstone, limestone, and dolomite laboratory formations (Alger et al. 1971).

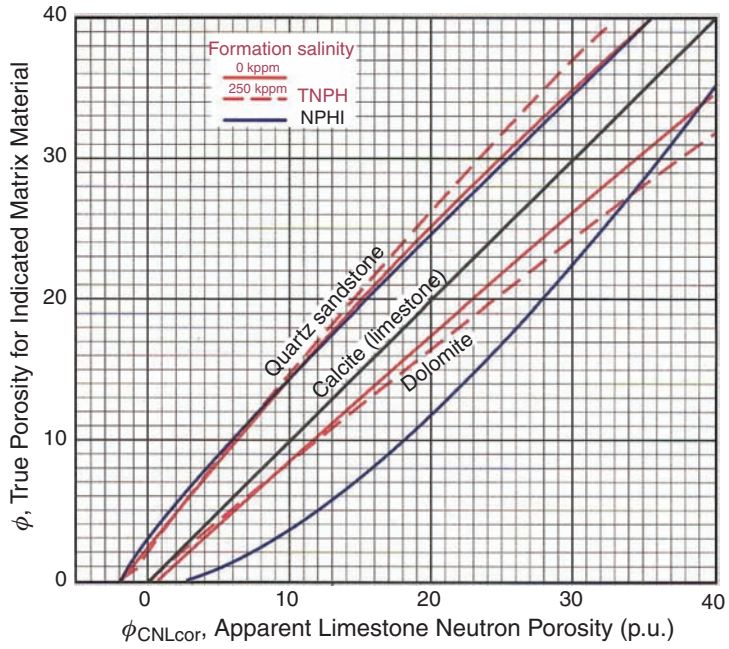


Fig. 18.7—Neutron porosity equivalence curves. Courtesy of Schlumberger.

TABLE 18.3—CONVERSION TO TRUE POROSITY

True Porosity in	Correction to ϕ_T "NPHI"	Correction to ϕ_T "TNPH"
Limestone	ϕ_{NLM}	ϕ_{NLM}
Sandstone	ϕ_{NLM} + 4.0 p.u.	ϕ_{NLM} + 4.0 p.u.
Dolomite	ϕ_{NLM} – 7.5 p.u.	ϕ_{NLM} – 2.5 p.u.

TABLE 18.4—CONVERSION TO EQUIVALENT LIMESTONE RESPONSE

Log Recorded on Setting for	Correction to Limestone Matrix "NPHI"	Correction to Limestone Matrix "TNPH"
Limestone	ϕ_{Log}	ϕ_{Log}
Sandstone	ϕ_{Log} – 4.0 p.u.	ϕ_{Log} – 4.0 p.u.
Dolomite	ϕ_{Log} + 7.5 p.u.	ϕ_{Log} + 2.5 p.u.

18.4 CNL Environmental Corrections

In general, CNL corrections for environmental factors are small. Of all corrections, the temperature and borehole pressure corrections are the largest. For "legacy" logs recorded before the advent of onboard computer systems, the appropriate corrections can be applied manually by reference to correction charts available form wireline service companies. For logs run after the changeover to onboard computer systems, most service companies automatically apply the appropriate environmental corrections, and the user can then work with the data directly in a log analysis routine.

18.5 Depth of Investigation

The depth of investigation of the CNL tool depends on both the porosity and the salinity of the mud filtrate (invading water) and formation water. It can be expressed in terms of a geometric factor *J*:

$$\phi_{CNL} = J\left(\phi_{CNL}\right)_{invaded} + \left(1-J\right)\left(\phi_{CNL}\right)_{uninvaded}, \quad (18.1)$$

where *J* is a function of the depth of invasion measured from the borehole wall. **Fig. 18.8** shows a typical set of *J* curves for the FDC, SNP, and CNL tools.

Note that the CNL tool reads much deeper into the formation than either of the other two tools. If the radial distance within which 90% of the measured signal received is measured, the FDC might be found to read 4 in. into the formation and the CNL to be reading 9 in. into the formation. This is a generalization, however; these figures can vary substantially depending on the formation fluid and the porosity.

18.6 Matrix Settings and Lithology Effects

When choosing a CNL logging scale and matrix setting, it is good practice to remain consistent with the standard operating procedure for the particular lithology expected in the well. This should be

Sand/shale sequences: Run the log with a sandstone-matrix setting and with a porosity scale of 60 to 0%, left to right across Tracks 2 and 3. If a density log is also recorded, scale it to an apparent sandstone porosity on the same scale (see Fig. 18.3 for an example of this sandstone-compatible scaling).

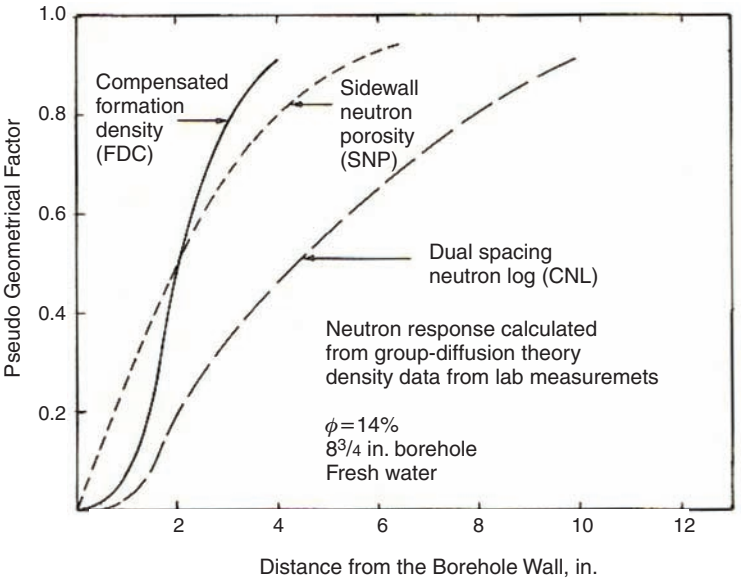


Fig. 18.8—Depth of investigation of FDC, CNL, and SNP tools (ϕ = 14%).

Carbonates/evaporates/generally unknown lithology: Run the log with the CNL on a limestone-matrix setting with a porosity scale of 45 to 15%, left to right across Tracks 2 and 3. If a density log is also recorded, a scale of 1.95 to 2.95 g/cm^3 is required **(Fig. 18.9).**

The advantage of the sandstone-compatible scales is (1) that gas can be easily spotted (the neutron curve reads less than the density curve) and (2) shales can be distinguished from sands (the neutron curve reads more than the density curve). The advantage of the limestone-compatible scales is that the curves coincide in limestone and that the neutron curve reads less than the density curve in sands and more than the density curve in dolomites and shales. These scaling schemes are covered more fully in the sections dealing with porosity and lithology and in Chapters 23 and 24.

18.7 Gas Effects

Because the neutron tool is sensitive to hydrogen, it will respond with an abnormally low reading if the concentration of hydrogen is low, for example, in gas-bearing formations. Making corrections for gas effects on neutron logs requires additional data such as a density log. The mechanics of making these corrections are covered in Chapter 23. In a manner that is entirely analogous to the approach taken with the density tool, the response of the neutron tool in gas-bearing formations may be written as

$$\phi_N = \phi_{Nma}(1-\phi) + \phi_{Nmf} S_{xo} + \phi_{Nhy}\phi(1-S_{xo}), \quad \ldots\ldots\ldots\

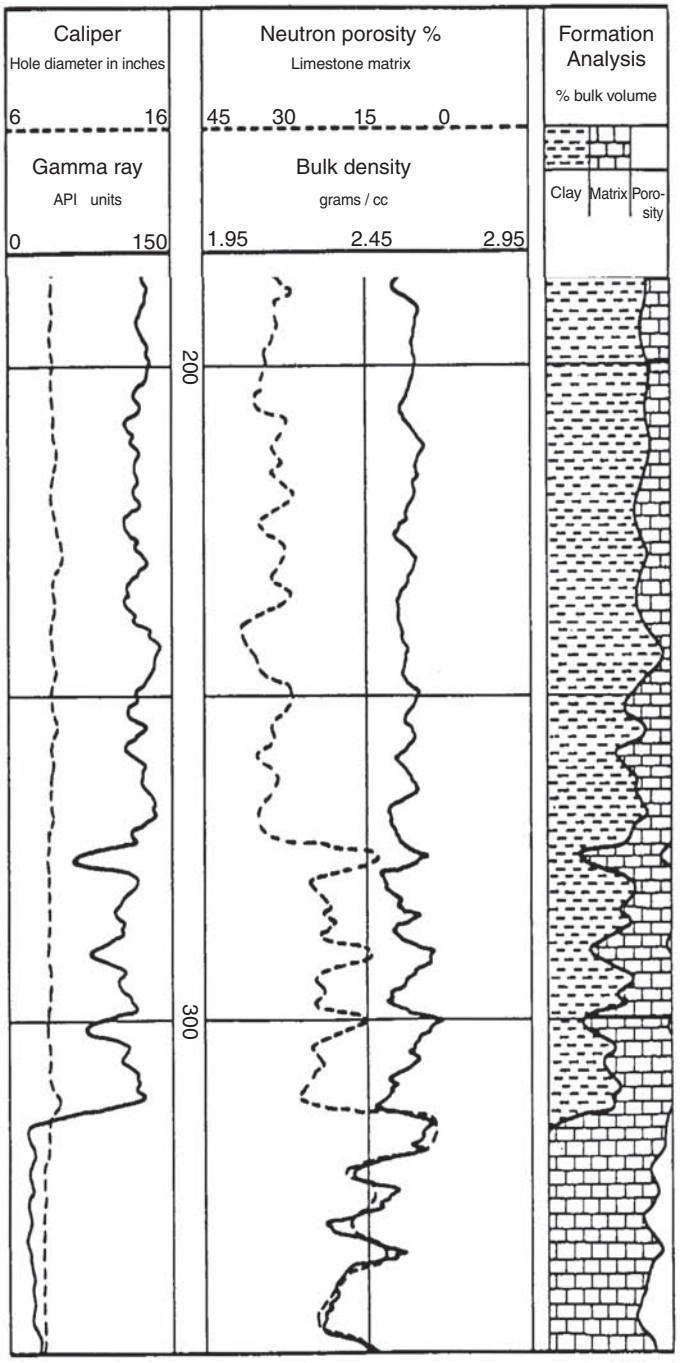


Fig. 18.9—Example of CNL-FDC presentation in complex lithology (modified from Goetz et al. 1977). Reprinted by permission from the Indonesian Petroleum Association.

Rearrangement of the terms gives:

$$\phi = \frac{\phi_N - \phi_{Nma}}{\phi_{Nhy} - \phi_{Nma} + S_{xo}\left(\phi_{Nmf} - \phi_{Nhy}\right)} \quad \ldots\ldots\ldots\

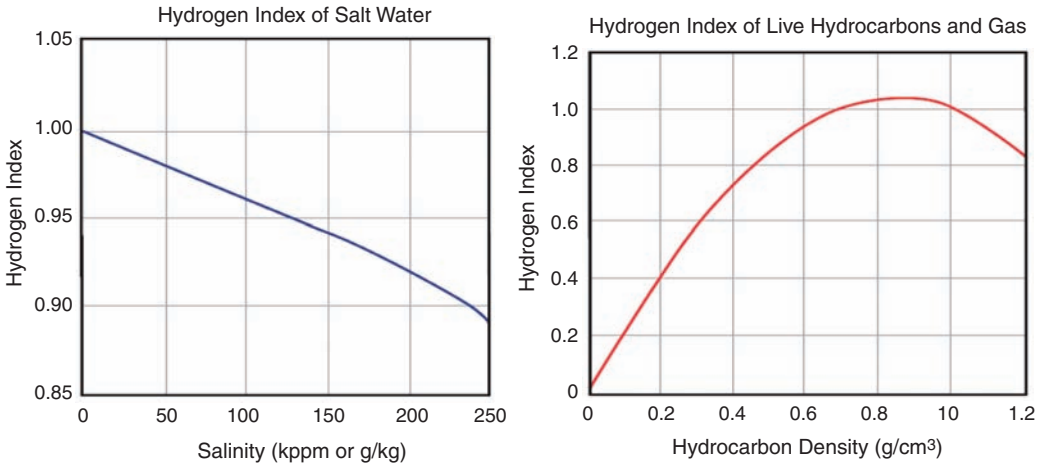


Fig. 18.10—Hydrogen index as a function of water salinity and hydrocarbon density. Courtesy of Schlumberger.

Because S_{xo} is always less than unity, it follows that ϕ_N in hydrocarbon-bearing formations is always less than ϕ.

QUESTION 18.3. On the log shown in Fig. 18.3, find a gas-bearing interval and give its top and base.

18.8 Shale Effects

In general, the response of the neutron log may be written in the form:

$$\phi_N = \phi_T + V_{sh}\phi_{Nsh}, \quad \ldots\ldots\ldots\

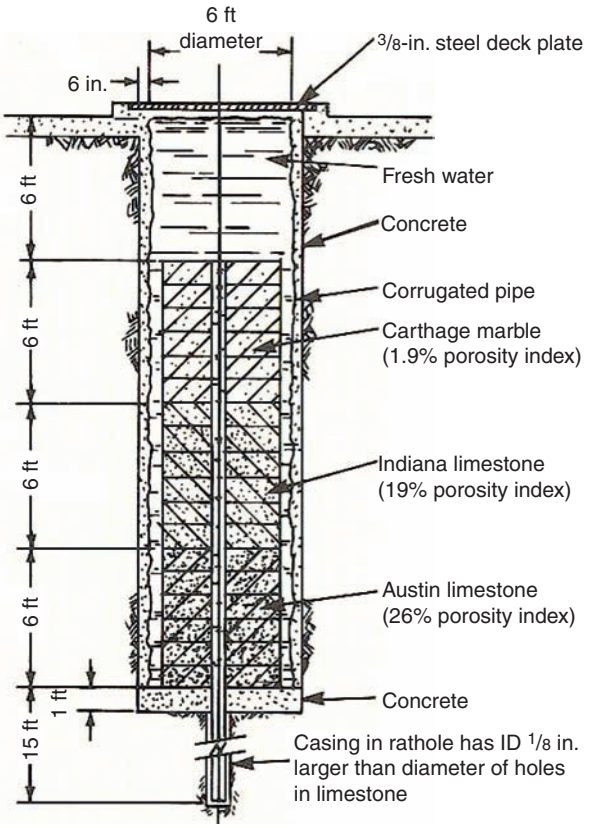


Fig. 18.11—University of Houston "test well" for neutron-logging tools.

18.10 CNL Calibration and Quality Control

The primary calibration standard for neutron-logging tools is a "test well" maintained at the University of Houston. It consists of a series of limestone blocks of known porosity, as shown in **Fig. 18.11.** Wireline service companies can use this facility to perform initial calibrations of their logging tools. Thereafter, local field standards are used, which are large water-filled tanks that serve for local shop calibrations carried out at 60-day intervals. Practical quality control can be monitored by the usual criteria for all logging measurements (repeatability and before- and after-logging wellsite calibration for tail consistency), plus two natural benchmarks, salt ($\phi_{NLM} = -1.5\%$) and anhydrite ($\phi_{NLM} = 0.0\%$). Apparent neutron and density porosities should agree in clean, water-bearing zones where the lithology is known.

References

Alger, R.P., Locke, S., Nagel, W.A. et al. 1971. The Dual-Spacing Neutron Log (CNL). Paper SPE 3565 presented at the SPE Annual Meeting, New Orleans, 3–6 October. http://dx.doi.org/10.2118/3565-PA.

Bateman, R.M. 1984. *Cased-Hole Log Analysis and Reservoir Performance Monitoring*. Boston, Massachusetts: IHRDC.

Goetz, J.F., Prins, W.J., and Logar, J.F. 1977. Reservoir Delineation by Wireline Techniques. Presented at the Sixth Annual Convention of the Indonesian Petroleum Association, Jakarta, 23–24 May.

Gilchrist Jr., W.A. 2009. Tutorial: Compensated Neutron Log Response Issues. *Petrophysics* **50** (5): 416–426.

Schlumberger. 2009. *Log Interpretation Charts*.

General References

Allen, L.S., Tittle, C.W., Mills, W.R., and Caldwell, R.L. 1967. Dual-Spaced Neutron Logging for Porosity. *Geophysics* **32** (1): 60–68.

Ellis, D.V., Case, C.R., and Chiaramonte, J.M. 2004. Porosity From Neutron Logs, I: Measurement. *Petrophysics* **44** (6): 383–395.

Ellis, D.V., Case, C.R., and Chiaramonte, J.M. 2004. Porosity From Neutron Logs, II: Interpretation. *Petrophysics* **45** (1): 73–86.

Galford, J.E., Flaum, C., Gilchrist Jr., W.A., et al. 1986. Enhanced Resolution Processing of Compensated Neutron Logs. SPE paper 15541 presented at the SPE Annual Technical Conference and Exhibition, New Orleans, 5–8 October. http://dx.doi.org/10.2118/15541-PA.

Gilchrist Jr., W.A., Galford, J.E., Flaum, C., et al. 1986. Improved Environmental Corrections for Compensated Neutron Logs. SPE paper 15540 presented at the SPE Annual Technical Conference and Exhibition, New Orleans, 5–8 October. http://dx.doi.org/10.2118/15540-PA.

Kienitz, C., Flaum, C., Olesen, J.-R. et al. 1986. Accurate Logging in Large Boreholes. *Trans.,* SPWLA 27th Annual Logging Symposium, Houston, 9–13 June.

Poupon, A., Clavier, C., Dumanoir, J. et al. 1970. Log Analysis of Sand-Shale Sequences: A Systematic Approach. *J. Pet Tech* **22** (7): 867–881. http://dx.doi.org/10.2118/2897-PA.

RP 33, Recommended Practice for Standard Calibration and Form for Nuclear Logs. 1959. Washington, DC: API.

Segesman, F. and Liu, O. 1971. The Excavation Effect. *Trans.,* SPWLA 12th Annual Logging Symposium, Dallas, 2–5 May.

Sherman, H. and Locke, S. 1975. Effect of Porosity on Depth of Investigation of Neutron and Density Sondes. Paper SPE 5510 presented at the SPE Annual Technical Conference and Exhibition, Dallas, 28 September–1 October. http://dx.doi.org/10.2118/5510-MS.

Tittle, C.W. 1961. Theory of Neutron Logging I. *Geophysics* **26** (1): 27–39.

Tittman, J., Sherman, H., Nagel, W.A., et al. 1966. The Sidewall Epithermal Neutron Porosity Log. *J. Pet Tech* **18** (10): 1351–1362. *Trans.,* AIME, **237.** SPE-1180-PA. http://dx.doi.org/10.2118/1180-PA.

Tixier, M.P., Martin, M., and Tittman, J. 1956. Fundamentals of Logging. Lecture 6, Petroleum Engineering Conference, University of Kansas, Lawrence Kansas.

Truman, R.B., Alger, R.P., Connell, J.G., et al. 1972. Progress Report on Interpretation of the Dual-Spacing Neutron Log (CNL) in the US. *Trans.,* SPWLA 13th Annual Logging Symposium, Tulsa, 7–10 May.

Wahl, J.S., Nelligan, W.B., and Frentrop, A.H. 1970. The Thermal Neutron Decay Time Log. *SPE J.* **10** (4): 365–379. http://dx.doi.org/10.2118/2252-PA.

Wahl, J.S., Tittman, J., and Johnstone, C.W. 1964. The Dual Spacing Formation Density Log. *J. Pet Tech* **16** (12): 1411–1416. *Trans.,* AIME, **231.** SPE-989-PA. http://dx.doi.org/10.2118/989-PA.

Weinberg, A.M. and Wigner, E.P. 1958. *The Physical Theory of Neutron Chain Reactors.* Chicago: University of Chicago Press.

Answers to Questions

QUESTION 18.1.
$\phi_T = 19.2\%$.

QUESTION 18.2.
$\phi_{NLM} = 18\%$.

QUESTION 18.3.
5,276–5,312 ft.

Chapter 19

Nuclear Magnetic Resonance

embellishment-a decorative detail or feature added to something to make it more attractive

19.1 Applications of NMR

NMR has applications both in the medical field and in subsurface formation evaluation. Although early forms of this measurement for petrophysical analysis have been around since the 1960s, modern implementations stem from work done in the 1980s and 1990s. Research and development is ongoing, so with each passing year, another useful embellishment is added to the veritable smorgasbord of information about rocks and their fluid contents that can be gathered from NMR data. In particular, NMR can be used to measure:

- Mineral-independent porosity
- Fluid saturations of oil, gas, and water
- Permeability
- Pore-size distributions
- Viscosity of hydrocarbons present

Such is the versatility of the NMR process that these measurements may be applied to several different parts of the overall formation evaluation task, including:

- Openhole wireline logging
- Measurements on drillpipe
- Core analysis
- Fluid identification while performing formation tests

19.2 NMR vs. Conventional Logging and Log Analysis

Conventional wireline logging tools are heavily influenced by the rock matrix itself. However, the analyst's chief concern is with the storage space (the porosity) and the contents of the pores (the fluid saturations and the types of hydrocarbon). Because, in most cases, the rock matrix occupies more than two-thirds of the volume sensed by the logging tools, the conventional forms of log analysis leave many questions unresolved. The analyst does not always know the precise grain density of the matrix or the resistivity of the water(s) in the pore space. Because there was no tool in conventional logging that directly detected porosity or oil, it was fair to say that the loggers measured everything they could, subtracted it from the universe, and what was left had to be oil. With the advent of modern NMR, a step has certainly been taken in the right direction.

19.2.1 NMR and Conventional Log Analysis Models. To appreciate this advance, the reader is referred to **Fig. 19.1,** which depicts, from right to left:

- A conventional Archie model of a clean formation,
- A shaly formation with typical NMR semidirect measurements, and
- A shaly formation with conventional log analysis responses.

Note that the model has six components: *matrix and dry clay*, which together sum to give the **solid**; *clay-bound water*, *capillary-bound water*, *free water*, and *hydrocarbon*, which together sum to give the **liquid.** In the nomenclature used in this figure,

- Solid = matrix + dry clay
- Liquid = clay-bound water (*MCBW*) + capillary-bound water (*BVI*) + free water (ϕ_w) + hydrocarbon (ϕ_h)

These, in turn, can be further defined in petrophysical terms as

- Clay-bound water = $(\phi_T - \phi_e) = MCBW$
- Capillary-bound water = $BVI = (MPHI - FFI)$
- Free water = $FFI - \phi_h$
- V_{shale} = dry clay + clay-bound water (*MCBW*)
- *FFI* = free water + hydrocarbon
- *MPHI* = effective porosity (ϕ_e) = $FFI + BVI = \phi_T - MCBW$

19.2.2 Uncertainties of Conventional Log Analysis. In the Archie model (on the right of Fig. 19.1), the analyst might use a density log, for example, to deduce the porosity, in this case defined as the sum of ϕ_h and ϕ_w, but might still be dogged by the lack of certainty about the values of ρ_{matrix}, $\rho_{hydrocarbon}$, and S_{xo}, and hence about the value of ρ_{fluid}. Even if the analyst guesses all these values correctly, there still remains the impossibility of knowing how much of the water is free and how much is irreducible (capillary-bound water). Moreover, conventional log analysis offers little help in determining permeability.

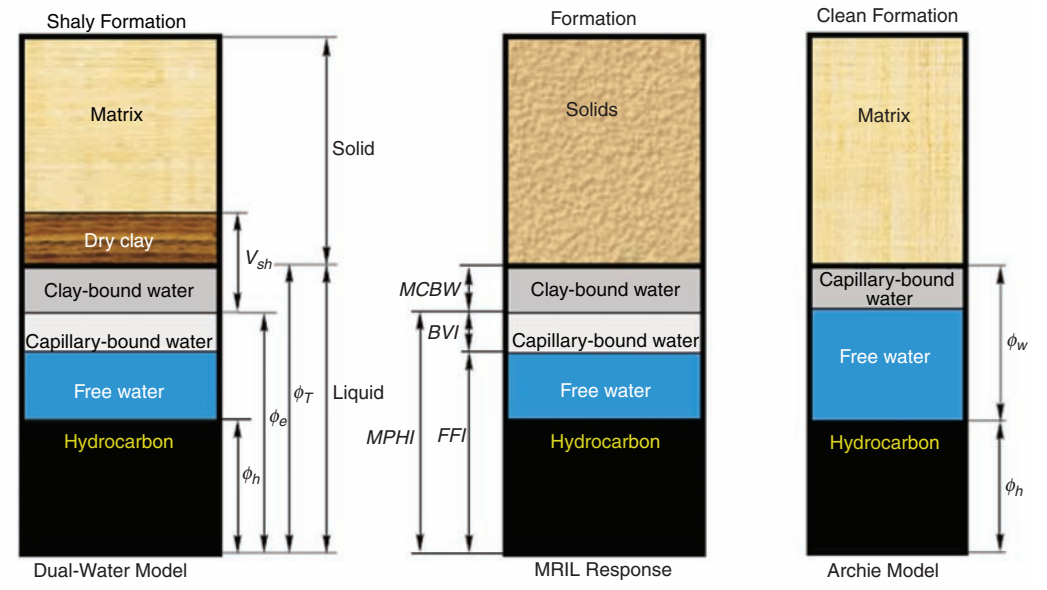


Fig. 19.1—Formation models with conventional and NMR responses (after Coates et al. 1999). Courtesy of Halliburton.

On the left side of Fig. 19.1 is a conventional model for shaly-sand analysis in terms of total porosity (ϕ_T), effective porosity (ϕ_e), and V_{shale} (which is the sum of dry clay and clay-bound water). A complete solution of this sort of model requires multiple conventional logging measurements, all of which are subject to the vagaries of rugose hole conditions, vertical and radial resolution mismatches, unknown values for R_w and R_{mf}, and many other factors.

The middle panel of Fig. 19.1 shows that with essentially three basic NMR measurements, the major components of the puzzle can be solved. *MPHI, BVI,* and *MCBW* provide answers regardless of matrix type, clay type, pore structure, hole conditions, or invasion pattern. This is the advantage offered by NMR. **Fig. 19.2** summarizes this contrast between conventional and NMR measurements and analysis.

19.3 NMR Measurements

The basic measurements made by NMR tools of any kind are:

- T_1, the longitudinal relaxation time
- T_2, the transverse relaxation time
- D, the diffusion constant

Because these technical terms from the world of nuclear physics are unintelligible to the average log analyst, they are (fortunately) presented to the user as familiar petrophysical quantities, including:

- *MPHI,* the effective porosity
- *FFI,* the free-fluid index
- *MCBW,* the clay-bound water

These in turn may be used to compute permeability, free-water saturation, and irreducible-water saturation, enabling the analyst to predict what a given formation is likely to produce, with what water cut, and at what flow rate.

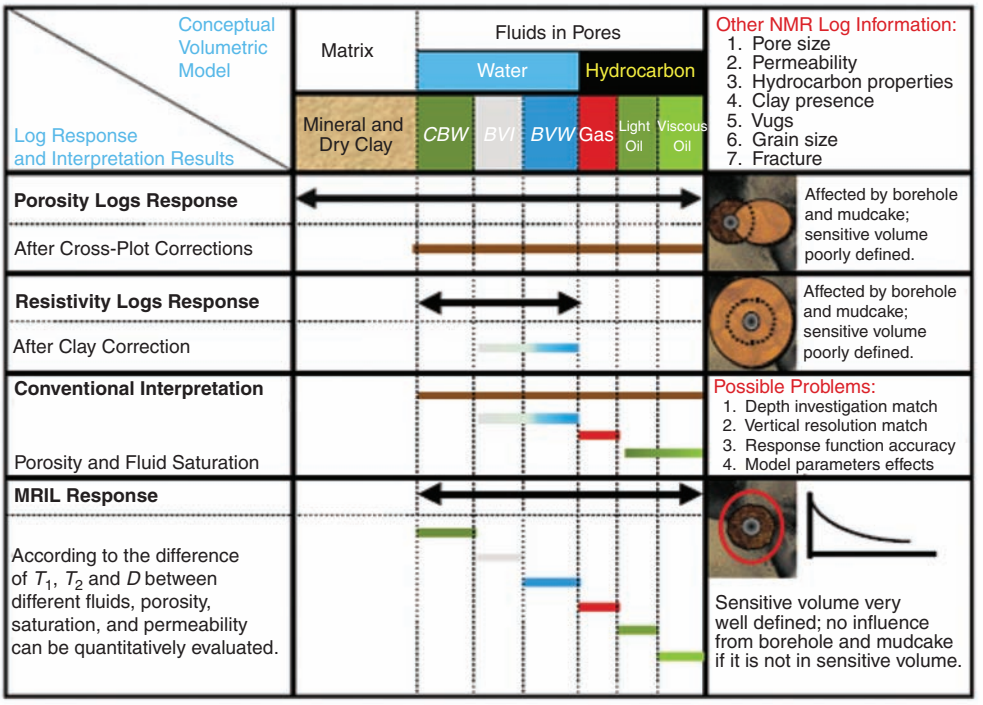


Fig. 19.2—Comparison of NMR and conventional log analysis (Coates et al. 1999). Courtesy of Halliburton.

19.4 NMR Free Fluid and Permeability

The NMR measurement of T_2 at any given depth in the well is not a single number, like R_t, but a distribution over time of a series of values that gives the analyst a picture of the porosity and the pore-size distribution. A typical T_2 distribution is shown in **Fig. 19.3.**

In Fig. 19.3, the total area under the curve gives the effective porosity, ϕ_e (*MPHI*), provided that the only fluid in the pore space is water. In cases where light hydrocarbons, gas, or both are present, the form of the T_2 distribution may become somewhat distorted.

The logarithmic time axis tells the analyst how much of the porosity is distributed where: in the clay-bound water-filled tiny pore spaces; in the capillary-bound small pores that hold the immovable (irreducible) water; or in the connected pores that allow fluid flow. The points on the T_2 time axis that divide the three pore types are located at approximately 3 and 33 ms (see **Fig. 19.4**), although these cutoffs can vary from one formation type to another.

Although the effective porosity is given by the total area under the curve, the permeability is related to the area under the curve to the right of the 33-ms cutoff line. The general form of the equation relating permeability and the measured quantities is:

$$k = \left(\frac{\phi}{C}\right)^4 \left(\frac{FFI}{BVI}\right)^2, \quad \ldots\ldots\ldots\

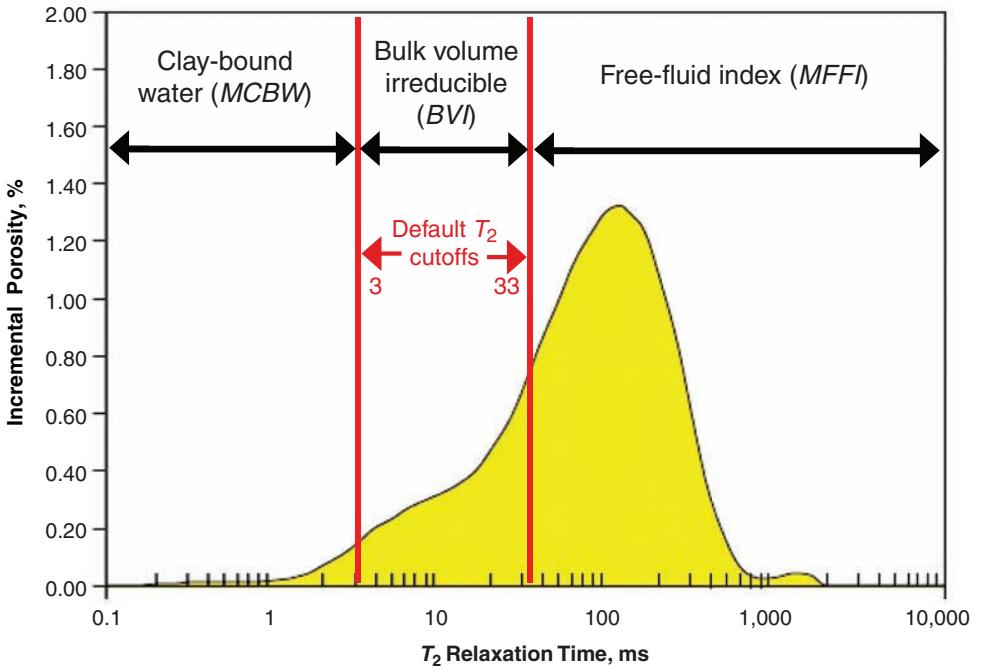


Fig. 19.4—T_2 cutoffs between free fluids and immovable fluids (Coates et al. 1999). Courtesy of Halliburton.

19.5 The Physics of NMR

Certain elements have a nucleus with an odd number of protons (for example, hydrogen, carbon, and sodium). The nuclei of these elements can therefore act like bar magnets and align with an external magnetic field. In the case of hydrogen, there is only one proton in the nucleus, and this fact provides the basis for both medical and oilfield NMR activities because hydrogen is found in water (and in hydrocarbons), which are found in the pore spaces of porous rocks. The protons are also free to spin, and therefore they act like a combination of a top and a bar magnet.

These properties are used to extract information by deliberately aligning the protons with an externally applied magnetic field and then sending a radio frequency (RF) pulse that knocks them out of alignment. When the pulse is removed, the protons precess back to their original alignment at a precise frequency known as the Lamor frequency. For hydrogen, the Lamor frequency is given by:

$$f = \frac{\gamma B_o}{2\pi}, \quad \ldots\ldots\ldots\

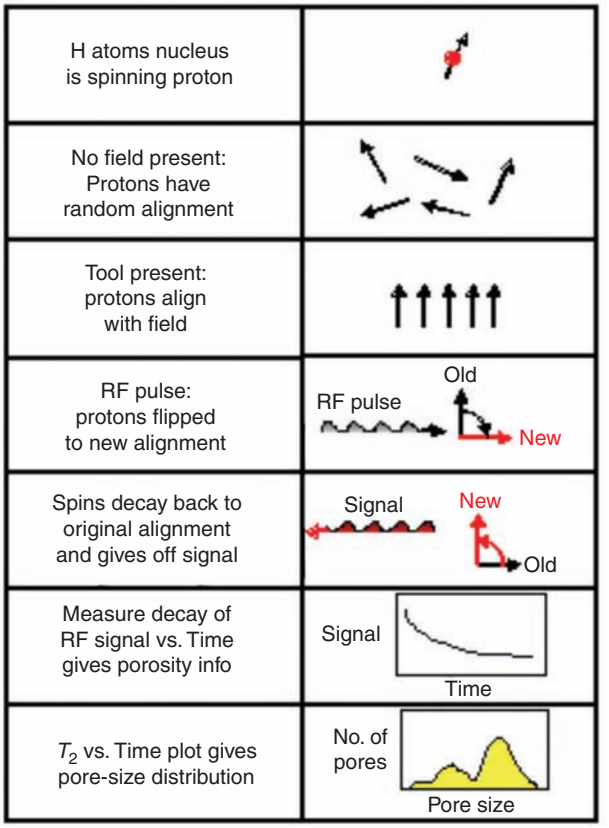


Fig. 19.5—Schematic of NMR measurement cycle.

Fig. 19.6 shows two relaxation curves, one for a high-permeability sample and one for a low-permeability sample. Although both samples have the same porosity, the *FFI* to *BVI* ratio of the two samples is very different. The lower curve represents a sample with a very high percentage of small pores and very little free fluid, resulting in a permeability of only 6.7 md. By contrast, the upper curve, where the spinning protons decay back to their original alignment much more slowly, represents a sample with a relatively small percentage of clay-bound and capillary-bound water in the smallest pores and a high free-fluid index; this sample has a healthy 4.2 darcy permeability value.

19.6 NMR Logging

There are two basic types of NMR wireline logging tools: the centered type, and the eccentered or pad-contact type. The centered tool was developed by NUMAR and was subsequently bought by Halliburton and licensed to other wireline operators. The pad-contact tool was introduced by Schlumberger in 1995 and is known as the combinable magnetic resonance (CMR) tool. Both these tools surpass the now-obsolete NMR tool that relied on the earth's magnetic field and required special doping of the mud in the borehole to eliminate the effect of the protons in the borehole itself.

19.6.1 Pad-Contact CMR Tool. A CMR tool is illustrated in **Fig. 19.7.** A pad is forced into contact with the formation wall by an opposing bowspring. The volume of rock investigated is a relatively small cylinder of formation rock a few inches from the pad in the invaded zone. **Fig. 19.8** shows a detailed plan view of the sensed zone.

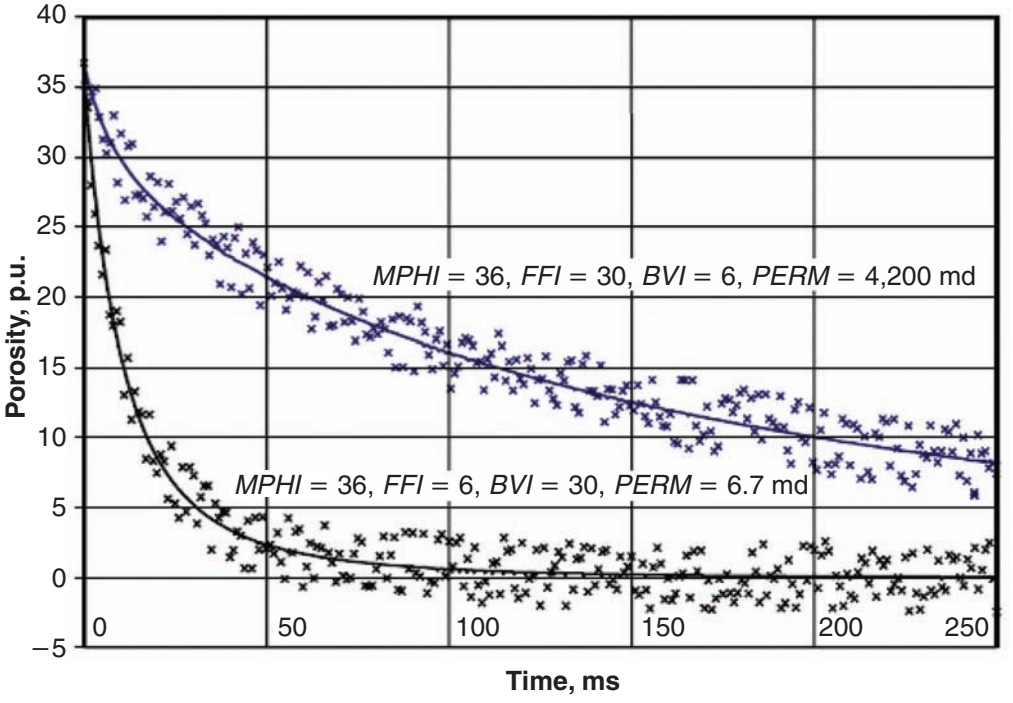


Fig. 19.6—Relaxation curves for high- and low-permeability samples (Coates et al. 1999). Courtesy of Halliburton.

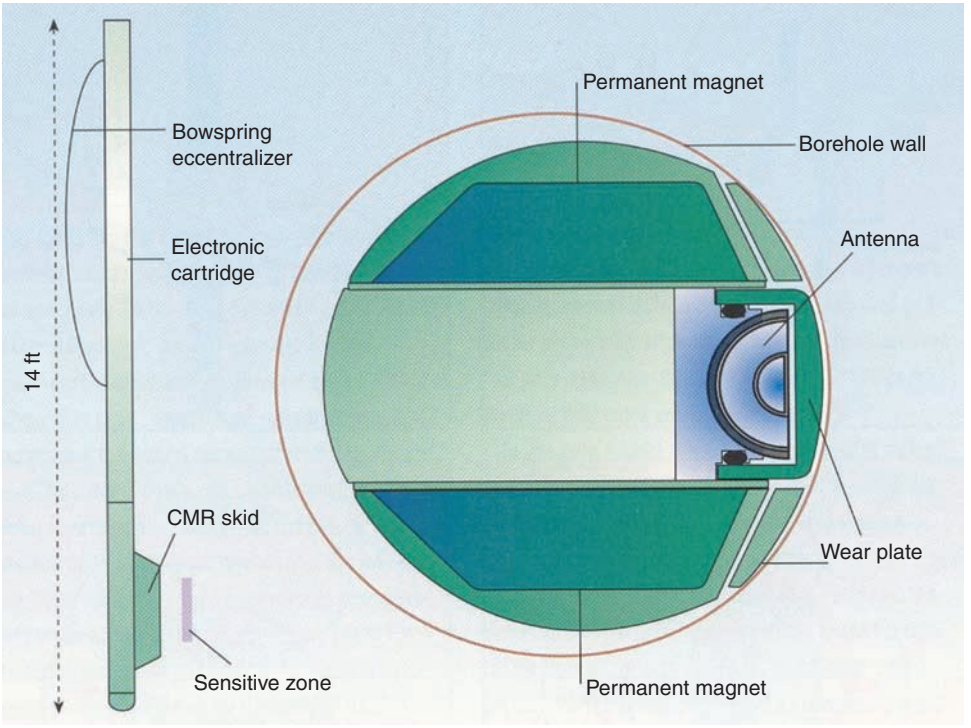


Fig. 19.7—CMR tool and cross section of pad. Courtesy of Schlumberger.

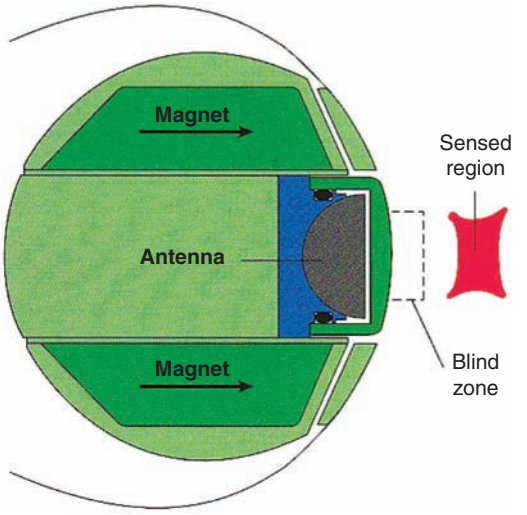


Fig. 19.8—Detail of CMR magnet, antenna, and sensed region. Courtesy of Schlumberger.

By changing the frequency of the RF pulse used to flip the protons, this tool can make measurements at different depths of investigation radially outward from the tool into the formation, as illustrated in **Fig. 19.9.**

19.6.2 Centered MRIL Tool. The MRIL tool is run centered in the borehole and is less affected by borehole rugosity than the pad-contact devices. **Fig. 19.10** shows a juxtaposition of the tool, the borehole wall, and the sensed region of the formation.

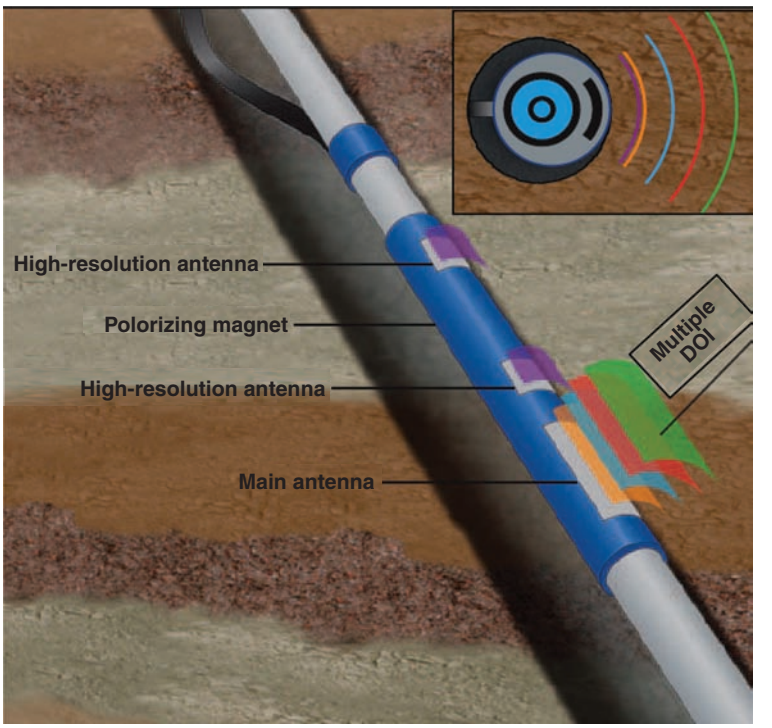


Fig. 19.9—Variable depth of investigation with CMR tool (Schlumberger 2006). Courtesy of Schlumberger.

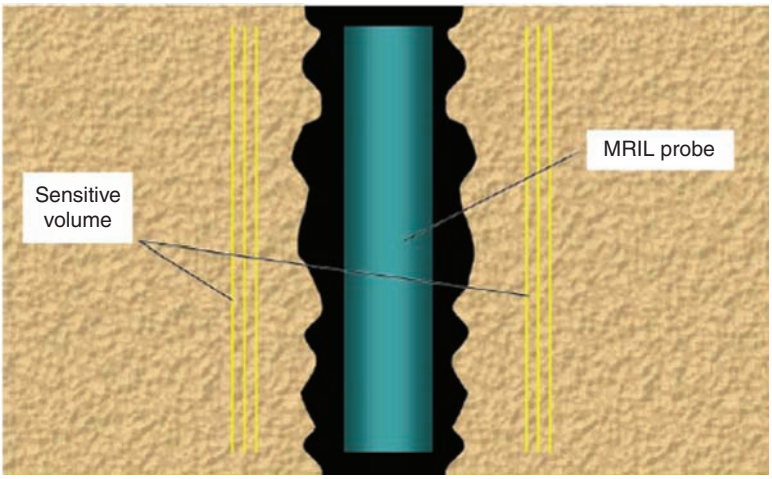


Fig. 19.10—Centered MRIL tool. From Coates et al. (1999). Courtesy of Halliburton.

The magnetic field from the MRIL permanent magnet drops off radially from the tool axis into the surrounding formation. Therefore, the strength of the field, coupled with the operating frequency of the RF pulses, enables the tool to look at thin annular cylindrical volumes of the formation at different radial distances from the tool. **Fig. 19.11** shows one such annular shell defined by the radial position at which the field has dropped to 175 gauss and the Lamor frequency is 750 kHz.

Fig. 19.12 gives a plan view of the tool in the borehole and the sensible volume in the formation for one particular RF frequency.

Thus, by use of multiple operating frequencies, the MRIL tool can also investigate a range of annular volumes of the formation at different distances from the tool axis, as illustrated in **Fig. 19.13.**

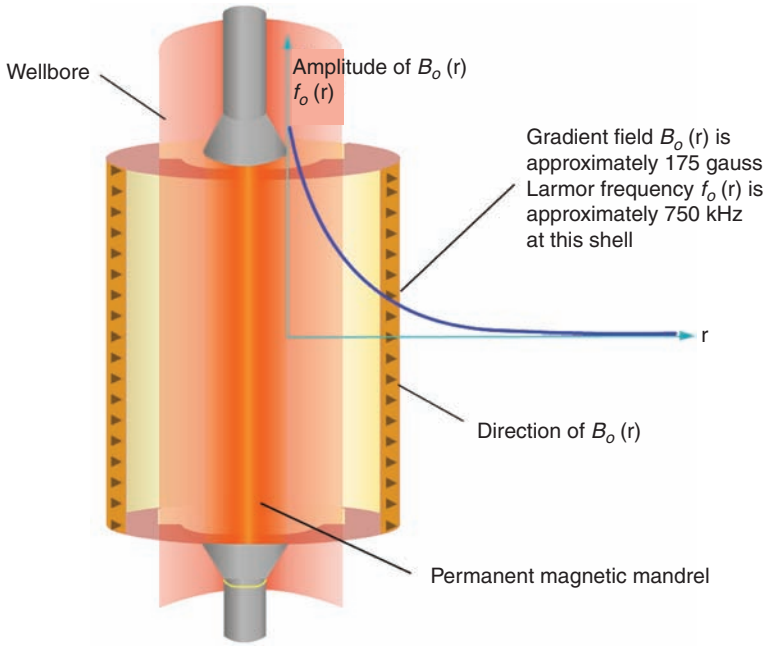


Fig. 19.11—Magnetic field surrounding centered MRIL tool (Coates et al. 1999). Courtesy of Halliburton.

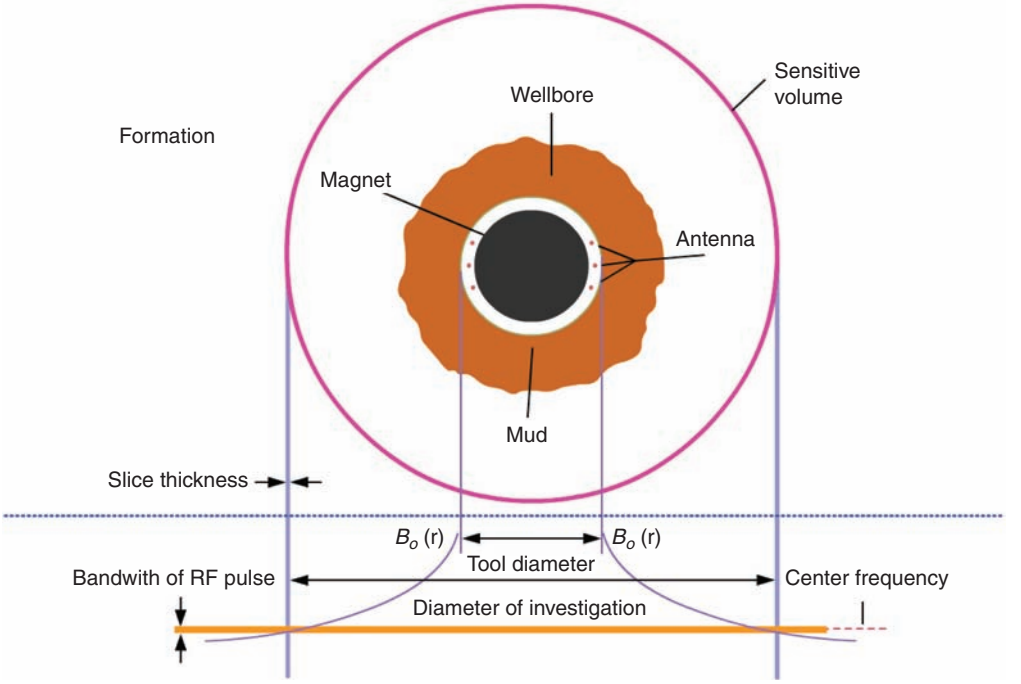


Fig. 19.12—Plan view of MRIL tool in the borehole showing sensible volume of formation (Coates et al. 1999). Courtesy of Halliburton.

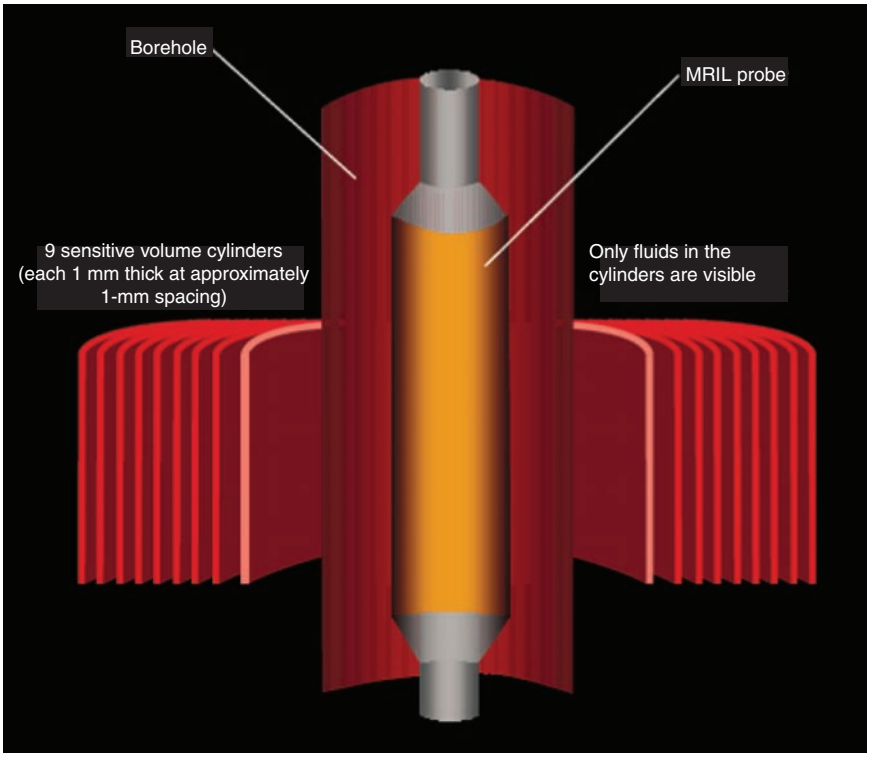


Fig. 19.13—Multiple sensible volumes surrounding MRIL tool (Coates et al. 1999). Courtesy of Halliburton.

19.6.3 NMR Use in Formation Testing. NMR measurements are not confined to deducing rock properties because the same NMR principles can be applied to fluids. Bulk relaxation can be measured for a fluid in a container large enough that surface relaxation effects are insignificant. In such cases, T_{2bulk} is approximately equal to T_{1bulk}, which is given by:

$$\text{For water}: \quad T_{1bulk} \cong 3\left(\frac{T_K}{298\eta}\right) \quad \ldots\ldots\ldots\

19.7 NMR Log Interpretation

The basic level of formation evaluation with an NMR log is the visual inspection of a strip log on which a T_2 distribution curve has been plotted at fixed depth increments along the borehole. The analyst should be able to pick, in conjunction with other ancillary data such as a gamma ray scan, depth intervals with good porosity and permeability. **Fig. 19.15** shows a presentation of a CMR-processed NMR data set.

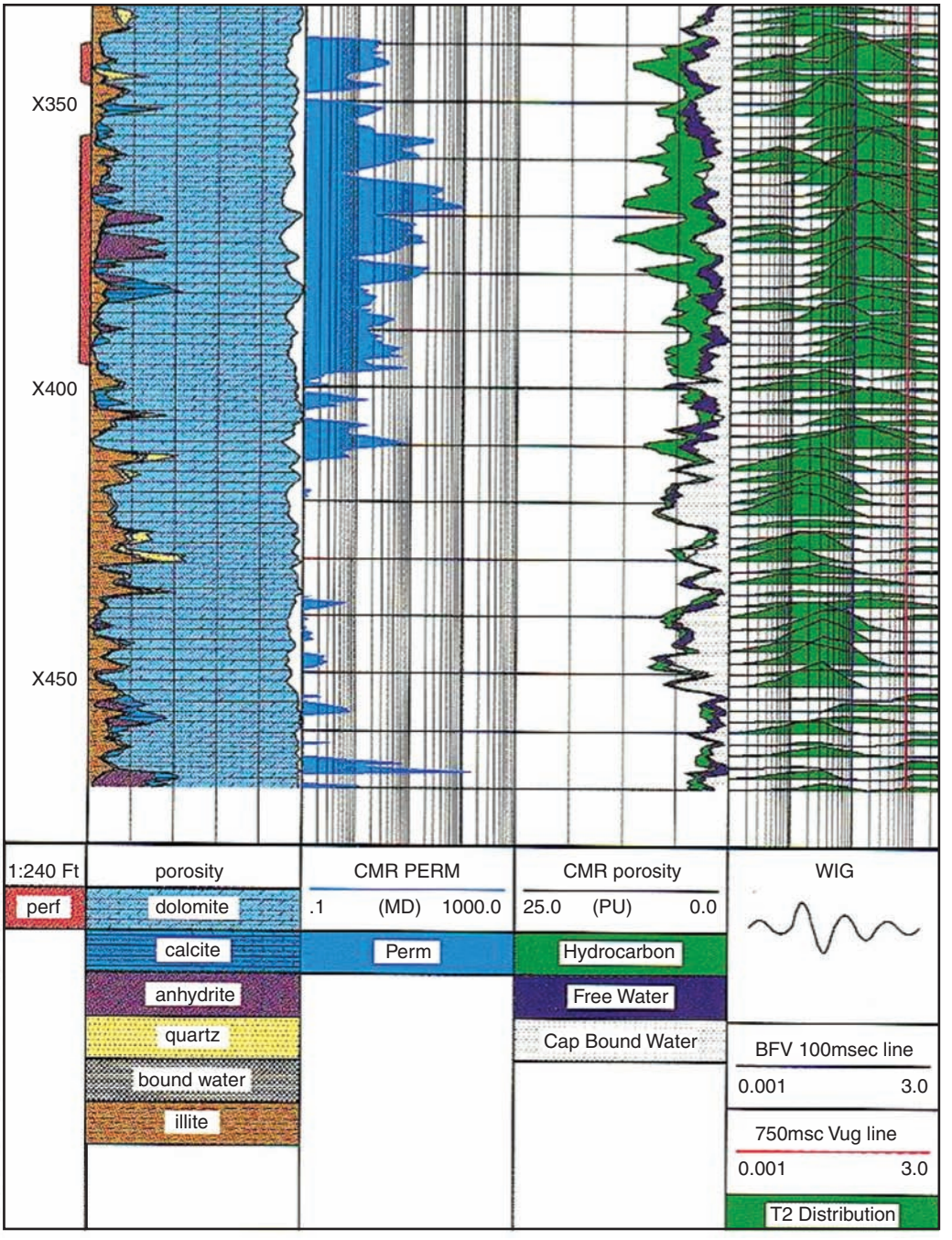


Fig. 19.15—Presentation of processed CMR data. Courtesy of Schlumberger.

QUESTION 19.2. Inspect the log shown in Fig. 19.15 and answer the following questions:

1. What is the predominant lithology of the logged column?
2. In the interval X415 to X470, are the pore fluids free or bound?
3. What fluids would you expect to flow from the perforated interval?
4. What is the significance of the red line at 750 ms on the T_2 display?

NMR alone cannot perform a complete analysis that includes free and bound-water saturations; conventional deep and shallow resistivity devices are still needed. NMR tools, of whatever type, can, at best, make measurements near the borehole in the invaded zone where mud filtrate has invaded and the saturation is S_{xo}. An example of a full analysis that combines both MRIL and conventional data is shown in **Fig. 19.16.**

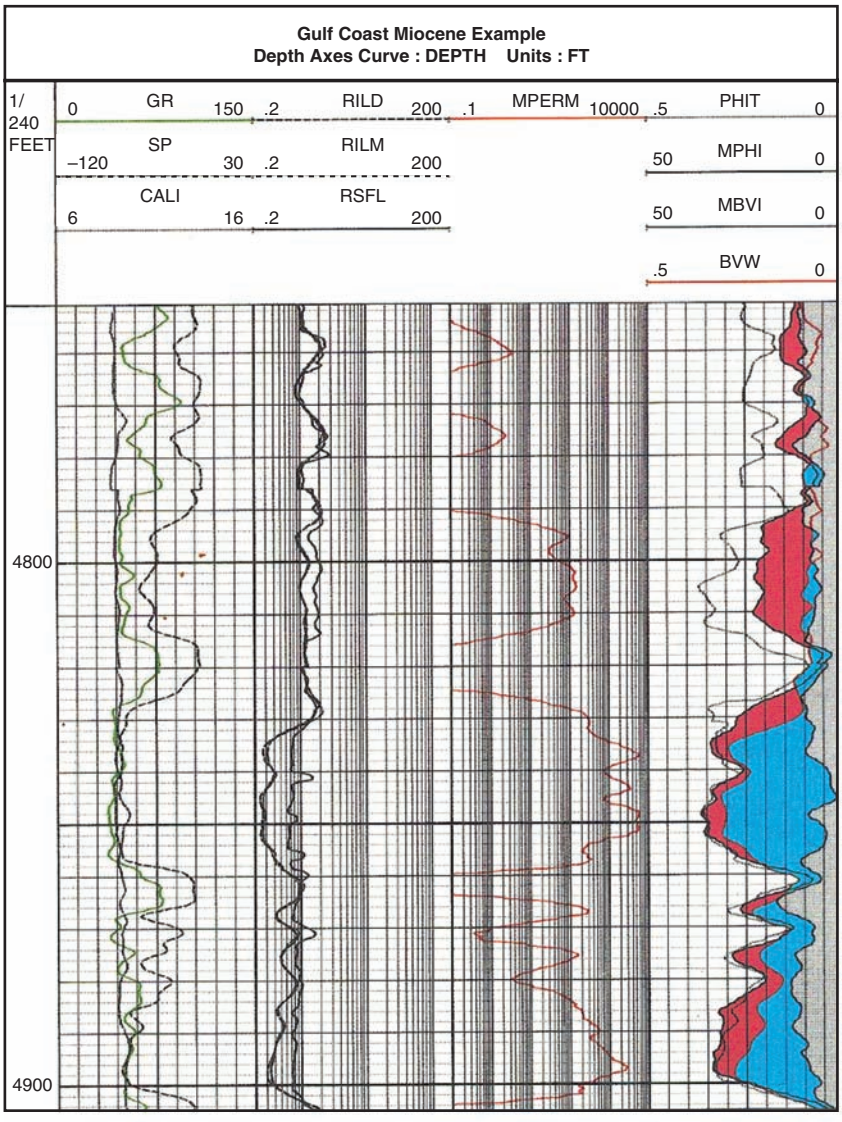


Fig. 19.16—Log analysis in shaly sand combining MRIL and conventional logs.

QUESTION 19.3. Inspect the log shown in Fig. 19.16 and answer the following questions:

1. What interval shows a clean water-bearing zone?
2. What is the permeability in the wet zone?
3. What interval shows producible hydrocarbons?
4. What are the porosity and permeability in the hydrocarbon zone?
5. Why is *PHIT* so much larger than *MPHI* in this zone?

19.7.1 NMR Porosity and Permeability. Do NMR-derived porosity and permeability values compare well with values from core analysis? The answer is "yes." Many studies on wells where both core and NMR wireline logs have been run confirm that there is excellent agreement between the two measurements. **Fig. 19.17** shows an example with core analysis results plotted as points on the strip log of computed CMR porosity and permeability.

Note that with CMR, it is common to use a slightly different relationship to calculate permeability. Instead of using the Coates equation (given in Eq. 19.1), the "Geometric Mean T_2" is used as the input to the equation:

$$k = a\phi^4 T_{2gm}^2, \quad \ldots\ldots\ldots\

QUESTION 19.4. Inspect the log shown in Fig. 19.17:

1. In the interval XX41 to XX48, what is the CMR porosity?
2. In the same interval, what is the mean value of T_2?
3. Based on these two log readings, what is the permeability (Eq. 19.5)?
4. Does this value agree with the core porosity?

19.7.2 Hydrocarbon Typing. So far, only the NMR response to water-filled pore space has been discussed. 100% water is said to have an HI of one. Oil, light oil, and gas have fewer hydrogen atoms per unit volume than water and are therefore said to have an HI of less than one. The discussions in Chapter 18 on the response of thermal neutron tools covered similar ground and accounted for the observation that the neutron tool reads less that true porosity in gas and light oil.

The presence of gas and light hydrocarbons in the pore space thus distorts the normal (water-filled) T_2 vs. incremental porosity graph. **Fig. 19.18** illustrates this phenomenon, which also depends on the gradient of the magnetic field in the zone under investigation. In the absence of a gradient, the T_2 distribution is as shown in Fig. 19.18a. The light hydrocarbons fall between 100 and 1000 ms. In the presence of a gradient, molecules move with more or less alacrity, depending on their viscosity, and will shift to the left on the T_2 time axis, as shown in Fig. 19.18b. MRIL-type tools are capable of providing the gradient needed for this kind of analysis.

To account fully for these hydrocarbon effects, two additional factors need to be determined, T_1 and the diffusivity, D, which is a measure of the mean square displacement of molecules observed during a given period. D varies with fluid type and temperature. In the case of a gas, D also varies with gas density and is therefore pressure-dependent. The reader is referred to the literature for technical details of how NMR tools can be programmed for field recording of these inputs for hydrocarbon typing. **Table 19.1** lists values for T_1, T_2, and D for brine, oil, and gas as well as ranges for HI and viscosity.

A useful crossplot for hydrocarbon typing is one in which the diffusivity factor, D, is crossplotted with T_1, as shown in **Fig. 19.19.**

Fig. 19.20 gives a guide using T_1, T_2, and D to the presence of various solids and fluids in the sensed volume of the formation, including clay-bound water, capillary-bound water, movable water, heavy oil, light oil, and gas. This petrophysical jigsaw puzzle is nothing if not complex, and although the means are available to solve the puzzle, the analyst would be well advised to

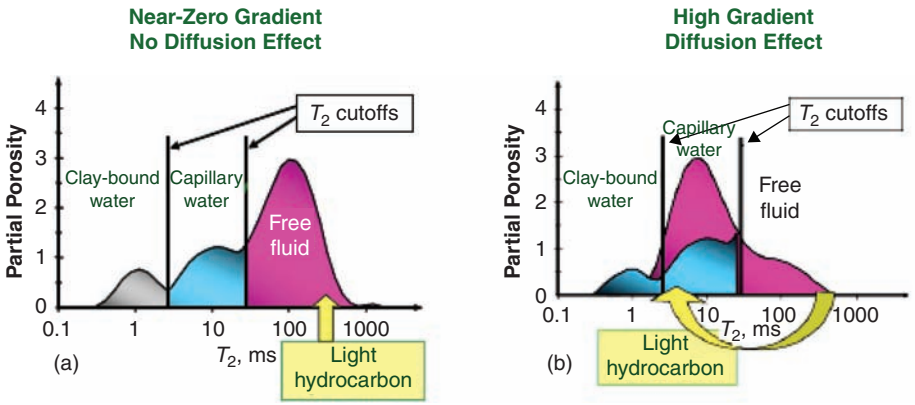


Fig. 19.18—Light hydrocarbon effect on T_2 distribution plot: (a) without and (b) with field gradient (Borghi et al. 2005). Courtesy of Baker Hughes.

TABLE 19.1—NMR PROPERTIES OF RESERVOIR FLUIDS (Coates et al. 1999)
Courtesy of Halliburton

Fluid	T_1 (ms)	T_2 (ms)	Typical T_1/T_2	HI	η (cp)	$D_0 \times 10^{-5}$ (cm^2/s)
Brine	1–500	1–500	2	1	0.2–0.8	1.8–7
Oil	3,000–4,000	300–1,000	4	1	0.2–1,000	0.0015–7.6
Gas	4,000–5,000	30–60	80	0.2–0.4	0.011–0.014 methane	80–100

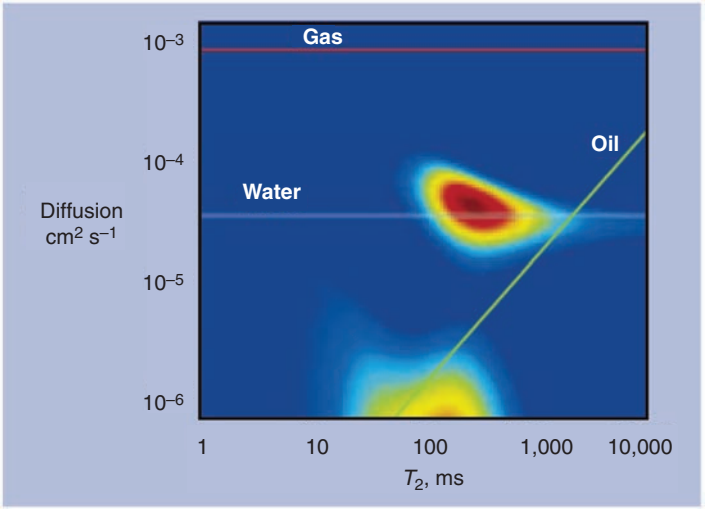


Fig. 19.19—Hydrocarbon typing crossplot, *D* vs. T_2 (Schlumberger 2006). Courtesy of Schlumberger.

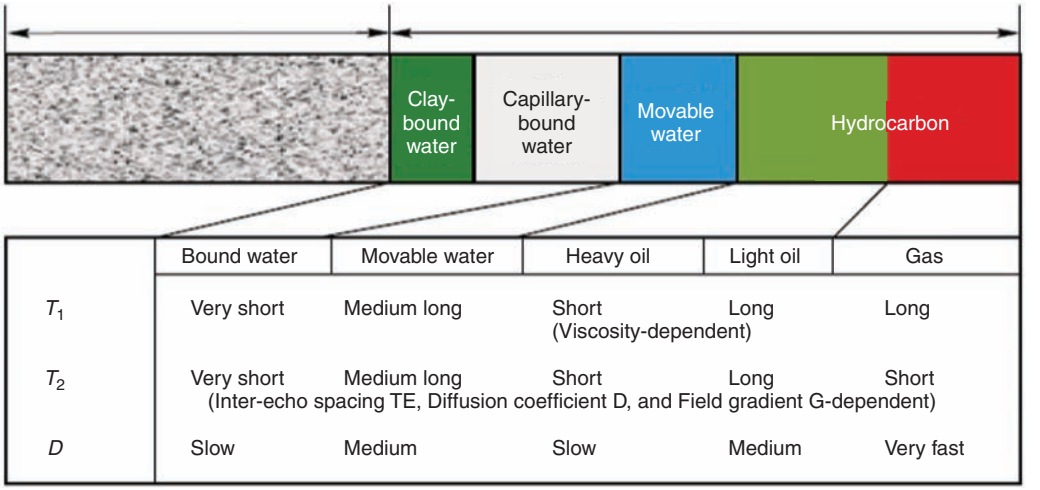


Fig. 19.20—Guide to T_1, T_2, and *D* in various solids and fluids (Coates et al. 1999). Courtesy of Halliburton.

take a more detailed course on this topic before claiming to be an expert on the setup for NMR recording and interpretation.

19.8 NMR Vertical and Horizontal Resolution

The vertical precision of NMR tools depends on:

- The length of the magnet
- The length of the RF antenna
- The number of different frequencies used (for different depths of investigation)
- The duty cycle for repeating measurements (for signal-to-noise improvement)
- The logging speed

Fig. 19.21 gives a pictorial guide to vertical-resolution issues and their controlling factors. It is not possible to represent the vertical resolution of either the centered or the pad-type tool by a single number. Suffice it to say that the average vertical resolution is similar to that of the neutron-density combination at between 1 and 2 ft. Likewise, the average depth of investigation of NMR-type tools is similar to that of the neutron-density combination at 5 in.

19.9 NMR Calibration

Fig. 19.22 illustrates the primary calibration procedure for the MRIL tool. The calibration takes place in a fiberglass tank with a thin metal coating that acts as a Faraday cage to block out unwanted RF radiation.

The interior of the tank contains a number of concentric chambers that are filled with appropriately doped water to simulate the borehole and the formation. In addition to monthly checks in this calibrator, the usual pre- and post-logging calibrations should be run and checked for conformity with published norms.

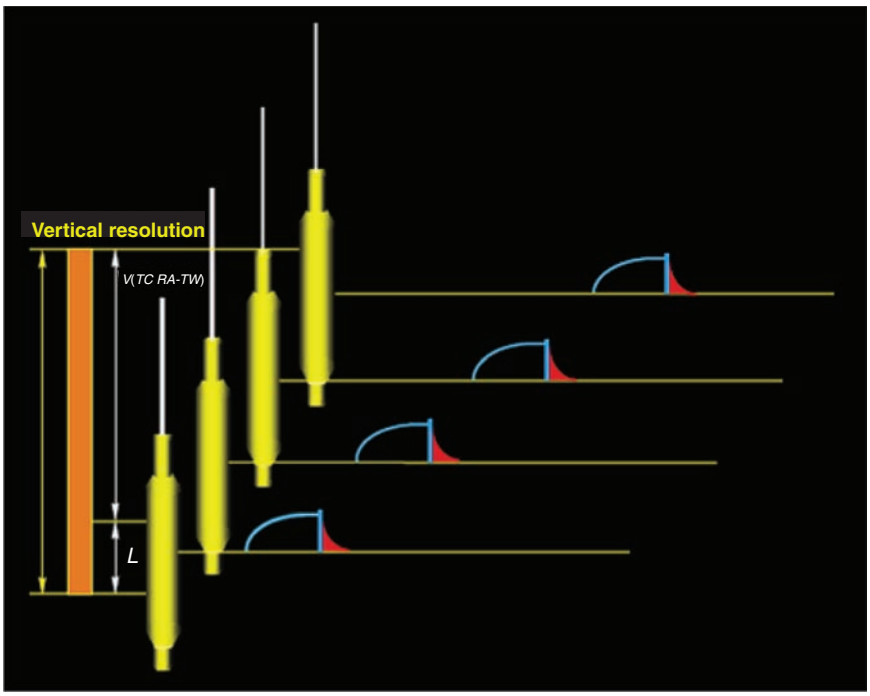


Fig. 19.21—NMR vertical resolution (Coates et al. 1999). Courtesy of Halliburton.

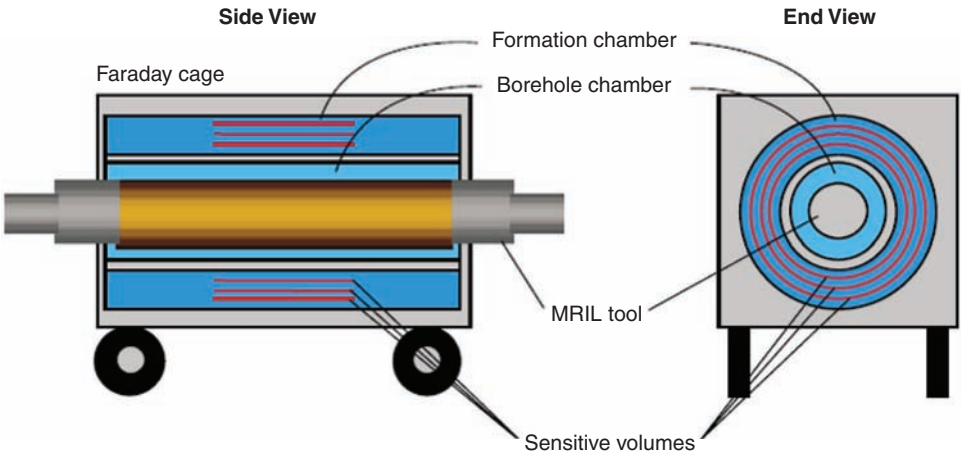


Fig. 19.22—MRIL calibration tank (Coates et al. 1999). Courtesy of Halliburton.

19.10 NMR Limitations

Although instrumentation and logging savoir-faire have reached new heights with the introduction of modern NMR, it should never be thought that NMR alone can solve all log analysis and petrophysical problems. The chief limitation of NMR-type measurements is their relatively shallow depth of investigation radially into the formation. This limits their sensible volume to the invaded zone where the fluid saturations are not the same as in the undisturbed zone farther away from the borehole. The reader is encouraged to continue to combine as many formation-evaluation tools as can be assembled to understand fully the pore system and its fluid content. Every effort should be made to relate log and laboratory measurements back to the rocks themselves.

References

Borghi, M., Porrera, F., Lyne, A. et al. 2005. Magnetic Resonance While Drilling Streamlines Reservoir Evaluation. *Trans.,* SPWLA 46th Annual Logging Symposium, New Orleans, 26–29 June.

Coates, G.R., Xiao, L., and Prammer, M.G. 1999. *NMR Logging Principles and Applications*. Publication H02308, Halliburton Energy Services, Houston, Texas, USA.

Schlumberger. 2006. MR Scanner, http://www.slb.com/~/media/Files/evaluation/brochures/wireline_open_hole/petrophysics/nmr/mrscanner_br.ashx, (accessed 13 February 2012).

General References

Anand, V. and Freedman, R. 2009. New Methods for Predicting Properties of Live Oils From NMR. *Trans.,* 50th Annual SPWLA Logging Symposium, 21–24 June, The Woodlands, Texas, Paper AAAA.

Cheng, Y., Karrat, A.M., and Badry, R. et al. 2009. Power-Law Relationship Between Viscosity of Heavy Oils and NMR Relaxation. *Trans.,* SPWLA 50th Annual Logging Symposium, 21–24 June, The Woodlands, Texas, Paper BBBB.

Clavier, C., Coates, G., and Dumanoir, J. 1977. The Theoretical and Experimental Bases for the Dual Water Model for Interpretation of Shaly Sands. Paper SPE 6859 presented at the SPE Annual Technical Conference and Exhibition, Denver, 9–12 October. http://dx.doi.org/10.2118/6859-PA.

Coates, G.R., Miller, M., Gillen, M., et al. 1991. The MRIL in Conoco 33-1: An Investigation of a New Magnetic Resonance Imaging Log. *Trans.,* SPWLA 32nd Annual Logging Symposium, Midland, Texas, USA, 16–19 June, Paper DD.

Coope, D.F., Quinn, T.H., Frost, E. Jr., et al. 2009. A Rock Model for Shale Gas and its Application using Magnetic Resonance and Conventional LWD Logs. *Trans.,* SPWLA 50th Annual Logging Symposium, 21–24 June, The Woodlands, Texas, USA, Paper CCCC.

Ostroff, G.M., Shorey, D.S., and Georgi, D.T. 1999. Integration of NMR and Conventional Log Data for Improved Petrophysical Evaluation of Shaly Sands. *Trans.,* SPWLA 40th Annual Logging Symposium, Oslo, Norway, 30 May–3 June.

Straley, C., Rossini, D., Vinegar, H., et al. 1997. Core Analysis by Low Field NMR. *The Log Analyst* **38** (2): 84-94.

Timur, A. 1968. Effective Porosity and Permeability of Sandstones Investigated through Nuclear Magnetic Principles. *Trans.,* SPWLA 9th Annual Logging Symposium, New Orleans, 23–26 June, Paper K. Later published in the 1969 *The Log Analyst* **10** (1): 3–11.

Vinegar, H.J. 1995. SPWLA short course on NMR, Houston, Texas, USA.

Answers to Questions

QUESTION 19.1.

$k = 352$ md.

QUESTION 19.2.

1. Dolomite.
2. Bound.
3. Oil (practically water-free).
4. Levels with T_2 above 750 ms have vuggy porosity.

QUESTION 19.3.

1. 4826–4858 and 4825–4902.
2. 1 to 6 darcy.
3. 4792–4815.
4. $\phi_{av} = 23\%$, $k_{av} = 100$ md.

QUESTION 19.4.

1. CMR porosity is between 9 and 11%.
2. Logarithmic mean T_2 is between 2 and 3 ms.
3. k from Eq. 19.5 is between 1.8 and 6 md.
4. k core in the same interval is between 1 and 10 md.

Chapter 20

Dipmeter and Borehole Imaging

The earliest attempts at borehole imaging were directed toward determination of the bed dip and azimuth using a relatively simple three-arm, three-electrode dipmeter tool that provided the minimum information required (three points) to determine the orientation of a given plane in space. Later on, this technology advanced with the introduction of contact-pad-carrying four-arm and six-arm tools on which, in some cases, two or more electrodes were installed. This led to better definition of bed dips, especially because these advances in hardware were matched by advances in software, digital sampling, and recording density. These technological advances culminated in tools with multiple pads, each of which held multiple electrodes, giving rise to formation microimaging tools that could generate an almost 360° electrical image of the borehole.

These advances opened the door for the analyst, not only to obtain reliable dip and dip-azimuth data, but also to see the texture of the borehole wall and thus to identify the presence and orientation of fractures and, where present, vugs. In many instances, the clarity of the images obtained was sufficient to enable direct comparison between a full-core photograph and the logged image. However, these tools all operated by measuring electrical resistivity. When oil-based mud was used as the drilling fluid, these tools behaved poorly or were entirely unable to produce a usable survey from which dips or borehole images could be computed.

Given this inconvenience, the industry moved ahead with the introduction of other methods of imaging the borehole wall, including both ultrasonic scanners and downhole cameras conveyed on wireline. At about the same time, the ability to obtain logging data on drillpipe by means of LWD sensors opened up yet another possibility for formation imaging. If the drilling process involves the rotation of the bit by the drillpipe, then a directional sensor on an LWD sub will scan 360° around the borehole with each full rotation of the bit. (If the drilling is performed by means of a mud motor, then such imaging is not possible.)

In this chapter, both conventional dipmeters and other scanning devices and their modes of recording will be covered. In addition, the use of the image data obtained will be addressed for both structural and sedimentary features of the formations logged.

20.1 Definitions

A dipmeter survey records data on how the subsurface layers of rock were deposited and have subsequently been moved. The raw data consist of *orientation information*, which indicates where the downhole tool is located with respect to vertical and geographic coordinates, and *correlation information*, which can be used to determine the orientation of bedding planes with respect to the tool. The field log does not indicate formation dip. Computer processing of the raw data is required before any geological information can be extracted. The two most important parameters obtained from computer-based processing are the *bed-dip magnitude* and the *dip azimuth.* By studying how these two parameters vary with depth, much valuable information can be obtained. It is worthwhile to review the definitions of dip and dip azimuth:

The *dip angle* is the angle formed between a normal to a bedding plane and the vertical. A horizontal bed has a dip angle of 0°, and a vertical bed has a dip angle of 90° **(Fig. 20.1).**

The *dip azimuth* is the angle formed between geographic north and the direction of greatest slope on a bedding plane. Dip azimuth is conventionally measured clockwise from north, so that a plane dipping to east has a dip azimuth of 90° and one dipping to west, a dip azimuth of 270° **(Fig. 20.2).**

20.2 Applications of Dipmeters and Borehole Imaging Devices

Dipmeter surveys have a variety of applications. At the lowest level, the raw data may be used:

- To compute a deviation survey and true vertical depth
- To compute the integrated hole volume
- As an aid to fracture detection

At a higher level, computed dipmeter results may be used to determine:

- Gross geologic structural features crossed by the wellbore
- Sedimentary details within the reservoir (e.g., grading, bioturbation)
- Thin-bed analysis
- The depositional environment (e.g., paleocurrents)
- True stratigraphic thickness and true vertical thickness

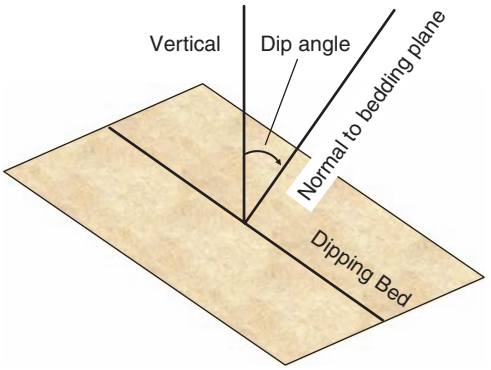


Fig. 20.1—Definition of dip angle.

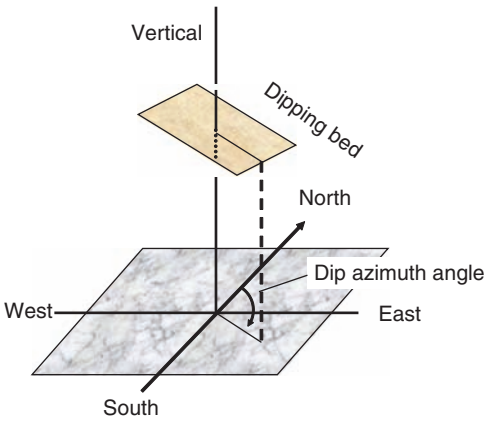


Fig. 20.2—Definition of dip azimuth.

At the highest level, computed dipmeter results from many wells may be combined to produce:

- Structural cross sections
- Trend-surface maps
- Detailed views of rock texture

The most important applications of the dipmeter survey are in exploration drilling, to help identify local structure and stratigraphy, and in development drilling, to help map the productive horizons and indicate directions to follow for further field development.

20.3 Tools Available

A number of dipmeter tools are available. Historically, three-arm dipmeter tools were used for many years, but have now been entirely superseded by four-arm and six-arm tools. **Fig. 20.3** illustrates a commonly used four-arm dipmeter tool. All currently used dipmeter tools have the following common characteristics:

An *orientation section* that measures:

a. Tool deviation from vertical
b. Tool azimuth with respect to north
c. Orientation of the reference electrode pad either to north or to the low side of the hole

A *caliper section*, which measures two or more hole diameters

A *microelectrode array* that records the resistivity of the formation in the very localized area where the pads contact the formation (correlation traces)

A *gross-correlation device* that will supply a moderately deep resistivity curve or a gamma ray or SP curve.

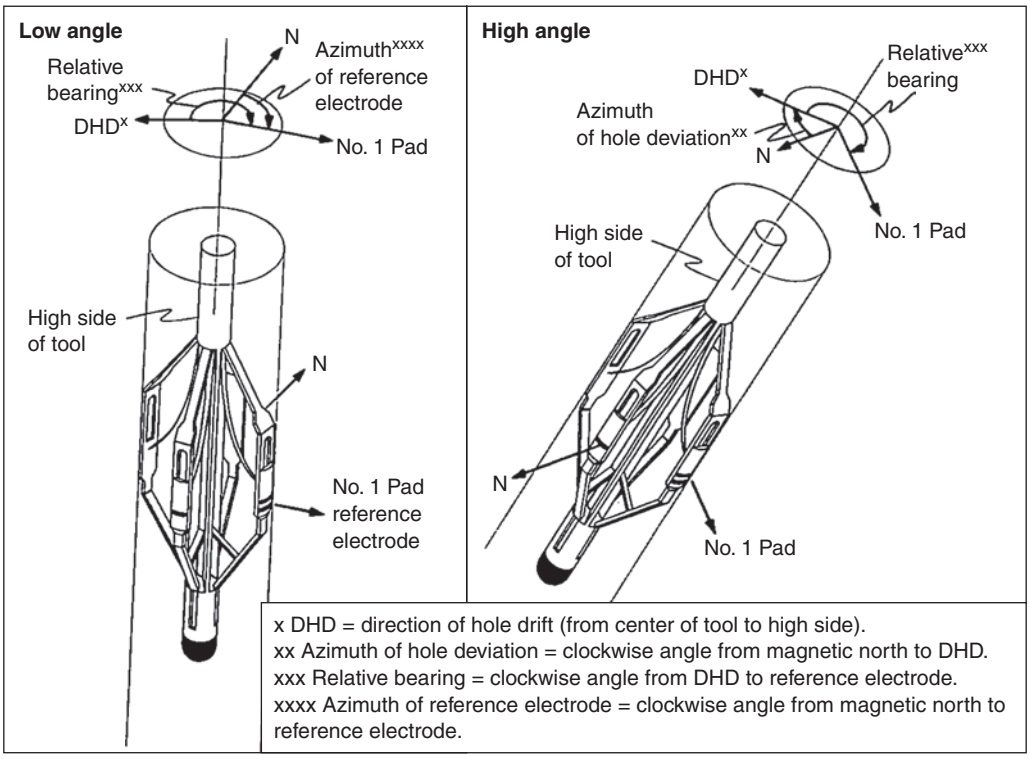


Fig. 20.3—Four-arm dipmeter tool. Courtesy of Schlumberger.

Whereas orientation was traditionally measured with a pendulum to indicate deviation from vertical, and a magnetic compass was used to indicate tool rotation relative to magnetic north, now fluxgate magnetometers, gyroscopes, accelerometers, or a combination of these are used to deduce tool position and orientation.

The microresistivity pads carry small button electrodes for water-based muds and knife-edge electrodes for oil-based muds, although the latter are not always very effective.

20.4 Field Presentation

In the field, the norm is to supply a printout of the orientation curves, the correlation traces, and the caliper curves. All data are recorded on magnetic media. If the service company is authorized to compute the raw data, the field engineer will retain the digital record. Otherwise, it should be delivered along with the field printouts to the operator's representative for processing elsewhere.

On rare occasions, it may be desirable to compute dip results from an optical record rather than from the digital data, for which a paper printout on a much-expanded scale (60 in. = 100 ft, or 1:20 depth scale) will be required. **Fig. 20.4** illustrates a 5-in. (1:240 or 1:200) dipmeter presentation; **Fig. 20.5** illustrates the far more detailed 60-in. presentation.

20.5 Dipmeter Computation

The basic principle of dipmeter computation may be grasped by considering the case of a thin bed crossing a borehole. If the dip of the bed is greater than zero, then at its intersection with the borehole, it will appear shallower in the well on the updip side of the wellbore than on the down-dip side. If the bed in question has a resistivity different from the resistivity of the surrounding beds, then a resistive (or conductive) anomaly will exist that appears higher on one side of the borehole than on the other. The computation of dip and dip azimuth is therefore reduced to a trigonometric calculation. Any plane can be uniquely defined by three points in space. A four-arm dipmeter provides four points. If the bedding planes are uniformly thick and plane at the intersection with the wellbore, only three of the dipmeter's available four points are necessary to compute the dip.

However, it is frequently found that one or another of the correlation traces is substandard as a result of hole conditions or recording technique, in which case the four traces provide a margin of safety. **Fig. 20.6a** shows a cross section of a borehole with a four-arm dipmeter tool. Fig. 20.6b is a schematic of the correlation curves that might be recorded by the four-arm dipmeter.

Displacement of an anomaly shown on one correlation curve to another correlation curve is the key to computing the formation dip. **Fig. 20.7** illustrates the displacements to be expected when a dipping plane cuts across a borehole.

Dip computation starts with the correlation of one trace with another to discover the relevant displacement. Computer-based correlation can be performed with a variety of techniques, such as pattern recognition, Fourier analysis, and conventional correlograms. The most commonly used technique is the construction of correlograms. A short length of one correlation curve is compared with an equal length of another correlation curve. Starting some distance uphole and sliding down to some distance downhole, the two segments are cross-multiplied. This correlation function reaches a maximum at the point where the curves coincide. Three parameters are used to control the process of correlation: the correlation interval, the search angle, and the step distance **(Fig. 20.8).**

The length of the correlation interval can be from a fraction of a foot up to several feet, depending on the information sought. For fine stratigraphy, and if the quality of the raw data supports it, a correlation interval of 3 in. to 2 ft may be used. For standard work, a 2 to 6 ft length may typically be used. For structural information, 6 to 18 ft may be used.

The search angle defines how far up and down the hole to seek a correlation, and, depending on the hole size, this in turn reflects the analyst's guess of the greatest dip angle to be expected. Computation time requirements become a concern at this point. Searching for a 30° dip in a 12-in. hole requires correlation to start $12 \times \tan 30°$ uphole and to stop at $12 \times \tan 30°$ downhole (a search over 13.86 in.). Searching for a 60° dip requires starting at $12 \times \tan 60°$ uphole and ending at

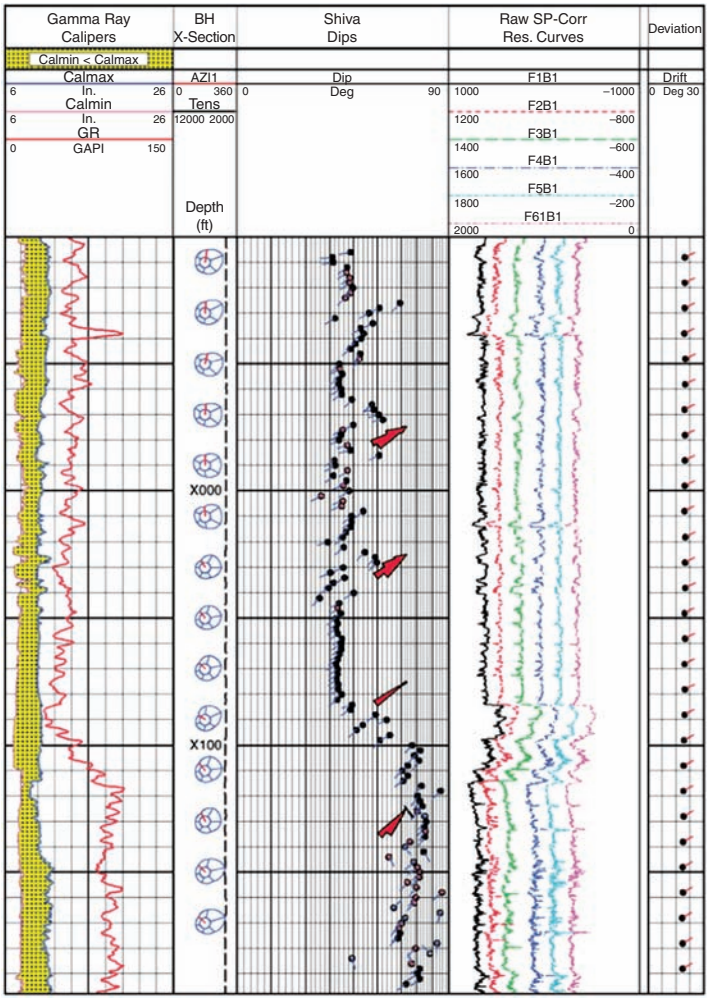


Fig. 20.4—5-in. to 100-ft six-arm dipmeter presentation (Halliburton 2007). Courtesy of Halliburton.

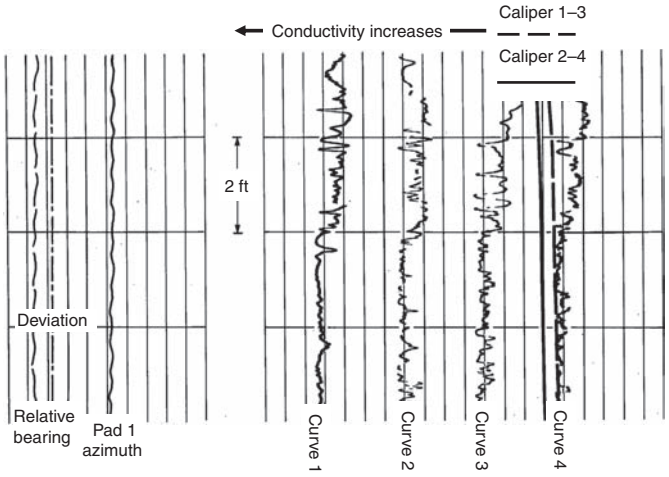


Fig. 20.5—60-in. to 100-ft four-arm dipmeter presentation.

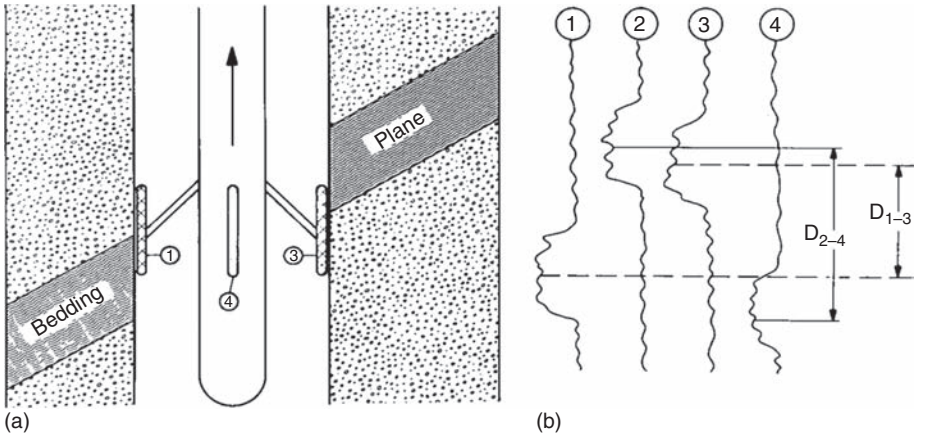


Fig. 20.6—(a) Cross section of four-arm dipmeter tool and the formation around it; (b) schematic of dipmeter log.

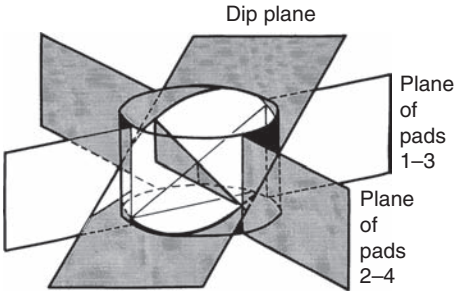


Fig. 20.7—Dipping plane crossing a borehole.

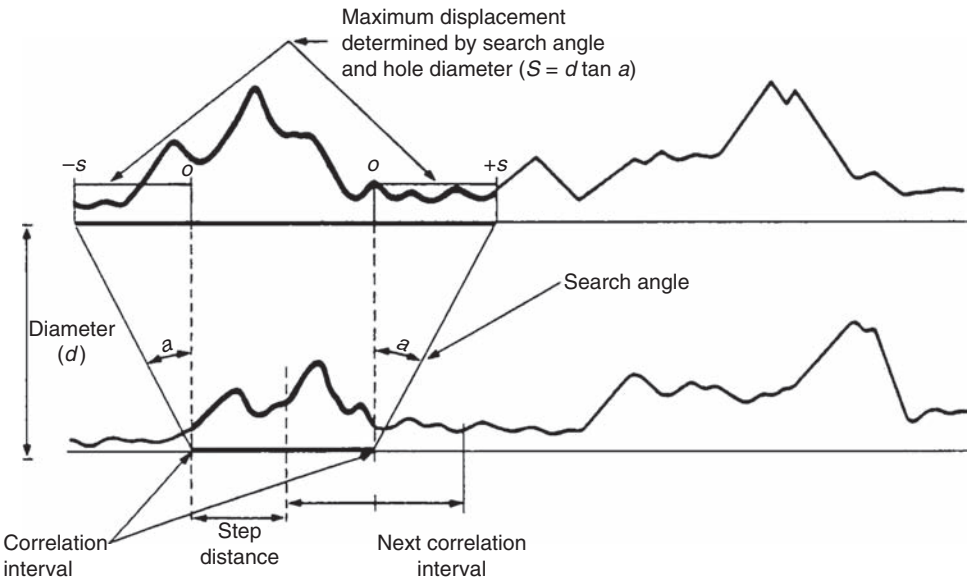


Fig. 20.8—Correlation interval, search angle, and step distance.

$12 \times \tan 60°$ downhole (a search over 41.57 in.). Therefore, doubling the dip angle means tripling the time required. Some programs are structured to perform an initial search in the 30 to 35° range and to search further only if a satisfactory correlation has not been found.

The step distance defines the depth increment to be used for the next round of correlations. It is usually set to half the correlation interval. Therefore, a dipmeter computation at 4 ft × 2 ft × 35° means that a correlation interval of 4 ft was used with a step distance of 2 ft and a search angle of 35°.

Because only three points are required to define a plane, a four-arm dipmeter survey defines an overdetermined system. Any three curves of the four can define a dipping plane. Three items may be selected among four in four ways by leaving out any one of the four pad traces. Potentially, therefore, four dip computations may be performed at the same depth. It has been found in practice that the four often do not agree. For the same reason that four-legged stools tend to wobble on an uneven floor, but three-legged stools do not, a number of dip values are possible simply because nature has not provided us with bedding planes that are perfectly flat at the scale of one borehole diameter. Add to this the effects of borehole rugosity, floating pads, and so on, and the result is a scatter diagram of possible dip angles. The choice of the correct dip then becomes an exercise in common sense, which has come to be known as *clustering.* Simply stated, if at any level in the well, the majority of the possible dip angles agree with each other and agree with the majority of the dips at adjacent levels in the well, then these are the most probable dip angles. The criteria for judging the worth of any type of dipmeter computation is of course its ability to reflect the known geologic facts.

20.6 Computed Log Presentations

There are a number of ways of presenting the computed results of a dipmeter survey. These include:

- Tadpole or arrow plots
- SODA* plots
- Listings
- Azimuth frequency plots
- Histograms
- Polar plots
- Stick plots
- Stratigraphic plots

A typical *tadpole plot is* shown in **Fig. 20.9.** The dip magnitude is read from the position at the base of the tadpole on the plot. The dip azimuth is read by observing the direction in which the tail of the tadpole points. The azimuth convention is to measure angles clockwise from north. Thus, a north dip points uphole, an east dip to the right, a south dip downhole, and a west dip to the left.

SODA plots separate dip and azimuth as distinct points on separate tracks of the results plot. A typical listing is shown in **Fig. 20.10.** In addition to the dip angle and dip azimuth, these listings may include further details such as dip quality and hole volume.

Azimuth frequency diagrams (or rose plots) present statistical information for a certain depth interval in the well, usually 100 or 500 ft. Within that interval, a polar plot is constructed by plotting the number of dips with a dip azimuth of a particular direction as a circular histogram **(Fig. 20.11).** These diagrams are most useful for making a quick scan of the geologic column for trends in dip direction with depth. Conventional histograms **(Fig. 20.12)** of both dip angle and dip azimuth can also be presented.

Polar plots can be constructed in two ways. One way, the rose plot, has just been described. The other way is to scale the plot with zero dip at the outside and 90° at the middle. In this way, the azimuth of the lowest dip becomes more apparent. This type of plot (see **Fig. 20.13**) is popular for identifying structural dip.

*Separation of dip and azimuth.

Why is the eccentricity of an ellipse important?
The eccentricity of an ellipse refers to how flat or round the shape of the ellipse is. The more flattened the ellipse is, the greater the value of its eccentricity. The more circular, the smaller the value or closer to zero is the eccentricity.

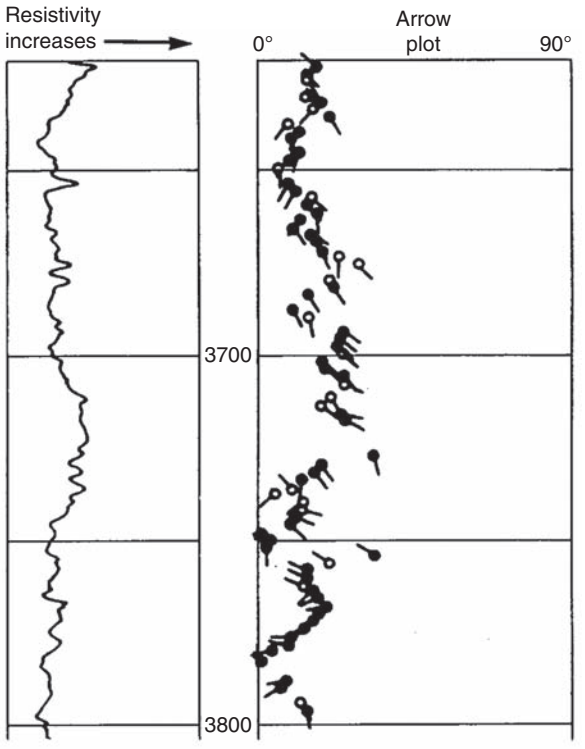


Fig. 20.9—Tadpole plot.

		Dip			Hole			Hole Diameter		Eccentricity		Integrated
Depth	Angle	Dir	Grade		Angle	Dir		1–3	2–4	Size	Dir	Voulme
14003.0	1.7	286	1	•	2.4	102	•	10.8	10.5	0.23	332	297.00
14005.0	2.3	282	1	•	2.4	101	•	10.7	10.4	0.24	325	296.64
14007.0	5.2	302	1	•	2.4	102	•	10.6	10.3	0.24	316	295.43
14009.0	5.5	315	1	•	2.4	102	•	10.5	10.3	0.19	309	294.24
14011.7	4.9	318	1	•	2.4	102	•	10.4	10.3	0.14	301	293.06
14013.7	5.1	296	1	•	2.4	103	•	10.3	10.2	0.14	295	291.90
14015.7	2.3	313	1	•	2.2	104	•	10.1	10.1	0.00	•••	290.75
14017.7	2.4	313	1	•	2.2	105	•	9.9	10.0	0.14	13	289.64
14019.7	3.7	273	1	•	2.2	105	•	9.9	9.9	0.00	•••	288.56
14021.7	3.0	270	1	•	2.2	105	•	9.8	9.8	0.00	•••	287.49
14023.7	2.7	296	1	•	2.2	107	•	9.7	9.8	0.14	355	286.44
14025.7	3.3	299	1	•	2.2	107	•	9.7	9.7	0.00	•••	285.40
14027.7	1.6	303	1	•	2.2	109	•	9.6	9.7	0.14	344	284.38
14029.7	2.1	291	1	•	2.2	110	•	9.5	9.7	0.20	339	283.37
14031.7	3.2	283	1	•	2.2	109	•	9.4	9.6	0.20	331	282.36
14033.7	2.8	291	1	•	2.2	110	•	9.4	9.5	0.14	325	281.30
14035.7	1.9	330	1	•	2.2	110	•	9.4	9.4	0.00	•••	280.40
14037.7	2.0	328	1	•	2.2	110	•	9.4	9.5	0.14	312	279.44
14039.7	1.5	251	2	•	2.2	111	•	9.5	9.6	0.14	308	278.47
14041.7	3.0	275	1	•	2.2	111	•	9.5	9.6	0.14	304	277.47
14043.7	3.1	253	1	•	2.2	113	•	9.5	9.6	0.14	301	276.40
14045.7	2.4	247	1	•	2.2	114	•	9.4	9.5	0.14	298	275.48
14047.7	1.6	89	2	•	2.2	115	•	9.4	9.5	0.14	295	274.51
14049.7	2.8	28	1	•	2.2	115	•	9.5	9.5	0.00	•••	273.54
14051.7	2.9	24	1	•	2.2	114	•	9.6	9.6	0.00	•••	272.55
14053.7	0.8	221	1	•	2.2	114	•	9.6	9.7	0.14	285	271.55
14055.7	1.9	243	1	•	2.2	115	•	9.7	9.7	0.00	•••	270.53
14057.7	2.0	278	3	•	2.2	116	•	9.7	9.7	0.00	•••	269.51
14059.7	3.2	231	1	•	2.2	116	•	9.7	9.7	0.00	•••	268.48
14061.7	1.3	267	1	•	2.2	115	•	9.7	9.7	0.00	•••	267.45
14063.7	1.9	27	1	•	2.2	115	•	9.7	9.7	0.00	•••	266.43
14065.7	2.6	14	1	•	2.2	115	•	9.7	9.7	0.00	•••	265.41
14067.7	9.7	240	1	•	2.2	115	•	9.7	9.7	0.00	•••	264.38

Fig. 20.10—Dipmeter listing.

Stick plots **(Fig. 20.14)** show a series of short lines inclined to the horizontal. Each line represents the dip angle as projected onto some line of a cross section. It is normal to distort the horizontal and vertical scales on these plots to fit the geologist's mapping requirements. Stick plots are normally used in multiwell projects to generate cross sections. They are particularly helpful

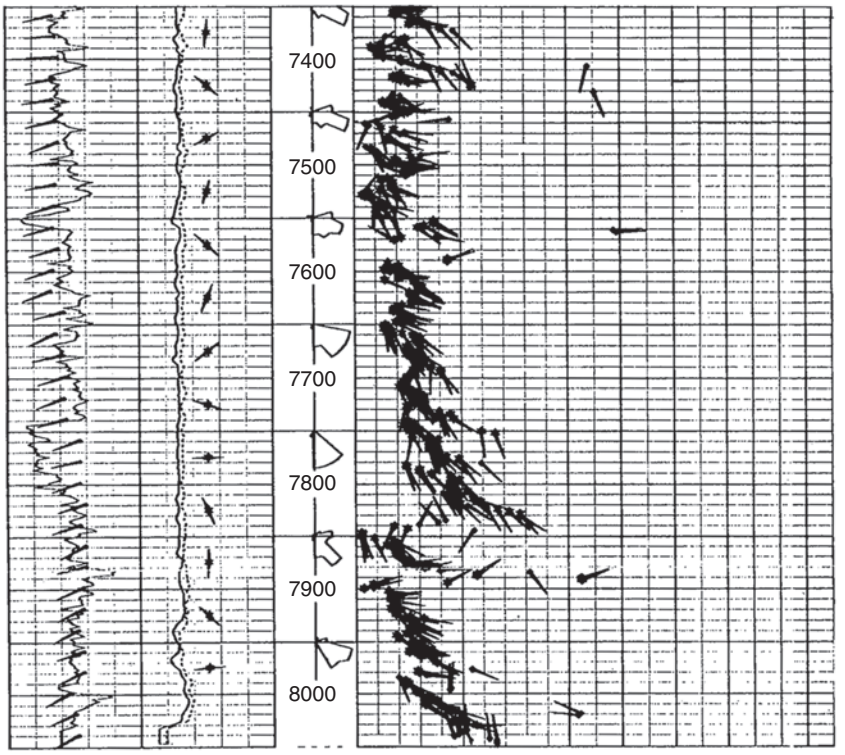


Fig. 20.11—Azimuth frequency diagram (shown in depth track).

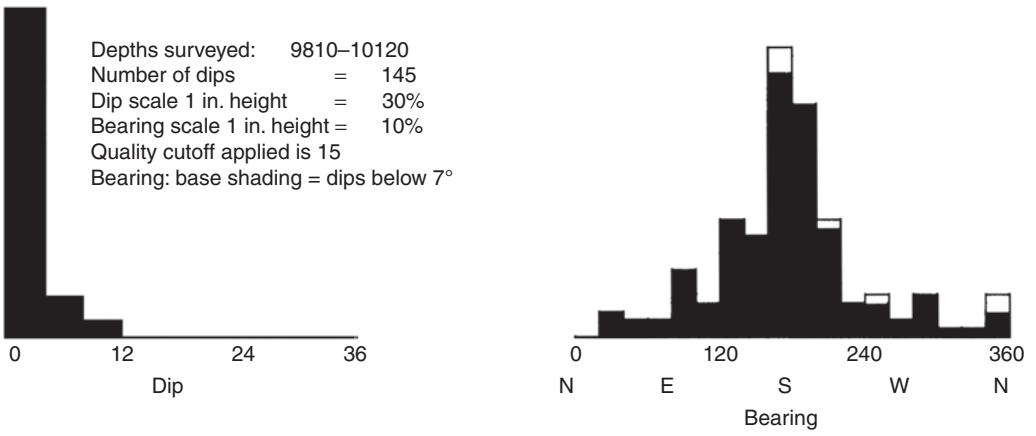


Fig. 20.12—Histogram of dip angle and dip azimuth.

where the interwell correlation is not immediately obvious from conventional logs alone. Note that, on a stick plot, a flat dip is flat whatever the azimuth of the section, but a highly dipping bed will appear (a) as an inclined line in the section viewed 90° from the dip azimuth, but (b) flat if viewed in the direction of the dip azimuth.

Stratigraphic plots **(Fig. 20.15)** attempt to provide a visual representation of bed stratigraphy. Each dip can be represented by the trace of its bedding plane on the borehole wall. If the trace could be "unwrapped" and laid on a flat surface, a sine wave would be visible, with its amplitude reflecting the dip magnitude and its low point indicating the dip azimuth.

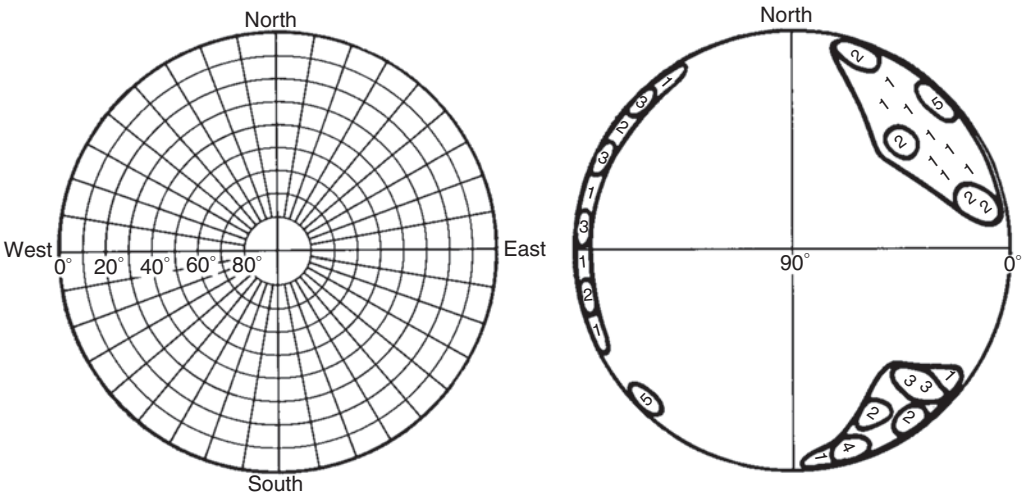


Fig. 20.13—Polar plot.

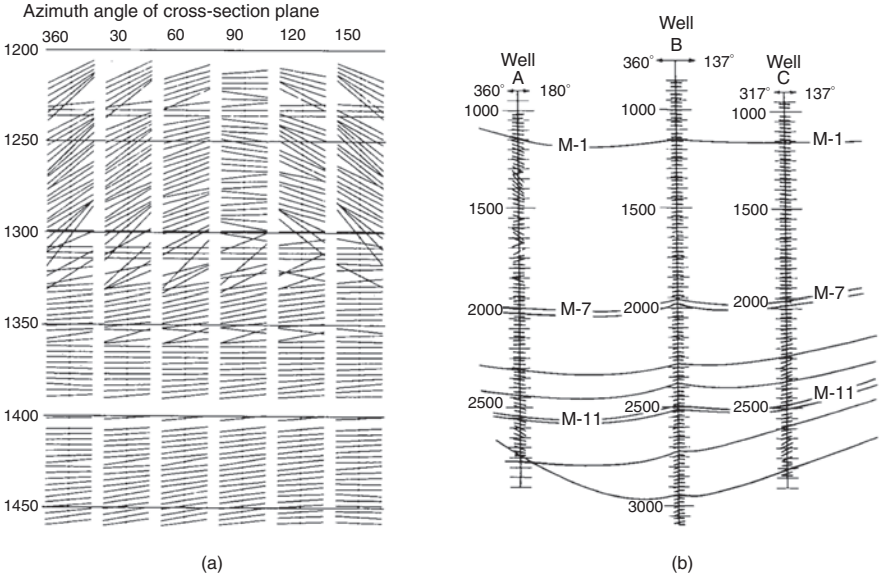


Fig. 20.14—Stick plots in (a) a single well (six different sections) and (b) three wells (helpful for interwell correlation).

20.7 Interpretation

Dipmeter plots can be interpreted by observing the variation of dip and dip azimuth in conjunction with openhole logs. To aid in this type of analysis, it is helpful to highlight certain types of patterns. Conventionally, a group of dips of more or less constant azimuth, but showing an increase in dip magnitude with depth, is colored red. A group of dips of more or less constant azimuth, but showing a decrease in dip magnitude with depth, is colored blue. A group of dips of constant low dip magnitude and more or less constant azimuth is colored green. **Fig. 20.16** illustrates these patterns.

Broadly speaking, dip interpretation may be split into two parts, structural and sedimentary. Gross structural characteristics, such as unconformities, folds, anticlines, and synclines, produce

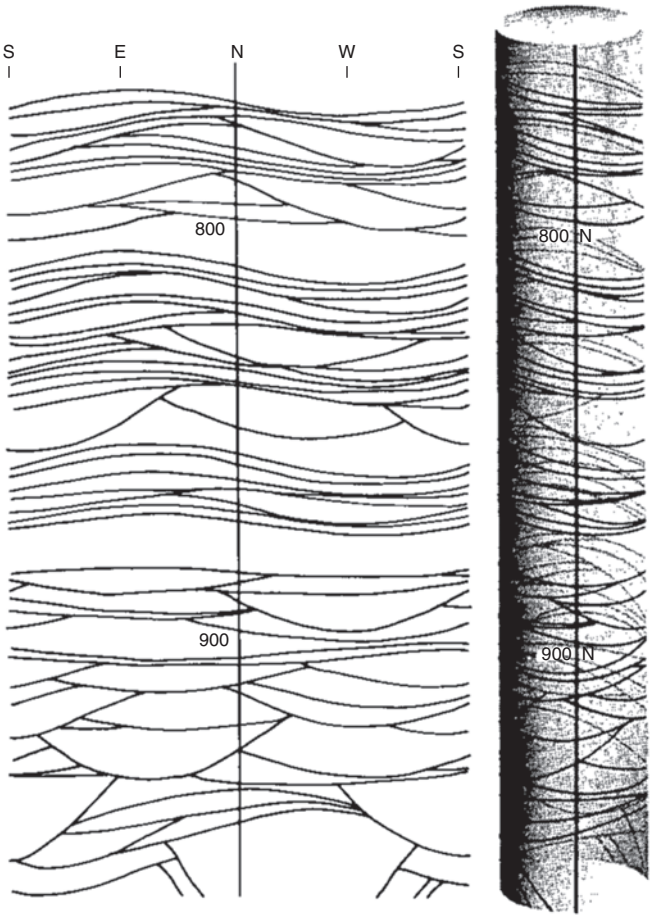


Fig. 20.15—Stratigraphic plot.

patterns that vary gradually over hundreds of feet. Sedimentary characteristics such as cross bedding appear only within sedimentary beds and are localized to a few feet to tens of feet. Some of these patterns and their associated geologic features are described below.

20.7.1 Folded Structure. Fig. 20.17 shows a folded structure. Note that in the shallow part of the well, dips are moderate and to the north. In the deeper section, the well has crossed the axial plane of the fold, and dips are more pronounced and to the south. Where the well crosses the axial plane, dips are flat; it is here that a hydrocarbon trap exists. From the dips on the flanks, it is possible to compute both the tilt of the axial plane and the plunge of the fold.

20.7.2 Unconformity. Fig. 20.18 illustrates an unconformity. A series of sediments in the deeper part of the well were originally deposited flat. Later, these sediments were tilted and then eroded, and a new set of beds was deposited. At the interface between the old and new sediments, an abrupt change of dip takes place.

20.7.3 Faults. Faults may be identified from dip patterns by observing the drag patterns, if present, on either side of a fault. A normal fault with drag is illustrated in **Fig. 20.19.** Above the intersection of the wellbore with the fault, a red pattern will develop (dip increasing with depth). Below the intersection of the wellbore with the fault, a blue pattern will develop (decreasing dip with depth). At the intersection of the wellbore with the fault plane, the dip of the fault plane itself

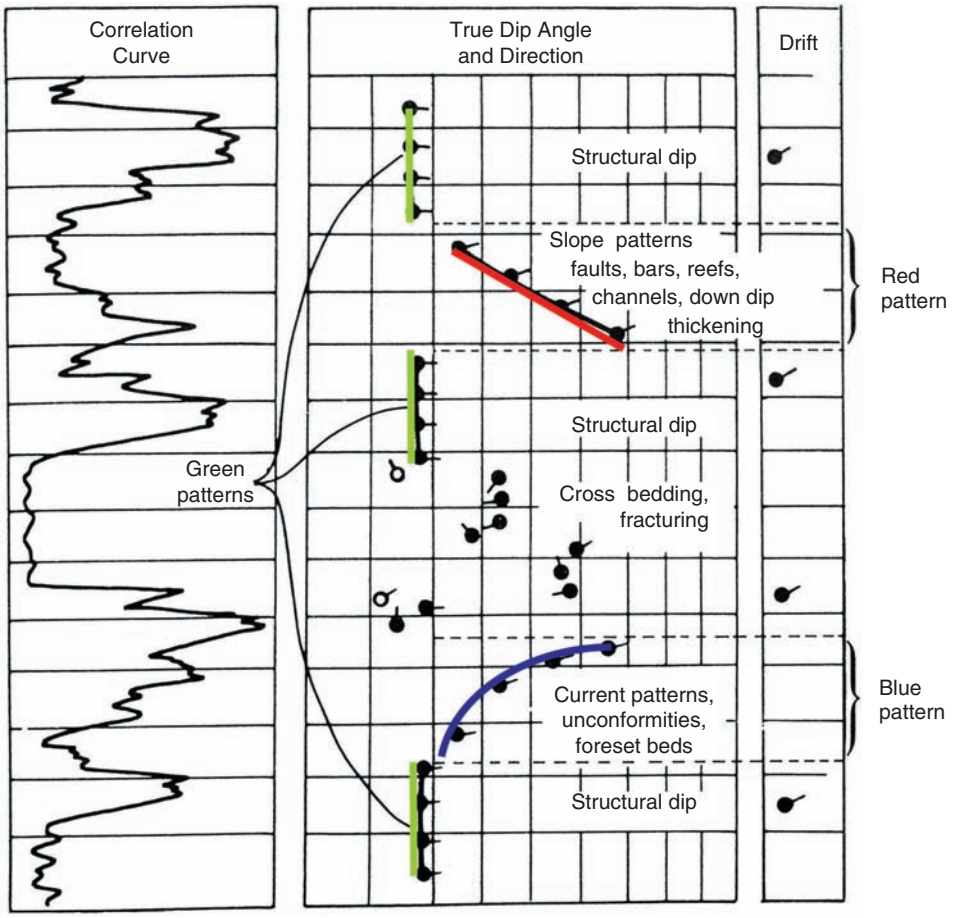


Fig. 20.16—Common dip patterns and color code.

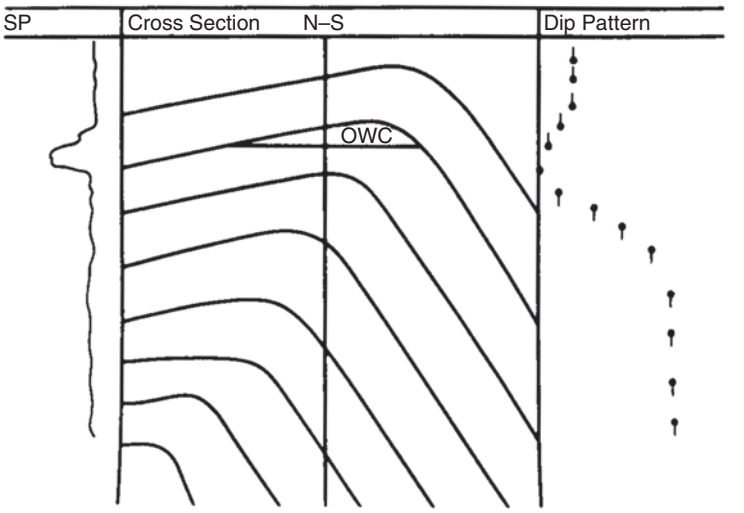


Fig. 20.17—Folded structure.

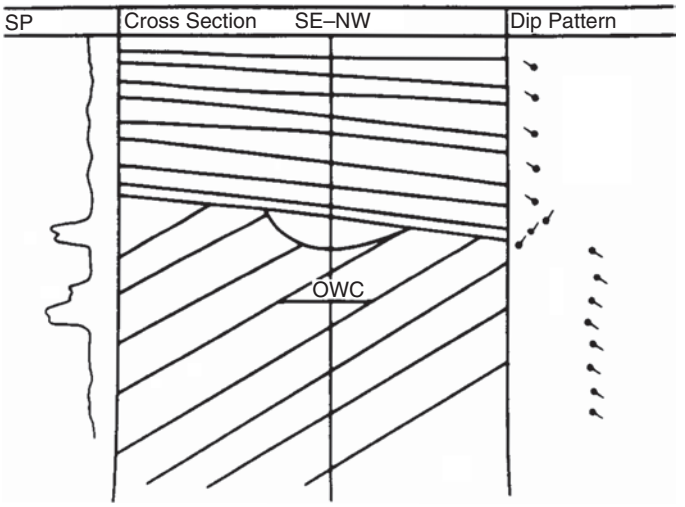


Fig. 20.18—Unconformity.

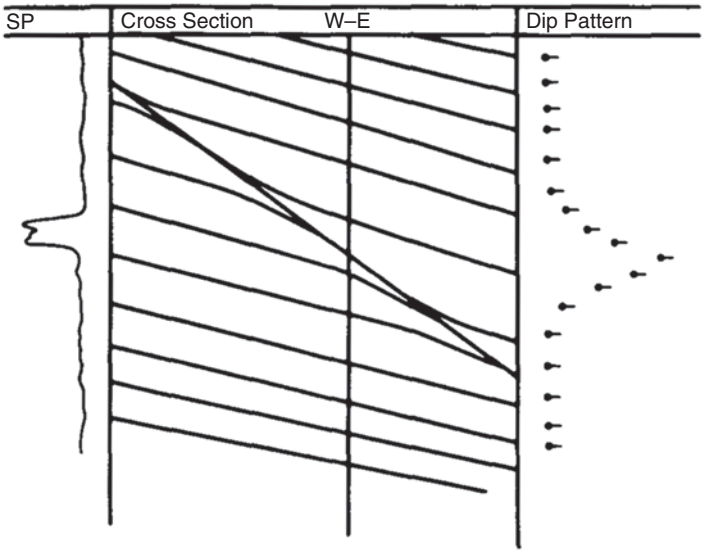


Fig. 20.19—Normal fault with drag.

may occasionally be seen. Note that the fault dips down in the direction of the azimuth of the drag pattern; it strikes perpendicular to that direction.

20.7.4 Current Bedding. Among the sedimentary details that may be inferred from a dipmeter plot is the direction of transportation of sediments by streams. **Fig. 20.20** shows the sort of pattern to be expected in such a case. Here, blue patterns develop, with the dip azimuth in the patterns pointing downstream.

Depending on where the well is drilled, it may be of interest to move upstream toward the source or downstream to finer sediments or broader deposits.

20.7.5 Channel Cut and Fill. A common type of deposit results when a channel is cut and then refilled with reservoir sand. A red pattern will develop together with a characteristic SP shape, broadening to

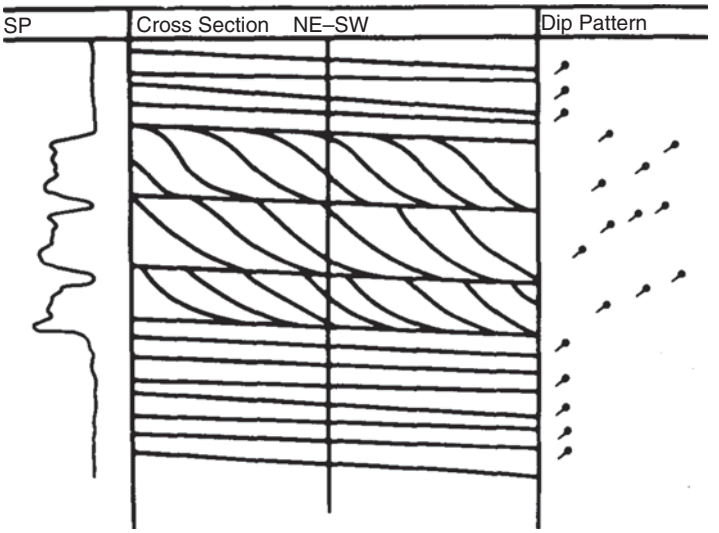


Fig. 20.20—Current bedding.

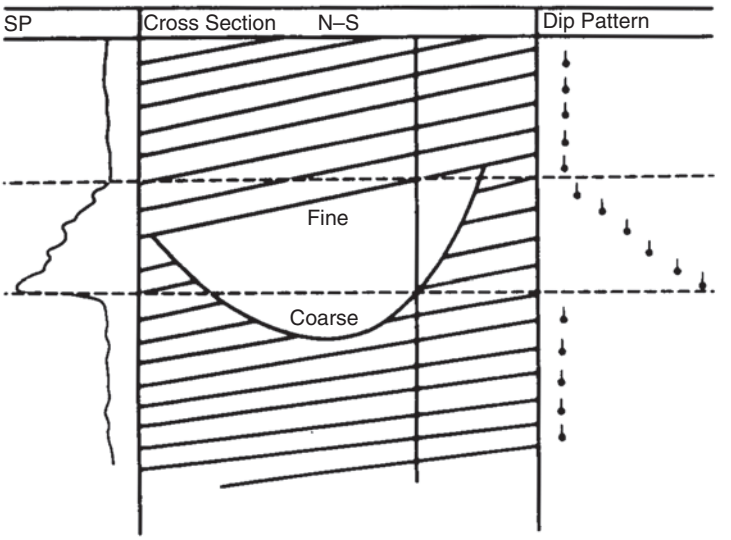


Fig. 20.21—Channel cut and fill.

the base. When drilling such deposits, it is useful to know in which direction the channel extends and in which direction it thickens. Referring to **Fig. 20.21,** note that the well was drilled off the axis of the channel. Had it been drilled to the north, a thicker section of sand would have been found.

To move to the center of a channel, offset the well in the direction indicated by the red-pattern tadpoles. To follow the channel, move at right angles to the red-pattern dip azimuth, in this case, either east or west.

20.7.6 Buried Bar With Shale Drape. Another common feature is a buried bar over which subsequent shale deposits have been draped. Here (see **Fig. 20.22**), dips within the sand body decrease with depth (blue), but above the sand body, dips in the shale increase with depth (red). The SP will usually show a characteristic pattern, broad at the top. To follow the bar, wells should

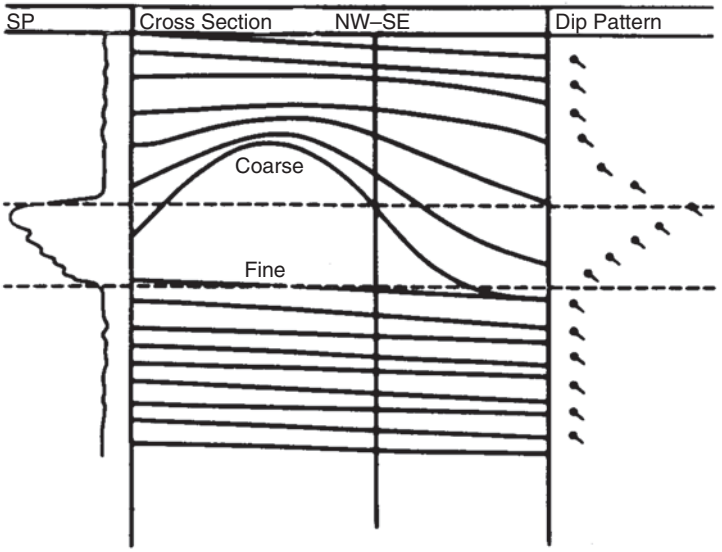


Fig. 20.22—Buried bar with shale drape.

be offset at right angles to the dip azimuth seen within the bar. To drill a thicker section, a well should be offset in the opposite direction to the dip seen in the bar.

20.8 Fracture Finding

Another application of the dipmeter survey is the detection of fractures. There are many methods available for fracture detection, but none, on its own, is a completely reliable diagnostic test. The dipmeter should be viewed as one of many methods for fracture finding and should be used to complement other methods.

The theory is very simple. An open fracture will be invaded by mud filtrate and will therefore offer a less resistive path to electric current than the surrounding formation. If one of the dipmeter pads happens to lie in front of a fracture, it will record a low resistivity value. Another pad at the same depth may not be in front of a fracture and will record a higher resistivity. Comparison of adjacent pad traces should reveal the presence of a fracture when the two resistivity values are different. Various ways are available to display these curves to highlight such differences. **Fig. 20.23** shows one such presentation. Note that because the orientation of the dipmeter tool is known, the orientation of the fracture can also be deduced.

20.9 Dipmeter Log-Quality Control

Good dip information requires good raw data. To ensure good raw data, the following guidelines are suggested.

1. Recondition the hole before running the dipmeter.
2. Use a swivel-head adapter to reduce tool rotation while logging.
3. Log at 1,800 to 2,400 ft/hr to reduce tool jerking. Slow down even more if the tension on the line is erratic.
4. Reject sections of log where the tool rotates once in less than 60 ft of hole.
5. Make repeat sections or overlaps of 100 to 200 ft every time logging is interrupted for any operational reason whatsoever.
6. Inspect the raw log for dead correlation curves, insensitive curves, stuck calipers, and so on. As a last resort, three good correlation curves are sufficient, but four are much better.

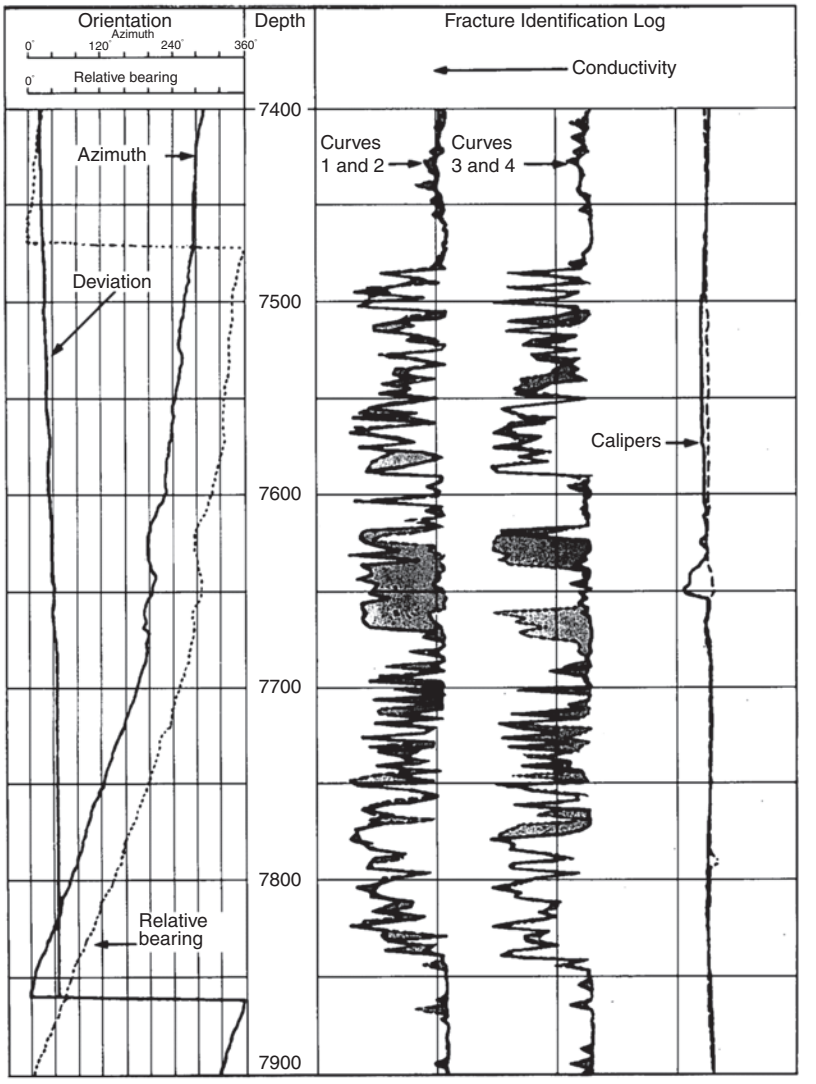


Fig. 20.23—Fracture presentation of dipmeter data.

7. Carefully inspect the orientation curves for nonsense readings such as a hole deviation less than zero.
8. On a computed log, check the dip against field controls for consistency. Many dipmeter surveys have been off by 90 or 180° because of incorrect pad wiring or an erroneous computation.

Fig. 20.24 shows a field printout of a dipmeter survey. From the orientation curves, it is evident that the tool was rotating too frequently. Such a log should be rerun.

20.10 Borehole Imaging

Although dipmeters and the information they gather provide valuable insights into the structural and sedimentary features of the reservoir, they lack the fine detail that a full borehole image can provide. In general, processed raw dipmeter data give a good and useful indication of bed dip and azimuth; they may also indicate the presence of fractures, but in the absence of special processing

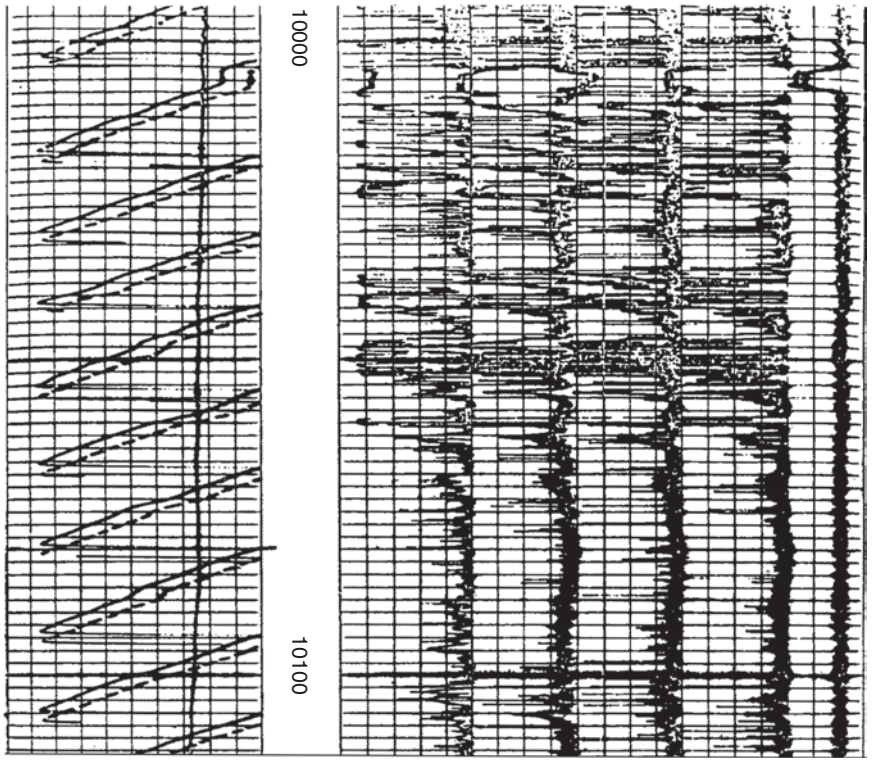


Fig. 20.24—Dipmeter field printout showing excessive tool rotation.

software,* they cannot tell the analyst very much about high-angle fracture-plane azimuths. Dipmeters are equally silent on the matter of rock texture.

Borehole imaging tools, by contrast, are able to provide the analyst with the very detailed images that are lacking from standard dipmeter logs. In addition to confirmation of bed dip angle and azimuth, borehole imaging devices provide textural information, thus pinpointing vugs, fractures, and other fine sedimentary details unobtainable from dipmeters alone.

These devices rely on their ability to "scan" most or all of the internal periphery of the borehole, either by using a single sensor that physically rotates through 360° as the device is drawn up the borehole on wireline, or if mounted on an LWD drill collar, as the drilling progresses downhole. Other wireline tools rely not on a physical rotation so much as on a multitude of sensors that cover a high percentage of the full circumference of the borehole itself.

Wireline imaging devices rely on two measurement principles: fine variations in formation resistivity and variations in the travel time and strength of an ultrasonic pulse sent out from a rotating transducer and reflected back from the formation wall (the sonar principle).

Drillpipe-conveyed LWD imaging devices take advantage of the fact that during the drilling process, the drillstring is rotating, and therefore a single directional sensor can record variations in formation properties as it moves through each full 360° rotation. Depending on the sensor used, the image may be semicontinuous or segmented, providing finer or courser images respectively. The sensors used include focused (azimuthal) resistivity, formation density, and gamma ray.

20.10.1 Wireline Imaging Tools. ***Electrical Imaging.*** **Fig. 20.25a** shows a typical wireline formation microimaging tool equipped with multiple resistivity electrode buttons mounted on articulated pads attached to arms that are closed when the tool is descending to the bottom of the well

*For example, Bateman (1980).

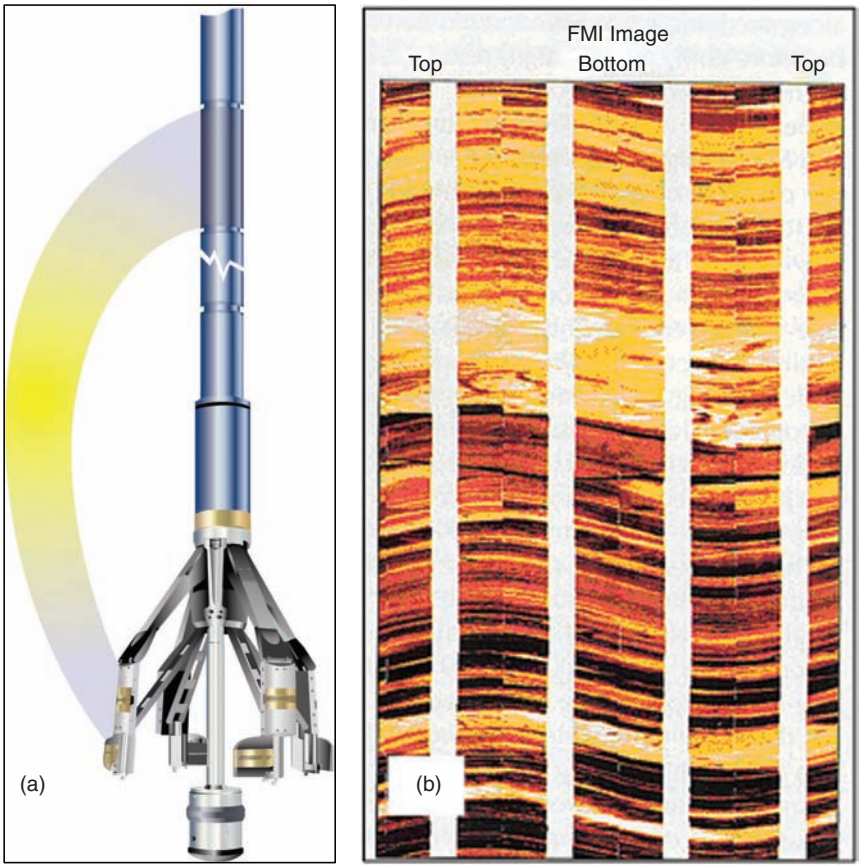


Fig. 20.25—Wireline formation microimaging. Courtesy of Schlumberger.

but opened to make intimate contact with the borehole wall for the logging run made coming up the hole. Fig. 20.25b shows the image produced by such a tool, in which differences in resistivity are translated into color variations between localized portions of the borehole wall.

Note that there are four vertical white bands on the image corresponding to the part of the borehole wall not covered by the electrode-carrying pads. Depending on the tool used, the number of individual electrodes may be as few as five or as many as 16 dozen.

Acoustic Imaging. **Fig. 20.26** shows an acoustic imaging tool with a rotating transducer. In general, the acoustic imaging tools have lower resolution than their electrical cousins but provide full 360° coverage and can be run in both water- and oil-based muds. **Fig. 20.27** shows a plan view of an acoustical scanning tool and illustrates that both the strength and the travel time of the reflected signal are routinely recorded.

The degree of detail obtained with these devices depends on the speed of rotation of the transducer in rps, the number of samples taken in each 360° rotation, and the logging speed. If n is the number of samples taken per 360° revolution and λ is the number of revolutions per second, then the sampling rate per second is given by $n\lambda$. Tools are available with between 100 and 500 samples per revolution (on average approximately 200) and between 4 and 12 rev/sec (on average 8), which yield possible sample rates of between 500 and 5,000 (on average 1,600) samples per second. By use of the actual logging speed, these sample rates over time can be translated into sampling rates per foot. For example at a logging speed of one foot per second (3,600 ft/hr), one might expect 1,600 samples per foot. The area of the borehole wall of one vertical foot of an 8½-in. hole is approximately 320 in.^{2}, giving a resolution of 0.2 in.^{2}. Put another way, the tool

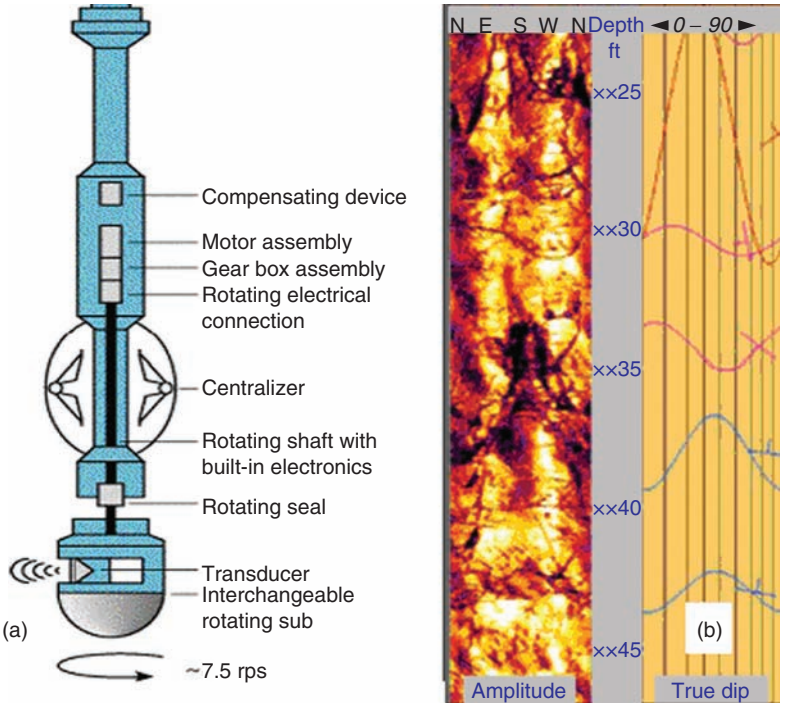


Fig. 20.26—(a) Acoustic imaging tool (courtesy of Schlumberger); (b) acoustic image log (showing high-angle fractures; courtesy of Halliburton).

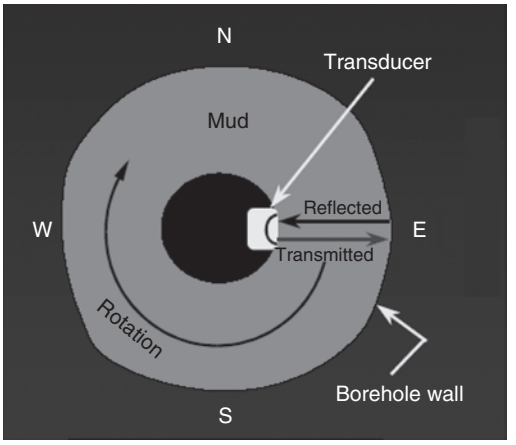


Fig. 20.27—Plan view of acoustic imaging tool. Courtesy of Halliburton.

produces images made up of "acoustic pixels" 0.45 in. (1.1 cm) on a side. Logging at a slower speed of 1,800 ft/hr would double the precision to 0.1 in.[2] and provide pixels 0.32 in. (0.8 cm) on a side.

Tele-Imaging. Direct visual images of the borehole can be obtained where borehole conditions allow it by use of a TV camera mounted to look either vertically downwards or radially outwards. Both types of tele-imaging require that the hole be air-drilled or filled with a clear completion fluid. **Fig. 20.28** shows a view of the inside of a borehole as seen by a camera mounted to view radially.

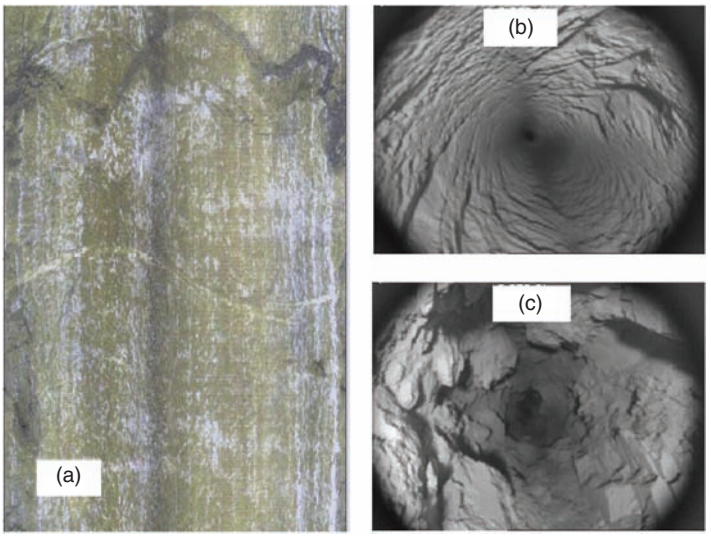


Fig. 20.28—Visual borehole images: (a) looking radially, (b) looking down a smooth borehole, and (c) looking down a rugose section.

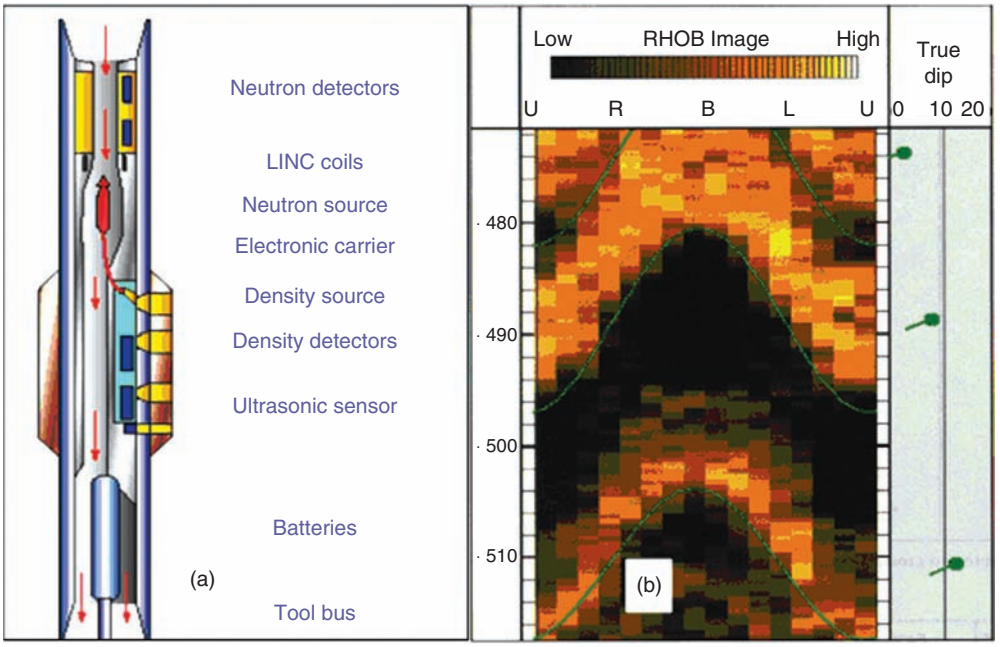


Fig. 20.29—(a) Azimuth neutron-density LWD tool; (b) corresponding ρ_B image. Courtesy of Schlumberger.

20.10.2 Drillpipe-Conveyed Imaging Devices. Measurements on drillpipe are covered in detail in Chapter 3, where the mechanics of LWD and the parameters that can be measured are discussed. Here only a subset of these will be addressed, namely borehole imaging systems. Drillpipe-conveyed imaging devices use a single directional sensor to produce a scanned image as the drillpipe is rotated during the drilling process and the bit (and the sensor) advance along the drilled borehole. Commonly used LWD tools of this type rely on azimuthal resistivity, density, and gamma ray measurements.

Density Imaging. **Fig. 20.29** shows a drillpipe-conveyed neutron-density LWD sub and a corresponding borehole image that maps formation density variations in false color. Note that although

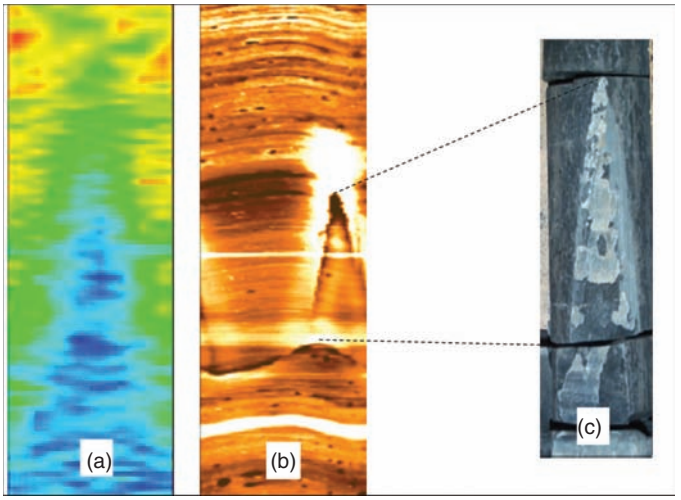


Fig. 20.30—LWD images: (a) gamma ray, (b) electrical, and (c) core photo. Courtesy of Baker Hughes.

the image is segmented into 16 azimuthal slices, the apparent bed dip angle and azimuth (relative to the wellbore itself) are clearly evident and quantifiable.

Resistivity Imaging. **Fig. 20.30** shows an LWD resistivity image over a section of a well from which a full-diameter core has been cut. For comparison purposes, the core photo is shown to the right of the electrical image, and a gamma ray image is shown to the left.

Note that the resolution of the resistivity image is superior to that of the gamma ray image. Indeed, in general, it can be said that electrical and acoustic images are of higher quality than those generated by the active or passive radioactive measurements of formation density by use of natural gamma rays.

References

Fitzgerald, D.D. 1980. Obtaining Valid Dipmeter Surveys in Deviated Wells. *World Oil* (November).

Halliburton. 2007. Wireline and Perforating Services: Six Arm Dipmeter (SED™), http://www.halliburton.com/public/lp/contents/Data_Sheets/web/H/H00826.pdf (accessed 15 February 2012).

Schlumberger. 1981. *Dipmeter Interpretation: Volume 1—Fundamentals*.

Schlumberger. 1983. *Dipmeter Interpretation: Volume 1—Fundamentals*.

General References

Bateman, R.M. 1981. Four-Arm Dipmeter Computation and Stereographic Dip Manipulation. In *Manual of Geophysical Hand-Calculator Programs*. Tulsa: Society of Exploration Geophysicists.

Bateman, R.M. 1986. Determination of High-Angle Fracture Plain Orientation From SHDT Dipmeter Recording Using a Microcomputer. *Canadian Well Logging Society* **15** (1): 85–100.

Gilreath, J.A. and Stephens, R.W. 1975. Interpretation of Log Response in a Deltaic Environment. Paper presented at the American Association of Petroleum Geologists, Marine Geology Workshop, Dallas, April.

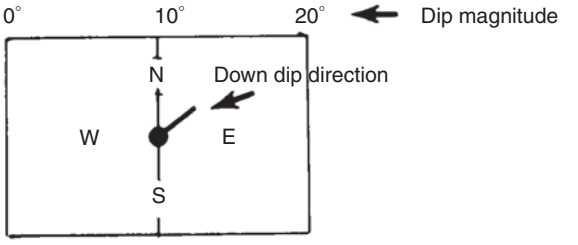
Prammer, M.G., Morys, M., Knizhnik, S., et al. 2007. Field Testing of an Advanced LWD Imaging/Resistivity Tool. *Trans.*, SPWLA 48th Annual Logging Symposium, Austin, Texas, 3–6 June.

Ritter, R.N., Chemali, R., Lofts, J., et al. 2005. High Resolution Visualization of Near Wellbore Geology Using While-Drilling Electrical Images. *Petrophysics* **46** (2): 85–95.

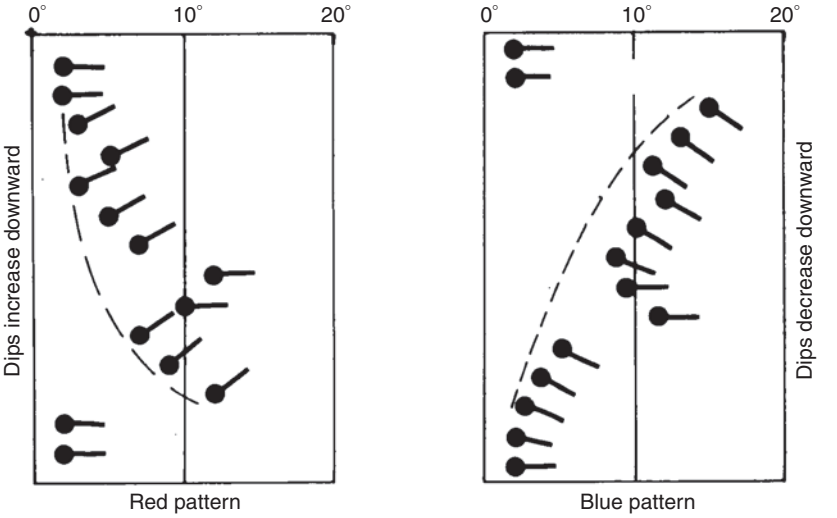
Appendix 20A: Dipmeter Interpretation Rules

METHOD OF PLOTTING

Appendix 20 has been reproduced with kind permission of J.A. Gilreath, Schlumberger Offshore Services, New Orleans.

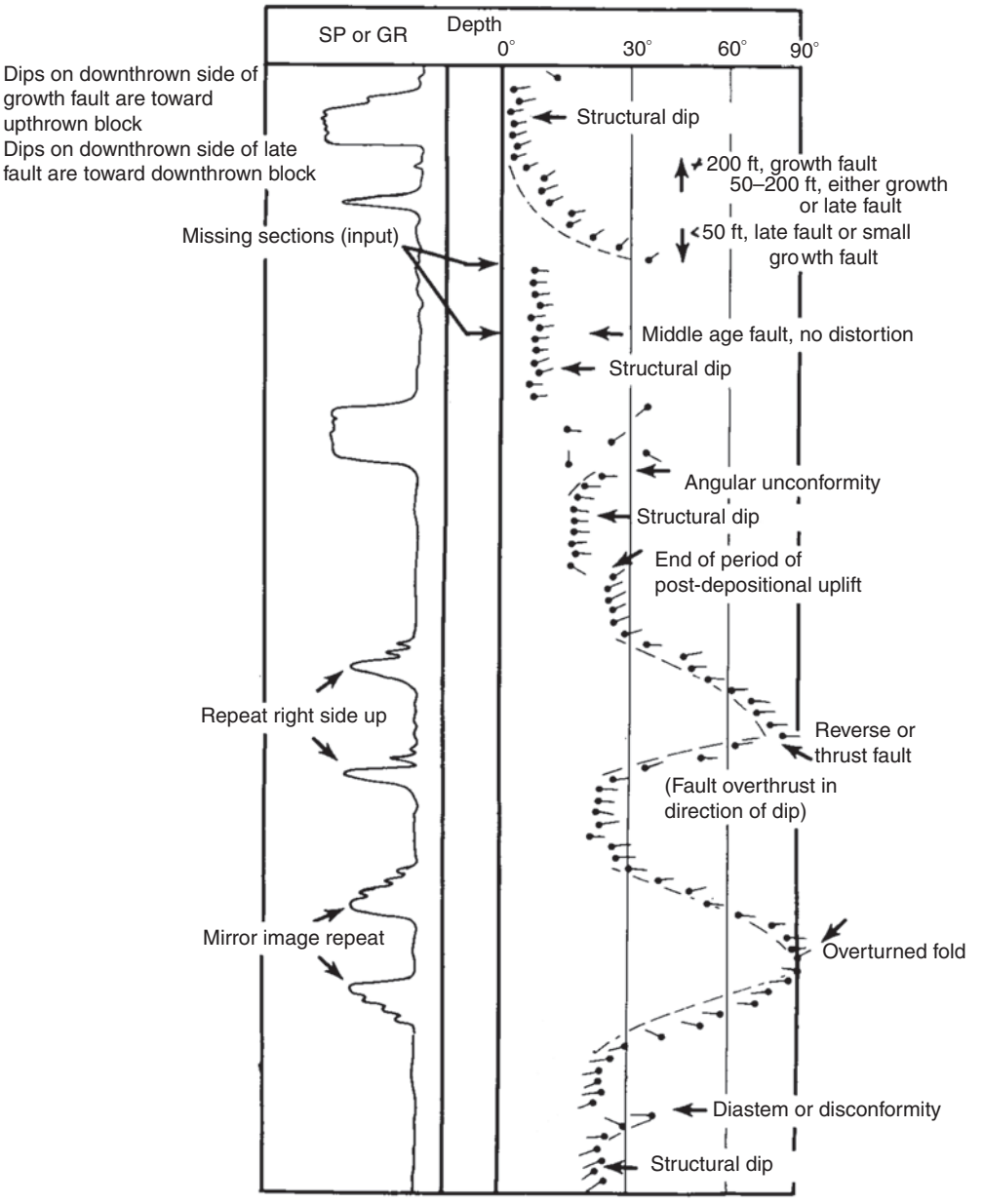


Example 10°N 45°E

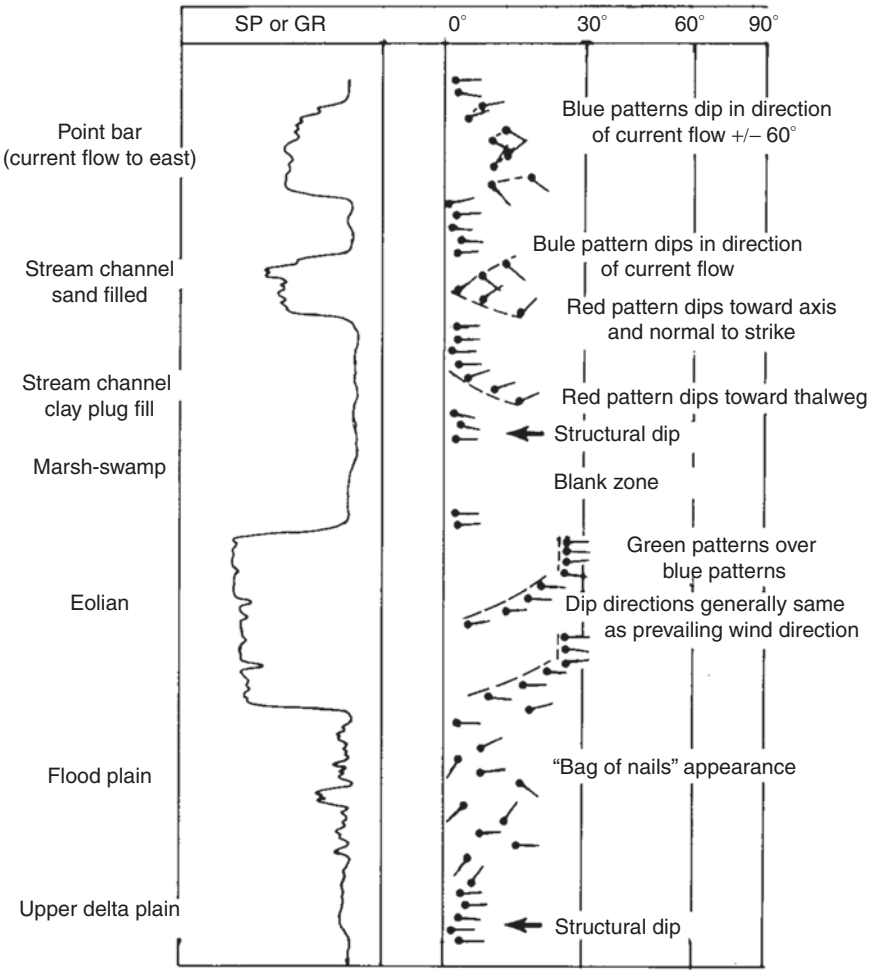


These patterns, along with other information, are used for both fault and stratigraphic interpretations.

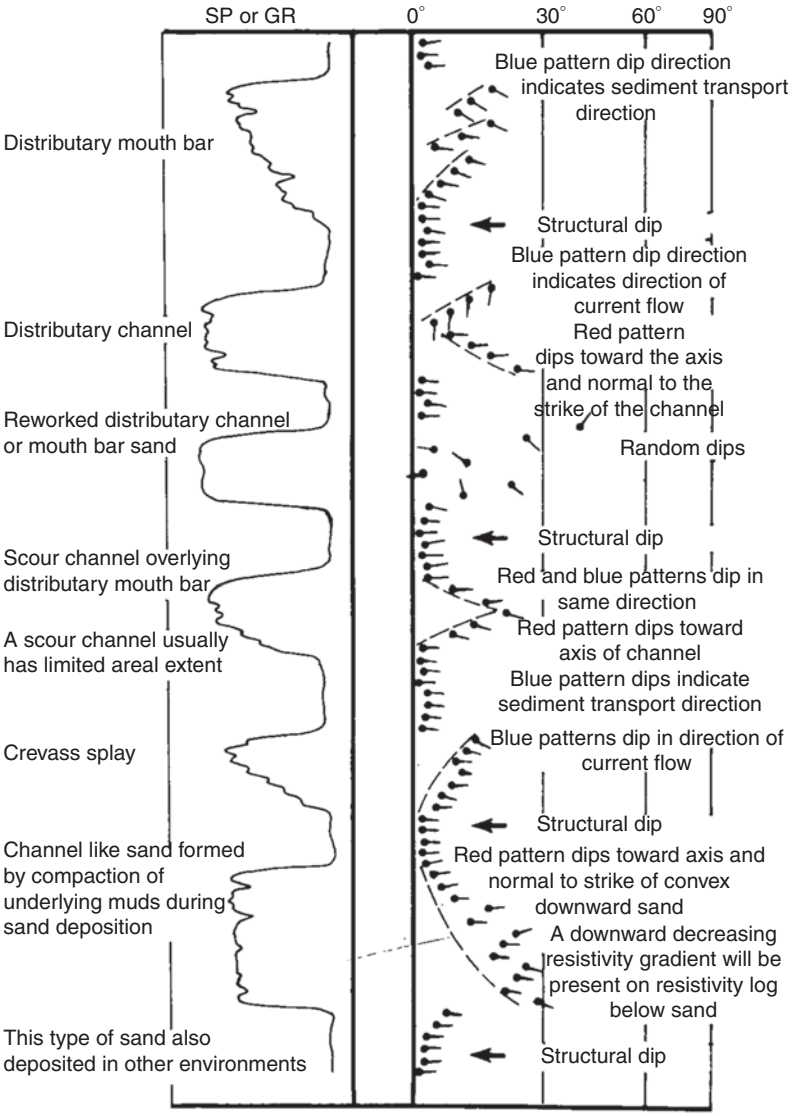
MISSING and REPEAT SECTIONS



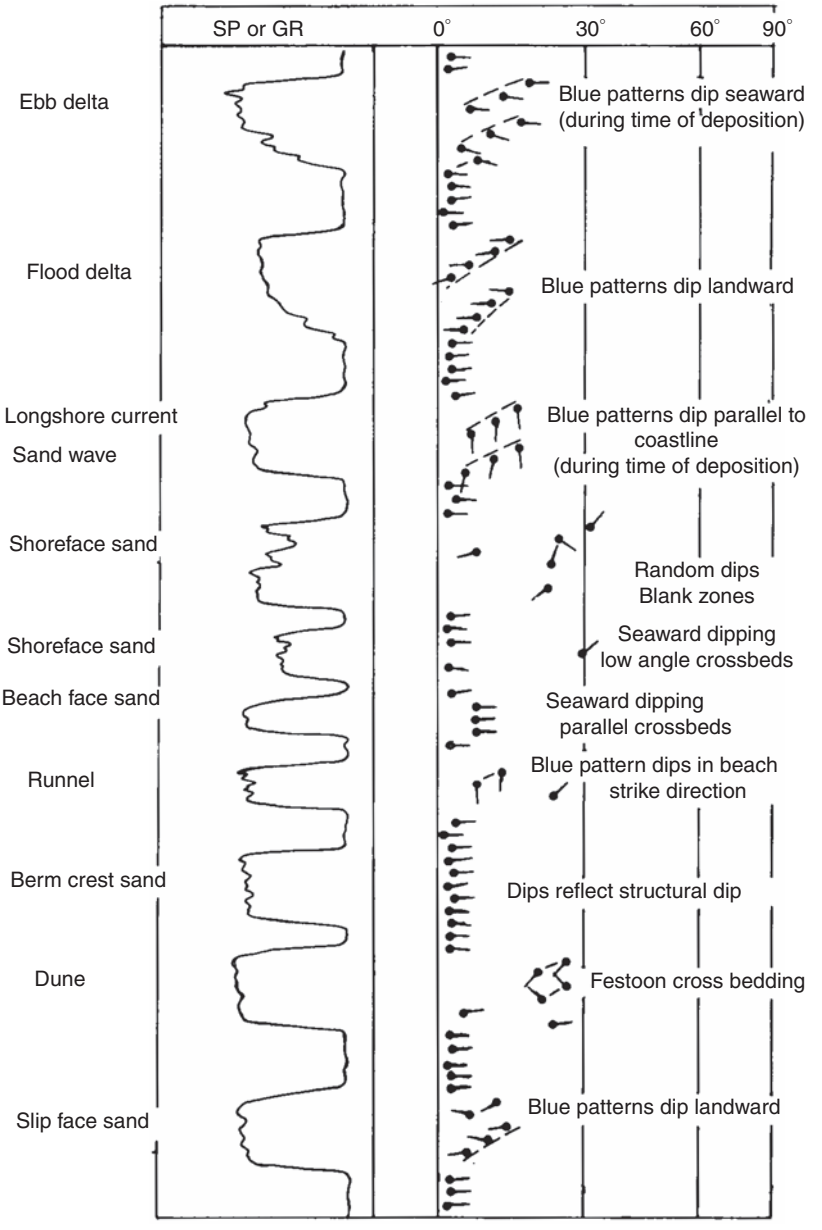
STRATIGRAPHIC INTERPRETATION CONTINENTAL ENVIRONMENT



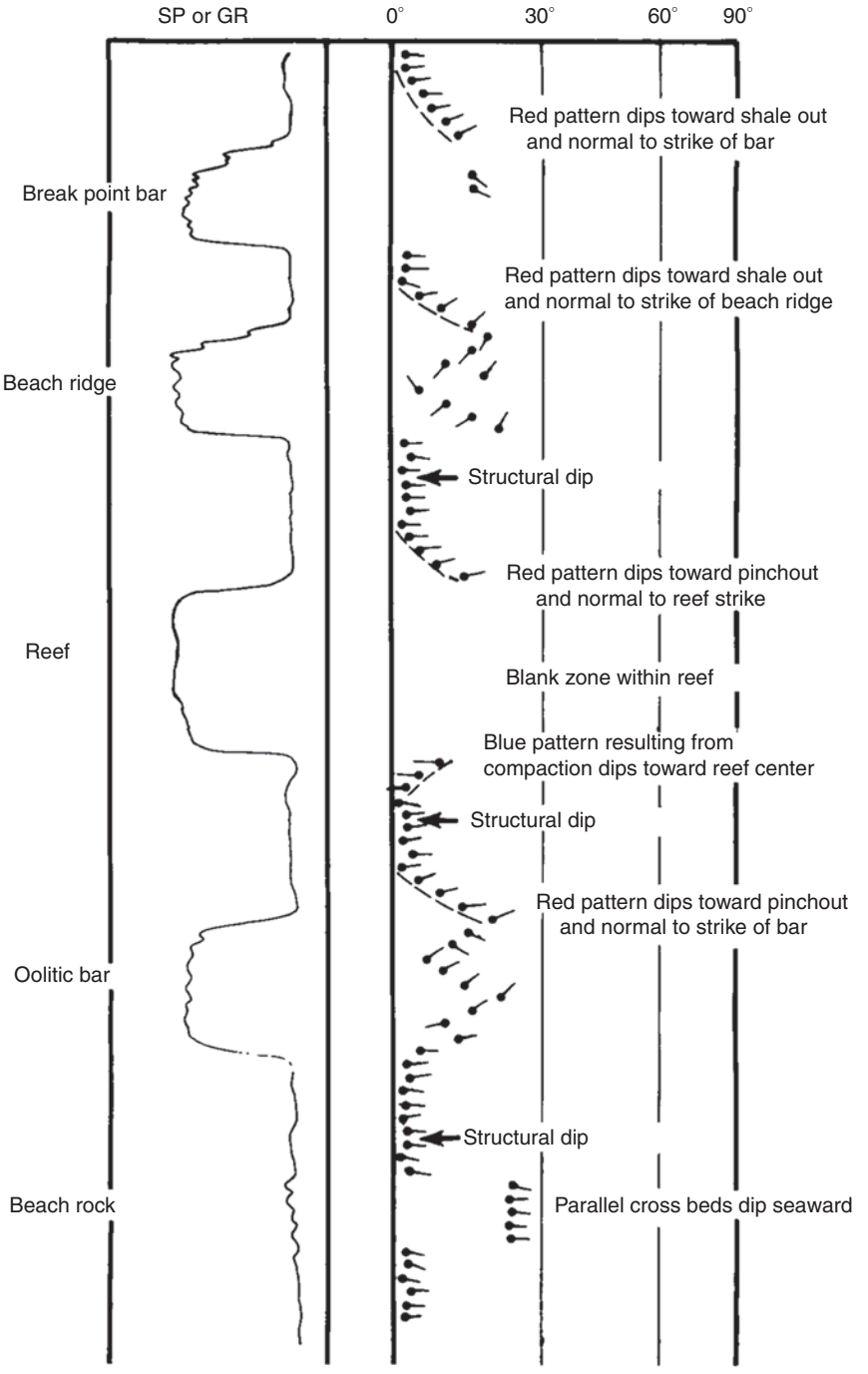
STRATIGRAPHIC INTERPRETATION
CONTINENTAL SHELF
DELTA DOMINATED



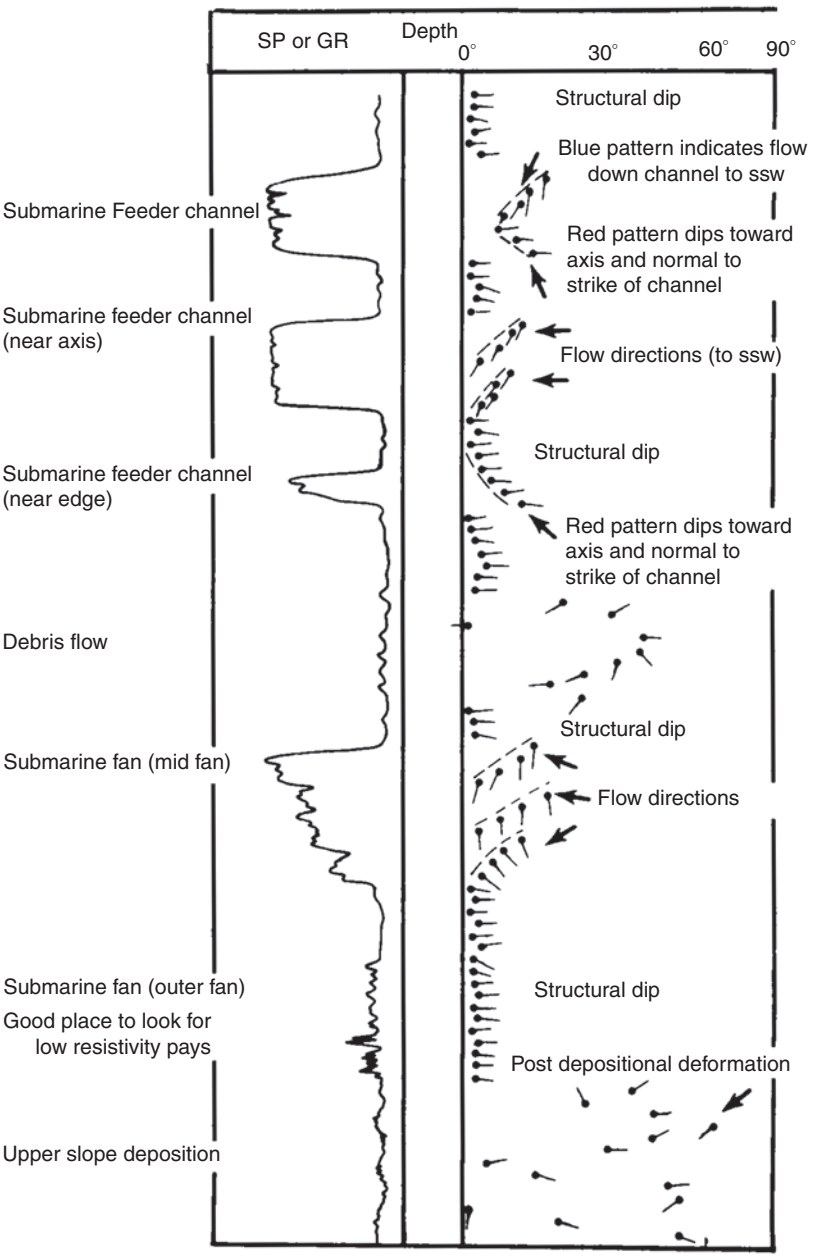
STRATIGRAPHIC INTERPRETATION
CONTINENTAL SHELF
TIDE/WAVE DOMINATED



STRATIGRAPHIC INTERPRETATION
CONTINENTAL SHELF
TIDE/WAVE DOMINATED



STRATIGRAPHIC INTERPRETATION CONTINENTAL SLOPE AND ABYSSAL ENVIRONMENTS



Part IV—Analysis of Logs and Cores

Chapter 21

Interpretation Techniques

General Philosophy

Well logs can be interpreted on a variety of levels, depending on the requirements of the user. These distinct levels can be classified as:

1. One point from one zone in one well: This method might be used, for example, to pick a top, or the location of some marker bed as a guide to further drilling, choosing a casing point.
2. A few zones in one well: This method might be used for completion and testing decisions.
3. An entire well: This method might be used for reserve studies, correlation of the well to nearby wells, and completion and testing decisions.
4. Many wells in a field: This method might be used in some field study as a starting point for mapping porosity, oil in place, and other characteristics over an entire field.

According to the requirements, the analyst may perform only a quick evaluation or consume hours of computer time in the analysis of the log data. Consciously or not, all analysts use some kind of physical model as a basis for analysis. It is worthwhile to reflect on these models before discussing the techniques of mathematical interpretation.

Suppose that a device existed that read porosity. Suppose further that this device could be made as small or as large as desired **(Fig. 21.1).** Now assume that it is 100 times smaller than a grain of sand. In a porous formation, this tiny tool will either find itself in a pore space and read 100% porosity, or it will find itself in a sand grain and read 0% porosity; that is, it has only two possible states. If the tool were placed at a large number of random points in the formation, a statistical distribution of 100 and 0% porosity readings would be developed that would provide a description of the porosity of the formation.

Now assume that the device is made very large, for example, a cubic mile in size. This large tool measures a porosity of 20%. This is not a very useful piece of information because there is no knowledge of the homogeneity of the cubic mile being measured. In fact, half the measured volume could have a porosity of 40% and half could have a porosity of 0%, and the difference would never be known. In reality, porosity tools investigate a formation volume of a few liters, so that variations at the granular level are not measurable. In that case, there is no guarantee that the porosity 10 ft from the borehole is the same as the porosity near the wellbore. The lesson is that any petrophysical measurement is a function of the way it is measured. Rather like Heisenberg's uncertainty principle, a very accurate value of porosity can be known (small device), but with no guarantee that the measurement is representative; or a macro-reading of the value of porosity can be made, but with no certainty about what volume of rock it represents.

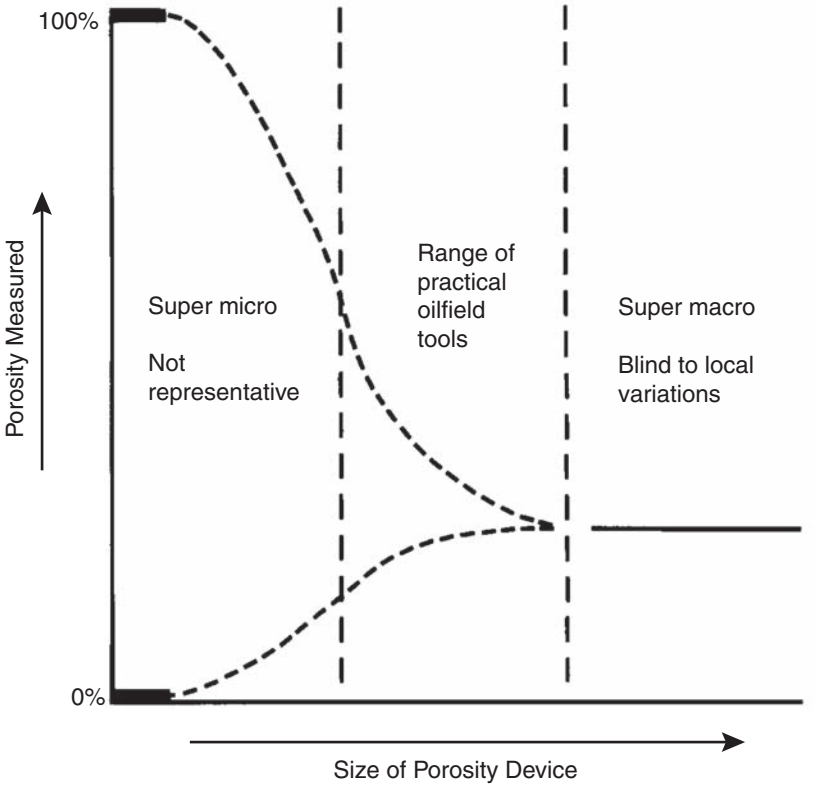


Fig. 21.1—Effect of tool size on measured parameter.

QUESTION 21.1. If a 10-acre field extends to a depth of 10,000 ft and 20 wells are drilled with a hole diameter of 12 in., what proportion of the total reservoir volume has actually been sampled?

A similar problem is that of determining the length of the coastline of an island. **Fig. 21.2** shows the mythical isle of Fractaland. A first attempt at defining the length of its coastline is made using the map, and a figure of 1000 km is obtained. Later, a more-detailed map on a much larger scale is found, and more details can be determined as the coastline bends into estuaries and juts back out into peninsulas. This map, when measured, gives a coastline length of 1500 km. Next, a hardy hiker sets out with a measuring wheel and actually walks all around Fractaland at the high-tide level on the beach, dodging around rocks and into crevices and caves, and, somewhat exhausted, comes up with a figure of 3000 km. Not to be outdone, a mad marine biologist takes a 10-year leave of absence from Fractaland U and remeasures the coastline taking into account the extra distance involved in passing the line over each barnacle on each rock on the beach and comes up with a figure of 5000 km. What, therefore, is the correct figure for the length of the coastline of Fractaland?

The moral of the story is that with any measurement problem, the answer is a function of how the measurement was made. Never was this more true than in well logging. Each practical logging tool involves a trade-off between local precision, which can be extrapolated fieldwide only at great risk of inaccuracy, and global averaging, which is blind to local inhomogeneities. If different tools are used to investigate similar rock volumes, their measurements may be combined with impunity. However, if one tool is reading a local property and another a global one, the combination of the two measurements can produce interpretive results that are either meaningless or flat wrong.



Fig. 21.2—Coastline of Fractaland.

The analyst should bear all this in mind before launching into the purely mathematical aspect of log analysis. In **Fig. 21.3,** an attempt has been made to place these concepts in perspective by crossplotting vertical resolution against radius of investigation for a number of commonly used logging tools.

21.1 Models

To apply quantitative analysis to well logs, some physical model is required to relate the log response to the mineral and fluid contents of the formation and their distribution therein. Common models used include:

- Clean formations
- Shaly formations
- Multimineral mixed lithologies
- Unconventional reservoirs

21.1.1 Clean Formations. Clean formations conform to Archie's model in which porosity may be deduced from a single porosity device (e.g., the density tool) and all formation conductivity is due to the connate water in the pore spaces. This water saturation can be determined from the standard relationship:

$$S_w^n = F \times R_w / R_t \quad \ldots\ldots\ldots\

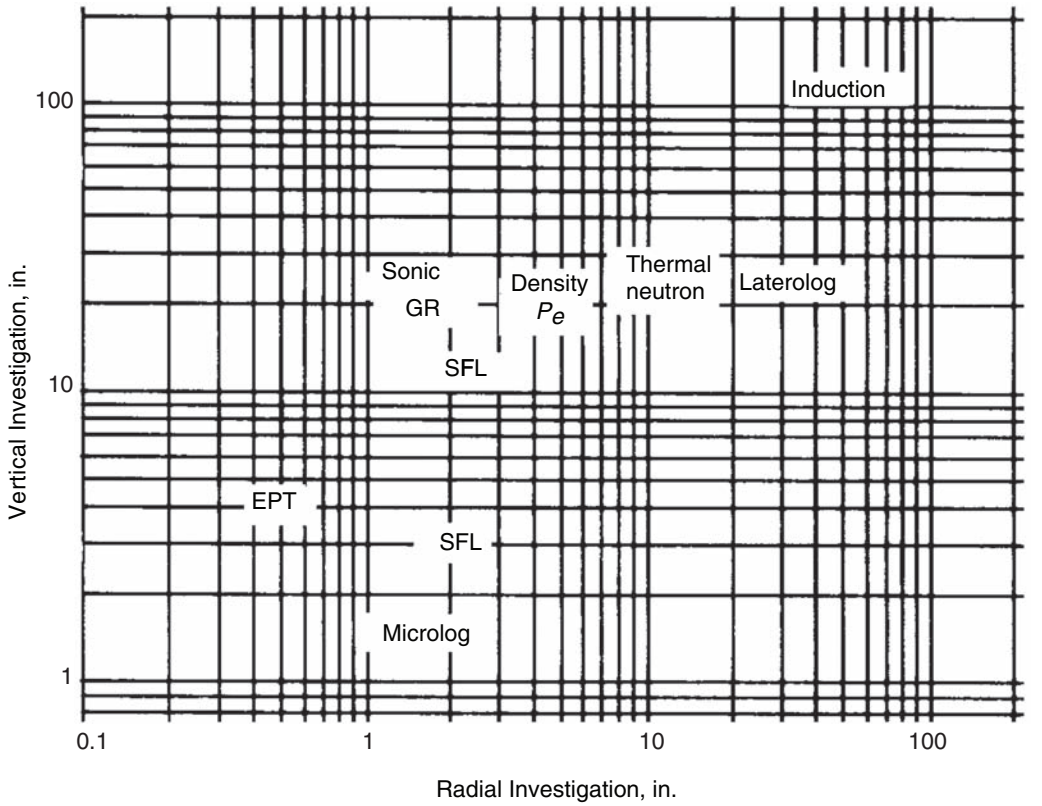


Fig. 21.3—Vertical and radial investigation characteristics of common logging tools.

Treatment of shaly sand models requires considerable care to match the log readings to the type, amount, and distribution of clays present in the formation. The specific treatment of these models is reviewed in Chapter 28.

21.1.3 Multimineral Mixed Lithologies. Where the effects of clay materials do not pose serious modeling problems, another problem with mixed minerals may exist. Carbonate and evaporite sequences may be present in the logged column. This case is most easily handled by logical application of the response equations of the individual tools, as discussed in Chapter 29.

21.1.4 Unconventional Reservoirs. Unconventional reservoirs include tight gas, shale gas, and coal bed methane (CBM). These reservoirs require specialized log and core analysis techniques that are covered in Chapter 30.

21.2 Structured Approach

A frequently asked question is, Where do I begin? This section will suggest a structured approach to log analysis. Dividing the task into logical units or sequential steps will clarify the process. These steps are:

1. Data gathering
2. Quality checks
3. Reconnoitering
4. Picking the model
5. Determining the computation parameters

6. Performing the calculations
7. Reporting conclusions

21.2.1 Data Gathering. Find all the logs. You may think that you will need only a "triple combo" log, but get the rest of the logs, too. Maybe the dipmeter will pinpoint a fault. Get the formation water analysis, core analysis, the mud log if there is one, and any drillstem-test results; you need all the data you can get. The search for data may reveal that the file is full of previous log analysis results and that the job you had planned to do is unnecessary!

21.2.2 Quality Checks. Read the headings on the log. Log headings contain all sorts of useful information on mud type, hole size, operating difficulties, bad tools, and so on. Look for bad logs, baseline shifts, noise, and any other problems.

21.2.3 Reconnoitering. Start with a log print on a scale of 1 or 2 in./100 ft (1/500 or 1/1000 for metric). Visually examine the log from top to bottom, looking for trends or formations of interest. Use a colored marker for quick delineation of shales, evaporites, and porous and permeable zones. Make a few quick calculations for lithology. If necessary, determine whether the formation of interest is a shaly sand or a carbonate.

21.2.4 Picking the Model. Having made the reconnoitering pass to locate formations of interest, the next step is to choose a model so that you will know what analysis techniques to use. For a shaly sand, try to determine whether it is a laminated shale or a dispersed shale. For a carbonate reservoir, try to determine which minerals are likely to be present. Geological reports, sidewall cores, or bit-cuttings analysis carry a wealth of information about lithology.

21.2.5 Determining Parameters. A variety of parameters will be needed. The particular selection depends on the model used and on the complexity of the case. At a bare minimum, you will need to know the value of R_w, the F-to-ϕ relationship, and how to determine porosity and R_t. The more sophisticated models require tool-response endpoints for various lithologies, shale responses to porosity tools, shale resistivities, and other information. Computer-generated crossplots can help with parameter selection.

TABLE 21.1—LOG ANALYSIS OUTLINE

Log Used	Objectives	Parameters Required
SP, GR	(Find reservoir rocks)	
Neutron, Density	ϕ	Neutron matrix setting
Sonic, *Pe*	(Find porosity and lithology)	ρ_{ma}, ρ_f, ρ_b
		Δt_{ma}, Δt_f, Δt
Laterolog	S_w	R_t, R_w, ϕ
Induction	(Find water saturation)	*a, m, n*
SFL, μSFL	S_{xo}	R_{xo}, R_w, ϕ
	(Find S_{xo})	a, m, n
Neutron, Density	ρ_{hy}	ϕ_N, ϕ_D, S_{xo}
	(Determine hydrocarbon type)	
	h	ϕ , S_w, h
	(Find pay thickness)	OIP, area, β_o, β_g, recovery factor
	OIP	
	(Find oil-in-place)	
	N	
	(Find reserves)	

21.2.6 Performing the Calculations. Calculation of saturation and porosity values is the least of your worries. This can be accomplished by the use of nomograms or by means of a scientific calculator. Programmable calculators save time here. Interactive and batch computer programs are also available. Service companies offer computer-based log analysis.

21.2.7 Reporting Conclusions. An analysis should end with a definitive conclusion. It could be simply that sand A is indicated to be productive and should be tested, or it could be in the form of a computer log indicating the locations of oil, gas, lithology, net pay, and so on. Whatever form the report takes, it must document two things: (1) the model used and (2) the parameters (R_w, ρ_{ma}, etc.) used, so that another analyst can make a judgment in an informed manner.

Table 21.1 shows an outline of steps that the reader may find useful for performing desktop analysis. A summary of the most useful log analysis equations can be found in the appendix at the end of this book.

General References

Goetz, J.F., Prins, W.J., and Logar, J.F. 1977. Reservoir Delineation by Wireline Techniques. *The Log Analyst* **18** (5): 12–55.

Raymer, L.L. and Burgess, K.A. 1980. The Role of Well Logs in Reservoir Modeling. Paper SPE 9342 presented at the SPE Annual Technical Conference and Exhibition, Dallas, 21–24 September. http://dx.doi.org/10.2118/9342-MS.

Timur, A. 1982. Open Hole Well Logging. Paper SPE 10037 presented at the SPE International Petroleum Exhibition and Technical Symposium, Beijing, 18–26 March. http://dx.doi.org/10.2118/10037-MS.

Answer to Question

QUESTION 21.1.

1 acre-ft = 43,560 ft^3.

Rock volume = 10 acres × 10,000 ft = 3.365×10^9 ft^3.

Volume of wells = 20 wells × 10,000 ft × π $(0.5)^2$ = 1.571×10^5 ft^3.

Proportion = 1:27,730.

Chapter 22

Quick-Look Interpretation, Crossplots, and Overlays

The term "quick-look log analysis" refers to a number of techniques for plotting log data in a reasonably effortless and simple way that reveals either the formation content or the formation lithology. These methods are widely used by log analysts for wellsite evaluations. Their great appeal lies in their simplicity and subtlety. Most quick-look methods can be applied without any special equipment and produce acceptable results. Broadly speaking, there are three types of quick-look analysis:

- Compatible overlays of curves
- Crossplots of selected curve readings
- Simple algorithms for calculators

In general, *compatible overlays* manage to eliminate some unknown quality by taking a ratio, while revealing some other quality that is of interest, for example, water saturation. *Crossplots* are indispensable for computer-based analysis but also offer a quick and convenient means of determining endpoints such as R_w. *Calculator algorithms* offer a quick and simple means to calculate items of interest such as porosity and water saturation. They are widely incorporated into computer-based log analysis routines.

22.1 Compatibly Scaled Overlays

22.1.1 Theory. Compatibly scaled overlays compare two or more log curves. In practice, a display will be generated with one logging parameter's analog curve overlaid on top of another, producing a composite of the two curves. In general, the relative deflection between the two curves is indicative of some formation property of interest. It is necessary for all overlays that the curves being compared be compatibly scaled (i.e., both must be in the same system of units). Apples must be compared to apples, not to oranges. Many of the quick-look overlays in use today are fairly subtle in that they eliminate some quantity that is either unknown or of no interest. The most commonly used overlays are

SP with R_{xo}/R_t	Hydrocarbon detection
R_o with R_t	
EPT porosity with porosity	Lithology, porosity and hydrocarbon typing
Neutron porosity with density porosity	
Density porosity with sonic porosity	

22.1.2 *SP* With R_{xo}/R_t. This overlay is by no means universally applicable because it requires conditions that result in healthy SP development. When those conditions are met (i.e., in wells drilled with fresh mud having salty connate water), this approach is an elegant way to detect hydrocarbons without needing to know porosity. Therefore, it is a natural candidate for wells with a minimal log suite (e.g., where only an induction SP log is available). It is usually produced at the time the log is run because it requires some manipulation of the raw data in the service company's surface equipment, but it may equally be used on legacy material with the aid of log manipulation software packages. Inputs required are an SP value, a deep resistivity measurement (usually a deep induction reading), and a shallow resistivity measurement (usually a short-normal, SFL, or similar reading). The theory behind the method depends only on Archie's equation and the SP relationship and may be expressed as follows:

$$SP = -K \log(R_{mf}/R_w) \quad (22.1)$$

Note that for the purposes of this overlay, R_{mf} and R_w are used rather than their equivalent values, R_{mfe} and R_{we}.

Archie's equation, if written for both the invaded and undisturbed zones, makes it possible to form a ratio that eliminates F, the porosity-dependent formation factor:

$$S_w^n = FR_w/R_t \quad (22.2)$$

$$S_{xo}^n = FR_{mf}/R_{xo} \quad (22.3)$$

$$\left(\frac{S_w}{S_{xo}}\right)^n = \frac{R_w}{R_{mf}}\frac{R_{xo}}{R_t} \quad (22.4)$$

If it is assumed that S_{xo} is related to S_w, for example, by the established working rule

$$S_{xo} = S_w^{1/5}, \quad (22.5)$$

then the quantity $(S_w/S_{xo})^n$ can be replaced by $S_w^{8/5}$ if n is assumed equal to 2. The term R_{mf}/R_w can then be replaced by $(R_{xo}/R_w)\, S_w^{5/8}$ and the SP equation rewritten as

$$-SP = K \log\left[\left(R_{xo}/R_t\right) S_w^{5/8}\right] \quad (22.6)$$

or

$$-SP = K\left[\log\left(R_{xo}/R_t\right) + \log S_w^{5/8}\right]. \quad (22.7)$$

In a water-bearing zone with $S_w = 1$, the $K \log S_w^{5/8}$ term is equal to zero, and therefore the $K \log (R_{xo}/R_t)$ term is numerically equal to $-SP$. In an oil-bearing zone with S_w less than 1; however, the $\log S_w^{5/8}$ term will be less than 1, and hence the $K \log (R_{xo}/R_t)$ term will be numerically less than $-SP$. Provided that there is no substantial SP reduction resulting from the presence of hydrocarbons, which is usually the case in all but very shallowly invaded formations (see Chapter 9), a comparison of the actual SP with the quantity $K \log (R_{xo}/R_t)$ will have the following characteristics:

- In wet zones, the two curves will track each other.
- In hydrocarbon-bearing zones, the $K \log (R_{xo}/R_t)$ curve will separate from the SP curve (see **Fig. 22.1**).

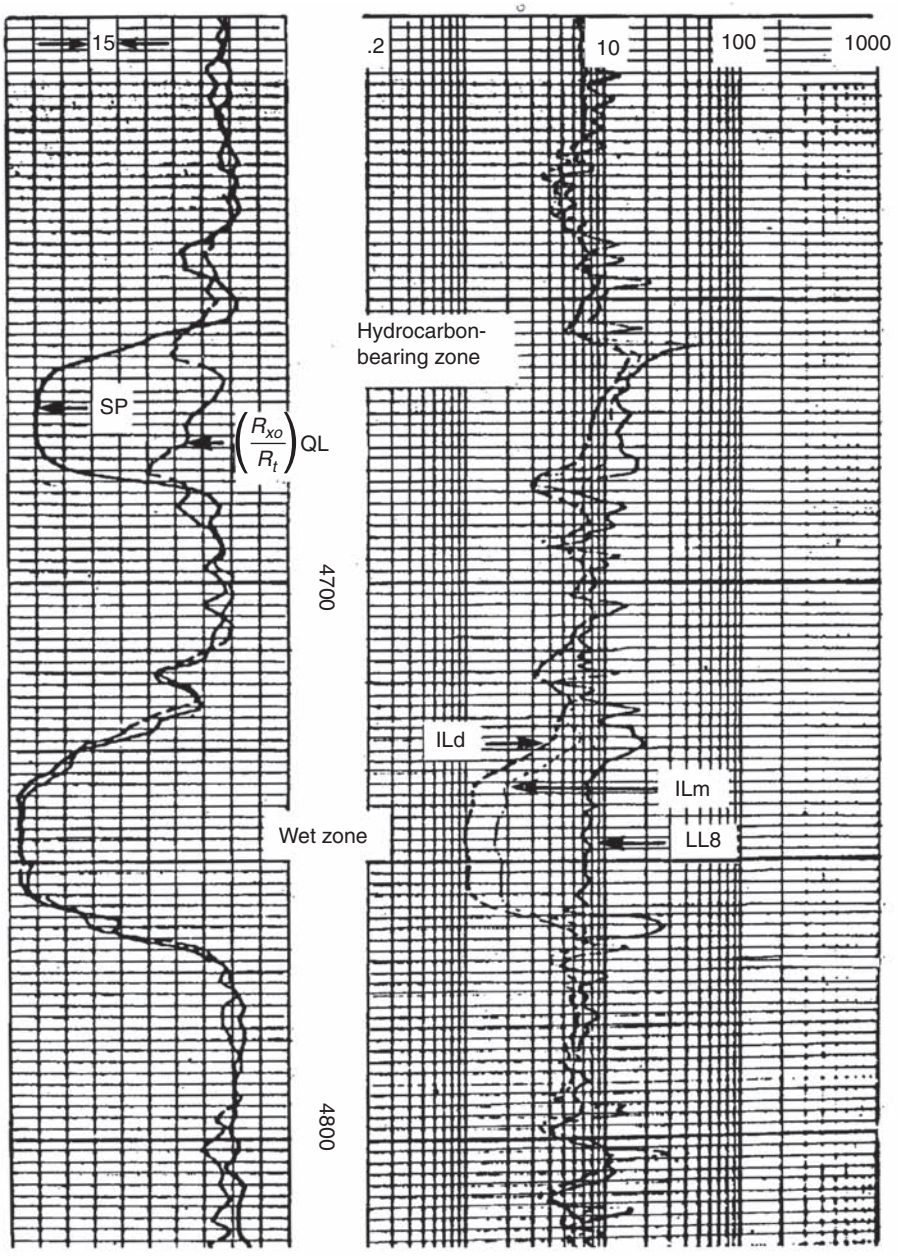


Fig. 22.1—SP with R_{xo}/R_t overlay.

Note that in the lower sand, which is wet, the SP and the massaged (R_{xo}/R_t) ratio closely coincide, while in the upper sand, which is hydrocarbon-bearing, the two curves separate. In shales, because the (R_{xo}/R_t) ratio is close to 1, the massaged R_{xo}/R_t is effectively 0. In practice, some experimentation is usually required to obtain a valid overlay with the two traces aligned in both shales and wet zones. This requires the correct K value to be used for the formation temperature in question and to correct offsetting of either the SP baseline or the massaged R_{xo}/R_t curve.

In summary, use the SP–R_{xo}/R_t overlay method by all means if you have sand/shale sequences and good SP development (high R_{mf}/R_w ratio) and if the data set you are working with lacks a reliable porosity determination. This method cannot be used with oil-based mud. A variation of the method, which is not widely used, makes use of the SP to generate a pseudo-R_{xo}/R_t ratio, which

may then be compared with the actual R_{xo}/R_t ratio. A refinement to this method enables a more accurate computation of the real R_{xo}/R_t ratio by accounting for invasion effects. In deeply invaded formations, for example, the ratio of R_{SFL} to R_{LLd} will not be as large as the real R_{xo}/R_t ratio (see Chapter 12). This refinement requires that a solution to the tornado chart be available in the analyst's software package.

22.1.3 R_o with R_t: The F Overlay. Another popular and extremely effective overlay is the F overlay, which effectively compares R_o with R_t. If Archie's equation is written as:

$$S_w^n = FR_w/R_t \quad \ldots\ldots (22.8)$$

and logarithms are taken of both sides of the equation, then:

$$n \log S_w = \log F + \log R_w - \log R_t \quad \ldots\ldots (22.9)$$

F is available from porosity measurements, for example, from a density log. Bulk density may be converted to an F value by use of the standard relationships:

$$\phi = (\rho_{ma} - \rho_b)/(\rho_{ma} - \rho_f) \quad \ldots\ldots (22.10)$$

and

$$F = a/\phi^m \quad \ldots\ldots (22.11)$$

In clean formations of known lithology, this conversion is a simple matter for the service company's surface equipment. It merely requires values of ρ_{ma}, ρ_f, a, and m to be entered. F then appears as an output. In practice, this F curve is displayed on a logarithmic scale, and the analyst then compares the F curve with a logarithmically displayed R_t curve (from a deep induction or deep laterolog). In the manner of a slide rule, the two curves may be normalized so that one will overlay with the other in clean, water-bearing zones. By so doing, the log F curve has in fact been shifted by an amount equal to log R_w. Because the product of F and R_w is R_o, the net effect is an overlay that compares R_o to R_t **(Fig. 22.2).**

Wherever the two curves separate, with R_t greater than R_o, the implication is that S_w is less than 1, and therefore that hydrocarbons are to be expected. Note that in the water-bearing section (Fig. 22.2), the normalized F curve (i.e., R_o) coincides with the R_t curve and that in the hydrocarbon-bearing section, the R_t curve separates from the R_o curve. This separation can be quantified in S_w units by use of an appropriate logarithmic scaler, as illustrated (not to scale) in **Fig. 22.3.**[*] This scaler is used as follows: Place the scaler across the log display in such a way that its long axis is parallel to the depth lines on the log. Place the $S_w = 100$ mark on the normalized F curve. Now read off the S_w value at the R_t curve.

Another useful feature of the F overlay is that R_w need not be known. The act of normalizing the F curve to the deep resistivity trace in a wet zone effectively computes R_w automatically. If the F curve is on top of the resistivity log when the normalization is made, then locate the 100 line of the F scale at the top of the F log and read the resistivity value on the resistivity scale that lies directly beneath it. This value will be numerically equal to 100 times R_w. For example, after normalizing in a wet zone, $F = 100$ lies over the R_t scale line corresponding to 20 Ω·m. This means that R_w is 0.2 Ω·m.

[*]For the scaler shown to be correctly dimensioned, the distance between the 1 and the 100 should be 5 in.

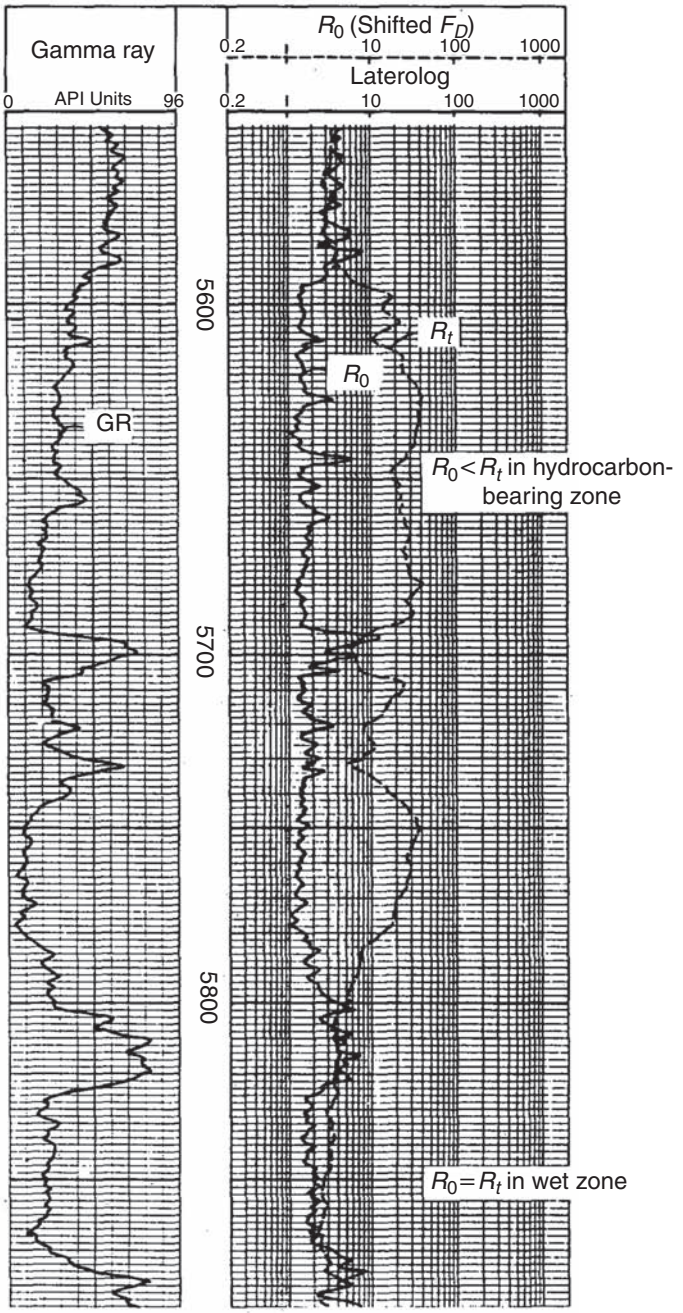


Fig. 22.2—*F* overlay (R_o with R_t).

22.1.4 The Logarithmic Movable-Oil Plot. The logarithmic movable-oil plot is an extension of the *F* overlay. This plot requires the display of two normalized traces instead of one; the first, as before, indicates S_w, and the second indicates S_{xo}. In practice, both overlays are prepared as a single display, and the result is a movable-oil plot (MOP) on a logarithmic scale.

The production of an MOP proceeds in two stages. First, the *F* curve is normalized to R_t in a water-bearing zone, and the resulting R_o curve is displayed with the resistivity log. Second, the *F* curve is normalized to an R_{xo} trace (such as a μSFL) in the water-bearing zone, and the resulting R_{xoo} curve ($R_{xoo} = R_{xo}$ in a rock 100% saturated with a fluid of resistivity R_{mf}) is displayed with

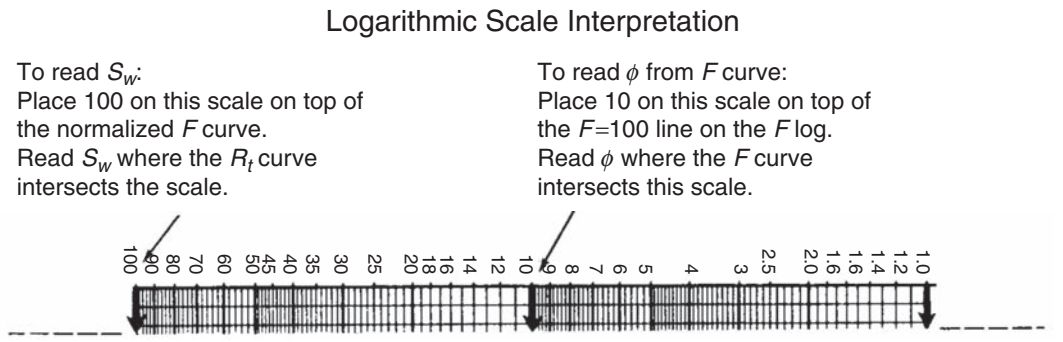


Fig. 22.3—*F* overlay scaler for S_w (not to scale).

the shallow resistivity log. The resulting display will be as shown in **Fig. 22.4.** Note that the area between the R_o and R_t curves represents the hydrocarbon-filled pore space. The MOP adds a further dimension by subdividing that space into two parts, one containing residual oil and the other movable oil. This presentation is therefore helpful in assessing the most productive intervals (i.e., the ones with high movable oil).

Consider the bulk-volume model shown in **Fig. 22.5**. Note that in the undisturbed zone, the saturating fluids are connate water and oil and that the water saturation is S_w. In the invaded zone, however, the saturating fluids are mud filtrate and residual oil, and the water saturation is S_{xo}. If S_{xo} is high, ROS is low, and a large fraction of the oil in place has been moved by the miniwaterflood affected by the drilling process.

If, however, S_{xo} is close to S_w, very little of the oil in place has been moved; in such cases, a formation may be less productive. On the MOP, the area between the R_o curve and the R_{xo} curve is a measure of the residual-oil saturation, and the area between the R_{xoo} curve and the R_t curve is a measure of the movable-oil saturation. In practice, once a display of this sort has been prepared, it is common to color in the appropriate areas with highlighters of different colors (e.g., red for residual oil, yellow for movable oil, and blue for water) as shown in **Fig. 22.6.**

Note that the zero-porosity point never appears on such a logarithmic plot because the F or R_t value corresponding to zero porosity is infinity. Some arbitrary line is, therefore, chosen as the right-hand limit for the purpose of coloring in water with a blue highlighter.

22.1.5 The Neutron-Density Overlay. The neutron-density overlay is probably the most commonly used presentation for quick-look log analysis. The two logs are nearly always run together and together supply an enormous wealth of information, even from a cursory inspection.

Two distinct types of neutron-density overlay will be considered: the compatible sandstone-scaled overlay and the compatible limestone-scaled overlay. The former is needed in sand/shale sequences and the latter in carbonate/evaporite sequences. The compatibly scaled sandstone presentation requires that the neutron log (and here the dual-spacing thermal neutron log is the norm) be recorded on a sandstone-matrix setting and displayed on a 0 to 60% scale. The bulk density recording, ρ_b, should be converted to an apparent sandstone-porosity curve by choice of an appropriate value for ρ_{ma} (2.65 or 2.68 g/cm^3, for example) and displayed on the same scale as the neutron log. The choice of a scale, be it 0 to 60% or 0 to 50%, is immaterial provided that both curves are on the same scale and the shale readings do not exceed the high end of the scale (i.e., a presentation on a 0-to-30% scale is inappropriate if ϕ_N in the shales is 45% and therefore off-scale).

In the neutron-density overlay shown in **Fig. 22.7,** note that in shales, ϕ_N is much larger than ϕ_D (dotted curve to the left of the solid curve) and that in water-bearing intervals, ϕ_N equals ϕ_D if the formation is clean. In gas-bearing zones, note that ϕ_N reads a lower apparent porosity than does ϕ_D and that the traces tend to be mirror images of each other. Even in oil-bearing sections, it is common to see ϕ_N reading slightly less than ϕ_D. Fig. 22.7 demonstrates that on one plot, it is possible to

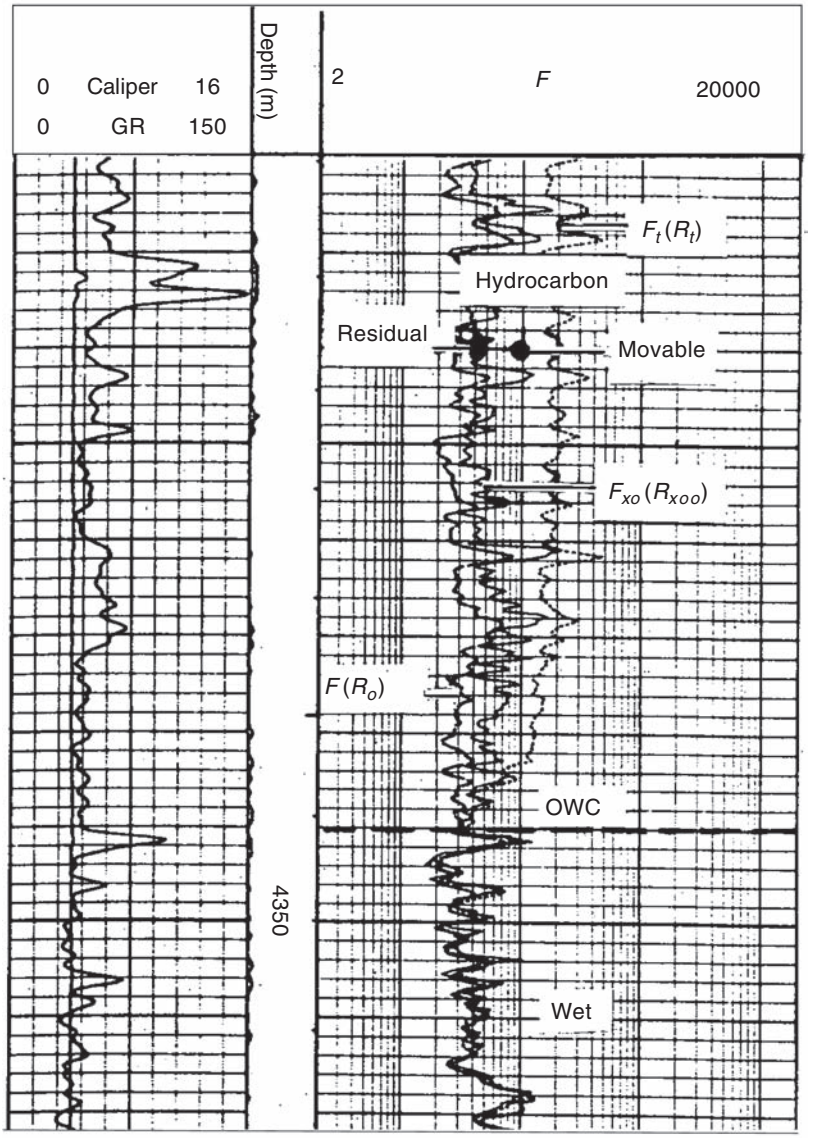


Fig. 22.4—Logarithmic MOP.

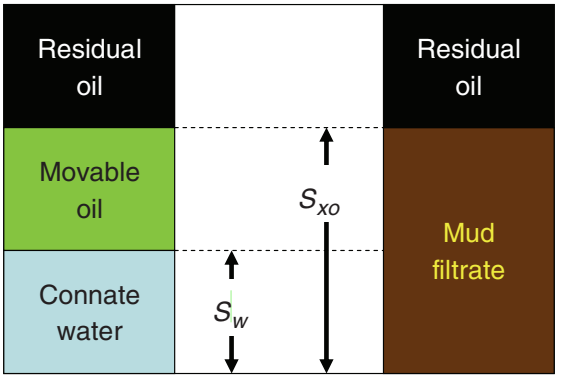


Fig. 22.5—Bulk-volume model for movable and residual oil.

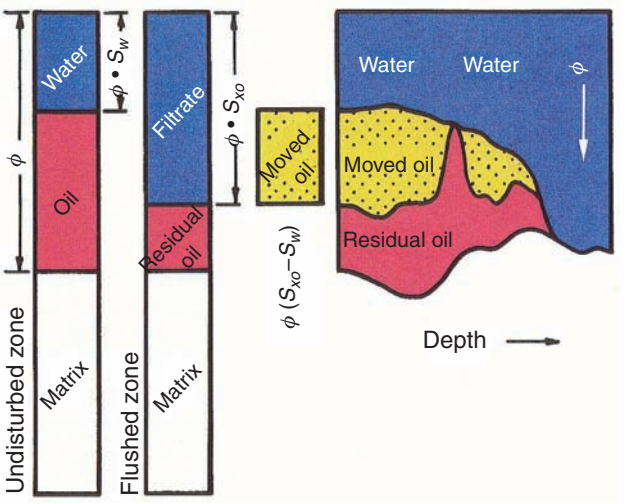


Fig. 22.6—Color-coded MOP showing movable and residual hydrocarbons.

distinguish quickly porous and permeable sections from shales and, within the potential reservoir rocks so defined, to distinguish gas, oil, and water.

A slightly different presentation is used in carbonate reservoirs because the purpose is slightly different. Here, the norm is not sandstone or shale, but limestone and possibly evaporites. Porosities in general are lower in carbonate reservoirs than in sandstone reservoirs, and dolomite may be present as well. The compatible limestone-scaled overlay therefore calls for a neutron log on a limestone matrix setting and a density log on an apparent limestone porosity basis. Because dolomite and anhydrite may have computed apparent porosities less than zero on a limestone basis (remember that ρ_{ma} for dolomite is higher than ρ_{ma} for limestone), an appropriate scale for this type of overlay is 45 to −15% (left to right). Although, in some locations, 30 to −10% is favored, the 45 to −15% scale has an added advantage: All is not lost if the bulk density curve has not been converted to an apparent porosity curve. By appropriate shifting, the neutron porosity and the bulk density curves may be overlaid so that 2.95 g/cm^3 coincides with −15% on the neutron log and 1.95 g/cm^3 coincides with 45% on the neutron log. The reader may verify that 1.95 g/cm^3 translates to approximately 45% porosity on a limestone scale and 2.95 g/cm^3 to −15%.

The neutron-density limestone-scaled overlay in **Fig. 22.8** is constructed for a formation porosity of 15%. Note that in limestone, the two traces coincide; in dolomite, the apparent neutron porosity is higher than the apparent density porosity, and in sandstone, the reverse is true. This sandstone crossover is due entirely to the matrix effects in the two porosity devices and is the result of the limestone porosity scaling used. It should not be confused with crossover produced by gas. Note that in the sandstone intervals, both curves have a similar character, although they are separated from one another. The mirror-imaging effect of gas is not evident. If gas were present, it would manifest itself by an additional separation, with neutron porosity even lower than density porosity.

Shale and the evaporites salt and anhydrite are also shown in Fig. 22.8. Such a presentation is extremely valuable as a quick-look guide to rock types in the column drilled and is a very good starting point for further, more detailed analysis.

22.1.6 Density-Sonic Overlay. Although not as widely used as the neutron-density overlay, the density-sonic overlay is particularly useful for detection of secondary porosity (vugs and fractures). **Fig. 22.9** shows a formation with both matrix (intergranular) porosity and fracture porosity. Provided that the matrix is known, the density porosity will be equal to the total porosity:

$$\phi_D = \phi_T = \phi_{\text{matrix}} + \phi_{\text{secondary}} \quad \ldots\ldots\ldots\

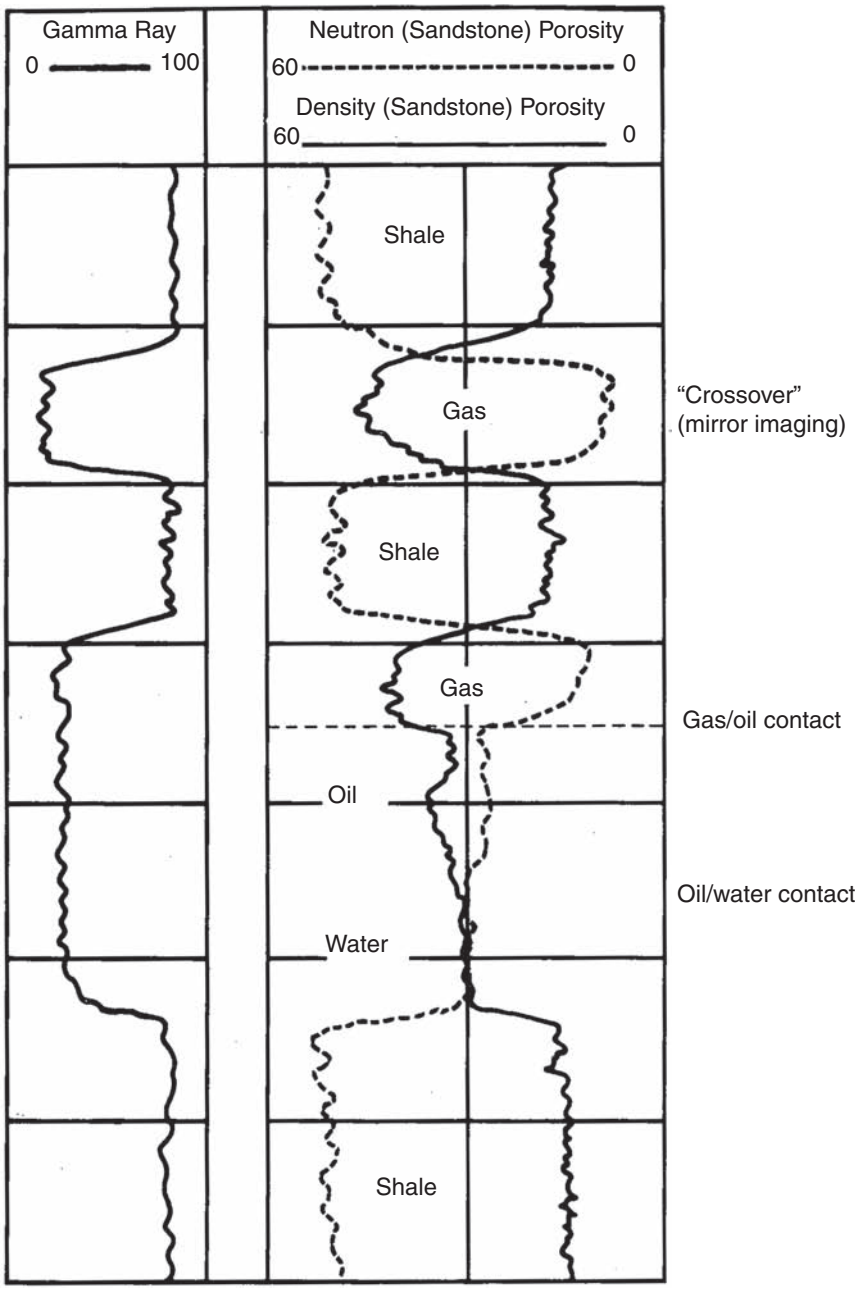


Fig. 22.7—Neutron-density overlay: sandstone presentation.

The sonic tool, however (responding as it does to the first compression wave arrival; see Chapter 16), will respond only to the matrix porosity. Compression waves traveling through a vertical, fluid-filled fracture, for example, will travel more slowly than those traveling through the matrix system. Because the sonic tool triggers on the first (faster-traveling) arrival, the later arrivals (having passed through the fracture system) will be ignored. Therefore,

$$\phi_S = \phi_{\text{matrix}} \quad \ldots\ldots\ldots\

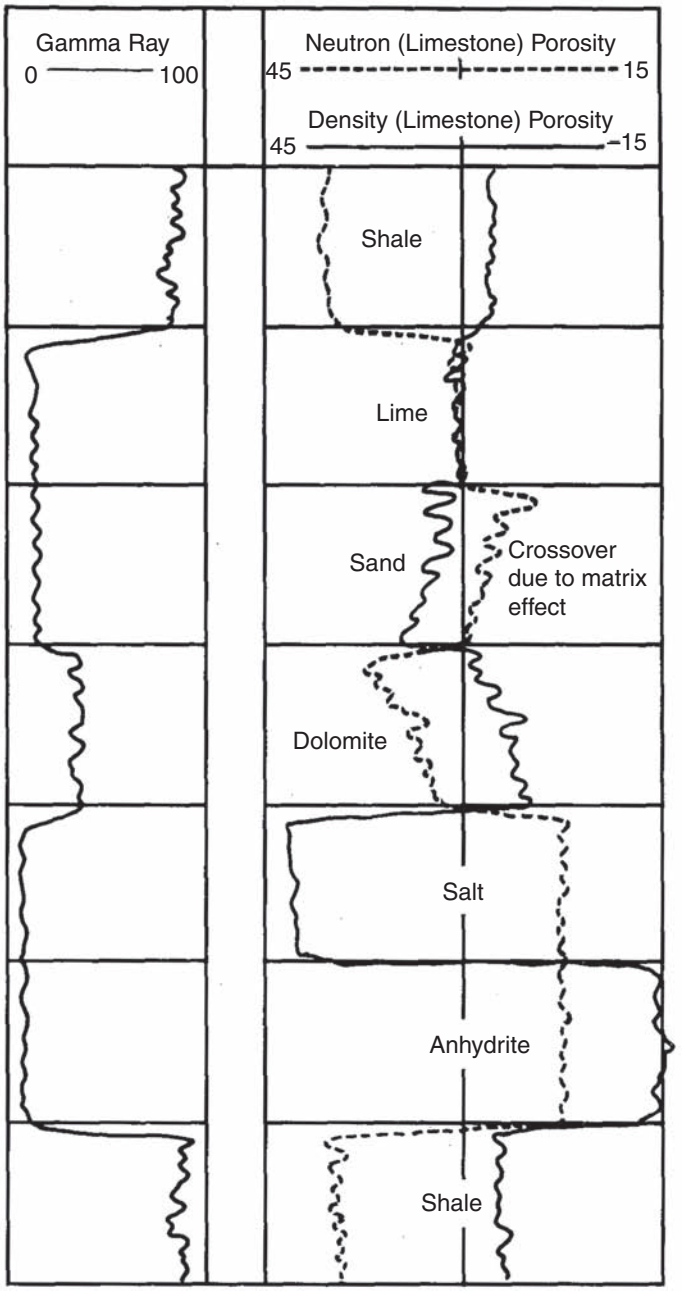


Fig. 22.8—Neutron-density overlay: Limestone presentation.

for density sonic overlays. Compatible limestone scaling of 45 to −15% (left to right) is generally adequate. If bulk density and Δt are to be overlaid, compatible scaling is 1.95 to 2.95 g/cm^3 (left to right) for ρ_b and 108 to 28 μs/ft (left to right) for Δt (equivalent to 40 μs/ft per track). In metric units, a scaling of 366 to 86 μs/m is adequate (equivalent to 70 μs/m per track).

22.1.7 EPT-Porosity Overlay. The compatible porosity overlay of an EPT-derived porosity with another porosity curve is useful for quick-look hydrocarbon detection. The theory behind the overlay is simple. An EPT-derived porosity effectively represents the water-filled pore space,

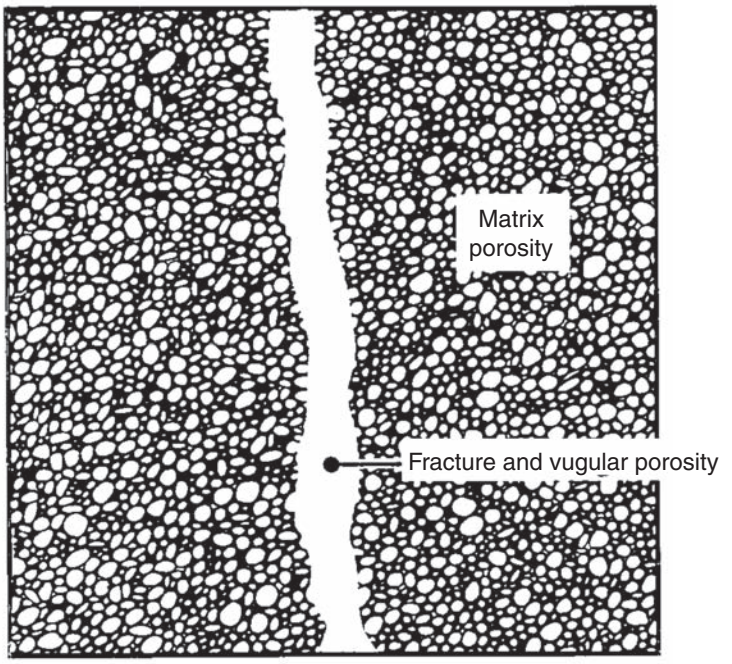


Fig. 22.9—Matrix and fracture porosity.

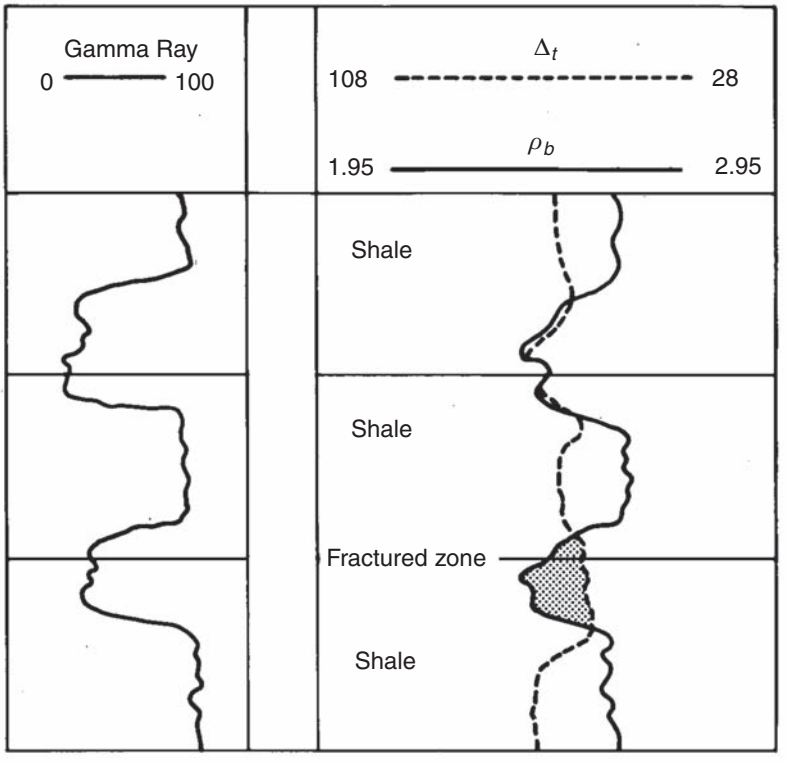


Fig. 22.10—Density-sonic overlay for fracture determination.

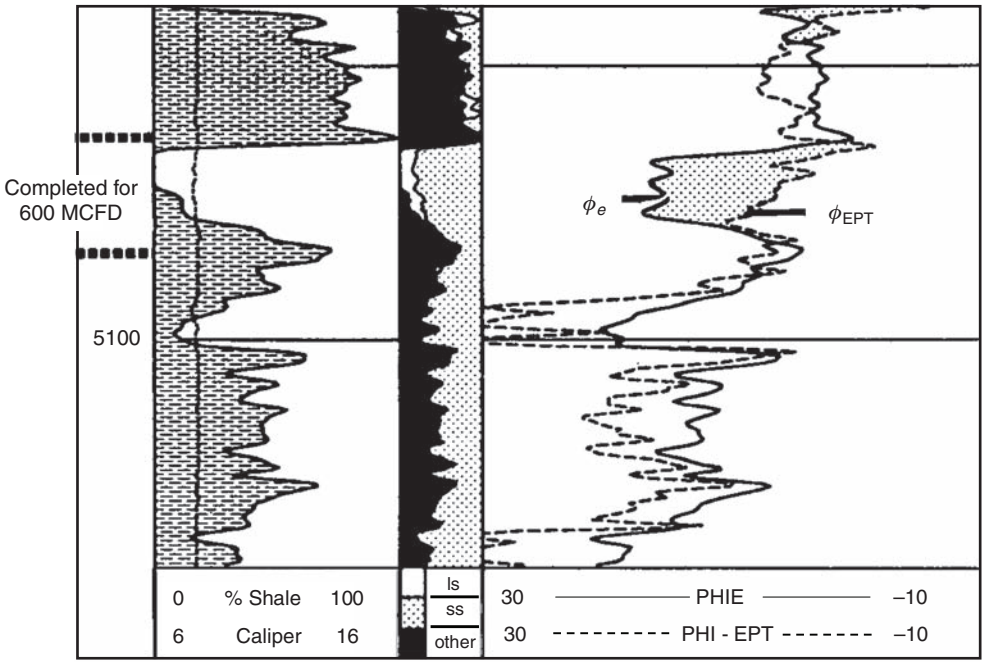


Fig. 22.11—EPT-porosity overlay for hydrocarbon detection (Eck and Powell 1983).

whereas a density porosity, for example, effectively represents the total porosity. If the formation is wet, the traces will match. In hydrocarbon-bearing zones, separation is probable **(Fig. 22.11).** The usual cautions are appropriate, that is, such an overlay requires clean formations and the correct choice of matrix parameters in computing the two porosities. Chapter 15 deals with the derivation of EPT porosity in more detail.

22.2 Crossplots

22.2.1 Theory. Crossplots of log data are indispensable tools for the analyst. Although widely used in conjunction with computer processing of log data, crossplots may, of course, be prepared by hand using only limited amounts of data "eyeball" filtered by the analyst. The end result of using a crossplot will be the picking of some parameter (e.g., R_w) needed for quantitative log analysis. Crossplots come in a variety of flavors, and the purpose of this section will be to give the reader an overall view of crossplotting techniques. More detailed work with the individual crossplots will follow in the appropriate chapters on lithology, porosity, R_w, and saturation.

22.2.2 Crossplots as Maps. A crossplot may be thought of as a map. It is a 2D representation of data variation with respect to two or more properties. For example, any animal can be classified by its weight and its height. A crossplot of animal weight versus animal height is, therefore, a valid method of mapping animal species. In the hypothetical plot of **Fig. 22.12,** for example, point **A** might represent a short fat man and **B** a tall skinny one. **C** might represent an elephant and **D** a giraffe. By typing a population in this manner, the crossplot gives a visual meaning to what would otherwise be a listing of heights and weights, which is not as easy to assimilate.

22.2.3 Trend Analysis and Groupings. The above plot of height against weight, if made more complete by adding tens or hundreds of different animal species, would start to show groups of points typical of a type of animal. In logging terms, crossplots can likewise be used to discern trends or groups. Suppose that a well has been extensively cored and that core analysis has been

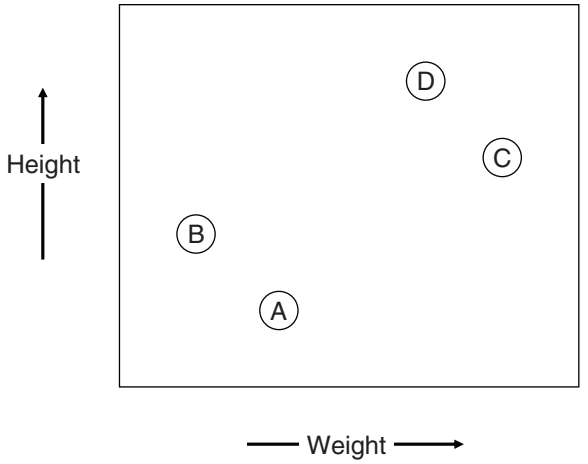


Fig. 22.12—Crossplot of height vs. weight for animals.

performed to determine porosity and permeability throughout the section. A plot of permeability against porosity might look like the plot shown in **Fig. 22.13.** Note that three distinct rock types are revealed by the crossplot. Rock type **A** is of low porosity and permeability (perhaps a carbonate); rock type **B** is of moderate porosity and high permeability (perhaps a sandstone); and rock type **C** is of high porosity and moderate permeability. Crossplots provide a visualization of trends and groupings of data points that helps in understanding the nature of the population being plotted.

22.2.4 Extrapolations. Extrapolation is a useful feature of the crossplot. In the year 1766, Titius Wittenberg noticed in his study of the planets that a relatively simple rule could be applied to relate the orbital radius of a planet to its sequence number (e.g., counting Mercury as 1, Venus as 2, Earth as 3). This later became known as Bode's law, which states that the radius of a planetary orbit, in units of the radius of the Earth's orbit, is given by:

$$\text{Orbital Radius of Planet } n = 0.4 + 0.3 \times 2^{(n-2)} \quad \ldots\ldots\ldots\

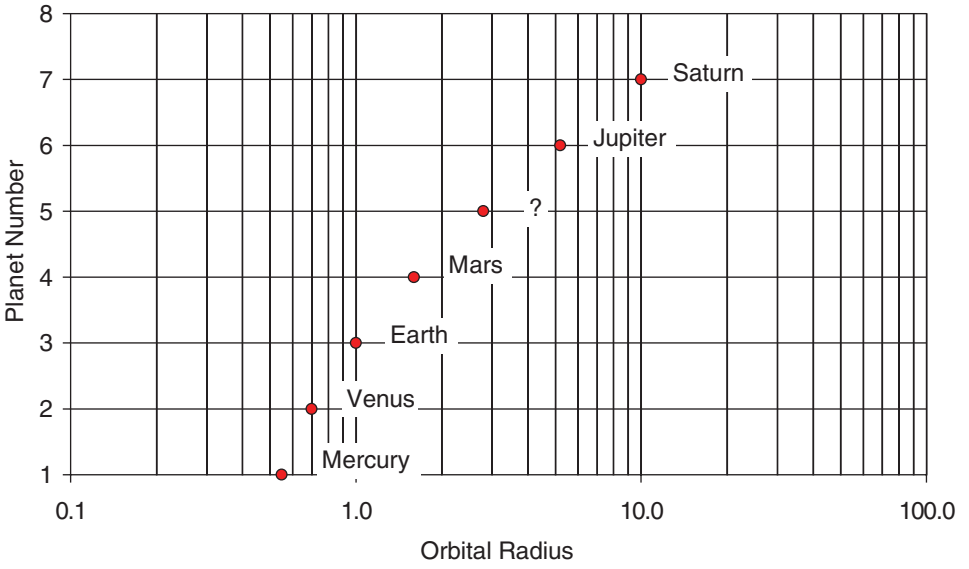


Fig. 22.14—Crossplot for finding planets (orbital radius predicted by Bode's law).

Fig. 22.14 plots planet sequence number against the Bode-predicted orbital radius. At the time this predictive plot was first made, no planet was known to exist between Mars and Jupiter. Observations at the expected orbital radius led to the discovery of the asteroids. Later discoveries of Neptune and Pluto, albeit with some serendipity, have also been ascribed to the same technique. The extrapolation of patterns and trends on crossplots is an extremely valuable tool for predicting key log-analysis parameters such as R_w.

22.2.5 Frequency Plots. Computers are particularly adept at manipulating log data to produce frequency plots, which are crossplots on which the number of occurrences of a particular pair of data points is printed at a particular map location. **Fig. 22.15** shows a neutron-density frequency crossplot for data from a section logged through a sand/shale sequence. For illustrative purposes, the plot shown has each axis divided into one-porosity-unit cells. There are, therefore, $50 \times 50 = 2{,}500$ cells on the plot. Each data point on the log is inspected, and its ϕ_N and ϕ_D coordinates are used to place a point on the plot. Where many points fall in the same cell, their total number is accumulated, and this number (or frequency) is the item printed on the final plot at that particular cell address.

Note that where no data are found, the plot remains blank, and where the majority of the points lie, the plot provides a good visual image of the distribution of formation properties in the logged section. Such plots are used extensively for normalization of log data (i.e., recalibration shifts), shale picks, and so on.

22.2.6 Z Plots. The Z plot is a companion plot to the conventional frequency crossplot (or X-Y plot) described previously. The purpose of the Z plot is to map the distribution of three variables instead of two. Given the limitations of a 2D sheet of paper, this task is accomplished by printing the scaled average of the third variable (z) at any given x-y cell address.

For example, on Fig. 22.15, there were eight occurrences of the condition ϕ_N (Phi-N, the x-axis) = 26% and ϕ_D (Phi-D, the y-axis) = 12%. The same cell on the Z plot shown in **Fig. 22.16** shows the scaled average of a third parameter, the gamma ray measurement. At the chosen address, the

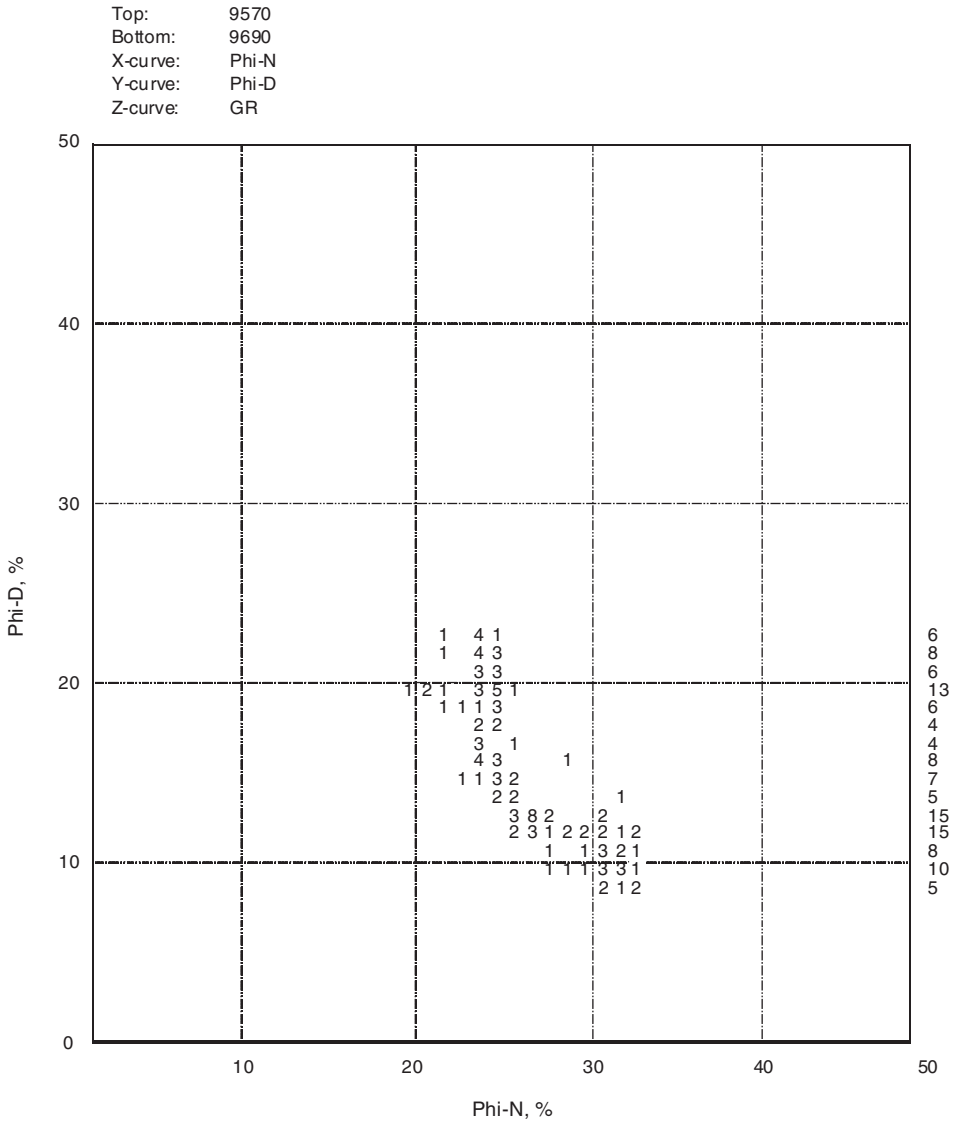


Fig. 22.15—Neutron-density frequency crossplot.

scaled average of the eight values of the gamma ray measurement occurring at $\phi_N = 26\%$ and $\phi_D = 12\%$ is seen to be 8. On this particular plot, the scaling of the z-axis was accomplished as follows:

$$z = \frac{GR - GR_{\min}}{GR_{\max} - GR_{\min}} \times 10, \quad \ldots\ldots\ldots\

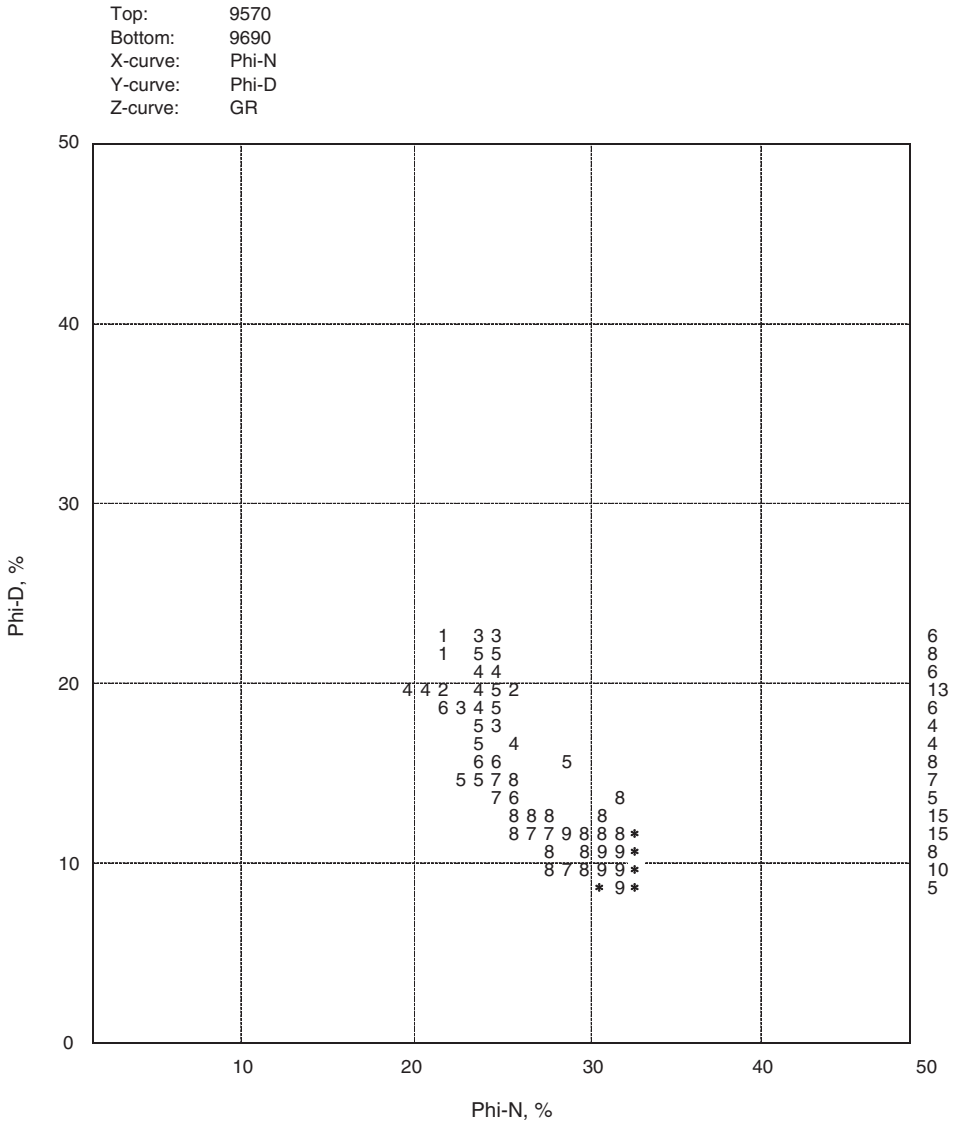


Fig. 22.16—Neutron-density crossplot with gamma ray on z-axis.

22.3 Histograms

Histograms of raw log data and of computed log analysis results are also useful tools for the analyst. **Fig. 22.17** illustrates such a histogram. The y-axis of the plot is scaled either in actual number of occurrences or as a percentage of the total number of data points analyzed. The x-axis is scaled over the useful range of the data analyzed. Among the better-known uses for histograms are:

- Picking minima and maxima
- Rescaling logs
- Checking the validity of computed results

Illustrations of particularly useful histograms will be given in the appropriate chapters when discussing particular aspects of log analysis.

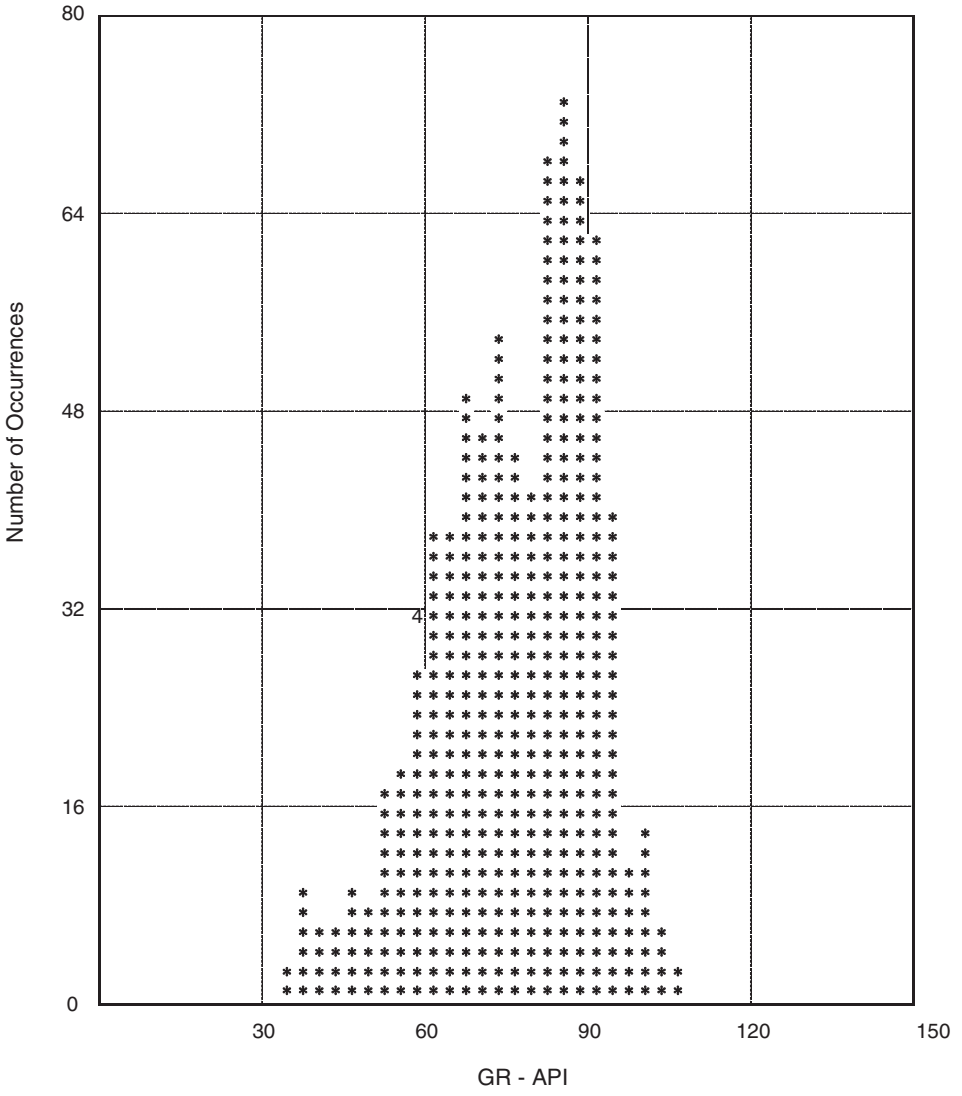


Fig. 22.17—Histogram of raw log data.

22.4 Quick-Look Algorithms

With the advent of the laptop computer, log analysts have tended to condense their wisdom into algebraic manipulations to ease their daily toil. Today, much of what used to be done by reference to charts is now done using spreadsheets or log-processing software packages. This has advantages and disadvantages. On the plus side, obviously more data points can be analyzed in a shorter time and with greater precision. On the minus side, however, the analyst is no longer free to shift points on a chart to obtain an immediate feel for the sensitivity of a computed answer to a change in the raw data values used.

Algorithms for performing many of the common manipulations that log analysts use are given in the appropriate chapters where the particular analysis method is discussed. As a convenience, these algorithms are also included in the appendix.

A word of caution is in order. Although the computer is a terribly clever device for crunching numbers and relieves the analyst of that chore, it also places a greater burden on the analyst: that

of ensuring (a) that the model fits the circumstances and (b) that legitimate data are submitted to be processed. A more precise answer should not be confused with a more accurate one.

References

Eck, M.E. and Powell, D.E. 1983. Application of Electromagnetic Propagation Logging in the Permian Basin of West Texas. Paper SPE 12183 presented at the SPE Annual Technical Conference and Exhibition, San Francisco, 5–8 October. http://dx.doi.org/10.2118/12183-MS.

Chapter 23

Porosity

Devices that measure porosity are sensitive both to the rock matrix and to the fluid filling the pore space. Therefore, the readings from porosity tools reflect not only porosity but also the type of rock, the clay content, and the fluid type. As yet, no tool has been invented that reads only porosity, although the NMR measurement (see Chapter 19) comes very close to this ideal. This characteristic of the conventional devices used to measure porosity is a blessing in disguise because it enables the analyst to derive more information than just porosity from combinations of different porosity tools. The term *porosity tools* includes compensated neutron, compensated formation density (with or without photoelectric-factor measurement), and sonic tools.

Clean (shale- and clay-free) water-bearing formations of known lithology represent the simplest environments for porosity determination because the effects of mixed lithology, clay, and hydrocarbons do not confuse the issue. Before discussing techniques for their analysis, a review of the scales used on porosity logs and the procedures and techniques to be used in reading them will be presented.

Three things must be determined before reading a porosity log:

1. The type of curve recorded (e.g., bulk density, ρ_b, or apparent porosity, ϕ_D)
2. The scale (e.g., 45 to −15% or 60 to 0% on a neutron log)
3. The actual lithology of the formation and the nature of the fluid occupying the pore space.

Once all three of these are known, true porosity can be determined in those intervals where the particular porosity device under consideration can reasonably be expected to work; for example, with a pad-contact device such as the density tool, no readings should be attempted in washed-out zones.

Porosity is the volume fraction of pore space in the rock and is expressed as a fraction of the bulk volume of the rock. The normal convention in reservoir engineering is to express porosities in percentage units; for example, a porosity of 0.3 is referred to as 30% porosity. Another term is also frequently used: the porosity unit, or p.u. By using units rather than percentages, much confusion is avoided, for example, when comparing a 20 p.u. sandstone with a 25 p.u. sandstone. The latter is 5 p.u. higher than the former. This avoids the confusion caused by saying that one is 5% better than the other or 25% better than the other, depending on which way the difference is expressed.

23.1 Reading Porosity From the Density Log

Normal scaling for the density log is from 2.00 to 3.00 g/cm^3 from left to right across two tracks, or 20 divisions. Each division, therefore, represents 0.05 g/cm^3. On this basis, it is a simple matter to find the bulk density, ρ_b, in g/cm^3. The range of bulk densities encountered in sandstone, for example, is from 1.00 g/cm^3 (water) at 100% porosity to 2.65 g/cm^3 at zero porosity. A spread of

1.65 g/cm^3, therefore, represents a spread of 100 p.u., and each of the 20 log-scaling divisions represents 0.05 g/cm^3. The number of p.u. in a scale division can be determined as follows:

$$1.65 \text{ g/cm}^3 = 100 \text{ p.u.}$$
$$0.05 \text{ g/cm}^3 = 0.05/1.65 \times 100.$$
$$= 3.03 \text{ p.u.}$$

For all practical purposes, the log scale can be marked off in increments of 3 p.u., starting with 0 p.u. at 2.65 g/cm^3. The error at 30 p.u. is only 0.3 p.u., or 1%.

23.2 Combinations of Porosity Tools

Frequently a combination of porosity devices can be run into the wellbore together. In many cases, these combination tools can define porosity better than any single porosity device by itself. The most commonly available pair is the density-neutron combination.

When working with well logs generated by such a tool combination, the log scales should be checked carefully before jumping to conclusions. Probably more confusion exists about density-neutron combinations and their presentations than about any other device on the market today.

23.2.1 Density-Neutron Combinations. The compensated density log can be recorded either as a bulk density curve (ρ_b) in g/cm^3 or as a porosity curve (ϕ_D) if certain assumptions about ρ_{ma} and ρ_f are made. The neutron log can be recorded with one of three matrix settings. The important items to note on each porosity log are the zero porosity point and the porosity scale. If these parameters have been chosen correctly, comparing the two logs will be like comparing apples with apples. More often than not, however, density-neutron combinations will be comparing apples to pears because porosity scales are different or the zero points do not coincide.

A common rule is to record both logs on compatible limestone scales, that is, so that both logs would be reading the true porosity if the lithology were limestone. To accomplish this, the neutron log is run using a limestone matrix setting, and the density log is recorded as a bulk density curve and shifted so that the zero of the neutron scale coincides with a ρ_b value of 2.70 g/cm^3. Alternatively, and a little more accurately, ρ_b can be converted into a porosity curve by using $\rho_{ma} = 2.71$ and an appropriate value of ρ_f, depending on the salinity of the mud filtrate.

For predominantly sandstone reservoirs, two methods can be used:

1. Run the neutron log on a sandstone matrix using a porosity scale of 60 to 0%. Run the density log as a ρ_b curve on a scale of 1.65 to 2.65 g/cm^3. The zero point for both will now be at the extreme right of Track 3.
2. Alternatively, ρ_b can be run as a ϕ_D curve and scaled as for the neutron log on a 60 to 0% porosity scale.

For predominantly carbonate reservoirs, or when the lithology is not well known, the best method is to use compatible limestone scales. In other words, run the neutron log on a limestone matrix using a 45 to −15% porosity scale, and run the density log using a ρ_b scale of 1.95 to 2.95 g/cm^3.

In analyzing combination density-neutron logs, some unusual combinations of scales may be encountered. If this happens, reason back to the zero point for each log and begin the analysis there.

23.2.2 Uses of Combination Porosity Logs. Three parameters can be determined by combining two porosity logs: porosity, lithology, and fluid content of the pore space. Regardless of the actual lithology, an extremely good approximation to true porosity can be made by combining the neutron limestone porosity (ϕ_{NLM}) with the density limestone porosity (ϕ_{DLM}) in the following manner:

$$\phi_X = \left(\phi_{NLM} + \phi_{DLM}\right)/2, \quad \text{.....(23.1)}$$

where ϕ_X is referred to as the crossplot (Xplot) porosity.

If both logs are recorded on limestone porosity scales and the lithology is limestone, both logs will read the same porosity value. If the lithology is sandstone, then ϕ_{DLM} will be too high and ϕ_{NLM} will be too low, but the average will be close to the actual porosity value. If gas or light hydrocarbons are present, use of the average-porosity formula will result in porosity values that are good only to a first-order approximation. When light hydrocarbons are present, better porosity values can be determined by the Gaymard (1968) method, which is discussed later.

23.3 Density Porosity (ϕ_D)

The simple relation,

$$\phi(\text{fractional}) = \frac{\rho_{ma} - \rho_b}{\rho_{ma} - \rho_f} \quad \ldots\ldots\ldots\

23.4 Neutron Porosity (ϕ_N)

Compensated neutron tools are run on a matrix setting chosen by the logging engineer or the company witness. If the actual lithology coincides with the chosen matrix setting, porosities may be read directly from the log. This is seldom the case, however, and if the matrix is something other than that used in running the log, the porosity reading from the log will not be correct. Moreover, in most instances, the lithology is not known before the well is logged. Therefore, a standard matrix setting is normally used.

A convenient standard for the neutron log is the neutron porosity index (limestone). This is the value (ϕ_{NLM}) that the tool would have read had it been recording on a limestone scale. **Fig. 23.2** plots the porosity measured by the neutron tool set for a limestone matrix against the true porosity for the indicated lines of constant lithology. This chart can be used to determine the true porosity if the actual lithology is known. Because of "generational" changes in neutron-tool design, some service-company charts may show, on a single chart, the response of an older tool (for example the blue lines in Fig. 23.2) together with the response lines from a newer tool (red lines). The analyst should match the interpretation chart to the tool used to record the logs in all cases.

QUESTION 23.2. Use Fig. 23.2 to find the true porosity in dolomite if the neutron porosity index (ϕ_{NLM}) is 20%.

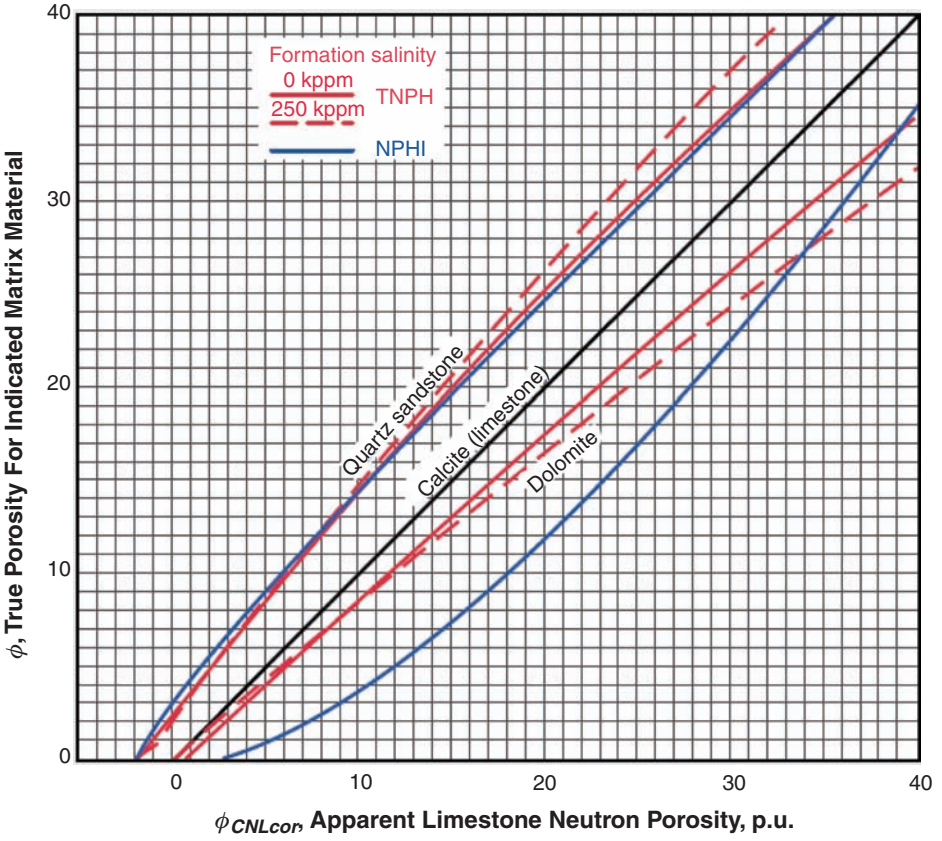


Fig. 23.2—Neutron porosity chart (Schlumberger 2005a). Courtesy of Schlumberger.

23.5 Sonic Porosity

Sonic porosity can be estimated from the Wyllie (1956) time-average equation:

$$\phi_S = \frac{\Delta t - \Delta t_{ma}}{\Delta t_f - \Delta t_{ma}} \quad (23.3)$$

This equation is represented graphically in **Fig. 23.3.** The interval transit time, Δt in μs/ft, is plotted against porosity. Lines on the chart correspond to various matrix velocities in ft/sec. The blue colored lines correspond to the Wyllie time-average equation.

Common reservoir rocks have matrix velocities in the range of 18,000 ft/sec (sandstone) to 26,000 ft/sec (dolomite). Fluid velocities depend on fluid type (oil, gas, or water) and the temperature, pressure, and salinity of the fluid; a working range is 5,000 to 5,300 ft/sec. **Table 23.1** provides a convenient summary.

Unconsolidated formations do not conform to the simple Wyllie-time-average equation. A correction factor is used in these cases to extend the usefulness of Fig. 23.3. This correction factor is the B_{cp} term, which is also known as the compaction factor (the "*cp*" is an abbreviation for *compaction*). The value of B_{cp} is usually determined for a given formation from core analysis and existing sonic logs. Effectively, the B_{cp} factor is used as a fudge factor according to Eq. 23.4:

$$\phi_S = \frac{\Delta t - \Delta t_{ma}}{\Delta tf - \Delta t_{ma}} \times \frac{1}{B_{cp}} \quad (23.4)$$

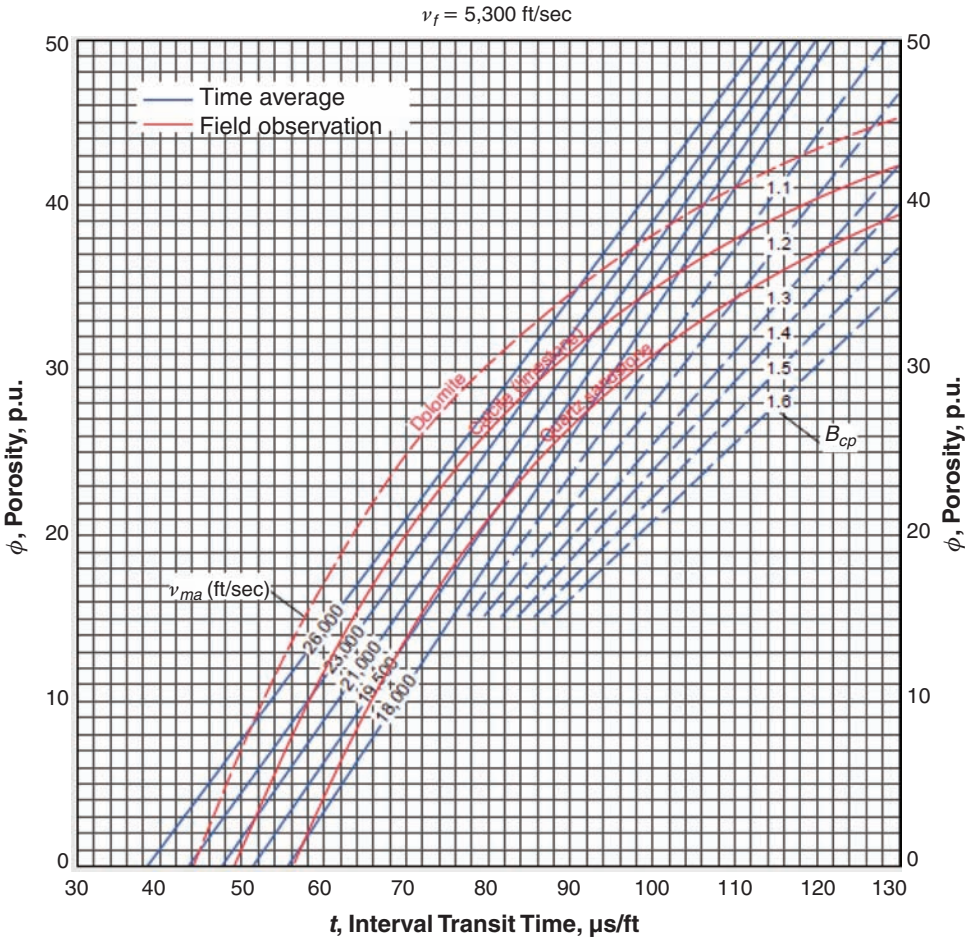


Fig. 23.3—Sonic porosity chart (Schlumberger 2005a). Courtesy of Schlumberger.

TABLE 23.1—SONIC LOG RESPONSES IN COMMON RESERVOIR ROCKS

	V_{ma} (ft/sec)	Δt_{ma} (μs/ft)
Sandstones	18,000–19,500	55.5–51.3
Limestones	21,000–23,000	47.6–43.5
Dolomites	23,000–26,000	43.5–38.5

Alternatively, the Hunt transform (the red lines on Fig. 23.3) can be used as outlined in Chapter 16.

QUESTION 23.3. Use Fig. 23.3 to find the sonic porosity in limestone (V_f = 21,000 ft/sec) if Δt = 70 μs/ft.

23.6 Neutron-Density Crossplot

Where lithology is unknown, no single porosity tool can uniquely define the porosity, which must then be determined by combining two tools such as the neutron and density logs. **Fig. 23.4** shows the neutron porosity index (ϕ_N) plotted against bulk density (ρ_b, from the density log). The lines of constant porosity are substantially straight lines that are parallel to the NW-SE axis. Thus, regardless of the lithology, readings of ρ_b and ϕ_N are sufficient to define a porosity value. One qualification for use of the chart is that the formation under investigation be water-filled; hydrocarbon effects will complicate the use of this chart.

A simple working rule for finding a neutron-density crossplot porosity is to express ρ_b as an apparent limestone porosity, add this value to the neutron limestone porosity, and divide by two:

$$\phi_{X(N-D)} = \left[\phi_{N(\text{Lime})} + \phi_{D(\text{Lime})}\right] / 2 \quad \ldots\ldots\ldots\

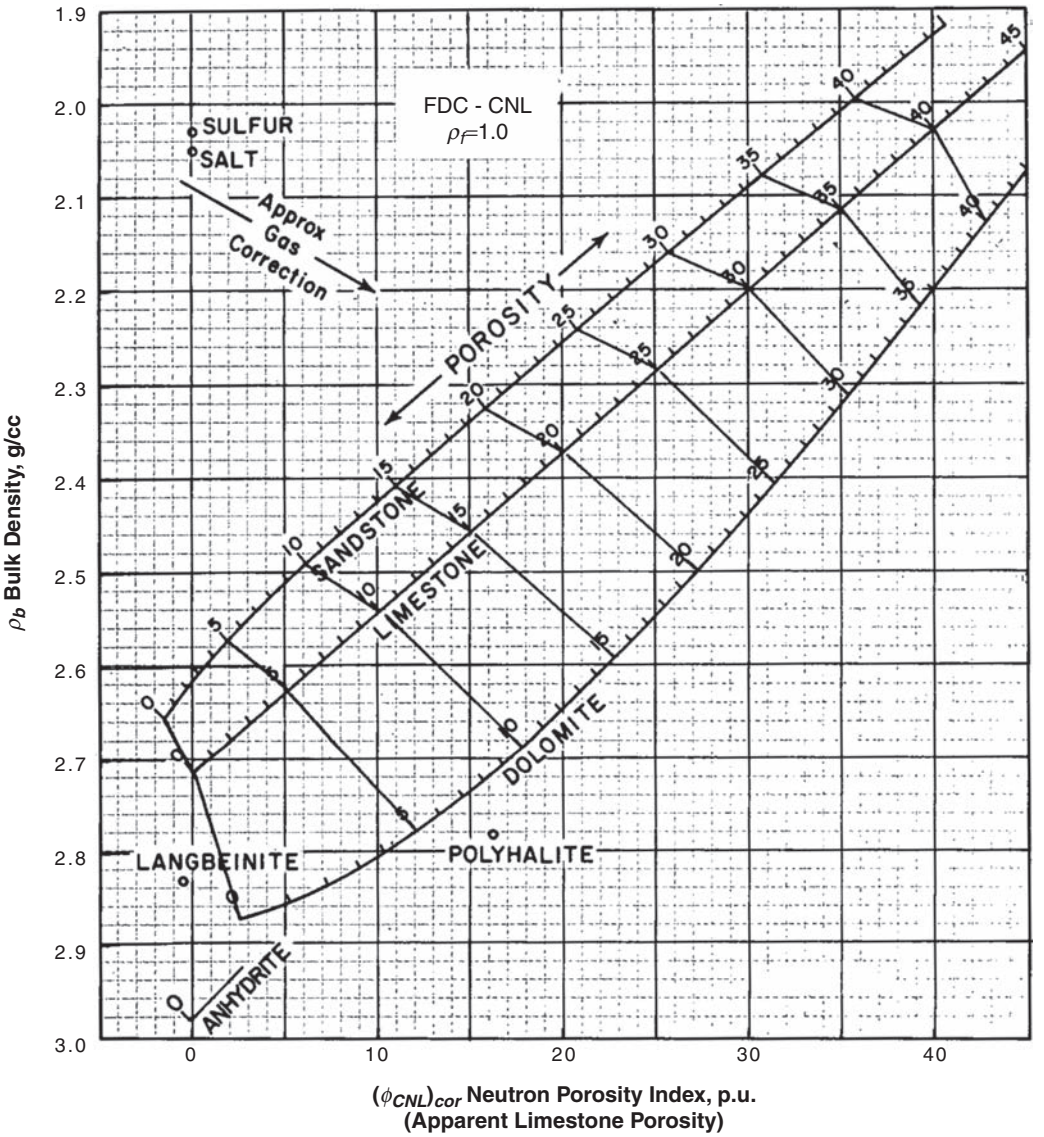


Fig. 23.4—Neutron-density crossplot showing ϕ_x. After Schlumberger (2005b). Courtesy of Schlumberger.

development is somewhat generalized. A more complete treatment of shaly sands is to be found in Chapter 28.

If a porosity device P reads ϕ_P on the log and ϕ_{Psh} in the foreign material (clay fillers or shale laminae), then the response of the device can be written as:

$$\phi_P = \phi + (1 - \phi - V_{sh})\phi_{Pma} + V_{sh}\phi_{Psh}, \quad \ldots\ldots\ldots\

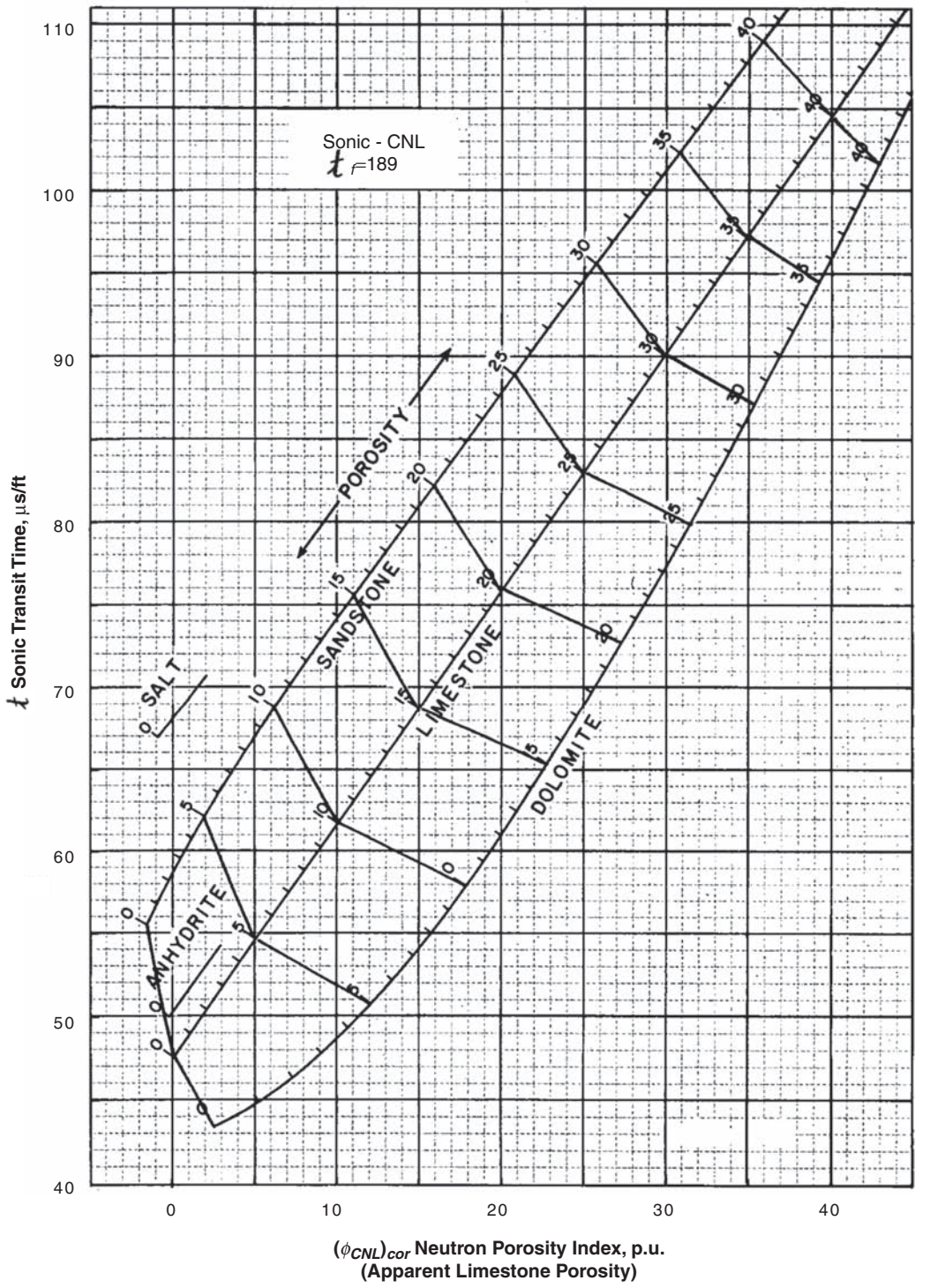


Fig. 23.5—Neutron-sonic crossplot for ϕ_x. After Schlumberger (2005b). Courtesy of Schlumberger.

and by rearrangement,

$$\phi = \phi_P - V_{sh}\phi_{Psh} \quad (23.8)$$

This generalized equation may be applied to each of the porosity devices. For the density tool, for example,

$$\phi = \phi_{D\log} - V_{sh}\phi_{Dsh} \quad (23.9)$$

Typical values of ϕ_{Dsh} range from 20 to −10% depending on the bulk density of the extraneous materials. For example, if a density log reads 20% for the assumed matrix, and an independent indicator (such as a gamma ray) reveals that 30% of the bulk volume is occupied by shale (V_{sh} = 30%), which has an apparent density porosity of 15%, the equation for ϕ can be written as:

$$\phi = 20 - 0.3(15) = 15.5\% \quad (23.10)$$

In most cases, shaly formations will at first sight appear more porous than they actually are. For the neutron log, the equation can be written as:

$$\phi = \phi_{N\log} - V_{sh}\,\phi_{Nsh} \quad (23.11)$$

and for the sonic log,

$$\phi = \phi_{S\log} - V_{sh}\,\phi_{Ssh} \quad (23.12)$$

Typical values for ϕ_{Nsh} lie between 15 and 50%, and typical values for ϕ_{Ssh} are in the same range.

Again, the combination of two devices can eliminate unknown qualities. For example, a simultaneous solution of the neutron and density equations for porosity in shaly formations leads to a useful result:

$$\phi_D = \phi + V_{sh}\phi_{Dsh} \quad \text{and} \quad \phi_N = \phi + V_{sh}\phi_{Nsh} \quad (23.13)$$

Eliminating V_{sh}, these equations can be combined to give:

$$\phi = \frac{\phi_{Nsh}\phi_D - \phi_{Dsh}\phi_N}{\phi_{Nsh} - \phi_{Dsh}} \quad (23.14)$$

QUESTION 23.7. If ϕ_{Nsh} = 36%, ϕ_N = 29%, ϕ_{Dsh} = 12%, and ϕ_D = 23%, use Eq. 23.14 to find ϕ.

The simultaneous equations may equally well be solved in the reverse fashion to eliminating ϕ, in which case a simple expression giving V_{sh} is:

$$V_{sh} = \frac{(\phi_N - \phi_D)}{(\phi_{Nsh} - \phi_{Dsh})} \quad (23.15)$$

QUESTION 23.8. Using the data from question 23.7, compute V_{sh}.

23.9 Secondary Porosity in Complex Lithology

Neutron and density logs respond to total porosity regardless of its form or distribution. Sonic logs, however, tend to ignore irregular porosity (such as vugs) and fracture porosity. Compression waves passing through the formation find a path through the rock matrix around the water-filled vugs and fractures that are faster than the path through the water in them. Because the sonic tool registers the first arrival time of the compression wave, it follows that ϕ_S represents the primary porosity. This effect may be turned to good advantage. A comparison of ϕ_D and ϕ_S should indicate when secondary porosity is present. If ϕ_D is greater than ϕ_S, vugs, fractures, or both are likely to be present in the formation.

This poses the problem of how to compute ϕ_S and ϕ_D in complex lithology when neither ρ_{ma} nor Δt_{ma} is accurately known. The solution to the problem requires use of all three porosity devices, the neutron, density, and sonic tools, and is described in detail in Chapter 29.

23.10 Hydrocarbon Effects

Neutron tools respond to the hydrogen index. Gas and light oils have a low hydrogen index and, therefore, make neutron readings lower than they would have been had water occupied the pore space instead of hydrocarbons. Density tools respond to electron density and because of hydrogen's unique Z/A ratio, gas and light oils (which contain hydrogen) appear lighter than water. Sonic tools measure the transit time of compression waves, which travel more slowly through gas than through water. Therefore, in the presence of gas and light hydrocarbons:

- The neutron log indicates less than true porosity.
- The density log indicates more than true porosity.
- The sonic log indicates more than true porosity.

To quantify the effects of light hydrocarbons, two items must be known: (1) the volume of the pore space containing hydrocarbons in the annular volume of the formation in which the tool makes its measurement, and (2) the response of the tool to hydrocarbons. In general, the porosity tools are shallow-investigation devices; that is, the majority of their measurements are made in the filtrate-invaded zone (see **Fig. 23.6**), where the saturation is S_{xo}. Therefore, the bulk volume of the hydrocarbon "seen" by the tool is $\phi\ (1 - S_{xo})$.

The equivalent porosity of a hydrocarbon depends on its density, as shown in **Fig. 23.7.** For neutron and density tools, fair approximations of the functions shown in Fig. 23.7 are:

$$\phi_{Nhy} = 2.2\rho_{hy} - 1.2(\rho_{hy})^2 \quad \text{and} \quad \phi_{Dhy} = 1.7 - 0.7\rho_{hy}. \qquad (23.16)$$

The response of the density tool can be described by:

$$\phi_D = \phi_T + \phi_{Dhy}(1 - S_{xo}). \qquad (23.17)$$

Therefore,

$$\phi_T = \frac{\phi_D}{S_{xo} + \phi_{Dhy}(1 - S_{xo})}. \qquad (23.18)$$

In gas-bearing formations, ϕ_{Dhy} is much larger than ϕ_T, and hence ϕ_D is larger than ϕ_T. For example, if $\phi_{Dhy} = 1.7$, $\phi_T = 30\%$, and $S_{xo} = 75\%$, the density log reading can be calculated as:

$$\phi_D = 0.3\left[0.75 + 1.7(1 - 0.75)\right] = 0.325. \qquad (23.19)$$

or 35.25% porosity.

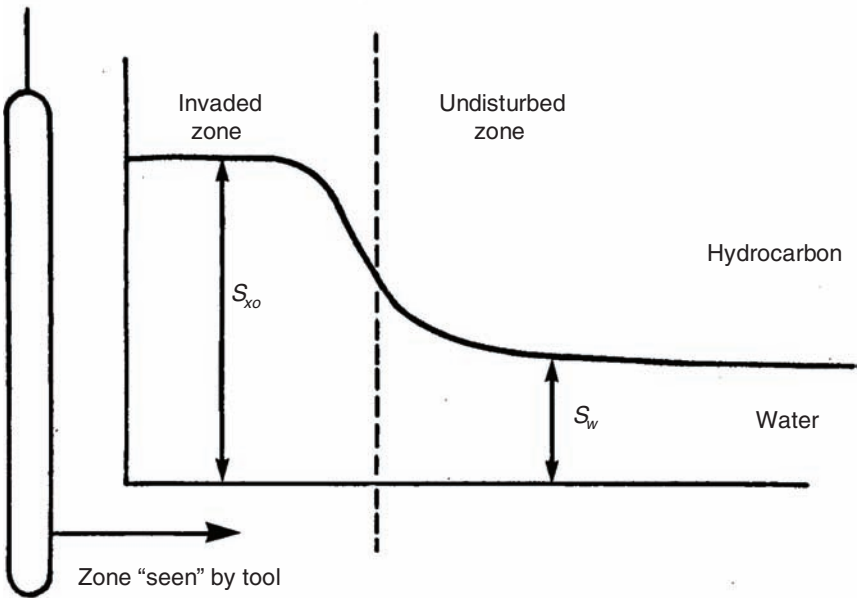


Fig. 23.6—Saturation profile "seen" by porosity logging tools.

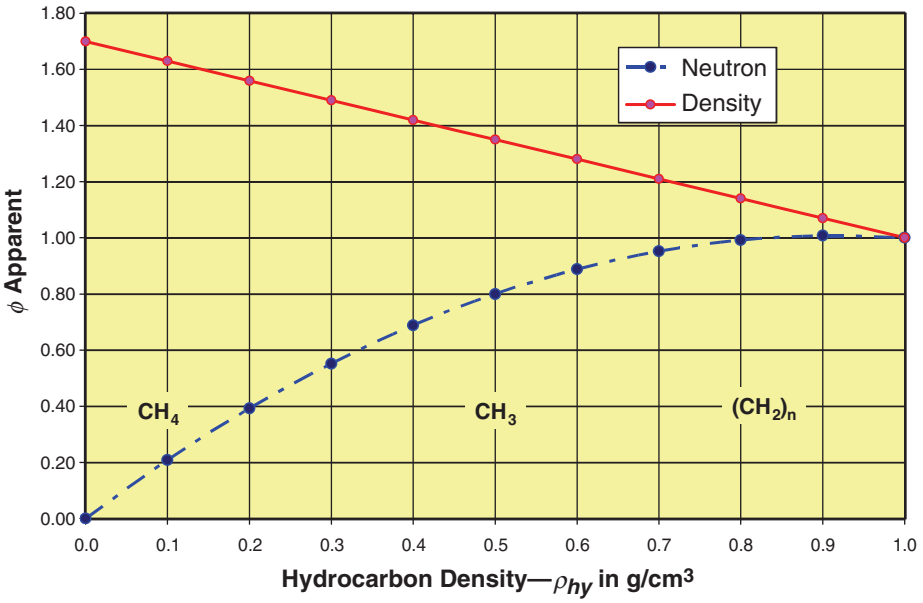


Fig. 23.7—Equivalent porosities of hydrocarbons ϕ_{Dhy} and ϕ_{Nhy} vs. ρ_{hy}.

A neutron tool under the same conditions would have a ϕ_{Nhy} of zero and

$$\phi_N = 0.3\left[0.75 + 0(1-0.75)\right] = 0.225. \quad (23.20)$$

or 22.5% porosity.

In gas-bearing formations, the log analyst has the problem of deducing porosity from a measurement that has been distorted by the fluid contained in the pore space. If single porosity measurements are available, working rules that can be used include:

$$\phi_T = 0.8\,\phi_D \quad \text{.....(23.21)}$$

$$\phi_T = 1.25\,\phi_N \quad \text{.....(23.22)}$$

A better solution can be obtained by combining the two measurements. A quick-look method for this is provided by the Gaymard (G) relationship:

$$\phi_G = \left(\frac{\phi_N{}^2 + \phi_D{}^2}{2} \right)^{1/2} \quad \text{.....(23.23)}$$

In the previous example with $\phi_N = 22.5\%$ and $\phi_D = 35.25\%$, the Gaymard formula gives:

$$\phi_G = \left[\frac{(0.225)^2 + (0.325)^2}{2} \right]^{1/2} = 0.2957 \quad \text{.....(23.24)}$$

or 29.57%, which is a very close approximation to the true porosity of 30%. More rigorous solutions can be found using iterative procedures that refine the value of porosity and S_{xo}, but these methods require computer-based processing.

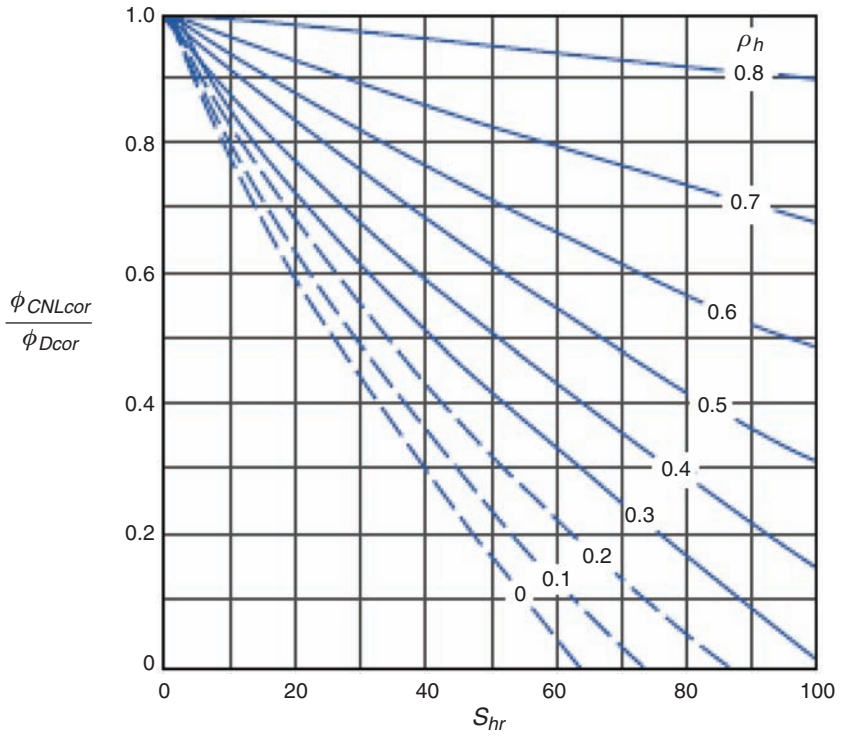


Fig. 23.8—Quick determination of ρ_{hy} (Schlumberger 2005a). Courtesy of Schlumberger.

23.11 Hydrocarbon Density

Fig. 23.8 offers a quick solution to the determination of hydrocarbon density (ρ_{hy}). The ratio ϕ_N/ϕ_D is plotted against S_{xo} or the hydrocarbon saturation S_{hy} (which is numerically equal to $(1 - S_{xo})$. The curved lines represent constant values of ρ_{hy}.

QUESTION 23.9. Use Fig. 23.8 to determine ρ_{hy} when $\phi_N = 12.5\%$, $\phi_D = 33\%$, and $S_{xo} = 55\%$.

23.12 Summary

In clean formations of known lithology, porosity can be determined from any one of the three commonly available porosity tools. When lithology is unknown, the safest quick-look porosity determination is the neutron-density crossplot porosity (ϕ_X). When light hydrocarbons are present, the Gaymard quick-look formula (ϕ_G) should be used.

In shaly formations, a simultaneous solution of any two of the three porosity-tool response equations gives an adequate effective porosity value for quick-look purposes. Complex cases, where mixed lithology, clays, and light hydrocarbons all coexist, call for a more sophisticated approach that combines the various methods already discussed with some new ones that are covered in Chapters 28 and 29.

References

Gaymard, R. and Poupon, A. 1968. Response of Neutron and Formation Density Logs in Hydrocarbon Bearing Formations. *The Log Analyst* **9** (5): 3–20.

Schlumberger. 2005a. *Log Interpretation Charts*, 05-FE-007. Sugar Land, Texas: Schlumberger Marketing Communications.

Schlumberger. 2005b. *Historical Log Interpretation Charts*, 05-FE-006.

Wyllie, M.R.J., Gregory, A.R., and Gardner, L.W. 1956. Elastic Wave Velocities in Heterogeneous and Porous Media. *Geophysics* **21** (1): 41–70.

General References

Burke, J.A., Campbell, R.L. Jr., and Schmidt, A.W. 1969. The Litho-Porosity Cross-Plot. *The Log Analyst* **10** (6): 25–43.

Raymer, L.L., Hunt, E.R., and Gardner, J.S. 1980. An Improved Sonic Transit Time-to-Porosity Transform. *Trans.,* SPWLA 21st Annual Logging Symposium, Lafayette, Louisiana, USA, 8–11 July.

Schlumberger. 2009. *Log Interpretation Charts*, 09-FE-0058. Sugar Land, Texas: Schlumberger Marketing Communications.

Answers to Questions

QUESTION 23.1.
$\phi_D = 15.2\%$.

QUESTION 23.2.
$\phi_{NLm} = 12\%$.

QUESTION 23.3.
$\phi_S = 16\%$.

QUESTION 23.4.
$\phi_X = 14\%$.

QUESTION 23.5.
$\phi_X = 14\%$.

QUESTION 23.6.
$\phi_X = 20\%$.

QUESTION 23.7.
$\phi = 20\%$.

QUESTION 23.8.
$V_{sh} = 25\%$.

QUESTION 23.9.
$\rho_{hy} = 0.2$ g/cm^3.

Chapter 24

Lithology/Mineralogy

Logs can be used as indicators of lithology. The most useful logs for this purpose are:

- Density log: ρ_b and P_e
- Neutron log: ϕ_N
- Sonic log: Δt
- Gamma ray log: natural gamma and gamma ray spectra

With the exception of the photoelectric factor measurement, P_e, and the natural gamma ray spectral log, no single tool measurement will by itself give a direct indication of lithology. However, much useful information can be gathered by combining the measurements from more than one porosity tool. The most useful combinations are:

- Crossplots such as ϕ_N vs. ρ_b, ϕ_N vs. Δt, and Δt vs. ρ_b
- The M-N plot
- The MID plot
- Combination of the above with P_e

It is often possible to scale porosity logs in such a way that two curves, when overlaid, immediately give a visual indication of the rock type. These methods are to be encouraged. A very good picture of a geologic column may be gained simply by color-coding an appropriately scaled combination of porosity logs. In a mixed lithology, it is essential to identify the rock type to choose correct values for the parameters needed to perform other log analysis calculations for porosity and water saturation. Correct identification of lithology will also assist in well-to-well correlation tasks.

24.1 The Neutron-Density Crossplot

The neutron-density crossplot shown in **Fig. 24.1** appears in two versions. Fig. 24.1 is to be used in the case of fresh-mud filtrates with $\rho_{mf} = 1.0$, and **Fig. 24.2** is to be used in the case of salt-mud filtrates, with $\rho_{mf} = 1.1$. The differences between the two are slight. Lithology (and/or mineralogy) is indicated by the location of the plotted point. The positions of various nonporous minerals are shown on the charts, as well as lines for the porous reservoir rocks. Shales typically fall in the area delineated by the boundaries

$$30 < \phi_N < 40 \quad \text{and} \quad 2.35 < \rho_b < 2.5.$$

As an exercise, it is suggested that this rectangular shale area be boxed off on Fig. 24.1 and colored in.

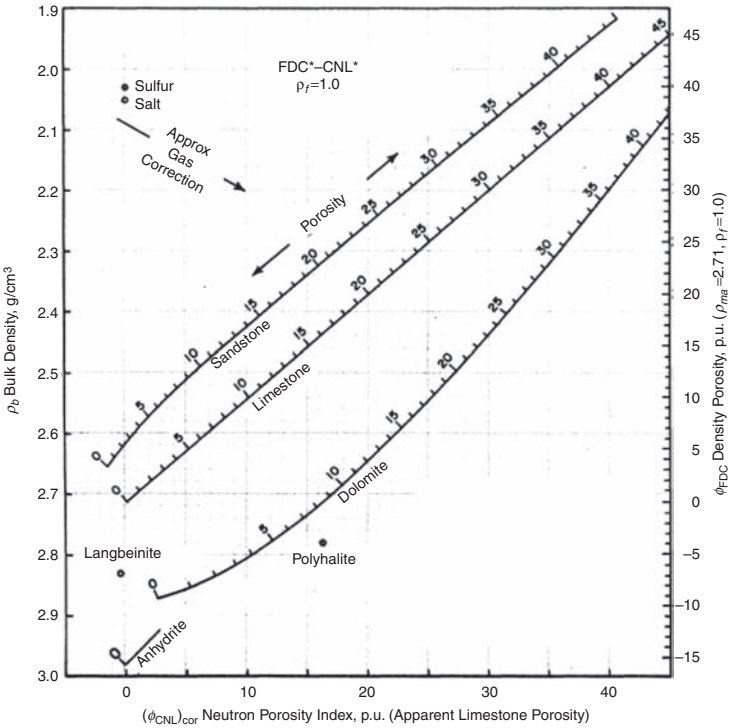


Fig. 24.1—The neutron-density crossplot: fresh muds (Schlumberger 2005a). Courtesy of Schlumberger.

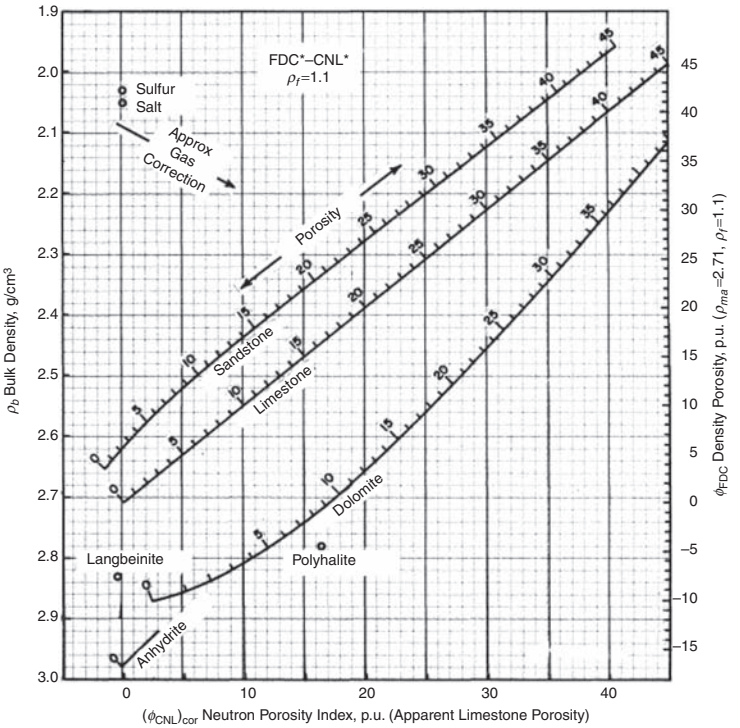


Fig. 24.2—The neutron-density crossplot: salt muds (Schlumberger 2005a). Courtesy of Schlumberger.

QUESTION 24.1. $\rho_b = 2.5$ g/cm^3, $\phi_N = 27\%$, and $\rho_{mf} = 1.0$ g/cm^3. What lithology is indicated?

QUESTION 24.2. $\rho_b = 2.5$ g/cm^3, $\phi_N = 6\%$, and $\rho_{mf} = 1.1$ g/cm^3. What lithology is indicated?

The same kind of information can be gained visually from a log display on compatible limestone scales (see **Fig. 24.3**). Note that the scale for the density log is from 2 to 3 g/cm^3 across Tracks 2 and 3. The neutron log, in limestone porosity units, is scaled from 42 to −18% across the same tracks. The 0% limestone point, therefore, coincides for both devices at four divisions from the right of Track 3. Sandstone is indicated where the neutron curve lies to the right of the density curve. This corresponds to the area to the northwest of the limestone line on Fig. 24.1. Likewise,

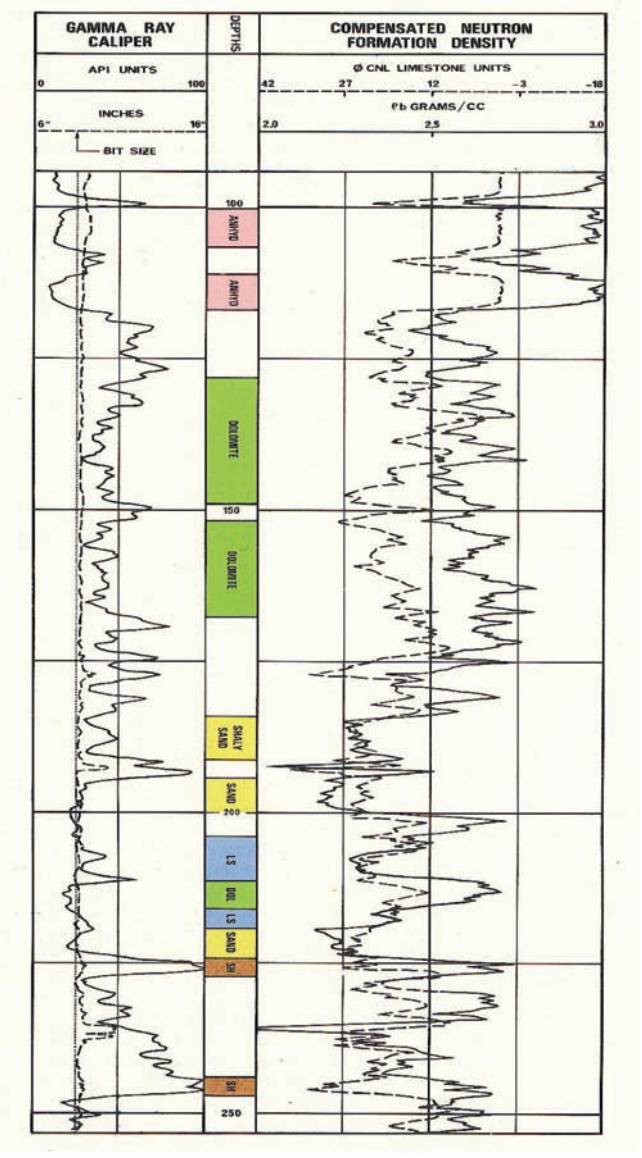


Fig. 24.3—Neutron and density curves on compatible limestone scales for lithology identification.

when the neutron curve lies to the left of the density curve, dolomite or shale (check the gamma ray) is indicated. This corresponds to the area to the southeast of the limestone line on Fig. 24.1. When the two curves coincide, limestone is indicated. Large separations, such as in anhydrite, are easily recognized.

24.2 The Neutron-Sonic Crossplot

Another frequently used pair is formed by the combination of neutron and sonic devices. When a density log is missing or suffers from bad hole effects, this plot should be used. A neutron-sonic crossplot is shown in **Fig. 24.4.** It is used in much the same way as the neutron-density crossplot. Shales typically fall into the area delineated by the boundaries:

$$30 < \phi_N < 40 \quad \text{and} \quad 70 < \Delta t < 100.$$

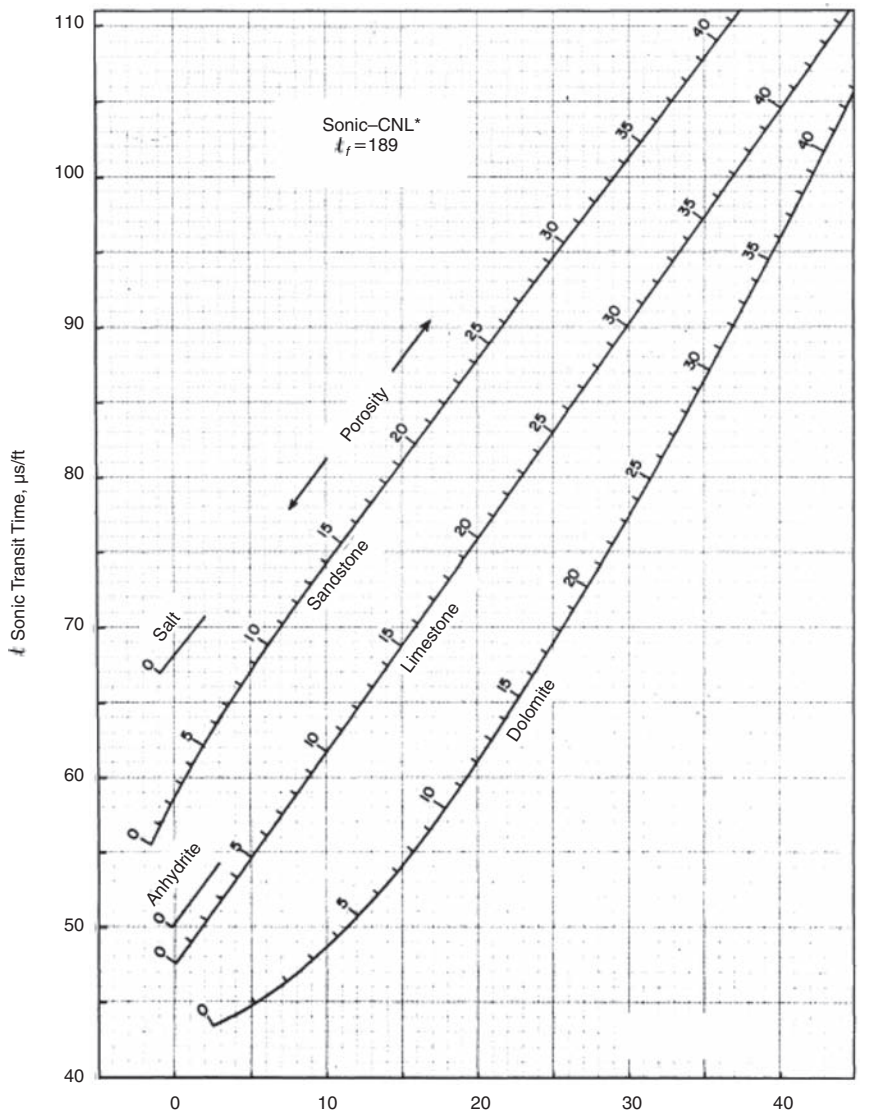


Fig. 24.4—The neutron-sonic crossplot. After Schlumberger (2005a). Courtesy of Schlumberger.

As an exercise, it is suggested that this rectangular shale area be boxed off on Fig. 24.4 and colored in.

24.3 The Sonic-Density Crossplot

The sonic-density crossplot is particularly useful for identifying minerals in addition to reservoir rocks. This plot is illustrated in **Fig. 24.5.**

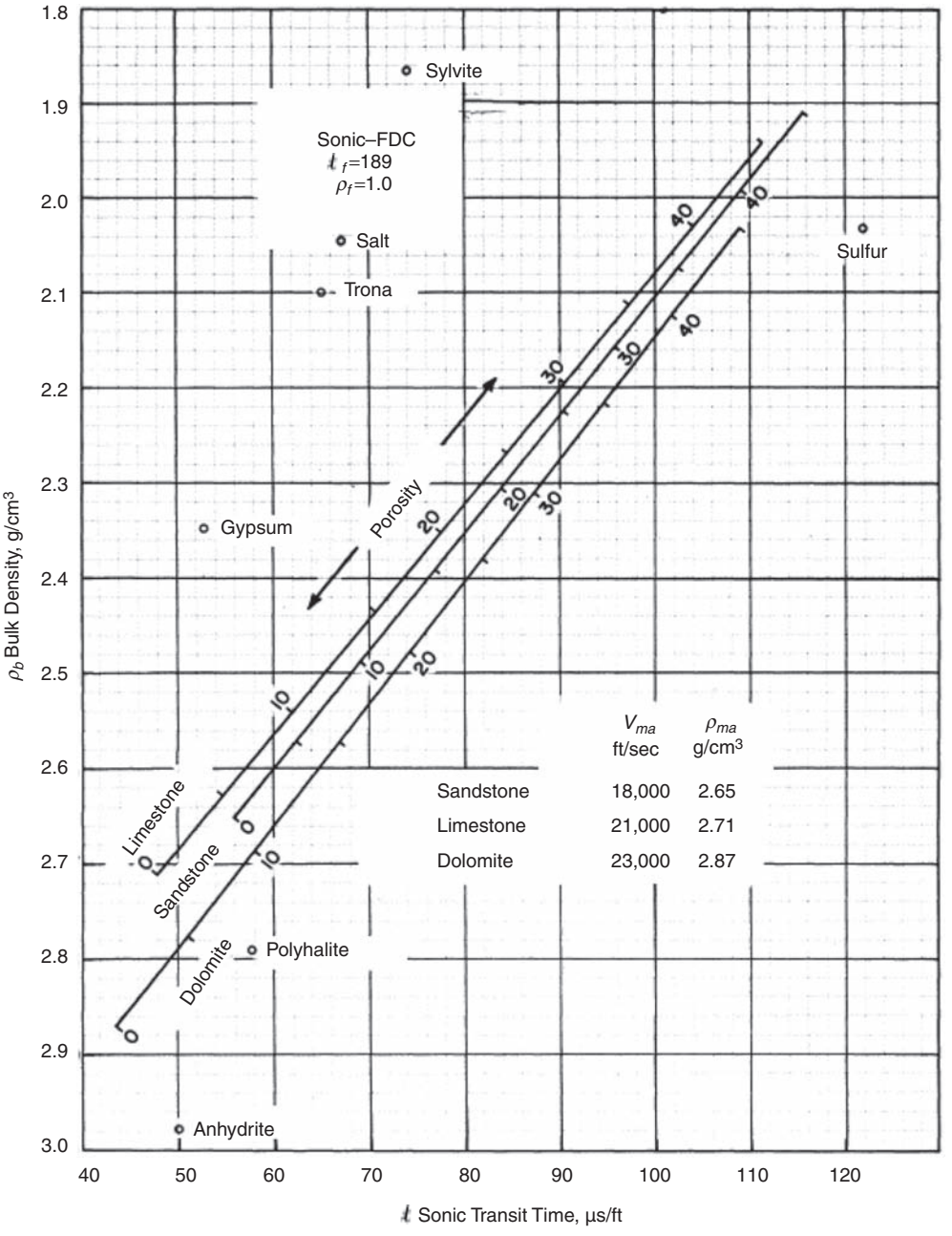


Fig. 24.5—The sonic-density crossplot. Courtesy of Schlumberger.

QUESTION 24.3. $\Delta t = 89$ μs/ft and $\phi_N = 20.5\%$. Determine the lithology.

QUESTION 24.4. $\Delta t = 89$ μs/ft and $\phi_N = 10\%$. Determine the lithology.

QUESTION 24.5. $\rho_b = 2.1$ g/cm^3 and $\Delta t = 65$ μs/ft. What mineral is this?

QUESTION 24.6. $\rho_b = 2.98$ g/cm^3 and $\Delta t = 50$ μs/ft. What mineral is this?

24.4 The M-N Plot

Sometimes three, not two, porosity devices are available. If a 3D plot could be constructed with x-, y-, and z-axes corresponding to the neutron, density, and sonic responses, then identifiable minerals would occupy unique points in space. Cases where a lithologic mixture exists could be more easily interpreted. For example, a mixture of sand and dolomite could appear as limestone on the neutron-density and neutron-sonic plots but would be identified by the sonic-density plot. Various attempts have been made to resolve the problem of reducing three log readings to a 2D crossplot. One of the first was the M-N plot. This requires that the two parameters M and N be defined as

$$M = \frac{\Delta t_f - \Delta t}{(\rho_b - \rho_f) \times 100} \quad (24.1)$$

$$N = \frac{(\phi_{Nf} - \phi_N)}{(\rho_b - \rho_f)} \quad (24.2)$$

Note that ϕ_N needs to be in fractional units and that ϕ_{Nf} is assumed to be 1.0. Effectively, these two definitions are algebraic methods of finding the slope of a line that passes through a plotted point and the 100% porosity point. Because any pure reservoir rock will plot on a line on the crossplots, and the slope of this line is substantially constant, then that slope is a characteristic of the rock type. Having defined M and N and determined them for a given point on the log, their values can be plotted on an M-N plot, as shown in **Fig. 24.6.**

QUESTION 24.7. Assume fresh-mud filtrate with $\rho_f = 1.0$ g/cm^3 and $\Delta t_f = 189$ μs/ft.
a. If $\Delta t = 69$ μs/ft and $\rho_b = 2.5$ g/cm^3, find M.
b. Where does this plot on the $\Delta t - \rho_b$ crossplot?
c. If $\phi_N = 10\%$, find N.
d. Where does this plot on the $\phi_N - \rho_b$ crossplot?
e. Plot the values of M and N on the M-N plot.
f. What does this point reveal about the lithology mixture?

The M-N plot suffers from a number of shortcomings. For example, it is not truly porosity-independent in the case of dolomite because the neutron response is not linear. Another annoying feature is that the plotted point depends on ρ_{mf}, the filtrate density. Finally, the actual values of M and N for common minerals and reservoir rocks are not easily remembered and have no particular significance in themselves. Although the M-N plot is still used by some analysts, it has largely been superseded by another plot that accomplishes the same end result more elegantly: the MID plot.

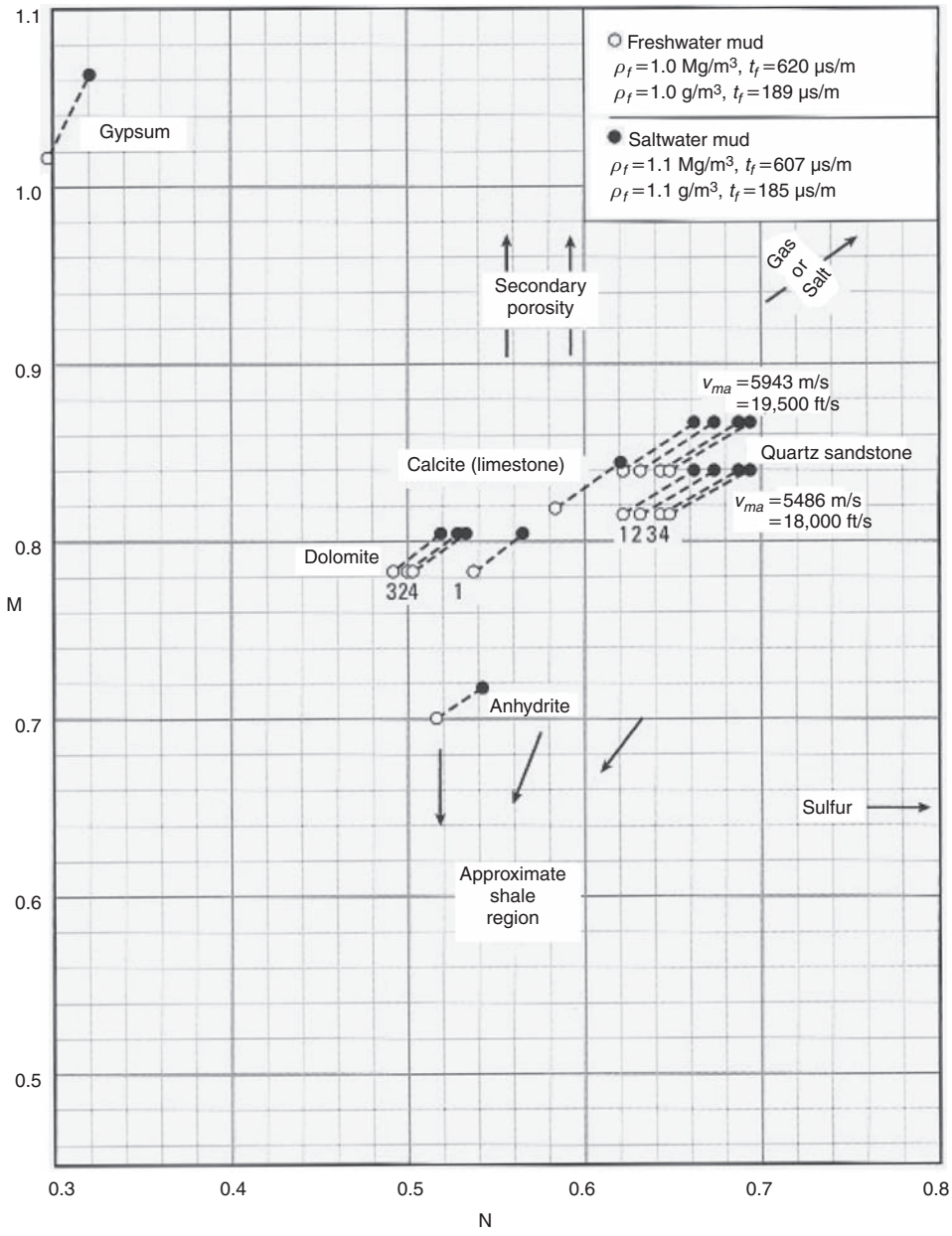


Fig. 24.6—M-N plot for mineral identification (Schlumberger 2005b). Courtesy of Schlumberger.

24.5 The Matrix Identification Plot (MID)

The MID plot requires three porosity tools as inputs. Its main advantages over the M-N plot include its independence from porosity and mud type and the fact that it uses meaningful parameters directly related to rock properties that are easily remembered. The neutron and density logs are combined to define an apparent matrix density, ρ_{maa}. The neutron and sonic logs are combined to define an apparent matrix travel time, Δt_{maa}. These two parameters are then crossplotted to define lithology mixtures.

The value of ρ_{maa} can be computed from the equation:

$$\phi_x = \left(\phi_{D\text{Lime}} + \phi_{N\text{Lime}}\right)/2. \quad \ldots\ldots\ldots\

whence

$$\rho_{maa} = \frac{\rho_b - \phi_x \times \rho_f}{1 - \phi_x} \quad (24.4)$$

and

$$\Delta t_{maa} = \frac{\Delta t - \phi_x \times \Delta t_f}{1 - \phi_x} \quad (24.5)$$

However, in practical log evaluation, these values can be found more simply from charts. For example, **Fig. 24.7** defines ρ_{maa} for any ρ_b, ϕ_N pair, and **Fig. 24.8** defines Δt_{maa} for any Δt, ϕ_N pair. Once ρ_{maa} and Δt_{maa} have been determined, they are crossplotted to generate the MID-plot chart shown in **Fig. 24.9.**

QUESTION 24.8. $\rho_b = 2.5$ g/cm^3 ($\rho_f = 1.0$), $\phi_N = 21\%$, and $\Delta t = 72$ μs/ft.
Find ρ_{maa} and Δt_{maa}. Plot these two values on **Fig. 24.10.** What lithology mix does this point indicate?

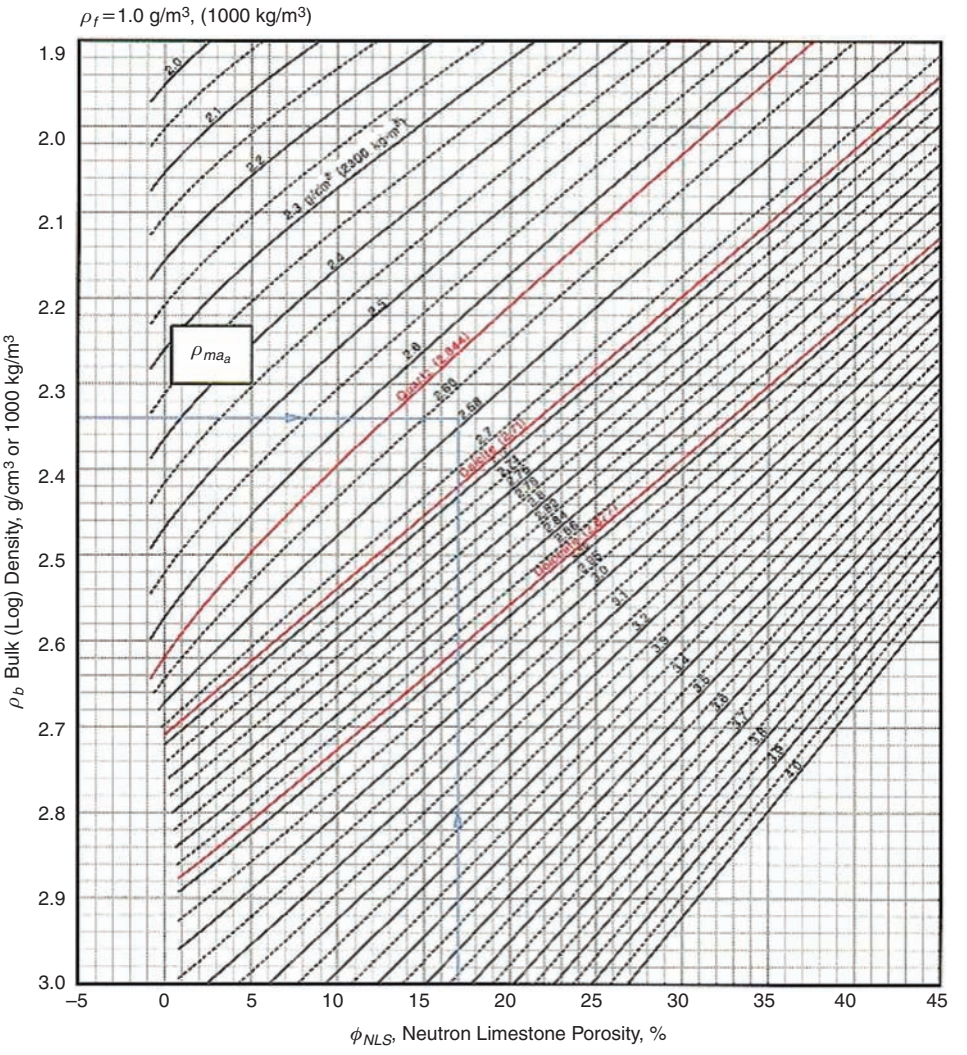


Fig. 24.7—Determination of ρ_{maa} from neutron and density logs in fresh muds. Courtesy of Schlumberger.

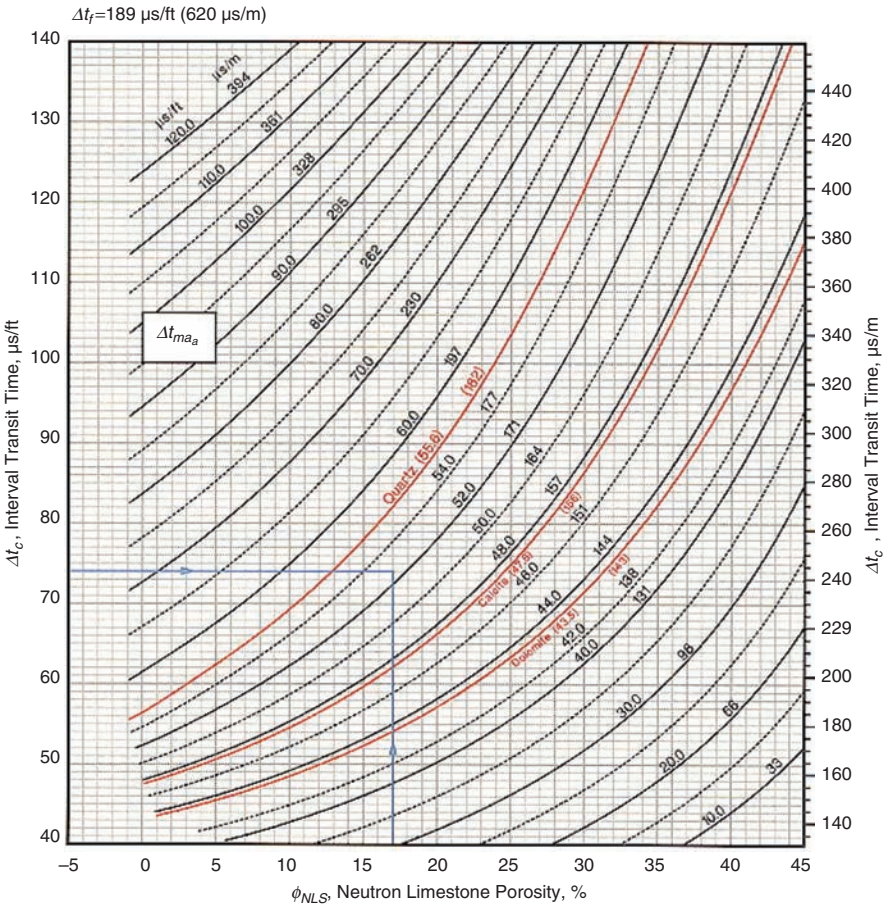


Fig. 24.8—Determination of Δt_{maa} from neutron and sonic logs. Courtesy of Schlumberger.

When using either the MID plot or the M-N plot, it is useful to have available a reference table similar to **Table 24.1**. This table summarizes the values of ρ_{maa}, Δt_{maa}, M, and N for common minerals and reservoir rocks.

24.6 The Litho-Density Log and the Photoelectric Factor P_e

Details of the litho-density tools and their measurement principle are given in Chapter 17 together with a quick-look guide to interpretation of the P_e curve. The more detailed discussion that follows here is designed to shed more light on the usefulness of the P_e measurement when combined with other log readings.

Table 24.2 lists typical values of densities and photoelectric indices for the most common minerals. A more complete list is given in the appendix at the end of the book. In most lithologies, combinations of minerals exist, and the overall photoelectric index is not a linear function of the P_e values of the individual components. A new term, the volumetric photoelectric absorption index (U), must be calculated. This index is the product of electron density and the photoelectric factor:

$$U = \rho_e \times P_e \quad \ldots\ldots\ldots\

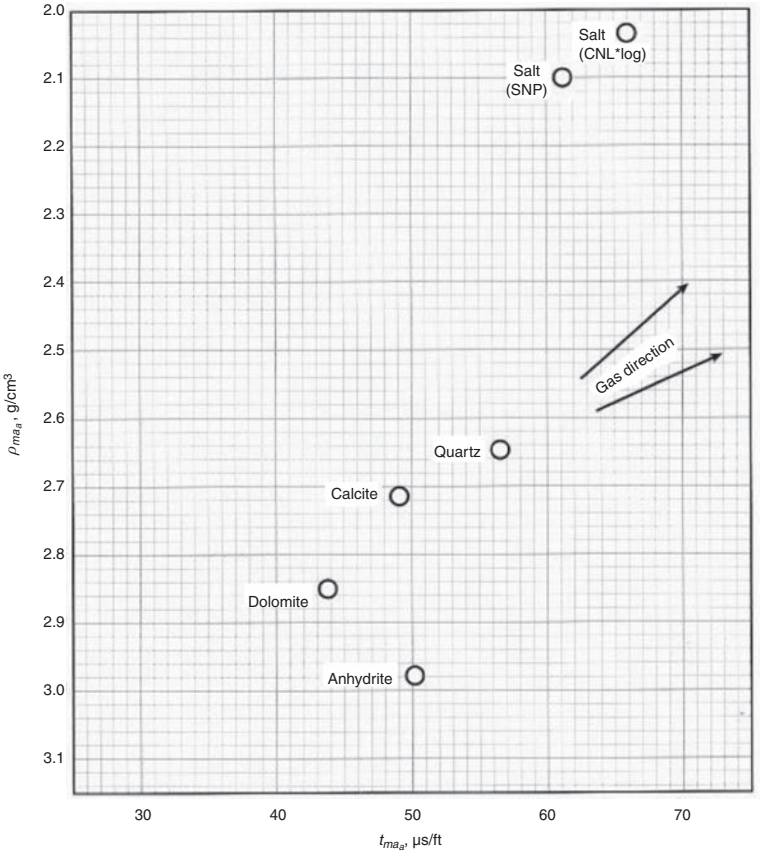


Fig. 24.9—MID plot (Schlumberger 2005b). Courtesy of Schlumberger.

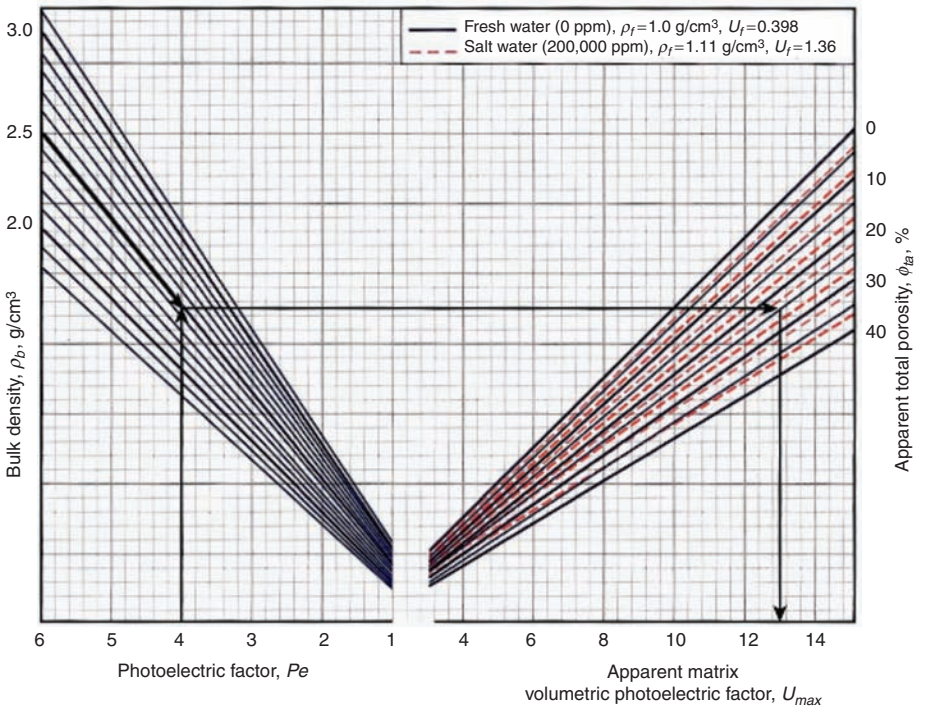


Fig. 24.10—Nomogram to determine U_{maa} from P_e, ρ_b, and ϕ_x (Schlumberger 2005b). Courtesy of Schlumberger.

TABLE 24.1—LITHOLOGY INDICATORS FOR COMMON MINERALS (Schlumberger 2005b)

Mineral	ρ_b	ρ_{ma}	ϕ_{CNL}	Δt_{ma}	M	N
Sand	2.65	2.648	–1.5	55.5	0.84	0.64
Limestone	2.71	2,710	0.0	47.5	0.85	0.60
Dolomite	2.87	2.876	2.5	43.5	0.80	0.53
Anhydrite	2.96	2.977	0.0	50.0	0.72	0.52
Halite	2.17	2.032	0.0	67.0	1.24	1.02
Sylvite	1.98	1.863	0.0	74.0	1.41	1.23
Gypsum	2.32	2.351	60	52.0	1.05	0.31

sum of the individual volumetric photoelectric absorption indices weighted by their relative proportions in the formation

$$U = U_1V_1 + U_2V_2 + ...U_nV_n, \quad \text{.....(24.7)}$$

where

U_n = volumetric photoelectric absorption index of mineral n,

V_n = volumetric fraction of mineral n in the formation,

For a porous single-mineral shaly formation containing hydrocarbons, a general equation can be written as

$$U = (1-\phi-V_{sh}) \times U_{ma} + \phi \times S_{xo} \times U_f + \phi(1-S_{xo}) \times U_{hy} + V_{sh} \times V_{sh}. \quad \text{.....(24.8)}$$

matrix term | water term | hydrocarbon term | shale term

TABLE 24.2—DENSITY AND PHOTOELECTRIC INDEX FOR COMMON MINERALS (Schlumberger 2005b)

Mineral	P_e	ρ_{maa}	U_{maa}	ρ_b	U
Dolomite	3.14	2.88	9.11	2.88	9.05
Limestone	5.08	2.71	13.78	2.71	13.78
Sandstone	1.81	2.65	4.79	2.65	4.79
Magnesite	0.83	3.00	2.50	2.98	2.47
Anhydrite	5.05	2.98	15.06	2.98	15.06
Gypsum	3.99	3.69	18.76	2.35	9.38
Halite	4.65	2.36	12.44	2.04	9.49
Sylvite	8.51	2.25	23.08	1.86	15.83
Chlorite*	6.30	3.39	23.63	2.76	17.39
Illite*	3.45	2.92	10.97	2.52	8.69
Kaolinite*	1.83	2.96	6.14	2.41	4.41
Montmorillonite*	2.04	2.89	7.29	2.12	4.32
Muscovite	2.40	2.97	7.35	2.82	6.77
Biotite	6.27	3.10	19.80	2.99	18.75
Glauconite*	6.37	3.05	21.52	2.54	16.18
Coal (bituminous)	0.17	1.99	0.87	1.24	0.21
Barite	267	4.09	1091	4.09	1091
Hematite	21.50	5.27	113.5	5.18	111.3
Freshwater	0.36			1.00	0.36
Salt water (330 ppk)	1.64			1.19	1.95
Oil	0.12			0.88	0.11

*Average values.

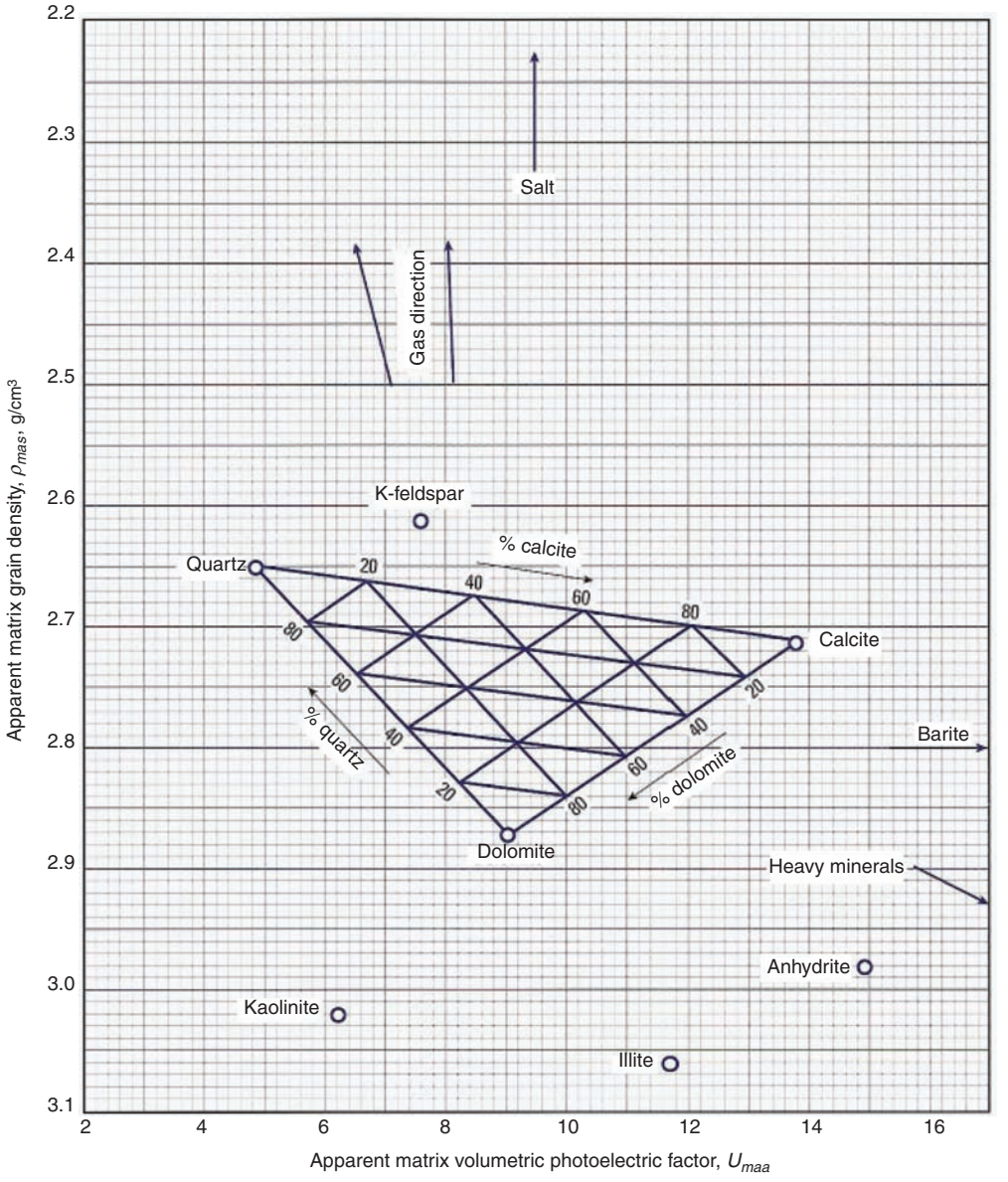


Fig. 24.11—Chart to determine lithology fractions from U_{maa}-ρ_{maa} crossplots (Schlumberger 2005b). Courtesy of Schlumberger.

It can be seen from the data in Table 24.2 that the absorption coefficient U_f of fresh water is substantially lower than any of the matrix coefficients U_{ma} and can, therefore, be neglected without introducing a major error. Only if very salty muds are used would the term need to be included. The hydrocarbon contribution can also be neglected because U_{hy} is less than 0.12. If the shale content of the formation is included in the matrix, the foregoing equations can be combined to produce the relationship:

$$U_{ma} = \frac{P_e \times \rho_e}{1-\phi} \quad \ldots\ldots\ldots\

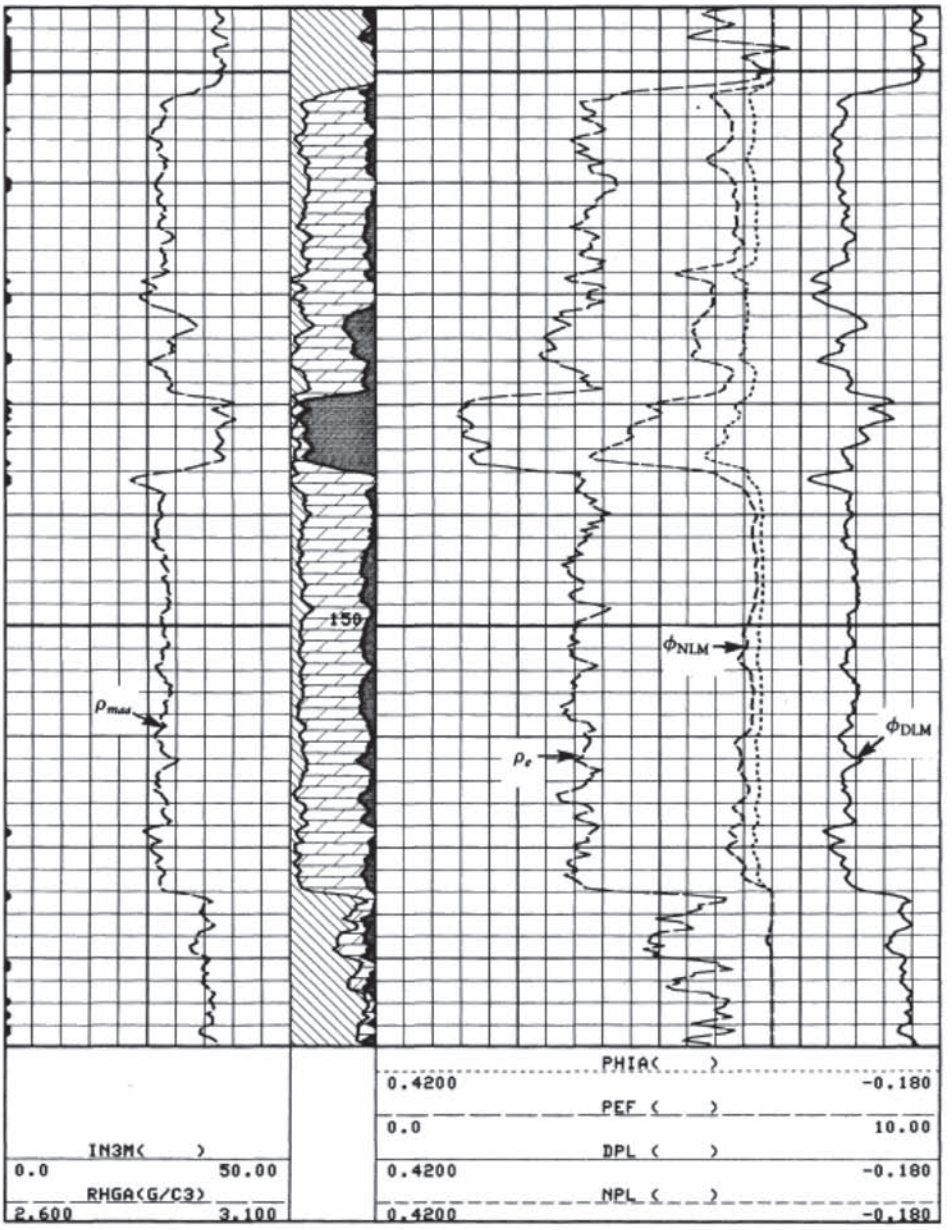


Fig. 24.12—Example of wellsite computation in mixed lithology.

This equation can be solved using the nomogram shown in **Fig. 24.10.** For a quick-look interpretation, the porosity ϕ can be taken from a neutron-density crossplot.

In complex lithology (a mixture of two or more minerals), a second physical parameter is needed to define the individual minerals and the volume percentage of each in the formation. The apparent matrix density ρ_{maa}, derived from the neutron-density crossplot, may be used and can be calculated using the standard formula:

$$\rho_{ma} = \frac{\rho_b - \phi_x \times \rho_f}{1 - \phi_x}, \quad \ldots\ldots\ldots\

where

ρ_f = fluid density in the invaded zone, and

ϕ_X = apparent porosity from the density and neutron data.

The apparent volumetric photoelectric absorption index of the matrix, U_{maa}, can be calculated for any mineral composition if the apparent porosity is used:

$$U_{maa} = \frac{P_e \times \rho_b}{1 - \phi_x} \quad \text{.....(24.11)}$$

Once the values of ρ_{maa} and U_{maa} have been calculated, they can be crossplotted against one another to help in identifying lithology. **Fig. 24.11** shows such a crossplot. Using known values for matrix parameters, an overlay can be constructed which, when placed over the crossplot, indicates the most probable mineral composition. Of course, geological knowledge and cuttings analysis are a substantial help in selecting the main contributing components. When the main mineral components of the formation have been identified, a plot can be constructed to determine their relative proportions. Fig. 24.11 is an example of a plot that is valid for a quartz/calcite/dolomite composition with a grid already established. Continuous computation of the relative proportions of up to three minerals is possible using this approach, as shown in the example illustrated in **Fig. 24.12.**

24.6.1 Limitations. Both gas in the formation pore space and barite in the mud have a marked effect on the measurements made by litho-density type tools. These effects can be detected on an U_{maa}-ρ_{maa} crossplot (see Fig. 24.11). Because of its high atomic number, barite moves the U_{maa} points toward the right (higher U_{maa}). Gas influences the ρ_{maa} values but has little effect on U_{maa}, and therefore moves the points upward. By picking the U_{maa} and ρ_{maa} values of the minerals according to the crossplots rather than using their theoretical values, the relative proportions of the three minerals can still be determined in some cases.

References

Schlumberger. 1976. *Well Evaluation Conference*: Iran.

Schlumberger. 1977. *Log Interpretation Charts*.

Schlumberger. 1982a. *Litho-Density Tool Interpretation*. M086108.

Schlumberger. 1982b. *Well Evaluation Developments: Continental Europe*.

Schlumberger. 2005a. *Historical Log Interpretation Charts*, 05-FE-006.

Schlumberger. 2005b. *Log Interpretation Charts*, 05-FE-007. Sugar Land, Texas: Schlumberger Marketing Communications.

General References

Burke, J.A., Campbell, R.L. Jr., and Schmidt, A.W. 1969. The Litho-Porosity Cross-Plot: A New Concept for Determining Porosity and Lithology From Logging Methods. *Trans.,* SPWLA 10th Annual Logging Symposium, Houston, 25–28 May, Paper Y.

Burke, J.A., Curtis, M.R., and Cox, J.T. 1966. Computer Processing of Log Data Improves Production in Chaveroo Field. Paper SPE 1576 presented at the SPE Annual Meeting, Dallas, 2–5 October. http://dx.doi.org/10.2118/1576-PA.

Clavier, C. and Rust, D.H. 1976. Mid Plot: A New Lithology Technique. *The Log Analyst* **17** (6): 16–24.

Edmundson, H. and Raymer, L.L. 1979. Radioactive Logging Parameters for Common Minerals. *Trans.,* SPWLA 20th Annual Logging Symposium, Tulsa, 3–6 June.

Gardner, J.S. and Dumanoir, J.L. 1980. Litho-Density Log Interpretation. *Trans.*, SPWLA 21st Annual Logging Symposium, Lafayette, Louisiana, USA, 8–11 July.

Nugent, W.H., Coates, G.R., and Peebler, R.P. 1978. A New Approach to Carbonate Analysis. *Trans.,* SPWLA 19th Annual Logging Symposium, El Paso, Texas, USA, 13–16 June.

Poupon, A., Hoyle, W.R., and Schmidt, A.W. 1971. Log Analysis in Formations With Complex Lithologies. *J. Pet Tech* **23** (8): 995–1005. http://dx.doi.org/10.2118/2925-PA.

Raymer, L.L. and Biggs, W.P. 1963. Matrix Characteristics Defined by Porosity Computations. *Trans.,* SPWLA 4th Annual Logging Symposium, Oklahoma City, Oklahoma, USA, May 23–24.

Savre, W.C. 1963. Determination of a More Accurate Porosity and Mineral Composition in Complex Lithologies With the Use of Sonic, Neutron, and Density Surveys. *J. Pet Tech* **15** (9): 945–959. http://dx.doi.org/10.2118/617-PA.

Schmidt, A.W., Land, A.G., Yunker, J.D., and Kilgore, E.C. 1971. Applications of the Coriband Technique to Complex Lithologies. *Trans.,* 12th Annual SPWLA Logging Symposium, Dallas, 2–5 May, Paper Z.

Serra, O. 1990. *Elemental Mineral Rock Catalog*. Schlumberger.

Tilly, H.P., Gallagher, B.J., and Taylor, T.D. 1982. Methods for Correcting Porosity Data in a Gypsum-Bearing Carbonate Reservoir. *J. Pet Tech* **34** (10): 2449–2454. http://dx.doi.org/10.2118/9716-PA.

Tixier, M.P. and Alger, R.P. 1968. Log Evaluation of Non-Metallic Mineral Deposits. *Trans.,* SPWLA 9th Annual Logging Symposium, New Orleans, 23–26 June, Paper R.

Answers to Questions

QUESTION 24.1. Dolomite.

QUESTION 24.2. Sandstone.

QUESTION 24.3. Sandstone.

QUESTION 24.4. Limestone (or is it sand and dolomite?).

QUESTION 24.5. Trona.

QUESTION 24.6. Anhydrite.

QUESTION 24.7.
a. M = 0.8.
c. N = 0.6.
f. Sand-dolomite mixture.

QUESTION 24.8.
$\rho_{maa} = 2.80$.
$\Delta t_{maa} = 46.0$.
Lime-dolomite mix.

Appendix

TABLE A-1—PHOTOELECTRIC FACTORS OF ELEMENTS AND MINERALS

Name	Formula	Molecular Weight	*Pe*	*Zeq*	*ρ*	*ρe*	*ρb*	*C*
Elements								
Hydrogen	H	1.000	0.00025	1				1.9840
Carbon	C	12.011	0.15898	6				0.991
Oxygen	O	16.000	0.44784	8				1.0000
Sodium	Na	22.991	1.4093	11				0.9566
Magnesium	Mg	24.320	1.9277	12				0.9868
Aluminum	Al	26.980	2.5715	13	2.700	2.602	2.596	0.9637
Silicon	Si	28.090	3.3579	14				0.9968
Sulfur	S	32.006	5.4304	16	2.070	2.066	2.022	0.9979
Chlorine	Cl	35.457	6.7549	17				0.9589
Potassium	K	39.100	10.081	19				0.9719
Calcium	Ca	40.080	12.126	20				0.9980
Titanium	Ti	47.900	17.089	22				0.9186
Iron	Fe	55.850	31.181	26				0.9311
Copper	Cu	63.500	43.500	29				
Strontium	Sr	87.630	122.240	38				0.8673
Zirconium	Zr	91.220	147.030	40				0.8770
Barium	Ba	137.360	496.720	56				0.8154
Minerals								
Anhydrite	$CaSO_4$	136.146	5.055	15.69	2.960	2.957	2.977	0.9989
Barite	$BaSO_4$	233.366	266.800	47.20	4.500	4.011		0.8913
Calcite	$CaCO_3$	100.090	5.084	15.71	2.710	2.708	2.710	0.991
Carnalite	KCl· MGC12· $6H_2O$	277.880	4.089	14.79	1.610	1.645	1.573	1.0220
Celestite	$SrSO_4$	183.696	55.130	30.40	3.960	3.708		0.9363
Corundum	Al_2O_3	101.960	1.552	11.30	3.970	3.894		0.9808
Dolomite	$CaCO_3$· $MgCO_3$	184.420	3.142	13.74	2.870	2.864	2.877	0.9977
Gypsum	$CaSO_4$· $2H_2O$	172.180	3.990	14.07	2.320	2.372	2.350	1.0222
Halite	NaCl	58.450	4.650	15.30	2.165	2.074	2.040	0.9580
Hematite	Fe_2O_3	159.700	21.480	23.45	5.240	4.987		0.9518
Ilmenite	$FeOTiO_2$	151.750	16.630	21.87	4.700	4.460		0.9489
Magnesite	$MgCO_3$	84.330	0.829	9.49	3.037	3.025	3.049	0.9961
Magnetite	Fe_3O_4	231.550	22.080	23.65	5.180	4.922		0.9501
Marcasite	FeS_2	119.980	16.970	21.970	4.875	4.708		0.9668
Pyrite	FeS_2	119.980	16.970	21.96	5.000	4.834		0.9668
Quartz	SiO_2	60.090	1.081	11.78	2.654	2.650	2.648	0.9985
Rutile	TiO_2	79.900	10.080	19.02	4.260	4.052		0.9512
Siderite	$FeCO_3$	115.860	14.690	21.09	3.940		3.890	
Sylvite	KCl	74.557	8.510	18.13	1.984	1.916	1.862	0.9657
Zircon	$ZrSiO_4$	183.310	69.100	32.45	4.560	4.279		0.9383

TABLE A-1—PHOTOELECTRIC FACTORS OF ELEMENTS AND MINERALS (CONT'D)

Name	Formula	Molecular Weight	*Pe*	*Zeq*	*ρ*	*ρe*	*ρb*	*C*
Liquids								
Water	H_2O	18.016	0.358	7.52	1.000	1.110	1.0000	1.1101
Salt water	(120,000 ppm)		0.807	9.42	1.068	1.185	1.0800	1.0918
Oil	CH_{16}		0.119	5.53	0.850	0.948	0.8260	1.1157
	CH_2		0.125	5.61	0.850	0.970	0.8800	1.1407
Misc.								
Berea sandstone			1.745	11.67	2.308	2.330	2.3050	0.9993
Pecos sandstone			2.700	13.18	2.394	2.414	2.3950	1.0000
Average shale			3.420	14.07	2.650	2.645	2.6420	0.9980
Anthracite coal	C:H:O = 95:3:4		0.161	6.02	1.700	1.749	1.6830	1.0287
Bituminous coal	C:H:O = 82:5:13		0.180	6.21	1.400	1.468	1.3830	1.0485

Chapter 25

R_w Determination

Until this point in the discussions, the value of R_w has been assumed. However, in many cases, its value cannot be assumed and must be found. Various methods are available for determining the resistivity of the formation water, R_w:

- Direct measurement of a water sample
- Computation from chemical analysis of a water sample
- Use of the SP
- The R_{wa} technique
- The ratio technique
- Various types of crossplots
- Use of overlays

The following is a detailed discussion of each of these means for finding the value of R_w.

25.1 Direct Measurement

Direct measurement of R_w from a water sample requires two things: an uncontaminated representative sample of formation fluid and a resistivity cell. The sample could come from:

a. A drillstem test
b. A wireline formation test
c. A produced sample collected at the separator

In all cases, collection of the water sample should be made in a clean, dry glass container that is stoppered to prevent evaporation. In cases (a) and (b), care should be taken to assure that the recovered sample is really formation water and not mud filtrate. A nitrate tracer added to the drilling mud is an easy way to distinguish drilling mud- or filtrate-contaminated samples from formation water. Nitrates are never found in natural formation water, so the presence of nitrate in a recovered water sample is indicative of contamination by mud filtrate. Normally, a concentration of 100 ppm NO_3 is maintained in the mud. Most mud companies are equipped to measure nitrate concentrations at and below this concentration.

Resistivity cells are found in laboratories, logging trucks, and mud loggers' briefcases. Mud loggers like the battery-operated type, which invariably have dead batteries, are usually out of calibration, and have very condensed scales that inhibit accurate measurement. Moreover, they operate on DC current and are prone to polarization effects. The resistivity cells in logging trucks are more sophisticated, accept larger samples of water, work on AC current, and can be calibrated before each reading. For these reasons, they are preferable for measuring R_w values.

The measurement will be in Ω·m at a given temperature. At 75°F (a normal ambient temperature), fresh waters have a resistivity ranging from half an ohm to several ohms, and brines have a resistivity of a tenth of an ohm or less. Seawater normally has a resistivity of 0.2 Ω·m. These figures are approximate. Conversion of a resistivity measured at one temperature to an equivalent resistivity at another temperature can be performed by use of **Fig. 25.1.** Note that this chart assumes a NaCl solution and may not be strictly valid for waters containing ions other than Na and Cl.

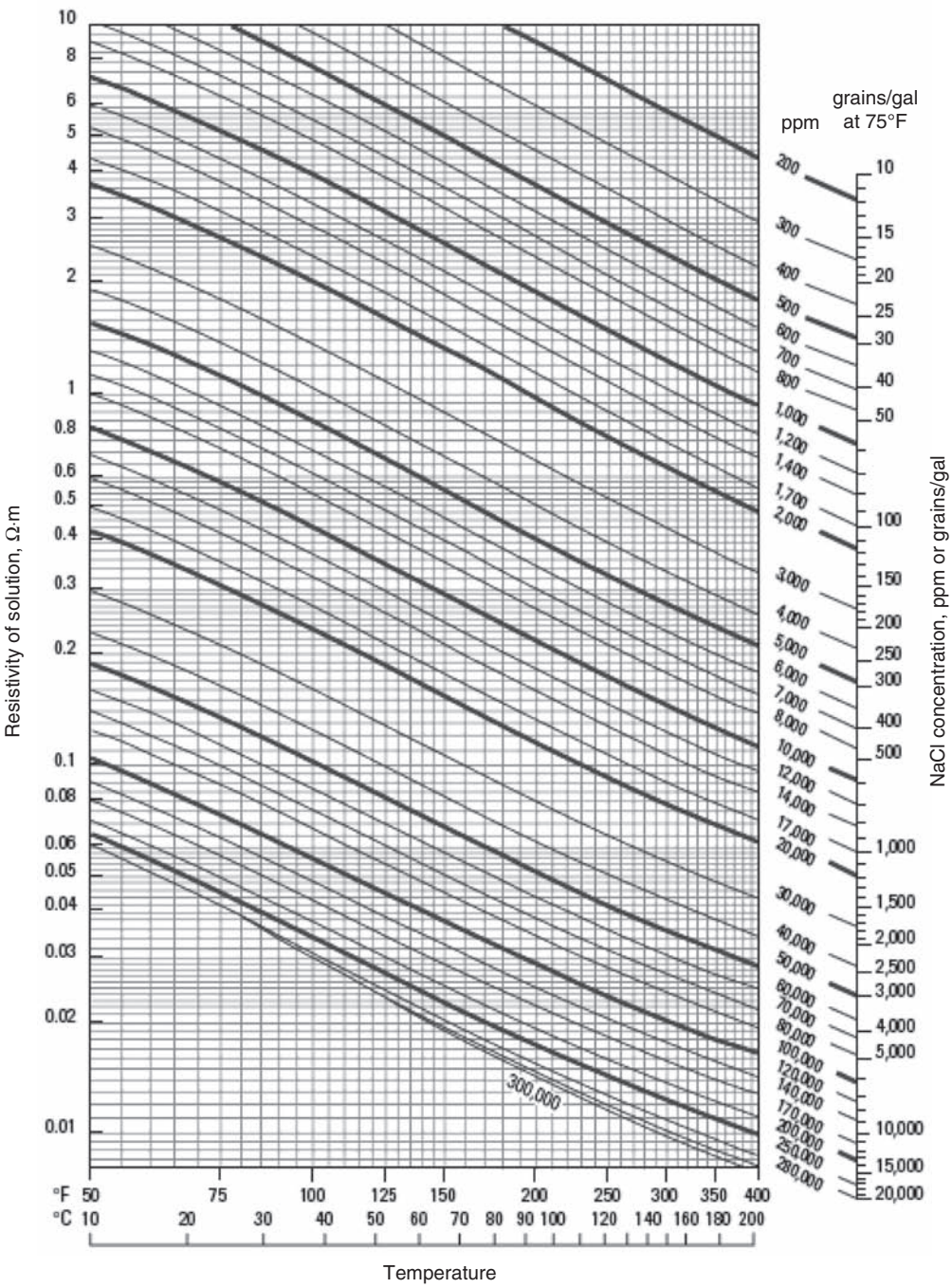


Fig. 25.1—Resistivity nomograph for NaCl solution (Schlumberger 2005). Courtesy of Schlumberger.

25.2 R_w Computed From Chemical Analysis

If Na^+ and Cl^- are the only ions present in a solution, computation of an R_w value is a simple matter. Fig. 25.1 can be used by entering the chart with a total NaCl concentration and a temperature and exiting with an R_w value in Ω·m.

QUESTION 25.1. An NaCl solution is shown by chemical analysis to contain 20,000 ppm NaCl. What is its resistivity at 175°F?

Titration-test results are frequently quoted as ppm of chlorides. This is merely an indication of the chemistry of the method used. To convert ppm of chlorides to the equivalent ppm of NaCl, the value of chlorides in ppm should be multiplied by 1.65.

QUESTION 25.2. A recovered DST water sample titrated out at 87,000 ppm chlorides.
a. What would be the equivalent ppm NaCl?
b. At 75°F, what resistivity would this solution exhibit?

When working with formation waters that contain ions other than Na^+ and Cl^-, the effect of these other ions on the electrical behavior of the electrolyte must be considered. The two factors that must be taken into consideration are (1) the charge carried by the ion and (2) its mobility through an electrolyte in the presence of an electric field. Obviously, a bivalent or trivalent ion carrying multiple charges (for example, calcium and magnesium ions carry two positive charges each) will contribute more conductivity than a monovalent ion such as Na^+ or Cl^-. However, these multivalent ions are normally surrounded by oppositely charged ions; for example, a Ca^{++} ion may be surrounded by a couple of OH^- (hydroxide) ions. These attached ions tend to slow down the Ca^{++} ion in its progress through the electrolyte. So even though a Ca^{++} ion delivers more charge per trip, it may end up making the trip through the electrolyte so slowly that a monovalent ion would do the charge-carrying job better because it moves more quickly.

These two opposing effects, charge-carrying capability and mobility (speed), are very sensitive to the total ionic concentration in the electrolyte. At low concentrations, the bivalent ions can move around freely and are better charge carriers than the monovalent ions. At high concentrations, the reverse is true. A practical method of dealing with this problem is to use multipliers for each ion to compute its effective charge-carrying power relative to Na^+ and Cl^-. In **Fig. 25.2,** the y-axis gives the value of the multiplier and the x-axis the total solids concentration in ppm. Lines on the chart show the behavior of each type of common ion found in naturally occurring waters.

Consider the following example: chemical analysis has revealed that a water sample contains the following ions at their respective concentrations **(Table 25.1).**

The first step is to find the total concentration in ppm, which is 46,000 for this water sample. On Fig. 25.2, a line can be drawn vertically through the point on the x-axis at 46,000 (46K) ppm. Where this line intersects the corresponding line for each ion present in the mixture, the multiplier can be read. The next step is to multiply each ion's concentration by its own multiplier **(Table 25.2).**

The effective concentrations are then summed. For the water in this example, the total ion concentration is 33,450 ppm. This value is the ppm of NaCl that would have the same electrical resistivity as the actual mixture of ions present in the formation water.

The final step is to determine the resistivity of the electrolyte solution containing these 33,450 ppm of equivalent NaCl ions. For example, R_w at 200°F is approximately 0.075 Ω·m (Fig. 25.1). If the actual concentrations of the ions had been used (without accounting for the ability of each individual ion to conduct electricity), an R_w value of 0.056 Ω·m would have been determined, resulting in an error of 25%.

Significant errors in determining R_w values for formation waters frequently occur (a) in formations in or near evaporites or carbonate formations, and (b) in shallow freshwater formations,

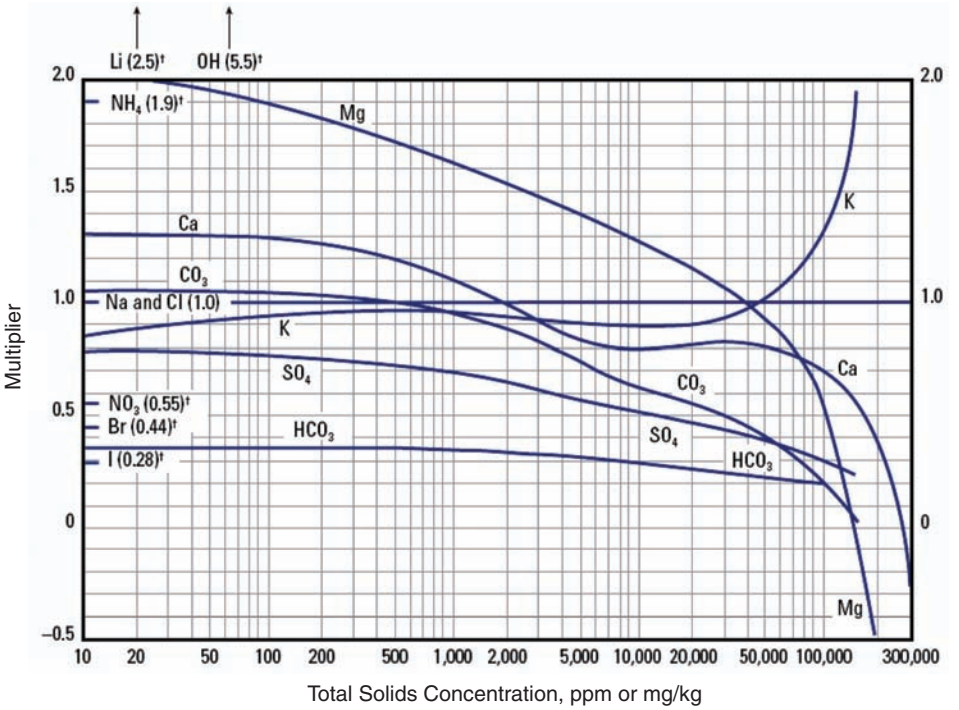


Fig. 25.2—Multipliers and total solids concentrations for various ions (Schlumberger 2005). Courtesy of Schlumberger.

TABLE 25.1—IONIC CONCENTRATION IN A SAMPLE SOLUTION

Ion	Symbol	Concentration (ppm)
Sodium and chloride	Na^+ and Cl^-	25,000
Carbonate	CO_3^{--}	2,000
Sulfate	SO_4^{--}	5,000
Bicarbonate	HCO_3^-	10,000
Magnesium	Mg^{++}	4,000
Total		**46,000**

TABLE 25.2—MULTIPLIERS AND EFFECTIVE CONCENTRATIONS

Ion	Concentration (ppm)	Multiplier	Effective Concentration
Sodium and chloride	25,000	1.00	25,000
Carbonate	2,000	0.40	800
Sulfate	5,000	0.37	1,850
Bicarbonate	10,000	0.20	2,000
Magnesium	4,000	0.95	3,800
Total	**46,000**		**33,450**

especially near mountains. When drilling in an area where evaporites and carbonate formations occur, for example, a recovered water sample may be classified as a "saturated brine"; R_w will be calculated at 0.015 Ω·m on the assumption that the only ions present are Na^+ and Cl^-, and using this low R_w value, log evaluation will indicate the presence of oil in numerous formations. Therefore, numerous drillstem tests will be planned. Then, one after the other, all the formations will produce only water during the DSTs. After much head scratching, it dawns on the eager engineer that something went wrong.

To understand the effect of carbonates on R_w, the behavior of Mg^{++} and Ca^{++} ions must be considered. At a total concentration of 200,000 ppm, the Mg^{++} multiplier is a *negative* value (–0.65), and the Ca^{++} multiplier is only 0.35, as shown in **Table 25.3.** Assuming that this solution has the concentrations of ions given in Table 25.3, the effective NaCl ppm can be computed using the appropriate multipliers:

The effective NaCl equivalent concentration is only 85,000 ppm. For a formation temperature of 240°F, the correct R_w is 0.029 Ω·m instead of the 0.015 originally computed. The effect of carbonates on the computation of water saturation is dramatic. Formations where water saturation was calculated to be 40% using an R_w value of 0.015 will have a calculated value of 56% using an R_w value of 0.029.

The problem with freshwater-bearing formations is different. A frequently found component in fresh formation water is the bicarbonate ion, HCO_3^-. Its multiplier remains less than 1.00 throughout the range of normal formation waters. For example, consider a freshwater sample reported as having a total ion content of 5,000 ppm. Based on the assumption of NaCl content only, such a solution would be expected to have a resistivity of 0.56 Ω·m at 150°F. If half the ions present are bicarbonate ions, however, the situation changes radically, as shown in **Table 25.4.**

The resistivity of a 3,250 ppm NaCl solution at 150°F is 0.85 Ω·m, or 52% higher than would be expected on the assumption that sodium and chloride were the only ions present.

The bivalent cations Mg^{++} and Ca^{++} can also occur in fresh waters. In dilute solutions, these ions can cause difficulties because they are very good charge carriers and create massive SP deflections. Thus, they cause R_w values to appear too low.

In summary, NaCl is not the only substance found in formation waters. Other ions, even in small concentrations, can alter the resistivity characteristics of the water. To account adequately for these other ions, a chemical analysis is required. The effect of bivalent cations at high concentrations (total ppm) is to make a solution less conductive (to raise R_w). At low total concentrations, bivalent cations have the reverse effect and make a solution more conductive (they lower R_w). Bicarbonates always reduce conductivity (they raise R_w).

TABLE 25.3—EFFECTIVE CONCENTRATIONS IN HIGH SALINITY BRINES

Ion	Concentration (ppm)	Multiplier	Effective Concentration
Na^+ and Cl^-	100,000	1.00	100,000
Ca^{++}	50,000	0.35	17,500
Mg^{++}	50,000	–0.65	–32,500
Total	**200,000**		**85,000**

TABLE 25.4—EFFECTIVE CONCENTRATIONS AT LOW SALINITIES

Ion	ppm	Multiplier	Equivalent ppm NaCl
HCO_3^-	2,500	0.30	750
Na^+ and Cl^-	2,500	1.00	2,500
Total	**5,000**		**3,250**

25.3 R_w From the SP

This subject has been dealt with extensively in Chapter 9. However, one aspect of R_w determination from the SP will be enlarged on here. It is common practice to drill wells using potassium-based muds, mainly for control of problem shales. In these cases, conventional SP charts and nomograms are no longer applicable because the electrochemical properties of KCl are not the same as those of NaCl. When faced with this situation, the analyst should use **Fig. 25.3** to estimate R_{mfe} and **Fig. 25.4** to estimate the R_{mfe}/R_{we} ratio from the SP deflection.

QUESTION 25.3. A well is drilled with KCl mud.
R_{mf} at formation temperature of 200°F is 0.28.
The SP development is –40 mV.
Calculate R_w at formation temperature, assuming that connate water is an NaCl solution.

25.4 The R_{wa} Method

The R_{wa} technique relies on Archie's relationship:

$$S_w^n = F\,R_w/R_t \quad \ldots\ldots\ldots\

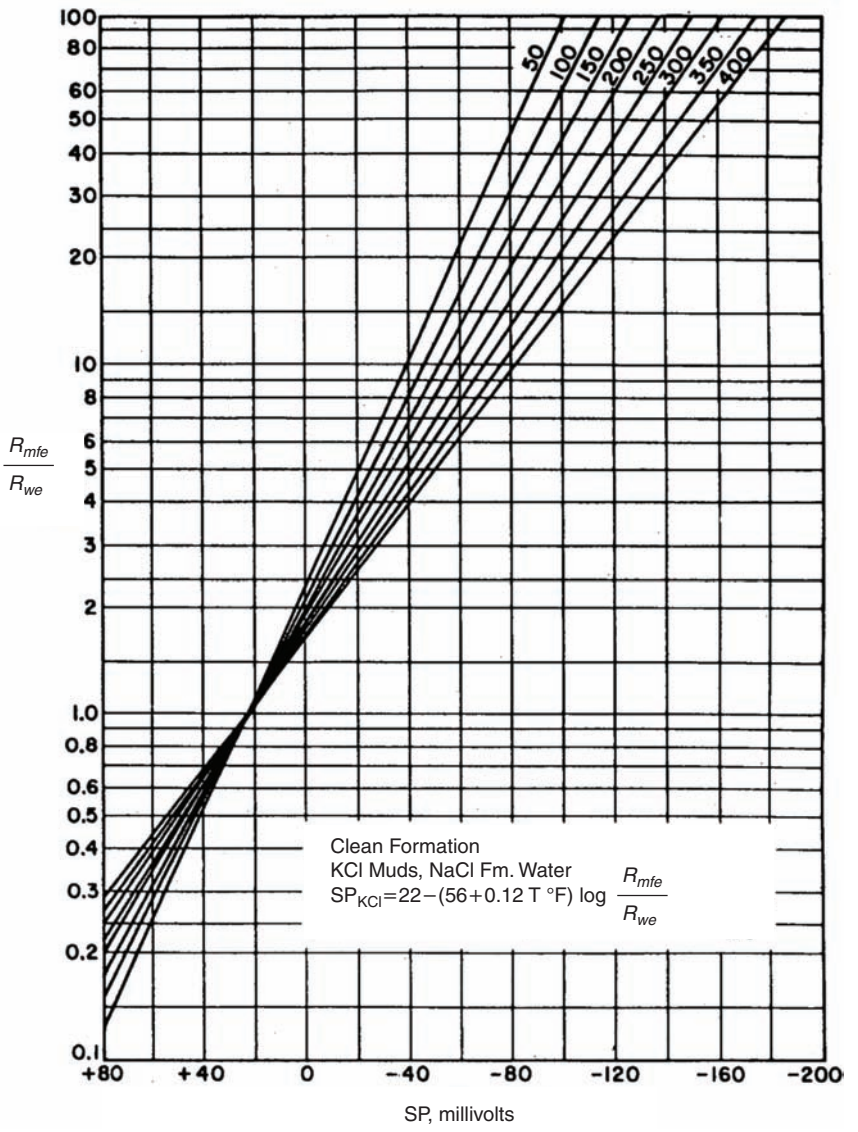


Fig. 25.4—SP vs. R_{mfe}/R_{we} for KCl muds (Cox and Raymer 1976). Reprinted by permission from the SPWLA.

With a little rearranging, this equation can be written as:

$$R_w = R_t S_w / F. \quad \ldots\ldots\ldots\

Remembering the relationship between F and ϕ,

$$F = a/\phi^m \quad (25.4)$$

Substitution into Archie's equation results in an expression for R_{wa} in terms of porosity:

$$R_{wa} = \phi^m R_t / a \quad (25.5)$$

The simplest form of this equation for use on a calculator is

$$R_{wa} = \phi^2 R_t, \quad (25.6)$$

where m is assumed equal to 2 and a equal to 1.

QUESTION 25.4. Table 25.5 lists porosities and resistivities as depth increases through a zone. Compute R_{wa} at each level, assuming $R_{wa} = \phi^2 R_t$, and pick a minimum value for R_w. Remember that the formula for R_{wa} expects the porosity to be expressed as a fraction of 1.

The question then arises of which porosity device one should use. What about shale effects and the influence of filtrate invasion on R_t? Usually the choice will be between a neutron porosity log and a density porosity log. Shale will generally cause neutron porosity to read higher than true porosity, and the presence of shale will generally reduce the resistivity of a formation. Therefore, a combination of the two is to some extent self-compensating. A neutron-derived R_{wa} value is referred to as an $R_{wa\text{-}N}$ value. In pure shale beds, R_{wa} may compute *lower* than R_w. Distinguishing these spuriously low values of R_{wa} from legitimate measurements requires some independent indicator of shale, such as a gamma ray curve.

The R_{wa} technique is most easily applied by computing R_{wa} over long intervals of logs and reviewing the analog printout of the resulting curve. This approach calls for a computer. Modern computerized logging trucks can generate this curve during the logging run. The R_{wa} plot is a very useful quick-look tool. Not only is it simple to find R_w but also quick estimates of S_w can be made. Minor rearrangement of Archie's equation will suffice to show that

$$S_w^n = R_w / R_{wa} \quad (25.7)$$

Therefore, if the logged section includes both a water-bearing interval and a hydrocarbon-bearing interval, it is a simple matter to compute water saturation.

TABLE 25.5—DATA FOR R_{wa} EXERCISE

Level	Porosity (%)	R_t	R_{wa}
1	23	19.5	
2	17	36	
3	19	18	
4	22	6.5	
5	18	5.5	
6	20	4	
7	16	6.5	

QUESTION 25.5.

a. Inspect the logs shown in **Fig. 25.5.**

b. Identify a wet interval and read the minimum value of R_{wa}.

c. Find a hydrocarbon-bearing interval and compute S_w.

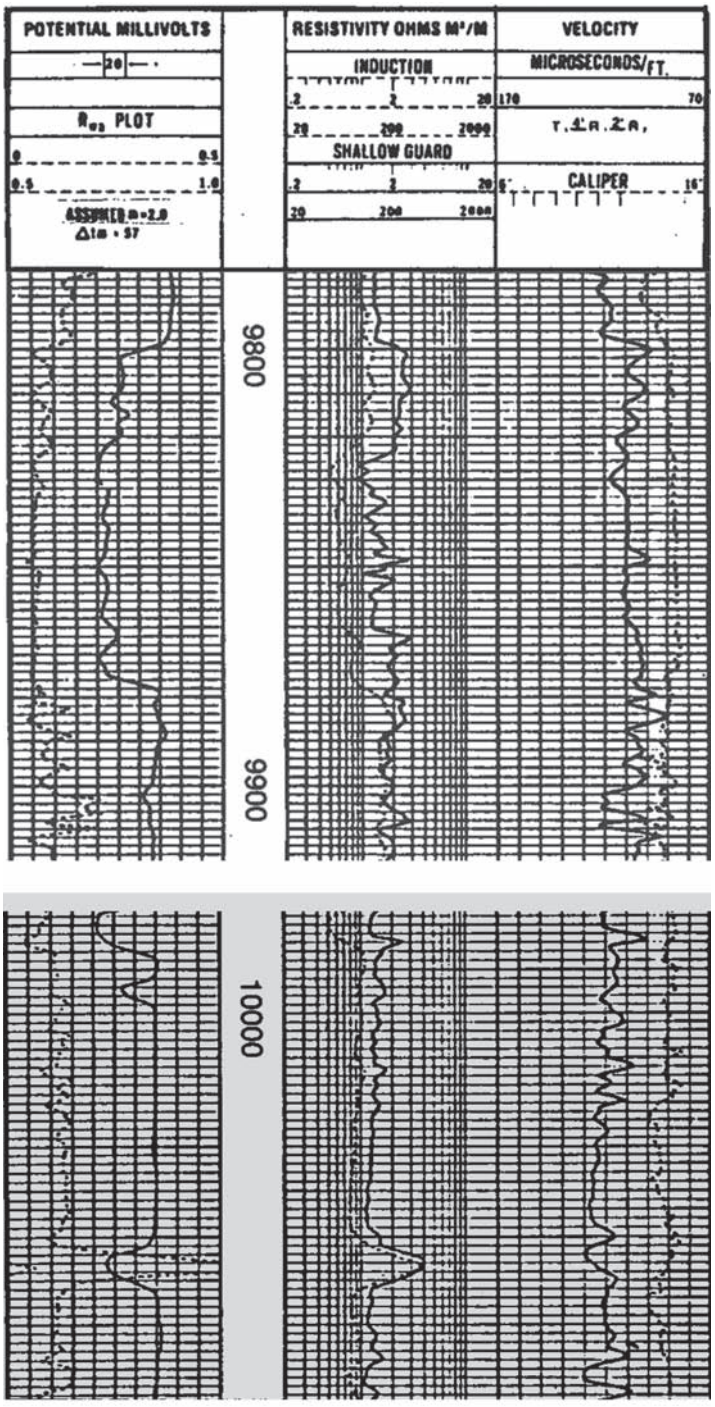


Fig. 25.5—Example of a continuous R_{wa} plot.

25.5 The Ratio Technique

The ratio technique is fairly easy to use because it eliminates the need to know every variable. The equation for water saturation in the undisturbed portion of the formation is:

$$S_w^n = F\left(R_w/R_t\right), \quad (25.8)$$

and in the zone invaded by the drilling-mud filtrate, the equation is:

$$S_{xo}^n = F\left(R_{mf}/R_{xo}\right). \quad (25.9)$$

If only 100% water-saturated zones are considered, then $S_w = S_{xo} = 1$. By taking a ratio of the two above equations, the need to know F is eliminated, and

$$R_{mf}/R_w = R_{xo}/R_t. \quad (25.10)$$

and, therefore,

$$R_w = R_{mf}\left(R_t/R_{xo}\right) \quad (25.11)$$

If reliable values of R_t, R_{xo}, and R_{mf} are available, a value of R_w can be determined. Provided that invasion effects do not materially affect the R_t and R_{xo} measurements made by the deep and shallow investigation resistivity devices, the technique works well and has the advantage of being independent of porosity.

QUESTION 25.6. If R_{mf} (at 80°F) = 0.15 Ω·m,
T_{form} = 175°F,
R_t = 2.5 Ω·m, and
R_{xo} = 1.5 Ω·m,
find R_w at formation temperature.

25.6 R_w From Crossplots

The use of crossplots can also give good indications of R_w. Again, Archie's relation can be modified to produce a workable system. Some analysts favor plots on linear axes and others plots on logarithmic axes. Both types will be covered here.

25.6.1 Linear Crossplots. Archie's equation may be rearranged to read

$$1/R_t = S_w^n \phi^m / aR_w \quad (25.12)$$

If $n = m = 2$, then

$$\sqrt{1/R_t} = S_w\phi/\sqrt{a/R_w} \quad (25.13)$$

Therefore, in a 100% water-bearing interval, a plot of $\sqrt{1/R_t}$ vs. ϕ will produce a straight line of slope $\sqrt{1/aR_w}$, as shown in **Fig. 25.6.**

Because the parameter $\sqrt{1/R_t}$ is rather awkward to handle, special sheets of graph paper can be prepared with a reciprocal root scale already marked (see **Fig. 25.7**). This method is referred

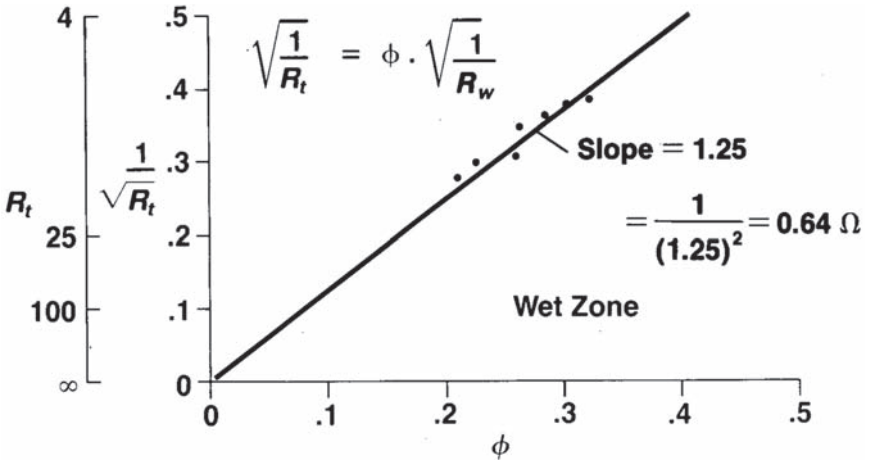


Fig. 25.6—Plot of ϕ against $\sqrt{1/R_t}$ in wet zone.

to as the Hingle plot. The practical procedure is straightforward; points are taken at regular intervals over the gross thickness of a formation and plotted for both oil- and water-bearing sections. A water-bearing line is drawn from the origin $\sqrt{1/R_t} = 0$, $\phi = 0$, through the most northwesterly points plotted. The slope of this line determines R_w. Note that only water-bearing points will fall on a line. Points for which S_w is less than 1 will fall below the line. This kind of plot has two other uses, which will be discussed later: saturation determination and matrix response for the porosity tool involved.

QUESTION 25.7. Plot the following points from Table 25.6 on Fig. 25.7 and deduce R_w.

R_w is determined by calculating the square of the porosity value (expressed as a fraction) corresponding to an R_t value of 1. If this does not fall conveniently on the graph, R_w can equally be well determined by calculating 10 times the square of the porosity corresponding to an R_t value of 10.

25.6.2 Logarithmic Plots. Archie's equation may equally well be written in logarithmic form such that:

$$n \log S_w = \log a + \log R_w - m \log \phi - \log R_t, \quad \ldots\ldots\ldots\

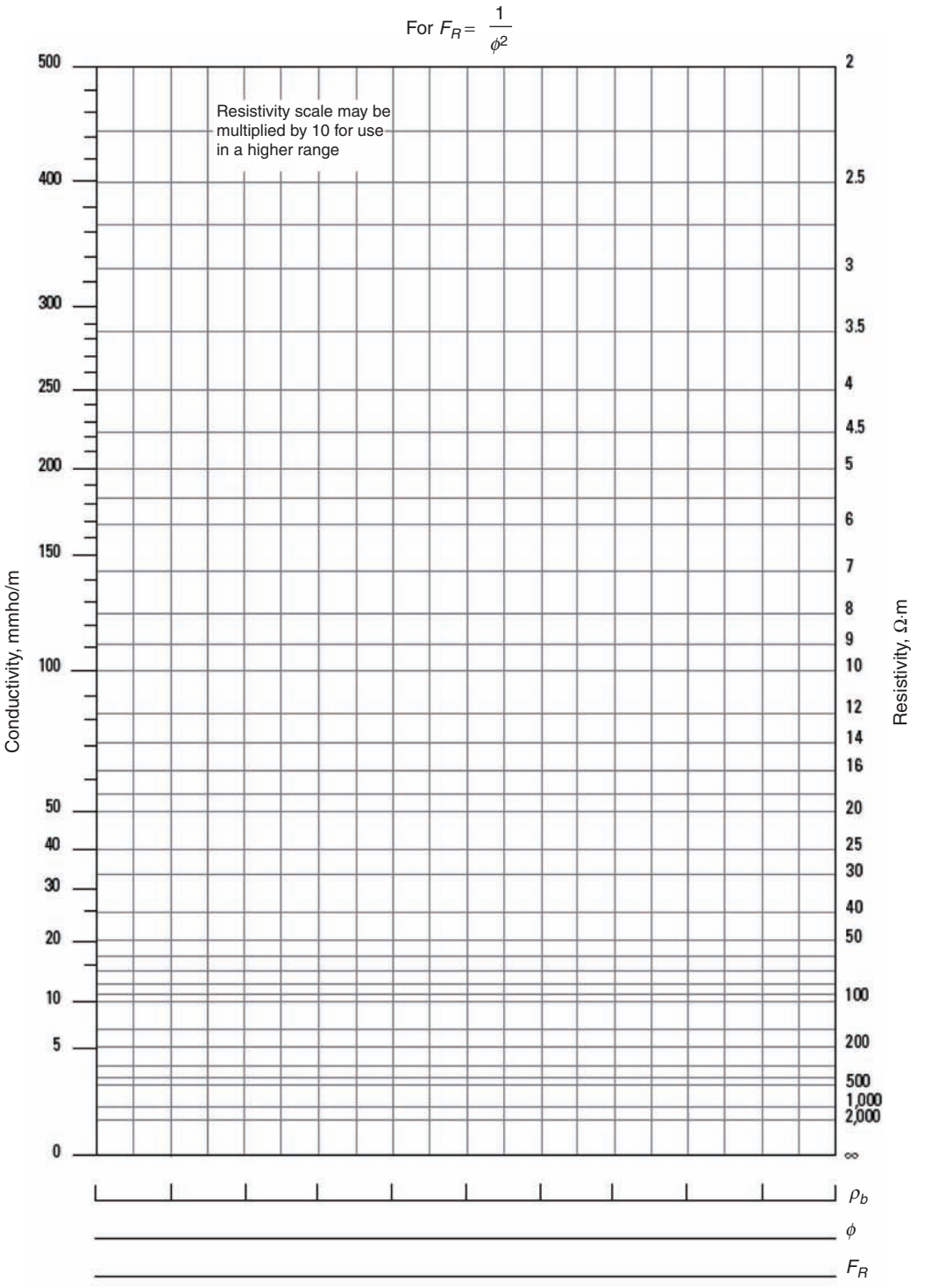


Fig. 25.7—Specially scaled graph paper for plotting $\sqrt{1/R_t}$ vs. ε (Schlumberger 2005). Courtesy of Schlumberger.

TABLE 25.6—DATA FOR HINGLE PLOT	
ϕ (%)	R_t ($\Omega m^2/m$)
19	4.2
15	6.7
12	10.4
17	5.2
13	8.9
18	4.6
14	7.7
16	5.9

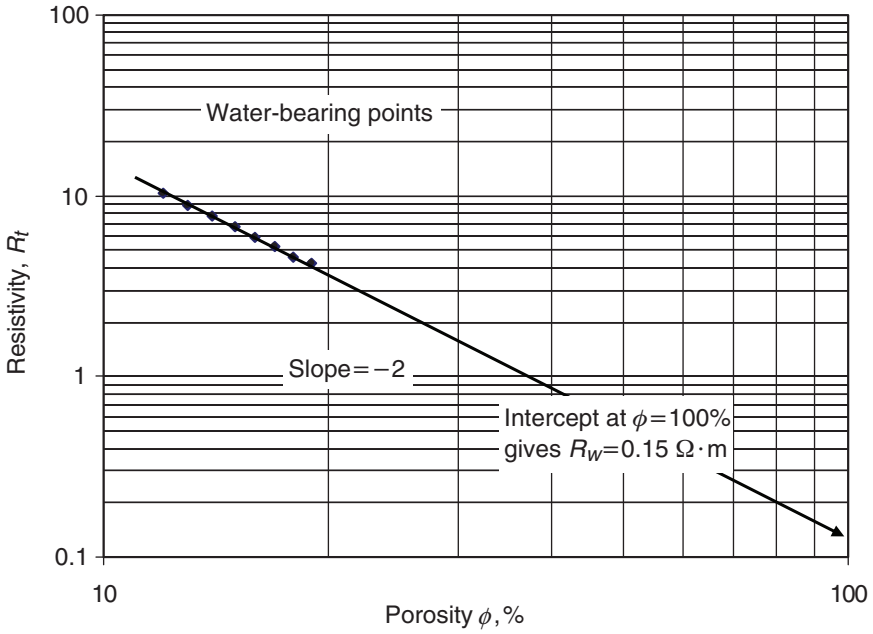


Fig. 25.8—Plot of log ε vs. log R_t for R_w determination.

If $S_w = 1$, then $\log S_w = 0$, and therefore,

$$\log R_w = \log R_t - \log F \quad \ldots\ldots\ldots\

R_w in various formations. For the explorer in a wildcat situation, an R_w catalog will not be of any great use.

References

Cox, J.W. and Raymer, L.L. 1976. The Effect of Potassium Salt Muds on Gamma Ray and Spontaneous Potential Measurements. *Trans.,* SPWLA 17th Annual Logging Symposium, Denver, 9–12 June.

Schlumberger. 2005. *Log Interpretation Charts*, 05-FE-007. Sugar Land, Texas: Schlumberger Marketing Communications.

General References

Desai, K.P. and Moore, E.J. 1969. Equivalent NaCl Concentrations From Ionic Concentrations. *The Log Analyst* **10** (30): 12–21.

Gondouin, M., Tixier, M.P., and Simard, G.L. 1957. An Experimental Study on the Influence of the Chemical Composition of Electrolytes on the SP Curve. SPE-657-G. *Trans.,* AIME **210:** 58–72.

Lowe, T.A. and Dunlap, H.F. 1986. Estimation of Mud Filtrate Resistivity in Fresh Water Drilling Muds. *The Log Analyst* **27** (2): 77–84.

Answers to Questions

QUESTION 25.1.
0.13 $\Omega \cdot m^2/m$.

QUESTION 25.2.
a. 143,550 ppm NaCl.
b. 0.59 $\Omega \cdot m^2/m$.

QUESTION 25.3.
0.065 $\Omega \cdot m^2/m$ at 200°F.

QUESTION 25.4.
0.160 $\Omega \cdot m^2/m$.

QUESTION 25.5.
a. Wet zone 9,800 to 9,880 ft
$R_w = 0.05\ \Omega \cdot m^2/m$.
b. Pay zone 10,052 to 10,060 ft
$R_{wa} = 0.55\ \Omega \cdot m^2/m$.
$S_w = 30\%$.

QUESTION 25.6.
0.12 $\Omega \cdot m^2/m$

QUESTION 25.7.
0.15 $\Omega\, m^2/m$.

Chapter 26

Water Saturation

This chapter will review in detail various methods of determining the water saturation of a rock system. Water saturation can be used to determine whether hydrocarbon production is probable and to calculate the volume of oil in a unit volume of rock (e.g., how many barrels per acre).

Water saturation (S_w) is defined as the fraction of the pore volume occupied by water. This is shown schematically in **Fig. 26.1.** The actual bulk volume of water in a unit volume of porous rock is given by the product $\phi\, S_w$, and the bulk volume of hydrocarbons is given by $\phi\,(1-S_w)$. This latter value is also referred to as the hydrocarbon pore volume (HCPV).

QUESTION 26.1. A rock sample has a volume of 100 cm^3. It contains 30 cm^3 of pore space, of which 10 cm^3 is occupied by water.

a. What is the porosity (ϕ)? $\phi =$

b. What is the water saturation (S_w)? $S_w =$

c. What is the hydrocarbon pore volume? HCPV =

26.1 Methods Available To Determine S_w

Many methods are available for finding the water saturation of a rock sample. They include

- Core analysis
- Dielectric measurements
- Nuclear measurements
- Archie's equation
- The ratio technique (SP vs. R_{xo}/R_t)
- Crossplots
- F overlays
- Shaly sand methods

26.1.1 Core Analysis. Core analysis is covered in detail in Chapter 27; however, it is worthwhile to mention here, in the context of water-saturation determination, that generally only native-state cores can be relied on to provide representative figures for S_w. It is perhaps equally important to mention the role of permeability measurements from cores. As will be discussed in Chapter 28, many low-resistivity pay sections with very high apparent water saturations do in fact produce water-free hydrocarbons. In general, these are formations of low permeability. These troublesome formations can be evaluated properly through adequate core analysis.

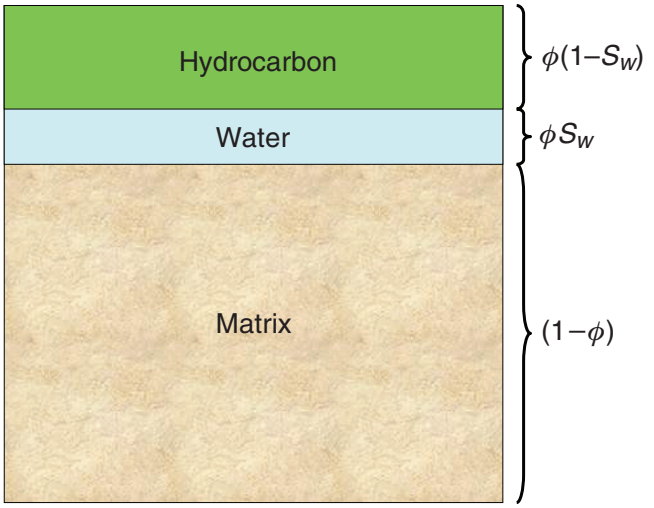


Fig. 26.1—Definition of water saturation.

26.1.2 Dielectric Measurements. Dielectric measurements include logging measurements, such as the EPT covered in Chapter 15, and also measurements made on cores using laboratory apparatus. These methods will not be covered here in detail. However, it should be noted that wireline dielectric-type logging tools may record at two or more different frequencies and with two or more transmitter/receiver spacings. As a result, the depth of investigation of these tools may vary from the S_{xo} zone, very close to the wellbore, outward toward the undisturbed zone where the saturation is closer to S_w than to S_{xo}. Therefore, although dielectric measurements have traditionally been associated with finding S_{xo}, this should not necessarily be assumed with the more complex tools now available.

26.1.3 Nuclear Methods. Nuclear methods include log measurements from pulsed neutron logs of the thermal neutron-capture cross section (Σ) of the formation and inelastic gamma ray measurements from carbon/oxygen logs. These measurements are commonly made in cased holes and are covered in Bateman (1985).

26.2 The Basic Method: Archie's Equation

Archie (1942) combined three measurable observations into one equation.* By saturating a rock sample with salt solutions of different salinities, he found that the resistivity of the wet (water-saturated) rock (R_o) was related to the resistivity of the saturating water (R_w) by the relation:

$$R_o = FR_w, \quad \ldots\ldots\ldots\

$$S_w^n = R_o/R_t, \quad \ldots\ldots (26.3)$$

where n is the *saturation exponent*. A combination of these relationships gives Archie's equation:

$$S_w^n = \frac{aR_w}{\phi^m R_t} \quad \ldots\ldots (26.4)$$

The values of a, m, and n, when they are unknown, can be set to the following generally accepted values (although for serious petrophysical analysis, they should be determined by core analysis):

Sandstones:	$a = 0.81$	$m = 2$	$n = 2$ or less
or	$a = 0.62$	$m = 2.15$	$n = 2$ or less
Carbonates:	$a = 1$	$m = 2$	$n = 2$ or more

Thus, three commonly used versions of Archie's equation are:

$$\text{Sandstones: } S_w = \left(\frac{0.81R_w}{\phi^2 R_t}\right)^{1/2} \quad \ldots\ldots (26.5)$$

$$\text{or } S_w = \left(\frac{0.62R_w}{\phi^{2.15} R_t}\right)^{1/2}; \quad \ldots\ldots (26.6)$$

$$\text{Carbonates: } S_w = \left(\frac{R_w}{\phi^2 R_t}\right)^{1/2} \quad \ldots\ldots (26.7)$$

The analyst should avoid a mindset that locks the conventional values for a, m, and n into any and all log analysis evaluations. Some crossplot methods enable one or another of these parameters to be deduced, but there is no substitute for rigorous core analysis to pin down the precise values required for each reservoir unit.

26.3 The Saturation Exponent *n*

While n is usually assumed to be two, its exact value may vary depending on the wettability of the rock. Oil-wet systems usually exhibit an n greater than two. Some water-wet systems show an n less than two. To find n, a core sample is prepared at a number of different water saturations, and for each saturation, the ratio of R_o to R_t is determined. By taking the logarithm of Archie's equation, it is transformed into:

$$n \log S_w = \log\left(R_o/R_t\right) \quad \ldots\ldots (26.8)$$

Therefore, a plot of log (S_w) vs. log (R_o/R_t) should produce a straight line of slope n. **Fig. 26.2** illustrates the method.*

QUESTION 26.2. A core from the Fubar formation was measured in the laboratory to have the following resistivities and saturations:

S_w	R_t
100%	1.00
75%	1.73
50%	3.73
25%	14.0

Plot these results on the log-log graph paper of **Fig. 26.3** and find the value of n.

---

*See also discussions in Chapter 27.

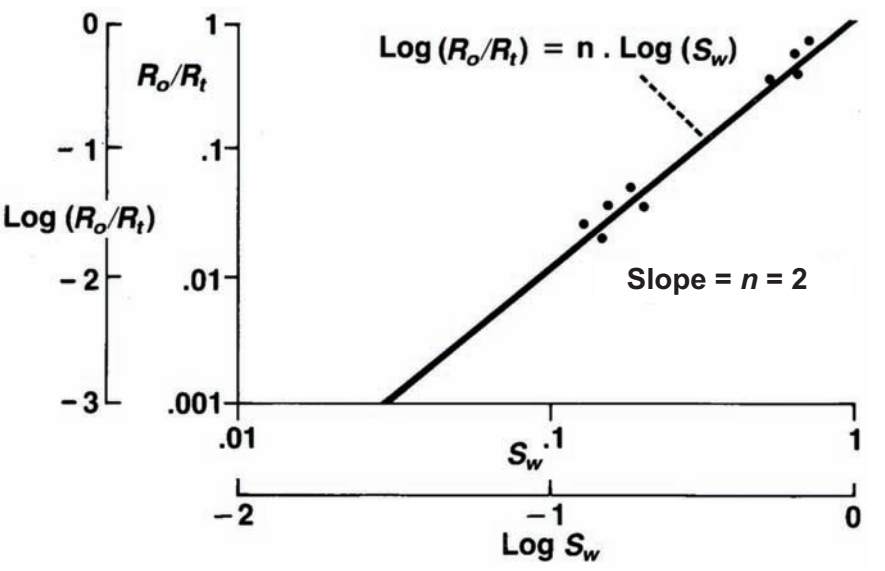


Fig. 26.2—Determination of saturation exponent *n*.

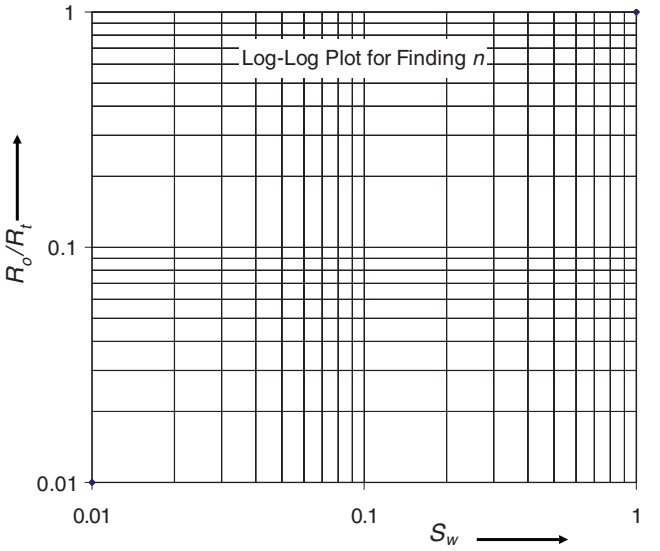


Fig. 26.3—Determination of *n* from core analysis.

It is worthwhile to explore the sensitivity of S_w to the value of n. Suppose that a calculation of S_w is made using $n = 2$ and that the resulting value of S_w is 0.5, or 50%. It can then be deduced that:

$$S_w = \left(\frac{FR_w}{R_t}\right)^{1/2} = 0.5 \quad \ldots\ldots (26.9)$$

and hence that

$$\left(\frac{FR_w}{R_t}\right) = 0.5^2 = 0.25 \quad \ldots\ldots (26.10)$$

Having determined that FR_w/R_t is 0.25, it is now possible to play a "what-if" game and to explore the results of increasing n to, say, 2.2:

$$S_w = \left(\frac{FR_w}{R_t}\right)^{1/2.2} = (0.25)^{1/2.2} = 0.533 \quad \text{or} \quad 53.3\% \ldots\ldots (26.11)$$

Decreasing n to, say, 1.7 gives

$$S_w = (0.25)^{1/1.7} = 0.442 \quad \text{or} \quad 44.2\% \ldots\ldots (26.12)$$

In summary, other factors remaining the same, raising n raises S_w, and conversely, lowering n lowers S_w.

26.4 Formation Factor and Porosity: Finding *a* and *m*

Each rock type has its characteristic formation factor vs. porosity relationship. Core measurements to determine this relationship require a range of core samples of different porosities. At each porosity, a measurement is made of R_o, the resistivity of the rock at 100% water saturation. If the value of R_w is known, the formation factor F can be deduced by use of the definition $F = R_o/R_w$. Note that the solution used to saturate the core should be of the same NaCl concentration as the connate water found in the formation. By taking the logarithm of both sides of the equation relating formation factor to porosity, the result is

$$\log F = \log a - m \log \phi \ldots\ldots (26.13)$$

Thus, a plot of log (F) vs. log (ϕ) should give a line of slope $-m$ and an intercept at $\phi = 1$ of a (see **Fig. 26.4**).

QUESTION 26.3. Use the following measurements of F and ϕ to deduce a and m by plotting the points on **Fig. 26.5.**

ϕ	F
32	9.8
27	14.1
22	21.6
17.5	35.0
12	77.3

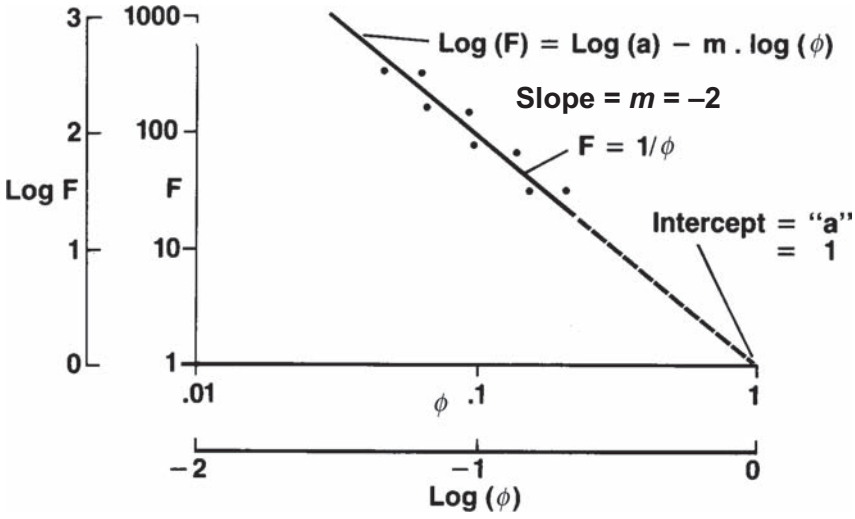


Fig. 26.4—Determination of *a* and *m*.

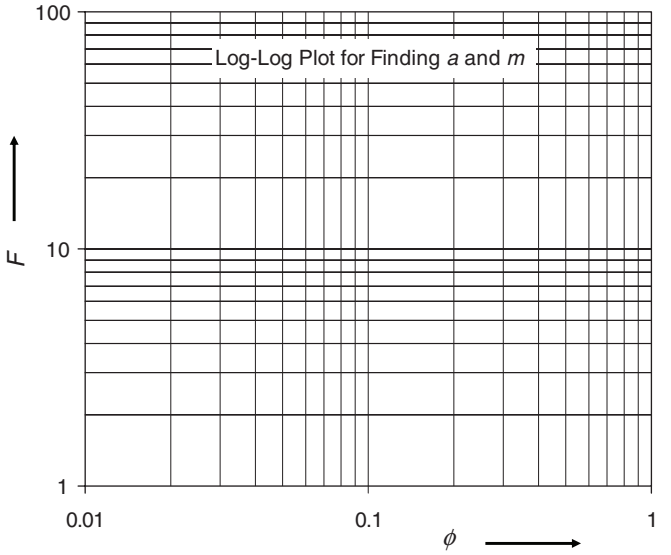


Fig. 26.5—Determination of *a* and *m* from core analysis.

Various formation-factor/porosity relationships have been proposed, such as the Shell formula for low-porosity carbonates, which boosts the value of m at low porosities according to the relationship

$$m = 1.87 + (0.019/\phi) \quad \ldots\ldots\ldots\

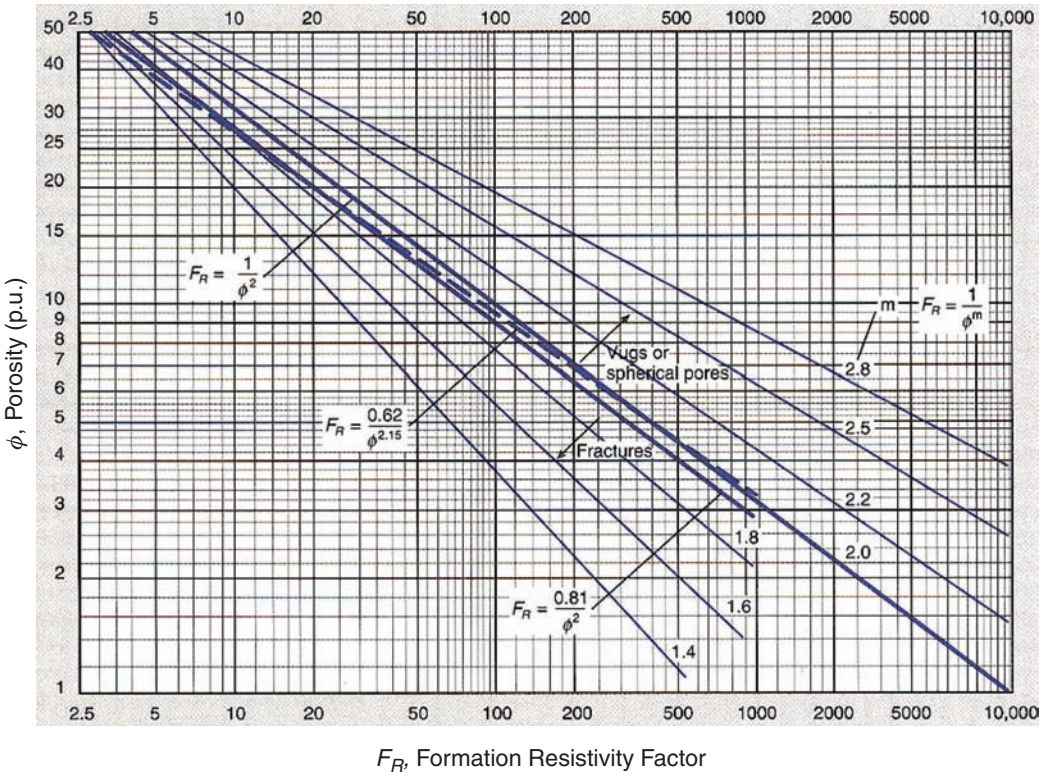


Fig. 26.6—Formation-factor/porosity relationships (Schlumberger 2005). Courtesy of Schlumberger.

Dividing the second equation by the first, the formation factor is eliminated. This method is useful if no porosity log is available.

$$\left(\frac{S_{xo}}{S_w}\right)^2 = \frac{R_{mf}}{R_w} \times \frac{R_t}{R_{xo}} \quad \ldots\ldots\ldots\

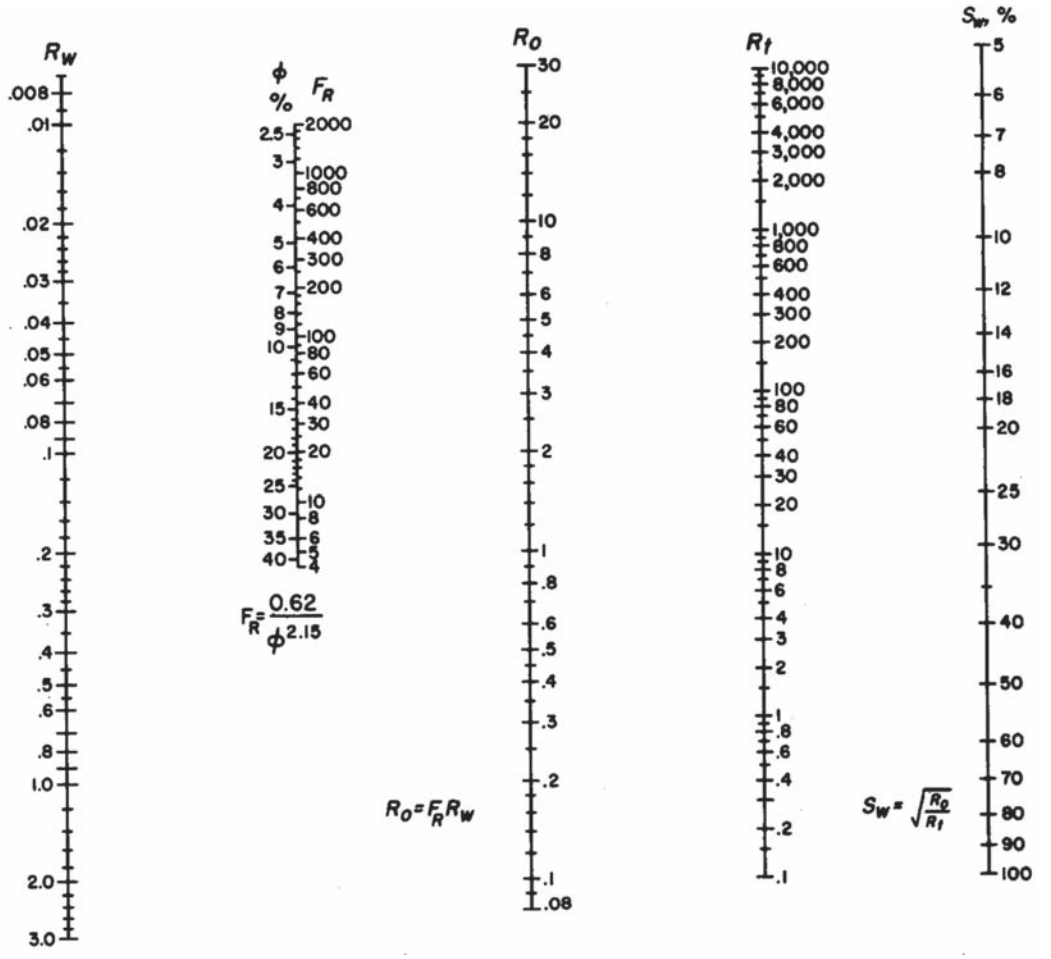


Fig. 26.7—Nomogram for water saturation in clean formations (Schlumberger 2005). Courtesy of Schlumberger.

$$S_w = \left(\frac{R_{xo}}{R_t} \times 10^{SP/K} \right)^{5/8} \quad \ldots\ldots\ldots\

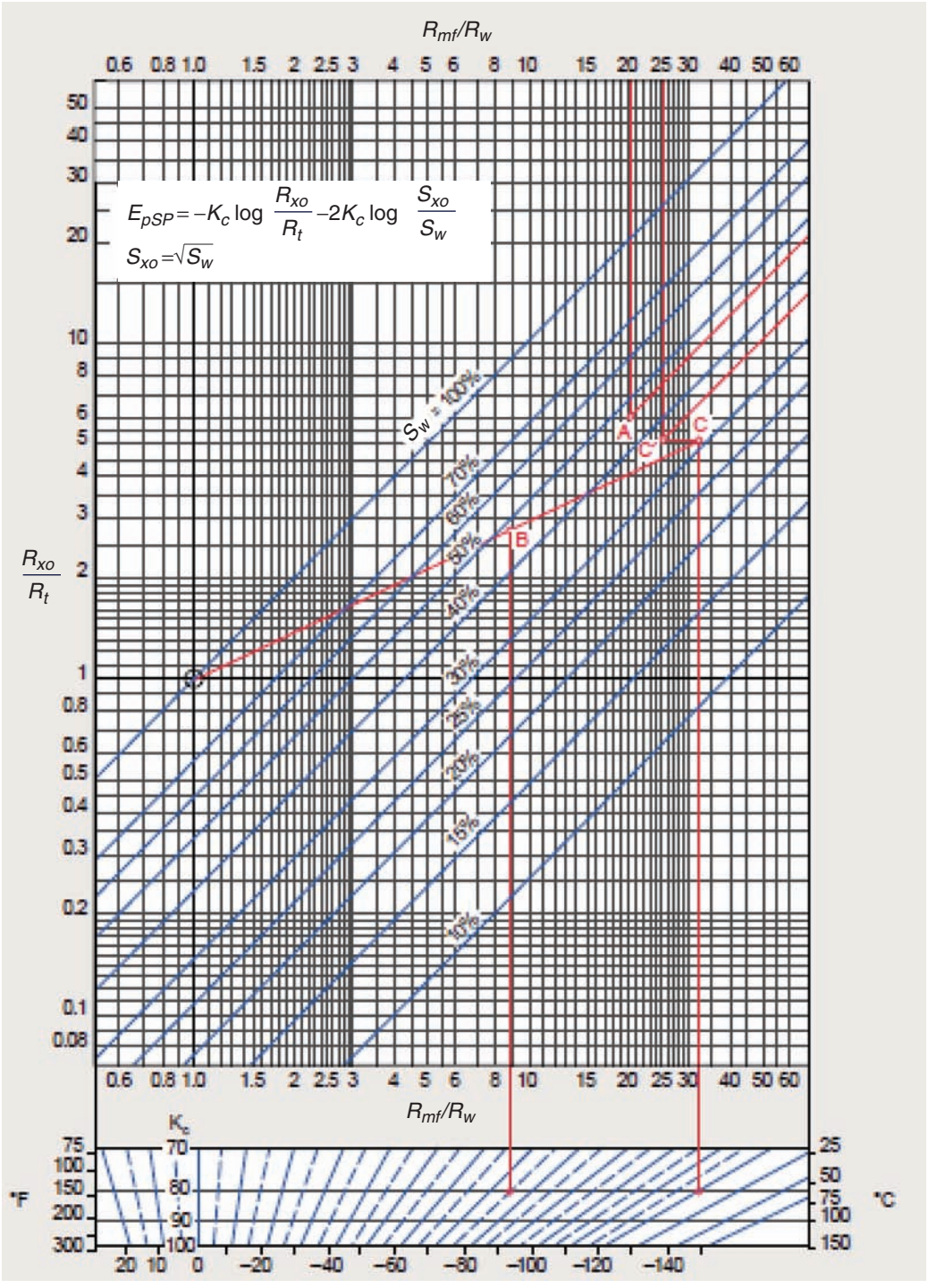


Fig. 26.8—Saturation determination using the ratio method (after Schlumberger 2005). Courtesy of Schlumberger.

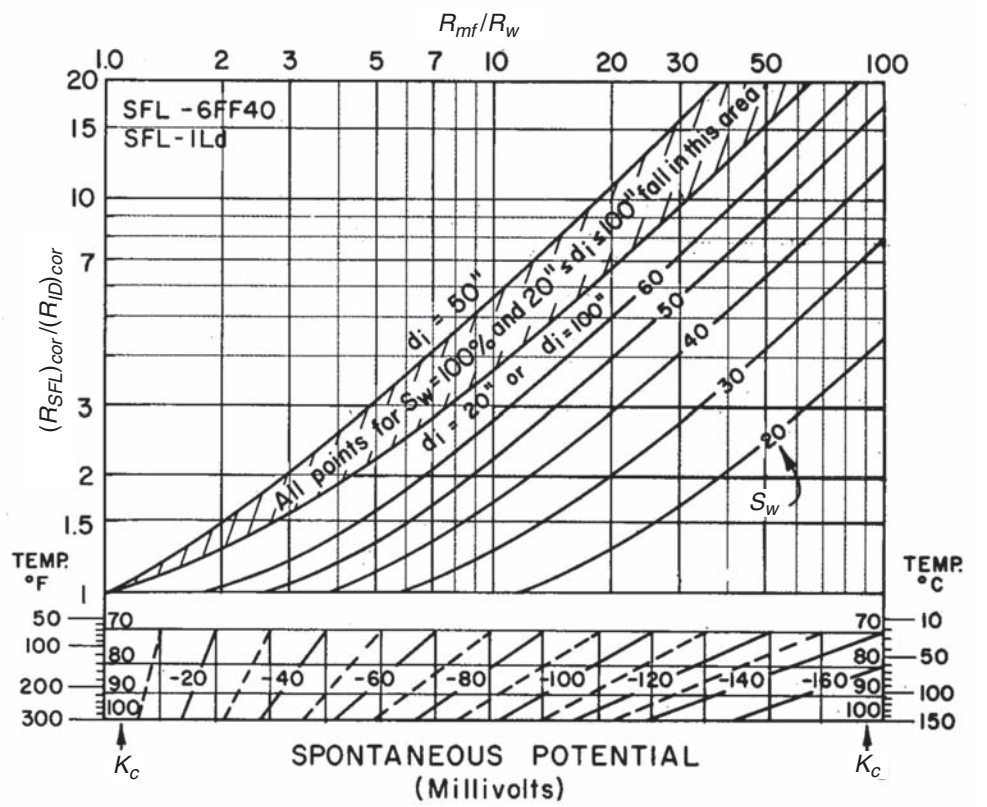


Fig. 26.9—Ratio method using R_{ID} and R_{SFL} (20 in. <d_i <80 in.). Courtesy of Schlumberger.

the logs in this fashion. An alternative method for determining the value of R_{xo}/R_t is shown in **Fig. 26.9,** which was prepared for the induction-SFL combination. This method takes into account filtrate-invasion effects.

QUESTION 26.6.
R_{SFL} = 40 Ω·m,
R_{ID} = 10 Ω·m,
T = 200°F,
SP = −115 mV.
Find S_w =

This R_{xo}/R_t ratio method can be extended to produce a continuous overlay. This can be generated at the wellsite or on playback at the analyst's work station by computing the R_{xo}/R_t ratio scaled according to K (temperature) and raising the result to the 5/8 power. This pseudo-SP is then superimposed on the real SP curve. Where the two curves coincide, S_w is 100%. Where the two curves separate, S_w is less than 100%, and the zone is immediately identified for further study. An example of this kind of presentation is given in Chapter 21.

26.5.3 Crossplots. Crossplot methods are useful when many points need to be analyzed together—for example, where computer-based processing of digital log files is available. However, these same methods can be applied manually using convenient charts or plain graph paper.

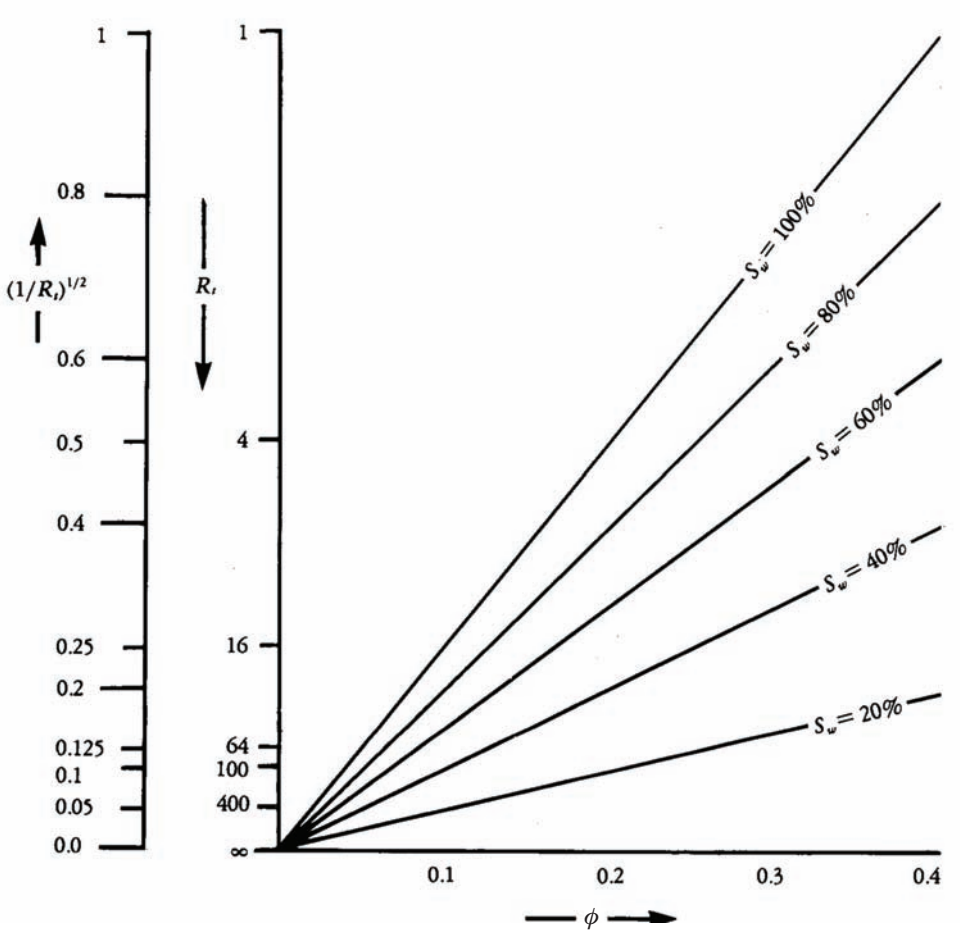


Fig. 26.10—Resistivity-vs.-porosity crossplot for saturation determination.

Archie's equation can be rearranged to give the following equation:

$$\frac{1}{R_t} = \frac{S_w^n \phi^m}{aR_w} \quad \ldots\ldots\ldots\

This crossplot has another interesting application. If ρ_b or Δt rather than porosity is plotted on the x-axis, it is possible to determine the matrix point provided that there is a fairly wide range of wet points at different porosities, as also explained in more detail in Chapter 24. The following question illustrates this method.

QUESTION 26.7. Readings from sonic and induction logs at various points throughout an interval of interest give:

Depth	R_t	Δt
1	200	70
2	150	74
3	400	62
4	125	76
5	70	66
6	30	70
7	14	68
8	13	64
9	4.5	78
10	20	60
11	16	62
12	9	68
13	5	76

Use **Fig. 26.11** and scale the x-axis in μsec/ft so that porosity increases to the right. Assuming that $\Delta t_f = 188$ μs/ft, find the following from the plot:

a. R_w
b. Δt_{ma}
c. S_w in the pay

26.5.4 *F* Overlay. The *F* overlay is a powerful interpretation technique for quick analysis of resistivity and porosity logs. An *F* log can be overlaid with the deep resistivity log (both logs on a logarithmic scale) so that the two logs coincide in a clean wet zone. The departure between the two curves may then be used to determine S_w using an appropriately marked scaler, as described in Chapter 22. When the *F* curve has been normalized in a wet zone (the *F* curve coincides with the deep resistivity curve in a clean wet zone), a useful side benefit is a quick method of finding R_w. Where the $F = 100$ line overlays the resistivity log scale, that value of R_t equals $100 \times R_w$.

26.5.5 Using an R_{wa} Curve. If an R_{wa} display is available (see Chapter 25 for details of how to generate an R_{wa} value), it is a simple matter to deduce S_w in a hydrocarbon-bearing zone by taking the *n*-th root of the ratio of R_{wa} read in a wet zone to the R_{wa} value read in a hydrocarbon-bearing zone. If the value of *n* is two, then a simple square-root function is all that is required.

$$S_w = \sqrt[n]{\frac{R_{wa-\text{wet zone}}}{R_{wa\text{-hc zone}}}} \quad \ldots\ldots\ldots\

For $F_R = \frac{1}{\phi^2}$

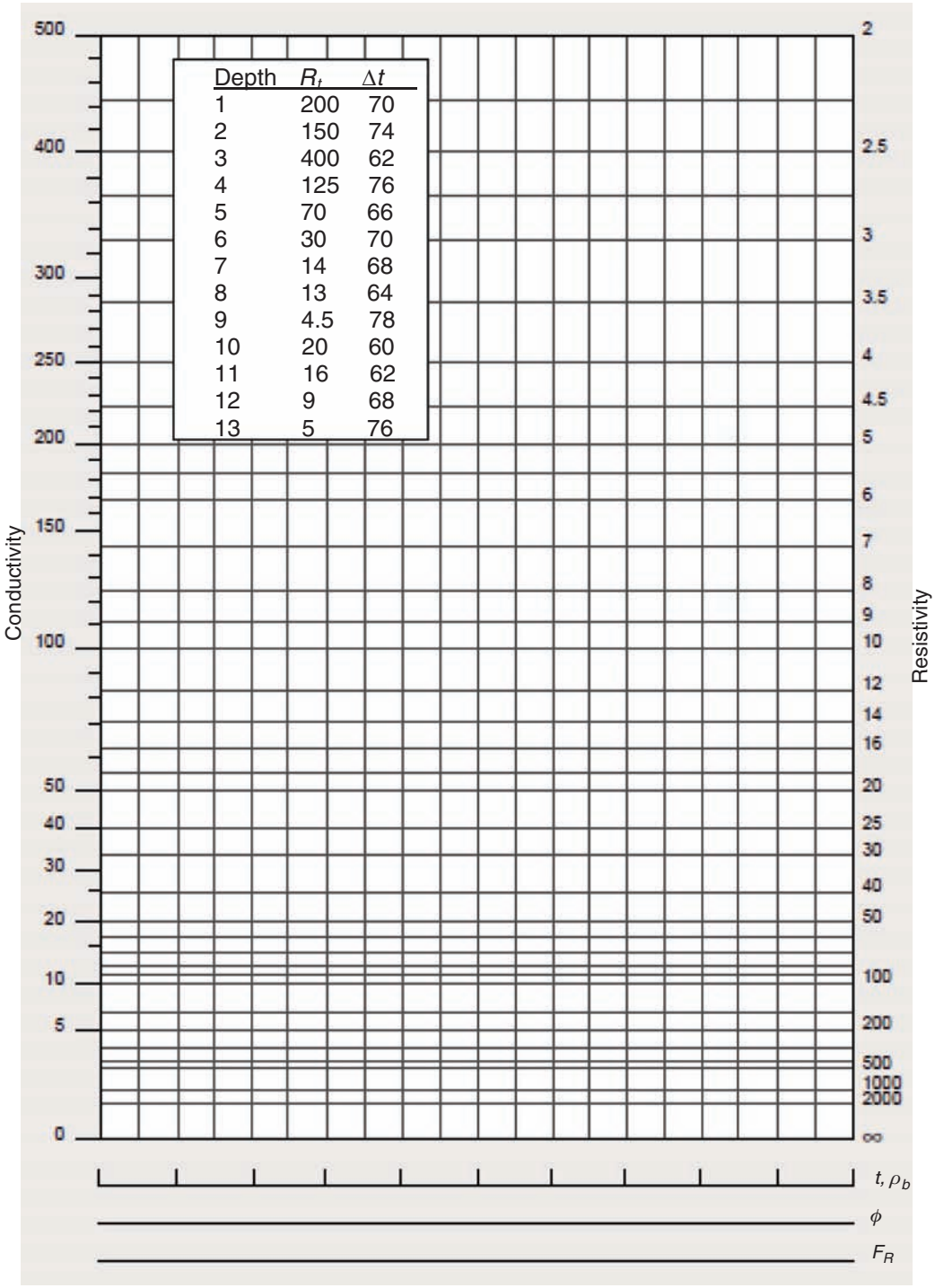


Fig. 26.11—Resistivity-vs.-porosity crossplot ($F = 1/\phi^2$) (Schlumberger 2005). Courtesy of Schlumberger.

challenges to resistivity tools when the thickness of the laminae is small in comparison with the resolution of the logging tool. Methods of making allowances for these perturbing effects are covered more completely in Chapter 28.

26.7 Summary

1. Use the Archie technique when the formation is clean, when a deep resistivity log and a porosity log are available, and when the value of R_w is known.
2. Use the ratio technique when a porosity log is missing, but when deep and microresistivity logs are available together with an SP log.
3. Use crossplots to reconnoiter a porosity and resistivity log if the value of R_w, the matrix type, or both are questionable. Use the position of a plotted point on the crossplot as an indicator of S_w when it falls away from the 100% S_w line through the water-bearing trend.
4. Use the F overlay technique for quick analysis when a logarithmic F and deep resistivity logs are available and when a wet zone is present where the two curves can be normalized. Use this normalization to deduce the exact value of R_w, and use the separation at any given depth as an indicator of the value of S_w.
5. Take advantage of a continuous computation of R_{wa} for quick S_w estimates.

References

Archie, G.E. 1942. The Electrical Resistivity Log as an Aid in Determining Some Reservoir Characteristics. SPE- 942054-G. *Trans.,* AIME **146:** 54–62.

Bateman, R.M. 1985. *Cased-Hole Log Analysis and Reservoir Performance Monitoring*. Boston: IHRDC.

Schlumberger. 1977. *Log Interpretation Charts*. New York: Schlumberger Ltd.

Schlumberger. 2005. *Historical Log Interpretation Charts*, 05-FE-006.

Schlumberger. 2009. *Log Interpretation Charts*. 09-FE-0058. Sugar Land, Texas. Schlumberger.

Tixier, M.P. 1958. Porosity Balance Verifies Water Saturation Determined From Logs. *J. Pet Tech* **10** (7): 161–169. http://dx.doi.org/10.2118/1024-G.

General References

Poupon, A., Loy, M.E., and Tixier, M.P. 1954. A Contribution to Electric Log Interpretation in Shaly Sands. *J. Pet Tech* **6** (6): 27–34. http://dx.doi.org/10.2118/311-G.

Answers to Questions

QUESTION 26.1.
a. $\phi = 30\%$.
b. $S_w = 33.3\%$.
c. HCPV = 0.2.

QUESTION 26.2.
$n = 1.9$.

QUESTION 26.3.
$a = 0.9$.
$m = 2.1$.

QUESTION 26.4.
$S_w = 23$.

QUESTION 26.5.
$S_w = 50\%$.

QUESTION 26.6.
$S_w = 50\%$.

QUESTION 26.7.
a. $R_w = 0.25\ \Omega\cdot m$.
b. $\Delta t_{ma} = 44\ \mu s/ft$.
c. $S_w = 20\%$.

Chapter 27

Core Analysis

Rock samples suitable for laboratory analysis may come from a variety of sources; for example,

- Cuttings
- Sidewall cores (percussion- or rotary-drilled)
- Conventional cores (full-diameter or plugs)

The sophistication of the analysis performed depends on the source of the sample and the objectives of the analysis. At least, a good idea of the rock type and oil presence can be obtained; at most, a vast range of rock and fluid properties. Those that can be determined in a routine core analysis include:

- Porosity
- Lithology
- Fluid saturations
- Permeability
- Grain-size distribution
- Grain density
- Effects of overburden stress
- Hydrocarbon analysis
- Pore water analysis
- Core gamma and spectral gamma logs
- Core imaging photographs

Those that require tests that are not normally available from routine core analysis demand special core-analysis laboratory equipment and procedures and include:

- Relative permeability
- Wettability
- Capillary pressure
- Pore-throat distribution
- Mineral composition and clay typing
- Electrical properties
- Sensitivity to fluids
- Mechanical properties
- Acoustical properties
- Computed Tomography (CT) scans
- X-ray diffraction
- NMR analysis

Inasmuch as most of these properties of a rock/fluid system are of vital interest to the formation evaluator, it is of critical importance to learn more about core-analysis methods and the application of their results to log analysis in particular and formation evaluation in general.

27.1 Sample Selection and Preparation

The analyst may be able to select only samples that originate from the depth interval of interest. To some extent, a selection is made at the time the sample is taken; for example, sidewall cores are usually recovered at selected depths determined from wireline logs. Cuttings are usually collected at 2-, 5-, 10-, or 20-ft intervals (see Chapter 5) and should be properly lagged and identified as to source (depth). Whole cores are usually cut to driller's depth, which may be different from wireline-logging depths. Therefore, a good starting point for whole-core analysis is a gamma ray scan of the core. The core is laid out and moved relative to a gamma ray counter that records a graph of radioactivity vs. distance traveled along the core. This record may then be compared directly with a wireline gamma ray log (see **Fig. 27.1**) to determine the correction required to match the core depth to the log depths.

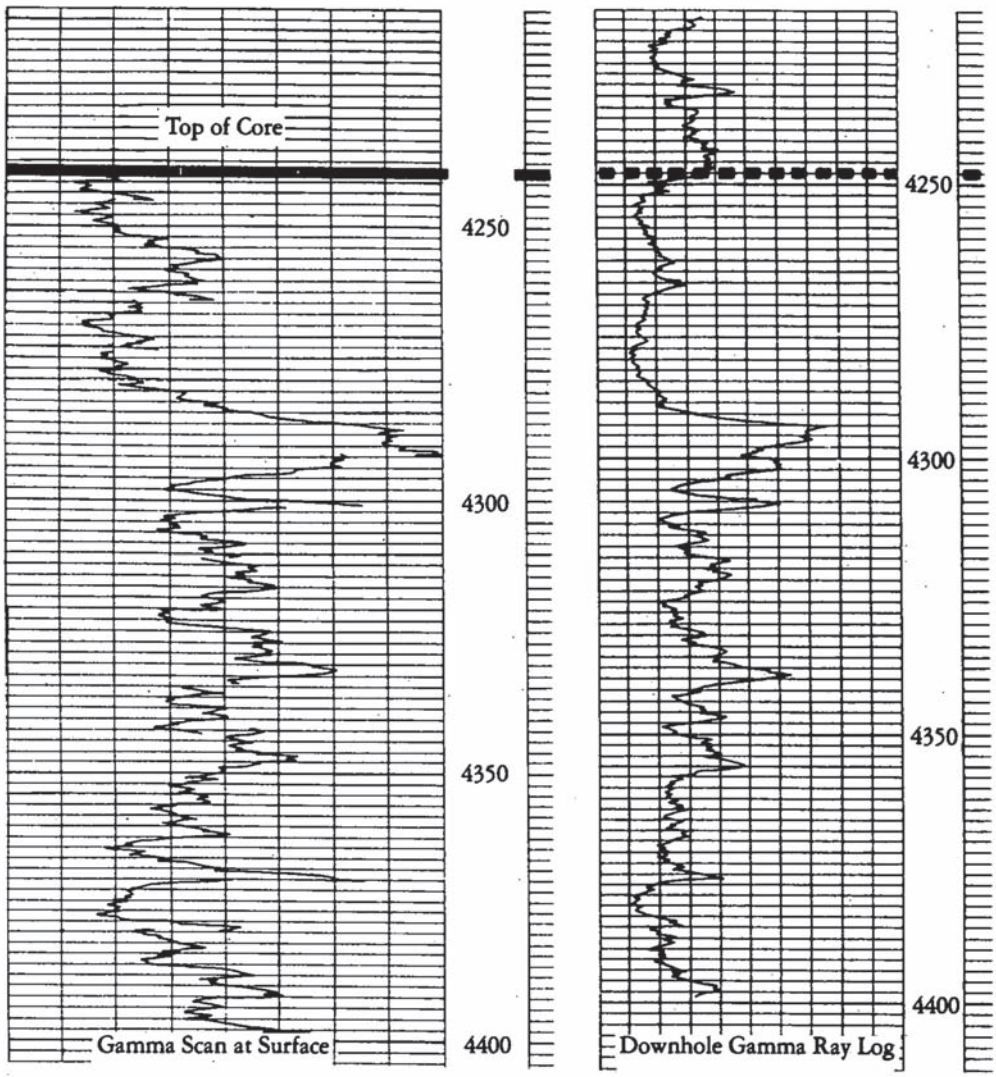


Fig. 27.1—Comparison of core gamma scan with wireline openhole gamma ray log. Courtesy of Core Lab.

QUESTION 27.1. Inspect the logs shown in Fig. 27.1 and estimate the differences between core depths and log depths.

When cutting conventional cores, it is wrong to assume that the only formations of interest are the clean reservoir rocks. Useful data may be extracted from shales as well, and the temptation to high-grade the core at the wellsite by discarding shale sections should be resisted. If necessary, the total length of the whole core should be described so that samples to be tested as well as shale locations and their depths are recorded. The core gamma ray scan, for example, would be useless if the radioactive section of the core were missing. Conventional core analysis uses a plug cut from the whole core, whereas full-diameter core analysis uses the whole core. Plugs are typically 1 to 1½ in. in diameter and 1 to 3 in. long. Whole-core diameter varies but is often approximately 5 in. Samples for analysis are cut into right cylinders up to 10 in. long. Cores can be classified as follows:

Fresh Cores are cores cut with water- or oil-based muds and are tested or preserved without any cleaning.

Native-State Cores are cores cut with lease crude as the coring fluid to minimize changes in water saturation and location and rock wettability. This term, although used historically, is not currently in use.

Restored-State Cores are cores that have been cleaned and dried, then re-exposed to reservoir fluids with the intent to restore reservoir wettability. In such samples, the wettability and fluid distributions may be changed.

Cores may be epoxy-coated, jacketed in heat-shrinkable tubing or metal (for unconsolidated cores), or coated with Lucite.

27.2 Measurement of Basic Rock Properties

27.2.1 Porosity. There are two components in a porous rock system: the grain volume (V_G) and the pore volume (V_P). The sum of the two gives the bulk volume (V_B).

$$V_B = V_G + V_P \quad (27.1)$$

Porosity is defined as the ratio of the pore volume to the bulk volume:

$$\phi = V_P / V_B \quad (27.2)$$

It can be calculated in a number of ways; for example,

$$\phi = (V_B - V_G)/V_B \quad \text{or} \quad \phi = V_P/(V_G + V_P) \quad (27.3)$$

In other words, provided that any two of the three quantities are measured, porosity can be deduced. Among the commonly used methods of measuring porosity are:

The Summation of Fluids Method uses a fresh, nonextracted core to determine the volumes of water, oil, and gas, which are independently measured and then summed to give V_P. V_B of percussion sidewall cores is measured with a volumetric mercury-displacement pump. Conventional core analysis combines data from a displacement pump with the retort-sample weight to yield V_B. This is the most rapid technique because an uncleaned core is used.

The Boyle's Law Method uses core that is cleaned and dried. Air or another gas is allowed to fill the pore space. When the sample is connected to a second chamber filled with gas

(normally helium) at a higher pressure, the gas in the second chamber expands into the pore spaces in the core. The final pressure in the system enables deduction of V_P or V_G (depending on the configuration used to enclose the core) by use of Boyle's (Charles') law. V_B is deduced from the dimensions of the core or calculated by summing V_P and V_G.

Grain-Density Methods require that both the grain volume (V_G) and the dry weight of the cleaned and dried sample be determined. Grain density is calculated by dividing the dry weight by the grain volume. The most common technique uses the Boyle's Law method to determine V_G in a two-cell porosimeter.

The accuracy of conventional drillplug-core porosity measurements is claimed to be within 1/2 p.u. Methods that require the core to be cleaned and dried are subject to error when the core contains hydrated clay material. Retorting or oven drying such a sample will drive off the water of hydration, and therefore the measured porosity will be greater than the effective porosity. Removal of all water of hydration will yield a porosity value referred to as ϕ_T, or total porosity. This value is used in selected log calculations. Currently, it is believed that effective porosity, as defined by log analysis, falls between the oven-dried core porosity and ϕ_T. Use of a humidity-controlled oven to dry samples will assist in alleviating this problem because two or more molecular layers of water will be retained on pore-space mineral surfaces.

The use to which a porosity value is put should be governed by the analyst's knowledge of the heterogeneity of the reservoir. A core plug is very localized, and core-plug porosities may be higher than whole-core porosities if the whole core includes portions of lower-porosity rock. The selection of where to take a plug from a whole core is somewhat subjective, and the "best-looking spot" may be picked. Plug porosities may be lower than the full-diameter porosity of a vuggy core because vugs cannot be sampled. A good geological description and photographs of the core will assist in evaluating the representative pay zone and sample-selection points.

Sidewall core plugs can produce porosities that are either higher or lower than the true porosities of the producing interval. This may result from inappropriate selection of depth, porosity range, or both. **Fig. 27.2** illustrates this effect by plotting sidewall-core porosity vs. conventional-core porosity. In general, low-porosity formations tend to be better cemented, and they fracture when sidewall-core bullets strike them. This creates additional pore volume, while poorly indurated higher-porosity rock is compacted. Fig. 27.2 illustrates that sidewall porosity in the 30% range yields reasonable porosity values.

Porosity measurements on cuttings may be made on samples as small as a cubic centimeter or less. Such measurements can compare well to core-plug porosities (within one p.u.), but suffer from inaccurate knowledge of sample depth and an inadequate selection of representative cuttings of sufficient size.

27.2.2 Permeability. Permeability (k) is measured by causing a fluid to flow through the core sample. Measurements required to deduce permeability include the cross-sectional area A, the length L, the pressure drop Δp, the flow rate q, and the fluid viscosity μ. Darcy's equation can be applied to deduce permeability:

$$k = q\mu L / A\Delta p \quad \ldots\ldots (27.4)$$

Historically, permeability was derived using steady-state flow techniques with a constant Δp and flow rate. Currently, unsteady-state techniques are also available and offer faster and more-reliable results. Both gas permeability and equivalent liquid permeabilities are quickly available from a single unsteady-state measurement. In addition, overburden effects on permeability are more easily and quickly obtained from unsteady-state measurements.

The fluid used in routine core analysis is nitrogen, helium, or air. Gases and liquids do not behave in the same fashion while flowing. Gas permeabilities measure higher than liquid permeabilities. Klinkenberg (1941) studied gas flow and determined that gas permeability is a function

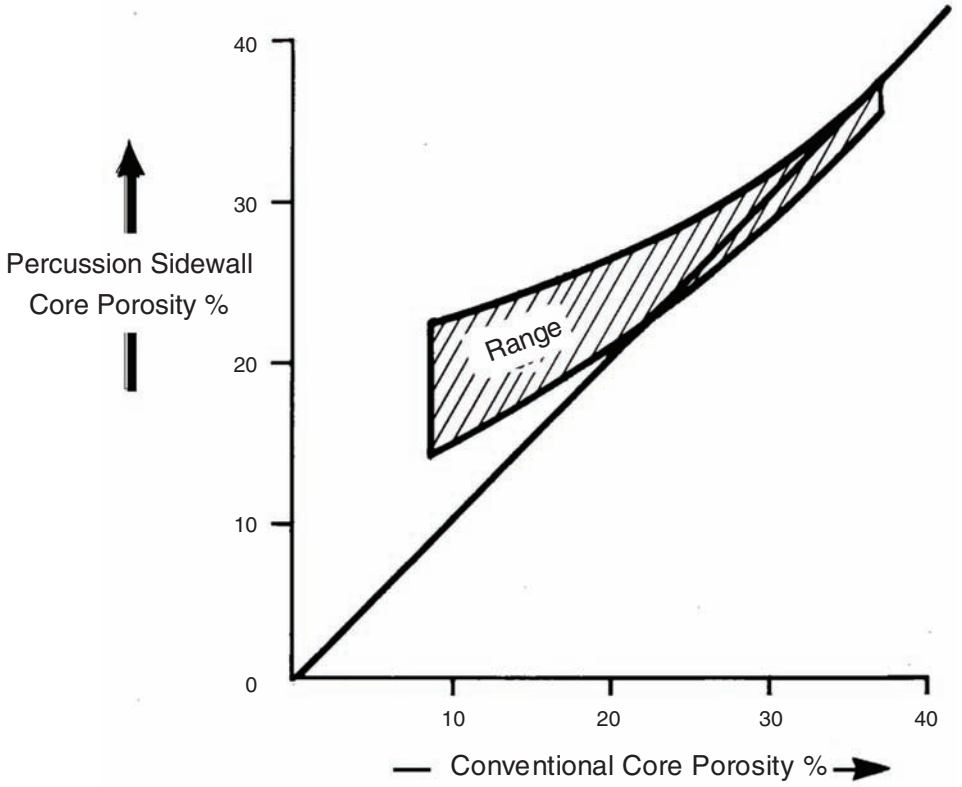


Fig. 27.2—Comparison of conventional and percussion sidewall core porosities. After Core Lab.

of both the gas composition and the mean pressure in the core. At infinite mean pressure, the gas behaves as a nonreactive liquid, and its permeability is referred to as the *equivalent liquid permeability*. It is common therefore to convert laboratory air permeabilities, normally measured at low mean pressure in the core, to lower equivalent liquid permeabilities using a Klinkenberg correction. **Table 27.1** lists laboratory-determined Klinkenberg corrections for air. These data are time-consuming to use and were developed on sandstone and uniform carbonates. Unsteady-state measurements supply both measured air permeability and equivalent liquid permeability and are now offered in routine core analysis.

When reading a core-analysis report, always check to see whether permeability was measured with gas and whether the values reported have been corrected for the Klinkenberg effect.

Note that k_L is often used as the symbol for "equivalent liquid permeability" and will be higher than an actual brine permeability in a rock containing water-sensitive mineral clays.

TABLE 27.1—KLINKENBERG CORRECTION FACTORS [AFTER CORE LAB]

Air Permeability (md)	Correction Factor	Equivalent Liquid Permeability (md)
1000	0.95	950
100	0.88	88
10	0.78	7.8
1	0.68	0.68
0.18	0.66	0.12

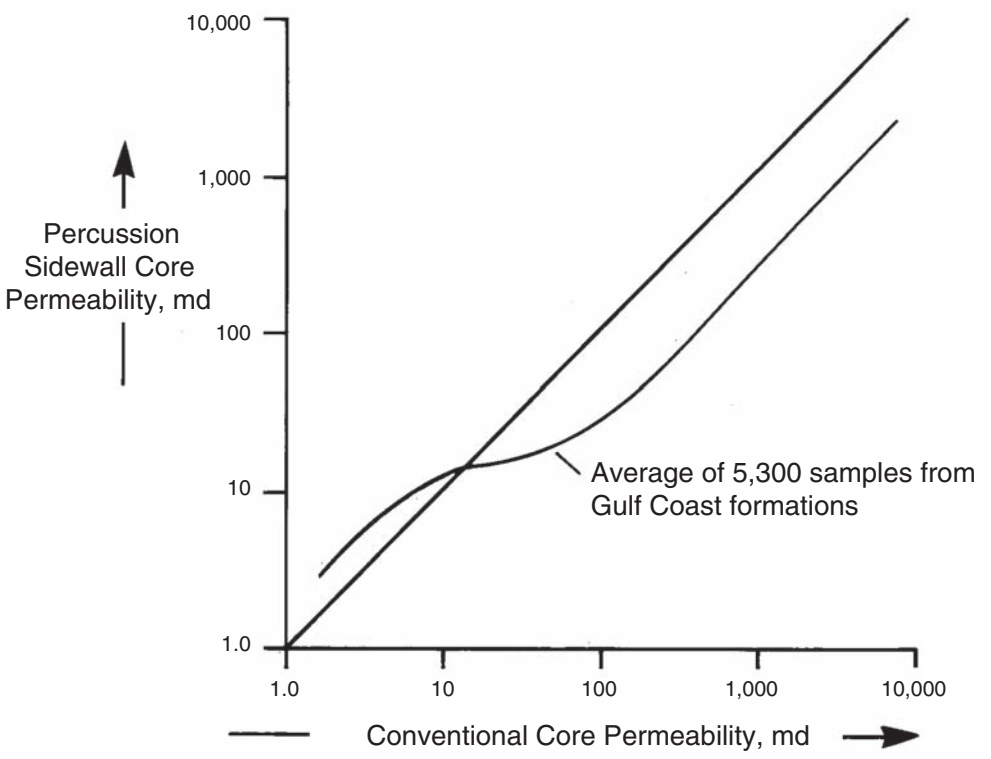


Fig. 27.3—Comparison of conventional and percussion sidewall core permeabilities. After Core Lab.

Like the porosity measurements from sidewall cores, permeability measurements from percussion sidewall cores may be higher or lower than the true value. **Fig. 27.3** shows a comparison of measured conventional-core permeability and measured percussion sidewall-core permeability.

Because of the small sample size of percussion sidewall cores and the observed inadequacy of the measured permeability values, textural features of the sample are often used to estimate permeability. These features include grain size and distribution, shaliness, and porosity. Currently, computerized particle-size analysis can provide actual measurement of the core grain size and distribution, including the percentage of silt and clay in each sample. Permeability estimates from textural features are typically reliable and more closely match conventional permeability values than those measured on percussion sidewall cores.

27.2.3 Relative Permeability, Wettability, and Sensitivity. Tests for relative permeability and wettability require samples from native-state core, if possible, to minimize the chances that the rock wettability and pore-water distribution have been altered as a result of coring or preparation procedures. Wettability tests include contact-angle measurements using lease crude and a polished silica or carbonate surface to simulate the formation rock. These tests depend to some extent on how long the wetting fluid remains in contact with the surface being tested. For these reasons, sufficient time must be allowed for rock, oil, and water to reach equilibrium.

A more commonly used technique monitors the quantity of oil and water that is imbibed by and then flushed from a fresh core. The wetting fluid spontaneously invades the core and displaces the nonwetting fluid. The equipment required is a specially shaped imbibition tube that enables measurement of the displacing fluid. The rock sample is typically a cylindrical plug similar to that used for permeability and Boyle's Law method porosity. The wettability at the time of testing represents the state of the core following exposure to the coring fluid, recovery, handling, and transportation and may not represent wettability at reservoir conditions. **For reliable results, careful**

attention to the selection of coring fluid and proper handling is required. Some prefer to clean the sample of all fluids and then restore the sample to reservoir saturation of oil and water. The oil is then displaced with crude oil, and the sample is soaked for several weeks at reservoir pressure and temperature. Imbibition tests can then be run. Reported data support this approach, although others prefer that these tests be made on a fresh core recovered with a coring fluid tested to ensure that it does not alter wettability. Common testing techniques are the *Amott* method, the *USBM* method (that uses a centrifuge in the testing procedure), and a combination of the two procedures.

Sensitivity tests may be performed to determine whether fresh water has damaged in any way the permeability of the core. These tests are routinely performed in a special-core-analysis laboratory, but may not be available in a routine-core-analysis laboratory. X-ray-diffraction measurements can be used to define clay type and quantity. Scanning-electron-microscope (SEM) images can identify clay morphology and location. These measurements aid in the selection of procedures to reduce or eliminate damage.

It is quite common to find that fresh water dislodges fines from the surfaces of the grains and that these fines subsequently bridge together and create obstructions in pore throats. Some clays hydrate and swell in place. Permeability may or may not be restored by flushing with saline water. Clay sensitivity, damage prevention, and treatment can be investigated. Depending on the type of clay present, an appropriate treatment can be recommended. What works for one situation may create problems in another. For example, hydrofluoric acid (HF) will cause calcium fluoride to precipitate in rocks with calcite present, but hydrochloric acid (HCl) works well. Chlorite is liable to produce iron hydroxide precipitates when exposed to oxygen-rich systems with a pH greater than 4. Other clay types are susceptible to treatment with HCl and HF if freshwater systems have already caused damage. The addition of potassium, calcium, or other additives to water-based muds or the use of oil-based mud may be required to prevent formation damage during the drilling process.

27.2.4 Fluid Saturation (Summation of Fluids).

Gas Saturation can be measured in two ways, depending on the sample size and the analysis selected. In the first, a sidewall or conventional core sample is subjected to injection of mercury at approximately 750 psi, which causes all the gas present to go into solution with the liquids in the pore system. The volume of mercury injected gives the fraction of V_P occupied by gas. In the second, a whole-core analysis is performed on a full-diameter core sample up to 10 in. long. The whole-core sample is subjected to rapid evacuation of all free gas. Water is then forced into the sample, and the increase in weight is used to measure the fraction of V_P that held gas. Typically, the injection of mercury results in a sample that is not suitable for certain measurements; consequently, this method is not recommended for drilled sidewall cores.

Oil Saturation is measured by a retorting process in which the core sample is heated to between 450 and 1,200°F (according to the technique used) and the oil distilled off is collected in a calibrated condenser. This volume of oil is corrected for volume shrinkage and represents the fraction of V_P that contained residual oil resulting from flushing by the coring fluid, expulsion by gas drive during recovery, and oil shrinkage during pressure drop to atmospheric.

Water Saturation is measured at the same time as oil saturation when the retorting methods are used. Oil and water recovered by the distillation are separated, and their volumes are measured individually. The water volume represents connate water plus any water added by the coring-fluid filtrate.

27.2.5 Fluid Saturation (Dean-Stark Distillation). The Dean-Stark distillation process is the favored technique for non-sidewall plug samples and for rotary-drilled sidewall cores. It can also be used for whole-core analysis, but is very time-consuming. The drilled sidewall core sample is trimmed into a right cylinder, weighed, and then placed in a Dean-Stark apparatus,

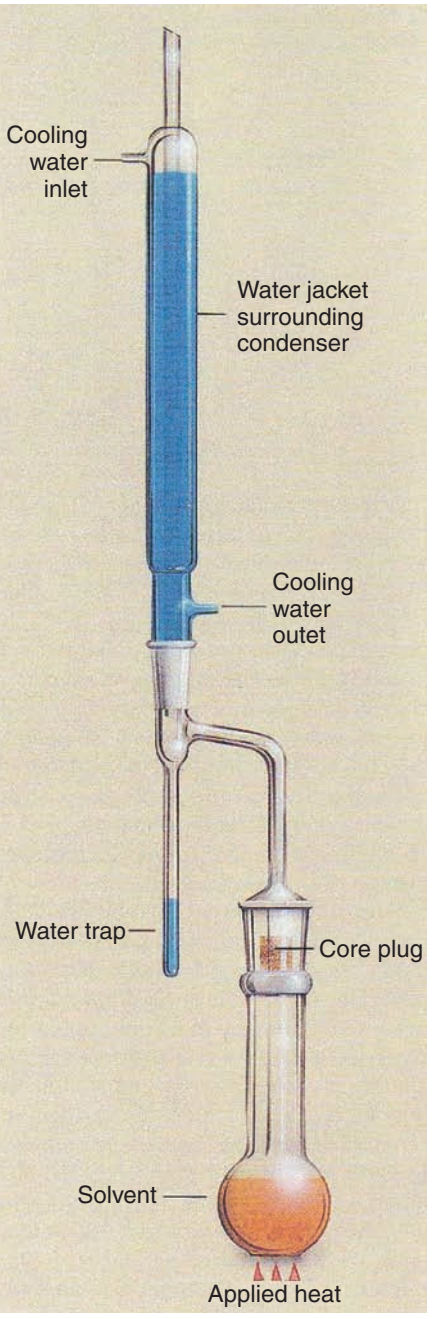


Fig. 27.4—Dean-Stark apparatus.

as shown in **Fig. 27.4.** A distillation process using a solvent such as toluene is used to recover and measure the pore water. The distillation process removes all the oil. The sample is removed from the Dean-Stark apparatus, dried, and weighed. A weight balance supplies the weight of residual oil in the core. Oil weight divided by oil density yields the oil volume. The pore volume of the clean dry sample is determined by the Boyle's Law method. Water and oil volumes are subtracted from the pore volume to yield gas volume, and the volumes are divided by V_p to yield saturations.

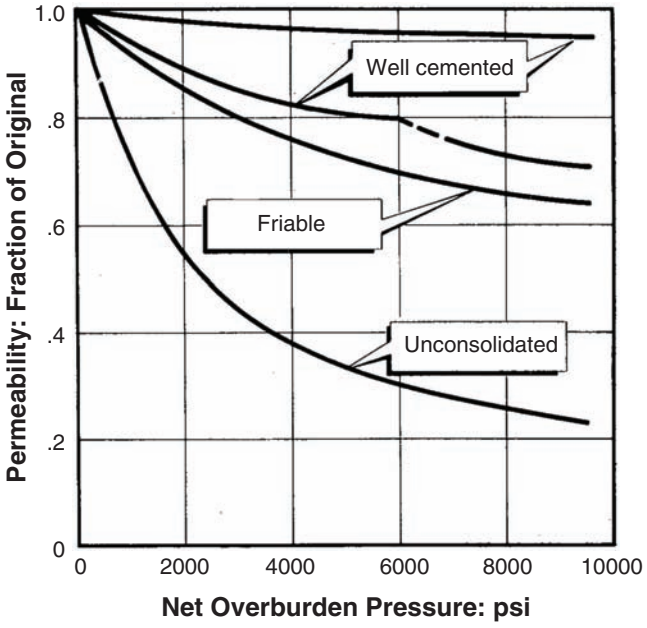


Fig. 27.5—Effects of net overburden pressure on permeability measurements. Courtesy of Core Lab.

27.3 Effects of Overburden Pressure

Although most basic rock properties are measured at atmospheric conditions, in some cases it is important to make measurements (especially of porosity and permeability) at simulated reservoir conditions. Both rock matrix and pore fluids are compressible, and measurements at standard conditions therefore give overly optimistic values for ϕ and k. The tests illustrated in **Fig. 27.5** show, for example, that increasing overburden pressure can reduce permeability by as much as 80%, depending, of course, on the type of material tested.

Permeability is an intrinsic rock property that is independent of the fluid in the pore space as long as no rock/fluid interaction occurs and there is no change in net confining pressure. When discussing reduced porosity caused by changes in pressure, however, the total rock/fluid system must be considered because both the rock matrix and the fluids in the pore space are compressible.

Therefore, both overburden stress and pore pressure come into play. Compressibilities are expressed in vol/vol/psi. It would not be uncommon to find a 10% reduction in porosity resulting from compression; that is, if a sample measured 20% in the laboratory, the porosity at depth might be 18%. Laboratory measurements of oil, water, and rock compressibility can be made and the pore reduction factor deduced if reservoir pore pressure and overburden stress are known. Data show that the defining parameter is the pressure difference between the confining stress and the pore pressure, and therefore measurements are often made with pore pressure at atmospheric value while the confining stress is increased.

Other pressure-sensitive parameters include acoustic velocity and formation factor. Both should be determined under a net confining stress equal to that in the reservoir. Measured values on stressed cores often differ dramatically from data on unstressed cores. Formation factor and acoustic velocity normally increase as net confining stress is increased. This increase in stress results from a drop in reservoir pressure as production occurs.

27.4 Measurements of Capillary Pressure

Capillary pressure is a force that retains water in the reservoir as hydrocarbons accumulate. It is a function of pore-throat-radius distribution, reservoir-fluid properties, and rock wettability, as covered in Chapter 6. A number of techniques are used to measure capillary pressure. Their basic

TABLE 27.2—CONTACT ANGLE AND INTERFACIAL TENSION FOR VARIOUS FLUID PARTS [AFTER CORE LAB]

Environment	Fluids	Contact Angle θ (degrees)	Interfacial Tension (dynes/cm)	$T \cos \theta$
Laboratory	Air/water	0	72	72
	Air/mercury	140	480	367
	Air/oil	0	24	24
	Oil/water	30	48	42
Average Reservoir	Water/oil	30	30	26
	Water/gas	0	50	50

principle is to force a fluid into the core and to measure how much fluid goes in at a fixed pressure or how much fluid is displaced. Techniques include injection of mercury (which renders the core sample useless for further analysis), use of a centrifuge, and core desaturation through a porous plate in a closed cell. Both imbibition and drainage conditions can be simulated. The end results consist of a set of paired readings of saturation and pressure. Because the contact angles and interfacial tensions of the fluids used in the laboratory may differ from those that exist in the reservoir, it is necessary to convert the laboratory measurements to equivalent reservoir capillary pressures. The reservoir values are converted to a plot of water/oil or water/gas saturations in the reservoir as a function of height above the free-water level. **Table 27.2** may be consulted for typical conversion factors. Reservoir values vary with pressure and temperature as well as with hydrocarbon composition. Water/gas values are reduced with increased reservoir depth, reservoir pressure, and reservoir temperature and approach water/oil values as a lower limit.

Remembering from Chapter 6 that height above the free-water level may be expressed as:

$$h = P_{c\,\text{Reservoir}} / \left(\rho_w - \rho_{hy}\right)_{\text{Reservoir}} \quad \ldots\ldots\ldots\

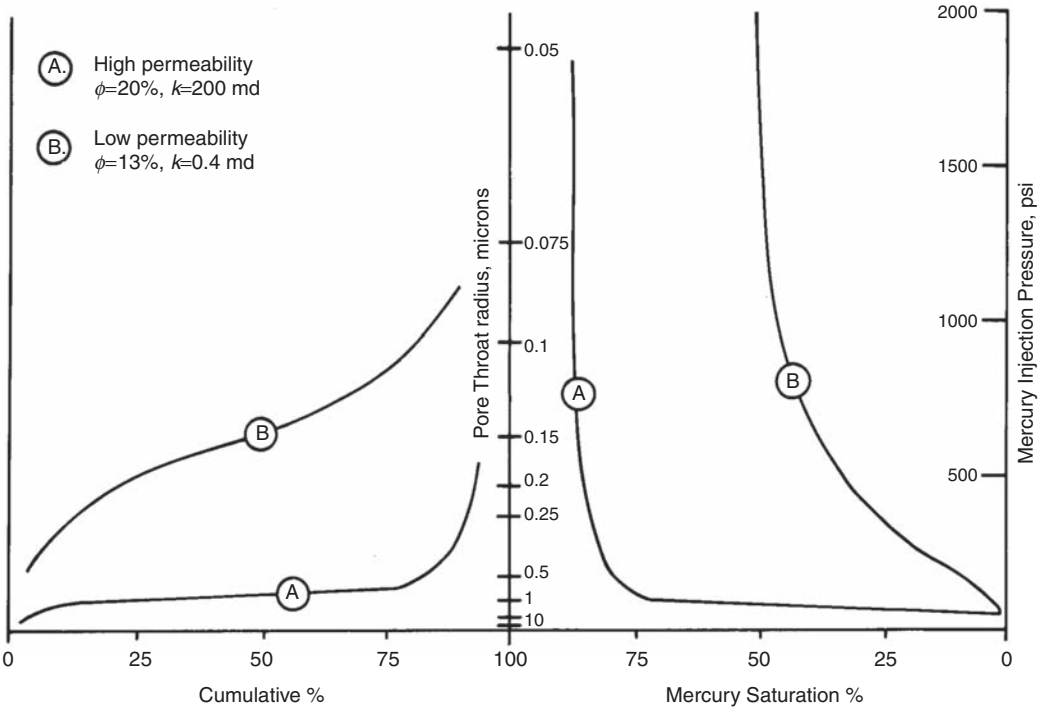


Fig. 27.6—Interrelationships between capillary pressure and pore-throat distribution.

where

r is in μm,

T is in dynes/cm,

P_c is in psi, and

c is a constant (to take care of units) that is equal to 1.45×10^{-3}.

The relationship between mercury-injection capillary pressure and pore-throat distribution is illustrated schematically in **Fig. 27.6.** A capillary pressure of 100 psi in the air/mercury system represents a radius (r) of approximately (1.0) μm.

Sieve analysis is a useful technique for gauging grain size and distribution. These data are used in designing gravel packs for unconsolidated formations. Laser diffraction is now a commonly used technique for grain-size analysis. It defines a classification of particles, including silt and clay, and is highly reproducible and rapid, and it requires a sample of only 1 g or less for the analysis.

27.5 Petrographic and Other Measurements

Petrographic studies of cores provide descriptions of texture, rock type, mineralogy, and other formation characteristics. Techniques used include:

- Thin sections
- X-ray diffraction
- SEM and focused ion-beam SEM (FIBSEM)
- Cathodoluminescence
- CT and micro-CT scanning
- Hydrocarbon analysis
- NMR

Thin sections (usually 1-in.^{2}) are prepared from any core-sample source. Before cutting and polishing the section, the core may be injected with colored plastic to fill the pore spaces.

The section is examined under the microscope to determine grain sizes, distribution (sorting), depositional history, and other properties.

X-ray diffraction measurements yield a quick and accurate analysis of both matrix and clay types. The normal procedure is to separate a crushed rock sample into clay fines (particles with a diameter less than four μm) and larger fragments using a centrifuge so that the matrix and clay portions can be analyzed separately. Each fraction is then sampled by the X-ray diffraction technique to "fingerprint" the crystal structure. Only 5 or 10 g of material is required to make the measurement. Results are normally quoted by weight percentage of the whole rock. A typical report might read:

Bulk Rock Analysis by wt%

Quartz	42	
Feldspar	28	
Calcite	21	
Fubarite	6	
Kaolinite	1	
Chlorite	TR	clays constitute 3% by weight of total rock
Illite	TR	
Montmorillonite	TR	

Clay Fractions

Kaolinite	31	% of clay present
Chlorite	10	
Illite	55	
Montmorillonite	4	

X-ray diffraction should be considered accurate to within 5 or 10%.

SEM studies enable a much closer look at individual grains and pore-filling minerals all the way down to clay-sized particles. Samples are first prepared by a special process that plates the grain surfaces with a conductive film such as carbon, gold, or palladium by use of a sputter or evaporative coater. Then, under high vacuum, the sample is scanned using a beam of electrons. Very high magnification is possible (up to 40,000X) with this technique. It is usually combined with a KEVEX-type system that also measures elemental composition using the energy-dispersive X-ray (EDX) technique **(Fig. 27.7).** For a very complete "dictionary" of the appearance and distribution of clays and other minerals, the reader is referred to the AAPG *SEM Petrology Atlas* (Welton 1984). Samples of SEM photos are shown in **Fig. 27.8.**

Micro- and Nanoscanning involve advances in SEM analysis and include the following categories:

- *Sample preparation*: argon-ion milling prepares a cross section with minimal artifacts and creates a fresh, debris-free surface for follow-up SEM examination.
- *High-resolution electron microscopy*: the field-emission SEM (FESEM) is preferred over standard thermionic SEM methods because of its better spatial resolution.
- *FIB systems*: these operate in a fashion similar to an SEM except that, rather than a beam of electrons, FIB systems use a finely focused beam of ions (usually gallium) that can be operated at low beam currents for imaging or high beam currents for site-specific sputtering or milling.

Fig. 27.9 shows an example of a FIBSEM scan of a shale core sample showing porosity and kerogen networks; the yellow indicates the 3D kerogen network, and the red indicates porosity. In this sample, all porosity occurs within the kerogen itself.

Cathodoluminescence occurs when a thin section of rock (30 to 100 μm thick) is bombarded with electrons in a vacuum. Different minerals glow in different colors depending on the mineral composition and the depositional and geochemical history of the rock. The electron emitter is mounted on a petrographic microscope, enabling immediate comparison of

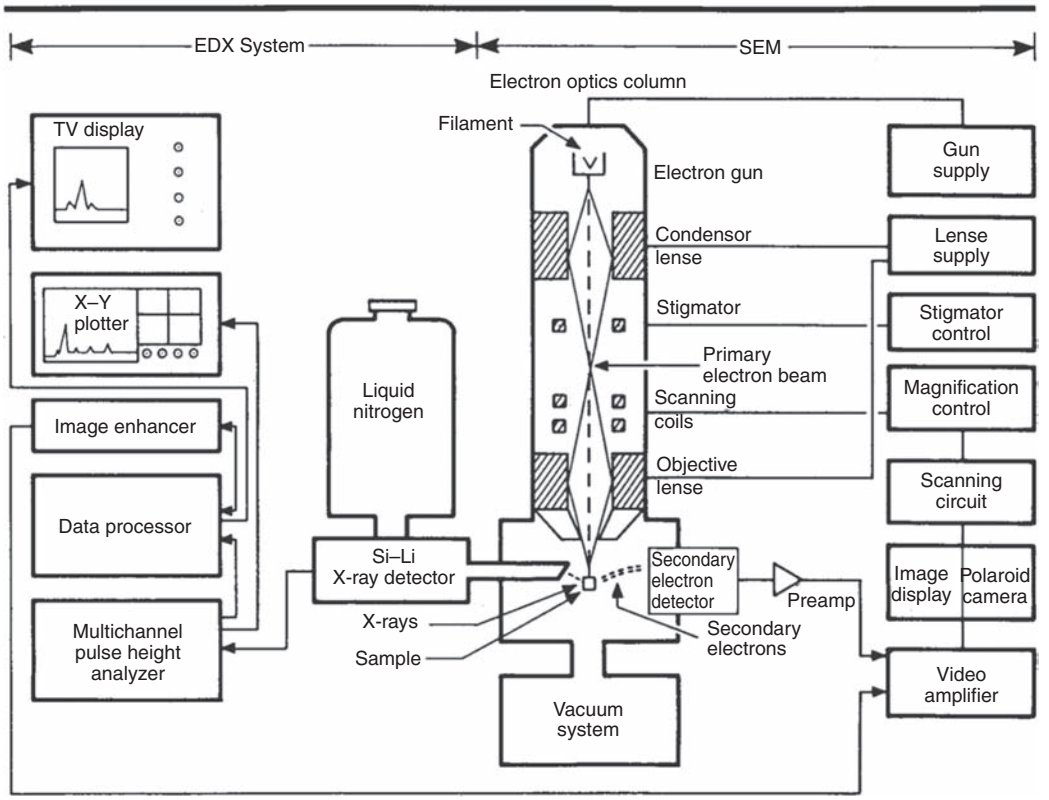


Fig. 27.7—Schematic of SEM/EDX system (Welton 1984; modified from H.M. Beck, schematic drawing of SEM/EDX system, unpublished). AAPG © 1984, reprinted by permission of the AAPG whose permission is required for further use.

samples by polarized light and luminescence. Growth rings similar to those of trees are observed in individual crystals. These rings are reported to correlate over large distances, and they reflect trace elements present in formation waters at various stages of the crystal history. The color offers insight into water temperature and chemistry (e.g., fresh water vs. marine cement precipitation). **Fig. 27.10** illustrates the cathodoluminescence method.

CT Scanning of small samples can produce striking 3D images with as many as 8×10^9 voxels on core plugs up to 6 cm in diameter and with resolutions down to 2 μm. This enables the 3D pore space of a rock and the fluid distributions within the pores to be imaged over several orders of magnitude. **Fig. 27.11** shows an example.

QEMSCAN consists of an SEM combined with four EDX spectrometers. The SEM images the field of view using backscattered electrons (BSE) to determine particle boundaries. The EDX captures a spectrum for each "pixel" of the particles. The EDX spectra are compared against a lookup table of known minerals to generate a mineralogy map. **Fig. 27.12** compares three images of a rock sample: one obtained in visible light, by one BSE, and one through the QEMSCAN system that reveals mineralogical detail as well.

Hydrocarbon Analysis of residual hydrocarbons may be carried out by heating a core sample and passing the vaporized hydrocarbons directly to a chromatographic column. This technique is referred to as *pyrochromatic analysis.* The chromatographic analysis gives the percentage of each hydrocarbon component. If the cumulative percentage is plotted vs. the hydrocarbon number, the resulting curve can be compared with "type" curves for gas, oil, and nonproductive formations **(Fig. 27.13).**

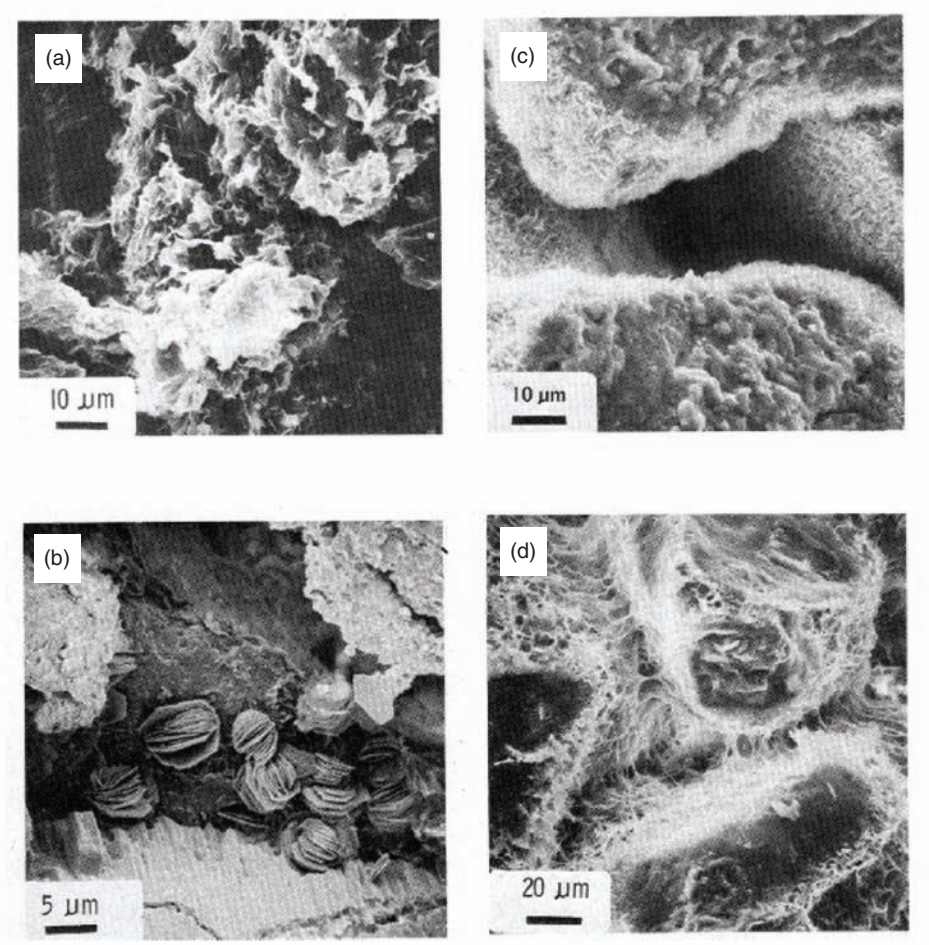


Fig. 27.8—Examples of SEM photos of clays in sandstone formations: (a) smectite; (b) authigenic kaolinite partially filling pore space (ϕ = 20.3%, k = 7.7 md);(c) authigenic chlorite lining pores (ϕ = 14%); (d) authigenic illite lining pores and filling pore throats between sand grains (ϕ = 11.3%, k = 7.7 md). Pittman and Thomas (1979).

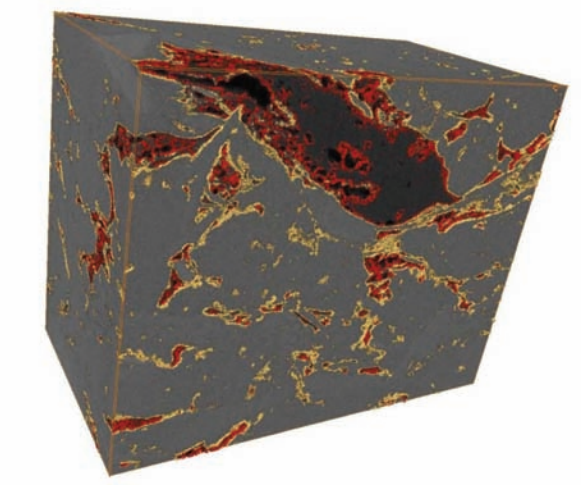


Fig. 27.9—FIBSEM scan. Courtesy of Weatherford.

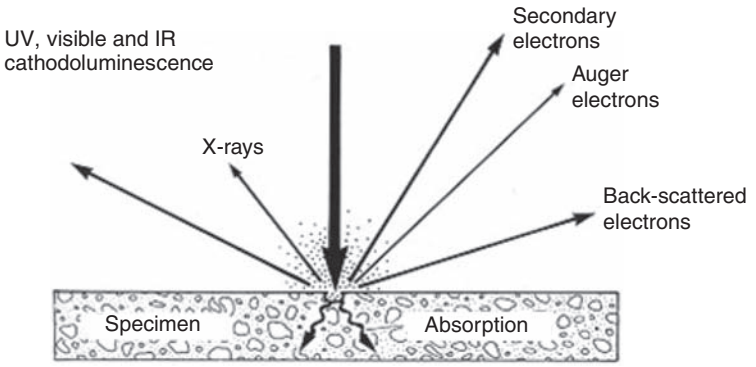


Fig. 27.10—Cathodoluminescence from electron bombardment of a rock sample.

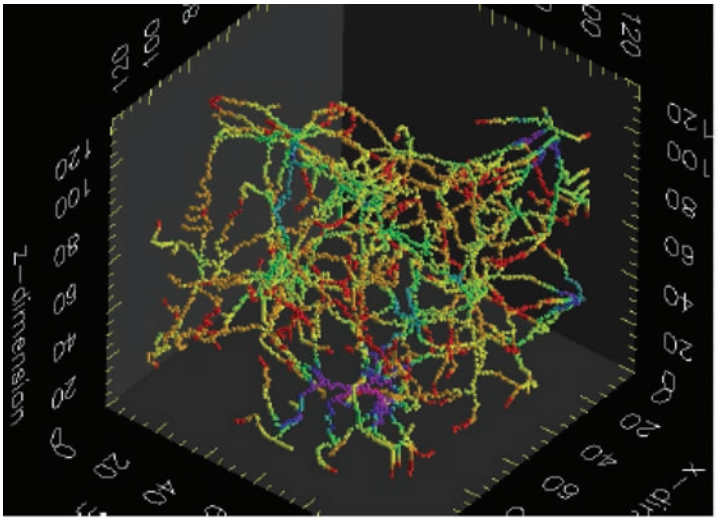


Fig. 27.11—3D image of small core sample. The color code is red for relatively small pore openings and violet for relatively large pore openings (pore volume and grains are not depicted). Dimensions are approximately 1100 × 1100 × 1100 μm^3.

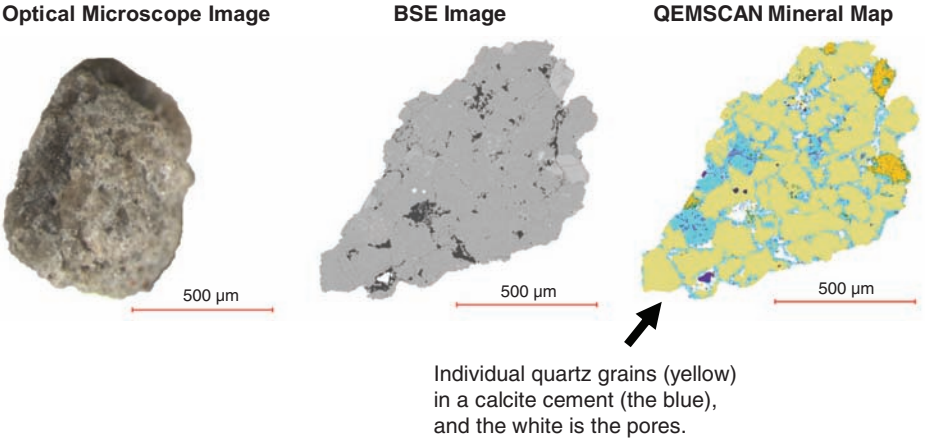


Fig. 27.12—Imaging comparisons. Courtesy of SGS (ARQS).

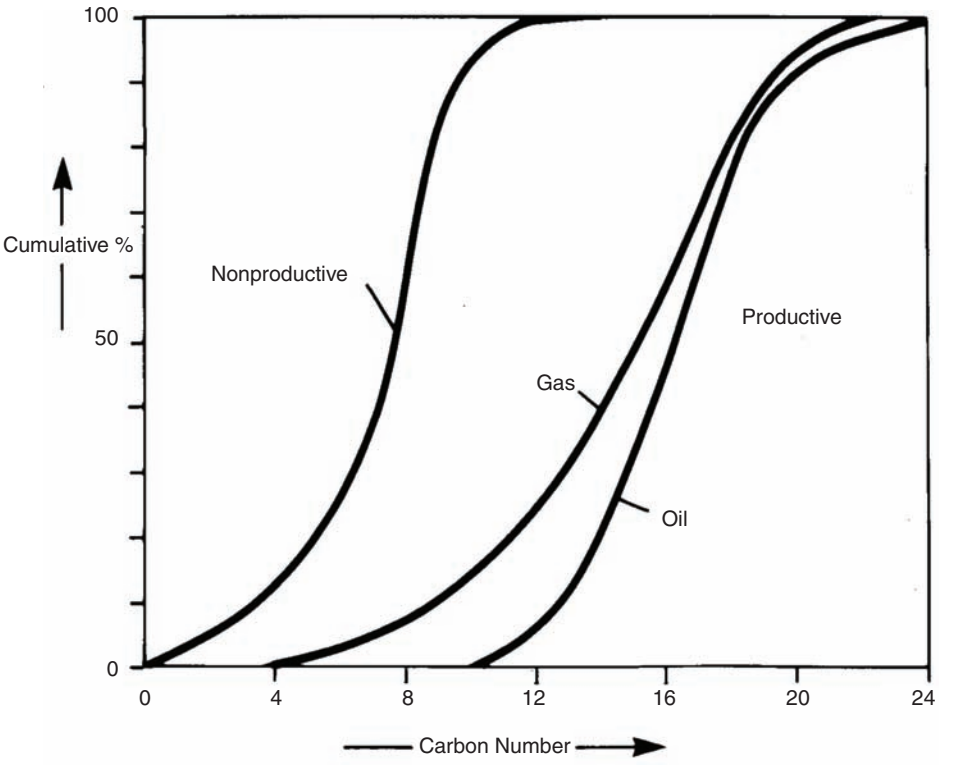


Fig. 27.13—Chromatographic "type" curves for residual hydrocarbon in core samples. After Maness and Price (1979).

Newer methods of analyzing crude oils depend on the optical density of an oil sample to light (both visible and near infrared) at different wavelengths. A typical spectrum obtained by shining light through the crude oil is shown in **Fig. 27.14.**

In addition to optical density, fluorescence is another tool in the core analyst's toolkit. Chapter 2 has already described the value of using a UV light source to detect hydrocarbons in the cuttings retrieved from the shale shaker as a well is drilled. The same technology may be used to "type" the hydrocarbons found in a core sample in the laboratory by use of UV light with a spread of wavelengths so that the fluorescence can be depicted as a characteristic spectrum to identify crude-oil types. **Fig. 27.15** shows an example of this type of analysis.

NMR measurements provide invaluable information about porosity, permeability, saturation, hydrocarbon types, and pore-size distribution in a core sample. The same physical principle is used in logging devices (both on wireline and on the drillstring) for subsurface formation evaluation in boreholes and is covered in Chapter 19.

27.6 Electrical and Related Measurements

Electrical measurements on cores are conducted using specialized cells that enable parameters such as R_o and R_t to be determined at various saturations. Because these parameters vary with salinity and confining stress, they should be measured under conditions that approximate reservoir conditions. Cells of the four-electrode type should be used. Such measurements make possible the deduction of formation factors and saturation exponents. Specifically, the constants a, m, and n in the Archie relationships can be calculated from the measured data. Details are covered in Chapter 26.

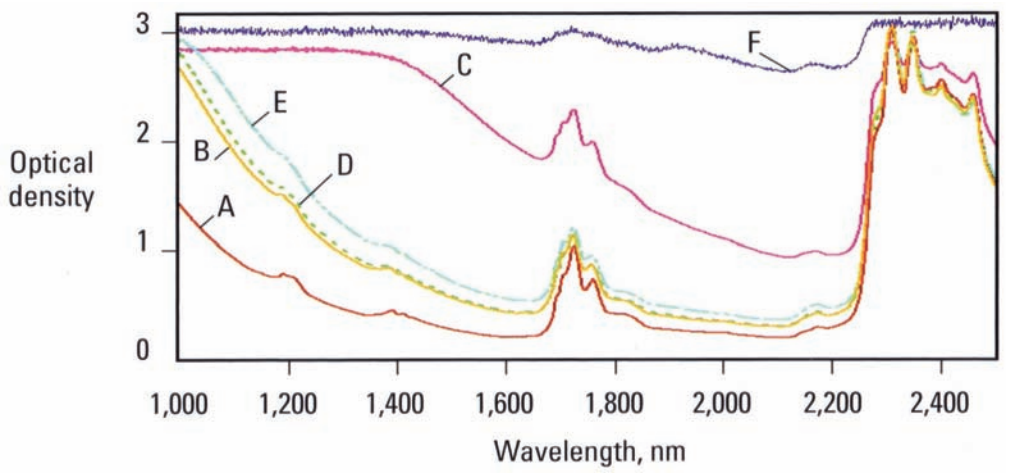


Fig. 27.14—Examples of optical spectra of six different crude oils (Mullins 2008). Courtesy of Schlumberger.

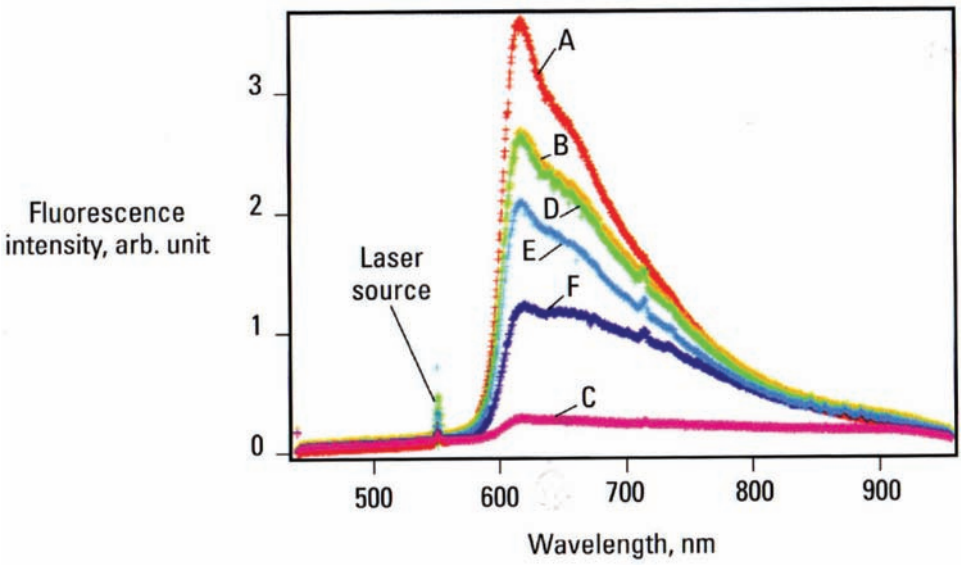


Fig. 27.15—Examples of fluorescence spectra of six different crudes (Mullins 2008). Courtesy of Schlumberger.

In shaly cores, cation-exchange capacity (CEC) can be measured by a chemical titration technique. Other techniques exist, but they are more time-consuming and often of limited availability. Controversy exists regarding the accuracy of CEC measurements on cores because different techniques can give different results.

27.7 Summary

The formation evaluator would do well to acquire an intimate knowledge of core-analysis techniques. Only then can coring programs be designed properly and core-analysis results used correctly. It is hoped that this brief discussion of a vast topic has at least sensitized the reader to some of the benefits and pitfalls of coring and core analysis, while at the same time opening up for consideration some of the possibilities that exist to enhance other forms of formation evaluation.

References

Klinkenberg, L.J. 1941. *Drilling and Production Practice,* pp. 200–213. Washington, DC: API.

Maness, M. and Price, J.G.W. 1979. Well Formation Characterization by Residual Hydrocarbon Analysis. *J. Pet Tech* **31** (1): 118–120. http://dx.doi.org/10.2118/6860-PA.

Mullins, O.C. 2008. *The Physics of Reservoir Fluids*. Houston: Schlumberger Press.

Pittman, E.D. and Thomas, J.B. 1979. Some Applications of Scanning Electron Microscopy to the Study of Reservoir Rock. *J. Pet Tech* **31** (11): 1375–1380. http://dx.doi.org/10.2118/7550-PA.

Welton, J.E. 1984. *SEM Petrology Atlas*. Tulsa: American Association of Petroleum Geologists.

General References

Amott, E. 1959. Observation Relating to the Wettability of Porous Rock. *Trans.,* AIME **216:** 156–162.

API. 1998. *API RP 40, Recommended Practices for Core Analysis,* second edition. Washington, DC: API.

Arns, C.H., Knackstedt, M.A., Pinczewski, W.V., and Martys, N.S. 2004. Virtual Permeametry on Microtomographic Images. *J. Pet. Sci. Eng.* **45:** 41–46.

Bobek, J.E., Mattax, C.C., and Denekas, M.O. 1958. Reservoir Rock Wettability: Its Significance and Evaluation. *Trans.,* AIME **213:** 155–160.

Dupuy, M., Morineau, Y., and Simandoux, P. 1966. About the Importance of Small Scale Heterogeneities on Fluid Flow in Porous Media. Paper presented at the 58th Annual AIChE Meeting, Dallas, 8 February.

Fatt, I. and Davis, D.H. 1952. Reduction in Permeability with Overburden Pressure. *Trans.,* AIME **195:** 329.

Geffen, T.M., Owens, W.W., Parrish, D.R., and Morse, R.A. 1951. Experimental Investigation of Factors Affecting Laboratory Relative Permeability Measurements. *Trans.,* AIME **192:** 99–110.

Hall, H.N. 1953. Compressibility of Reservoir Rocks. *Trans.,* AIME **198:** 309–311.

Hassker, G.L., Brunner, E., and Deahl, T.J. 1944. The Role of Capillarity in Oil Production. *Trans.,* AIME 155: 155–174.

Hill, H.J., Klein, G.E., Shirley, O.J. et al. 1979. Bound Water in Shaly Sands: Its Relation to Q_v and Other Formation Properties. *The Log Analyst* **20** (3): 3–19.

Jones Jr., F.O. 1964. Influence of Chemical Composition of Water on Clay Blocking of Permeability. *J. Pet Tech* **16** (4): 441–446. http://dx.doi.org/10.2118/631-PA.

Keelan, D.K. 1982. Core Analysis for Aid in Reservoir Description. *J. Pet Tech* **34** (11): 2483–2491. http://dx.doi.org/10.2118/10011-PA.

Kieke, E.M. and Hartmann, D.J. 1973. Scanning Electron Microscope Application to Formation Evaluation. *Trans.,* Gulf Coast Association of Geological Societies **23:** 60–67.

Knackstedt, M.A., Arns, C.H., Sakellariou, A., Senden, T.J., Sheppard, A.P., and Sok, R.M. 2007. X-Ray Micro-Tomography Applications of Relevance to the Petroleum Industry. *AIP Conference Proceedings* **902** (1): 135–138.

Martin, P. and Dacy, J. 2004. Effective Q_v by NMR Core Tests. *Trans.,* SPWLA 45th Annual Logging Symposium, Noordwijk, The Netherlands, 6–9 June.

Monaghan, P.H., Salathiel, R.A., Morgan, B.E. et al. 1959. Laboratory Studies of Formation Damage in Sands Containing Clays. *Trans.,* AIME **216:** 209–215.

Osoba, J.S., Richardson, J.G., Kerver, J.K. et al. 1951. Laboratory Measurements of Relative Permeability. *Trans.,* AIME **192:** 47–56.

Price, J.G.W. 1985. Thermal Extraction Chromatography: A New Technique for Rapid Wellbore Evaluation. *J. Cdn Pet Tech* **24** (5): 64–68. http://dx.doi.org/10.2118/85-05-07.

Sok, R., Varslot, T., Ghous, A., Latham, S., Sheppard, A.P., and Knackstedt, M.A. 2010. Pore Scale Characterization of Carbonates at Multiple Scales: Integration of Micro-CT, BSEM and FIBSEM. *Petrophysics* **51** (6): 379–387.

Sheppard, A.P., Arns, J.-Y., Knackstedt, M.A. et al. 2005. Volume Conservation of the Intermediate Phase in Three-Phase Pore-Network Models. *Transport in Porous Media* **59** (2): 155–173.

Stewart, C.R. and Spurlock, J.W. 1952. Analysis of Large Core Samples. *Oil & Gas J.* **51** (17 September).

Talabi, O., Alsayari, S., Blunt, M.J., Dong, H., and Zhao, X. 2008. Predictive Pore-Scale Modeling: From Three-Dimensional Images to Multiphase Flow Simulations. Paper SPE 115535 presented at the SPE Annual Technical Conference and Exhibition, Denver, 21–24 September. http://dx.doi.org/10.2118/115535-MS.

Warren, J.E., Skiba, F.F., and Price, H.S. 1961. An Evaluation of the Significance of Permeability Measurements. *J. Pet Tech* **13** (8): 739–744.

Wyllie, M.R.J., Gregory, A.R., and Gardner, G.H.F. 1958. An Experimental Investigation of Factors Affecting Elastic Wave Velocity in Porous Media. *Geophysics* **23** (3): 459–493.

Answer to Question

QUESTION 27.1. Approximately 8 ft.

Chapter 28

Formation Evaluation in Shaly Sands

28.1 Objectives

The problem the log analyst faces when confronted by shaly sands is formidable. The objective is to define porosity, hydrocarbon content, permeability, and productivity from logs and any other data that may be available, in a situation where no adequate model exists and where the fundamental electrical behavior of the rock system is poorly understood. The problem arises either where clay material is present with a quartz matrix and formation waters are fresh, in which case conventional log analysis overestimates water saturation, or where formation waters are relatively salty and abnormally low formation resistivities are observed in pay zones. Both cases lead to bypassed production unless adequate steps are taken to identify these difficult zones.

The fundamental reason behind the problem is the failure of the classical Archie relationships to hold under the conditions encountered in shaly sands. The postulate that C_o, the wet-rock conductivity, is linearly related to C_w, the water conductivity, has been found to be false in shaly sands. **Fig. 28.1** shows that, as formation water conductivity increases, C_o increases through a nonlinear zone until it reaches a plateau at some conductivity offset X above the clean-sand line. The form of the C_o vs. C_w plot is a function of the shaliness of the sand. **Fig. 28.2** shows that the apparent formation factor F_a ($= C_w/C_o$) decreases with increasing shale content. Note that at high values of C_w (salty formation waters), F_a approaches the classical Archie formation factor. The problem, therefore, is to explain the source of the "excess" conductivity, X.

Over the years, many workers have tackled this problem. In general, the approach has been first to model the behavior of the 100%-wet shaly sand system and then to transpose the model to include nonconductive hydrocarbons as well. A very large body of published material is available on the subject, and the reader is referred to the comprehensive bibliography at the end of this chapter.

28.2 Clay Types and Distributions

In discussions of shaly sands, a distinction is usually made between the terms *clay* and *shale* (see discussion in Chapter 10). In this discussion, "clay" or "dry clay" will be used to refer to dehydrated clay minerals, and "shale" will be used to refer to hydrated clay materials. The potter works with wet clay, but you eat off china (dry clay). In some of the literature, the terms are used interchangeably, which can confuse the issue. The effect of shale on the response of standard logging tools depends on:

- The distribution of the clay material
- The type of clay material
- The amount of clay material
- The salinity of the formation water
- The water saturation

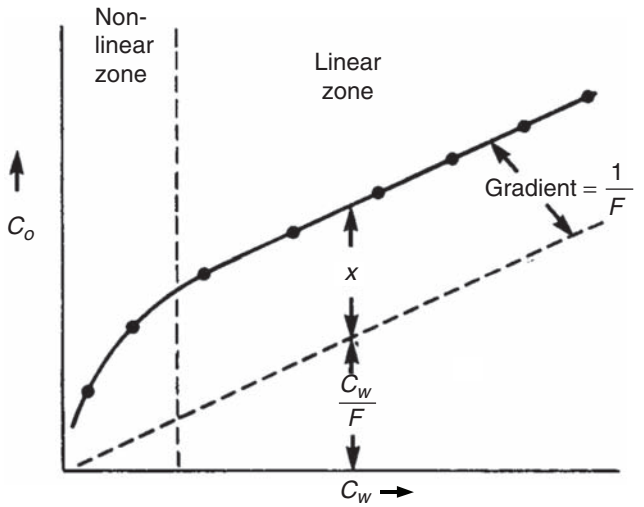


Fig. 28.1—C_o vs. C_w for shaly sand (Worthington 1985). Reprinted by permission from the SPWLA.

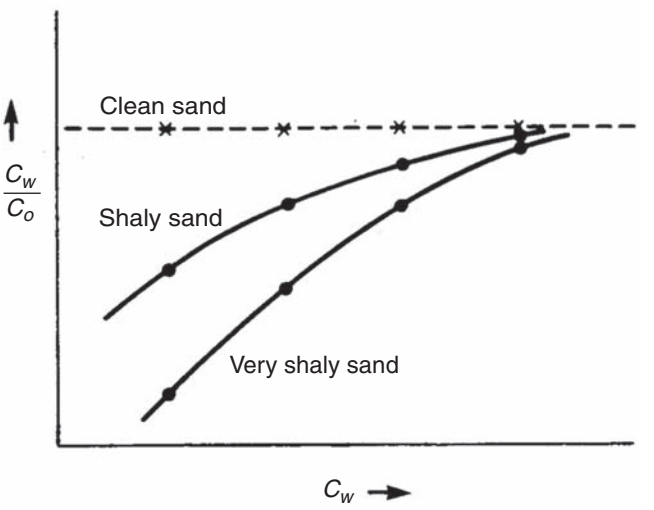


Fig. 28.2—C_w/C_o as a function of C_w and shale content (Worthington 1985). Reprinted by permission from the SPWLA.

28.2.1 Distribution. Fig. 28.3 illustrates three different ways in which clay materials may be distributed:

Dispersed shale is an inexact term used to describe clay overgrowths on the matrix material (for example, sand grains). These clay particles reduce porosity and permeability within the pore structure of the sandstone.

Laminated shale can occur as layers of compacted clay, mudstone, or siltstone and meets this model definition provided that it has zero effective porosity. In a laminated sand/shale sequence, an added complication can be the matter of logging-tool bed resolution.

Structural shale is a term used to describe the random replacement of grains of primary matrix material with fragments of lithified reworked shale.

28.2.2 Clay Types. There are two ways of defining shales. One is by grain size, and the other is by mineralogical description. For example, the standard definitions by grain size (diameter) are:

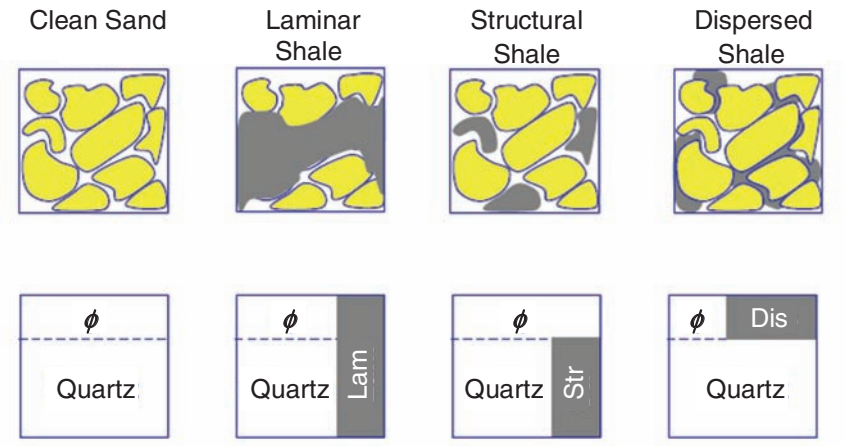


Fig. 28.3—Physical models of shale distribution.

- Sand: 0.05 to 2 mm (50 to 2000 μm)
- Silt: 0.004 to 0.05 mm (4 to 50 μm)
- Clay: less than 0.004 mm (less than 4 μm)

Mineralogical analysis defines the common clay minerals as:

- Montmorillonite (smectite)
- Illite
- Kaolinite
- Chlorite

These are various molecular arrangements of aluminosilicates with various quantities of quartz and feldspar, which can be subclassified further by their origin:

> *Detrital clays are* deposited with the sandstone at the time the sediments are laid down.
> *Authigenic clays* appear as precipitates from solution at a later time.

A schematic of the molecular building blocks and their various arrangements to form clay crystals is shown in **Fig. 28.4.**

The most important aspect of these minerals is their ability to hold adsorbed water on their grain surfaces. **Table 28.1** lists the specific areas of porous formations.

Fig. 28.5 generalizes the relationship between grain size and grain surface area. As grain diameter decreases, so too does pore-throat radius.

As noted in Chapter 6, this decrease in pore-throat radius is accompanied by an increase in capillary pressure and hence an increase in the amount of water that can be imbibed into the system. When silt- and clay-sized particles are present, microporosity accounts for a large percentage of total porosity. Under these circumstances, irreducible water saturation can be very high. To provide a visual understanding of where and how the micropore system develops, **Fig. 28.6** shows SEM photos of the major clay types.

Crystal surfaces have what are known as *exchange sites,* where ions can temporarily reside because of the charge imbalance on the external surface of the clay's molecular building blocks. These exchange sites effectively offer an electrical path through the clay by means of surface conductance. A dry clay is an insulator, of course, but a wet clay is not. The CEC can be measured to quantify the conductivity of wet clays. It will come as no surprise to find that the larger the specific surface area, the larger is the CEC; or in other words, the clay type *per se* is not important, only its specific surface area. Even quartz sand grains, if sufficiently small, exhibit surface

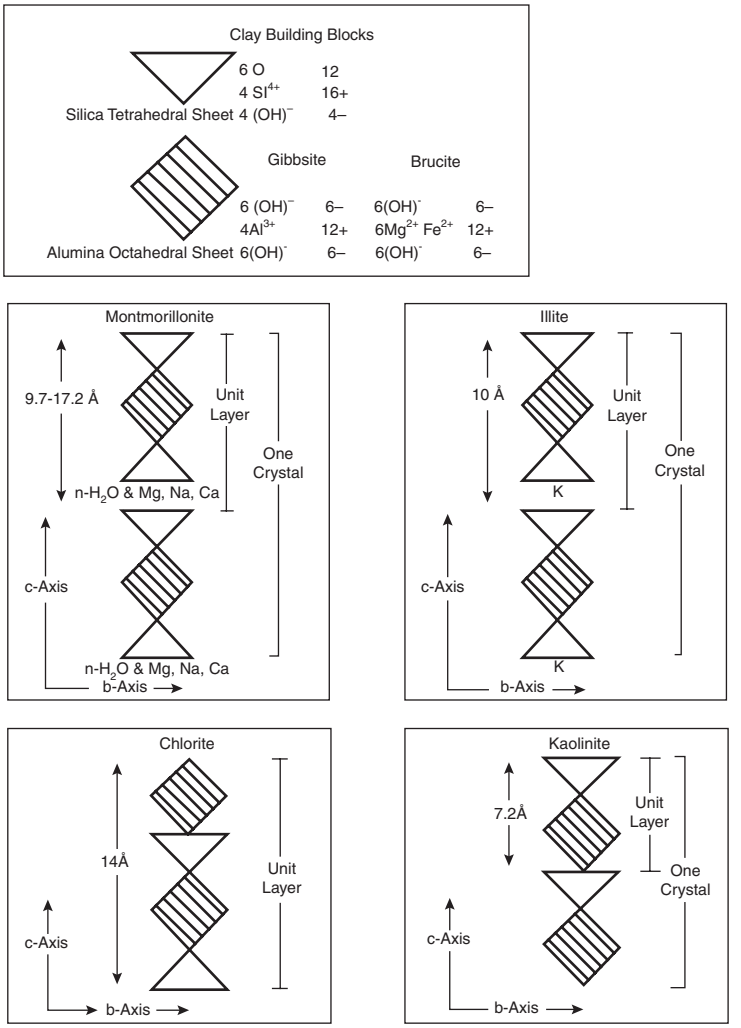


Fig. 28.4—Schematic of clay crystal structure. After Moore (1960).

TABLE 28.1—SPECIFIC AREAS OF POROUS FORMATIONS

Formation	m^2/cm^3	$acres/ft^3$
Montmonrillonite	900	6300
Illite	280	1960
Kaolinite	50	350
Sands (100 grains)	—	0.1 to 0.2

conductance and can be ascribed a CEC value. **Fig. 28.7** shows the relation between CEC and surface area.

Unfortunately, log measurements do not permit direct measurement of either CEC or surface area. **Table 28.2** lists the properties of, and log responses to, the common clay minerals. It can be seen that there is no general correlation between the CEC or specific-area numbers and any *one* clay indicator. Perhaps the best hope for determining clay type from logs is to note that the least electrically active clays have a large neutron-density difference and the most active clays have a small one.

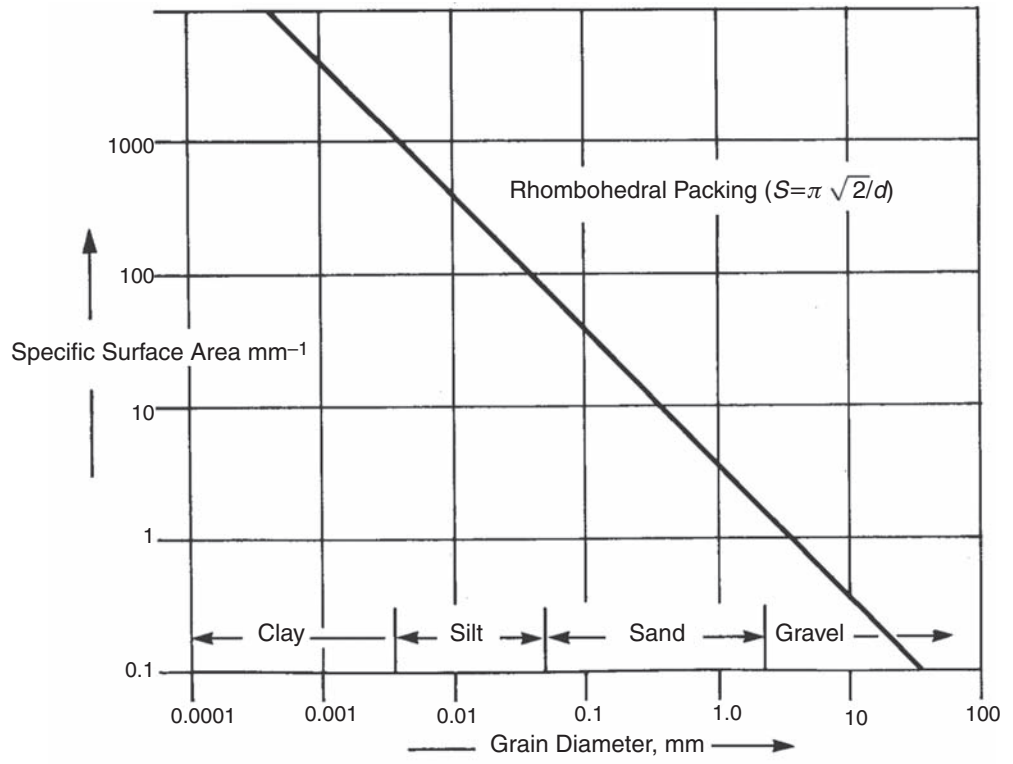


Fig. 28.5—Specific grain surface area as a function of grain diameter for granular formations.

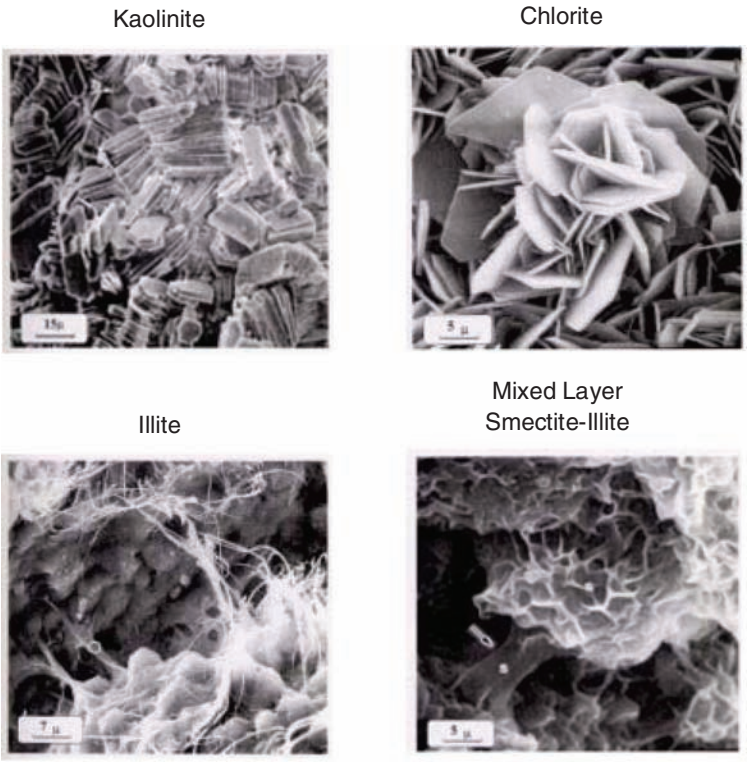


Fig. 28.6—SEM photos of the major clay types and associated micropore structure.

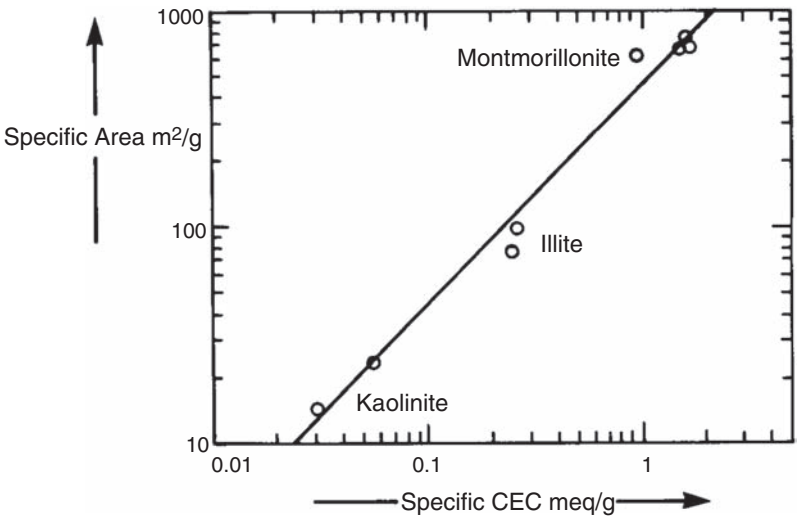


Fig. 28.7—Relation between specific CEC and specific area for API standard clays. After Patchett (1975).

TABLE 28.2—PROPERTIES OF LOG AND RESPONSES TO COMMON CLAY MATERIALS

	Chlorite	Kaolinite	Illite	Montmorillonite
ρ_{ma} g/cm^3	2.6–2.96	2.6–2.7	2.6–2.9	2.2–2.7
(ρ_{ma}) *av* g/cm^3	2.79	2.63	2.65	2.53
CEC meq/100 g	10–40	3–15	10–40	80–150
GR (relative)	1	9	100	5
Σ_{ma} cu	25	14	17.2	11.2
P_e	6.33	1.84	3.55	2.3
(ϕ_{Nsh}) *av* %	52	37	30	44
(ϕ_{Dsh}) *av* %	–7	15	8	32
$\phi_{Nsh} - \phi_{Dsh}$ %	59	22	22	12
ϕ_T %	29.5	26	19	38

28.3 Models

There must be some physical model for analysis of shaly sand logs to produce quantitative results that are of practical use. A number of these models will be considered here, including:

- Laminated shales and sands
- Dispersed clay systems
- Structural shales
- Electrochemical models

The following sections provide a discussion of each model, together with some commonly used equations for determining effective porosity and water saturation for each.

28.3.1 Laminated Shale Model. The model for analysis of laminated shale proposes a multilayer sandwich of alternating layers of clean sand and shale (lithified clay materials). The thickness of each layer is small in relation to the vertical resolution of the porosity and resistivity devices used to log it. Therefore, both porosity and resistivity devices "see" an "average" that is not a true indicator of the properties of either the clean-sand laminae or the intervening shales. **Fig. 28.8**

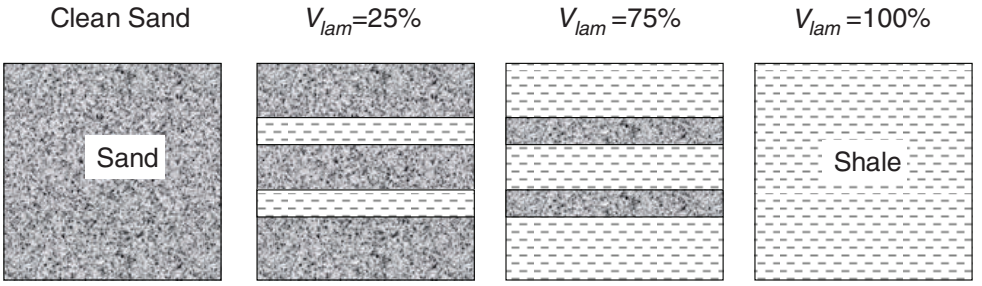


Fig. 28.8—Laminated-shale physical model.

illustrates schematically that as the proportion of shale laminae (V_{lam}) increases, the amount of clean sandstone is reduced. The porosity in the clean sand remains unchanged, but there is progressively less and less of the clean sand present.

In the laminated-shale model, porosity as measured by the density tool can be expressed by:

$$\phi_D = V_{\text{lam}}\phi_{Dsh} + (1 - V_{\text{lam}})\phi_e, \quad \ldots\ldots (28.1)$$

where ϕ_{Dsh} is the apparent density porosity in the shale and ϕ_e is the true porosity in the clean sand. A similar equation can be written for the neutron log:

$$\phi_N = V_{\text{lam}}\phi_{Nsh} + (1 - V_{\text{lam}})\phi_e \quad \ldots\ldots (28.2)$$

Combining these two equations results in equations for true porosity and shale content in a laminated shale:

$$\phi_e = \frac{\phi_{Nsh}\phi_D - \phi_{Dsh}\phi_N}{(\phi_{Nsh} - \phi_{Dsh}) - (\phi_N - \phi_D)} \quad \ldots\ldots (28.3)$$

$$V_{\text{lam}} = \frac{\phi_N - \phi_D}{\phi_{Nsh} - \phi_{Dsh}} \quad \ldots\ldots (28.4)$$

This is represented graphically in **Fig. 28.9.**

QUESTION 28.1. In a laminated sandstone/shale sequence, $\phi_N = 31\%$ and $\phi_D = 19\%$. If $\phi_{Nsh} = 40\%$ and $\phi_{Dsh} = 10\%$, find ϕ_e and V_{lam}.

The resistivity model for water saturation in laminated shale assumes that there are two resistivities in parallel, that of the shale and that of the sandstone. This may be looked at schematically **(Fig. 28.10)** as a measurement of an R_t that is the parallel resistivity of the sand and shale fractions, or in other words, a total rock conductivity that is the weighted sum of the conductivities of its components:

$$C_t = C_{\text{sand}}(1 - V_{\text{lam}}) + C_{sh}V_{\text{lam}} \quad \ldots\ldots (28.5)$$

If C_{sand} is considered to be the conventional Archie conductivity, then

$$C_{\text{sand}} = \frac{\phi_e^m S_w^n}{aR_w} \quad \text{and} \quad C_{sh} = \frac{1}{R_{sh}} \quad \ldots\ldots (28.6)$$

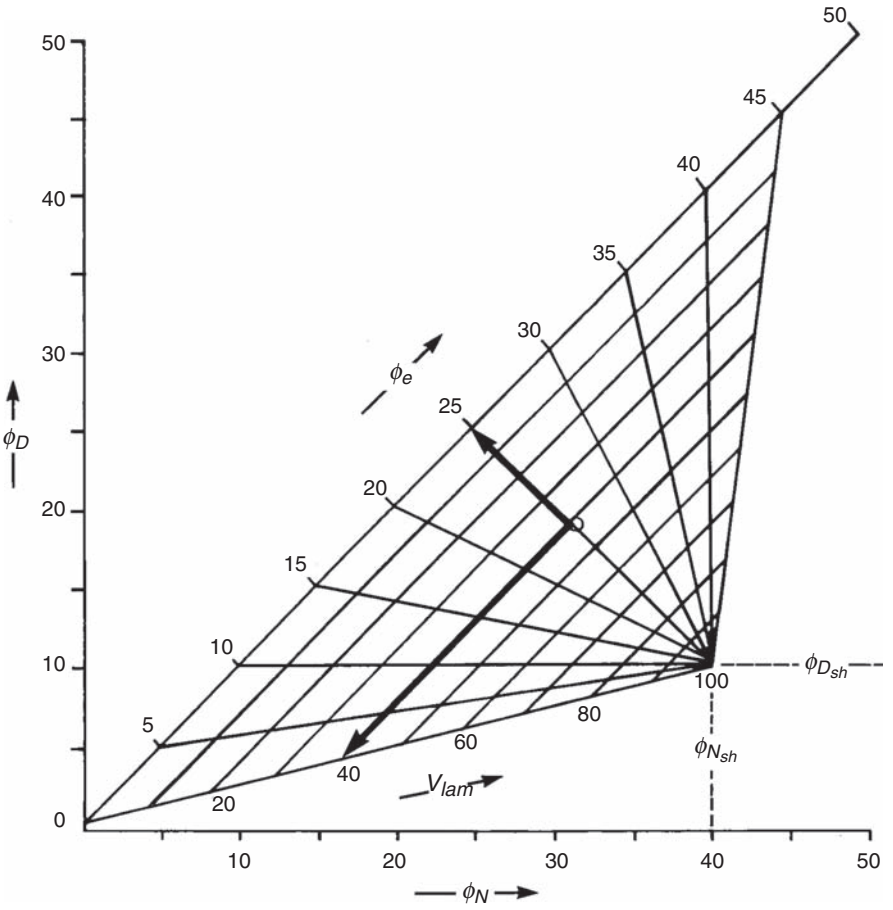


Fig. 28.9—Neutron/density crossplot in a laminated sand/shale sequence.

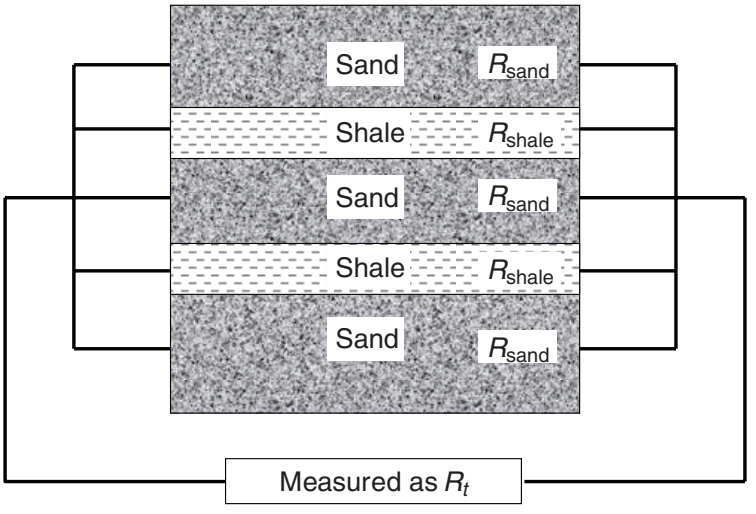


Fig. 28.10—Electrical model of laminated shaly sand.

Hence, S_w will be related to the other parameters by:

$$\frac{1}{R_t} = \frac{(1-V_{\text{lam}})\phi_e^m S_w^n}{aR_w} + \frac{V_{\text{lam}}}{R_{sh}}, \quad \ldots\ldots\ldots\

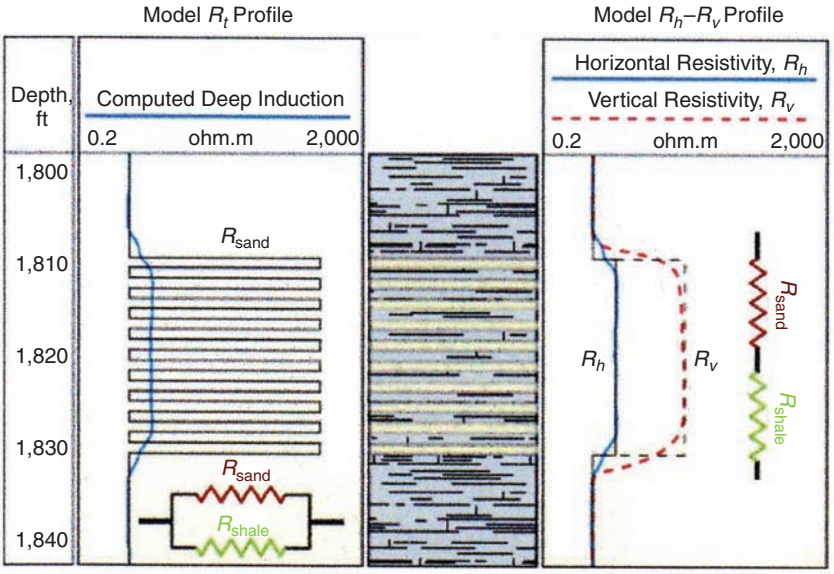


Fig. 28.11—Measurement of vertical and horizontal resistivities in laminated sand/shale sequence (Anderson et al. 2008). Courtesy of Schlumberger.

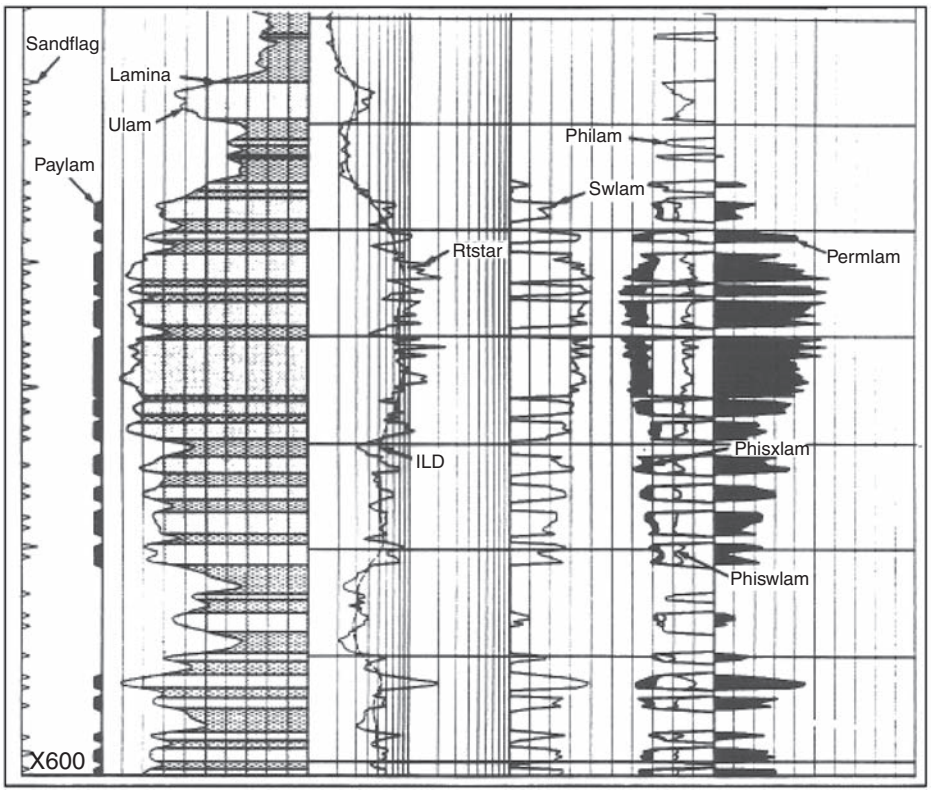


Fig. 28.12—Output of a binary lithology model in a laminated sand/shale sequence (after Bateman 1990). Reproduced by permission from the SPWLA.

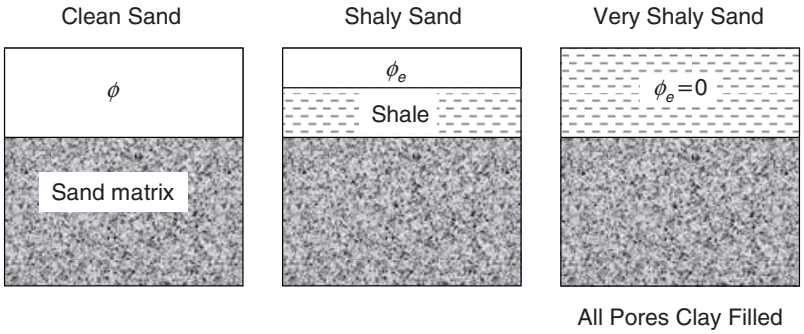


Fig. 28.13—Dispersed-clay physical model.

28.3.2 Dispersed Shale Model. The dispersed-shale model proposes that clay fines and clay overgrowths on the sand grains progressively replace pore space. They bring with them very large surface areas on which large quantities of water are adsorbed. Therefore, high water saturations are likely to be calculated if Archie's clean model is used.

Fig. 28.13 illustrates schematically that the dispersed clays replace porosity. The maximum value of V_{dis} is equal to the original porosity, but the volume of matrix material (sandstone) remains unchanged.

In the dispersed-shale model, porosity measured by the density log will be expressed by:

$$\phi_D = \phi_e + V_{dis}\phi_{Dsh}, \quad \ldots\ldots (28.10)$$

and for the neutron log, porosity is expressed by

$$\phi_N = \phi_e + V_{dis}\phi_{Nsh} \quad \ldots\ldots (28.11)$$

By combining these two equations, an expression for true porosity can be developed:

$$\phi_e = \frac{\phi_{Nsh}\phi_D - \phi_{Dsh}\phi_N}{\phi_{Nsh} - \phi_{Dsh}} \quad \text{and} \quad V_{dis} = \frac{\phi_N - \phi_D}{\phi_{Nsh} - \phi_{Dsh}} \quad \ldots\ldots (28.12)$$

These equations can be solved graphically using **Fig. 28.14.**

The electrical model of the dispersed clay system considers the total porosity to be filled with a mixture of clay slurry of resistivity R_{dis} and free water and hydrocarbons, if any. Therefore, the total formation conductivity can be considered to be the sum of an Archie term referred to as the total porosity (representing both the freely interconnected pores and the slurry-filled pores) and a clay-conductivity term that depends both on water saturation and on the clay fraction (see **Fig. 28.15**).

Therefore, for the dispersed case,

$$C_T = \frac{\phi_T^2 S_{wT}^2}{aR_w} + \frac{\phi_T S_{wT} V_{\text{dis}}}{a}\left(\frac{1}{R_{\text{dis}}} - \frac{1}{R_w}\right) \quad \ldots\ldots (28.13)$$

and

$$S_{we} = 1 - \frac{\phi_T}{\phi_e}\left(1 - S_{wT}\right) \quad \ldots\ldots (28.14)$$

For practical purposes, ϕ_T, ϕ_e, and V_{dis} can be calculated from the neutron-density crossplot (some prefer to take ϕ_T from the sonic log). R_{dis} can be calculated at the shale point as $R_{sh}\,(\phi_{Tsh})^2$.

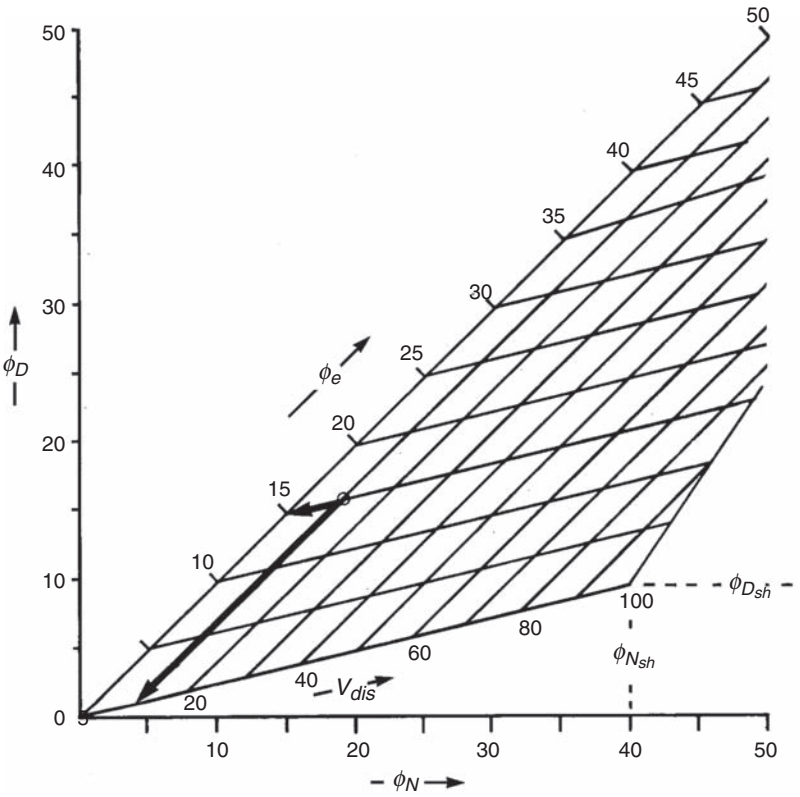


Fig. 28.14—Neutron/density crossplot in dispersed clays.

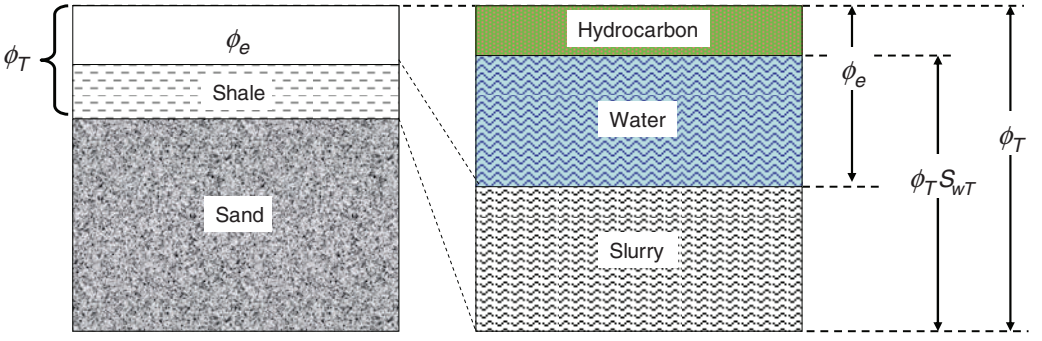


Fig. 28.15—Dispersed-clay electrical model.

QUESTION 28.3. Assuming a dispersed-clay model, solve for ϕ_e and V_{dis} for a case where $\phi_N = 19\%$ and $\phi_D = 16\%$, if $\phi_{Nsh} = 40\%$ and $\phi_{Dsh} = 10\%$. Then, solve the dispersed saturation equation for S_{wT} and S_{we} given $R_{sh} = 2$, $R_w = 0.1$, and $R_t = 8$.

28.3.3 Structural-Shale Model. The structural-shale model proposes that the grains of the sand matrix are progressively replaced with grains of shale. To the extent that the replacement grains may have a different grain density and hydrogen index, this process will have an effect on the neutron- and density-log response. The maximum theoretical fraction of shale in this case is $(1-\phi_e)$ **(Fig. 28.16).**

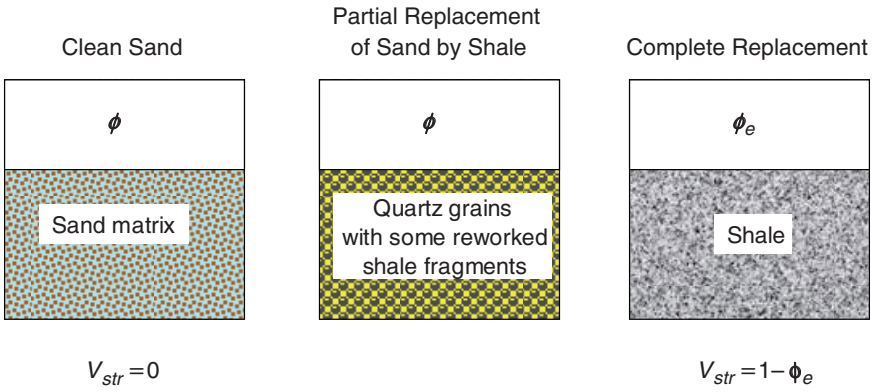


Fig. 28.16—Structural-shale physical model.

The response of the neutron and density tools can be written as:

$$\phi_D = \phi_e + (1-\phi_e) V_{sh} \phi_{Dsh} \quad \ldots\ldots\ldots\ldots (28.15)$$

and

$$\phi_N = \phi_e + (1-\phi_e) V_{sh} \phi_{Nsh}, \quad \ldots\ldots\ldots\ldots (28.16)$$

which gives

$$\phi_e = \frac{\phi_D \phi_{Nsh} - \phi_N \phi_{Dsh}}{\phi_{Nsh} - \phi_{Dsh}} \quad \ldots\ldots\ldots\ldots (28.17)$$

and

$$V_{str} = \frac{\phi_N - \phi_D}{\phi_{Nsh}(1-\phi_D) - \phi_{Dsh}(1-\phi_N)} \quad \ldots\ldots\ldots\ldots (28.18)$$

This is illustrated graphically in **Fig. 28.17.**

The electrical model for the structural case assumes that, in addition to the Archie term, a simple shale-conductivity term can be added such that:

$$C_t = \frac{\phi_e^m S_w^n}{a R_w} + \frac{V_{str}}{R_{sh}}, \quad \ldots\ldots\ldots\ldots (28.19)$$

whence

$$S_w^n = \left(\frac{1}{R_t} - \frac{V_{str}}{R_{sh}} \right) \frac{a R_w}{\phi_e^m} \quad \ldots\ldots\ldots\ldots (28.20)$$

When in doubt as to the actual distribution of shale or clay in the formation, an alternative approach is to use one of the so-called *total-shale* relationships that is nonspecific to the model selected. A commonly used formula is:

$$\frac{1}{R_t} = \frac{\phi_e^m S_w^n}{a R_w (1-V_{sh})} + \frac{V_{sh} S_w}{R_{sh}} \quad (\text{modified total shale}) \quad \ldots\ldots\ldots\ldots (28.21)$$

Although none of these relations has any sound experimental basis, the most widely used is probably the modified total-shale relationship.

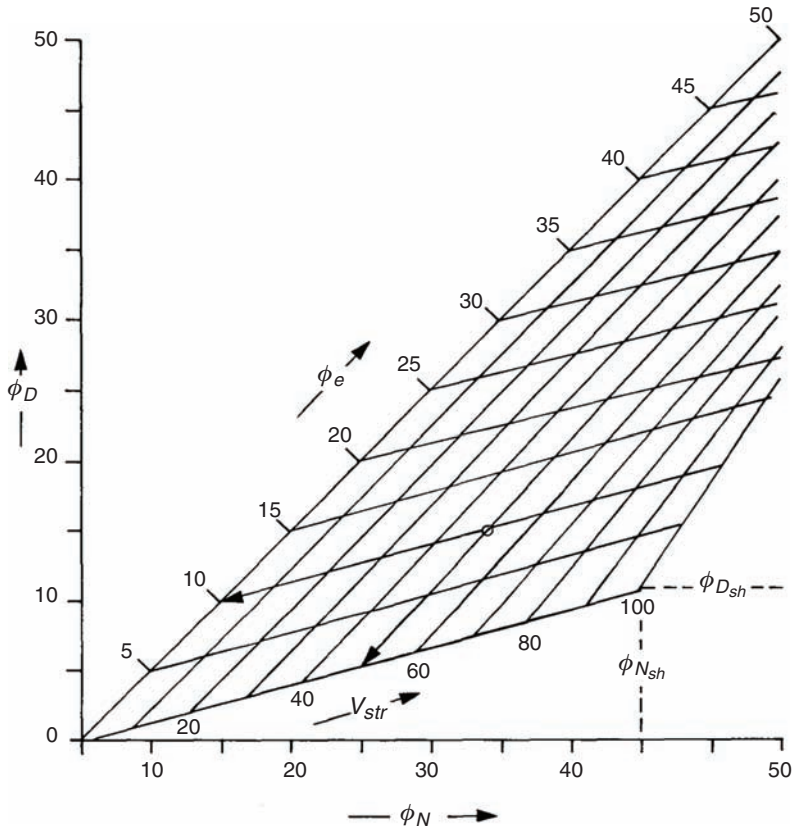


Fig. 28.17—Structural-model neutron/density crossplot.

28.4 Other Shaly Sand Models

28.4.1 Waxman-Smits Technique. Physical chemists can measure the ability of a crystal surface to adsorb water by finding the number of sites available for ionic exchange. This is referred to as the CEC. Different materials have different CEC values. Quartz in the form of sandstone has practically none, but illite and montmorillonite, because of their high specific (surface) areas, have higher CEC values.

Waxman and Smits (1968) derived an equation to express S_w in shaly sands as a function of the CEC of the clay disseminated in the sand:

$$\frac{1}{R_t}=\frac{S_w^2}{F^*R_w}+\frac{BQ_vS_w}{F^*}, \quad \ldots\ldots\ldots\

core measurements of CEC and other log measurements (e.g., GR, ϕ_N, ϕ_D). However, no practical means exists to use this method if only well log data are available. Modifications of the Waxman-Smits method by Juhász (1979) have made it more directly applicable to measurements from logs.

28.4.2 Dual Water Model. The dual water model proposes that two distinct waters can be found in the pore space. Close to the surface of the grains, *bound* water of resistivity R_{wB} is encountered. This water is fresher (more resistive) than the remaining water farther away from the grain surface. This *far* water of resistivity R_{wF} is more saline (less resistive) than the bound water and is free to move in the pores. The model suggests that the amount of bound water is directly related to the clay content of the formation. Therefore, as clay volume increases, the portion of the total porosity occupied by bound water increases. This is illustrated schematically in **Fig. 28.18.**

For a water-bearing shaly sand, the model proposes a total bulk volume of water $\phi_T S_{wT}$ that is made up of a bulk volume of bound water $\phi_T S_{wB}$ and a bulk volume of free water $\phi_e S_{we}$, where ϕ_T is the *total* porosity and ϕ_e is the *effective* porosity. The resistivity model for this mixture of waters requires that the effective mixed-water resistivity be such that:

$$\frac{1}{R_{\text{fluid mixture}}} = \frac{(1-S_{wB})}{R_{wf}} + \frac{S_{wB}}{R_{wB}}, \quad \ldots\ldots\ldots\

conductivity of such a system after accounting for both clay and hydrocarbons can be expressed by the relation:

$$C_t = \frac{C_w S_w^2}{F_o} + \frac{(C_{wB} - C_w) V_Q Q_v S_w}{F_o}, \quad \ldots\ldots\ldots\

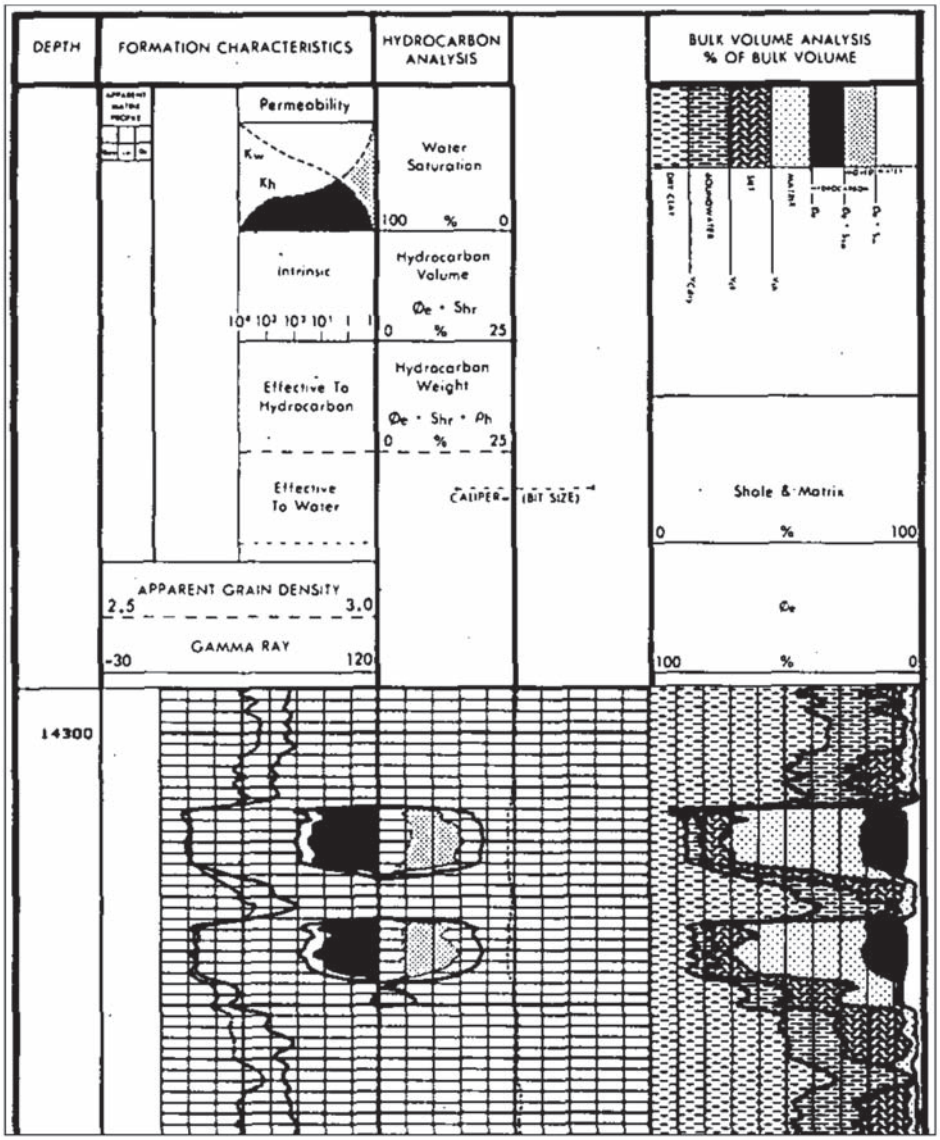


Fig. 28.19—Computer-generated shaly sand presentation. Courtesy of Schlumberger.

gamma ray alone is used as a shale indicator. Many sandstones, on the other hand, have a high potassium feldspar content and are therefore radioactive. The method suggested here should cover both eventualities by combining both gamma ray and neutron/density logs for shale measurement.

Step 0: Compute R_w in a clean wet zone.
Compute R_{wB} in a a shale using $R_{sh}\phi_T^2$.
Step 1: Compute V_{sh} from the gamma ray log in the conventional fashion:

$$V_{sh} = \frac{GR - GR_{cl}}{GR_{sh} - GR_{cl}} \quad \ldots\ldots\ldots\

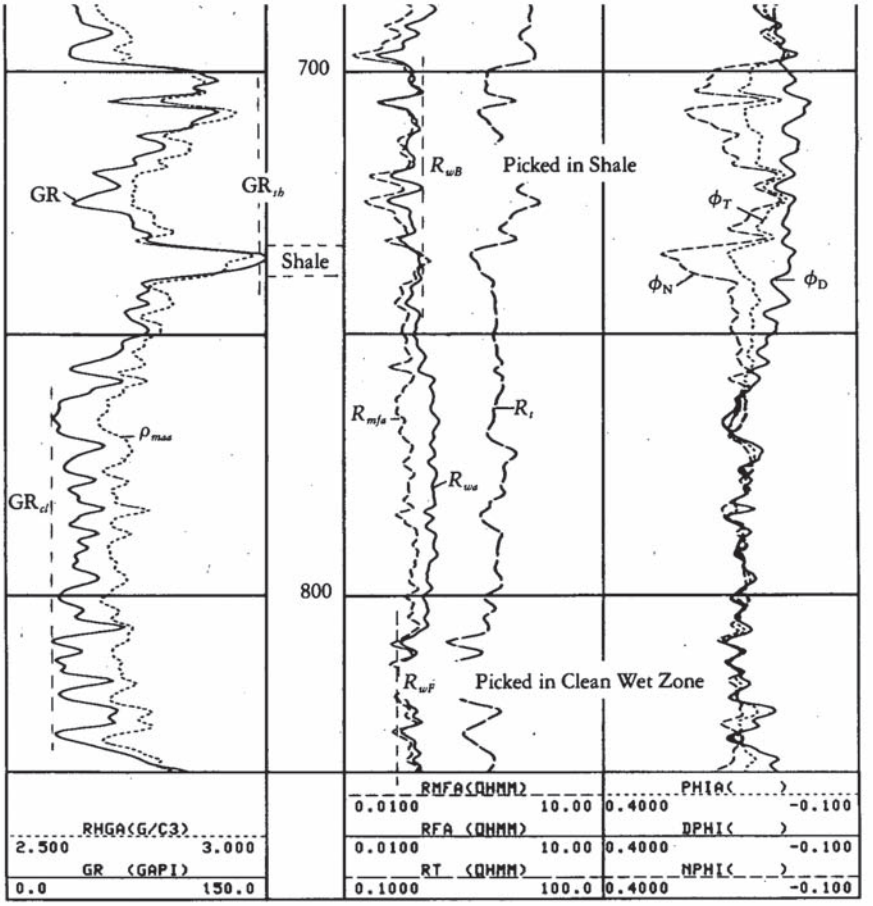


Fig. 28.20—Shaly-sand first-pass presentation for parameter selection. Courtesy of Schlumberger.

If the corrected values are such that $\phi_{Ncor} < \phi_{Dcor}$, then one of two factors could be the cause. Either light hydrocarbons are influencing ϕ_N and ϕ_D, or radioactive matrix such as K-feldspar is present. In either case, compute ϕ_e as:

$$\phi_e = \left(\frac{\phi_N^2 + \phi_D^2}{2} \right)^{1/2} \quad \ldots\ldots\ldots\

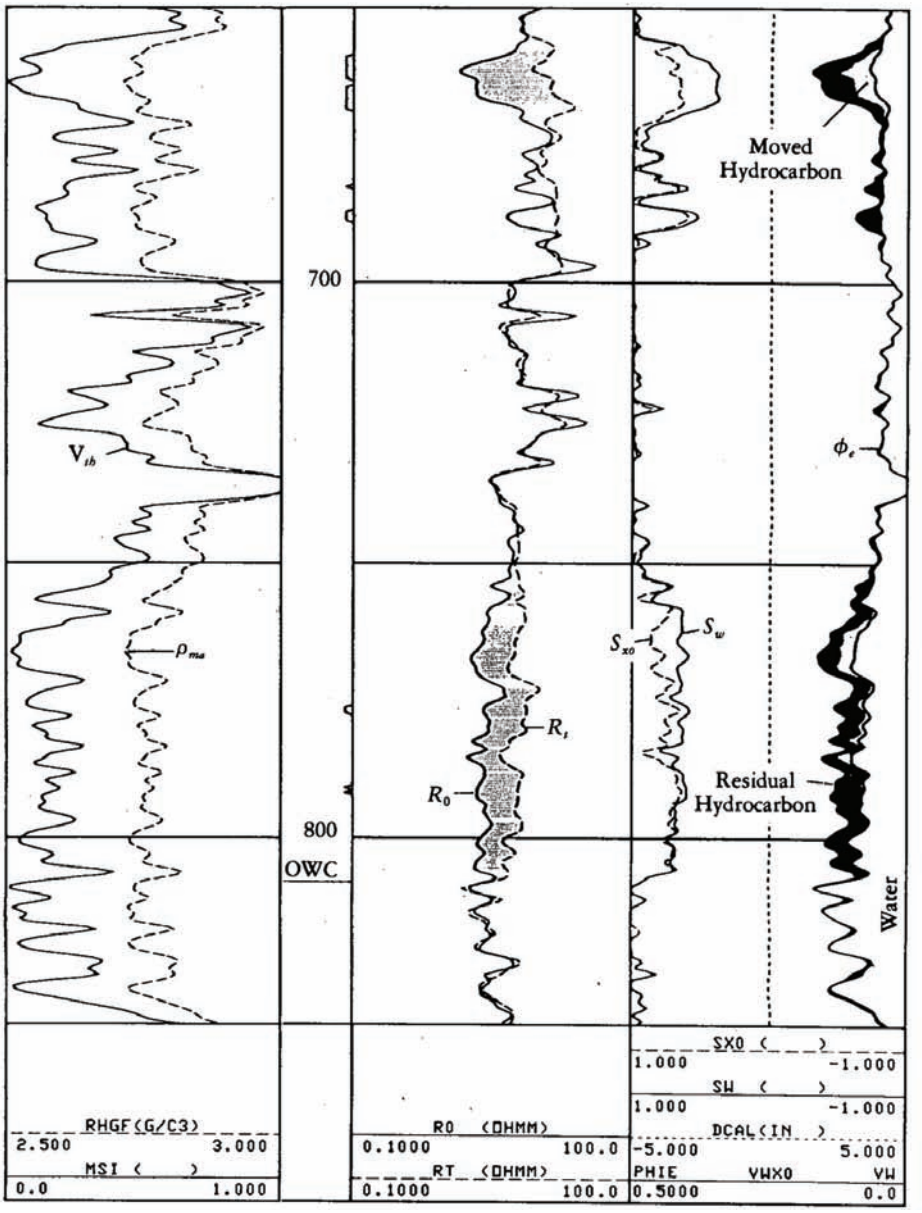


Fig. 28.21—Final presentation for shaly sand using the dual-water model. Courtesy of Schlumberger.

Step 4: Compute ϕ_T from the neutron and density logs as:

$$\phi_T = \frac{\phi_N + \phi_D}{2} \quad \ldots\ldots\ldots\

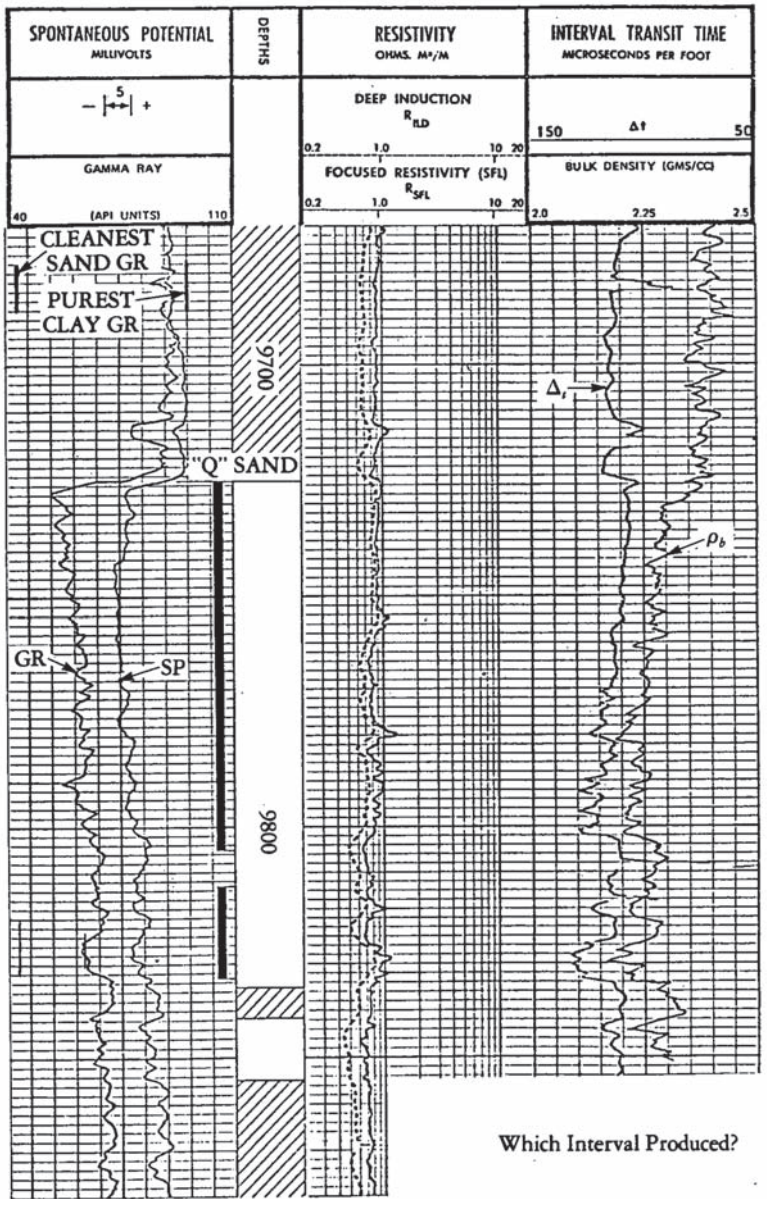


Fig. 28.22—Example log suite, US Gulf Coast well (Vajnar et al. 1977). Reprinted by permission from the SPWLA.

Step 6: Compute effective water saturation as:

$$S_{we} = 1 - \frac{\phi_T}{\phi_e}\left(1 - S_{wT}\right) \quad \ldots\ldots\ldots\

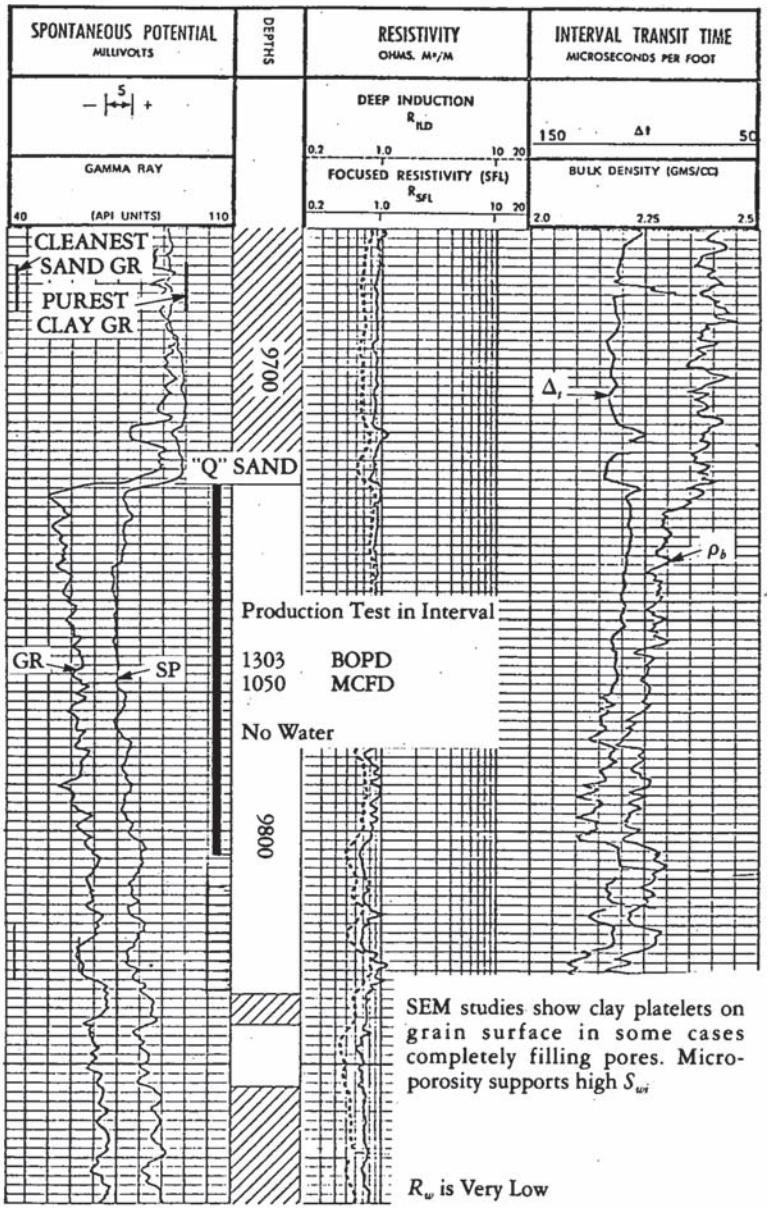


Fig. 28.23—Surprising results in low-resistivity formation (Vajnar et al. 1977). Reprinted by permission from the SPWLA.

A second example is from a North Sea well. The log is presented in **Fig. 28.24.** Again, try to guess the test results from the various marked (gray crosshatched) intervals. The unbelievable, but true, results are shown in **Fig. 28.25.**

28.8 Unconventional Reservoirs

Since the new millennium was ushered in, an ever-increasing number of wells have been drilled in tight-gas sands and in shale-gas and shale-oil plays. Formation evaluation in these low-porosity, low-permeability reservoirs requires special attention, and the reader is directed to Chapter 30, which covers mud logging, coring, and logging measurements and analysis techniques appropriate for these relatively new resources.

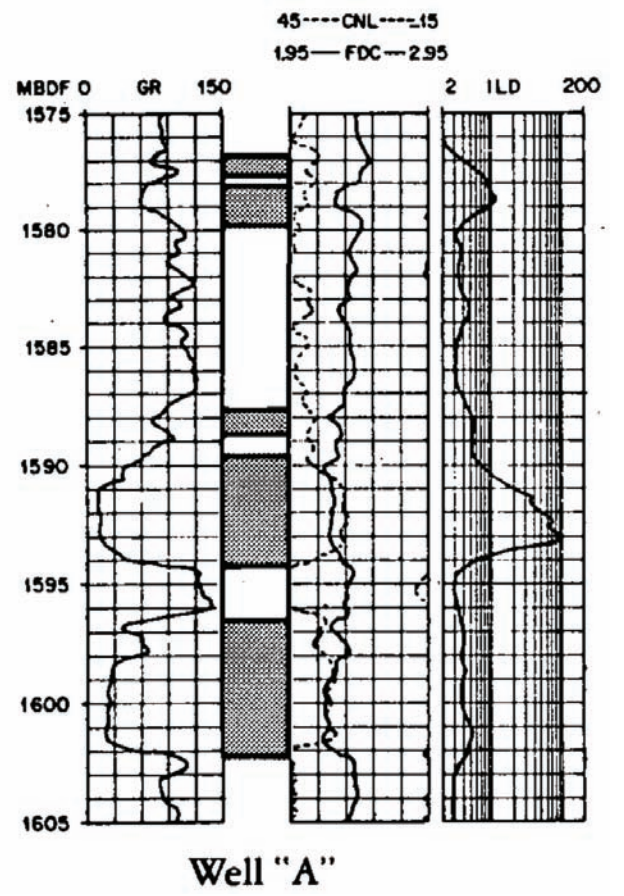


Fig. 28.24—Example log suite from North Sea well (Bos 1982). Reprinted by permission from the SPWLA.

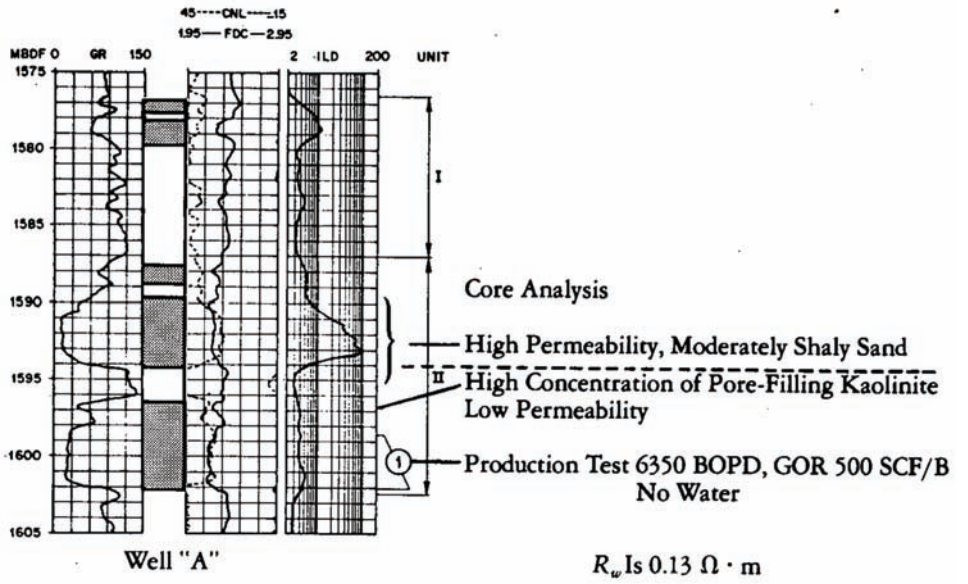


Fig. 28.25—Prolific production from apparent wet interval (Bos 1982). Reprinted by permission from the SPWLA.

28.9 Summary

Log analysis in shaly sands is difficult. Anyone who tells you otherwise is out of date. The easy-to-find pay has mostly been found already. What was not economical to explore and produce a few years ago is now the target of ambitious drilling programs. There is no doubt that more and more shaly reservoirs will have to be evaluated and produced. It is worth pondering that in all probability many prolific producers have already been plugged and abandoned because of lack of adequate formation evaluation.

The key to successful log analysis in these troublesome formations lies in the experimental sciences. The observations are available. What is lacking is an adequate theory to explain the observations and adequate logging tools to make the necessary measurements.

References

Anderson, B., Barber, T., Leveridge, R. et al. 2008. Triaxial Induction—A New Angle for an Old Measurement. *Oilfield Review* **20** (2): 64–84.

Bateman, R.M. 1990. Thinbed Analysis with Conventional Log Suites. *Trans.,* SPWLA 31st Annual Logging Symposium, Lafayette, Louisiana, USA, 24–27 June.

Bos, M.R.E. 1982. Prolific Dry Oil Production From Sands With Water Saturations in Excess of 50%: A Study of a Dual Porosity System. *The Log Analyst* **23** (5): 17–23.

Herrick, D.C. and Kennedy, W.D. 2009. A New Look at Electrical Conduction in Porous Media. *Trans.,* SPWLA 50th Annual Logging Symposium, The Woodlands, Texas, USA, 21–24 June.

Juhász, I. 1979. The Central Role of Q_v and Formation-Water Salinity in the Evaluation of Shaly Formations. *Trans.,* SPWLA 20th Annual Logging Symposium, Tulsa, 3–6 June, Paper AA.

Lee, M.W. 2011. Connectivity Equation and Shaly-Sand Correction for Electrical Resistivity. U.S. Geological Survey Scientific Investigations Report 2011–5005.

Montaron, B. 2009. Connectivity Theory: A New Approach to Modeling Non-Archie Rocks. *Petrophysics* **50** (2): 102–115.

Moore, J.E. 1960. How to Combat Swelling Clays: Clay Mineralogy Problems in Oil Recovery. *The Petroleum Engineer* (February): B78–101; (March): B40–47.

Patchett, J.G. 1975. An Investigation of Shale Conductivity. *Trans.,* SPWLA 16th Annual Logging Symposium, New Orleans, 4–7 June, Paper U.

Schlumberger. 1972. *Log Interpretation: Volume I—Principles*.

Schlumberger. 1982. *Well Evaluation Developments: Continental Europe*.

Vajnar, E.A., Kidwell, C.M., and Haley, R.A. 1977. Surprising Productivity From Low-Resistivity Sands. *Trans.,* SPWLA 18th Annual Logging Symposium, Houston, 5–8 June.

Waxman, M.H. and Smits, L.J.M. 1968. Electrical Conductivities in Oil-Bearing Shaly Sands. *SPE J.* **8** (2): 107–122. http://dx.doi.org/10.2118/1863-A.

Worthington, P.F. 1985. The Evolution of Shaly-Sand Concepts in Reservoir Evaluation. *The Log Analyst* **26** (1): 23–40.

General References

Archie, G.E. 1942. The Electrical Resistivity Log as an Aid in Determining Some Reservoir Characteristics. SPE- 942054-G. *Trans.,* AIME **146:** 54–62.

Almon, W.R. 1979. A Geologic Appreciation of Shaly Sands. *Trans.,* SPWLA 20th Annual Logging Symposium, Tulsa, 3–6 June, Paper WW.

Alguero, A.J., Fabris, A., Watt, H.B., et al. 1973. Effective Porosity and Shale Volume Determinations From Neutron Lifetime and Sidewall Neutron Logs. *Trans.,* SPWLA 14th Annual Logging Symposium, Lafayette, Louisiana, USA, 6–9 May, Paper X.

Carothers, J.E. 1968. A Statistical Study of the Formation Relation. *The Log Analyst* **9** (5): 13–20.

Chilingar, G.V., Rieke III, H.H., Sawabini, S.T., et al. 1969. Chemistry of Interstitial Solutions in Shales Versus That in Associated Sandstones. Paper SPE 2527 presented at the SPE Annual Meeting, Denver, 28 September–1 October. http://dx.doi.org/10.2118/2527-MS.

Clavier, C., Coates, G., and Dumanoir, J. 1977. The Theoretical and Experimental Bases for the Dual-Water Model for the Interpretation of Shaly Sands. Paper SPE 6859 SPE Annual Technical Conference and Exhibition, Denver, 9–12 October. http://dx.doi.org/10.2118/6859-PA.

deWitte, A.J. 1957. Saturation and Porosity from Electric Logs in Shaly Sands. *Oil & Gas J.* **55:** 89.

de Witte, L. 1955. A Study of Electric Log Interpretation Methods in Shaly Formations. *Trans.,* AIME **204:** 103–110.

de Witte, L. 1950. Relations between Resistivities and Fluid Contents of Porous Rocks. *Oil & Gas J.* **49:**120–132.

Doll, H.G. 1950. The SP Log in Shaly Sands. *Trans.,* AIME **189**: 205–214.

Fertl, W.H. 1979. Gamma-Ray Spectral Data Assists in Complex Formation Evaluation. *The Log Analyst* **20:** 3.

Heslop, A. 1972. Gamma-Ray Log Response of Shaly Sandstones. CWLS Symposium **5** (1): 29.

Heslop, A. 1975. Porosity in Shaly Sands. *Trans.,* SPWLA 16th Annual Logging Symposium, New Orleans, 4–7 June, Paper F.

Hill, H.J. and Milburn, J.D. 1956. Effect of Clay and Water Salinity on Electrochemical Behavior of Reservoir Rocks. *Trans.,* AIME **207:** 65–72.

Hill, H.J., Shirley, O.J., and Klein, G.E. 1979. Bound Water in Shaly Sands: Its Relation to Q*v* and Other Formation Properties. *The Log Analyst* **20** (3): 3–19.

Hodson, G., Fertl, W.H., and Hammack, G.W. 1976. Formation Evaluation in Jurassic Sandstones in the Northern North Sea Area. *The Log Analyst* **17** (1): 22–32.

Hossin, A., Delvaux, P., Quint, M.A. et al. 1970. Application to the Hassi-Messaoud Cambrian Reservoir of a New Quantitative Interpretation Method for Shaly Sands. *Trans.,* SPWLA 11th Annual Logging Symposium, Los Angeles, California, USA, 3–6 May, Paper H.

Hoyer, W.A. and Rumble, R.C. 1976. Dielectric Constant of Rocks as a Petrophysical Parameter. *Trans.,* SPWLA 17th Annual Logging Symposium, Denver, 9–12 June, Paper O.

Johnson, W.L. and Linke, W.A. 1977. Some Practical Applications to Improve Formation Evaluation of Sandstones in the Mackenzie Delta. *Proc.,* 6th Formation Evaluation Symposium of the CWLS, Calgary, 24–26 October, Paper R.

Kern, J.W., Hoyer, W.A., and Spann, M.M. 1977. High Temperature Electrical Conductivity of Shaly Sands. *Trans.,* SPWLA 18th Annual Logging Symposium, Houston, 5–8 June, Paper U.

Kern, J.W., Hoyer, W.A., and Spann, M.M. 1976. Low Porosity Gas Sand Analysis Using Cation Exchange and Dielectric Constant Data. *Trans.,* SPWLA 17th Annual Logging Symposium, Denver, 9–12 June, Paper PP.

Kennedy, D. 2007. The Porosity-Water Saturation-Conductivity Relationship: An Alternative to Archie's Model. *Petrophysics* **48** (5): 335–361.

Marett, G., Chevalier, P., Souhaite, P. et al. 1976. Shaly Sand Evaluation Using Gamma Ray Spectrometry Applied to the North Sea Jurassic. *Trans.,* SPWLA 17th Annual Logging Symposium, Denver, 9–12 June, Paper DD.

Lee, M.W., Collett, T.S., Anderson, B.J. et al. 2011. Evaluation of Long-Term Gas Hydrate Production Testing Locations on the Alaska North Slope. Paper OTC 22149 presented at the OTC Arctic Technology Conference, Houston, 7–9 February. http://dx.doi.org/10.4043/22149-MS.

Neasham, J.W. 1977. The Morphology of Dispersed Clay in Sandstones and Its Effect on Sandstone Shaliness, Pore Space, and Fluid Flow Properties. Paper SPE 6858 presented at the SPE Annual Technical Conference and Exhibition, Denver, 9–12 October. http://dx.doi.org/10.2118/6858-MS.

Ohirhian, P.U. 1998. An Explicit Form of the Waxman-Smits Equation for Shaly Sands. *The Log Analyst* **39** (3): 54–57.

Passey, Q.R., Dahlberg, K.E., Sullivan, K.B. et al. 2006. *Petrophysical Evaluation of Hydrocarbon Pore-Thickness in Thinly Bedded Clastic Reservoirs*, AAPG Archie Series, No. 1, Chaps. 1, 2, and 3. Tulsa, AAPG Special Volumes, AAPG.

Patnode, H.W. and Wyllie, M.R.J. 1950. The Presence of Conductive Solids in Reservoir Rocks as a Factor in Log Interpretation. *Trans.,* AIME **189:** 47–52.

Porter, C.R. and Carothers, J.E. 1970. Formation Factor-Porosity Relation Derived From Well Log Data. *Trans.,* SPWLA 11th Annual Logging Symposium, Los Angeles, California, USA, 3–6 May.

Poupon, A. and Gaymard, R. 1970. The Evaluation of Clay Content from Logs. *Trans.*, SPWLA 11th Annual Logging Symposium, Los Angeles, California, USA, 3–6 May, Paper G.

Poupon, A. and Leveaux, J. 1971. Evaluation of Water Saturation in Shaly Formations. *Trans.*, SPWLA 12th Annual LoggingSymposium, Dallas, 2–5 May, Paper O.

Poupon, A., Loy, M.E., and Tixier, M.P. 1954. A Contribution to Electrical Log Interpretation in Shaly Sands. *J. Pet Tech* **6** (6): 27–34; *Trans.,* AIME, **201.** SPE-311-G. http://dx.doi.org/10.2118/311-G.

Poupon, A., Clavier, C., Dumanoir, J. et al. 1970. Log Analysis of Sand Shale Sequences: A Systematic Approach. *J. Pet Tech* **22** (7): 867–881. http://dx.doi.org/10.2118/2897-PA.

Ransom, R.C. 1977. Methods Based on Density and Neutron Well Logging Responses to Distinguish Characteristics of Shaly Sandstone Reservoir Rocks. *The Log Analyst* **18** (3): 47–62.

Rink, M. and Schopper, J.R. 1974. Interface Conductivity and Its Implications for Electric Logging. *Trans.,* SPWLA 15th Annual Logging Symposium, Houston, 5–8 June.

Ruhovets, N. and Fertl, W.H., 1981. Digital Shaly Sand Analysis Based on Waxman-Smits Model and Log-Derived Clay Typing. Paper presented at the 7th European Logging Symposium, Paris, 21–23 October.

Simandoux, P. 1963. Dielectric Measurements on Porous Media: Application to the Measurement of Water Saturations. *Revue de L Institut Français du Pétrole,* Vol. 18, supplementary issue, 193–215; (translated text in shaly sand reprint volume, SPWLA, Houston, IV, 97–124).

Simandoux, P. 1963. Dielectric Measurements in Porous Media and Application to Shaly Formations (Mesures Diélectriques en Milieu Poreux, Application à la Mesure des Saturations en Eau, Etude du Comportement des Massifs Argileux), *Revue de l'Institut Français du Pétrole,* Vol. 18, supplementary issue, 193–215.

Smits, L.J.M. 1968. SP Log Interpretation in Shaly Sands. *SPE J.* **8** (2): 123–136. http://dx.doi.org/10.2118/1863-PA.SPWLA. 1982. Reprint Volume: *Shaly Sand*.

Thomas, E.C. 1976. The Determination of Q_v from Membrane Potential Measurements on Shaly Sands. *J. Pet Tech* **28** (9): 1087–1096. http://dx.doi.org/10.2118/5505-PA.

Thomas, E.C. and Stieber, S.J. 1975. The Distribution of Shale in Sandstones and Its Effect Upon Porosity. *Trans.,* SPWLA 16th Annual Logging Symposium, Denver, 9–12 June, Paper T.

Tixier, M.P., Morris, R.L., and Connell, J.G. 1968. Log Evaluation of Low-Resistivity Pay Sands in the Gulf Coast. *The Log Analyst* **9** (6): 3–20.

Waxman, M.W. and Thomas, E.C. 1974. Electrical Conductivities in Oil-Bearing Shaly Sands—I. The Relation between Hydrocarbon Saturation and Resistivity Index; II. The Temperature Coefficient of Electrical Conductivity. *SPE J.* **26** (2): 213–225. http://dx.doi.org/10.2118/4094-PA.

Wilson, M.D. 1982. Origins of Clays Controlling Permeability in Tight Gas Sands. *J. Pet Tech* **34** (12)**:** 2871–2876. http://dx.doi.org/10.2118/9843-PA.

Wilson, M.D. and Pittman, E.D. 1977. Authigenic Clays in Sandstones: Recognition and Influence on Reservoir Properties and Paleoenvironmental Analysis. *Journal of Sedimentary Research* **47** (1): 3–31.

Winsauer, W.O. and McCardell, W.M. 1953. Ionic Double Layer Conductivity in Reservoir Rocks. *Trans.,* AIME **198:** 129–134.

Worthington, A.E. 1973. An Automated Method for the Measurement of Cation Exchange Capacity of Rocks. *Geophysics* **38** (1): 140–153.

Wyllie, M.R.J. and Southwick, P.F. 1954. An Experimental Investigation of the SP and Resistivity Phenomena in Dirty Sands. *J. Pet Tech* **6** (2): 44–57. http://dx.doi.org/10.2118/302-G.

Answers to Questions

QUESTION 28.1.
$\phi_e = 25\%$.
$V_{lam} = 40\%$.

QUESTION 28.2.
a. $S_w = 30\%$.
b. $S_w = 119\%$.
c. $S_w = 66\%$.

QUESTION 28.3.
$\phi_e = 15\%$.
$V_{\text{dis}} = 10\%$.
$S_{wT} = 67.7\%$.
$S_{we} = 62.3\%$.

QUESTION 28.4.
a. $S_w = 25\%$.
b. $\rho_{hy} = 0.4$ g/cm$^{3.}$
c. $k_o = 30$ md.
d. $\rho_{ma} = 2.65$ g/cm^3.

QUESTION 28.5.
a. $R_{wF} = 0.04\ \Omega$·m.
b. $R_{wB} = 0.08\ \Omega$·m.
c. $GR_{cl} = 26$.
d. $GR_{sh} = 145$.
Yes, gas at 660–670.

Chapter 29

Formation Evaluation in Complex Lithology

29.1 Objectives

The objectives of an analyst faced with the problem of formation evaluation in complex lithology may differ from those of an analyst evaluating shaly sands. In the former case, the problem is to account adequately for an unknown mixture of rock types, some of which may be reservoir rocks containing recoverable hydrocarbons. Conventionally, these reservoirs are classified as hard rock and are characterized by low porosity, low permeability, and the existence of secondary porosity in the form of vugs and fractures.

Although most of the log analysis principles already covered (see Chapter 24) are valid in this situation, the way in which they are applied to form a coherent method of foot-by-foot analysis is of most interest here. Some problem formations defy conventional analysis techniques and must be addressed by specific working rules. Among these may be included conglomerates, which in some areas are prolific producers, and oolitic formations, where porosity evaluation is difficult. Analysis of other unconventional reservoirs such as tight gas sands, coalbed methane, and shale gas is covered in Chapter 30. Some important types of analysis, such as geothermal projects and mineral logging for uranium, potassium, and sulfur, are unfortunately beyond the scope of this present work.

29.2 Exactly Determined Systems

A classical method of solving multimineral log response problems is historically known as the Chaveroo method. It was developed when the Chaveroo field was being actively drilled and logged in the 1960s. The method reduces the problem to a simple inversion of a "response" matrix. It is most easily understood by reference to the Martini Problem:*

A log analyst, after a hard day's work, sought comfort and deserved repose in a bar. He ordered a martini and was immediately struck by the harmonious and mellow proportions of its ingredients. Wishing to learn the secret of the "perfect martini," he asked the bartender to tell him how much gin, dry vermouth, and sweet vermouth had been used. The barman (a geologist perhaps?) could only reply that it was mostly made of gin with occasional vermouthian tendencies. The analyst thereupon set out to back calculate the relative proportions of the mix using the alcohol and sugar contents of the ingredients and of the mixture. He "logged" his martini to find that it contained 35% alcohol and 3.4% sugar. He consulted a reference book to find the amount of alcohol and sugar in each ingredient. **Table 29.1** shows what he found:

*I am indebted to John Doveton of the Kansas Geological Survey for the original Martini Problem, which I have adapted slightly for the present purpose.

TABLE 29.1—MARTINI MATRIX		
	Alcohol	Sugar
Martini	35%	3.4%
Gin	47%	0.0%
Dry Vermouth	18%	3.0%
Sweet Vermouth	16%	14.0%

He solved the problem by setting up three simultaneous equations:

$$\text{Alcohol}: \quad 35 = V_G \times 47 + V_{DV} \times 18 + V_{SV} \times 16. \quad (29.1)$$

$$\text{Sugar}: \quad 3.4 = V_G \times 0 + V_{DV} \times 3 + V_{SV} \times 14. \quad (29.2)$$

$$\text{Material Balance}: \quad 1 = V_G + V_{DV} + V_{SV}, \quad (29.3)$$

where V_G is the fraction of gin, V_{DV} the fraction of dry vermouth, and V_{SV} is the fraction of sweet vermouth. He then solved the three equations to find V_G, V_{DV}, and V_{SV}, the respective fractions of gin, dry vermouth, and sweet vermouth.

QUESTION 29.1. Compute the values of V_G, V_{DV}, and V_{SV}.

This is not a trivial example. Each logging tool can be used to set up a response equation describing a lithology mix. If V_L, V_D, and V_S are the bulk volumes of limestone, dolomite, and sandstone in some lithology mixture, then, for example, the density of the mixture can be expressed in terms of the relative quantities of each and the density-tool response to each:

$$\rho_b = V_L \times 2.71 + V_D \times 2.87 + V_S \times 2.65 + \phi \times 1.0. \quad (29.4)$$

In a similar fashion, the sonic and neutron logs can also define a response equation:

$$\Delta t = V_L \times 47.5 + V_D \times 43.5 + V_S \times 55.5 + \phi \times 189. \quad (29.5)$$

$$\phi_N = V_L \times 0 + V_D \times 0.07 + V_S \times (-0.03) + \phi \times 1. \quad (29.6)$$

Finally, the material-balance equation reveals that

$$1 = V_L + V_D + V_S + \phi. \quad (29.7)$$

QUESTION 29.2.
Given Δt = 69 μs/ft,
ρ_b = 2.49 g/cm^3, and
ϕ_N = 16.5%,
find the porosity and the fractions of limestone, dolomite, and sandstone in the mixture.

Elaboration of examples such as these should convince even the most mathematically inclined analyst that level-by-level solutions to matrix inversion problems using only a hand-held calculator are not to be recommended. Clearly, this type of processing is best left to a computer that has been fed log data in digital form.

In the example of Question 29.2, three independent formation measurements were combined to solve for four unknowns: porosity and the volume fractions of limestone, dolomite, and sandstone. Because four equations are required to solve for four unknowns, the material-balance equation (stating that the sum of the component fractions is equal to unity) provided the missing equality. Therefore, in general, given **n** independent logging measurements, a solution can be found for **n + 1** components. For example, if in addition to neutron, density, and sonic measurements, measurements of P_e and gamma ray were also available, then a solution could be sought for two additional components (anhydrite and salt, for example).

The mathematics of this approach (the Chaveroo method) is straightforward. The weakness of the method lies in the analyst's choice of the components for which to solve. What happens, for example, if a heavy mineral (e.g., a pyrite with $\rho_{ma} = 4.99$ g/cm^3) is present but not specified as a component to be solved for? There is a good chance that in such a case, the point in question will fall outside the solution polygon and will result in an apparently negative quantity of one of the other specified components.

Many computer-based programs have been written to implement the Chaveroo approach to log analysis in multimineral environments. Some include elegant logic to handle cases in which an unspecified component appears or a negative quantity of a specified component results. Such programs have their place and their application in situations where the lithology is reasonably well known (e.g. from experience or core analysis) and when a knowledgeable analyst is involved who can select both the components and their correct endpoints. An example of the results obtained from this kind of processing is shown in **Fig. 29.1.** The column logged is predominantly anhydrite and dolomite with occasional appearances of sand and gypsum. The well was completed in the intervals shown, acidized and fractured, and put on production at 609 BOPD and 6 BWPD.

The Chaveroo method can generate only one answer set for a given input-data set because the system is exactly determined. Once the response equations are written and the endpoints chosen for each component, then for any given set of log data, one and only one solution can be found. What happens if the log data are subject to statistical variations (neutron, density, gamma ray) or the response model is inaccurate? Logically, the answers produced will also suffer from these variations and inaccuracies, and there will be no way to assess the magnitude of the error. In general, it can be stated that the most accurate assessment made by Chaveroo processing will be porosity. However, if the inaccuracies are to be estimated properly, another type of processing is called for.

29.3 Overdetermined Systems

Overdetermined systems, unlike exactly determined systems, have more equations than unknowns. For example, with five log measurements (ρ_b, ϕ_N, Δt, P_e, and GR), finding the relative proportions of three components (sand, limestone, and dolomite) is a relatively simple problem. Instead of only one possible solution, there are many possible solutions. Any three log measurements suffice to form an exact solution subset, and in this case, there are ten different ways to choose three logs out of five. (The reader may satisfy himself on this score by writing down all possible combinations of any two log measurements to be omitted.) If the log measurements are perfect and the model is perfect, all ten possible solutions will coincide. In practice, this never happens, and the result is a set of ten possible answers for each component. Which one is correct? For each possible answer, a value for the original log measurements may be back-calculated. For example, the density-tool response equation can be written as:

$$\rho_b = \rho_1 V_1 + \rho_2 V_2 + \cdots \rho_n V_n, \quad (29.8)$$

where ρ_1, ρ_2, … are the log responses to Components 1, 2, … and V_1, V_2, … are the volume fractions of Components 1, 2, …. If $V_{1,1}$ is the estimated value of V_1 from the first of the ten possible answer sets, then the back-calculated value of ρ_b will be:

$$\rho_{b1} = \rho_1 V_{1,1} + \rho_2 V_{2,1} + \cdots + \rho_n V_{n,1}. \quad (29.9)$$

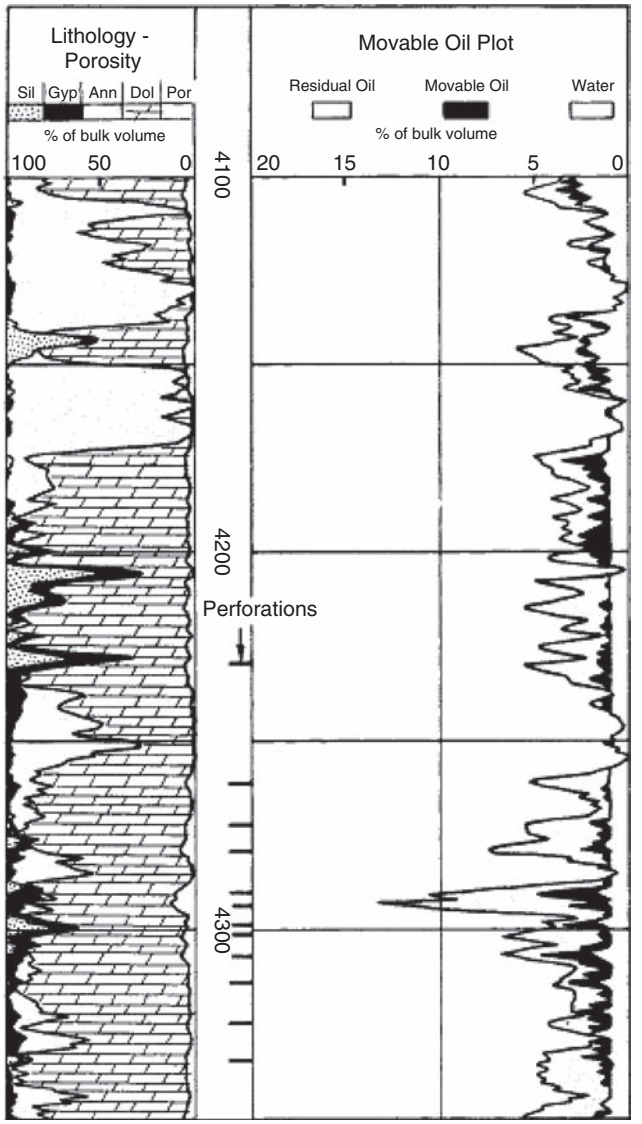


Fig. 29.1—Example of Chaveroo log processing (Burke et al. 1966).

This can then be compared with the actual log reading of ρ_b and an error function defined as:

$$E\rho_b = \rho_b - \rho_{b1} \quad \ldots\ldots\ldots\

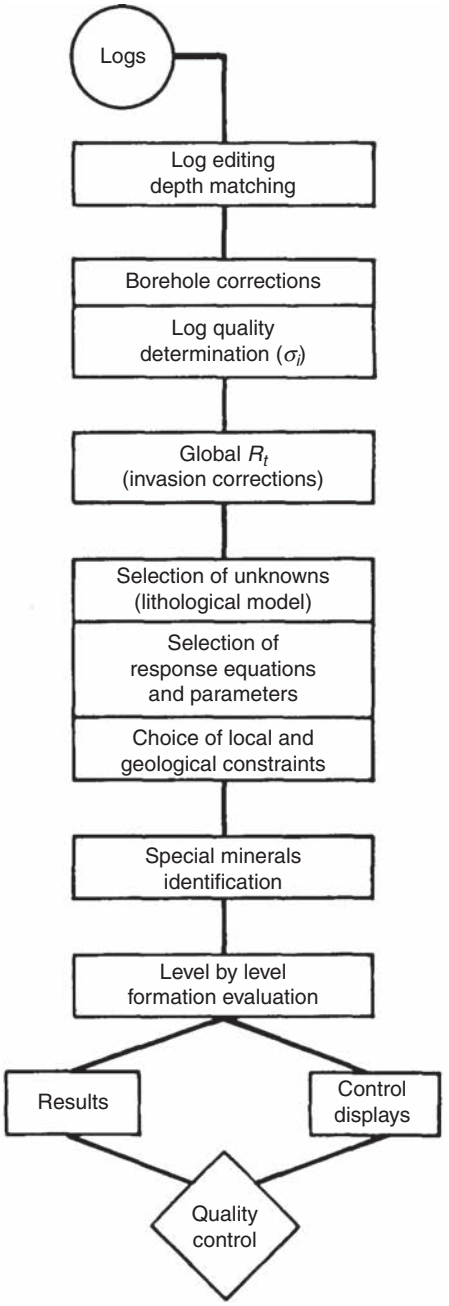


Fig. 29.2—Logical steps for global log processing. Courtesy of Schlumberger.

Of particular interest on Fig. 29.3 is that Track 1 displays a continuous plot of "reduced incoherence." This is a measure of the reliability of the results obtained, which in this example is good. The remainder of the plot is fairly conventional, with S_w, $\phi\ (1 - S_{xo})$, and $\phi\ (1-S_{xo})\rho_{hy}$ in Track 2 (indicating gas pay), a movable-oil plot in Track 3, and a lithology breakdown in Track 4 solved for porosity, siderite, quartz, silt, and clay.

The advantages of global-type processing* are that in places where the raw log data are unreliable, this unreliability will become evident, and that in zones of special interest, the analyst will

*Many commercial (service-company) packages are available for this kind of computer-based log analysis of complex lithology. Some of the trade names are ULTRA™, Elan, and MultiMin.

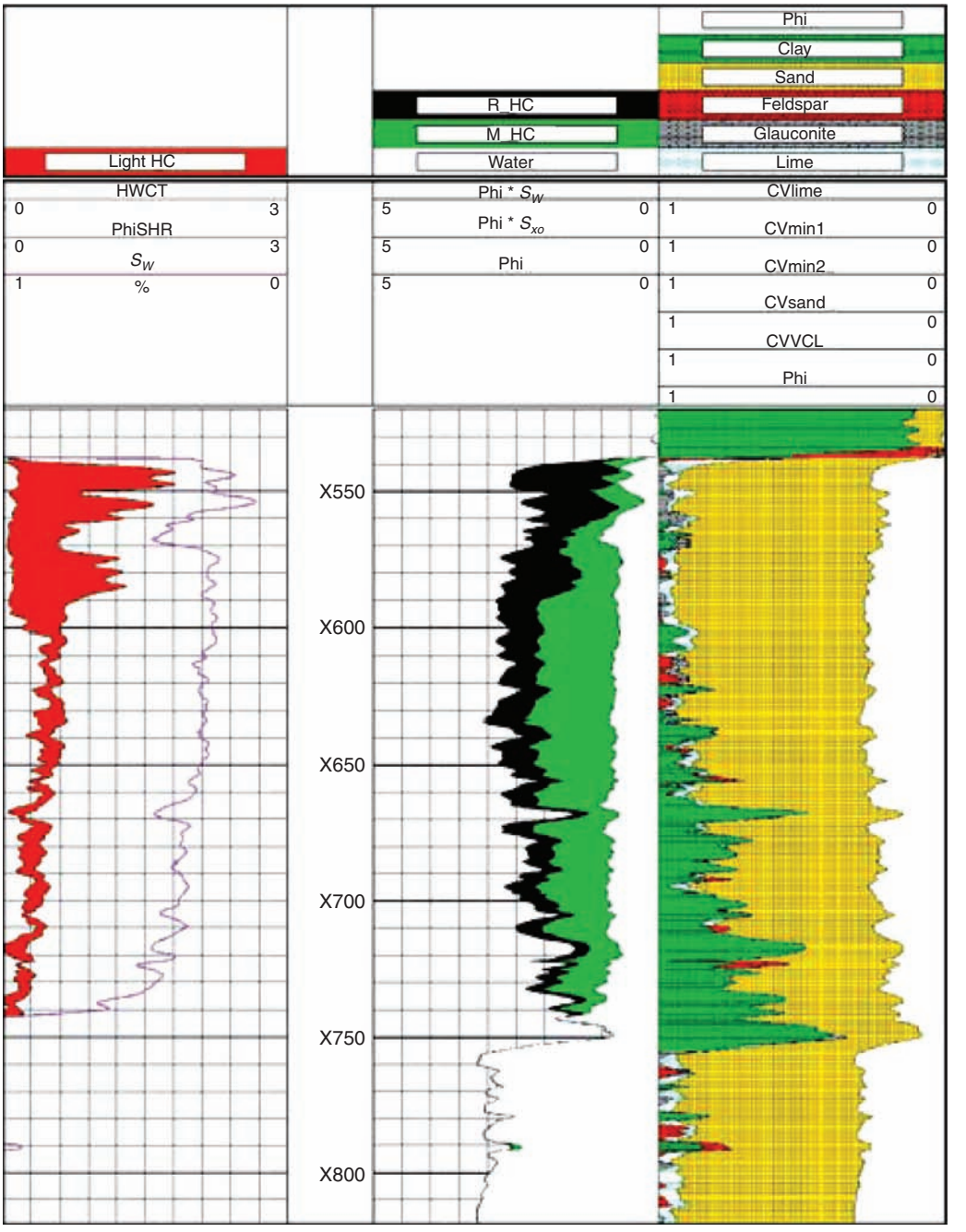


Fig. 29.3—Example of log analysis using ULTRA™ (Halliburton Wireline and Perforating Products and Services). Courtesy of Halliburton.

have a rigorously mathematical estimate of the probability that the analysis is correct. The disadvantages include the complexity of the processing and the need for specialists to use it.

29.4 Crossplot-Based Systems

Straddling the Chaveroo and global methods are more-generalized methods based on crossplot analysis. These methods rely on a neutron/density crossplot to resolve the question of porosity and lithology in a more general way. No special effort is made to determine the exact fractions of the

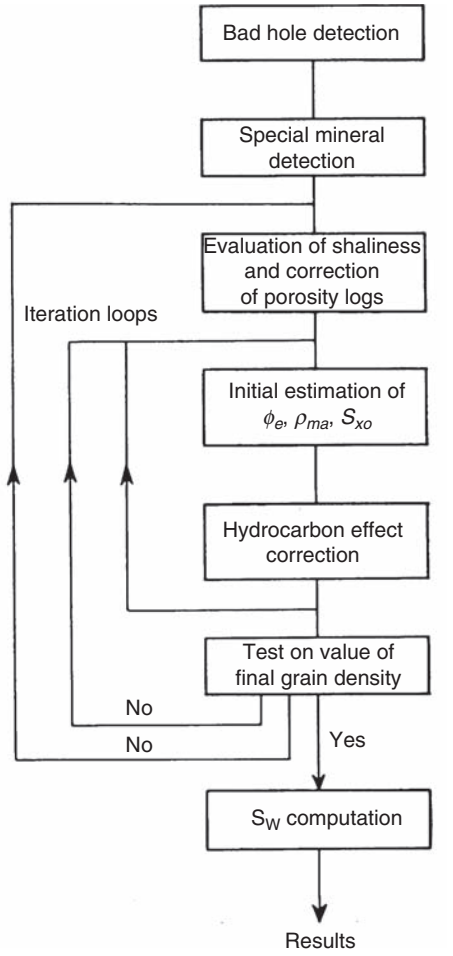


Fig. 29.4—Complex-lithology log-analysis flow diagram. Courtesy of Schlumberger.

different lithologic components; rather, an apparent matrix density is computed, and the analyst is left to his own devices to interpret its significance. The key steps in this logical chain include

- Determination of adverse hole conditions
- Identification of special minerals (e.g., coal, salt)
- Initial estimates of porosity and saturations
- Estimation of hydrocarbon effects on porosity logs
- Reiteration to satisfy constraints
- Final computations including S_w

Because of the nature of the problem (the number of unknowns), conventional wisdom calls for the analyst to assume the most-probable minerals present and to assume a value for the hydrocarbon density ρ_{hy}. Normally, available log data are insufficient to resolve enough unknowns to avoid the need for these assumptions. There are many logical ways to perform such an analysis, the choice of which depends on the whim of the analyst who supplies the required input parameters.

Service and petrophysical consulting companies offer crossplot log processing under a number of trade names. The advantages of these services include continuous processing over the entire section of interest and the speed with which results can be produced. The disadvantages of crossplot systems include the lack of operator control over the computation parameters used and the options selected in the processing chain. **Fig. 29.4** gives a general outline of the logic flow in

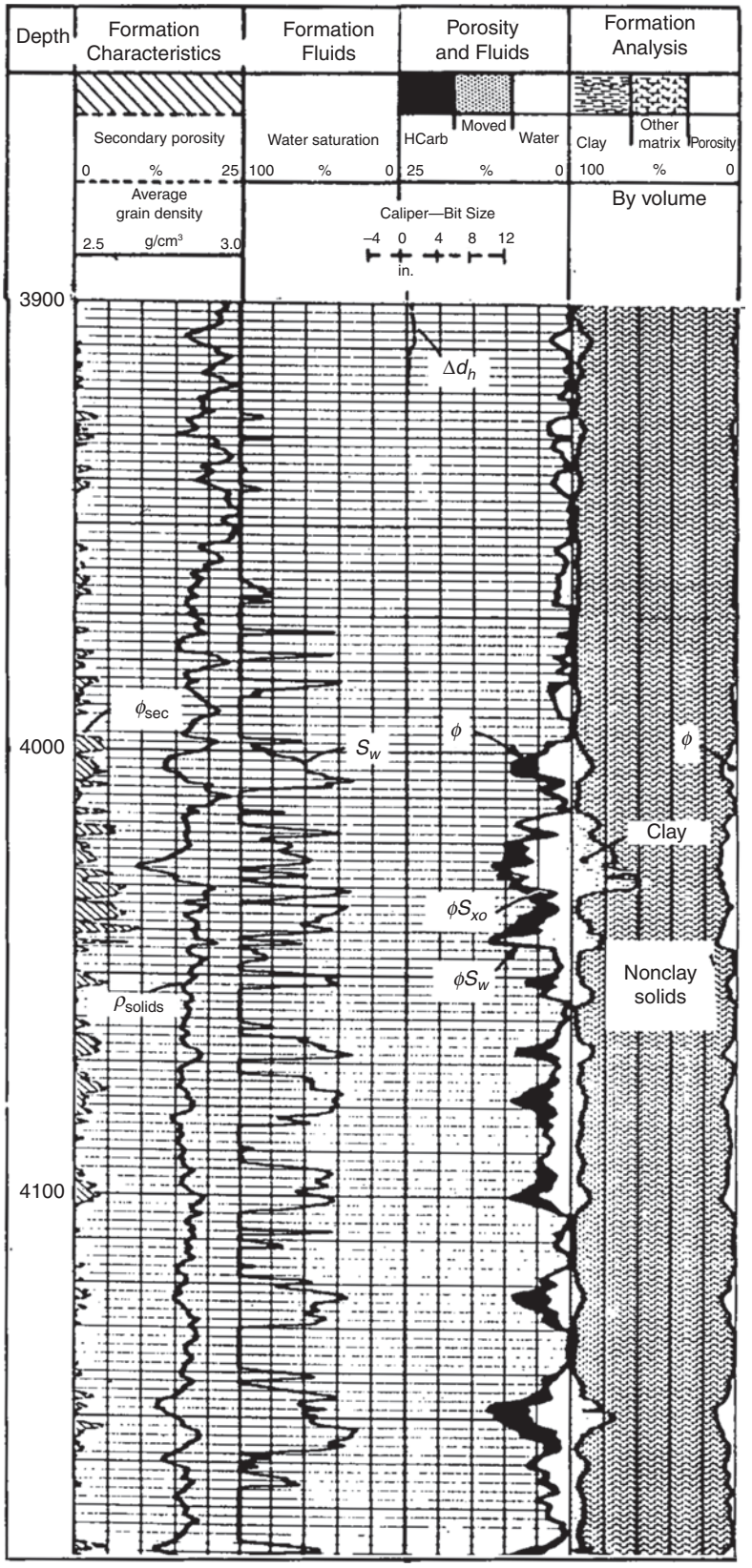


Fig. 29.5—Example of complex-lithology log-processing output (Poupon et al. 1971).

TABLE 29.2—KEY TO COMPUTED OUTPUTS FOR FIG. 29.5

Track	Parameter
1	ρ_{maa} and secondary porosity, ϕ_2
2	S_w
3	ϕ, ϕS_w and ϕS_{xo} (movable oil plot)
4	V_{sh} and ϕ (coded lithology track)

this kind of processing chain. An example of crossplot-processing output is given in **Fig. 29.5,** which shows the computer-based processing results for a shaly carbonate section with some secondary porosity. The format of the presentation is as given in **Table 29.2.**

When checking such computer-generated results, look in the headings or listings for indications of the model used and the mineral options that were entered. All these software packages require that the analyst enter a fixed value for the hydrocarbon density, so that value also should be checked.

29.5 Practical Quick-Look Methods

Although analysis of complex lithology is a natural candidate for computer processing, under certain conditions, the analyst will need to perform his own evaluation with recourse only to a set of log analysis charts and a calculator. In that case, some logical guidelines are in order. The steps might be ordered as follows:

1. Handpick levels of obvious interest using such criteria as GR and resistivity response.
2. Tabulate raw log readings.
3. Compute shale volume (V_{sh}) from available indicators (e.g., GR, SP).
4. Correct ρ_b, ϕ_N, and Δt readings to equivalent clean-formation values.
5. Calculate crossplot porosity (ϕ_X) and ρ_{maa}.
6. Calculate S_w and S_{xo}.
7. If the bulk volume of hydrocarbons in the invaded zone, $\phi\,(1 - S_{xo})$, exceeds 0.1, consider an iteration to correct ρ_b and ϕ_N further for the effects of light hydrocarbons.
8. Calculate Δt_{maa} and ϕ_S as a check for secondary porosity.

Most of these steps already have been covered elsewhere in the text. The relevant relationships are restated in the form of a flow chart in **Fig. 29.6.**

The computation of Δt_{maa} for the purpose of estimating secondary porosity deserves some further explanation. The procedure is as follows:

a. Use ρ_b and ϕ_N to find ϕ_X.
b. At the plotted point, estimate the matrix density.
c. Use this value of matrix density to estimate the most probable matrix travel time, Δt_{maa}.
d. Use this matrix travel time to compute a value for ϕ_S.
e. Compare ϕ_X with ϕ_S.

The estimation of ρ_{ma} in Step (b) can be made by using the MID plot (see Chapter 24) or by calculation using the relationship:

$$\rho_{ma} = \frac{\rho_b - \phi_X \rho_f}{1 - \phi_X} \quad \ldots\ldots\ldots\

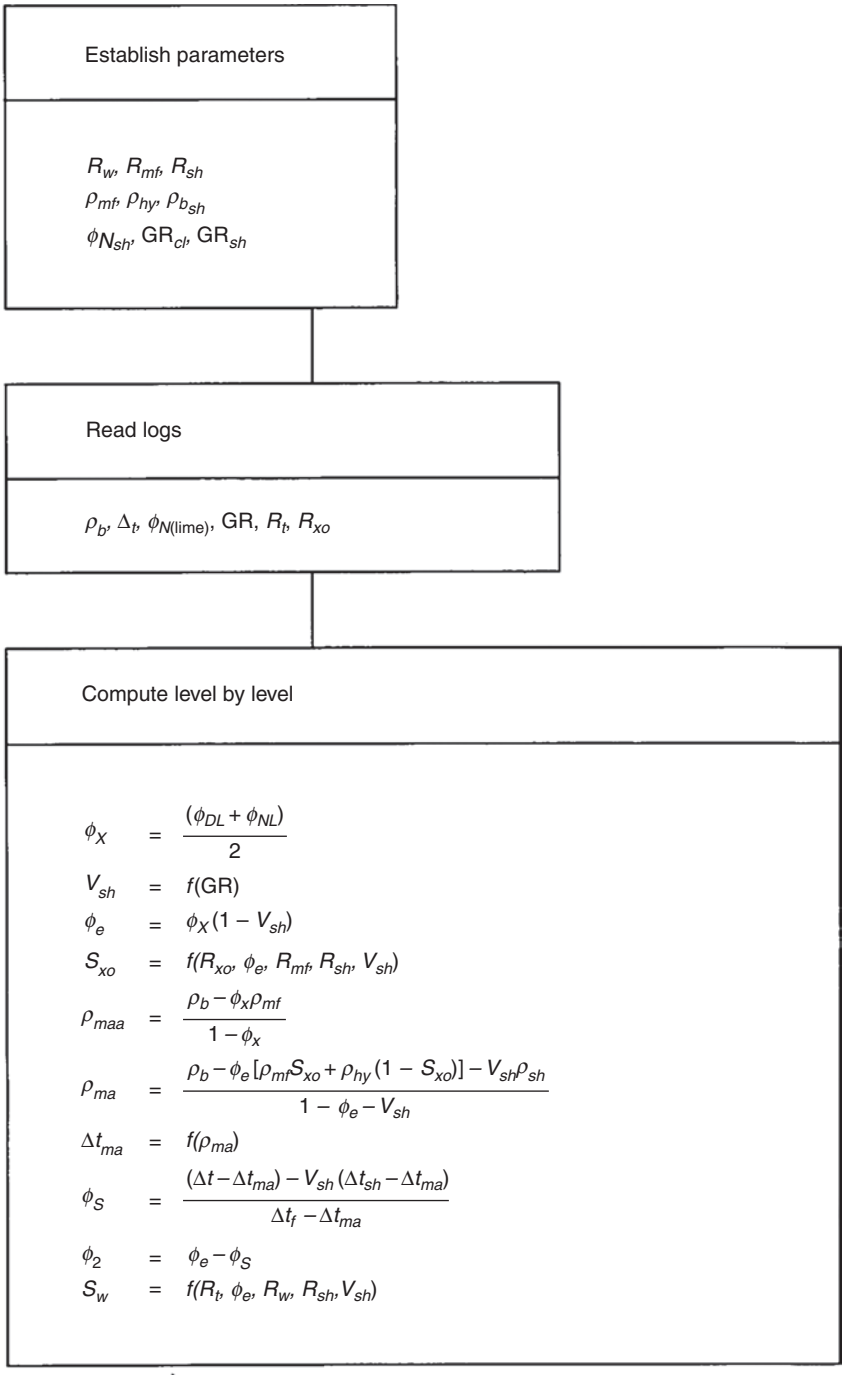


Fig. 29.6—Simplified flowchart for analysis of complex lithology.

QUESTION 29.3. Apply the preceding method to the following data:
$\rho_b = 2.575$ g/cm^3,
$\phi_{N\ (lime)} = 11\%$, and
$\Delta t = 55.5$ μs/ft.
Is there any secondary porosity?

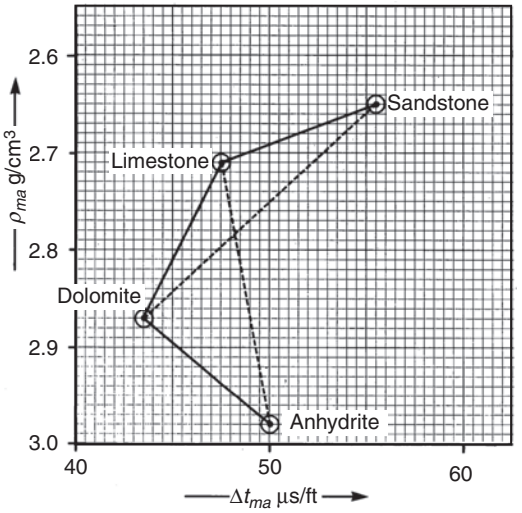


Fig. 29.7—Complex/Lithology: θ_{ma} vs. Δt_{ma}.

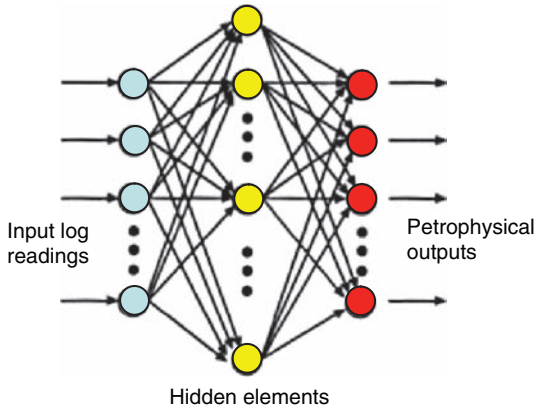


Fig. 29.8—Principle of a neural network.

29.6 Neural Networks

Another branch of complex-lithology log analysis is based on the use of neural networks. A number of commercial "packages" are available for the analyst to "train" a network to recognize mineralogy, porosity, and hydrocarbon presence from a base set of logs for which the "answers" are already known. Then the trained "brain" is set to work on a log data set to produce "answers." **Fig. 29.8** illustrates the concept.

Input log readings (blue circles) are normalized, weighted, and combined to produce a "hidden layer" (yellow circles). These, in turn, are recombined and reweighted to match known petrophysical outputs (in training mode) or to produce a complete petrophysical interpretation (in application mode).

The same principle is also used to "invent" logging curves that are missing because of recording or archival mishaps. **Fig. 29.9** shows an example in which a neural network was used with cased-hole pulsed-neutron measurements to estimate openhole log values. The surprisingly good agreement between the neural-network estimated values and the actual values is shown in **Fig. 29.10.**

29.7 Elemental Logging Tools

Advances in nuclear-logging-tool design and implementation have opened the door to what is commonly called "elemental logging." The principle used is that of atomic excitation by neutron bombardment of the formation and the subsequent analysis of the energy spectrum of the gamma rays thus produced.

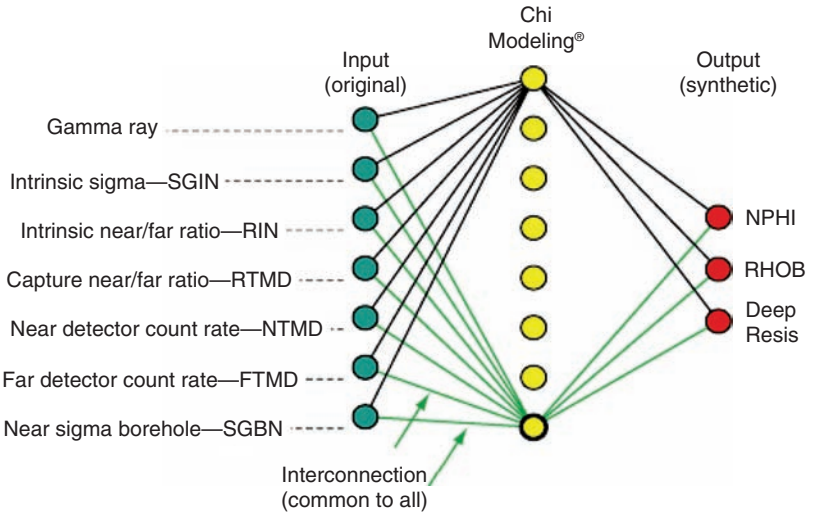


Fig. 29.9—Use of a neural network to simulate a missing openhole log (Halliburton Wireline and Perforating Products and Services). Courtesy of Halliburton.

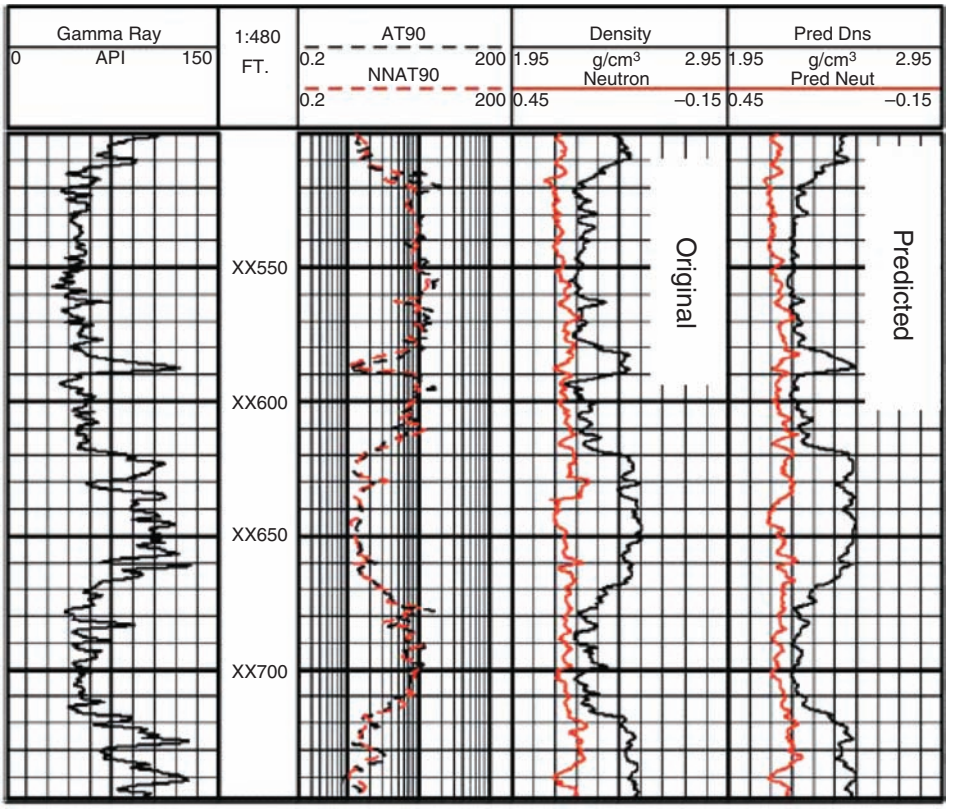


Fig. 29.10—Comparison between actual and neural-network-derived curves (Halliburton Wireline and Perforating Products and Services). Courtesy of Halliburton.

Elemental logging systems* use either an electronically pulsed source or a standard Am/Be neutron-logging source to send high-energy neutrons into the surrounding formation. These

*Service-company trade names for this service include ECS, FLEX, and GEM.

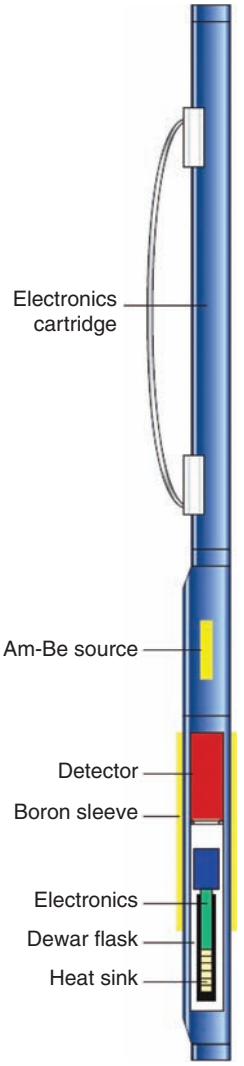


Fig. 29.11—Elemental-concentration logging tool (Schlumberger 2006). Courtesy of Schlumberger.

neutrons lose energy as a result of scattering, after which they are absorbed by the various atoms present in the rock matrix and the fluids in the pore space. **Fig. 29.11** shows an elemental-logging-tool schematic.

The inelastically scattered neutrons, as well as the absorbed neutrons, cause the atoms of the various elements in the formation to emit gamma rays with characteristic energies. These are measured with a large bismuth germanate (BGO) scintillation detector, resulting in both inelastic and capture gamma ray energy spectra. Wellsite processing uses a multichannel gamma ray energy spectrum analyzer to provide readings for:

Dry-weight elements [clay, carbonate, anhydrite + gypsum (from S and Ca), QFM (quartz + feldspar + mica), pyrite, siderite, coal, and salt].

Matrix properties (from elements) including matrix grain density and matrix thermal and epithermal neutron-capture cross-sectional Σ (sigma).

The first step involves spectral deconvolution of the composite gamma ray energy spectrum by use of a set of elemental standards to produce relative elemental yields. The relative yields are then converted to dry-weight elemental-concentration logs for the elements Si, Fe, Ca,

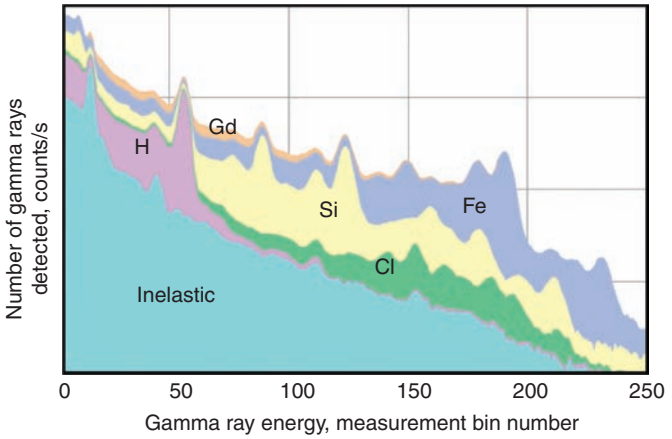


Fig. 29.12—Energy spectra for elemental logging tools (Schlumberger 2006). Courtesy of Schlumberger.

S, Ti, and Gd using an oxides closure method. Matrix properties and quantitative dry-weight lithologies are then calculated from the dry-weight elemental fractions by means of empirical relationships derived from an extensive core chemistry and mineralogy database. **Fig. 29.12** illustrates how the gamma ray energy spectrum is used to characterize the elements found in the formation.

A matrix-inversion spectral-fitting algorithm is used to analyze these spectra to separate the total response into its individual elemental components. The prominent measured elements associated with subsurface rock formations include calcium, silicon, magnesium, carbon, sulfur, aluminum, and iron. Tool response is characterized for each individual element by calibrating it in laboratory formations of known chemical composition.

The assessment begins with elemental formation weights and follows with an interpretation of lithology and mineralogy. The primary elements measured in both open and cased holes are silicon (Si), iron (Fe), calcium (Ca), sulfur (S), titanium (Ti), gadolinium (Gd), chlorine (Cl), barium (Ba), and hydrogen (H). The lithologies deduced from the elemental readings are divided into general categories, including sand, shale, coal, carbonates, and evaporites. Potentially identifiable minerals include quartz, potassium-feldspar, albite, calcite, dolomite, siderite, anhydrite, illite/smectite, kaolinite, glauconite, chlorite, and pyrite.

These elemental logging tools and their associated mineralogical interpretation routines find particular application in unconventional reservoirs (see Chapter 30). An illustration of the use of this complex-lithology logging and analysis technique is found in **Fig. 29.13.**

29.8 Logging-Tool Responses to Reservoir Rocks and Minerals

Whatever the method selected to perform log analysis in complex lithology, a detailed knowledge of logging-tool response is required. The work of Edmundson and Raymer (1979) is particularly useful here. See also the appropriate tables in the appendix to this chapter.

29.9 Summary

Analysis of complex lithology need not be complex if the analyst has a clear understanding of log-response equations and logging-tool response to reservoir rocks and minerals. Problems of clay conductivity can, as a rule, be ignored without prejudice. The analyst's main concern need be only the degree of mathematical complexity of the data analysis. If in doubt, the simplest approach often gives the most reliable result because the impact of gross computational errors is immediately obvious and simply corrected. The sensitivity of the end result to changes in input parameters is not always easy to see or to anticipate when using more-complex methods.

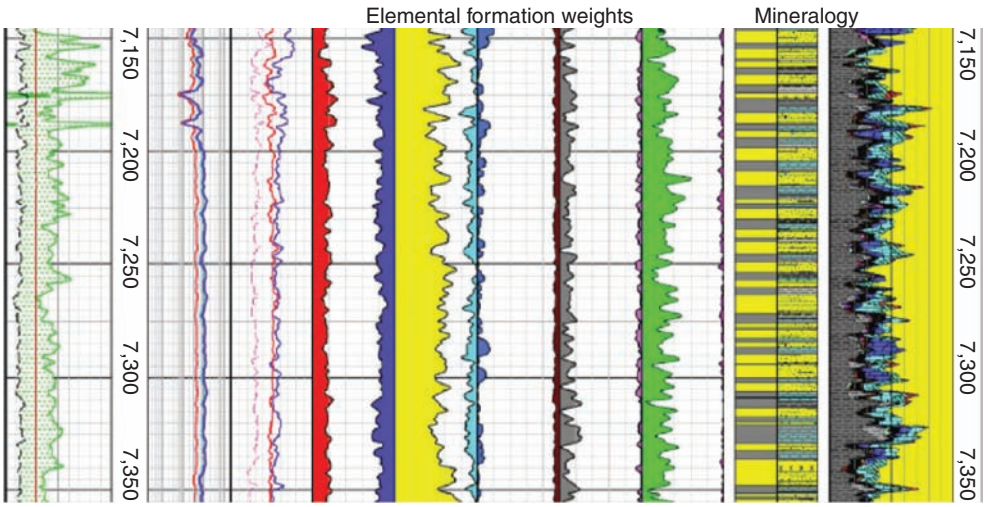


Fig. 29.13—Example of elemental analysis in the Barnett shale. Courtesy of Baker Hughes.

References

Burke, J.A., Curtis, M.R., and Cox, J.T. 1966. Computer Processing of Log Data Enables Better Production in Chaveroo Field. Paper SPE 1576 presented at the SPE Annual Meeting, Dallas, 2–5 October. http://dx.doi.org/10.2118/1576-PA.

Edmundson, H. and Raymer, L.L. 1979. Radioactive Logging Parameters for Common Minerals. *Trans.,* SPWLA 20th Annual Logging Symposium, Tulsa, 3–6 June.

Halliburton Wireline and Perforating Products and Services, http://www.halliburton.com/public/lp/contents/Books_and_Catalogs/web/WPS_PS_Catalog/Web/WPS_PS_CAT.pdf (accessed 20 February 2012).

Poupon, A., Hoyle, W.R., and Schmidt, A.W. 1971. Log Analysis in Formations With Complex Lithologies. *J. Pet Tech* **23** (8): 995–1005. http://dx.doi.org/10.2118/2925-PA.

Schlumberger. 1981. Well Evaluation Conference South East Asia. October.

Schlumberger. 1982. Litho Density Tool Interpretation. M 086108.

Schlumberger. 1982. Well Evaluation Developments, Continental Europe.

Schlumberger. 2006. ECS Elemental Capture Spectroscopy Sonde, http://www.slb.com/~/media/Files/evaluation/brochures/wireline_open_hole/petrophysics/porosity/ecs_brochure.ashx (accessed 20 February 2012).

General References

Alberty, M. and Hashmy, K.H. 1984. Application of ULTRA to Log Analysis. *Trans.,* SPWLA 25th Annual Logging Symposium, New Orleans, 10–13 June, Paper Z.

Balwin, J.L. and Bateman, R.M. 1989. Computer Emulation of Human Mental Processes: Application of Neural Network Simulators to Problems in Well Log Pattern Recognition. Presented at the Artificial Intelligence in Petroleum Exploration and Production Conference, Texas A&M University, College Station, Texas, USA.

Baldwin, J.L., Wheatley, C.L., and Bateman R.M. 1990. Application of a Neural Network to the Problem of Mineral Identification from Well Logs. *The Log Analyst* **31** (5): 279–293.

Burke, J.A., Campbell, R.L. Jr., and Schmidt, A.W. 1969. The Litho-Porosity Cross-Plot: A New Concept for Determining Porosity and Lithology From Logging Methods. *Trans.,* SPWLA 10th Annual Logging Symposium, Tulsa, 25–28 May.

Kristianto, A., Jong, Y., and Moinard, L. 2008. Comparison of Conventional Log Interpretation With Neutron Spectroscopy Log and X-Ray Diffraction Laboratory Analysis: A Case Study. Paper IPTC 12849 presented at the International Petroleum Technology Conference, Kuala Lumpur, 3–5 December. http://dx.doi.org/10.2523/12849-MS.

Mayer, C. and Sibbit, A. 1980. GLOBAL, A New Approach to Computer-Processed Log Interpretation. Paper SPE 9341 presented at the SPE Annual Technical Conference and Exhibition, Dallas, 21–24 September. http://dx.doi.org/10.2118/9341-MS.

Nugent, W.H., Coates, G.R., and Peebler, R.P. 1978. A New Approach to Carbonate Analysis. *Trans.,* SPWLA 19th Annual Logging Symposium, El Paso, Texas, USA, 13–16 June.

Pemper, R., Sommer, A., Guo, P. et al. 2006. A New Pulsed Neutron Sonde for Derivation of Formation Lithology and Mineralogy. Paper SPE 102770 presented at the SPE Annual Technical Conference and Exhibition, San Antonio, Texas, USA, 24–27 September. http://dx.doi.org/10.2118/102770-MS.

Savre, W.C. 1963. Determination of a More Accurate Porosity and Mineral Composition in Complex Lithologies with the Use of Sonic, Neutron and Density Surveys. *J. Pet Tech* **15** (9): 945–959. http://dx.doi.org/ 10.2118/617-PA.

Raymer, L.L. and Biggs, W.P. 1963. Matrix Characteristics Defined by Porosity Computations. *Trans.,* SPWLA 4th Annual Logging Symposium, Oklahoma City, Oklahoma, USA, 23–24 May.

Schmidt, A.W., Land, A.G., Yunker, J.D., and Kilgore, E.C. 1971. Applications of the Coriband Technique to Complex Lithologies. *Trans.*, SPWLA 12th Annual Logging Symposium, Dallas, 2–5 May, Paper Z.

Serra, O. 1990. *Elemental Mineral Rock Catalog*. Schlumberger.

Tilly, H.P., Gallagher, B.J., and Taylor, T.D. 1982. Methods for Correcting Porosity Data in a Gypsum-Bearing Carbonate Reservoir. *J. Pet Tech* **34** (10): 2449–2454. http://dx.doi.org/10.2118/9716-PA.

Answers to Questions

QUESTION 29.1.
Gin 60%.
Dry vermouth 20%.
Sweet vermouth 20%.

QUESTION 29.2.
$\phi = 15\%$.
$V_{\text{lime}} = 40\%$.
$V_{\text{dol}} = 30\%$.
$V_{\text{sand}} = 15\ \%$.
Total = 100% bulk volume.
Hence, the fractions of matrix materials are
Limestone: 40:85 = 47%.
Dolomite: 30:85 = 35%.
Sandstone: 15:85 = 18%.
Total: = 100% solids.

QUESTION 29.3.
$\phi_X = 9.45\%$.
$\rho_{maa} = 2.74$ g/cm^3.
$\Delta t_{maa} = 46.75$ μsec/ft.
$\phi_S = 6.15\%$.
Secondary porosity = 9.45−6.15 = 3.3%.

Appendix 29 A—Properties of Evaporites and Coals

TABLE A-1—PROPERTIES OF EVAPORITES AND COALS (COURTESY OF SCHLUMBERGER)

Name	Formula	M	ρ g/cm^3	ρ_{Log} g/cm^3	Δtc µs/ft	Δts µs/ft	P_e	U	Z	$GR_k 10^{15}$ atoms/g	Σ c.u.	ϕ_{SNP} p.u.	ϕ_{CNL} p.u.
Evaporites													
Halite	$NaCl$	58.44	2.17	2.04	67	120	4.65	9.5	15.3	—	754.2	–2	–3
Anhydrite	$CaSO_4$	136.14	2.96	2.98	50		5.05	15.0	15.7	—	12.5	–1	–2
Gypsum	$CaSO_4\ (H_2O)_2$	172.17	2.32	2.35	52		3.99	9.4	14.7	—	18.5	50+	60+
Trona	$Na_2CO_3NaH{\cdot}CO_3H_2O$	208.02	2.12	2.08	65		0.71	1.5	9.1	—	15.9	24	35
Tachydrite	$CaCl_2(MgCl_2)_2{\cdot}(H_2O)_{12}$	517.60	1.68	1.66	92		3.84	6.4	14.5	—	406.0	50+	60+
Sylvite	KCl	74.55	1.98	1.86			8.51	16.0	18.1	953.15	564.6	–2	–3
Carnalite	$KClMgCl_2{\cdot}(H_2O)_6$	277.86	1.61	1.57			4.09	6.4	14.8	255.51	369.0	41	60+
Langbeinite	$K_2SO_4(MgSO_4)_2$	414.99	2.83	2.82			3.56	10.0	14.2	342.46	24.2	–1	–2
Polyhalite	$K_2SO_4MgSO_4{\cdot}(CaSO_4)2(H_2O)_2$	602.94	2.78	2.79			4.32	12.0	15.0	235.72	23.7	14	25
Kainite	$MGSO_4KCl{\cdot}(H_2O)_3$	248.97	2.13	2.12			3.50	7.4	14.2	285.42	195.1	40	60+
Kieserite	$MgSO_4H_2O$	138.38	2.57	2.59			1.83	4.7	11.8	—	14.0	38	43
Epsomite	$MGSO_4(H_2O)_7$			1.71			1.20	2.0			21.0	50+	60+
Bischofite	$MgCl_2(H_2O)_6$			1.54	100		2.60	4.0			323.0		
Barite	$BaSO_4$	233.40	4.48	4.09			267	2.0	47.2	—	6.8	–1	–2
Celestite	$SrSO_4$	183.68	3.97	3.79			55.19	4.0	30.5	—	22.5	–1	–1
Sulfides													
Sulfur	S	32.06	2.07	2.02	122		5.43	11.0	16.0	—	20.2	–2	–3
Pyrite	FeS_2	119.97	5.00	4.99	39.2	62.1	16.97	85.0	22.0	—	90.1	–2	–3
Marcasite	FeS_2	119.97	4.80	4.87			16.97	83.0	22.0	—	88.1	–2	–3
Pyrrhotite	Fe_7S_8	647.41	4.60	4.53			20.55	93.0	23.2	—	94.2	–2	–3
Sphaterite	ZnS	97.44	4.00	3.85			35.93	138	27.0	—	25.3	–3	–3
Chalcopyrite	$CuFeS_2$	183.51	4.20	4.07			26.72	109	24.9	—	102.1	–2	–3
Galena	PbS	239.26	7.50	6.39			1631	10,400	78.1	—	13.4	–3	–3
Coals													
Anthracite	$CH_{.358}N_{.009}O_{.022}$	—	1.51	1.47	105		0.16	0.23	6.0	—	8.7	37	38
Bituminous	$CH_{.793}N_{.015}O_{.078}$	—	1.27	1.24	120		0.17	0.21	6.1	—	14.3	50+	60+
Lignite	$CH_{.849}N_{.015}O_{.211}$	—	1.23	1.19	160		0.20	0.24	6.4	—	12.8	47	52

Appendix 29 B—Properties of Silicates, Carbonates, Oxidates, Phosphates, and Feldspars

TABLE B-1—PROPERTIES OF SILICATES, CARBONATES, OXIDATES, PHOSPHATES, AND FELDSPARS (COURTESY OF SCHLUMBERGER)

Name	Formula	M	ρ g/cm^3	ρ_{Log} g/cm^3	Δtc µs/ft	Δts µs/ft	P_e	U	Z	$GR_k 10^{15}$ atoms/g	Σ c.u.	ϕ_{SNP} p.u.	ϕ_{CNL} p.u.
Silicates													
Quartz	SiO_2	60.09	2.65	2.64	56.0	88.0	1.81	4.8	11.78		4.3	–1	–2
β Cristobalite	SiO_2	60.09	2.19	2.15			1.81	3.9	11.78		3.5	–2	–3
Opal 3.5% H_2O	$SiO_2(H_2O)$ .1209	62.26	2.16	2.13	58.0		1.75	3.7	11.68		5.0	4	2
Opal 6.33% H_2O	$SiO_2(H_2O)$ .2253	64.15	2.10	2.07			1.70		11.60		6.1	7	6
Opal 8.97% H_2O	$SiO_2(H_2O)$ .3285	66.00	2.04	2.01			1.66		11.52		7.1	11	11
Garnet	$Fe_3Al_2 \cdot (SiO_4)_3$	497.76	4.32	4.31			11.09	48.0	19.51		44.9	3	7
Hornblende	$Ca_2NaMg_2Fe_2AlSi_8O_{22} \cdot (O, OH)_2$	900.13	3.20	3.20	43.8	81.5	5.99	19.0	16.44		18.1	4	8
Tourmaline	$NaMg_3Al_6B_3Si_6 \cdot O_2(OH)_4$	558.78	3.03	3.02			2.14	6.5	12.35		7450	16	22
Zircon	$ZrSiO_4$	183.31	4.67	4.50			69.10	311.0	32.43		6.9	–1	–3
Carbonates													
Calcite	$CaCO_3$	100.09	2.71	2.71	49.0	88.4	5.08	13.8	15.71		7.1	0	–1
Dolomite	$CaCO_3Mg \cdot CO_3$	184.41	2.87	2.88	44.0	72.0	3.14	9.0	13.74		4.7	2	1
Ankerite	$Ca(Mg,Fe) \cdot (CO_3)2$	240.25	2.90	2.86			9.32	27.0	18.59		22.2	0	1
Siderite	$FeCO_3$	115.86	3.94	3.89	47.0		14.69	57.0	21.09		52.3	5	12

TABLE B-1—PROPERTIES OF SILICATES, CARBONATES, OXIDATES, PHOSPHATES, AND FELDSPARS (COURTESY OF SCHLUMBERGER) (CONT'D)

Name	Formula	M	ρ g/cm^3	ρ_{Log} g/cm^3	Δtc µs/ft	Δts µs/ft	P_e	U	Z	$GR_K 10^{15}$ atoms/g	Σ c.u.	ϕ_{SNP} p.u.	ϕ_{CNL} p.u.
Oxidates													
Gibbsite	$Al(OH)_3$	78.01	2.44	2.49			1.10		10.28		23.1	50+	60+
Hematite	Fe_2O_3	159.69	5.27	5.18	42.9	79.3	21.48	111	23.44		101.4	4	11
Magnetite	Fe_3O_4	231.54	5.18	5.08	73.0		22.24	113	23.67		103.1	3	9
Geothite	FeO(OH)	88.86	4.37	4.34			19.02	83	22.66		85.4	50+	60+
Limonite	$FeO(OH)\cdot(H_2O)2.05$	125.79	3.50	3.59	56.9	102.6	13.00	47	20.39		71.1	50+	60+
Phosphates													
Hydroxyapatite	$Ca_5(PO_4)_3O\cdot H$	502.33	3.15	3.17	42.0		5.81	18	16.30		9.6	5	8
Chlorapatite	$Ca_5(PO_4)_3Cl$	520.78	3.18	3.18	42.0		6.06	19	16.50		130.2	–1	–1
Fluorapatite	$Ca_5(PO_4)_3F$	504.32	3.20	3.21	42.0		5.82	19	16.31		8.5	–1	–2
Carbonapatite	$(Ca_5(PO_4)_3)_2\cdot CO_3H_2O$	1048.67	3.11	3.13			5.58	17	16.20		9.1	5	8
Feldspars-Alkali													
Orthoclase	$KAlSi_3O_8$	278.34	2.55	2.52	69.0		2.86	7.2	13.39	255.29	15.5	–2	–3
Anorthoclase	$KAlSI_3O_8$	278.34	2.62	2.59			2.86	7.4	13.39	255.29	15.9	–2	–2
Microcline	$KAlSi_3O_8$	278.34	2.56	2.53			2.86	7.2	13.39	255.29	15.6	–2	–3
Feldspars—Plagioclase													
Albite	$NaAlSi_3O_8$	262.23	2.62	2.59	49.0	85.0	1.68	4.4	11.55		7.5	–1	–2
Oligoclase	10–30% Anorthite												
Andesine	30–50% Anorthite												
Labradorite	50–70% Anorthite												
Bytownite	70–90% Anorthite												
Anorthite	$CaAl_2Si_2O_8$	278.22	2.76	2.74	45.0		3.13	8.6	13.73		7.2	–1	–2

Interpolate linearly between Albite and Anorthite

Appendix 29 C—Properties of Clays, Zeolites, and Micas

TABLE C-1—PROPERTIES OF CLAYS, ZEOLITES, AND MICAS (COURTESY OF SCHLUMBERGER)

Name		Formula	M	ρ g/cm^3	ρ_{Log} g/cm^3	Δtc µs/ft	Δts µs/ft	P_e	U	Z	$GR_k 10^{15}$ atoms/g	Σ c.u.	ϕ_{SNP} p.u.	ϕ_{CNL} p.u.
Clays														
Kaolinite	W	$Al_4Si_4O_{10}\cdot(OH)_8$	—	2.42	2.41			1.83	4.40	11.8	7.79	14.1	34	
Kaolinite	D		—	2.44	2.44			1.84		11.9	7.85	14.0	33	36
Chlorite	W	$(Mg,Fe,Al)_6\cdot(Si,Al)_4O_{10}\cdot(OH)_8$	—	2.77	2.76			6.30	17.00	16.7	1.06	24.9	37	52
Chlorite	D		—	2.79	2.79			6.33		16.7	1.07	24.9	36	51
Illite	W	$K_{1\text{-}1.5}Al_4\cdot(Si_{7\text{-}6.5},Al_{1\text{-}1.5})\cdot O_{20}(OH)_4$	—	2.53	2.52			3.45	8.70	14.1	86.68	17.6	20	30
Illite	D		—	2.65	2.63			3.55		14.2	89.26	17.2	15	24
Mixed Layer														
Aggregate 1	W		—	2.37	2.37			3.96		14.7	25.91	18.8	35	44
Aggregate 1	D		—	2.70	2.70			4.32		15.0	28.23	18.0	20	29
Aggregate 2	W		—	2.36	2.35			2.23		12.5	105.07	15.2	25	33
Aggregate 2	D		—	2.57	2.26			2.36		12.7	111.38	14.1	16	22
Aggregate 3	W		—	2.62	2.61			3.01		13.6	41.84	13.6	13	19
Aggregate 3	D		—	2.67	2.67			3.05		13.6	42.42	13.3	10	15
Montmorillonite	W	$(Ca,Na)_7\cdot(Al,Mg,Fe)_4\cdot(Si,Al)_8$	—	2.12	2.12			2.04	4.00	12.2	3.89	14.1	40	44
Montmorillonite	D	$O_{20}(OH)_4\cdot(H_2O)_8$	—	2.53	2.52			2.30		12.6	4.45	11.2	20	24
Zeolites														
Heulandite	W	$(Ca,Na_2)\cdot Al_2Si_7\cdot O_{18}(H_2O)_6$	—	2.23	2.23			2.86		13.4	18.44	11.8	25	
Heulandite	D		—	2.34	2.34			2.96		13.5	17.78	12.6	31	36
Laumontite	W	$CaA_{12}Si_4\cdot O_{12}\cdot(H_2O)_{3.5\text{-}4}$	—	2.53	2.53			2.64		13.1	3.94	11.2	22	26
Laumontite	D		—	2.56	2.56			2.67		13.1	3.99	11.0	20	24
Mordenite	W	$(Na_2,K_2,Ca)Al_2Si_{10}O_{24}\cdot(H_2O)_7$	—	2.24	2.24			1.91		12.0	4.39	11.6	27	31
Mordenite	D		—	2.39	2.38			1.99		12.1	4.60	10.3		23
Analcine	W	$NaAlSi_2O_6\cdot H_2O$	—	2.45	2.43			1.56		11.3	4.52	11.8	17	23
Analcine	D		—	2.45	2.44			1.56			4.53	11.8	17	23

TABLE C-1—PROPERTIES OF CLAYS, ZEOLITES, AND MICAS (COURTESY OF SCHLUMBERGER) (CONT'D)

	Name		Formula	M	ρ g/cm^3	ρ_{Log} g/cm^3	Δtc µs/ft	Δts µs/ft	P_e	U	Z	$GR_k 10^{15}$ atoms/g	Σ c.u.	ϕ_{SNP} p.u.	ϕ_{CNL} p.u.
	Micas														
	Muscovite		$KAl_2{\cdot}(Si_3AlO_{10}){\cdot}(OH)_2$	398.32	2.83	2.82	49.0	149.0	2.40	6.70	12.8	178.40	16.9	12	20
Glauconite	Sample 1	W	$K_2(Mg,Fe)_2{\cdot}Al_6(Si_4O_{10})_3{\cdot}(OH)_{12}$	—	2.51	2.49			6.77		17.0	90.51	25.3		
	Sample 1	D		—	2.71	2.69			7.11		17.3	94.86	25.7	18	
	Sample 2	W	$K_2(Mg,Fe)_2{\cdot}Al_6(Si_4O_{10})_3{\cdot}(OH)_{12}$	—	2.53	2.52			5.32	14.00	15.9	113.22	22.4	23	≈38
	Sample 2	D		—	2.69	2.67			5.53	14.00	16.1	117.53	2239	16	≈38
	Sample 3	W	$K_2(Mg,Fe)_2{\cdot}Al_6(Si_4O_{10})_3{\cdot}(OH)_{12}$	—	2.65	2.63			7.04		17.2	112.44	26.7	21	
	Sample 3	W		—	2.80	2.77			7.27		17.4	115.92	27.1	16	
Biotite	Sample 1	W	$K(Mg,Fe)_3{\cdot}(AlSi_3O_{10}){\cdot}(OH)_2$	—	3.08	3.06			6.22		16.6	119.81	29.6	8	
	Sample 1	D		—	3.12	3.10	50.8	224.0	6.26	19.00	16.6	120.54	29.8	6	≈21
	Sample 2	W	$K(Mg,Fe)_3{\cdot}(AlSi_3O_{10}){\cdot}(OH)_2$	—	2.95	2.93	50.8	224.0	6.32	19.00	16.7	136.25	30.0	14	≈21
	Sample 2	D													

Chapter 30

Formation Evaluation in Unconventional Reservoirs

30.1 Overview of Unconventional Reservoirs

The term *unconventional reservoir* embraces a broad continuum from tight gas sands at one extreme through shale in the middle to coal at the other extreme.

- At the left end of the spectrum **(Fig. 30.1),** tight gas sands are characterized by a lack of organic content (kerogen), permeabilities less than 0.1 md, and intergranular pore spaces filled with water and gas.
- At the right end of the spectrum are coals, with between 50 and 100% organic matter, which may act as a reservoir for gas adsorbed on the surfaces of micropores (cleats).
- Between these two lie shales, with up to 50% organic content and permeabilities less than 0.001 md.

The purpose of this chapter is to give the reader a practical guide to the evaluation of these resources. Starting with a theoretical basis for the analytical tools that can be used to find the "sweet spots," this guide will discuss mud logging, core measurements, and log measurements that can be used to assess the production potential of unconventional hydrocarbon resources. Then, the application of geomechanics to completion planning will be coupled to fracture-treatment monitoring and hydrocarbon production.

In practice, the sequence of events in the exploitation of unconventional resources may follow this path:

- Initial drilling of an exploration well
- Analysis of cuttings and mud gas during the drilling process
- Formation logging, either by measurements on drillpipe (MOD) or by wireline tools
- Cutting, retrieval, and wellsite handling of cores (either full cores or sidewall cores)
- Analysis of cores for gas content, porosity, permeability, and organic material
- Log analysis for porosity, gas saturation, total organic content (TOC), fractures, formation anisotropy, and elastic constants (Young's modulus, Poisson's ratio)
- Estimation of hydrocarbons in place, recovery factors, and reserves
- Decisions on field development and optimal well designs for maximum production
- Completion planning (if warranted) on any given well
- Formation stimulation and completion monitoring

These topics will be discussed more or less sequentially, but there will be some overlap of topics because it is impossible to divorce core analysis entirely from gas-in-place estimates or log analysis from a discussion of geomechanics.

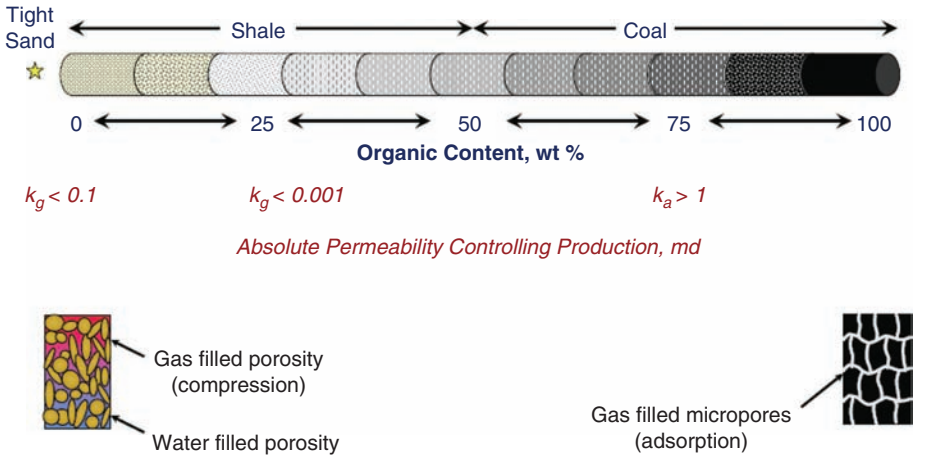


Fig. 30.1—The unconventional-reservoir spectrum (Hartman et al. 2008). Courtesy of Weatherford.

30.1.1 Location of Unconventional Reservoirs. On a global scale, unconventional reservoirs are found on all continents (**Table 30.1**), and organics-rich source-rock basins are estimated to hold between 500 and 1,000 Tcf of natural gas. Although these resources have yet to be fully explored on a global scale, the North American continent has seen a veritable boom in activity, with the drilling of thousands of wells in unconventional reservoirs.

It is notable that North America holds one-quarter of the world's unconventional gas reserves and that almost one-half these reserves are in the form of shale gas.

30.1.2 Unconventional Gas Production. Curiously, actual gas production is greatest from tight gas sands, exceeding that from shales by a factor of six. Even coalbed-methane (CBM) production is greater than shale-gas production. **Fig. 30.2** documents actual and projected unconventional gas production.

TABLE 30.1—GLOBAL DISTRIBUTION OF UNCONVENTIONAL GAS (AS OF 2010)

	Gas-In-Place Tcf				
Region	Coal-bed Methane	Shale Gas	Tight-Sand Gas	Total	% of Total
North America	3,017	3,840	1,370	8,227	25%
Former Soviet Union	3,957	627	901	5,485	17%
Centrally planned Asia and China	1,215	3,526	353	5,094	16%
Pacific OECD	470	2,312	705	3,487	11%
Latin America	39	2,116	1,293	3,448	11%
Middle East & North Africa	0	2,547	823	3,370	10%
Sub-Saharan Africa	39	274	784	1,097	3%
Western Europe	157	509	353	1,019	3%
Other Asia Pacific	0	313	549	862	3%
South Asia	39	0	196	235	1%
Central and Eastern Europe	118	39	78	235	1%
World	**9,051**	**16,103**	**7,405**	**32,559**	**100**
% of Total	28%	49%	23%	**100%**	

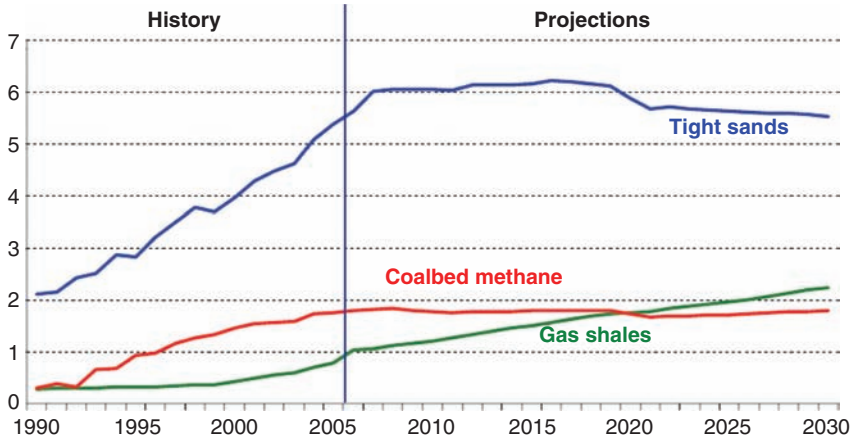


Fig. 30.2—Unconventional gas production in Tcf. Courtesy of the Energy Information Administration, U.S. Department of Energy.

30.1.3 Commonalities of Unconventional Reservoirs. When it comes to formation evaluation, tight gas, shale gas, and CBM share a number of characteristics. To varying degrees, these unconventional reservoir rocks have high kerogen (TOC) content, which may act as both the source and the reservoir rock and may be mixed with clay minerals, although these may not be the primary rock components.

Proper analysis demands that the type, maturity, and amount of organic matter be quantified from logs and cores and that the total hydrocarbon content be assessed properly, be it in the form of free, absorbed, or dissolved gas.

To meet these objectives effectively, special coring and core-analysis techniques are called for along with specialized logs required to detect the presence of natural fractures or the susceptibility of the rock to induced fracturing by calculation of rock brittleness.

Finally, the formation evaluator may be of great assistance in proper planning and monitoring of unconventional well completions.

Fig. 30.3 presents a generalized diagram showing conventional and unconventional oil and gas accumulations. The continuous chalk, shale-oil, and shale-gas accumulations shown in the diagram are representative of mature, fractured shales such as the Barnett or Eagle Ford shales.

30.1.4 Synopsis of Unconventional-Play Types.

CBM. Production requires a proper understanding of the mechanism by which gas molecules are stored in the coal cleats by adsorption. To remove these molecules from their storage sites and move them into the wellbore for production and sale requires first a desorption process and then a Darcy flow through a very thin crack in the coal matrix. The determinant of actual gas-flow rate from a given well will, therefore, depend on which process offers the greatest resistance to flow.

An added complication is the likely presence of water along with the gas, and the initial stage of CBM-well production will involve "dewatering." The design of a CBM production well will, therefore, not only have to strive for maximum exposure of coal-cleat surfaces, but will also have to include a mechanism for producing the associated water and preventing it from reflooding the reservoir and blocking the vital desorption process.

Tight Gas. Tight gas, as its name implies, is an extension of a conventional gas reservoir into a realm where porosities are in the single digits and permeabilities are in the range of 0.01 or 0.001 md **(Fig. 30.4).** These reservoirs present several challenges. For example, the measurement of extremely low permeabilities in cores requires techniques that are not needed or used in conventional core analysis. Production from tight gas also requires stimulation and fracture treatments that would not normally be required in a conventional high-porosity, high-permeability gas sand. Relative permeability effects can on occasion produce situations in which the relative

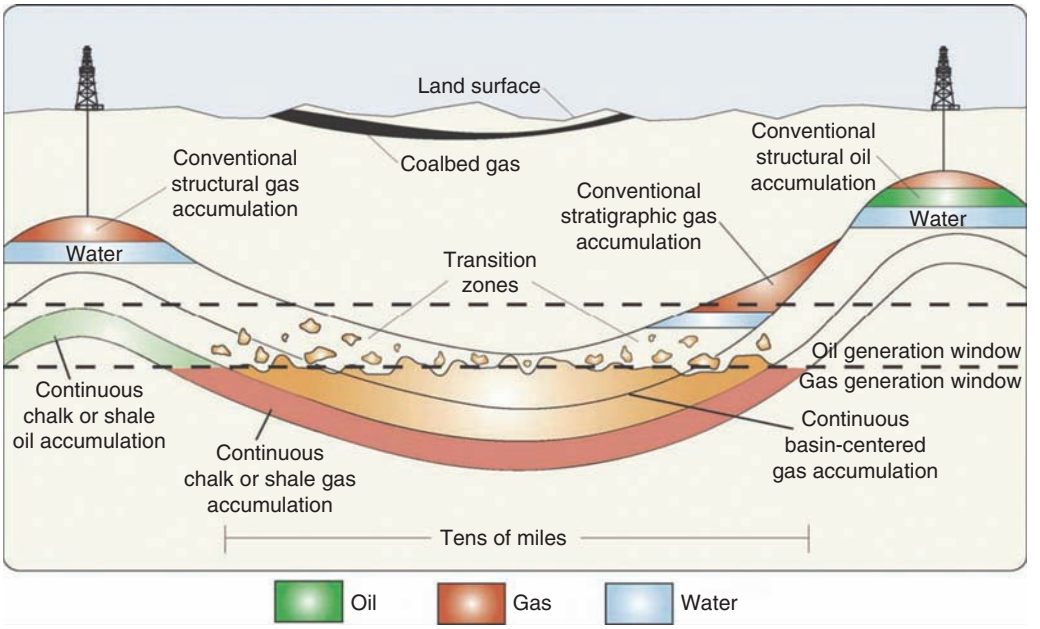


Fig. 30.3—Conventional and unconventional oil and gas accumulations (Pollastro et al. 2003). AAPG © 2003, reprinted by permission of the AAPG whose permission is required for further use.

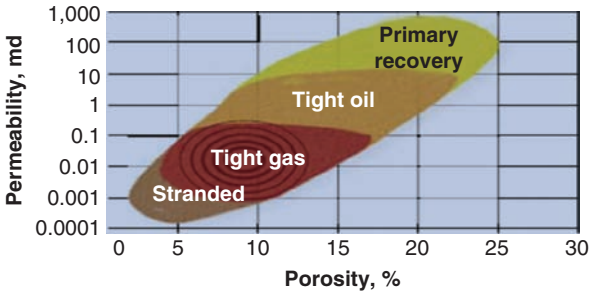


Fig. 30.4—Position of tight gas in the permeability/porosity spectrum (Shehata et al. 2010).

permeability to gas and to water are both so low that effectively nothing can move, creating the so-called "permeability jail."

Shale Gas and Shale Oil. Shale gas and shale oil are present in organics-rich rocks where, surprisingly, the porosity is attributable to the organic material and not to the "conventional" matrix material (for example, in the pore spaces between sand grains). As a result, the gas may exist as free gas, as adsorbed gas, and as gas dissolved in the accompanying water (or oil, or both) in the pore spaces. Assessment of the gas content of such systems is a nontrivial problem. Innovative core handling and analysis techniques that have been developed for tight gas sands have wider applications, but might not have been developed without the important economic value of this resource.

30.2 Geochemistry of Unconventional Rocks

The nature of unconventional reservoirs is that they contain organic matter that is both the source and the reservoir. The challenge is to develop methodologies to identify the nature of the hydrocarbon storage and optimize its connection to permeable pathways.

Organic materials preserved in rocks came from the decay of plants. Depending on the time and temperature at which these materials were "cooked," greater or lesser quantities of liquid or

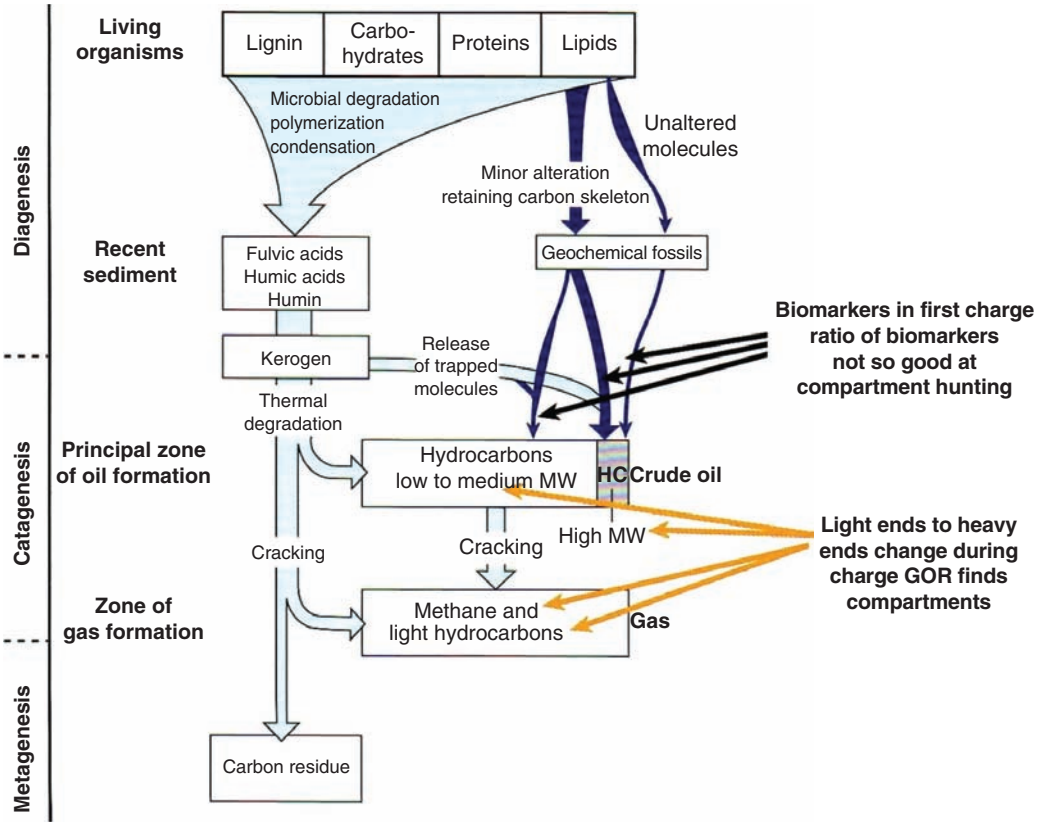


Fig. 30.5—Transformation of living organisms into hydrocarbons (after Cubitt et al. 2004). Used with permission of The Geological Society Publishing House.

gaseous hydrocarbons generated, and what remained coals. The transformation of living organisms through diagenesis into kerogen, through catagenesis into oil and gas, and finally through metagenesis into carbon residue is illustrated in **Fig. 30.5.**

30.2.1 Quantity of Organic Matter. Adequate quantities of organic material must be present for a geologic unit to be considered a potential source rock. A variety of geochemical parameters can be used to measure the petroleum potential of a source rock on the basis of the amount of organic material present. These parameters are listed in **Table 30.2.** Geoscientists assess the quantity of organic material in sedimentary rocks by evaluating several indicators, including TOC

TABLE 30.2—PETROLEUM POTENTIAL OF SOURCE ROCK (From Peters and Cassa 1994)
AAPG © 1994, reprinted by permission of the AAPG whose permission is required for further use.

	Organic Matter					
	TOC	Rock-Eval Pyrolysis		Bitumen		Hydrocarbons
Petroleum Potential	(wt%)	S_1	S_2	(wt%)	(ppm)	(ppm)
Poor	0–0.5	0–0.5	0–2.5	0–0.05	0–500	0–300
Fair	0.5–1	0.5–1	2.5–5	0.05–0.10	500–1000	300–600
Good	1–4	1–2	5–10	0.10–0.20	1000–2000	600–1200
Very Good	2–4	2–4	10–20	0.20–0.40	2000–4000	1200–2400
Excellent	>4	>4	>20	>0.40	>4000	>2400

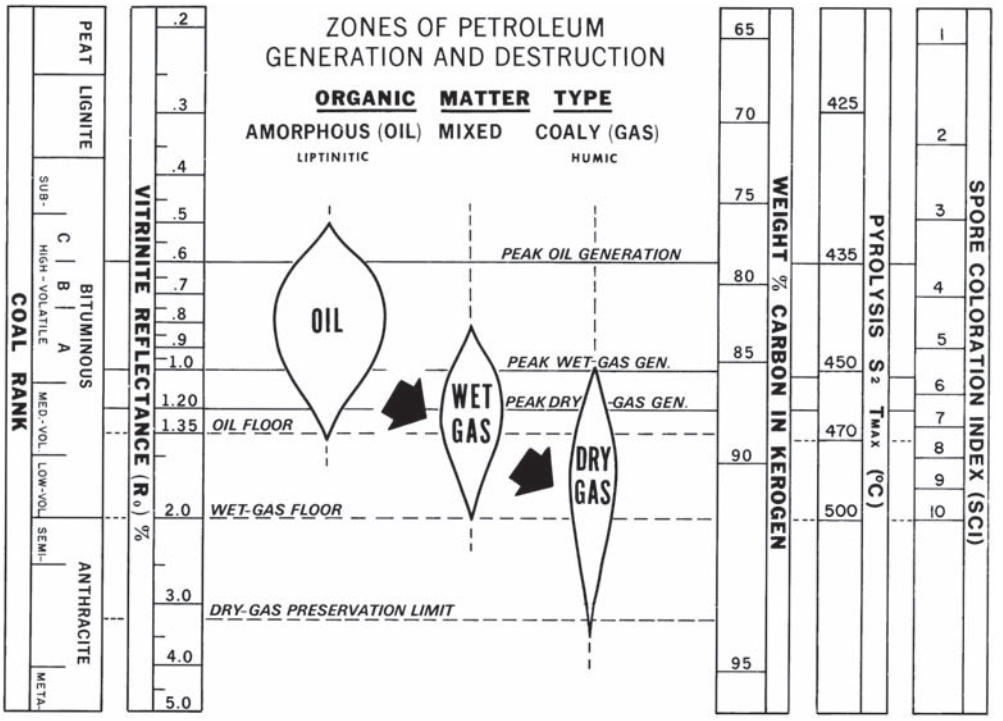


Fig. 30.6—Hydrocarbon-generation schematic. This historical figure is provided courtesy of the former Robertson Research, now Fugro Robertson Ltd.

and Rock-Eval® pyrolysis.* Such assessments can be made from properly cut core samples that have been correctly handled at the wellsite and in transportation to the laboratory (see later in this chapter for details of coring and core-analysis techniques and other log-derived methods for assessment of TOC).

30.2.2 Hydrocarbon Generation. Fig. 30.6 graphically combines a number of related factors that either control or give indications of the hydrocarbon-generating potential of buried sediments. These include, in order of increasing age, depth of burial, and temperature,

- Coal rank (peat ⇨ lignite ⇨ bituminous ⇨ anthracite)
- Vitrinite reflectance [from dull to shiny (0.2 ⇨ 5)]
- Weight percentage of carbon in kerogen (65 ⇨ 95)
- Pyrolysis S2 temperature (425°F ⇨ 525°F)

30.2.3 Kerogen and Bitumen.

Kerogen. This is the portion of organic matter preserved in sedimentary rocks that is insoluble in organic solvents. It derives from the breakdown and diagenesis of plant and animal matter disseminated in fine-grained sediments. Kerogen includes both marine- and land-derived organic matter. The latter is identical to the components of coal.

There are four types of kerogen: the liptinites (Types I and II), the vitrinites (Type II), and the inertinites (Type IV). In discussions of kerogen, the term *maceral* is often used, which may not be familiar to nongeochemists. A maceral is to coal what a mineral is to rock. Rocks are composed of minerals; coal is composed of macerals. However, minerals often have reasonably well-defined

*Rock-Eval® is a trade name for an apparatus that combusts organic matter in the absence of oxygen.

chemical and physical characteristics. Macerals cannot be categorized so neatly. They are the remains of plants and degraded plant materials; they also have some characteristic chemistries and physical attributes. Unfortunately, these characteristics are more loosely defined than for minerals (see the Appendix to this chapter). Liptinite-rich rocks have high oil- and gas-producing potential. Vitrinite-rich rocks tend to be prone to gas generation. Inertinites are not prone to oil or gas generation.

Bitumen. This is the portion of organic matter in sedimentary rocks that is soluble in organic solvents. Hunt (1996) broadly defined bitumen as any native substance of variable color, hardness, and volatility, composed principally of carbon and hydrogen, and sometimes associated with mineral matter, the nonmineral constituents being largely soluble in carbon disulfide. The term *bitumen* is also used to describe organic matter that may be thermally extracted from rocks, and it may be used informally to mean tar, pitch, and asphalt.

Thus, by judicious use of the various indicators available from core and log analysis, the geologist and geochemist can gain a good understanding of the source potential of any rock. **Fig. 30.7** shows a schematic of the solids and fluids present in source and nonsource rocks.

30.2.4 TOC. TOC is a measure of the organic richness of a rock: that is, the quantity of organic carbon (both kerogen and bitumen) in a rock sample (Jarvie 1991; Peters and Cassa 1994).

TOC is reported as a weight percentage (wt%) carbon, (e.g., 1.0 wt% carbon means that in 100 g of rock sample, there is 1 g of organic carbon). TOC is useful as a qualitative measure of petroleum potential. The qualifiers for petroleum potential that are used here (e.g., fair) apply to rocks at a thermal maturity equal to vitrinite reflectance (R_o) of 0.6% (at the beginning of the oil window). It is important to realize that TOC decreases with increasing thermal maturity.

- A TOC of 0.5 wt% is widely regarded as the minimum value for defining a petroleum source rock, but most geochemists consider rocks with less than 1.0 wt% TOC as organically lean and as unlikely sources of commercial hydrocarbon accumulations (Peters and Moldowan 1993; Hunt 1996).
- The worldwide average TOC of all shales is approximately 0.9 wt%, and the average TOC of source-rock shales is 2.2 wt% (Miles 1989).
- The average TOC of calcareous shale source rocks and carbonate (mudstone) source rocks is 1.9 wt% and 0.7 wt%, respectively.
- The worldwide average TOC of all source rocks is 1.8 wt%, a value much higher than the oft-quoted minimum of 0.5 to 1.0 wt%.
- It is recommended to use a TOC of 1.0 wt% as a minimum value for defining potential source rocks.

30.3 Unconventional Formation Evaluation

The task of the petrophysicist working with unconventional reservoirs is to quantify the amount of organic material in the formation and its maturity. The tools available to accomplish this goal

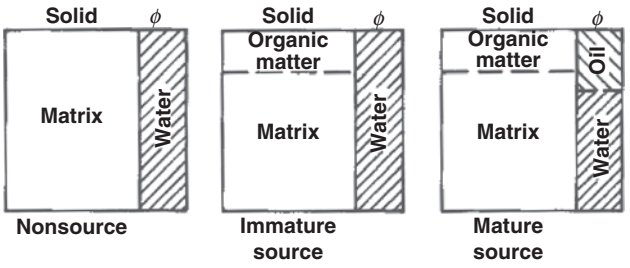


Fig. 30.7—Schematic of immature and mature source rocks.

include mud logging, cores and core analysis, and either wireline or MOD logs. A short discussion of each method follows.

30.3.1 Mud Logging. Not all wells drilled in unconventional reservoirs will necessarily have a mud-logging unit on location. Those that do have one may not have the specialized equipment that the proper evaluation of unconventional reservoirs demands. In this segment, the basics of mud-logging sensors and analysis will be reviewed.

The basics of mud logging have been covered in Chapter 2. The analysis of the solids and fluids recovered is presented on the mud log as curves plotted against depth, which tell the user useful things about the lithology, the drilling rate, and the kind of rock drilled through and present a breakdown of the gases recovered at the gas trap into subcomponents by carbon (C) number. However, certain mud-logging techniques are particularly pertinent when dealing with unconventional reservoirs.

Fracture Detection. A first indication of a fractured formation may indeed come from the mud log, and the analyst should be on the lookout for:

- Unusual "nonparallel" pattern of gas curves (e.g., C3 much stronger than C2, C4)
- Rate of penetration (ROP) highly erratic
- Total-gas-curve spikes that are not connection gas
- Shale density markedly different
- Mineralized fracture surfaces seen in cuttings

Carbon-Isotope Analysis. The carbon atom occurs naturally in two forms called *isotopes*. **Fig. 30.8** illustrates the difference between two methane molecules with different carbon isotopes.

One isotope has a nucleus (^{12}C) with six protons and six neutrons, and the other has a nucleus (^{13}C) with an "extra" neutron. Only approximately 1% of the carbon nuclei in nature are ^{13}C. However the *ratio* of the abundance of the two carbon isotopes tells a story related to the maturity of the source of the organic material found in a formation being drilled through. **Fig. 30.9** documents the decrease of ^{13}C as one moves from deep dry gas up through oil-related gas to shallow bacterial methane.

Gas liberated during the drilling process and captured at the gas trap **(Fig. 30.10)** from mud returns may have a different isotopic composition from gas that is liberated from a cored rock sample preserved in a pressure chamber where adsorbed gas can be liberated. The latter is referred to as "head" gas. These differences are indicators of permeability variations, fracturing, or both.

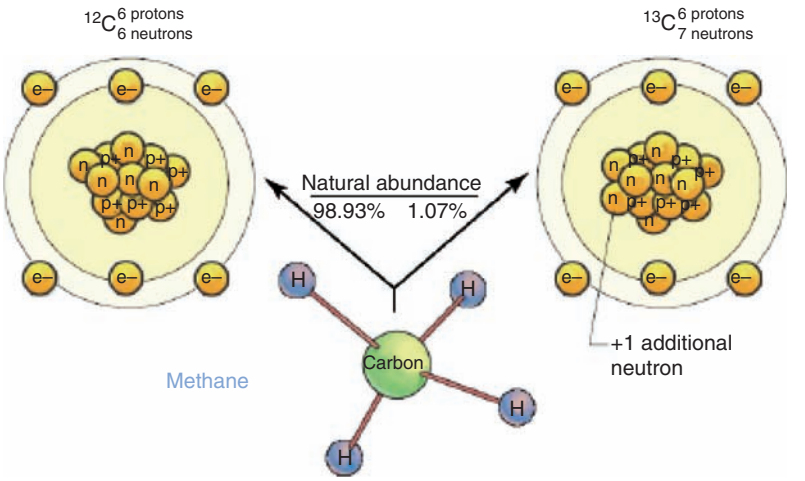


Fig. 30.8—Carbon isotopes. After *Oil & Gas Journal* (May 2003).

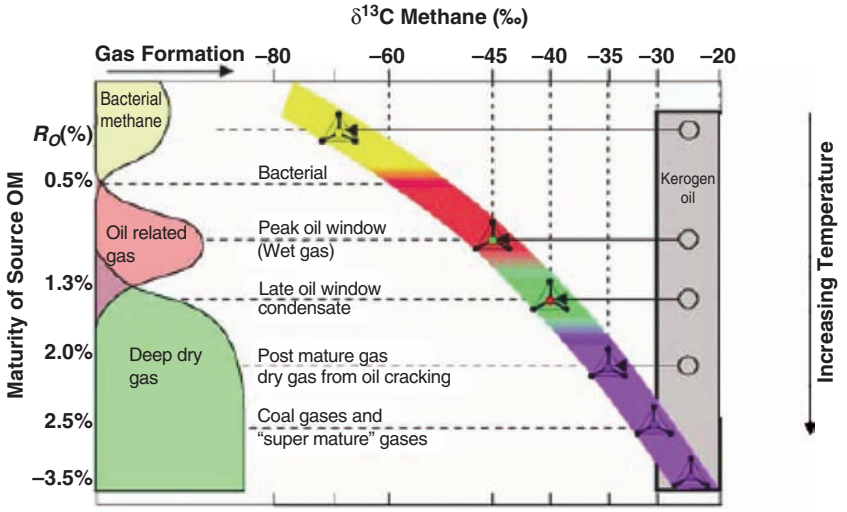


Fig. 30.9—Carbon-isotope ratios vs. maturity.

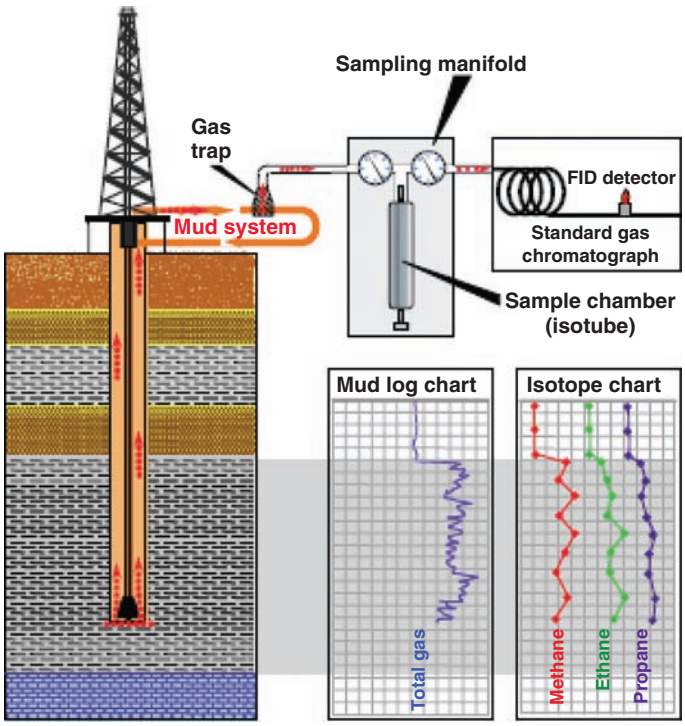


Fig. 30.10—Mud-gas isotopic chromatography.

Fig. 30.11 illustrates the origins of "free" mud gas and adsorbed "head" gas.

There is a clear isotopic difference between methane from mud gases (black squares) and the headspace gases (purple squares). The mud gas includes free and solution gas, but the headspace gas comes from the adsorbed gas. Large differences between the two correlate with increased permeability.

C-Number Ratios as Hydrocarbon Type Indicators. Analysis of mud-logging gas ratios has proved useful in predicting whether the gas produced from a shale will be dry or wet (i.e.,

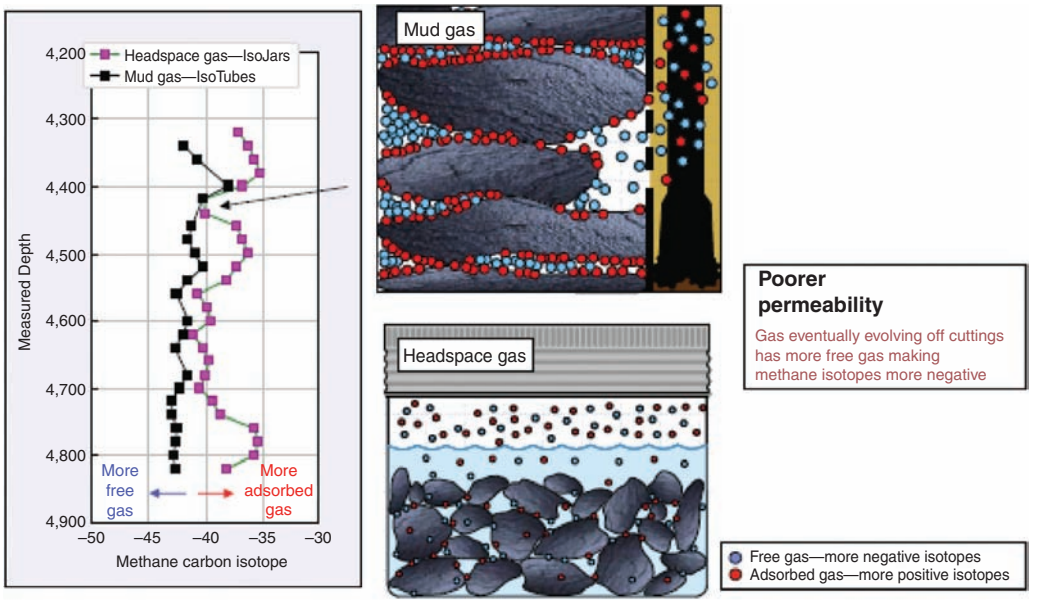


Fig. 30.11—Shale-gas analysis as a permeability indicator.

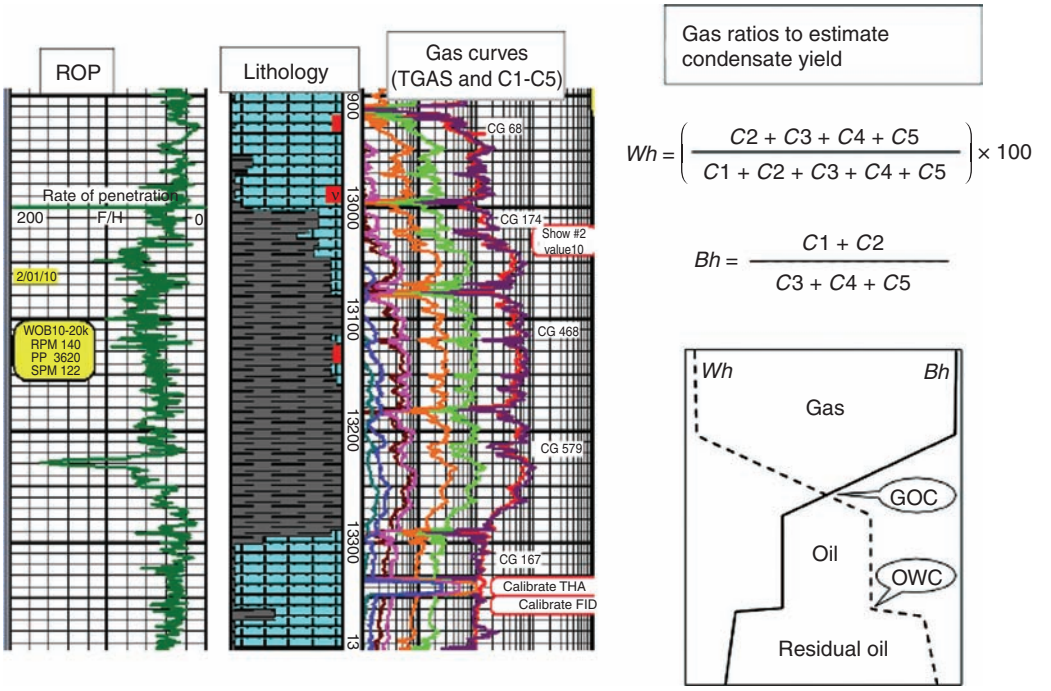


Fig. 30.12—Mud-logging gas ratios and condensate yield (after Haworth et al. 1985). Courtesy of Pioneer.

providing a condensate that also generates an income stream from the sale of hydrocarbon liquids). The ratios used in the example shown in **Fig. 30.12** are:

$$Wh = \left(\frac{C2 + C3 + C4 + C5}{C1 + C2 + C3 + C4 + C5} \right) \times 100 \quad \ldots\ldots\ldots\

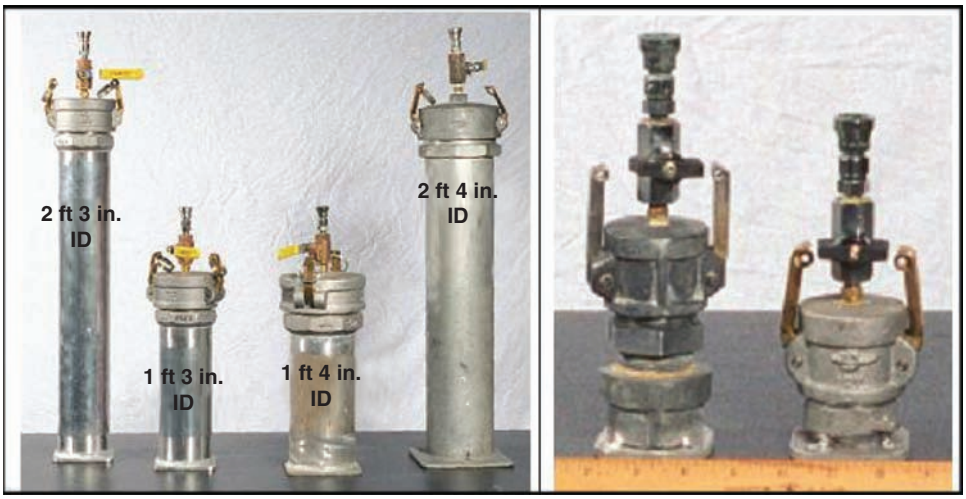


Fig. 30.13—Canisters used for full-diameter cores (left) and rotary sidewall cores (right).

$$Bh = \left(\frac{C1 + C2}{C3 + C4 + C5} \right) \quad \ldots\ldots\ldots\

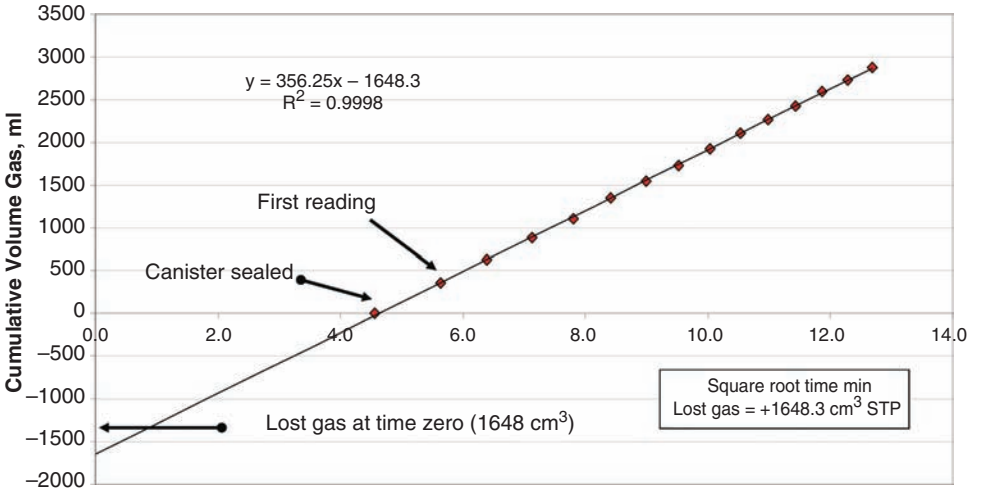


Fig. 30.15—Estimation of "lost gas."

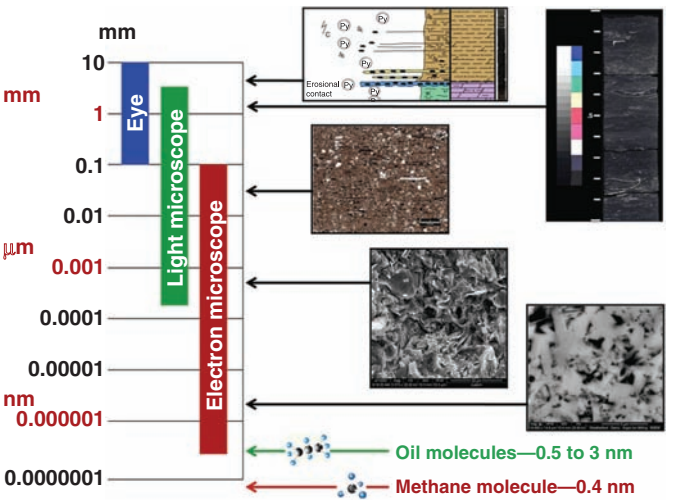


Fig. 30.16—Scales of inspection of core material.

The lost gas is summed with the recovered gas to give a figure for total gas. In certain cases, some residual gas may be trapped in dead-end pores and can be released by grinding up the core sample in the laboratory. This gas can then be added to the total that will be used as an indicator of the gas in place in the reservoir.

Core-Sample Analysis. Rock samples suitable for laboratory analysis may come from a variety of sources (e.g., cuttings, sidewall cores or plugs, and conventional cores). Chapter 27 covers standard core-analysis procedures. In the case of unconventional reservoirs, the standard methods used for routine and special core analysis are inadequate, and special laboratory procedures have been developed fairly recently to measure extremely low permeabilities and to understand the mechanisms by which gas molecules are stored in unconventional reservoir rocks and by adsorption to the surfaces of coal cleats.

Core material can be investigated at three levels: the human eye (visible-light range), under the light microscope, and with the SEM **(Fig. 30.16).***

*Personal communication with M. Walker and M. Dixon. 2010. Houston: Weatherford Laboratories.

Recent advancements in SEM analysis of shales can be categorized as follows:

- *Sample preparation*: argon-ion milling prepares a cross section with minimal artifacts and displays a fresh, debris-free surface for follow-up SEM examination.
- *High-resolution electron microscope*: The FESEM is preferred over standard thermionic SEM methods because of better spatial resolution.
- *Focused ion beam (FIB)* systems operate similarly to an SEM, except that, rather than a beam of electrons, FIB systems use a finely focused beam of ions (usually gallium) that can be operated at low beam currents for imaging or high beam currents for site-specific sputtering or milling.

30.3.3 Logging Unconventional Reservoirs. The term *logging* encompasses mud logging, wireline logging, and measurements on drillpipe. All three logging methods provide the analyst with crucial data that make it possible to pinpoint formations of interest and to calculate their porosity, permeability, hydrocarbon content, and potential produceability. By appropriate use of logging tools and methods, the analyst may expect to gain knowledge of:

- TOC and its maturity
- Porosity, permeability, and gas saturation
- Lithology and mineralogy
- Geologic characterization
- Structural features, layering, and fractures
- Geomechanical reservoir characteristics
- Optimal placement of a horizontal lateral well
- Effectiveness of well stimulations and completions

Logging measurements, while useful and essential, attain their maximum value only when integrated in an overall petrophysical context. **Fig. 30.17** illustrates how multiple logging and core data types can be integrated to provide an overall picture of the unconventional reservoir.

It is a challenge to know what logging parameters are most useful and how log and core measurements can be combined for optimal interpretation when developing unconventional reservoirs. It is my hope that, this section can serve as a useful guide in this endeavor.

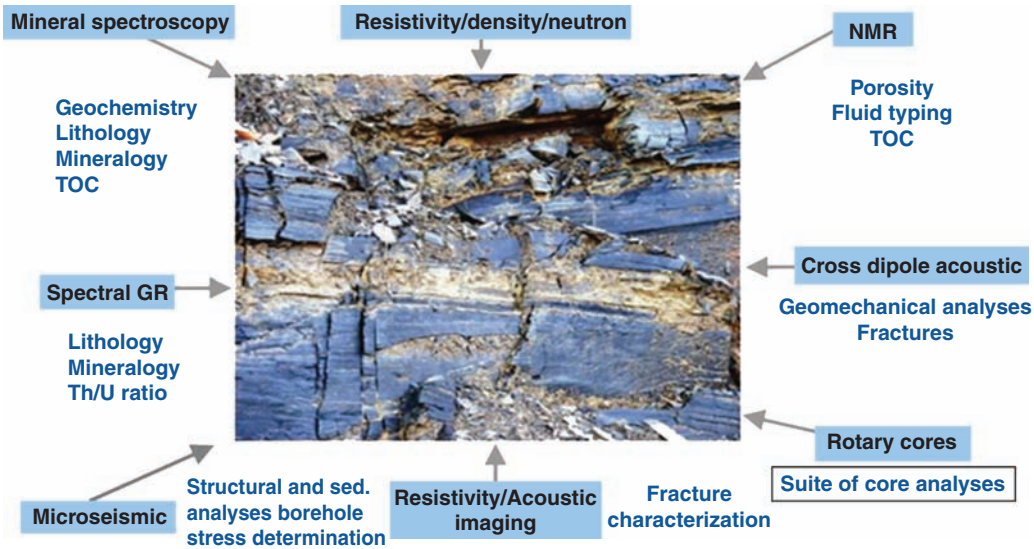


Fig. 30.17—Petrophysical integration. Courtesy of Baker Hughes.

Openhole Wireline Logging. Openhole wireline logging is a standard data-gathering tool in vertical and near-vertical wells. However, it is common, when developing unconventional reservoirs, to construct highly deviated or even horizontal wells. These pose a challenge to normal wireline logging operations. The solution is to use either logging sensors mounted on specially adapted drill collars or to transport the standard wireline logging tools to the bottom of the well on drillpipe. In this segment, only those measurements and analysis techniques that apply to shale gas, tight gas, or CBM are discussed. A common operational practice is to record a "standard" set of logging measurements with a single run in the hole using a so-called "triple combo" that includes both resistivity and neutron-density measurements as well as ancillary measurement of gamma ray, spontaneous potential, and hole caliper.

Gamma Ray Logging. As covered in detail in Chapter 10, gamma ray logging tools come in two versions. The standard logging tool measures the total incident gamma rays coming from the formation. In general, conventional porous matrix materials and evaporites have low gamma ray activity, while shales and volcanic ash have high activity, as shown in **Fig. 30.18.** The more sophisticated gamma ray detectors measure in addition how much of the total gamma radiation comes from the three sources of naturally occurring gamma rays (i.e., potassium, thorium, and uranium). Of particular interest to the analyst working with unconventional reservoirs is the uranium content of the formation because this can be correlated with the total organic carbon (TOC) content, as shown in Fig. 30.18b.

Resistivity. Resistivity logs respond to the water content of the formation. Most formation-matrix materials are insulators (with the exception of iron-bearing minerals such as pyrite), and therefore the only path open for electrical conductivity is through the ionic salt(s) that are dissolved in the water in the pore spaces. In conventional sandstone and carbonate reservoirs, this is the only conductive path available, and the electrical resistivity of such rocks is controlled by the porosity (ϕ), the water saturation (S_w), and the resistivity of the connate water (R_w), which in turn is a function of salt concentration and temperature. Archie's equation is used for quantitative analysis and estimation of hydrocarbons in place:

$$S_w^n = \frac{a}{\phi^m} \times \frac{R_w}{R_t} \quad \ldots\ldots\ldots\

Unconventional reservoirs do not behave as simple "Archie rocks," either because of their high clay content or because of the unconventional nature of the matrix, which may be both the source rock and the reservoir. Clays provide an additional conductive path because of surface conductance effects related to their CEC, which in turn depends on the specific surface area of the clay crystals. Not all clays are equally "active" in this respect, and a proper understanding of the resistivity of an unconventional reservoir rock requires knowledge of the clay type, quantity, and distribution.

Sonic Logs. Sonic logs perform multiple important roles in the petrophysical analysis of unconventional reservoirs. Not only are they used for formation porosity estimates, but they are also used for estimation of organic content (TOC) and for measurements of formation anisotropy. Sonic logging tools also come in a variety of "flavors," including tools that are:

- Simple two-receiver uncompensated
- Multisource, multireceiver borehole compensated
- Long-spaced versions of the aforementioned
- Arrayed receiver versions for semblance processing
- Dipole-sourced with directional receivers
- Versions with both compression and shear energy sources

The analyst should be familiar with the functions of these devices and be sure that the tool selected for logging will provide the parameters needed for analysis (Δt_c and Δt_s, for example).

Neutron Logging. Neutron logging* requires a (chemical) source of high-energy neutrons. On entering the formation, these become scattered, slowed down, and finally captured by other nuclei, which then emit gamma rays of capture. At various stages of this progression, detectors may measure the backscattered neutrons re-entering the borehole or the gamma rays of capture. Other versions use a particle accelerator that can be switched on and off to produce pulsed "bursts" of neutrons; these tools are used mostly in cased holes to determine porosity and saturation behind the casing. Yet other versions are used for what is called *elemental spectral analysis,* which detects the presence and volumetric fractions of matrix materials in the formation. **Fig. 30.19** shows a schematic of a generic neutron-logging tool.

Density Logging. In unconventional reservoirs, the measurement of formation density alone is insufficient to describe porosity fully because the matrix itself is a mixture of sand, shale, and kerogen. The mineralogy of shale-gas reservoirs is complex, hence the need for multiple logging-tool measurements to evaluate them fully. The complexity of the problem can be perceived from **Table 30.3,** which lists the typical components of a shale-gas formation.

If the reservoir rock is well known and a core analysis is available, it may be possible to "calibrate" the reading of a density log in terms of TOC. **Fig. 30.20** gives an example of such a calibration.

Photoelectric Factor, P_e. A sophisticated version of the density logging tool can also produce an indicator of lithology known as the photoelectric factor, or P_e. This indicator is useful in performing a detailed log analysis.** It is particularly useful in unconventional reservoirs, where it is critical to pinpointing the makeup of the rock matrix. **Table 30.4** lists the values of P_e for common rock-matrix materials. Proper interpretation of the formation-density measurement therefore calls for sophisticated log-analysis routines.

Fig. 30.21 shows a mineralogical analysis of a Barnett shale section based on measurements from neutron, density, gamma ray, and other logs.

NMR. NMR provides the analyst with a quasicomplete "picture" of the formation porosity and type of porosity because it is sensitive to the pore-size *distribution*. This, in turn, enables surprisingly good estimates of formation permeability. In addition, the NMR measurement gives

*See Chapter 18 for a fuller discussion of neutron logging.

**See Chapter 17.

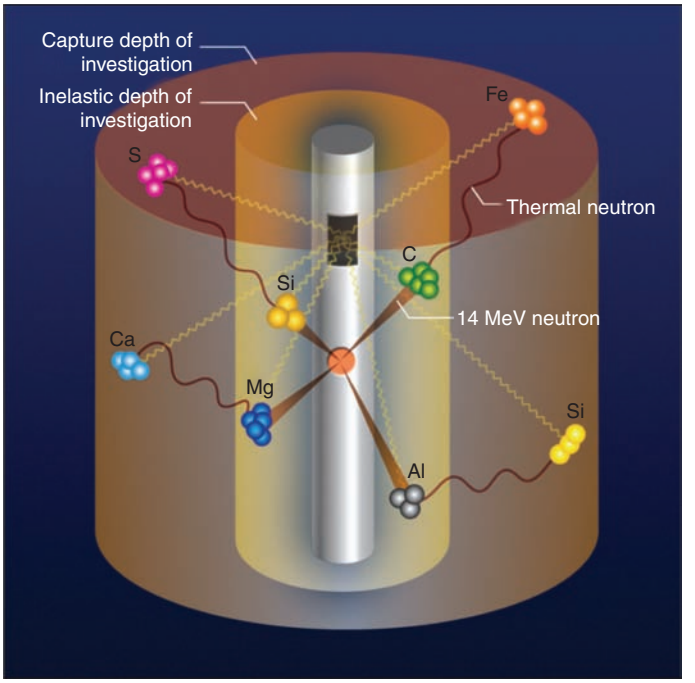


Fig. 30.19—Generic neutron-logging tool. Courtesy of Baker Hughes.

TABLE 30.3—SHALE GAS MINERALS COMPONENTS (COURTESY OF BAKER HUGHES)

Name	Formula	Density, g/cm^3
Quartz	SiO_2	2.64
K-Feldspar	$KAlSi_3O_8$	2.54–2.57
Albite	$NaAlSi_3O_8$	2.59
Calcite	$CaCO_3$	2.71
Dolomite	$CaMg(CO_3)_2$	2.85
Siderite	$FeCO_3$	3.89
Apatite	$Ca_5(PO_4)_3F$	3.21
Anhydrite	$CaSO_4$	2.98
Gypsum	$CaSO_4{\cdot}2H_2O$	2.35
Illite	$K_{0.67}[Al_2](Al_{0.67}Si_{3.3})O_{10}(OH)_2$	2.52
Smectite	$Na_{0.33}[Al_2](Al,Si)_4O_{10}(OH)_2 - nH_2O$	2.41–2.52
Chlorite	$[Mg_3Fe_3](AlSi_3)_4O_{10}(OH)_8$	2.76
Kaolinite	$Al_2Si_2O_5(OH)_4$	2.41
Glauconite	$K_{0.8}[Fe_{1.2}Al_{0.4}Mg_{0.4}](Al_{0.35}Si_{3.65})O_{10}(OH)_2$	
Pyrite	FeS_2	4.9
Hematite	Fe_2O_3	5.18
Halite	NaCl	2.04
Sylvite	KCl	1.86
Zeolite	$(Ca,Na)_{2-3}Al_3(Al,Si)_2Si_{13}O_{36}{\cdot}12(H_2O)$	2.1–2.47
Excess C	Coal, Kerogen, or Oil	

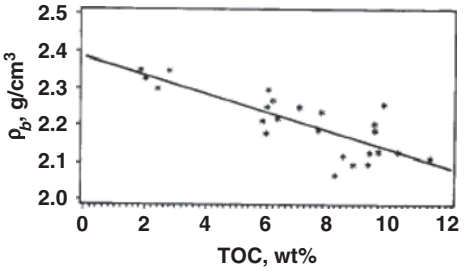


Fig. 30.20—Bulk-density-to-TOC calibration.

TABLE 30.4—*Pe* VALUES FOR MATRIX MATERIALS

Matrix	*Pe*
Quartz	1.81
Kaolinite	1.80
K-Feldspar	2.90
Dolomite	3.14
Salt	4.65
Illite	3.50
Calcite	5.08
Anhydrite	5.05

an indication of the presence and types of hydrocarbons. The main drawbacks of NMR tools* are that they make their measurements very close to the borehole wall in a zone that has probably been altered in some way by the drilling process (shattering and filtrate invasion) and that they are expensive and time consuming to run (logging speed is 900 ft/hr).

NMR logging in unconventional reservoirs has not yet been proved to be indispensable, and many operators omit this tool from their logging programs for shale-gas wells.

Electrical Imagers. Electrical images are available from formation microimaging tools, examples of which are shown in **Fig. 30.22.** In the left panel, layered beds are clearly visible, and their dip and azimuth can be determined from the borehole images. The right-hand panel shows the results that can be expected in a CBM well where fractures, cleats, and breakouts are clearly visible.

Acoustic Imagers. Acoustic imagers use a rotating ultrasonic beam to scan the inside of the borehole in a helical path as the tool is moved along the well. The reflected acoustical signal is monitored both for time traveled and intensity. Travel time is a gauge of hole size, and intensity is related to rock texture. The resolution of the image obtained depends on the speed of rotation of the sensor and the logging speed. **Fig. 30.23** shows an acoustic imaging tool and a typical log.

Acoustic imaging tools work equally well in oil-based and water-based muds. Wireline-conveyed imaging devices have their limitations, especially in highly deviated or horizontal holes. Many of the same sensors used on wireline logging tools can also be used on drill collars in MOD versions. In normal drilling operations, the drill collar will rotate, and therefore a single electrode or other sensor (gamma ray, neutron, or density) can be used to "scan" the borehole in a 360° sweep. The ability to detect fractured intervals from the image logs is particularly valuable because these are the zones that enhance the production of hydrocarbons in shale-gas and coal reservoirs.

*See Chapter 19.

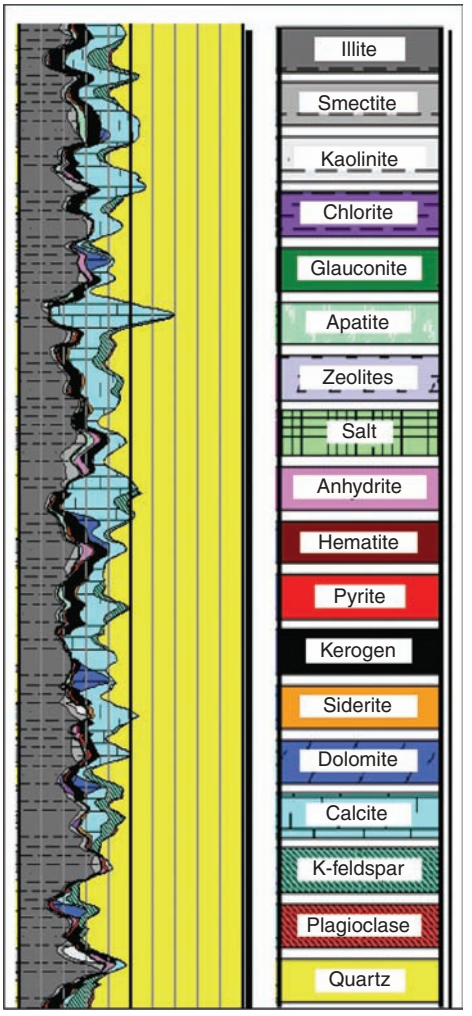


Fig. 30.21—Barnett shale log analysis. Courtesy of Baker Hughes.

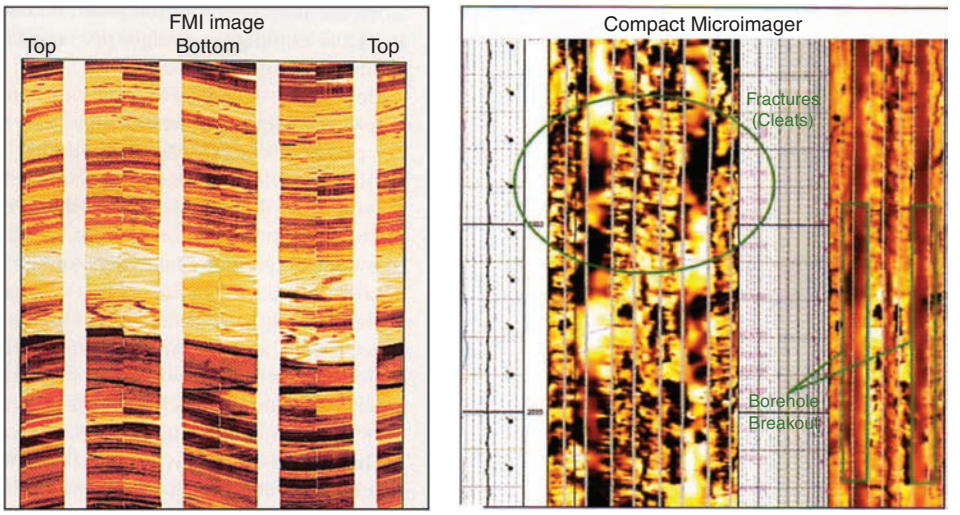


Fig. 30.22—Electrical borehole images.

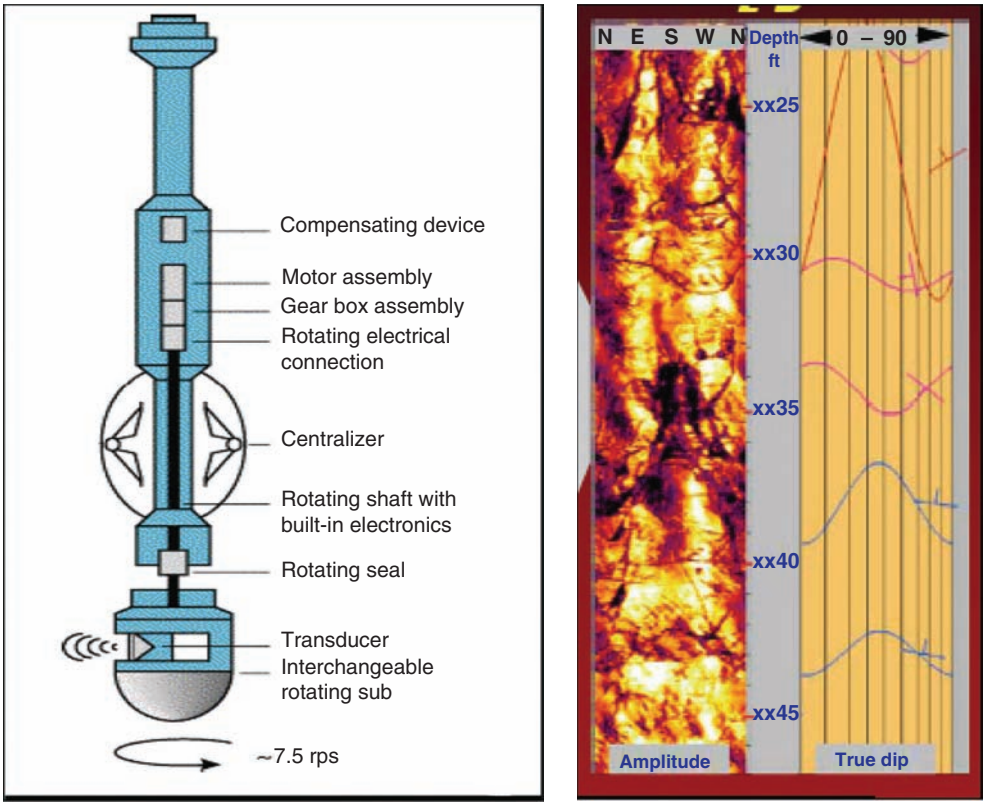


Fig. 30.23—Ultrasonic borehole imaging device (left panel) courtesy of Schlumberger. Acoustical image (right panel) courtesy of Halliburton.

30.4 Assessment of TOC

Traditionally, core material is analyzed in a laboratory to determine its TOC. Secondary indicators, such as log measurements, are then correlated with the laboratory measurements. In subsequent drilling in the same field, these logs may then be used as indicators of TOC, thus eliminating the time and expense of coring every well.

30.4.1 Pyrolysis Parameters (S1 and S2). Pyrolysis is a powerful analytical tool that assesses the quantity, type, and thermal maturity of whole-rock and kerogen samples. **Fig. 30.24** shows a map of the pyrolysis process. The S1 and S2 values measured by pyrolysis provide information about the quantity of organics or the generative potential in the rock sample. S1 and S2 are reported in milligrams of hydrocarbon per gram of dry rock. Pyrolysis involves two heating steps: (1) volatization of hydrocarbons in the source rock and (2) pyrolysis of kerogen and conversion to free hydrocarbons. A third pyrolysis step releases trapped CO_2 and is an indicator of the oxygen trapped in the kerogens.

S1 indicates the oil already generated in the rock. This is the hydrocarbon already present in the sample, and it is distilled out of the sample upon initial heating of the sample to a temperature of 350°C. These values may be anomalously high because of migration or contamination by drilling fluids and mud. A minimum value of S1 for good source rocks is 1.0 mg hydrocarbon/g dry rock.

S2 indicates the amount of hydrocarbon generated through thermal cracking of nonvolatile organic matter. S2 is an indication of the quantity of hydrocarbons that the rock has the potential of producing should burial and maturation continue. This parameter normally decreases with burial depths >1 km. A minimum value of S2 for good source rocks is 5.0 mg HC/g dry rock.

S3 indicates the release of trapped CO_2 from kerogen in the sample.

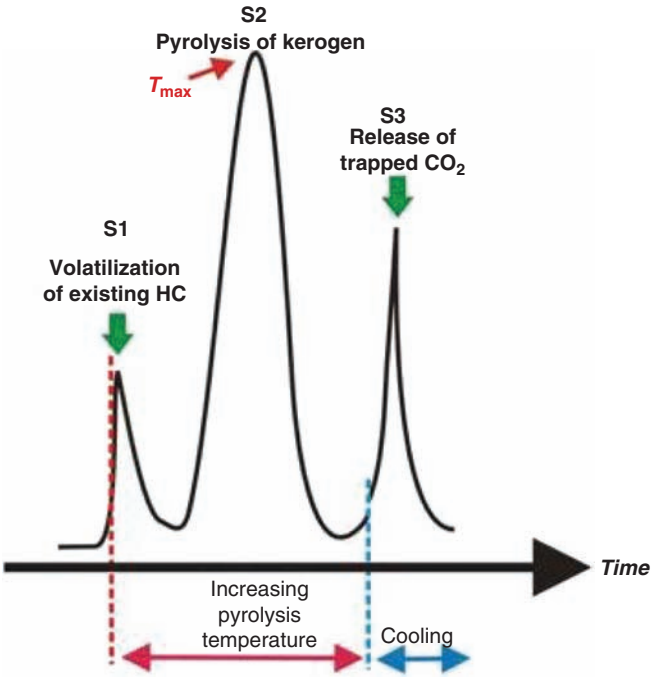


Fig. 30.24—Pyrolysis.

30.4.2 Vitrinite Reflectance. Vitrinite reflectance is commonly used as a maturation indicator. As coal rank increases, vitrinite becomes more reflective. Because the sample may be anisotropic, the reflectance measurement may be recorded either as $\mathbf{R}_v$ max % or as $\mathbf{R}_o$ %. The $\mathbf{R}_v$ max method uses a polarized light beam; the sample is rotated 360° under the microscope, and the average of the two maxima is recorded. The $\mathbf{R}_o$ method uses a nonpolarized light beam. Reflectance is measured as a percentage of the incident light beam that is reflected from the surface of a polished rock sample. The relative importance of each petroleum-generating zone depends on the composition of the original kerogen. In general, the deeper and hotter the sediment, the greater will be the maturity of the kerogen, as illustrated in **Fig. 30.25,** which plots vitrinite reflectance against depth and temperature for a number of different geologic periods from Cretaceous to Plio-Pleistocene.

Core-based evaluation of TOC can be performed by a commercial laboratory, which can return to the operator a log of all the hydrocarbon indicators. An example is given in **Fig. 30.26.** Such displays may also include the oxygen index (S3/TOC × 100) and T_{max}, the temperature at which S2 generation is a maximum.

Note that the lithology track indicates shale as the predominant lithology where the TOC track registers TOC as "good" or "very good." Note also the "maturity" track, which records the core measured values of vitrinite reflectance, R_o. The "hydrogen index" is computed as S2/TOC × 100.

30.4.3 Assessment of TOC From Logs. A number of correlations between TOC and measured parameters from logs have been suggested and are in use today, including:

- Sonic-log Δ-T and formation-resistivity overlays
- Sonic shear slowness
- Spectral gamma ray-derived formation uranium content
- Thermal neutron-porosity index
- Pulsed-neutron ratio curve
- Bulk density

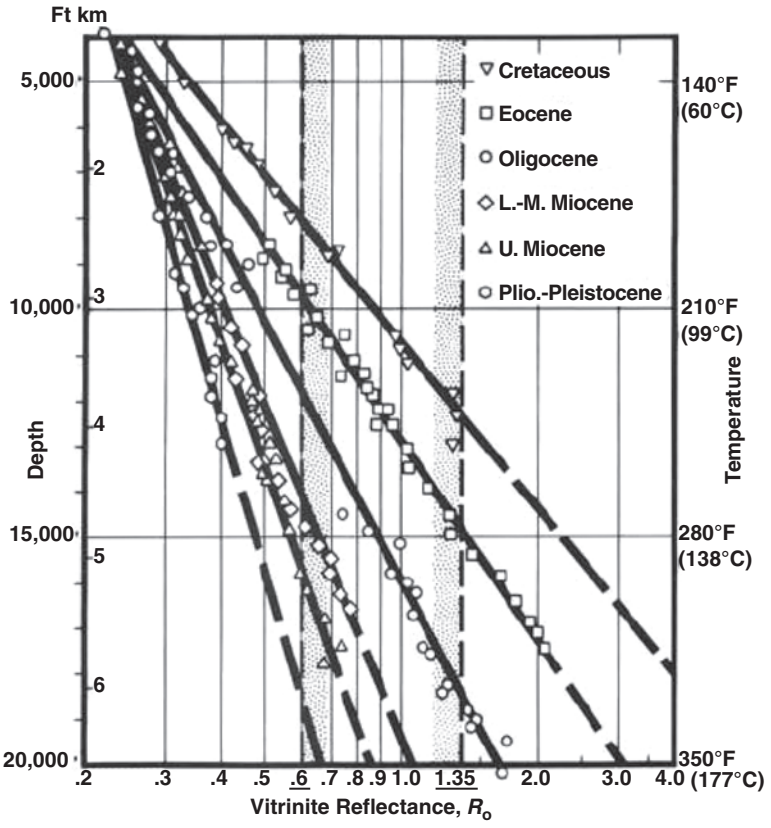


Fig. 30.25—Vitrinite reflectance vs. depth and temperature. Courtesy of Robertson Research. This historical figure is provided courtesy of the former Robertson Research, now Fugro Robertson Ltd.

dLog R Method. The so-called "dLog R" method was proposed by Passey et al. (1990). This method uses the overlay of an appropriate scaled porosity log with a deep resistivity log. The porosity log normally used is the sonic log, which shows values of Δt (slowness).

Referring to **Fig. 30.27,** it can be seen that in water-saturated organics-lean rocks, the two curves parallel each other and can be overlaid because both curves respond to changes in formation porosity. In either hydrocarbon-bearing reservoir rocks or organics-rich nonreservoir rocks, a separation between the curves appears. Using a gamma ray curve, the conventional reservoir intervals can be identified and eliminated from the analysis.

The separation of the organics-rich intervals results from two effects: The porosity curve responds to the presence of low-density, low-velocity kerogen, and the resistivity curve responds to the formation fluid. In an immature, organics-rich rock where no hydrocarbons have been generated, the observed separation is solely the result of the porosity-curve response. In mature source rocks, in addition to the porosity-curve response, the resistivity increases because of the presence of generated hydrocarbons.

The magnitude of the curve separation in nonreservoir rocks may be calibrated to TOC and maturity, which enables depth profiling of organic richness in the absence of core samples. In the preceding example, the relative scaling of the resistivity and sonic logs is 50 μs/ft for each decade on the logarithmic resistivity display. The baseline interval equates 1 Ω·m of resistivity with 100 μs/ft of Δt. This interval has a level of maturity (LOM) of between 6 and 7 and contains Type II kerogen.

The parameter "Δ log R" is obtained from the curve overlays. Algebraically, this is given by the equation:

$$\Delta \log R = \log_{10}\left(R/R_{\text{baseline}}\right) + 0.02 \times \left(\Delta t - \Delta t_{\text{baseline}}\right) \ldots\ldots\ldots\

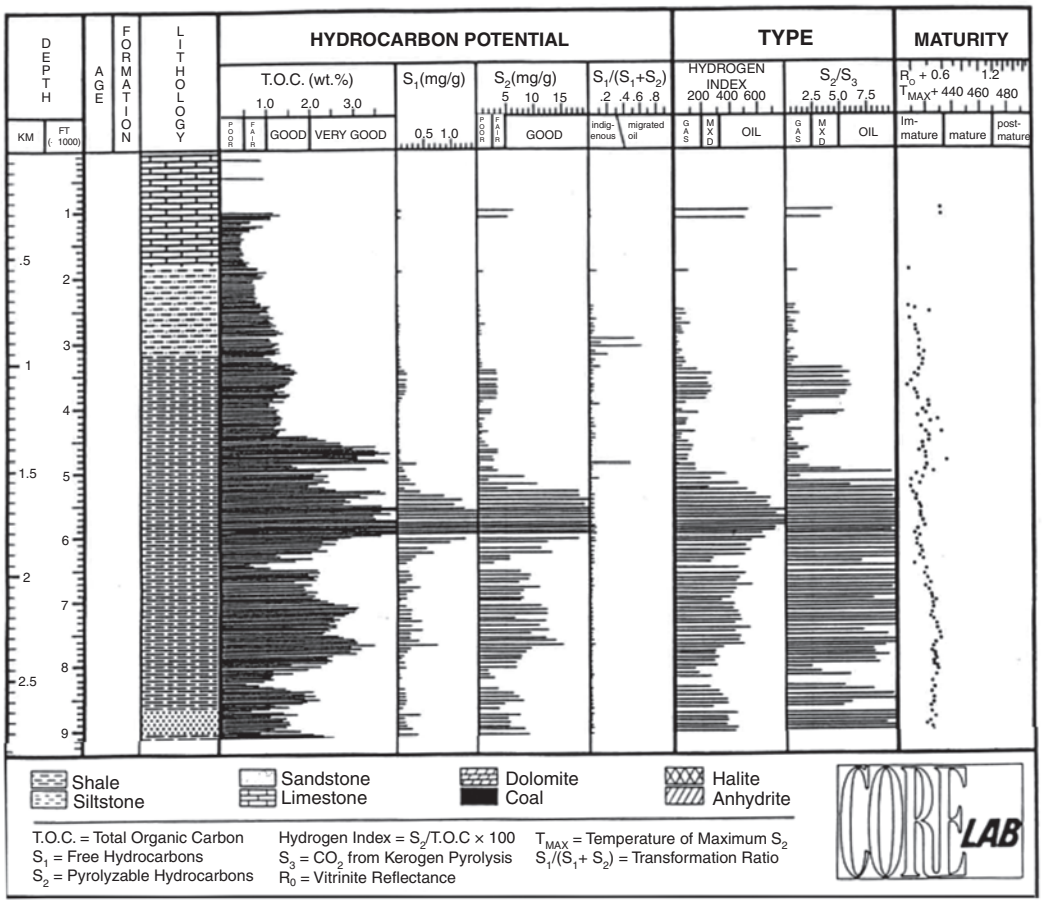


Fig. 30.26—Geochemical well profile. Courtesy of Core Lab.

In turn, "Δ log R" is indirectly related to TOC through previous knowledge of the LOM. **Fig. 30.28** shows this relationship.

Use of this method requires additional data for the LOM, which is not directly available from logs, but which can be inferred from vitrinite-reflectance measurements. The lines plotted on the TOC vs. "Δ Log *R*" can be expressed algebraically by the equation:

$$TOC = (\Delta \log R) \times 10^{(2.297 - 0.1688 \times LOM)}, \quad \ldots\ldots\ldots\

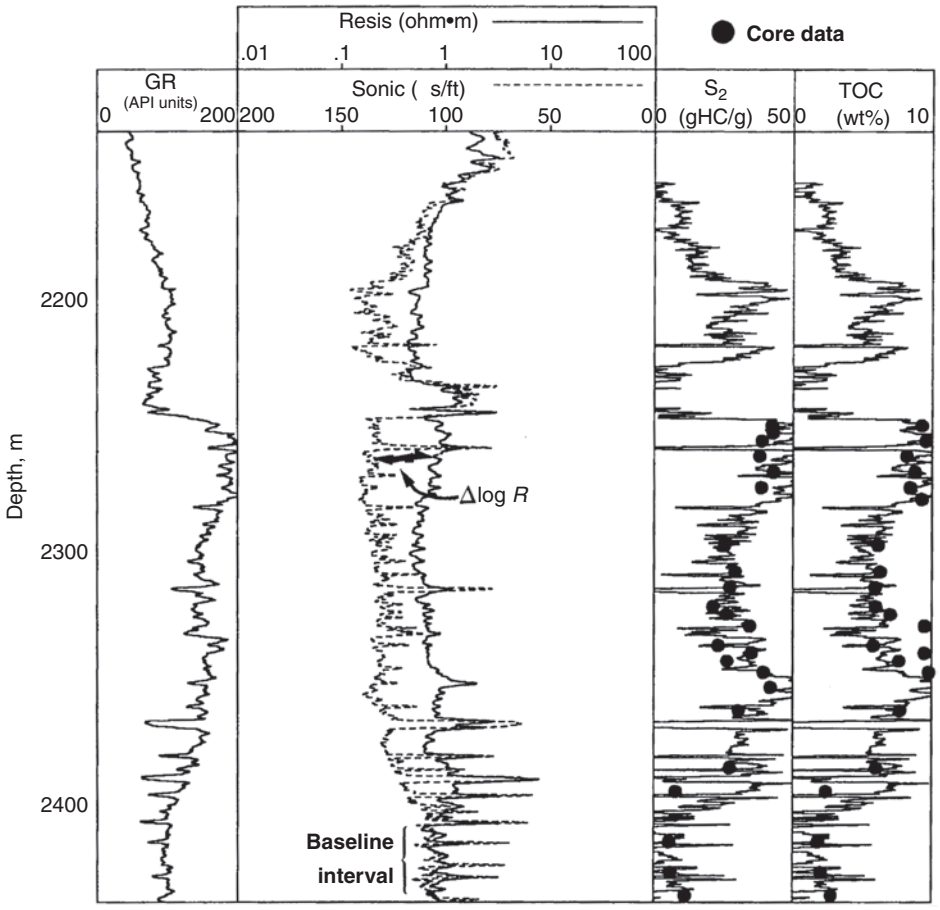


Fig. 30.27—Sonic resistivity overlay for TOC assessment (Passey et al. 1990). AAPG © 1990, reprinted by permission of the AAPG whose permission is required for further use.

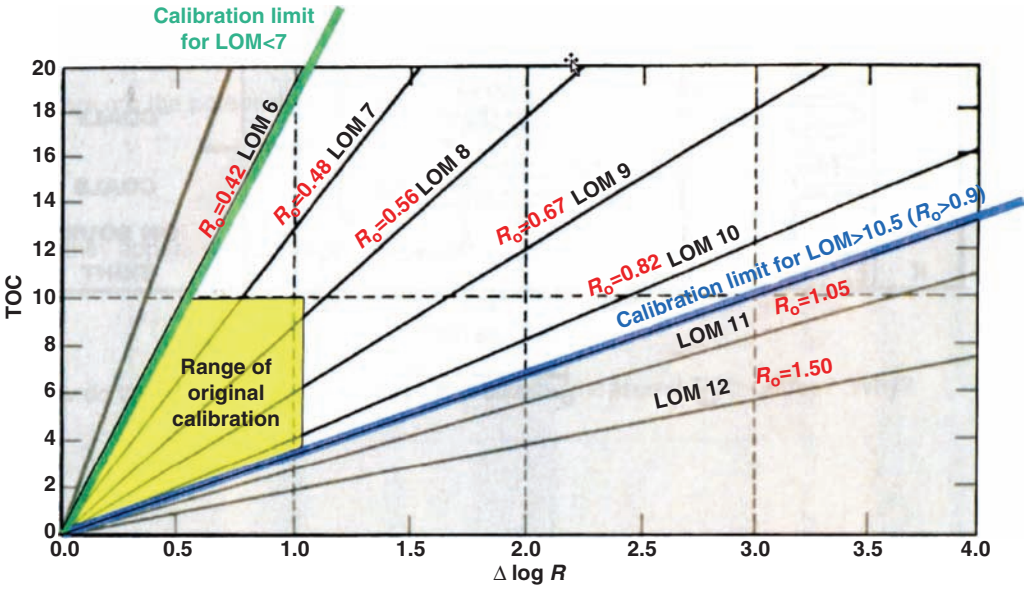


Fig. 30.28—TOC dependence on Δ log *R* and LOM (Passey et al. 1990). AAPG © 1990, reprinted by permission of the AAPG whose permission is required for further use.

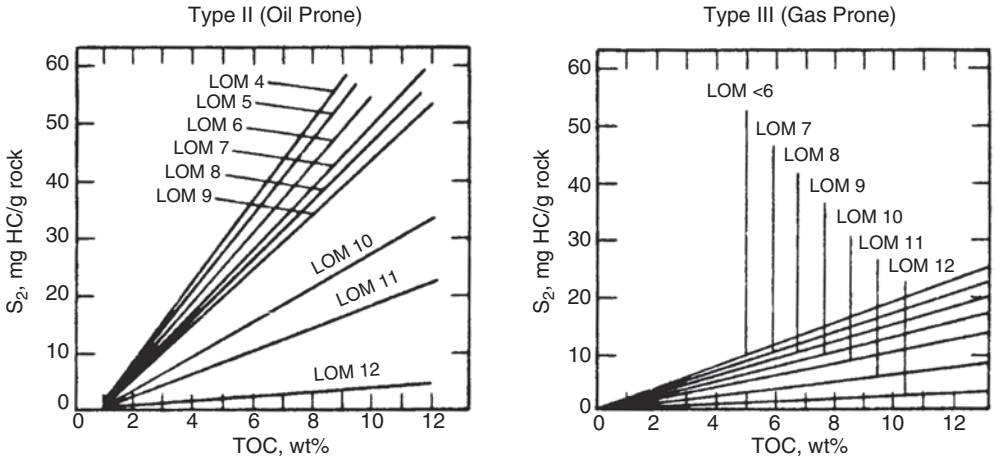


Fig. 30.29—TOC dependence on S2 values (Passey et al. 1990). AAPG © 1990, reprinted by permission of the AAPG whose permission is required for further use.

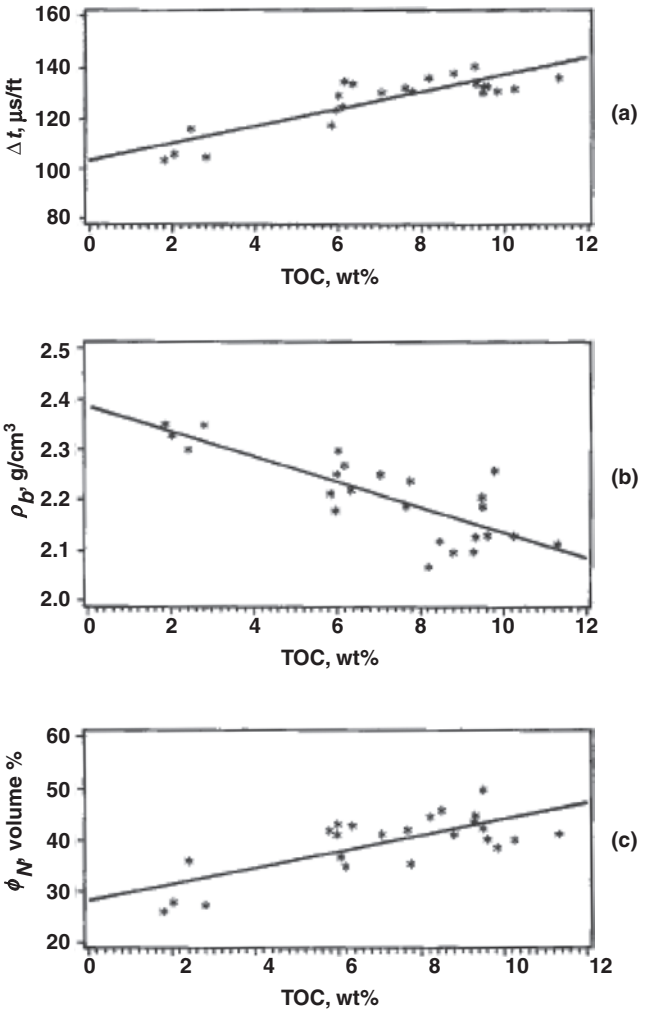


Fig. 30.30—Correlations for (a) Δt, (b) ρ_b, and (c) ϕ_N with TOC (Passey et al. 1990). AAPG © 1990, reprinted by permission of the AAPG whose permission is required for further use.

The fit of TOC to bulk density can be expressed algebraically as:

$$\Delta \log R = \log 10\left(R/R_{\text{baseline}}\right) - 2.5 \times \left(\rho_b - \rho_{\text{baseline}}\right), \quad (30.7)$$

and the fit of TOC to neutron porosity can be expressed algebraically as:

$$\Delta \log R = \log 10\left(R/R_{\text{baseline}}\right) + 4 \times \left(\phi_N - \phi_{N\,\text{baseline}}\right). \quad (30.8)$$

The "best-fit" lines shown in Fig. 30.30 can also be expressed as:

$$TOC = \Delta t \times 0.343 - 36$$
$$TOC = 96 - 40 \times \rho_b$$
$$TOC = \phi_N \times 0.7 - 20, \quad (30.9)$$

where TOC is in wt%, Δt is in μs/ft, ρ_b is in g/cm^3, and ϕ_N is in %.

A summary chart for the Passey method is given in **Fig. 30.31.**

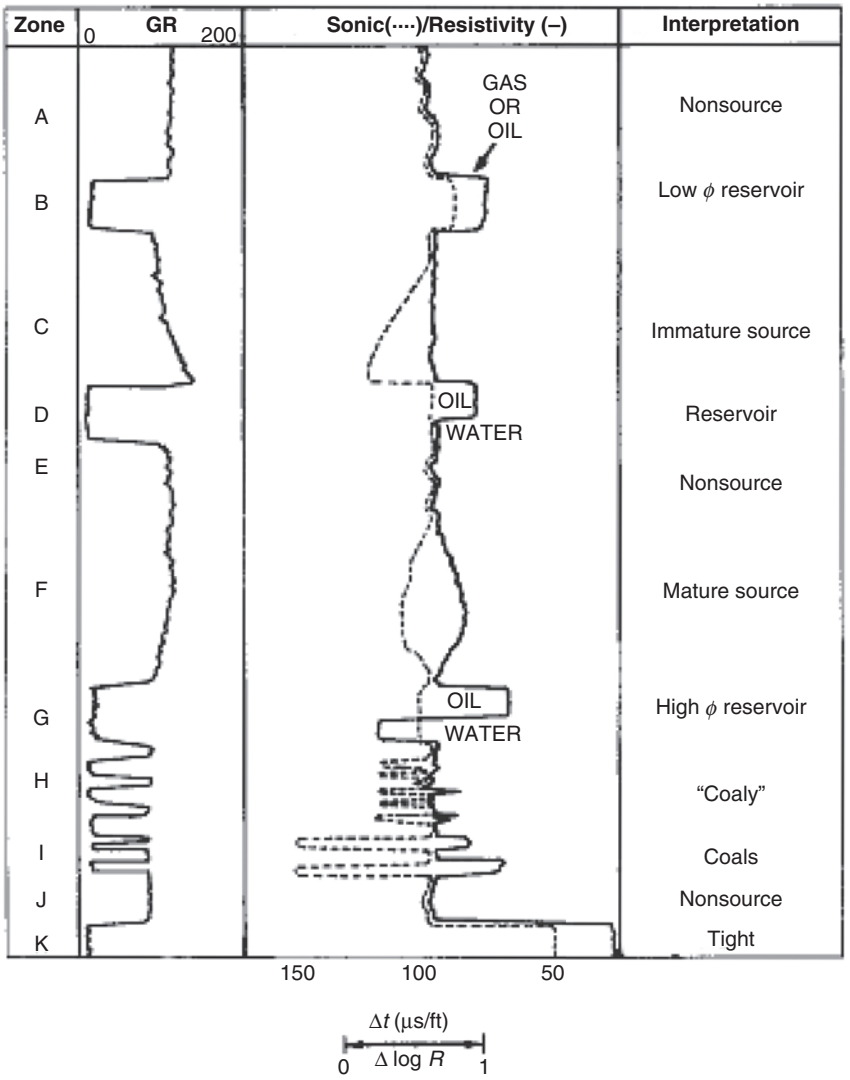


Fig. 30.31—Summary chart for Passey method (Passey et al. 1990). AAPG © 1990, reprinted by permission of the AAPG whose permission is required for further use.

TABLE 30.5—SHALE PLAY TOC COMPARISONS (COURTESY OF TEXAS KEYSTONE)

	Marcellus	Barnett (Core)	Barnett (SW)	Fayetteville	Arkoma Woodford
Avg. TOC	2–10%	3.5–8%	3.5–5%	4–9.5%	3–10%
Av. Total Porosity	6%	4–6%	3–4.8%	2–8%	6–8%
GIP, Bcf/Section	70–150	50–200	50–125	25–65	40–120
Silica Content	40–60%	40–60%		20–60%	60–80%

TABLE 30.6—GEOCHEMICAL PARAMETERS BARNETT SHALE SAMPLES

Sample	Immature	Mature
Vitrinite Reflectance (%)	0.44	1.15
Maceral Composition		
Amorphous (%)	93	91
Exinite (%)	1	1
Vitrinite (%)	5	3
Inertinite (%)	1	5
Rock-Eval and Total Organic Carbon		
TOC (%)	5.51	4.51
S_1 (mg HC/g rock)	2.39	1.73
S_2 (mg HC/g rock)	19.1	3.07
S_3 (mg CO_2/g rock)	1.08	0.23
T_{max} (°C)	441	463
HI (mg HC/G TOC)	346	68
OI (mg CO_2/g TOC)	20	5
PI	0.12	0.36
S_2/S_3	17.68	13.35
Elemental Composition		
Carbon	32.56	22.78
Hydrogen	3.79	2.02
Oxygen	4.39	4.7
Sulfur	9.9	N.D.
Nitrogen	<0.01	N.D.
H/C	1.41	1.06
O/C	0.1	0.15

Shale-Play Petrophysical Comparisons. **Table 30.5** compares a number of shale plays with average TOC values ranging from 2 to 10%, average porosities ranging from 2 to 8%, and gas-in-place values ranging from 25 to 200 Bcf/section.* **Table 30.6** gives a breakdown for some Barnett Shale samples.

*A **section** is 1 sq mile, or 640 acres.

30.5 Matrix and Pore Volumetrics

Historically, conventional petrophysics and log analysis were crafted to handle clean, porous, and permeable formations that conformed to a simple model of an impervious solid matrix material in which interconnected pores provided both the storage volume and the pathways for fluid flow. Direct detection of hydrocarbons was not possible with early oilfield technology, and there was a saying that log analysts measured as much as they possibly could, subtracted it from the universe, and what was left had to be oil. The equivalent saying today would be that gas is where you find it.

In such a model, a unit volume of the formation contained a porosity ϕ and a matrix volume V_{matrix} equal to $1-\phi$. The water-filled pore space was simply the product of the water saturation S_w and the porosity ϕ. By difference, the hydrocarbon-filled pore space was given by the product of the porosity and $1-S_w$. This led to the volume-balance equation:

$$V_{\text{matrix}} + V_{\text{water}} + V_{\text{hydrocarbon}} = 1 \quad \text{or} \quad (1-\phi) + \phi S_w + \phi(1-S_w) = 1 \ldots\ldots\ldots\ldots\ldots\ldots\ldots\ldots (30.10)$$

As unconventional reservoirs became economically important, efforts were made by petrophysicists, core analysts, and log analysts to create new models that could account for a number of new factors that were not accommodated by conventional logging and coring tools and techniques. In particular, these new models have to account for:

- Inorganic matrix materials (both clay and nonclay)
- Organic matrix materials
- Free water
- Capillary-bound water
- Clay-bound water
- Free gas
- Adsorbed gas
- Gas dissolved in water
- Isolated pores

For each of these elements, accurate values are needed for the density of each component to compute its volume. This poses a challenge. For example, adsorbed methane molecules on the surface of cleats or fractures can have a much higher density than the density of free gas, and the density of organic and inorganic materials may be difficult to pinpoint from conventional logging tools. Other factors, never before considered, must now be quantified—for example, gas solubility in water, which depends on gas composition and water salinity as well as temperature and pressure. Suggested component density values are:

$\rho_{\text{inorganic matrix}} = 2.60$ to 2.68 g/cm^3
$\rho_{\text{organic matrix}} = 1.3$ to 1.4 g/cm^3
$\rho_{\text{fluid}} = 0.4$ to 1.0 g/cm^3.

An example of the sorts of models being used today is shown in **Fig. 30.32.**

Modeling at the molecular level suggests that when methane is adsorbed onto the surfaces of the minute cracks in the organic material that afford storage space (porosity) and contribute to permeability, it gets "packed in" at a higher density than that of free gas. **Fig. 30.33** illustrates such a molecular-modeling simulation. The orange spheres represent methane molecules, and the black surfaces are graphite fracture walls.

Such models reveal that the density of adsorbed gas can be as high as 1.8 g/cm^3 immediately adjacent to the pore walls, but drops off rapidly with distance **(Fig. 30.34).** If an average is taken over a typical nanometer pore, the gas density ranges from 0.35 to 0.45 g/cm^3 **(Fig. 30.35).**

To move from log reading and core analysis to a full evaluation of scf/ton involves many assumptions and unknowns. Service-company products that attempt to perform this challenging

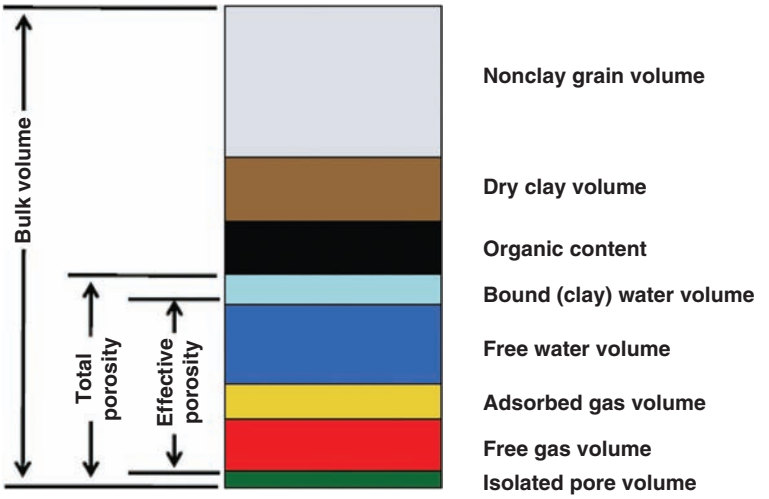


Fig. 30.32—Petrophysical model of an unconventional reservoir rock (Ambrose et al. 2010). Courtesy of Weatherford.

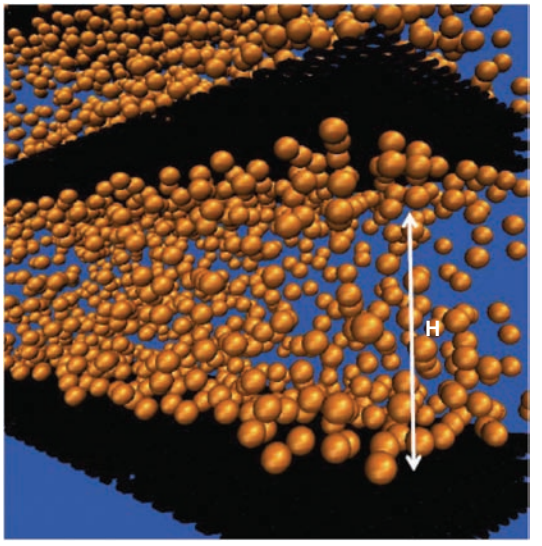


Fig. 30.33—Molecular-dynamics simulation model (Ambrose et al. 2010). Courtesy of Weatherford.

analysis are not always totally transparent about the algorithms used, or (even if published) what the units of measurement are. The advice to the newcomer to this strange world would be "caveat emptor."

Fig. 30.36 provides a good illustration of what is possible when cores and logs are integrated. Note the tracks on this display. Counting from the left, the user is afforded a lithology track (showing porosity, quartz, clay, and organic content), a TOC track, a quartz/clay track, neutron and density logs, a saturation track (water, free gas, and adsorbed gas), and a gas-storage track for both free and adsorbed gas.

Industry practices vary with regard to both core and log analysis. At this time, there is no universally agreed-upon "best way" to handle the calculation of TOC or gas-in-place (GIP). The equivalent of an "Archie's Law" has yet to emerge in this rapidly evolving unconventional industry.

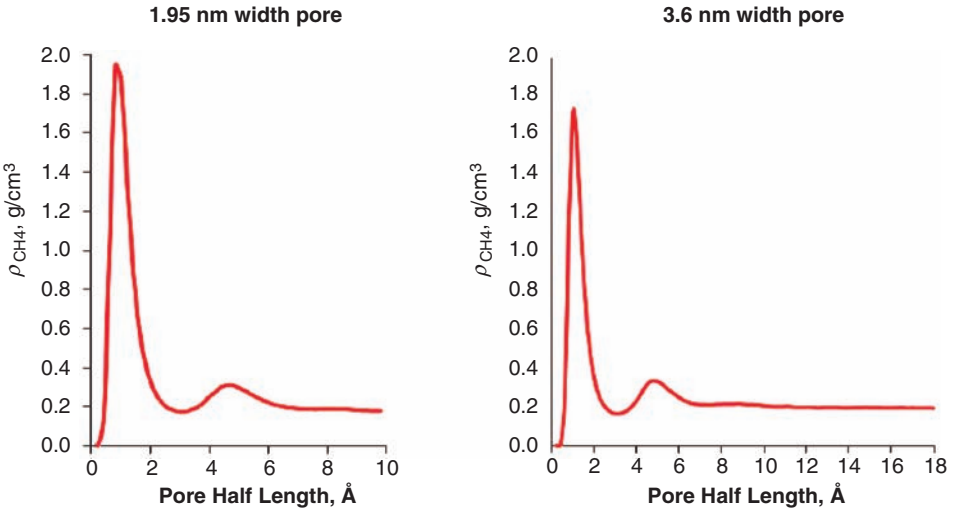


Fig. 30.34—Adsorbed-methane density profile (Ambrose et al. 2010). Courtesy of Weatherford.

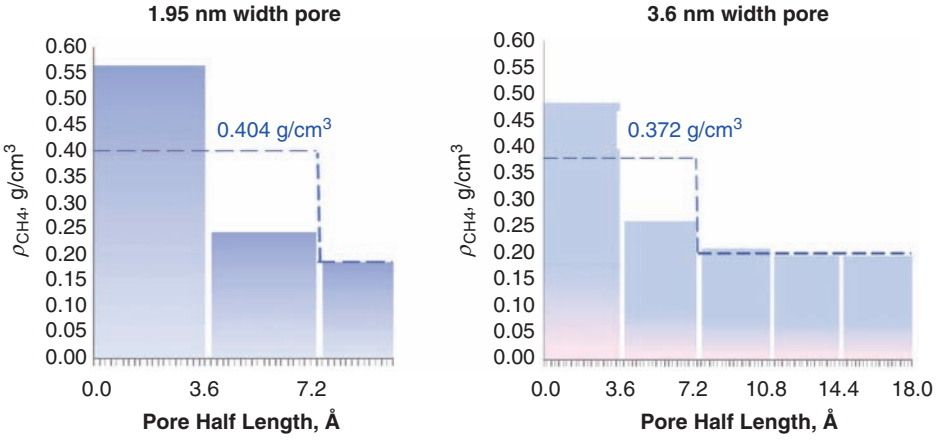


Fig. 30.35—Volume-average methane densities (Ambrose et al. 2010). Courtesy of Weatherford.

30.5.1 Unconventional Gas Reserves. It should be remembered that GIP refers to the volume of gas that is stored in the unconventional reservoir by whatever means: free, dissolved, or adsorbed. This is expressed in standard cubic feet (scf) adjusted for the difference between reservoir pressure and temperature conditions and standard conditions (14.7 psi and 60°F).* *Reserves*, on the other hand, refer to the portion of the GIP that can be economically produced and sold. Reserves are also measured in scf (or Bcf or Tcf), but represent only the portion of the GIP that can be recovered and sold at a profit after the cost of producing it has been covered. This in turn depends on reservoir parameters, production technology, and economic factors such as current operating costs and gas price. The expected ultimate recovery (EUR) of GIP for most modern shale-gas wells is in the 15 to 35% range.

Shale-Gas Production. The production rate from a shale-gas well can in general be related to factors such as TOC and thermal maturity (R_o). **Fig. 30.37** illustrates low potential flow from biogenic source rocks and increasing flow potential as one moves through thermogenic rocks to

*In some states in the United States, slightly different "standard" temperature and pressure conditions prevail.

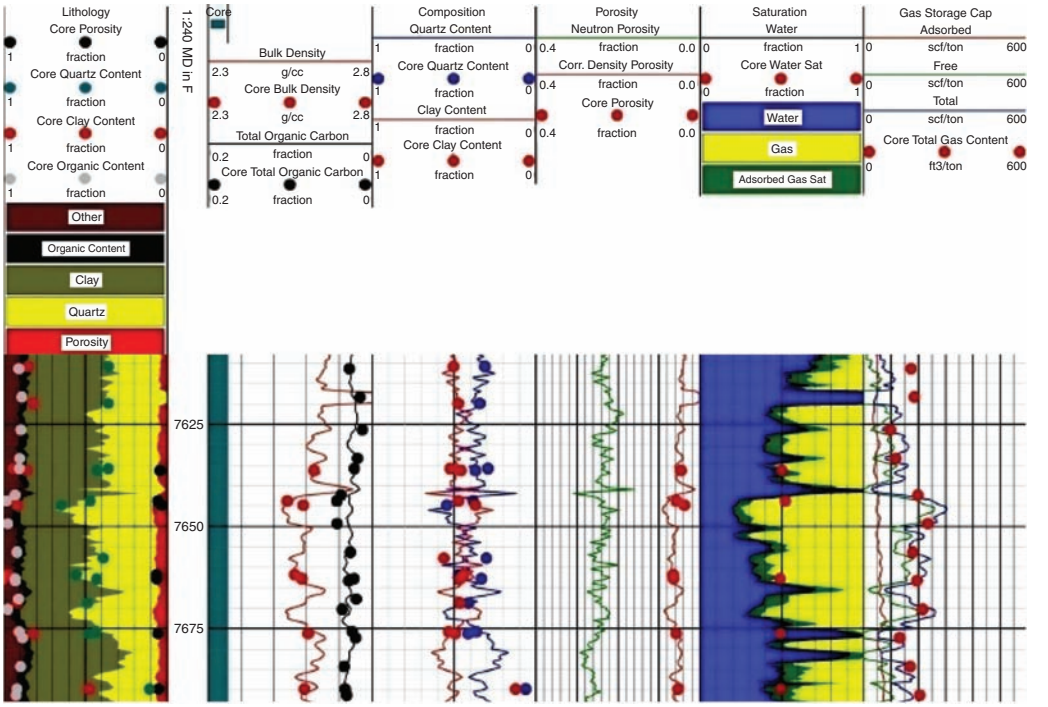


Fig. 30.36—Marcellus-core calibrated log interpretation (Ambrose et al. 2010). Courtesy of Weatherford.

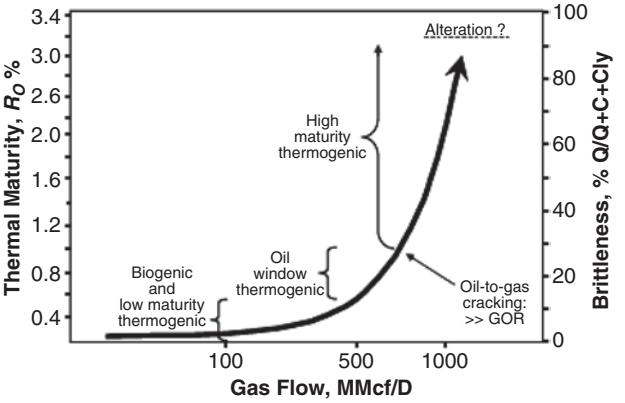


Fig. 30.37—Shale-gas well flow rate and source-rock organic richness.

the high-maturity end of the spectrum, where a rate of 1 MMcf/D can be expected, other things being equal.

Barnett-Type Well Production. **Fig. 30.38** maps an average production-decline curve using data from more than 1,000 Barnett horizontal shale-gas wells.

The decline curve shown in Fig. 30.38 is typical of a shale-gas well and follows a "stretched exponential" curve of the form:

$$q = q_0\, e\left(\frac{t}{\tau}\right)^n, \quad \ldots\ldots\ldots\

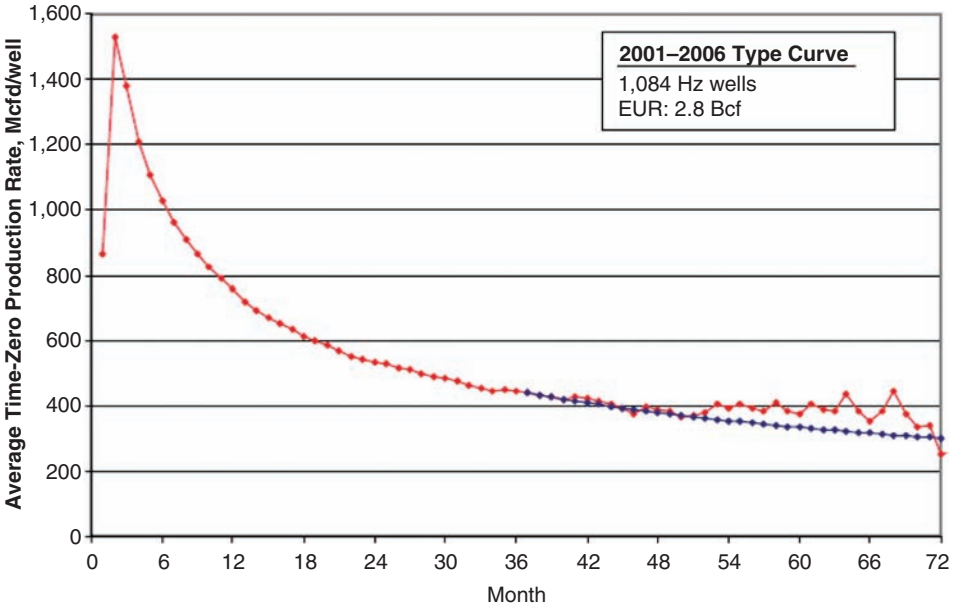


Fig. 30.38—Barnett-shale-type gas-well production profile. Courtesy of Advanced Resources International.

where:

q = flow rate at time t

q_0 = flow rate at time zero

τ = time constant

n = fitting exponent.

In the example shown, if t is in months, then by setting $\tau = 25$ and $n = 0.5$, an acceptable fit is obtained. Thus, estimates of future cumulative production can be made for shale-gas wells.

CBM Gas Production. Coalbed production is characterized by three stages, as illustrated in **Fig. 30.39.** During the early life of the well (Stage I), production is dominated by water. During Stage II, gas production increases as the mobile water is produced. As water saturation decreases, the relative permeability to gas increases. In Stage III, both gas- and water-production rates decline.

Tight-Gas-Sand Production. Tight gas sands are characterized by low porosity, very low permeability, high irreducible water saturation, and extremely low relative permeability to gas. One of the best sources for a detailed petrophysical analysis of the factors in play is available from Cluff and Byrnes (2010). They explain the origin of the so-called "permeability jail," where conditions of water saturation can occur such that both the relative permeability to gas, k_{rg}, and the relative permeability to water, k_{rw}, are so low that neither phase can flow.

30.5.2 Unconventional Gas Accounting. The estimation of GIP for conventional reservoirs is routinely performed by use of the following relationship:

$$GIP = \phi(1 - S_w) hA \times \left(\frac{1}{B_g}\right), \quad \ldots\ldots\ldots\

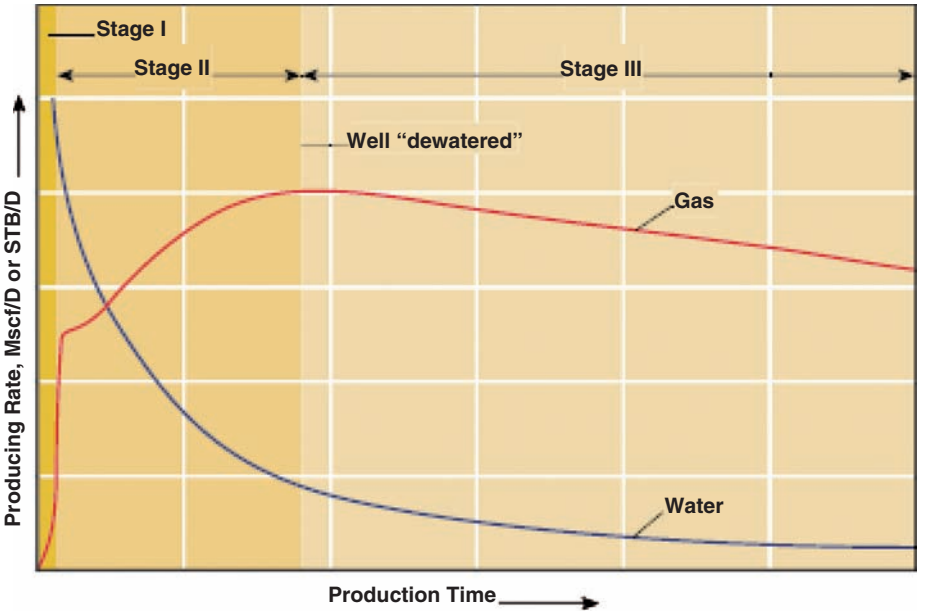


Fig. 30.39—CBM-type well production profile. Courtesy of Schlumberger.

h = net formation thickness
A = formation areal extent
$1/B_g$ = gas formation volume factor, which is turn in a function of the formation pressure and temperature and the supercompressibility factor Z of the gas in question.

If A is measured in acres and h in feet, the units of GIP will be acre-feet. Because there are 43,560 ft^2 in an acre, it follows that an acre-foot contains 43,560 ft^3. To convert to Bcf, this acre-feet value should be multiplied by 4.356×10^{-5}.

In a conventional reservoir, porosity is determined from well logs—for example, from a density log:

$$\phi = \frac{\rho_{ma} - \rho_b}{\rho_{ma} - \rho_{fl}}, \quad \ldots\ldots\ldots\

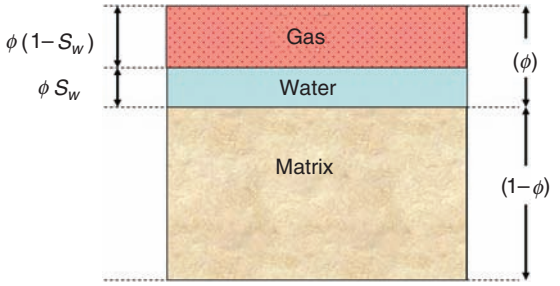


Fig. 30.40—Clean-formation model.

Note that a number of different geoscientific disciplines are involved in deriving the final value for GIP. The geologist and geophysicists will supply A. The reservoir engineer will supply $1/B_g$. The petrophysicist and the log analysts will supply ϕ, S_w, and h.

The actual gas reserves will depend on the proportion of the GIP that can be recovered economically. In conventional reservoirs, it is normal to achieve a potential recovery as high as 85% of the GIP. However, the actual recovery may also be dictated by economic factors; for example, a low gas price may lead to conditions in which further production operations are no longer economical.

It is useful to have a model of the formation to appreciate the differences between conventional and unconventional analysis for GIP. **Fig. 30.40** shows a conventional (clean) formation.

Unconventional reservoir models must account for the presence of organic matter as well as the actual gas-storage mechanism. This may include conventional "free" gas (contained in the pore space), "adsorbed" gas (held on the surfaces of the cleats in coal, for example), and "dissolved" gas (in the water in the pore space available). Furthermore, the simple derivation of a porosity from a density log becomes a more complicated exercise because of the added components.

GIP for Tight Gas Reservoirs. Tight gas sands are low-porosity, low-permeability formations. A typical porosity will be depth-dependent and will follow a relation such as:

$$\phi = 10^{-\left(\frac{Depth}{a}+b\right)}, \quad \ldots\ldots\ldots\

Permeability is the key to tight gas production. In general, it can be related back to irreducible water saturation. Typically, it can be estimated by a relationship of the form:

$$\log_{10} k = \frac{C - \log_{10} S_{wi}}{D}, \quad \ldots\ldots(30.17)$$

where:

k = permeability (md)
S_{wi} = irreducible water saturation (%)
C = lithology factor (close to 1.18)
D = regional factor (close to 0.187).

For example, with $S_{wi} = 52.5\%$, k computes as 0.00129 md, or 1.29 microdarcies. At a water saturation of 52.5% in a microdarcy rock, the relative permeability to gas (k_{rg}) is on the order of 10%, meaning that the permeability to gas (k_g) is approximately 0.1 microdarcy.

Once ϕ, S_w, and k_g have been assessed, then standard log analysis may be used for GIP calculations, but completion for gas production will be heavily dependent on considerations of permeability and relative permeability to gas, as documented by Cluff and Byrnes (2010).

GIP for Shale-Gas Reservoirs. In shale-gas reservoirs, the presence of organic material must be accounted for. An appropriate model for such a formation is shown in **Fig. 30.41.**

For example, the response of the density tool is given by:

$$\rho_b = \rho_{ma}\left(1 - V_{TOC}\right) + \rho_{TOC} V_{TOC} + \rho_{fl}\phi, \quad \ldots\ldots(30.18)$$

where

ρ_{ma} = formation inorganic matrix density
ρ_{gr} = grain density of solid organic + inorganic material
ρ_b = formation bulk density (read from the density log)
ρ_{fl} = density of the fluid in the pore space
ρ_{TOC} = density of the organic material
V_{TOC} = volume fraction of organic material.

The solution for porosity is:

$$\phi = \frac{\left(\rho_{ma} - \rho_b\right) - V_{TOC}\left(\rho_{ma} - \rho_{TOC}\right)}{\left(\rho_{ma} - \rho_{fl}\right)} \quad \ldots\ldots(30.19)$$

It is also possible to derive expressions for V_{TOC} and for ρ_{gr}:

$$V_{TOC} = \frac{\rho_{ma} - \rho_{gr}}{\rho_{ma} - \rho_{TOC}}, \quad \ldots\ldots(30.20)$$

$$\rho_{gr} = \frac{\rho_b - \rho_{fl}\,\phi}{\left(1 - \phi\right)} \quad \ldots\ldots(30.21)$$

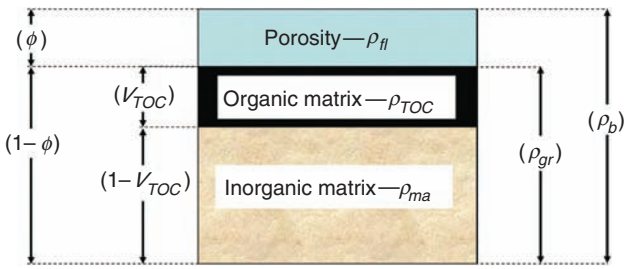


Fig. 30.41—Formation model for shale gas.

GIP for CBM. GIP can be calculated for a coal using the following relationship:

$$GIP = 1.464 \times 10^{-6}\, h \rho V, \quad \ldots\ldots\ldots\

From a knowledge of the elastic constants for the formation of interest (as derived from sonic and density logs), it is then possible to calculate what horizontal stress will be needed to induce a vertical fracture. A number of commercial software packages are available to compute formation mechanical properties and predict the fracture pressures that may be needed for specific formations at specific depths. An example of the output of such an analysis is given in Fig. 16.27 (see Chapter 16).

Once Poisson's ratio μ and the bulk compressibility K_B are known, the fracture-closure pressure (FCP) can be estimated. This is the pressure required to hold open and extend a hydraulic fracture in any given zone. The FCP is calculated as:

$$FCP = \alpha P_p + \left[\mu/(1-\mu)\right] \times \left(P_o - \alpha P_p\right), \quad (30.25)$$

where:

$$\alpha = 1 - \left(C_{ma}/C_B\right). \quad (30.26)$$

and

P_p is the pore pressure,
P_o is the overburden (lithostatic) pressure, and
C_{ma} is the compressibility of the matrix with zero porosity.

These parameters will vary from well to well and from depth to depth. Typically, P_p will be in the range of 0.43 to 0.45 psi/ft, P_o from 1.0 to 1.1 psi/ft, and C_{ma} close to 8×10^{-6} psi^{-1}. A comparison of FCP in the zone of interest with the values of FCP above and below may give indications of the vertical extent that may be expected for a given fracture treatment.

30.6.1 Unconventional-Reservoir Completions. Unconventional reservoirs are uneconomical without stimulation. This normally takes the form of fracture stimulation. For the fracturing to be successful, the target formation must be brittle. If it is ductile, then it will not be possible to maintain a flow path for gas from the formation to the wellbore. Designing where and how to fracture a formation therefore requires knowledge of formation brittleness.

Prospective unconventional gas-shale reservoirs in fact have low clay content (less than 40%) and should be described as "shilts or shands" (Britt and Schoeffler 2009). One way to gauge brittleness is by combining Young's modulus and Poisson's ratio into a single "brittleness coefficient." **Fig. 30.42** shows a crossplot of E and μ that illustrates the concept that the points for more-ductile shale will fall to the upper right and those for more-brittle shale to the lower left. The "brittleness coefficient" can be quantified by the equation:

$$\text{Brittleness Coefficient} = 50 \times \left[\left(\frac{E-1}{7}\right) + \left(\frac{0.4-\mu}{0.25}\right)\right]. \quad (30.27)$$

This coefficient may be computed on a continuous foot-by-foot basis from well logs (density and sonic ΔT_c and ΔT_s) and used to choose the intervals to be fractured, taking into consideration that the more-ductile shales will form needed fracture barriers. In the plot shown in Fig. 30.42, two-color coding has been used to indicate the most-brittle shales in red and the most-ductile in green.

An example of the geomechanical portion of a petrophysical analysis that shows mineralogy, shale classification, brittleness closure stress, fracture barriers, fracture width, Poisson's ratio, and Young's modulus is shown in **Fig. 30.43.** On the basis of the plot, it can be seen that Zones B, D, and G are the best candidates for a fracture with low closure stress and acceptable fracture width. The calculation of fracture width depends on the pumping rate and the viscosity of the fluid used.

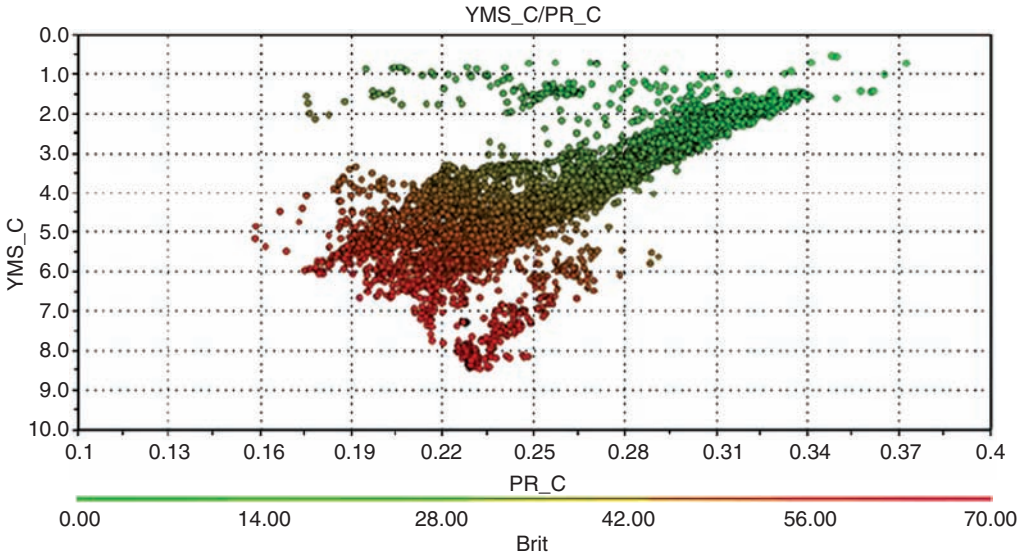


Fig. 30.42—Young's modulus and Poisson's ratio crossplot for brittleness (Rickman et al. 2008). Courtesy of Halliburton.

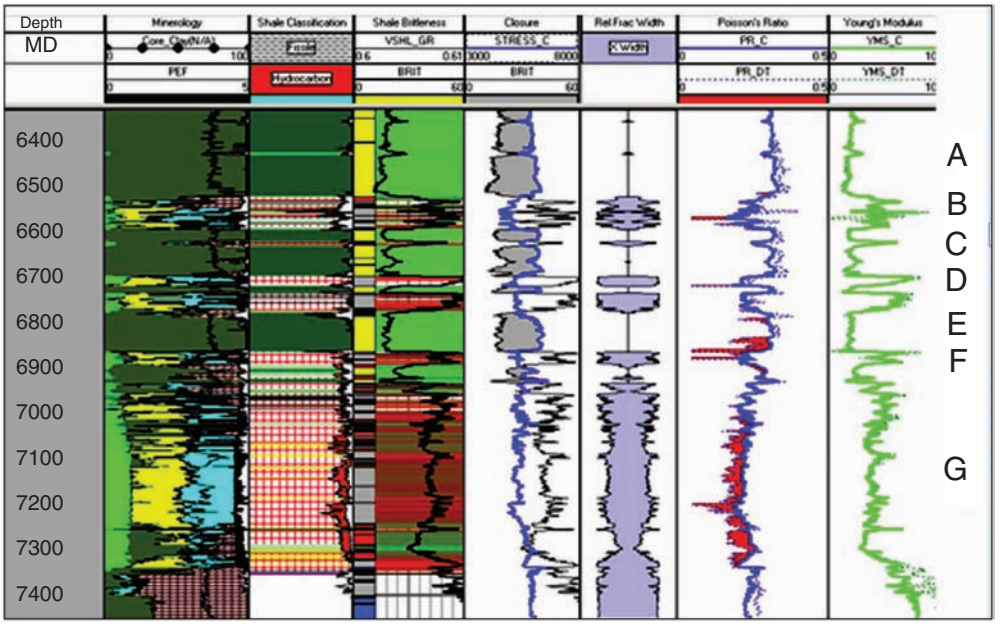


Fig. 30.43—Geomechanics deduced from petrophysical logging data (Rickman et al. 2008). Courtesy of Halliburton.

30.6.2 Fracture Monitoring. There are two ways to monitor fracturing. The first is applicable in real time and requires a conveniently close observation well (or wells) equipped with directional geophones to record microseismic events associated with the fracturing process. **Fig. 30.44** illustrates a pseudo-3D display of microseismic events recorded during a multistage fracture job.

The second method requires the use of radioactive tracers that are used to "dope" the solids and fluids used in the fracturing. By choosing different radioisotopes for the preflush, the proppant, and the fracturing fluid itself, the efficiency and effectiveness of the operation can be monitored

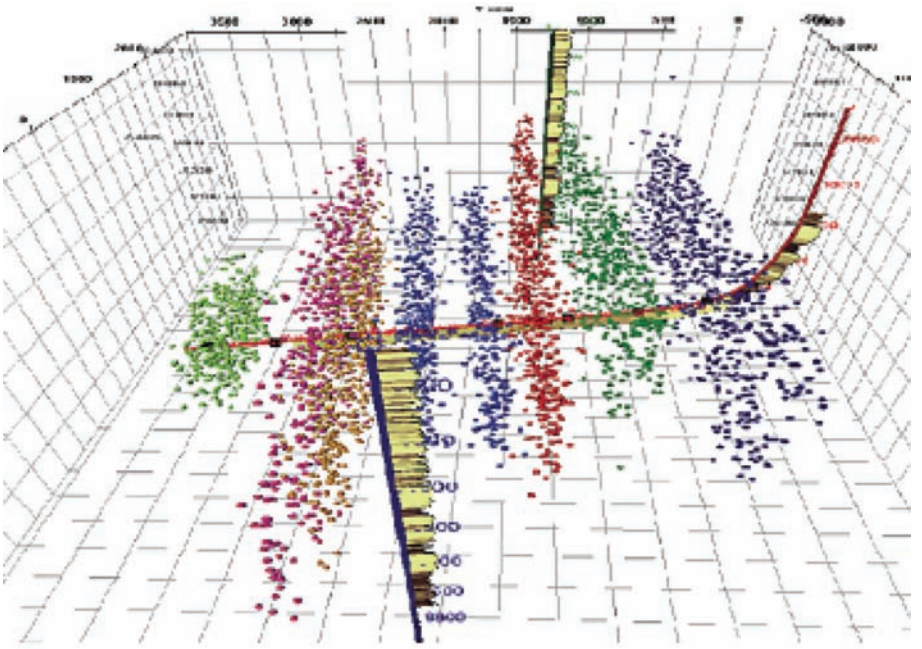


Fig. 30.44—Microseismic monitoring of staged fracturing job.

by running a post-frac spectral gamma ray log in the wellbore. Because the relative proportions of uranium, thorium, and potassium are different in the fluids and in the proppant, it is possible to "see" where the fracturing fluids and the proppant entered (or did not enter) the formation. A typical tracer-log presentation is shown in **Fig. 30.45.**

30.7 Unconventional Well Construction

Almost without exception, unconventional reservoirs are developed by use of directional wells. A first well in a prospective field may be drilled vertically and assessed by coring and logging to measure the geomechanical and geochemical properties, which if favorable, delineate the "sweet spot." Thereafter, the field is developed by means of horizontal wells through the "sweet spot." Such wells not only are aimed to remain in the "sweet spot" for the longest possible interval, but also are oriented with respect to the stress field inherent in any anisotropic formation.

Reservoir contact for a typical 8½-in. borehole increases significantly when hydraulic fracturing is used. When combined with horizontal drilling, the growth in reservoir contact is exponential, as shown in **Fig. 30.46.**

Depending on the horizontal well section orientation with respect to the minimum and maximum stress, the fractures will propagate either transversely or longitudinally **(Fig. 30.47).**

Determination of the far-field stress directions is therefore a key factor in well design and completion. As already seen in Section 7, formation stress and other formation geomechanical properties can be deduced from well logs, particularly when dipole sonic tools are used. If the sonic logging tool is equipped with crossed dipole sources and receivers and an orientation package, then it is possible to deduce the direction of the major and minor formation stresses and also the degree of anisotropy that the prospective formation may have.

30.7.1 Fractures and Complexity. The objective of both well placement and fracture stimulation is to expose the maximum possible area of the target formation to a flow path to the wellbore. The more interconnection or complexity that can be generated, the better the flow will be. Looking at either a horizontal (plan) view **(Fig. 30.48—left)** or a vertical section (elevation) view (Fig. 30.48—right) gives an idea of the complexity involved.

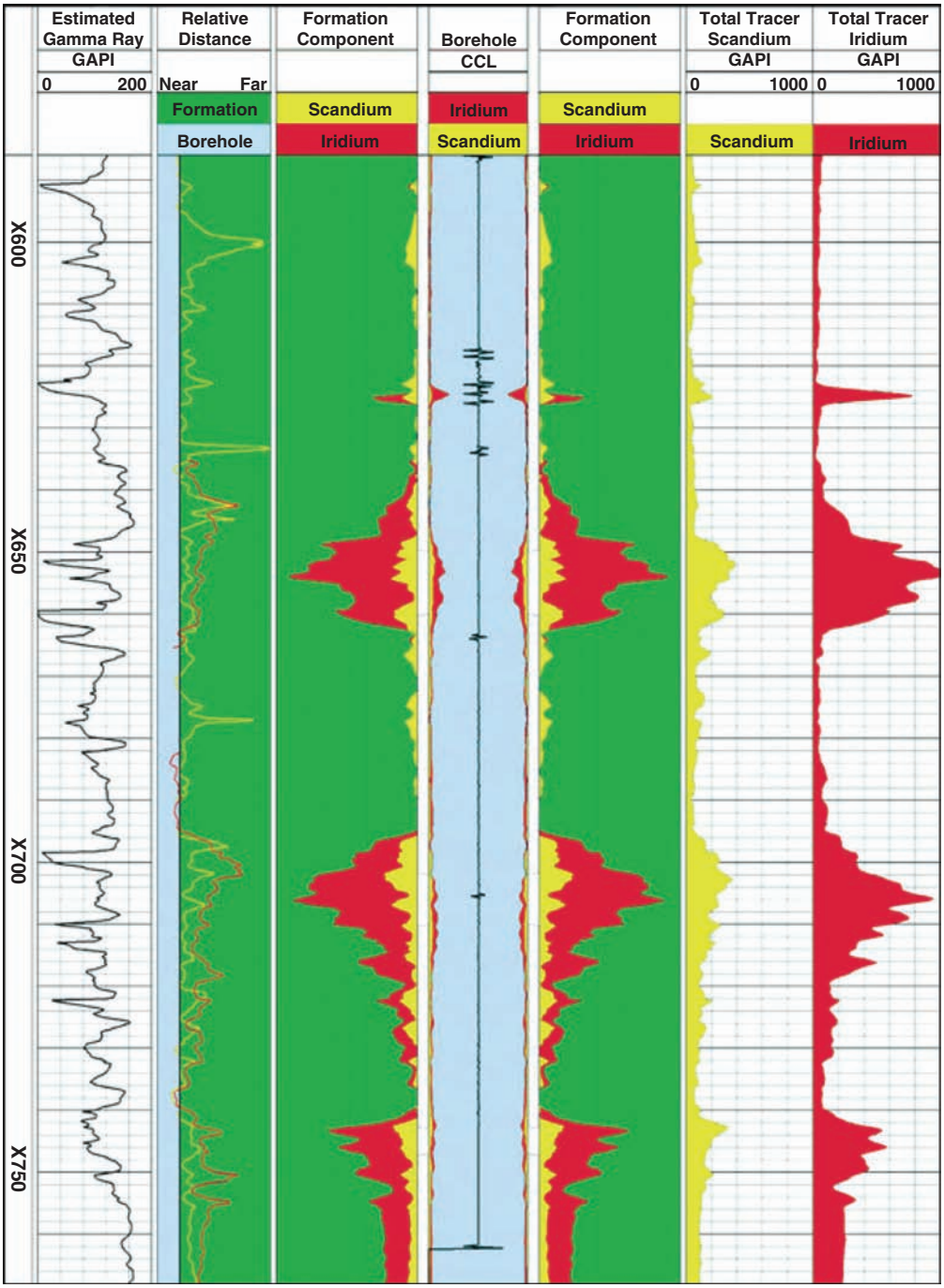


Fig. 30.45—Radioactive tracers used to monitor proppant placement.

Complexity is controlled by:

- Heterogeneity—(bedding planes and fractures)
- Misalignment between fracture strike and maximum horizontal stress
- Stress similarity of horizontal stresses

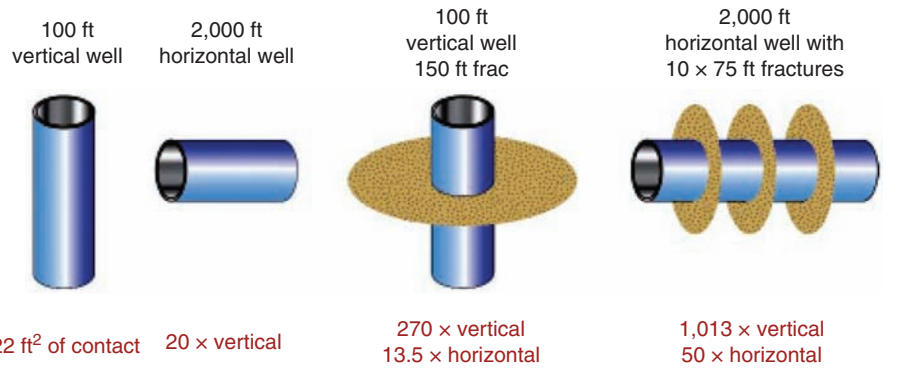


Fig. 30.46—Contact area in vertical, horizontal, and fractured wells. Courtesy of Schlumberger.

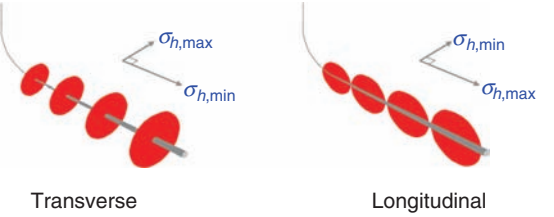


Fig. 30.47—Fracture-propagation orientation and in-situ formation stresses. Courtesy of Schlumberger.

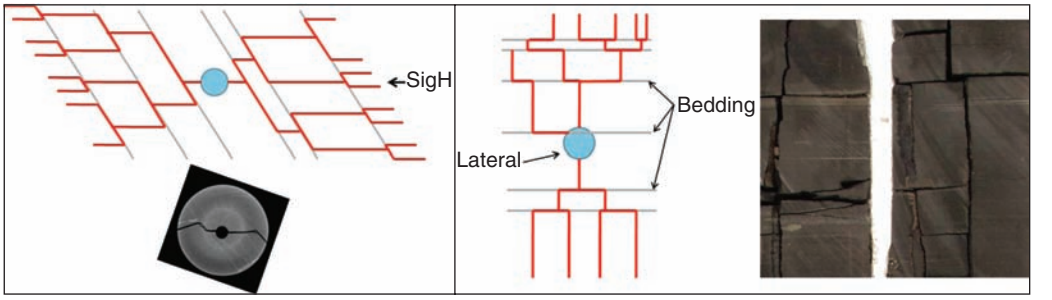


Fig. 30.48—Fracture complexity (seen horizontally on left, vertically on right). Courtesy of Tom Bratton.

Complexity is confirmed by

- Images, acoustics, and outcrop rock mechanics
- Laboratory and field experiments
- Observations described using rock-physics models

This can be appreciated even better by a view of layered and fragmented formations as seen in visible light and by a formation micro-imaging tool, as shown in **Fig. 30.49.** It should be noted that the horizontal fractures are more "continuous," but the vertical fractures, if connected through the silty zones by artificial stimulation, would greatly increase the drainage to a horizontal borehole.



Fig. 30.49—Fracture complexity (wireline formation micro-imager and outcrop). Courtesy of Tom Bratton.

30.7.2 Anisotropy.

An isotropic formation has the same elastic properties in all three directions (one vertical and two horizontal) and is labeled **ISO** in **Fig. 30.50.**

A transverse isotropic formation has the same elastic properties in two directions, either horizontally (labeled **HTI**) or vertically (labeled **VTI**).

An orthotropic formation has different elastic constants in all three directions (labeled **ORT**).

Formation anisotropy can occur in three distinct ways, which are detailed in Fig. 30.50.

These cases can be distinguished by use of the shear slowness in the *x*- and *y*- direction coupled with the shear from a Stoneley-wave recording. In the isotropic case, all three will read the same. In the transverse isotropic cases, at least two will read the same. In orthotropic formations, all three will read differently (**Fig. 30.51**).

An example from the Upper Barnett shale play showing multiple layers and no natural fracturing is given in **Fig. 30.52.**

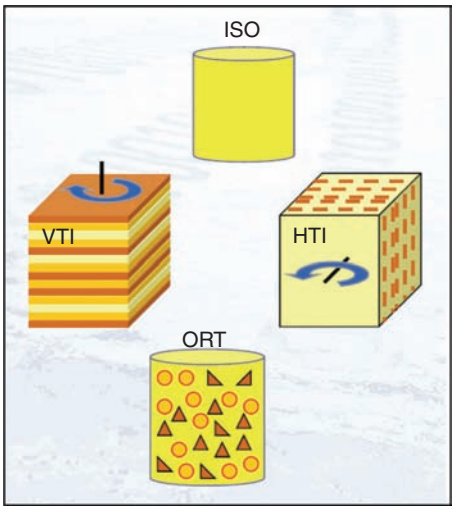


Fig. 30.50—Three types of anisotropy. Courtesy of Tom Bratton.

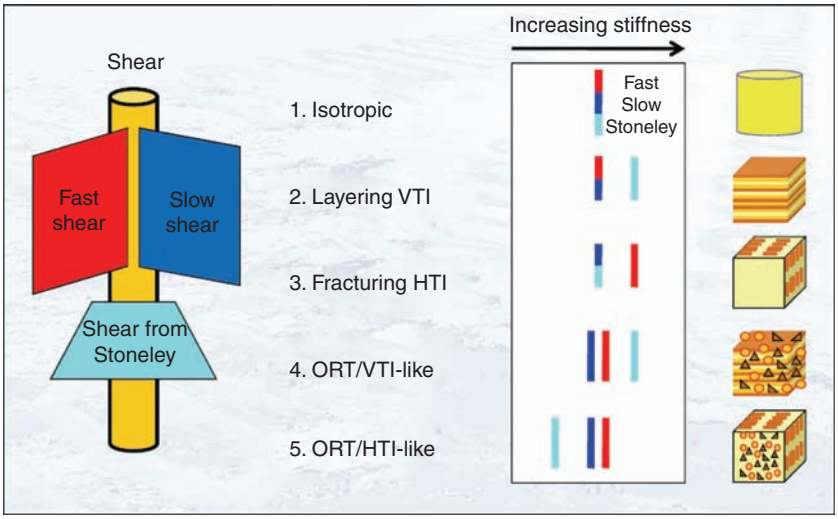


Fig. 30.51—Formation anisotropy from shear-slowness measurements. Courtesy of Tom Bratton.

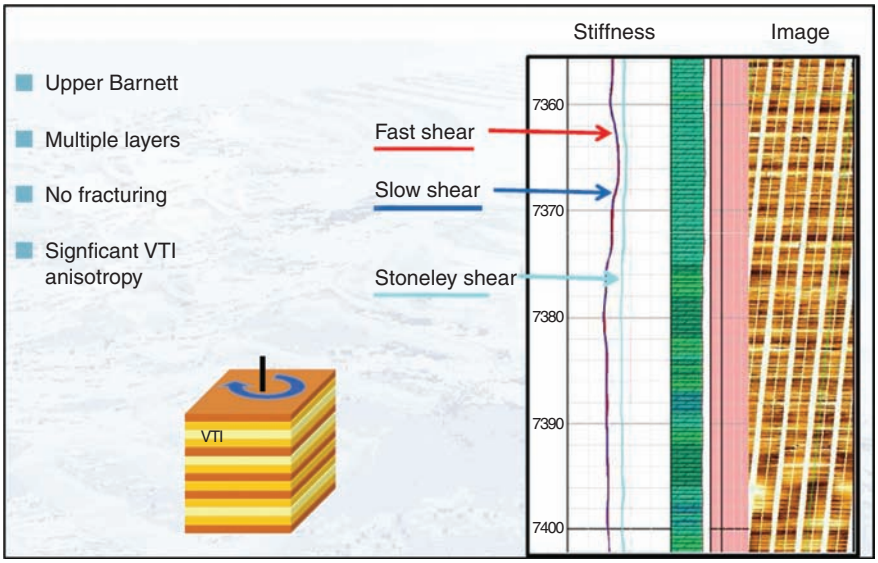


Fig. 30.52—Transverse isotropy in the Upper Barnett shale. Courtesy of Tom Bratton.

A further example **(Fig. 30.53)** from the Lower Barnett shows multiple vertical fracturing superimposed on structural anisotropy, although the central zone (indicated by the arrow) has every indication of being isotropic, with all three slowness indicators reading the same.

The log display shown in **Fig. 30.54** shows zones with transverse vertical anisotropy in the upper and lower sections and a zone of fractured horizontal anisotropy in the central zone.

30.7.3 Coalbed Cavity Completion. In the San Juan and Bowen (Australia) basins, it is common practice to complete CBM wells with a "mined" cavity. It takes from 1 to 3 weeks to complete the installation, which entails flushing out an annular cavity, as shown in **Fig. 30.55.**

In the Powder River basin, for example, it is common to use openhole or "barefoot" completions, as illustrated in **Fig. 30.56.** The well is cased down to the top of the coal seam to be produced,

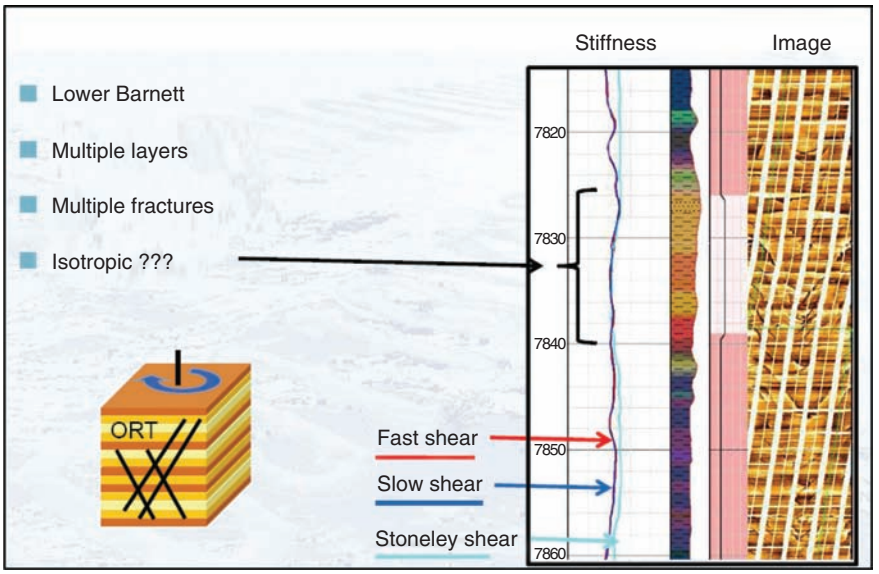


Fig. 30.53—Transverse isotropy in the Lower Barnett shale. Courtesy of Tom Bratton.

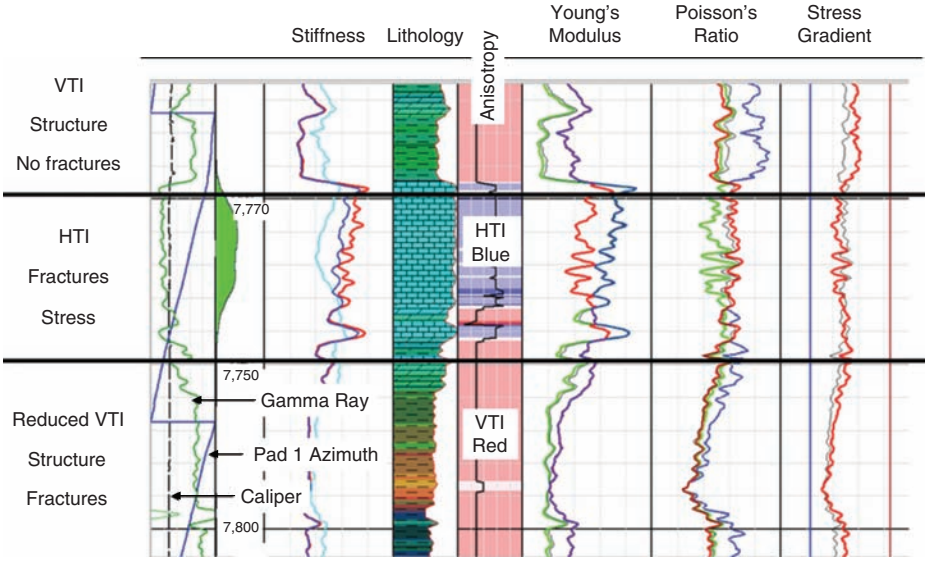


Fig. 30.54—Log display indicating central HTI fractured zone. Courtesy of Tom Bratton.

but the coal section is left open. An electric submersible pump sends the water produced up the tubing for disposal or further use, depending on water quality. Gas is then free to produce up the tubing/casing annulus.

Fig. 30.57 shows alternative multizone approaches.

30.7.4 Horizontal CBM Completions. Horizontal completions in CBM wells commonly have laterals up to 6,000 ft long. Such completions are indicated where the target coalbeds are thin or the coal has low permeability. Such completions have better success where the coals are dry and "stiff" and less likely to wash out or have wellbore-stability problems.

The improvement in production that can be expected from a horizontal well vs. the production from the same coal seam in a vertical well can be judged from the plot shown in **Fig. 30.58.** This

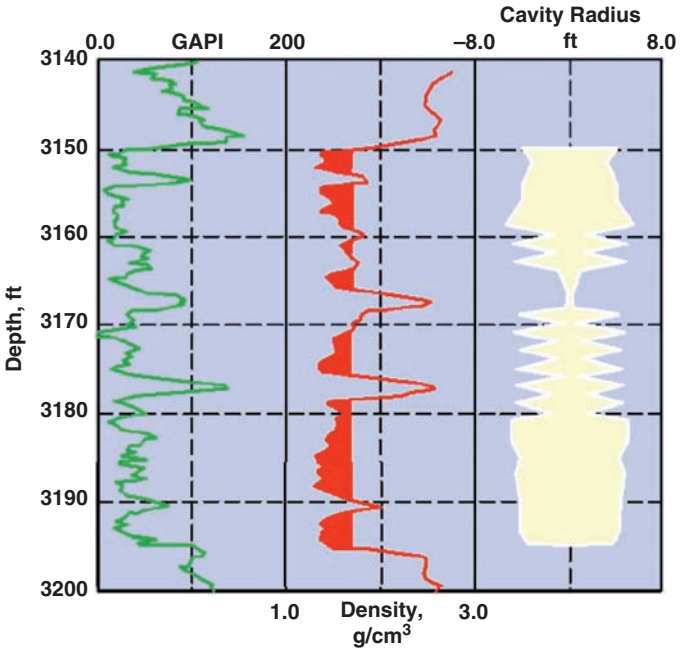


Fig. 30.55—Cavity completion for CBM well. Courtesy of MHA Petroleum Consultants.

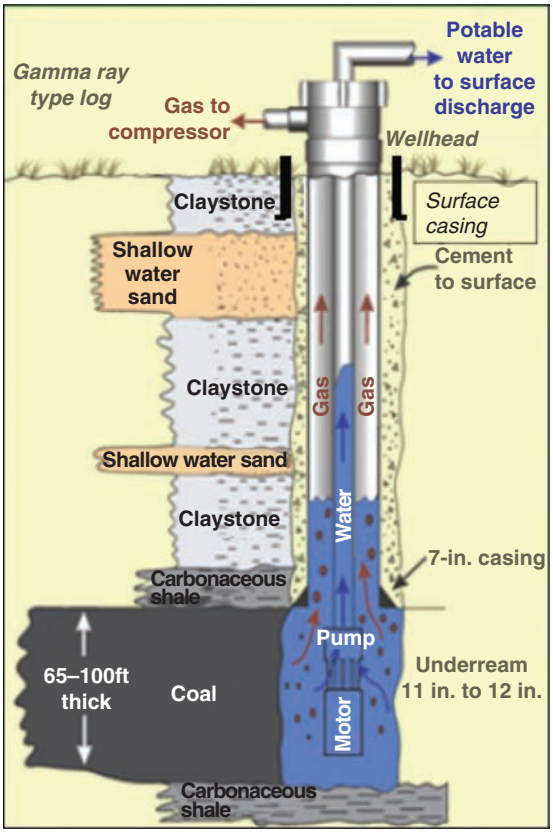


Fig. 30.56—CBM openhole completion. Courtesy of Barrett Resources.

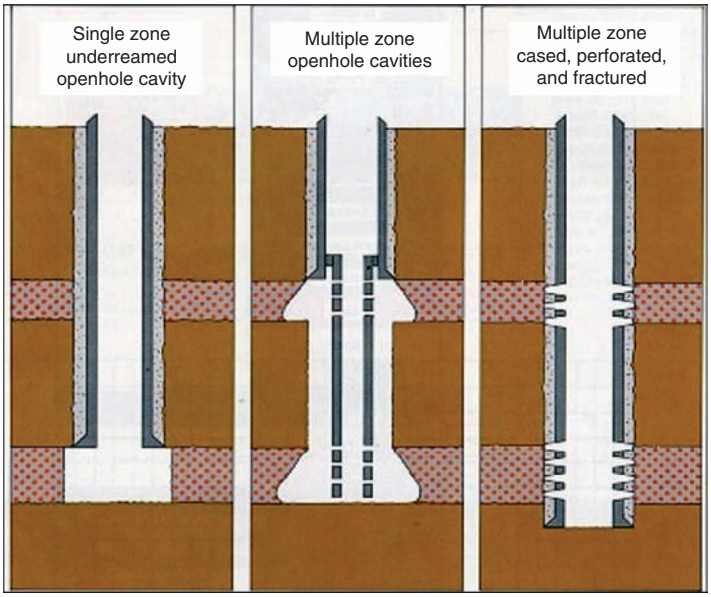


Fig. 30.57—Multizone variants for barefoot CBM completions.

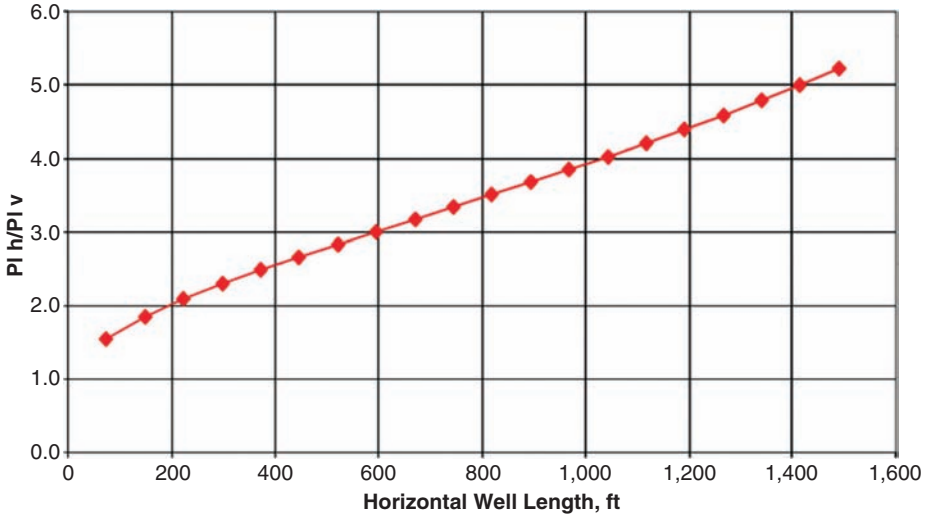


Fig. 30.58—Productivity improvement as a function of horizontal-well length. Courtesy of MHA Petroleum Consultants.

plot was constructed for a given set of conditions (bed thickness of 5 ft, drainage area of 160 acres, wellbore radius of 0.2 ft, vertical well skin = −2) and is based on a productivity- improvement factor (PIF) that can be approximated by the following equation:

$$PIF = \frac{L}{h}\sqrt{\frac{k_v}{k_h}}, \quad \ldots\ldots\ldots\

Acknowledgments

The author would like to acknowledge kind assistance from the Department of Earth & Environmental Sciences, University of Kentucky; the Bureau of Economic Geology, Jackson School of Geosciences, The University of Texas at Austin; Alfred Lacazette, Mike Walker, and Mike Dixon (Weatherford); D. Jarvie (Worldwide Geochemistry); Roger Sassen (Texas A&M University); Gigi Zhang (Baker Hughes); and Michael J. Manning (Samson).

References

Ambrose, R.J., Hartman, R.C., Diaz-Campos, M., et al. 2010. New Pore-Scale Consideration for Shale Gas in Place Calculations. Paper SPE 131772 presented at the SPE Unconventional Gas Conference, Pittsburgh, Pennsylvania, USA, 23–25 February. http://dx.doi.org/10.2118/131772-MS.

Cluff, R.M. and Byrnes, A.P. 2010. Relative Permeability in Tight Gas Sandstone Reservoirs: The "Permeability Jail" Model. Presented at the SPWLA 51st Annual Logging Symposium, Perth, Australia, 19–23 June.

Cubitt, J.H., England, W.A., and Larter, S. 2004. *Understanding Petroleum Reservoirs: Towards an Integrated Reservoir Engineering and Geochemical Approach*, Vol. 237, 1–5. London: Special Publications, The Geological Society.

Haworth, J., Sellens, M., and Whittaker, A. 1985. Interpretation of Hydrocarbon Shows Using Light (C1-C5) Hydrocarbon Gases From Mud-Log Data. *AAPG Bulletin* **69** (8): 1305–1310.

Hunt, J.M. 1996. *Petroleum Geochemistry and Geology*, second edition. New York: W.H. Freeman and Co.

Jarvie, D.M. 1991. Total Organic Carbon (TOC) Analysis. In *Treatise of Petroleum Geology: Handbook of Petroleum Geology: Source and Migration Processes and Evaluation Techniques*, ed. R.K. Merrill, 113–118. Tulsa: American Association of Petroleum Geologists.

Lake, L.W. 2006. *Petroleum Engineering Handbook*. Richardson, Texas: SPE.

Oil & Gas J. (May 2003).

Passey, Q.R., Creaney, S., Kulla, J.B., et al. 1990. A Practical Model for Organic Richness from Porosity and Resistivity Logs. *AAPG Bulletin* **74** (12): 1777–1794.

Pemper, R., Sommer, A., Guo, P. et al. 2006. A New Pulsed Neutron Sonde for Derivation of Formation Lithology and Mineralogy. Paper SPE 102770 presented at the SPE Annual Technical Conference and Exhibition, 24-27 September, San Antonio, Texas, USA. http://dx.doi.org/10.2118/102770-MS.

Peters, K.E. and Cassa, M.R. 1994. Applied Source Rock Geochemistry. In *The Petroleum System—From Source to Trap*, ed. L.B. Magoon and W.G. Dow, Memoir 60, 93–117. Tulsa: American Association of Petroleum Geologists.

Peters, K. E. and Moldowan, J. M. 1993. *The Biomarker Guide: Interpreting Molecular Fossils in Petroleum and Ancient Sediments*. Englewood Cliffs, New Jersey: Prentice Hall.

Pollastro, R.M., Hill, R.J., Jarvie, D.M. et al. 2003. Assessing Undiscovered Resources of the Barnett-Paleozoic Total Petroleum System, Bend Arch–Fort Worth Basin Province, Texas. Online adaptation of presentation at AAPG Southwest Section Meeting, Fort Worth, Texas, USA, 1–4 March.

Rickman, R., Mullen, M., Petre, E. et al. 2008. A Practical Use of Shale Petrophysics for Stimulation Design Optimization: All Shale Plays Are Not Clones of the Barnett Shale. Paper SPE 115258 presented at the SPE Annual Technical Conference and Exhibition, Denver, 21–24 September. http://dx.doi.org/10.2118/115258-MS.

Shehata, A., Aly, A., and Ramsey, L. 2010. Overview of Tight Gas Field Development in the Middle East and North Africa Region. Paper SPE 126181 presented at the North Africa Technical Conference and Exhibition, Cairo, Egypt, 14–17 February. http://dx.doi.org/10.2118/126181-MS.

General References

AAPG Bulletin **91** (4).

American Society for Testing and Materials. 1979. Annual Book of Standards, Part 26, Gaseous Fuels; Coal and Coke; Atmospheric Analysis. Philadelphia, Pennsylvania: American Society for Testing and Materials.

API. 1988. *RP40, Recommended Practices for Core Analysis*, second edition, Washington, DC: API.

Amott, E. 1959. Observations Relating to the Wettability of Porous Rock. *Trans.,* AIME **219:** 156–162.

Bobek, J.E., Mattax, C.C., and Denekas, M.O. 1958. Reservoir Rock Wettability: Its Significance and Evaluation. *Trans.,* AIME **213:** 155–160.

Britt, L.K. and Schoeffler, J. 2009. The Geomechanics of a Shale Play: What Makes a Shale Prospective. Paper SPE 125525 presented at the SPE Eastern Regional Meeting, Charleston, West Virginia, USA, 23–25 September. http://dx.doi.org/10.2118/125525-MS.

Carpenter, A.M. 1988. *Coal Classification*. London: IEA Coal Research.

Cluff, S.G. and Cluff, R.M. 2004. Petrophysics of the Lance Sandstone Reservoirs in Jonah Field, Sublette County, Wyoming. *In Jonah Field: Case Study of a Tight-Gas Fluvial Reservoir,* ed. J.W. Robinson and K.W. Shanley, No. 52, 215–241. Tulsa, Oklahoma: Studies in Geology AAPG.

Cumella, S. and Scheevel, J. 2008. The Influence of Stratigraphy and Rock Mechanics on Mesaverde Gas Distribution, Piceance Basin, Colorado. *In Understanding, Exploring, and Developing Tight-Gas Sands: 2005 Vail Hedberg Conference,* ed. S.P. Cumella, K.W. Shanley, and W.K. Camp, first edition, 137–155. Tulsa, Oklahoma: Hedberg Series 3, AAPG.

Decker, A.D., Hill, D.G. and Wicks, D.E., 1993. Log-Based Gas Content and Resource Estimates for the Antrim Shale, Michigan Basin. Paper SPE 25910 presented at the Low Permeability Reservoirs Symposium, Denver, 26–28 April. http://dx.doi.org/10.2118/25910-MS.

Dupuy, M., Morineau, Y., and Simandoux, P. 1966. About the Importance of Small-Scale Heterogeneities on Fluid Flow in Porous Media. Paper presented at the 58th Annual AIChE Meeting, Dallas, 7–10 February.

Fatt, I. and Davis, D.H. 1952. Reduction in Permeability With Overburden Pressure. SPE- 952329-G. *Trans.*, AIME **195:** 329.

Geffen, T.M., Owens, W.W., Parrish, D.R., and Morse, R.A. 1951. Experimental Investigation of Factors Affecting Laboratory Relative Permeability Measurements. *Trans.,* AIME **192:** 99–110.

Hall, H.N. 1953. Compressibility of Reservoir Rocks. *Trans.,* AIME **198:** 309–311.

Harris, N.B., Ko, T.-W., Philp, R. et al. 2009. Natural Gas Compositions From Large Tight Gas-Sand Fields in the Rocky Mountains: A Clue to How These Reservoirs Fill. *Trans.,* Gulf Coast Association of Geological Societies **59:** 347–350.

Hartman, C., Bhatta, N., and Lasswell, P. 2008. Recent Advances in the Analytical Methods used for Shale Gas Reservoirs Gas-in-Place Assessment. AAPG 2008 Annual Convention and Exhibition, 23 April 2008.

Holditch, S.A. 2006. Tight Gas Sands. *J. Pet Tech* **58** (6): 86–93. http://dx.doi.org/10.2118/103356-MS.

Hood, A., Gutjahr, C.M., and Heacock, R.L. 1975. Organic Metamorphism and the Generation of Petroleum. *AAPG Bulletin* **59** (6): 986–996.

Hyland, C.R. 1983. Pressure Coring: An Oilfield Tool. Paper SPE 12093 presented at the SPE Annual Technical Conference and Exhibition, San Francisco, 5–8 October. http://dx.doi.org/10.2118/12093-MS.

International Committee for Coal Petrology. 1963. *Handbook of Coal Petrography*, second edition. Paris: Centre National de la Recherche Scientifique.

Jones, F.O. Jr. 1964. Influence of Chemical Composition of Water on Clay Blocking of Permeability. *J. Pet Tech* **16** (4): 441–446. http://dx.doi.org/10.2118/631-PA.

Jaeger, J. and Cook, N.G. 2007. *Fundamentals of Rock Mechanics*. Oxford, UK: Blackwell Publishing.

Jensen, J., Clarkson, C.R., and Blasingame, T.A. 2011. Reservoir Engineering for Unconventional Gas Reservoirs: What Do We Have to Consider? Paper SPE 145080 presented at the SPE North American Unconventional Gas Conference and Exhibition, The Woodlands, Texas, USA, 14–16 June.

Keelan, D.K. 1982. Core Analysis for Aid in Reservoir Description. *J. Pet Tech* **34** (11): 2483–2491. http://dx.doi.org/10.2118/10011-PA.

Kieke, E.M. and Hartmann, D.J. 1973. Scanning Electron Microscope Application to Formation Evaluation. *Trans.,* Gulf Coast Association of Geological Societies, Vol. 23.

Klinkenberg, L.J. 1941. The Permeability of Porous Media to Liquids and Gases. *API Drilling and Production Practice*. American Petroleum Institute, 200–213.

Maness, M. 1979. Well Formation Characterization by Residual Hydrocarbon Analysis. *J. Pet Tech* **31** (1): 118–120. http://dx.doi.org/10.2118/6860-PA.

Mullins, O.C. 2008. *The Physics of Reservoir Fluids*. Schlumberger.

Pittman, E.D. and Thomas, J.B. 1979. Some Applications of Scanning Electron Microscopy to the Study of Reservoir Rock. *J. Pet Tech* **31** (11): 1375–1380. http://dx.doi.org/10.2118/7550-PA.

Schapiro, N. and Gray, R.J. 1960. Petrographic Classification Applicable to Coals of All Ranks. *Proc.,* 68th Illinois Mining Institute, 83–97.

Shelley, R.F. and Soliman, M.Y. 2010. Evaluating the Effects of Well-Type Selection and Hydraulic-Fracture Design on Recovery for Various Reservoir Permeabilities Using a Numeric Reservoir Simulator. Paper SPE 130108 presented at the SPE Europec/EAGE Annual Conference and Exhibition, Barcelona, Spain, 14–17 June. http://dx.doi.org/10.2118/130108-MS.

Shanley, K.W., Cluff, R.M., and Robinson, J.W. 2007. Prolific Gas Production from Low-Permeability Sandstone Reservoirs, Part II: Reconciling Basin History, Fluid Saturations, Gas Shows, and Capillary Pressure. Oral presentation given at the AAPG Annual Convention on Searching for Success, Long Beach, California, USA, 1–4 April.

Shanley, K.W., Cluff, R.M., and Robinson, J.W. 2004. Factors Controlling Prolific Gas Production From Low-Permeability Sandstone Reservoirs: Implications for Resource Assessment, Prospect Development, and Risk Analysis. *AAPG Bulletin* **88** (8): 1083–1121.

Stopes, M.C. 1935. On the Petrology of Banded Bituminous Coal. *Fuel* **14** (1): 4–13.

Lake, L.W. 2006. *Petroleum Engineering Handbook*. Richardson, Texas: SPE.

Stewart, C.R., and Spurlock, J.W. 1952. Analysis of Large Core Samples. *Oil & Gas J.* **51** (17 September): 4–13.

Talabi, O., Alsayari, S., Blunt, M.J. et al. 2008. Predictive Pore-Scale Modeling: From Three-Dimensional Images to Multiphase Flow Simulations. Paper SPE 115535 presented at the SPE Annual Technical Conference and Exhibition, Denver, 21–24 September. http://dx.doi.org/10.2118/115535-MS.

Welton, J.E. 1984. *SEM Petrology Atlas*. Tulsa: AAPG.

Wyllie, M.R.J., Gregory, A.R., and Gardner, G.H.F. 1958. An Experimental Investigation of Factors Affecting Elastic Wave Velocities in Porous Media. *Geophysics* **23** (3): 459–493.

Appendix 30.1—Macerals

- Type I—Liptinite (Exinite) Maceral Group
  - Waxy, lipid-rich, and resinous parts of plants
  - Ultraviolet (UV) fluorescence strong yellow or green
  - Reflectance low
- Type II—Liptinite (Exinite) Maceral Group
  - Green and blue-green algae, common in anoxic shales where vitrinite is very rare
- Type III—Vitrinite Maceral Group
  - UV fluorescence, none or poor
  - Reflectance moderate
  - The most common maceral (organic component in most humic coals)
  - A common constituent of organic source rocks
  - Remains of cell lumens (cell walls); woody tissues of stems, branches, leaves, and roots of plants; and the precipitated gels from these materials
- Type IV—Inertinite Maceral Group
  - UV fluorescence, none
  - Reflectance very high
  - Peats that were oxidized early in their formation
  - Bark, stems, leaves, and roots

Appendix 30.2

TABLE A-1—LARGEST TIGHT GAS FIELDS IN THE MIDDLE EAST AND NORTH AFRICA

Country	Field Name	Location of Field	Geologic Age	Type of Formation	Reservoir Properties		Applied Technology
					(Φ, %)	(K, md)	
Oman	Huge khazzan and makarem gas field	Central Oman, west of the giant saih Rawl gas field	Ordovician	Sandstone	7	0.1	• Wide azimuth seismic • Directional drilling • Underbalanced drilling • Hydraulic fracture
Saudi Arabia	Gawaher	Northwest	Ordovician/ Silurian	Sandstone	12	>1	• 3D seismic • Horizontal drilling • Multi hydraulic frac stages
Saudi Arabia	Mushayab		Ordovician	Sandstone	4–6	0.001–0.008	• Horizontal drilling • Fracturing horizontal wells • Multi hydraulic frac stages
Egypt	Obaiyed	Western desert	Middle Jurassic	Sandstone	7–13	0.1–600	• Hydraulic fracture • Directional drilling
Egypt	Abu gharadig	Western desert	Upper Cretaceous	Sandstone	8.5	.01–200	• Directional drilling • Hydraulic fracture
Algeria	Teguentour	Southwest of Algeria	Silurian–Lower Devonian	Sandstone	20.1	<1	• Underbalanced drilling • Horizontal drilling • Fracturing horizontal wells • Multi hydraulic frac stages
Algeria	Krechba	Southwest of Algeria	Silurian–Lower Devonian	Sandstone	8.5	<1	• 2D seismic • Horizontal drilling • Geosteering • Multi hydraulic frac stages
Algeria	In Salah	Southwest of Algeria	Silurian–Lower Devonian	Sandstone	10		• 3D multi azimuth seismic survey • NMR • Directional drilling • Hydraulic fracture • Improved proppants
Iraq	Akkas	Northwest of Iraq	Upper Ordovician	Sandstone	7.6	0.13	• Wide azimuth seismic • Underbalanced drilling • Directional drilling • Multi hydraulic frac stages
Jordan	Risha	Northeast of Jordan	Upper Ordovician	Sandstone with silty clay	3–7	Less than 0.124	• Directional drilling • Hydraulic fracture
Syria	Arak		Carboniferous	Sandstone interbedded with shale layer	13	>1	• 2D seismic • Directional drilling • Coiled tubing drilling • Acidizing the formation matrix

Part V—Formation Testing

Chapter 31

Wireline Formation Testing

Wireline formation testers serve a number of useful purposes, including:

- Obtaining a sample of formation fluid
- Gauging formation permeability
- Measuring formation pressure
- Determining formation pressure gradients
- Finding fluid contacts: Oil/Water (OWC), Gas/Oil (GOC), or Gas/Water (GWC)

Wireline formation testers have been used for many years to recover samples of formation fluid in both open and cased holes. Nevertheless, these traditional tools suffered from a number of drawbacks. One was the lack of resolution and accuracy of their pressure gauges; another was the inability of the instrumentation to tell the operator whether or not a good packer seal was obtained until it was too late to rectify a bad situation; and. finally, there was no way to monitor in real time what fluids were being sampled, nor was there any means to discard unwanted fluids and sample only uncontaminated ones.

These inadequacies have now largely been overcome by the introduction of a number of key features of modern wireline formation-tester tools, including quartz-crystal pressure gauges, pretest capabilities that allow the operator to rectify a bad seal before it leads to undesirable results, and pumpout capabilities that include real-time monitoring of the physical properties of the fluids extracted from the near-wellbore region being sampled. Methods for monitoring the flow stream coming from the formation include fluid resistivity, density and pH measurements, fluorescence, and discrimination among oil, water, and gas using spectroscopic optical fluid analysis.

A bonus is the ability of these tools to perform pressure tests independently of sample taking. Indeed, in current practice, it is quite common to use these tools solely to perform pressure tests.

31.1 Tool Characteristics and Applications

Most service companies now offer a wireline formation tester with the following features:

- Pretest chambers
- Sample chambers
- High-resolution pressure gauges in addition to strain gauges
- Pump-through/pump-out capability
- Monitoring of extracted-fluid resistivity and pH
- Analysis of extracted fluids using optical spectroscopy, fluorescence, or NMR

The hardware available to make these measurements comes as a wide variety of modular units that may be combined in a "mix-and-match" fashion to suite the purpose of the test to be performed and the wellbore conditions. Among the choices to be made are between single or dual probes and between single or dual packers. Wireline formation testers are particularly useful:

- When investigating a zone of interest where conventional drillstem tests are not feasible, such as too far above the bottom of the hole or total depth (TD), lack of good intervals to set straddle packers, or a very short interval where depth control is critical
- When trying to pin down OWC, GOC, or GWC
- Where rig time is critical
- Where pressure control is critical because of time of day or rig location

When ordering this service, give plenty of notice to the service company. The desired choice of variables such as sample-chamber sizes, packer hardnesses, choke sizes, pressure gauges, and water cushions may not be universally available. If a sample of recovered hydrocarbons is needed for pressure/volume/temperature (PVT) lab analysis, a special pressure cylinder should be requested.

When running the tool, a valid test may be considered one that recovers significant quantities of fluid, records formation and hydrostatic pressure, or both. A dry test is indeterminate, and the tool should be repositioned several times to determine if (1) the formation is impermeable (in which case all tests will be dry) or (2) the tool was set in a shale or a tight streak (in which case repositioning should result in a valid test). A lost packer seal also results in an indeterminate test, and the tool should be repositioned. Openhole logs are particularly helpful in resolving dry tests and lost packer seals. The microlog, if available, is useful as an indicator of tight streaks, and caliper logs, particularly the four-arm type, are useful for avoiding hole conditions that lead to lost packer seals.

31.2 Operating Principles

31.2.1 Mechanics. Fig. 31.1 shows a wireline formation tester in the open (or set) position for pressure measurement and sample taking.

31.2.2 Hydraulics. Communication between the formation and the tool interior is established through the probe. **Fig. 31.2** shows a schematic of the tool's sampling system. Note the details of

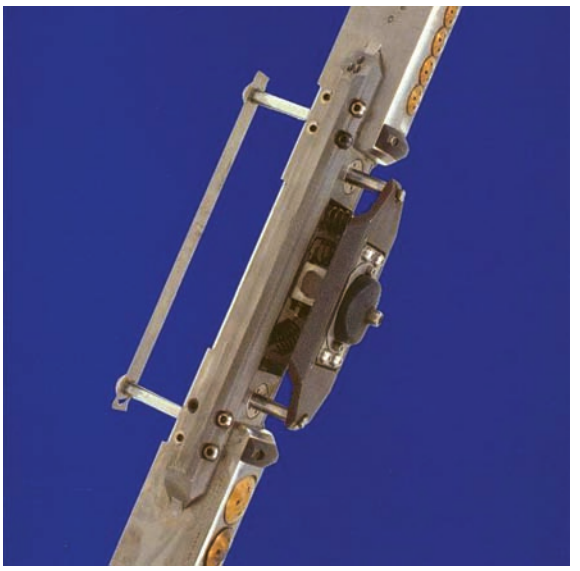


Fig. 31.1—Wireline-formation-tester tool.

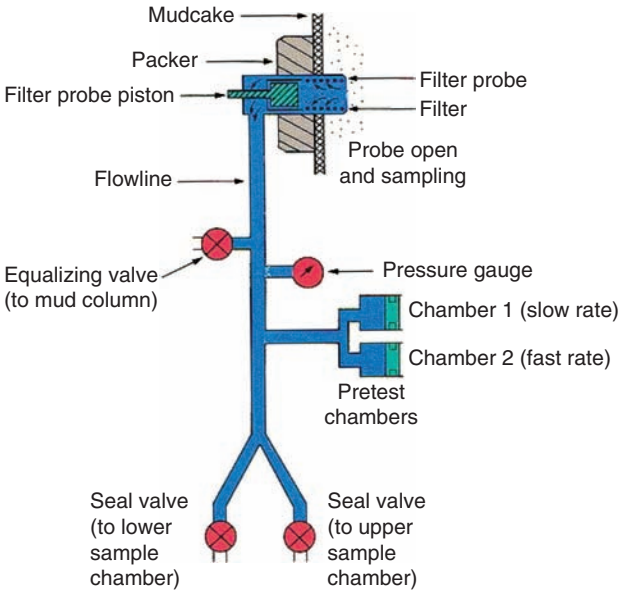


Fig. 31.2—Wireline-formation-tester sampling-system schematic. Courtesy of Schlumberger.

actuation of the filter probe, which in the setting cycle is forced to cut through any mudcake and during the sampling cycle is retracted to leave an open path for the formation fluids.

Note also the pretest chambers and the position of the sample chambers. The two pretest chambers, automatically activated every time the tool is set, withdraw 10 cm^3 of formation fluid. Chamber 2 has a higher flow rate than Chamber 1. The actual rates of fluid withdrawal vary with the tool and the downhole conditions, but are in the neighborhood of 50 cm^3/min for Chamber 1 and 125 cm^3/min for Chamber 2, resulting in pretest times of roughly 12 and 5 seconds, respectively. The pretest samples are expelled back into the mud column and are not saved.

Fig. 31.3 shows a typical log produced during a test. Because the tool is stationary in the hole during the test, the recording is made on a time scale with time increasing in the downhole direction on the log. Note that in Track 1, pressure is recorded in analog form. Four subtracks record the units, tens, hundreds, and thousands of pounds.

QUESTION 31.1. Read the pressure from the log in Fig. 31.3 at time T
a. from the analog curve
b. from the digital display

Each record shows the following pressures:

1. Hydrostatic pressure before tool is set
2. Drawdown pressure during pretest
3. Buildup pressure after pretest
4. Shut-in pressure after buildup

These four regions of the pressure record are marked on Fig. 31.3.

31.2.3 Pressure Gauges. Although some testers still use strain gauges calibrated by a deadweight tester, the *de facto* standard today is a high-precision quartz gauge. Accuracy of this instrument is within

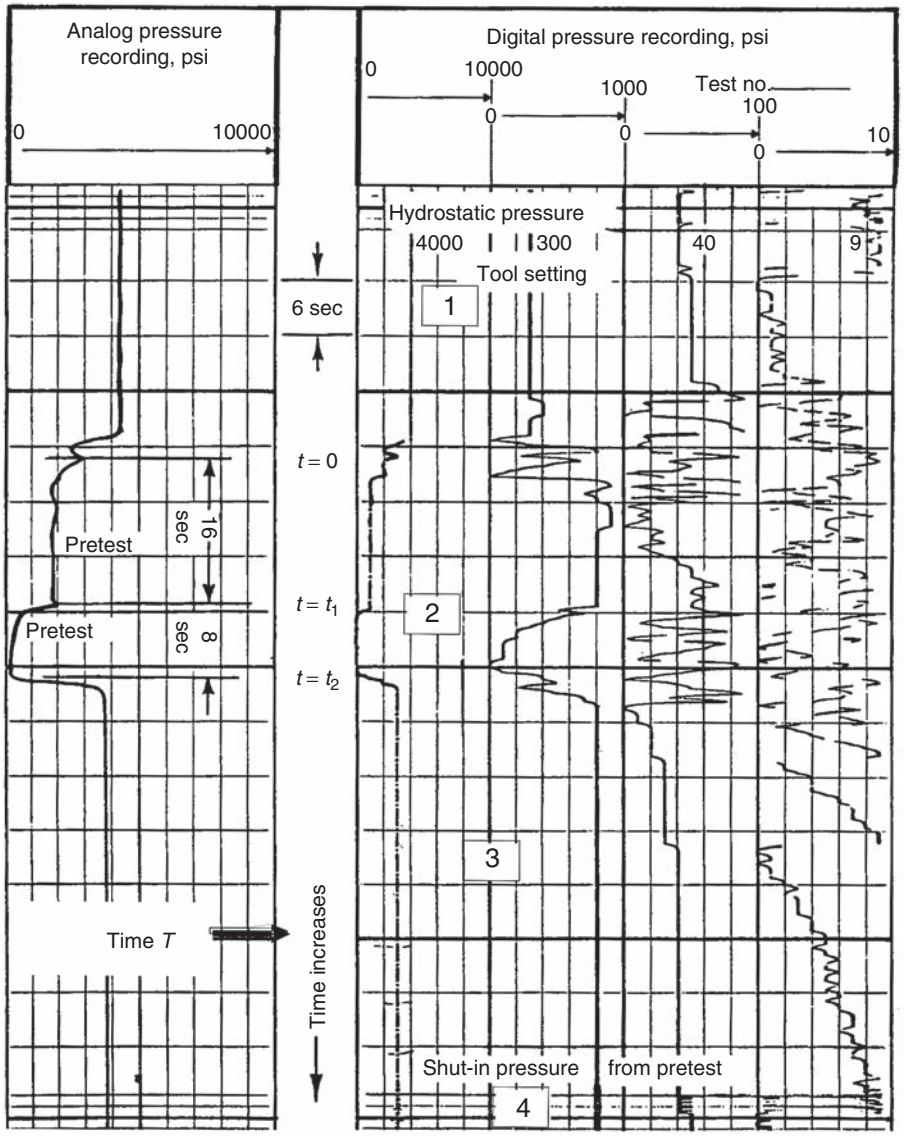


Fig. 31.3—Wireline-formation-tester pressure recording (Smolen and Litsey 1979).

1 psi, and resolution is on the order of 0.01 psi. Note that in some tools, multiple pressure gauges may be physically located at different points along the tool axis with respect to the reference measurement point (which is where the probe contacts the formation) and that, therefore, the pressure recorded by the various gauges may differ because of the hydrostatic head of the column of silicone oil in the tubes connecting the sensors. In some cases, a further pressure difference may be noted between gauges because of gauge calibration differences (e.g., one may be in psig and another in psia).

31.3 Interpretation

To make the most effective use of tester data, the analyst should be able to interpret the following types of records:

- Pretest records for packer seal and preliminary formation permeability
- Post-pretest buildup for formation permeability

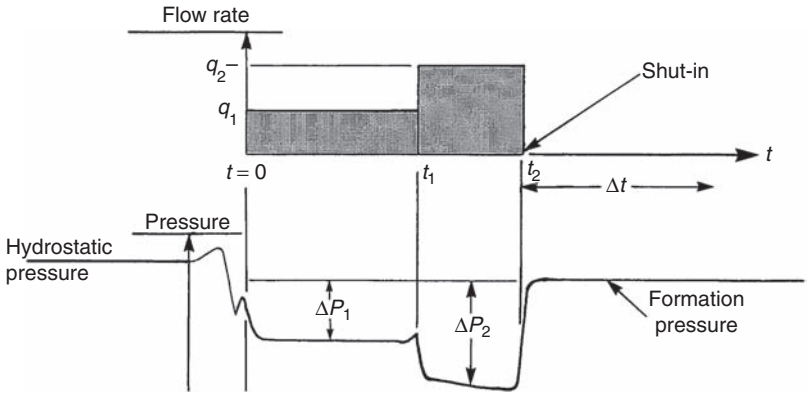


Fig. 31.4—Wireline-tester analog pretest pressure recording (Smolen and Litsey 1979).

- Large-sample fill-up time for formation permeability
- Sequential pressure readings vs. depth for pore-pressure gradients and fluid contacts
- Large-sample collection data for expected formation production

Fig. 31.4 shows a typical pretest record. In reality, only one pretest is required to estimate formation permeability. The magnitude of the pressure differential Δp between pretest sampling pressure and formation pressure, coupled with the flow rate during pretest, is sufficient to define permeability. In general, this may be found by a relation of the form:

$$k = ACq\mu/\Delta p, \quad \ldots\ldots\ldots\

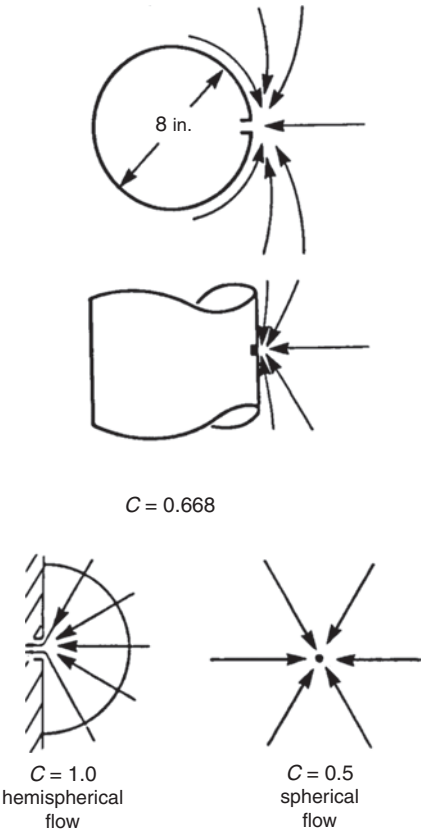


Fig. 31.5—Flow-shape factor C.

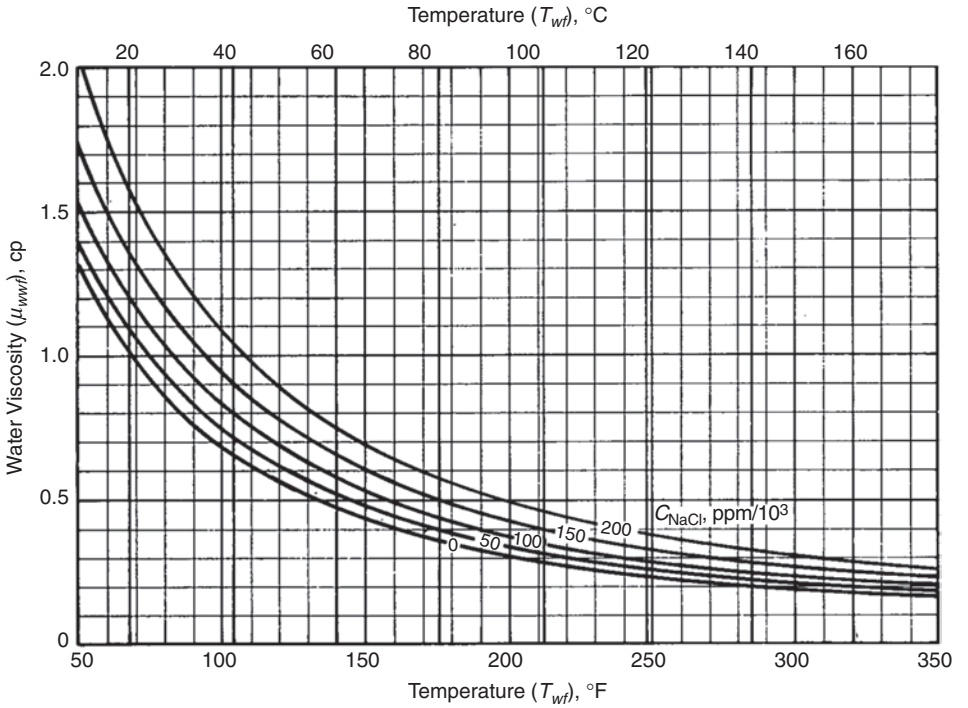


Fig. 31.6—Estimation of water viscosity. Courtesy of Schlumberger.

formation permeability correctly, the analyst should obtain the correct value of the constant *A* used in Eq. 31.1 from the service company involved for the specific tool used.

QUESTION 31.3. If a normal probe and packer are used and
shut-in formation pressure = 3,520 psi,
first pretest pressure = 3,257 psi,
time to fill first pretest = 10 seconds,
second pretest pressure = 2,993 psi,
time to fill second pretest = 5 seconds,
filtrate salinity = 50,000 ppm, and
formation temperature = 175°F,
find the formation permeability in md.

The limitations of the pretest method for determination of permeability are:

a. If the permeability is very high, the drawdown is very small and cannot be measured accurately.
b. If the permeability is very low, the sampling pressure may drop below the bubblepoint, in which case gas or water vapor is liberated and the flow rate of the liquid withdrawn is less than the volumetric displacement of the pretest pistons.

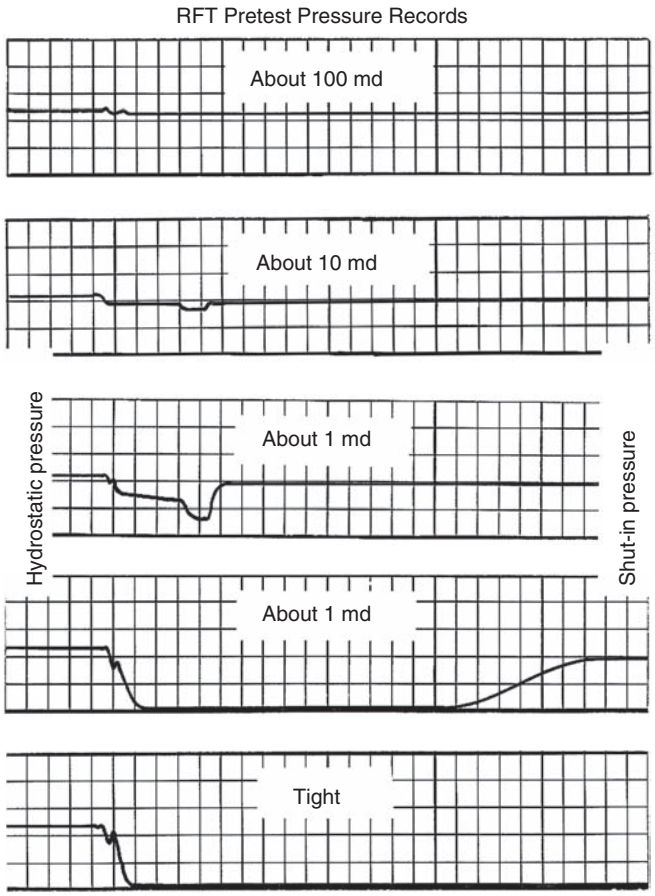


Fig. 31.7—Permeability estimates from pretest pressure records. Courtesy of Schlumberger.

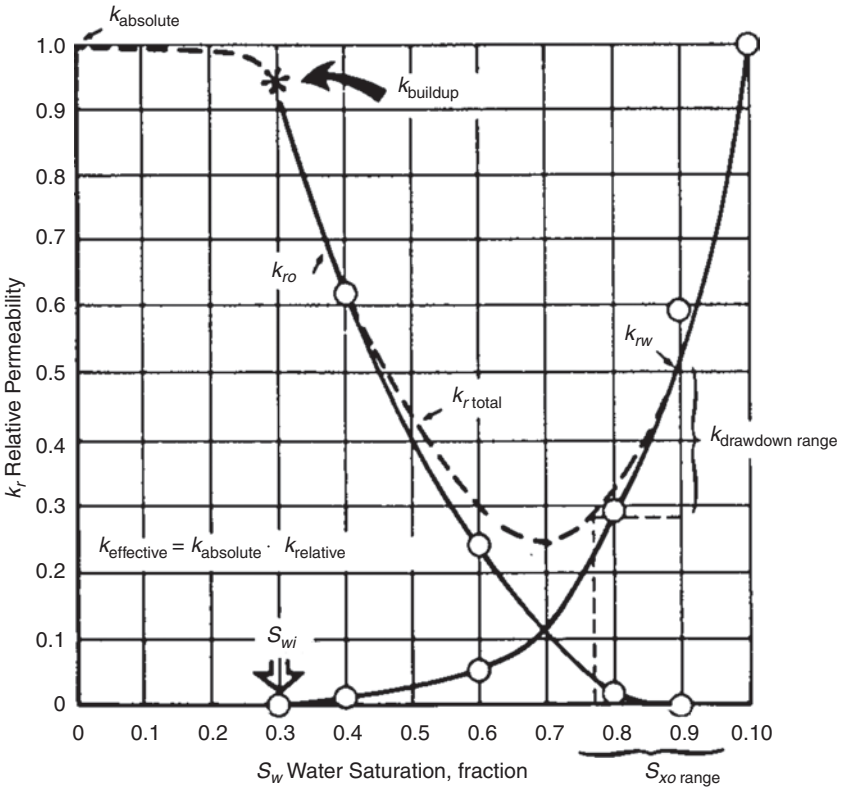


Fig. 31.8—Relative permeability curves. Courtesy of Schlumberger.

c. If the volume of formation investigated is small, the permeability measured may be that of the damaged zone, if present, and therefore not representative of the formation as a whole.

In general, a good estimate of formation permeability may be obtained from a visual inspection of the pretest record. **Fig. 31.7** shows a number of pretest records and their corresponding permeabilities.

31.3.1 Post-Pretest Buildup for Formation Permeability. Permeabilities obtained from a pretest may be subject not only to the errors just mentioned, but also to measuring *relative permeability* to water in the flushed zone instead of *absolute permeability*. **Fig. 31.8** marks the pretest region on a set of relative permeability curves, from which it can be deduced that pretest permeabilities are less than half the absolute permeability when measured in an invaded oil zone.

A preferred method of calculating permeability is to analyze the late-time portion of the pressure-buildup record after the pretest disturbance has been made. A much larger rock volume can be investigated with this method. Effectively, the method will measure k_{ro} at a saturation close to S_{wi}, which will be very close to $k_{absolute}$ (Fig. 31.8) provided that the measurement is made above the transition zone.

Fig. 31.9 illustrates two modes of propagation of a pressure disturbance: spherical and cylindrical. If a test is conducted in a thin bed, the cylindrical mode will predominate, but in a thick bed, the spherical mode will predominate.

31.3.2 Spherical Buildup. The probe pressure response during buildup is obtained by superposition of the two single-drawdown responses, and calculations based on spherical flow in an infinite homogeneous medium lead to the expression:

$$P_i - P_s = \frac{8\times10^4 q_1 \mu \left(\phi\mu C_t\right)^{1/2}}{\left(k_s\right)^{3/2}} \times f_s\left(\Delta t\right), \quad \ldots\ldots\ldots\

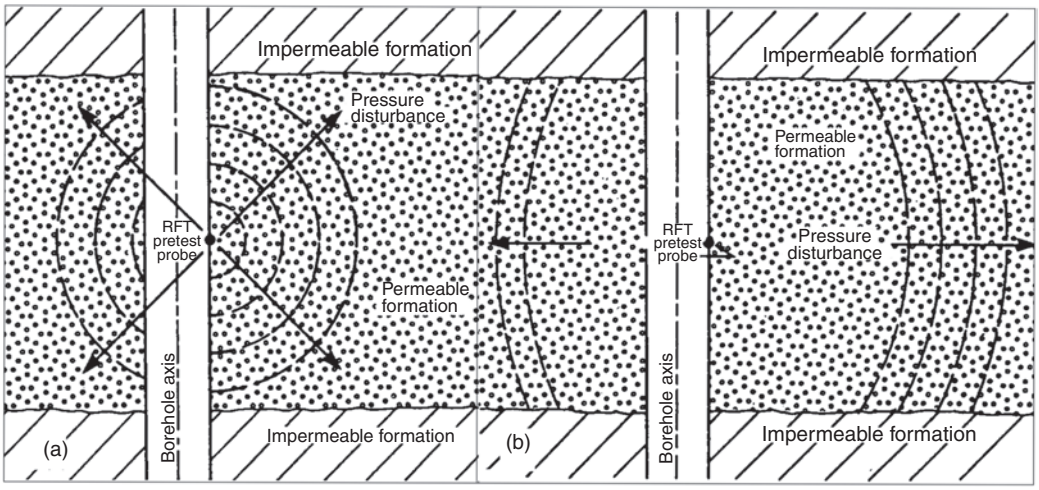


Fig. 31.9—Modes of propagation: (a) spherical, (b) cylindrical. Courtesy of Schlumberger.

where

$$f_s(\Delta t) = \frac{\frac{q_2}{q_1}}{\sqrt{\Delta t}} - \frac{\frac{q_2}{q_1} - 1}{\sqrt{T_2 + \Delta t}} - \frac{1}{\sqrt{T_1 + T_2 + \Delta t}} \quad \ldots\ldots\ldots\

31.3.3 Cylindrical Buildup. In relatively thin beds, a radial-cylindrical flow pattern predominates, and the buildup is affected only by the horizontal permeability. The buildup equation can then be written as:

$$P_i - P_c = 2687\mu\left(q_1\mu/k_r h\right)\times f_c\left(\Delta t\right), \quad \ldots\ldots\ldots\

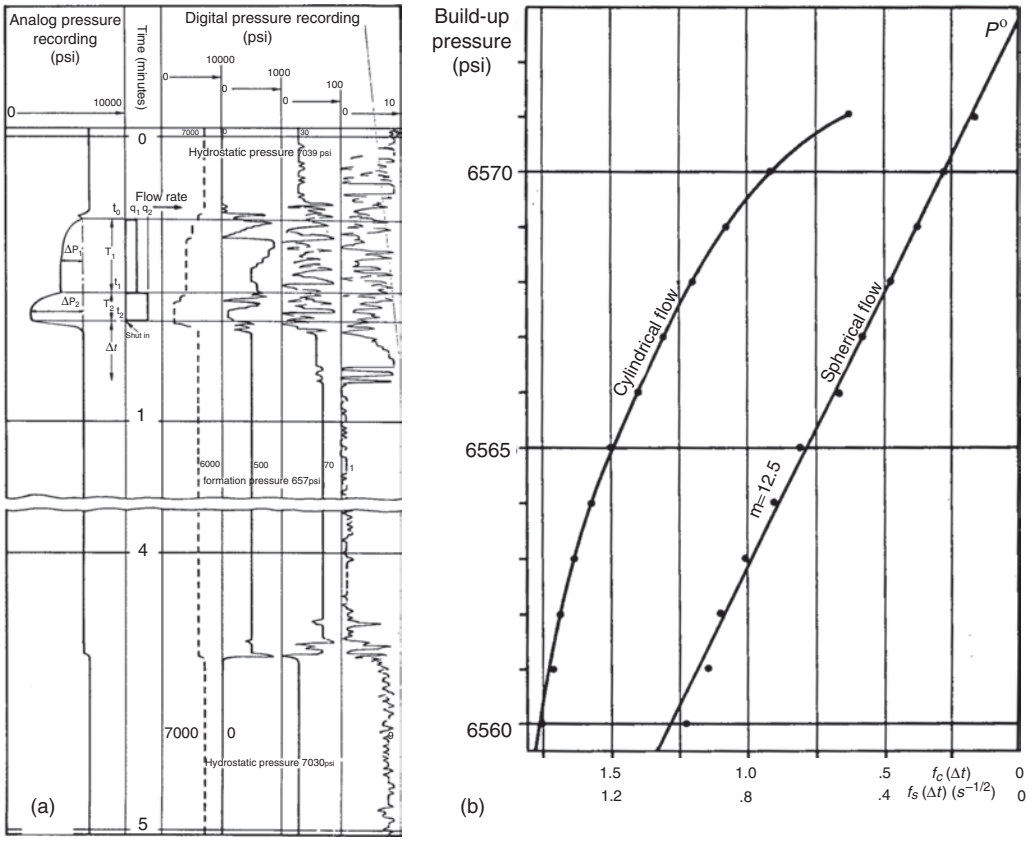


Fig. 31.10—Pressure-buildup permeability: (a) pressure record; (b) buildup plot. Courtesy of Schlumberger.

193	4,004
217	4,006
249	4,008
290	4,010
347	4,012
431	4,014
565	4,016
816	4,018

Bed thickness is 0.5 m.

31.3.4 Large-Sample Fill-Up Time for Formation Permeability. When a large sample of formation fluid is recovered, the time taken to fill the sample chamber can be used as an indicator of permeability. In this case, the drawdown is considered to be the formation pressure itself because the sample chamber is for all practical purposes at atmospheric pressure. This may not hold true if the fill-up time is limited by a water cushion and a choke, so this method should be used with discretion and taken for what it is, a "quick and dirty" method of finding permeability. The equation is:

$$k = \frac{4388Cq\mu}{p}, \quad \ldots\ldots\ldots\

where

k = fill-up permeability (md),
C = flow-shape factor,
q = flow rate (cm^3/s),
μ = fluid viscosity (cp), and
p = drawdown pressure (psi).

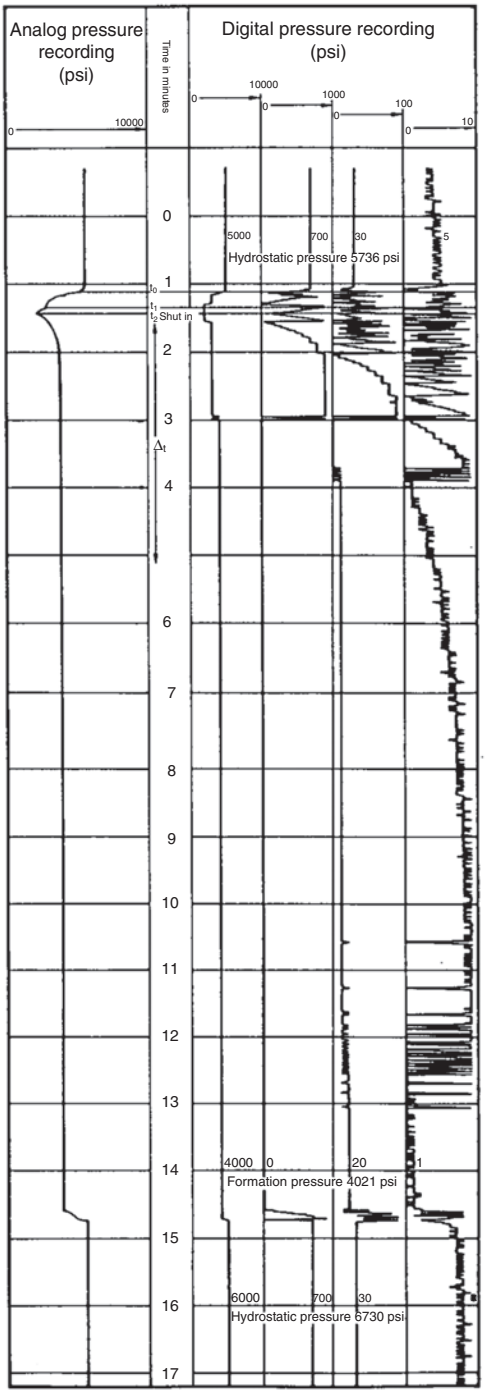


Fig. 31.11—Pressure-buildup recording for Question 31.5. Courtesy of Schlumberger.

QUESTION 31.6. A large sample is collected in a 2¾-gal sample chamber that took 5 seconds to fill. Given that the formation pressure is 3,542 psi, $\mu = 0.5$ cp, and $C = 0.75$, find k.

31.4 Fluid Sampling

Recovering representative samples of uncontaminated reservoir fluids requires two important additions to the basic wireline formation tester. The first is a means to extract quickly and selectively only the fluids of interest and to discard the contaminating mud filtrate that may be in the invaded zone adjacent to the wellbore. This mud filtrate is unceremoniously pumped back into the mud column and discarded. The second is a means to detect when the flow stream entering the tool has reached a state in which an uncontaminated sample can be captured.

31.4.1 Multielement Packers and Probes. The first step to hasten the arrival of uncontaminated formation fluid is accomplished in modern tools with a pump-out capability coupled with specially positioned or shaped packer elements or probes.

Fig. 31.12 illustrates the difference between a conventional single-probe and a dual-probe system including an outer annular element probe that diverts mud filtrate away from the main central sampling probe and thus enables acceptable sample capture significantly more quickly.

31.4.2 Monitoring Sampled Fluid. The second step in monitoring the physical and chemical characteristics of the fluid entering the tool is accomplished by a series of sophisticated sensors that enable real-time analysis for optical density, fluid resistivity, pH, temperature, and density by means of a fluid analyzer. **Fig. 31.13** shows an optical fluid-analysis apparatus, including a fluorescence detector.

Using visible and near-infrared light, the optical density (OD) of the flow stream is measured. The wavelength ranges are optimized for the detection and analysis of hydrocarbon and CO_2 components in crude oil and natural gas, as well as for the determination of water content and pH. The measurement of OD is simply the base-10 logarithm of the ratio of incident light to transmitted light through a cross section of reservoir fluid in the flowline. OD is presented as a dimensionless unit, meaning that one OD absorbance unit implies a tenfold reduction in light intensity. For example, OD = 0 means that 100% of the light is transmitted, OD = 1 indicates that 10% of the light is transmitted, and OD = 2 means that 1% of the light is transmitted.

Fig. 31.14 shows a typical OD spectrum with characteristic responses for oil and water. In practice, the operator monitors the composition of the flow stream from a recording such as that shown

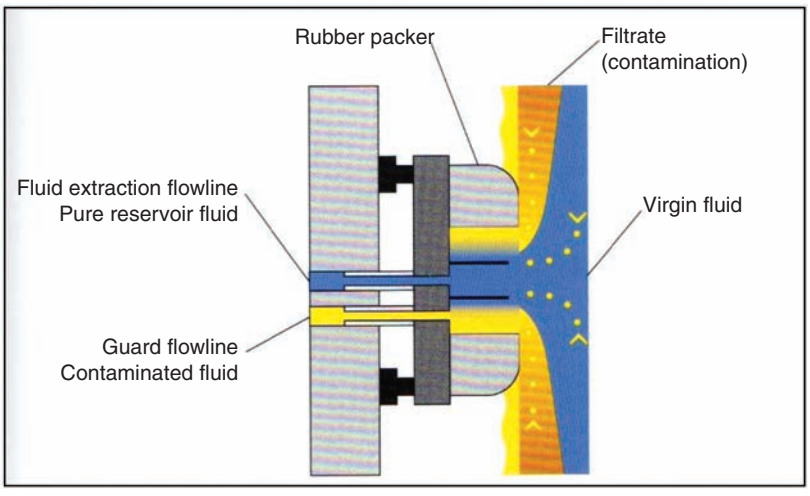


Fig. 31.12—Packer/probe design for quick fluid sampling.

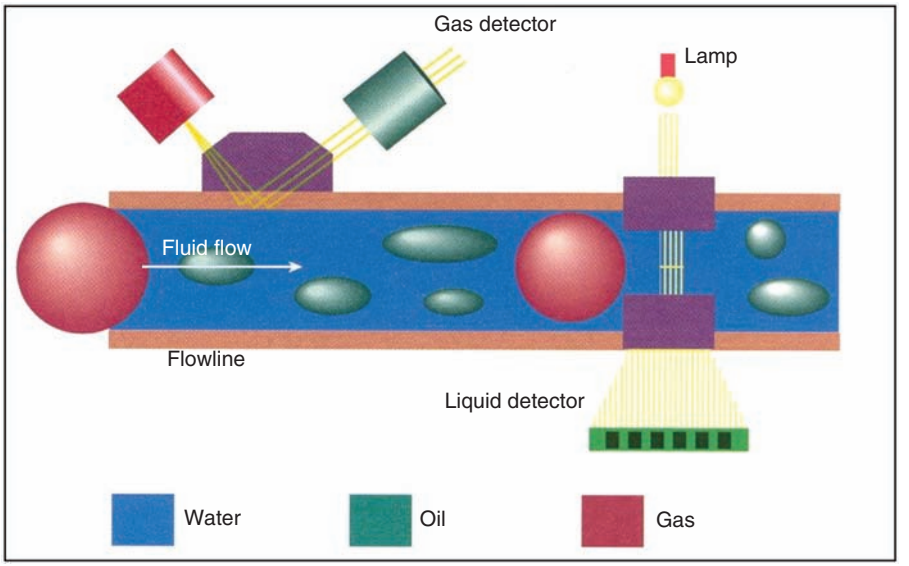


Fig. 31.13—Optical fluid analyzer (Mullins 2008). Courtesy of Schlumberger.

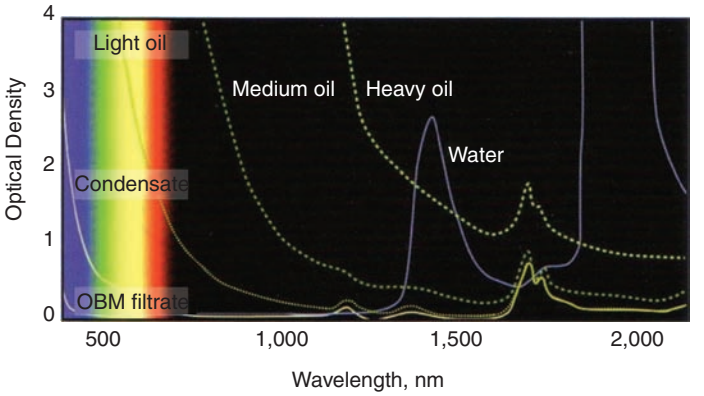


Fig. 31.14—OD spectra for oil(s), water, and mud filtrate.

in **Fig 31.15.*** When the indications are favorable and show that any contaminating mud filtrate has been flushed from the sampling line, then the uncontaminated fluid is diverted to a sample container that is subsequently retrieved when the tool returns to surface.

31.5 Sequential Pressure Readings vs. Depth for Pore-Pressure Gradient

Because many formation-pressure measurements can be made on one trip into the hole, pressure readings can be plotted against depth and fluid gradients can be calculated.

The easiest way to do this is to plot formation pressure against depth. **Fig. 31.16** shows an example of this kind of plot. It is also useful to plot hydrostatic pressure on the same plot. GOCs and OWCs are evident on a plot of this nature. In this example, a GOC is indicated at 7,150 ft and an OWC at 7,177 ft. The fluid density in g/cm^3 can be deduced from the pressure gradient in psi/ft, using

* Note that the record is on a time axis because the tool is stationary; time increases down the page.

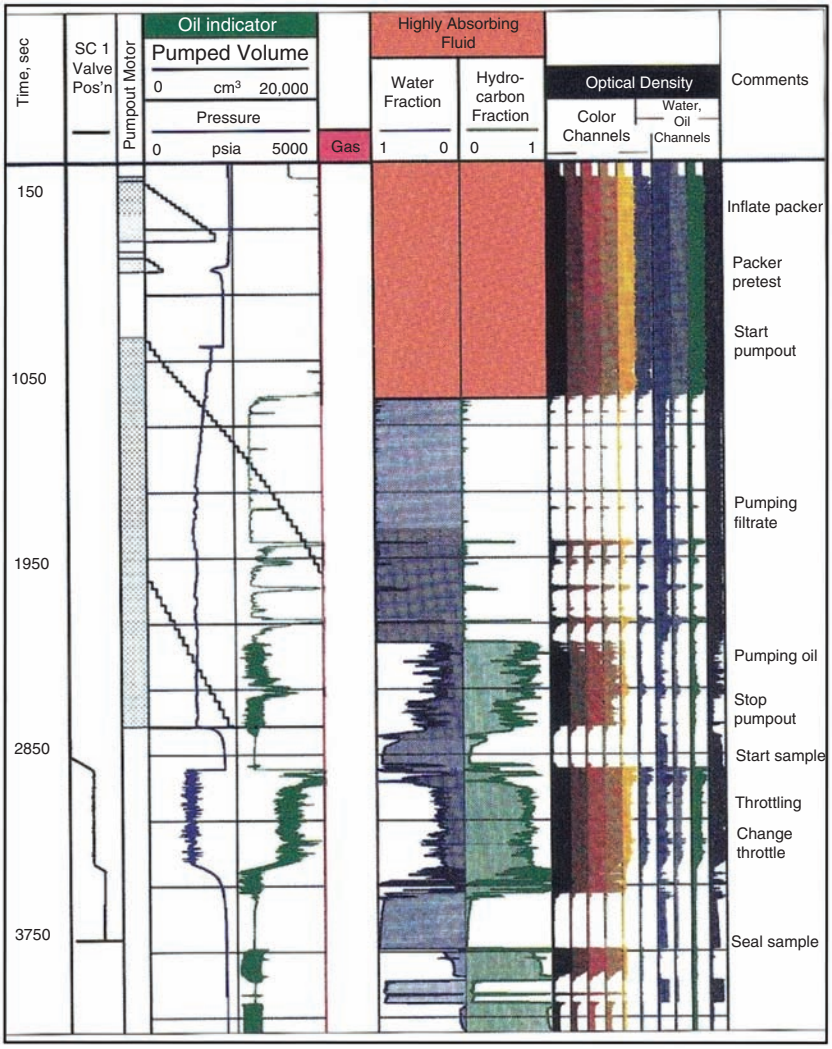


Fig. 31.15—Sequential record of formation-fluid sampling.

$$\text{fluid density} = \text{pressure gradient}\,(\text{psi/ft}) \times 2.3072 \quad \ldots\ldots\ldots\

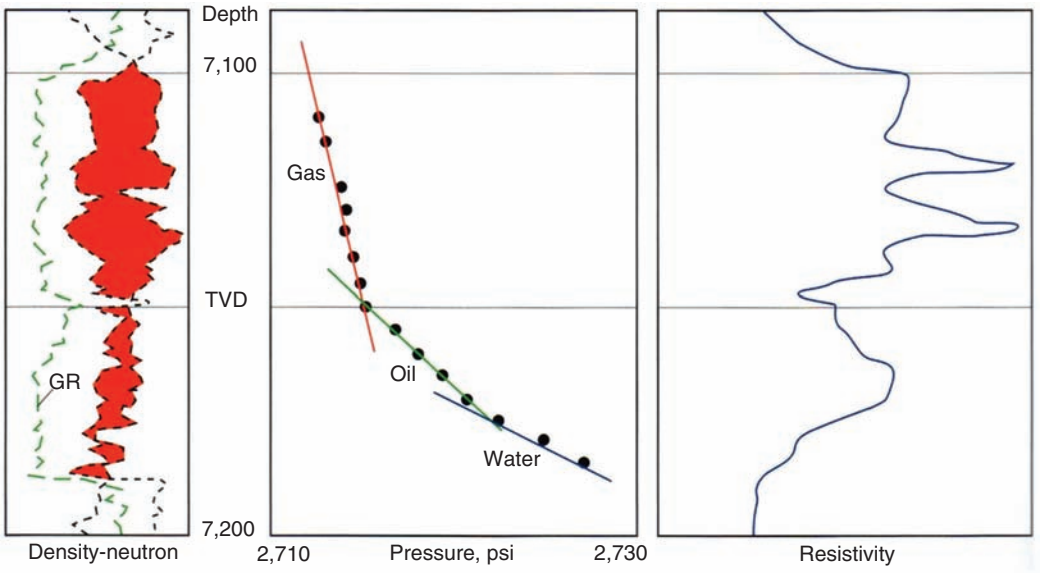


Fig. 31.16—Formation pressure vs. depth plot.

Empirical charts then link recovered volumes to predicted production. **Fig. 31.19** shows a plot of oil recovery (in cm^3) vs. gas recovery (in scf). Three areas are delineated on the chart indicating formations that are gas-, oil-, and water-productive. An "estimate" of water cut can also be made using

$$\text{water cut } \% = \frac{\text{volume of formation water}}{\text{volume of formation water} + \text{volume of oil}} \times 100 \cdot \quad \ldots\ldots\ldots\ldots\ldots\ldots (31.16)$$

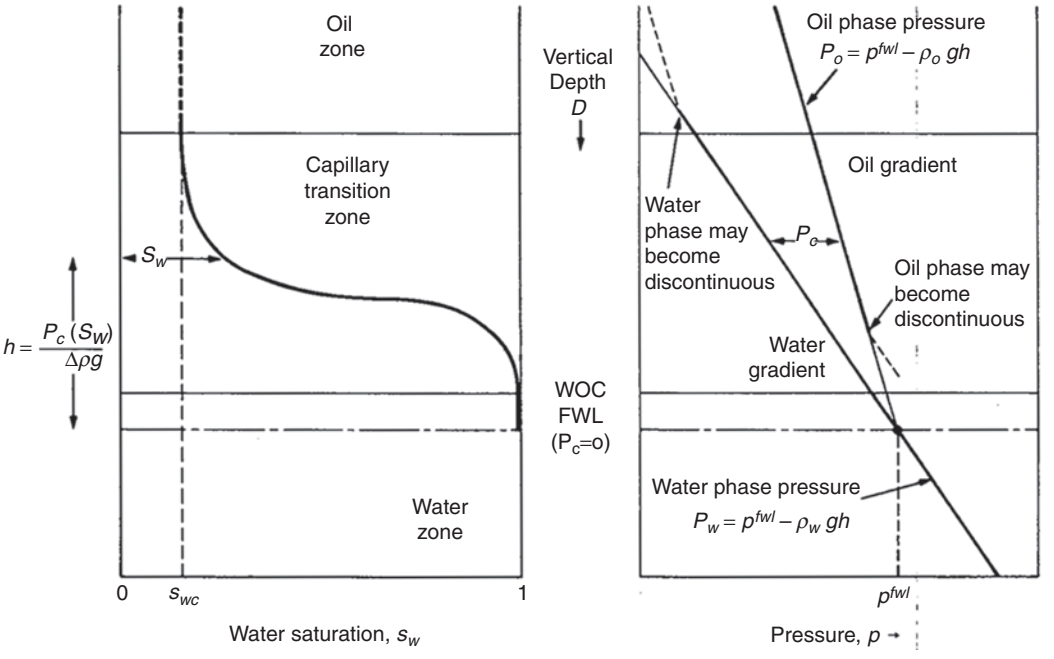


Fig. 31.17—Pressure gradients around the OWC. Courtesy of Schlumberger.

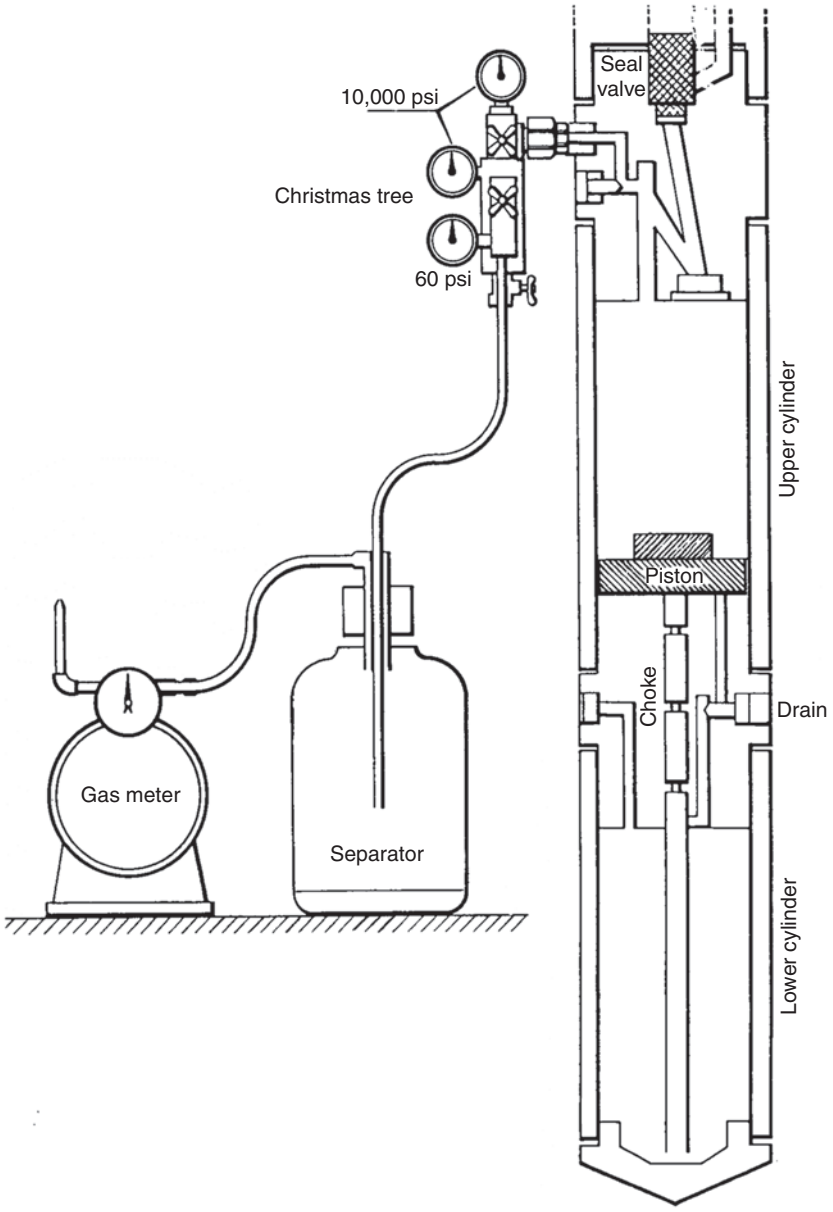


Fig. 31.18—Formation tester sample recovery measurement.

QUESTION 31.7. On a wireline formation test, the following recoveries were measured at the surface:
Gas: 23 scf,
Oil: 7250 cm^3,
Water: 1350 cm^3.
The resistivity of the recovered fluid was 0.88 Ω·m at 78°F.
The resistivity of the mud filtrate was 1.9 Ω·m at 78°F.
The resistivity of the formation water was 0.32 Ω·m at 78°F.
Use Eqs. 31.15 and 31.16 to predict water cut.
Use Fig. 31.19 to predict oil and gas production.

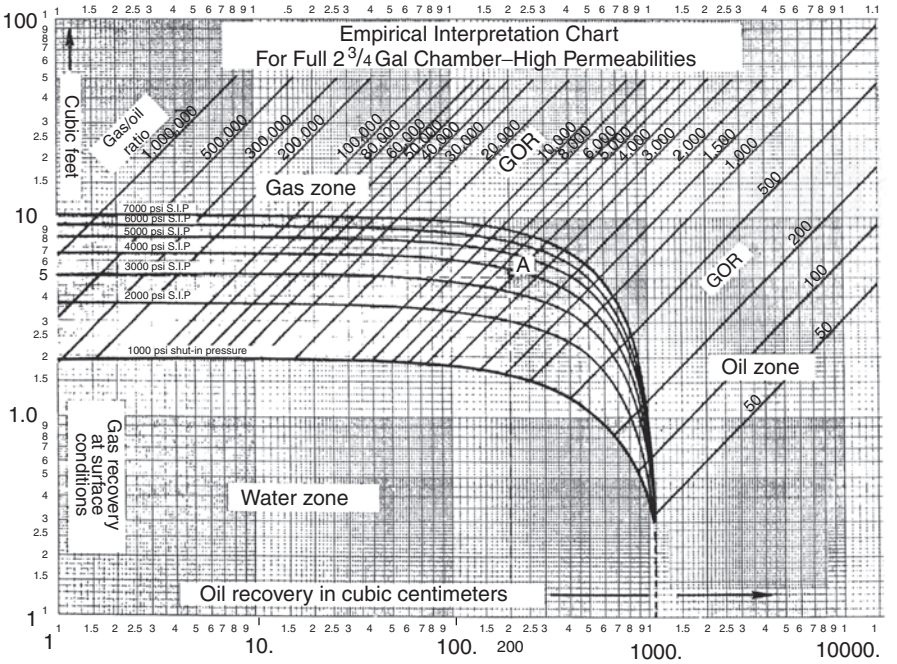


Fig. 31.19—Empirical estimation of productivity.

References

Mullins, O.C. 2008. *The Physics of Reservoir Fluids*. Schlumberger.

Mullins, O.C. and Schroer, J. 2000. Real-Time Determination of Filtrate Contamination During Openhole Wireline Sampling by Optical Spectroscopy. Paper SPE 63071 presented at the SPE Annual Technical Conference and Exhibition, Dallas, 1–4 October. http://dx.doi.org/10.2118/63071-MS.

Mullins, O.C., Schroer, J., and Beck, G.F. 2000. Real-Time Quantification of OBM Filtrate Contamination During Openhole Wireline Sampling by Optical Spectroscopy. *Trans.,* SPWLA 41st Annual Logging Symposium, Dallas, 4–7 June, Paper SS.

Mullins, O.C., Beck, C.F., Cribs, M.E. et al. 2001. Downhole Determination of GOR on Single-Phase Fluids by Optical Spectroscopy. *Trans.*, SPWLA 42nd Annual Logging Symposium, Houston, 17–21 June, Paper M.

Mullins, O.C., Elshahawi, H., Hashem, M.N. et al. 2005. Identification of Vertical Compartmentalization and Compositional Variation by Downhole Fluid Analysis: Towards a Continuous Downhole Fluid Log. *Trans.*, SPWLA 46th Annual Logging Symposium, New Orleans, 26–29 June, Paper K.

Mullins, O.C., O'Keefe, M., Elshahawi, H. et al. 2009. The Impact of Reservoir Fluid Compositional Variation and Valid Sample Acquisition on Flow Assurance Evaluation SS-FA. Paper OTC 20204 presented at the Offshore Technology Conference, Houston, 4–7 May. http://dx.doi.org/10.4043/20204-MS.

Schlumberger. 1966. *Formation Tester Interpretation: Methods and Charts*. Houston: Schlumberger.

Schlumberger. 1974. *Fluid Conversions in Production Logging*.

Schlumberger. 1981. *The Essentials of Wireline Formation Tester*.

Schlumberger. 1982. *RFT Essentials of Pressure Test Interpretation*. Document M-081022. Paris: Schlumberger.

Schlumberger. 2006. *Fundamentals of Formation Testing*, 06-FE-014. Sugar Land, Texas: Schlumberger Marketing Communications.

Smolen, J. and Litsey, L. 1979. Formation Evaluation Using Wireline Formation Tester Pressure Data. *J. Pet Tech* **31** (1): 25–32. http://dx.doi.org/10.2118/6822-PA.

General References

Blakeman, E.R. 1965. Dimensionless Time Function Tables for Pressure Buildup Analysis. *The Log Analyst* **6** (3): 21–36.

Del Campo, C., Dong, C., Vasques, R. et al. 2006. Advances in Fluid Sampling With Formation Testers for Offshore Exploration. Paper OTC 18201 presented at the Offshore Technology Conference, Houston, 1–4 May. http://dx.doi.org/10.4043/18201-MS.

Dresser Atlas. 1980. *Formation Multi-Tester Interpretation Manual*.

Hashem, M.N., Elshahawi, H., and Ugueto, G. 2004. A Decade of Formation Testing: Do's and Don'ts and Tricks of the Trade. *Trans.,* SPWLA 45th Annual Logging Symposium, Noordwijk, The Netherlands, 6–9 June, Paper L.

Stewart, G. and Wittmann, M.J. 1979. Interpretation of the Pressure Response of the Repeat Formation Tester. Paper SPE 8362 presented at the SPE Annual Technical Conference and Exhibition, Las Vegas, Nevada, USA, 23–26 September. http://dx.doi.org/10.2118/8362-MS.

Stewart, G., Wittmann, M.J., and van Golf-Racht, T. 1981. The Application of the Repeat Formation Tester to the Analysis of Naturally Fractured Reservoirs. Paper SPE 10181 presented at the SPE Annual Technical Conference and Exhibition, San Antonio, Texas, USA, 5–7 October. http://dx.doi.org/10.2118/10181-MS.

Weinheber, P. and Vasques, R. 2006. New Formation Tester Probe Design for Contamination Sampling. *Trans.,* SPWLA 47th Annual Logging Symposium, Veracruz, Mexico, 4–7 June, Paper Q.

Answers to Questions

QUESTION 31.1.
3,845 psi.

QUESTION 31.2.
$\mu_{wwf} = 0.43$ cp.

QUESTION 31.3.
Pretest 1: $k = 8.61$ md.
Pretest 2: $k = 8.59$ md.

QUESTION 31.4.
Spherical.

QUESTION 31.5.
Formation pressure = 4,022.6 psi.
$k = 0.06$ md.

QUESTION 31.6.
$k = 967$ d.

QUESTION 31.7.
$R_{mf}/R_w = 5.94$.
$R_{mf}/R_{rf} = 2.16$.
Formation water % = 21.
Formation water volume = 284 cm^3.

$$\text{Water cut} = \frac{284}{7,250+284} = 4\%.$$

Gas and oil recoveries plot in oil zone with GOR = 500. Well actually produced 120 BOPD, no water.

Chapter 32

Drillstem-Testing Objectives

The purposes of running a drillstem test (DST) are:

- To ascertain whether the formation can achieve sustained production
- To establish the type of production (oil or gas)
- To collect formation fluids for laboratory analysis (e.g., PVT, water salinity)
- To establish formation pressure
- To estimate formation permeability

Although a wireline repeat formation tester may provide some of this information, the DST is the only proof positive that recoverable hydrocarbons are present in the formation and will flow once the well is put on production. For this reason, the DST is a popular formation-evaluation technique.

32.1 Mechanics of DST

The mechanics of running a DST is straightforward. The drillpipe is lowered into the open hole with a testing assembly on the bottom of the string. This assembly consists of a packer and a system of valves. The drillpipe itself is kept empty or partially so (with a water cushion, for example). When the assembly reaches the bottom of the hole, the packer is set to seal off the bottom of the test assembly from the mud column. The flow valve is then opened, and the formation is placed in communication with the inside of the drillpipe, which is then at a much lower pressure than the formation. Fluids therefore flow into the drillpipe. If formation pressure and permeability are sufficiently high, formation fluids will flow to the surface. **Fig. 32.1** illustrates the principle.

When testing is completed, the test valve is closed, and a pressure-equalizing valve is opened so that the mud in the formation and the drillpipe annulus once again comes into contact with the formation and kills further flow. The packer can then be unseated and the formation fluid still in the drillpipe circulated out of the hole through a reverse-circulating valve.

32.2 Pressure Recording

The test assembly normally carries two pressure recorders: One is placed in the flow stream and one outside the tool. If any differences are noted between the readings of the two pressure recorders, tool plugging is indicated. A typical pressure recording is shown in **Fig. 32.2.**

By plotting the observed pressure as a function of time, it is possible to determine formation permeability, reservoir limits, formation damage (reduced permeability adjacent to the wellbore) if present, and formation pressure. A number of plotting techniques are used for these purposes, including the *Horner plot,* in which pressure is plotted vs. the log of $(T + \Delta T)/\Delta T$, where T is the time during which the formation was open to flow and ΔT is the cumulative time since flow started **(Fig. 32.3).** If both the first and second buildup extrapolate to the same formation pressure, it may be assumed that the reservoir is homogeneous and that the flow periods were of the correct duration.

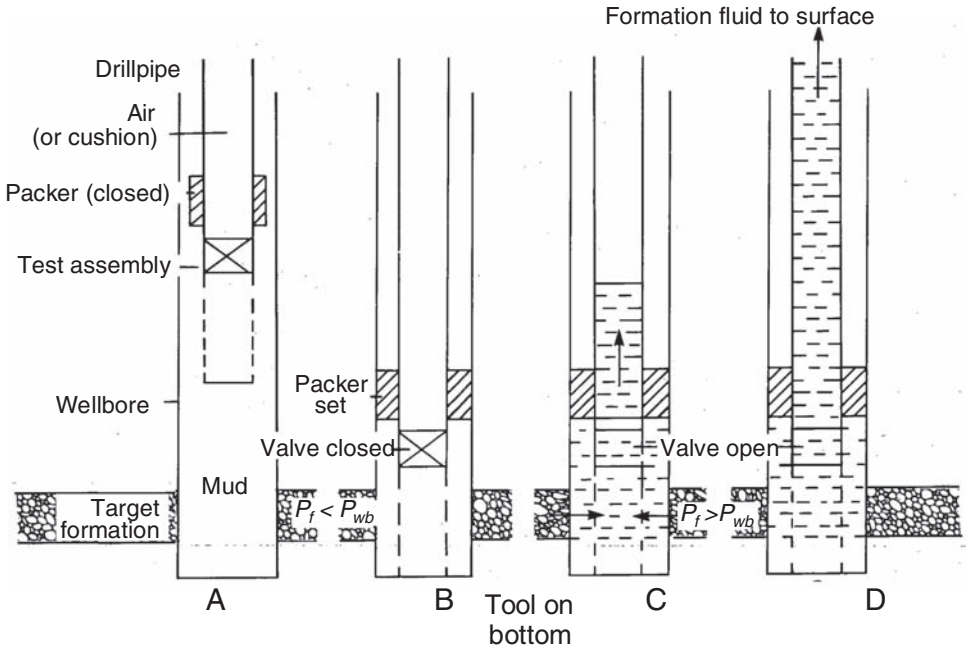


Fig. 32.1—Principles of drillstem testing: (a) running in hole, (b) setting packer, (c) opening flow valve, (d) fluids to surface.

32.3 Planning the DST

When planning the DST, a number of points are worth remembering:

1. In deep wells, a water or other cushion will be needed to prevent collapse of the drillpipe. Normally, a water or pressurized-nitrogen-gas cushion will be used to limit the initial drawdown on the formation to 4,000 psi or less.

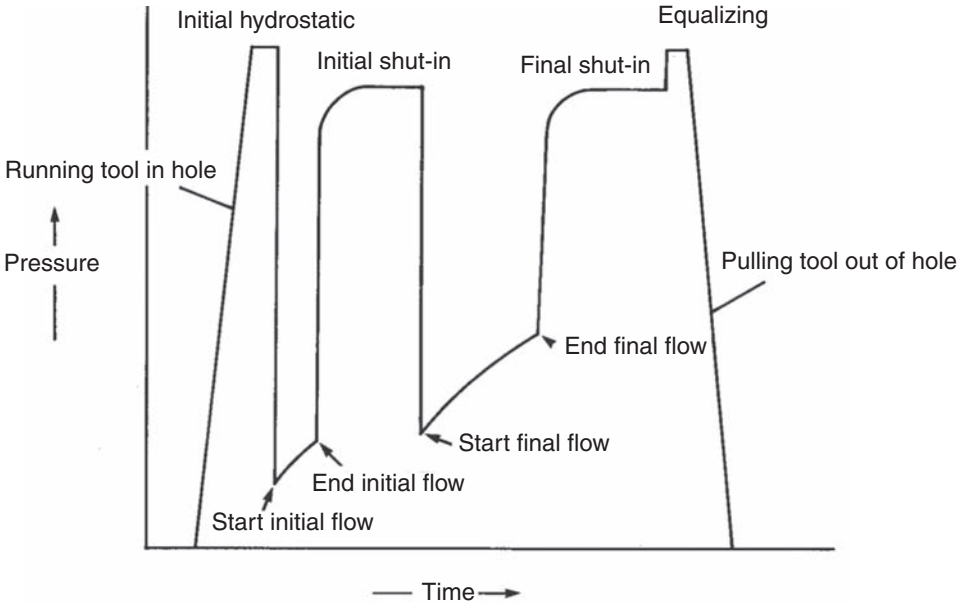


Fig. 32.2—Typical DST plot of pressure vs. time.

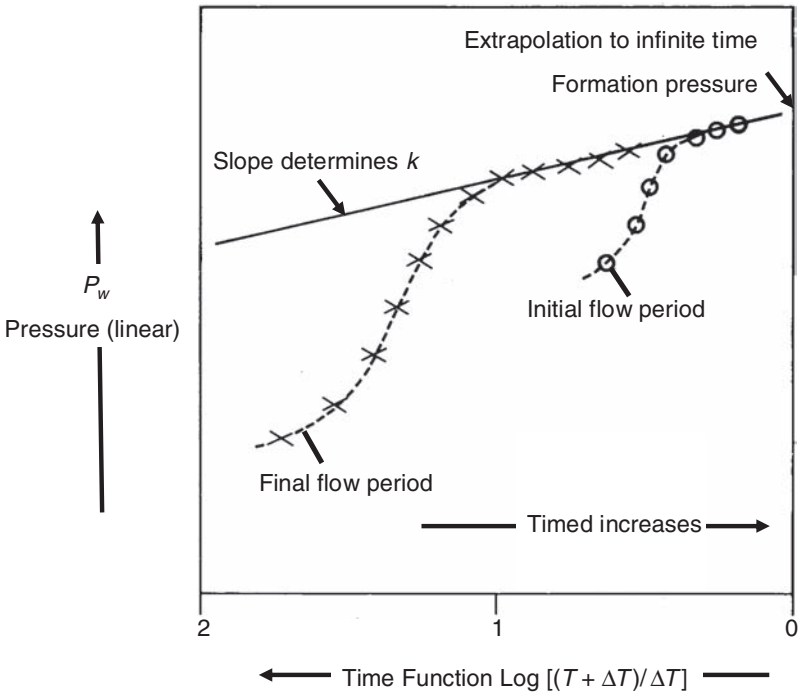


Fig. 32.3—Horner plot for DST data.

2. Consult the openhole logs to choose the depth at which to set the packer. Avoid unconsolidated or fractured formations and washouts.
3. Plan to adjust the flow and buildup periods according to the following guidelines:

Initial flow:	3–5 minutes.
Initial shut-in:	75–90 minutes, depending on the blow during the initial flow period. Less time is required if the blow was strong, and vice versa.
Final flow:	60–120 minutes or longer if flow rates are to be gauged. If the well dies, shut it in.
Final shut-in:	One and one-half to three times the final flow period, depending on the blow. A strong blow requires less final shut-in time, and vice versa. If the well has been produced for any length of time, the shut-in time should equal the final flow time.

32.4 Perspective

The DST should be viewed in perspective along with all the other formation-evaluation techniques. By its nature, it measures macro formation properties. Because of the large pressure drawdown created, the pressure disturbance travels much farther into the formation than any other formation-evaluation tool can reach. A skilled interpreter of DST records can associate neighboring faults or other boundaries with the reservoir and can estimate reservoir size and producibility. That kind of information is of inestimable value. A DST is the "acid test" for all other formation evaluation techniques.

However, a DST cannot evaluate the rock type or identify the precise porosity and water saturation, so it is not the be-all and end-all of all tests. It is a powerful tool, and the analyst should combine all the available data to help in deciding where and when to use the DST and then use the additional data gathered to improve the overall picture of the reservoir.

References

Horner, D.R. 1951. Pressure Build-Up in Wells. *Proc.,* Third World Petroleum Congress, Leiden, Holland, Sec. II, 503.

General References

Amyx, J.W., Bass, D.M., and Whiting, R.L. 1960. *Petroleum Reservoir Engineering Physical Properties*. New York: McGraw-Hill.

Lee, J. 1982. *Well Testing*. Richardson, Texas: Textbook Series, SPE.

Miller, C.C., Dyes, A.B., and Hutchinson, C.A. Jr. 1950. The Estimation of Permeability and Reservoir Pressure From Bottom-Hole Pressure Build-Up Characteristics. SPE-950091-G. *Trans.,* AIME **198:** 91–104.

Part VI—Integrated Formation-Evaluation Plan

Chapter 33

Integrated Formation-Evaluation Plan

33.1 Objectives

When a serious formation evaluation program is considered, objectives must be set and plans made to achieve them. In this chapter, the goals and strategies involved will be laid out.

In its broadest sense, the objective of a formation-evaluation program should be to gather sufficient data before, during, and after drilling the well so that all subsurface formations and their contents can be completely evaluated. Therefore, many disciplines must be involved.

The *geophysicist* must plan where to run seismic lines, quality check the actual shooting, and then interpret the data to assist in choosing a drilling location. The *geologist* and the *geochemist* must work together to map the locations of traps, reservoir rocks, and source rocks. The *drilling engineer* must plan how the well is to be drilled and supervise the drilling process and any testing or completion work. The *reservoir engineer* must work with the *petrophysicist* and the *log analyst* to provide the *manager* with reserves figures and production-decline estimates so that logical economic decisions can be made regarding field development.

Seldom do all these professionals work in the same group, in the same office building, or even in the same city, and seldom is there one line manager with enough authority over these diverse groups to command an integrated formation-evaluation plan. Too often, each group optimizes its own plan to suit its immediate objectives without regard to the overall plan, with the result that many of the data required to perform a complete formation evaluation are lost or cannot be gathered. At the end of the day, the loss is an economic one that must eventually return to haunt the captains of the industry. Which of us has not heard of leases abandoned by one company, only to be proved productive and profitable by another company more willing or able to evaluate fully the formations drilled?

Who, then, can coordinate all these individual efforts so that the objectives are met? Surely it must be the formation evaluator. In his/her hands lie the keys to economic success. All other efforts are directed toward providing the data required to evaluate fully the formations drilled. The formation evaluator must therefore be somewhat of a politician to succeed and to acquire the necessary authority to ensure that all phases of the operation dovetail logically and harmoniously. This is not an easy task. Good luck to the intrepid person who attempts it!

33.2 Planning

Before a well is drilled, it is customary to make detailed plans, including:

- Bit size
- Mud type
- Logging points
- Casing points
- Intervals to be cored
- Intervals to be tested

Many of the decisions involved interact with each other. In particular:

33.2.1 Drilling. The *hole size* should be planned so that where wireline logs are required, the tools can reasonably be expected to provide valid measurements. Many logging tools will not give representative readings in overly large holes, and in these cases, it is best to plan on drilling a modest-sized hole that, after logging, can be underreamed to an appropriate diameter to accommodate the casing string.

33.2.2 Mud System. The *mud type* can seriously affect the response of logging tools and also the validity of saturation measurements from cores. Situations can arise in which no amount of tinkering with the mud chemistry can satisfy all the requirements of all the interested parties. At least, an attempt should be made to ensure:

- Control of problem shales
- Low water loss (to reduce invasion effects)
- Compatibility with core-analysis requirements

33.2.3 Logging Points. *Logging points* are usually picked to coincide with bit changes, casing points, or other naturally occurring interruptions in the drilling of the well. On occasion, wells have been logged on such festive days as Christmas Day or Super Bowl Sunday, or even over just plain old golfing weekends. Understandable though such practices are, they usually lead to situations in which data quality is compromised.

33.2.4 Logging Suites. *Logging suites* should be planned to complement the type of mud and the objectives of the formation evaluation. With modern multiple-tool strings, the practice of foregoing a particular survey because of time considerations is in most cases no longer valid. **Table 33.1** can be used as a guide to the logging programs that may be appropriate for a number of different mud systems and well types.

33.3 Monitoring

While the well is being drilled, continuous monitoring of the mud log is vital for several reasons:

- Detection of hydrocarbon shows
- Detection of adverse drilling conditions
- Safety

In particular, a drilling break combined with mud-log shows may call for either cutting of a core or a DST. Such occurrences can never be exactly anticipated in advance, and if the opportunity is lost, the data that could have been gathered from a core analysis or a DST can never be collected. Equally important is the monitoring of wireline log quality. Once pipe is set in the well, no further openhole log can be run.

TABLE 33.1—SUGGESTED LOGGING PROGRAMS

	Exploration			Development		
Mud System	Fresh	Salt	Oil Based	Fresh	Salt	Oil Based
Neutron	X	X	X	X	X	X
Density				X	X	X
Litho-Density	X	X	X			
Sonic	X	X	X			
Induction	X		X	X		X
Laterolog		X			X	
Micro-XX	X	X		X	X	
Sidewall Coring	X	X	X			
Dipmeter	X	X				
Borehole Imaging	X	X	X			
GR				X	X	X
Spectral GR	X	X	X			
SP	X	X		X	X	
NMR	X	X	X			

33.4 Data Analysis

33.4.1 Normalization. Before any kind of data analysis is attempted, all types of recording should be normalized to a common system of depth measurement. This calls for reconciliations between:

- Driller's depths
- Mud logger's depths
- Wireline log depths
- Cored intervals
- DST points
- VSP and seismic surveys

Often this becomes a monumental task. Many horror stories are told of wells drilled in meters and logged in feet; of holes with unintentional sidetracks with the mud log in one bifurcation and the wireline log in the other; of core barrels turned top to bottom; and many others. Only when all records refer to the same depth can any serious data analysis begin.

33.4.2 Environmental Effects. All wireline logs, to some extent, suffer from wellbore environmental effects caused by such factors as temperature, pressure, salinity, hole size, and mud weight, and they require appropriate corrections before quantitative analysis can be attempted. Mud-log gas shows likewise need adjustment for background gas before any calculations can be made. When brought to the surface, core samples are relieved of overburden stress, and their measured porosities and permeabilities do not therefore truly reflect the formation properties in situ. All these effects must be accounted for before data from different sources can be combined into a total formation-evaluation package.

33.4.3 Rock Typing. Once all the data—be they from mud logs, wireline logs, cores, or DSTs—have been gathered, normalized, and corrected, the next step will be to establish rock types. In

simple reservoirs, only one rock type may be present, in which case the task is simplified. However, the norm is to find several different rock types, each of which has its own petrophysical characteristics, such as the relationship between (for example):

- F and ϕ
- ϕ and k
- S_w and R_o/R_t

These relationships must be established properly through core analysis or other means. Usually, simple crossplots will suffice to establish the existence of different rock types, and with the help of logs, appropriate core sections can be selected for analysis.

33.4.4 Log Calibration. The next step in the chain is to calibrate logs to some known standard. Like it or not, even the most carefully planned and quality-checked logging suites can still contain records that are systematically shifted or skewed with respect to the true response. Of help in this respect are various techniques such as comparison of log response in one well with the cumulative average response of logs in other wells in the same field at a particular horizon. Core-analysis measurements are also of great value in this respect.

At this time, it is also of value to attempt to establish the types of clay minerals associated with the reservoir rock, particularly if it is a shaly sand. X-ray-diffraction and SEM photos are of particular help in this task.

33.4.5 Numerical Computations. Once a well-calibrated data set is available, the analyst may then embark on numerical computations based on the log data. A number of choices exist, including:

- Selective level-by-level analysis with a calculator or a chart book
- Interactive computer-based analysis over limited intervals of digitized data
- Batch processing of the entire logged column from the original data recording

Each method has its advantages and disadvantages. Although laptop-based analysis does not usually include iterative processing (because it is complex and time consuming), it at least gives the analyst some immediate feedback regarding the choice of parameters and the sensitivity of the computed results to those parameters.

The interactive mode enables far more data to be processed in a much shorter time using more-complex logic, but it opens the door to endless recomputations when the analyst decides to play "what-if" games and attempts to vary the method of analysis to suit some preconceived notion of what the final answer should be.

Batch processing of large databases is a time-consuming business, but it permits the most-modern and -complex algorithms to be used. However, some loss of feedback between the analyst and the processing algorithm is to be expected. The output from batch processing can at times be overwhelming, and valuable time can be lost sifting through voluminous output files in the search for a simple item such as the integrated hydrocarbon pore feet.

33.5 Summary

Formation evaluation will be effective only when it is planned to be effective. If integrated formation evaluation is a serious objective, as indeed it should be, then plans should be made with the active participation of many different groups. If the plan is to succeed, one party must be responsible, and that party must be given authority appropriate to the responsibility. As a guide to formation evaluators, a flowchart **(Table 33.2)** is offered as a starting point.

It is also useful to have a "road map" to guide the analyst in an orderly fashion when confronted with formation-evaluation tasks. **Table 33.3** lists a suggested order for the tasks necessary to

TABLE 33.2—INTEGRATED FORMATION EVALUATION PLAN FLOW CHART

Formulate Plan	Geophysicist Geologist Drilling engineer Log analyst Petrophysicist
Select	Well geometry Mud type Logging suites Coring intervals Testing intervals
Monitor	Mud logging Wireline logging Coring Testing
Normalize	Driller's depths Mud log depths Wireline depths Core depths DST depths Sonic and Seismic
Correct data	Environmental effects
Rock Typing	Cuttings Cores Logs
Log Calibration	Core Analysis Logs
Computations	

TABLE 33.3—SUGGESTED LOG ANALYSIS WORKFLOW

Workflow	Chapter(s)
Delineate porous and permeable sections	7, 9, 10
Identify intervals with water, oil and/or gas	6, 7, 22
Establish porosity log scaling and rock type	2, 23, 24, 27, 29
Mark zero porosity line	16, 17, 18
Mark fluid contacts (OWC and GOC) and top transition zone	6, 7, 22
Compute crossplot porosities in zones of interest	23
Read values of R_t and R_{xo}	11, 12, 13, 14, 15
Analyze wet zone and compute R_w from multiple methods	9, 25
Compute values for S_w and S_{xo}	7, 26, 28, 29
Sum net oil and gas	8
Estimate permeability in zones of interest	6, 7, 19
Write report	32

determine the key rock and fluid parameters. The table includes references to the chapters in this work that are most relevant to each task.

General References

Bateman, R.M. 1993. Building a Reservoir Description Team: A Case Study. *Proc.,* 15th European Formation Evaluation Symposium, Stavanger, 5–7 May, Paper EE.

Crain, E.R. 1980. Economics of Log Evaluation for Large Projects. *Trans.,* SPWLA 21st Annual Logging Symposium, Lafayette, Louisiana, USA, 8–11 July, Paper A.

Johnson, H. 1966. The Role of the Log Analyst. *The Log Analyst* 7 (1): 21–24.

Pirson, S.J. 1965. The Education of a Log Analyst. *Trans.,* SPWLA 6th Annual Logging Symposium, Dallas, 4–7 May.

Threadgold, P. 1975. The Function and Training of a Log Analyst. *The Log Analyst* **16** (5): 11–13.

Towle, G., 1965. The Log Analyst with a Service Company. *Trans.,* SPWLA 6th Annual Logging Symposium, Dallas, 4–7 May.

Appendix

Log Analysis Equation Summary*

Table of Contents

Saturation
- Archie
- Ratio–R_{wa}
- EPT

Spontaneous Potential
Capillarity
Permeability, Relative Permeability, and Fluid Flow
- NMR
- Conventional Log Analysis
- Transition-Zone Resistivity Gradient
- Absolute and Relative Permeability
- Water Cut and Movable Oil

Volumetrics
- HCPV and Oil in Place
- Recovery Factors
- Bed/Well Geometry

V_{Shale}/V_{clay} **Estimation**
- From SP
- From Gamma Ray
- From Neutron-Density

Resistivity
Porosity
- Clean Formations
- Shaly Formations
- Gas-Bearing Formations
- Vuggy Formations

Hydrocarbon Typing
R_w

*The reader is encouraged to use this appendix as an aide-mémoire only. The limitations and applicability of each equation is completely explained only in the text of each chapter. Particular attention should also be given to using these equations with the correct units of measurement.

Porosity-Resistivity Crossplots
- Hingle
- Pickett
- F-Overlay

Lithology
- M and N
- MID Plot

Core Analysis

Shaly Sands
- Laminated Model
- Dispersed-Clay Model
- Structural-Shale Model
- Total-Shale Model
- Electrochemical Model
- Dual-Water Model

Unconventional Reservoirs

Formation Tester

Saturation

Archie

$$R_o = FR_w \quad (26.1)$$

$$F = a/\phi^m \quad (26.2)$$

$$S_w^n = R_o/R_t \quad (26.3)$$

$$S_w^n = F\left(R_w/R_t\right) \quad (25.8)$$

$$S_{xo}^n = F\left(R_{mf}/R_{xo}\right) \quad (25.9)$$

$$S_w^n = \frac{aR_w}{\phi^m R_t} \quad (26.4)$$

$$S_w = \left(\frac{0.81R_w}{\phi^2 R_t}\right)^{1/2} \quad (26.5)$$

$$S_w = \left(\frac{0.62R_w}{\phi^{2.15} R_t}\right)^{1/2} \quad (26.6)$$

$$S_w = \left(\frac{R_w}{\phi^2 R_t}\right)^{1/2} \quad (26.7)$$

Ratio—R_{wa}

$$S_w = \left(\frac{R_{xo}}{R_t} \times 10^{SP/K}\right)^{5/8} \quad (26.20)$$

$$S_w^n = R_w/R_{wa} \quad (25.7)$$

EPT

$$S_{xo} = \frac{1}{\phi_T} \frac{t_{p0} - t_{pma}}{t_{pw0} - t_{pma}} = \frac{\phi_{EPT}}{\phi_T} \quad \text{.....(15.12)}$$

Spontaneous Potential

$$E_{Total} = E_{lj} + E_m = SP \quad \text{.....(9.1)}$$

$$SP = -K \log\left(R_{mfe}/R_{we}\right) \quad \text{.....(9.9)}$$

$$SP = -K \log(R_{mf}/R_w) \quad \text{.....(26.19)}$$

$$-SP = K \log\left[\left(R_{xo}/R_t\right) S_w^{5/8}\right] \quad \text{.....(22.6)}$$

$$K = \left(T + 505\right)/8 \quad \text{.....(9.3)}$$

$$R_{mfe}/R_{we} = 10^{-SP/K} \quad \text{.....(9.13)}$$

Capillarity

$$h = P_{c\text{Reservoir}} / \left(\rho_w - \rho_{hy}\right)_{\text{Reservoir}} \quad \text{.....(27.5)}$$

$$P_c = 2T \cos\theta / r \quad \text{.....(27.6)}$$

$$h = 2.3 P_c / \Delta\rho \quad \text{.....(27.7)}$$

$$r = c \times 2T \cos\theta / P_c \quad \text{.....(27.9)}$$

$$2\pi r T \cos\theta = \left(\rho_w - \rho_a\right) \pi r^2 \quad \text{.....(6.6)}$$

$$h = \frac{2T \cos\theta}{r\left(\rho_w - \rho_a\right)} \quad \text{.....(6.7)}$$

Permeability, Relative Permeability, and Fluid Flow

NMR

$$k = \left(\frac{\phi}{C}\right)^4 \left(\frac{FFI}{BVI}\right)^2 \quad \text{.....Coates .....(19.1)}$$

$$k = a\phi^4 T_{2gm}^2 \quad \text{.....CMR .....(19.6)}$$

Conventional Log Analysis

$$k = \frac{8581\phi^{4.4}}{S_{wi}^2} \quad \text{.....(Timur 1968) .....(6.17)}$$

$$k = \left(\frac{250\phi^3}{S_{wi}}\right)^2 \quad \text{.....(Oils—Wyllie and Rose 1950). .....(6.18)}$$

$$k = \left(\frac{79\phi^3}{S_{wi}}\right)^2 \quad \text{.....(Dry Gas—Wyllie and Rose 1950) .....(6.19)}$$

$$k = \frac{10000\phi^{4.5}}{S_{wi}^2} \quad \text{(Schlumberger 2009)} \quad (6.20)$$

$$k = \phi\left\{\frac{122}{h\left(\rho_w - \rho_o\right)}\right\}^2 \quad \text{(Oil/Water—Raymer and Freeman 1984)} \quad (6.21)$$

$$k = \phi\left\{\frac{140}{h\left(\rho_w - \rho_g\right)}\right\}^2 \quad \text{(Gas/Water—Raymer and Freeman 1984)} \quad (6.22)$$

Transition-Zone Resistivity Gradient

$$k = c\left(\frac{2.3a}{\left(\rho_w - \rho_h\right)}\right)^2 \quad (6.23)$$

$$a = \frac{\Delta R}{\Delta D} \times \frac{1}{R_o} \quad (6.24)$$

Absolute and Relative Permeability

$$k_o = \frac{q_o \mu_o L}{\Delta p A} \quad \text{and} \quad k_w = \frac{q_w \mu w L}{\Delta p A} \quad (6.8)$$

$$k_{ro} = k_o / k \quad \text{and} \quad k_{rw} = k_w / k \quad (6.9)$$

$$k_{ro} = \left(\frac{0.9 - S_w}{0.9 - S_{wi}}\right)^2 \quad \text{and} \quad k_{rw} = \left(\frac{S_w - S_{wi}}{1 - S_{wi}}\right)^3 \quad (6.10)$$

$$q_o = k_o \Delta p A / \mu_o L \quad (6.11)$$

$$q_w = k_w \Delta p A / \mu_w L \quad (6.12)$$

Water Cut and Movable Oil

$$WOR = k_w \mu_o / k_o \mu_w \quad (6.13)$$

$$WC = q_w / \left(q_w + q_o\right) \quad (6.14)$$

$$WC = WOR / \left(1 + WOR\right) \quad (6.15)$$

$$WC = WOR\beta_o / \left(\beta_w + WOR\beta_o\right) \quad (6.16)$$

$$\%OOIP \text{ moved} = \frac{S_{xo} - S_w}{1 - S_w} \times 100 \quad (14.4)$$

Volumetrics

HCPV and Oil in Place

$$HCPV = \phi\left(1 - S_w\right) \quad (8.1)$$

$$OIP = \Sigma\phi\left(1 - S_w\right)hA \quad (8.2)$$

$$\frac{\Sigma\phi(1-S_w)h}{\Sigma h} \quad (8.3)$$

$$N = C\Sigma\phi(1-S_w)hAr/B \quad (8.4)$$

Recovery Factors

$$r_{WD} = 54.9\left[\phi(1-S_w)/B_o\right]^a\left(k\mu_w/\mu_o\right)^b\left(S_w\right)^c\left(p_i/p_a\right)^d \quad (8.5)$$

$$r_{SG} = 41.82\left[\phi(1-S_w)/B_{ob}\right]^a\left(k/\mu_{ob}\right)^b\left(S_w\right)^c\left(p_b/p_a\right)^d \quad (8.6)$$

Bed/Well Geometry

$$TST = MT\ \mathrm{Cos}\,\alpha \quad (8.7)$$

$$TST = MT\mathrm{Cos}\beta \quad (8.8)$$

$$TST = MTCos(\alpha+\beta) \quad (8.9)$$

$$TST = MT\left[\mathrm{Cos}\alpha\,\mathrm{Cos}\beta - \sin\alpha\,\mathrm{Sin}\beta\,\mathrm{Cos}\,(HAZ-DAZ)\right] \quad (8.13)$$

$$TVT = \frac{TST}{\mathrm{Cos}\beta} = \frac{MT\mathrm{Cos}(\alpha+\beta)}{\mathrm{Cos}\beta} \quad (8.10)$$

$$TVT = MT\left[\mathrm{Cos}\alpha - \mathrm{Sin}\alpha\,\mathrm{Tan}\beta\,\mathrm{Cos}\,(HAZ-DAZ)\right] \quad (8.15)$$

V_{shale}/V_{clay} Estimation

From SP

$$\left(V_{sh}\right)_{SP} = \left(SP - SP_{\mathrm{sand}}\right)/\left(SP_{\mathrm{shale}} - SP_{\mathrm{sand}}\right) \quad (9.15)$$

From Gamma Ray

$$V_{sh} = \frac{GR - GR_{cl}}{GR_{sh} - GR_{cl}} \quad (28.27)$$

$$\text{Gamma Ray Index } (X) = \frac{GR - GR_{\min}}{GR_{\max} - GR_{\min}} \quad (10.1)$$

$$\text{Linear } V_{\mathrm{clay}} = X \quad (10.2)$$

$$\text{Clavier } V_{\mathrm{clay}} = 1.7 - \sqrt{3.38 - \left(X+0.7\right)^2} \quad (10.3)$$

$$\text{Steiber } V_{\mathrm{clay}} = \frac{0.5X}{(1.5-X)} \quad (10.4)$$

$$\text{Bateman } V_{\mathrm{clay}} = X^{(X+GR\ \mathrm{Factor})} \quad (10.5)$$

From Neutron-Density

$$V_{sh} = \frac{\left(\phi_N - \phi_D\right)}{\left(\phi_{Nsh} - \phi_{Dsh}\right)} \quad (23.15)$$

Resistivity

$$\text{conductivity} = \frac{1}{\text{resistivity}} \quad (11.2)$$

$$T_{\text{form}} = T_{\text{surf}} + \text{Depth} \times \text{Temperature Gradient} \quad (9.10)$$

$$R_2 = R_1 \frac{(T_1 + 7)}{(T_2 + 7)} \quad (9.11)$$

$$R_{mf} = \left\{ R_m^{\,1.065} \right\} \times 10^{\left[(9-W)/13\right]} \quad (9.4)$$

$$R_{mc} = \left\{ R_m^{\,0.88} \right\} \times 10^{\left[(W-10.4)/7.6\right]} \quad (9.5)$$

$$R_{mf} = 0.75 \times R_m \quad (9.6)$$

$$R_{mc} = 1.5 \times R_m \quad (9.7)$$

$$\frac{1}{R_{ID}} = \frac{G}{R_{xo}} + \frac{1-G}{R_t} \quad (12.5)$$

$$\frac{1}{R_{IM}} = \frac{G'}{R_{xo}} + \frac{1-G'}{R_t} \quad (12.8)$$

$$R_{SFL} = JR_{xo} + (1-J)R_t \quad (12.9)$$

$$R_{LL} = JR_{xo} + (1-J)R_t \quad (13.5)$$

Porosity

Clean Formations

$$\rho_b = \rho_{ma}(1-\phi) + \rho_f \phi \quad (17.9)$$

$$\phi_D = \frac{\rho_{ma} - \rho_b}{\rho_{ma} - \rho_f} \quad (17.10)$$

$$\Delta t\,(\mu\text{s/ft}) = 10^6/V, \text{ in ft/s} \quad (16.5)$$

$$\phi_S = \frac{\Delta t - \Delta t_{ma}}{\Delta t_f - \Delta t_{ma}} \quad (23.3)$$

$$\phi_S = \frac{\Delta t - \Delta t_{ma}}{\Delta tf - \Delta t_{ma}} \times \frac{1}{B_{cp}} \quad (23.4)$$

$$B_{cp} = \Delta t_{sh}/100 \quad (16.7)$$

$$\phi_S = \frac{1}{\rho_{ma} - \rho_f}\left(1 - \frac{\Delta t_{ma}}{\Delta t}\right) \quad (16.8)$$

$$\phi_X = (\phi_{NLM} + \phi_{DLM})/2 \quad (23.1)$$

$$\phi_{EPT} = \frac{t_{po} - t_{pma}}{t_{wo} - t_{pma}} \quad (15.11)$$

Shaly Formations

$$\rho = (1 - V_{sh} - \phi)\rho_{ma} + V_{sh}\rho_{sh} + \phi\rho_f \quad \text{(17.11)}$$

$$\phi = \frac{(\rho_{ma} - \rho_b) - V_{sh}(\rho_{ma} - \rho_{sh})}{(\rho_{ma} - \rho_f)} \quad \text{(17.12)}$$

$$\phi = \phi_D - V_{sh}\phi_{D_{sh}} \quad \text{(17.13)}$$

$$\phi_N = \phi_T + V_{sh}\phi_{Nsh} \quad \text{(18.5)}$$

$$\phi_e = \phi_N - V_{sh}\phi_{Nsh} \quad \text{(18.6)}$$

$$\phi_P = \phi + (1 - \phi - V_{sh})\phi_{Pma} + V_{sh}\phi_{Psh} \quad \text{(23.6)}$$

$$\phi_P = \phi + V_{sh}\phi_{Psh} \quad \text{(23.7)}$$

$$\phi = \phi_P - V_{sh}\phi_{Psh} \quad \text{(23.8)}$$

$$\phi = \phi_{D\log} - V_{sh}\phi_{Dsh} \quad \text{(23.9)}$$

$$\phi = \phi_{N\log} - V_{sh}\,\phi_{Nsh} \quad \text{(23.11)}$$

$$\phi = \phi_{S\log} - V_{sh}\,\phi_{Ssh} \quad \text{(23.12)}$$

$$\phi_D = \phi + V_{sh}\phi_{Dsh} \quad \text{and} \quad \phi_N = \phi + V_{sh}\phi_{Nsh} \quad \text{(23.13)}$$

$$\phi = \frac{\phi_{Nsh}\phi_D - \phi_{Dsh}\phi_N}{\phi_{Nsh} - \phi_{Dsh}} \quad \text{(23.14)}$$

Gas-Bearing Formations

$$\phi_G = \left(\frac{\phi_N{}^2 + \phi_D{}^2}{2}\right)^{1/2} \quad \text{(23.23)}$$

$$\phi_{CNL} = J(\phi_{CNL})_{\text{invaded}} + (1 - J)(\phi_{CNL})_{\text{uninvaded}} \quad \text{(18.1)}$$

$$\phi_N = \phi_{Nma}(1 - \phi) + \phi_{Nmf}S_{xo} + \phi_{Nhy}\phi(1 - S_{xo}) \quad \text{(18.2)}$$

$$\phi = \frac{\phi_N - \phi_{Nma}}{\phi_{Nhy} - \phi_{Nma} + S_{xo}(\phi_{Nmf} - \phi_{Nhy})} \quad \text{(18.3)}$$

$$\phi = \phi_N / S_{xo} \quad \text{(18.4)}$$

$$\phi_{Nhy} = 2.2\rho_{hy} - 1.2(\rho_{hy})^2 \quad \text{and} \quad \phi_{Dhy} = 1.7 - 0.7\rho_{hy} \quad \text{(23.16)}$$

$$\phi_D = \phi_T + \phi_{Dhy}(1 - S_{xo}) \quad \text{(23.17)}$$

$$\phi_T = \frac{\phi_D}{S_{xo} + \phi_{Dhy}(1 - S_{xo})} \quad \text{(23.18)}$$

$$\phi_T = 0.8\,\phi_D \quad (23.21)$$

$$\phi_T = 1.25\,\phi_N \quad (23.22)$$

Vuggy Formations

$$\phi_D = \phi_T = \phi_{\text{matrix}} + \phi_{\text{secondary}} \quad (22.12)$$

$$\phi_S = \phi_{\text{matrix}} \quad (22.13)$$

Hydrocarbon Typing

$$\rho_{hy} = 1 - \left[\frac{\phi_D - \phi_T}{0.7\left(1 - S_{xo}\right)\phi_T} \right] \quad (14.5)$$

R_w

$$R_w = R_o/F = R_o\phi^m/a \quad (7.3)$$

$$R_w = R_t S_w/F \quad (25.2)$$

$$R_{wa} = \phi^m R_t/a \quad (25.5)$$

$$R_w = R_{mf}\left(R_t/R_{xo}\right) \quad (25.11)$$

Porosity-Resistivity Crossplots

Hingle

$$\sqrt{\frac{1}{R_t}} = \phi S_w \sqrt{\frac{1}{R_w}} \quad (26.22)$$

Pickett

$$n\log S_w = \log a + \log R_w - m\log\phi - \log R_t \quad (25.14)$$

F-Overlay

$$n\log S_w = \log F + \log R_w - \log R_t \quad (25.16)$$

Lithology

M and N

$$M = \frac{\Delta t_f - \Delta t}{\left(\rho_b - \rho_f\right)\times 100} \quad (24.1)$$

$$N = \frac{\left(\phi_{Nf} - \phi_N\right)}{\left(\rho_b - \rho_f\right)} \quad (24.2)$$

MID Plot

$$\rho_{maa} = \frac{\rho_b - \phi_x \times \rho_f}{1 - \phi_x} \quad (24.4)$$

$$\Delta t_{maa} = \frac{\Delta t - \phi_x \times \Delta t_f}{1 - \phi_x} \quad (24.5)$$

$$U_{maa} = \frac{P_e \times \rho_b}{1 - \phi_x} \quad (24.11)$$

Core Analysis

$$V_B = V_G + V_P \quad (27.1)$$

$$\phi = V_P / V_B \quad (27.2)$$

$$\phi = (V_B - V_G) / V_B \quad \text{or} \quad \phi = V_P / (V_G + V_P) \quad (27.3)$$

$$k = q\mu L / A\Delta p \quad (27.4)$$

Shaly Sands

Laminated Model

$$\phi_D = V_{\text{lam}}\phi_{Dsh} + (1 - V_{\text{lam}})\phi_e \quad (28.1)$$

$$\phi_N = V_{\text{lam}}\phi_{Nsh} + (1 - V_{\text{lam}})\phi_e \quad (28.2)$$

$$\phi_e = \frac{\phi_{Nsh}\phi_D - \phi_{Dsh}\phi_N}{(\phi_{Nsh} - \phi_{Dsh}) - (\phi_N - \phi_D)} \quad (28.3)$$

$$V_{\text{lam}} = \frac{\phi_N - \phi_D}{\phi_{Nsh} - \phi_{Dsh}} \quad (28.4)$$

$$C_t = C_{\text{sand}}(1 - V_{\text{lam}}) + C_{sh}V_{\text{lam}} \quad (28.5)$$

$$C_{\text{sand}} = \frac{\phi_e^m S_w^n}{aR_w} \quad \text{and} \quad C_{sh} = \frac{1}{R_{sh}} \quad (28.6)$$

$$\frac{1}{R_t} = \frac{(1 - V_{\text{lam}})\phi_e^m S_w^n}{aR_w} + \frac{V_{\text{lam}}}{R_{sh}} \quad (28.7)$$

$$S_w^n = \left[\frac{1}{R_t} - \frac{V_{\text{lam}}}{R_{sh}}\right] \frac{aR_w}{\phi_e^m (1 - V_{\text{lam}})} \quad (28.8)$$

$$HCPV = \phi_e (1 - S_w)(1 - V_{\text{lam}})h \quad (28.9)$$

Dispersed-Clay Model

$$\phi_D = \phi_e + V_{\text{dis}}\phi_{Dsh} \quad (28.10)$$

$$\phi_N = \phi_e + V_{\text{dis}}\phi_{Nsh} \quad (28.11)$$

$$\phi_e = \frac{\phi_{Nsh}\phi_D - \phi_{Dsh}\phi_N}{\phi_{Nsh} - \phi_{Dsh}}, \quad V_{dis} = \frac{\phi_N - \phi_D}{\phi_{Nsh} - \phi_{Dsh}} \quad (28.12)$$

$$C_T = \frac{\phi_T{}^2 S_{wT}{}^2}{aR_w} + \frac{\phi_T S_{wT} V_{\text{dis}}}{a}\left(\frac{1}{R_{dis}} - \frac{1}{R_w}\right) \quad (28.13)$$

$$S_{we} = 1 - \frac{\phi_T}{\phi_e}\left(1 - S_{wT}\right) \quad (28.14)$$

Structural-Shale Model

$$\phi_D = \phi_e + \left(1 - \phi_e\right) V_{sh} \phi_{Dsh} \quad (28.15)$$

$$\phi_N = \phi_e + \left(1 - \phi_e\right) V_{sh} \phi_{Nsh} \quad (28.16)$$

$$\phi_e = \frac{\phi_D \phi_{Nsh} - \phi_N \phi_{Dsh}}{\phi_{Nsh} - \phi_{Dsh}} \quad (28.17)$$

$$V_{str} = \frac{\phi_N - \phi_D}{\phi_{Nsh}\left(1 - \phi_D\right) - \phi_{Dsh}\left(1 - \phi_N\right)} \quad (28.18)$$

$$C_t = \frac{\phi_e^m S_w^n}{aR_w} + \frac{V_{str}}{R_{sh}} \quad (28.19)$$

$$S_w^n = \left(\frac{1}{R_t} - \frac{V_{str}}{R_{sh}}\right) \frac{aR_w}{\phi_e^m} \quad (28.20)$$

Total-Shale Model

$$\frac{1}{R_t} = \frac{\phi_e^m S_w^n}{aR_w\left(1 - V_{sh}\right)} + \frac{V_{sh} S_w}{R_{sh}} \quad \left(\text{modified total shale}\right) \quad (28.21)$$

Electrochemical Model

$$\frac{1}{R_t} = \frac{S_w^2}{F^* \times R_w} + \frac{BQ_v S_w}{F^*} \quad (28.22)$$

$$Q_v = \frac{CEC\left(1 - \phi\right)\rho_{ma}}{100\phi} \quad (28.23)$$

$$C_t = \frac{C_w S_w^2}{F_o} + \frac{\left(C_{wB} - C_w\right) V_Q Q_v S_w}{F_o} \quad (28.26)$$

Dual-Water Model

$$\phi_T = \frac{\phi_N + \phi_D}{2} \quad (28.32)$$

$$\phi_e = \frac{\phi_D \phi_{Nsh} - \phi_N \phi_{Dsh}}{\phi_{Nsh} - \phi_{Dsh}} \quad (28.30)$$

$$V_{sh} = \frac{\phi_N - \phi_D}{\phi_{Nsh} - \phi_{Dsh}} \quad (28.31)$$

$$\frac{1}{R_{\text{fluid mixture}}} = \frac{\left(1 - S_{wB}\right)}{R_{wf}} + \frac{S_{wB}}{R_{wB}} \quad (28.24)$$

$$R_o = \frac{R_{wF} R_{wB}}{\left[R_{wB} + S_{wB}\left(R_{wF} - R_{wB}\right)\phi_T{}^2\right]} \quad (28.25)$$

$$S_{wT} = \left[\frac{R_w}{R_t \phi_T^2} - \frac{R_w}{R_{wB}} \left(1 - \frac{\phi_e}{\phi_T} \right)^2 \right]^{1/2} \quad \ldots\ldots (28.33)$$

$$S_{we} = 1 - \frac{\phi_T}{\phi_e} \left(1 - S_{wT} \right) \quad \ldots\ldots (28.34)$$

Unconventional Reservoirs

$$Wh = \left(\frac{C2 + C3 + C4 + C5}{C1 + C2 + C3 + C4 + C5} \right) \times 100 \quad \ldots\ldots (30.1)$$

$$Bh = \left(\frac{C1 + C2}{C3 + C4 + C5} \right) \quad \ldots\ldots (30.2)$$

$$S_w^n = \frac{a}{\phi^m} \times \frac{R_w}{R_t} \quad \ldots\ldots (30.3)$$

$$\Delta \log R = \log_{10} \left(R / R_{\text{baseline}} \right) + 0.02 \times \left(\Delta t - \Delta t_{\text{baseline}} \right) \quad \ldots\ldots (30.4)$$

$$TOC = \left(\Delta \log R \right) \times 10^{(2.297 - 0.1688 \times LOM)} \quad \ldots\ldots (30.5)$$

$$TOC = \left(\Delta \log R \right) \times 10^{(2.3 - LOM/6)} \quad \ldots\ldots (30.6)$$

$$\Delta \log R = \log 10 \left(R / R_{\text{baseline}} \right) - 2.5 \times \left(\rho b - \rho_{\text{baseline}} \right) \quad \ldots\ldots (30.7)$$

$$\Delta \log R = \log 10 \left(R / R_{\text{baseline}} \right) + 4 \times \left(\phi N - \phi N_{\text{baseline}} \right) \quad \ldots\ldots (30.8)$$

$$TOC = \Delta t \times 0.343 - 36$$
$$TOC = 96 - 40 \times \rho b \quad \ldots\ldots (30.9)$$
$$TOC = \phi N \times 0.7 - 20$$

$$V_{\text{matrix}} + V_{\text{water}} + V_{\text{hydrocarbon}} = 1 \quad or \quad (1 - \phi) + \phi S_w + \phi (1 - S_w) = 1 \quad \ldots\ldots (30.10)$$

$$q = q_0 \, e \left(\frac{t}{\tau} \right)^n \quad \ldots\ldots (30.11)$$

$$GIP = \phi (1 - S_w) \, h \, A \times \left(\frac{1}{B_g} \right) \quad \ldots\ldots (30.12)$$

$$\phi = \frac{\rho_{ma} - \rho_b}{\rho_{ma} - \rho_{fl}} \quad \ldots\ldots (30.13)$$

$$S_w = \sqrt[n]{\left(\frac{a}{\phi^m} \times \frac{R_w}{R_t} \right)} \quad \ldots\ldots (30.14)$$

$$\phi = 10^{-\left(\frac{\text{Depth}}{a} + b \right)} \quad \ldots\ldots (30.15)$$

$$\log_{10} S_{wi} = A - B \log_{10} \phi \quad \ldots\ldots (30.16)$$

$$\log_{10} k = \frac{C - \log_{10} S_{wi}}{D} \quad \ldots\ldots (30.17)$$

$$\rho_b = \rho_{ma}(1 - V_{TOC}) + \rho_{TOC} V_{TOC} + \rho_{fl}\phi \quad (30.18)$$

$$\phi = \frac{(\rho_{ma} - \rho_b) - V_{TOC}(\rho_{ma} - \rho_{TOC})}{(\rho_{ma} - \rho_{fl})} \quad (30.19)$$

$$V_{TOC} = \frac{\rho_{ma} - \rho_{gr}}{\rho_{ma} - \rho_{TOC}} \quad (30.20)$$

$$\rho_{gr} = \frac{\rho_b - \rho_{fl}\,\phi}{(1 - \phi)} \quad (30.21)$$

$$GIP = 1.464 \times 10^{-6}\, h\, \rho\, V \quad (30.22)$$

$$\text{Pore Pressure (psi)} = \text{Depth (ft)} \times 0.43 \quad (30.23)$$

$$\text{Overburden Stress (psi)} = \text{Depth (ft)} \times 1.1 \quad (30.24)$$

$$FCP = \alpha P_p + \{\mu/(1-\mu)\} \times \{P_o - \alpha P_p\} \quad (30.25)$$

$$\alpha = 1 - (C_{ma}/C_B) \quad (30.26)$$

$$\text{Brittleness Coefficient} = 50 \times \left[\left(\frac{E-1}{7}\right) + \left(\frac{0.4-\mu}{0.25}\right)\right] \quad (30.27)$$

$$PIF = \frac{L}{h}\sqrt{\frac{k_v}{k_h}} \quad (30.28)$$

Formation Tester

$$\text{Fluid Density} = \text{Pressure Gradient (psi/ft)} \times 2.3072 \quad (31.14)$$

AUTHOR INDEX

A
Alger, R.P., 333
Allaud, L., 204, 205
Aly, A., 548
Ambrose, R.J., 572–574
Anderson, B., 227, 506
Archer, D.L., 111
Archie, G.E., 116–119, 123

B
Badruzzaman, A., 322
Bair, F.K., 322
Barber, T., 227, 506
Barnes, S., 322
Bassiouni, Z., 166, 168, 170
Bateman, R.M., 6, 87, 121, 142, 144, 145, 166, 169, 299, 337, 506
Boatman, E.M., 112
Bonner, S., 62, 65
Borghi, M., 355
Bos, M.R.E., 518
Brown, H.D., 300
Burgess, T., 65
Burke, J.A., 526
Byrnes, A.P., 575, 578

C
Cassa, M.R., 549, 551
Chevalier, P., 191
Clark, B., 65
Cluff, R.M., 575, 578
Coates, G.R., 342–345, 347, 349, 350, 354, 356–358
Combaz, A., 191, 192
Cox, J.T., 526
Cox, J.W., 172, 452, 453
Creaney, S., 565–569
Cubitt, J.H., 549
Curtis, M.R., 526

D
Diaz-Campos, M., 572–574
Dunlap, H.F., 160, 161

E
Eck, M.E., 408
Edmundson, H., 536
England, W.A., 549
Evans, C.J., 261, 262

F
Fertl, W.H., 191, 196, 197, 199–201
Fitzgerald, D.D., 381
Fraser, H.J., 104
Fredette, M., 62
Freeman, P.M., 114
Frondel, C., 198

G
Gardner, G.H.F., 286, 289
Gardner, L.W., 419
Gaymard, R., 417
Gilchrist, W.A., 332
Gilreath, J.A., 382
Goetz, J.F., 106, 336
Graton, L.C., 104
Gregory, A.R., 286, 289, 419
Grigalva, V.E., 300
Grimaldi, P., 234, 235, 243
Grosso, D.S., 61
Gurvis, R.L., 44

H
Haley, R.A., 516, 517
Hartman, R.C., 572–574
Harvey, A.H., 112
Hassan, M., 191, 192
Haworth, J.H., 44, 554
Herrick, D.C., 512
Hill, R.J., 548
Honarpour, M., 112
Hossin, A., 191, 192
Hoyle, W.R., 530
Hunt, J.M., 551

J
Jarvie, D.M., 548, 551, 590
Johnson, R., 261, 262
Juhász, I., 511

K
Kennedy, W.D., 512
Kidwell, C.M., 516, 517
Klinkenberg, L.J., 480, 481
Knox, C.C., 87
Koederitz, L.F., 112
Konen, C.E., 144, 145, 166, 169
Kulla, J.B., 565–569
Kunz, K.S., 207, 208

L
Larter, S., 549
Lee, M.W., 512
Letton, W., 283, 284
Leveridge, R., 227, 506
Litsey, L., 600, 601
Little, T.M., 283, 284
Locke, S., 333
Logar, J.F., 106, 336
Lovell, J., 62
Lyne, A., 355

M
Maness, M., 492
Marett, G., 191

Martin, M., 204, 205
Mason, K.L., 294
Moldowan, J.M., 551
Molina, N.N., 112
Montaron, B., 512
Moore, J.E., 500
Moran, J.H., 207, 208
Morris, C.F., 283, 284
Mullen, M., 581
Mullins, O.C., 493, 610
Muskat, M., 141

N
Nagel, W.A., 333
Neinast, G.S., 87
Nettle, R.L., 112

P
Park, A., 96, 97
Passey, Q.R., 565–569
Patchett, J.G, 502
Peters, K.E., 549, 551
Petre, E., 581
Pirson, S.J., 112
Pittman, E.D., 490
Pollastro, R.M., 548
Porrera, F., 355
Poston, S.W., 141
Poupon, A., 234, 235, 243, 417, 530
Powell, D.E., 408
Prammer, M.G., 342–345, 347, 349, 350, 354, 356–358
Price, J.G.W., 492
Prins, W.J., 106, 336

R
Radar, D., 61
Ramsey, L., 548
Raymer, L.L., 114, 172, 300, 452, 453, 536
Raynal, J.C., 61
Raza, S.H., 111
Rickman, R., 581
Rose, W.D., 114, 115

S
Schlumberger, C., 231, 232, 237–240, 242, 244, 245
Schmidt, A.W., 530
Segesman, F., 172
Sellens, M.P., 44, 554
Shehata, A., 548
Silva, P., 166, 168, 170
Smits, L.J.M., 510
Smolen, J., 600, 601
Souhaite, P., 191
Stapp, W.L., 191
Stieber, S.J., 188
Suau, J., 234, 235, 243

T
Theys, P., 87
Thomas, E.C., 188
Thomas, J.B., 490
Timur, A., 114
Tittman, J., 182
Treiber, L.E., 111

V
Vaello, D.B., 191
Vajnar, E.A., 516, 517

W
Waxman, M.H., 510
Welton, J.E., 488, 489
Whittaker, A., 554
Williams, H., 160, 161
Worthington, P.F., 498
Wyllie, M.R.J., 114, 115, 286, 289, 419

X
Xiao, L., 342–345, 347, 349, 350, 354, 356–358

SUBJECT INDEX

A

acoustic imaging, 378–379
acoustic logging. *See* sonic logging
anisotropy
  lower Barnett shale, 586, 587
  shear-slowness measurements, 585, 586
  types, 585
  upper Barnett shale, 585, 586
anti-Delaware effect, 242, 244
API gamma ray standard, 180, 184
API gravity of oil, 43–44
Archie's law, 572
array induction tool (AIT), 22, 224–225
array laterolog device, 25, 231
array sonic tools
  coherence function, contour plot, 281, 284
  recordings, 281, 283
  slowness, 282, 285

B

bed resolution, microresistivity measurements, 253–256
BHC tools. *See* borehole-compensated (BHC) tools
bismuth germanate (BGO), 535
Bode's law, 409, 410
borehole-compensated (BHC) tools, 277–279
borehole-compensation (BHC) array, 261
borehole environment
  nomenclature for zones, 79, 80
  radial resistivity profile, 81
  symbols, 79, 80
borehole gravimeters, 14
borehole imaging. *See* dipmeter and borehole imaging
bulk-volume model
  clean gas-bearing formation, 316
  movable and residual oil, 402, 403
  porous rock formation, 312
  shaly formation, 315
butterfly chart, laterologs, 239–240

C

calcimetry, 44
calculator algorithms, 397
calibration
  compensated neutron log (CNL), 338
  formation density log, 321–322
  gamma ray detectors, 180, 182
  induction logging, 216
  measurements on drillpipe (MOD), 66–67
  microresistivity measurements, 258
  nuclear magnetic resonance (NMR), 357, 358
caliper logs, 14
carbon/oxygen logging, 13
catalytic combustion detector (CCD), 41
cathodoluminescence, 488–489, 491
cation-exchange capacity (CEC), 493
CBL. *See* cement bond log (CBL)
cementation exponent (*m*)
  derivation, 268–270
  finding methods, 270–271
cement bond log (CBL)
  CBL-VDL display, 299, 300
  CBL-VDL tool, 296, 299
  receiver output signal, 299
Chaveroo method
  definition, 523
  example of, 526
coalbed methane (CBM)
  cavity completion, 586, 588
  horizontal completion, 587
  openhole completion, 586, 588
compaction effects, 289–291
compatibly scaled overlays
  density-sonic
    overlay
    fracture determination, 405–407
    matrix and fracture porosity, 404–405, 407
  EPT-porosity overlay, 406, 408
  F overlay, 400–402
  movable-oil plot
    bulk-volume model, 402, 403
    logarithmic, 401–403
    movable and residual hydrocarbons, 402, 404
    stages, 401–402
  neutron-density overlay
    limestone presentation, 404, 406
    sandstone presentation, 402, 404, 405
    types of, 402
  SP with R_{xo}/R_t, 398–400
  theory, 397
compensated neutron log (CNL)
  borehole compensation, 330, 332
  calibration and quality control, 338
  depth of investigation, 334, 335
  dolomite and sandstone porosity values, 330–331, 333–334
  environmental corrections, 334
  example of, 331
  limestone porosity values, 330–331, 333–334
  matrix settings and lithology effects, 334–336
  neutron porosity index, 329–330
  thermal neutron flux, 330, 332
complex lithology
  Chaveroo log processing, 525, 526
  crossplot-based systems, 528–531
  elemental logging tools, 533–536
  martini problem, 523
  material-balance equation, 525
  neural networks, 533
  objectives, 523
  overdetermined systems, 525–528
  practical quick-look methods, 531–532
  properties
    carbonates, 540–541
    clays, 542–543

evaporites and coals, 539
feldspars, 540–541
micas, 542–543
oxidates, 540–541
phosphates, 540–541
silicates, 540–541
zeolites, 542–543
reservoir rocks and minerals, 536
computerized logging truck, 71, 74
computerized logging units
logging engineers console, 84
log presentations and calibrations, 85–87
conductivity, 204
core analysis
capillary pressure
contact angle and interfacial tension, 485–486
pore-throat distribution, 487
cathodoluminescence, 488–489, 491
vs. CMR porosity and permeability, 354
CT scanning, 489, 491
Dean-Stark distillation process, 483–484
electrical measurements, 492–493
gas saturation, 483
hydrocarbon analysis, 489, 492
NMR, 492
oil saturation, 483
overburden pressure, 485
permeability, 480–482
porosity
Boyle's law method, 479–480
conventional vs. percussion sidewall core porosities, 480, 481
fluids method, summation of, 479
grain-density methods, 480
QEMSCAN system, 489, 491
relative permeability, 482–483
sample selection and preparation, 478–479
SEM and focused ion-beam SEM, 488–490
sensitivity tests, 483
thin sections, 487–488
water saturation, 461, 483
a and *m,* determination of, 466
n, determination of, 464
wettability tests, 482–483
X-ray diffraction, 488
core-sample analysis, 556
coring
basics, 6–7
conventional core, 96–97
coring fluid
changes in saturation, 98–99
effects of, 97–98
recommended coring fluids, 98
special core handling, 99–100
wireline coring
percussion sidewall cores, 93–94
rotary sidewall coring, 94–96
crossplots
extrapolations, 409, 410
height vs. weight for animals, 408, 409
neutron-density frequency, 410, 411
permeability vs. porosity, 408–409
R_w determination
linear crossplots, 456–458
logarithmic plots, 457, 459
theory, 408
water saturation, 470–473
Z plot, 410–412
cycle skipping and noise, 284–285
cylindrical buildup, 606–607

D

Dean-Stark distillation process, 483–484
Delaware effect, 242, 243
Δt ratio
in micaceous sands, 291, 293
for rock types, 292, 294
travel-time correction factor, 292, 294
density tools, 13
detectors
calibration, mud logging, 41–42
gamma ray
calibration, 180, 182
Geiger-Mueller, 180
operating principle, 180
scintillation, 180, 183
dielectric constant, 259, 260
dielectric logging tools, 13
dielectric measurements
cementation exponent (*m*)
derivation, 268–270
finding methods, 270–271
electromagnetic propagation tools (EPT), 259
antenna configuration and signal paths, 261, 262
electromagnetic propagation signals, 261, 262
standard EPT log presentation, 261–263
interpretation methods, 264–266
multispacing, multifrequency dielectric tool
high-frequency dielectric tool (HFDT), 263–264
hydrocarbon zones, 264, 266
two-transmitter, eight-receiver antenna arrangement, 264, 265
physical principle, 259–261
wellsite interpretation
matrix propagation time determination, 268, 269
sonic porosity vs. EPT porosity, 267, 268
water and hydrocarbons, log readings for, 268, 269
dielectric permittivity, 260
dipmeter and borehole imaging
applications of, 362–363
characteristics, 363
computation principle of, 364, 366–367
computed log presentations
azimuth frequency diagrams, 367, 369
dip angle and azimuth, histogram of, 369
polar plots, 367, 370
SODA plots, 367, 368
stick plots, 368, 370
stratigraphic plots, 369, 371
tadpole plot, 368
definition
bed-dip magnitude, 361

correlation information, 361
dip angle, 362
dip azimuth, 362
orientation information, 361
drillpipe-conveyed imaging devices
density imaging, 380
resistivity imaging, 381
excessive tool rotation, 377
field presentation, 364, 365
four-arm dipmeter tool, 363
fracture finding, 375, 376
interpretation
buried bar, shale deposits, 374–375
channel cut and fill, 373–374
current bedding, 373, 374
dip patterns and color code, 370, 372
folded structure, 371, 372
normal fault, 371, 373
rules, 382–388
unconformity, 371, 373
openhole logging tool, 31
quality control, 375–376
reservoir geometry indicator, 14
wireline imaging tools
acoustic imaging, 378–379
electrical imaging, 377–378
tele-imaging, 379–380
dipole sonic tools, 282
dispersed-clay electrical model, 508
dispersed-clay physical model, 507
drillstem-testing objectives
Horner plot, 617, 619
mechanics, 617, 618
perspective, 619
planning, 618, 619
pressure recording, 617–619
principles, 617, 618
dual induction log, 19
dual laterolog resistivity log, 126, 128
dual laterolog (DLL) tools
anomalous behavior
anti-Delaware effect, 242, 244
Delaware effect, 242, 243
Groningen effect, 244
shoulder-bed corrections, 244–245
characteristic behavior, 240–241
current paths, 233, 234
equivalent circuit, 236
invasion correction chart, 239–241
openhole logging tools, 24
operation principle, 232, 234
pseudoradial geometric factor, 236, 237
radial distribution of resistivity, 233, 235
resistivity curves, 232, 233
dual-spacing epithermal neutron logs, 337

E

elastic constants, 274–275
elastic waves propagation, 273–274
electrical borehole imager, 34
electrical imaging, 377–378
electromagnetic propagation tools (EPT), 259
antenna configuration and signal paths, 261, 262
electromagnetic propagation signals, 261, 262
standard EPT log presentation, 261–263
estimation of uncertainty in volumetrics, and reserve, 149–150

F

first electric log, 203, 205
flame-ionization detector (FID), 41
fluid distribution in reservoir
capillary pressure curves, 109–110
capillary pressure effects, 108–109
capillary tube, 107–108
depositional environments, interrelationships of, 106
pore system, 108–109
in water-wet reservoir, 107
wettability and contact angle, 109–110
fluid sampling
monitoring sampled fluid, 609–611
multielement packers and probes, 609
focused electric logs, 209
formation density log
calibration, 321–322
compensated density log, 305, 306
density porosity, 312–315
depth of investigation, 317–318
dual-spacing device, 305, 307
electron density, 310–312
elements and minerals, photoelectric factors of, 324–325
gas effects, 315–317
litho-density tools
measurement theory, 318–320
P_e curve, 320–321
physical principle, 318, 319
mudcake compensation, 307, 309
operating principle
detector count rates vs. formation density measurements, 308
gamma ray mass absorption coefficient, 305, 307
mass absorption coefficient vs. gamma ray energy, 306, 308
near and far count rates, 308
safety, 322
shale effects, 314–315
formation evaluation
complex lithology (*see* complex lithology)
coring, 6–7
logging devices
auxiliary tools, 14
evolution, 9, 11–12
formation fluid content indicators, 11–13
porosity-lithology indicators, 13–14
reservoir geometry indicators, 14
logging while drilling (LWD), 7
log measurements, 5
measurements while drilling (MWD), 7
modern logging tools
combination tool strings, 9
components, 8, 9
logging terms, 9, 10
triple combo example, 9, 10

mud logging, 6
openlog logging, 7–8
orders of magnitude, 3–5
processes, 5–6
range of physical principles, 3, 4
roles of researchers, 3–5
shaly sands (*see* shaly sands)
testing, 7
unconventional reservoirs (*see* reservoirs, unconventional)
formation fluid content indicators, 11–13
F overlay
compatibly scaled overlays, 400–401
R_w determination, 457, 459
water saturation, 472

G

gamma ray
detectors
calibration, 180, 182
Geiger-Mueller, 180
operating principle, 180
scintillation, 180, 183
index, 186
logs
calibration, 180, 182
clay content estimation, 186, 188–189
vs. core gamma scan, 478–479
logging speed effects, 184, 185
perturbing effects, 185–187
presentation, 179, 183
time constant, 182–185
uses, 179
origin of, 179
quartz and clay solids, 188
radioactive disintegration series, 179, 181
spectral log
interpretation techniques, 191–194
schematic representation, 189, 191
spectroscopy, 189, 190
gamma ray neutron tools (GNT), 328
gas chromatography, 42–43
gas effects
formation density log, 315–317
neutron logs, 335–337
gas-in-place (GIP), 572
shale-gas reservoirs, 578–579
tight gas reservoirs, 577–578
generalized neutron-logging tool, 328
geochemistry
bitumen, 551
hydrocarbon generation, 550
kerogen, 550–551
organic matter, 549–550
TOC, 551
geomechanics
completions, 580, 581
fracture monitoring, 581–583
Groningen effect, 244

H

HCPV. *See* hydrocarbon pore volume (HCPV)
high-frequency dielectric tool (HFDT), 263–264
high-resolution induction, 21, 223–224
hot-wire gas detector, 41
Hunt-Raymer transform, 289–291
hydrocarbon density, 257
hydrocarbon effects, porosity, 424–426
hydrocarbon movability, 256–257
hydrocarbon pore volume (HCPV), 139–140, 461
hydrogen index (HI), 335–337

I

induction geometric factor (*G*), 220–221
induction logging
array induction tool (AIT), 224–225
basics, 213
bed-thickness corrections, 217–219
calibration, 216, 226–227
3D induction, 23, 226–227
environmental effects, 217, 218
high-resolution induction, 223–224
hole-size corrections, 220
induction current paths, 218–220
invasion effects, 220
dual-induction tornado chart, 222
induction geometric factor (*G*), 220–221
radial distribution of fluids, 221
phasor induction, 223
quick guide, 228–229
resistivity logging, 209
skin effect, 216–217
theory, two-coil induction log system, 215–216
tool development history, 214–215
types, 11
usage of logging devices, 214
integrated formation-evaluation plan
data analysis
environmental effects, 625
log calibration, 626
normalization, 625
numerical computations, 626
rock typing, 625–626
flowchart, 626, 627
log analysis workflow, 626, 627
monitoring, 624
objectives, 623
planning
drilling, 624
logging points, 624
logging suites, 624, 625
mud system, 624
interpretation techniques
calculation, 396
data gathering, 395
determining parameters, 395
Fractaland, coastline of, 392–393
model, picking of, 395
physical model
clean formations, 393
multimineral mixed lithologies, 394
sand/shale sequences, 393–394
unconventional reservoirs, 394
quality checks, 395
reconnoitering, 395

reporting conclusions, 396
tool size, effect of, 391–392

K
katharometer, 41

L
laminated-shale physical model, 503
Lamor frequency, 345
large-sample fill-up, 607–608
laterologs. *See also* dual laterolog (DLL) tools
borehole corrections, 237–239
butterfly chart, 239–240
early devices, 231, 232
invasion corrections, 237–239
types, 11
usage conditions, 231
liquid junction effect, 156, 157
litho-density log, 28
litho-density tools (LDTs)
measurement theory, 318–320
P_e curve, 320–321
physical principle, 318, 319
lithology/mineralogy
elements and minerals, photoelectric factors of, 444–445
indicators of, 429
litho-density log and photoelectric factor
index for common minerals, 437, 439
limitations, 442
U_{maa}-ρ_{maa} crossplots, 440, 442
wellsite computation, 441, 442
log analysis, 126, 128–130
MID plot, 435–438
M-N plot, 434–435
neutron-density crossplot
fresh-mud filtrates, 429–430
limestone scales, 431
salt-mud filtrates, 429, 430
neutron-sonic crossplot, 432–433
sonic-density crossplot, 433
log analysis
abbreviations, 18
dual laterolog resistivity log, 126, 128
generalized answer log, 126, 127
generalized log analysis
clay, shale, porosities, and clay-bound water, 135
logging sensors and seven-component formation model, 136
movable and bound fluids, 134–135
hydrocarbon type, 132
lithology, 126, 128–130
neutron-density porosity log, 126, 129
pay counting, 133–134
permeability, 134
porosity, 127, 129, 130
reservoir perspective, 125–126
water saturation
definition, 131
nomogram, saturation determination, 132, 133
log analysis equation
capillarity, 631
core analysis, 637
formation tester, 640
hydrocarbon typing, 636
lithology
M and N, 636
MID plot, 636–637
permeability, relative permeability, and fluid flow
absolute and relative permeability, 632
conventional log analysis, 631–632
NMR, 631
transition-zone resistivity gradient, 632
water cut and movable oil, 632
porosity
clean formations, 634
gas-bearing formations, 635–636
shaly formations, 635
vuggy formations, 636
porosity-resistivity crossplots
F-overlay, 636
Hingle, 636
Pickett, 636
resistivity, 634
R_w, 636
saturation
Archie, 630
EPT, 631
ratio–R_{wa}, 630
shaly sands
dispersed-clay model, 637–638
dual-water model, 638–639
electrochemical model, 638
laminated model, 637
structural-shale model, 638
total-shale model, 638
spontaneous potential, 631
unconventional reservoirs, 639–640
volumetrics
bed/well geometry, 633
HCPV and oil in place, 632–633
recovery factors, 633
V_{shale}/V_{clay} estimation
from gamma ray, 633
from neutron-density, 633
from SP, 633
logging cables
breaking cable at weakpoint, 76
differential pressure sticking, 76
fishing alternatives, 77
getting stuck, 75
head and the weakpoint, 74–75
monoconductor cables, 73
multiconductor cables, 73
logging devices
auxiliary tools, 14
evolution, 9, 11–12
formation fluid content indicators, 11–13
porosity-lithology indicators, 13–14
reservoir geometry indicators, 14
logging suite selection
depth, pressure, and temperature, 82
factors, 81
hole deviation, 82
hole size, 82

influence of mud program, 83–84
recommended general logging programs, 82–83
time to log, 84
logging tools
array induction, 22
array laterolog, 25
dielectric, 13
3D induction, 23
dipmeter, 31
dual induction log, 19
dual laterolog, 24
electrical borehole imager, 34
elemental, complex lithology, 533–536
high-resolution induction, 21
litho-density log, 28
LWD, 36
microlog, 26
modern tools
combination tool strings, 9
components, 8, 9
logging terms, 9, 10
triple combo example, 9, 10
natural gamma ray spectral log, 30
neutron-density, 27
neutron logs, 328
percussion sidewall coring, 32
phasor induction, 20
rotary sidewall coring, 33
sonic log, 29
ultrasonic borehole imager, 35
wireline logging operations
measure points and memorization distances, 77, 78
unmemorized and memorized logs, 77–79
logging trucks
components, 71
computerized logging truck, 71, 74
offshore units, 72, 74
logging while drilling (LWD)
azimuth neutron-density tool, 380
basics, 7
definition, 59
density or gamma ray sensors, 36
resistivity image, 381
log-quality control, 299
acceptance standards for logs, 88–90
necessity, 87–88
practical log quality checks, 88
long-spacing sonic (LSS) tools
vs. BHC, 278, 279
depth of investigation, 280
with four transit-time curves, 281, 282
long-spaced sonic “depth-derived” principle, 280–281
LSS tools. *See* long-spacing sonic (LSS) tools
LWD. *See* logging while drilling (LWD)

M

macerals, 592
material-balance equation, 525
matrix identification plot (MID), 435–438
measurements on drillpipe (MOD)
combination sensors, 66–67
common element, 59–60
data transmission methods and speeds, 61
downhole assembly, 61
future aspects, 68
morphing from wireline to MOD
measurements in extended-reach wells, 63
mud filtrate invasion effects, 62–63
sensor rotation, 62
petrophysical considerations, 63–64
for porosity and lithology, 65–66
quality control and sensor calibration, 66–67
for resistivity
EWR implementation, 64
gamma ray detection, 65
measurement of formation resistivity, 64–65
resistivity at bit (RAB), 64, 65
telemetry, 60–62
measurements while drilling (MWD)
basics, 7
definition, 59
membrane potential, 158
microfocused and microresistivity tools, 12–13
microlog (ML), 26, 250, 251
microresistivity measurements
bed resolution, 254, 256
calibration and quality control, 258
depth of investigation, 253–255
environmental corrections, 254, 255
hydrocarbon density, 257
S_{xo} and hydrocarbon movability, 256–257
tools
applications, 249–250
microlaterolog (MLL), 250–253
microlog (ML), 250, 251
microspherically focused log (MSFL), 252, 254
spherically focused log (SFL), 252–255
types and ratings, 249–250
uses, 249
microspherically focused log (MSFL), 232, 233, 235, 237, 252, 254
microwave devices, 209
MID. *See* matrix identification plot (MID)
M-N plot, 434–435
MOD. *See* measurements on drillpipe (MOD)
monoconductor cables, 73
movable-oil plot (MOP)
bulk-volume model, 402, 403
logarithmic, 401–403
movable and residual hydrocarbons, 402, 404
stages, 401–402
MRIL tool, centered
magnetic field, 349
multiple sensible volumes, 350
plan view of, 350
mud filtrate invasion effects, 62–63
mud logging
basics, 6
carbon-isotope analysis, 552–553
hydrocarbon type indicators, 513, 514
lithology
abbreviations, 49–57
symbols, 46–48
measurements
calcimetry, 44
detector calibration, 41–42

drilling process, 39–40
formation evaluation, 40–41
formation productivity estimation methods, 44–45
gas chromatography, 42–43
gas concentration, 41
hydrocarbon determination, 43–44
visual inspection, 42
written description, 43
multiconductor cables, 73
multispacing, multifrequency dielectric tool
high-frequency dielectric tool (HFDT), 263–264
hydrocarbon zones, 264, 266
two-transmitter, eight-receiver antenna arrangement, 264, 265
MWD. *See* measurements while drilling (MWD)

N

natural and spectral gamma ray logging, 13, 30
neural networks
principle, 533
use, 533, 534
neutron-density
lithology/mineralogy
fresh-mud filtrates, 429–430
limestone scales, 431
salt-mud filtrates, 429, 430
logging on drillpipe, 66
openhole logging tools, 27
porosity, 420, 421
porosity log, 126, 129
neutron logs
chemical sources, 327
compensated neutron tool
borehole compensation, 330, 332
depth of investigation, 334, 335
dolomite and sandstone porosity values, 330–331, 333–334
environmental corrections, 334
example of, 331
limestone porosity values, 330–331, 333–334
matrix settings and lithology effects, 334–336
neutron porosity index, 329–330
thermal neutron flux, 330, 332
dual-spacing epithermal neutron logs, 337
gamma ray neutron tools, 328
gas effects, 335–337
generalized neutron-logging tool, 328
inelastic gamma log, 337
properties, 327
pulsed sources, 327
shale effects, 337
slowing and capture cross sections, 328–329
SNP tool, 328, 335
stages, 327–328
test well, 338
neutron porosity index, 329
neutron-sonic crossplot
lithology/mineralogy, 432–433
porosity, 420, 422
neutron tools, 13
nuclear magnetic resonance (NMR)
applications of, 341
centered MRIL tool
magnetic field, 349
multiple sensible volumes, 350
plan view of, 350
vs. conventional logging and log analysis, 341–343
core analysis, 492
formation productivity indicators, 14
free fluid and permeability
immovable fluids, 345
T_2 distribution vs. incremental porosity, 344
horizontal resolution, 357
limitation of, 358
log interpretation
CMR data, presentation of, 352
CMR porosity and permeability vs. core analysis, 354
hydrocarbon typing, 355–357
MRIL and conventional logs, 353
measurement cycle, 345–346
measurements, 343
MRIL calibration tank, 357, 358
openhole logging tool, 38
pad-contact CMR tool
cross section of, 347
depths of investigation, 348
magnet, antenna, and sensed region, 348
porosity-lithology indicators, 13–14
relaxation curves, high-and low-permeability samples, 346, 347
vertical resolution, 357
wireline formation tester, 351

O

ohmmeter, 203–205
oil and gas in place estimates
generalized reservoir units, 139–140
hydrocarbon pore volume (HCPV), 139–140
oil in place (OIP), 139–141
optical density (OD), 609
optical fluid analyzer, 610

P

packer/probe design, 609
pad-contact CMR tool
cross section of, 347
depths of investigation, 348
magnet, antenna, and sensed region, 348
Passey method, 569
pay counting, 133–134
percussion sidewall coring, 32
permeability
log analysis, 134
measurements
radii of investigation, 113–114
Wyllie and Rose relationship, 115–116
relative
curves, 110–111
effective permeabilities, 109
imbibition and drainage, 112
ratio plot, 110–111
water/oil ratio (WOR), 113
reservoir rocks, 104–106
petrophysics. *See* rock/fluid systems
phasor induction, 20, 223

porosity
combination tools
density-neutron combination, 416
uses of, 416–417
core analysis
Boyle's law method, 479–480
conventional vs. percussion sidewall core porosities, 480, 481
grain-density methods, 480
summation of fluids method, 479
density log, 415–416
density porosity, 417
hydrocarbon
density, 426–427
effects, 424–426
and lithology, MOD, 65–66
log analysis, 127, 129, 130
measurement, 113
neutron-density crossplot, 420, 421
neutron porosity, 418
neutron-sonic crossplot, 420, 422
percentage units, 415
reservoir rocks, 103–104
secondary porosity, 424
shaly formations, 420–421, 423
sonic logging
compaction effects and Hunt-Raymer transform, 289–291
determination, 286, 288
fluid travel time, 287–289
matrix travel time, 287, 288
measurement, 286, 287
sonic porosity, 419–420
porosity-lithology indicators, 13–14
post-pretest buildup, 604, 605
practical quick-look methods, 531–532
pulsed neutron tools, 13
pyrochromatic analysis, 489, 492

Q

quality control
compensated neutron log (CNL), 338
dipmeter and borehole imaging, 375–376
litho-density tools (LDTs), 321–322
measurements on drillpipe (MOD), 66–67
microresistivity measurements, 258
sonic (acoustic) logging, 299
SP log, 173, 175
wireline logging operations
acceptance standards for logs, 88–90
necessity, 87–88
practical log quality checks, 88
quick fluid sampling, 609
quick-look log analysis
algorithms, 413–414
compatibly scaled overlays
density-sonic overlay, 404–407
EPT-porosity overlay, 406, 408
F overlay, 400–402
logarithmic movable-oil plot, 401–404
neutron-density overlay, 402, 404–406
SP with R_{xo}/R_t, 398–400
theory, 397
crossplots
extrapolations, 409, 410
height vs. weight for animals, 408, 409
neutron-density frequency, 410, 411
permeability vs. porosity, 408–409
theory, 408
Z plot, 410–412
histograms, 412–413

R

radioactive nuclei decay, 179, 180
ratio technique
R_w determination, 456
water saturation, 466–470
recovery factor, 141–142
reservoir geometry indicators, 14
reservoir rocks
permeability, 104–106
porosity, 103–104
reservoirs, unconventional
anisotropy, 585–586
Barnett-type well production, 574–575
CBM gas production, 575
coalbed cavity completion, 586–589
commonalities of, 547
coring and core analysis, 555–557
fractures and complexity, 582–584
gas production, 546–547
geochemistry
bitumen, 551
hydrocarbon generation, 550
kerogen, 550–551
organic matter, 549–550
TOC, 551
geomechanics
completions, 580, 581
fracture monitoring, 581–583
GIP
Middle East and North Africa, 593
shale-gas reservoirs, 578–579
tight gas reservoirs, 577–578
horizontal CBM completions, 587, 589
location, 546
logging
acoustic imagers, 561, 563
density logging, 559–561
electrical imagers, 561, 562
gamma ray logging, 558
neutron logging, 559, 560
NMR, 559, 561
openhole wireline logging, 558
petrophysical integration, 557
photoelectric factor, 559, 561, 562
resistivity, 558–559
sonic logs, 559
macerals, 592
matrix and pore volumetrics
molecular-dynamics simulation model, 571, 572
petrophysical model, 571, 572
mud logging
carbon-isotope analysis, 552–553
hydrocarbon type indicators, 513, 514
shale-gas production, 573–574

synopsis
CBM, 547
shale gas and shale oil, 548
tight gas, 547–548
tight-gas-sand production, 575
TOC
dLog R method, 565–568
Passey correlations, 566, 568–569
pyrolysis parameters, 563–564
shale-play petrophysical comparisons, 570
vitrinite reflectance, 564, 565
resistivity at bit (RAB), 64, 65
resistivity devices, 214
resistivity measurements
definition, ohmmeter, 203–205
factors affecting the measurements, 209–210
first electric log, 203, 205
focused electric logs, 209
hypothetical cross section, 203, 205
ideal resistivity measurements
electrical logging schematic, 204, 206
lateral resistivity device, 208
normal resistivity device, 207
induction logs, 209
microwave devices, 209
surface resistivity measurement device, 203
typical formation resistivities, 204
rhombohedral packing, 104
rock/fluid systems
averaging, 120, 122–123
fluid distribution in reservoir
capillary pressure curves, 109–110
capillary pressure effects, 108–109
capillary tube, 107–108
depositional environments, interrelationships of, 106
pore system, 108–109
in water-wet reservoir, 107
wettability and contact angle, 109–110
permeability measurements
radii of investigation, 113–114
Wyllie and Rose relationship, 115–116
permeability, relative
curves, 110–111
effective permeability, 109
imbibition and drainage, 112
ratio plot, 110–111
water/oil ratio (WOR), 113
porosity measurement, 113
product of porosity and water saturation crossplot, 120–122
reservoir rocks
permeability, 104–106
porosity, 103–104
saturation measurement
electrical formation factor, 117–120
saturation of core vs. resistivity, 119, 120
water resistivity, 116–117
rotary sidewall coring, 33
R_w determination
catalogs, 459–460
chemical analysis, 449–451
direct measurement, 447–448
F-overlay technique, 457, 459
linear crossplots, 456–458
logarithmic plots, 457, 459
ratio technique, 456
R_{wa} technique, 452–455
SP, 452, 453

S

saturation measurement
electrical formation factor
formation factor vs. porosity, 119
tortuous pore system, 117, 118
100%-water-saturated rock system vs. resistivity, 117, 118
saturation of core vs. resistivity, 119, 120
water resistivity, 116–117
scintillation detectors, 180, 183
seismic applications
borehole sonic logging and seismic logging, 295–296
range and resolution, 293–295
synthetic seismogram, 296, 297
transit-time integration, 296, 297
VSP, 296, 298
SFL. *See* spherically focused log (SFL)
shale effects
formation density log, 314–315
neutron logs, 337
shale indicator, SP log, 172, 175
shaly sands
clay types, 498–502
dispersed shale model, 507–508
distribution, 498
dual water model, 511–512
laminated shale model
electrical model, 504
hardware help, 505
neutron/density crossplot, 504
software help, 505
low-resistivity pay, 516–517
objectives, 497
percolation theory, 512
practical log analysis, 512–516
quick-look computer analysis, 512
service-company products, 512
structural-shale model, 508–510
unconventional reservoirs, 517–518
Waxman-Smits technique, 510–511
shoulder-bed correction chart
deep laterolog, 244
shallow laterolog, 244, 245
sidewall coring, 14
sidewall neutron porosity (SNP) tool, 328, 335
six-coil induction logging system, 217, 218
skin effect, 216–217
sonic/acoustic logging, 13
sonic-density crossplot, 433
sonic logging
apparent water resistivity, 291, 292
array sonic tools
coherence function, contour plot, 281, 284
recordings, 281, 283
slowness, 282, 285

cement bond log (CBL)
CBL-VDL display, 299, 300
CBL-VDL tool, 296, 299
receiver output signal, 299
compressional wave velocity and interval transit time, 302–303
cycle skipping and noise, 284–285
dipole sonic tools, 282
on drillpipe, 65–66
Δt ratio
in micaceous sands, 291, 293
for rock types, 292, 294
travel-time correction factor, 292, 294
elastic constants, 274–275
elastic wave propagation, 273–274
log quality control, 299
LSS tools
vs. BHC, 278, 279
depth of investigation, 280
with four transit-time curves, 281, 282
long-spaced sonic "depth-derived" principle, 280–281
mechanical properties, 292–295
openhole logging tools, 29
operating principles
basic device, 275–276
BHC tool, 277–278
maximum formation, 278–279
porosity
compaction effects and Hunt-Raymer transform, 289–291
determination, 286, 288
fluid travel time, 287–289
matrix travel time, 287, 288
measurement, 286, 287
seismic applications
borehole sonic logging and seismic logging, 295–296
range and resolution, 293–295
synthetic seismogram, 296, 297
transit-time integration, 296, 297
VSP, 296, 298
speed of compressional wave, 304
tools, 275–277
waveform recording
long-spaced sonic waveforms, 285, 286
variable-density display, 286, 287
spherical buildup, 604–606
spherically focused log (SFL)
bed resolution and radial investigation, 253, 254
electrode arrangement and current paths, 253, 255
vs. "intermediate"-resistivity devices, 252, 253
spontaneous potential (SP) log
alternative method, 166, 167, 170
definition, 155, 156
depositional patterns, 173
factors affecting SP, 168–169, 171–173
quality control, 173, 175
recording, 155, 157
as shale indicator, 172, 175
source
liquid junction effect, 156, 157
membrane potential, 158
normal and reverse SP deflections, 159, 160
overall SP, 158–159
water resistivity
conversion of solution to equivalent resistivity, 164, 166
formation temperature, 163
logic flow diagram, 166, 169
mud filtrate resistivity, 159
mud filtrate and mudcake resistivity estimation, 161–162
mud vs. mud filtrate resistivity, 160, 161
quick guide, 166, 168
solution resistivity vs. temperature and concentration, 164, 165
temperature vs. depth, 163
structural-shale physical model, 510
surface resistivity measurement device, 203
symbols, 16–17

T

tele-imaging, 379–380
thermal conductivity detector (TCD), 41
thermal neutron flux, 330, 332
3D induction, 23, 226–227
total organic content (TOC)
dLog R method, 565–568
Passey correlations, 566, 568–569
pyrolysis parameters, 563–564
shale-play petrophysical comparisons, 570
vitrinite reflectance, 564, 565
t_{po} interpretation method. *See* wellsite interpretation
true stratigraphic thickness (TST), 146
true vertical thickness (TVT), 146
two-coil induction log system, 215–216

U

ultralong-spacing electric logs, 14
ultrasonic borehole imager, 35

V

variable density log (VDL), 296, 299, 300
vertical seismic profile (VSP), 296, 298
volumetrics and reserve estimation
conversion factors, reserves, 148–149
depth and net pay measurements, 142–143
deviated wells and dipping beds
deviated wells and horizontal bed, 144
rotations, 146
true stratigraphic thickness (TST), 146
true vertical thickness (TVT), 146
vertical well and dipping bed, 144–145
formation volume factors, 142
oil and gas in place estimates
generalized reservoir units, 139–140
hydrocarbon pore volume (HCPV), 139–140
recovery factor, 141–142
reservoir volumes
area within net pay contour vs. depth, 147–148
net pay thickness isopach and structure cross section, 147
units multiplier, reserve estimates, 141
VSP. *See* vertical seismic profile (VSP)

W
water/oil ratio (WOR), 113
water resistivity
  saturation measurement, 116–117
  spontaneous potential (SP) log
    conversion of solution resistivities to equivalent resistivity, 164, 166
    formation temperature, 163
    logic flow diagram, 166, 169
    mud filtrate resistivity, 159
    mud filtrate resistivity and mudcake resistivity estimation, 161–162
    mud resistivity vs. mud filtrate resistivity, 160, 161
    quick guide, 166, 168
    solution resistivity vs. temperature and concentration, 164, 165
    temperature vs. depth, 163
water saturation (S_w)
  Archie's equation
    cementation exponent, 462
    formation factor, 462
    saturation exponent, 463
  clean formations
    Archie's equation, 466, 468
    crossplot methods, 470–473
    F overlay, 472
    ratio technique, 466–470
    R_{wa} curve, 472
  core analysis, 461, 483
  definition of, 131, 461, 462
  dielectric measurements, 462
  formation-factor/porosity relationships, 465–467
  nomogram, saturation determination, 132, 133
  nuclear methods, 462
  saturation exponent *n,* 463–465
  shaly sand methods, 472, 473
wellsite interpretation
  matrix propagation time determination, 268, 269
  sonic porosity vs. EPT porosity, 267, 268
  water and hydrocarbons, log readings for, 268, 269
wireline coring
  percussion sidewall cores, 93–95
  rotary sidewall coring, 94–96
wireline formation testing
  fluid sampling
    monitoring sampled fluid, 609–611
    multielement packers and probes, 609
  formation production estimates, 611–614
  interpretation
    cylindrical buildup, 606–607
    large-sample fill-up, 607–608
    post-pretest buildup, 604, 605
    spherical buildup, 604–606
  operating principles
    hydraulics, 598–600
    mechanics, 598
    pressure gauges, 599, 600
  sequential pressure readings vs. depth, 610–612
  tools, 14, 37, 598
    applications, 597–598
    characteristics, 597–598
wireline imaging tools
  acoustic imaging, 378–379
  electrical imaging, 377–378
  tele-imaging, 379–380
wireline logging operations
  borehole environment
    nomenclature for zones in and around the borehole, 79, 80
    radial resistivity profile, 81
    symbols, 79, 80
  computerized logging units
    logging engineers console, 84
    log presentations and calibrations, 85–87
  logging cables
    breaking cable at weakpoint, 76
    differential pressure sticking, 76
    fishing alternatives, 77
    getting stuck, 75
    head and the weakpoint, 74–75
    monoconductor cables, 73
    multiconductor cables, 73
  logging suite selection
    depth, pressure, and temperature, 82
    factors, 81
    hole deviation, 82
    hole size, 82
    mud program, influence of, 83–84
    recommended general logging programs, 82–83
    time to log, 84
  logging tools
    measure points and memorization distances, 77, 78
    unmemorized and memorized logs, 77–79
  logging trucks
    components, 71
    computerized logging truck, 71, 74
    offshore units, 72, 74
  log-quality control
    acceptance standards for logs, 88–90
    necessity, 87–88
    practical log quality checks, 88
  rigging up to run a log
    detailed diagram, 71, 72
    lower sheave tie-down arrangement, 71, 73
    setup for logging job, 71, 72
    top sheave and elevator arrangement, 71, 73
  service company nomenclature, 91